# Triassic to Early Jurassic sandstones in North Victoria Land, Antarctica: Composition, provenance, and diagenesis

**Dissertation**

zur Erlangung des akademischen Grades
doctor rerum naturalium (Dr. rer. nat.)

Vorgelegt dem Rat der Chemisch-geowissenschaftlichen Fakultät
der Friedrich-Schiller-Universität, Jena

von Dipl.-Geol. Martin Elsner
geboren am 27.02.1978 in München

1. Gutachter: Prof. Dr. Reinhard Gaupp (Jena)

2. Gutachter: Prof. Dr. Hilmar von Eynatten (Göttingen)

Tag der öffentlichen Verteidigung: 4. Februar 2011

# Triassic to Early Jurassic sandstones in North Victoria Land, Antarctica: Composition, provenance, and diagenesis

Martin Elsner

2010

## Zusammenfassung

Diese Arbeit befasst sich mit mesozoischen kontinentalen Siliziklastika der Victoria Group (Beacon Supergroup) in Nord Viktorialand, Antarktis. Diese Ablagerungen sind triassischen bis jurassischen Alters und wurden im Transantarktischen Becken abgelagert, das weite Teile des antarktischen Sektors von Gondwana umfasste. Sie werden in zwei Formationen unterteilt: Die Section Peak Formation (SPF) im Liegenden wird etwa 200 bis 250 m mächtig und besteht hauptsächlich aus Sandsteinen. Lokal sind auch Konglomeraten vorhanden. Untergeordnet kommen Pelite und Kohlen vor. Im obersten Teil der SPF sind felsische Tuffite eingeschaltet. Die überlagernde Shafer Peak Formation (SHF) erreicht etwa 50 m und besteht vorwiegend aus felsischen, tuffitischen Sandsteinen. Die gesamte Abfolge ist von jurassischen Lagergängen intrudiert (Ferrar dolerites) und wird von bis zu 1000 m mächtigen Flutbasalten (Kirkpatrick basalts, Ferrar Group) überlagert. Das absolute Alter sowohl der Lagergänge als auch der Flutbasalte beträgt etwa 184 Ma. Geländearbeit und Beprobung erfolgte im Rahmen der neunten German Antarctic North Victoria Land Expedition (GANOVEX IX) im Winter 2005/06.

Die Arbeit behandelt verschiedene Aspekte der Geologie Nord Victorialands. Für eine strukturgeologische Analyse wurde die erosive Sandstein-Basis (Top Basement) durch Inter- und Extrapolation sowohl veröffentlichter Höhendaten (z.B. aus Karten) als auch Geländemessungen modelliert. Das Modell stützt frühere Interpretationen, die Nord Victorialand als Teil eines dextralen Blattverschiebungsbereichs betrachteten. Ein tektonischer Einfluss während der triassischen bis jurassischen Sedimentation konnte ausgeschlossen werden.

Der umfänglichste Abschnitt dieser Arbeit befasst sich mit einer Liefergebietsanalyse der SPF. Dazu wurden petrographische (Leicht- und Schwerminerale), chemische (Gesamtgesteinschemie, Mineralchemie diagnostischer Minerale) und mineralogische Daten (Tonmineralogie von Siltsteinen) sowie Isotopendaten (Sm, Nd, Sr an Siltsteinen, U-Pb LA-ICPMS Altersdaten detritischer Zirkone) erfasst und interpretiert. So können sechs Sandstein-Typen mit unterschiedlichen Liefergebieten nachgewiesen werden. Fünf dieser Sandstein-Typen sind auf unterschiedliche lokale Quellen in Nord Victorialand und benachbarte Regionen zurückzuführen. Der sechste Sandstein-Typ repräsentiert ein axiales Abflusssystem entlang des Transantarktischen Beckens. In einigen der Sandstein-Typen lokaler Herkunft manifestiert sich der Einfluss eines magmatischen Bogens entlang der aktiven Plattengrenze von Gondwana. Im axialen Abflusssystem ist dieser Einfluss zunächst sehr gering, wird aber mit der Zeit bedeutend. Aufgrund der Beckengeometrie (Breite, Sedimentmächtigkeit, Winkel der Sedimentationsbasis), der petrographischen Zusammensetzung (z.B. der räumlichen Verteilung der Sandstein-Typen) und sedimentologischer Indikatoren (z.B. Sedimentationsrate) kann dieser Teil des Transantarktischen Beckens einer epikratonischen Lage zugeordnet werden. Dies ist möglicherweise auf einen relativ steilen Subduktionswinkel der Proto-Pazifischen (Panthalassa-) Platte unter Gondwana im Bereich von Nord Victorialand zurückzuführen. Im Gegensatz dazu war die Subduktion in anderen Teilen des Transantarktischen Beckens (z.B. im zentralen Transantarktischen Gebirge) wohl zumindest zeitweise relativ flach, wodurch sich dort ein Vorland-Becken entwickeln konnte.

Für die tuffitischen Ablagerungen der SHF werden anhand petrographischer und chemischer Daten Aussagen zu Herkunft und Genese gemacht. Dabei erfolgt stets auch ein Vergleich mit den im obersten Teil der Section Peak Formation eingeschalteten Tuffiten, die schon bei der Beprobung im Gelände lithologische Ähnlichkeiten zeigten. Eine (soda?)rhyodacitische Quelle für den juvenilen magmatischen Anteil der Tuffite ist sehr wahrscheinlich. Die zahlreichen felsischen Shards deuten auf distale, ultra-plinianische, Caldera-formende Ausbrüche hin, die höchstwahrscheinlich im Bereich des oben bereits angesprochenen magmatischen Bogens an der aktiven Plattengrenze von Gondwana stattfanden. Es können lithologische und stratigraphische Parallelen zur Hanson Formation im zentralen Transantarktischen Gebirge gezogen werden. Der zugemischte epiklastische Anteil der Tuffite ist mit den Ablagerungen der jüngsten SPF vergleichbar. Eine tuffitische Einschaltung in der obersten SPF ergab ein U-Pb (SHRIMP) Alter von 188,2 ± 2,2 Ma, was erstmals ein eindeutig jurassisches Alter (Pliensbach) der obersten SPF und der gesamten SHF beweist.

Letzter Abschnitt der Arbeit ist die diagenetische Entwicklung der Ablagerungen. Eine Versenkungstemperatur zwischen weniger als 90°C und maximal etwa 120°C wird auf die Platznahme der Ferrar-Laven zurückgeführt. Das gleiche trifft auf ein starkes Kompaktions-Ereignis zu, das nicht mit der Kompaktion durch sedimentäre Überlagerung zusammenhängt. Es wurden keine Hinweise auf Temperaturen über 120°C gefunden, und die Existenz eines kretazischen Beckens kann anhand der ermittelten Diagenese-Geschichte für das südliche Nord Victorialand ausgeschlossen werden.

## Abstract

Triassic to early Jurassic sediments (Victoria Group, Beacon Supergroup) in North Victoria Land, Antarctica, can be subdivided into two formations. The Section Peak Formation (SPF) directly covers a magmatic and metamorphic basement and consists predominately of sandstones of about 200-250 m thickness. Locally, conglomerates are present, and pelites and thin coal seams may be intercalated. In higher parts of the formation, felsic tuffaceous layers occur. The overlying Shafer Peak Formation (SHF) reaches about 50 m thickness and consists predominantly of tuffaceous sandstones.

The entire succession was deposited in the Transantarctic Basin, occupying large parts of the Antarctic sector of Gondwana. It is intruded by mafic sills (Ferrar dolerites) and overlain by an up to 1000 m succession of flood basalts (Kirkpatrick basalts, Ferrar Group). The absolute age of both, intrusive and effusive parts, is about 184 Ma. Field work and sampling took place during the ninth German Antarctic North Victoria Land expedition (GANOVEX IX) in the austral summer 2005/06.

This thesis deals with several different aspects of the geology in North Victoria Land. For a structural analysis, the erosive sedimentary base of the Beacon sediments (top basement) was modelled by inter- and extrapolation of published elevation data (e.g. from maps), and of field data. The model supports previous interpretations of North Victoria Land lying in a dextral strike-slip regime. As a main result, a tectonic influence on sedimentation during the Triassic and Early Jurassic can be excluded.

The most extensive part of this thesis treats with a provenance analysis for the SPF. This analysis includes petrographic (light and heavy mineralogy), chemical (whole rock geochemistry, mineral chemistry of diagnostic minerals), and mineralogical data (clay mineralogy of pelites) as well as isotope data (Sm, Nd, and Sr of pelites, U-Pb LA-ICPMS age data of detrital zircons), and their comprehensive interpretation. Six different sandstone types with distinct source areas can be distinguished. Five of them can be related to different local sources in North Victoria Land and adjoining regions. The sixth sandstone type represents an axial drainage system following the Transantarctic Basin. In some of the locally originating sandstone types the influence of contemporaneous magmatic activity was proved, that may be related to the magmatic arc along the active plate margin of Gondwana. In the axial drainage system, this influence is very minor at the start of sedimentation, but increases strongly through time. Due to the basin geometry (e.g. basin width, thickness of sediments, angle of sedimentation base) deduced from the identified sources, from petrographic (e.g. the spatial and stratigraphic relation of the sandstone types), and from sedimentological (e.g. sedimentation rate) indicators the North Victoria Land sector of the Transantarctic Basin can be related to an epicratonic setting. This may be related to a relatively steep subduction angle of the Panthalassan (Proto-pacific) plate underneath Gondwana in the North Victoria Land sector, while other parts of the Transantarctic Basin (e.g. in the Central Transantarctic Mountains) possibly experienced a flat-plate subduction at least during times of their evolution, leading to formation of a (retro-arc) foreland basin in these areas.

Petrographic and chemical data were used to define origin and genesis of the tuffaceous sandstones of the SHF. They are compared to the tuffaceous sandstones intercalated in the upper parts of the SPF, as already during field work lithological similarities became obvious. A (soda?)rhyodacitic source is most likely for the juvenile magmatic portion of the tuffaceous sandstones. Numerous felsic shards point towards distal, ultra-plinian, caldera forming events, which presumably took place at the magmatic arc along the active plate margin of Gondwana. Lithologic and stratigraphic equivalent deposits can be found in the Hanson Formation in the Central Transantarctic Mountains. The composition of the epiclastic fraction of the tuffaceous sandstones is similar to sandstones from the youngest SPF. A tuffaceous layer within the upper SPF revealed a U-Pb SHRIMP age of 188.2 ± 2.2 Ma and proves an Early Jurassic age of the uppermost SPF and the entire SHF (Pliensbachian stage).

Finally, the diagenetic history of the deposits is reconstructed. Authigenic phases and reactions are described in detail, with emphasis on temperature sensitive processes and products (e.g. zeolites). A burial temperature between less than 90°C and maximal 120°C is explained by the emplacement of Ferrar lavas shortly after deposition, as is a strong compactional event that can be distinguished from compaction due to increasing sedimentary overburden. No mineralogical indications of temperatures higher than 120°C were found, and the existence of a major sedimentary basin during the Cretaceous, as previously assumed, can be excluded for the area of southern North Victoria Land.

## Acknowledgement

I am particularly grateful to Dr. Robert Schöner (Universität Jena), who initiated this work. He helped and encouraged me in many phases of the thesis and improved it considerably by valuable suggestions and numerous discussions. Together with Prof. Lothar Viereck-Götte (Universität Jena), Prof. Jörg Schneider (Bergakademie Freiberg), and Dr. Benni Bomfleur (Universität Münster), he spent some weeks in the field for sampling and logging. The Bundesanstalt für Geowissenschaften und Rohstoffe (BGR) supported the field work. The entire field party is thanked for discussing my results in a wider context.

I sincerely thank my supervisor Prof. Dr. Reinhard Gaupp, who encouraged me during the work and showed great interests in the results. The German Research Foundation (DFG) funded this project (grants GA 457/11-1, 13-2, 13-3) within the scope of the DFG-Research Program (SPP) 1158: "Antarctic research with comparative investigations in Arctic Sea Ice Areas".

At the Institut für Geowissenschaften in Jena, Sigrid Bergmann and Frank Linde carried out extensive sample preparation. Michael Ude accomplished the measurements of X-ray fluorescence; Dr. Ulrich Bläss and Steffi Richter helped with X-ray diffractometry.

Many results of this work were only possible by using analytical techniques not available in Jena. I therefore thank geoscientist from other institutions, introducing me to their subjects. Dr. Andreas Kronz (GZG, Universität Göttingen) and his assistant D. Harries supported me during the electron microprobe measurements in Göttingen. Dr. Axel Gerdes (Universität Frankfurt a. M.) introduced me into LA-ICPMS isotope analytics and helped in data evaluation and interpretation. Dr. Jens Götze (Bergakademie Freiberg) helped me with the hot cathodoluminescence microscopy.

Dr. Ilka Schönberg (GZG, Göttingen) performed the Sm-Nd-Sr-isotope measurements. U-Pb (SHRIMP) isotope analyses were carried out by Dr. Nikolai Rodionoff and Dr. Sergei Sergeiev at the VSEGEI, St. Petersburg (Russia). Prof. G. Franz (Berlin) evaluated the amphibole analyses, and Robert Bsteh prepared some of the thin section photographies and one of the X-ray diffractogram.

Ina Zander and Fabian Jähne are thanked for their help in using GIS for the modelling of the sub-Beacon-unconformity. Dr. Franz Tessensohn helped in interpretation of the modelling results.

The interpretation of the tuffaceous sandstones was improved by helpful suggestions of Prof. Lothar Viereck-Götte and Dr. Ricarda Hanemann.

I am also grateful for many stimulating discussions about my work with friends, fellows, and colleagues in Jena, especially with Dr. Dieter Pudlo, Dr. Thomas Voigt, Dr. Michael Abratis, and Prof. Jonas Kley.

Dr. Franz Elsner considerably improved spelling and grammar of this work and provided important IT-support. Christa Berroth helped during the finalization by keeping my little daughter busy. Last, but not least, I sincerely thank my wife Gabriele Weidel for her patience, especially during the last year of the work, and my children for teaching me the really important things in life.

# Contents

## Abbreviations

| | |
|---|---|
| AFT | Apatite fission track |
| apfu | Atoms per formula unit |
| a.s.l. | Above sea level |
| AG | Anderton Glacier |
| AI | Admiralty Intrusives |
| AN | Archambault Ridge North |
| BSE | Back-scattered electron |
| b.s.l. | Below sea level |
| CE | Mt. Carson East Ridge |
| CHW | Chisholm Hills West |
| CL | Cathodoluminescence |
| CTM | Central Transantarctic Mountains |
| EDX | Energy dispersive X-ray microanalysis |
| EHF | Exposure Hill Formation |
| EHT | Exposure Hill Type |
| EMP | Electron microprobe |
| ER | Eisenhower Range |
| EWM | Ellsworth-Whitmore Mountains |
| GANOVEX | German North Victoria Land expedition |
| GHI | Granite Harbour Intrusives |
| IGV | Intergranular volume |
| MA | Mt. Adamson |
| MBL | Marie-Byrd-Land |
| NVL | North Victoria Land |
| pfu | Per formula unit |
| PR | Priestley Glacier |
| PT | Pt. 3350 |
| RB | Roberts Butte |
| SHA | Shafer Peak A |
| SHB | Shafer Peak B |
| SHC | Shafer Peak C |
| SHF | Shafer Peak Formation |
| SHS | Shafer Peak South |
| SP | Section Peak |
| SPF | Section Peak Formation |
| SPP | Section Peak Plateau |
| SR | Skinner Ridge |
| ST | Stewart Heights |
| SVL | South Victoria Land |
| TAM | Transantarctic Mountains |
| TI | Timber Peak |
| TP | Thern Promontory |
| XRD | X-ray diffraction |
| XRF | X-ray fluorescence |

# 1 General introductory remarks

## 1.1 Introduction

### 1.1.1 Context and motivation

This thesis covers some aspects of the larger research subject “Initiation of Jurassic Ferrar Group Magmatism in North Victoria Land, Antarctica: stratigraphic age, composition, and depositional environment of volcaniclastic and epiclastic sediments of the Exposure Hill and Section Peak Formation, Beacon Supergroup” within the scope of the DFG-Research Program (SPP) 1158: "Antarctic research with comparative investigations in Arctic Sea Ice Areas".

As the Ferrar magmatism and its South African equivalent (Karroo province) are regarded as symptoms of the beginning break-up of Gondwana, sedimentary products from this time are important records of the processes acting during early stages of the break-up of this super-continent.

### 1.1.2 Outline of this study

The thesis is divided into four parts, each of which is dealing with different aspects of the geology of North Victoria Land (NVL). In addition, a preliminary section describes the working area and its geological evolution. Subject of section 2 is the structural geology of NVL. As a supposition for both, provenance analysis and diagenetic evolution, a marker horizon was modelled to detect syn- or post-sedimentary tectonic movements and to define tectonic blocks as possible diagenetic compartments. Section 3 comprises the main part of this study, and deals with composition and provenance of sandstones of the Section Peak Formation (SPF) in order to further refine the model of the Transantarctic Basin and to characterize the processes shortly before the break-up of Gondwana. Petrography, geochemistry, mineral chemistry and U-Pb dating of detrital zircons were the most important methods used. In the fourth section the composition of tuffaceous sandstones of overlying Shafer Peak Formation (SHF) is discussed. They are compared with similar sediments within the uppermost SPF. One of the tuffaceous sandstones yielded the first absolute age of the Beacon sedimentation in NVL so far (U-Pb age of magmatic zircons). Finally, in section 5 the diagenetic history of the SPF is reconstructed. Especially a maximal burial temperature and depth was ascertained in order to figure out the processes in NVL taking place after deposition of the sediments.

### 1.1.3 Study area

#### 1.1.3.1 Geography and geomorphology

The working area is located in the southern part of NVL, Antarctica (Fig. 1.1). It lies approximately between 160° and 164° East and between 72.5° and 74.5° South and covers about 200 by 80 km. NVL is part of the Transantarctic Mountains (TAM), which stretch for more than 3000 km along the margin of the East Antarctica and reach elevations of more than 4000 m above sea level.

Outlet glaciers from the polar ice cap have formed deeply cutting valleys into the TAM, resulting in extremely steep gradients in altitude. Fig. 1.2 shows a hillshade of a digital elevation model (USGS/EROS et al. 1996).

In the working area, the Priestley glacier and the Campbell glacier are the most prominent glaciers, flowing from the Polar Plateau towards the Ross Sea (Fig. 1.3). The Reeves glacier in the south and the Aviator glacier in the north are located shortly outside the working area, both flowing towards the Ross Sea as well. Northern parts of the working area

are drained by the Rennick glacier, following the depression of the Rennick graben towards the Pacific Ocean. The polar climate of NVL is relatively dry, with short austral summers and long winters.

In most of the analysed sections the underlying basement is exposed. Many sections are capped by dolerite sills of the Ferrar Group. A detailed description of the sections including sedimentological features is given by Schöner et al (in review). The most important characteristics of the analysed sections (locality, elevation, etc.) are given in the appendix. Fig. 1.3 displays their position in a map of the working area, and Fig. 1.8 shows their lithology in a simplified cross section.


Fig 1.1: Geographic map of Antarctica and adjoining areas. The working area is indicated by the red rectangle.

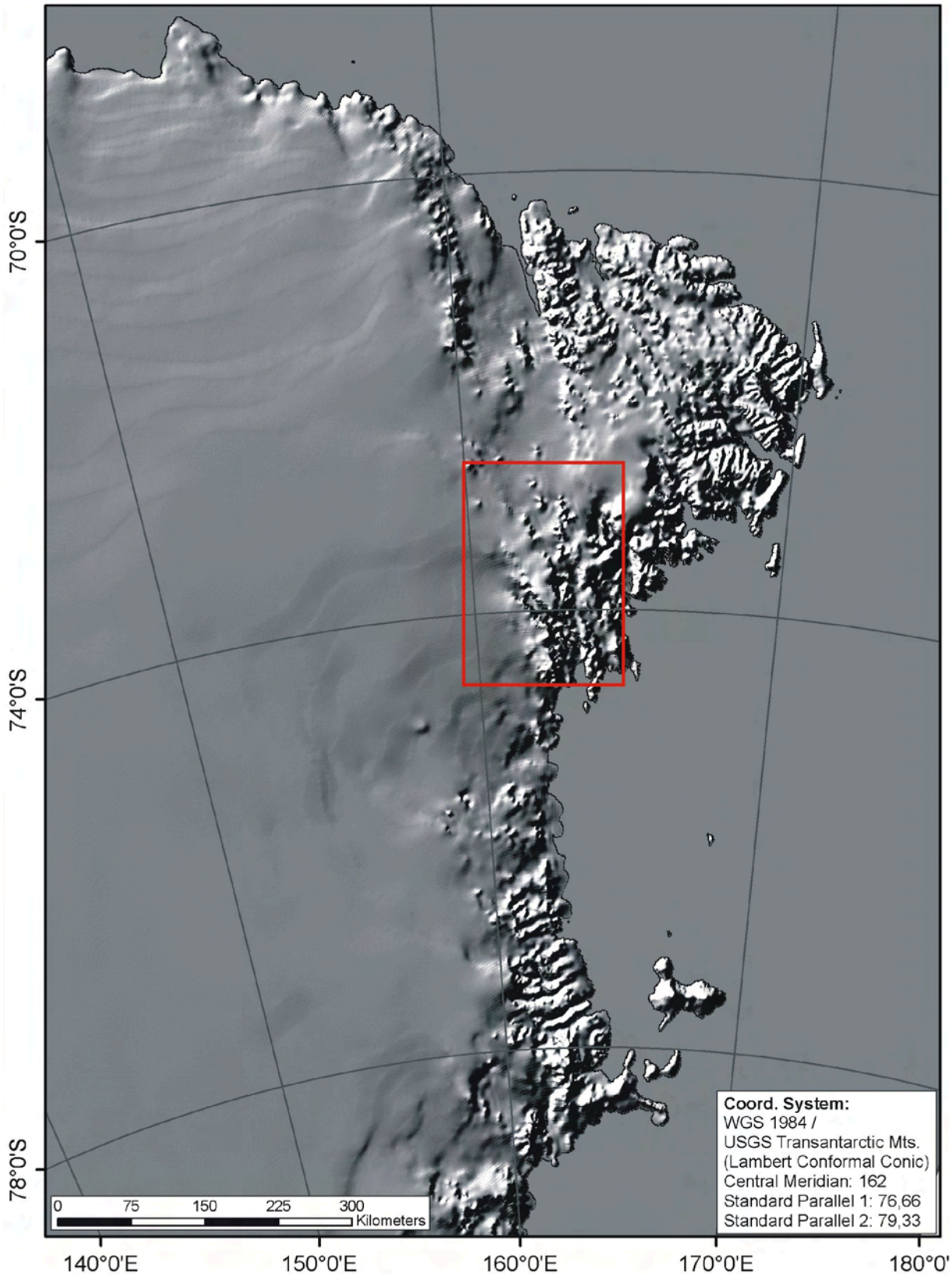


Fig. 1.2: Hillshade of a digital elevation model of Victoria Land (USGS/EROS et al. 1996). The coastal parallel Transantarctic Mountains dip westwards under the ice cap of the polar plateau. The red rectangle marks the working area as shown in the map of Fig. 1.3.

### 1.1.3.2 Field work, analysed sections

In total, 22 representative sections were investigated in detail during the GANOVEX IX in the austral summer 2005/06 by R. Schöner (Jena, sedimentology), J. Schneider (Freiberg, palaeontology), B. Bomfleur (Münster, palaeobotany) and L. Viereck-Götte (Jena, igneous petrology). The author did not attend the field investigations, but concentrated on analysis of the samples provided. Therefore, 19 out of the 22 measured sections were chosen to be investigated in detail. However, information from the other sections, for instance, sedimentology, petrography, or palaeoflow directions, were also taken into account.

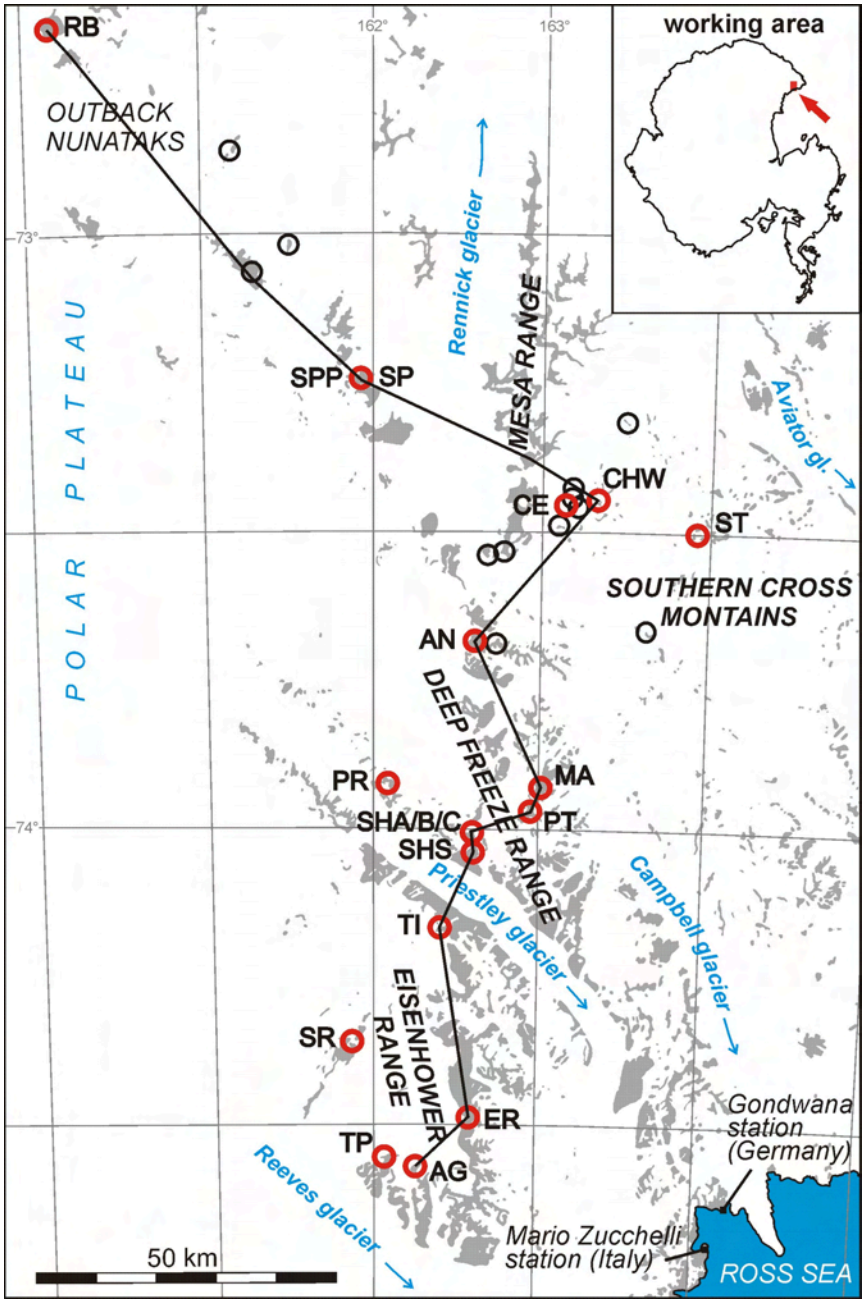


Fig. 1.3: Map of the working area in southern NVL (modified from Schöner et al. 2007). Red circles indicate localities from which samples have been investigated in this study. Thin black circles indicate other localities visited during the GANOVEX IX expedition in 2005/06.
Abbreviations: AG: Anderton Glacier; AN: Archambault Ridge North; CE: Mt. Carson East Ridge; CHW: Chisholm Hills West; ER: Eisenhower Range; MA: Mt. Adamson; PR: Priestley Glacier; RB: Roberts Butte; SHA/B/C: Shafer Peak A, B, C; SHS: Shafer Peak South; SP: Section Peak; SPP: Section Peak Plateau; SR: Skinner Ridge; ST: Stewart Heights; TI: Timber Peak; TP: Thern Promontory.

## 1.2 Geological evolution of North Victoria Land

### 1.2.1 Pre-'Beacon' evolution

#### 1.2.1.1 Introduction

From their amalgamation in the Late Neoproterozoic to Cambrian until its break-up during the Mesozoic, the continents of today's southern hemisphere including India were forming a large single landmass, the super-continent Gondwana (Veevers 2004). Subduction of the Proto-Pacific (Panthalassan) oceanic plate under the Gondwana cratons took place from the Late Neoproterozoic through the Palaeozoic and Mesozoic with phases of accretion, metamorphism and (arc) magmatism, resulting in a complex and lateral variable assemblage of different tectonic units (e.g. Encarnación and Grunow 1996; Vaughan and Pankhurst 2008, see also Fig. 1.4). These units are sometimes hard to correlate (Bradshaw 2007) and single orogenic phases may be difficult to separate from each other (Foster and Gray 2000).

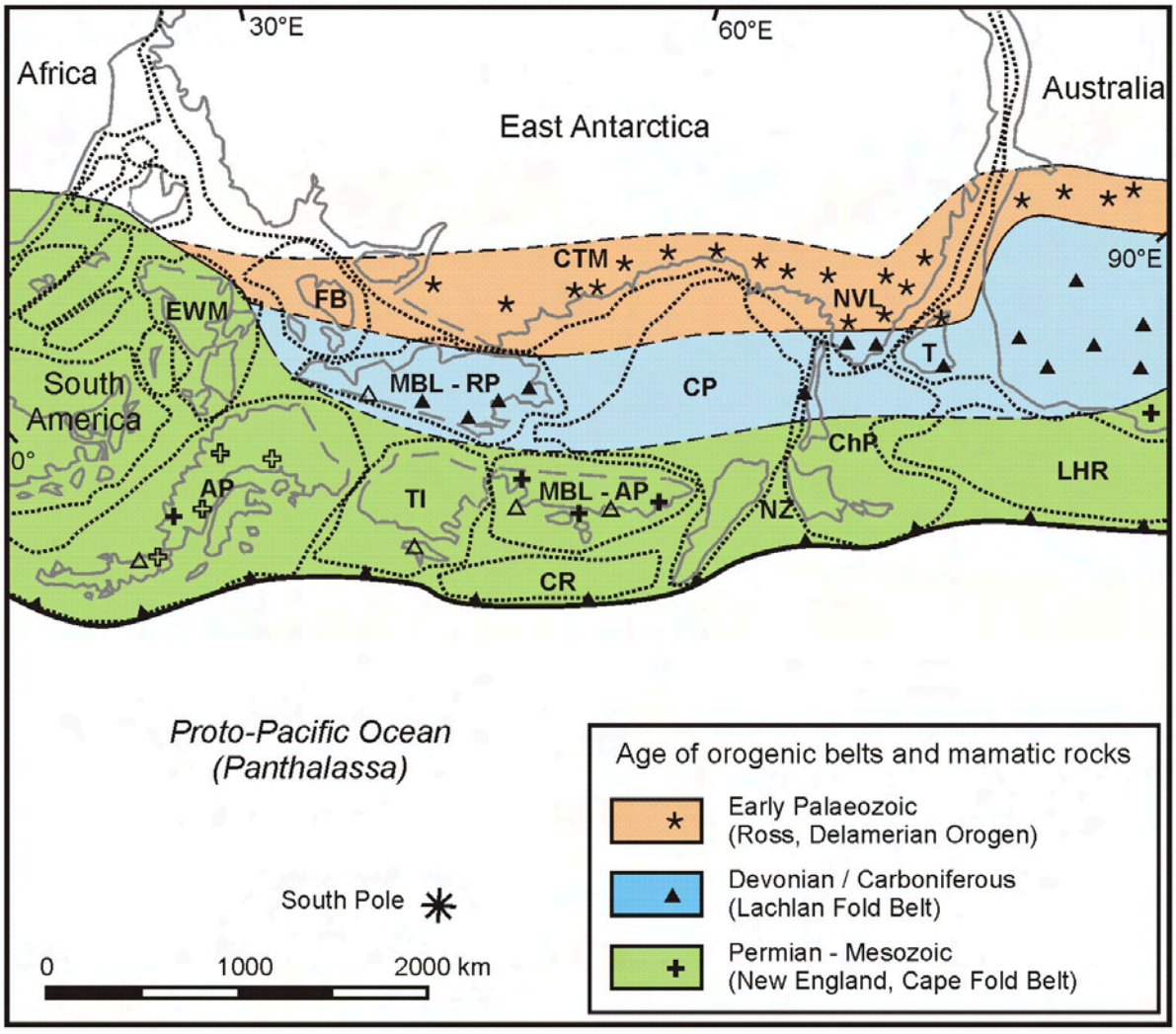


Fig. 1.4: Palaeogeographic reconstruction of the active plate-margin of Gondwana during the Late Triassic/Early Jurassic (Elliot and Fanning 2008; Veevers 2004; Willan 2003). The ages of the orogenic belts are indicated by colours, related magmatic rocks by symbols. Open symbols indicate metamorphically overprinted rocks of the same age.
Abbreviations: AP: Antarctic Peninsula; ChP: Challenger Plateau; CP: Campbell Plateau; CR: Chatham Rise; CTM: Central Transantarctic Mountains; EWM: Ellsworth-Whitmore Mountain Block; FB: Filchner Block; LHR: Lord Howe Rise; MBL-AP: Marie-Byrd-Land, Amundsen Province; MBL-RP: Marie-Byrd-Land, Ross Province; NVL: North Victoria Land; NZ: New Zealand; T: Tasmania; TI: Thurston Island Block.

The basement rocks of NVL and most parts of the TAM formed during one of these phases, namely the Ross Orogeny in the Early Palaeozoic (Federico et al. 2006; Kleinschmidt and Tessensohn 1987). Since then and until the Cretaceous rifting, marking the end of Gondwana, NVL and the TAM were located between the stable East Antarctic continental interior and the active Gondwana plate margin, along which subduction of the proto-pacific and the related magmatism formed a mountain belt. Here, the Transantarctic Basin was located (Collinson et al. 1994), and both sides of the basin are potential source areas for its siliciclastic filling.

The basement of NVL can be divided into three, approximately NW-SE trending terranes accreted during the Ross Orogeny (Fig. 1.5). From east to west, these are the Wilson, Bowers and Robertson Bay terrane (Kleinschmidt and Tessensohn 1987). Both, an autochthonous and an exotic origin of these terranes have been discussed (Tessensohn and Henjes-Kunst 2005).The term 'terrane' has been under debate (Roland et al. 2004), but is used here as a tectono-stratigraphic unit.

Evidence from detrital zircon ages seems to suggest at least one more tectonic unit in between the Wilson terrane and the East Antarctic Craton below the Antarctic ice sheet (Sircombe 1999). This unit may be interpreted as accretionary and magmatic complex equivalent to the Ross Orogen, but older.

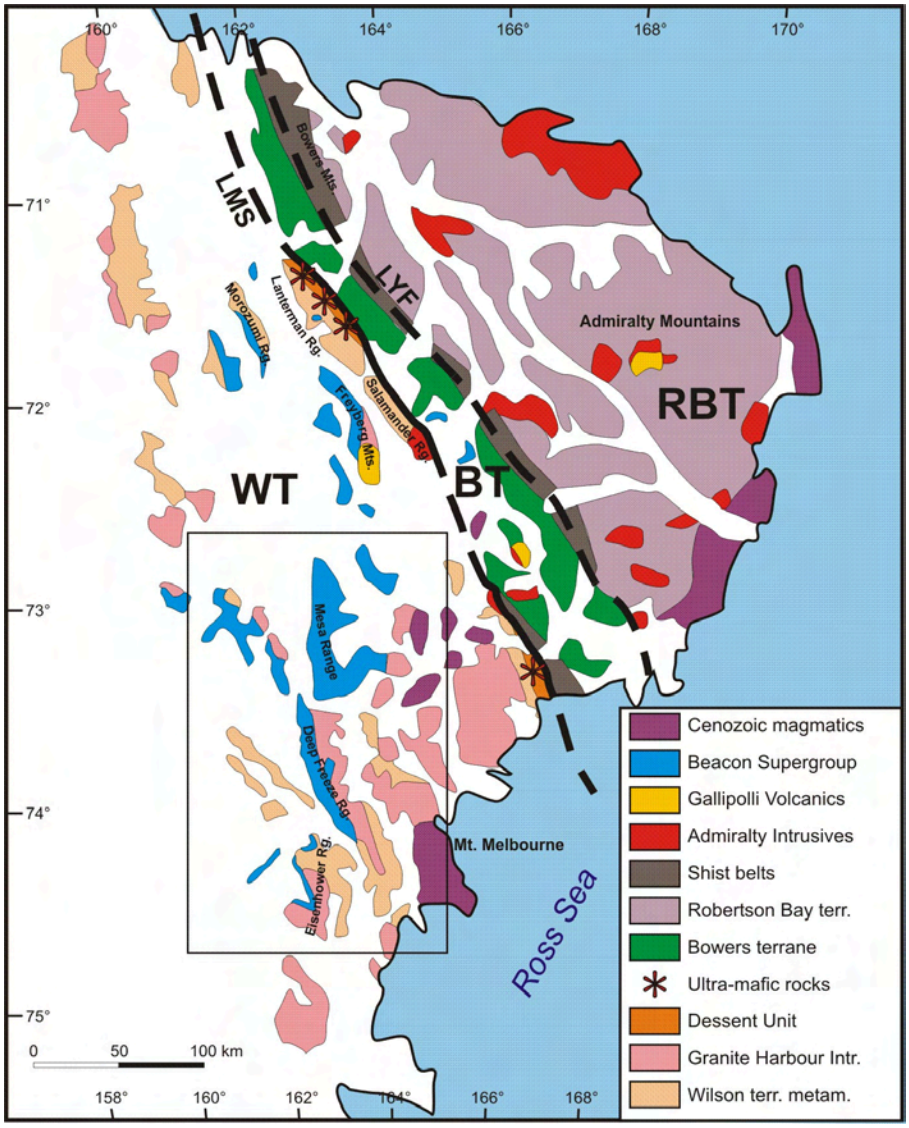


Fig. 1.5: Geological sketch map of NVL showing the three different terranes (redrawn after Henjes-Kunst and Kreuzer 2003; Hornig and Wörner 2003; Ricci et al. 1996; Tessensohn and Henjes-Kunst 2005). The tectonic transport during the Ross Orogeny was towards the NE. Rocks of the Beacon Supergroup (Victoria and Ferrar group) are shown in light blue. The location of the working area is marked by the black rectangle (compare Fig 1.3). BT: Bowers terrane; LMS: Lanterman-Mariner suture; LYF Leap Year fault; RBT: Robertson-Bay terrane; WT: Wilson terrane.

All three terranes of NVL can be traced to Tasmania (Jago 1980) and further on to Australia (Stump et al. 1986). Thereby, the Wilson terrane shows stratigraphic and tectonic similarities to the Delamerian Orogen in Australia, whereas the Bowers terrane and the Robertson Bay terrane are more comparable to the Lachlan Fold Belt (Foster and Gray 2000). However, in NVL, the three terranes are regarded as parts of the Ross Orogen and thus of a single orogenic phase, highlighting the difficulties in delimiting and tracing tectonic units or phases laterally in a setting of continuous subduction (Bradshaw 2007).

The boundary between the Wilson terrane and the Bowers terrane is a major fault zone, known as Lanterman Fault or Lanterman-Mariner-Suture. Along this fault, lenses of ultramafic rocks of centimetre to kilometre size can be found (Kleinschmidt et al. 1987; Ricci et al. 1996). The metamorphic grade within the Wilson terrane increases towards the fault and culminates in ultra-high pressure rocks (Ghiribelli et al. 2001; Palmieri et al. 2003).

The boundary between Bowers terrane and Robertson Bay terrane is less distinct, but characterised by a shist belt of variable thickness. The old name, Leap Year Fault, is rarely used in more recent publications, but is shown in the map in Fig. 1.5 for consistency. The shist belt comprises rocks from both adjoining units which have been incorporated during the tectonic movement (Tessensohn and Henjes-Kunst 2005).

Although these faults originate in the Ross Orogen and are thus of Early Palaeozoic age, they have been re-activated in a regime of dextral strike-slip shearing during Eocene opening of the Southern Ocean and the separation of Australia from Antarctica (Rossetti et al. 2003b).

#### 1.2.1.2 The Wilson terrane

The Wilson terrane is the westernmost exposed unit of the Ross Orogen and thus the relatively closest one to the craton. Most common rock types are gneisses (e.g. Wilson Gneiss, Murchison Formation), shists (e.g. Rennick Shists, Priestley Shists) and phyllites (Morozumi Phyllites). Their metamorphic grade is characterized by low pressure and low to high temperature (Tessensohn and Henjes-Kunst 2005).

The protoliths are siliciclastic sediments, rarely volcanic rocks. Time of protolith formation was Early to Middle Cambrian, although some parts may be from the Latest Neoproterozoic. In areas with low metamorphic grade, a monotonous turbiditic series and more variegated shallow water deposits (limestones, marls, sandstones, mudstones) were identified (Tessensohn and Henjes-Kunst 2005). The age of metamorphism varies around 500 Ma, but ages of 550 Ma to 610 Ma have also been reported (Federico et al. 2006; GANOVEX-Team 1987bb). Some rocks show multiple phases of deformation (Kleinschmidt and Skinner 1981).

Syn- to post-tectonic the calc-alkaline Granite-Harbour-Intrusives intruded at about 480 ± 20 Ma during the Late Cambrian to Early Ordovician (Tonarini and Rocchi 1994). These rocks include granodiorites, ‘adamellites’, tonalities and granites of both, I- and S-type. The Granite-Harbour-Intrusives are interpreted as remnants of the Ross Orogenic magmatic arc (Armienti et al. 1990), as are the locally occurring volcanic equivalents (Molzahn et al. 1996). Of similar age are small gabbroic intrusions, close to the terrane boundary to the Bowers terrane (compare Encarnación and Grunow 1996).

#### 1.2.1.3 The Bowers terrane

The Bowers terrane comprises a highly variable volcanic and sedimentary assemblage, covering the evolution from an oceanic island-arc setting to shallow shelf sediments and terrestrial siliciclastics. The entire succession is summarized as Bowers Supergroup and thought to be of Cambrian to lower Ordovician age (Federico et al. 2006; Tessensohn and Henjes-Kunst 2005).

The lowermost parts of the Bowers Supergroup are formed by oceanic (pillow-)lavas (Glasgow Volcanics), interfingering with mudstones, turbiditic sandstones and few conglomerates rich in volcaniclastic detritus (Molar Group). These sediments grade locally into regressive limestones and sandstones of the Mariner Group, which are in turn overlain by a thick sequence of fluvial to deltaic siliciclastic sediments (Leap Year Group) of continental origin (Laird et al. 1982).

#### 1.2.1.4 The Robertson Bay terrane

The Robertson Bay terrane consists mainly of uniform turbiditic sandstones rich in lithic fragments, alternating with mudstones. This succession reaches probably a few thousand meters, but the base is unknown (GANOVEX-Team 1987bb). The uppermost part is specified as Handler Formation, which is characterized by increasingly intercalations of reddish slates, quartzose conglomerates and exotic limestone blocks of Tremadocian age. This succession is interpreted as regressional sequence caused by tectonic movements of the beginning Ross Orogeny (Wright and Brodie 1986).

Both the Robertson Bay terrane and the Bowers terrane described above were affected by extrusive and intrusive magmatism during the Late Devonian and Early Carboniferous. As these rocks are part of the Beacon Supergroup, they are described in the following section.

### 1.2.2 The Beacon Supergroup

#### 1.2.2.1 Introduction

Erosion, subsequently following the Ross Orogeny, led to formation of the Kukri erosion surface that can be traced throughout the TAM (Isbell 1999). This erosion surface is sometimes referred to as sub-Beacon peneplain. It forms a regional marker horizon, and can be used for the determination of younger tectonic movements. However, the relief of the Kukri surface is locally considerable, reaching up to 700 m south of the Byrd glacier (Anderson 1979, in Elliot and Fanning 2008). Above this erosion surface, deposition started again in the Devonian with the Beacon Supergroup, which is divided into the Devonian Taylor Group, the Late Carboniferous to Early Jurassic Victoria Group, and the Jurassic Ferrar Group. The Beacon Supergroup was deposited in the Transantarctic Basin, occupying the Antarctic sector of Gondwana and possibly extending to adjacent areas in Africa and Australia (Collinson et al. 1994). The stratigraphy of the Victoria and Ferrar Group is shown in the chart in Fig. 1.6.

#### 1.2.2.2 The Transantarctic Basin

The Transantarctic Basin is regarded as the accommodation space generated in between the East Antarctic craton and a mountain belt that can be ascribed to subduction of the proto-pacific ocean and the related magmatic arc. The Transantarctic Basin lasted from the Devonian to the Jurassic, but was subject to substantial changes in shape and orientation during this time.

The reconstruction of the basin is based on the interpretation of sedimentary relicts from a few regions, located along the axis of the Transantarctic Mountains and being separated by as many as hundreds of kilometres from each other. Important outcrops of the filling of the basin are the Ellsworth and Pensacola Mountains, the CTM (Beardmore Glacier area and Queen Maud Mountains) and South and North Victoria Land.

The sedimentary record is most complete and thickest in the CTM, where only Late Devonian to Early Carboniferous sediments are missing. Towards the Pensacola and Ellsworth Mountains only Palaeozoic sediments are preserved, while in South Victoria Land (SVL), and even more in NVL, sedimentation started increasingly later and gaps in the sedimentary record become larger and more widespread (Collinson et al. 1994).

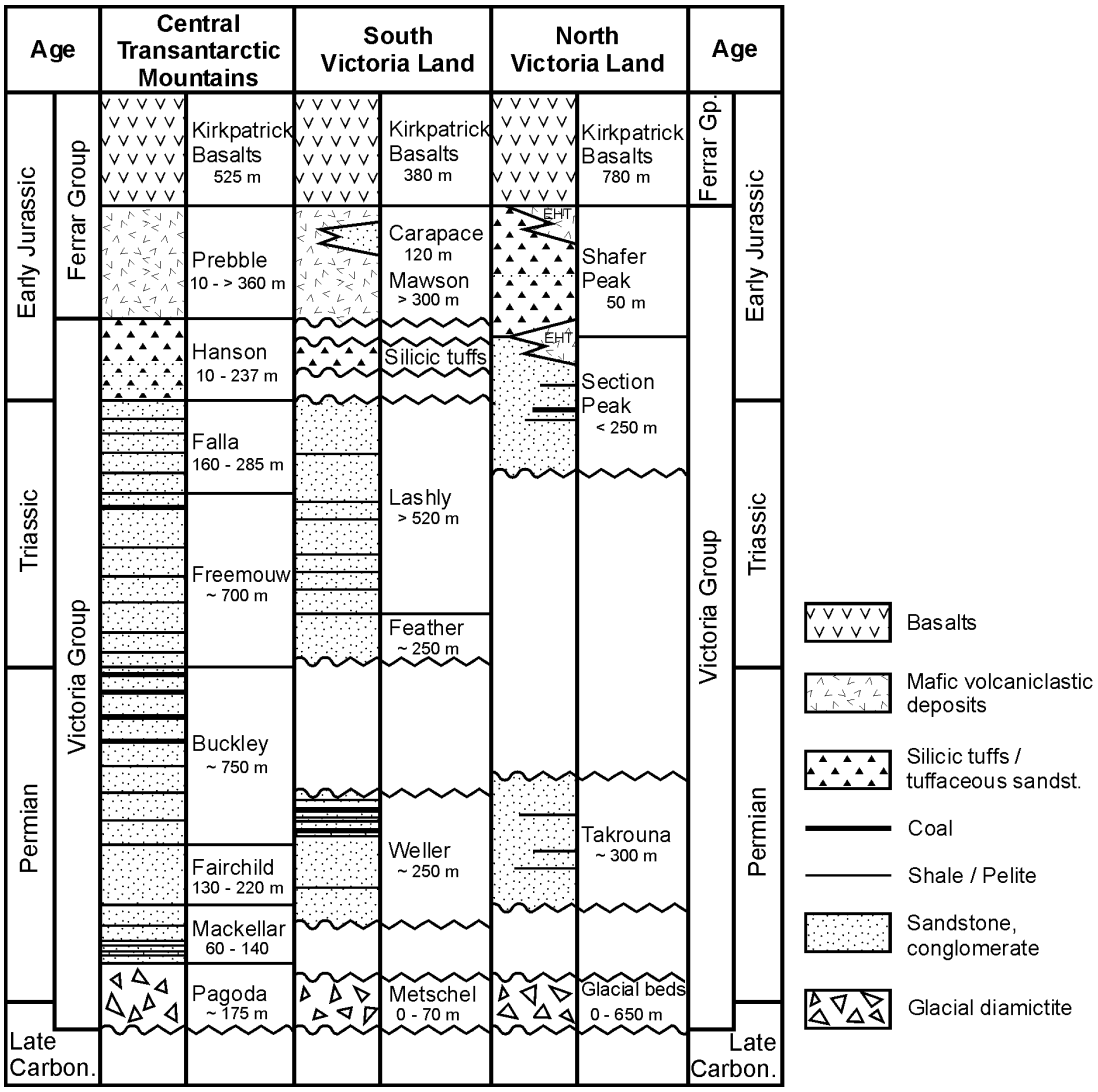


Fig. 1.6: Stratigraphy of the Victoria and Ferrar Group in the Transantarctic Mountains. Modified after Elliot and Fanning (2008) and Schöner et al. (2007). The mafic volcaniclastic deposits are allocated to the Ferrar Group in the CTM and in SVL (Elliot and Fanning 2008), but to the Victoria Group in NVL (Schöner et al. 2007).

The tectonic setting of the Transantarctic Basin system is ambiguous for different stages of basin evolution. Dalziel and Elliot (1982) discussed the basin as a retro-arc foreland basin, with an extensional setting inferred during the Carboniferous and Permian (Collinson et al. 1994). During the Early Permian, one or more coal-bearing epicontinental basins ('epicratonic Victoria sub-basin') on the craton side in Victoria Land can be distinguished from a foreland basin on the arc side (CTM, Pensacola and Ellsworth Mountains) by sedimentary detritus and palaeoflow in opposite directions (Collinson et al. 1994; Isbell and Cúneo 1996). A foreswell, the Ross High, is assumed to have divided these basins (see Fig. 1.7, upper panel). It probably extended from almost the present South Pole acute-angled to the axis of the TAM towards Australia and apparently became inactive in the Middle Triassic, when drainage was towards Australia throughout the basin system (Barrett, 1991; Collinson et al., 1994) and one continuous (foreland?) basin developed along the Transantarctic Mountains. This major change in the drainage system is believed to be related to the development of a fold-and-thrust belt, which is documented in the Ellsworth and Pensacola Mountains (Collinson et al. 1994). In the following, the entire basin including the Victoria sub-basin was flooded with volcaniclastic detritus derived from the magmatic arc (Collinson et al. 1994, see also Fig. 1.7, lower panel).

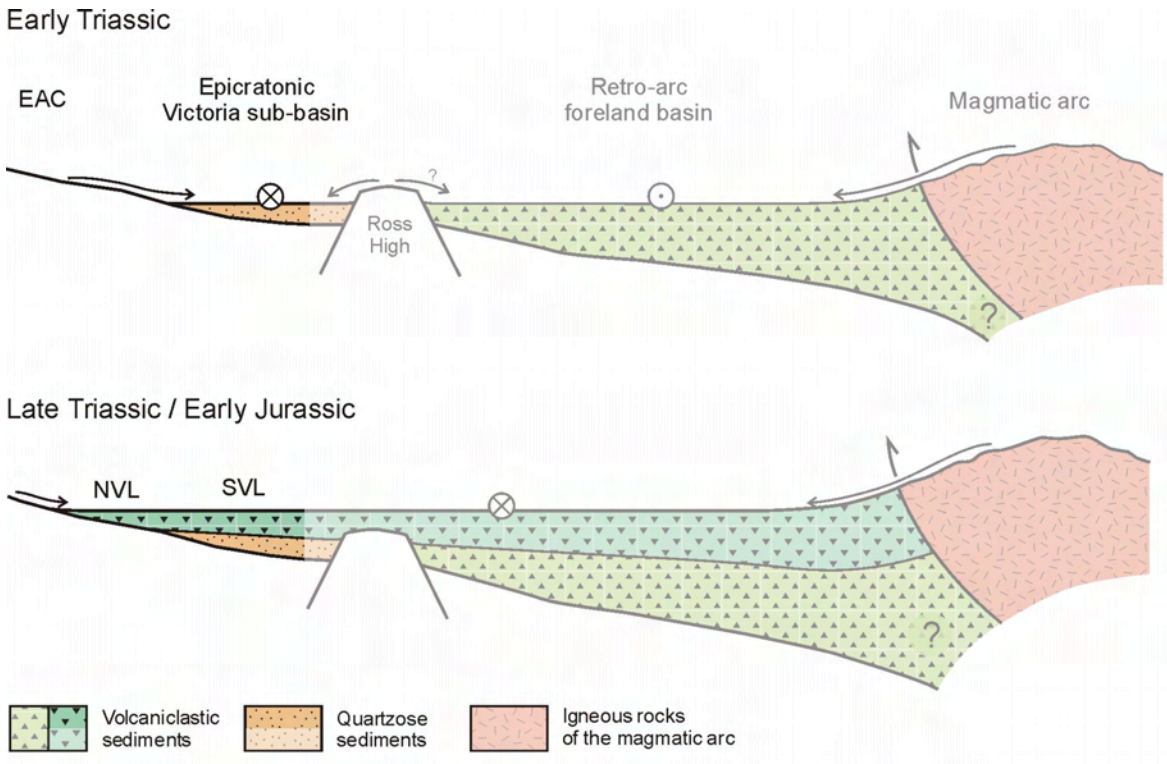


Fig. 1.7: Schematic cross sections of the Transantarctic Basin in the NVL sector (not to scale) as proposed by Collinson et al (1994) for the Early Triassic (upper panel) and the Late Triassic / Early Jurassic (lower panel). The little symbols indicate the different directions of palaeo-drainage. Information in the pale areas is derived from other parts of the TAM, hundreds to thousands of km apart from Victoria Land. The structure of the basin close to the magmatic arc is uncertain.

A different model interprets the Mesozoic Victoria Group in NVL as filling of a tectonic graben contemporaneously to Ferrar igneous activity (Casnedi and Di Giulio 1999), and thus entirely Jurassic in age. This model is based on the assumption that some of the Ferrar sills are lava flows, but, however, there is no field evidence for this (L. Viereck-Götte 2007, pers. comm.). Additionally, this model can not explain the Triassic biota found frequently (e.g. Norris 1965; Tessensohn and Mädler 1987).

#### 1.2.2.3 The Devonian

In SVL, Devonian terrestrial sediments of the Taylor Group reach a thickness of approximately 1400 m (Collinson et al. 1994). In the CTM, erosional relicts of about 300 m can be found, with uncertain amounts of the presumably originally thicker succession being removed before deposition of the Victoria Group. Farther along the TAM, in the Ohio Range, shallow marine Devonian sediments have been found (Collinson et al. 1994), indicating a transition from continental to marine conditions in this direction along the TAM (Barrett 1991).

In contrast to these areas, major sedimentary successions from this time are missing in NVL. Instead, the Devonian to Early Carboniferous is represented by the rhyolitic and andesitic Gallipolli Volcanics from about 357 Ma to 369 Ma (Adams et al. 1986; Henjes-Kunst and Kreuzer 2003). They may reach up to 2000 m thickness with minor intercalated plant-bearing sediments (GANOVEX-Team 1987b). The Gallipolli Volcanics are restricted to few outcrops outside the working area, for example in the Admiralty Mountains (Robertson Bay terrane) or at their type locality, the Gallipolli Heights, in the southern Freyberg Mountains (Wilson terrane, Fig. 1.5).

The prevalently granodioritic Admiralty Intrusives (Meccheri et al. 2003) with cooling ages between 354 ± 1 Ma and 371 ± 3 Ma (Henjes-Kunst and Kreuzer 2003) are thought to represent intrusive equivalents of the Gallipolli Volcanics. They occur mainly in the Robertson Bay terrane, with their type locality in the Admiralty Mountains, but also in the Bowers terrane and along the eastern margin of the Wilson terrane. Of similar age, but not related otherwise, is the Salamander Granite Complex (Borg et al. 1986) in the Salamander Range (Wilson terrane).

#### 1.2.2.4 The Carboniferous to Permian

A Permo-Carboniferous glaciation of NVL is inferred from isolated occurrences of yet unnamed, up to 350 m thick glacigenic deposits resting unconformably on basement rocks (e.g. Laird and Bradshaw 1981; McKelvey and Walker 1983; Skinner 1981). They represent the basal deposits of the Victoria Group. Their age is constrained by their stratigraphic position directly below plant-bearing Permian sediments (Takrouna Formation, see below) and from correlations with glacigenic deposits from SVL (Metschel Formation) and the CTM (Pagoda Formation, Barrett 1991) as well as from Tasmania (Banks 1981; Crowell and Frakes 1971). The deposits represent a variety of depositional settings (Laird and Bradshaw 1981; McKelvey and Walker 1983), and have been interpreted as remnants of valley fills (Collinson and Kemp 1983).

The Permian Takrouna Formation in NVL is at least 300 m thick (Collinson et al., 1986) and either conformably overlies glacigenic strata described above, or rests unconformably on igneous or metamorphic basement rocks, with its base being an erosional unconformity with a relief of up to 100 m on a regional scale (Sturm and Carryer 1970). Its age is constrained by a flora dominated by *Gangamopteris*, *Glossopteris* and *Vertebraria* (Dow and Neall 1974).

The dominant lithologies of the Takrouna Formation are fluvial channel sandstones with intercalated mudstones and minor coal (Collinson et al. 1986). Sediments appear to become finer-grained and more carbonaceous from east to west. This probably represents a proximal to distal trend from the margin to the centre of a trough-like depression, that coincides with the modern Rennick Graben (Collinson et al. 1986). Mean palaeocurrent directions indicate a dominant transport to the north towards Tasmania, but there is considerable variation between the outcrops.

Equivalent sediments in SVL are the Weller Coal Measures (250 m), consisting of sandstones, mudstones, and coal, which have been deposited within a similar (or possibly even the same) basin as the Takrouna Formation (Isbell and Cúneo 1996). The trough-shaped Permian basin in SVL was probably 100-150 km wide and characterized by traverse flow from the hinterland across the two basin margins, and axial flow towards NVL and Tasmania (Isbell and Cúneo 1996).

Late Carboniferous and Early Permian deposits in Tasmania (Parmeener Supergroup) are interpreted as filling of a glacially excavated depression (e.g. Banks 1981; Crowell and Frakes 1971; Hand 1993). The Tasmanian Basin was approximately 150 km wide and 270 km long and comprises basal diamictites, followed by terrestrial, coastal and cold-water shallow marine deposits (e.g. Clarke et al. 1989; Martini and Banks 1989).

In the CTM, the Permian Mackellar, Fairchild, and Buckley Formation together reach a thickness of about 1000 m in total (Collinson et al. 1994). Palaeocurrents indicate a sediment transport towards the southeast (Isbell 1991; Vavra et al. 1981), and thus in the opposite direction than in Victoria Land. Palaeoflow data are supported by a change of lithofacies from continental to brackish and marine conditions from the CTM towards the Pensacola and Ellsworth Mountains (Barrett 1991; Collinson et al. 1994).

Inferred source areas of the Takrouna Formation in NVL, and presumably for the Weller Coal Measures of SVL as well, are the foreswell of the Ross High and the East Antarctic Craton (Collinson and Kemp, 1983; Collinson et al., 1986). The upper boundary of the Takrouna Formation is unknown (Collinson et al. 1986), and a direct transition to Triassic sediments has not been observed. This indicates an erosional phase following the end of Permian sedimentation.

#### 1.2.2.5 The Triassic to Jurassic

With one possible exception (Sturm and Carryer 1970; Norris in Sturm and Carryer 1970), Triassic rocks have only been observed in the southern part of NVL. The Mesozoic sediments of the Victoria Group in NVL are divided into the Section Peak Formation (SPF), the Shafer Peak Formation (SHF) and the Exposure Hill Type events/Exposure Hill Formation (EHT/EHF). SPF and SHF are intruded by mafic sills (Ferrar Dolerites) and overlain by an up to 1000 m thick succession of Kirkpatrick (Ferrar Group) lava flows (Elliot and Foland 1986, see also Fig. 1.8). The absolute age of both, intrusive and effusive parts, is about 184 Ma (Encarnación et al. 1996; Minor and Mukasa 1997).

The Section Peak Formation (SPF)

The term Section Peak Formation was introduced in 1986 for the Triassic part of the Beacon sandstones in NVL, with the Section Peak defined as type locality (Collinson et al. 1986). In the working area, the formation overlies directly more or less intensely weathered metamorphic and plutonic rocks of the Ross Orogen (e.g. Rennick Shists, Granite Harbour Intrusives). At their base, the sub-Beacon erosion surface shows a minor relief on meter scale. Their age has been assigned due to palynomorphs and the occurrence of a *Dicroidium*-flora (Gair et al. 1965; Norris 1965; Tessensohn and Mädler 1987), although some authors suggested a Jurassic age for the upper part (Musumeci et al. 2006; Norris 1965; Pertusati et al. 2006) or for the entire SPF (Di Giulio et al. 1997; Elliot et al. 2007). The first absolute age dating for Beacon sediments in NVL was carried out during this study by U-Pb dating of magmatic zircons from a tuffaceous interbed (see Sect. 4).

The SPF reaches about 200 m thickness and consists predominantly of light-coloured sandstones of fluvial origin. Thin mudstones are rarely interbedded, but become locally more important (e.g. at Shafer Peak), and are in few sections associated with thin coal seams (at Timber Peak). Basal conglomeratic braided stream deposits of up to 70 m are present in southern parts of NVL (Schöner et al. in review; Schöner et al. 2008).

Northwards, the conglomerates give way to sandstones, typically showing large scale trough cross-bedding. They are interpreted as deposits of a sand-dominated braid plain. Carbonaceous fine-grained sandstone to shale as well as coal layers are interbedded in the upper part, representing floodplain, swamp and lacustrine environments (Schneider et al. 2006). Within the uppermost 20 meters of the SPF, tuffaceous sandstones are interbedded at Shafer Peak in the southern Deep Freeze Range. Plant fossil assemblages within the SPF have been found at a variety of locations and are sometimes extraordinarily well preserved (Bomfleur et al. in review; Tessensohn and Mädler 1987). Compositional types and source areas of the SPF were analyses for this study. The results are presented in Sect. 3.

The Shafer Peak Formation (SHF)

The SHF was introduced shortly after the GANOVEX IX (Schöner et al. 2007). At the type locality (Shafer Peak, southern Deep Freeze Range) the SHF overlies lacustrine black shale on top of mafic volcaniclastic deposits of an Exposure Hill Type Event (or Exposure Hill Formation) described below. SHF deposits crop out also at the eastern ridge of Mt. Carson. Basal parts and underlying deposits are not exposed here.

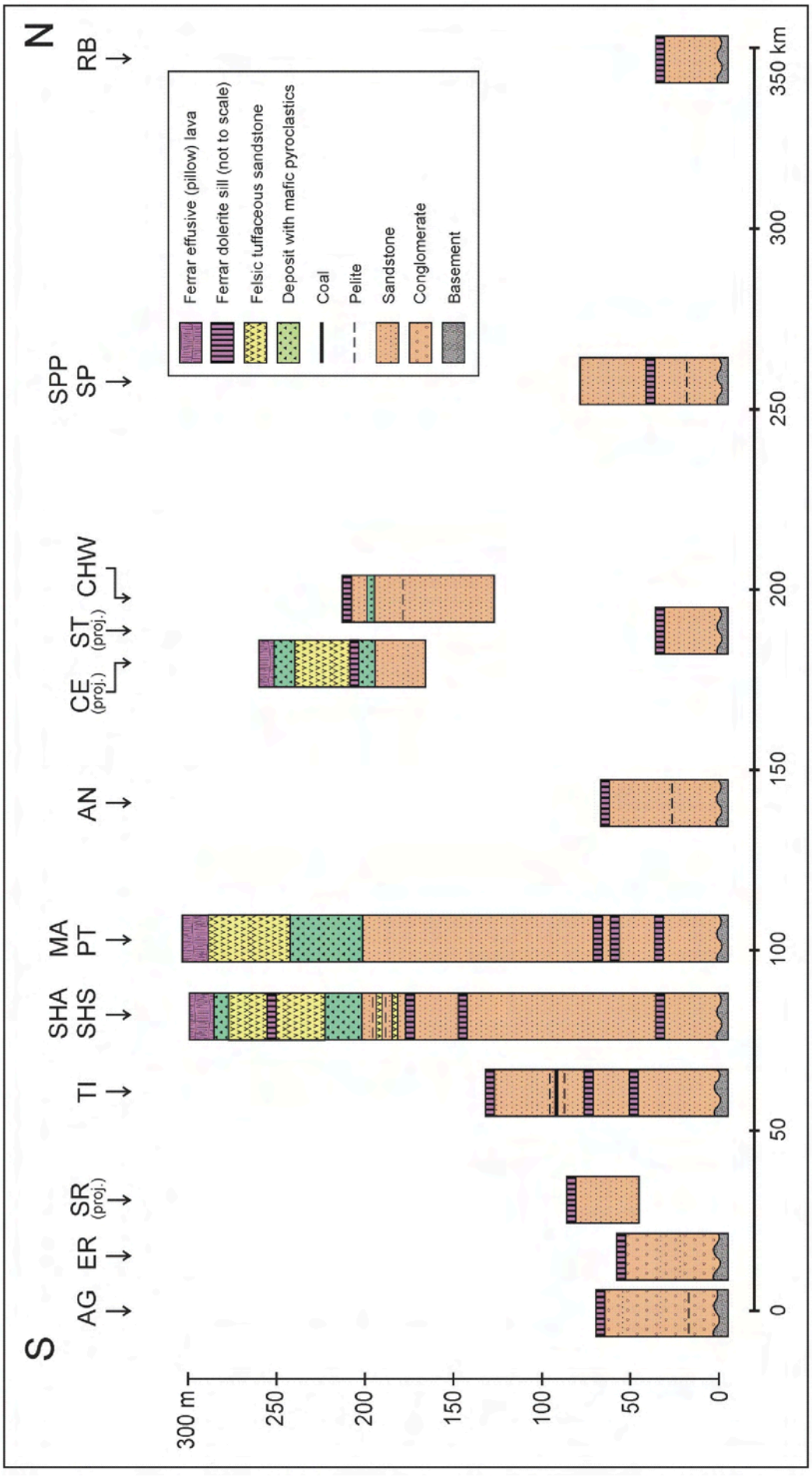


Fig. 1.8: Simplified cross section of the Beacon sediments in southern NVL (after Schöner et al. in review). The trace of the cross section is shown in Fig. 1.3. The lower part of the sequence consists mainly of siliciclastic sandstones (conglomerates in the south), in which locally pelites, coal, and felsic tuffaceous sandstone are intercalated (SPF). Tuffaceous sandstones also form the upper part of the succession (SHF). Both formations contain deposits with mafic pyro-/hydroclastic components, allocated to EHT events. The entire succession is intruded and overlain by mafic igneous rocks of the Ferrar group. The basement is formed by metamorphic and plutonic rocks of the early Palaeozoic.

The deposits of the SHF consist of sand- to silt-sized tuffaceous material often showing ripple cross-lamination and climbing ripples, indicating fluvial reworking. The beds are divided by thin, greenish-grey pelite horizons. Layers rich in pelitic intraclasts are frequent. Plant fossils are dominated by cycadophytes and dipterid ferns, whereas *Dicroidium* is absent, pointing to a Jurassic age. In addition, by the relationship to the syn-sedimentary to shortly post-sedimentary Ferrar magmatites, the age of the SHF can be constrained to be minimal about 184 Ma (see above). Composition and provenance of the SHF are part of Sect. 4.

The Exposure Hill Type Events / Exposure Hill Formation

At several stratigraphic levels, though possibly not throughout NVL, volcaniclastic sediments (breccias, sandstones, block- and lapilli-bearing tuffs) occur, reaching several tens to more than 150 m thickness (Schöner et al. 2007). They have been found in between the SPF and the SHF, and within upper parts of the SHF. These sediments contain juvenile mafic igneous clasts beside sedimentary rafts of the underlying SPF and SHF. As they are steeply crosscutting the sedimentary layering of the SPF and SHF, respectively, they are interpreted as diatreme fillings. Lateral these diatreme fillings can be traced to stratified, intraformational volcaniclastic sedimentary units of up to 50 m.

Regardless of their status as a formation (Elliot et al. 1986) the Exposure Hill type deposits are interpreted as remnants of local hydromagmatic explosive events, triggered by intrusion of dolerite sills of the Jurassic Ferrar Group (Viereck-Götte et al. 2007).

In SVL, the Triassic part of the Victoria group is represented by the Feather Conglomerate of approximately 250 m thickness and the Lashly Formation, which reaches at least 520 m (Collinson et al. 1983). The Lashly Formation is assumed to be Triassic only, with younger parts possibly being removed by erosion. Within the Lashly Formation, quartzose sandstones supposed to be derived from the East Antarctic continental interior, can be distinguished from sandstones rich in volcaniclastics, presumably shed from a magmatic arc source, and indicating the Ross High was not a blocking swell anymore (Collinson et al. 1994). From the Early Jurassic, silicic tuffs are known, which may be correlatives to the SHF in NVL. Both the Mawson and Carapace formation are mafic volcaniclastic breccias and sandstones, respectively, and as the Exposure Hill deposits in NVL they may be related to the emplacement of the Ferrar sills (Elliot 2000).

In the CTM, the Triassic is represented by the Freemouw and the Falla Formation, together reaching about 900 m (Barrett et al. 1986). As in SVL, a quartzose and a volcaniclastic facies can be distinguished (Collinson et al. 1994). Both formations are regarded to be Triassic, although from the upper Falla formation intercalated silicic tuffs yielded an Rb-Sr isochron age of $186 \pm 9$ Ma (Faure and Hill 1973) and thus strong evidence for a continuation of sedimentation during the Early Jurassic. However, these ages may have been influenced by pervasive zeolitization related to emplacement of Ferrar igneous rocks (Elliot 1996).

Above the Falla Formation and Early Jurassic in age (Hammer et al. 1994), the Hanson Formation (more than 200 m) consists predominantly of volcaniclastic and tuffaceous sandstones with intercalated tuffs (Elliot 1996), thus exhibiting lithological and stratigraphic similarities to the silicic tuffs in SVL and NVL (Elliot 2000).

Below the overlying Ferrar lava, the Prebble formation consists of up to 300 m thick mafic breccias, and similar to the Mawson and the Carapace formations in SVL and the Exposure Hill deposits in NVL it may be related to emplacement of Ferrar sills (Elliot 2000).

Palaeoflow directions in the CTM and in SVL indicate a sediment transport along the axis of the TAM towards NVL, and thus the opposite direction than during the Permian. This reversal of palaeoslope in the Late Permian has been related to the Late Permian to Early Triassic Gondwanide Orogeny or Weddel Orogeny, respectively (Ford 1972, in Barrett 1991), and the

uplift of the Cape Fold Belt and adjoining areas in Antarctica (Barrett 1991). It coincides with a change from quartzose to volcaniclastic sandstone composition in SVL (Collinson et al. 1994).

In Tasmania, the highest unit of the Upper Parmeener Supergroup is of Carnian to Norian age and comprises a non-marine succession of predominantly lithic sandstone with minor lutite and coal. The lithic sandstone is largely of intermediate to felsic volcanic provenance, which is also indicated by rare conglomerates with common rhyolitic clasts. In the upper parts of this succession thin (< 1 m) felsic tuffs from a calc-alkaline volcanic source are interbedded (Bacon and Everard 1981).

Younger sediments of Jurassic age (Toarcian) are known from only a single locality at Lune River, where they are capped by arc-like tholeiithic basalts (Bromfield 2004). Fossil logs indicate a transport direction of the volcanolithic sandstones towards the north to northwest. An originally wider distribution of the Jurassic sediments can be inferred, but attempts to constrain their thickness are inconclusive (Hergt et al. 1989). However, they may have been at least 800 m of post-Norian cover at the time of Ferrar sill intrusion (Bacon et al. 2000, and references therein)

### 1.2.2.6 Late Carboniferous to Early Jurassic climate in North Victoria Land

Palaeomagnetic data indicate that the position of the magnetic South pole moved from eastern Africa through southern India (around 330 Ma), the East Antarctic craton, and reached the area of the present CTM at about 290 Ma (McElhinny et al. 2003). During the Permian, the South Pole migrated either further into the palaeo-Pacific (McElhinny et al. 2003), or towards south-eastern Australia (Grunow 1999; Veevers et al. 2006). However, both scenarios place NVL at high to very high latitudes during the Late Carboniferous and Permian, certainly higher than 75°S. A high latitude is also indicated by the Permo-Carboniferous glacial beds and sedimentological features throughout the Transantarctic Basin, indicating that Permian sedimentation occurred in ice-marginal, peri-glacial or glaciomarine settings (Miller and Waugh 1987; Miller and Waugh 1991).

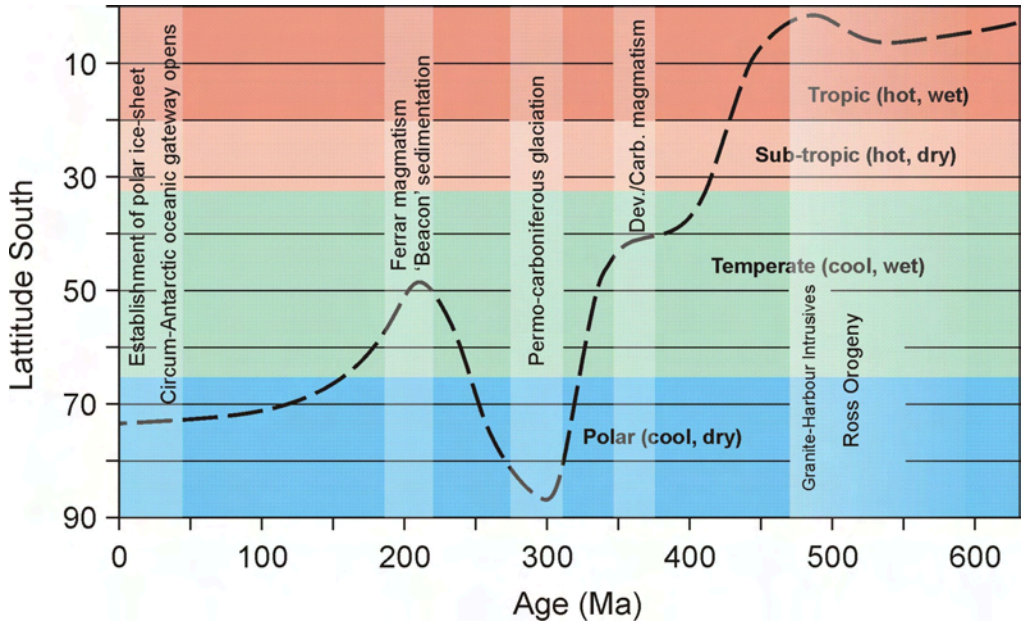


Fig. 1.9: Reconstruction of the latitude of NVL and likely climatic conditions since the Latest Proterozoic (adopted from Torsvik et al. 2008). Apparently, the sedimentation of the SPF took place under temperate conditions of mid-latitudes.

The global climatic transition to greenhouse conditions in the Late Permian to Triassic resulted in relatively warm and consistently humid polar conditions (e.g. Taylor et al., 1992; McLoughlin et al., 1997; Rees et al., 1999; Kerp, 2000; Kidder and Worsley, 2004). Paleosols in the Early Triassic lower Feather Conglomerate of SVL indicate persistence of a temperate, sub-humid or humid climate over thousands of years (Barrett and Fitzgerald 1985). An equable, more sub-humid to semi-arid climate has been suggested for the Triassic of southern Gondwana (Lindstrom and McLoughlin 2007).

For the Late Triassic and Early Jurassic, sediments from NVL can be used as climatic indicators. Sedimentological features indicate a high ground water table and thus a humid climate during deposition. Rare mudcracks in the uppermost parts of the SPF seem to point towards a change to more semi-arid conditions (R. Schöner and J. Schneider, 2008, pers. comm.).

## 1.2.3 Post-'Beacon' evolution

### 1.2.3.1 The remaining Mesozoic

During the Cretaceous, an extensional regime started to form the West Antarctic Rift System (Siddoway 2007). Although no volcanic rocks are known from this time, hydrothermal events are indicated by resetting of various K-Ar and Ar-Ar ages, the last of which has been dated from newly precipitated Apophyllite to about 96 Ma (Molzahn et al. 1999).

Apatite fission track data (AFT) seem to indicate a deeper burial of parts of NVL as deduced by the obtained overlying Ferrar rocks alone, thus leading to the presumption of an Antarctic-Australian Victoria basin, with the basin filling of 3 to 5 km being later removed completely again (Lisker and Läufer 2007). The diagenetic evolution of the Beacon sandstone yields important information about burial temperature and depth (see Sect. 5).

### 1.2.3.2 The Cenozoic

A second phase of extension started around 50 Ma (Ross Sea, Weddel Sea) in a slightly different direction than during the Cretaceous (Rossetti et al. 2003b) resulting in the division of East and West Antarctica (Siddoway 2007) and the uplift of the TAM and NVL as shoulder of an asymmetric rift structure. A crust of about 40 to 45 km thickness below the TAM (Bentley 1983) and only 17 to 21 km under the Ross Sea and parts of West Antarctica is indicated by geophysical data (Behrendt et al. 1991). Lateral heat transfer probably increased the uplift of the TAM and led to present heights of more than 4000 m above sea level. This extensional phase was accompanied by extrusion and, to a lesser extend, intrusion of alkaline magmatic rocks (e.g. McMurdo Volcanic Group) along the Ross Sea margin (Hornig and Wörner 2003; Jordan et al. 2003).

During this phase, the Rennick Graben and many of the tectonic structures in NVL were formed (Roland and Tessensohn 1987; Rossetti et al. 2003b). The interior of the graben today comprises the only area in NVL, in which Kirkpatrick Basalts are preserved in a larger extent, revealing a minimum thickness of about 1000 m (e.g. in the Mesa Range). The structure of NVL has been reconstructed using the basement top (sub- Beacon unconformity) as a marker horizon. The results and an interpretation can be found in the following Sect. 2.

In the Middle to Late Eocene, relative motion between terranes south and west of Tasmania, and the final detachment from Antarctica led to opening of the first circum-Antarctic oceanic gateway (South Tasman Sea), causing radical changes in oceanic circulation patterns (Brown et al. 2006; Lawver et al. 1992). In combination with a general global cooling an extensive Antarctic polar ice sheet formed, at the latest during the Oligocene (Breza and Wise 1992; Whitehead et al. 2006). However, smaller ephemeral ice sheets may have been existed already since the Cretaceous (Miller et al. 2007).

# 2 Structural geology of North Victoria Land

## 2.1 Introduction

### 2.1.1 Objectives and regional situation

The understanding of structural geology is crucial to detect possible tectonic influences on sedimentation. These could result in abrupt or smooth changes in sediment thickness or sedimentation rates, in marked changes in flow directions or in variable depositional styles or facies.

For the detection of tectonic movements during or after sedimentation of the Beacon sandstone in NVL, the base of the Beacon Supergroup is an excellent marker horizon (e.g. Roland and Tessensohn 1987). The sedimentary base is referred to as Kukri erosion surface in SVL and the CTM, or as sub-Beacon peneplain, and can be traced along the TAM (Isbell 1999, compare Sect. 1). To visualize tectonic movements affecting Beacon sediments, this marker horizon was modelled by inter- and extrapolation of outcrop data. In the northern part of the modelled area, Beacon sedimentation started in the Carboniferous, and in the southern part in the upper Triassic (Sect. 1).

Victoria Land and adjoining regions were part of a dextral transtensional system since the late Cretaceous. The extension direction changed from the initial E-W direction to a NW-SE extension during the Tertiary (Rossetti et al. 2003b, see Fig. 2.1). A digital elevation model (DEM) of the modelled area is shown in Fig. 2.2.

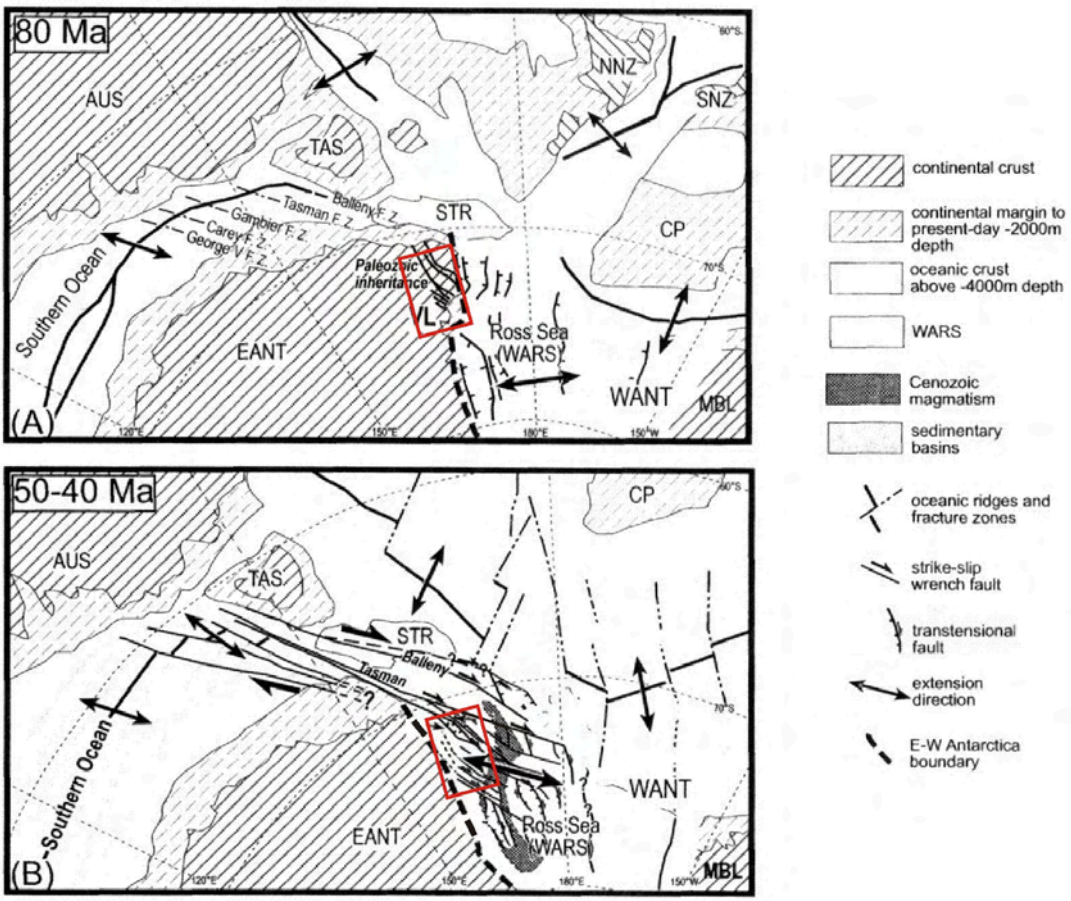


Fig. 2.1: Tectonic setting of the Ross Sea region in the late Cretaceous (A) and Palaeogene (B), modified after Rossetti et al. (2003b). AUS: Australia; CP: Campbell Plateau; EANT: East Antarctica; MBL: Mary-Byrd-Land; NNZ: North New Zealand; SNZ: South New Zealand; STR: South Tasman rise; VL: Victoria Land; WANT: West Antarctica; WARS: West Antarctic Rift System. The area shown in Fig. 2.2 is marked in red.

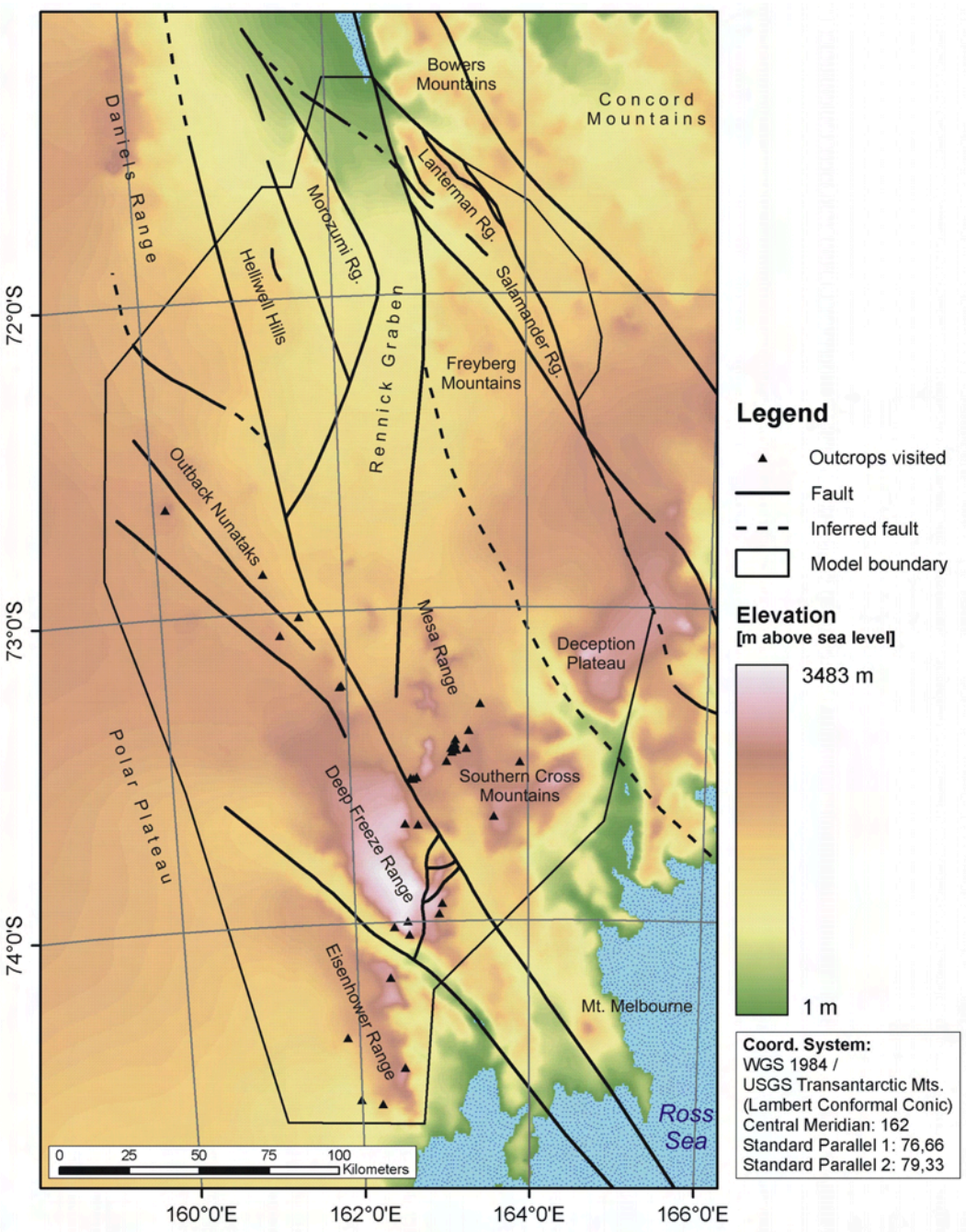


Fig. 2.2: Digital elevation model (USGS/EROS et al. 1996) of the modelled area showing the locations of outcrops visited during the GANOVEX IX in 2005/06 (see also Sect. 1). The faults are adopted from various sources defined in the text. This model was used to calculate the 'thickness map' of Fig. 2.11.

### 2.1.2 Methods

The sub-Beacon unconformity was constructed using the elevation of digitized, georeferenced points, following the outcropping basement top. Other outcrops allow estimating the range of possible positions for this surface and have been used complementary (see Fig. 2.3). According to the quality of the outcrops, the reliability of the reconstructed basement top is variable. In some regions it is only possible to provide upper and lower bounds to its position.

Faults were adopted from the geological map (GANOVEX-Team 1987a), structural analyses (Lisker et al. 2006; Roland and Tessensohn 1987; Rossetti et al. 2003a; Rossetti et al. 2003b), geophysical evidence (Salvini et al. 1997), and field data collected during the GANOVEX IX (L. Viereck-Götte and R. Schöner 2009, pers. comm.). As in most cases the dip angle of the faults is unknown, a vertical position has been assigned consistently.

The final interpolation was performed using the Spatial Analyst of Arc Map (GIS 9.2), utilizing the 'Spline with Barriers' method at a grid resolution of 300 m. The resulting model was used for further calculations like slope calculation, and relation of sedimentary base to topography, by using standard analysis tools in Arc Map.

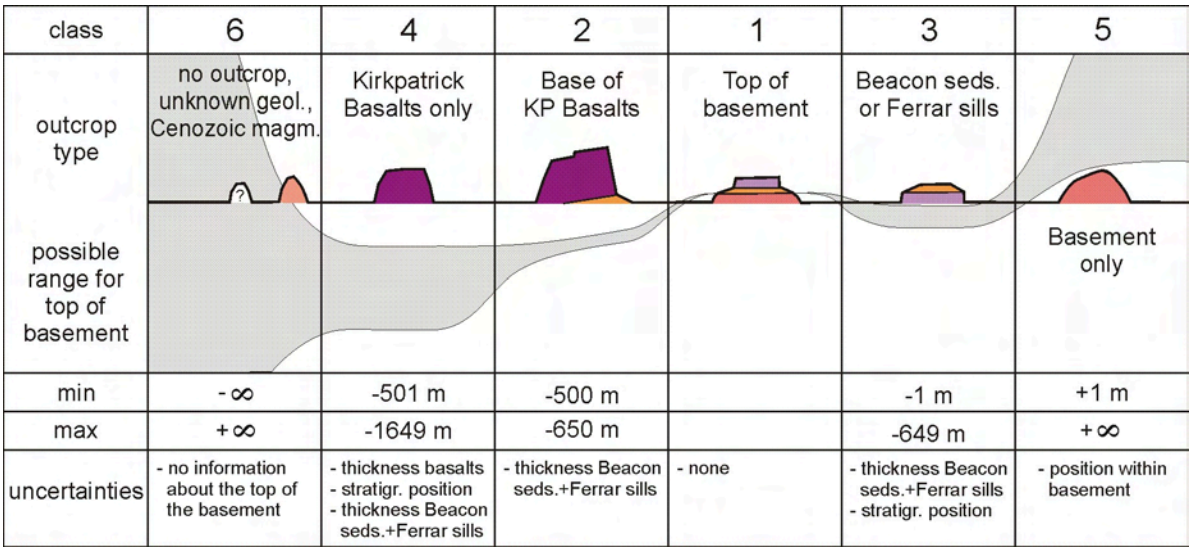


Fig. 2.3: Virtual cross section to visualize the outcrop classification for the construction of the sub-Beacon unconformity. The range of possible positions of the surface (light grey shaded) was used to define six outcrop classes. A thickness of 1000 m for the Kirkpatrick basalts and 500 - 650 m for the Beacon sediments plus Ferrar dolerites has been assumed. In practice, the uncertainty is reduced by the thickness of the exposed strata.

The model boundaries are defined by the locations of outcropping Beacon sediments, and are marked in Fig. 2.2. The fault-bounded Lanterman and Salamander Range were not modelled. In the former the Beacon base (about 600-2000 m a.s.l.) is displaced by thrusts associated with transpressive flower structures (e.g. Lisker et al. 2006). In the latter, the Beacon sediments have been eroded, thus only a minimum elevation of 2100 m for the Beacon base can be given, without information about dip direction or angle.

Using a reference horizon, the detectable faults are limited to those including a major vertical displacement (normal faults, reverse faults, oblique strike-slip faults). Faults without a major vertical component (less than about 50 m) may possibly remain undetected. From the northern part of the modelled area, where Permian sediments are present, syn- as well as post-sedimentary normal faults have been reported (Walker 1983). The intrusion of Ferrar dolerites were not affected by this faulting.

To determine the position of the sub-Beacon unconformity relative to topography, the digital elevation model GTOPO30 (USGS/EROS et al. 1996) was used, providing a horizontal grid spacing of 30 arc seconds. This is approximately 1 kilometre in N-S direction only, but, due to the high latitude of NVL, about 300 m in E-W direction.

### 2.1.3 Quality assessment

To show the various uncertainties and to allow for quality assessment, three separate maps have been drawn. The first shows the outcrop density throughout the modelled area (Fig. 2.4). A nunatak was regarded as a single outcrop; regardless of its possible extend over several square kilometres. This approach was chosen for simplification. The resulting map mainly recovers the topography. Faults were not considered in this map.

As the outcrops are of different importance for construction of the basement top, the second map (Fig. 2.5) assesses the outcrop quality following the classification scheme of Fig. 2.3.

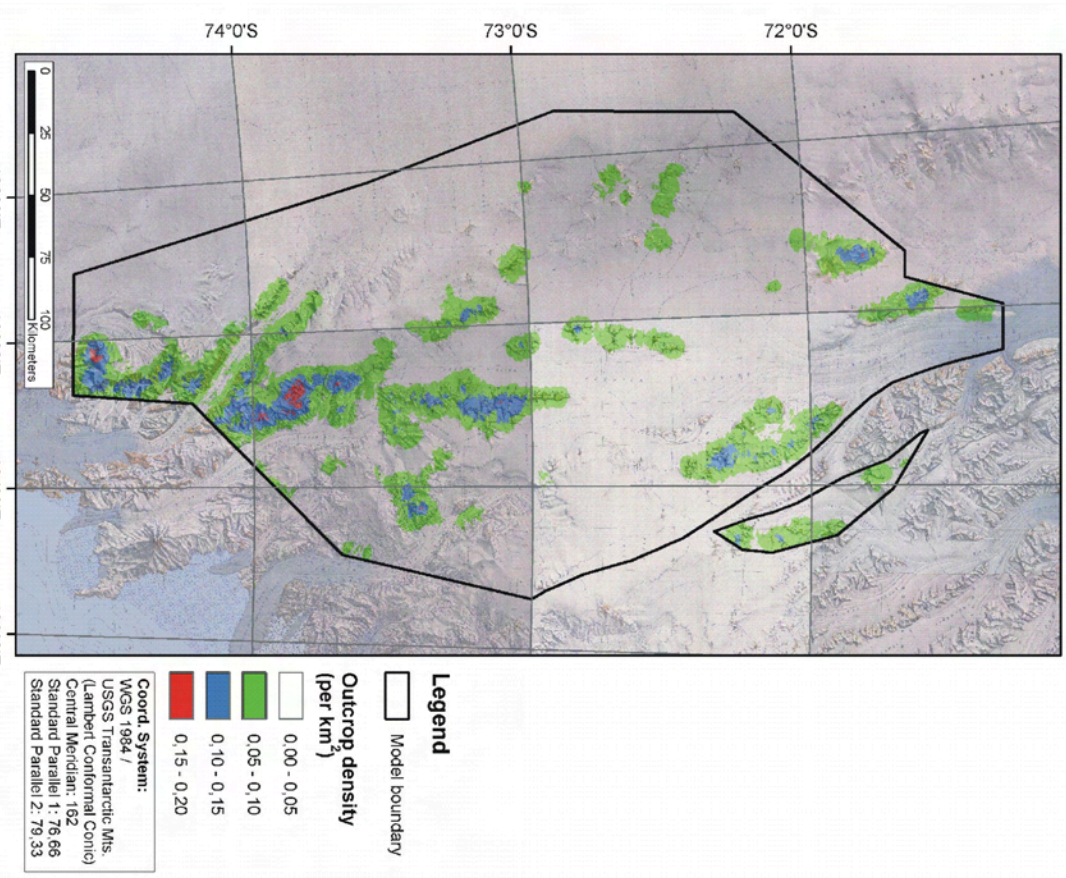


Fig. 2.4: Outcrop density within the modeled area. For simplification, a nunatak was considered as a single outcrop regardless of its actual size.

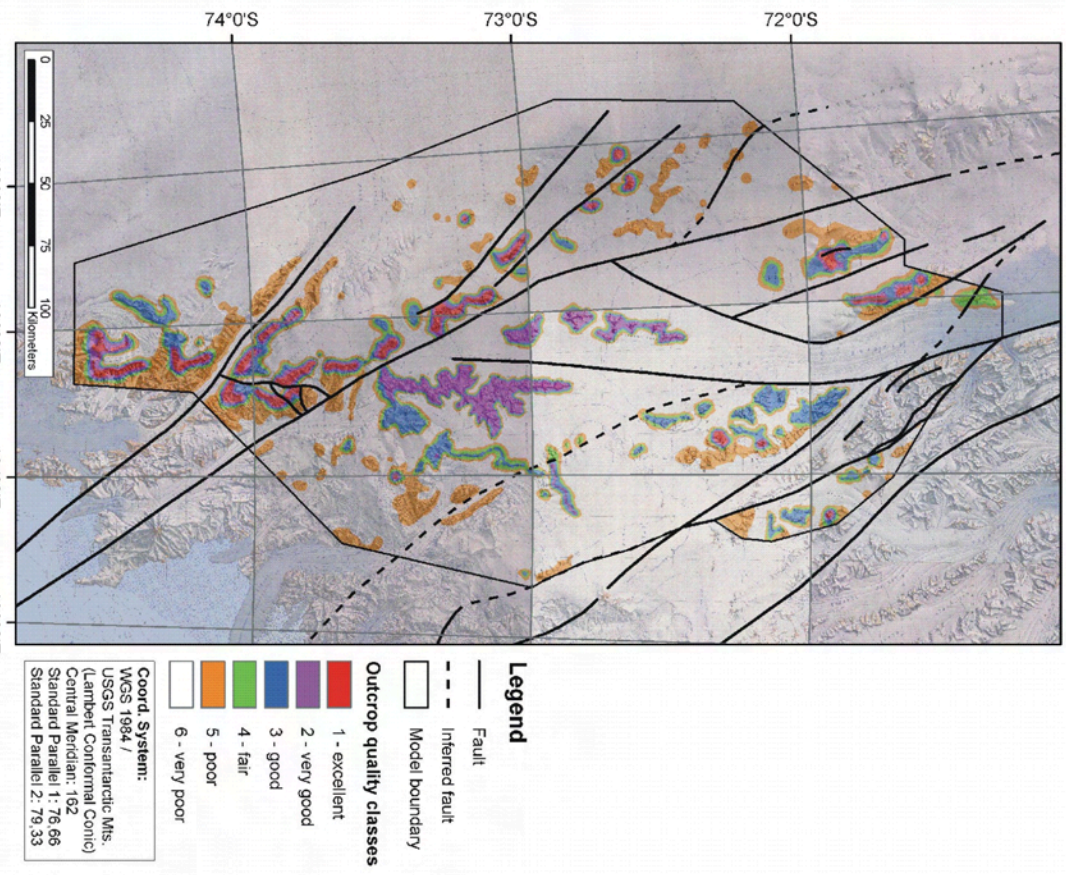


Fig. 2.5: Outcrop quality considering the possible range of the position of the sub-Beacon unconformity following the classification scheme of fig.2.3.

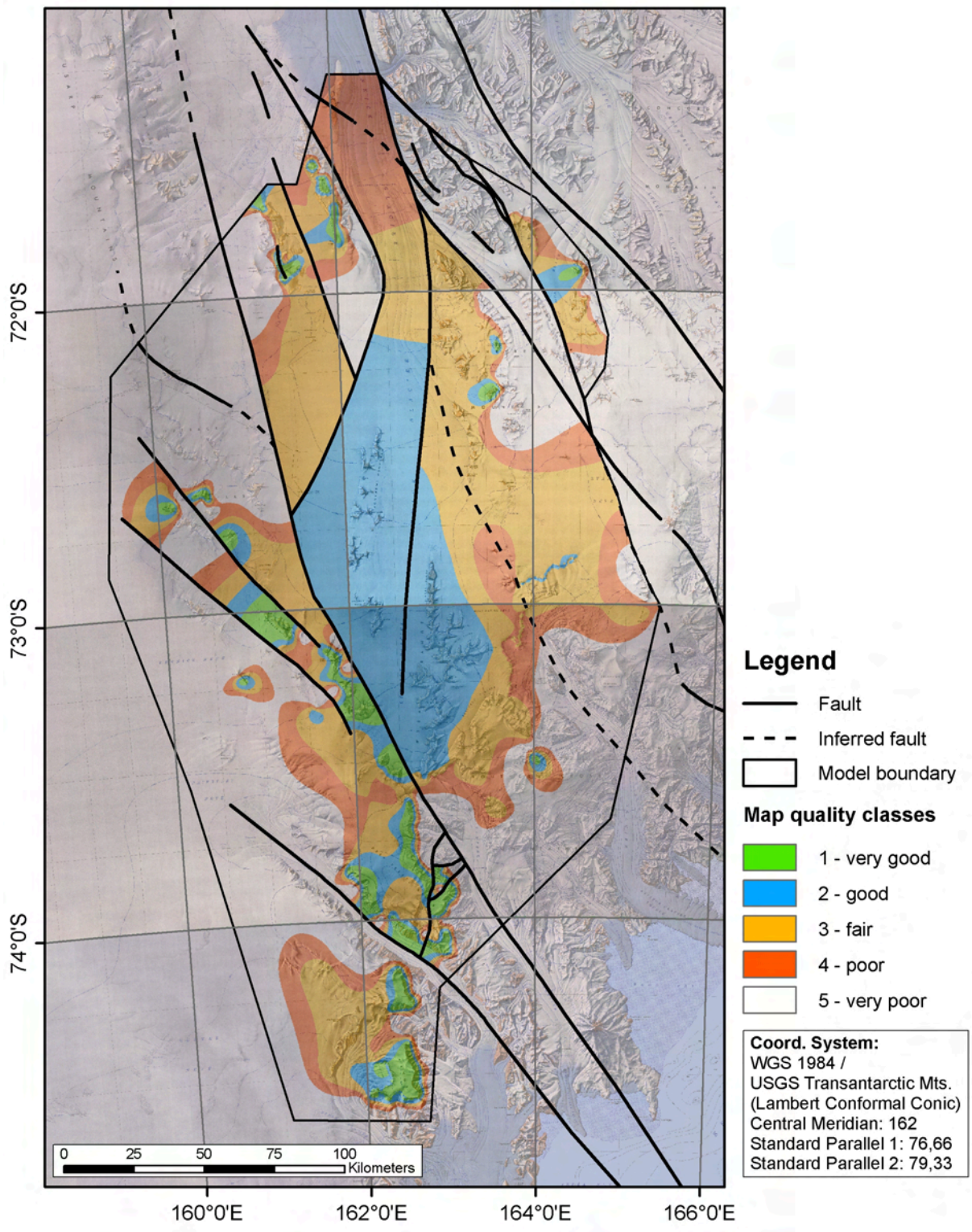


Fig. 2.6: Map showing the quality classes of the model following the classification scheme in Fig. 2.3. 'Good' and 'very good' grade is given mainly for the Eisenhower and Deep Freeze Range, the Outback Nunataks, the Helliwell Hills, Morozumi Range, and for the Mesas in the central part of the modelled area. Areas next to the model boundaries are mostly classified as 'poor' or 'very poor'.

In the third map for quality assessment, the outcrop quality as given in Fig. 2.5 was extrapolated to define regions of different degrees of uncertainty within the modelled area. In this analysis faults were considered. In general, areas with exposed sedimentary base show a very good quality (e.g. Eisenhower Range, Deep Freeze Range, Outback Nunataks). Regions,

where the base of Ferrar lava (e.g. Mesa Range), Beacon sediments, or Ferrar sills are exposed, are classified as ‘good’ or ‘fair’. All other outcrops including basement rocks, and the absence of any outcrops at all, was flagged as ‘poor ‘or ‘very poor’. Especially areas at the margins of the model show these classes. In these areas, the contour lines of the model of the sub-Beacon unconformity are drawn stippled to visualize the uncertainty (Fig. 2.6).

## 2.2 Modelling of the sub-Beacon unconformity

### 2.2.1 Elevation of the sub-Beacon unconformity

#### 2.2.1.1 Introduction

The input data for the model of the sub-Beacon unconformity comes mainly from the geological map of NVL (GANOVEX-Team 1987a). Additional data from structural analyses (Lisker et al. 2006; Rossetti et al. 2003a), analysis of aerial photographies (Petri et al. 1997), geophysical evidences (Ferraccioli and Bozzo 1999) and from field measurements (R. Schöner and L. Viereck-Götte 2009, pers. comm.) were included.

#### 2.2.1.1 Results

The modelled sub-Beacon unconformity is shown in Fig. 2.7, and the slope of the unconformity is shown in Fig. 2.8.The elevation of the sub-Beacon unconformity within the modelled area is lowest in the northern part of the Rennick Graben (about 580 m b.s.l.). As the graben continues outside the modelled area towards the Pacific, the basement top is most likely to reach progressively lower elevations further towards the north.

In the center of the syncline between Helliwell Hills and Morozumi Range, the basement top lies relatively low at about 400 m a.s.l.. As outcrops are missing from the center of the syncline, this height is extrapolated from the exposed basement top in the Helliwell Hills and the Morozumi Range and therefore relatively uncertain.

Low elevations can also be found west of the Eisenhower and Deep Freeze Range, towards the Polar Plateau, although the top basement surface is extrapolated here and relatively uncertain due to the low number of outcrops. However, a dip of the strata towards the west under the Polar Plateau as shown by the model matches the tectonic situation of the TAM as uplifted shoulder of the Ross Sea rift (Fitzgerald 2002, see also Sect. 1), and is also evident from field data (R. Schöner 2009, pers. comm.).

The highest parts of the surface in the modelled area reach nearly 3700 m a.s.l. in the southern parts of the Daniels Range. Similar elevations of up to 3400 m are realized in the south-east, where it rises towards the Ross Sea. Here, the rise of the surface is thought to be interrupted outside the modelled area by roughly N-S trending normal faults running about parallel to the coastline (Salvini and Storti 1999). The amount of vertical displacement is uncertain, as no Beacon sediments but only basement rocks are exposed here.

The dip angle of the sub-Beacon unconformity (Fig. 2.8) is less than about 5° in most parts of the modelled area. However, in northern parts of the working area, where Permo-Carboniferous sediments are present, relatively high values of up to 26° are present locally in four approximately parallel, NNW trending zones. They are located in areas where the map quality is ‘good’ or even ‘very good’ (compare Fig 2.6 for quality assessment) due to exposure of the unconformity.

Outside these high class zones the dip angle appears to become smaller again. However, this finding may be seriously affected by the lower outcrop quality that allows assigning upper and lower limits to the elevation of the sub-Beacon unconformity only. Thus the steeply dipping areas may extend further away from the high class zones.

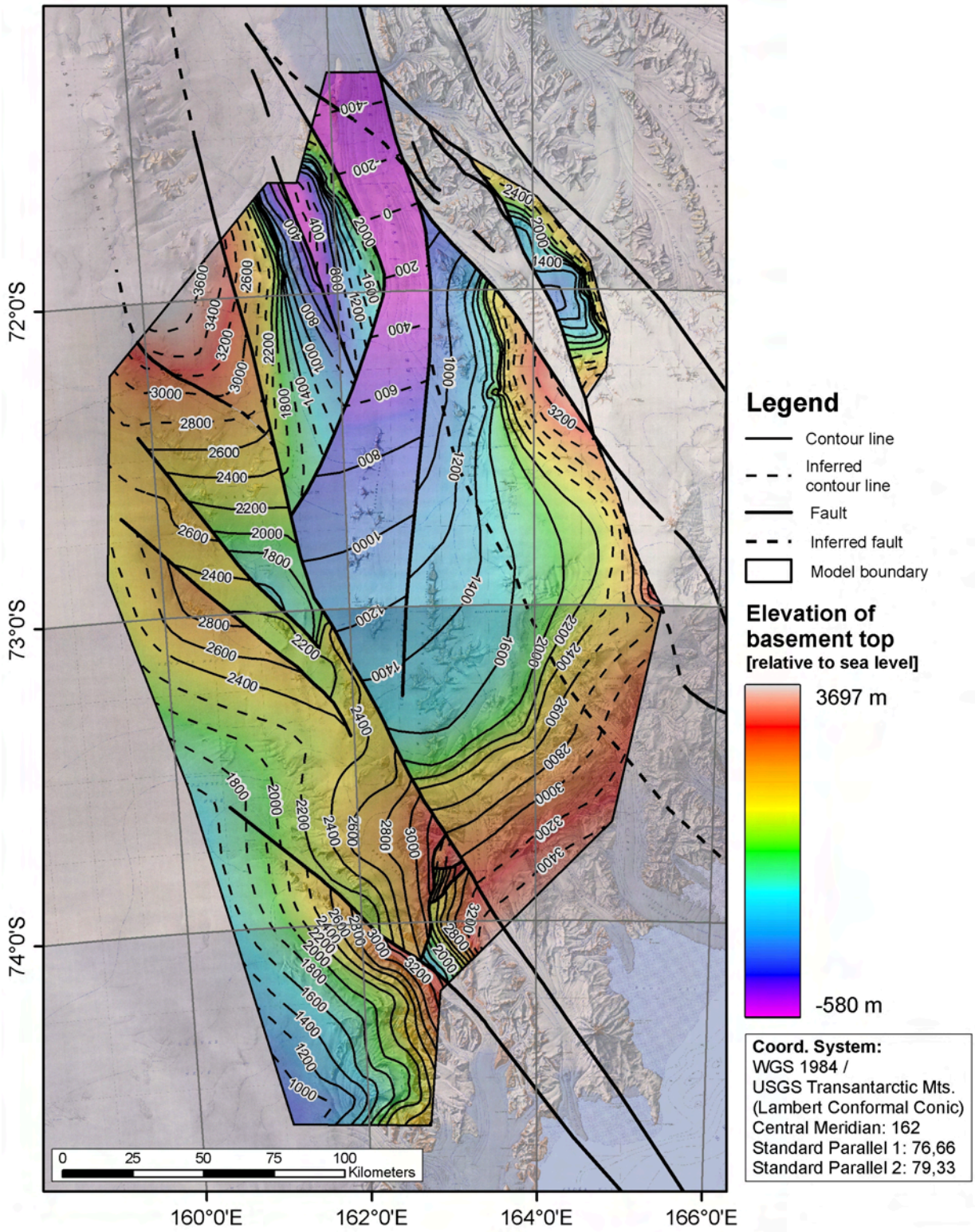


Fig. 2.7: Construction of the elevation of the basement top (sub-Beacon unconformity) in NVL. A height of more than 3000 m is reached in south-eastern and eastern parts, as well as in the northwest. The deepest position of the basement top is located in the Rennick Graben, where it slopes down below sea level. Contour lines are spaced by 200 m.

The local presence of steeply dipping zones may be an indication of faults, either affecting the Beacon sediments directly, or being present within the basement below, leading to monoclinal (flexural) folding of the overlying sedimentary strata (growth structure). Syn- as well as post sedimentary faulting has been reported for the Permo-Carboniferous sediments in the north

(Walker 1983). They trend approximately parallel to the palaeoflow direction during the Permian (Collinson et al. 1986). As similarly steep dipping zones within the Triassic/Jurassic strata in the southern part of the modelled area are absent, their formation most likely took place between the latest Permian and the Middle to Late Triassic.

Alternatively, an originally high relief of the sub-'Beacon' unconformity is possible. A relief of up to 100 m on a regional scale has been described for the Permian Tacrouna Formation (Sturm and Carryer 1970), and the relief below the Carboniferous glacigenic deposits interpreted as valley fills (Collinson and Kemp 1983) is likely to be even higher and steeper.

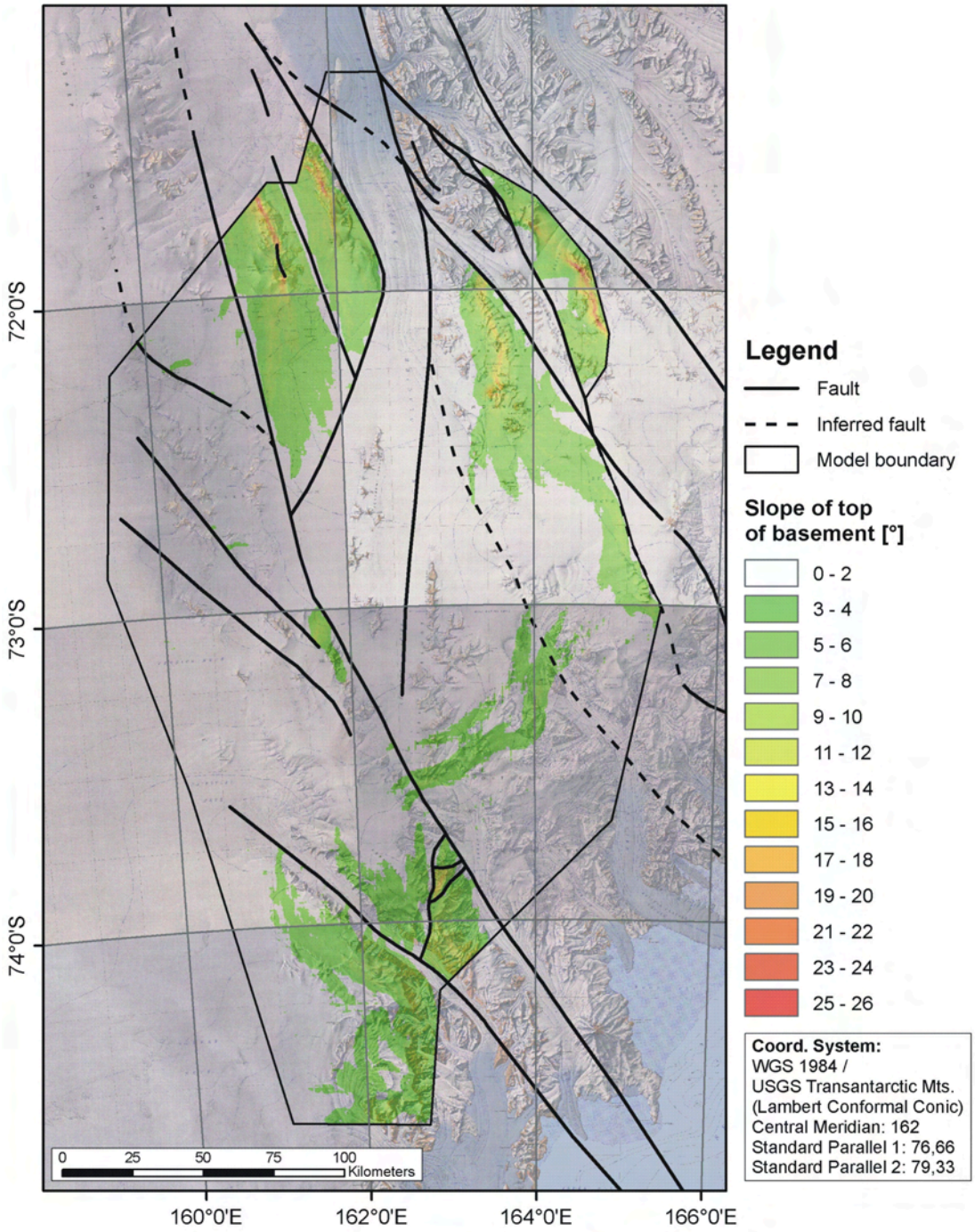


Fig. 2.8: The slope of the base of Beacon sediments is mostly very small, but shows larger values especially in northern parts of the modelled area. These zones can be interpreted as caused by faults, but may also be related to a high relief of the Permo-Carboniferous sedimentary base, in contrast to the Triassic sediments in the south.

The model of the sub-Beacon unconformity presented as a map in Fig. 2.7 is shown as a 3D image in tenfold vertical exaggeration in Fig. 2.9 and 2.10 from two different directions. In the following, the tectonic blocks marked in both figures are described in detail.

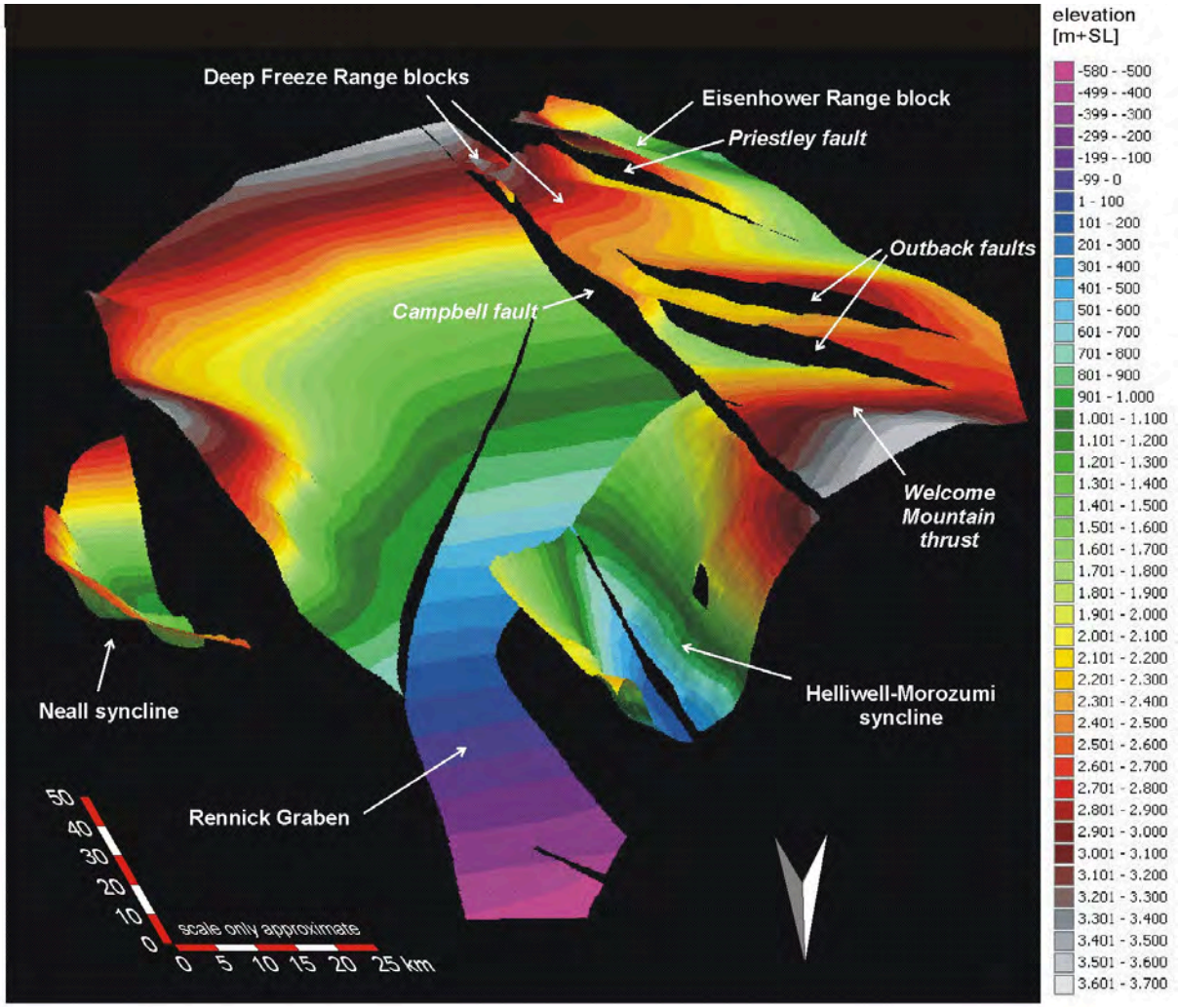


Fig. 2.9: A 3D visualization of the modelled sub-Beacon unconformity using Arc Scene. Faults (appearing as 'black holes') were assumed to be vertical. Tectonic elements described in the text are labelled. Along the Welcome Mountain thrust the tectonic transport was towards the south. For this reason, it can hardly be identified in this picture. Tenfold vertical exaggeration, view from the north.

## The Rennick Graben

The Rennick Graben shows to be more like an asymmetric half-graben, or even as a pull-apart basin. This is related to the orientation of the westward bounding fault, which changes from a NNE orientation to the SSE direction of the Campbell fault. Additionally, the vertical displacement on the eastern bounding fault decreases towards the south until the fault cannot be traced further in the Mesa Range (see Fig. 2.2).

The vertical displacement is strongly asymmetric and generally larger along the western fault. While the graben interior is downthrown more than 2000 m along the western fault at the Morozumi Range, it is only up to 800 m along the eastern fault.

## The Helliwell-Morozumi syncline

Helliwell Hills and Morozumi Range are located between the lower Rennick Graben and the northern segment of the Campbell fault. The opposite dip directions of the sub-Beacon

unconformity in the Helliwell Hills (eastward) and the Morozumi Range (westward) led to their interpretation as two separate blocks tilted towards each other and being divided by a oblique strike-slip fault (Lisker et al. 2006). This idea has been adopted in this model, although a simple syncline without fault could also explain the observed shape of the sub-Beacon unconformity.

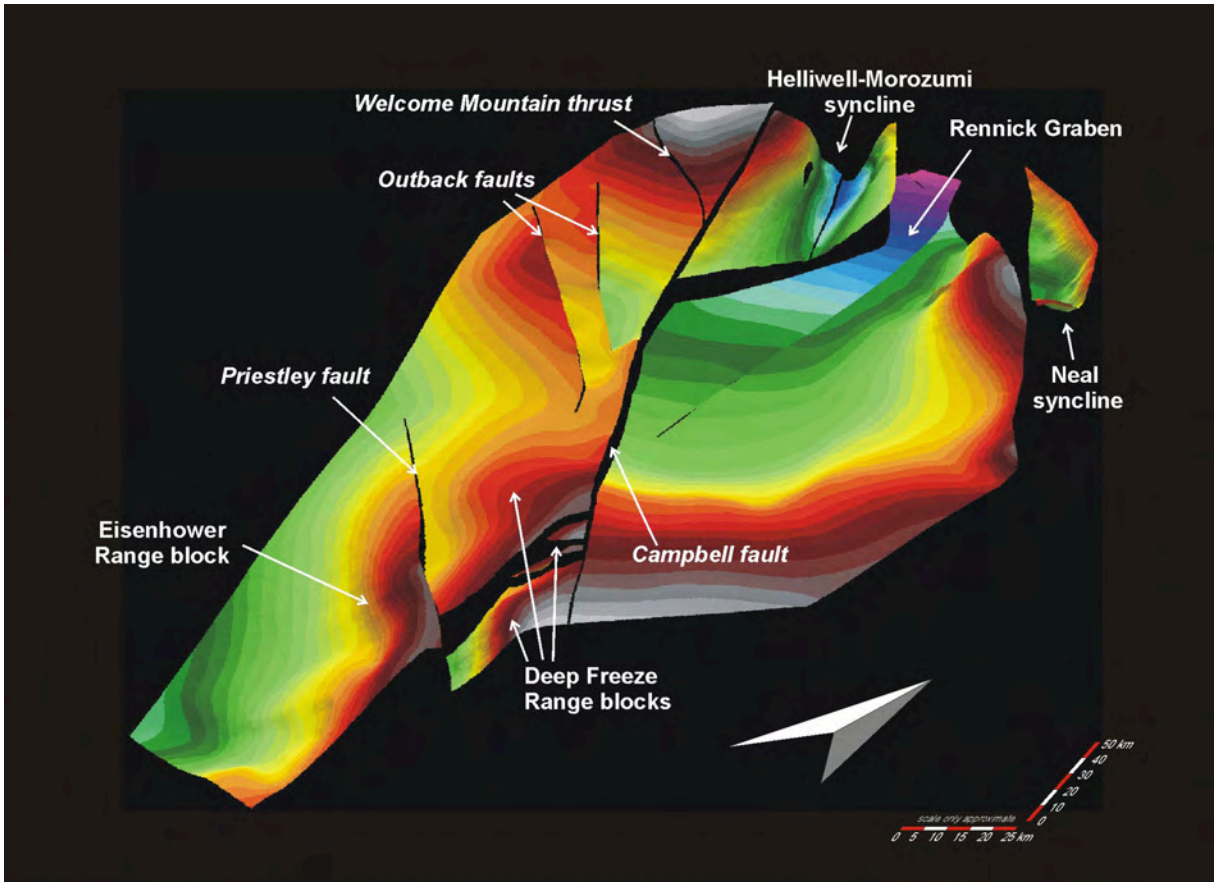


Fig. 2.10: A 3D visualization of the modelled sub-Beacon unconformity. Tectonic elements described in the text are labelled. Tenfold vertical exaggeration, view from the south-east. Colour chart as in Fig. 2.9.

## The Eisenhower Range block

The Eisenhower Range block is bounded in the north by the Priestley Glacier following the trace of the Priestley fault. Outside the modelled area, its southern boundary is set by the Reeves Glacier, presumably following a dextral strike-slip fault zone (Salvini and Storti 1999). To the west, the block dips gently under the Polar Plateau. The highest elevations of the sub-Beacon surface with more than 3000 m a.s.l. are reached in the northeast along the Priestley fault, and thus at the boundary to the neighbouring Deep Freeze Range blocks.

Immediately east of the Eisenhower Range the sub-Beacon surface is down faulted by a system of approximately north-south trending normal faults (Salvini and Storti 1999). Because only basement rocks are cropping out here, this area was not modelled.

A NW-SE directed dextral strike-slip fault, crossing the Eisenhower Range block, has been suggested by some authors (Salvini and Storti 1999; Storti et al. 2001). In the proposed scenario, the fault splits from and merges later again with the Priestley fault. It is not included into this model, because no evidence of a vertical displacement can be detected by using the sub-Beacon unconformity as a reference horizon.

The Deep Freeze Range blocks

In the Deep Freeze Range north of the Priestley glacier the sub-Beacon unconformity dips gently under the Polar Plateau. Thus the situation is comparable to the Eisenhower Range block described above. The highest elevations of the sub-Beacon surface are present in the south-eastern part of the DFR, with more than 3000 m above sea level.

A set of about N-S to NE-SW trending normal faults dissects the Deep Freeze Range forming smaller, downthrown puzzle pieces contrasting a larger block in the east. Along these faults, the strike-slip movement along the Campbell fault may overstep to the Priestley fault in the south (see Sect. 2.2.3).

The Neall syncline

Around the upper Black Glacier and the Neall Massiv northeast of the Salamander Range, Beacon sediments and Ferrar sills overlie basement rocks of the Bowers terrane. They form an apparently simple syncline cut in the southwest by the Lanterman Mariner Suture. This is the only known exposure of Beacon rocks outside the Wilson terrane (GANOVEX-Team 1987a).

## 2.2.2 The sub-Beacon unconformity relative to topography

### 2.2.2.1 Introduction

The difference of the sedimentary base to topography divides areas in which sediments may be preserved (if the difference is positive) from those where they have been eroded (if the difference is negative). It also indicates the possible thickness of preserved strata or the amount of erosion. However, as parts of the working area are covered by ice, the DEM used to calculate this map (GTOPO30) is not capable of reconstructing the rock surface. As a result, the actual rock surface position may lie well below the elevation given by the DEM. Thus, parts with a considerable ice cover may be shown as underlain by sediments, although this is actually not the case (e.g. under the Polar Plateau west of the Eisenhower and Deep Freeze Range).

Similarly, areas of Cenozoic magmatism may lie higher than the modelled base of the Beacon sediments. Hence, they appear to comprise sediments, although they may have been eroded already before the onset of magmatism (e.g. at the Berlin Dome and Deception Plateau). Small nunatak comprising Beacon rocks appear to lie below the sub-Beacon unconformity, because of the low resolution of the DEM (e.g. at Vulcan Hills).

### 2.2.2.2 Results

The result of calculating the difference between the modelled sub-Beacon unconformity and the topography is shown as map in Fig. 2.11. The relicts of the Beacon Supergroup are most complete in the Mesa Range and in the Rennick Graben, where they were downthrown and protected from erosion. Towards the Ross Sea, the amount of erosion increases as the sub-Beacon unconformity rises, and reaches more than 3000 m in places. However, a little distance outside the modelled area and approximately N-S trending, normal faults are present (e.g. Salvini et al. 1997), and no Beacon rocks are preserved, making it difficult to reconstruct the sub-Beacon unconformity. In this area, the amount of erosion becomes uncertain, although no indication for a further increase was found.

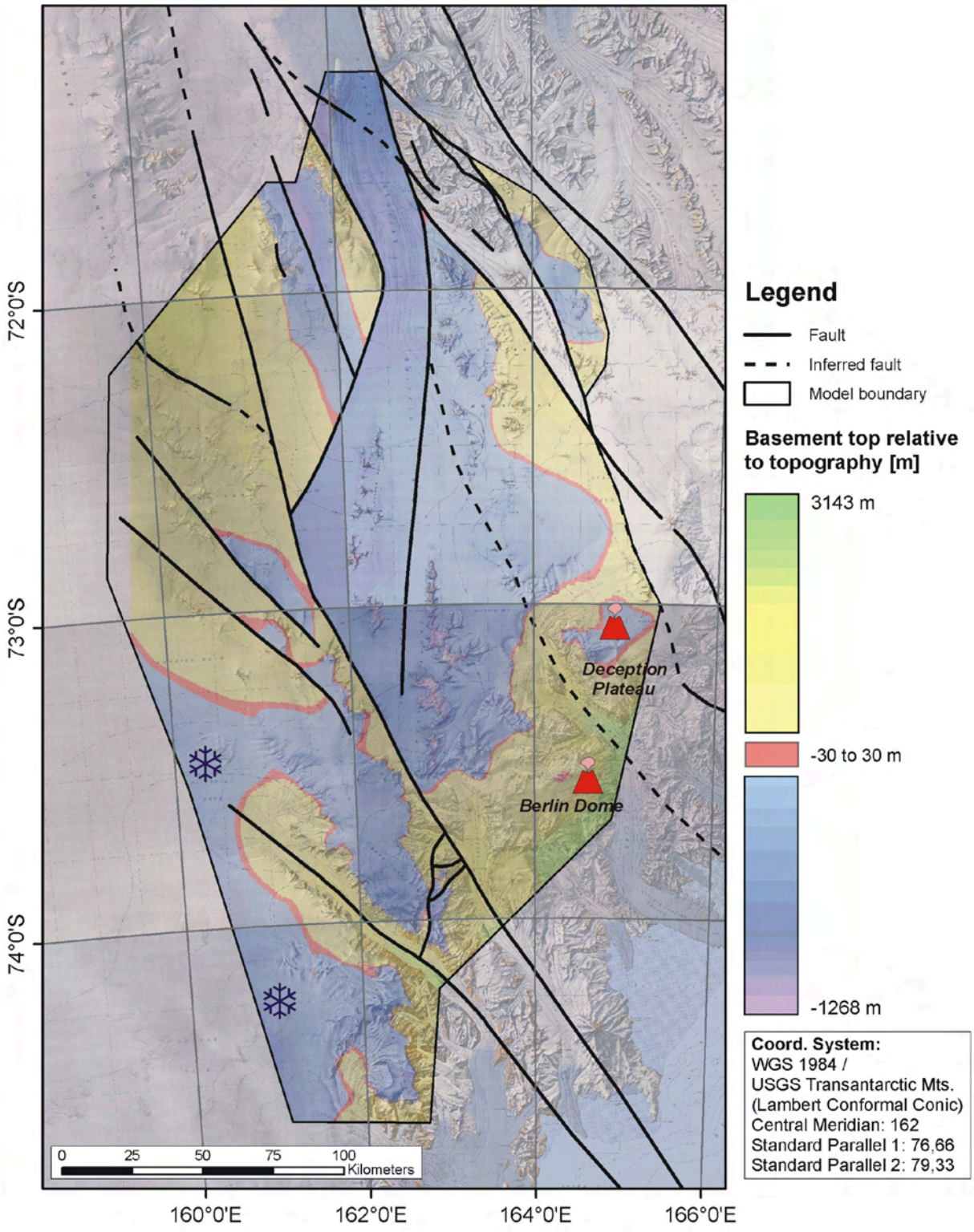


Fig. 2.11: Difference of the modelled sub-Beacon erosion surface and the topography. Yellow and green colours show areas where the modelled surface is higher than the topography, and Beacon sediments have been eroded. Regions, where both surfaces lie at approximately the same height (± 30 m), are marked in red, representing the position of the sedimentary base. In blue and purple areas are flagged, where the sedimentary base is lower than the topography. Beacon sediments may be preserved here; however, this is not always the case due to the presence of ice and younger Cenozoic volcanics. Those areas are marked by the little symbols.

## 2.2.3 Faults

### 2.2.3.1 Introduction

The interpretation of faults is based on the modelled sub-Beacon unconformity and on published (field) data and their interpretations. The relative orientation of the faults to each other was used to determine the structural processes leading to their formation. A dextral strike-slip regime was assumed from the results of many previous studies including field investigations (e.g. Lisker et al. 2006; Salvini et al. 1997; Salvini and Storti 1999; Storti et al. 2001).

### 2.2.3.2 Results

In the following, the most important faults are described. Their position is indicated in the 3D Figs. 2.9 and 2.10, and in the map of Fig. 2.12.

The Welcome Mountain thrust

The fault exposed at the Welcome Mountains has a NW-SE orientation and is interpreted as a thrust fault (Lisker et al. 2006). It is located within basement rocks, and Beacon sediments are missing here. Thus the displacement may also be pre-sedimentary, but as the thrust orientation is perpendicular to the tectonic transport during the Ross Orogeny, and similar to the post-sedimentary thrusts reported from other areas in NVL (e.g. in the Lanterman Range, or in the Rennick Graben), a younger age of the Welcome Mountain thrust is assumed. In Fig. 2.9 the Welcome Mountain thrust is not visible due to the view from the hanging wall side perpendicular to the fault.

The Outback faults (OF)

The Outback faults are two NW-SE trending faults. The maximal vertical displacement along the Outback faults is about 600 to 800 m for each of the fault. Along the faults, the vertical displacement becomes less towards the northwest and southeast. A strike-slip component of the faults cannot be excluded. The south-eastern end of the northern Outback fault ends relatively abrupt. Here a monocline, possibly as a result of an underlying growth fault, has been interpreted to account for the height difference between Myosotis Nunatak and Caudal Hills. Due to the strike similarly to the Welcome Mountains thrust an equally thrusting character but in opposite direction towards the NE can be assumed for the Outback faults.

The Priestley fault (PF)

The eastern sector of the Priestly fault, mainly lying outside the modelled area, has been described as a dextral strike-slip fault (Storti et al. 2001). Following the model presented here, an additional major vertical component must be assumed (see Fig. 2.7). About north to northeast of the Eisenhower Range and thus outside the modelled area, the Priestley fault splits up into several faults in a ‘principal displacement zone’, and transforms into a N-S trending extensional system that can be traced offshore into the Terror Rift (Storti et al. 2001).

While this eastern part of the Priestley fault runs parallel to the Campbell fault, the western parts shows a slightly different orientation, parallel to the Outback faults and the Welcome Mountain thrust. Therefore, this western part may be a thrust with a likely dextral strike-slip component. Apart from the orientation, there are no (field) indications for this hypothesis, but this may be due to the extensive erosion of the Priestley glacier.

The vertical displacement increases along the Priestley fault towards the southeast and reaches a maximum of about 1700 m. Offshore, the Priestley fault may merge with the Campbell fault (compare Salvini et al. 1997).

The Campbell fault (CF)

The Campbell fault can be traced through the entire modelled area, bounding the Rennick Graben in its southern segment. As it runs parallel to the eastern segment of the Priestley fault, an oblique dextral strike-slip movement can be assumed. The maximal vertical displacement is about 1300 m. It decreases to the southeast until it vanishes eastwards of the Deep Freeze Range. This implies a shift of the maximum strike-slip movements from the Campbell to the Priestley fault along an approximately N-S trending zone, crossing the Deep Freeze Range at Mt. Gibbs, and resulting in smaller scale faulting. This may either be interpreted as normal block faulting, or as a negative flower-structure, including minor strike-slip movements. A far offshore continuation of the Campbell fault seems rather unlikely. Instead, it may merge with the Priestley fault, which becomes increasingly important to the southeast.

In general, a set of about NW-SE to NNW-SSE trending faults is most obvious; they can be further traced offshore (e.g. Salvini et al. 1997). Their orientation is pre-defined by the Palaeozoic terrane boundaries (thrusts with tectonic transport to the NE) of the Ross Orogen. Many of these have been proved to be normal faults by field evidence, others have been proved to be thrusts; especially important in this case is the Welcome Mountain thrust within the modelled area (Lisker et al. 2006), other thrusts lie outside the modelled area (GANOVEX-Team 1987a). By analogy, the Outback fault and the Priestley fault, showing the same trend as the thrusts, are equally interpreted in this model as thrusts. This interpretation assumes a formation of these faults during the same tectonic event.

Many of the outlet glaciers flowing from the Polar Plateau towards the Ross Sea follow at least in parts the NW/NNW – SE/SSE direction (e.g. Priestley Glacier, Campbell Glacier, and Mariner Glacier). The Cenozoic magmatic activity does not show a clear spatial relationship to this trend.

In addition, a N-S to NE-SW oriented fault system is present, that becomes more important east of the modelled area towards and within the Ross Sea (Salvini et al. 1997; Storti et al. 2001). This system comprises normal faults that accommodate the horizontal displacement associated with the West Antarctic Rift System (WARS), and the opening of the Ross Sea (Salvini et al. 1997). The coastline from Victoria Land to the CTM follows this trend. Within the Ross Sea, the most important depositional troughs and highs are oriented roughly N-S (e.g. the Victoria Land Basin, the Central High, or the Terror Rift). Also, the extrusive and intrusive magmatic bodies of late Cenozoic age are aligned along this trend, both on- and offshore (GANOVEX-Team 1987a; GANOVEX-Team 1987b).

Some of the outlet glaciers flowing south-eastward towards the Ross Sea show a suspicious bend in N-S direction, parallel to the coast, before turning again and ending in the Ross Sea. Most intriguing examples are the Mariner and the Priestley Glacier. These bends can be associated with N-S aligned faults. The Campbell Glacier shows a similar bend, but this may possibly be related to the Cenozoic volcanism of the Mt. Melbourne, forcing the glacier to change its flow direction.

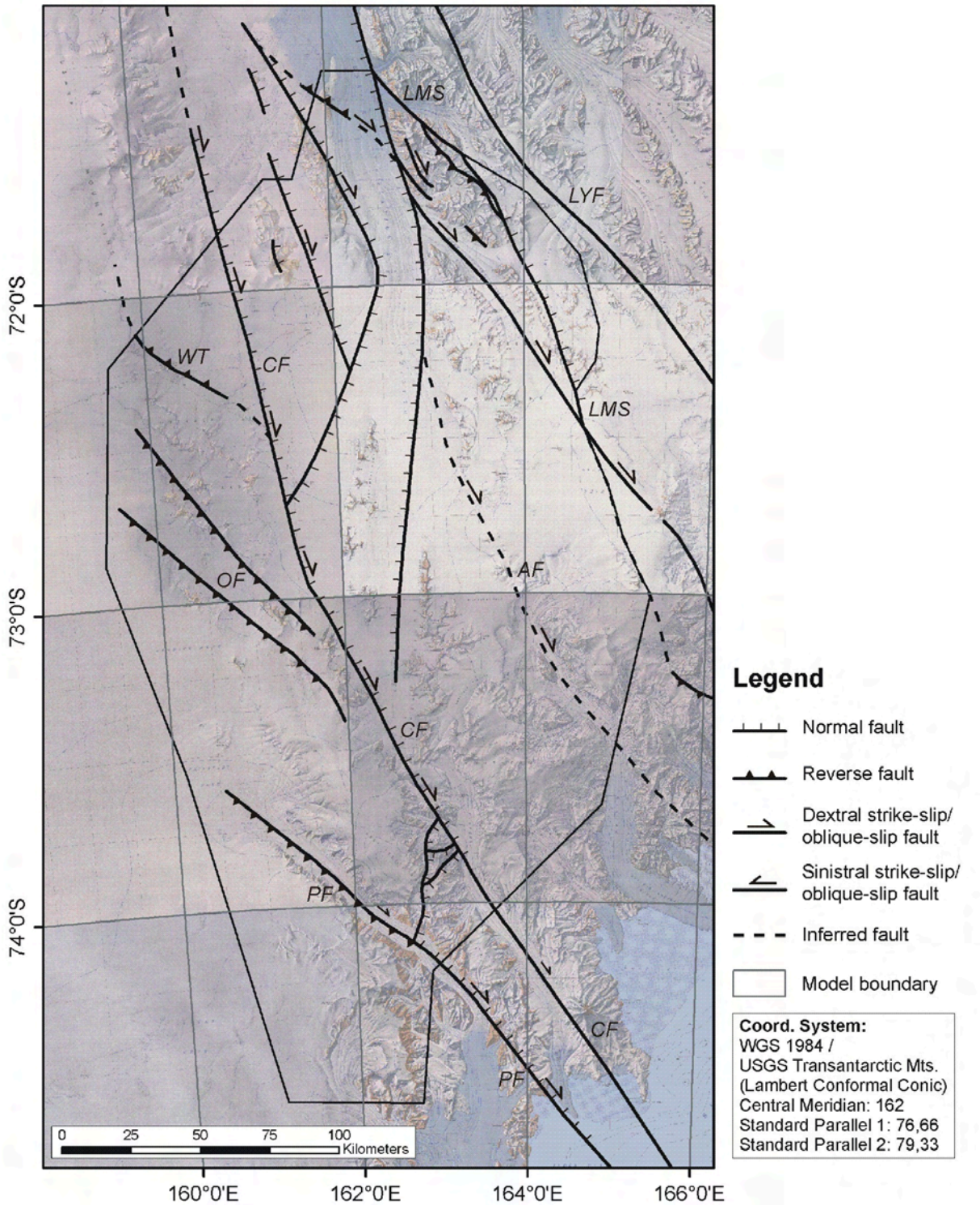


Fig. 2.12: Interpretation of the fault characteristics and the tectonic movement based on the modelled sub-Beacon unconformity and published data (explained in the text). AF: Aviator fault; CF: Campbell fault; LMS: Lanterman-Mariner suture; LYF: Leap-Year fault; OF: Outback faults; PF: Priestley fault; WT: Welcome Mountains thrust.

### 2.2.3.3 Estimation of horizontal displacement

The horizontal displacement $\mathbf{d_h}$ can be estimated from the vertical displacement $\mathbf{d_v}$ and the dip of the faults $\boldsymbol{\alpha}$ according to $\mathbf{d_h = d_v / \tan \alpha}$. For calculation, a fault dip of 60° was assumed for the normal faults. This calculation is only a first approximation, as displacement may also be accommodated by folding, or by shearing along diffuse structures. In addition, the dip of the

faults may vary. However, in this particular tectonic setting folding appears to be relatively unimportant. As most of the faults include strike-slip movements, they are unlikely to flatten towards the depth, but more likely to continue in a relatively steep angle.

The vertical displacement across the Rennick Graben along the Morozumi Range is about 2000 m at the western flank, and about 600 m at the eastern flank, resulting in a horizontal extension of about 1500 m. In the middle to southern part (Mesa Range) of the Rennick Graben, the vertical displacement is only about 1300 m at the western flank and 100 m at the eastern flank. Therefore the horizontal displacement is only 800 m in this area, and thus about 700 m smaller than in the north. These 700 m may have been accommodated along one or more strike-slip faults (e.g., the Aviator fault, see Fig. 2.12). Alternatively, a clockwise rotation of the north-eastern part of NVL relatively to the south-western part may also explain the observed discrepancy.

### 2.2.4 Indicators for syn-sedimentary faulting

#### 2.2.4.1 Introduction

The detection of syn-sedimentary tectonic movements is a basic prerequisite for the basin evolution, as discussed in Sect. 3. The Triassic and Early Jurassic parts of the Beacon sediments in NVL are preserved mainly in southern parts of the working area, where they were investigated and sampled during the GANOVEX IX in 2005/06. However, the Permian Beacon sediments from the northern part of the working area are not regarded in what follows.

#### 2.2.4.2 Results

To detect syn-sedimentary tectonic movements the comparison of the sedimentary thickness on two sides of a fault is helpful. This can be done in the Deep Freeze Range, where a normal fault divides sections SHS and SHA in the west from sections PT and MA in the east. Sediment thicknesses on both sides are similar, giving no evidence for fault activity during sedimentation. Other examples are the sections SHS/SHA and TI, separated by the Priestley fault, where the sediment thickness does not show remarkable differences again (R. Schöner 2009, pers. comm.). In general, the thickness of sedimentary strata is very thin (less than about 300 m) compared to the basin extension (at least 300 x 200 km), without evidence for locally higher values or strong variations. However, excellent outcrops are present only within the Deep Freeze Range, while elsewhere either the top (e.g. Eisenhower Range) or the base of the sediments (e.g. Mesa Range) is missing.

Palaeoflow directions give no evidence for syn-sedimentary fault activity as well. For example in sections SP and SPP, located close to the Campbell fault, palaeoflow was directed parallel to acute-angled to the fault strike, and not perpendicular, as would have been expected for the foot-wall of a fault-bounded half-graben.

## 2.3 Summary and interpretation

The displacement of the sub-Beacon unconformity is in concordance to the dextral strike-slip system in NVL already stated by previous authors. However, the Outback faults and the western segment of the Priestley fault have not been interpreted as thrusts before. If a formation of these faults during the same tectonic regime is assumed, this is a necessary conclusion drawn from the alignment of the proved thrusts and the derived regional stress field. Strike-slip movements appear to be overstepping from the Campbell fault to the Priestley fault along a N-S oriented zone crossing the Deep Freeze Range (possibly a negative flower-structure).

The fault pattern interpreted can be explained to be the result of the same tectonic regime, thus a stress field in NNE-SSW direction during the Late Cretaceous and Early Tertiary related to the rifting between Australia and Antarctica and to the opening of the Ross Sea. However, a formation of all structures during the same event is not necessary. Alternatively, a slight rotation of the stress field and formation of faults during two separate events could also explain the situation. A rotation of the stress field has been proved on a larger scale, from E-W extension in an early phase of Ross Sea rifting to a NW-SE extension later (see Fig. 2.1).

No evidence for syn-sedimentary fault movements during the sedimentation in the Triassic and Early Jurassic was found; accordingly, significant tectonic movements at faults considered in this study must at least be younger than the deposition of the Section Peak Formation. However, evidence for fault activity during Ferrar magmatism has been found in the southernmost Mesa Range, where sills and lavas of the Ferrar Group show a slightly increasing tilting towards the Campbell fault (L. Viereck-Götte 2008, pers. comm.). A rifting phase as suggested in earlier publications (Elliot 1992; Schmidt and Rowley 1986) can not be deduced from this observation alone, as much more distinct displacements are to be expected in this scenario.

# 3 Composition and provenance of the SPF

## 3.1 Introduction

The following part deals with the analysis of petrography and provenance of the Section Peak Formation (SPF) in NVL. The SPF represents the upper Triassic to lower Jurassic part of the 'Beacon sandstone' in NVL. It is correlated with similar sediments in SVL and the CTM and overlain by Early Jurassic mafic plateau lavas of the Ferrar large igneous province.

In general, sediments may record and preserve information about geology, geography, and the environmental conditions (climate, vegetation) of the region and the time they were deposited, as well as their source region. Therefore, the composition of sediments provides valuable information to reconstruct the geological history and evolution of a sedimentary basin. Sedimentary provenance is of particular importance in cases where the source region is inaccessible, does exist no longer, or was subject to substantial changes since the time of deposition. Possible causes therefore are, for instance, covering by younger sediments, or (plate) tectonic processes like orogenies.

Due to the cover of the Antarctic polar ice sheet, erosional processes or younger plate tectonic movements large parts of possible source areas of the 'Beacon'-sediments are not well known. Provenance analysis is a valuable tool to predict geological structure of those areas, and may additionally help to better understand the processes that were taking place along the Antarctic part of the Gondwana margin shortly before the break-up of this super-continent.

## 3.2 Petrography

### 3.2.1 Texture of sandstones and provenance of pebbles

#### 3.2.1.1 Texture of sandstones

The sandstones of the SPF are predominantly white to yellowish-grey and medium- to coarse-grained. Rounding and sorting ranges usually from 'moderately well' to 'poor'. Rounding and sphericity of (quartz) grains do not show any remarkable differences in the working area.

Although generally a reduction of grain size with increasing transport distance has been observed, it is not possible to determine a transport distance from grain-size for sand-sized material (Frings 2008). Reasons therefore may be different modes of transportation or the mineralogical composition.

#### 3.2.1.2 Lithology and provenance of pebbles

Pebbles are larger than sand-sized lithoclasts and therefore often easier to analyse. However, pebbles occur only locally and at the base of the SPF. In general, they are rarely found in higher stratigraphic levels. A comprehensive analysis of pebble lithology was therefore impossible, and the results may not be representative for the entire SPF.

A detailed description of the lithology of pebbles (and cobbles) is given by Schöner et al (in review). The conglomerates in the southernmost sections (TP, AG, ER) comprise mostly granitic rock fragments, quartz, grey slates, K-feldspar, and whitish fine grained igneous rocks (kaolinized rhyolite or aplite vein clasts). The cobbles reach a maximal diameter of about 15 cm, and may be derived locally from the Wilson terrane.

In sections AN and ST, pebbles are of metamorphic rocks. In AN, pebbles are mica-shists comprising biotite or chlorite, with chlorite indicating a low metamorphic grade. Pebble size in this section is less than 5 cm. In ST, amphibolite clasts are present, indicating a medium grade metamorphic source. Here also quartz pebbles occur. Maximal grain size is about 15 cm. As for the cobbles in the southern Eisenhower Range, local sources from the Wilson terrane are possible.

In contrast to sand-sized material, the size of the largest pebbles has been proved to correlate with the distance of their source (McBride and Picard 1987). However, this approach is limited by the regional geological (lithology, weathering intensity, etc.) and the local topographic situation (relief). It may therefore not give an exact result in other cases, but at least the order of magnitude of the transport length can expected to be reliable. Applying the formula of McBride and Picard (1987) to the largest clasts found in the SPF (about 15 cm) results in a distance of about 26 km. Regarding the uncertainties mentioned above, the source area for the basal sandstones in the southern Eisenhower Range and on Stewart Heights can be expected to be in the range of a few tens of km. This distance gives (at least for the cobbles) strong evidence for the Wilson terrane as source, supporting the information derived from lithology.

For all other sections, and for sandstones in higher stratigraphic ranges within the two areas mentioned, no distance information can be given, as pebbles are either absent or too small to expect a reliable result using this approach. However, a distance larger than the value given above may be obvious from the smaller grain size alone.

## 3.2.2 Light minerals and lithoclasts

### 3.2.2.1 Introduction

Light minerals and lithoclasts are by far the most abundant constituents of siliciclastic sandstones. Their occurrence and proportions are the most basic information for provenance studies.

### 3.2.2.2 Methods

In total, 108 thin sections of representative rock samples out of 16 sections throughout the working area were prepared. To this end, the rock samples were cut in cuboids of about 20 x 40 mm with a thickness of 10 mm perpendicular to bedding. They were imbued with blue coloured epoxy resin and leaved to dry and harden before being ground on one side with grinding powder (9 µm). This side was mounted on a polished glass slide with Araldite® before the largest part of the cuboids was finally removed and the remaining sample was ground with decreasing powder sizes (23 – 3 µm) to about 0.03 mm thickness. Thin sections chosen for mineral analytical purposes, were polished with 0.5 µm diamond abrasion paste.

After a semi-quantitative evaluation of all samples, 52 representative thin sections were chosen for point-count analysis. Point-counting was performed on a Zeiss Axioplan® stereomicroscope by determination of at least 300 counts each. The exact results are comprised in the appendix. To estimate the statistical error, the analysis was repeated in seven cases, revealing neglectable discrepancies (van der Plas and Tobi 1965).

In contrast to the method of Gazzi-Dickinson (Zuffa 1985), point-counting followed the classical way in order to obtain information stronger related to provenance itself. A mineral grain $> 63$ µm within a (poly-mineralic) aggregate was therefore counted as the aggregate it occurs in. Possible negative effects, as the limited comparability of results of sandstones with different grain sizes, or with geochemical data, were accepted. To minimize the impact of this well known problem, samples of similar grain sizes (medium grained, 0.2-0.63) were preferentially chosen for quantification.

Minerals and lithoclasts were classified according to the detailed description given in the following section. Contrary to earlier petrographic analyses of the sandstones of the SPF (Di Giulio et al. 1999), a more detailed classification of rock fragments was pursued. The clasts discriminated are listed in Tab. 3.1.

| | | | |
|---|---|---|---|
| Q | Quartz | L | Lithoclast |
| Qm | Monoquartz | Lt | Total lithoclast (incl. Qp) |
| Qp | Polyquartz | Lv | Volcanic lithoclast |
| $Qp_{2-3}$ | Polyquartz (2 or 3 subgrains) | Lvm | Mafic volcanic lithoclast |
| $Qp_{>3}$ | Polyquartz (> 3 subgrains) | Lvf | Felsic volcanic lithoclast |
| Qc | Chert | Lm | Metamorphic lithoclast |
| F | Feldspar | Lmm | Metamorphic lithoclast, mica-rich |
| Kf | Kalifeldspar | Lmq | Metamorphic lithoclast, quartz-rich |
| Mi | Microcline | Ls | Sedimentary lithoclast |
| Pl | Plagioclase | Lss | Sedimentary lithoclast, sandstone |
| Mi | Mica | Lsm | Sedimentary lithoclast, mudstone |
| Bi | Biotite | Lgr | Granitic rock fragments |
| Mu | Muscovite | Li | Illitic lithoclast |
| HM | Heavy mineral | Lu | Unknown rock fragment |
| Opq | Opaque mineral | | |

Tab. 3.1: Light minerals and lithoclasts discriminated in this study, and their abbreviations.

### 3.2.2.3 Description of light minerals and lithoclasts and possible source lithologies

The following list is based on various publications (e.g. Folk 1968; Von Eynatten 1996), tailored to the particular needs of the sandstones of the SPF. Photographs of the most common types can be found in the appendix.

Monoquartz (Qm)

This type comprises all monocrystalline quartz grains without inclusion or adhesion of another rock-indicative mineral, like biotite. Fluid inclusions (vacuoles) or inclusions / adhesions of non-rock-indicative minerals (e.g. opaque grains), were not regarded. The bulk of monoquartz in the SPF shows undulose extinction. However, as this property does not seem to be necessarily related to any certain rock type (Blatt, in Folk, 1980), it was not analysed in greater detail. The bulk of the grains may have a plutonic or high grade metamorphic source, but volcanic quartz grains with dissolution embayments have also been recorded. In general, a recycling of grains from older sediments can not be excluded.

Polyquartz (Qp)

Quartz grains with at least two subgrains, but without any other rock-indicative mineral, were attributed to this type. Two subgroups of polyquartz, with 2 or 3 subgrains ($Qp_{2-3}$) and more than three subgrains ($Qp_{>3}$), were distinguished. The latter are commonly found in low rank metamorphic gneisses or slates, especially if subgrains show oriented C-axes (Basu et al. 1975), while the former may also be of higher metamorphic grade or of magmatic origin.

Chert (Qc)

Subgrains of chert are usually smaller than 20 µm (microcrystalline). Impurities like clay minerals may be present. In some cases, chert can hardly be distinguished from quartz-rich felsic volcanic rock fragments, if the latter do not show any other mineral diagnostic for its origin, like biotite. Chert usually forms as sediment.

K-feldspar (Kf) and Microcline (Km)

K-feldspar may be confused with quartz grains, though it often shows cleavage and dissolution, or alteration features. The typical twinning of K-feldspar is often spaced too widely to be recognized in sand-sized grains. Microcline as sub-type of K-feldspar, can be easily identified due to its typical twinning feature. K-feldspar is a common constituent of felsic igneous and metamorphic rocks, microcline typically occurs in felsic plutonic rocks. Recycling from sedimentary rocks is possible, though less common than for quartz.

Plagioclase (Pl)

The characteristic plagioclase twinning is mostly closely spaced, thus plagioclase grains can be easily tagged. Due to its chemical composition plagioclase is less stable during weathering

than K-feldspar. Plagioclase typically occurs in mafic igneous and some metamorphic rocks. Due to its lower stability to weathering, recycling of plagioclase from older sedimentary rocks is unlikely.

Mica (Mi)
Micas are sub-classified in white muscovite (Mu) and dark biotite (Bi). They occur in magmatic, as well as in metamorphic rocks. Their sheet structure allows micas to be transported in suspension, thus the grains are less affected by mechanical abrasion. Due to its Fe-component, biotite is less resistant to weathering than muscovite and therefore usually less abundant in sediments.

Translucent heavy mineral (HM)
Although very frequent in few samples (placer), translucent (non-opaque) heavy minerals are usually too rare to be reliably analysed in thin sections by point-counting. However, as excellent provenance indicators, they were analysed separately (Sect. 3.3).

Opaque mineral (Opq)
Many of the opaque minerals are heavy minerals like magnetite, ilmenite, or pyrite. Although they carry information about provenance, they were not studied as detailed as the translucent heavy minerals, because of the greater effort needed for their identification.

Volcanic lithoclast (Lv)
Volcanic clasts have been divided into felsic (Lvf), mafic (Lvm) and vitreous fragments (Lvv). Especially the vitreous clasts are often altered or weathered or unidentifiable due to secondary minerals. Felsic clasts comprise quartz and K-feldspar, often as porphyric crystals, in a fine-crystalline ground mass. Mafic clasts are characterised by lath-like plagioclases, which in some cases exhibit preferential flow orientations. The groundmass is typically opaque due to secondary minerals, most likely replacing original Fe-/Mg-minerals, for instance pyroxenes.

Metamorphic lithoclast (Lm)
Metamorphic rock fragments were sub-classified in mica rich (Lmm) and quartz rich (Lmq) clasts. White mica is a common constituent of quartz-rich metamorphic clasts. With a preferential orientation of mineral axes, they may be distinguished from plutonic aggregates consisting of identical minerals. Transitions to poly-crystalline quartz grains ($Qp_{>3}$) are self-evident. Mica-rich clasts may comprise white mica, dark mica, chlorite, or quartz. Biotite and chlorite point towards a low grade metamorphic origin.

Sedimentary lithoclast (Ls)
Sedimentary lithoclasts comprise sand-, silt- and mudstones. The finer grained types may often be rip-up clasts, as they are unlikely to be transported over long distances. Sandstones and coarser siltstones usually contain quartz and feldspar, but all other types of minerals may also be present. Chert is counted separately.

Granitic lithoclast (Lgr)
All aggregates of quartz, feldspar, and possibly mica without preferential mineral orientation were attributed to this group. Due to the relatively large mineral size of plutonic rocks, point-counting results of sandstones with different grain sizes are very sensitive to this group.

Illitic lithoclast Li
Some lithoclasts have been considerably altered and only small illite flakes can be recognized. These clasts may have been clay-rich sedimentary or low grade metapelitic rocks once, possibly even fine-crystalline volcanic rocks. A classification to a certain rock type is therefore not possible.

Unknown rock fragments Lu

It was impossible to attribute all grains to one of the groups described above. Some grains were strongly weathered or just too small to be identified. In some sections, strong mechanical compaction has squeezed instable rock fragments to form pseudomatrix. Many of this group are probably of volcanic origin, but this could not be further verified.

### 3.2.2.4 Results

Following the QFL diagram for sandstone classification (McBride 1963), the SPF sandstones show considerable variations (Fig. 3.1, left panel). Many samples are lithic subarkoses to sublitharenites, but also (feldspathic) litharenites and lithic arkoses are present.

A comparable variation is shown by the Qm-F-Lt diagram for provenance determination (Dickinson 1985), where a quartzose and transitional recycled orogen is indicated as a dissected and transitional arc and a mixed source (Fig. 3.1, right panel).

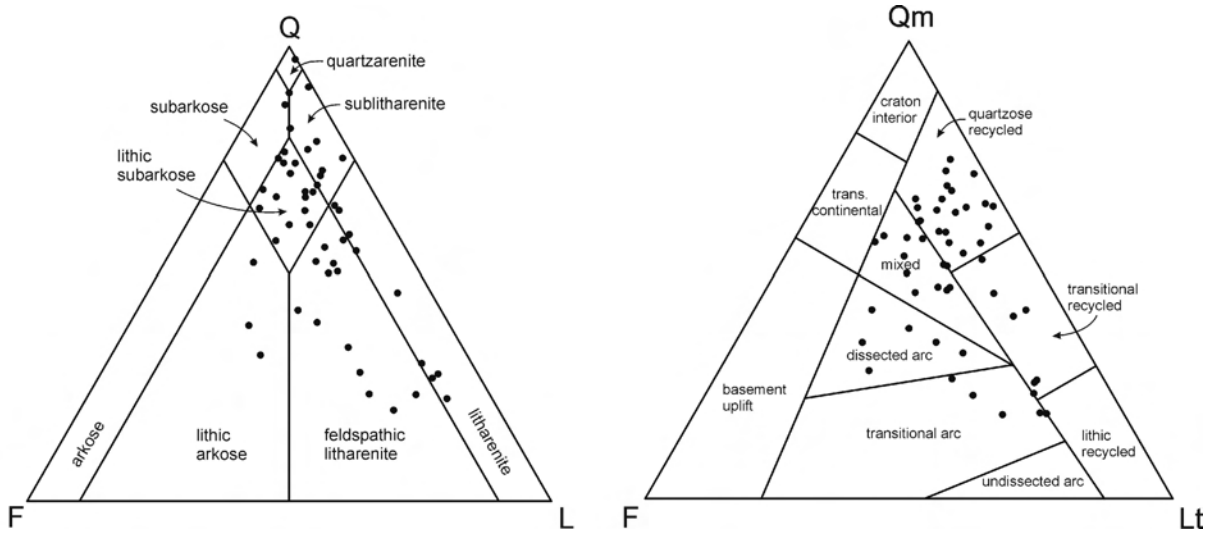


Fig. 3.1: Sandstone classification diagram (left panel, McBride 1963) and provenance diagram (right panel, Dickinson 1985) for the detrital mode of SPF sandstones. The samples scatter widely and no distinct single source can be identified. Instead, a mixing of various sources seems probable.

The most southerly sections (TP, AG, and ER) in the Eisenhower Range, comprise lithic (sub-)arkoses with large amounts of biotite (up to 16.5 % in sample TP05, see Fig. 3.2). On average the two southernmost sections TP and AG comprise more biotite than the section ER (up to 5 % in the latter). Many of these biotites are distinctly altered to a pale yellowish colour (see also Sect. 3.2.2.6). Nevertheless, they can be identified easily in thin sections. Lithoclasts and plagioclase are absent or very rare in these sections.

The section TI is located at the northern margin of the Eisenhower Range. In Fig. 3.3, the results of the petrography are presented along with those of section SR east of the Eisenhower Range. The sandstones of these two sections form two subgroups, (feldspatic) litharenites, and lithic subarkoses to feldspathic litharenites. Especially volcanic lithoclasts are frequent, and mafic volcanics with up to 20 % are more common than in other sandstones. Although metamorphic lithoclasts are present, garnet is rare. Less rigid volcanic clasts are often squeezed to form pseudomatrix. Porosity and intergranular volume (IGV) is generally low in these sandstones. Plagioclase has a share of about 20 % of the total feldspar content.

An exception is the uppermost part of section TI. In contrast to the other TI samples, quartz is much more abundant and garnet is the dominant heavy mineral. This sample resembles sandstones from the sections north of the Priestley Glacier described below.

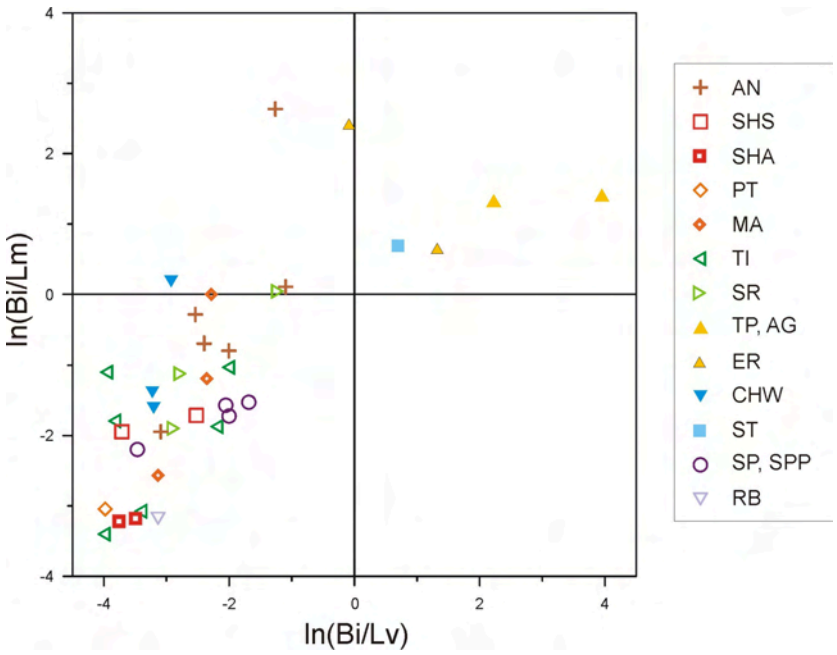


Fig. 3.2: Logratios of biotite relative to volcanic (X-axis) and metamorphic lithoclasts (Y-axis). Most samples plot in the lower left quadrant, thus containing less biotite than volcanic and metamorphic lithoclasts. However, this is not the case for the samples from the southern part of the Eisenhower Range (TP, AG, ER). Only exception is a sample from section ST, in which metamorphic and volcanic lithoclasts are extremely rare, thus the still rare biotite appears to be relatively frequent.

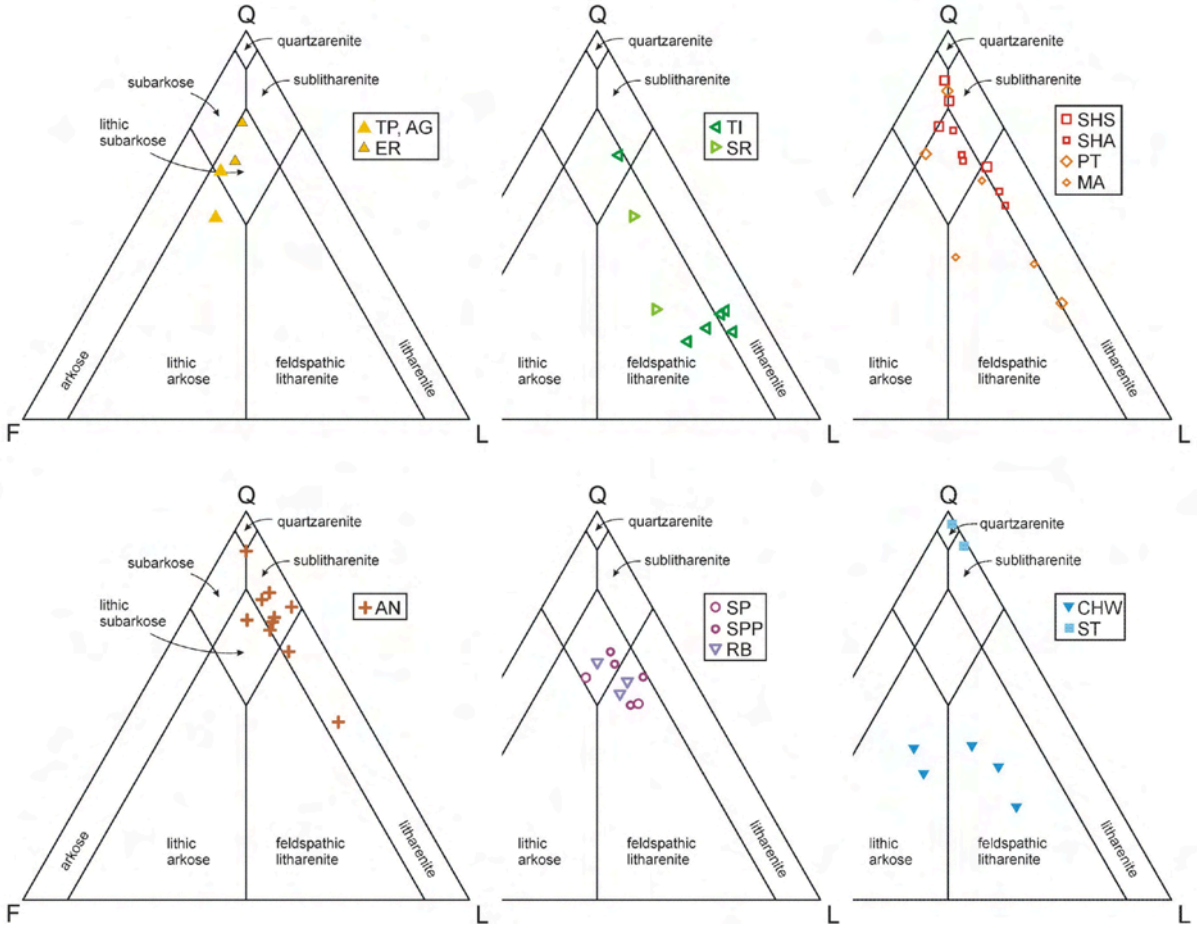


Fig. 3.3: Point-count data grouped by geographical relations. The location of the sections is shown in Fig. 3.4.

The four sections SHS, SHA, PT, and MA are lying not far away from each other in the Deep Freeze Range north of the Priestley glacier; their petrographic analysis is jointly summarized here. They cover different stratigraphic sections, with SHS and PT representing the base of the SPF, and SHA and MA representing the upper part. Point-counting data vary significantly (Fig. 3.3, upper right diagram). The base of PT (e.g. sample PT02) is formed by lithoclast-rich sandstones. At section SHS, sample SHS01 is similar rich in lithoclasts but additionally contains quartz grains clearly larger than the lithoclast-rich matrix.

Apart from these basal parts, all four sections are quartz-rich. Among these quartz rich samples, lithoclasts are generally more common than feldspars, with volcanic lithoclasts (felsic more than mafic) being the most prevalent group. On average, the fraction of volcanic lithoclasts is higher in the stratigraphic higher sections SHA and MA, compared with the stratigraphic lower sections SHS and PT. The same is true for the ratio of plagioclase to total feldspar. While this ratio is about 0 to 1 % in the lower stratigraphic parts, it increases to more than 20 % in higher parts.

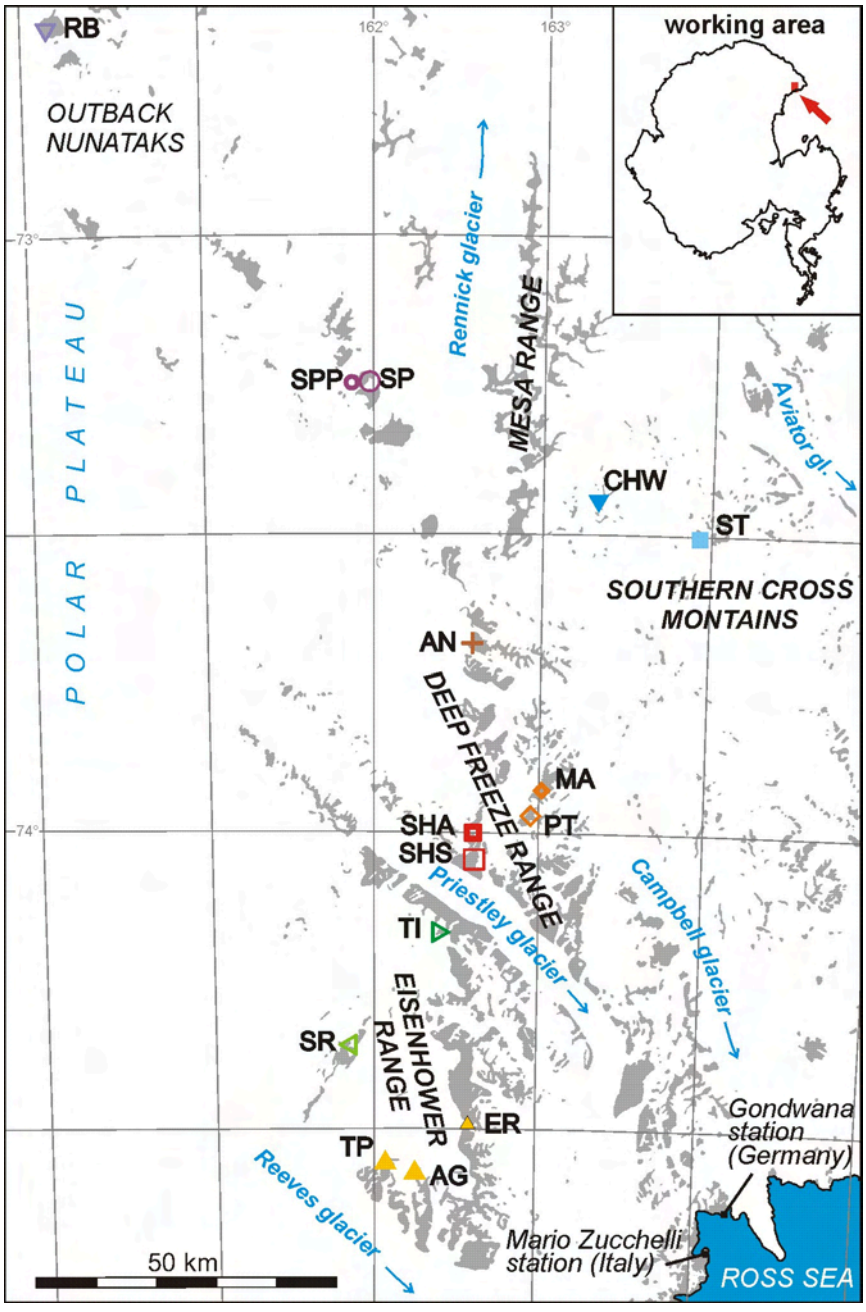


Fig. 3.4: Locations of the sections from which samples were quantitatively analysed. The symbols are the same as in Figs. 3.2 and 3.3, and in the following figures.

Section AN is located at the northern end of the Deep Freeze Range, close to the southern end of the Mesa Range. The composition of the sandstones is less variable compared to the southerly sections of the Deep Freeze Range, but only the basal 60 m of the SPF are exposed. In the QFL diagram, the AN sandstones are clustering in or around the field 'sublitharenite' (Fig. 3.3). An obvious exception is the stratigraphically highest sample AN18, which contains more lithoclasts and is classified as litharenite. Although strongly affected by diagenetic alteration, this sample resembles the lithoclast rich samples of the lower TI section, described above. Altered biotites, reported from sections PT, AG, and ER above, occur only in the lowermost sample (AN01a) to a notable extent. As in the southern Deep Freeze Range, in the quartz rich samples the proportion of plagioclase relative to total feldspar increases slightly towards the uppermost samples.

The sandstones in the north-eastern sections SP, SPP, and RB in the Outback Nunataks, exhibit similar compositions as the samples from the Deep Freeze Range, though slightly more lithoclasts and feldspar have been found. Felsic volcanics are the most abundant lithoclasts. The compositional variation of samples from these sections is relatively low, and all samples can be classified as lithic subarkoses to feldspathic litharenites. Plagioclase content relative to total feldspar is low in the lower stratigraphic part (section SP: 0-2 %), and higher in the upper stratigraphic part (section SPP: 6-9 %). In section RB, the plagioclase content is between 4 and 13 %.

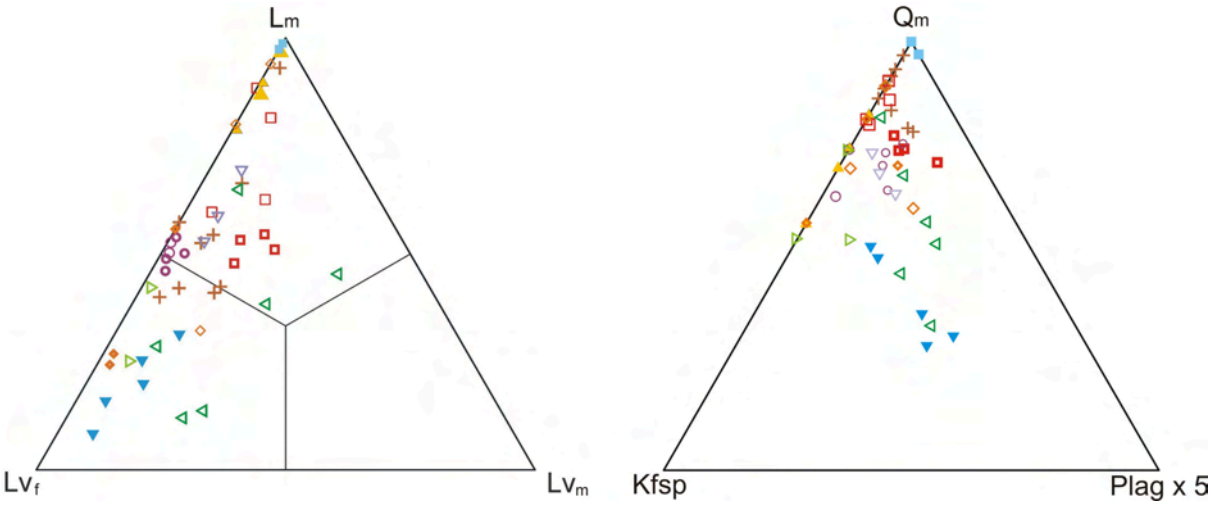


Fig. 3.5: The ternary diagrams Lm-Lvf-Lvm (left panel) and Q-Kfsp-Plagx5 (right panel). Mafic lithoclasts are generally rare, but more abundant in samples from section TI. In CHW samples, felsic volcanics are relatively frequent, while in samples from sections TP, AG, ER, or ST, metamorphic lithoclasts are relatively abundant. As plagioclase is rare, for a better visualization, its proportion was increased fivefold. Lithoclast rich samples (sections TI and CHW) show the largest fraction of plagioclase. Legend as in Fig. 3.2.

Sections ST and CHW are located north-west of the Deep Freeze Range in the Southern Cross Mountains, with the former comprising the lower, and the latter an upper stratigraphic interval of the SPF. Considerable differences exist between both sections. The only quartz-arenites within the SPF were found in section ST, grading upward into sublitharenites. Feldspar is very rare to absent in samples from this section.

In contrast, the sandstones of the section CHW contain high abundances of both, K-feldspar and plagioclase. Predominantly felsic, but also mafic volcanic lithoclasts are frequent. Metamorphic rock fragments are less common than in sandstones from section TI (Fig. 3.5). Plagioclase contributes about 8 to more than 20 % to the total amount of feldspar.

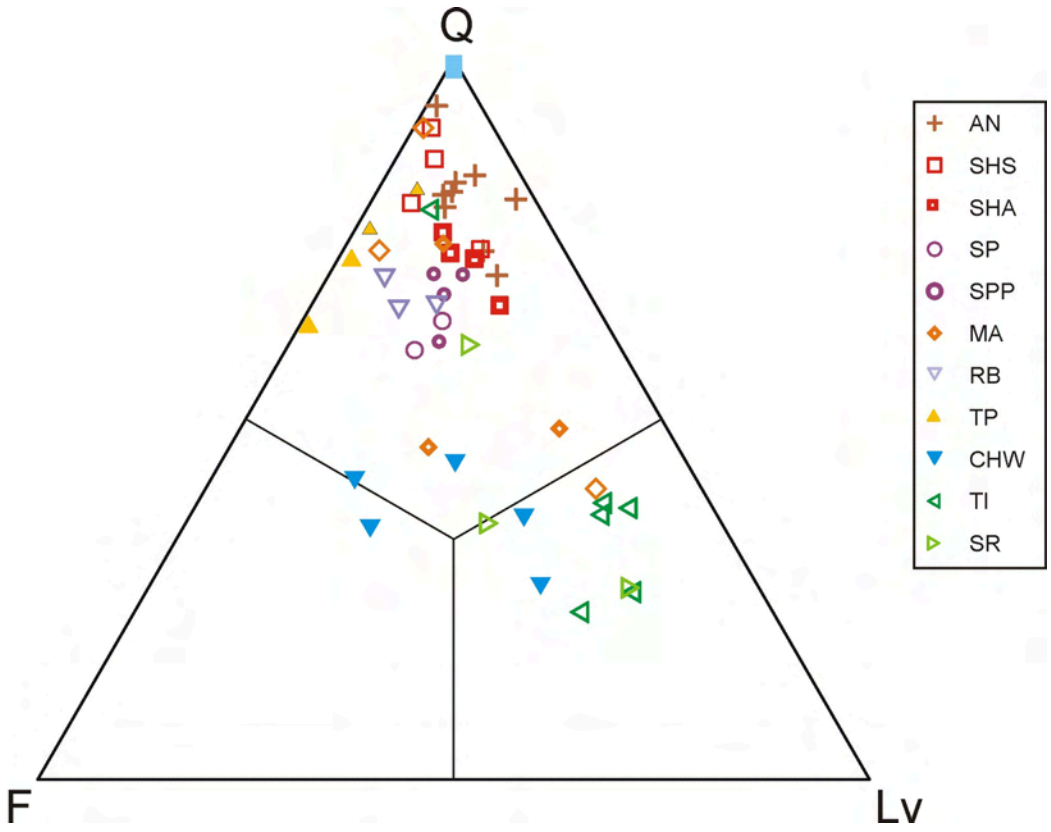


Fig. 3.6: Q-F-Lv ternary diagram for sandstone discrimination. Two sample groups are obvious: a quartz richer group on the top, and a group richer in feldspar and volcanic lithoclasts below.

### 3.2.2.5 Altered biotite as an indicator mineral

As stated above, in some samples distinctly altered biotites are present. These altered biotites are pale yellowish in thin section with low birefringence, but can clearly be identified as originally biotites (e.g. by shape and cleavage). Electron microprobe analysis (EMP) revealed alkali (earth) metals to be very rare, and Si and Al as only noteworthy constituents in about equal proportions, thus pointing to halloysite or kaolinite as alteration product (e.g. Kretzschmar et al. 1997), forming pseudomorphs after biotite.

Biotite pseudomorphs are present in sections in the Eisenhower Range and in some sections in the Deep Freeze Range, while they have not been found in the northern working area. They are most frequent in the Eisenhower Range. In the southerly sections AG and TP, they account for up to 17 % (point-counting data). In samples of section ER, they reach up to 5 %, and in section SR up to 8 %. In other sections, they only have been detected sporadically, for example in section TI (TI11, c. 5 %), in section AN (AN01a, c. 4 %; AN16, c. 0.7 %), or section SHS (SHS04-16, c. 0.3 %).

## 3.2.3 Heavy minerals

### 3.2.3.1 Introduction

Heavy mineral analysis is a very sensitive technique for determining provenance and therefore widely used. By definition, the density of heavy minerals is larger than about 2.9 g/cm$^3$. They usually occur as accessory minerals only, making special separation necessary before an analysis is possible. Many heavy minerals can be attributed to a certain source lithology, making them excellent indicator minerals. However, besides mineralogy of the parent rocks, a large variety of control mechanisms exist for the heavy mineral assemblage in sandstones, of which physical sorting, mechanical abrasion and dissolution are the most important ones (Morton and Hallsworth 1999). A naive use of heavy mineral compositions of sandstones may result in erroneous conclusions. For example, the fraction of volcanic source rocks may be underestimated, because the grain size of their heavy mineral fraction may be too small for sand sized samples. Although opaque heavy minerals have proved to be valuable for provenance determination in some cases (e.g. Grigsby 1990), they were not analysed in detail here. The focus was set on translucent heavy minerals instead, as these can be identified more easily by means of optical methods.

The exact order of succession of resistance to mechanical and chemical abrasion is under debate. However, the classification of the most common non-opaque heavy minerals as shown in Tab. 3.2 is widely accepted in literature (e.g. Boenigk 1983; Mange and Maurer 1991).

| Mineral / Mineral group | Density [g/cm$^3$] | Mohs hardn. | Igneous rocks | | | Metamorphic rocks | | | Sed. Rocks (recycled) |
|---|---|---|---|---|---|---|---|---|---|
| | | | Mafic | inter. | felsic | low | med. | high | |
| Very resistant: | | | | | | | | | |
| Zircon | 4.60–4.79 | 7,5 | | x | x | x | x | x | x |
| Tourmaline | 3.00–3.25 | 6.5 – 7 | | | x | x | x | | x |
| Rutile | 4.23–5.50 | 6 – 6.5 | | (x) | | (x) | x | x | x |
| Resistant: | | | | | | | | | |
| Apatite | 3.1–3.35 | 5 | (x) | x | x | x | x | | x |
| Spinel | 3.55–5.09 | 7.5 - 8 | x | | | (x) | (x) | (x) | x |
| Garnet | 3.4–4.3 | 6.5 – 7 | | | (x) | (x) | x | x | x |
| Staurolite | 3.74–3.83 | 7 – 7.5 | | | | | x | | x |
| Moderately res.: | | | | | | | | | |
| Sphene | 3.45–3.55 | 5 – 5.5 | | x | x | x | x | | (x) |
| Kyanite | 3.53–3.65 | 4.5 / 7 | | | | | x | x | (x) |
| Epidote | 3.38–3.49 | 6 – 7 | | | | x | | | (x) |
| Poorly resistant: | | | | | | | | | |
| Andalusite | 3.13–3.16 | 6 – 7.5 | | | | x | | | |
| Sillimanite | 3.23–3.27 | 6 – 7 | | | | | | x | |
| Amphibole | 2.85–3.57 | 5 – 6 | | x | | x | x | x | |
| Non resistant: | | | | | | | | | |
| Pyroxene | 2.96–3.96 | 5 – 6 | x | x | (x) | | (x) | x | |
| Olivine | 3.22–4.39 | 6.5 – 7 | x | | | | | | |
| For comparison: | | | | | | | | | |
| Quartz | 2.65 | 7 | (x) | x | x | x | x | x | x |
| Feldspar | 2.53-2.76 | 6 – 6.5 | x | x | x | x | x | x | (x) |

Tab. 3.2: Summary of the most important heavy minerals ranked by resistance and possible source rocks (Mange and Maurer 1991). The most abundant light minerals quartz and feldspar are shown for comparison. Metamorphic rocks include para- and ortho-metamorphic rocks, as well as metasomatic rocks. Mafic igneous rocks include ultra-mafics. No discrimination between extrusive and intrusive igneous rocks has been made.

### 3.2.3.2 Methods

For heavy mineral separation, 24 sandstone samples were crushed and carefully disintegrated using 10 % acetic acid. The size fraction of 63-125 µm was separated with sieves, and heavy minerals with a density of more than 2.9 g/cm$^3$ were cut off using heavy liquid sodium polytungstate ($3Na•2WO_4•9WO_3•H_2O$). After repeated washing, a portion of the separates were mounted between two glass slides using Meltmount 1.660®. Additional 12 samples were mounted on a glass slide with Araldite® and polished for further mineral chemical analyses (see Sect. 3.4).

Heavy mineral analysis and counting was performed on 23 out of the 25 samples with an optical polarization microscope Zeiss Axioplan®, using the ribbon counting method. In two mounts (both from section AN), too many minerals were encrusted with Fe-oxides and thus they were excluded from the analysis. At least 200 non-opaque minerals were counted in order to keep statistical error small (Mange and Maurer 1991; Von Eynatten 1996). In samples with high garnet abundances (up to 80 %), more than 300 minerals (on average about 350) have been counted to include enough grains of the other mineral species into the statistical analysis.

For the study of zircon morphology, 17 heavy mineral samples have been analysed optically, to reveal possible zircon sources and changes between or within various sections. The zircons were classified as ‘elongated’, with a length:width ratio of more than two, and as ‘compact’otherwise. Additionally, the zircons were classified as ‘roundish’, ‘subroundish’, ‘edgy’ and ‘irregular’. Common terms as for example ‘rounded’ or ‘angular’ were avoided, as they already imply sedimentary processes (transport, abrasion) that have not necessarily taken place, as ‘roundish’ zircons can form already primary in case of polyhedral growth and regular arrangement (e.g. Wu and Zheng 2004). For the same reason, crystallographic terms as ‘idiomorphic’ were avoided and the term ‘edgy’ used instead for zircons with an obvious (hyp-)idiomorphic structure, mainly with pyramid faces of the (101) or (301) type (Pupin 1980). Angular crystals without crystallographic planes were classified as ‘irregular’, as were aggregates, too. Subgroups for broken grains were also counted. In general, it is unclear if a ‘breakage’ occurred during sample preparation, or resembles in fact imperfect crystallisation (Larsen and Poldervaart 1957).

### 3.2.3.3 Description of heavy minerals and possible source lithologies

The most common translucent heavy minerals and mineral groups, regarded in this study, are described in the following. More detailed descriptions of heavy minerals can be found in standard references (e.g. Boenigk 1983; Mange and Maurer 1991).

Zircon (zrn)

Zircon typically forms in intermediate to felsic magmas, but can also occur in pegmatites. Due to its extreme resistance to mechanical and chemical abrasion, it is very frequent in both, sediments and meta-sediments (Mange and Maurer 1991). Sedimentary recycling and mineral overgrowth during metamorphosis is a typical feature, resulting in complex zonations.

zircons are usually uncoloured, although they may be yellowish, brownish, or pinkish. They can be distinguished from other heavy minerals by a high relief and a high birefringence. Pegmatitic zircons often are elongated due to special growth conditions. Inclusions are frequent, as are cracks due to radioactive elements (e.g. uranium, thorium), substituting zirconium in the crystal structure.

The radioactive elements found primarily in the zircon crystal lattice are the basis for (U-Pb) isotope age studies, as presented in Sect. 3.5 for detrital zircons within the SPF. In addition, juvenile magmatic zircons from a tuffaceous sandstone were analysed (Sect. 4).

Tourmaline (tou)
Tourmaline is common in some types of granite, granitic pegmatites, and pneumatolytic veins. It also occurs in a variety of metamorphic rocks. Authigenic rims can form during diagenesis. Due to their extraordinary high resistance to mechanical and chemical abrasion, tourmaline is a common heavy mineral in sandstones (Mange and Maurer 1991).

Due to recycling, tourmaline is often roundish, but can also exhibit a more idiomorphic, angular shape. It can show almost black (Fe-rich) to blue, green, brownish, or yellow colour. Typically pleochroism is very strong and cleavage is not visible. Refraction is slightly lower than that of Meltmount 1.660®.

Rutile (rtl)
Rutile is the most abundant among the three $TiO_2$ minerals (anatase, brookite). It forms prevailingly in metapelites or metabasites of medium to high metamorphic grade (Force 1980). Subordinately, rutile occurs in magmatic rocks as well, but in this case it is mostly too fine-grained or too sparse to be found in sand-sized sediments (Force 1980). Trace elements (e.g. Zr, Nb) in rutile can be used as a provenance indicators (Triebold et al. 2007; Zack et al. 2004b) or geothermometer (Zack et al. 2004a). Rutile can easily be identified by means of optical methods, due to its unique reddish-brown colour, its high relief, and its extremely high birefringence. It is extremely stable to chemical and physical abrasion.

The three minerals zircon, tourmaline and rutile show similar high resistance to abrasion and their proportion of the translucent heavy minerals (ZTR ratio) is therefore used as indicator of sediment maturity (Hubert 1962).

Garnet (grt)
Garnet is a cubic mineral group with various end members, and a common constituent of metamorphic rocks, rarely occurring also in magmatic rocks (Deer et al. 1982). It is mechanically stable (no cleavage), and therefore a common heavy mineral in sandstones. Although it is chemically unstable under acid conditions during diagenesis, it is still more resistant than apatite. Therefore, in the presence of apatite, dissolution of garnet is unlikely (Morton 1985).

The end members of the garnet group can hardly be determined under the microscope. Most end members are isotropic and can not be distinguished with optical methods. Only grossular shows a weak birefringence. Garnets are often roundish close to their idiomorphic shapes.

Cr-spinel (chr)
Primary Cr-spinel is almost exclusively restricted to ultramafic rocks (ophiolites), where it occurs as accessory mineral (Pober and Faupl 1988). Locally, it can also be present in primitive basalts, too (Von Eynatten 1996). It is chemically and physically sufficiently stable to be found in sand and sandstones. Even a recycling from older sediments is possible. Due to its restricted and characteristic origin, Cr-spinel is an excellent indicator mineral and widely used for provenance analysis, especially for reconstructions of orogenic processes (Zimmerle 1984). As other characteristic minerals of ultramafic rocks, like olivine or pyroxene, are much less resistant to weathering and transport, Cr-spinel often offers the only possibility to record ophiolitic material in the source area.

Cr-spinel is a cubic mineral and therefore one of the rare isotropic heavy minerals. Unlike garnet, its colour is of a deep red to reddish brown. Grains are often roundish reflecting the originally idiomorphic mineral shape (Mange and Maurer 1991).

In case of the SPF, the Cr-spinels do not show their usual distinctive colour, but are opaque and therefore not to be identified in regular heavy mineral mounts. Their fractions have been estimated from polished heavy mineral mounts. The reason for their opaquity remains unclear, but may be related to an oxidised ferric crust.

Epidote group minerals (ep)
Beside its typical occurrence in low grade metamorphic rocks, epidote occurs subordinately in veins and in zones of contact-metamorphism (Mange and Maurer 1991). Epidote is characterised by a high relief and green to yellowish-green colour. Very few clinozoisites have also been found, but not separately analysed.

Apatite (apa)
Apatite occurs in a variety of settings and its occurrence can therefore hardly be used for provenance determination. A variety of different igneous, hydrothermal and metamorphic rocks can host apatites, but it can form authigenic in sediments. It is unstable under acid diagenetic conditions (Deer et al. 1992).

Apatite is clear to yellowish, often hexagonal shaped or rounded. Its relief and birefringence is low, and inclusions can be common. Its refraction index is slightly lower than that of Meltmount 1.660®. In some samples of the SPF, beside typical apatites, other varieties are present, in which opaque minerals seem to have formed diagenetically within, or partly instead, of apatite. Thus, a great variety of 'altered' apatite exists, ranging from minerals with small opaque inclusions to opaque minerals with apatite only visible on edges. In some cases it remained unclear, if apatite has additionally formed authigenic during diagenesis.

Amphiboles (am)
Amphiboles are common in a variety of source rocks, with metamorphic rocks of low to medium grade among the most typical ones. However, they may occur in magmatic rocks of variable chemistry as well (Mange and Maurer 1991), for example in andesites.

Typical optical features are pleochroitic greenish to brownish colours and their cleavage. Blue sodic amphiboles are of special interest for reconstruction of plate tectonic and orogenic processes due to their restriction to high-pressure metamorphic rocks, typical for subduction zones (e.g. Mange-Rajetzky and Oberhänsli 1982; Till 1992; Winkler and Bernoulli 1986).

Other heavy minerals (oth)
Beside the heavy minerals described above, other minerals were occasionally found, such as sphene, kyanite or monazite. They were too rare for a detailed statistical analysis.

Unknown and altered heavy minerals (alt)
Altered and therefore unidentifiable as well as unknown heavy minerals were classified as unknown and altered heavy minerals. Their fraction depends mainly on the presence of hematitic crusts on grain surfaces.

#### 3.2.3.4 Results

The results of the heavy mineral analysis are visualized as bar plots in Fig 3.7. The exact assemblages of all samples are displayed in the appendix.

Sandstones from the southernmost sections TP and ER in the Eisenhower Range are rich in zircon, tourmaline, and apatite, but poor in typically metamorphic heavy minerals (e.g. garnet, rutile). Sample TP03 from does not contain garnet or rutile at all, while these minerals are present in the stratigraphically slightly higher samples from section ER (up to 5 %). The very frequent tourmaline (22-35 %) may be derived from granitoids or pegmatites. The ZTR ratio of these sandstones varies between 46 and 59. Apatite as a typical mineral of granitic rocks reaches about 30 % in all three samples. In sample ER04 a single Cr-spinel has been found. Cr-spinel occurs in ultra-mafic rocks along a suture within the underlying Ross Orogen (for a detailed discussion see Sect. 3.4).

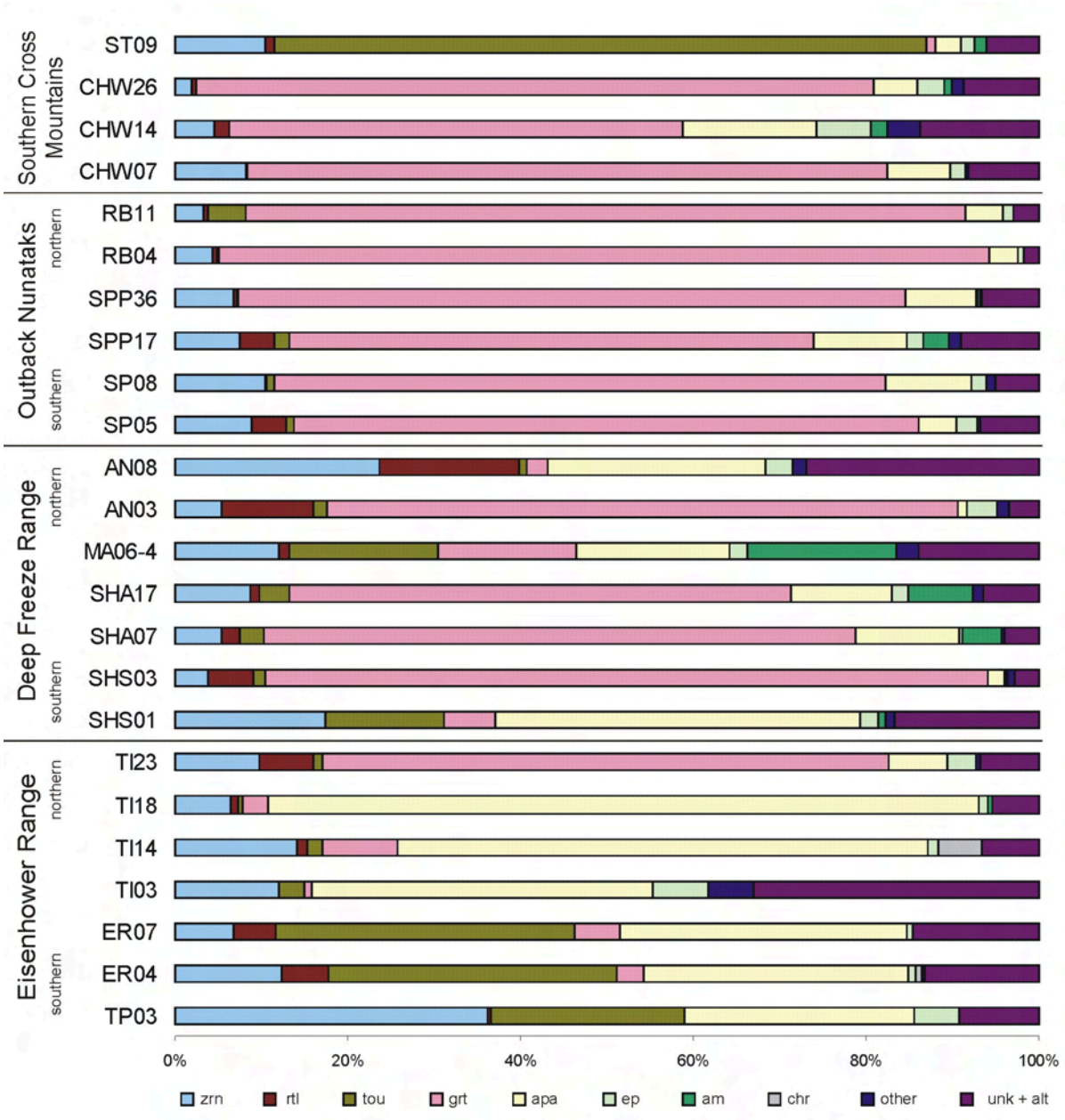


Fig. 3.7: The translucent heavy mineral suites of SPF sandstones ordered by location. In many samples, garnet is abundant. Other samples contain few or no garnet, but a great proportion of tourmaline or apatite instead. These three minerals are used in Fig. 3.8 to discriminate between the samples.

The heavy mineral assemblages of samples from the Timber Peak at the northern margin of the Eisenhower Range can be divided into two groups. The lower three samples (TI03, TI14, and TI18) are dominated by apatite (39 to more than 80 %). The metamorphic mineral garnet reaches less than 10 % in these samples. Rutile and tourmaline are rare (about 1 to maximal 3 %). The ZTR ratio varies between 8 and 17. As in sample ER04 described above, in sample TI14 Cr-spinel occurs, reaching about 5 %. This value was estimated from a polished heavy mineral concentrate due to the opaque crusts described above.

Sample TI23 from the uppermost part of section Timber Peak shows a different heavy mineral assemblage. Garnet is the most abundant constituent, reaching 66 % and therefore much more than in the samples from the underlying sandstones. Apatite on the other hand is much less frequent in this sample (7 %). The ZTR ratio of this sample is 17.

North of the Priestley Glacier, opposite of the Timber Peak and within the southern Deep Freeze Range, sections SHS and SHA are located relatively closely nearby. In sample SHS01, apatite is abundant (42 %); zircon (17 %) and tourmaline (14 %) are less frequent, and garnet is rare (6 %). This composition resembles the samples from the Timber Peak (except TI23), although the ZTR ratio is 31 and therefore somewhat higher.

In sample SHS03, SHA07, and SHA17, the heavy mineral spectra are similar to each other. Garnet as most abundant heavy mineral reaches 58 to 84 %. Apatite (2-12 %) and zircon (4-9 %) are less frequent and rutile and tourmaline are rare (less than 5 %). The ZTR ratio is between 10 and 13. In sample SHA07, and even more pronounced in sample SHA17, greenish-brownish amphiboles are present (3 and 8 %, respectively). The dominance of garnet resembles sample TI23 from the uppermost Timber Peak section.

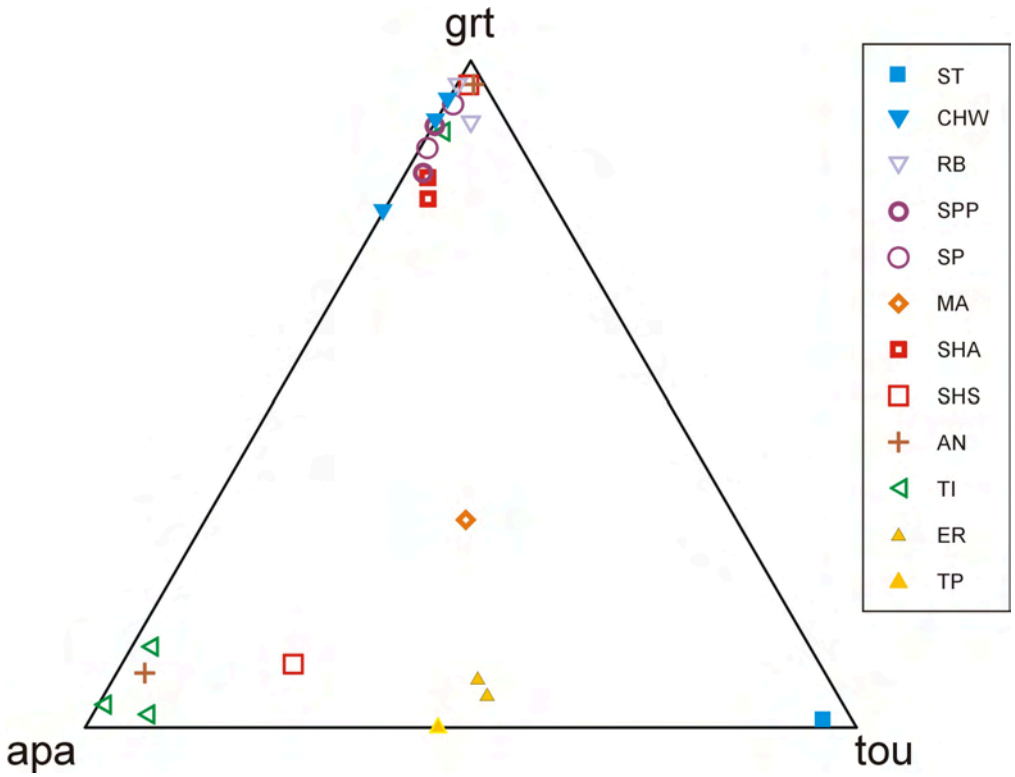


Fig. 3.8: Heavy mineral assemblages for all analysed samples in a tourmaline-garnet-apatite ternary diagram. The garnet dominated samples are most frequent. For locations of the sections see Fig 3.4.

Similar to the samples from SHA, in sample MA06-4 from the uppermost part of section Mount Adamson, greenish-brownish amphiboles (17 %) are present. The garnet content is only 16 %, but tourmaline (17 %) and zircon (12 %) are more frequent than in the samples from section SHA. The ZTR ratio is 30.

Section AN is located in the northern part of the Deep Freeze Range. Sample AN03 is very similar to the garnet rich assemblages described above (samples TI23, SHS03, SHA07, SHA17), with a garnet content of 73 % and less frequent zircon (5 %) and tourmaline (2 %). Rutile is present at 11 % and therefore more frequent than in the other garnet rich samples.

Sample AN08 is different with a garnet content of only 2 %, but a relatively high fraction of zircon (24 %) and rutile (16 %). Apatite is relatively frequent (25 %). The ZTR ratio is 41.

The samples from sections CHW, SP, SPP and SP from the Southern Cross Mountains show a relatively similar heavy mineral composition. It resembles in all cases the garnet rich assemblage described above, with a garnet content ranging from 54 to 89 %. Zircon (2-10 %) and apatite (3-16 %) are much less frequent, while rutile and tourmaline (both max. 4 %) are only accessories.

Sample ST09 from section Stewart Heights is dominated by tourmaline (76 %) and zircon (11 %). The typical metamorphic minerals rutile and garnet are present only at about 1 %. The ZTR ratio of this sample is 87, and thus the highest of all samples throughout the working area.

In sample SPP36 from Section Peak Plateau, among the fraction of opaques a non-magnetic mineral with cubic shape occurs. Microprobe EDX analysis revealed Fe and O as major elements with Si and Al occurring subordinately. The shape resembles pyrite, so it may be a pseudomorphosis of an impure iron oxide mineral after pyrite (possibly hematite due to the slightly reddish colour).

### 3.2.3.5 Statistical approach to heavy mineral assemblages by principal components

The advantages and possibilities of a statistical analysis of heavy mineral data have been demonstrated previously by various authors (Clemens and Komar 1988; Wagreich and Marschalko 1995). Motivated by their findings, a principal component analysis (PCA) was performed to identify possible clusters (Fig. 3.9). In addition to the classification scheme used above, the fraction of opaque minerals has been introduced as independent variable.

As shown in Fig. 3.9, the fractions of garnet, tourmaline, apatite, and opaque minerals are needed for maximal separation of the samples. The group of garnet rich samples clusters very well, as do the samples from the southern Eisenhower Range (ER, TP), which are similarly rich in zircon, tourmaline and apatite. All other samples do not show distinct clusters, and are therefore difficult to interpret.

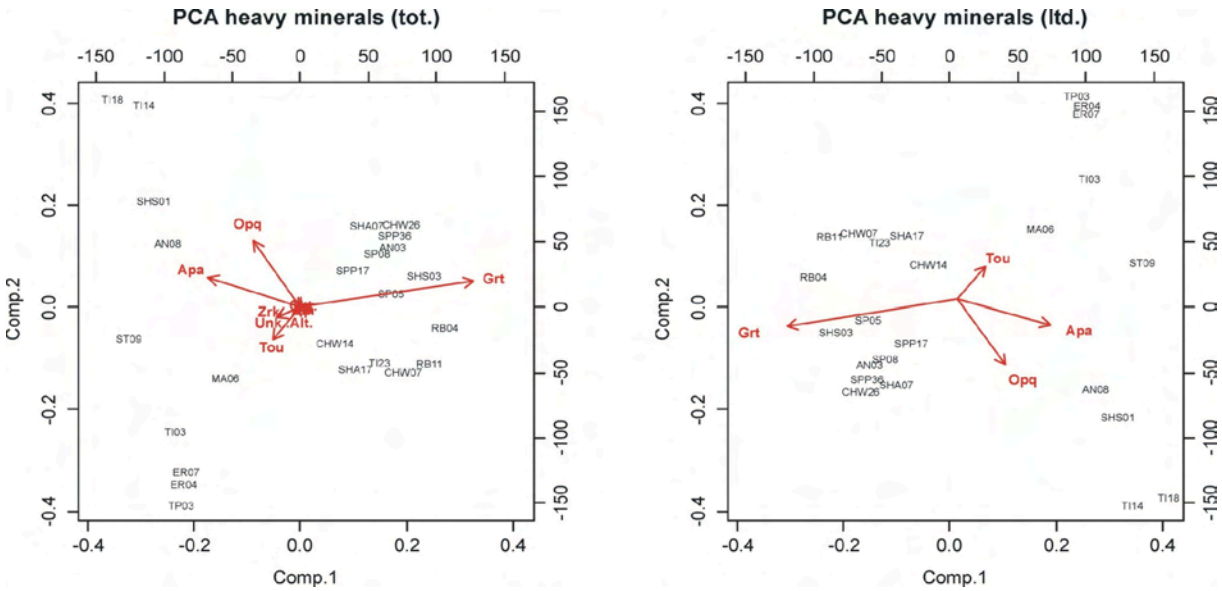


Fig. 3.9: Biplots of a PCA of all heavy mineral data (left panel) and of the fractions of garnet, tourmaline, apatite, and opaque minerals only (right panel). The garnet rich samples cluster very well, as do the samples from the southern Eisenhower Range (TP, ER).

### 3.2.3.6 Zircon morphology

Tracht and habit of zircons resembles the chemical and physical condition during mineral growth and may therefore be used as indicators for source rock lithology (Corfu et al. 2003; Hoppe 1962; Poldervaart 1950; Pupin 1980; Vavra 1990) . While the tracht of detrital zircons may be blurred due to abrasion, the morphology is usually well preserved and easy to determine. In general, strongly elongated crystals with a length:width ratio of more than three are considered to reflect fast crystal growth, and are most likely derived from pegmatites, while strongly rounded crystals are often recycled or metamorphic. In some cases, strongly elongated crystals have also been found in pyroclastic rocks (Mange and Maurer 1991), but those usually have grain sizes considerably smaller than zircons from pegmatites.

The classification scheme used in this study consisted primarily of eight classes as exemplified for sample TP03 in Tab. 3.3. The summarized results are given in Tab. 3.4. In some cases, the number of zircons is too small for a detailed statistical analysis (e.g. samples TI03, SHS01, MA06-4).

| TP03 | Absolute | | Relative | | Sum [%] |
|---|---|---|---|---|---|
| n = 141 | Compact | elongated | compact | elongated | |
| roundish | 0 | 0 | 1 % | 0 % | 1 % |
| ″ broken | 2 | 0 | | | |
| subroundish | 31 | 3 | 38 % | 2 % | 40 % |
| ″ broken | 23 | 0 | | | |
| edgy | 14 | 7 | 32 % | 12 % | 44 % |
| ″ broken | 31 | 10 | | | |
| irregular | 13 | 0 | 14 % | 0 % | 14 % |
| ″ broken | 7 | 0 | | | |
| Sum | 121 | 20 | 86 % | 14 % | 100 % |

Tab. 3.3: Example of the classification scheme of zircons showing results of sample TP03. The fraction of edgy (44 %) and elongated (14 %) crystals is relatively high compared with the other samples.

| Sample | Number (n) | Roundish | Edgy | Elongated |
|---|---|---|---|---|
| TP03 | 141 | 1 % | 44 % | 14 % |
| ER04 | 53 | 32 % | 9 % | 6 % |
| ER07 | 27 | 41 % | 7 % | 7 % |
| TI03 | 20 | 20 % | 20 % | 20 % |
| TI14 | 40 | 40 % | 10 % | 5 % |
| SHS01 | 28 | 14 % | 18 % | 18 % |
| SHS03 | 98 | 44 % | 5 % | 8 % |
| SHA07 | 40 | 38 % | 8 % | 5 % |
| SHA17 | 39 | 36 % | 8 % | 0 % |
| MA06-4 | 25 | 68 % | 4 % | 4 % |
| AN03 | 86 | 43 % | 3 % | 7 % |
| AN08 | 135 | 60 % | 4 % | 5 % |
| SP05 | 42 | 64 % | 0 % | 0 % |
| SPP36 | 71 | 46 % | 8 % | 7 % |
| CHW07 | 91 | 45 % | 7 % | 8 % |
| CHW14 | 33 | 48 % | 0 % | 3 % |
| CHW26 | 40 | 50 % | 8 % | 5 % |

Tab. 3.4: Number of analysed zircons and the fractions of roundish, edgy and elongated crystals for all analysed samples.

### 3.2.4 Summary and interpretation: Provenance by petrography

All sandstones found in the working area can be attributed to six classes, using a combination of heavy and light mineralogy. These classes are referred to as sandstone types A – F in the following. While especially type C is very frequent, others occur in single sections only (type E), or are even represented by a single sample (type F). A discrimination of the types by heavy mineralogy is possible in the garnet-apatite-tourmaline ternary diagram (Fig. 3.10), and by light mineralogy, in the Q-F-Lv ternary diagram (Fig. 3.11

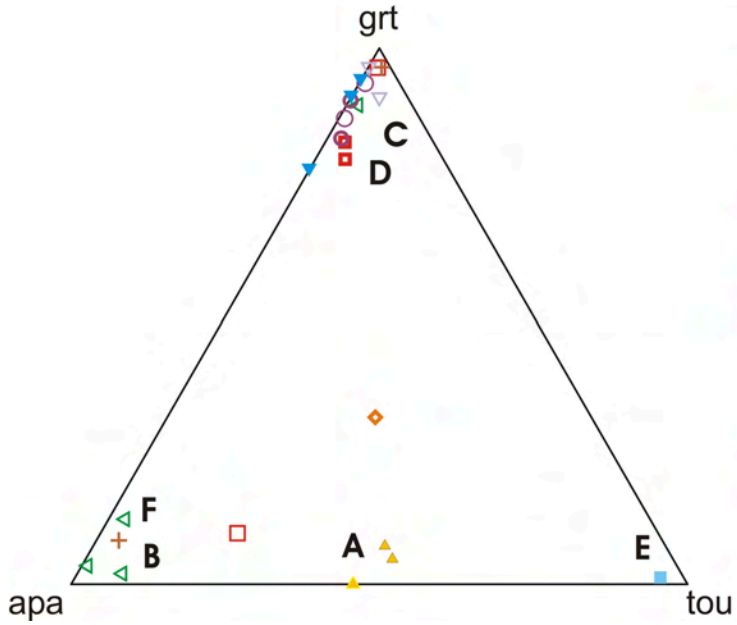


Fig. 3.10: The heavy mineral assemblages in the tourmaline-garnet-apatite ternary diagram. Sandstone types A to F are indicated. Types C and D, as well as type B and F, can not be discerned in this diagram. Note the two samples from SHS and MA, in between different sandstone types, indicating mixture. Sandstone type F refers to the single apatite rich sample from section AN, which can not be distinguished from type B samples in this diagram. Legend as in Fig. 3.11.

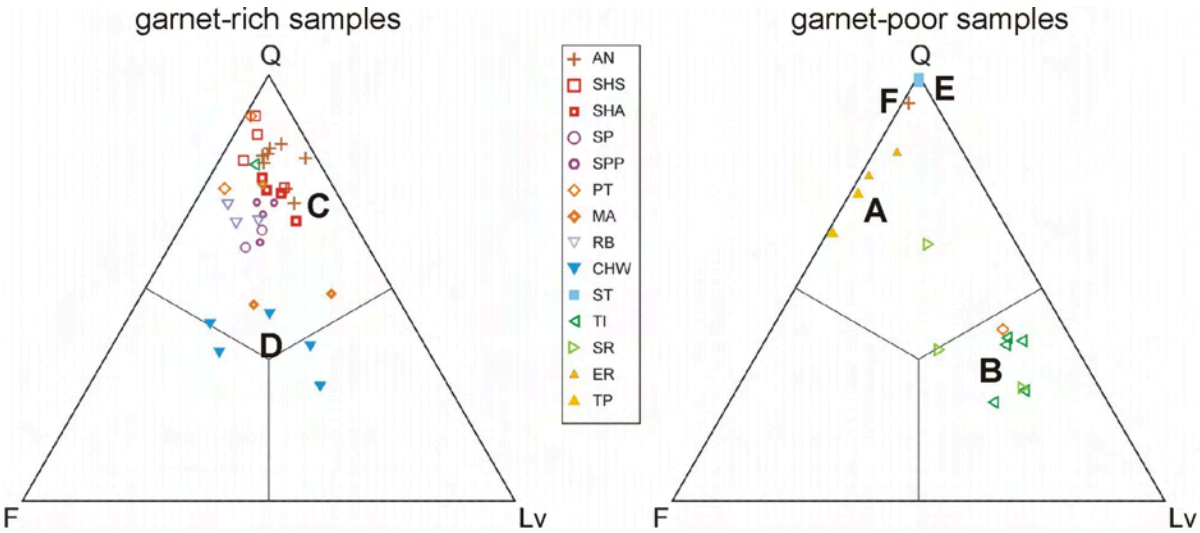


Fig. 3.11: Categorization of the six sandstone types A – F by means of light mineralogy in the Q-F-Lv ternary diagram. The left diagram includes the garnet-rich types C and D (grt : ZTR > 1), the right diagram the garnet-poor types A, B, E and F (grt : ZTR < 1). The sample between type A and B in the right diagram can be interpreted as mixture. Discrimination between groups A, E, and F can be done by heavy mineralogy (Fig. 3.10). Additionally, biotite is frequent in type A samples, but rare or absent in type E and F.

**Sandstone type A** is rich in tourmaline and apatite, with abundance of zircon varying strongly. Typical metamorphic heavy minerals like rutile or garnet are rare. The ZTR ratio is relatively high, reaching about 40 to 60. Light mineralogy shows a dominance of quartz. Feldspar is more abundant than lithoclasts. Biotite is relatively frequent (Fig. 3.12), but often altered to kaolinite or halloysite.

This sandstone type occurs predominantly in the southern part of the working area (sections TP, AG, ER), where it is associated with conglomerates. A predominantly felsic plutonic (granitoid) source can be assumed from both, the heavy mineralogy (tourmaline, apatite, zircon) and the light mineralogy (quartz, K-feldspar, biotite). A minor contribution of a metamorphic source (metamorphic lithoclasts, rutile, garnet) is characteristic for sandstone from section ER, but less evident in sections TP and AG. This difference can be explained by the locally different basement lithology (plutonic / metamorphic, GANOVEX-Team 1987a). On average, a 'mixed source' is indicated in the Qm-F-Lt diagram (Dickinson 1985) for this sandstone type (Fig. 3.13). At least for the basal parts of this sandstone type, cobbles indicate a transport distance from the source area in the range of a few tens of km. The sandstones from Mt. Nansen analysed by Di Giulio et al (1999) are also of type A according to the published mineral spectra.

The most basal sample from section AN (AN01a) in the northern Deep Freeze Range also resembles this sandstone type showing also altered biotites in a similar proportion. However, this sample only represents the basal 20 cm of the section. Thus the biotite is most likely derived from the local basement, with only minor transport.

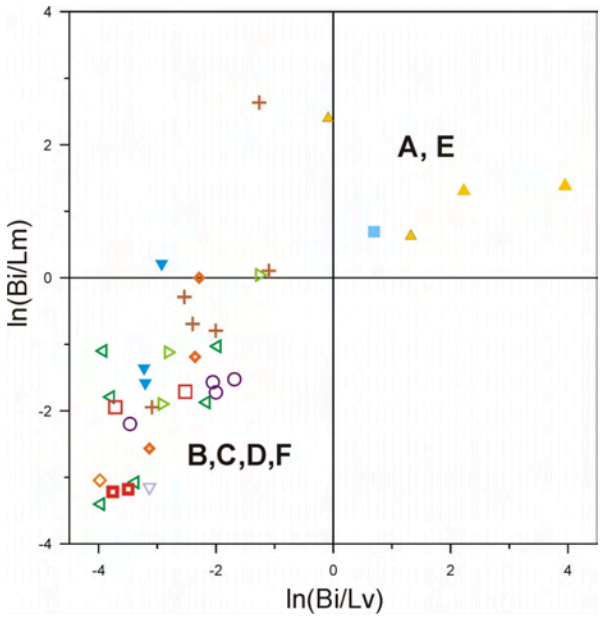


Fig. 3.12: Logratio of biotite vs. volcanic and metamorphic lithoclasts. Sandstones of type A and E can clearly be distinguished by their absolute biotite proportions. Legend as in Fig. 3.11.

In some samples, altered biotites are present next to unaltered ones. This can be interpreted as alteration prior to sedimentation. It is rather related to source area processes, or possibly even to a specific source. The abundance of these biotites is largest in the southernmost sections, and decreases towards the north. A relatively proximal source (few 10s of km) is implied by the conglomerates, though as for the cobbles the Wilson terrane may also be the likely source of the altered biotites.

In **sandstone type B** apatite is the most abundant heavy mineral, and zircon is usually the second most common. Tourmaline, rutile and garnet are rare. Cr-spinel may be present. The ZTR ratio is relatively low (< 20). Light mineralogy is dominated by lithoclasts, of which felsic volcanics are usually the most abundant. Mafic volcanic lithoclasts and metamorphic rock fragments are also frequent.

Sandstones of this type are present in southern to central parts of the working area. They occur in the lower part of section TI, the uppermost section SR, and in basal parts of section PT. Volcanic source rocks must be assumed from the light mineralogy, with a contribution from a metamorphic source. The abundance of apatite in the heavy mineral spectra may originate from the (felsic) volcanic source. In the Qm-F-Lt diagram, a transitional/lithic recycled orogen to transitional arc source is indicated (Fig. 3.13).

Sandstones from the lowermost part of section SHS can be interpreted as mixture of sandstone type A and B, as they exhibit characteristics of both types. The frequency of volcanic lithoclasts is higher than in other type A sandstones pointing towards a mixture with type B, but the tourmaline content and therefore the ZTR ratio is markedly higher than in type B sandstones, resembling type A. Clear quartz grains larger than the volcanic lithoclasts may also be derived from a plutonic (type A) source.

In addition, sandstones from the lower part of section SR may be a mixture of type A and B. This interpretation is based on light mineralogy only, as no heavy mineral analysis was conducted. However, this finding would suggest a gradual change from type A to type B sandstones in the Eisenhower Range.

According to the published data, some of the samples from Mt. New Zealand and from Skinner Ridge analysed by Di Giulio et al (1999) are also of type B.

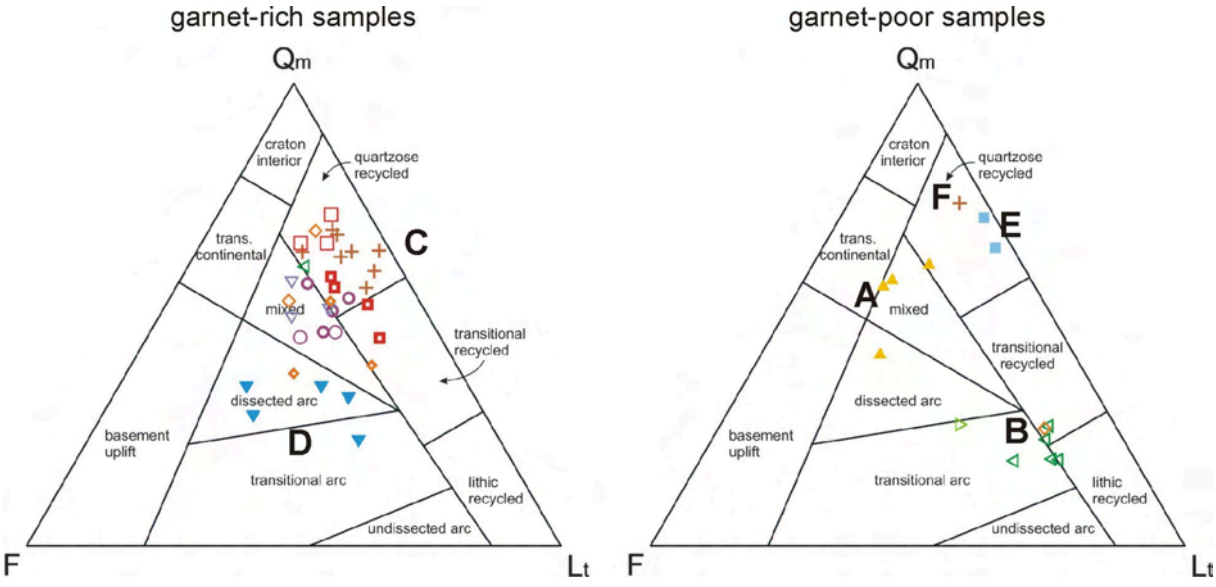


Fig. 3.13: Categorization of the six sandstone types A – F by means of light mineralogy in the Qm-F-Lt ternary diagram. The left diagram comprises the garnet-rich sandstone types C and D (grt : ZTR > 1), the right diagram the garnet-poor types A, B, E and F (grt : ZTR < 1). Note that the types C and D, or E and F, can hardly be discerned in this diagram. Legend as in Fig. 3.11.

**Sandstones of type C** show heavy mineral spectra dominated by garnet (more than 50 %, in some samples up to 90 %). Apatite and zircon are much less frequent, and rutile and tourmaline are rare. The ZTR ratio is relatively low (< 20), similar to sandstone type B. However, light mineralogy is dominated by quartz, lithoclasts are less frequent than in type B, but commonly more abundant than feldspar.

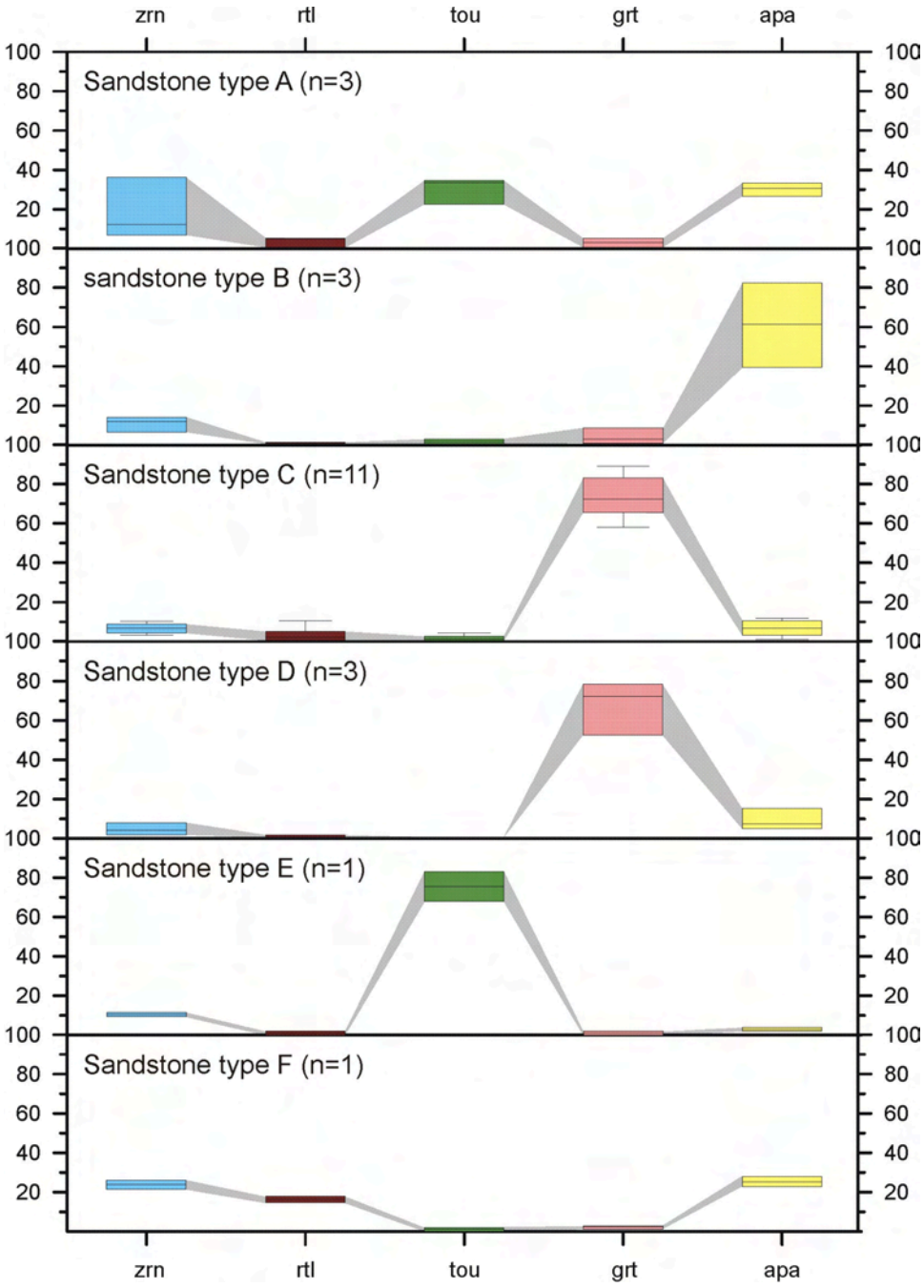


Fig. 3.14: Box-whisker plots of the average heavy mineral spectra of the six sandstone types (zircon, rutile, tourmaline, garnet, and apatite only). Other heavy minerals were not considered in this diagram. Note that type C and D can hardly be distinguished only by heavy mineralogy, although tourmaline is missing in type D. Samples representing a mixture between different types have not been regarded. For sandstone type E and F a range of ± 10 % around the point counting result of each sample is shown (n = 1 in both cases).

Sandstones of this type are the most frequent throughout the working area. They are present in the upper part of section TI, the Deep Freeze Range sections SHS, SHA, PR, PT, MA, and AN, as well as in the north-western sections SP, SPP and RB (Outback Nunataks). They have not been found in the sections of the southern Eisenhower Range and from sections CHW and ST in the north-eastern part of the working area.

The source of type C sandstones is predominantly metamorphic, as garnet is by far the most abundant heavy mineral. A contribution from a volcanic source is necessary to explain the presence of volcanic lithoclasts. Volcanic lithoclasts and plagioclase increase in

abundance in higher stratigraphic levels. This is most obvious in section SHA. Furthermore, the greenish-brownish amphiboles are more frequent in the heavy mineral assemblages in samples from higher stratigraphic levels (sections SHA, MA). A relation of both observations may be plausible, indicating a common source of plagioclases and amphiboles. The diagram in Fig. 3.13 implies a quartzose (transitional) recycled orogen as source for most samples and a 'mixed source' for the others.

Sample MA06-4 from the uppermost section MA does follow this trend with about 17 % amphiboles, but contrary to the other type C sandstones, it contains less garnet but more tourmaline. Its ZTR ratio is 30. This suggests the influence of a plutonic source. Possibly, this sample is a mixture of type C and type A.

**Sandstone type D** can not be distinguished from type C by means of heavy mineralogy, although tourmaline is missing. However, lithoclasts and feldspar are much more frequent here, while quartz is less abundant. Felsic and subordinately mafic volcanic rock fragments are the most abundant lithoclasts. A transition between type C and D type seems possible, but no direct evidence for this scenario has been found in the analysed samples.

Sandstones of type D have been found predominantly in section CHW, and subordinately in section MA. A mixture of a volcanic (lithoclasts) and metamorphic (garnet) source must be assumed, with type C and D sandstones being possibly arbitrarily chosen from a continuous mixing range. However, as the abundances of light minerals differ considerably, separate classes have been defined.

The dominance of metamorphic signatures in the heavy mineral assemblage, compared to the predominantly volcanic signal of the light mineralogy, can be explained by a grain size or frequency effect. Heavy minerals in volcanic rocks are usually small and often only accessories. In metamorphic rocks, however, they can be large and rock-forming (especially garnet), and therefore become much more frequent in the resulting sediments. A dissected arc is indicated as source by the Qm-F-Lt diagram (Fig. 3.13).

**Sandstone type E** has been defined by the sandstones in section ST. This is the only section throughout the working area, where this sandstone type has been found. The heavy mineral assemblage was determined from a single sample only. As the light mineralogy of all samples within the section is very similar, the same was assumed for the heavy mineralogy.

The heavy mineralogy is dominated by tourmaline. Zircon is much less frequent and other heavy minerals are very rare or absent. The light mineralogy shows a predominance of quartz. Feldspar and lithoclasts are absent to rare, but the proportion of volcanic and metamorphic lithoclasts increases slightly to higher stratigraphic levels.

A dominating plutonic source can be identified for this sandstone type, with very low but slightly increasing contributions from a volcanic and metamorphic source. The transport distance of cobbles at the base of the section is only a few tens of km, thus indicating a source within the Wilson terrane. The diagram in Fig. 3.13 suggests a quartzose recycled orogenic source, which is interpreted as the result of a very strong and deep reaching weathering of the source area, as observed for the basement at section ST (Schöner et al. in review).

**Sandstone type F** is actually defined by a single sample (AN08) only. However, as the heavy mineral assemblage is unique within the SPF, it cannot be attributed to one of the other sandstone types.

The heavy mineral spectrum comprises zircon and apatite, both with about 25 %. Rutile is present at about 16 % and thus significantly overabundant compared to the average rutile content of all other SPF samples of about 2 % (rejecting the AN samples). Garnet is very rare (2 %). The light mineralogy is quartz dominated, with few (volcanic) lithoclasts and feldspars. Therefore it is very similar to under- and overlying type C sandstones.

Sample AN03 from the same section also shows some similarity to type F, as it yields 11 % rutile in the heavy mineral spectrum. However, other heavy mineralogy (garnet 73 %) match type C sandstones, but a possible minor contribution of type F can be assumed.

A quartzose recycled orogenic source is indicated by the diagram in Fig. 3.13. Apatite and zircon may indicate an igneous source, and the high fraction of rutile points towards a metamorphic source. A diagenetic influence on heavy mineral assemblage (e.g. dissolution of garnet), is unlikely, because the existing garnet does not show dissolution features. Also, apatite is usually less stable than garnet, but frequent in this sample. Finally, this sample does not show any evidence of a specific diagenetic evolution different from the under- and overlying sandstones.

Some **ambigous sandstone samples** are difficult to classify in this scheme. They may be mixture of different sandstone types (see also Figs. 3.10 and 3.11). This is most likely type A and B for sample SHS01, which is also likely regarding the geographic relationship. A similar relation, though less obvious, can be presumed for the lower part of section SR.

Some samples from the higher part of section MA also exhibit characteristics of two sandstone types. Garnet is frequent in all samples, thus type C material is an important constituent. Sample MA06-3 contains many volcanic lithoclasts, thus an influence of the type B source is likely. In sample MA06-4, garnet is relatively rare, and tourmaline relatively frequent, what is interpreted as additional input of the type A source.

Zircon morphology is not well suited as a tracer to distinguish among different sandstone types. However, high fractions of roundish zircons were found in samples from sandstones of type C, D, and F (usually > 40 %), supporting a metamorphic source as indicated by the frequent metamorphic heavy minerals (garnet, rutile). Edgy and elongated crystals are rare in these samples.

In samples from the sandstone types A and B, the fraction of roundish zircons is mostly below 40 %, and edgy crystals are relatively abundant. This can be interpreted as pronounced input of an igneous source. In addition, the portion of elongated crystals in these sandstone types is higher, indicating the presence of zircons from pegmatitic origin. However, for samples of type B the data base is relatively poor, and the results have to be interpreted with caution. From sandstones of type E no sample was analysed with respect to zircon morphology. As only zircons of a single size fraction (63-125 µm) were analysed, differences in grain size could not be determined. However, this may be a possible criterion for future investigations.

| Type | Sections | Heavy mineralogy | Light mineralogy | Presumed source |
|---|---|---|---|---|
| A | TP, AG, ER | Zircon and tourmaline rich; garnet poor | Quartz rich, biotite rich; Lithoclast poor | Felsic plutonic |
| B | Lower TI, lower PT | Apatite rich; garnet poor | Volcanic and metam. lithoclasts, less quartz and feldspar | Volcanic, metamorphic (low grade?) |
| C | Upper TI, SHS, SHA, PR, MA, upper PT, AN, SP, SPP, RB | Garnet dominated; apatite and zircon | Quartz rich, few lithoclasts, few feldspars | Metamorphic (med.-high grade?) volcanic, plutonic? |
| D | CHW, MA | Garnet dominated; apatite and zircon | Lithoclast and feldspar rich | Volcanic, metamorphic (as type C) |
| E | ST | Tourmaline dominated; garnet poor | Quartz dominated | Felsic plutonic |
| F | AN08 | Zircon, apatite, rutile; garnet poor | Quartz rich, few lithoclasts / feldspars | Metamorphic (med.-high grade?) |

Tab. 3.5: Summary of some petrographic characteristics of the six sandstone types, and their presumed source areas.

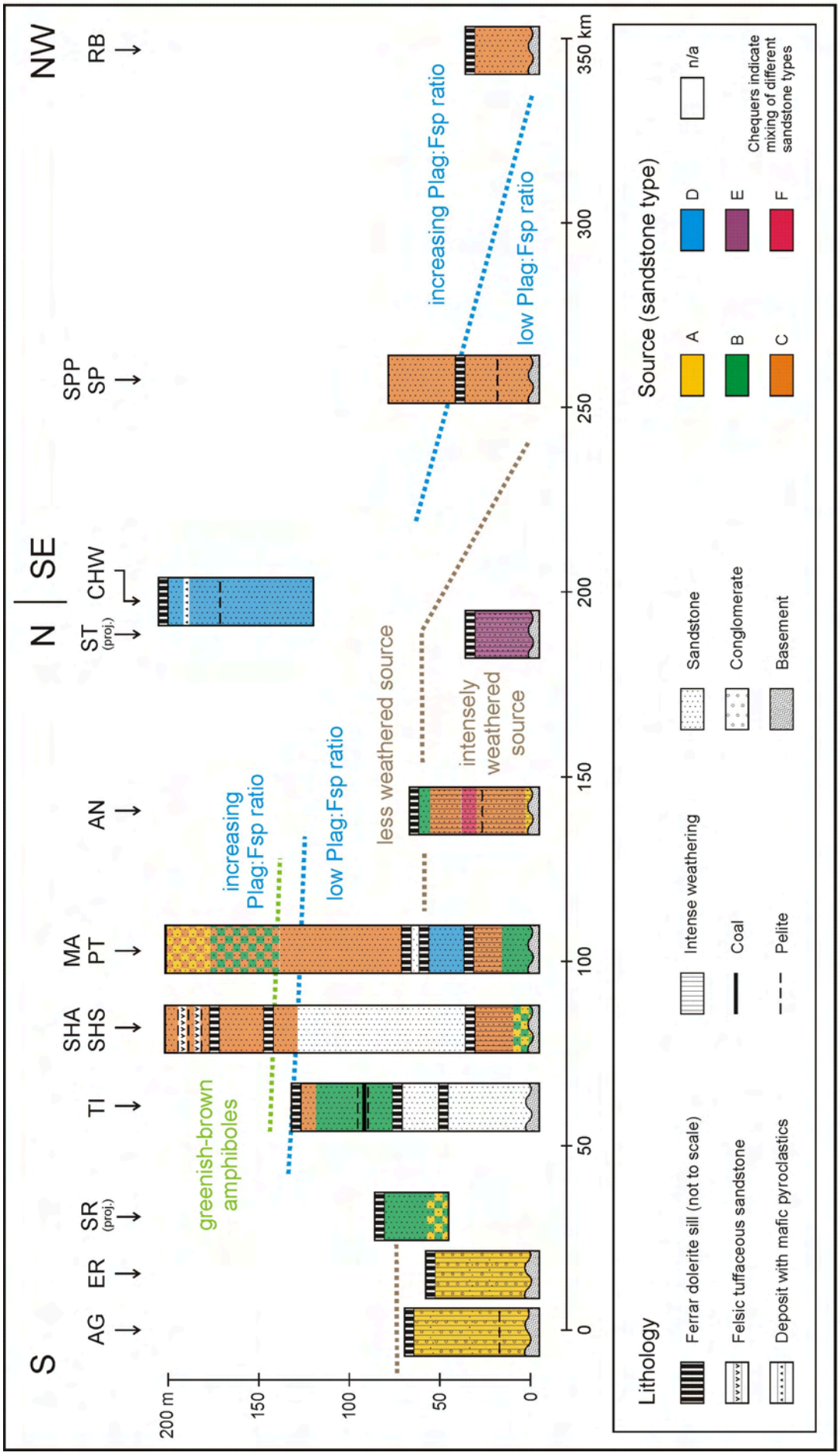


Fig. 3.15: Cross section visualizing the occurrence of the different sandstone types in the SPF in NVL as defined by petrography. For correlation, the inferred top of the sandstones derived from an intensely weathered source is given (type A, C, E, and F only). The beginning of the increase of the Plag:Fsp ratio, and the first appearance of greenish-brown amphiboles in sandstone type C are also shown. The trace of the cross section is indicated in Fig. 1.3.

# 3.3 Whole-rock geochemistry

## 3.3.1 Introduction

### 3.3.1.1 Geochemistry and provenance

Provenance determination by geochemical analyses tries to deduce from elements or element ratios to minerals, parent rocks and tectonic settings. Each step is rather indefinite so the results need to be interpreted with caution (McLennan et al. 1990; Ryan and Williams 2007). Nevertheless geochemical analysis is a frequently used method in provenance determination (Floyd et al. 1990; McCann 1991; Roser and Korsch 1999b) as it gives a quick overview and is easy to apply. Especially changes between various sections and trends within sections can be shown. However, to get reliable and interpretable results it should be combined with other methods, especially with thin section analysis. Table 3.6 comprises elements, the minerals they are allocated and common source rocks they are thought to indicate. For this study a total of 45 samples (sandstones and subordinately mudstones) from 11 sections were analysed. The results are listed in the appendix.

| Elements | Minerals | Common source rocks, provenance |
|---|---|---|
| Al | Clay minerals, mafic lithoclasts | Intensely weathered rocks, sediment recycling |
| K | Alkalifeldspar, mica, amphibole, illite | Felsic magmatites |
| Na | Alkalifeldspar (amphibole) | Mafic magmatites |
| Ca | Plagioclase, amphibole, pyroxene | Mafic magmatites |
| Mg, Fe, Mn | Biotite, amphibole, pyroxene | Mafic magmatites |
| Ti | Pyroxene, biotite, $TiO_2$-minerals | Mafic magmatites |
| Co, Sc, V | Mafic minerals | Mafic magmatites |
| Zr | Zircon | Felsic magmatites, possibly sediment recycling |
| Th, La, Ce, Y | Zircon, monazite | Felsic magmatites, possibly sediment recycling |
| Cr, Ni | Cr-spinel | Ultra-mafic magmatites |

Tab. 3.6: The elements used in this study, the minerals they are allocated and the provenance they are thought to indicate.

### 3.3.1.2 Methods

XRF measurements were carried out with a sequential wavelength dispersive spectrometer (WDXRF) Philips PW 2400, which uses single crystals of suitable materials to disperse the spectrum according to Bragg's law. Each characteristic spectral line has a discrete wavelength and a discrete Bragg angle. For determination of a specific element, this angle is set on a scanning goniometer and the resulting count rate is, as a first approximation, proportional to the concentration of the respective element. XRF only enables quantification by comparison with known count rates of certified standards, comprising of a set of 51 magmatic and sedimentary materials. Thereby the software Super-Q® was used.

Sample preparation started with powdering of about 30 to 100 g fresh rock material in a cleaned agate ring mill before following two different lines. Pressed powder tablets for determination of trace elements were made from six gram well desiccated (110°C) grinded sample powder, mixed with one gram of Hoechst Wax C as binding agent and inserted into a collapsible aluminium cup under pressure of 130 kN. Major elements were determined on fused beads (glass discs) in which the sample material was diluted with a flux agent (1:10) in order to minimize matrix effects. As flux Merck Spectromelt® was used (66 % Di-Lithiumtetraborate and 34 % Lithiummetaborate). After oxidizing the sample at 950°C for determination of loss on ignition (LOI), fusion was carried out within a high frequency induction furnace Lifumat 2.0-Ox. The relative error (1σ) is approximately ± 1 % for major elements (given as oxides) and ± 5 % for trace elements (M. Ude 2008, pers. comm.).

No attempt was made to distinguish between CaO in silicate and carbonate minerals. As carbonate clasts have not been recorded (see Sect. 3.2.2), and diagenetic carbonate cements are rare and easy to identify (see Sect. 5), the total CaO was assumed to be derived from silicate minerals.

### 3.3.2 Geochemical sandstone classification

A general classification of sandstones by geochemical data can be done by application of standard diagrams. The first uses the logarithms of the ratios $SiO_2/Al_2O_3$ and $Na_2O/K_2O$ (Pettijohn et al. 1972), in the second $Na_2O$ is replaced by $Fe_2O_3$ (Herron 1988). The $SiO_2/Al_2O_3$ ratio represents the maturity of the sample, while the alkali-ratio $Na_2O/K_2O$ is a measure of the feldspar content. $Fe_2O_3$ represents ferromagnesian minerals (pyroxenes, amphiboles etc.), which are very sensitive to weathering, and comprises therefore an additional representation of maturity.

Application of such diagrams generally may bear problems, as, for instance, diagenetic effects (e.g. leaching of alkalis) can distort the results (Rollinson 1993). However, these diagrams are useful to distinguish different sandstone types and in combination with thin section analysis they provide useful information.

In the diagram of Fig. 3.16 the analyses stretch mainly over the fields “Arkose”, “Litharenite” and “Greywacke”. The large percentage of the analysed samples apparently being classified as “Greywackes” – a result that is in conflict with thin section analysis – is probably be caused by the proportion of altered volcanic clasts being geochemical indistinguishable from a clayish matrix.

This diagram is suitable to discriminate the sandstones of the different sections. The samples from section TP are characterized by a very low $Na_2O$:$K_2O$-ratio, which may be related to an originally low ratio in a granitic, K-feldspar rich and plagioclase-poor source. Alternatively, an intense weathering may have lowered this ratio, as $Na_2O$ is less stable and leached faster than $K_2O$ (Nesbitt and Young 1984).

Samples from sections TI and SR show low $SiO_2$:$Al_2O_3$ ratios. These samples are lithoclast rich. The samples from section CHW are rich in lithoclasts and feldspars as well, which causes $SiO_2$:$Al_2O_3$ ratios nearly as high as in section TI. In the relatively mature sandstones from section AN and SHS, the $SiO_2$:$Al_2O_3$ ratio is the highest in the SPF.

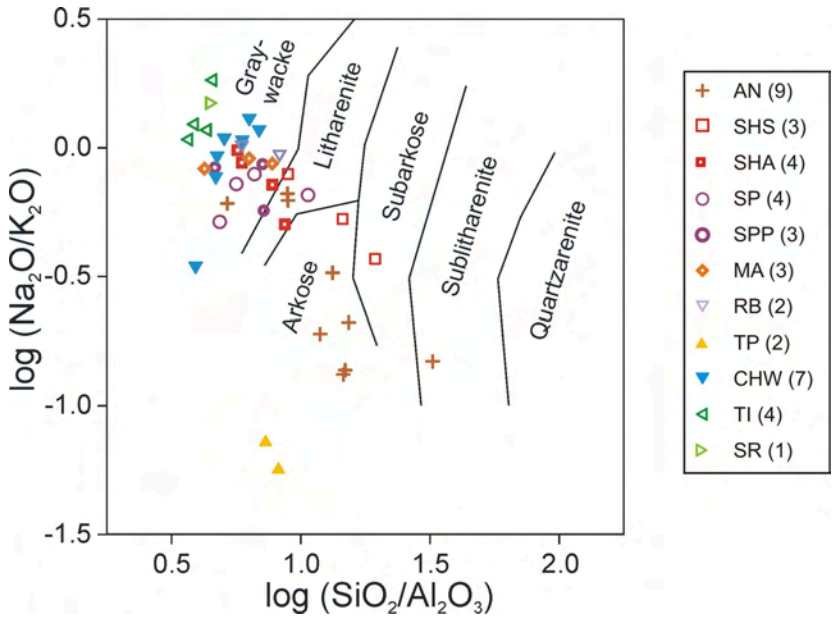


Fig. 3.16: Diagram for geochemical sandstone classification (Pettijohn et al. 1972). For explanations see text.

In the classification diagram of Fig. 3.17 (Herron 1988) samples are classified as "Subarkoses", "Arkoses", and "Wackes". Some samples from the AN section are plotting in the "Sublitharenite" or "Fe-Sand" field; this is related to authigenic iron (hydro-) oxides. As in the diagram in Fig. 3.16, the sandstones from the different sections can be discriminated.

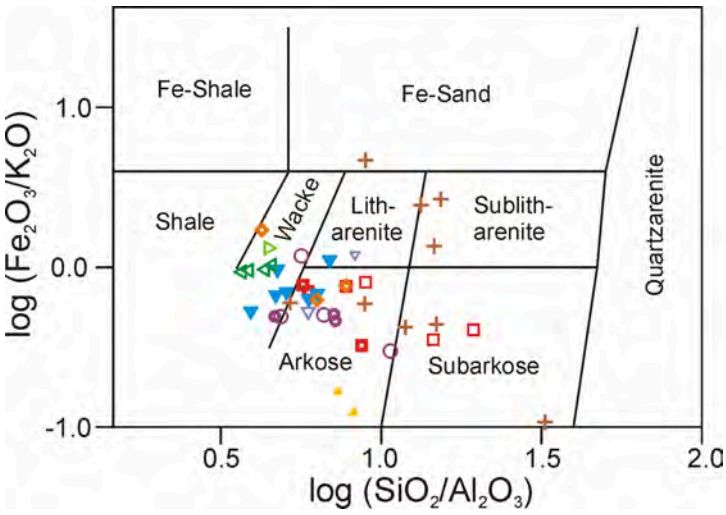


Fig. 3.17: Diagram for geochemical sandstone classification (Herron 1988). For explanations see text. Legend as in Fig. 3.16.

## 3.3.3 Provenance and weathering

### 3.3.3.1 Provenance using discrimination diagrams

To determine the average geochemical composition of a source area mathematical functions are used to discriminate sandstones by means of their geochemical composition (Roser and Korsch 1988). Only major elements $TiO_2$, $Al_2O_3$, $Fe_2O_3$, MgO, CaO, $Na_2O$ and $K_2O$ are used, which are weighted differently and combined with a constant. In diagrams the results can be compared with known provenances and classified to a felsic, an intermediate and a mafic igneous as well as a quartzose sedimentary provenance.

The validity of this approach has been called to question due to the specific regional settings used for definition of the standard diagrams. However, studies carried out to test their accuracy (e.g. Armstrong-Altrin and Verma 2005; Ryan and Williams 2007) showed that they are useful for discriminating between samples in principle, although the fields defined in the majority of diagrams cannot be universally applied.

The left diagram of Fig. 3.18 indicates a quartzose sedimentary to felsic igneous provenance for most samples. The samples from TI and SR group on the boundary to an intermediate igneous provenance. This can also be interpreted as caused by mixing of a felsic and a mafic source. In contrast, the discriminant functions in the right diagram are normalised to $Al_2O_3$. A similar discrimination as in the first case is not obvious. However, the indicated provenance is also largely a felsic igneous source.

The feldspar and lithoclast rich samples from section CHW are lying within the felsic igneous field. Although the relatively mature samples from section AN and SHS seem to be derived from a quartzose sedimentary provenance, this may also be caused by an intense weathering of the source area. Evidence for this is given by Fig. 3.19, showing that a heavy mineral (zircon) concentration typical for sediment recycling was not significant.

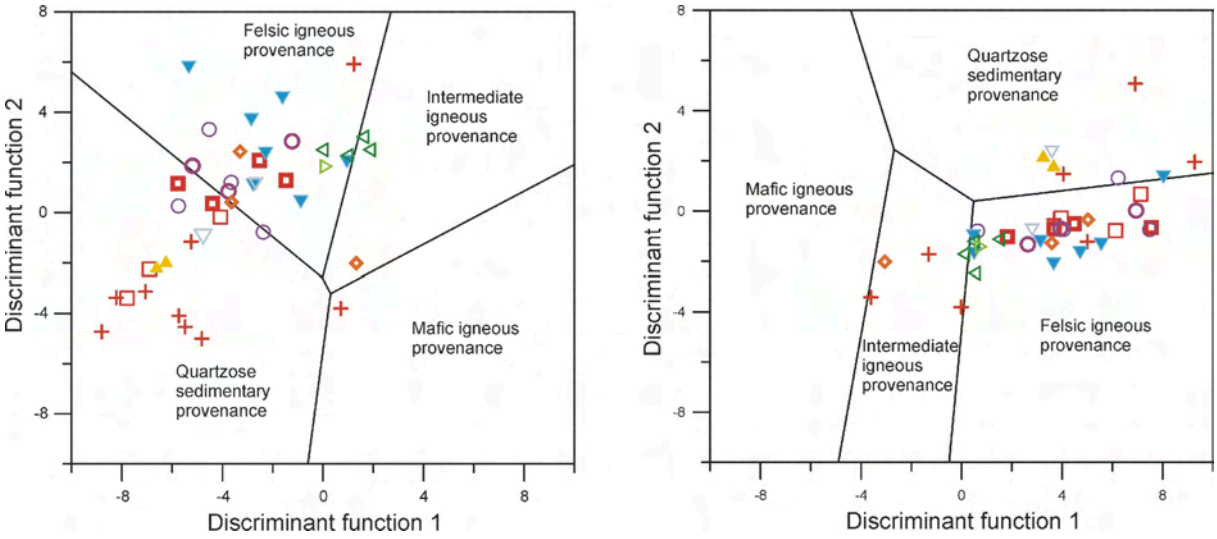


Fig. 3.18: Discrimination diagrams (Roser and Korsch 1988) to distinguish between felsic, intermediate and mafic igneous as well as quartzose sedimentary provenance. Legend as in Fig. 3.16.
The discriminant functions for the left diagram are:
Discriminant function 1 = -1.773*$TiO_2$ + 0.607*$Al_2O_3$ + 0.76*$Fe_2O_3$ - 1.5*MgO + 0.616*CaO + 0.509*$Na_2O$ - 1.224*$K_2O$ - 9.09; Discriminant function 2 =0.445*$TiO_2$ + 0.07*$Al_2O_3$ - 0.25*$Fe_2O_3$ - 1.142*MgO + 0.438*CaO + 1.475*$Na_2O$ + 1.426*$K_2O$ - 6.861
The discriminant functions for the right diagram are:
Discriminant function 1 = 30.638* $TiO_2/Al_2O_3$ - 12.541* $Fe_2O_3/Al_2O_3$ + 7.329* $MgO/Al_2O_3$ + 12.031* $Na_2O/Al_2O_3$ + 35.402* $K_2O/Al_2O_3$ - 6.382; Discriminant function 2 = 56.5* $TiO_2/Al_2O_3$ - 10.879* $Fe_2O_3/Al_2O_3$ + 30.875* $MgO/Al_2O_3$ -5.404* $Na_2O/Al_2O_3$ + 11.112* $K_2O/Al_2O_3$ -3.89

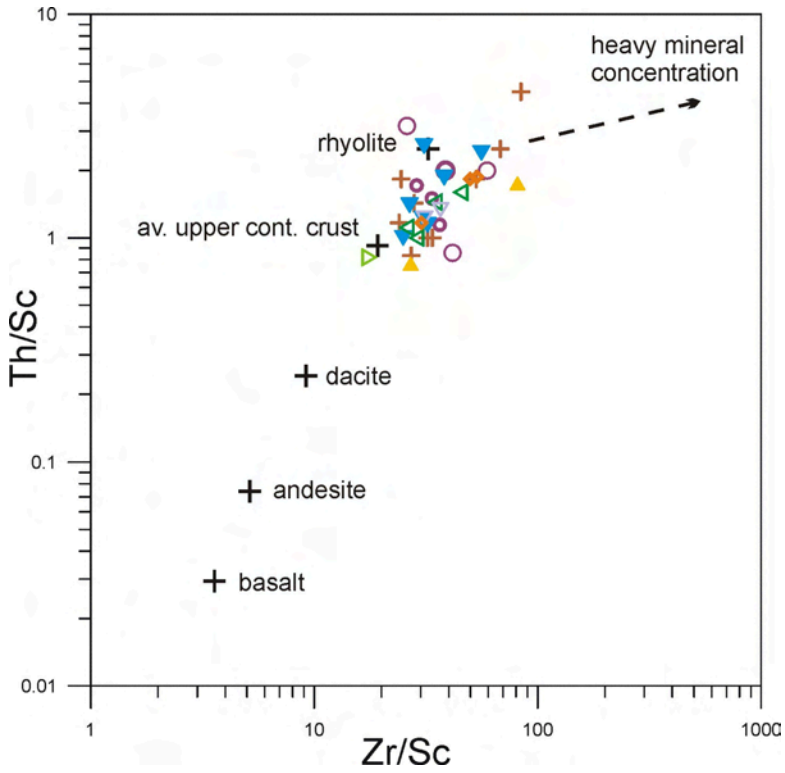


Fig. 3.19: Zr/Sc versus Th/Sc diagram (McLennan et al. 1993; Willan 2003) indicating that the sandstones are derived from a slightly more felsic source than the average upper continental crust displays. No systematic differences between the sandstones or sections, respectively, are obvious. A significant heavy mineral concentration (zircon) is not indicated by the chemical compositions. Legend as in Fig. 3.16.

### 3.3.3.2 Provenance revealed by reversed weathering trends

An average chemical composition of a source area can also be revealed by tracing back weathering trends. These trends exist due to the different mobility of elements during surface weathering. The most mobile and least resistant elements in silicates are Fe and Mg (mafic minerals), followed by Ca and Na. K is even less mobile and Al is rather immobile in relation to the mentioned elements. Suitable is the modified A-CN-K (that is Al – Ca+Na – K) diagram (Nesbitt and Young 1984; Nesbitt and Young 1989). The S-A-M (Si/10 – Na+K – Mg+Fe+Ti) diagram (Roser and Korsch 1999a; Willan 2003) is not as helpful (Fig. 3.20), because weathering trends are parallel to source rock composition and additionally maturity trends are affecting the result, too.

This method allows only prediction of average geochemical composition of the source area, which can be achieved by a variety of combinations of different rocks. Also (meta-) sedimentary source rocks can have different compositions than the grey shaded area of average upper continental crust in Fig. 3.20, as they may originate from already weathered material. Additionally, it is important that neither of these plots is suitable to predict the formation of weathering products like clay minerals, as they use whole rock compositions.

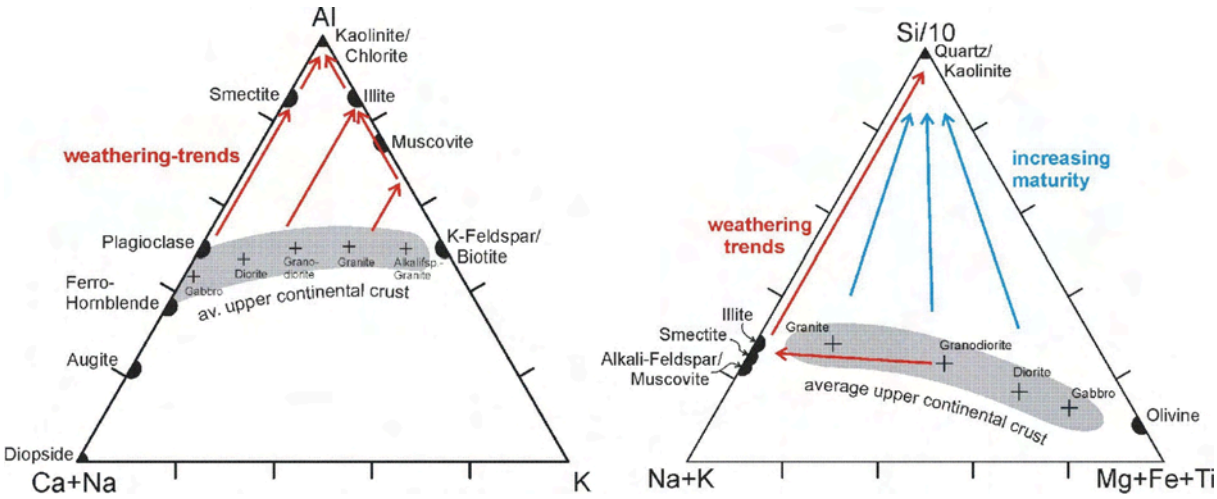


Fig. 3.20: Climate independent, general weathering trends for magmatic source rocks in the A-CN-K diagram (Nesbitt and Young 1984; Nesbitt and Young 1989) and in the S-A-M diagram (Roser and Korsch 1999a; Willan 2003). Elements are calculated in molar proportions and mineral formulas are based on ideal stoichiometry. For explanation see text.

For the diagrams in Fig. 3.21 samples were split up into the section or sections according to locality, to reveal systematic differences of the average geochemical composition of their source areas. The lithoclast-rich samples from section TI are therefore derived from a dioritic to granodioritic source, and the lithoclast and feldspar-rich samples from section CHW (apart from one sample) from a granodioritic source. The sandstones from the southern section TP and from section AN appear to be derived from a granitic to alkalifeldspar-granitic source.

Sections SHS/SHA as well as SP/SPP show an irregular trend from a granitic to a more granodioritic provenance, which can best be seen in section SHA. This trend can not be explained by weathering. It points to a gradual change in provenance from a granitic to a granodioritic source rock chemistry. This change matches the thin section data that show a gradual increase of the plagioclase : alkali-feldspar ratio (Sect. 3.2.2).

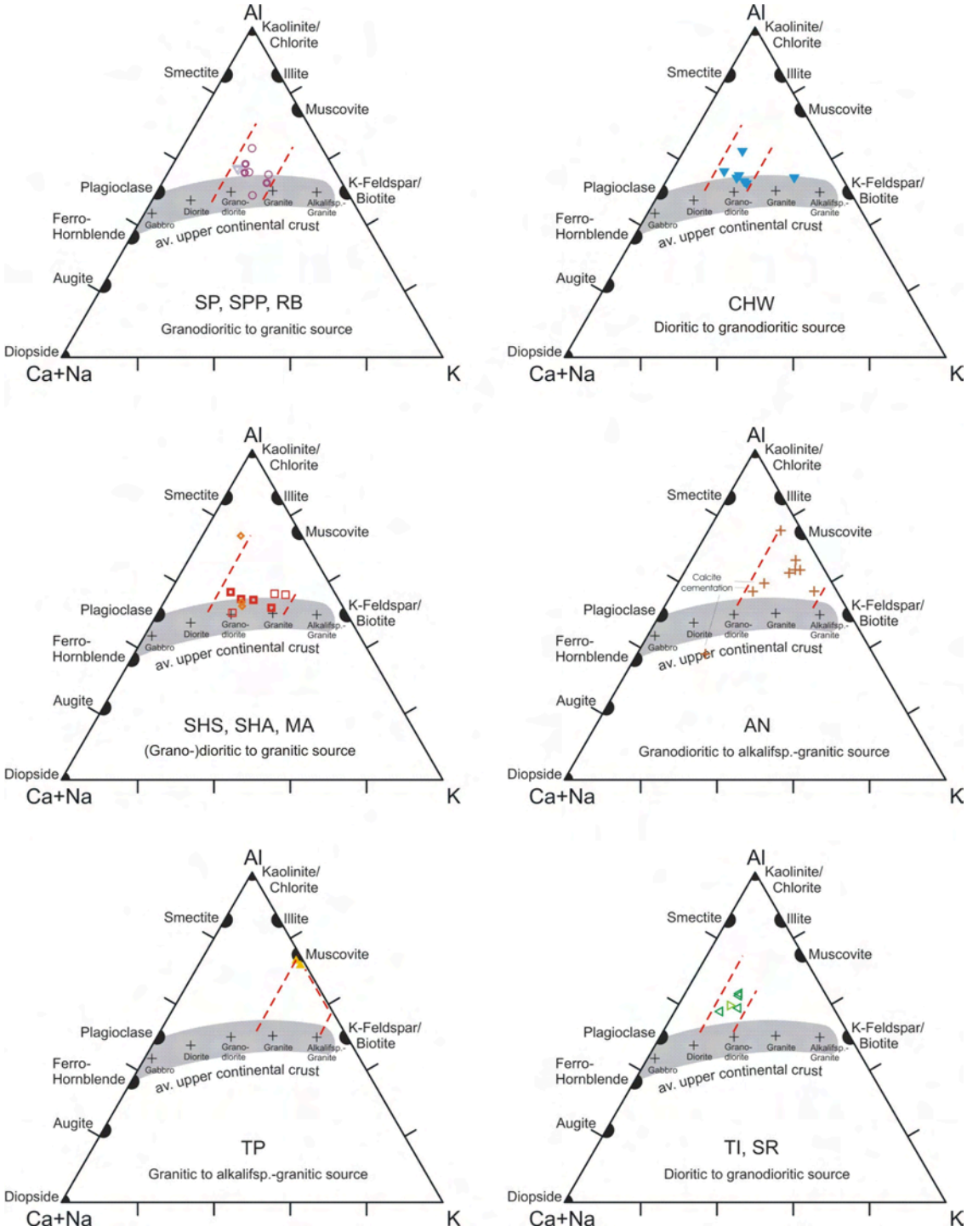


Fig. 3.21: The composition of the samples grouped after sections or closely adjoining sections, respectively, in the A-CN-K diagram (Nesbitt and Young 1984; Nesbitt and Young 1989). The average chemical compositions of the source area vary for the different sample localities from dioritic to alkalifeldspar-granitic. Legend as in Fig. 3.16.

As already stated, the S-A-M diagram (Roser and Korsch 1999a; Willan 2003) is not suitable to interpret weathering trends, as these are less differentiated than in the A-CN-K diagram and additionally parallel to rock composition. Therefore, source rock variations can easily be dismissed (Fig. 3.22). However, the diagram shows that samples from sections AN, SHS, and TP are the relatively most mature within the SPF.

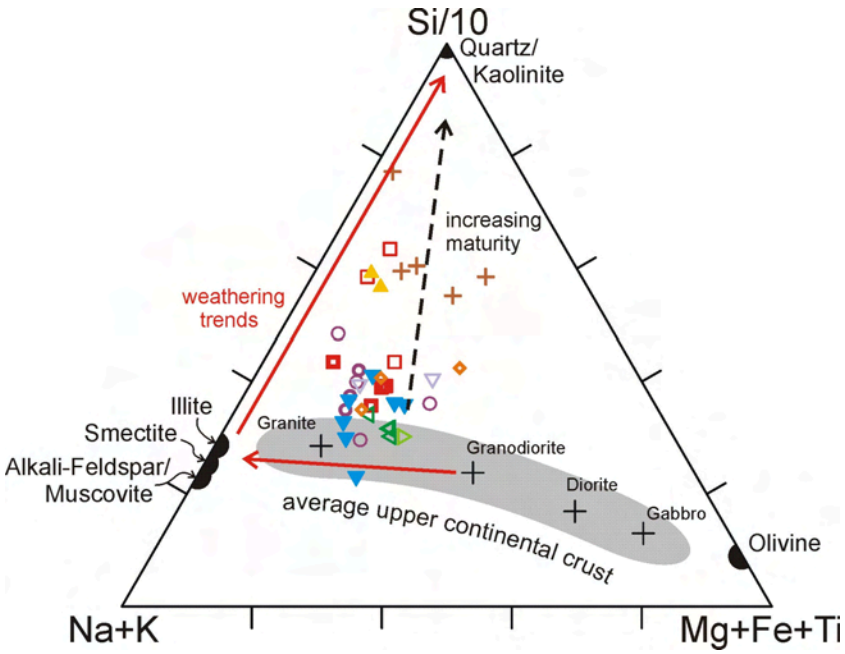


Fig. 3.22: All analyses plotted in the S-A-M-diagram (Roser and Korsch 1999a; Willan 2003). Differences in provenance can hardly be determined, as the weathering trend is blurring original source area variations. The grey area marks the composition of the upper continental crust. Legend as in Fig. 3.16.

### 3.3.3.3 Weathering intensity of the source areas

Many different weathering indices with different purposes have been introduced to literature (Fedo et al. 1995; Harnois 1988; Nesbitt and Young 1982; Parker 1970; Ruxton 1968; Vogt 1927). They all use major element oxides, mostly aluminium and alkalis, in different ways to obtain a value indicating the weathering of a sample. A compilation and critical review (Price and Velbel 2003) revealed only some of the indices to be reliable and suitable for provenance purposes. These indices are explained in Tab. 3.7.

| Weathering Index | | Calculation | Optimum fresh rock | Optimum weathered rock |
|---|---|---|---|---|
| V | Vogt's Residual Index | $(Al_2O_3+K_2O) / (MgO+CaO+Na_2O)$ | < 1 | infinite |
| WIP | Weathering Index of Parker | $100 * ((2Na_2O/0,35) + (MgO/0,9) + (2K_2O/0,25) + (CaO/0,7))$ | > 100 | 0 |
| CIA | Chemical Index of Alteration | $100 * (Al_2O_3 / (Al_2O_3 + CaO + Na_2O + K_2O))$ | ≤ 50 | 100 |
| CIW | Chemical Index of Weathering | $100 * (Al_2O_3 / (Al_2O_3 + CaO + Na_2O))$ | ≤ 50 | 100 |
| PIA | Plagioclase Ind. of Alteration | $100 * (Al_2O_3 - K_2O) / (Al_2O_3 + CaO + Na_2O – K_2O))$ | ≤ 50 | 100 |

Tab. 3.7: Summary of different important weathering indices after geochemical data (Price and Velbel 2003).

Although weathering indices are often used for classification and comparison of in situ weathering profiles and soils, they can as well be used for siliciclastic sediments (Fedo et al. 1996; Young 1999). In contrast to soils, they have undergone substantial transport and possibly even recyling; therefore results of thin section analysis concerning transport distance have to be taken into account. Additionally, only data from samples with similar grain size should be compared with each other to prevent misleading conclusions.

Thin section microscopy revealed no systematic differences in grain size and rounding for the SPF sandstones (see Sect. 3). The sandstone samples of the southernmost sections in the southern Eisenhower Range are the only one associated with conglomerates and therefore probably the most proximal. The weathering indices of the samples are plotted in the two diagrams of Fig. 3.23 and 3.24. Both diagrams show a good correlation of the compared indices.

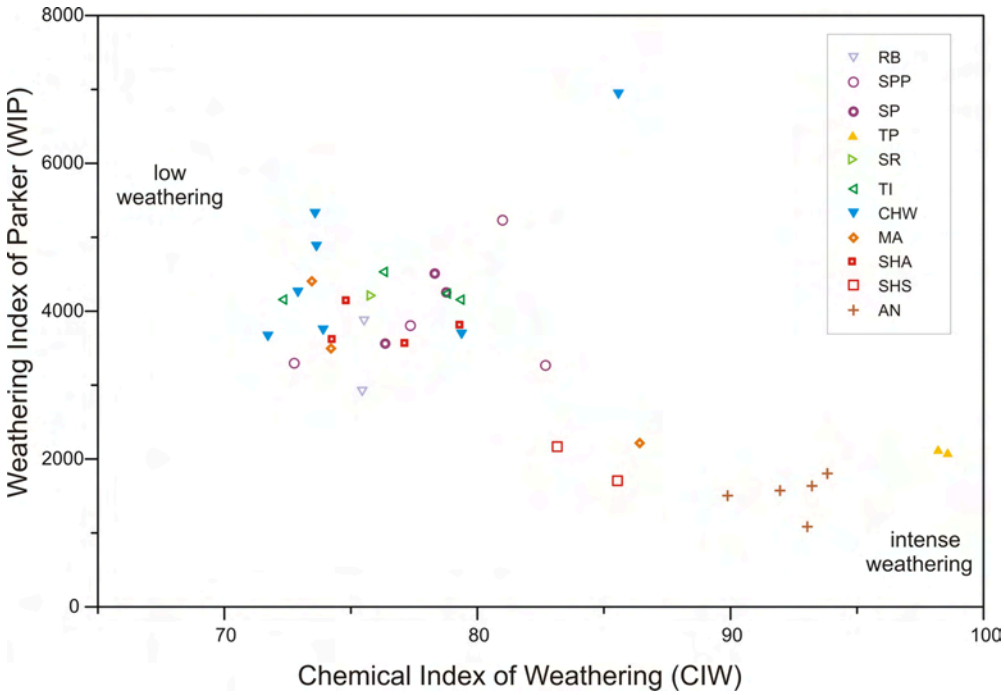


Fig. 3.23: Graphical representation of the Chemical Index of Weathering (CIW) plotted versus the Weathering Index of Parker (WIP). Samples with carbonate cementation were disregarded. For explanations see text.

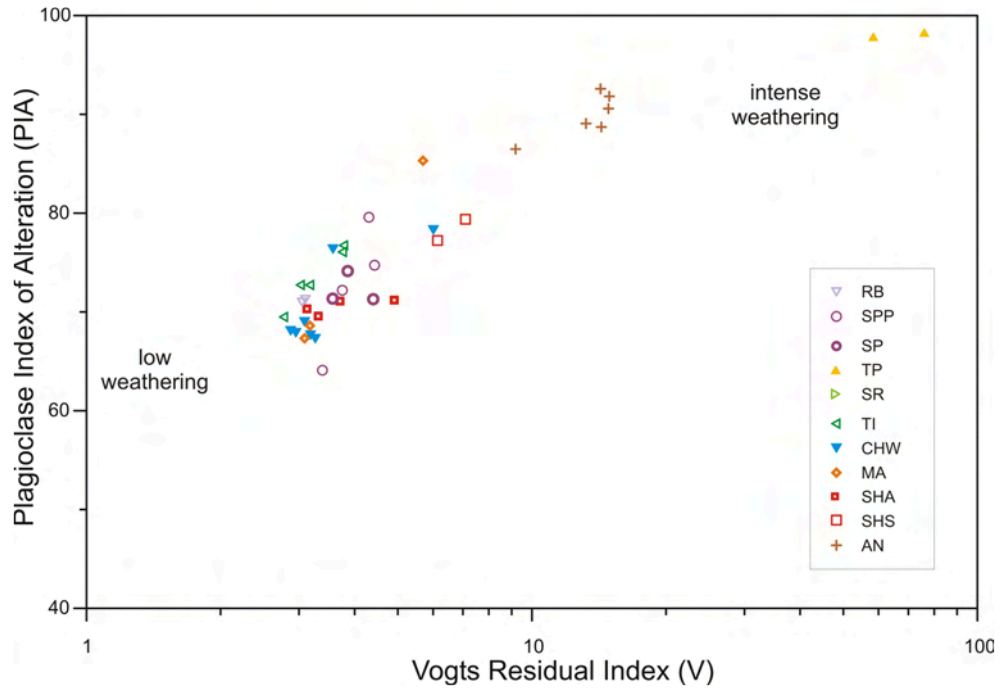


Fig. 3.24: Graphical representation of Vogt's Residual Index (V) plotted versus the Plagioclase Index of Alteration (PIA). Samples with carbonate cementation were disregarded. For explanations see text.

Samples from sections TP and AN have the highest weathering values of the analysed samples, and the values of section SHS are still relatively high. The bulk of all other samples shows lower and relatively similar weathering values.

The samples from section TP with the highest weathering values are intercalated with conglomerates and therefore most likely to be proximal. This proves an intense weathering of the source area prior to erosion and material transport, as the latter was presumably short (association with conglomerates).

Similarly highly weathered are samples from section SHS and AN, and – after thin section comparison, as no geochemical data are available – from section PT and ST. Samples with the highest geochemical weathering indices are found at basal parts of the SPF. The heavy mineral assemblages are not affected by different degrees of weathering (see Sect. 3.2.3), proving a common provenance. Most likely the surface of the source area was intensely (chemical) weathered prior sedimentation of the SPF. With beginning sedimentation (and subsequent erosion) the weathered 'crust' was first stripped off and was deposited at basal parts of SPF. At later stages chemical weathering could not keep up with erosion and fresher material was shed by the same source. A reason for the intensely weathered surface may be the long time span available for weathering, which lasted possibly since the end of the Permo-Carboniferous glaciation.

For the lithoclast richer samples from sections TI, SR and CHW no higher weathered equivalents have been found. These may lie in stratigraphic lower parts below the sampled sections, although they may also be absent. The existence of intensely and less weathered source areas side by side at the same time could be caused for example by different heights above sea level, with the steeper, higher parts being constantly more eroded and colder and therefore less weathered than adjoining low lying areas with a low relief, on which a deep weathering crust may form. Also young volcanic activity 'producing' fresh source rocks can be a reason, which in this case is possible for the lithoclast-rich sandstones. A different climate can also be important.

#### 3.3.3.4 Ophiolites in the source area

To determine an ophiolitic (ultra-mafic) sediment source by whole rock geochemical analysis Cr and Ni are used, which are typically found in Cr-spinel. Ophiolites commonly have a Cr:Ni ratio of about 1.6, in sandstones derived from such a source the ratio can exceed a value of 3 due to sedimentary processes (Garver et al. 1996).

Heavy mineral analysis revealed that some samples do contain Cr-spinel, although never in a high proportion (e.g. sample TI14, compare Sect. 3.2.3). The Cr:Ni ratio of all samples is between 0.1 and 1.3 and averages 0.6. The two highest ratios can be found in lithoclast-rich samples (SR03: 1.3; TI11: 1.0).

The two diagrams of Fig. 3.25 do not indicate ophiolitic source material, even though heavy mineral analyses do. Differences between the lithoclast richer and the lithoclast poorer sandstones are not evident. This example shows that geochemical data without accompanying petrographic analysis can be misleading, and the contribution of a small ultra-mafic source may not be detected.

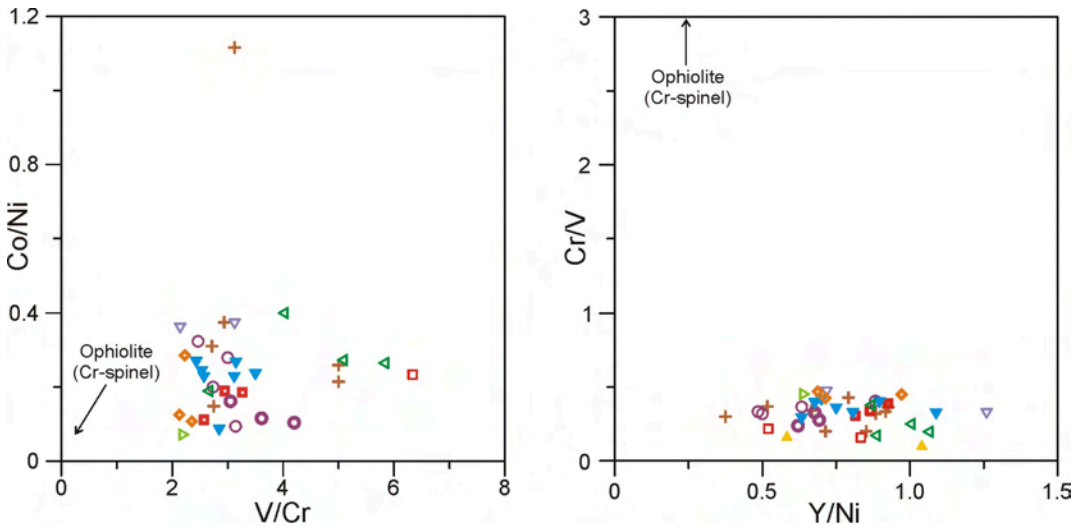


Fig. 3.25: Two plots for determination of a ophiolitic source area with whole rock geochemical analyses. The left diagram (Willscher 2004) uses the elements Co and V indicative for mafic minerals in relation to Ni and Cr, the indicators of Cr-spinel. An ophiolitic source would result in data points very close to the origin of the diagram. Similarly the right diagram (McLennan et al. 1993) uses V and Y in relation to Cr and Ni. It also gives no evidence for ophiolitic material. Legend as in Fig. 3.24.

## 3.3.4 Tectonic setting

### 3.3.4.1 Introduction

Generally different tectonic settings are thought to be characterized by distinctive provenance as well as by distinctive sedimentary processes (Rollinson 1993), but in individual cases it can be difficult to clue back from provenance to tectonic setting (Ryan and Williams 2007). This is especially the case where the eroded rocks are not related to basin formation processes itself. Tectonic settings of sedimentary basins are simplified to four types (Bhatia 1983; Bhatia and Crook 1986), that are:

- Oceanic island arc (fore-arc and back-arc basins on oceanic crust)
- Continental arc (fore-arc, inter-arc and back-arc basins on continental crust)
- Active continental margin (Andean-type/strike-slip basins on continental margins)
- Passive margin (sedimentary basins on or along thick continental crust)

These types are characterized be a decreasing importance of volcanic activity and an increase of differentiation of magmatic products due to increasing crustal thickness, and these are the trends geochemical classifications are based on. Additionally, the travel time from source to sink (erosion, transport, and sedimentation) may be faster in tectonically active regions than on low lying passive continental margins, thus weathering may possibly modify these trends (depending on climate). After all, for geochemical classification elements and element ratios are used that discriminate between mafic and felsic minerals or incorporate maturity indicators.

Tectonic setting is not the only control of sandstone composition, as are relief, weathering, transport and sorting, as well as diagenesis (Bhatia 1983; Kiminami and Fujii 2007). Therefore the results have to be interpreted carefully and compared to the results of other analytical methods.

In NVL, lying on the edge of the East Antarctic Craton in close vicinity to an active subduction zone, signatures from an “active continental margin”, a “continental arc” or a “passive margin” seem possible. Therefore the results are of special interest, because they may yield information about the basin forming processes. Only an “oceanic arc” setting seems to be unlikely from the palaeogeographic situation.

### 3.3.4.2 Tectonic setting using major elements

Major elements are controlled by light minerals and are traditionally used for discrimination. Their concentrations are given in weight percent of their oxide.

The diagram in Fig. 3.26 (Roser and Korsch 1986) exhibits the sandstones of the SPF to have formed in an active to passive continental margin setting. However, this plot is not suitable for sandstones with a negative $K_2O$:$Na_2O$ ratio, as found in some of the lithoclast rich samples (sections TI and SR). Also, a diagenetic (non-silicate) cementation (e.g. carbonates or clay minerals) and feldspar dissolution decreases ostensibly the absolute $SiO_2$ content. Weathering may also influence the $K_2O$:$Na_2O$ ratio and may distort the result.

For the diagrams of Fig. 3.27 and 3.28, the composition of Palaeozoic Australian sandstone samples were used (Bhatia 1983). In Fig. 3.27, additionally data from modern sands of known tectonic setting were incorporated.

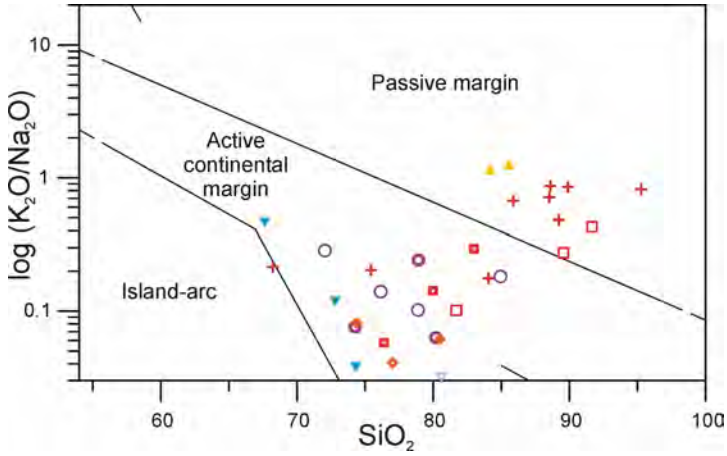


Fig. 3.26: Diagram revealing the tectonic setting plotting the logarithm of alkalis versus SiO2 content (Roser and Korsch 1986). For explanation see text. Legend as in Fig. 3.24.

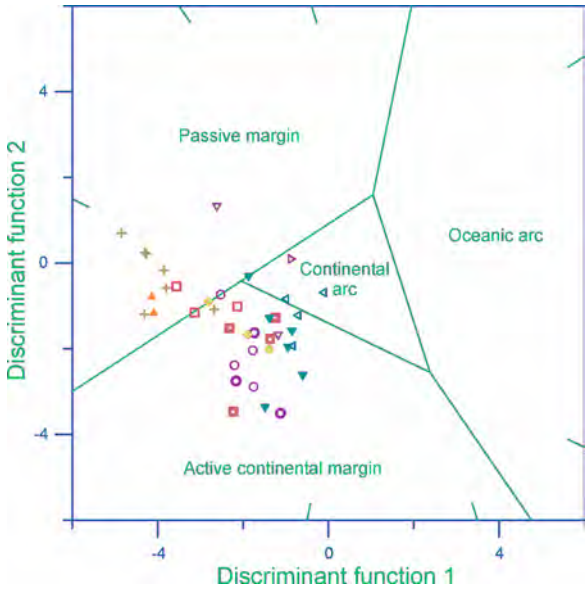


Fig. 3.27: This bivariate plot (Bhatia 1983) originally uses FeO and $Fe_2O_3$. However, this was not possible by XRF data. Therefore, $Fe_{tot}$ was used as $Fe_2O_3$, but even with $Fe_{tot}$ being totally FeO, the data points would only slightly shift to the lower right, and the result would not change substantially. Legend as in Fig. 3.24.
Discriminant function 1 = -0.447*$SiO_2$ - 0.972*$TiO_2$ + 0.008*$Al_2O_3$ - 0.267*$Fe_2O_3$ + 0.208*FeO - 3.082*MnO + 0.140*MgO + 0.195*CaO + 0.719*$Na_2O$ - 0.032*$K_2O$ + 7.510*$P_2O_5$ + 0.303;
Discriminant function 2 = -0.421*$SiO_2$ + 1.988*$TiO_2$ - 0.526*$Al_2O_3$ - 0.551*$Fe_2O_3$ - 1.610*FeO + 2.720*MnO + 0.881*MgO - 0.907*CaO - 0.177*$Na_2O$ – 1.840*$K_2O$ + 7.244*$P_2O_5$ + 43.57.

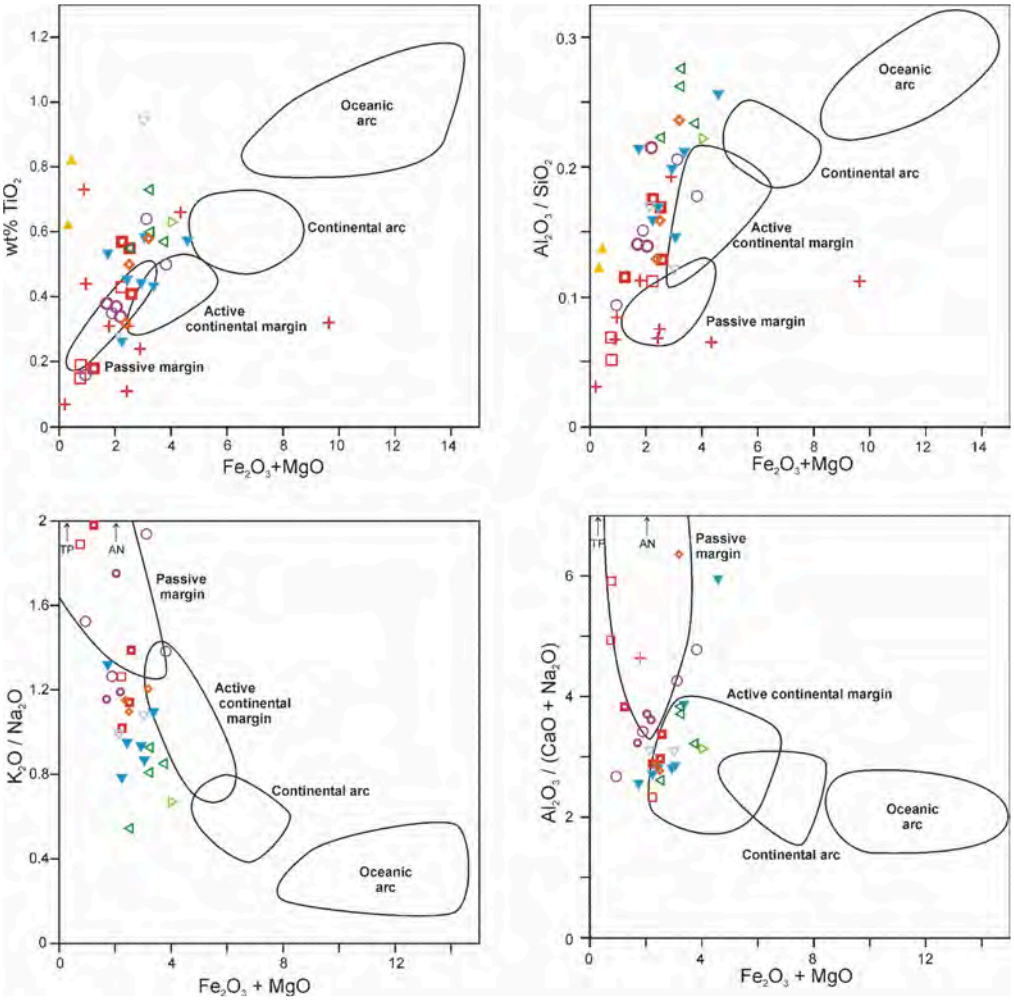


Fig. 3.28: Four discrimination diagrams (Bhatia 1983) plotting $Fe_2O_3$+MgO as proxy for mafic minerals versus $TiO_2$ (mafic minerals), $Al_2O_3/SiO_2$, (maturity), $K_2O/Na_2O$ (alkali ratio) and $Al_2O_3/CaO+Na_2O$ (clay minerals : feldspar ratio). Samples from TP and partly from AN are out of range of the lower diagrams. Further explanations in the text. Legend as in Fig. 3.24.

According to the discrimination diagrams of Fig. 3.27 and 3.28, the relatively mature sandstones (sections AN, SHS, TP) are allocated to a passive continental margin setting. All other samples seem to be derived from an active continental margin, with the lithoclast rich sandstones (section TI, SR, CHW), pointing towards a continental arc setting.

### 3.3.4.3 Tectonic setting using trace elements

Most trace elements are less mobile during diagenesis and therefore potentially more suitable for interpretation. Often but not always trace elements are derived from heavy minerals, which are resistant to weathering processes (zircon, monazite). Contrary to major elements concentrations of trace elements are given in ppm. Very low concentrations, especially those of La, Th and Sc were close to the detection limit, thus interpretation must be done carefully.

In the three ternary diagrams of Fig. 3.29 La, Th and Zr/10 are proxies for zircon and monazite, two minerals typically enriched in highly differentiated felsic rocks, whereas Sc and Co are common trace elements in mafic minerals. The two diagrams on the right indicate a continental arc to passive margin setting. In the left diagram active and passive continental margin are indistinguishable.

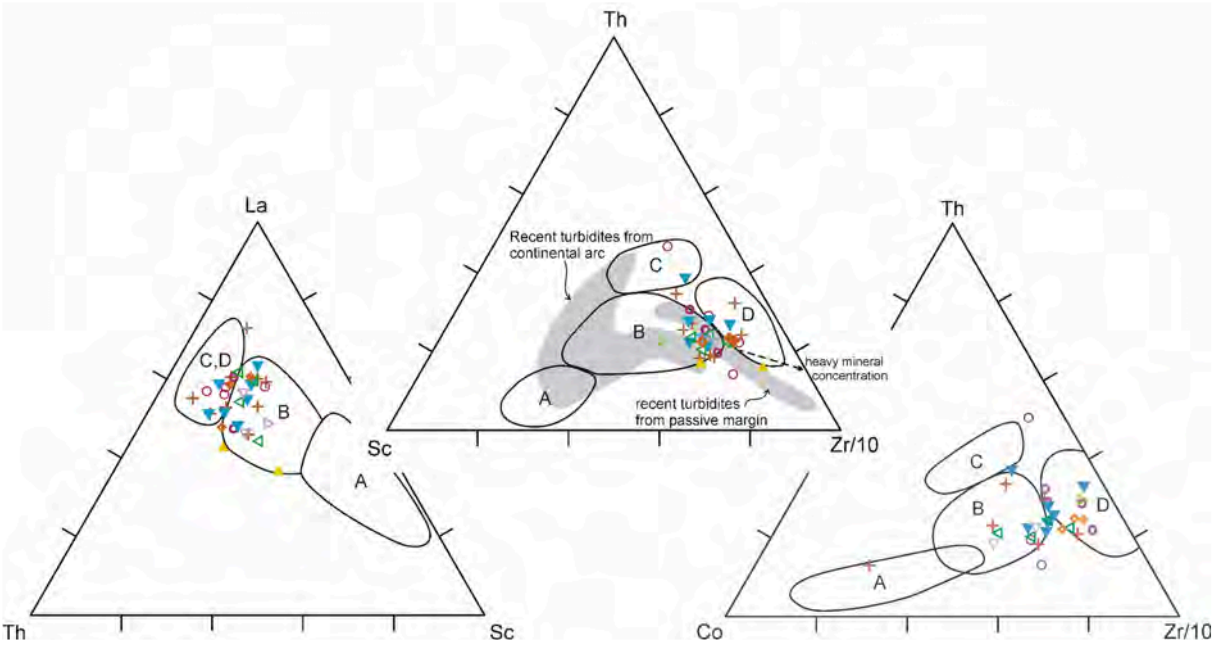


Fig. 3.29: Three ternary diagrams using trace elements (Bhatia and Crook 1986). In the middle diagram additionally fields for modern turbidite composition (McLennan et al. 1990) and a trend for heavy mineral concentration (Bhatia and Crook 1986; Willan 2003) are shown. A: Oceanic island arc; B: Continental island arc; C: Active continental margin; D: Passive margin. Legend as in Fig. 3.24.

The diagrams in Fig. 3.30 use the elements La, Th, Y and Zr being typical for highly differentiated magmatic rocks (granitoids) and Sc, Ti and Cr being typical for less differentiated magmatic rocks (basalts, ultra-mafic rocks) to discriminate sandstone types. The left diagram indicates a continental arc setting with active and passive continental margins being also possible for some samples. In the right diagram the data scatter strongly and even an oceanic island arc seems a possible tectonic setting. This result is in contrast to all other discrimination diagrams as well as to the general setting of NVL, and may therefore not be overinterpreted.

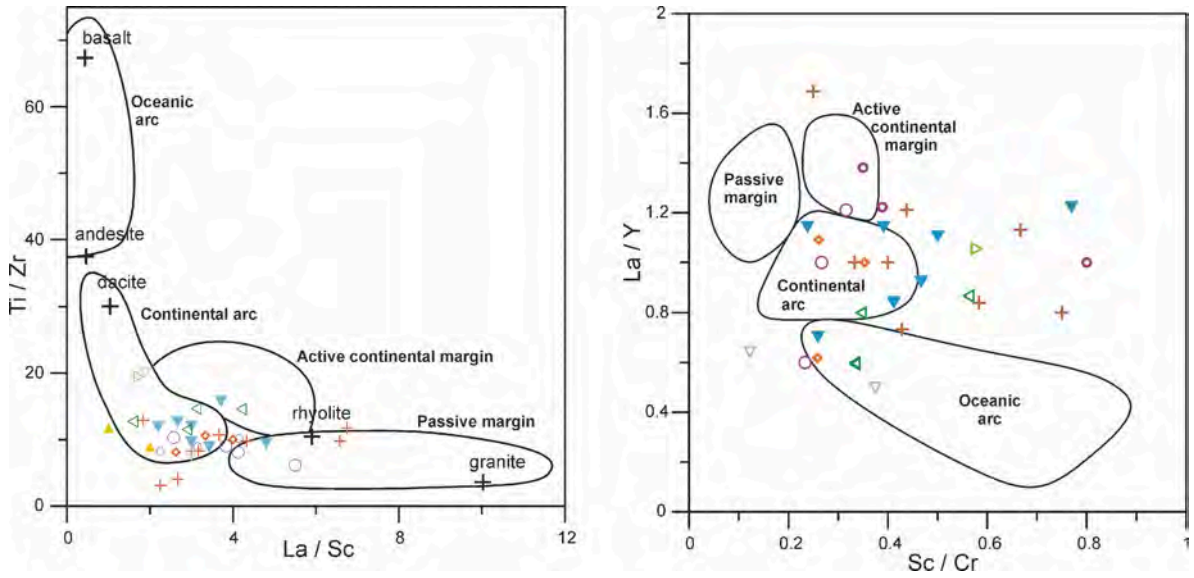


Fig. 3.30: Two scatter plots using trace element ratios for sandstone discrimination (Bhatia and Crook 1986; Roser 2000; Willan 2003). In the left plot ratios of typical source rocks are inserted (Roser and Korsch 1988). Legend as in Fig. 3.24.

Contrary to the diagrams using major elements in most of the diagrams using trace element the results do not show imaginary differences for the lithoclast richer and poorer samples. However, it is impossible to allocate the sandstones to a single tectonic setting. Considering all diagrams, the SPF has most likely formed in a setting with signatures from a continental arc, an active continental margin or a passive margin. This shows the limited possibilities of geochemical analyses. A further characterization of the tectonic setting is possible by an U-Pb age study of detrital zircons (Sect. 3.5).

### 3.3.5 Summary and comparison with petrography

In Sect. 3.2 six sandstone types (A-F) with different source regions were defined by petrography (heavy and light mineral composition). Of five of these types (except for type E) geochemical analyses were carried out. These sandstone types exhibit different geochemical characteristics with respect to provenance, tectonic setting, relative weathering intensity and the average geochemical composition of the source area.

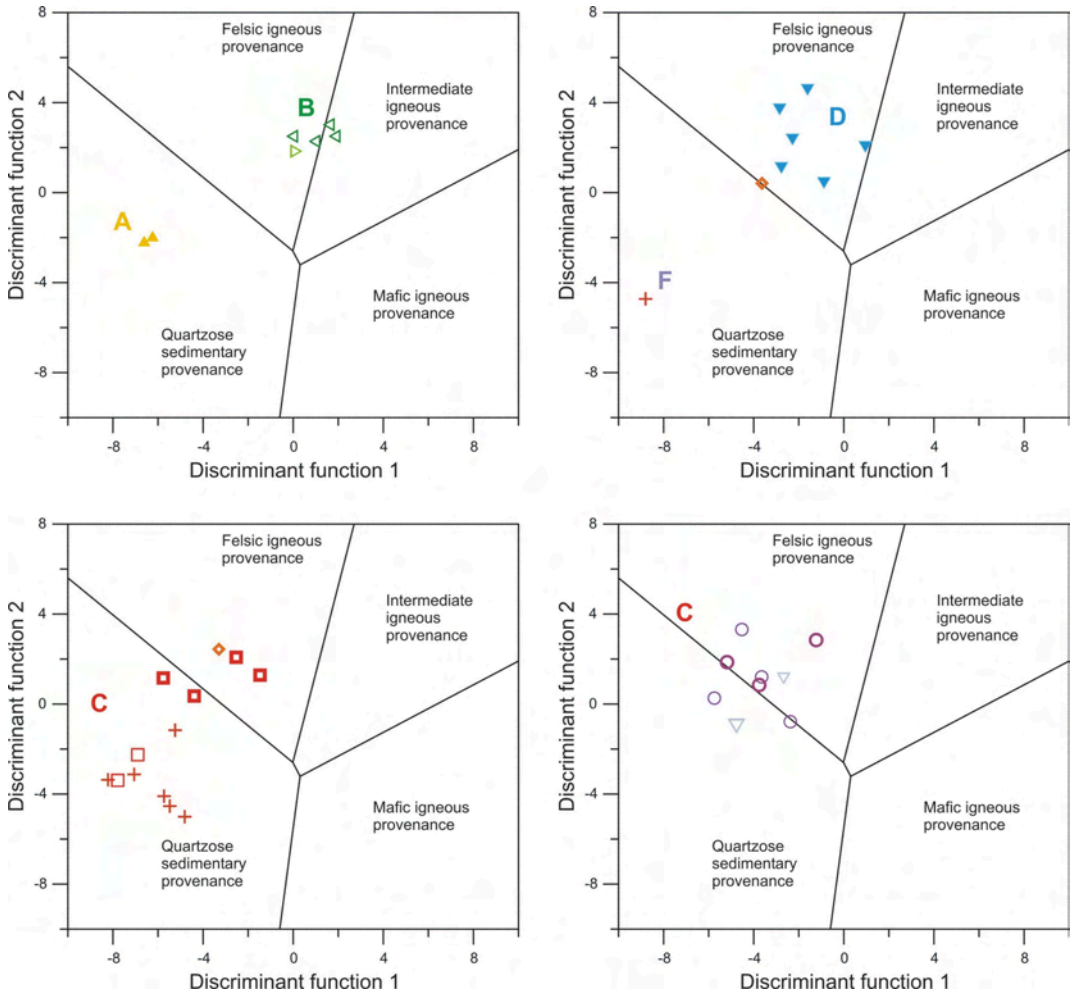


Fig. 3.31: Discrimination diagram (Nesbitt and Young 1984; Nesbitt and Young 1989) to distinguish between felsic, intermediate and mafic igneous as well as quartzose sedimentary provenance for the different sandstone types. For sandstones of type A and F a quartzose sedimentary provenance is indicated, type B points to a felsic to intermediate igneous source and type D sandstones are derived from a felsic igneous source. For type C sandstones of the Deep Freeze Range (lower left) a trend is obvious from a quartzose sedimentary source for stratigraphic lower samples (SHS) to a felsic igneous source for higher samples (SHA). Type C sandstones from the Outback Nunatak sections SP, SPP, and RB indicate a felsic igneous to quartzose sedimentary source similar to the samples from higher stratigraphic levels in the Deep Freeze Range sections MA and SHA. Legend as in Fig. 3.24, for discriminant functions see Fig. 3.18:

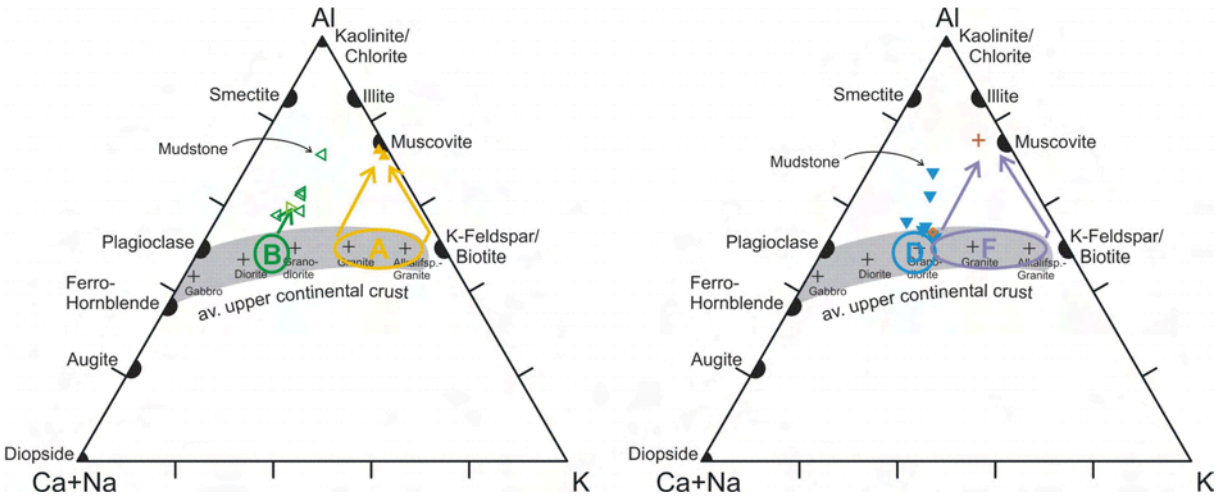


Fig. 3.32: Average geochemical composition of the sources of sandstone type A and B (left) and Type D and F (right) in the A-CN-K diagram (Nesbitt and Young 1984; Nesbitt and Young 1989). For sandstones of type A an (Alkalifeldspar-) granitic source is indicated, while type B is derived from a granodioritic to dioritic source. Type D samples point to a granodioritic source, and type F (only one sample) may be derived from a granodioritic to alkalifeldspar-granitic source. Legend as in Fig. 3.24.

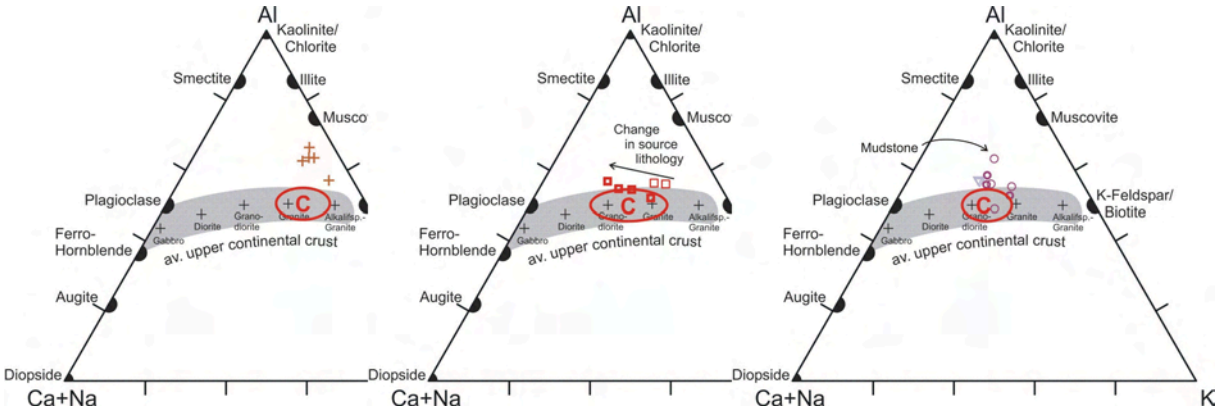


Fig. 3.33: Average geochemical composition of the sources of sandstone type C in the A-CN-K diagram (Nesbitt and Young 1984; Nesbitt and Young 1989). The samples are further divided by locality. Samples from section AN (left) indicate an (Alkalifeldspar-) granitic source, and samples from sections SHS and SHA (middle diagram) point to an granitic to granodioritic source. A trend is obvious in these sections from stratigraphic lower samples (SHS) to higher samples (SHA), which can not be explained by weathering but must be related to a change in provenance lithology. Samples from sections SP, SPP and RB are derived from an average granitic to granodioritic source similar to the samples from section SHA. Legend as in Fig. 3.24.

A distinction between the sandstone types by geochemical data alone is difficult, as the types often overlap at least partially with each other. However, the sandstone types may be further characterized by geochemical data, i.e. by additional information about the source area, or by exhibition of variations, or trend, related to provenance, transport, or sedimentation.

The following characterization of the sandstone types defined by petrography in Sect. 3.3 by their geochemical composition is based on the diagrams in Figs. 3.29 to 3.33. The results are summarized in Tab. 3.8.

Sandstones of **type A** occur at the southernmost parts of the working area (sections TP, AG, ER) and are associated with conglomerates. After geochemical constraints they are derived from a quartzose sedimentary source with on average (alkalifeldspar-) granitic composition. They are intensely weathered and show geochemical characteristics to sandstones of passive margin settings.

**Type B** sandstones occur mainly in section TI in the northern Eisenhower Range, in section SR, and in basal parts of section PT in the Deep Freeze Range. A felsic to intermediate igneous source rock composition can be deduced for these sandstones, with an on average dioritic to granodioritic composition. They show a relatively low weathering intensity. A continental arc setting is indicated applying standard geochemical provenance diagrams.

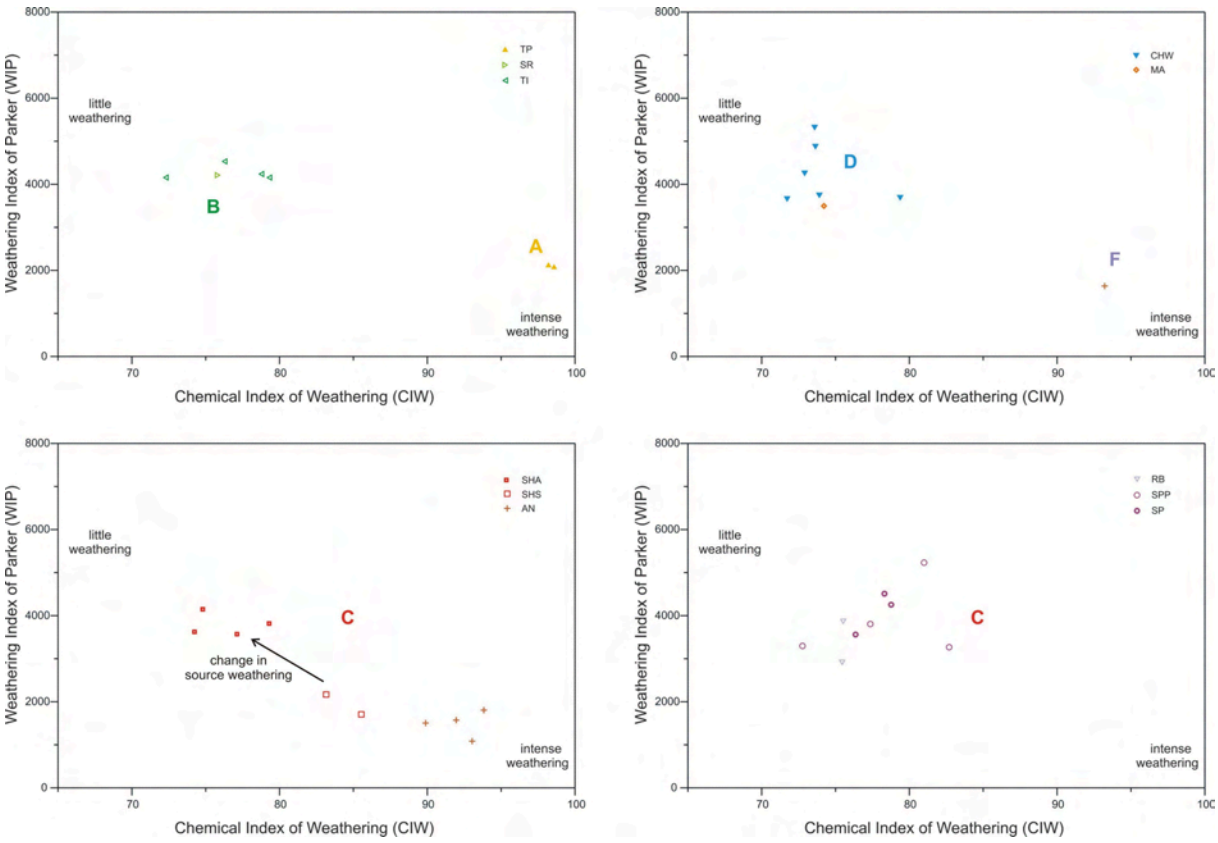


Fig. 3.34: Chemical Index of Weathering (CIW) plotted versus Weathering Index of Parker (WIP) for the different sandstone types. Type C samples have been divided into sections from the Deep Freeze Range (lower left) and sections from the Outback Nunataks (lower right). A trend of relatively intense weathered samples from the stratigraphic lower section SHS towards less weathered samples from the upper section SHA is obvious. More explanations in the text.

Sandstones of **type C** are the most frequent in the working area. They have been found mainly in the Deep Freeze Range (e.g. sections SHS, SHA, AN), in the northern Eisenhower Range (upper section TI), and in the Outback Nunatak sections RB, SP and SPP. In the Deep Freeze Range, they show a quartzose sedimentary to felsic igneous provenance, with a distinct trend for the samples of sections SHS and SHA. The stratigraphic lower samples exhibit a quartzose sedimentary provenance which changes gradually into a felsic igneous source for the stratigraphic higher samples. This trend coincides with the results of petrographic analyses, which indicate an increase of the plagioclase:total feldspar ratio and an increase of volcanic lithoclasts. Parallel to plagioclase, also the fraction of greenish-brownish amphiboles increases in the heavy mineral spectra.

The samples from the Outback sections SP, SPP and RB point to a felsic igneous provenance and no trend is obvious. Instead, all of the samples are similar to section SHA. Compositional equivalents to the basal sediments in the Deep Freeze Range (section SHS) are missing here.

On average, the source of type C sandstone has (alkalifeldspar-) granitic composition for section AN and granitic to granodioritic composition for sections SP, SPP and RB. For the sections SHS and SHA again a trend from granitic source for the basal samples towards a granodioritic provenance for the higher samples is obvious.

Intense weathering is deduced for stratigraphic lower samples (sections SHS, AN), while the upper samples are relatively less weathered. The provenance diagrams of Nesbitt and Young (1984; 1989) indicate a passive to active continental margin setting for type C sandstones. Again, the SHS and SHA samples show a trend from passive to active continental margin setting.

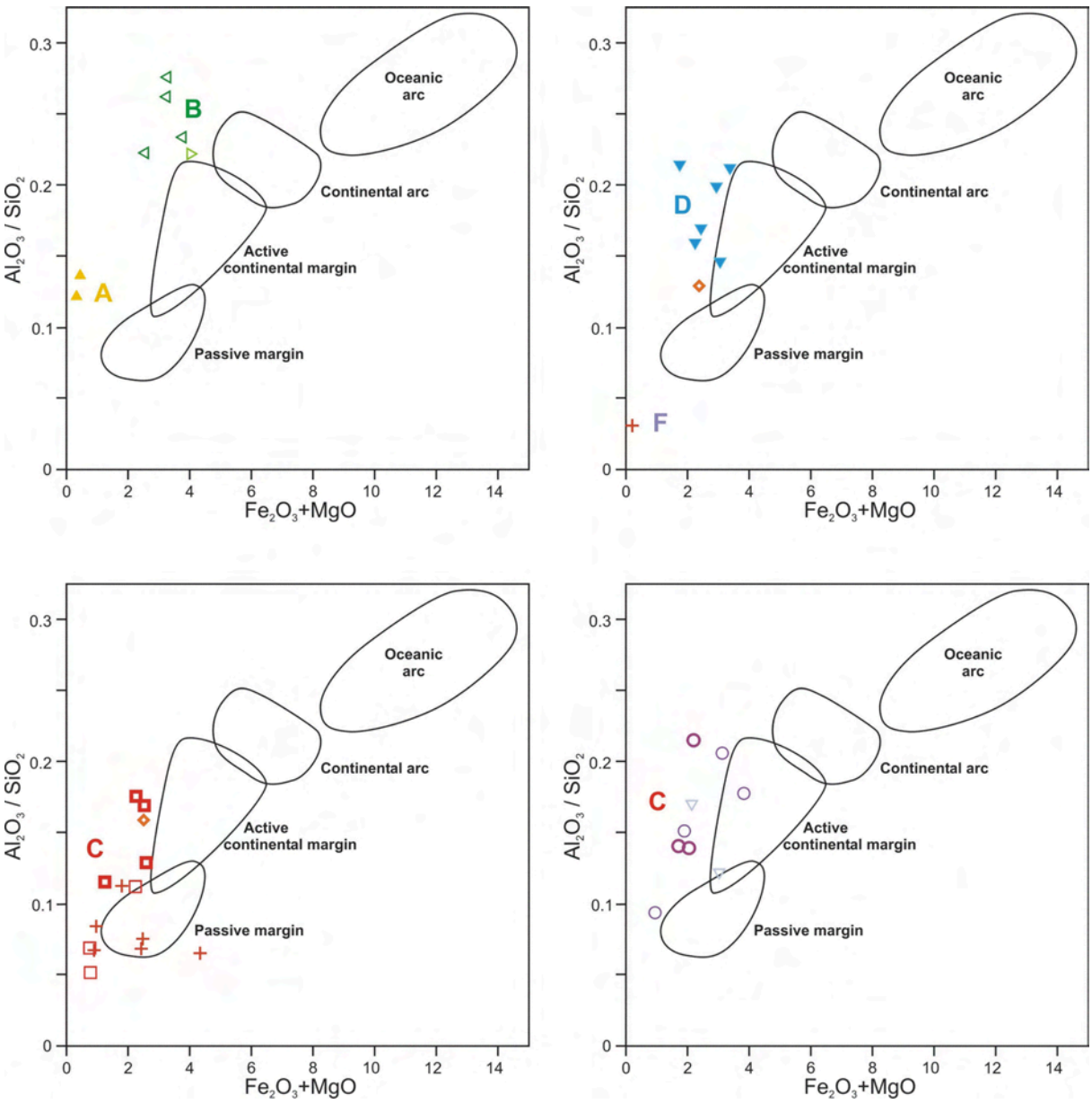


Fig. 3.34: Tectonic setting of the sandstone types in the $Fe_2O_3$+MgO vs. $Al_2O_3/SiO_2$ plot (modified after Nesbitt and Young 1984; Nesbitt and Young 1989). Sandstones of type C have been divided for clarity into Deep Freeze Range sections (SHS, SHA, MA, AN: lower left), and Outback sections (SP, SPP, RB).

Sandstones of **type D** occur mainly in section CHW in the north-eastern working area, and subordinately in section MA in the Deep Freeze Range. A felsic igneous provenance with on average granodioritic composition is indicated by geochemistry. The weathering intensity is relatively low. Sandstones of this type point towards an active continental margin setting.

**Type E** sandstones are mature quartz arenites and have been recorded from section ST in the north-eastern working area only. For sandstones of this type no geochemical analyses are available. However, petrographic analyses imply an intensely weathered source (dominating quartz) and an average (alkalifeldspar-)granitic composition (very frequent tourmaline and zircon).

Sandstone **type F** is represented by a single sample (AN08), but its heavy mineral assemblage (rutile rich) makes a separation necessary. This sandstone type is geochemically similar to stratigraphic lower type C sandstones (e.g. from section AN or SHS), showing a quartzose sedimentary provenance, a granodioritic to (alkalifeldspar-)granitic average source composition, an intense weathering of the source, and a passive margin setting.

The geochemical characteristics of the various sandstone types described above are summarized in Tab. 3.8.

| Sst.-type (n) | Provenance | Tectonic setting (major elements) | Relative weathering | Average source composition |
|---|---|---|---|---|
| A (2) | Quartzose sedimentary | Passive margin | Intense | (Alkalifeldspar-) granitic |
| B (6) | Felsic to intermediate igneous | Active continental margin to continental arc | Low | Dioritic to granodioritic |
| C (20) | Quartzose sedimentary to felsic igneous | Passive margin (to active continental margin) | Low, but intense in stratigraphic lower parts | Granodioritic to (Alkalifeldspar-) granitic |
| D (7) | Felsic igneous | Active continental margin | Low | Dioritic to granodioritic |
| F (1) | Quartzose sedimentary | Passive margin | Intense | Granodioritic to (Alkalifsp.-)granitic |

Tab. 3.8: Geochemical characterisation of the sandstone types defined by petrography. For sandstone type E no geochemical data are available. The numbers in brackets in the first column refer to samples that may be allocated clearly to one sandstone type by petrography (no mixing) without major diagenetic cementation that were used for the plots of Figs. 3.29 to 3.33. All of the described characteristics are based on geochemistry only and refer to the relating sections and figures above. Tectonic setting (column 3) is according to standard geochemical discrimination diagrams.

# 3.4 Mineral chemistry

## 3.4.1 Introduction

### 3.4.1.1 Mineral chemistry and provenance

Since the development of electron microprobe (EMP), mineral chemistry, especially of heavy minerals, has become an important tool in provenance analysis. A major advantage of the EMP is the quick chemical analysis of a very small sample volume; hence it is ideally suited for mineral grains in polished thin sections. It is especially useful for minerals that vary in composition, a property that may not be detected with mineral-optical examinations (e.g. garnet, amphibole, tourmaline), or for minerals, in which trace elements are important provenance indicators (e.g. rutile).

Mineral chemistry has been used for provenance analysis in numerous cases, particularly for garnet (e.g. Morton 1985; Morton 1987), Cr-spinel (e.g. Faupl et al. 2006; Lužar-Oberiter et al. 2009), amphiboles (e.g. Faupl et al. 2002; Von Eynatten and Gaupp 1999), and tourmaline (e.g. Henry and Dutrow 1992; Henry and Guidotti 1985). In this study, the heavy minerals garnet, tourmaline, Cr-spinel and amphibole, and the light minerals feldspar, white and dark mica were analysed, primarily to further refine provenance analysis, but also to reveal differences or similarities in mineral chemistry of the different sandstone types defined by petrography.

### 3.4.1.2 Methods

Quantitative mineral analyses were performed with a JEOL JXA 8900 RL electron microprobe (EMP), equipped with five wave-length dispersive spectrometers, at the Geowissenschaftliches Zentrum Göttingen of the Georg-August-Universität. An acceleration potential of 15 kV and a beam current of 12 nA was used. Beam diameter varied from 20 µm for light minerals (feldspar and mica) to 10 or 5 µm for heavy minerals. The oxides $SiO_2$, $Na_2O$, $K_2O$, CaO, FeO, $Al_2O_3$, MgO, MnO, BaO, SrO, and $TiO_2$ were analysed. For garnet and Cr-Spinel $Cr_2O_3$ was determined instead of BaO and SrO. For calibration, a set of natural mineral and synthetic (oxide) standards suitable for geological materials was available. Mineral identification was possible using energy dispersive spectrometer (EDX).

For analysis, in total 21 polished thin sections were chosen from various sections, covering different sandstone types in different stratigraphic positions. Additionally minerals from 3 polished heavy mineral separates were analysed. Sample preparation included heating in a vacuum-locker for at least 12 hours before carbon coating.

Back-scatter electron (BSE) images, as well as qualitative mineral identification (EDX) were additionally derived with a CAMECA SX50 at the Institut für Geowissenschaften, Friedrich-Schiller-Universität Jena.

## 3.4.2 Garnet

### 3.4.2.1 Introduction

A simplified general chemical formula of the minerals of the garnet-group is $A_3B_2[SiO_4]_3$, with the placeholder A for the elements Mg, Ca, $Fe^{2+}$, and $Mn^{2+}$. The most common element for B is Al. Important end members are almandine ($Fe^{2+}{}_3Al_2[SiO_4]_3$), pyrope ($Mg_3Al_2[SiO_4]_3$) grossular ($Ca_3Al_2[SiO_4]_3$) and spessartine ($Mn^{2+}{}_3Al_2[SiO_4]_3$). Besides these, other end members are less frequent, for example andradite ($Ca_3$ $Fe^{3+}{}_2[SiO_4]_3$), uvarovite ($Ca_3Cr_2[SiO_4]_3$) and knorringite ($Mg_3Cr_2[SiO_4]_3$). Even garnets containing (OH)-groups have been reported (Deer et al. 1992). Garnets are generally mixed crystals; pure end member compositions are extremely rare in nature.

In the SPF, garnet is the most frequent heavy mineral in sandstones of type C and D (up to 90 % of the non-opaque heavy minerals), while being very rare in sandstones of

type A, B, E, and F (see Sect. 3.2.3). Due to their chemical diversity, garnets are frequently used for provenance analysis. According to their chemical compositions they can be classified into three categories, which are thought to represent different source lithologies (Morton et al. 2005). To avoid confusion with the sandstone types A-F defined for the SPF, the garnet types originally named A, B, and C by Morton et al. (2005) were renamed in type 1, 2, and 3 here.

- Type 1 (low Ca and Mn, high Mg)
  high-grade metasediments or charnockites
- Type 2 (low Mg, variable Ca and Mn):
  medium to higher grade metasediments (amphibolites, acidic gneisses) and possibly granites
- Type 3 (high Mg, high Ca):
  high-grade basic gneisses and eclogites

The compositional boundaries of these garnet types are indicated in the diagram of Fig. 3.36. Garnets with a grossular-component of more than 50 % are not included in this classification. They are usually derived from calc-silicate-rocks or skarns (K. Pollok 2007 pers. comm.)

Analyses of garnets from possible source rocks in NVL have been published for Wilson metamorphics of amphibolite facies grade (Capponi et al. 1988; Kleinschmidt et al. 1984; Palmieri and Talarico 1988; Schubert et al. 1984; Ulitzka 1987) and granulite facies grade (Talarico et al. 1987) as well as for granitoid rocks of the Granite Harbour Intrusives (Biagini et al. 1991). These data are shown in Fig. 3.36.

Garnets (n = 59) of the SPF in NVL have already been analysed and used for provenance analysis (Di Giulio et al. 1999), but these samples cover neither the whole stratigraphic range nor the entire working area of this study. The dependence of garnet quantity and chemistry of sandstone type, as discussed in detail below, has not yet been unveiled.

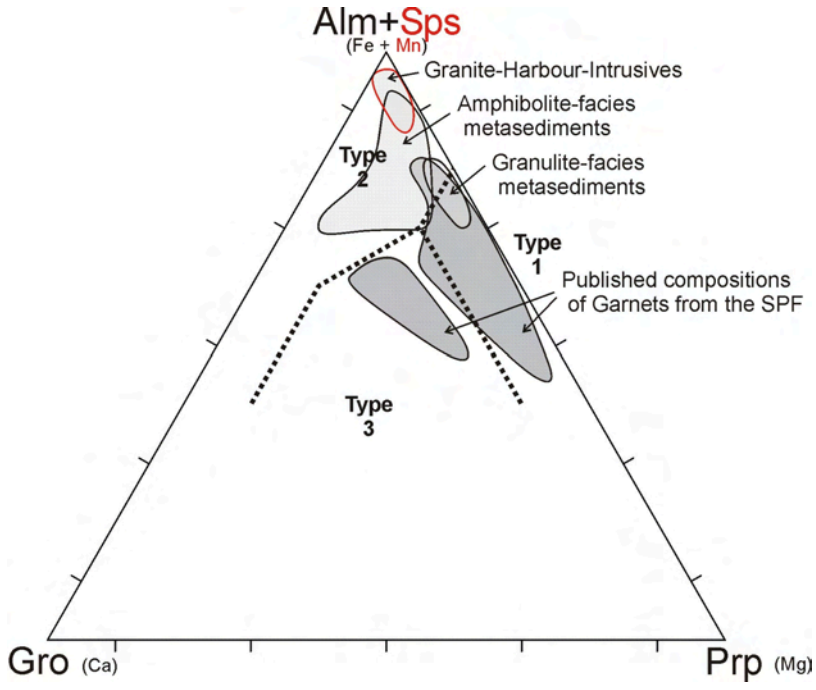


Fig. 3.36: Ternary diagram of garnet composition with the end members pyrope (Prp), almandine+spessartine (Alm+Sps) and grossular (Gro). The occurrences of garnets from Wilson metamorphics and Granite-Harbour Intrusives (red colour indicates Sps-component of more than 5 %) are displayed (see text for references), as well as the published data from the SPF (Di Giulio et al. 1999). Boundaries of the three garnet types 1, 2 and 3 after Morton et al. (2005) are also indicated.

### 3.4.2.2 Results

All analyses (n = 196) show sufficiently high Al-contents to exclude significant amounts of $Fe^{3+}$. Also, the Cr-content is very low (less than 0.03 apfu). Therefore, andradite or uvarovite components can be neglected and all results of the analyses can be represented in the pyrope – almandine+spessartine – grossular ternary diagram (Fig. 3.37). Sample locations, sample numbers, and numbers of analysed garnets as well as the associated sandstone type are summarized in Tab. 3.9.

The predominance of type 1 garnets is obvious, pointing towards a source lithology of high-grade metasediments or charnockites. A comparison with the available data indicates that the majority of the garnets do not originate from source rocks cropping out in NVL today, because these are mostly of garnet type 2. Therefore, the bulk of garnet has to be derived from one or more unknown sources.

| Section | Samples | n | Sst. type |
|---|---|---|---|
| Eisenhower Range | ER04 | 4 | A |
| Timber Peak | TI14 | 7 | B |
| Archambault Ridge North | AN15 | 23 | C |
| Shafer Peak | SHA05, SHA07 | 32 | C |
| Pt. 3350, Mt. Adamson | PT03, MA06-1, MA06-3 | 41 | C |
| Section Peak, Section Peak Plateau | SP08, SPP17, SPP31 | 43 | C |
| Roberts Butte | RB06 | 14 | C |
| Chisholm Hills West | CHW06, CHW26 | 31 | D |

Tab. 3.9: Sample locations, sample numbers and sandstone types of analysed garnets.

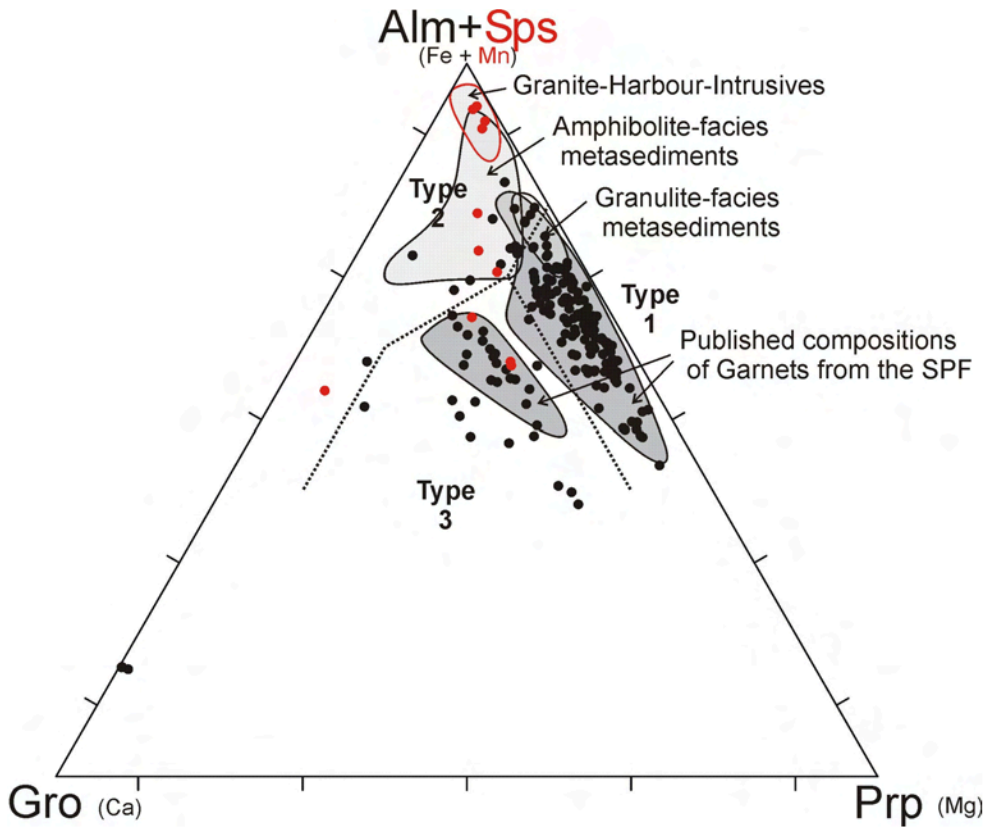


Fig. 3.37: Representation of all analyses of garnets (n = 196) in the Prp–Alm+Sps–Gro ternary diagram. Envelopes for Ross Orogen garnets and classification of garnet-types 1, 2 and 3 as in Fig. 3.36. (Prp: pyrope, Alm: almandine, Sps: spessartine, Gro: grossular). Red symbols indicate a Sps-component of more than 5 %, black symbols of less than 5 %. Garnet types 1,2, and 3 after Morton et al. (2005).

Although the bulk of garnets are not matching the composition of garnets from NVL today, this is not true for garnets from sandstone type B (Fig. 3.38). They can be associated to garnets from Granite Harbour Intrusives and Wilson metamorphic rocks of granulite facies about equal proportions. Only one garnet has been found not to show these compositions.

Within sandstone type A garnet is very rare and only four analyses were possible, three of which seem to represent a single but broken grain due to similar chemical composition (Fig. 3.38, section TP). Therefore, any interpretation of the data has to be done with caution. However, it cannot be excluded that garnets of the type A sandstones also originate from source rocks within the Ross Orogen.

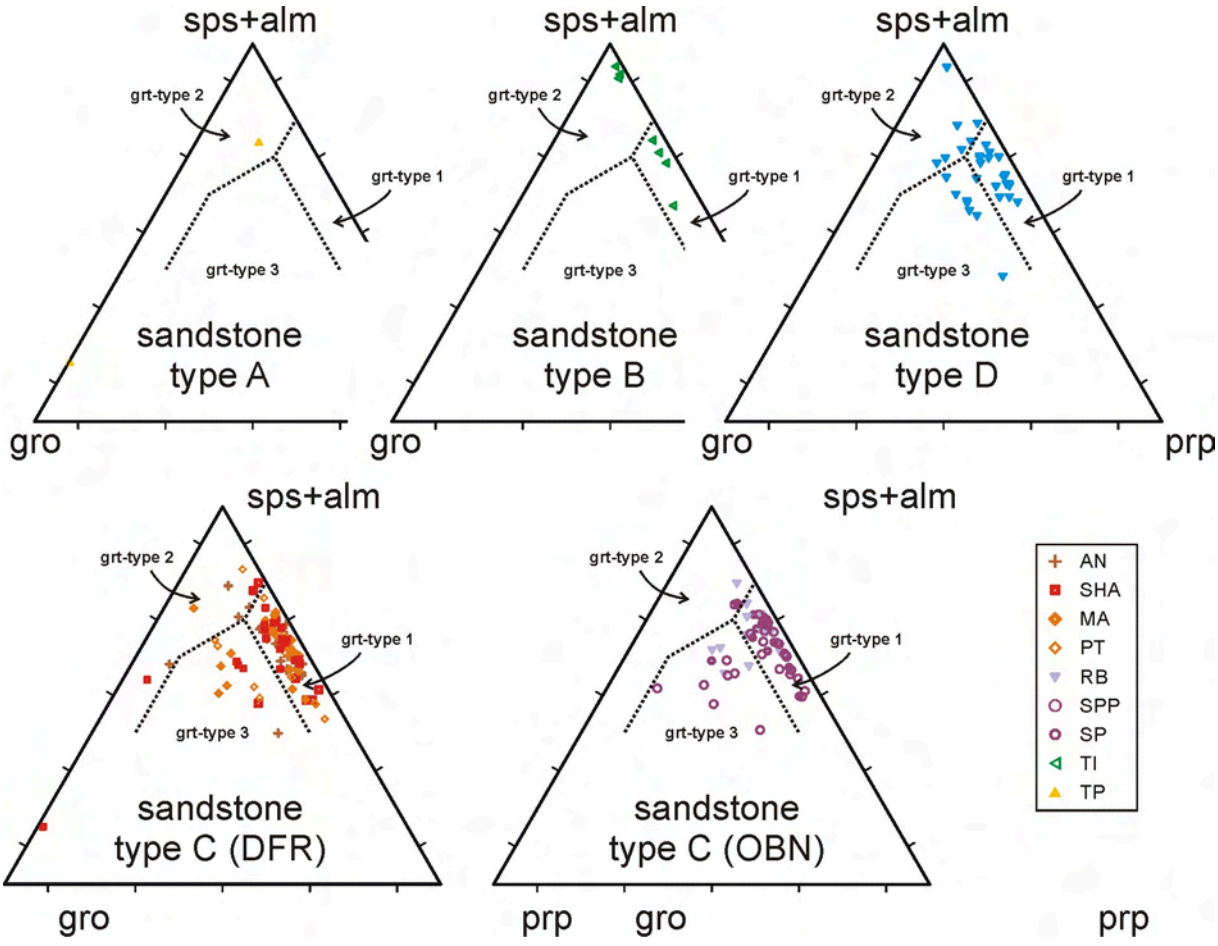


Fig. 3.38 Analyses of detrital garnets of different sandstone types. Type C samples have been subdivided into sections from the Deep Freeze Range (DFR, lower left) and from the Outback Nunataks (OBN, lower right). In sandstone types A and B, garnets are rare (see Sect. 3.2.3); therefore the number of analyses is limited. Type C and D sandstones show a predominance of type 1 garnets, pointing towards a high grade metamorphic source, with type 2 and 3 garnets being less frequent and about equally abundant. Garnet types 1,2, and 3 after Morton et al. (2005).

The fractions of the different garnet types 1, 2, and 3 are compared in Fig. 3.39. The ratios of garnets from sandstone type C are very similar regardless their geographic position in the Deep Freeze Range or in the Outback Nunataks. Thus, the same (high grade metamorphic) source of the garnets is most likely. Type 3 garnets are slightly more frequent than type 2 garnets. Basic gneisses or eclogites, and higher grade metamorphic rocks or granites, respectively, must have been present in the source region.

Garnets of type 1 are slightly less frequent in sandstone type D compared with type C sandstones. The difference in proportion of type 1 garnets may be a result of the relatively small number of analyses in type D sandstones (31). However, the ratio of type 2 and type 3 garnets is about equal, and thus similarly to type C sandstones. Therefore, it cannot be excluded that garnets of both type C and type D sandstones originate from the same source area.

In sandstones of type B, no garnets of type 3 have been found at all, and the fraction of type 2 garnets is significantly higher than in sandstones of type C and D. However, the number of analyses (7) is small.

Type A sandstones are rare in garnet. Apart from the three grossular analyses mentioned above only one type 2 garnet has been found.

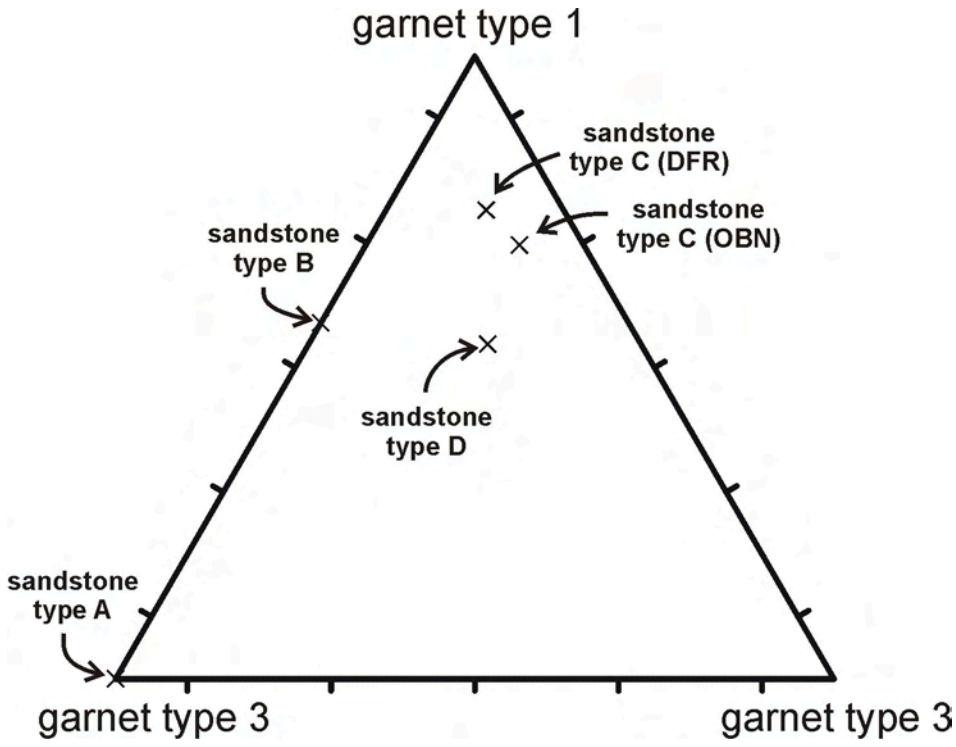


Fig. 3.39: The ratios of garnet types 1, 2, and 3 after Morton et al. (2005) compared for the different sandstone types in a ternary diagram.

### 3.4.2.3 Summary and interpretation

Most garnets of sandstone type B are probably descended from Wilson granulites and Granite Harbour Intrusives, and thus from the Wilson terrane (Ross Orogen), only few of them may possibly be from another source. The same can be inferred for garnets from type A sandstones, but the total number of analyses is very small.

The bulk of garnet from the sandstone types C and D does not match any known source in NVL. Their sources are presumably high-grade metasediments or charnockites (Garnet type 1). In addition, high-grade basic gneisses and eclogites (Garnet type 3) as well as higher grade metamorphic rocks or granites, respectively, must be present in the source region. Garnet has to be an important constituent of the rocks, as it is the most frequent heavy mineral in the two sandstone types C and D.

## 3.4.3 Tourmaline

### 3.4.3.1 Introduction

The general formula of tourmaline can be expressed as $A_{0-1}\ B_3\ C_6\ [Si_6O_{18}]\ (BO_3)_3\ (O,OH,F)_4$, with the placeholder A for Na, K or Ca, placeholder B for Li, Fe, Mg, Mn or Al, and placeholder C for Fe, Mg or Al. For stochiometric reasons, the A-site can be left empty. In rare cases, also Ti, Cr and V can be found in tourmalines (Deer et al. 1992).

The most common end members are elbaite $(Na\ (Li,Al)_3\ Al_6\ [Si_6O_{18}]\ (BO_3)_3\ (OH)_4)$, schorl $(Na\ (Fe,Mn)_3\ Al_6\ [Si_6O_{18}]\ (BO_3)_3\ (OH)_4)$, dravite $(Na\ Mg_3\ Al_6\ [Si_6O_{18}]\ (BO_3)_3\ (OH)_4)$ and uvite $(Ca\ Mg_3\ (MgAl_5)\ [Si_6O_{18}]\ (BO_3)_3\ (OH,F)_4)$. Elbaite and schorl are usually found in granites and their associated pegmatites, aplites and contact aureoles. On the other hand, dravite and uvite are common components of metasediments (Deer et al. 1992).

Due to its chemical variability and the possibility to associate chemical compositions to certain source rocks in the AFM (Al-Fe-Mg) and CFM (Ca-Fe-Mg) ternary diagrams (Henry and Guidotti 1985), tourmaline chemistry is a valuable tool for provenance analysis. However, analyses may point towards inconsistent source rocks in the two diagrams, so interpretation is not straightforward. Problems may also arise for zoned crystals, or for crystals with authigenic rims. Therefore, the interpretation should be restricted to clusters rather than arbitrary field boundaries. Table 3.10 summarizes sample locations, sample numbers and the number of analysed tourmalines, as well as associated sandstone types.

| Section | Samples | n | Sst. type |
|---|---|---|---|
| Thern Promontory | TP03 | 14 | A |
| Eisenhower Range | ER04 | 9 | A |
| Timber Peak | TI14 | 4 | B |
| Archambault Ridge North | AN15 | 1 | C |
| Shafer Peak | SHA07 | 1 | C |
| Section Peak, Section Peak Plateau | SP08, SPP17, SPP31 | 13 | C |

Tab. 3.10: Sample locations, sample numbers and sandstone types of analysed tourmalines.

### 3.4.3.2 Results

Classification of tourmalines from the SPF (Fig. 3.40) point towards Li-poor granitoid source rocks (fields 2 and 3) as well as to Ca-poor metapelites/metapsammites with or without Al-saturating phase, or quartz-tourmaline rocks (fields 4, 5, 6 and 10). However, as the number of analysed tourmalines is relatively small, a separation of tourmalines from magmatic ('granitoid') and from metamorphic sources seems appropriate, while a further subdivision of these sources is difficult. Due to the low number of analyses, samples of the same sandstone type as defined by petrography were summarized partially.

Sample TP03 (sandstone type A) contains a high proportion of tourmalines from granitoid sources. This group clusters relatively well, pointing towards a magmatic origin. The other tourmalines are derived from metapelites or metapsammites.

In sample ER04 (also sandstone type A) metamorphic tourmalines are more abundant than granitoid ones. While the tourmalines from the granitoid rocks differ slightly from the ones of the sample TP, the metamorphic tourmalines are similar and may originate from the same source.

In sample TI (type B) three out of four analysed tourmalines seem to be from a magmatic source. This is inferred from their position in the CFM diagram. In the AFM diagram, the analyses plot actually in a metamorphic field, but close to the boundary to

magmatic tourmalines. Possibly the differences between both diagrams are related to a hydrothermal overprint.

Tourmalines from sandstone type C are mostly of metamorphic origin and vary widely in composition. Tourmalines from other sandstone types have not been analysed.

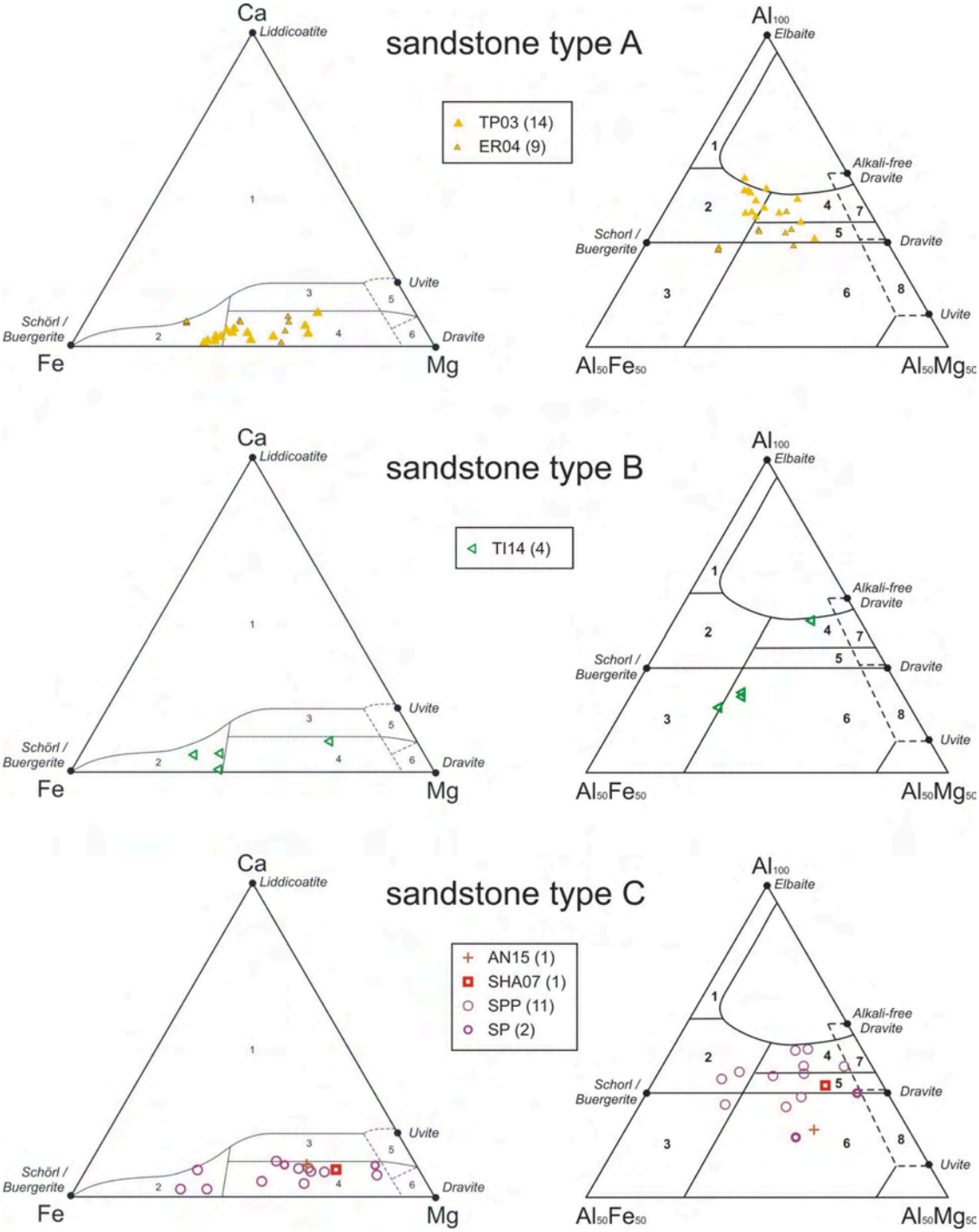


Fig. 3.40:Tourmaline analyses ordered by sandstone type plotted in the CFM (left panels) and AFM diagram (Henry and Guidotti 1985). In sandstone types A and B magmatic tourmalines are more frequent than in sandstone type C. (1) Li-rich granitoids, pegmatites and aplites; (2) Li-poor granitoids, pegmatites and aplites; (3) Hydrothermally altered granitoids; (4) Metapelites and –psammites (Al-saturating phase); (5) metapelites and -psammites (no Al-saturating phase); (6) $Fe^{3+}$-rich quartz-tourmaline rocks, calc-silicate rocks and metapelites; (7) Low Ca ultramafics and Cr-/V-rich metasediments; (8) Metacarbonates and –pyroxenites; (9) Ca-rich metapelites, -psammites and calc-silicates; (10) Ca-poor metapelites, -psammites and quartz-tourmaline rocks; (11) Metacarbonates; (12) Meta-ultramafics.

| Sandstone type | Samples | n | 'Granitoid' tourmaline | 'Metam.' tourmaline | Proportion of 'granitoid' tou |
|---|---|---|---|---|---|
| A | TP03 | 14 | 9 | 5 | 64% |
| A | ER04 | 9 | 3 | 6 | 33% |
| B | TI14 | 4 | 3 | 1 | 75% |
| C | AN15, SHA07, SP08, SPP17, SPP31 | 15 | 3 | 12 | 25% |

Tab. 3.11: Summary of tourmaline analyses from the SPF, ordered by sandstone type and samples, and subdivided into magmatic and metamorphic tourmalines. Samples from sandstone type C have been subsumed, as the number of analyses is very small in some samples and therefore not representative. The exact results are displayed in Fig. 3.40 in greater detail.

#### 3.4.3.3 Summary and interpretation

Tourmalines from type A sandstones are often descendent from granitoid rocks, but some are from metapelitic rocks. Both rock types can be found in the Ross Orogen (Granite Harbour Intrusives, Wilson metamorphics). The higher proportion of metamorphic tourmalines in sample ER04 compared with sample TP03 coincides with a higher fraction of metamorphic lithoclasts.

Also, a high proportion of tourmalines from type B sandstones may originate from granitoid rocks, although these are different from type A samples. This seems to point to a different source area, but the reason may also be a (possibly late magmatic) hydrothermal overprint.

Contrary to sandstone types A and B, tourmalines from type C are rather pointing towards a metamorphic source, although a small proportion may be of magmatic origin. The analyses scatter over a relatively wider area in the diagrams.

By means of the AFM and CFM diagrams, tourmalines from sandstones types A, B and C seem to be distinguishable from each other to a large extend, although their compositional variety overlaps partially. A greater number of analyses would be necessary to verify this statistically. Different tourmaline sources can be assumed for the three sandstone types A, B and C. Tourmalines from other sandstone types have not been analysed; in type D sandstones tourmalines have not been found.

### 3.4.4 Cr-spinel

#### 3.4.4.1 Introduction

Cr-spinel is a mixing crystal with the formula (Mg, $Fe^{2+}$)(Cr, Al, $Fe^{3+}$)$_2O_4$, with partial melting or fractional crystallisation controlling the composition. The compatible elements Cr and Mg are enriched in the crystals, while the less compatible Al remains in the (silicate) melt The $Fe^{2+}$:Mg-ratio strongly depends on magma temperature, whereas differences in the $Fe^{3+}$:$Fe^{2+}$-ratio can be explained by oxygen fugacity (Dick and Bullen 1984). Bivalent elements occupy the tetraeder position (A), trivalent elements the octaeder position (B). Other metals like $Mn^{2+}$, $Ni^{3+}$ or $Zn^{3+}$ can occur in traces. Ti may be found in the crystal lattice due to the coupled substitution of 2 $Fe^{3+}$→ $Fe^{2+}$ + $Ti^{4+}$ on the octaeder position to form ulvöspinel (Deer et al. 1982). A large component of ulvöspinel typically occurs in extraterrestrial Cr-spinel.

So far, only one analysis of Cr-spinel from NVL has been published. A small body of metamorphosed olivine-tremolite fels from the Lanterman Range (Wilson terrane, close to Lanterman-Mariner-Suture) was reported to contain Cr-spinel with a Mg: $Fe^{2+}$ ratio $X_{Mg} = 0.13$ and an Cr:Al ratio $X_{Cr} = 0.86$ (Kleinschmidt et al. 1987).

### 3.4.4.2 Results

As $Fe^{3+}$ occurs with at most 0.09 apfu, and the $TiO_2$-content is very low (max 0.25 wt%), all samples are presumably of peridotitic origin (Pober and Faupl 1988). The samples can be characterized by the four end member chromite ($Fe^{2+}Cr_2O_4$), picrochromite ($MgCr_2O_4$), hercynite ($Fe^{2+}Al_2O_4$) and spinel ($MgAl_2O_4$). If a common origin of the Cr-spinel is assumed, they most likely originate from supra-subduction zone peridotites (Fig. 3.41).

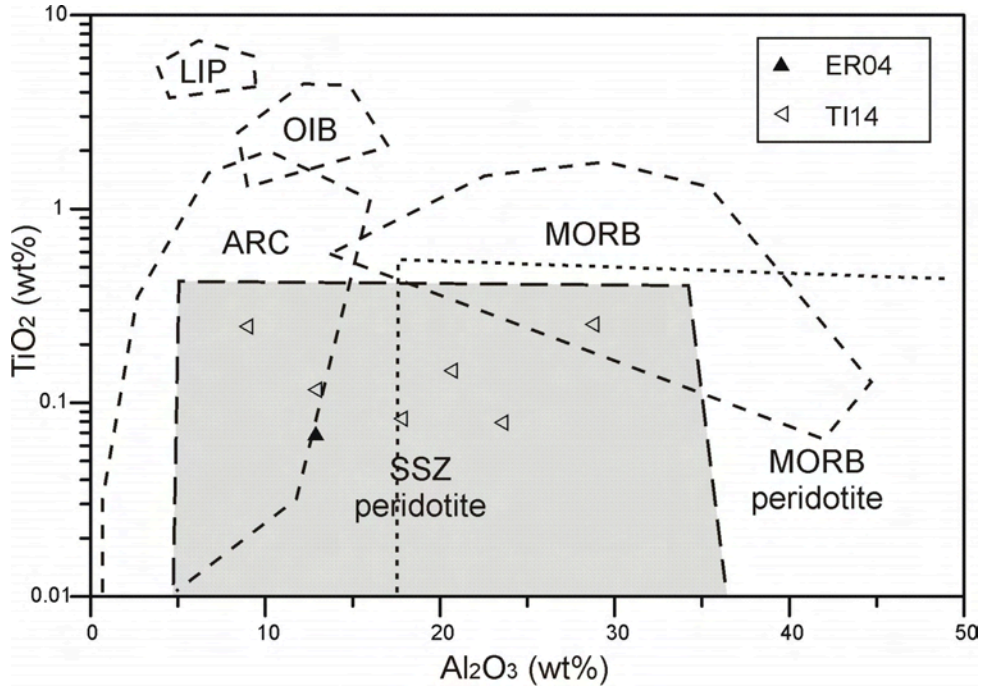


Fig. 3.41: $Al_2O_3$ versus $TiO_2$ diagram for the Cr-spinel. Fields indicate Cr-spinel composition typical for large igneous provinces (LIP), ocean island basalts (OIB), magmatic arcs (ARC), mid-ocean ridge basalts (MORB) as well as supra-subduction zone (SSZ) and MORB peridotite origin (Kamenetzky et al. 2001; Lenaz et al. 2000). Different possible sources are indicated for almost all samples; if a common origin is assumed, the results can easily be explained by SSZ peridotites.

Typically, the Cr:Al-ratio $X_{Cr}$ shows a stronger variation than the Mg:$Fe^{2+}$-ratio $X_{Mg}$. By means of $X_{Cr}$, chromites from harzburgites ($X_{Cr}$ between 0.4 and 0.8) can be distinguished from those from lherzolites ($X_{Cr}$ between 0.1 and 0.5). With $X_{Cr}$ between 0.48 and 0.81, the analysed chromites are most likely derived from harzburgites or dunites (see Fig. 3.42).

Besides this lithological classification, it is possible to assign a certain geotectonic setting to the composition of Cr-spinel. This can be done by comparing of recent abyssal peridotites with alpinotype peridotites (Dick and Bullen 1984), resulting in three types:

- Type-I-peridotites (chromites with $X_{Cr} < 0.6$) of Mid-Ocean Ridges (MOR)
- Type-II-peridotites (chromites with strongly varying $X_{Cr}$) of Island-Arc-Systems on oceanic crust (= transitional type)
- Type-III-peridotites (chromites with $X_{Cr} > 0.6$) of Island-Arc-Systems, oceanic plateaux and continental intrusives

This classification scheme has later been modified (Pober and Faupl 1988), as chromites with $X_{Cr}$ between 0.5 and 0.6 and high $X_{Mg}$ (> 0.65) are most likely to originate from chromitites, and thus most likely from type-III-peridotites. However, as $X_{Mg}$ of Cr-spinels of the SPF never exceeds 0.58, the original classification scheme was retained and an attribution to transitional type-II-peridotites is possible.

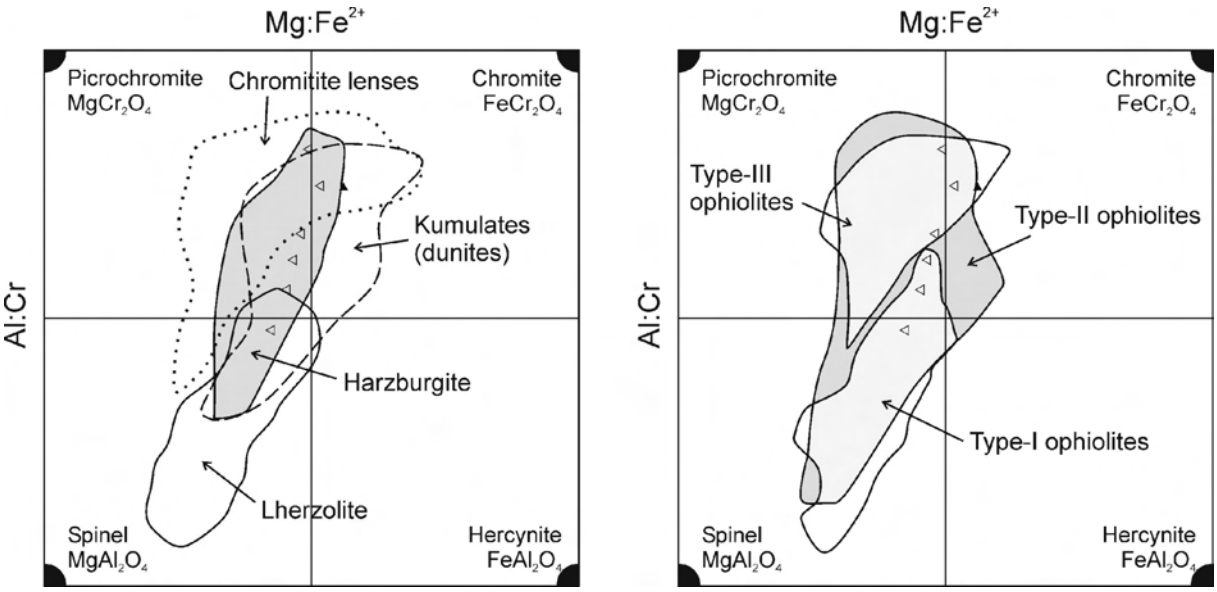


Fig. 3.42: Analysed Cr-spinels plotted in the Mg:Fe2+ versus Cr:Al – diagram compared to the compositions of chromites from different alpinotype peridotites in the left panel (Pober and Faupl 1988), and with different ophiolites in the right panel (Dick and Bullen 1984). Assuming a common origin of the Cr-spinel, an origin from harzburgitic type-II ophiolites is most likely.

### 3.4.4.3 Summary and interpretation

Cr-spinel of the SPF most likely originate from harzburgitic rocks, which may have been present in an oceanic island-arc (Dick and Bullen 1984) or in supra-subduction zone (SSZ) peridotites (Kamenetzky et al. 2001; Lenaz et al. 2000).

Various ultra-mafic rocks as possible sources are known within the Ross Orogen. They occur along the Lanterman-Mariner-Suture between Bowers terrane and Wilson terrane, and a SSZ peridotitic composition is likely according to their tectonic position (see Sect. 1). Known locations in Victoria Land are the Barber glacier area, the Lanterman Range, the Mariner glacier area, Reilley Ridge and Niagara Icefalls (Fiameni 2007). The Tiger Gabbro, a layered intrusion, also contains Cr-spinel (Engel 1987). Additionally, ultra-mafic rocks may be present at the Matusevich anomaly along the Matusevich glacier. This anomaly could be an important boundary within the Wilson terrane comparable to the other two terrane boundaries. Due to its sub-ice position, it is known from geophysical data only (F. Tessensohn 2008, pers. comm.). Cr-spinel may also be recycled from older sediments. Turbidites of the Morozumi Range contain Cr-spinel, in contrast to the turbidites of the Robertson-Bay terrane. Besides these known locations, other occurrences can be assumed along the offshore extensions of the terrane boundaries within the Ross Sea, particularly the Lanterman-Mariner suture.

A conclusive attribution to a specific location is impossible, because mineral chemical data for comparison are missing. In addition, the different sources may contain Cr-spinel of similar composition, as they may all have formed in a similar tectonic setting (type II ophiolites) during the same orogeny. Only Cr-spinel from the Tiger Gabbro (layered intrusion) possibly has a different composition (type III?). Therefore, the only possibility to further localize the source of the Cr-spinel, are palaeocurrent directions. For the type B sandstones (sample TI14), these point towards an easterly origin and thus to a source that today lies offshore in the Ross Sea (Schöner et al, in review).

## 3.4.5 Amphiboles

### 3.4.5.1 Introduction

Amphiboles are among the most complex mineral groups. A general formula for minerals of the amphibole group can be expressed as $A_{0-1}B_2C_5T_8O_{22}(OH,F,Cl)_2$ (Hawthorne and Oberti 2006; Leake et al. 2004). The most common elements are Na, K, Ca for A, Ca, Sr, Ba and Na for B, Al, Mg, Fe, Ti and Mn for C, and Si, Al for T. Depending on stoichiometry, the site A may be left empty. Due to the large number of elements possible in the amphibole structure, nomenclature is difficult (Fig. 3.43). Five groups are commonly distinguished (Leake et al. 2004):

- Mg-Fe-Mn-Li-amphiboles
- Calcic amphiboles
- Sodic-calcic amphiboles
- Sodic amphiboles
- Na-Ca-Mg-Fe-Mn-Li-amphiboles

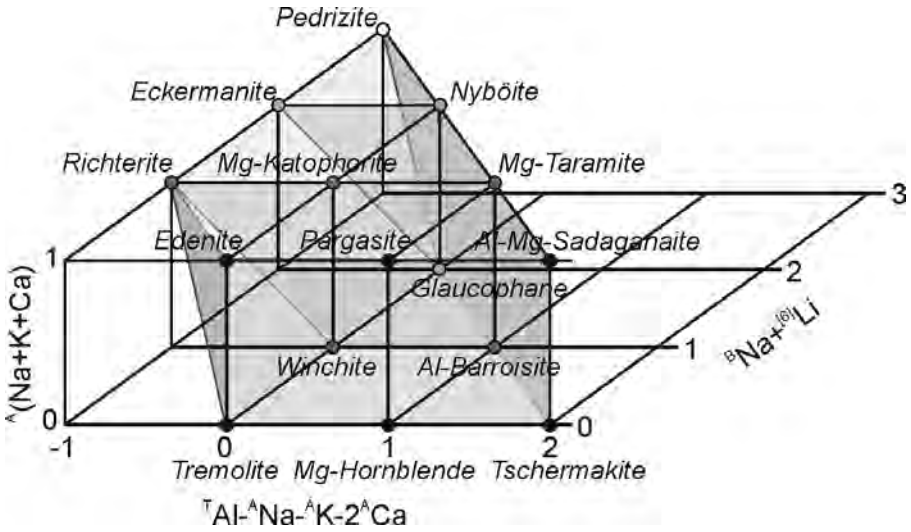


Fig. 3.43: This plot visualizes the very high chemical variability of amphiboles (Schumacher 2007). Amphiboles found in the SPF are calcic amphiboles and can be displayed in the Edenite – Al-Mg-Sadaganaite – Tschermakite – Tremolite square on the front side of the plot.

### 3.4.5.2 Results

The analyses of amphiboles are given in the appendix. All analyses show $^{B}Ca$ (this is Ca on position B) between 1.7 and 1.9 apfu and can be attributed to the group of calcic amphiboles. The fraction of $(Na+K)^{A}$ varies between 0.24 and 0.72, therefore two different diagrams are necessary for nomenclature purposes (Fig. 3.44).

As generally for EMP analyses the abundance of ferric iron is unknown, a calculation is necessary, resulting in a range of $Fe^{2+}$, and possibly causing nomenclature problems. For the calculations done here the 'average' $Fe^{2+}$ calculation (Schumacher 1997), has been used. $X_{Mg}$ exceeds 0.5 in nearly all cases.

Following the most recent classification scheme (Leake et al. 1997; Leake et al. 2004), the bulk of amphiboles are pargasites and magnesio-hornblendes, subordinately tschermakites and rarely edenites and ferro-pargasites.

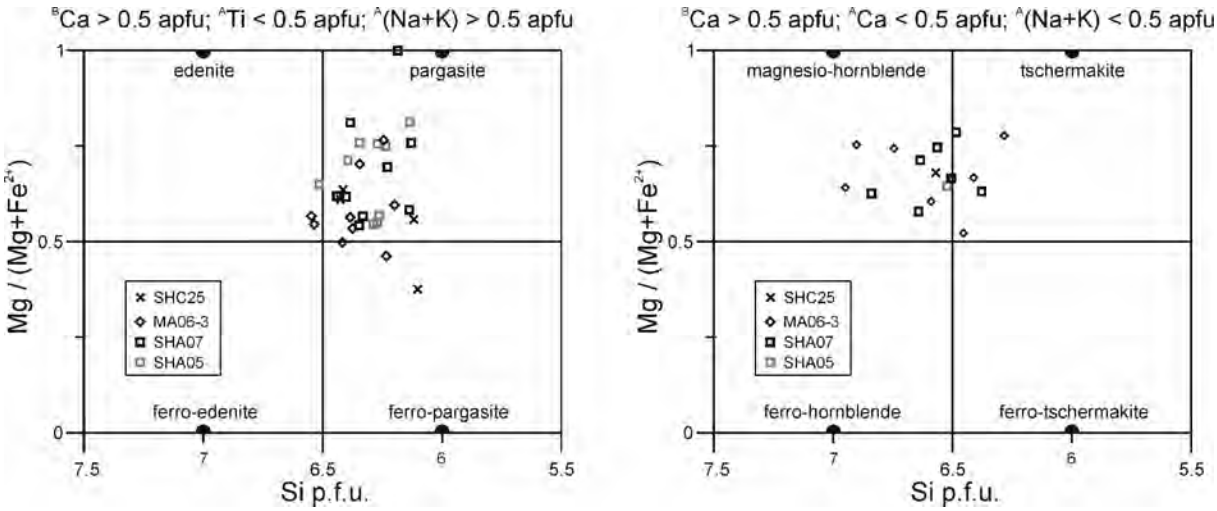


Fig. 44: Si pfu versus $X_{Mg}$ for $^{A}$(Na+K) ≥ 0.5 apfu (left diagram) and for $^{A}$(Na+K) < 0.5 apfu on the right (Leake et al. 1997). Analyses from the SHF (sample SHC25) are included. Most amphiboles are paragsites.

Although for brown hornblende a magmatic origin can generally be assumed (Von Eynatten 1996), colour alone is not a decisive criterion and its reliability should not be overvalued. Application of standard diagrams for determination of the origin of the amphiboles (Deer et al. 1997) give no clear result (Fig. 3.45).

A high Ti content is indicative for high temperatures, as is a glaucophan-component for high pressure, but no exact limits can be set. Here, the glaucophan-component is low and the Ti content ranges from about 0.05 to 0.35 apfu. However, the relatively homogeneous composition of the amphiboles is pointing to a magmatic origin (G. Franz 2008, pers. comm.).

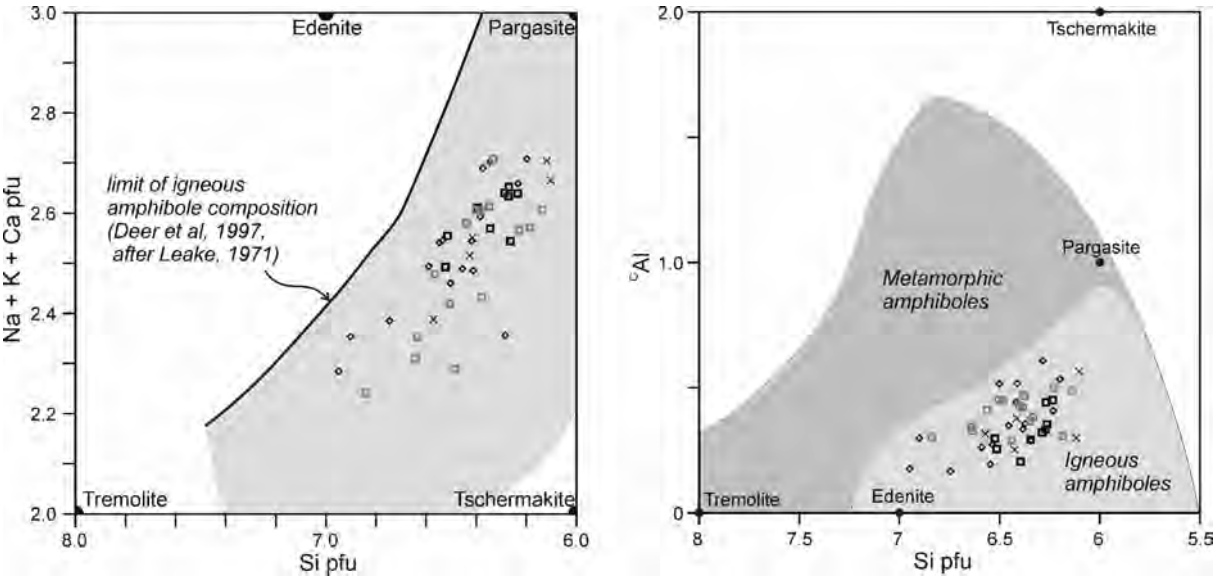


Fig. 3.45: Si pfu versus (Na+K+Ca) pfu (left panel), and versus $Al^{C}$ on the right (Deer et al. 1997). According to both diagrams a magmatic origin of the analysed amphiboles is possible, but a metamorphic origin cannot be excluded. Legend as in Fig. 3.44.

Temperature and pressure during amphibole formation can be estimated using Ti and Al on the C position (Colombi 1988, cited in Von Eynatten 1996). By application to the amphiboles in the SPF, the resulting pressures are very low, pointing towards a (sub-)volcanic formation of the amphiboles (Fig. 3.46).

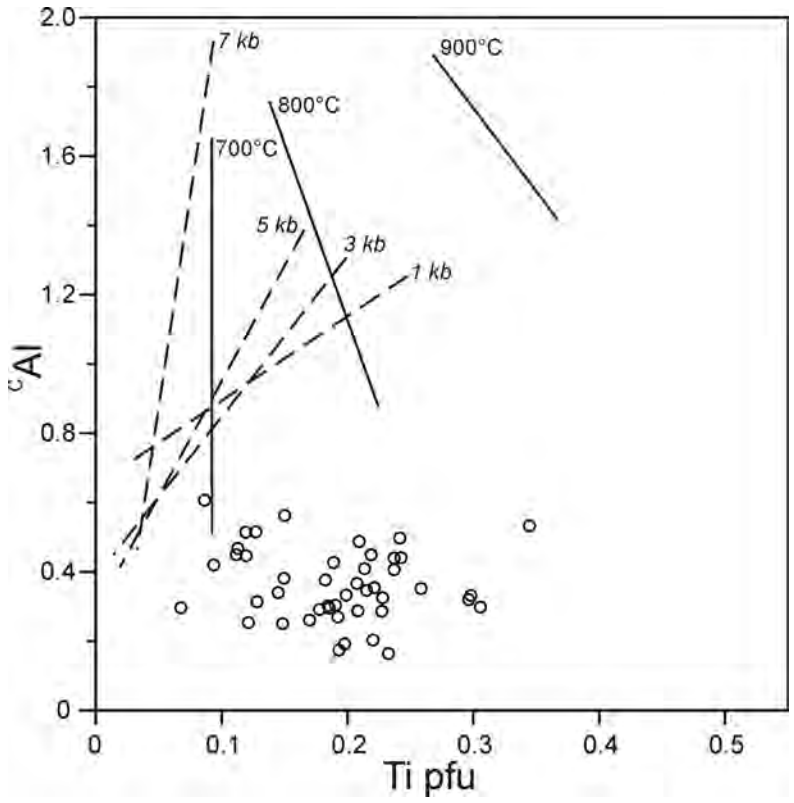


Fig. 3.46: Analyses of amphiboles in the Ti pfu versus $Al^{C}$ pfu diagram (after Colombi 1988, in Von Eynatten 1996) indicating very low pressure < 1 kb and temperatures between about 700 and 800°C. These conditions are typical for (sub-)volcanic rocks, or possibly contact metamorphism, but unlikely to occur during regional metamorphism.

Given a magmatic origin of the amphiboles, it is worth looking at the chemistry of their possible source rock. This can be done by comparing their chemistry with amphibole analyses from known magmatic rock types. According to Figs. 3.45 to 3.47 continental, calc-alkaline rocks of basaltic to andesitic composition are the most probable sources of the amphiboles.

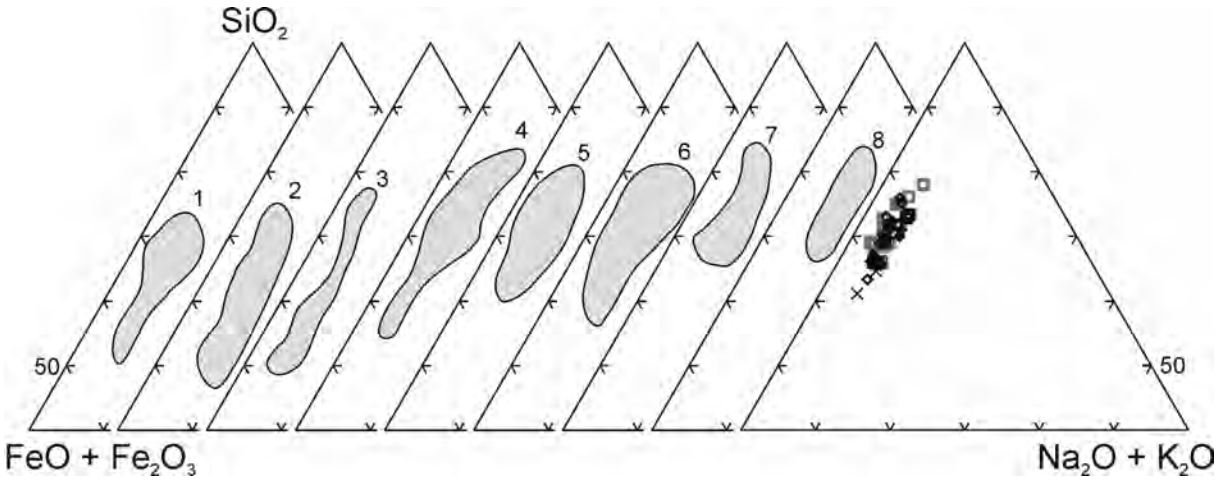


Fig. 3.47: Calcic amphibole composition in the iron-alkali-silica ternary diagram according to igneous rock type (Deer et al. 1997; Wones and Gilbert 1982). On average the range covered by the amphiboles of the SPF is similar to the typical range of amphiboles from dacitic, andesitic or basaltic rocks. 1 pegmatitic; 2 silica-undersaturated; 3 rhyolithic; 4 dacitic; 5 andesitic; 6 basaltic; 7 ultramafic; 8 xenolithic. Legend as in Fig. 3.44.

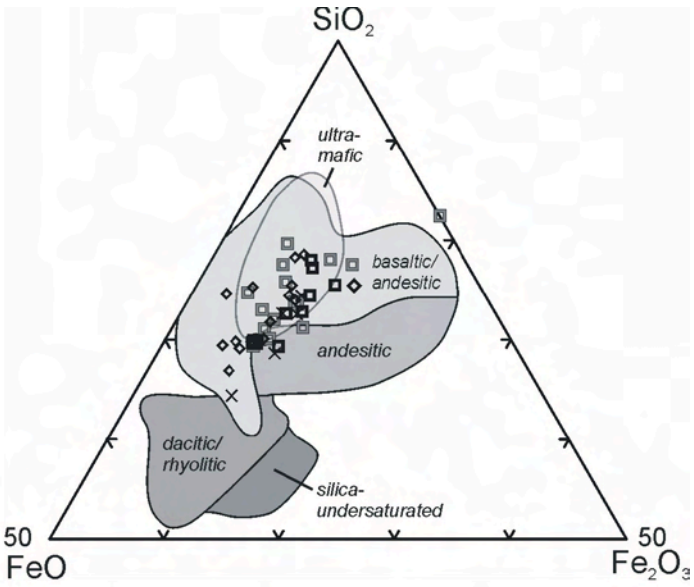


Fig. 3.48: Ternary discrimination diagram (Wones and Gilbert 1982) for igneous calcic amphiboles based on silica, ferric and ferrous iron. Analysed amphiboles from the SPF are in accordance with amphiboles from basaltic/andesitic or ultra-mafic rocks. Legend as in Fig. 3.44.

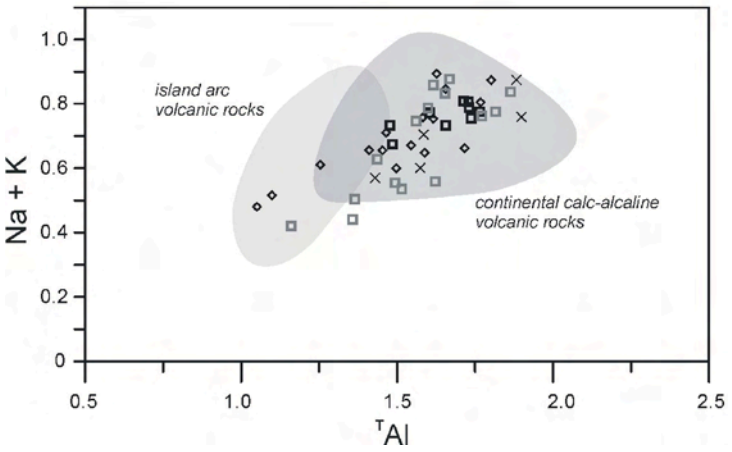


Fig. 3.49: Comparison of the analyses in a $Al^T$ versus Na+K diagram (Jakes and White 1972), indicating a continental calc-alkaline rather than an island arc source of the amphiboles. Legend as in Fig. 3.44

### 3.4.5.3 Summary and interpretation

The calcic amphiboles are mostly pargasites and magnesio-hornblendes. In all likelihood, they are originating from continental calc-alkaline rocks of presumably basaltic to andesitic composition. These rocks may have formed at the magmatic arc that developed along the subducting proto-pacific margin of Gondwana. This interpretation is consistent with the palaeogeographic and tectonic context (see Sect. 1). However, it predicts no formation age, as subduction was active along this plate margin since the Proterozoic. It could be related for example to the Devonian magmatic activity, from which andesitic rocks have been described (Gallipolli volcanics), but also to Permian or to syn-sedimentary Triassic/Jurassic volcanism. Additional information about formation of the amphiboles could be obtained from Ar-Ar age dating of the amphiboles.

The amphiboles can be found in the uppermost parts of the SPF only (sections SHA and MA, see Sect. 3.2.3). As in the upper part of the SPF the plagioclase : alkali-feldspar ratio increases with increasing stratigraphic height (see Sect. 3.2.2), a relation of both observations may be plausible. This indicates a common source of plagioclases and amphiboles, as for examples provided by andesitic extrusive rocks.

## 3.4.6 Feldspar

### 3.4.6.1 Introduction

Minerals of the feldspar group can be chemically classified in a ternary system on the basis of their end members K-feldspar ($KAlSi_3O_8$, orthoclase, Or), albite ($NaAlSi_3O_8$, Ab) and anorthite ($CaAl_2Si_2O_8$, An). Feldspar with a compositions between the end members K-feldspar and albite is referred to as alkali feldspar, whereas this with a composition between albite and anorthite is a plagioclase (Deer et al. 1992). A wide temperature, and, to a lesser extent, pressure dependent miscibility gap exists between anorthite and K-feldspar.

Besides a chemical classification, feldspars can be distinguished by their structural state in high-temperature (disordered) and low temperature feldspars (ordered). The former commonly originate from volcanic rocks that have undergone relatively rapid cooling, the latter typically from plutonic rocks, in which feldspars had time enough during crystallisation to form an ordered crystal lattice (Fig. 3.50).

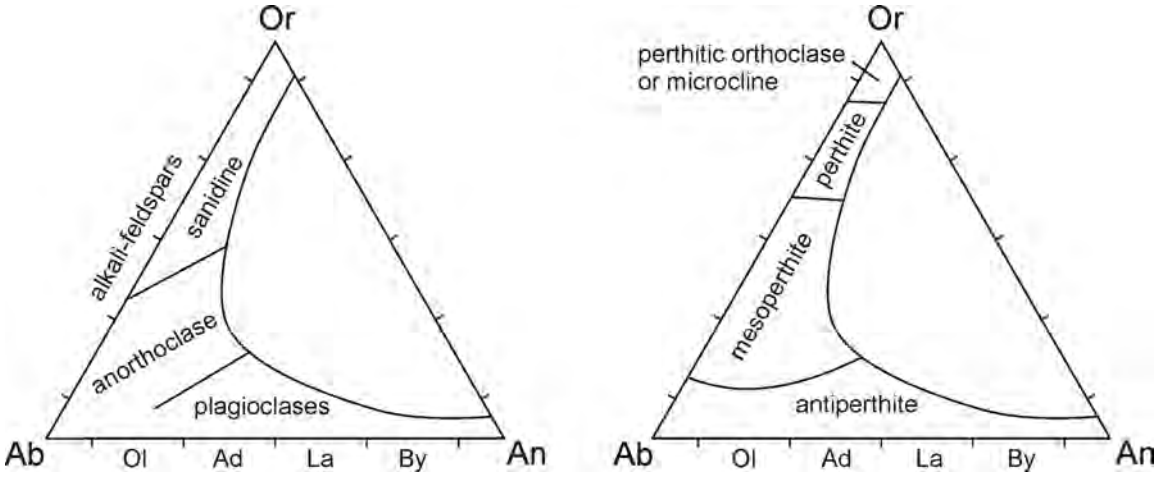


Fig. 3.50: Feldspar diagram with nomenclature for disordered ('volcanic', left panel) and for ordered ('plutonic', right panel) ternary feldspars (Deer et al. 1992). The miscibility gap for 1100°C and 5 kb is indicated.

Feldspars are the most abundant mineral group in igneous rocks, very common in gneisses and shists and – after quartz – they are the second most abundant minerals in sandstones. They are susceptible to weathering, with Na-rich feldspar and especially anorthite-rich plagioclase (Ca content) being substantially less resistant than K-feldspar, resulting usually in a change of end member abundance in sandstones relatively to the original source rocks. However, due to their common occurrence in sandstones and their chemical diversity, feldspars are good indicators for source rock lithology.

### 3.4.6.2 Results

A total of 404 feldspar grains and 15 feldspars within volcanic rock fragments from 13 samples of the SPF have been analysed. Mostly, these were K-feldspars with up to 40 % Ab component and plagioclases of $An_5$ to $An_{50}$ (Fig. 3.51). Few alkali feldspars were found with Ab component larger than 40 % (up to 65 %). Pure albites are most likely diagenetically in origin (see Sect. 5). The exact results are listed in the appendix.

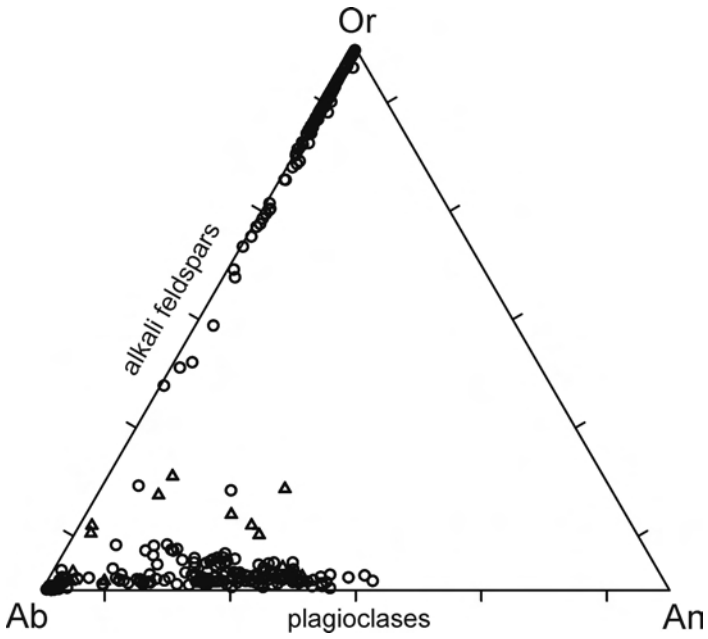


Fig. 3.51: All feldspar analyses plotted in the ternary feldspar diagram (An: Anorthite; Or: K-feldspar; Ab: Albite). Feldspars from volcanic rock fragments are displayed as triangles.

In the following figures the analyses are shown for the individual samples and ordered with respect to the associated sandstone type. Results of samples from the same section and for samples from similar stratigraphic positions are shown in conjunction.

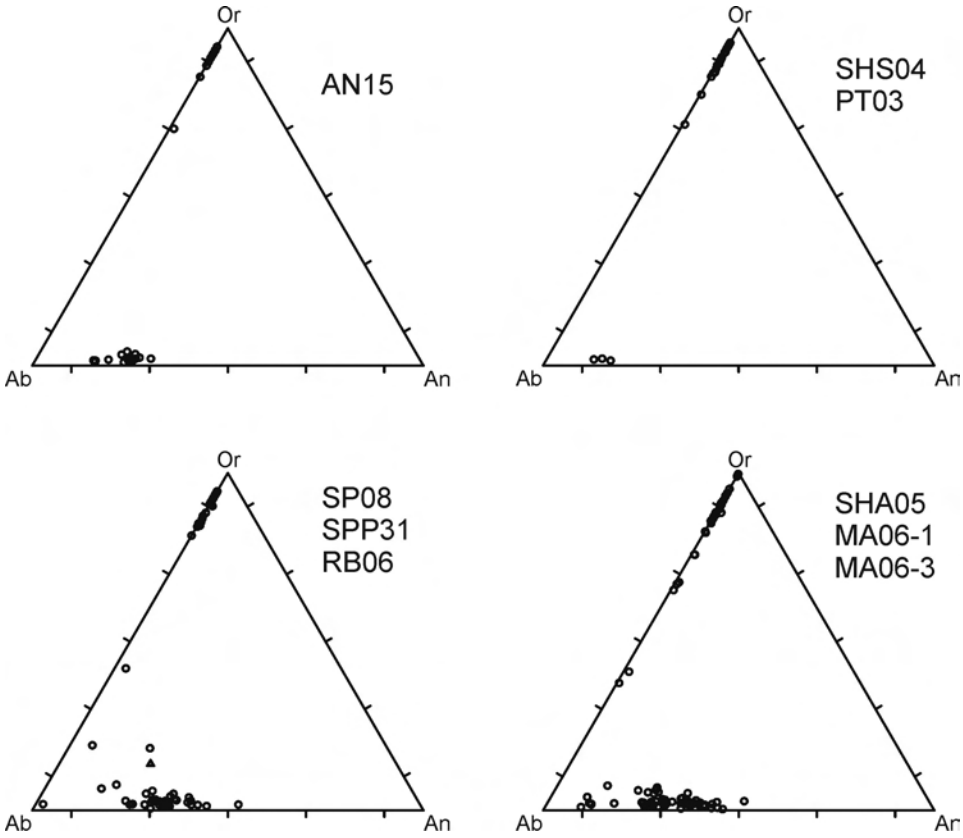


Fig. 3.52: Analyses of feldspars from type C sandstones, plotted in the ternary feldspar diagram. Feldspars from volcanic rock fragments are displayed as triangles.

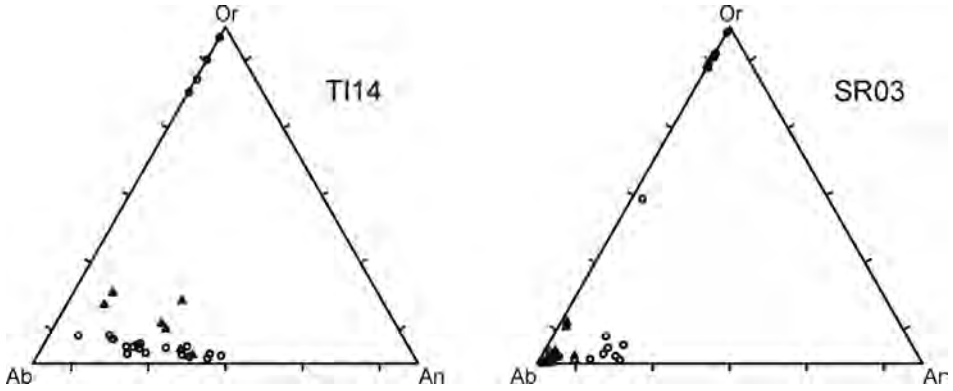


Fig. 3.53: Analyses of feldspars from type B sandstones, plotted in the ternary feldspar diagram.

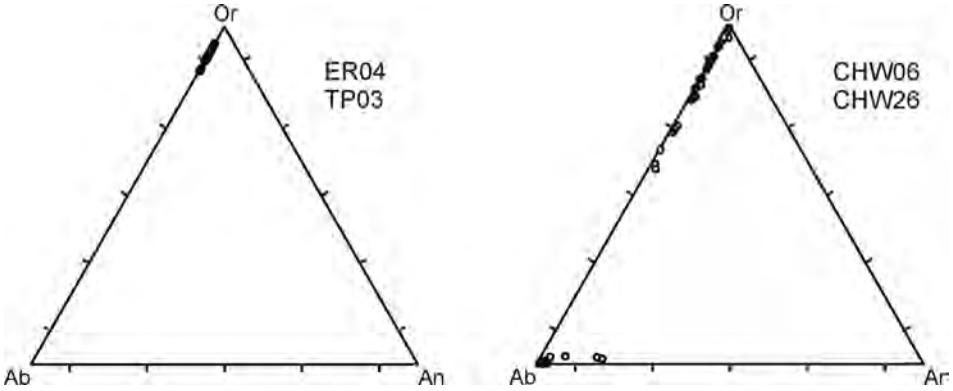


Fig. 3.54: Analyses of feldspars from the type A (left panel) and from type D sandstones (right panel), plotted in the ternary feldspar diagram.

The composition of feldspars from sandstone type C in lower stratigraphic parts (sample AN15, n = 27; SHS04, n = 20; PT03, n = 8) are similar, although in AN15, the plagioclases are more frequent and have a slightly higher An-component (Fig. 3.52, upper diagrams). Likewise, the feldspars from upper stratigraphic levels of sandstone type C are of comparable composition (sample SP08, n = 19; SPP31, n = 19; RB06, n = 24, see Fig. 3.52, lower left diagram, and sample SHA05, n = 24; MA06-1, n = 36; MA06-3, n = 37, see Fig. 3.52, lower right diagram).

Feldspars from sandstone type B (sample TI14, n = 22; SR03, n = 30, see Fig. 3.53) show similar compositions than those of type C. Sample SR03 contains many diagenetically albitised plagioclases, thus their original composition remains unknown.

Sandstone type A (sample TP03, n = 22; ER04 n = 16, see Fig. 3.54, left panel) exclusively comprises alkali feldspars, with a very narrow range of composition between $Or_{87}$ and $Or_{95}$. This is typical in (alkali-feldspar-) granites.

The K-feldspars from sandstone type D (sample CHW06, n = 54; CHW26 n = 39, see Fig. 3.54, right panel) resemble the analyses from type C sandstones. However, most of the plagioclases are albitised diagenetically, and their original composition remains unclear.

### 3.4.6.3 Summary and interpretation

Feldspars from type A sandstones are very homogeneous and presumably originating from granitoid source rocks. In NVL, plutons of the Cambro-Ordovician Granite-Harbour-Intrusives are frequent within the Wilson terrane, while the Devonian Admiralty Intrusives can be found in the Bowers and Robertson Bay terrane. Due to palaeocurrent directions and

the association of this sandstone type with conglomerates and thus a proximal source, the former seem to be more likely.

Within samples from sandstone type C, feldspars show a similar range in composition. Magmatic, as well as metamorphic origins are possible. The feldspars from sandstone type B have a similar range in composition, and thus cannot be distinguished chemically from type C. However, the fraction of plagioclase is higher (Sect. 3.2.2). The composition of K-feldspars from sandstone type D appears to be similar to that of type C, but as the plagioclases are commonly albitised diagenetically, their original composition is unknown.

## 3.4.7 Sheet silicates (mica)

### 3.4.7.1 Introduction

Micas show a considerable chemical variation, but due to their layered crystal structure they are platy with a perfect basal cleavage (Deer et al. 1992). A general formula of micas can be expressed as $A\,B_{2-3}\,\square_{1-0}\,T_4\,O_{10}\,X_2$ with interlayer cations for A (mostly K, Na, Ca), and octahedral cations (mostly Al, Mg, Fe) for Be. Up to 1 position in the octahedral layer can be deficient (as indicated by $\square_{1-0}$). For T tetrahedral cations (mostly Si, Al) are present, and X symbolises a ligand, mostly OH or F (Fleet 2003).

A subdivision of micas is possible by the number of cations on position B (octahedral) into di-octahedral ($B_2$) and tri-octahedral ($B_3$) micas, with the former being referred to as white mica, and the latter as dark mica**.** Dark mica is traditionally referred to as biotite, which is a generic name for the end member minerals annite ($KFe_3[AlSi_3O_{10}](OH,F)_2$), phlogopite ($KMg_3[AlSi_3O_{10}](OH,F)_2$), siderophyllite ($KFe_2Al[Al_2Si_2O_{10}](OH,F)_2$) and eastonite ($KMg_2Al[Al_2Si_2O_{10}](OH,F)_2$). White mica is not present in all samples, Due to their rare and often weathered or altered occurrence, reliable biotite analyses were difficult to obtain.

### 3.4.7.2 Results

In Fig. 3.55 the analyses of mica are plotted in the $(Mg,Fe,Al)^B$ versus $Al_{tot}$ diagram (Deer et al. 1992). Most of the white mica cluster on or around the vertical line $(Mg,Fe,Al)^B=2$ (di-octahedral mica). In the analysed mica to the right of that line ($(Mg,Fe,Al^B < 2$), one position is deficient or a cation not further specified, is present (possibly Li). Most mica are actually muscovites, few are phengites, and one Al-celadonite has also been found. Dark micas are further sub-classified in Fig. 3.57.

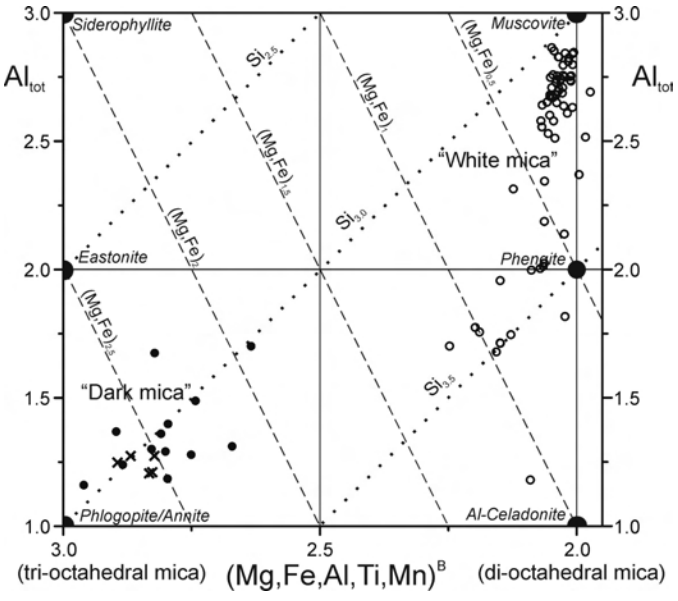


Fig. 3.55: Mica analyses from the SPF plotted in the $(Mg,Fe,Al)^B$ versus $Al_{tot}$ diagram (Deer et al. 1992). Crosses mark biotites from the tuffaceous sandstone SHA12 (see Sect. 4 for details).

The bulk of white micas are muscovites (K) with a low paragonite (Na) component (Fig 3.54, left panel). For some analyses the correlation of K and Na is poor and a substantial alkali leaching must be assumed (Fig 3.54, right panel). Exact analyses are listed in the appendix.

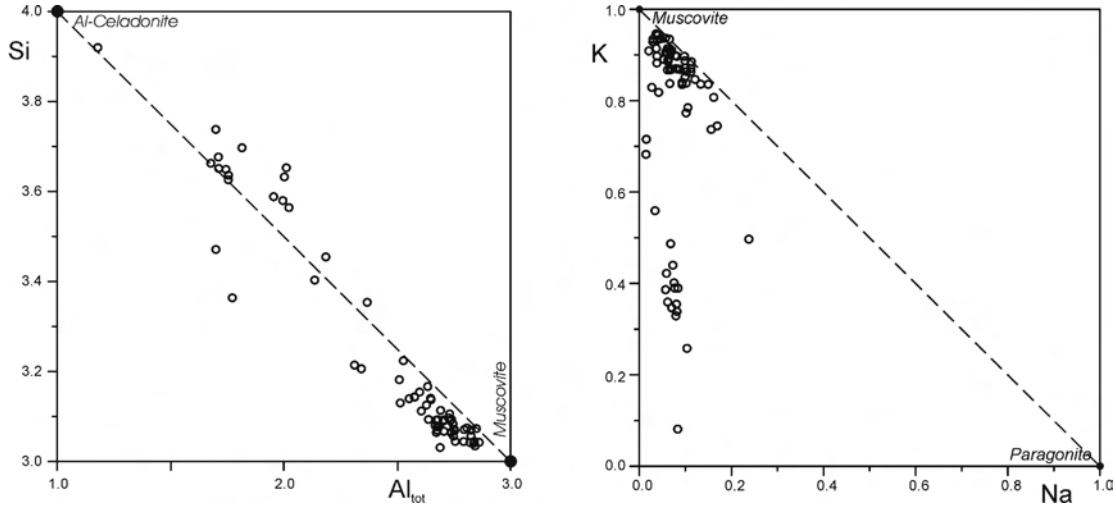


Fig. 3.56: The left diagram ($Al_{tot}$ vs. Si) indicates a tight correlation of Al and Si. In the right diagram (Na vs. K), alkali leaching is obvious for the analyses with weakly correlating K and Na content.

Mg is present in amounts of usually less than 0.15 apfu, only two white micas from sample AN15 have Si > 3.2 apfu and are therefore actually phengites. No high pressure mica with Si > 3.3 apfu was found. 'High' pressure means in this case a minimum pressure of 4 kb, depending on temperature and paragenesis (Massonne 1991; Massonne and Schreyer 1987, cited in Von Eynatten 1996).

Very few biotite analyses of only three samples from sandstone type C could be conducted (SP08, SPP31, and MA06-1); a comprehensive interpretation is therefore hardly possible. Detailed analyses are summarized in the appendix. Results are illustrated in Figs. 3.55 and 3.56. None of the reference data of biotites from the Granite Harbour Intrusives, the Rennick shists or from Marie-Byrd-Land migmatites are matching their composition; however, the number of analyses is very small.

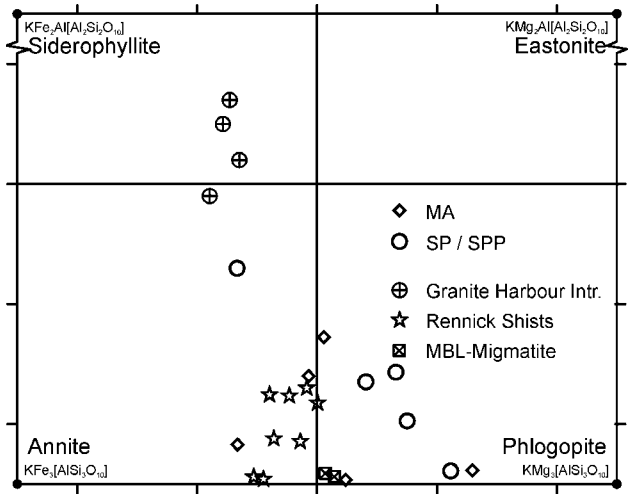


Fig. 3.57: Diagram plotting Mg/(Mg+Fe) vs. $Al^B$ of biotite analyses. The minerals are mostly Al-poor and follow the annite-phlogopite trend. Biotite analyses from the Granite-Harbour-Intrusives (Brigatti et al. 2000), from the Rennick Shists (Roland et al. 1989), and Marie-Byrd-Land granulites (Smith 1996) are plotted for comparison.

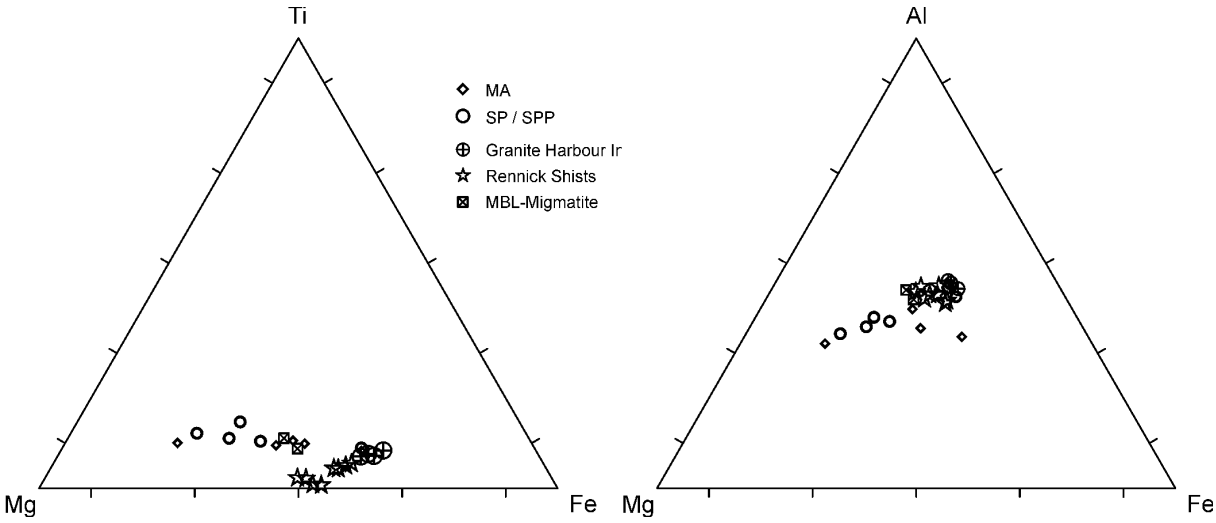


Fig. 3.58: Fe-Ti-Mg and Fe-Al-Mg ternary diagram for the biotite analyses. Reference data as in Fig. 3.57.

#### 3.4.6.3 Summary and interpretation

No high pressure mica with Si > 3.3 apfu was found and none of the reference data from the Granite Harbour Intrusives, the Rennick shists, or from Marie-Byrd-Land migmatites are matching the determined biotite composition. However, the total number of analyses of both, detrital mica and reference minerals, is very small; therefore, the results have to be interpreted with care.

### 3.4.8 Summary and comparison with petrography

In Sect. 3.2, six sandstone types (A-F) with different source regions were defined by petrography (heavy and light mineral composition). In four of these types (A, B, C, and D) selected minerals were analysed chemically. Garnet, tourmaline and feldspar exhibit a different composition in these four sandstone types, which can be related to different source rocks. The other minerals analysed are not suitable to distinguish sandstone types from each other, because they occur only locally (e.g. greenish amphiboles, Cr-spinel) or the number of analyses is too small (mica). However, these minerals yielded valuable information about provenance and source areas. The results are summarized in Tab. 3.12.
In sandstones of **type A** garnet is rare, and an interpretation of garnet chemistry is therefore difficult. A medium to high grade metamorphic or a plutonic source seems possible. Tourmaline composition points to a granitoid source, but the proportion of metamorphic tourmalines increases with stratigraphic position. Feldspars are most likely derived from a granitoid source. In summary, a granitoid source can be inferred for sandstones of type A by the composition of these minerals, with material from a metamorphic source becoming increasingly more frequent towards the upper part of the sections.

The composition of most of the garnets from **type B** sandstones matches the garnets from the Granite-Harbour-Intrusives or high-grade metamorphic rocks from the Wilson terrane. Only one analysis could not be allocated to these two sources. Tourmaline chemistry points towards a granitoid origin, with a possible hydrothermal overprint. Feldspars of type B sandstones are magmatic or metamorphic in origin. These three mineral groups indicate a source region with metamorphic and granitoid rocks (possibly from the Wilson terrane) beside the important volcanic source revealed by light mineralogy.

Additionally, a sample from type B sandstones (TI14) contains Cr-spinel, which most likely originates from harzburgitic rocks from suprasubduction zone (SSZ) peridotites. A provenance of this mineral from the Lanterman-Mariner-Suture within the Ross orogen is most likely.

Garnet composition in **type C** sandstones point to a high grade metamorphic source and the tourmalines are most likely metasedimentary in origin. Feldspars may also be metamorphic, but a magmatic origin is also possible. In summary a (high grade) metamorphic source lithology with possibly magmatic rocks can be inferred.

Greenish calcic amphiboles are important constituents only in the mineral spectra of type C sandstones in a higher stratigraphic range (section SHA and upper section MA). Their occurrence coincides with an increasing plagioclase : feldspar ratio. The amphiboles are most likely derived from effusive continental calc-alkaline rocks of basaltic to andesitic composition.

In **type D** sandstones tourmalines are missing. The composition of garnets is similar to that of type C sandstones (high grade metamorphic). Due to widespread diagenetic albitization feldspar analyses give no source rock information. Thus the mineral compositions of type D sandstones point towards a high grade metamorphic source, with magmatic rocks being a possible addition.

| Sst. type | Provenance of garnet | Provenance of tourmaline | Provenance of feldspar | Summary: source region |
|---|---|---|---|---|
| A | Medium/high grade metam. or plutonic | Granitoid, increasingly metamorphic | Granitoid | Granitoid, increasingly metamorphic |
| B | High grade metam. and plutonic (granitoid) | Granitoid (overprinted?) | Magmatic / Metamorphic | Granitoid; magmatic / metamorphic |
| C | Mostly high grade metamorphic | Metamorphic (few magmatic) | Magmatic / metamorphic | Metamorphic (high grade); magmatic |
| D | Mostly high grade metamorphic | - | Widespread albitization | Metamorphic (high grade); magmatic? |

Tab. 3.12: Summary of provenance information deduced from the compositions of garnet, tourmaline and feldspar.

# 3.5 U-Pb ages of detrital zircons

## 3.5.1 Introduction

### 3.5.1.1 General remarks to zircon age studies

Age data of detrital zircons provide useful information about magmatic and metamorphic events in the source area. For this reason, zircon studies are a powerful tool in provenance analysis and have been frequently used for determination and characterization of source areas, and tectonic reconstructions. In NVL, so far the distribution of detrital zircon ages has been analysed only in a single sample from the type locality at Section Peak (Goodge and Fanning 2010). Further analysed have been made in the CTM (Elliot and Fanning 2008; Goodge et al. 2002; Goodge et al. 2004) and in Australia (Sircombe 1999).

The youngest zircon age group provides an upper limit to the sedimentation age. This can be important for age dating and stratigraphic correlation, but is useful only if sedimentation was accompanied by contemporaneous volcanic activity, leading to a small spread between zircon age and stratigraphic age.

Zircons may survive one or even more orogenic cycles without losing the age information they carry. Mineral abrasion during sedimentary processes, magmatic resorption and overgrowth during metamorphic or magmatic events often result in a complex internal zoning (Corfu et al. 2003).

A zircon age study is most useful in combination with petrographic and geochemical analyses to obtain comprehensive provenance information. These later analyses are of great interest, as some rocks do not contain zircons or the zircons are too fine grained for preparation or analysis. These may be, for instance, ultra-mafic or mafic rocks, fine grained (meta-) pelites, or carbonates.

The Th/U-ratio of zircons is commonly regarded as a geochemical indicator of their genesis. Metamorphic zircons or zircons overprinted metamorphically typically possess lower Th/U-ratios compared to magmatic zircons. This is explained by the formation of separate Th-bearing phases in metamorphic rocks (e.g. monazite), which are lacking in magmatites. The Th/U-ratio of metamorphic zircons are typically less than 0.1 (Wu and Zheng 2004), but in some cases metamorphic zircons may reach significantly higher values (Vavra et al. 1999). Besides the Th/U-ratio, internal textures as show by CL images also may reveal the origin of zircons. Here, typically metamorphic textures are sector zoning, weakly or cloudy zoning (Schaltegger et al. 1999; Vavra 1990; Vavra et al. 1996; Wu and Zheng 2004).

### 3.5.1.2 U-Pb zircon ages in NVL and adjoining regions

The characteristics of the possible source areas have already been discussed in Sect. 1. Therefore, only a short summary with emphasis on zircon ages is given here. A detailed review is also given by Elliot and Fanning (2008). In comparison with other parts of the former super-continent Gondwana, age data in Antarctica are relatively rare.

The East Antarctic continental interior is inferred to consist of Archean cratons and Proterozoic domains, rimmed and amalgamated by belts of Grenville or Pan-African age (Fitzsimons 2000; Fitzsimons 2003). In the Australian sector of Antarctica, the Archean-Palaeoproterozoic Mawson craton (or Mawson continent) is presumed in the ice-covered hinterland of the TAM (Fanning et al. 1996; Fitzsimons 2003). However, there is evidence that in between the Mawson craton and the TAM, or between different parts of the Mawson continent, units dominated by pan-African ages (500-700 Ma) and possibly also Grenvillian ages (c. 800-1200 Ma) exist (Sircombe 1999; Veevers et al. 2006).

Within the TAM itself, the basement is formed by Neoproterozoic to Cambrian and Early Ordovician rocks that have been metamorphosed during the Ross Orogeny (Goodge et al. 2002; Goodge et al. 2004). Syn- and post-orogenic Cambrian to Ordovician Granite-Harbour Intrusives show cooling ages of about 480 ± 20 Ma.

| Code | Age [Ma] |
|---|---|
| d | 600-500 |
| d+ | 700-500 |
| dd | 725-650 |
| ddd | 1000-800 |
| c | 1300-900 |
| bb | 1400-1300 |

| Code | Age [Ga] |
|---|---|
| b | 1500-1300 |
| a | 1800-1500 |
| aa | 2100-1900 |
| aa’ | 2600-2500 |
| aaa | 2800-2600 |
| aaaa | 3050-2900 |

Tab. 3.13: Summary of zircon age clusters from East Antarctica (Veevers et al. 2005)

In NVL, the Admiralty Intrusives and the accompanying but mostly slightly younger rhyolitic and andesitic Gallipolli Volcanics as well as the rocks of the Salamander Granite Complex show a cooling age of about 360 ± 10 Ma (Henjes-Kunst and Kreuzer 2003). They occur mostly in the Bowers and Robertson-Bay terrane, but also in the Wilson terrane (Grindley and Oliver 1983).

As in NVL, magmatites of Devonian to Early Carboniferous age have been found in the Ross-Province of western Marie-Byrd-Land (Collinson et al. 1994), for example the Ford Granodiorite with a cooling age of 375 ± 5 Ma (Pankhurst et al. 1998). This province is characterized by Cambrian orthogneisses (about 505 Ma), and greywacks of about 420 - 440 Ma (Adams et al. 1995). Cambrian rocks are lacking in the Amundsen Province of central and eastern Marie-Byrd-Land. This province includes granitoids of 420 - 450 Ma and granitoid rocks of a Permian to Triassic magmatic arc, whose remnants are also found in the neighbouring Thurston Island – Ellis Coast block and in the Antarctic Peninsula (Mukasa and Dalziel 2000; Pankhurst et al. 1993).

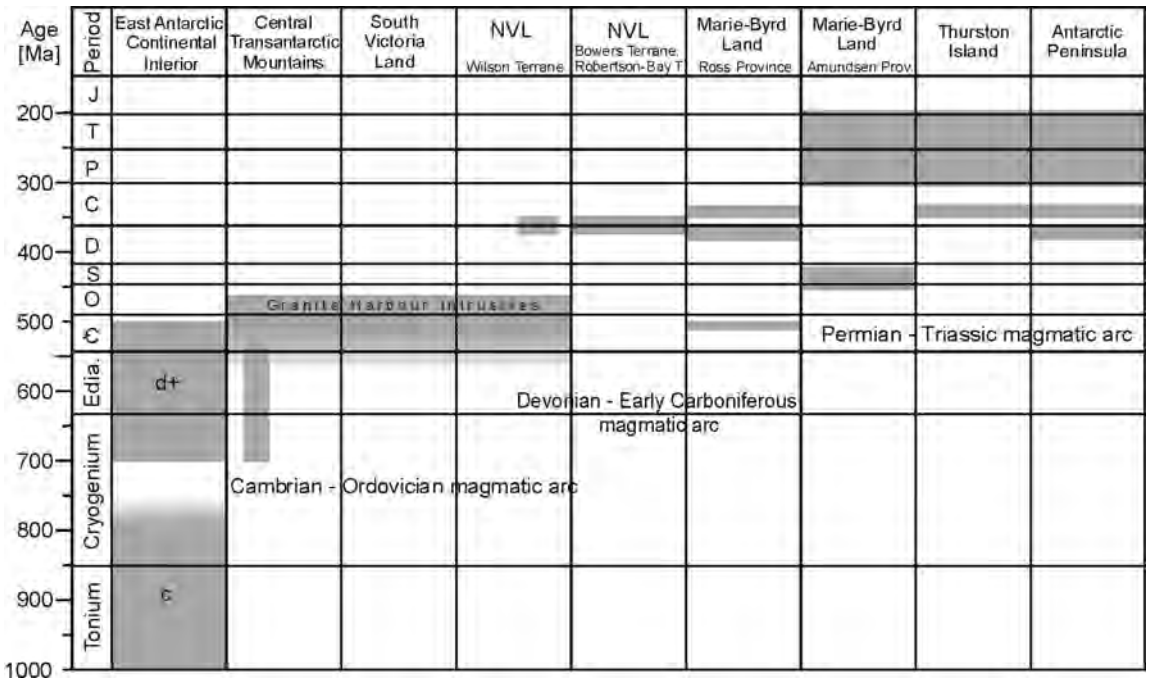


Fig. 3.59: Graphical representation of magmatic and metamorphic events in East and West Antarctica from the Neoproterozoic to the Triassic, which may be reflected by detrital zircon ages in the SPF. Based on a compilation of Elliot and Fanning (2008). The codes ‘c’ and ‘d+’ refer to the system of Veevers et al. (2005)

While Marie-Byrd-Land, the Antarctic Peninsula, and the Thurston Island – Ellis Coast block are relatively well exposed, other parts of the former and now dismembered Gondwana plate margin are not. The Campbell Plateau, the Challenger Plateau, and the Lord Howe Rise drifted away from their former positions close to the EAC by plate tectonic processes and are now largely covered with younger sediments. Therefore, information about their tectonic and stratigraphic history is derived from (sparse) outcrops and from a comparison with the formerly adjoining areas described above.

### 3.5.1.3 Methods

Eight samples from sandstones throughout the working area covering different stratigraphic levels of sandstone types A, B, C, and D classified by light and heavy mineral analysis, were chosen for zircon separation. Sandstones of type E and F were not regarded because of their limited regional and stratigraphic occurrence. Zircons were hand picked under a polarization microscope from heavy mineral concentrates (Sect. 3.3) and attached on planar glass slides using double-sided adhesive tape. A Frantz magnetic barrier separator was not used in order to avoid unnecessary biasing due to possible magnetic susceptibility of zircon (Sircombe and Stern 2002).

The zircons from four samples each were mounted on one glass slide to keep preparation procedure to a minimum and avoid time consuming sample exchange during measurements. A cylindrical plastic ring of 6 mm height and 25 mm (1 inch) outside diameter was placed on the glass slide surrounding all zircons, and filled up with Araldite®. After hardening, the mounts were abraded using decreasing powder sizes (23–3 µm) to uncover the embedded zircons. Final step was a polish with 0.5 µm diamond abrasion paste.

Reflected as well as transmitted light and microprobe BSE images of the zircons were taken for quality control and to allow orientation on the mounts during measurements. Cathodoluminescence (CL) imaging, performed at the Institut für Geowissenschaften of the Johann Wolfgang Goethe-Universität in Frankfurt a.M, revealed the internal structure of the zircons. It was chosen preferentially to BSE imaging for spot localization due to the wider range of intensity, allowing for a better assessment of zonings (Corfu et al. 2003).

Laser ablation – Inductively Coupled Plasma Mass Spectrometry (LA-ICPMS) analyses of U, Th, and Pb isotopes were carried out in the laboratory of Dr. A. Gerdes at the Institut für Geowissenschaften of the Johann Wolfgang Goethe-Universität in Frankfurt a.M., using a Thermo-Finnigan Element II™ sector field ICPMS coupled to a New Wave UP-213™ ultraviolet laser system. A teardrop-shaped, low-volume laser cell was used to enable sequential sampling of heterogeneous grains (e.g. growth zones) during time-resolved data acquisition (Janoušek et al. 2006). The laser spot size was 30 µm, with a depth of crater between 10 and 15 µm. Each analysis consisted of 20 s background monitoring followed by 35 s of data acquisition.

Raw data were corrected for background signal, common-Pb, laser-induced elemental fractionation, instrumental mass discrimination, and time-dependant elemental fractionation of Pb/Th and Pb/U using an analysis pipeline developed by Dr. A. Gerdes. The common-Pb correction based on interference- and background corrected $^{204}Pb$ signal and a model Pb composition (Stacey and Kramers 1975) was carried out, if the corrected $^{207}Pb/^{206}Pb$ was outside the internal errors of the measured ratios. Reported uncertainties were propagated by quadratic addition of the external reproducibility (standard deviation) obtained from the standard zircon GJ-1 (n = 13; about 0.6 % for the $^{207}Pb/^{206}Pb$ ration and 0.5-1.0 % for the $^{206}Pb/^{238}U$ ratio) during individual analytical sessions, and the within-run precision of each analysis (standard error, Linnemann et al. 2007). Concordia diagrams (2σ error ellipses) were produced using Isoplot 3.41b (Ludwig 2003), and frequency and relative probability plots using AgeDisplay (Sircombe 2004). Discordant analyses were generally interpreted with care.

The $^{207}Pb/^{206}Pb$ ages were preferentially taken for interpretation of zircons older than 1.000 Ma, and the $^{206}Pb/^{238}U$ ages for younger grains. For further details of the analytical protocol and data reprocessing see Gerdes and Zeh (2006).

The outermost parts of each zircon were analysed preferentially, intending to reveal the youngest events in zircon formation. However, in some cases, two ore even three spots in different growth zones of a single grain (core, mantle, rim) were analysed in order to assess overgrowth relationships.

### 3.5.2 Results

From each sample, usually more than 100 spots were analysed (Tab. 3.14), leading to up to 115 concordant ages. Here, two ages were classified as concordant, if they differ by at most 10 %. For two samples (ER04 and TI14) containing only about 60 zircons, there is still a 95 % probability to probe all zircon populations accounting for more than 10 % of all zircons in the source area (Vermeesch 2004). Discordant ages mostly support the result of the concordant ones, and the discordance itself is thought to reflect source area processes (Mezger and Krogstadt 1997). The results are plotted and listed in detail in the appendix.

| Sample | Sandstone type | Number of grains | Number of spots | Failed analyses | Measured spots | Concordant ages (90-110%) |
|---|---|---|---|---|---|---|
| ER04 | A | 57 | 71 | 3 (4.2 %) | 68 | 61 |
| TI14 | B | 60 | 73 | 3 (4.1 %) | 70 | 55 |
| SHS03 | C | 104 | 118 | 4 (3.4 %) | 114 | 109 |
| SHA07 | C | 117 | 133 | 0 (0 %) | 133 | 115 |
| SP08 | C | 85 | 110 | 2 (1.8 %) | 108 | 100 |
| SPP36 | C | 100 | 111 | 0 (0 %) | 111 | 106 |
| CHW07 | D | 91 | 111 | 4 (3.6 %) | 107 | 70 |
| CHW26 | D | 113 | 124 | 7 (5.6 %) | 117 | 98 |

Tab. 3.14: The eight zircon samples and sandstone types as given by petrographic results. The number of grains and spots is also given. Some analyses failed due to technical errors. The last two columns include the number of correctly analysed spots and concordant ages.

Several zircon age clusters can be distinguished from the results, although never all of them are present in a single sample. A cluster was defined by a minimum of 4 % of zircons in the relevant sample in one bin, or in two neighbouring bins (bin width 25 Ma). These clusters are (1) a Triassic/Early Jurassic peak ('T/J',< 251 Ma, with a variable lower limit controlled by the stratigraphic age of the sample), (2) a Permian peak ('P', 251 - 299 Ma), (3) a peak at around 325 - 400 Ma (Devonian and early Carboniferous), (4) a group between 460 and 550 Ma, that may be part of (5) a larger group between 460 and 650 Ma, which may again overlap in some samples with (6) a cluster between about 500 and 700 Ma, and finally (7) a grouping between about 800 and 1200 Ma that may actually consist of several sub-groups.

Generally, though not present in all samples, most pronounced are the groups of zircons from the Triassic/Early Jurassic (< 251 Ma), from between 500 and 700 Ma, and from between 800 and 1200 Ma. These three groups account for about 70 % to 90 % of the total number of determined zircon ages. However, the proportion of these peaks varies strongly. Relatively few zircon ages are lying outside these clusters. The combined probability plot and histogram for all analyses with ages below 1.600 Ma in Fig. 3.60 visualizes the most frequent clusters. Information about the few zircons older than this limit, and the complete analytical results, can be found in the appendix. Both, the peaks between 460 and 550 Ma and between 460 and 650 Ma cannot be shown in this plot, as they are present in a single sample only.

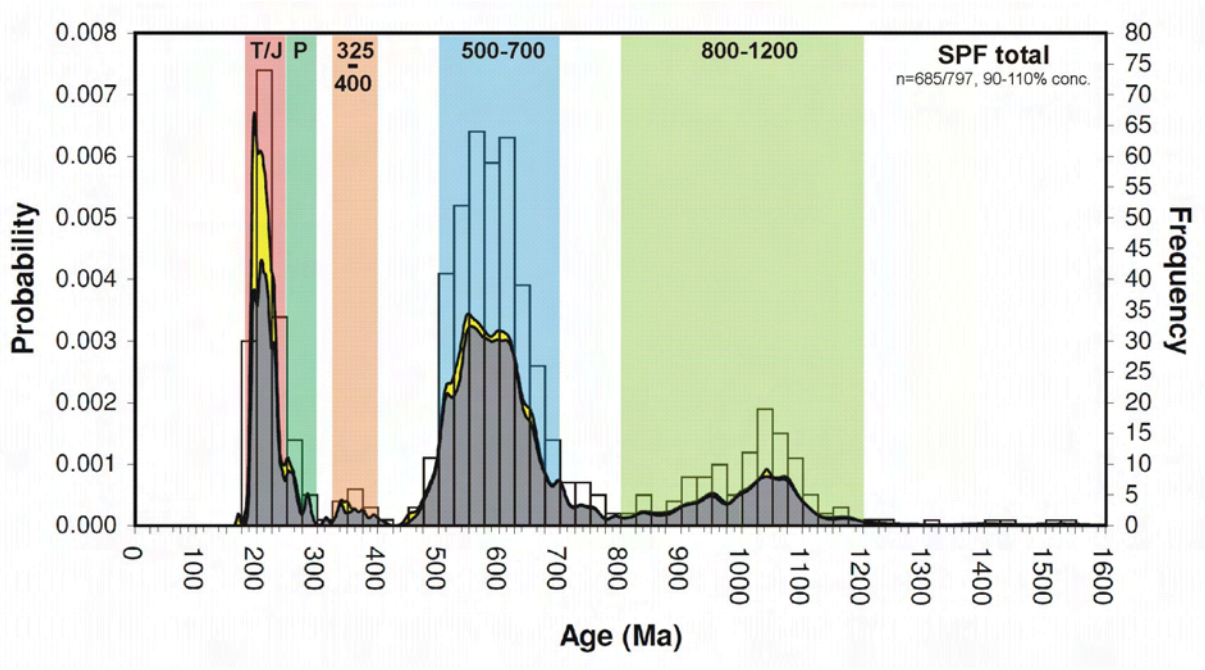


Fig. 3.60: Combined probability plot and histogram (bin width 25 Ma) for the age distribution of detrital zircons within the SPF (all eight samples). The grey area marks the sample probability of concordant zircons, the yellow area the sample probability including discordant ages. In general, though not present in all samples, the age groupings in the Triassic/Jurassic, from between 500–700 Ma, and from between 800–1200 Ma are most prominent.

In sample ER04 (sandstone type A, Fig. 3.61), the most pronounced peak lies between about 460 and 650 Ma, while zircons from the 800 – 1.200 Ma group are less abundant. Only one zircon has been found with Triassic, another one with Permian age. They are not highlighted in Fig 3.61, as they got rejected by the 4 %-criterion. The total number of determined zircon ages is relatively small in this sample.

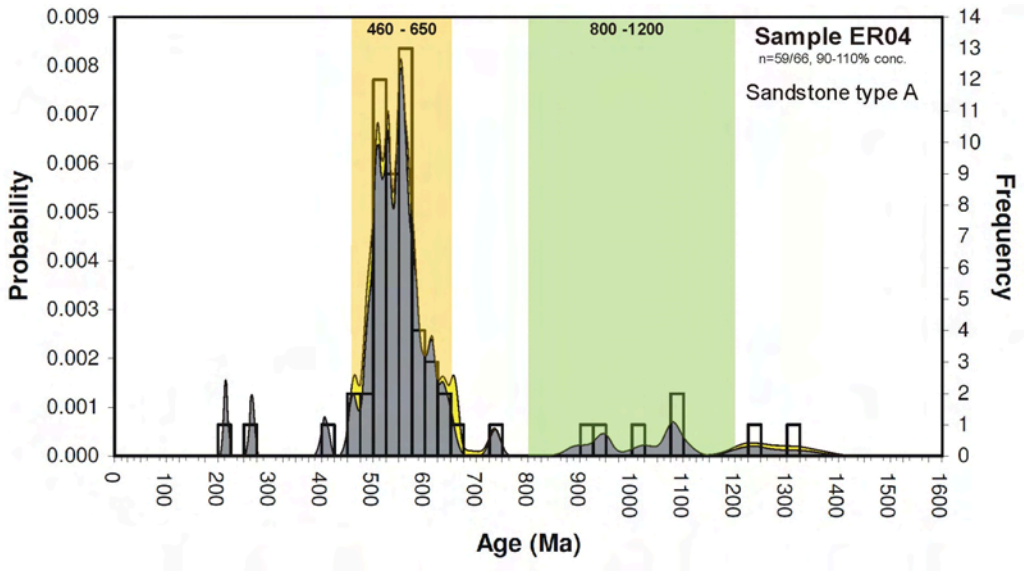


Fig. 3.61: Combined probability plot and histogram (bin width 25 Ma) for the age distribution of detrital zircons in sample ER04 (sandstone type A). Most pronounced is the age group between 460 and 650 Ma.

Sample TI14 (sandstone type B, Fig. 3.62) shows a strong predominance of zircons below 251 Ma (Triassic). A small group is of Permian age (251 - 299 Ma), another one from the Devonian to early Carboniferous (325 - 400 Ma), and some zircons show ages between 460 and 550 Ma.

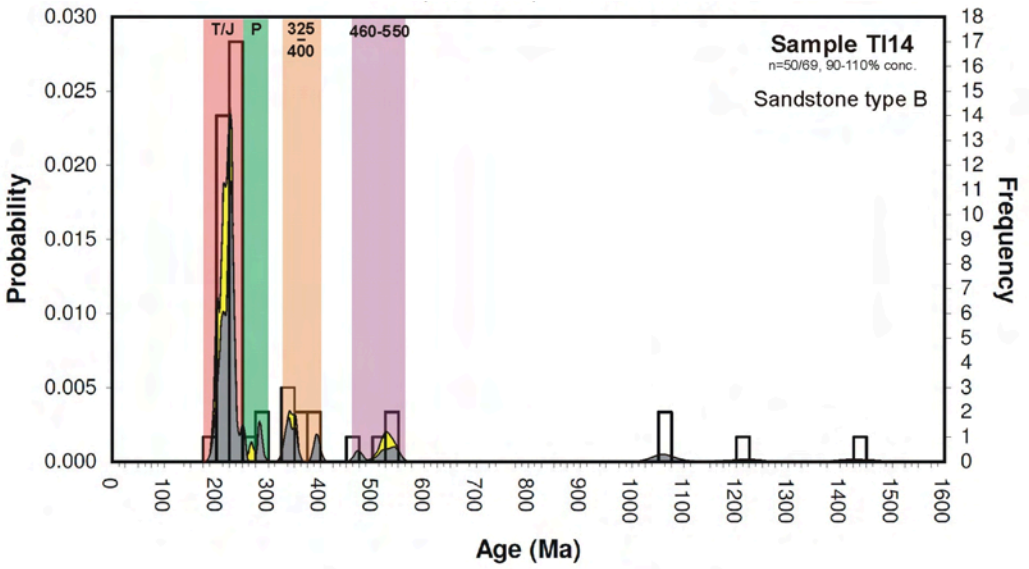


Fig. 3.62: Combined probability plot and histogram (bin width 25 Ma) for the age distribution of detrital zircons in sample TI14 (sandstone type B). Most prominent is the Triassic age group. Moreover, a Permian group, a Devonian/early Carboniferous group (325-400 Ma), and a group from 460-550 Ma can be distinguished.

Samples from sandstone type C (SHS03, SHA07, SP08, SPP36, Fig. 3.63) exhibit three prominent age groups. Besides the Triassic/Jurassic cluster, the 500 - 700 Ma and the 800 - 1.200 Ma group can be found in all four samples. However, in the stratigraphic higher samples SHA07 and SPP36, the Triassic/Jurassic peak is more pronounced than in the stratigraphic lower samples SHS03 and SP08. Contrary, zircons with ages between 500 and 700 Ma are more abundant in the two stratigraphically lower samples.

A relatively small peak of Permian age (251 - 299 Ma) can be identified in the two samples from upper parts of the SPF. In sample SP08, zircons of Permian age are also present, but contribute less than 4 % of the total number of determined zircon ages. Equally, zircons from the Devonian/early Carboniferous group described above, were found in three samples from sandstone type C (except SPP36), but they also fail to reach more than 4 %.

The zircon age distribution of sample SP08 is similar to the sample analysed by Goodge and Fanning (2010). Here, the youngest sub-population peaks at around 191 Ma, and further age cluster are about from between 500 – 700 Ma and from 950 – 1120 Ma. Also, two grains of Permain age are present.

Samples CHW07 and CHW26 from sandstone type D show a relatively similar zircon age distribution (Fig. 3.64 and 3.65), despite their different stratigraphic position. Most prominent are the Triassic/Jurassic peak, the 500 - 700 Ma, and the 800 – 1.200 Ma group. One Permian zircon in sample CHW26 and two Devonian/early Carboniferous zircons in CHW07 are less than 4 % of the total number of zircons in both cases.

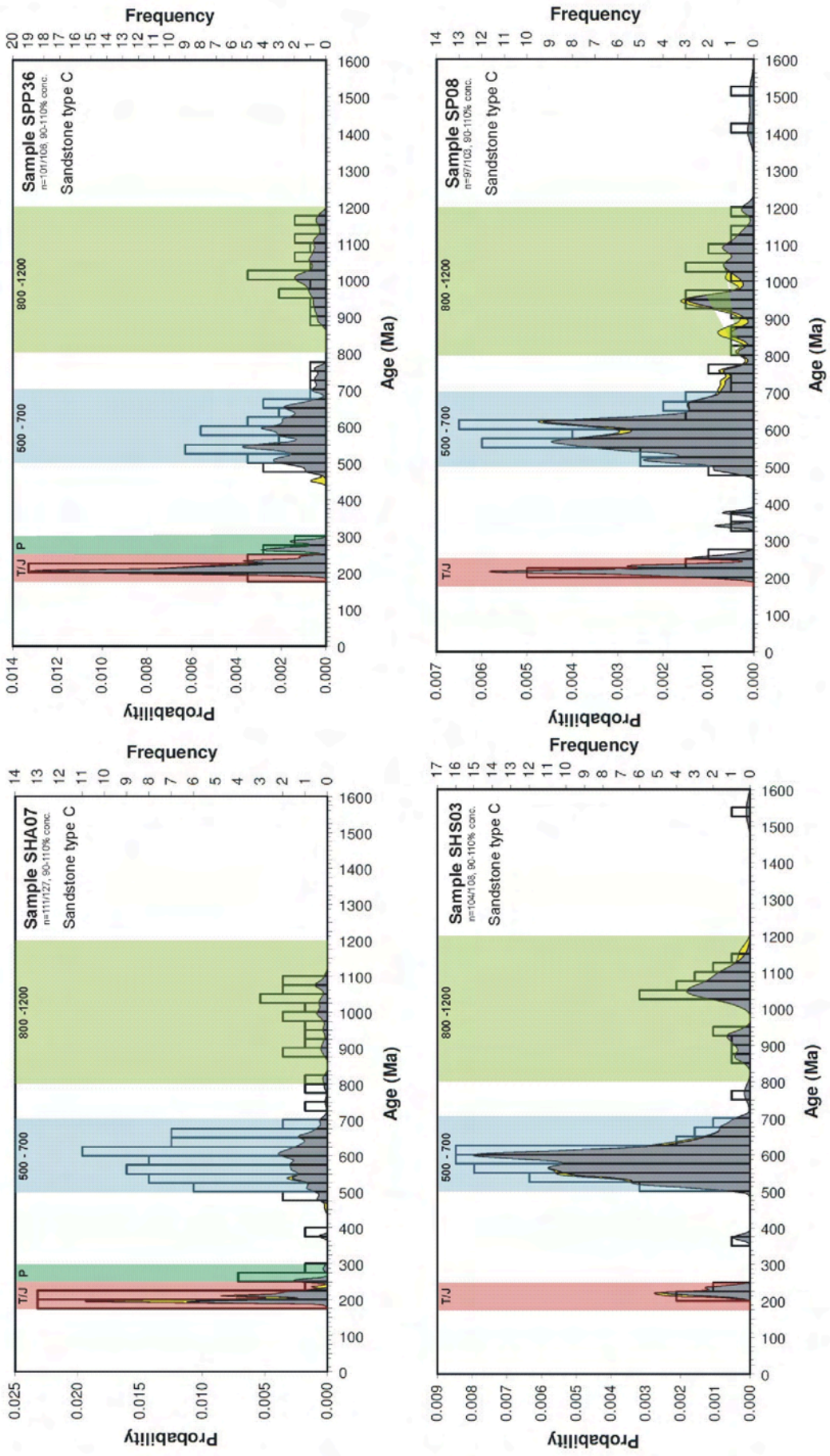


Fig. 3.63: Combined probability plots and histograms (bin width 25 Ma) for the age distribution of detrital Zircons in sample from sandstone type C (samples SHS03, SHA07, SP08, SPP36). The Triassic/Jurassic peak, the 500-700 Ma, and the 800-1200 Ma age group are present in all samples, although their proportion varies. Additionally, a Permian cluster can be identified in samples SHA07 and SPP36, both from higher stratigraphic levels.

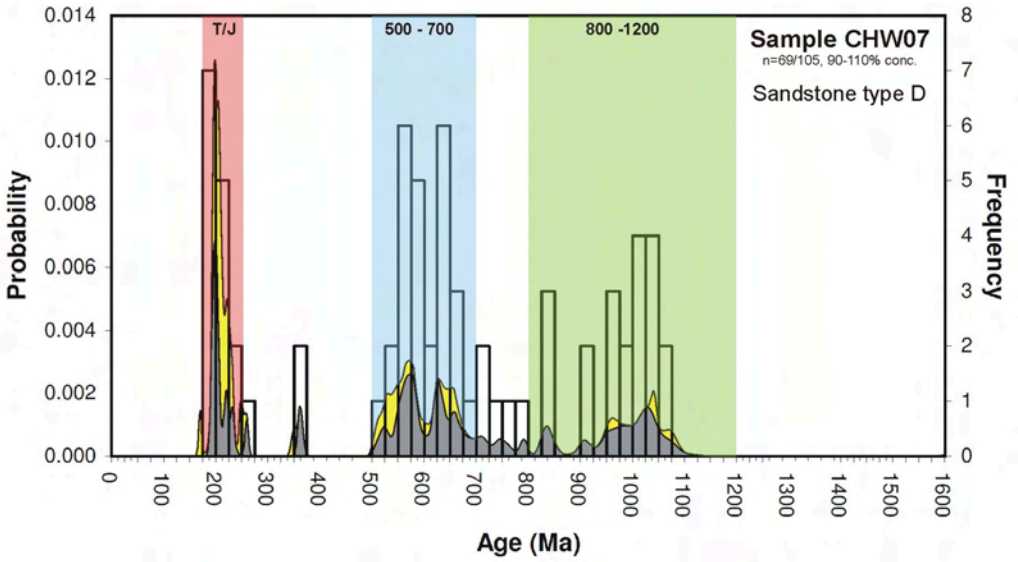


Fig. 3.64: Combined probability plot and histogram (bin width 25 Ma) for the age distribution of detrital zircons in sample CHW07 (sandstone type D). The Triassic/Jurassic peak, the 500 - 700 Ma, and the 800 – 1.200 Ma group are present. Two zircons and thus less than 4 % of the total number are from the Devonian/Early Carboniferous group.

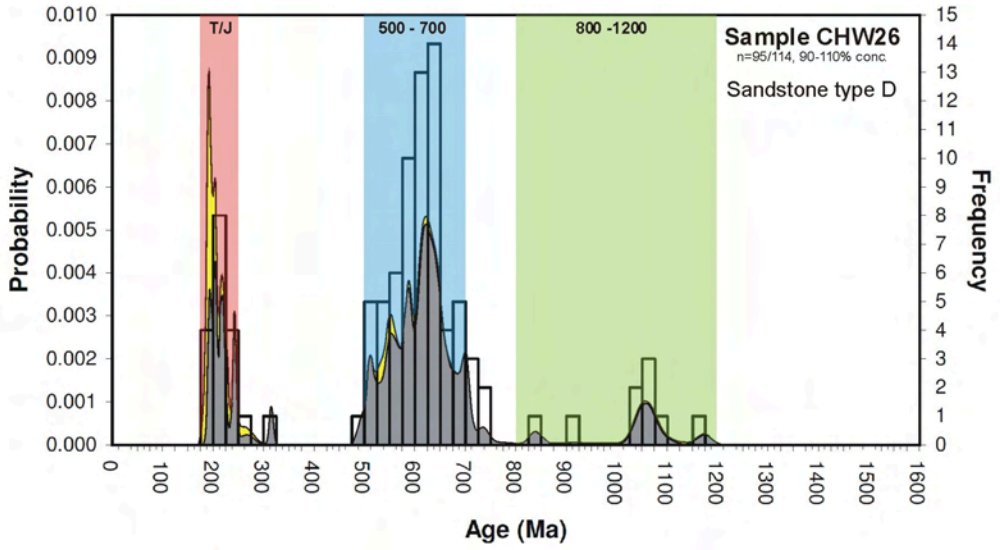


Fig. 3.65: Combined probability plot and histogram (bin width 25 Ma) for the age distribution of detrital zircons in sample CHW26 (sandstone type D). The Triassic/Jurassic peak, the 500 - 700 Ma group, and the 800 - 1.200 Ma group are present.

The ratio of the Triassic/Early Jurassic (< 251 Ma) cluster to the 500 - 700 Ma age group shows an inverse relationship in sandstones of type C and D (Fig. 3.66), most likely indicating a mixing between two separate sources. Contrary, the number of zircons from between 800 and 1.200 Ma is independent from both the proportion of Triassic/Early Jurassic zircons and the proportion of 500 - 700 Ma old zircons. An explanation for this observation is given below.

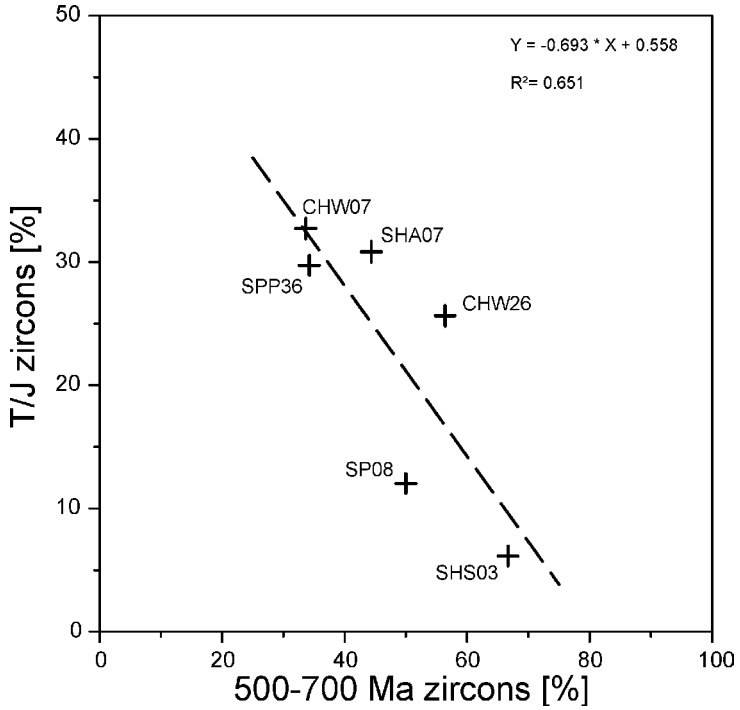


Fig. 3.66: Correlation of the proportions of the Triassic/Early Jurassic ('T/J', < 251 Ma) and the 500 - 700 Ma group within samples from sandstone types C and D. The inverse relationship is obvious. In the sample from sandstone type B (TI14) the 500-700 Ma peak is not present, and the samples from sandstone type A do neither contain a Triassic/Early Jurassic peak, nor a 500-700 Ma group.

The otherwise smooth sample frequency distribution of Th/U-ratios (Fig. 3.67) shows a significant discontinuity around 0.3 that may indicate a minimal Th/U-ratio of common magmatic zircons. However, to account for uncertainties, in this study a Th/U-ratio of less than 0.1 was assumed to point towards a metamorphic origin, whereas a value of more than 0.5 was regarded as indicator of a magmatic genesis. For zircons with Th/U-ratios in the range between 0.1 and 0.5, the origin was regarded as uncertain.

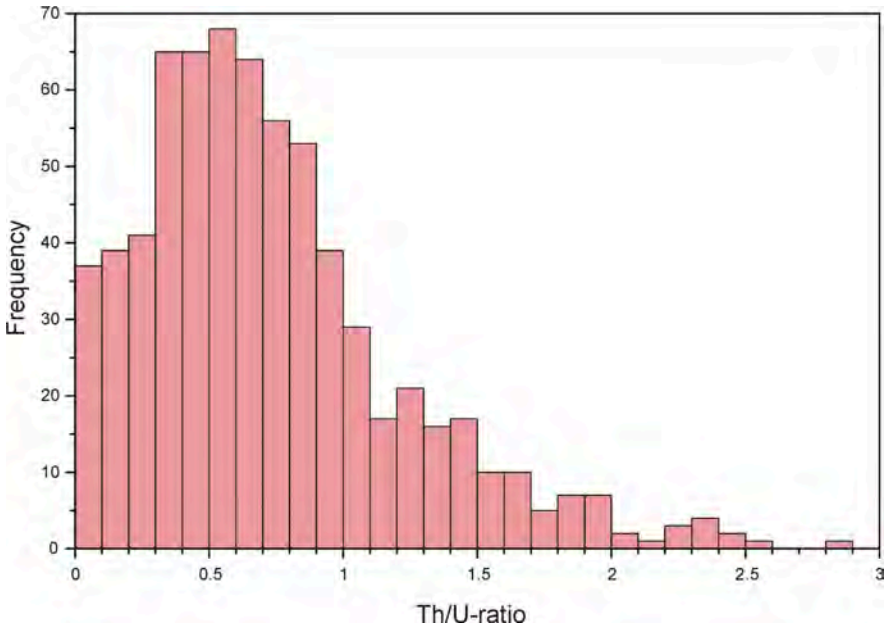


Fig. 3.67: Sample frequency distribution of Th/U-ratios of detrital zircons from the SPF. The significant increase in frequency at a Th/U-ratio around 0.3 may be caused by magmatic zircons showing dominantly Th/U-ratios higher than this value.

CL-images were used to test the results of the geochemical analysis. For very few zircons, the results of both approaches were contradictory. In these cases, the appearance of the internal structures was regarded as more reliable than the U/Th ratio. Nevertheless, the origin of some zircons remains unclear, as the interpretation of their CL images was uncertain.

The results of this combined geochemical/CL approach to define zircon genesis are given in the appendix. In Fig. 3.68, the Th/U-ratio versus the zircon age is drawn, in order to show the presumed origin of the different clusters.

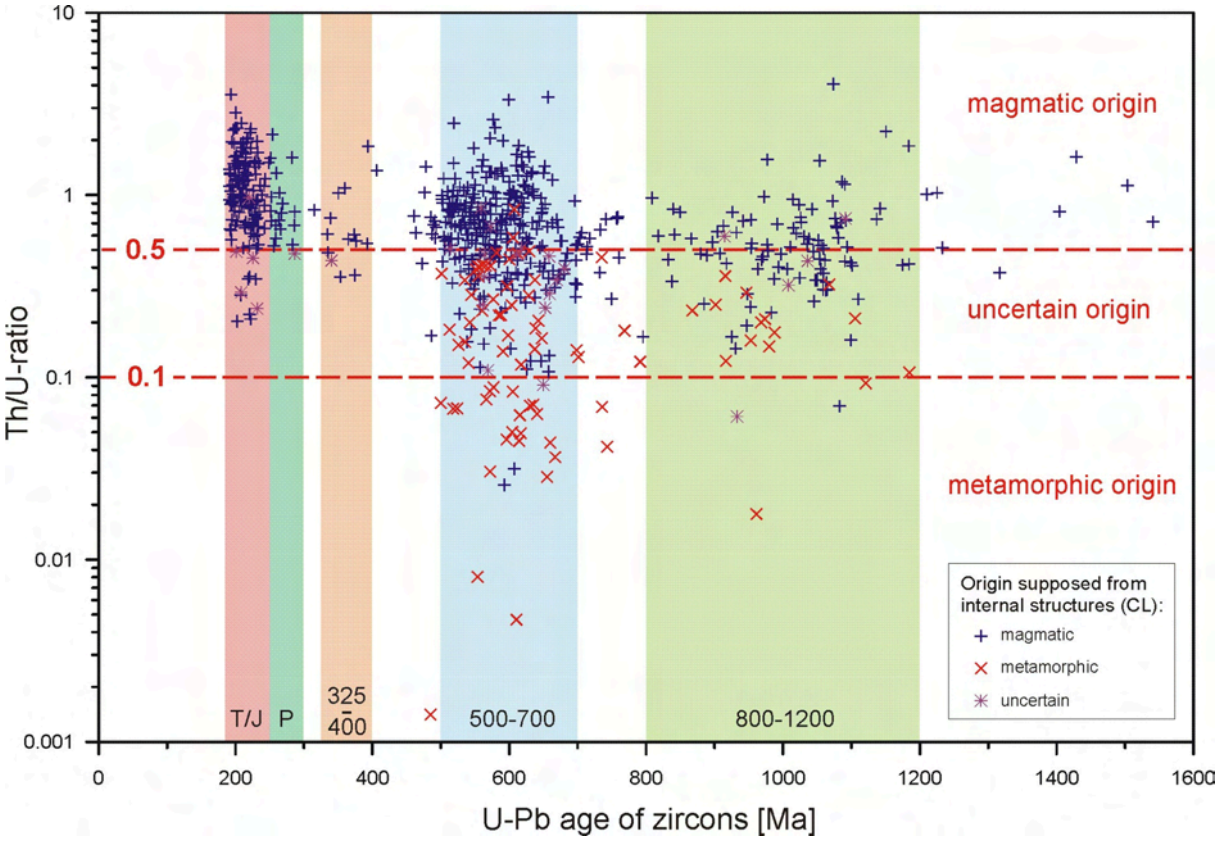


Fig. 3.68: Th/U-ratio and U-Pb ages of concordant zircons. While zircons of certain metamorphic origin are missing in the Triassic/Jurassic, in the Permian, and in the 325-400 Ma cluster, they are frequent in the 500 - 700 Ma group and in the 800-1.200 Ma age group.

The age correlations between different growth zones (core-rim, core-mantle, and mantle-rim) of single zircons are shown in Fig. 3.69. In many cases, both zones are of approximately the same age, and therefore originate from the same zircon forming event. This is especially the case for zircons of the Triassic/Early Jurassic (< 251 Ma) group, in which only one grain shows a core older than Triassic. However, zircons with external zones from between 500 and 700 Ma frequently exhibit significantly older internal zones, mostly showing ages of 800 - 1.200 Ma. This relation indicates, why the number of zircons from the 800 – 1.200 Ma group is independently distributed from the number of Triassic/Early Jurassic zircons.

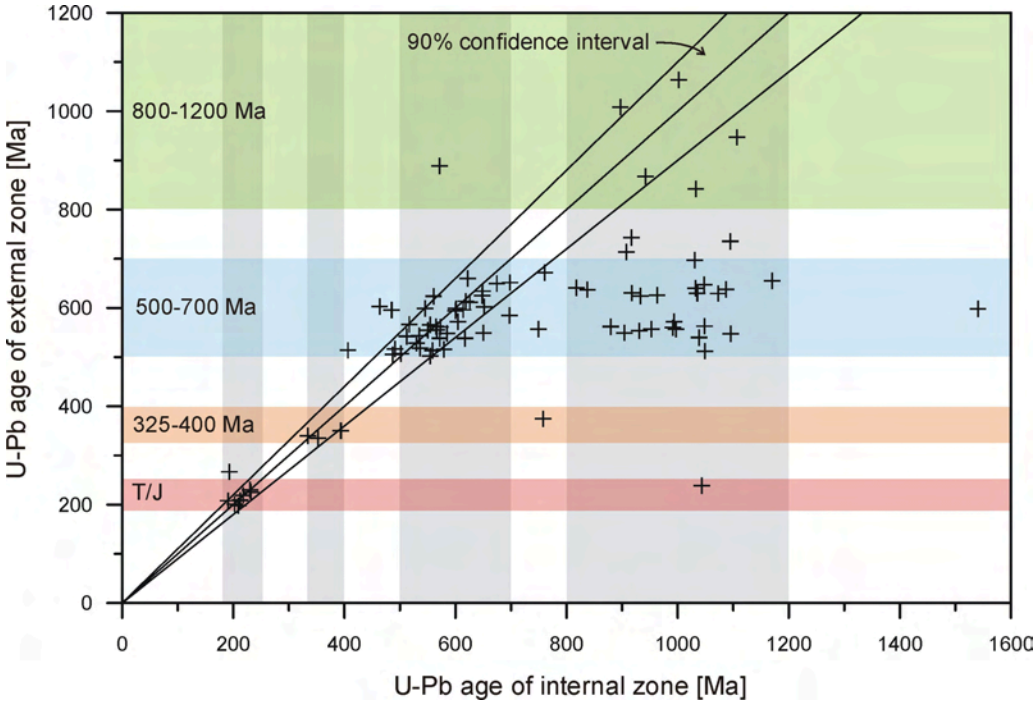


Fig. 3.69: Age relations of internal and external zones (defined by CL images) of concordant zircons. In many cases, both zones are approximately of the same age. However, zircons of the 500-700 Ma cluster frequently exhibit cores with ages between 800 and 1200 Ma. For one sample, the rim appears to be much older than the core – this may be due to an error in sample numbering.

### 3.5.3 Interpretation

The Triassic/Early Jurassic peak can be explained as originate from the magmatic arc along the active margin of Gondwana. The peak is more pronounced in samples rich in volcanic detritus, and less pronounced in samples where volcanic lithoclasts are rare (Fig. 3.70). The youngest zircon ages lie close to the stratigraphic age of the samples (palynologic data of B. Bomfleur 2008, pers. comm.), therefore providing upper limits to the sedimentation ages.

The relatively few zircons of Permian age present in some samples (TI14, SHA07, SPP36) point towards magmatites most likely of a similar, but earlier magmatic arc. Here, the zircons may also be of plutonic origin. Although they are also present in other samples, they are more frequent in stratigraphically higher samples (SPP36, SHA07, from the Early Jurassic). This can be interpreted as a result of unroofing and exhumation of Permian rocks at this time. Today, no Permian magmatic rocks are present in NVL, but they have been reported from the terranes of West Antarctica (Pankhurst et al. 1998).

Devonian to Lower Carboniferous zircons (325-400 Ma) are present in most samples, but they are frequent only in sample TI14. They may originate from the Admiralty Intrusives or from the Gallipolli Volcanics (Grindley and Oliver 1983; Henjes-Kunst and Kreuzer 2003). Alternatively, there are rocks of similar age in other tectonic units, for instance, in Marie-Byrd-Land Land (Collinson et al. 1994; Pankhurst et al. 1998).

The zircon group between 460 and 550 Ma in sample TI14 shows characteristic ages of Wilson terrane rocks, e.g. the Wilson metamorphics and the Granite Harbour Intrusives (Federico et al. 2006; Tonarini and Rocchi 1994). The 460-650 Ma peak present in sample ER04 covers this peak, but extends further to the past. This extension is difficult to interpret, but may represent earlier equivalents of the Granite Harbour Intrusives, or metamorphic rocks of the Wilson terrane not described so far. Following the general tectonic model for the Gondwana plate margin (Sect. 1) these may be located continent-wards, possibly today covered by the polar ice sheet.

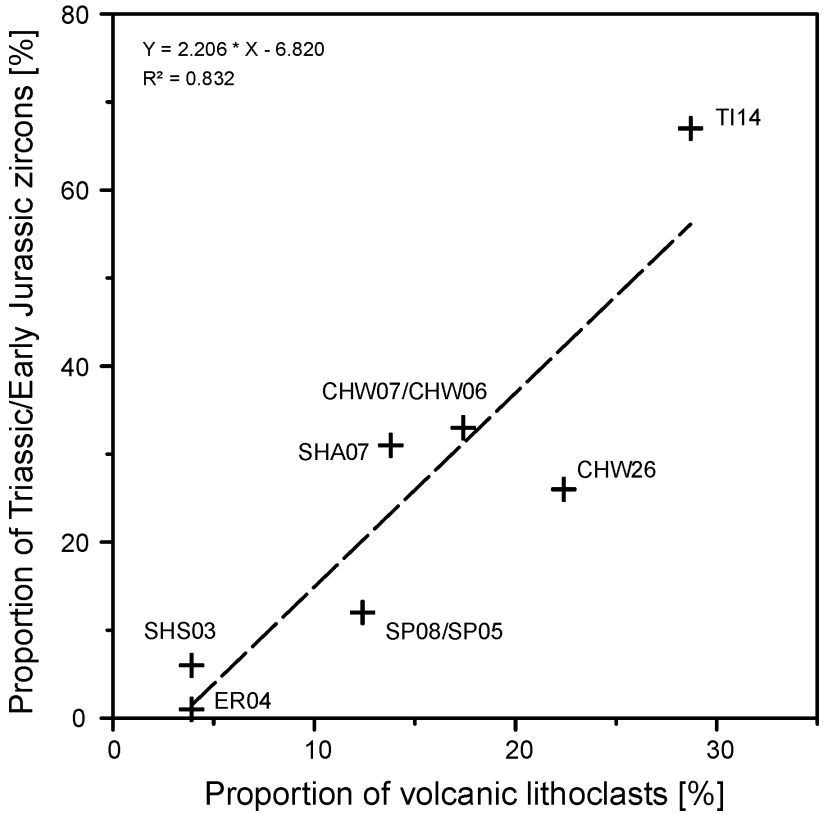


Fig. 3.70: Correlation of the fractions of volcanic lithoclasts (in % of total light minerals) and the zircons with Triassic/Early Jurassic ages (in % of total zircon ages). For samples SP08 and CHW07, no point-counting data are available, thus the results of the neighbouring – and after a semi-quantitative evaluation similar – samples SP05 and CHW06 were plotted in this diagram instead.

The 500-700 Ma age group has already been found in previous studies of detrital zircon ages along the margin of Gondwana. As 'Southwest Pacific-Gondwana age grouping' (Ireland et al. 1994; Sircombe 1999) the code d+ has been assigned to it (Veevers et al. 2005). The ages correspond to the Pan-African event. Zircons of this age have been reported from various locations along today's coastline of Antarctica (Yoshida et al. 2003). In this particular case, the source area may adjoin the Ross Orogen west of the TAM below the polar ice sheet. Here, especially the Wilkes subglacial basin has been presumed as a source area, possibly showing similarities to the Beardmore Microcontinent in the CTM (Sircombe 1999; Veevers et al. 2006).

The 800 – 1.200 Ma age group is more or less distinct in all samples. It is possibly not a single group but may be composed of several, partly overlapping peaks. This assumption may also explain the large width of the age distribution, and the lack of a clear maximum. In sample SHS03, for instance, two separate peaks can be found within this time span. However, the interpretation of this group is difficult, as the number of zircons is relatively small. The age spectrum of about 800 – 1.200 Ma resembles the Grenville age, or code c following the classification for Gondwana zircons of Veevers et al. (2005). The age relationships of different growth zones within zircons indicate that zircons of this age group have been reworked during the 500 - 700 Ma (Pan-African) event. This relationship has been observed previously in other parts of Gondwana, and was interpreted as a rejuvenation of Grenvillian crust during the following Pan-African event, taking place along more or less the same sutures (Yoshida et al. 2003). Thus, the source of the 800 – 1.200 Ma old zircons is most likely spatially related to that of the 500 - 700 Ma old zircons.

### 3.5.4 Implications on sedimentation rates

In three cases, two samples have been analysed from different stratigraphic levels within the same section (CHW07 and CHW26), or closely adjoining sections (SHS03 and SHA07; SP08 and SPP36). As the age of the youngest zircon or zircon group (derived from contemporaneous magmatites) lies close to the stratigraphic age of the samples, the age difference of zircons or zircon groups between the samples can be used to determine the relative sedimentation rates. This approach is limited, as all ages are not exact sedimentary ages but only upper limits thereof. However, as this limitation is valid for all samples, the difference of the sedimentary ages of two superimposed samples can be assumed to be approximately equal to the difference of their relevant maximum ages, as magmatism was contemporaneous and similar durations for erosion and transport may be assumed. The details for the sample pairs and the resulting sedimentation rates are shown in Tab. 3.15. Here, not the youngest zircon age was used, but the youngest maxima of zircon ages, thus the youngest group. Instead of the results of sample SHA07, the age of the tuffaceous sample SHA12 was used due to its higher accuracy (as discussed in Sect. 4).

| Lower sample | Youngest Max. [Ma] | Upper sample | Youngest Max. [Ma] | Age diff. [Ma] | Strat. diff. [m] | Approx. sed. rate [m/Ma] |
|---|---|---|---|---|---|---|
| SHS03 | 221 | SHA12 | 188.2 | 32.8 | 154 | 4.7 |
| CHW07 | 198 | CHW26 | 194 | 4 | 60 | 15.0 |
| SP08 | 215 | SPP36 | 206 | 9 | 55 | 6.1 |

Tab. 3.15: An estimation of sedimentation rates for the SPF by comparison of the maximal ages for various samples within their stratigraphic context, leading to values between about 4 and 15 m/Ma. Compaction was not regarded. Sample SHA12 is the tuffaceous sandstone discussed in Sect. 4.

Neglecting the effect of compaction, the sedimentation rates lie between 4 and 15 m/Ma. These rates are unusually low for sedimentation in active graben settings, as previously discussed for the SPF in the CTM (Elliot 1992; Elliot and Larsen 1993) and in NVL (Casnedi and Di Giulio 1999). Typically active downfaulting in continental settings leads to sedimentation rates at least one or two orders of magnitude higher (Einsele 2000). Rates of a few meters per million years, as found here, are more characteristic in epicratonic or distal foreland basins.

### 3.5.6 Summary and comparison with petrography

In the four sandstone types A, B, C, and D, classified by light and heavy mineral composition, different age distributions were identified. The six samples from sandstone type C and D show remarkable similarities, as do their heavy mineral assemblages (Sect. 3.2). Three prominent age groups were found in these two sandstone types. Their abundances vary, with the relative fraction of the 500 - 700 Ma and the Triassic/Early Jurassic group showing an inverse relationship. Ages from between 800 and 1.200 Ma (Grenvillian) are often present in cores of zircons reworked during the 500 - 700 Ma event (Pan-African). The Triassic/Early Jurassic zircons originate from volcanic rocks of the contemporaneously active magmatic arc along the Gondwana plate margin.

The 500 - 700 Ma cluster corresponds to the Southwest Pacific-Gondwana age group previously identified by various authors (e.g. Ireland et al. 1994; Sircombe 1999). In stratigraphic higher parts of the SPF, the influence from the arc increases, as shown by the total abundances of Triassic/Early Jurassic zircons. In parallel, the abundance of Permian zircons increases.

On the other hand, in sample ER04 (sandstone type A) and in sample TI14 (type B) zircon age spectra are different. Sample ER04 exhibits a very prominent peak between 460 and 650 Ma that apparently point towards a source within the Ross Orogen. Sample TI14 shows a prevalent Triassic group, besides of which a Permian, a Devonian/early Carboniferous, and a group between 460 and 550 Ma are present. A mixing of material from the Ross Orogen with arc-derived detritus is most likely for this sandstone type.

The results show similarities with zircon age spectra from Late Permian to Early Triassic sandstones in the CTM. Here, zircon populations reflect a contemporaneously (thus Permian) active magmatic arc source, a Devonian/Early Carboniferous source, an Early Palaeozoic (Cambrian in this case) Ross Orogen source, and a Neoproterozoic source (Elliot and Fanning 2008). Zircons of Cambrian and Neoproterozoic ages are interpreted as recycled from younger sedimentary rocks by these authors. However, this interpretation is not based on petrographic results, but only on general palaeogeographic and tectonic considerations. For NVL, major sedimentary recycling can be excluded (see Sect. 3.2).

## 3.6 Provenance of mudstones

### 3.6.1 Introduction

Mudstone chemistry, clay mineralogy, and isotopic composition can reveal information about provenance (Potter et al. 2005). This section covers clay mineralogy and isotopic composition with respect to Samarium, Neodymium and Strontium in order to further characterize source areas of the mudstones and the sandstone types they are intercalated.

### 3.6.2 Clay mineralogy

#### 3.6.2.1 Introduction

The mineralogy of clay can provide useful information about their source rocks, even if clay formation is also dependent on other factors like climate and weathering intensity. The most important clay minerals or clay mineral groups, respectively, are kaolinite group minerals (kaolinite, dickite), smectite minerals (montmorillonite, rectorite), illite, and chlorite group minerals (chamosite, corrensite). Their chemical formulas and their basal peak spacing under various conditions are given in Tab. 3.16.

| Mineral | Chemical formula | Air-dried | Glycolated | 550°C |
|---|---|---|---|---|
| Kaolinite (dickite) | $Al_2Si_2O_5(OH)_4$ | 7.15 | 7.15 | destroyed |
| Smectite (mont.) | $(Na,Ca)_{0,3}(Al,Mg)_2Si_4O_{10}(OH)_2 \cdot n(H_2O)$ | 12 – 15 | 17 | 10 |
| Illite | $(K,H_3O)(Al,Mg,Fe)_2(Si,Al)_4O_{10}[(OH)_2,(H_2O)]$ | 10 | 10 | 10 |
| Chlorite (Fe-rich) | $(Fe,Mg)_5Al(Si_3Al)O_{10}(OH,O)_8$ | 14.2 | 14.2 | 14.2 |
| Chlorite (Mg-rich) | $(Fe,Mg)_5Al(Si_3Al)O_{10}(OH,O)_8$ | 14.1 | 14.1 | 14.1 |

Tab. 3.16: Common clay minerals and clay mineral groups, their chemical formula and basal (d-)spacing [Å] after various treatments. The two chlorite types are difficult to distinguish by XRD.

Detrital clay minerals can be linked to certain source rocks or tectonic settings, respectively, and weathering intensity (Tab. 3.17). Deep burial can generally change primary compositions and especially the smectite-illite transformation is susceptible to diagenetic influences (see Sect. 5).

| Provenance / tectonic setting | Moderate weathering | Strong weathering |
|---|---|---|
| Igneous rocks: | | |
| Island arcs (mafic) | Smectite | Smectite, kaolinite |
| Continental arcs (felsic) | Smectite, illite | Smectite, illite, kaolinite |
| Basement uplifts (granitoid) | Illite | Kaolinite |
| Metamorphic rocks: | | |
| Mountain belts | Recycled chlorite, illite | Recycled chlorite, illite, kaolinite |
| Precambrian shields | Illite | Illite, kaolinite |
| Sedimentary rocks: | | |
| Fold-thrust belts / craton interiors | Recycled illite, chlorite, kaolinite, New smectite | Recycled illite, chlorite, kaolinite, New kaolinite |

Tab. 3.17: Detrital clay minerals typical for certain provenances/tectonic settings and different weathering intensities (Potter et al. 2005).

### 3.6.2.2 Methods

Claystones are extremely rare in the SPF, therefore siltstones were chosen for analysis here. Sample preparation followed standard procedures (Kinter and Diamond 1956; Shaw 1972). Fresh rock material was crushed carefully and disaggregated in deionised water. Sodium pyrophosphate ($Na_4P_2O_7$) was used to prevent flocculation of clay minerals. The fraction smaller then 2 µm was cut off using gravity settlement in an Atterberg cylinder. The suspended material was then dripped on ceramic carriers. Liquids were removed through the ceramic carrier using a suction pump to produce a flat, smooth oriented clay layer. Alternatively, and only for determination of authigenic minerals in sandstones (see Sect. 5), the material was mixed with ethanol, dripped carefully on a silicon carrier and leaved to dry.

For the treatment with glycol the mounted carrier was put in an airtight glass repository over Glycol vapour for at least 24 hours. For the heat treatment the samples were heated up over two hours in an annealing furnace to 550°C. This temperature was hold for one hour after which the sample was cooled again slowly.

XRD measurements were performed using a Seifert–FPM XRD 7 powder diffractometer and Cu-*K*α-radiation of 1.542 Å wavelength. The diffractometer was equipped with a point detector, secondary graphite-monochromator and a 30-fold sample changer. Standard cathode conditions were 40 kV and 40 mA.

Air-dried and heated samples were measured twice from 3-40° in 2θ with step width of 0.02° 2θ and a counting time of 3 seconds per step. Glycol-treated samples were measured from 3-30° 2θ only with equal step width of 0.02 2θ and a reduced measuring time of 1 second per step to avoid degassing of glycol from the sample during the measurement. Mineral identification was done with MacDiff® software after a 2θ multi-peak correction for quartz (or corundum from the ceramic carrier, in case of absent quartz) and standard references (Moore and Reynolds 1989; Petschick 2002).

### 3.6.2.3 Results

The XRD-patterns of the samples are plotted in Fig. 3.71. The interpretation was done qualitatively only by a simple comparison of the peak heights. Differences between the samples are obvious and summarized in Tab. 3.18. Illite is present in all samples and shows similar relative peak intensities.

| Sample | Sst. type | Smectite | Illite | Kaolinite | Chlorite | Other Minerals |
|---|---|---|---|---|---|---|
| AG08-JS | A | - | + | +++ | - | Qtz |
| TI13 | B | ++ | + | - | ++ | Qtz, KF |
| SHA08 | C | ++ | + | + | - | Qtz, KF, Pl, Clin/Heu |
| AN05 | C | ++ | + | +++ | - | Qtz, KF, Pl |
| SPP02 | C | +++ | + | ++ | - | Qtz, KF, Analcime |
| CHW24 | D | +++ | + | + | - | Qtz, Pl, Clin/Heu |

Tab. 3.18: Results of XRD clay mineralogy of the analysed samples and the sandstone type they are intercalated. (Relative peak intensity: - : none; + : present; ++ : distinct; +++ : very high). Smectite refers to expandable layers in illite/smectite mixed layer minerals as well.

The sample from section AG (type A sandstones) contains no smectite at all but is strongly dominated by kaolinite.

Sample TI13 (type B sandstones) is the only one of the analysed samples containing chlorite, most likely Fe-rich chamosite. Contrary to sample AG08-JS kaolinite is absent and smectite present.

The samples AN05, SHA08 and SPP02 are intercalated between sandstones of type C. They contain smectite and kaolinite, with the latter in very variable proportions.

Similar to these samples is sample CHW24 from a section of type D sandstones, which can not be distinguished from type C by XRD methods.

#### 3.6.2.4 Interpretation

Following the classification of Tab. 3.17 (Potter et al. 2005) the kaolinite-illite association in the type A siltstone (section AG) can be related to strongly weathered rocks from Precambrian shields or moderately to strongly weathered granitoid rocks (basement uplift). The former may most likely also comprise granitoid rocks or their metamorphic equivalent (felsic gneisses). A granitoid source is inferred for type A sandstones by petrography (see Sect. 3.2).

The chlorite-smectite-illite association in type B (sample TI13) is difficult to allocate to a certain source. However, chlorite and illite may be derived from metamorphic or sedimentary rocks from a moderately weathered mountain belt, whereas smectite (and illite) is most likely derived from igneous rocks (Tab. 3.17). A mountain belt comprising metamorphic rocks is the underlying Ross Orogen. Igneous rocks can also be found within the Ross Orogen (e.g. Granite Harbour Intrusives, Gallipolli Volcanics, see Sect. 1). The subduction related magmatic arc following the Gondwana plate margin comprises igneous rocks as well. Volcanic (predominantly felsic) and metamorphic lithoclasts are very frequent constituents in the sandstones of type B (Sect. 3.2), for which the Ross Orogen and the magmatic arc are inferred sources following the results of petrography and the ages of detrital zircons.

The kaolinite-illite-smectite association from type C (samples SHA08, AN05, SPP02) and D (sample CHW24) siltstones may be derived from a strongly weathered continental arc source, but a mixture of various rock types or settings is also possible (e.g. granitoids, Precambrian shields, igneous rocks, etc.; see Tab. 3.17). A mixture of higher grade metamorphic rocks with arc derived material is indicated by petrography and detrital zircon ages. Anyway, as chlorite is absent, the source is different from the type B source, and as smectite is present the source must also be different from type A source, both described above. The varying proportions of the associated clay minerals kaolinite and smectite (illite proportion appears to be relatively constant) may be related to minor changes or fluctuations within the source area, or to climate changes.

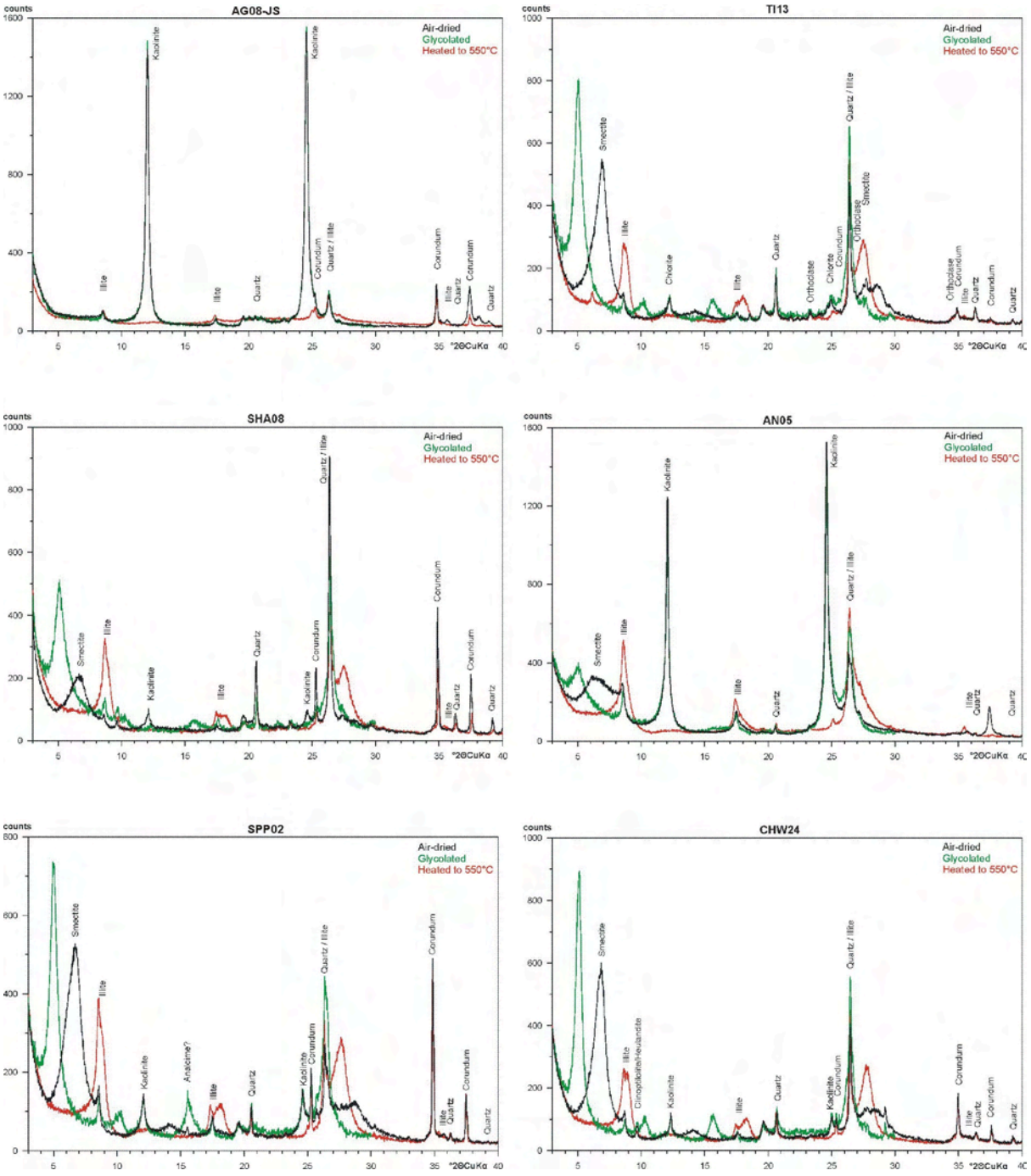


Fig. 3.71: XRD-patterns of the six analysed samples. The corundum peaks are caused by the ceramic carrier and were used for calibration in case quartz was absent.

## 3.6.3 Samarium, Neodymium, and Strontium isotopic composition

### 3.6.3.1 Introduction

Samarium (Sm) and Neodymium (Nd) are both Lanthanides (rare earth elements, REE) with seven naturally occurring isotopes. Radioactive $^{147}$Sm decays to $^{143}$Nd with a half-life of $1.06 * 10^{11}$ years (Gupta and Macfarlane 1970). Due to this large time span, the Sm-Nd method is well suited for dating Precambrian rocks. As stable reference isotope commonly $^{144}$Nd is used. Instead of an isotope ratio, the result is mostly given as $\varepsilon_{Nd}$ (De Paolo and Wasserburg 1976), that is as a relative deviation of a given reservoir, mostly the "chondritic uniform reservoir" (CHUR) or the depleted mantle reservoir (DM). Therefore, $\varepsilon_{Nd}$ can be used as a measure if the sample is derived from a source enriched in Nd ($\varepsilon_{Nd}$ negative), or from a depleted source ($\varepsilon_{Nd}$ positive).

Sm and Nd are very incompatible elements and behave chemically and physically more or less identical. A fractionation of isotopes during melting or crystallisation but also during exogenic processes like weathering can be excluded on a whole rock scale, and a once established isotope-ratio changes only due to radiogenic processes. Importantly, a Sm-Nd model-age therefore does not provide a stratigraphic age, but an average crustal segregation (or crust formation) age, i. e. the average time at which a rock or its precursor has segregated from mantle material (Arndt and Goldstein 1987). For sedimentary rocks (as found here) that means the model age averages the time at which the rocks of the source area or their precursors have segregated from the mantle (Faure 1986).

Although on a whole rock scale changes of the Sm-Nd ratio can be excluded, a metamorphism significantly later than crust formation may disturb the isotopic signal by a redistribution of Sm and Nd to newly formed metamorphic minerals like garnet or zircon (Nelson and De Paolo 1988). This is most important for the interpretation of isotopic data of sedimentary rocks derived from a metamorphic source, as mineral sorting during weathering and transport may result in a model-age no longer representing a crust formation age but a distinctly younger age closer to the age of metamorphism. The strength of this effect depends on the degree of mineral sorting. Analyses of fine grained rocks are thought to be robust, as these are more likely to carry a 'whole rock' isotopic signal than coarser grained rocks.

Strontium (Sr) is an alkali earth metal with four stable, naturally occurring isotopes. It readily substitutes Calcium in minerals, as its physical and chemical properties are similar. The isotope $^{87}$Sr is permanently produced by decay of the radioactive $^{87}$Rb (Rubidium), which has a half-life period of $4.88 * 10^{10}$ years (Faure 1986). As stable reference isotope commonly $^{86}$Sr is used. Sr is a compatible element being enriched in (highly differentiated) cratonic rocks with respect to the residual mantle and the subsequent volcanic rocks. It behaves totally different from Sm and Nd during endogenic or exogenic processes, making it an ideal supplement to the Sm-Nd system. The $^{87}$Sr/$^{86}$Sr ratio in provenance studies can be interpreted as a ratio of volcanic to cratonic source rocks, although diagenetic processes can alter this value (Potter et al. 2005).

Isotopic data for the possible source regions outlined in Sect. 1 are very sparse, so provenance can not be determined solely on the basis of isotopic data. However, some data have been published and shall be shortly summarized in what follows.

The East Antarctic Craton with presumably large areas Proterozoic or even Archean crust (James and Tingey 1983) shows a wide variation of $\varepsilon_{Nd}$ values between -7 and -46 and $^{87}$Sr/$^{86}$Sr ratios ranging from 0.71 to 0.78 (Basile et al. 1997; Borg et al. 1990; Walter et al. 2000; Wareham et al. 1998).

For metamorphic rocks of the Ross Orogen, very few isotopic data have been published (Goldie Formation, Beardmore Group, CTM), with $\varepsilon_{Nd}$ values varying from about -10 to -12 and $^{87}$Sr/$^{86}$Sr ratios between 0.73 and 0.78. Mafic igneous rocks of this region

yielded $\varepsilon_{Nd}$ values of about 4 to 6 (Borg et al. 1990). For Cambro-Ordovician intrusive rocks, $\varepsilon_{Nd}$ values between -12 and +2 and $^{87}Sr/^{86}Sr$ ratios between 0.704 and 0.822 are given.

The Granite Harbour Intrusives of northern Victoria Land show $\varepsilon_{Nd}$ values of about -25 to -30, which is slightly lower than the $\varepsilon_{Nd}$ values of the Devonian Admiralty Intrusives (-20 to -26) that occur in the Bowers and Robertson Bay Terrane only (Borg et al. 1987).

For the supposed volcanic arc along the proto-pacific margin, no data exists. The arc most likely comprised rocks with a depleted mantle isotopic signature as well as rocks with a more crustal signature due to assimilation or fractionation.

### 3.6.3.2 Methods

Five samples of greyish siltstones were analysed. They were intercalated in between sandstones of different types, as type B (sample TI13), type C (SHA11, SPP02), and type D (CHW14); thus they may most likely be derived from different source regions. Sample SHC29 is from the overlying SHF.

Sr, Sm, and Nd isotope analyses were performed on the Triton© TIMS of the isotope geology department at the Geowissenschaftliches Zentrum Göttingen of the Georg-August Universität. Samples were spiked with a $^{84}Sr$-tracer and a mixed $^{149}Sm$-$^{150}Nd$-tracer solution and dissolved in standard HF-$HNO_3$ acid mixture. Sr and REE were separated from one single rock digest using standard HCl-based cation exchange procedures. Subsequent separation of Sm and Nd was achieved using the reverse ion chromatographic procedure with HDEHP resin after Richard et al. (1976). Instrumental mass bias was corrected with $^{88}Sr/^{86}Sr$ of 0.1194 and with $^{146}Nd/^{144}Nd$ of 0.7219 using exponential law.

The Sm/Nd model-ages ($T_{DM}$) were calculated using present-day depleted mantle values of $(^{147}Sm/^{144}Nd)_{DM}$=0.222 and $(^{143}Nd/^{144}Nd)_{DM}$=0.513114, and a half-life period of $1.06*10^{11}$ for $^{147}Sm$ (Michard et al. 1985). $T_{DM}$ is given by $T_{DM} = 1/\lambda * \ln[(0.513114 - {}^{143}Nd/{}^{144}Nd) / (0.222 - {}^{147}Sm/{}^{144}Nd) + 1]$.

### 3.6.3.3 Results

The results for the five analysed samples are summarised in Tab. 3.19. The $\varepsilon_{Nd}$ vary but are all negative, implying a derivation from enriched sources with a lower Sm/Nd ratio than the depleted mantle. That means, their average source has separated from the mantle as a magma and not undergone periods of partial melting and differentiation (Potter et al. 2005).

| Sample | Sst.-type | $^{87}Sr/^{86}Sr$ | 2σ | $^{143}Nd/^{144}Nd$ | 2σ | $^{147}Sm/^{144}Nd$ | $\varepsilon_{Nd}$ | $T_{DM}$ [Ga] |
|---|---|---|---|---|---|---|---|---|
| **TI13** | B | 0.718939 | 1.33 E-05 | 0.512587 | 1.39 E-05 | 0.123576 | -1.00 | 0.82 |
| **SHA11** | C | 0.714250 | 1.69 E-05 | 0.512442 | 0.86 E-05 | 0.125312 | -3.82 | 1.06 |
| **SPP02** | C | 0.759938 | 7.12 E-05 | 0.512294 | 2.29 E-05 | 0.121706 | -6.70 | 1.24 |
| **CHW15** | D | 0.714367 | 2.36 E-05 | 0.512313 | 1.97 E-05 | 0.120153 | -6.34 | 1.20 |
| **SHC29** | - | 0.751802 | 2.65 E-05 | 0.512270 | 2.88 E-05 | 0.117494 | -7.17 | 1.23 |

Tab. 3.19: Sr-Sm-Nd isotopic data for the five analysed mudstones. Sst.-type refers to the type of sandstone after petrography the mudstone sample is intercalated. Sample SHC29 is from the Shafer Peak Formation (SHF). The complete results can be found in the appendix.

For samples SHA11 and CHW15 the $^{87}Sr/^{86}Sr$ ratio is very similar (~0.714), and for sample TI13 it is only slightly higher (~0.719). The remaining two samples SHC29 and SPP02 show very high ratios of ~0.752 and ~0.760, respectively. These high values point towards a very Rb rich initial source. As Rb may substitute K due to similar ionic radii and equal charge, a high Rb content may indicate K-rich rocks, as for example K-feldspar rich (meta-)granitoids.

The differences in $\varepsilon_{Nd}$ for the samples CHW15, SPP02 and SHC29 (the latter is from the SHF, see Sect. 4) are low. Similarly, the differences of their model-age are low ($T_{DM}$ = 1.20 - 1.24 Ga). The $\varepsilon_{Nd}$ and model-age for sample SHA11 ($T_{DM}$ = 1.06 Ga) are distinctly lower. Sample TI13 exhibits the lowest $\varepsilon_{Nd}$ and model age ($T_{DM}$ = 0.82 Ga) of all five samples. $^{87}Sr/^{86}Sr$ ratios and $\varepsilon_{Nd}$ are plotted in Fig. 3.72. Phanerozoic crust with high Rb/Sr ratio seems to be indicated as source area for all samples. However, as the sandstone types B, C, and D defined by petrography are all mixtures of different sources, their isotopic composition necessarily is a mixture. Thus, a proportion of archaic crust may also be present within the source area(s). However, the proportion of very old crust seems to be minor or neglectable due to the generally high to very high Rb/Sr content of all samples. Therefore, granulitic rocks presumed to comprise in the East Antarctic craton are unlikely to be a major source.

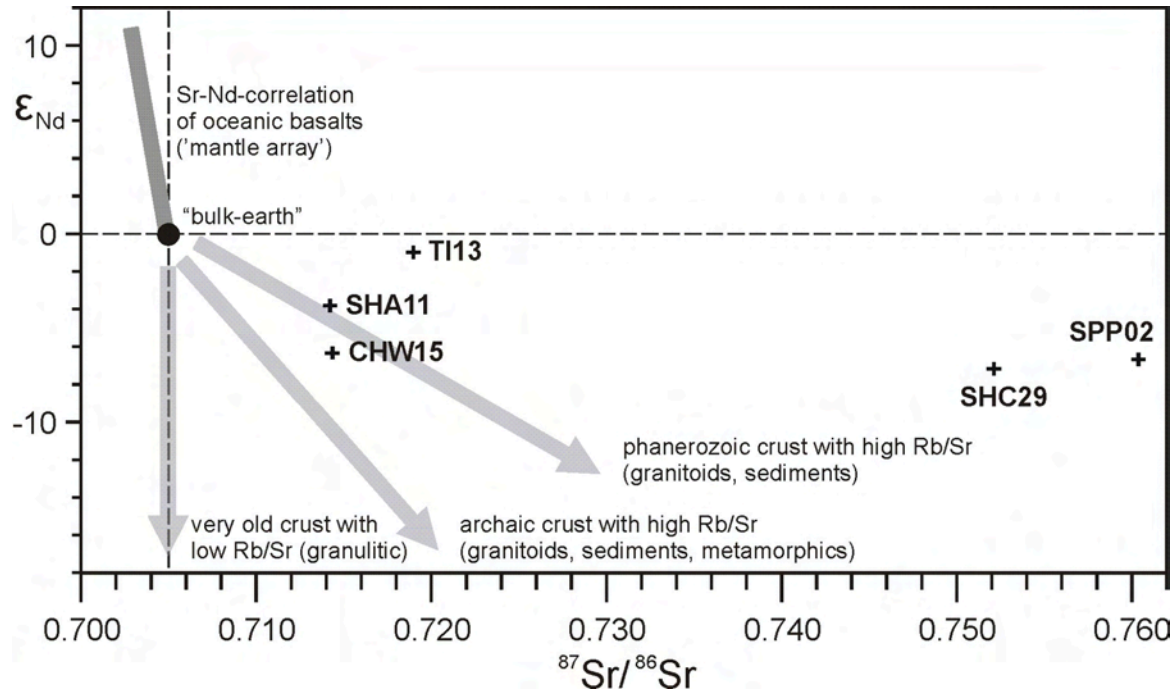


Fig. 3.72: $^{87}Sr/^{86}Sr$ ratios plotted versus $\varepsilon_{Nd}$, indicating Phanerozoic crust as source area. Admixture of older (Proterozoic or Archean) material can not be excluded, as these values are integrating a whole source area.

### 3.6.3.4 Interpretation

The sample TI13 is intercalated between sandstones rich in volcanic and metamorphic lithoclasts (type B). For these clasts, the underlying Ross Orogen and the magmatic arc are most likely source areas (see Sect. 3.2, 3.4, and 3.5). The 0.8 Ga crustal residence time may therefore be a mixture of the average model ages of these two sources.

Samples SHA11 and SPP02 are both intercalated in between sandstones of type C. An interpretation for the distinctly younger model-ages of the sample SHA11 is the presence of an additional relatively 'younger' source, i. e. material with a lower crustal residence time. This may have been juvenile volcanic material, as tuffaceous sandstones are occurring in under- as well as overlying samples (e.g. SHA06, SHA09, SHA12; see Sect. 4) and recycled tuffaceous material can be expected also in the intercalated mudstones. The model age of about 1.2 Ga of sample SPP02 most likely reflects the crustal residence time of the type C sandstones source. The lower $\varepsilon_{Nd}$ in comparison with sample TI13 (type B sandstone) correlates with the lower fraction of (presumably arc derived) volcanic lithoclasts.

Sample CHW15 is from a section dominated by type D sandstones. Its model age of about 1.2 Ga cannot be distinguished from that of sample SPP02 (type C sandstone). Both sandstone types show a very similar heavy mineral composition, but the proportion of volcanic lithoclasts is much higher in type D sandstones. As the heavy mineral assemblage, the model age of sample CHW15 may reflect the proportion of type C material only. This seems plausible, as volcanic rocks usually contain less of the incompatible elements Sm and Nd due to partial melting (e.g. of mantle material) and their isotopic signal may therefore be overwhelmed by the signal of the (metamorphic, plutonic) sandstone source C.
The model age of sample SHC29 from the SHF is very similar to the model age of samples CHW15 and SPP02 (sandstone type C and D) from the underlying SPF, but distinctly different from those of sample SHA11. As for the latter a proportion of juvenile magmatic material is inferred, this seems to be unlikely for sample SHC29, assuming a similar model age of the 'non-juvenile' part of the source area. In this case, this sample is derived from a source of equal crustal residence time as the other type C and D samples without juvenile material, as observed, for instance, in the sandstone sample SHC25 (see Sect. 4).

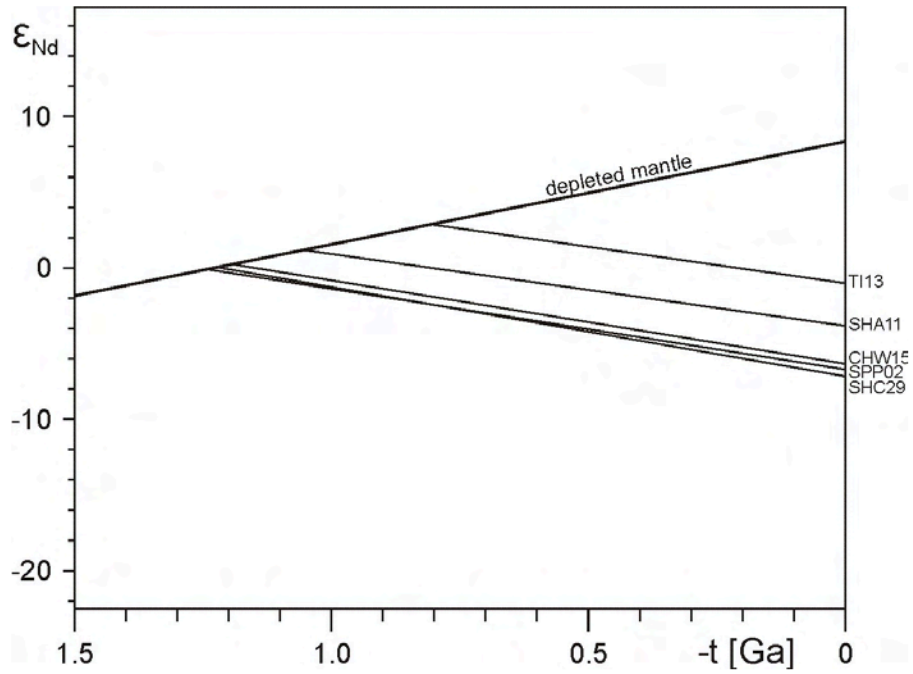


Fig. 3.73: $\varepsilon_{Nd}$ development of the depleted mantel and average source rock segregation at $T_{DM}$ of the five samples, resulting in different present-day $\varepsilon_{Nd}$ values.

## 3.7 Synthesis: Provenance of the SPF and basin evolution

### 3.7.1 The different sandstone types and their source areas

Six sandstone types (A-F) with different sources were identified by light and heavy mineralogy. The classification is consistent with whole-rock geochemical analyses. Mineral chemistry, zircon morphology, and especially U-Pb ages of detrital zircons confirmed the results and provided additional information. In the following, the detailed results are summarized in order to provide comprehensive information about lithology, age, and location of the source areas of the different sandstone types. These information are crucial for the understanding of the evolution of the NVL sector of the Transantarctic Basin presented in the following section. The distribution of the different sandstone types in cross section is shown in Fig. 3.75.

Sandstone **type A** is composed mainly of quartz and feldspar, while lithoclasts are rare. Most of the latter are of granitic origin, metamorphic and volcanic ones are less abundant. Distinctively altered biotites are frequent, pointing with quartz, feldspar and granitic rock fragments towards a predominantly granitoid source. Zircon, tourmaline and apatite as most frequent heavy minerals also indicate a granitoid source. Garnet and metamorphic lithoclasts are rare, but generally more frequent in section ER than in sections TP and AG. An influence of the local varying basement geology correlates with this variation. The contribution of a metamorphic source increases slightly in upper parts of the sections.

U-Pb zircon ages show a broad peak between 460 and 650 Ma of predominantly magmatic zircons, covering the 480 ± 20 Ma of the known Granite-Harbour Intrusives within the Wilson terrane. The other zircons comprising the largest part of this peak are probably mostly related to similar granitoid rocks. The subordinate metamorphic zircons of this age as well as the metamorphic lithoclasts may be derived from the Wilson terrane. The other units of the Ross Orogen (Bowers and Robertson Bay terrane) were not a major source, as the typical 360 ± 10 Ma range of zircon ages from the Admiralty Intrusives is not present. However, a Cr-spinel in sample ER04 indicates that the Lanterman-Mariner suture as boundary between the Wilson and the Bowers terrane was lying within the source area. In combination with the very rare volcanic rock fragments, a single magmatic Triassic zircon and another magmatic zircon from the Permian indicate a minor contribution of the magmatic arc along the active plate margin of Gondwana.

Type A sandstones have been found nearly exclusively in the southern Eisenhower Range (sections TP, AG, ER), where strongly varying palaeoflow directions indicate a transport from southerly directions (R. Schöner 2008, pers. comm.). The sandstones described here are intercalated in up to 70 m thick conglomerates, for which a transport distance of a few tens of km is likely. The frequent biotite indicates also a proximal source area. According to geochemical weathering indices, the source was intensely weathered.

At the basal parts of the SPF at Timber Peak (below section TI) also conglomerates are assumed (Schöner et al. in review), which may be similar in composition to the conglomerates in the southern Eisenhower Range. In the southern Deep Freeze Range, a sample at the base of the SPF (section SHS), is a mixture of type A and type B material. A sample at the top of the SPF (section MA) comprises a mixture of type A and type C material.

Due to its local and stratigraphic restriction, type A sandstones are interpreted as local input into the Transantarctic Basin shed mainly from a close source within the Wilson terrane. Despite the intense weathering, conglomerates are present; tectonic uplift of the source area may explain this apparent conflict. This uplift took place in a region close to the former Ross High foreswell, which so far has been assumed to be buried during the Middle Triassic (Collinson et al. 1994). The large time span of weathering (possibly since the Permian) may also be an additional or alternative explanation

If an axial flow following the axis of the Transantarctic Basin has existed already during this time, it may have been passing west of the Eisenhower Range with a more or less northward flow direction. A position of the basin axis east of the Eisenhower Range is unlikely, as from there type B sandstones were shed (see below). A possible alternative would be the presence of the Ross High foreswell, dividing the NVL part of the Transantarctic Basin from southern parts (SVL and the CTM), as it is proven until the Early Triassic. In this case, the axial flow must have crossed the magmatic arc towards the Proto-Pacific Ocean south of NVL to account for the presence of type B sandstones here. This scenario is highly unlikely, if the topography of the Triassic magmatic arc of Gondwana is assumed to be similar to that of the recent South American Andes.

Sandstone **type B** comprises eroded debris from an undissected, predominantly felsic, active volcanic arc, as shown by frequent volcanic lithoclasts, abundant apatite in the heavy mineral spectra and the predominance of magmatic zircons of Triassic/Jurassic age. This material is mixed with material from the Ross Orogen, providing metamorphic lithoclasts. The composition of the rare garnets in sandstone type B matches analyses from Granite Harbour Intrusives (GHI) and metamorphic rocks of the Wilson terrane. An age peak of detrital zircons around 360 Ma is typical for Admiralty Intrusives or Gallipolli Volcanics (Bowers/Robertson Bay terrane or Wilson terrane, respectively) and Cr-spinel of harzburgites are most likely derived from the Lanterman-Mariner suture within the Ross Orogen. Additionally, few zircons have Early Palaeozoic ages typical of the Ross Orogen. The ratio of arc material relative to Ross Orogenic material varies within the section, but does not show a distinct trend. The source area of type B sandstones is shown as a schematic cross section in Fig. 3.74.

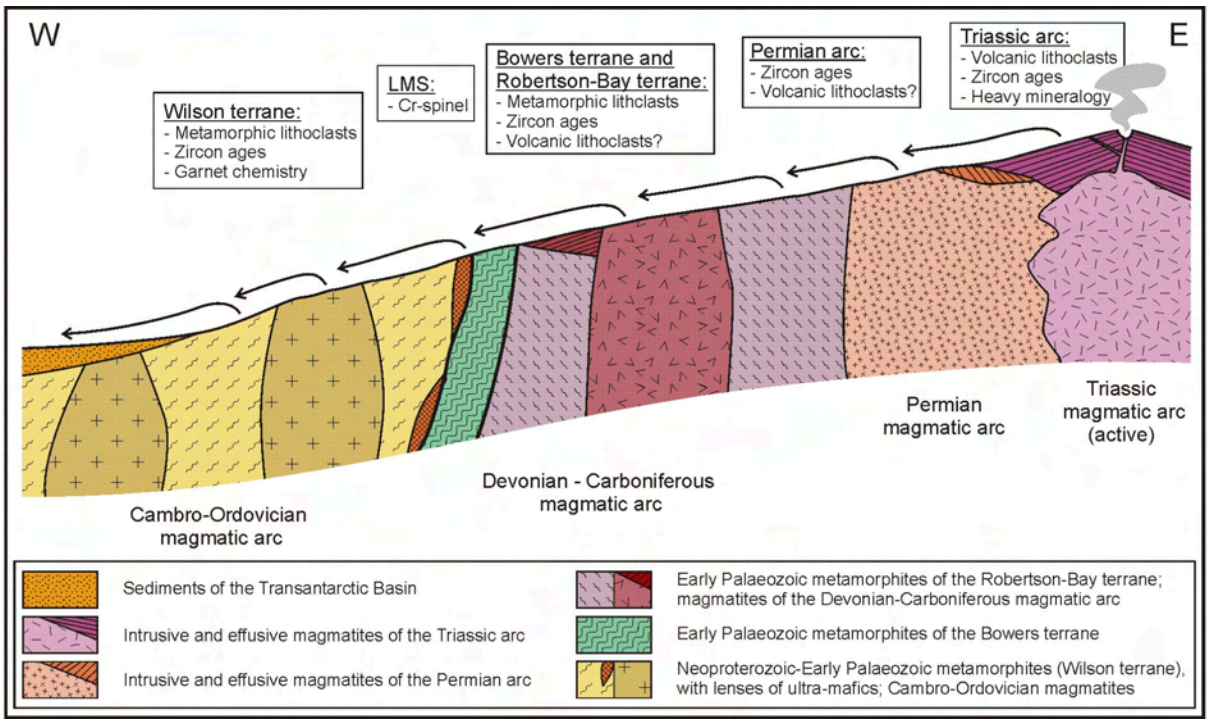


Fig. 3.74: Schematic cross section following the transport path of type B sandstones (E-W) to show their sources (not to scale). The continuously outcropping basement between NVL and the active magmatic arc stands in contrast to the basin model of Collinson et al. (1996, see also Fig. 1.7). LMS: Lanterman-Mariner-Suture.

The crustal residence time determined for one pelitic sample was about 0.8 Ga, and most likely reflects a mixture between an average model age of the terranes of the Ross Orogen and the magmatic arc. It may vary with the fractions of these sources.

Type B sandstones can be found in the northern Eisenhower Range (sections SR and lower TI) and in the southern Deep Freeze Range (sections SHS and PT). It is most abundant in section TI, where palaeoflow directions indicate an easterly source of this sandstone type (Schöner et al in review). Its composition thus proves that the Ross Orogen at this time was not totally covered by sediments but subject to erosion. If a regular south-eastward continuation of the Ross Orogenic terrane boundaries is assumed, the margin of the Transantarctic Basin in the NVL sector may have been less than about 100 km offshore east of the Eisenhower Range (latitude of Mt. Melbourne).

Due to the westward flow, material transport was about perpendicular to the axis of the Transantarctic Basin, which was about N-S trending following the strike of today's Ross Orogen. Consistently, this sandstone type is interpreted as a local, radial input into the basin. As in the southern Deep Freeze Range (sections SHS and PT), this sandstone type is found at basal parts of the SPF (in one sample mixed with type A), a presumed axial flow along the basin strike must therefore have been located westwards of these sections.

Garnet is by far the most abundant heavy mineral in the quartz rich **type C** sandstones. According to its composition, a high grade metamorphic source comprising metasediments/granulites and basic gneisses/eclogites is necessary. These source rocks can be correlated with the broad peak between 500 and 700 Ma in the U-Pb zircon age spectra, which is not present in samples missing those types of garnets. The source may be located in the ice-covered area of the East-Antarctic continental interior.

Another peak of Triassic/Jurassic zircon ages lying close to the relative sedimentary age, and the volcanic lithoclasts indicate material derived from the magmatic arc. Minerals (e.g. garnet) and zircon ages that can be clearly related to rocks of the Ross Orogen (e.g. 360 Ma Admiralty Intrusives, 480 Ma Granite Harbour Intrusives) are rare. An average crustal residence time of about 1.2 Ga was determined. However, the tuffaceous sandstones in the upper part of the SPF may have distinctly younger model ages.

According to geochemical indices, the source area was intensely weathered during deposition of basal parts of the SPF (in the Deep Freeze range, sections AN, SHS, PT). However, a high maturity due to long distance transport may also cause a similar effect. Towards higher stratigraphic ranges, the proportion of arc derived material increases, as is shown by the proportions of volcanic lithoclasts, the plagioclase : feldspar ratio, greenish calcic ampiboles in the heavy mineral assemblage and the ratio of Triassic/Jurassic zircon ages relative to the peak between 500 and 700 Ma. This finds expression in apparently lower weathering indices.

The abundance of zircons of Permian age also increases with time, indicating further exhumation and erosion of the Permian magmatic arc, at least in the source area of type C sandstones. An ocean-wards shift of the zone of active (Triassic) magmatism is a plausible mechanism, and trench roll-back or a steepening of the subduction zone may be the related causes. Additionally, greenish-brownish amphiboles become increasingly more abundant, in parallel to an increasing plagioclase : feldspar ratio in the uppermost stratigraphic intervals. Both observations can be explained by effusion and erosion of andesitic igneous rocks, most likely along the active magmatic arc.

Sandstones of type C can be found almost in the entire working area except for the Southern Cross Mountains (ST, CHW) and the Eisenhower Range (PT, AG, SR). In the latter, only basal parts of the SPF are exposed. Type C sandstones possibly have been present in higher stratigraphic levels here, as they are in the nearby section TI, where they overly type B

sandstones. In the Southern Cross Mountains (section CHW), type D sandstones show a similar heavy mineral spectrum to type C sandstones.

The palaeoflow directions for type C indicate mostly northern (to north-western) material transport (Schöner et al. in review). This orientation matches best the presumed basin axis (roughly N-S) of the Transantarctic Basin, thus this type most likely represents an axial flow. However, from some localities in the Outback Nunataks, other flow directions have been reported (Collinson et al. 1986, Schöner et al. in review), but they are not representative due to the small number of measurements.

Because this sandstone type is missing at the base of the SPF in the southern Eisenhower Range, the basin axis at this time was located west of the Eisenhower Range, as from the east type B sandstones were shed (see above). The most intensely weathered type C sandstones in section AN are interpreted to represent the earliest deposits of the axial flow. Alternatively, the axial flow may have been established at later stages of basin evolution and the deposits in the Eisenhower Range are slightly older. The increasing fraction of arc-derived material is concordant to a possible tectonic progradation of the active magmatic arc, thus agreeing with the interpretation of the Transantarctic Basin as a (retro-arc) foreland basin (Collinson et al. 1996). However, other controlling factors for the abundance of arc derived material are also possible, for instance, changes in drainage system, magmatic activity, or tectonic uplift.

In **type D** sandstones, volcanic lithoclasts and feldspars are very frequent and a dissected magmatic arc as source is likely. However, the heavy mineralogy is very similar to type C, although tourmaline is absent. Thus the high-grade garnet-bearing metamorphic source for type C sandstones was also a (minor) source of this sandstone type. The reason of the heavy mineralogy pointing to a different source than the light mineralogy can be explained by a smaller grain size and a lower abundance of (stable) heavy minerals in volcanic rocks compared with metamorphic or plutonic rocks. Therefore, the metamorphic source dominates the heavy mineralogy although it is overall less important for sandstone composition. The zircon age spectra are also similar to type C, containing a 500-700 Ma and a Triassic/Jurassic peak close to the sedimentation age of the sample and derived from the magmatic arc.

Although a gradual, lateral transition between sandstones of type D and type C has not been observed, this seems possible from a eastern (arc) to western (craton) side. In this case, type C and type D sandstones would be part of a continual mixing range. However, even in this case, the differentiation between two types may be useful and justifiable, although it may be difficult to define a boundary.

Type D sandstones comprise section CHW in the Southern Cross Mountains and are present in a sample within section MA in the southern Deep Freeze Range. In section CHW, the composition of underlying strata is unknown. However, basal parts of the SPF in this area, which are described below, are exposed at nearby section ST. In contrast to type B sandstones, no Cr-spinel was found. However, some zircons of Devonian/Carboniferous age are present in a sample from the lower part of the section, indicating that the Ross Orogen was a (minor) source. The model age of about 1.2 Ga determined for this source may reflect the age of the type C source only, as does the heavy mineral assemblage.

Few palaeoflow measurements that may not cover the entire stratigraphic range of this sandstone type indicate an easterly source for type D sandstones (Schöner et al. in review). This direction is also likely due to the abundance of arc derived material (volcanic lithoclasts, Triassic/Jurassic magmatic zircons), and the wider palaeogeographic context. However, mixing with a small amount of type C material that was most likely shed from the south along the basin axis (see above) is necessary. Recycling of already deposited type C material is a possible explanation. Although heavy mineral indicators argue against this hypothesis, their reliability is uncertain in this case (unlike for other sandstone types), as the high proportion of

a volcanic source may mask minor additional sediment recycling. Type D sandstones are interpreted as a local, lateral input to the Transantarctic Basin, which has experienced some mixing with material transported along the basin axis. However, the regularity of the mixing without greater variance throughout the stratigraphic range is enigmatic. Following this interpretation, the abundance of type C material decreases eastwards until a sandstone composition similar to type B is reached finally – a hypothesis that possibly may never been tested due to missing outcrops east of the Southern Cross Mountains.

Amphiboles as in type C sandstones have not been found, although a similar stratigraphic range of both sandstone types was analysed. Therefore, the andesitic rocks the amphiboles are most likely derived from were restricted to southern parts of the magmatic arc outside the NVL sector of the Transantarctic Basin.

**Type E** sandstones are the only quartz arenites found within the SPF. With tourmaline being the most important heavy mineral, a felsic plutonic provenance is likely. Cobbles and pebbles indicate a proximal source, which was presumably intensely weathered (as type A sandstones). In stratigraphic higher intervals metamorphic and volcanic lithoclasts become slightly more abundant, but are still very rare. This indicates an increasing contribution from a metamorphic and volcanic source, interpreted as enlargement of the catchments area.

Type E sandstones have been found in section ST only. Their originally overlying cover possibly consists of type D sandstones found at the close section CHW. A transition to type D sandstones has not been observed.

Both, the volcanic and the metamorphic lithoclasts may be derived from the Ross Orogen. As garnets are missing, the metamorphic source described for sandstones of type C and D is excluded. Alternatively, the volcanic lithoclasts may originate from the Permian or the Triassic arc.

Due to its local and stratigraphic restriction, sandstone type E is interpreted as local input to the Transantarctic Basin. Palaeoflow directions are unknown, but may be directed westward as for type D sandstones. A relative proximal source within the underlying Ross Orogen is inferred, most likely a plutons of the Granite Harbour Intrusives, as can be found in the western Southern Cross Mountains. Detrital zircon ages, however, have not been determined to prove this assumption.

**Type F** sandstone has been found in a single sample only (AN08), but a separate classification seems justifiable due to the unique, rutile rich heavy mineral spectrum. The sample is very quartz rich, whereas feldspar and lithoclasts (volcanic and metamorphic) are very rare. According to geochemical weathering indices, the source was highly weathered.

Palaeoflow directions point to a westerly source (Schöner et al. in review); however, the reliability of the low number of measurements from a single stratigraphic horizon is uncertain. Nevertheless, this sandstone type is the only one determined that may originate from the continental side of the basin. The limited spatial and stratigraphic range of type F sandstones makes a local source within the Ross Orogen (Wilson terrane) reasonable, but zircon ages have not been analysed to test this assumption.

Fig. 3.75: Cross section of the SPF in NVL showing the occurrence of the different sandstone types. Sandstones of mixed types are checked in the respective colours. Palaeoflow directions (after Schöner et al. in review) are plotted relative to the direction of the cross section. Biostatigraphic ages were provided by B. Bomfleur (pers. comm. 2009). In addition, for section CHW, a Jurassic age can be derived from the nearby section CE (not shown in the cross section). Roman numbers I to IV indicate the time slices of the maps in Figs. 3.76 to 3.79.

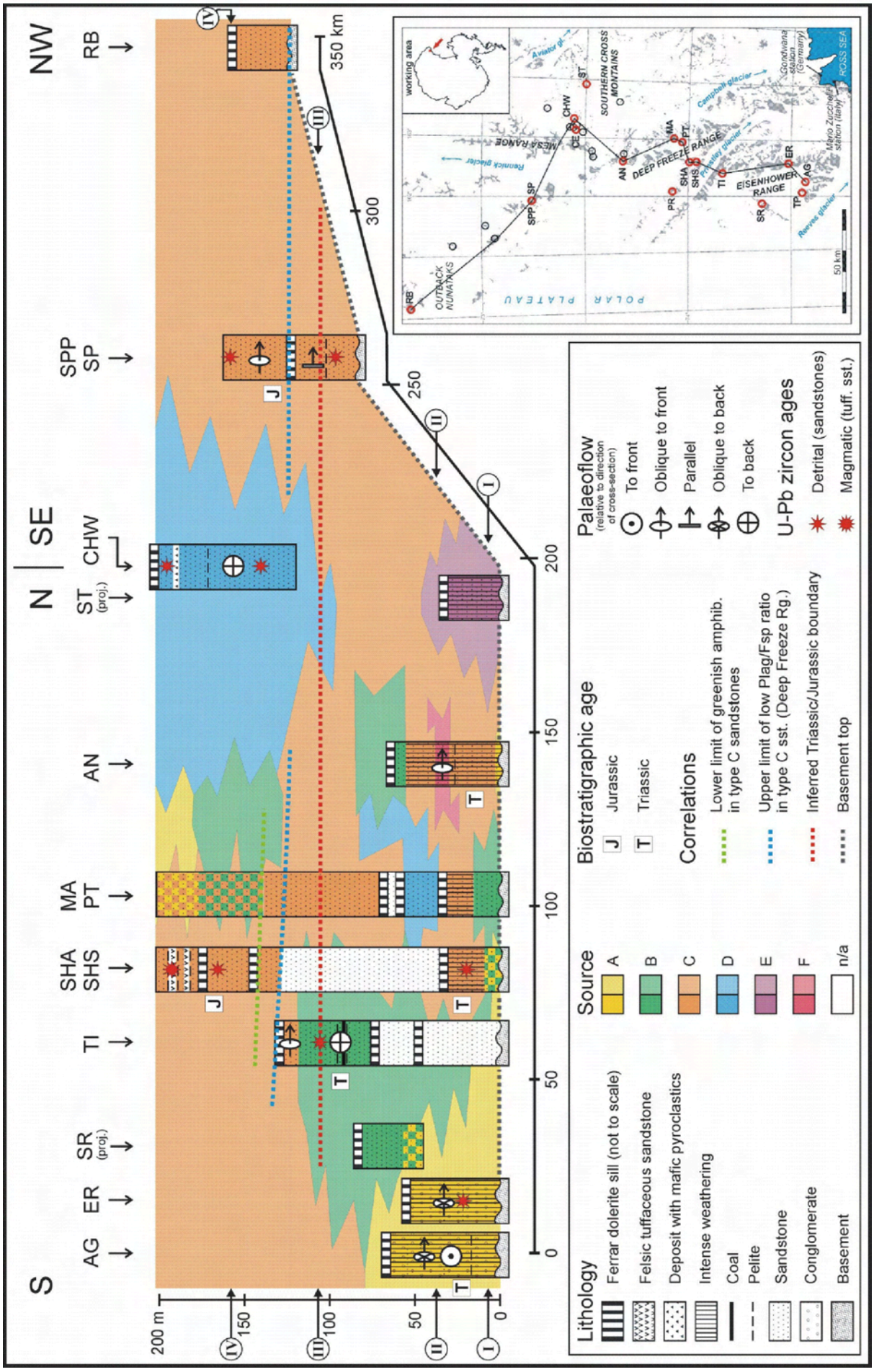
S
AG
ER
SR (proj.)
TI
SHA
SHS
MA
PT
AN
ST (proj.)
CHW
SPP
SP
RB
NW
N | SE
350 km
300
250
200
150
100
50
0
200 m
150
100
50
0
I
II
III
IV
J
T
working area
SOUTHERN CROSS MOUNTAINS
MESA RANGE
DEEP FREEZE RANGE
EISENHOWER RANGE
POLAR PLATEAU
OUTBACK NUNATAKS
Aviator gl.
Campbell glacier
Reeves glacier
Mario Zucchelli station (Italy)
Gondwana station (Germany)
ROSS SEA
50 km
Lithology
Ferrar dolerite sill (not to scale)
Felsic tuffaceous sandstone
Deposit with mafic pyroclastics
Intense weathering
Coal
Pelite
Sandstone
Conglomerate
Basement
Source
A
B
C
D
E
F
n/a
Biostratigraphic age
J Jurassic
T Triassic
Correlations
Lower limit of greenish amphib. in type C sandstones
Upper limit of low Plag/Fsp ratio in type C sst. (Deep Freeze Rg.)
Inferred Triassic/Jurassic boundary
Basement top
Palaeoflow
(relative to direction of cross-section)
To front
Oblique to front
Parallel
Oblique to back
To back
U-Pb zircon ages
Detrital (sandstones)
Magmatic (tuff. sst.)

### 3.7.2 Evolution of the NVL-sector of the Transantarctic Basin

Supplementary to the cross section shown in Fig. 3.75, in this section the evolution of the NVL sector of the Transantarctic Basin is shown in four palaeogeographic maps. The time assumed for the maps is only approximate, and reconstructed from detrital zircon ages and preliminary palynomorphs data (B. Bomfleur, pers. comm.). Each map contains a small insert, schematically visualizing the source area of type C sandstones, which is assumed to lie outside the NVL sector of the Transantarctic Basin (possibly in the CTM or in SVL).

For simplification, possible variations of the source areas themselves within the stratigraphic range of the SPF were not regarded, and the basement geology in the NVL sector was assumed to be more or less static during sedimentation of the SPF (thus for about 25 Ma). Small-scale, rapid, alternating petrographic variations were primarily regarded as the result of sedimentary processes, and not variations in the source areas (e.g. the variable fractions of the volcanic and metamorphic lithoclasts in section TI). However, for gradational, continual changes, source area changes were taken into account (e.g. the increasing volcanic material in type C sandstones).

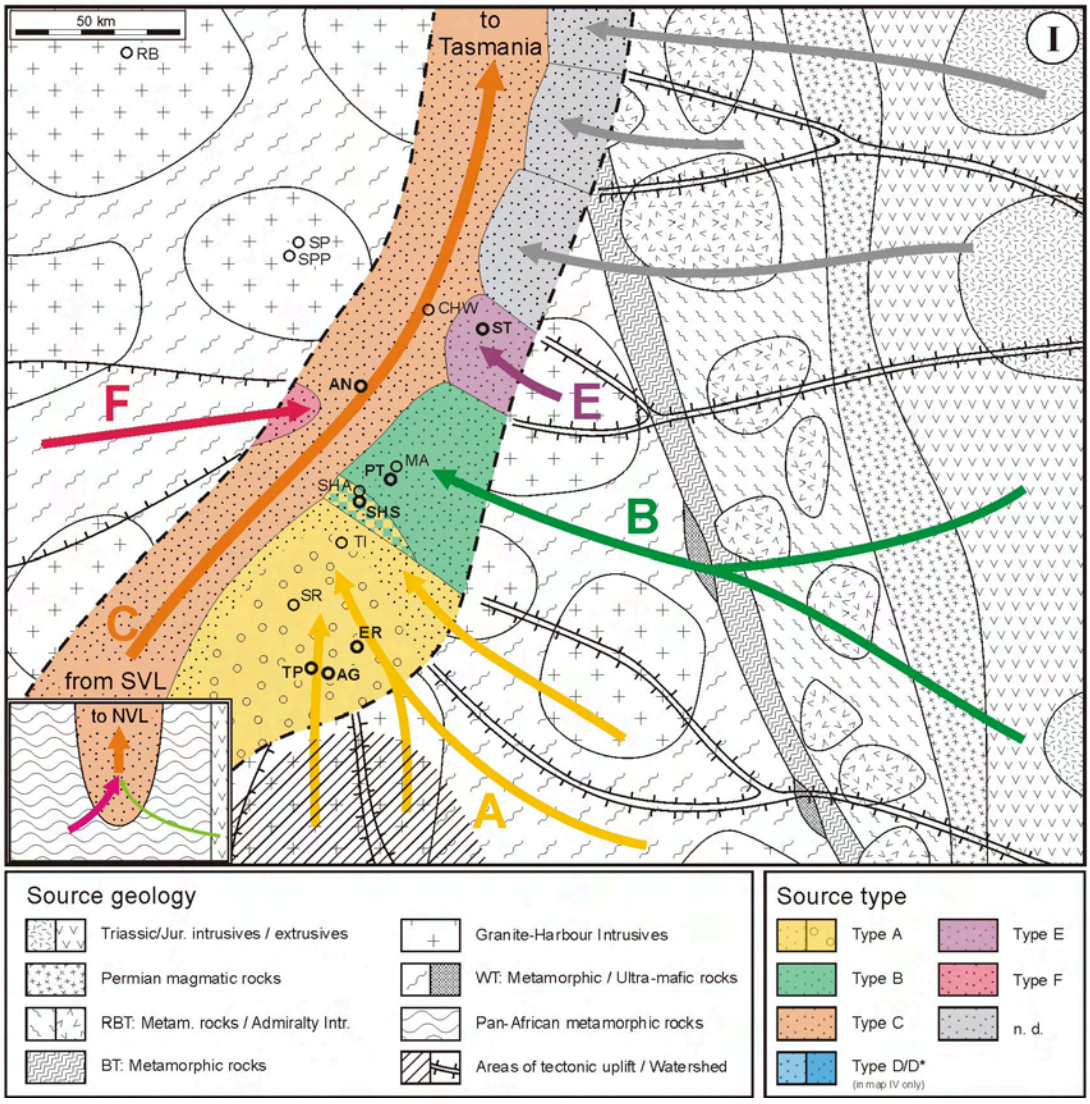


Fig. 3.76: Palaeogeographic reconstruction for the initial sedimentation of Beacon sediments in NVL (around 215 Ma). Sections covering the stratigraphic position of this time are bold, others are show for orientation. The scale is valid for the left part of the map only; positions and lithology of the Permian and Triassic/Jurassic arc are schematic only. The insert maps (lower left) in this and the following figures schematically show the relative fractions of the type C source at this time, as given by petrography or zircon age spectra.

As sedimentation starts in NVL, the axial flow (type C, as found in section AN) is dominated by detritus of Pan-African metamorphic rocks, and the input from the arc is very small. In relation, the radial contributions to the basin (especially types A and B) were large. Generally, contribution to the basin was stronger from the eastern (arc) side, and smaller from the western (continental) side, from which only type F sandstones have been identified. According to this observation, the axial flow was most likely not following the centre of the basin, but was located further to the western, continental side – at least during times of high material input from local sources.

The conglomerates in the Eisenhower Range (type A, sections TP, AG, ER, and possibly below TI) imply a proximal, uplifted region to the south. Type B sandstones form the basal units in section PT. In the nearly section SHS, a mixture of type B sandstones with (minor) type A sandstones are found. Type D and F sandstones have not been found at that stratigraphic level.

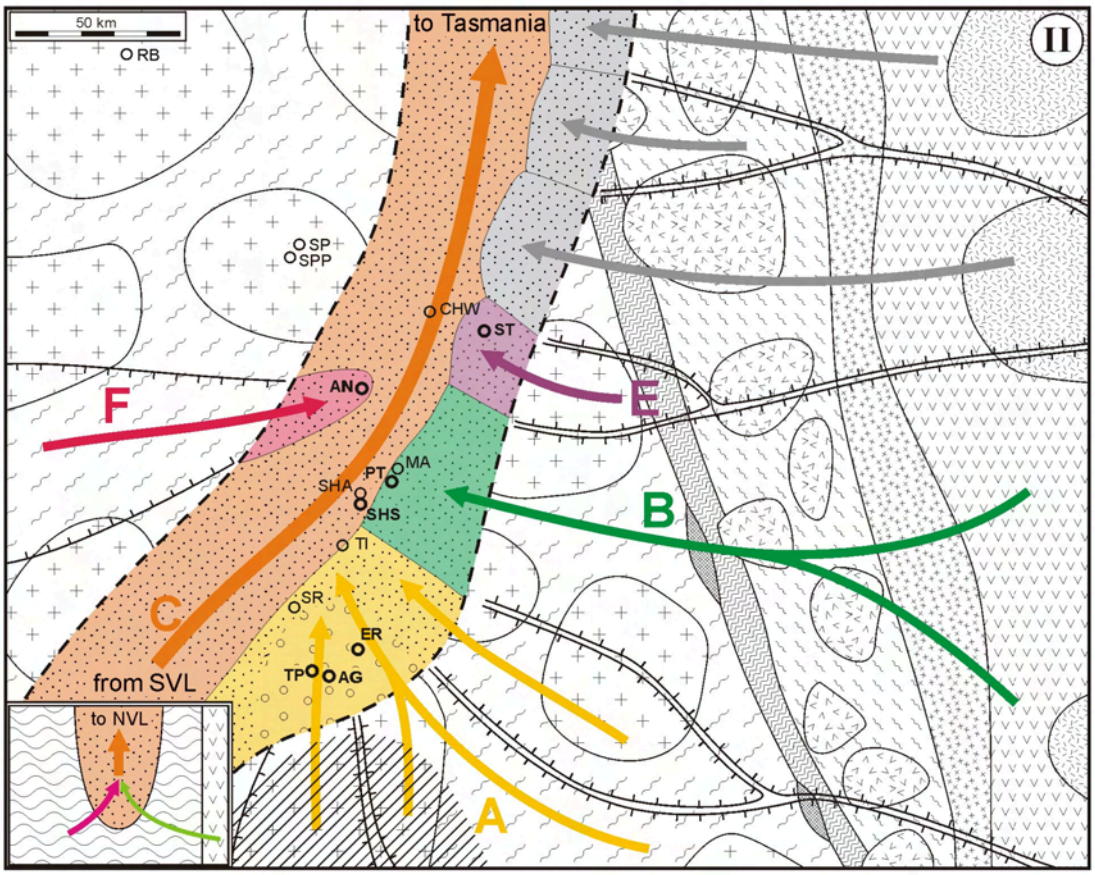


Fig. 3.77: Palaeogeographic reconstruction for the time around 210 Ma. For explanations and legend see Fig. 3.76.

At around 210 Ma, the range of the radial flows (type A and B) has become smaller, and the axial flow shifted to the east, now covering section SHS. Both the processes may be interrelated and may have triggered each other. The advance of type F sandstones from the west may also provide a possible explanation for a local east-ward shift of the axial flow.

In type C sandstones, arc derived material has become slightly more frequent, but is still minor, as shown by the zircon age spectra of sample SHS03. In the southern Eisenhower Range, conglomerates are continually deposited, but their range is smaller. The influence of the proximal source south of the Eisenhower Range is about to end, possibly because the tectonic uplift has stopped.

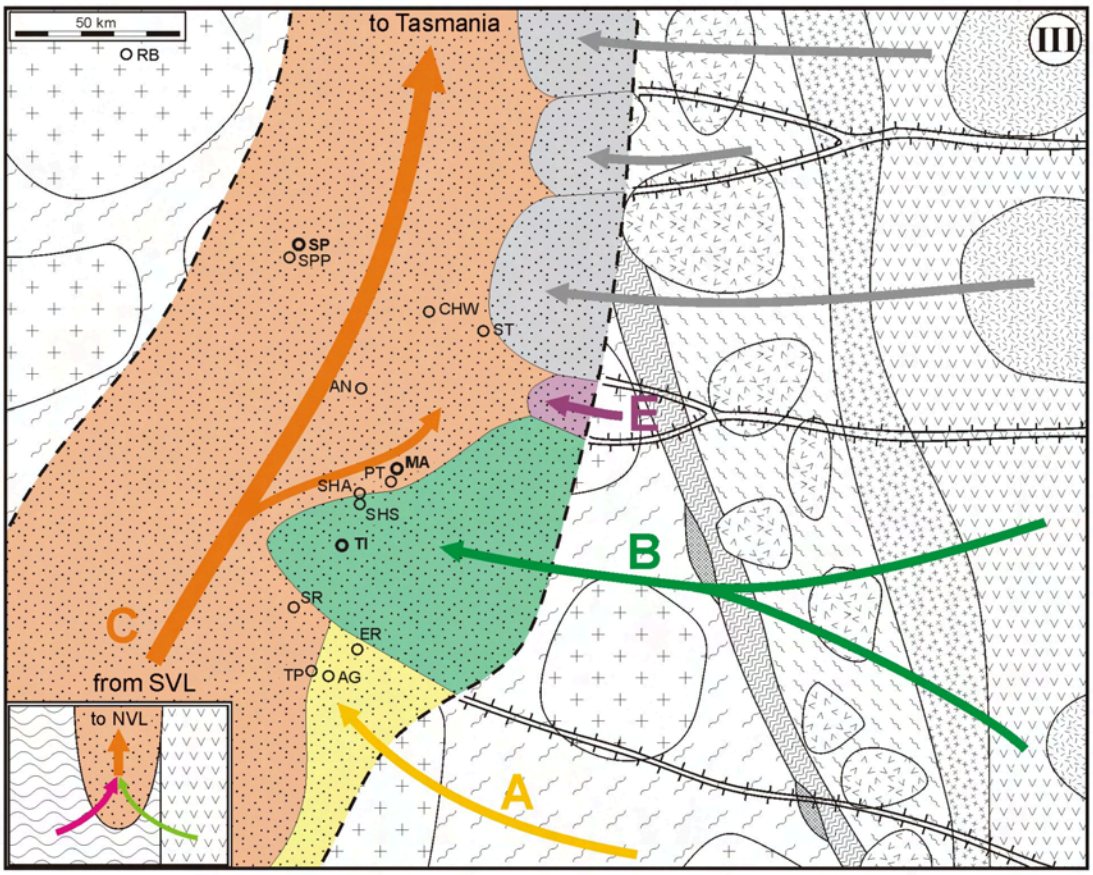


Fig. 3.78: Palaeogeographic reconstruction for the time around 200 Ma around the Triassic/Jurassic boundary. For explanations and legend see Fig. 3.76.

Approximately at the Triassic/Jurassic boundary, at around 200 Ma, the basin has enlarged considerably to the west, and sedimentation started in section SP. The quantity of the axial flow (sandstones of type C) has increased, in parallel with the abundance of arc derived material, as indicated by zircon age spectra of sample SP08 and the frequency of volcanic lithoclasts and plagioclases. No indications for a radial flow from the western (continental) side of the basin were found for this time, as present with type F sandstones earlier. In the east, a contribution of radial flows were found only in section TI (type B, see also Fig. 3.78). Similarly, this is interpreted as enlargement of the basin to the east. Possibly, the enlargement of the basin coincides with the end of deposition of conglomerates in the southern Eisenhower Range (as drawn in Fig. 3.78). However, sediments to prove this assumption are not exposed, and the age of the youngest conglomerates is not well defined.

At around 190 Ma, the basin has further enlarged to the western (continental) side, and sedimentation in section RB started (Fig. 3.79). The axial flow now covers large parts of the basin, possibly caused by the again higher fraction of arc derived material in sandstone type C. The increasing plagioclase : feldspar ratio and the greenish brown amphiboles in this sandstone type indicate erosion of large volumes of continental calc-alkaline rocks of basaltic to andesitic composition, most likely originating from the active magmatic arc. By comparison with the age distribution of arc-derived zircons, effusion of these rocks can be determined to be younger than about 195 Ma.

A northward material transport has been assumed for type C despite otherwise directed palaeoflow measurements in some of the Outback Nunatak sections (Collinson et al. 1986; Schöner et al. in review) , as the number of measurements is small and limited to few stratigraphic horizons.

Detritus of the Permian magmatic arc also contribute to type C, as shown by detrital zircons from that time in sample SHA07 and SPP36. However, as their proportion is very small, the area of the Permian arc is not shown in the insert map on the lower left of Fig. 3.79.

Radial flows of type A and B have not been found at this time within the working area, but the composition of the higher section MA indicates a mixture of type C material with type A and type B (see Fig. 3.75), thus both contributions may be still active. Alternatively, erosion of previously deposited material may also be an explanation, but petrographic indicators (e.g. heavy mineral enrichment) argue against this scenario.

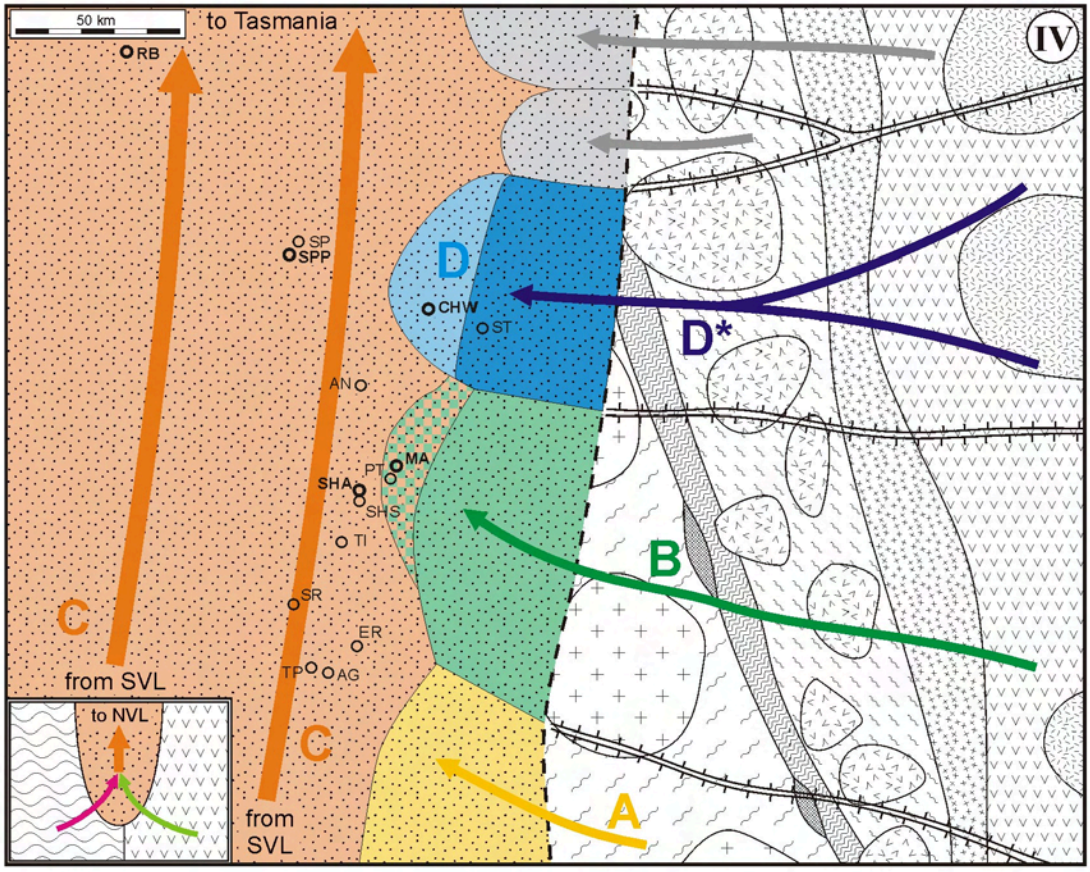


Fig. 3.79: Palaeogeographic reconstruction for the time around 190 Ma, at which the first tuffaceous layers were deposited. For explanations and legend see Fig. 3.76. The dark blue coloured D* sediments indicate the predicted, arc-derived sediments which have been mixed with type C material. The exact position and extend of these sediments is uncertain.

In contrast to the previous maps, at the time shown in Fig. 3.79, type D sandstones are present. They are indicated as radial flow from the arc side to account for westward palaeoflow directions (Schöner et al. in review). However, the heavy mineral assemblage of this sandstone type indicates a small contribution of type C material. Thus, a mixing with axially transported material must have taken place, either by lateral interfingering of both flows, or possibly by erosion of previously deposited type C material. The regularity of mixing throughout the entire CHW-section is difficult to explain with both models. However, as for the upper section MA, for the latter no indication was found (e.g. heavy mineral enrichment), thus a mixing of axially transported type C material with a radial flow is assumed. The arc-derived fraction of type D is indicated as D* in Fig. 3.79.

### 3.7.3 Geometry and setting of the NVL-sector of the Transantarctic Basin

According to the palaeogeographic situation of the Transantarctic Basin located in between the East Antarctic continental interior as part of Gondwana and the magmatic arc along the Gondwana plate margin, a roughly N-S oriented, elongated to belt shape of the basin is widely assumed (Collinson et al. 1994). The outcrops in NVL analysed in this study thus represent only a small sector of the entire basin. Due to distribution and palaeoflow directions of the sandstone types an axial transport system, represented by sandstones of type C, with more or less northward palaeoflow direction, can be distinguished from local inputs, oriented roughly perpendicular to the basin axis (e.g. type B, westward flow). The axial flow may have originated in the CTM, or in SVL, and possibly continued further on towards Tasmania. Besides arc derived volcaniclastic material, the local inputs to the basin indicate different sources within the Ross Orogen, which thus were not covered by sediments but subject to erosion at this time. Particularly the composition of type B sandstones implies a location of the basin margin in the NVL sector less than about 100 km offshore today's coastline. Although representing an early stage of basin evolution in NVL, type A and type E sandstones imply a basin margin even closer as they originate most likely from source rocks within the Wilson terrane (< 50 km).

According to the stratigraphic range of the Beacon sediments in the different outcrops, a gradual enlargement of the basin was proved, at least towards the continental (Gondwana) side (west). Besides the stratigraphic data from palynomorphs (B. Bomfleur 2009, pers. comm.), also petrography (plagioclase : feldspar ratio), and U-Pb ages of detrital zircons, yielding a maximum age of the samples, point towards a younger start of sedimentation in the (north-)western outcrops (Outback Nunatak sections) relatively to the sections in the Deep Freeze Range and Eisenhower Range. The difference in sedimentary thickness between the sections in the Deep Freeze Range (SHS, SHA, PT, MA) and the westernmost section RB is about 100 m, at a (projected) east-west extend of about 80 km. This results in an original dip angle of the sedimentary base (sub-Beacon unconformity) of about 0.1°. Extrapolation of this value beyond the westernmost section RB results in a basin margin about 40 km further westwards. In combination with the presumed distance to the eastern (arc) margin of the basin, a total width of the Transantarctic Basin in the NVL sector of maximal 250 km can be assumed. Thus, today's outcrops in the Eisenhower Range and in the Deep Freeze Range are located approximately along the former axis of the basin.

While therefore the western, 'continental' side of the basin appears to be characterized by onlapping of Beacon sediments and overstepping of the basement, the geometry of the eastern (arc) side is unclear, because this side is not exposed. Here, basically two different shapes are possible, an asymmetric and a symmetric one. Both cases are discussed in detail below.

Because the overstepping described above has been observed for the Transantarctic Basin in total, and thus on a much larger scale, it has been interpreted as a (retro-arc) foreland basin, and a wedge-shaped geometry in cross section has been suggested (see Sect. 1). Following this interpretation, the thickness of sediments (and possibly also of the Ferrar magmatites), must increase towards the magmatic arc, thus leading to an asymmetric basin shape in cross-section. Opposite to the western (distal) basin margin, the eastern margin in this scenario is bound by thrusts. As detritus from the Ross Orogen has been identified in some sandstone types, a retro-arc thrusting, affecting not only the magmatic arc but also parts of the crystalline basement of the Ross Orogen is necessary. However, there is no evidence for a thrusting phase since the Ross orogeny in NVL, nor in the Ross Sea, despite several thousand kilometres of seismic lines here. In addition, the original dip angle of the sedimentary base of about 0.1° is very small for a foreland basin, although this depends strongly on crust thickness

and rheology (Miall 1995). For comparison, in the North Alpine Molasse Basin as a typical collisional foreland basin, the dip angle of the base of the Tertiary, approximately representing the base of Molasse sedimentation, is about 2° in distal and 4° in proximal parts of the basin (Lemcke 1988; compare Miall 1995).

For the SPF, a sedimentation rate of about 5-15 m/Ma has been determined. Although this value is only a first approximation, it is definitely far less than the sedimentation rates common in foreland basins, which are usually one to two orders of magnitude higher (Einsele 2000; Flemings and Jordan 1990; Jordan 1995). In addition, foreland basins are characterized by an upwards coarsening of sediments, reflecting tectonic prograding of source areas by active thrusting. Although this is furthermore dependent on the axial material transport rates, in the SPF, however, well exposed and analysed sections (SHA) rather show a fining-upward trend. In section TI, the local basin input of type B sandstones is overlain by longitudinally transported material of type C, thus a retrogradation is present. Also, no indication for major sedimentary recycling ('cannibalism') has been found in this study (e.g. heavy mineral enrichment). Single of these arguments may not be sufficient to reject the hypothesis of the NVL part of the Transantarctic Basin being a (retro-arc) foreland basin, either because proximal basin parts are missing, or because of possible regional individualities of the Transantarctic Basin of any kind. However, in combination, these arguments make clear that the Transantarctic Basin in NVL cannot be described as a foreland basin.

The second possible scenario is a basin margin more or less symmetric to the western (craton) side, and thus a gradual decrease of sedimentary thickness towards the east. In this setup, thrusting is absent, thus no coarsening-upwards of sediments, progradation of radial sources, or sedimentary recycling is necessary. The dip angle of the sedimentary base on the eastern margin may be similar to the western side.

In this case, the basin forming subsidence mechanisms are unclear. From the basin position alone, a 'back-arc' environment seems likely, though it was certainly not behind an island arc as is commonly implied by this term. Subsidence rates, tectonics, and basin history in the NVL part of the Transantarctic Basin may rather be compared to an intra-plate (epicratonic) setting (Ingersoll and Busby 1995). Early sub-crustal processes finally leading to production of Ferrar magmatites may provide possible explanations for the formation and the evolution of the basin in NVL.

### 3.7.4 Implications for the Transantarctic Basin

While the Transantarctic Basin shows characteristics of a (retro-arc-)foreland basin in the Ellsworth-Whitmore-Mountains (EWM) and possibly in the CTM (see Sect. 1), this work has shown that its setting is rather epicratonic in NVL (actually 'pericratonic', as it is not located on a craton). To combine the different basin settings along the active Gondwana margin, a new model is proposed (Fig. 3.80), in which both settings are present side by side. Alternatively, the foreland setting was only a stage during basin evolution, and the setting may also have changed in the Late Triassic for the entire basin to an epicratonic setting.

For a co-existence of different tectonic settings at the same time, several reasons are possible, which all point towards large-scale tectonic differences along the active plate margin. These are the subduction angle (dip), the azimutal angle of plate convergence and subduction, the shape of the two plates, and the degree of coupling of the two plates.

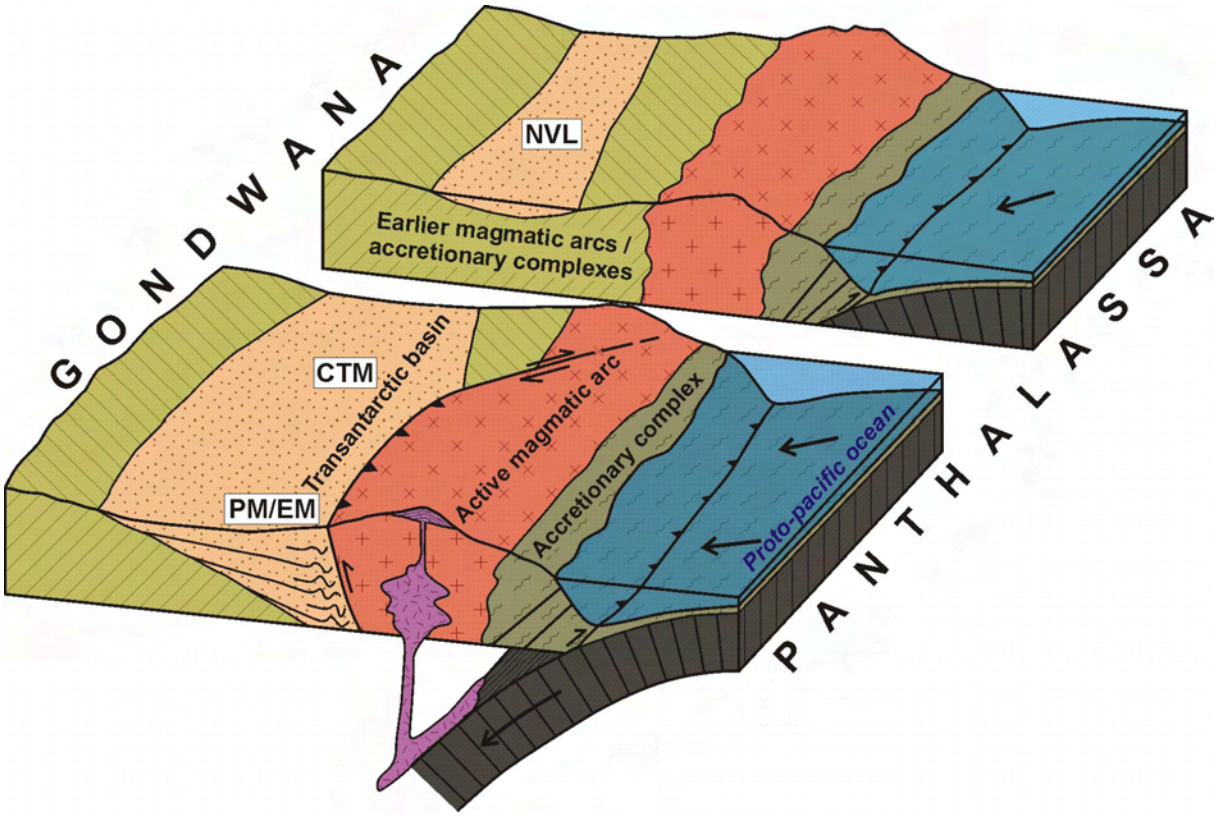


Fig. 3.80: Sketch of the proposed model of the Transantarctic Basin (not to scale) at the active Gondwana margin during deposition of the SPF (Late Triassic/Early Jurassic). The (retro-arc) foreland setting in the Pensacola and Ellsworth mountains (PM/EM) and in the CTM is proposed by Collinson et al. (1994). For NVL, a different setting is deduced from the results of this work.

From the arguments listed, the difference in subduction angle may be the most intriguing one. The dip depends mainly on the rate of convergence and on the temperature of the subducted lithosphere. A flat plate subduction is inferred for the Cape Fold belt in South Africa, at least during times of its evolution (Lock 1980), and for the (palaeo-)neighbouring Pensacola and Ellsworth Mountains in Antarctica (Elliot 1975). A strong coupling of the subducted and the overriding lithosphere can be inferred for these areas.

From recent investigations on today's South American active continental margin, which may be a representative equivalent for the Gondwana active continental margin in the Mesozoic, the subduction angle is known to vary considerably along the plate boundary between about 15° and more than 40° (Zeil 1986). Here, smooth and gradual variations are also present as abrupt changes, which are interpreted to be caused by breaks in the subducted (oceanic) plate.

A low subduction angle in South America, South Africa, and the adjoining parts of Antarctica during the Late Permian and the Triassic/Early Jurassic may also be responsible for the relatively wide magmatic arc here, compared with Australia and the remaining part of Antarctica, where the magmatic arc was narrower. This observation allows the separation of a western part of the active continental margin with likely flat plate subduction and an adjacent foreland basin, from an eastern part with steeper subduction and an 'epicratonic' basin in a back-arc position (Fig. 3.81). An exact boundary cannot be drawn due to the many uncertainties. For the western part, a higher degree of coupling can be inferred, resulting in a fold and thrust belt, as described from the Ellsworth-Whitmore Mountains. In the eastern area, similar tectonic features are unlikely. However, this cannot be verified, as the proximal parts of the basin are missing here due to later ocean spreading.

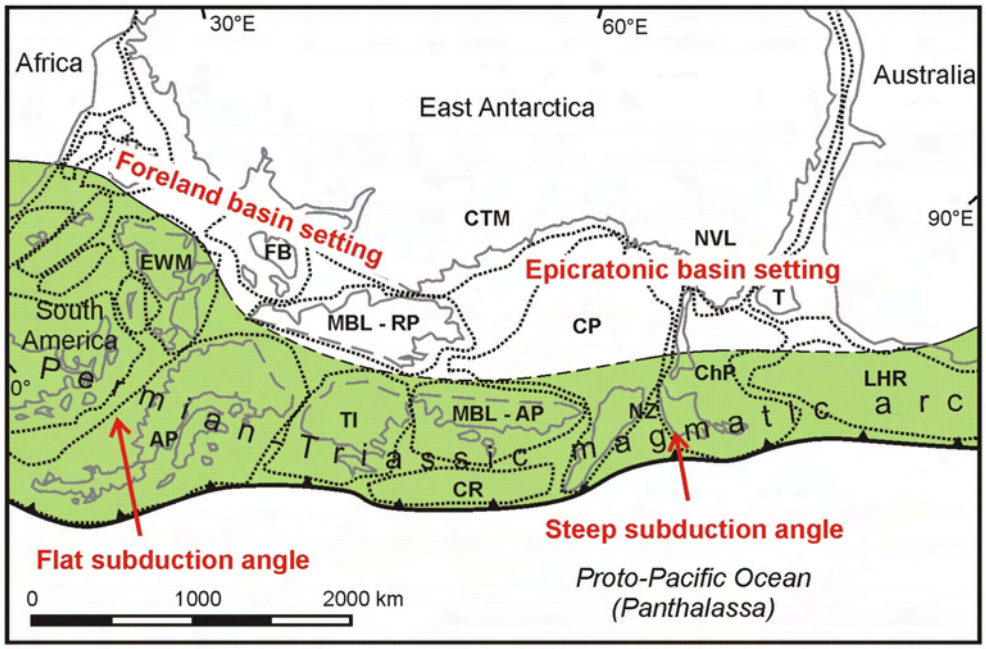


Fig. 3.81: Palaeogeographic reconstruction of the active plate-margin of Gondwana during the Late Triassic/Early Jurassic (Elliot and Fanning 2008; Veevers 2004; Willan 2003). The larger width of the magmatic arc in the African sector of Gondwana may point towards a flatter subduction angle compared to the NVL sector. Abbreviations: AP: Antarctic Peninsula; ChP: Challenger Plateau; CP: Campbell Plateau; CR: Chatham Rise; CTM: Central Transantarctic Mountains; EWM: Ellsworth-Whitmore Mountain Block; FB: Filchner Block; LHR: Lord Howe Rise; MBL-AP: Marie-Byrd-Land, Amundsen Province; MBL-RP: Marie-Byrd-and, Ross Province; NVL: North Victoria Land; NZ: New Zealand; T: Tasmania; TI-EC: Thurston Island Block.

# 4 Composition and provenance of the SHF

## 4.1 Introduction

The SHF was described during the GANOVEX IX 2005/06 as a more than 50 m thick homogeneous unit of reworked tuffs containing abundant silicic shards. It was proposed by Schöner et al. (2007) as a separate formation, between the SPF and the Ferrar Group. However, the tuffaceous rocks itself have been previously described (Musumeci et al. 2006). Lithologically similar deposits are known from the Hanson Formation in the CTM (Barrett 1991; Bryan et al. 2002; Elliot 1996), and from SVL, where they have been found as reworked clasts only, but not in situ (Bradshaw 1987).

The best outcrops in NVL have been found in the Mount Carson area (Mt. Carson East Ridge, CE) and in the Deep Freeze Range (Shafer Peak, SHC, Fig 4.1). Only the latter provides a complete, well exposed section and was therefore proposed as type locality (Schöner et al. 2007). From both localities, samples were chosen for investigation.

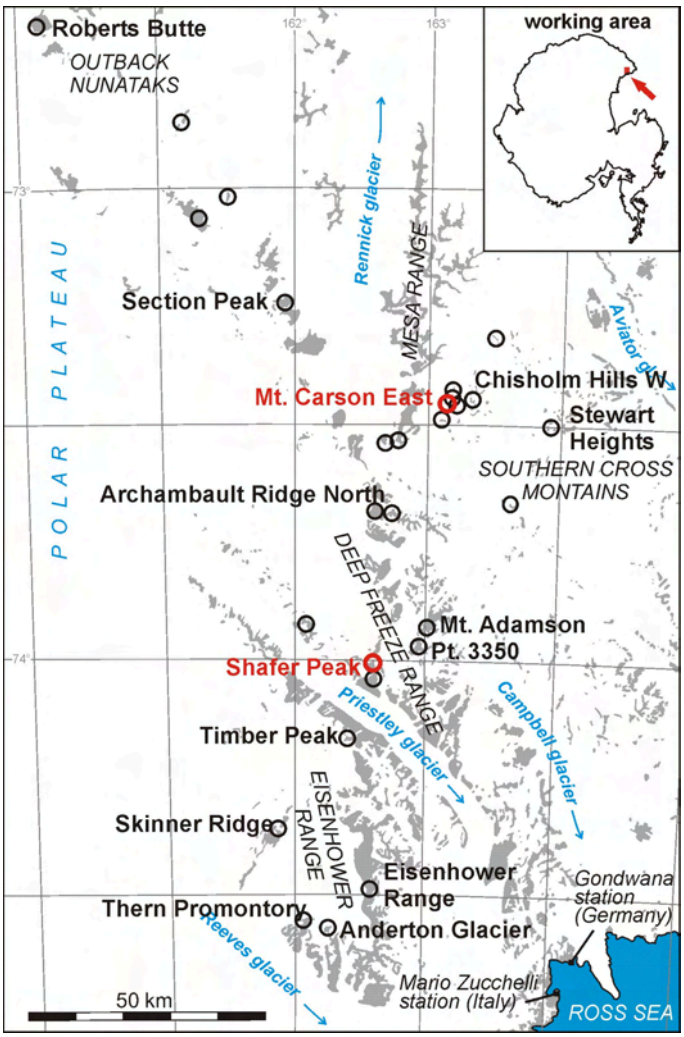


Fig. 4.1: Map of the working area showing the locality of outcrops visited during the GANOVEX IX in 2005/06. Outcrops of the SHF are marked in red.

In this section, the SHF is compared with similar deposits from the SPF. Here, the occurrence of whitish-grey, fine-grained tuffaceous sandstones is limited to the uppermost parts of section SHA. They are intercalated in a sandstones-mudstones suite (Fig. 4.2), and overlain by sediments containing mafic pyroclasts that were attributed to an Exposure Hill type event

(EHT, Viereck-Götte et al. 2007). The thickness of tuffaceous sandstone beds ranges from a few decimetres up to 2 m. In most cases, indications of fluvial reworking are present (e.g. ripple-cross lamination); clear fallout layers, however, could not be identified.

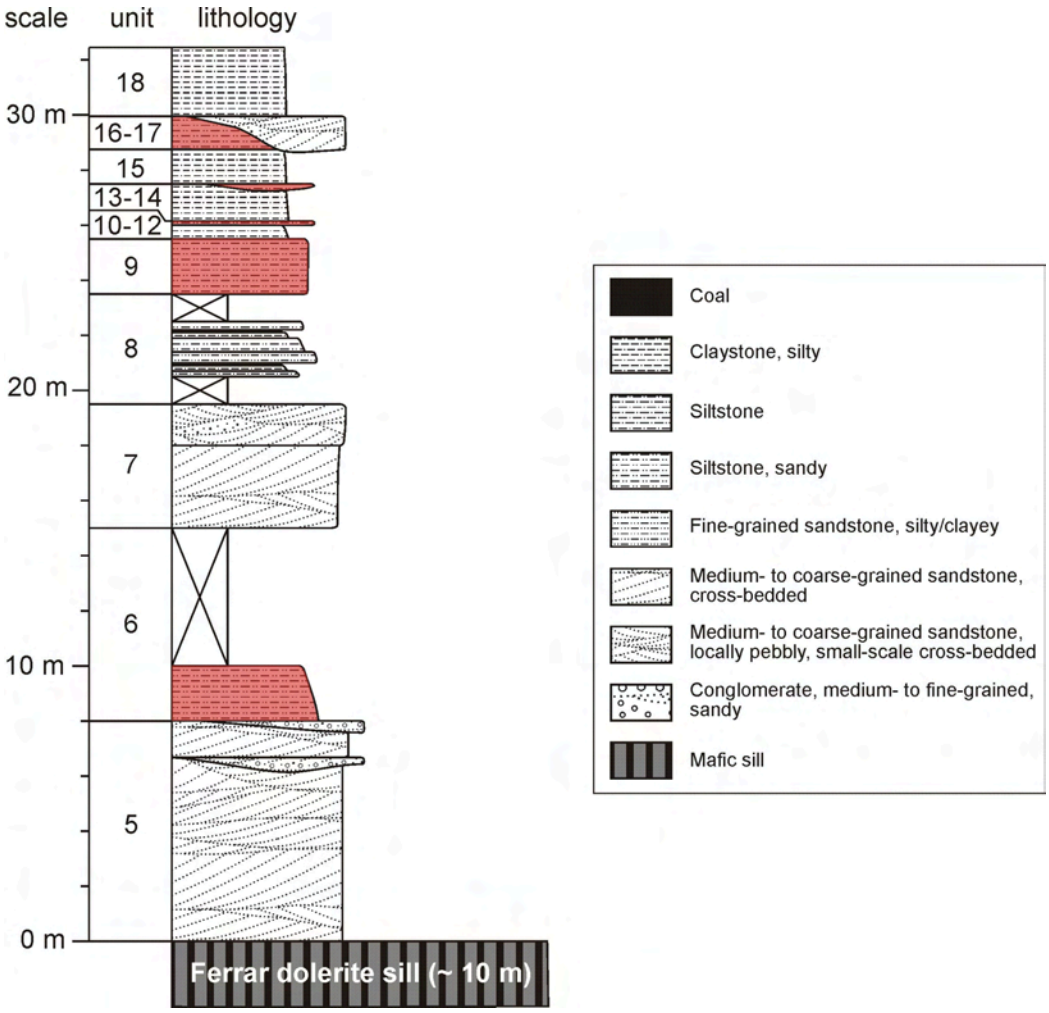


Fig. 4.2: Stratigraphic log of the upper part of section SHA, showing an intercalation of (mostly cross-laminated) sandstones and mudstones (by courtesy of R. Schöner and B. Bomfleur). Tuffaceous sandstones (units 6, 9, 12, 14, and 16) are marked in red. The uppermost shown unit 18 is directly overlain by sediments containing mafic pyroclasts that are attributed to an Exposure Hill type event.

## 4.2 Petrography

### 4.2.1 Texture, grain size

The SHF comprises about 53 m of greyish to light brownish tuffaceous sandstones in beds of about 0.5 to 2 m each with thin (mm-dm) clayish interbeds (Schöner et al. 2007). The average grain size of tuffaceous sandstones in the SHF usually varies between about 50 and 70 µm (coarse silt to fine sand) for section CE, which is similar to the tuffaceous sandstones in the SPF (section SHA). The tuffaceous sandstones in section SHC are slightly coarser grained (median diameter of about 60-80 µm). The sorting is generally good to very good. Medium to coarse grained sandstones (as known from the underlying SPF) are lacking. The coarsest sample (SHC25) is a fine-grained sandstone (median diameter of about 100 µm), however, it is not tuffaceous in origin but compositionally similar to type C sandstones from the uppermost SPF (see Sect. 3).

Ripple cross-lamination, climbing ripples, horizontal lamination and pelite intraclasts are the most obvious depositional features indicating fluvial reworking and rapid sedimentation from sediment-loaded rivers (Schöner et al. 2007). Traces of roots are present in some beds, but further evidence of long-lasting exposition is lacking. In many samples plant debris is present, consisting of cycadophytes and dipterid ferns, whereas *Dicroidium* is absent, thus indicating a Jurassic age (Bomfleur et al. 2007; Bomfleur et al. in review).

### 4.2.2 Methods

Besides optical microscopy (see Sect. 3.2 for details), cathodoluminescence microscopy was used for petrographic analysis. CL was performed at the laboratory of Prof. J. Götze at the Institut für Mineralogie of the Bergakademie Freiberg, using a hot-cathodoluminescence device (model HC1-LM). Polished thin-sections were carbon coated and studied under standard conditions at $p < 10^{-6}$ bar vacuum, acceleration voltage of 14 kV, and a current density of 10 µA/mm². CL images were recorded with a digital camera (KAPPA 961-1138 CF20 CXC).

### 4.2.3 Results

By optical microscopy, five tuffaceous sandstone units have been identified within the upper SPF (section SHA, Fig. 4.2). They were distinguished from epiclastic sandstones by the occurrence of vitric shards. The shards are altered to secondary zeolites (clinoptilolite/heulandite, see Sect. 5). However, they still show their original platy or cuspate shape that is interpreted as bubble-wall or bubble-junction, respectively, of a rapidly chilled and fragmented magma (Fisher and Schmincke 1984). In few cases, the fragmentation was not complete. Such shards show a structure of glass walls enclosing a roundish cavity, thus resembling pumice fragments (Fig. 4.3). Besides shards, the tuffaceous layers contain monomineral grains (mostly quartz, feldspar, or rarely mica). Some samples additionally contain few lithic fragments, or are rich in plant debris.

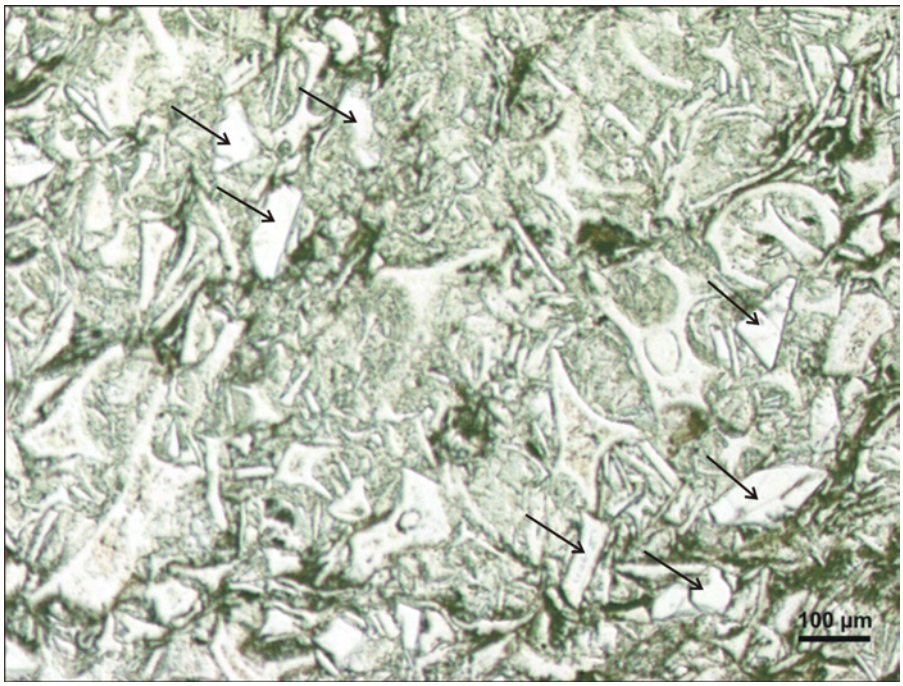


Fig. 4.3: Thin section image of the tuffaceous sandstone SHA12 from the SPF showing numerous vitric shards. Some minerals or mineral fragments (quartz or feldspar) are marked by arrows. Right to the image centre, there is an example of a not completely fragmented, pumice-like shard.

Contrary to the whitish-grey tuffaceous sandstones in the SPF, samples from the SHF generally appear more brownish-grey in optical microscopy. Also, shards within the SHF are mostly roundish or platy. As in the SPF, the shards are secondarily altered to clinoptilolite/heulandite (XRD-analysis, Sect. 5).

Besides the characteristic silicic glass shards, the tuffaceous sandstones contain quartz and feldspar as most abundant crystalline constituents. Accessories are white and dark mica, zircon, opaque heavy minerals, and, rarely, lithic fragments. Apart from biotite, mafic minerals have not been observed within the tuffaceous sandstones. However, the epiclastic sandstone sample SHC25 contains amphiboles (see Sect. 4.4).

In general, quartz and feldspar are mostly subangular to angular. Quartz clasts with corrosion and resorption features are rare, but present. Crystals are more abundant in the tuffaceous sandstones of the SHF compared with those of the SPF. This becomes evident in the classification diagram in Fig. 4.4, according to which some of the tuffaceous sandstones of the SHF can be classified as crystal tuffs, whereas the SPF samples (section SHA) are vitric tuffs.

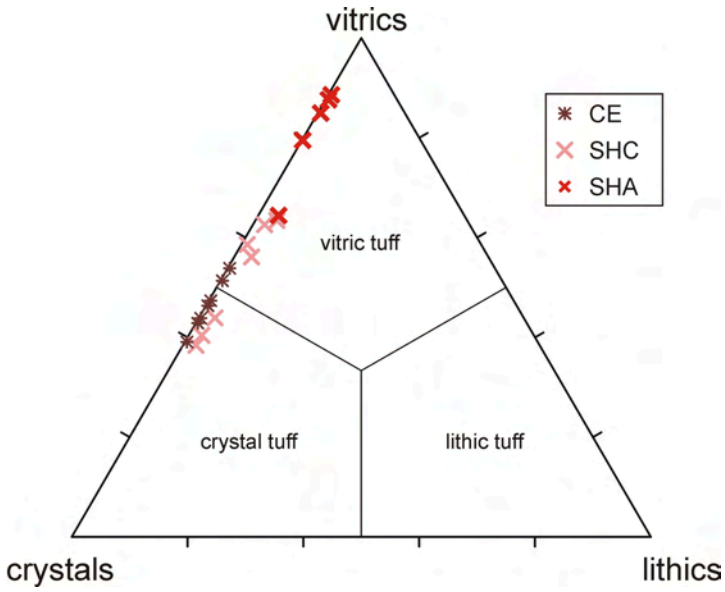


Fig. 4.4: Classification of tuffaceous sandstones of SPF and SHF according to clast types (Füchtbauer 1988). In contrast to most of the samples from SPF (section SHA), crystals are more frequent in the SHF (sections SHC, CE). The epiclastic sandstone sample SHC25 would lie on the base line, close to the crystal-side of the diagram.

### 4.2.4 Cathodoluminescence microscopy

CL was performed on two samples from the SPF, containing shards and minerals or mineral fragments. In SHA06, K-feldspar is the most abundant mineral; plagioclase and quartz are rare (Fig. 4.5, left panel). Besides shards, in sample SHA12 plagioclase is abundant, and quartz and K-feldspar are rare (Fig. 4.5, right panel).

Uniform CL-colours of plagioclases in sample SHA12 indicate a uniform chemical composition, and thus a common origin of the crystals. The plagioclase most likely originates from the same magma as the shards. A juvenile origin for sample SHA12 is therefore reasonable, with epiclastic material being virtually absent.

In contrast, sample SHA06 comprises more K-feldspar than plagioclase. The variable colours of K-feldspar in this sample are most likely related to different chemical compositions. This points towards different sources, with an epiclastic origin being the most obvious explanation. However, different CL colours can also be the result of variable growth conditions within the same magma.

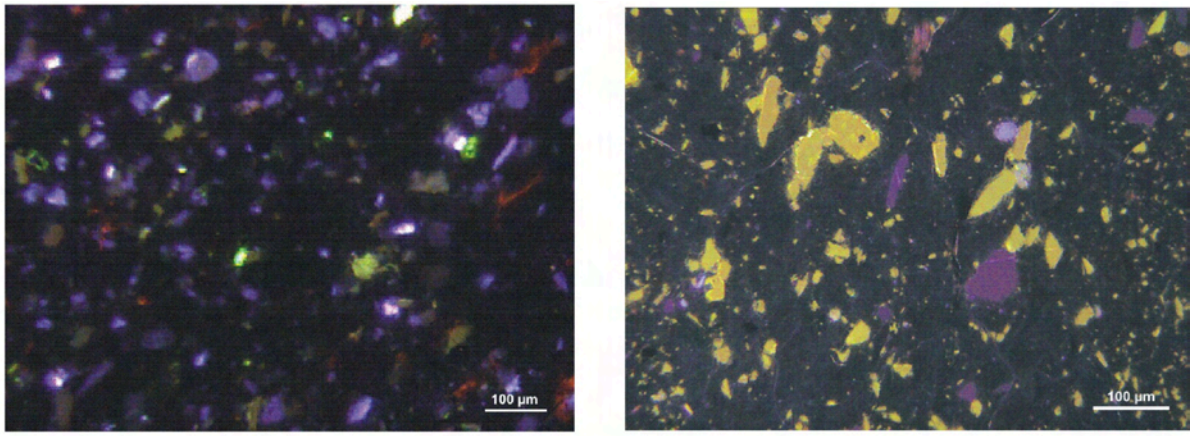


Fig. 4.5: CL images of two tuffaceous sandstones from the SPF. Secondary zeolites, replacing vitric shards, are non-luminescent. In sample SHA06 (left panel), K-feldspar with variable violet luminescence colours is the dominant mineral. Plagioclase (greenish colours) is rare. In sample SHA12 (right panel), plagioclase of uniform yellow-greenish luminescence colour is the most abundant mineral besides quartz (dark violet), and K-feldspar (light violet).

### 4.2.5 Summary and interpretation

In general, a juvenile magmatic origin of the vitric shards, and a non-juvenile origin of lithic fragments stands to reason. The crystals, however, may be xenoliths or juvenile in origin, or they may be mixed in during sedimentary reworking as detrital, epiclastic material. In sample SHA12, however, the uniform CL colours of the most abundant plagioclase indicate a common source, which can best be explained by formation within the same magma. As conclusion, no epiclastic material has been mixed by the sedimentary processed following the fallout of the tephra in this particular sample.

Contrary, feldspar grains in sample SHA06 exhibit different CL-colours, and the presence of non-juvenile material is likely. This epiclastic portion may have been mixed in during fluvial reworking, or, possibly, already during the (explosive) eruption event (e.g. due to vent erosion).

For all other samples, the estimation of a possible epiclastic portion by petrography alone is difficult. However, the higher amount of crystals and the less angular shape of shards within tuffaceous sandstones from the SHF relative to those from the SPF may indicate longer fluvial transport. Therefore, a higher portion of epiclastic material seems probable, though it cannot be stated from petrographic results.

## 4.3 Geochemistry

### 4.3.1 Introduction

Due to the relatively similar petrographic composition (quartz, feldspar, vitric shards, few lithoclasts), and the small grain size of the tuffaceous sandstones, focus was set in this study on their whole-rock geochemical composition. An important goal was the determination of the chemical composition of the original magma.

For fine grained rocks, analysis of whole-rock geochemistry may provide useful information about their petrogenesis or provenance (e.g. Saleemi and Ahmed 2000). This method is generally an important tool to describe and classify magmatic rocks or volcaniclastic sediments (e.g. Spears et al. 1999).

Whole-rock geochemical analyses were carried out with a sequential wavelength dispersive spectrometer (WDXRF) Philips PW 2400 (for details see Sect. 3.3).

### 4.3.2 Results

In the IUGS classification diagram (Fig. 4.6), the SHF samples plot within the rhyolite field. In contrast, the tuffaceous sandstones from the SPF are rhyodacitic in composition. As the $Na_2O$-content is higher than the $K_2O$ content, it appears to be soda-rhyodacitic. For the SHF-samples, this is generally not the case. However, the content and the ratio of alkalis may be subject to change during diagenesis (e.g. by zeolitisation of shards, albitization of plagioclases).

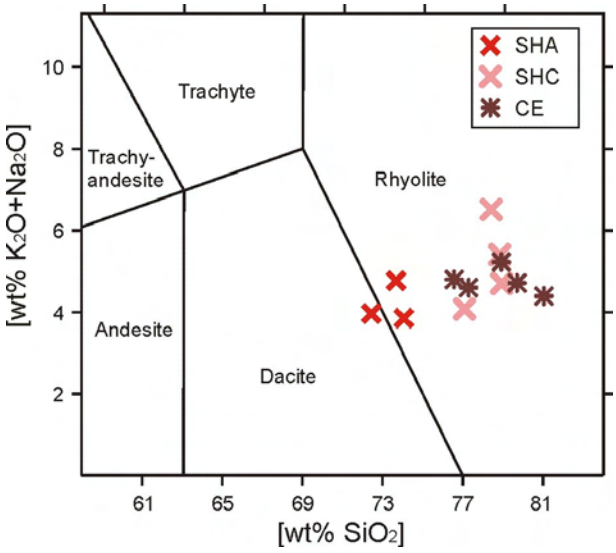


Fig. 4.6: Detail of the IUGS classification diagram for volcanic rocks (Le Maitre 1984; 2002). The tuffaceous sandstones of the SHF (sections SHC and CE) show a higher $SiO_2$ content and a (on average) slightly higher $K_2O+Na_2O$ content compared with the tuffaceous sandstones of the SPF (section SHA).

In contrast to the IUGS diagram, the classification diagram of Winchester and Floyd (1977) uses ratios of immobile trace elements (Fig. 4.7), which are less likely to be affected by diagenetic alterations. In this diagram, the samples from both formations can be classified as rhyolites. The samples from the SPF can clearly be distinguished from those of the SHF.

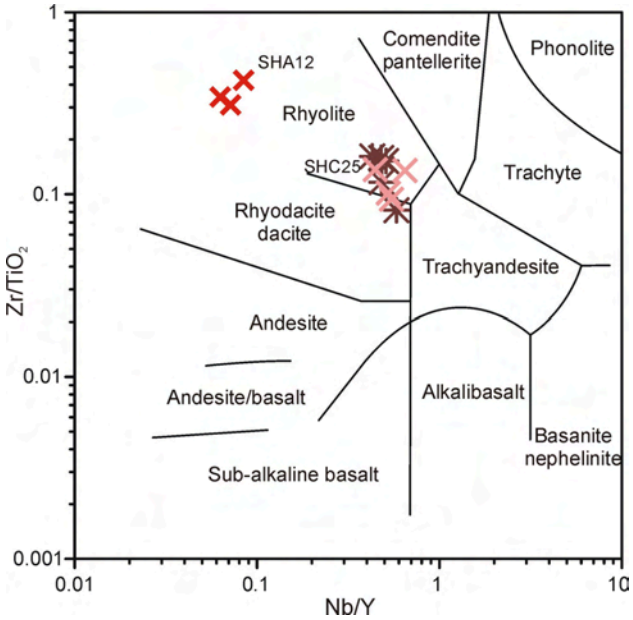


Fig. 4.7: The tuffaceous sandstones in the $Zr/TiO_2$ versus Nb/Y classification diagram after Winchester and Floyd (1977). Legend as in Fig. 4.6. The samples of the SPF can be distinguished from those of the SHF.

According to the diagrams in Fig. 4.8 (after Pearce et al. 1984, 1996) using the trace elements Y, Nb, and Rb, a volcanic arc source is most likely for the juvenile sample SHA12. All other samples, including the sandstone sample SHC25, also plot in the same field.

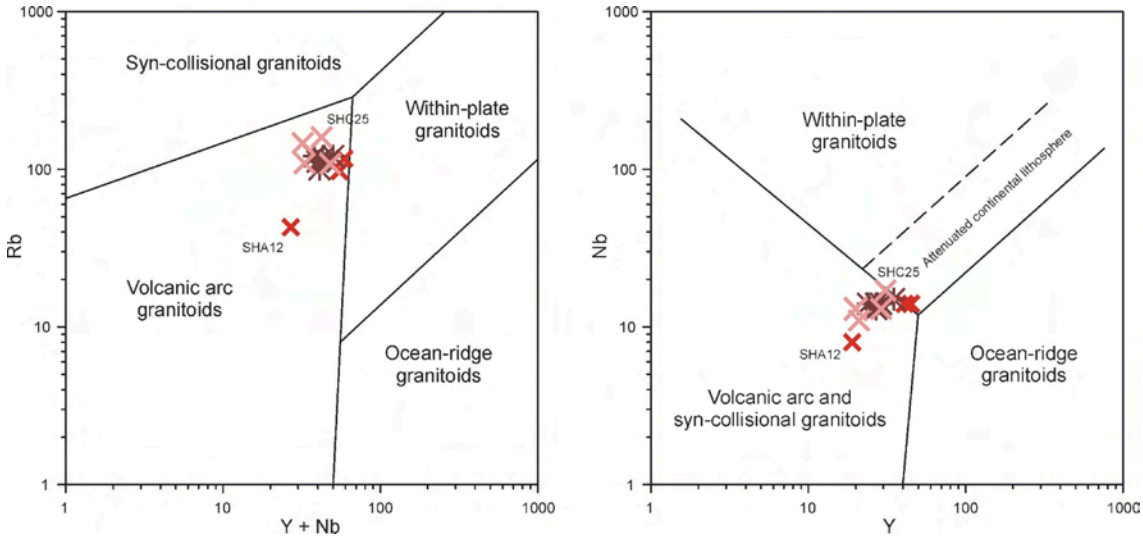


Fig. 4.8 Rb versus Y+Nb (left panel) and Nb versus Y (right panel) discrimination diagrams (Pearce 1996; Pearce et al. 1984). Legend as in Fig. 4.6.

The A-CN-K diagram can be used to determine provenance by reversion of the weathering trend (see Sect. 3.3 for details). However, the composition of tuffaceous sandstones follows a trend that can not be explained by weathering (Fig. 4.9). The bulk of samples fall within an interval bounded by sample SHA12, representing juvenile material, and sample SHC25, which is lacking shards and interpreted as epiclastic sandstone. Thus, all samples may be product of mixing these two sandstone types. Magmatic processes (e.g. fractionation) also may provide a possible explanation; however, the trend does not follow the stratigraphy. The samples from the SHA are lying closer to the juvenile source defined by sample SHA12.

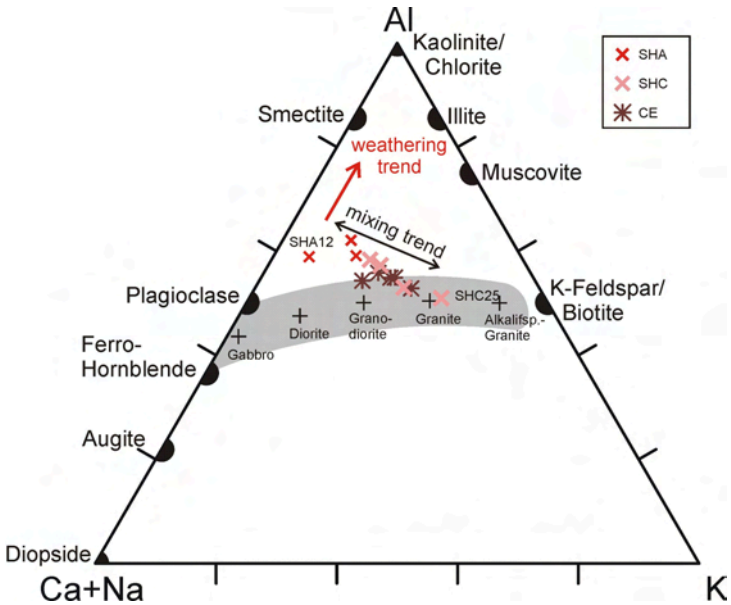


Fig. 4.9: A-CN-K diagram (after Nesbitt and Young 1984; 1989) indicating that all samples may be derived from a mixing of juvenile magmatic material as comprised in sample SHA12 (left) with epiclastic material as found in sample SHC25 (right). The SPF samples (section SHA) comprise less epiclastic material than the SHF samples (sections SHC and CE), as is also indicated by petrography. The grey shaded area marks the typical compositional range of upper continental crust.

A reversion of the weathering trend seems to indicate a dioritic / andesitic magma for sample SHA12. However, the $SiO_2$-content as an important factor in classification of magmatic rocks is not considered in this diagram. Therefore, the (soda-)rhyodacitic composition derived from the IUGS-diagram above seems to be more reliable. For the epiclastic source of sandstone SHC25 an on average granitic composition is indicated.

As already observed in thin-section, the weathering intensity of the samples from the SHF and SPF is low (Fig. 4.10) and similar to those of the bulk of the sandstones from the SPF (Sect. 3). No regular differences in weathering are obvious between samples from the two formations. However, as in Fig. 4.9, the bulk of samples is lying in between the juvenile sample SHA12 and the epiclastic sandstone SHC25, again indicating mixing of juvenile magmatic with epiclastic material.

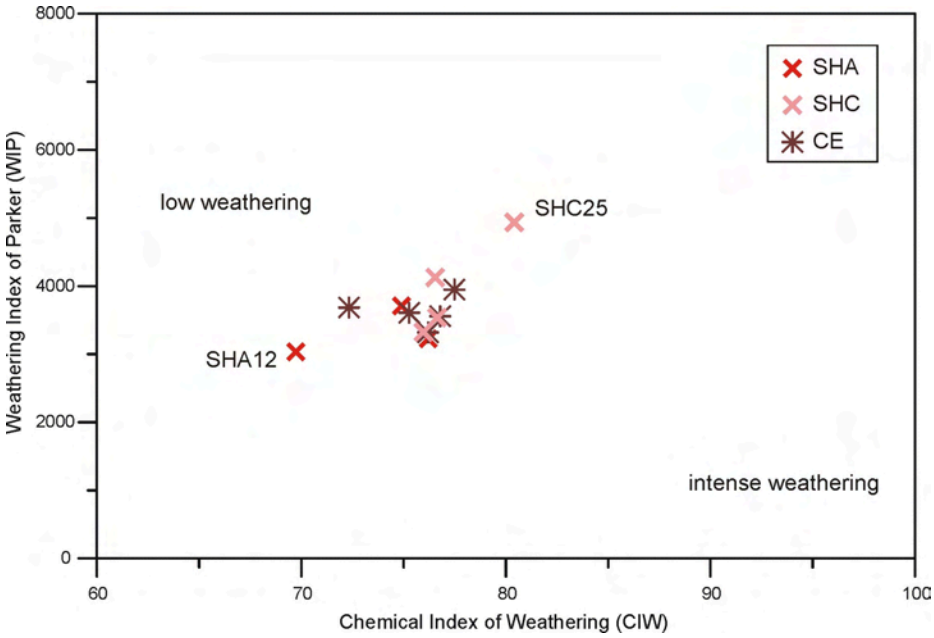


Fig. 4.10: Chemical Index of Weathering (Harnois 1988) plotted versus Weathering Index of Parker (1970) for the tuffaceous sandstone samples. The weathering intensity is relatively low, and no discrimination is possible by weathering intensity between the samples of the SHF (sections SHC and CE) and the SPF (section SHA). However, a mixing trend between juvenile material (represented by sample SHA12) with epiclastic material (sample SHC25) is reasonable.

In the spider diagrams of Fig. 4.11 (major elements) and 4.12 (trace elements), all samples are normalized to the juvenile magmatic composition of SHA12 in order to characterize geochemical differences of the tuffaceous sandstones relative to this juvenile sample. All samples from both formations are depleted in $P_2O_5$, $Na_2O$ and CaO as well as the trace elements Sr and Ba. On the other hand, they are enriched relatively to SHA12 in $K_2O$, $TiO_2$ and $SiO_2$ as well as in the trace elements V, Ni, Cu, Rb, Y, Zr and Nb. For most samples, MgO and Zn are enriched. MnO, $Fe_2O_3$ and $Al_2O_3$ as well as Pb and S do not follow a certain trend.

The concentrations of Cu, Zn, and Pb, are close to the detection limit of the RFA, and the variation of these elements may not be overinterpreted. EMP (EDX) analyses indicate that $P_2O_5$ as well as S in this case are often associated within plant debris, thus variations of these elements are not suitable to determine source rock or magma characteristics.

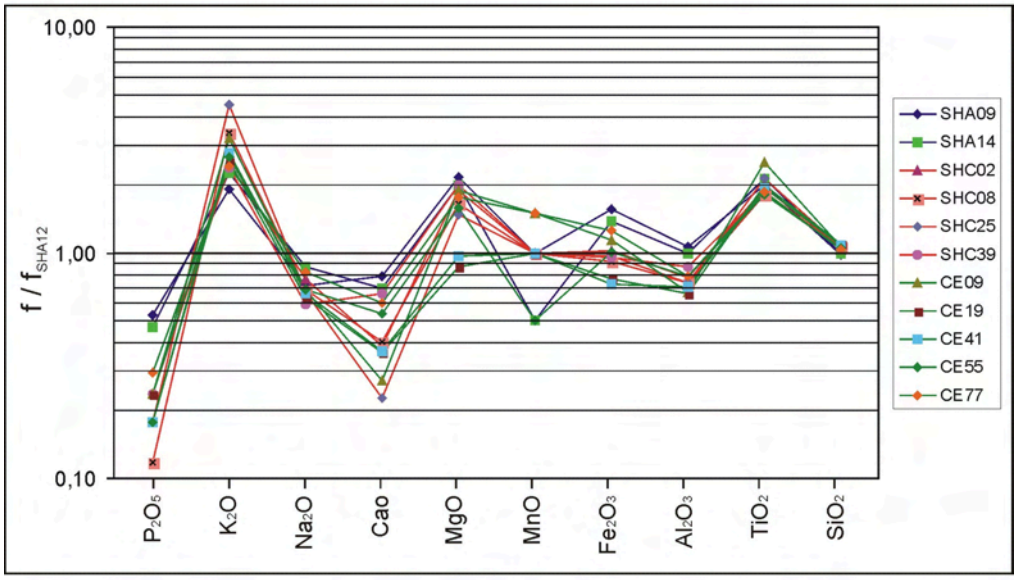


Fig. 4.11: Spider diagram for major elements (as oxides) normalized to sample SHA12. The SHF and SPF samples show similar trends of enrichment or depletion.

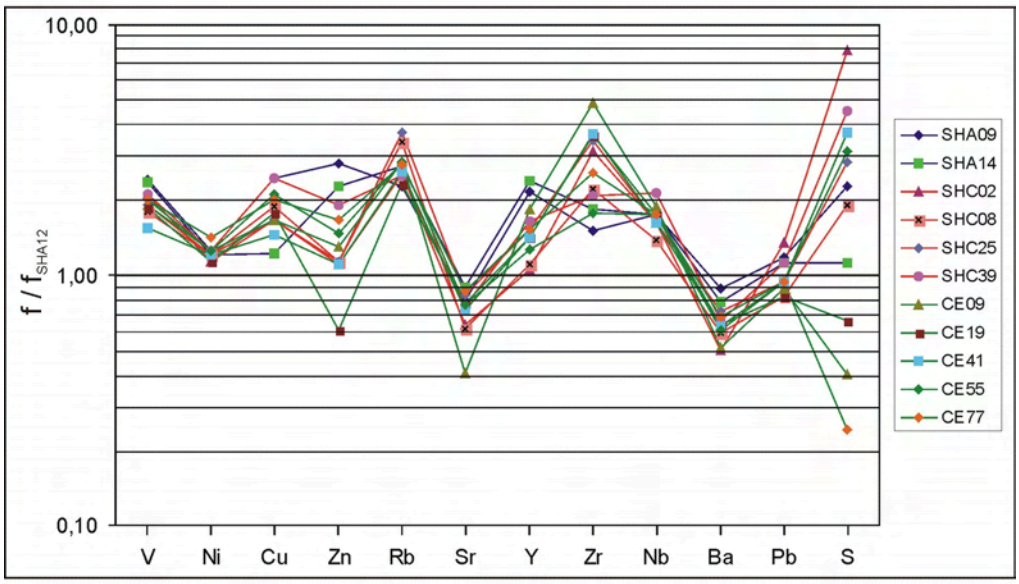


Fig. 4.12: Spider diagram for trace elements normalized to sample SHA12. The SHF and SPF samples show similar trends of enrichment or depletion.

In general, the trends of enrichments and depletions relatively to sample SHA12 are similar for both the samples from the SHF and from the SPF. However, the composition of samples from the SPF appears to be closer to the juvenile SHA12 than the composition of SHF-samples. In many cases, the epiclastic sandstone sample SHC25 differs most from all samples relatively to SHA12 (e.g. in $K_2O$ and CaO).

The enrichment in $K_2O$ and Rb, and the depletion in $Na_2O$, CaO, Sr, and Ba, can be explained by a higher K-feldspar : plagioclase ratio relatively to sample SHA12. This has been observed by CL for sample SHA06 (Sect. 4.2), and may also be valid for the other samples, as plagioclase is very abundant and K-feldspar is very rare in sample SHA12. The positive correlations of $K_2O$ and Rb common in K-feldspar, and of CaO and Sr, both found in plagioclase, is shown in Fig. 4.13.

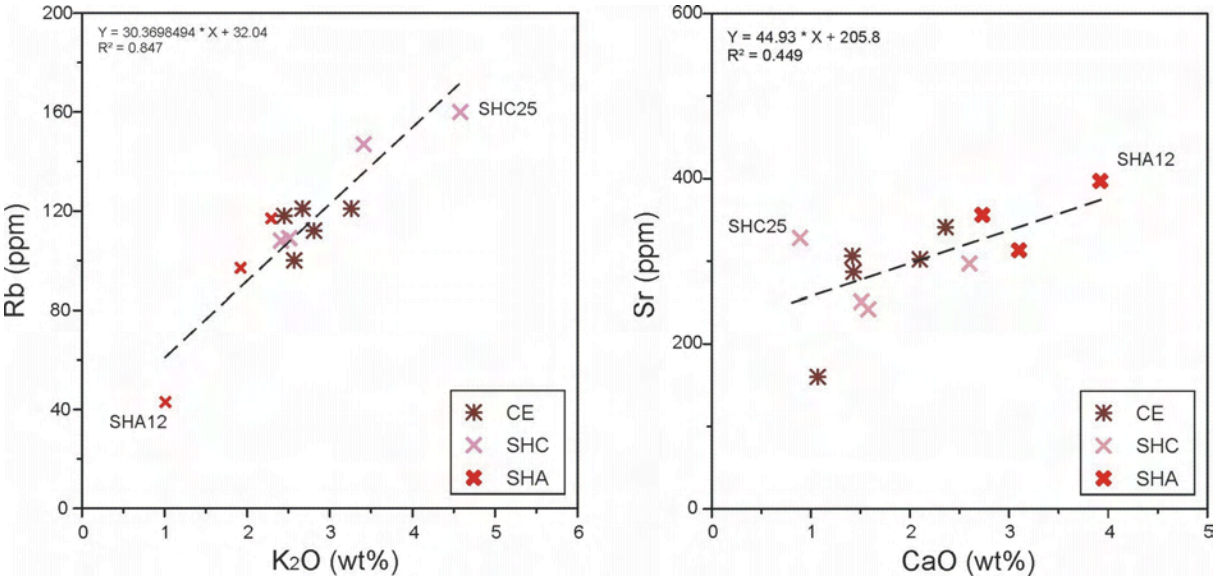


Fig. 4.13: A positive correlation is obvious between $K_2O$ and Rb (both as proxy for K-feldspar, left panel) and CaO and Sr (both as proxy for plagioclase, right panel) for the tuffaceous sandstones. Most samples lie between the juvenile sample SHA12 and the epiclastic sample SHC25. The samples from the SPF (section SHA) are closer to the juvenile source than the samples from the SHF.

Ba correlates positively with CaO, and $Na_2O$, indicating that this element is bound to plagioclase (Fig. 4.14). Despite its ionic radius and electric charge being similar to K, Ba correlates negatively with $K_2O$. Ba also correlates positively with the abundance of vitric shards (Fig. 4.15). In the juvenile sample SHA12, rich in shards and plagioclase, the concentration of Ba is highest of all tuffaceous samples analysed (1082 ppm), and the tuffaceous sandstone from the SPF also show relatively high Ba contents.

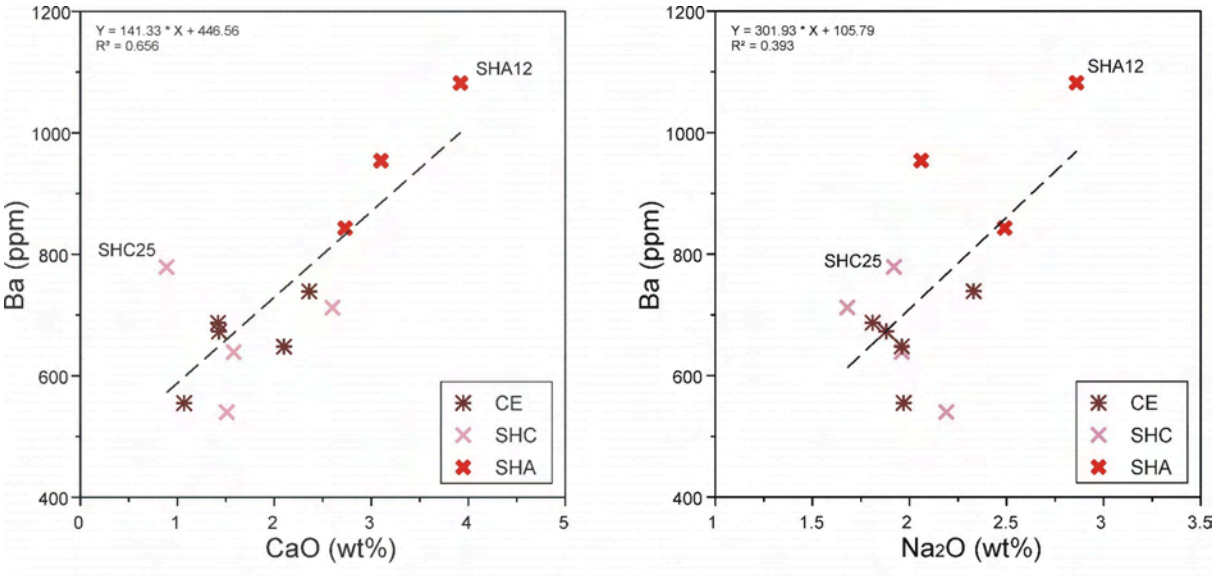


Fig. 4.14: The positive correlation of Ba with CaO (left panel) and $Na_2O$ (right panel) points towards plagioclase as Ba-bearing phase. In the juvenile sample SHA12, showing the highest fraction of plagioclase, also the Ba content is highest among all analysed samples.

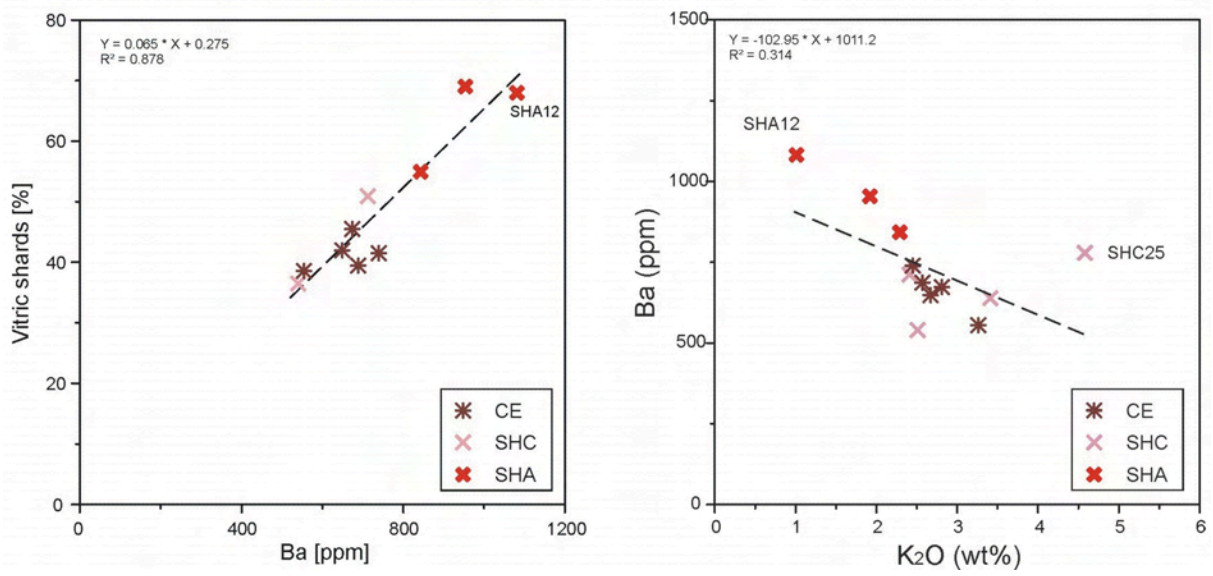


Fig. 4.15: A positive correlation of Ba with the fraction of vitric shards (given in percent of total constituents) is obvious. Despite their similar ionic radii and equal electronic charge Ba and K (plotted as $K_2O$) correlate negatively (lower right panel).

### 4.3.3 Summary and interpretation

For the juvenile magmatic sample SHA12, the pristine magma chemistry was most likely (soda-)rhyodacitic. A magmatic arc source is indicated by standard diagrams, pointing towards the active Gondwana plate margin as likely origin of the juvenile material. The composition of all other samples analysed can be explained by sedimentary mixing of igneous shards and crystals, similar to those in SHA12, with clasts from lithic sources like those that make up the sandstones in the SPF. The latter is represented by the slightly coarser sample SHC25, which does not contain shards.

The composition of the tuffaceous sandstones from the SPF resembles closer the juvenile magma chemistry than the tuffaceous sandstones from the SHF. This supports the petrographic interpretation (based, for instance, on the abundance and shape of shards) that the fraction of juvenile material is higher in the tuffaceous sandstones of the SPF. In contrast, SHF samples contain more epiclastic material.

The enrichment of the SHF samples in Mg, Fe, Ti, V, and Ni, relatively to SHA12, which are typically present in mafic minerals, is unlikely to be related to magmatic fractionation processes, as those must lead to a depletion of these elements. Instead, the enrichment may be caused by mixing with detrital material from the epiclastic source. This may also be the case for Zr and Y, but in contrast to the elements above the enrichment of these elements may also be caused by fractionation during the development of an evolved, felsic magma.

As the concentration of Ba is highest in the samples with the least proportion of epiclastic material and a high amount of vitric shards, this element may be predominantly derived from the juvenile source.

## 4.4 Mineral chemistry

### 4.4.1 Introduction

Mineral chemistry of juvenile minerals from tuffaceous sandstones may reveal information about the original magma chemistry. Therefore, in sample SHA12 feldspar and biotite were analysed by EMP. For direct comparison, sample SHA06 was selected for mineral analysis. In addition, minerals were analysed semi-quantitatively by EDX in two samples from section CE (CE15, CE77). The mineral chemical composition of diagenetic alteration products (zeolites, replacing vitric shards and filling pores) is evaluated in detail in Sect. 5.

In the epiclastic sandstone sample SHC25, feldspar, greenish-brown amphibole, garnet, and mica were analysed quantitatively in order to detect provenance variations relatively to sandstones from the SPF. However, for garnet and mica the total number of analyses was too small for a statistical evaluation. Only the composition of feldspar and amphibole is explained in detail here. All analyses can be found in the appendix.

Mineral chemical analyses were performed with a JEOL JXA 8900 RL electron microprobe at the Geowissenschaftliches Zentrum Göttingen of the Georg-August-Universität. Qualitative mineral identification (EDX) was derived with a CAMECA SX50 at the Institut für Geowissenschaften, Jena. Details to the methodology can be found in Sect. 3.4.

### 4.4.2 Results

The plagioclases of sample SHA12 show a relatively uniform composition with an anorthite component of about 28-31 %, and a K-feldspar component of about 6% (Fig. 4.14). In contrast, the plagioclases from sample SHA06 vary strongly between 20 and 60 % anorthite component. The nearly pure albitic composition of two analysed feldspars is most likely diagenetically in origin (albitization). Many of the plagioclases in the semi-quantitatively analysed samples from section CE are also albitised.

Biotites from the tuffaceous sandstone SHA12 exhibit a uniform composition with approximately 45% phogopite-/55% annite-component and a low Al-content (Fig. 4.15). In SHA06, no biotites are present.

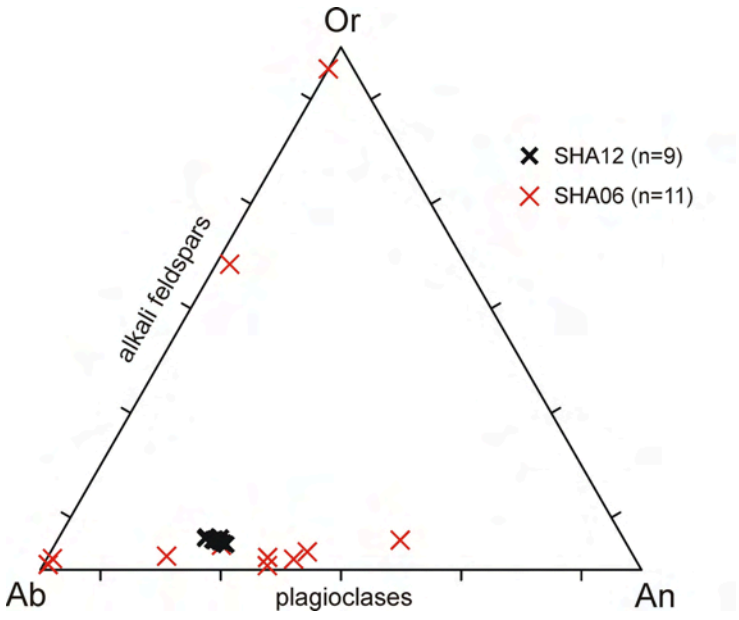


Fig. 4.14: The analyses of plagioclases from the tuffaceous sandstones within the SPF plotted in the ternary feldspar diagram. The plagioclases from sample SHA12 show a uniform composition ($An_{28}$-$An_{31}$), whereas the composition of plagioclases in sample SHA06 varies strongly. Or: K-feldspar; Ab: albite; An: anorthite.

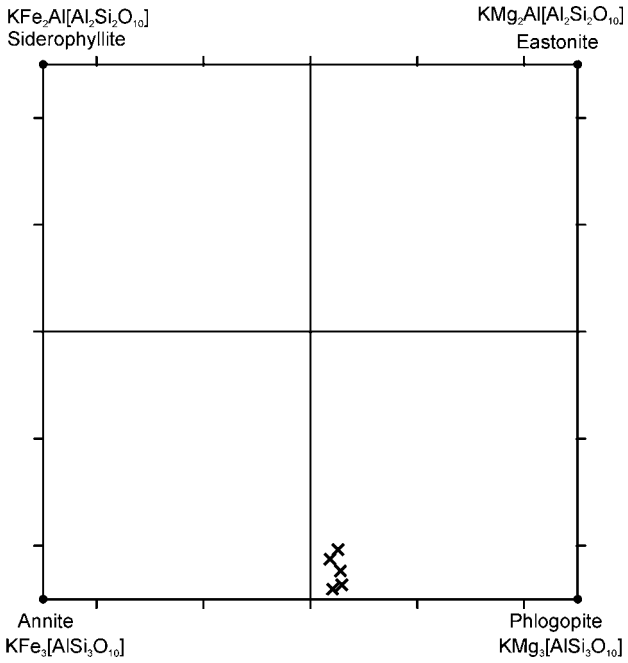


Fig. 4.15: Biotites from tuffaceous sandstone SHA12 in the Mg/(Mg+Fe) versus $Al^B$ diagram. The composition of all five analysed biotites is very similar, indicating a common, most likely magmatic origin.

In the epiclastic sandstone sample SHC25 feldspar and amphibole were analysed. Their composition is compared to analyses of sandstones from higher stratigraphic levels of the SPF in the southern Deep Freeze Range (samples SHA05, SHA07, MA06-1, and MA06-3) in order to test for a common source. These samples are classified as sandstone type C (see Sect. 3) and are geographically and stratigraphically close to section SHC.
The compositional range of feldspars (Fig. 4.16) in sample SHC25 lies for plagioclase in between about 12 and 38 % An. K-feldspar shows about 95% K. The same range was also semi-quantitatively determined from samples of section CE. These values lie within the wider range of samples from the upper SPF. They also resemble the analyses from sample SHA06, plotted in Fig. 4.14.

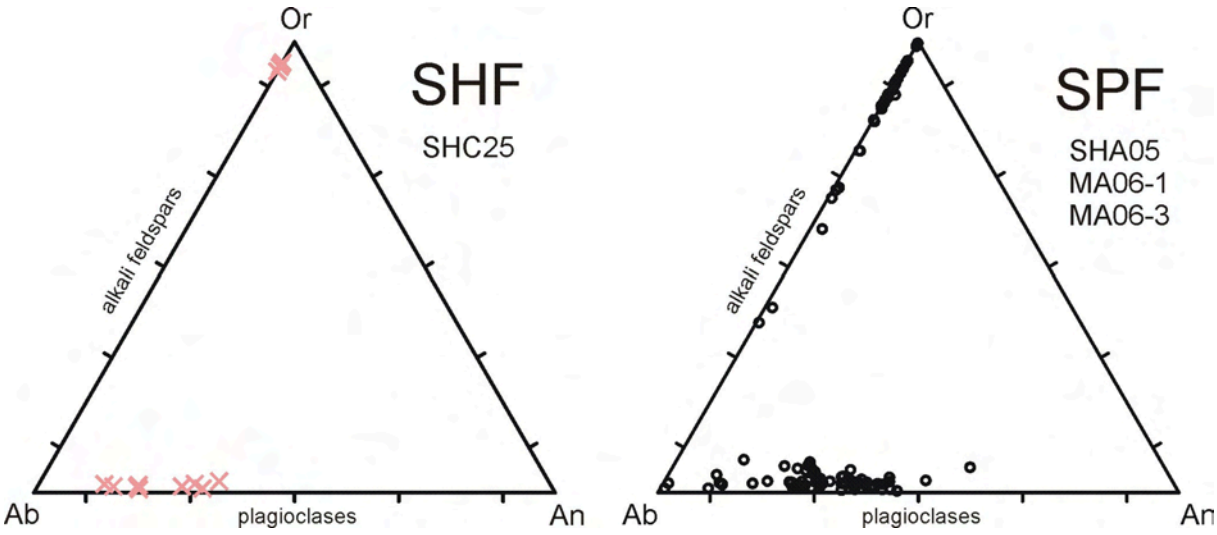


Fig. 4.16: Feldspar analyses from the SHF (left panel) and from upper stratigraphic levels of the SPF in the southern Deep Freeze Range (right panel) plotted in the ternary feldspar diagram. The feldspars may be derived from the same source.

The composition of greenish-brown amphiboles from sample SHC25 is also similar to those from SPF-sandstones (Fig. 4.17). However, the number of analyses from the SHF is relatively small (n = 4).

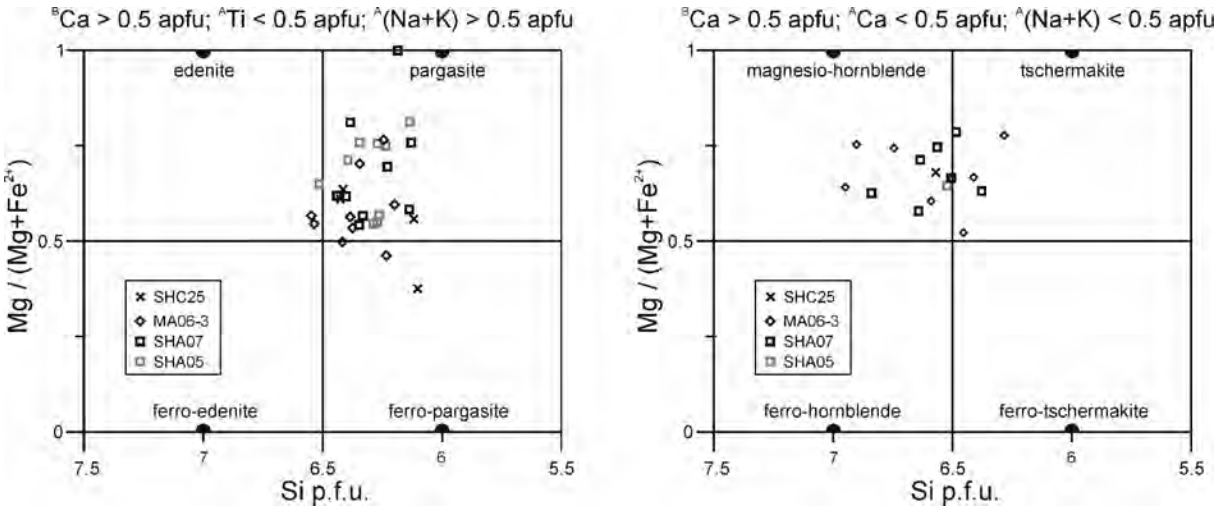


Fig. 4.17: Si pfu versus $X_{Mg}$ for $^{A}$(Na+K) ≥ 0.5 apfu in the left diagram, and for $^{A}$(Na+K) < 0.5 apfu on the right diagram (Leake et al. 1997). Amphiboles from the SHF (sample SHC25) exhibit a similar composition to those from the underlying SPF (samples SHA05, SHA07, MA06-3).

### 4.4.3 Interpretation

The formation of feldspars with the wide compositional range given for sample SHA06 is unlikely to have taken place within the same magma. Instead, an epiclastic origin of these crystals and a mixing with juvenile, shard-bearing material is more likely. The wide range of composition matches the different CL colours observed in this sample. White mica and epidote, found in sample SHA06, are not typical for felsic magmas and are therefore probably epiclastic components. It is not possible to conclude whether the admixture of the epiclastic material has taken place during the eruption process (e.g., by wall-rock erosion), or later during fluvial reworking. However, due to the compositional range of feldspars in the underlying sandstones a mixing during fluvial reworking appears probable.

In contrast, the compositional uniformity of plagioclases and biotites in sample SHA12 indicates formation from the same magma. The uniformity of plagioclases has already been inferred from the uniform CL-colours. White mica and epidote as in sample SHA06 have not been found.

In sample SHA12, biotites and $An_{30}$-plagioclases (oligoclase-andesine) together with quartz and K-feldspar (no analyses, petrographic result), matches a (soda-)rhyodacitic magma as deduced from whole rock geochemistry, although the plagioclase content is very high. However, in andesites, plagioclase usually contains 50-75 % Anorthite (Wimmenauer 1985) and thus significantly more than in SHA12. Epiclastic material has not been detected in this sample, thus supporting the petrographic result that SHA12 consists of juvenile magmatic material only.

Feldspar and amphibole composition of sample SHC25 do not raise the need for a source different from that of the upper sandstones from the underlying SPF (sandstone type C). Although the number of amphibole analyses is relatively small, their presence alone indicates a common source. Greenish-brown amphiboles have been found neither in other sandstone types, nor in other locations. Also, the presence of garnet (analyses not explained in detail) is characteristic for type C sandstones in the SPF.

## 4.5 U-Pb (SHRIMP) zircons ages

### 4.5.1 Introduction

So far, absolute sedimentation ages for the Beacon sandstone in NVL are missing. Biostratigraphic data points towards an Early Jurassic age for the uppermost SPF (Bomfleur et al. in review; Norris 1965; Pertusati et al. 2006). A Rb-Sr whole-rock isochron of a tuffaceous sandstone from the Falla Formation in the CTM yields an age of 186 ± 9 Ma (Faure and Hill 1973). However, due to pervasive zeolitisation, this age has been questioned (Elliot 1996), and lithological correlations over such a large distance (> 2000 km) may be misleading.

To determine the age of both, the youngest SPF and the SHF, four tuffaceous sandstones (two for SPF and SHF each) were chosen for a Zircon U-Pb age analysis with a Sensitive High-Resolution Ion-Microprobe (SHRIMP).

### 4.5.2 Methods

Zircon grains were hand selected and mounted in epoxy resin together with chips of the TEMORA (Middledale Gabbroic Diorite, New South Wales, Australia) and the 91500 (Geostandard zircon) reference zircons. The mounted grains were sectioned and polished. Reflected and transmitted light photomicrographs together with cathodoluminescence (CL) SEM images were taken for all zircons. The CL images were used to decipher the internal structures of the sectioned grains and to target specific areas within the zircons.

The U-Pb analyses of the Zircons were performed using SHRIMP-II ion microprobe at the Centre of Isotopic Research, VSEGEI, St. Petersburg (Russia) by Dr. N. Rodionoff and Dr. S. Sergeyev. Each analysis consisted of 5 scans through the mass range. Spot size was about 25 µm in diameter, with a primary beam intensity of about 4 nA. The data have been reduced similarly to a procedure described by Williams (1998) using the pipeline of Ludwig (2000). The Pb/U ratios have been normalized to a value of 0.0668 for the $^{206}Pb/^{238}U$ ratio of the TEMORA reference Zircons, corresponding to an age of 416.75 Ma (Black et al. 2003). Uncertainties for individual analyses (ratios and ages) are given at the 1σ level; however, the uncertainties in calculated concordia ages are reported at 2σ level. The Ahrens-Wetherill concordia plot (Wetherill 1956) of Fig. 4.18 was prepared using ISOPLOT/EX (Ludwig 1999).

### 4.5.3 Results and interpretation

During preparation of the mounts at the VSEGEI, the two samples from the SHF were irrecoverably lost, and only one non-magmatic zircon remained in a sample from the SPF. This accident may have been a result of the small grain size. Anyway, for this reason an age could only be obtained for sample SHA12 from the upper SPF, where 11 spots on 8 zircon grains were analysed (see Fig. 4.19 and Tab. 4.1). CL images can be found in the appendix.

One analysis (spot 6.2) was excluded from the age determination due to contamination with common lead. The other ten results lead to an age of 188.2 Ma ± 2.2 Ma (2σ), which is interpreted as crystallization age of the zircons within the magma chamber or during the eruption process. This age (Pliensbachian stage) thus confirms an Early Jurassic sedimentation age of the uppermost SPF, and provides a lower limit for sedimentation of the SHF.

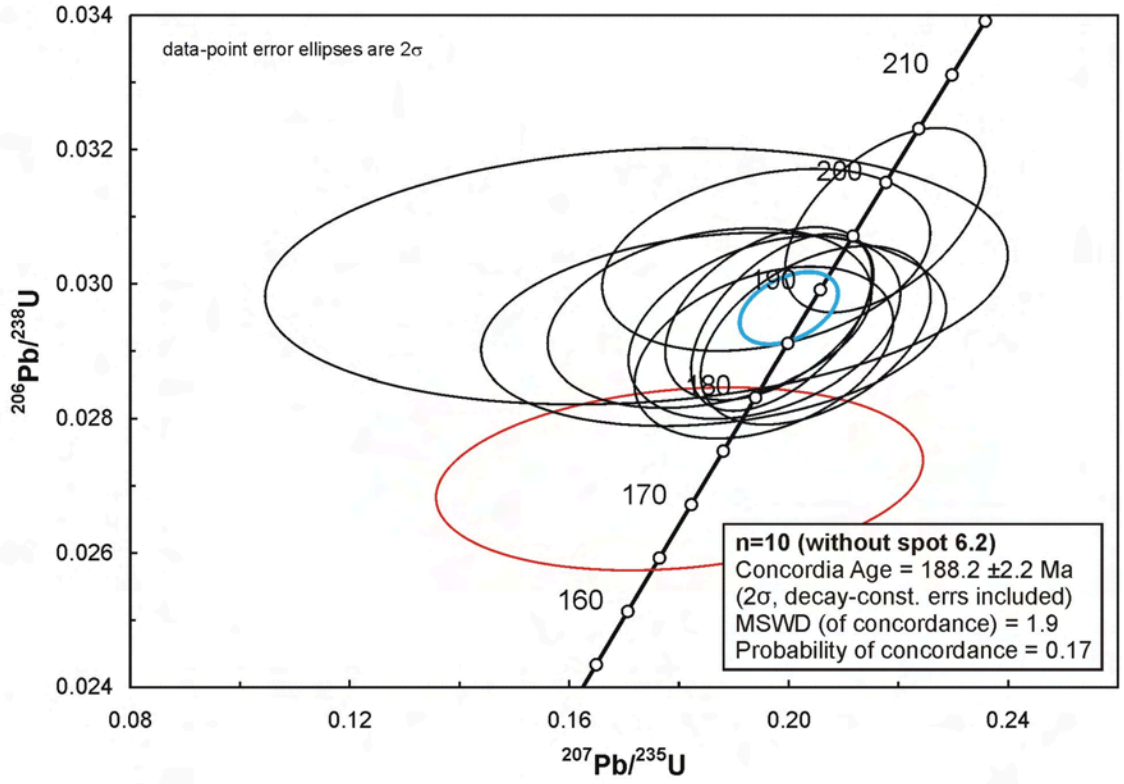


Fig. 4.19: Concordia plot of the U-Pb age results (SHRIMP) for sample SHA12 from the upper SPF. Error ellipses are 2σ. Spot 6.2 (marked in red, age 172.4 ± 3.5 Ma) has been excluded from the statistical age evaluation of the sample due to contamination with common lead. The blue ellipse indicates the concordia age of 188.2 ± 2.2 Ma calculated from the other 10 analyses.

| Spot | $^{206}Pb_c$ [%] | U [ppm] | Th [ppm] | $^{232}Th/^{238}U$ | $^{206}Pb^*$ [ppm] | $^{206}Pb/^{238}U$ age [Ma] [1] |
|---|---|---|---|---|---|---|
| SHA12–1.1 | 0.47 | 346 | 292 | 0.87 | 8.77 | 186.5 ± 3.5 |
| SHA12–1.2 | 0.73 | 344 | 297 | 0.89 | 8.79 | 187.4 ± 3.4 |
| SHA12–2.1 | 1.03 | 193 | 222 | 1.19 | 4.91 | 186.3 ± 3.7 |
| SHA12–2.2 | 1.22 | 48 | 26 | 0.55 | 1.27 | 191.3 ± 4.9 |
| SHA12–3.1 | 0.04 | 331 | 265 | 0.83 | 8.36 | 187.0 ± 3.4 |
| SHA12–4.1 | – | 332 | 222 | 0.69 | 8.83 | 196.5 ± 3.5 |
| SHA12–5.1 | 0.28 | 485 | 503 | 1.07 | 12.3 | 187.8 ± 3.3 |
| SHA12–6.1 | 0.23 | 440 | 423 | 0.99 | 11 | 184.2 ± 3.3 |
| SHA12–6.2 [2] | 0.92 | 174 | 138 | 0.82 | 4.08 | 172.4 ± 3.5 |
| SHA12–7.1 | 0.28 | 283 | 174 | 0.64 | 7.12 | 185.8 ± 3.4 |
| SHA12–8.1 | 0.61 | 383 | 347 | 0.94 | 10 | 192.8 ± 3.5 |

Table 4.1: Results of the U-Pb age analysis (SHRIMP) of sample SHA12. Errors are 1-sigma; $Pb_c$ and Pb* indicate the common and radiogenic portions, respectively. Error in Standard calibration was 0.64%. The complete results are given in the appendix.

[1] Common Pb corrected using measured $^{204}Pb$.

[2] Spot SHA12-6.2 was excluded for determination of the sample age due to contamination with common lead.

## 4.6 Summary: Provenance of the tuffaceous sandstones

Sample SHA12 from the uppermost SPF was identified by petrographic and mineral chemical analyses as a tuffaceous layer comprising of juvenile magmatic material only. This sample originates from a distal, explosive eruption of a (soda-)rhyodacitic magma, formed most likely at the active plate margin of Gondwana. Eruption resulted in fragmentation of the glassy material in numerous vitric shards. Before deposition, minor fluvial reworking took place. $An_{30}$-plagioclase is the most abundant mineral constituent, besides of which quartz and K-feldspar occur as accessories. Biotite as the only mafic mineral is very rare.

Zircons from this sample gave a U-Pb (SHRIMP) age of 188.2 ± 2.2 Ma. This result suggests that deposition of the SPF persisted at until the Early Jurassic (Pliensbachian). As a minimum age of 183.6 ± 2.1 Ma is given for the SHF by the age of the overlying Ferrar lavas (Encarnación et al. 1996), the depositional age of this formation is fairly well bracketed, and can be confirmed as Early Jurassic (Pliensbachian).

The other tuffaceous samples from both, the SPF and the SHF, are products of mixing of juvenile magmatic material similar to that of sample SHA12, with epiclastic material. Especially mineral chemical analyses of feldspar and greenish-brown amphiboles (and even the presence of the latter alone) indicate a common source for both the epiclastic portion of the tuffaceous sandstones and the sandstones in the uppermost part of the SPF (Deep Freeze Range, sandstone type C). Thus, the volcanism was not accompanied by major changes in source area or drainage system within the NVL sector of the Transantarctic Basin. No evidence was found for an additional admixture of epiclastic material during the explosive eruptions itself (e.g. by vent erosion). Plant debris in many samples indicates that vegetation was present during deposition.

Tuffaceous sandstones from the SPF usually contain a smaller portion of epiclastics than these of the SHF. Therefore, tuffaceous sandstones from both formations can be distinguished petrographically (SHF: less and stronger abraded shards), and geochemically (SHF: more $SiO_2$, $Na_2O < K_2O$). The higher abrasion and smaller abundance of shards within the SHF in combination with the higher amount of epiclastic material can be interpreted as result of longer fluvial transport prior to deposition. Alternatively, these observations may be explained by a more intense weathering before (fluvial) deposition, but geochemical weathering indices argue against this scenario.

In general, petrographic (vitric shards) and geochemical similarities of the tuffaceous sandstones from the two formations indicate a common provenance of the juvenile magmatic material. Distal, ultra-plinian events can be inferred from fragmentation and dispersion of the volcaniclastic material, which was then further transported fluvially, reworked and thereby mixed with epiclastic material. Pyroclastic fall deposits from ultra-plinian events may cover areas of several thousands to several ten thousands of square kilometres, and the volume of these pyroclastic deposits may exceed 3000 km³ (Fisher and Schmincke 1984). Calderas with diameters of up to 20 km are commonly formed during the eruptions (Fisher and Schmincke 1984).

Similar deposits in a comparable stratigraphic position as the SHF have been found in the upper Hanson Formation (formerly Upper Falla Formation) in the CTM (Barrett 1991; Bryan et al. 2002; Elliot 1996). In the Hanson Formation, an intercalation of sandstones with tuffaceous sandstone at the base grades into a tuffaceous unit with intercalated tuffs and volcaniclastic sandstones. The upper part of the Hanson Formation comprises more than 100 m of finely bedded, vitric felsic tuffs (Elliot 1996) of soda-rhyolitic composition (Barrett et al. 1986). Accretionary and armoured lapilli in these deposits indicate a relatively proximal source (Elliot 1996). A Rb-Sr-whole-rock-isochron of this unit gave an age of 186 ± 9 Ma (Faure and Hill 1973).

The occurrence of tuffaceous sandstones or tuffites with similar chemical composition in the Transantarctic Basin at the same stratigraphic level more than 2000 km apart, indicates a major volcanic province. A possible source with silicic magmatic activity at that time has been reported from the Chon Aike Province (e.g. Bryan et al. 2002, and references therein). It was located above the subduction zone of the Panthalassa (Proto-pacific) oceanic plate underneath Gondwana, today exposed in the Antarctic Peninsula and in Patagonia (Fig. 4.20).

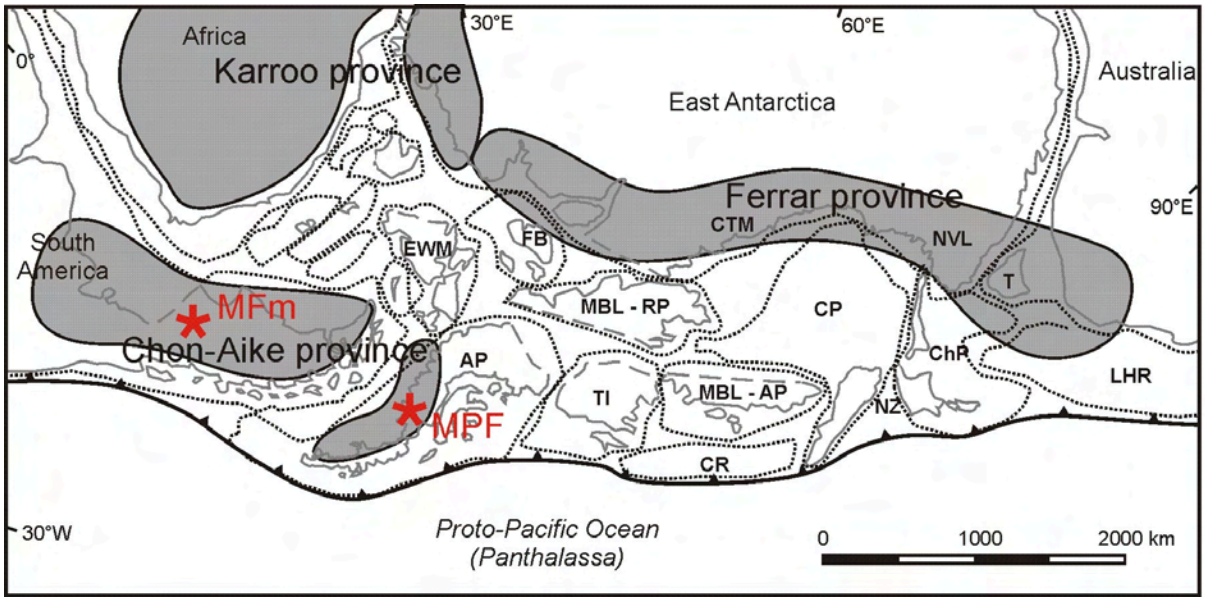


Fig. 4.20: Palaeogeographic reconstruction of the active Gondwana margin during the Early Jurassic (after Willan. 2003, Riley et al. 2001), indicating the position of the Chon Aike, the Karoo, and the Ferrar Large Igneous Province. The Mount Poster Formation (MPF) and the Marifil Formation (MFm) are possible sources of the tuffaceous sandstone in NVL and in the CTM. However, there may be further eruption centres on the magmatic arc along the Proto-pacific margin, e.g. on the Campbell Plateau.
Abbreviations: AP: Antarctic Peninsula; ChP: Challenger Plateau; CP: Campbell Plateau; CR: Chatham Rise; CTM: Central Transantarctic Mountains; EWM: Ellsworth-Whitmore Mountain Block; FB: Filchner Block; LHR: Lord Howe Rise; MBL-AP: Marie-Byrd-Land, Amundsen Province; MBL-RP: Marie-Byrd-Land, Ross Province; NVL: North Victoria Land; NZ: New Zealand; T: Tasmania; TI: Thurston Island Block.

In Patagonia, the Marifil Formation (188-178 Ma, with a peak around 184 Ma), dominated by rhyolitic ignimbrites, correlates stratigraphically with the tuffaceous deposits in SPF and SHF (Riley et al. 2001). On the Antarctic Peninsula, the Mount Poster Formation in the Latady Basin matches the stratigraphic range of the upper SPF and SHF (Hunter et al. 2006). However, the palaeogeographic distance of both Patagonia and the Latady Basin to the CTM stands in contrast to the observation of a relatively proximal source of the uppermost Hanson Formation (see Fig. 4.20). Therefore, other areas of contemporaneous volcanic activity lying closer to the CTM or NVL may be more likely as sources for the tuffaceous material. They may have formed in a tectonic setting equivalent to the Chon Aike Province and on the same magmatic arc, but, possibly, are now covered by younger sediments (e.g. on the Campbell Plateau). In any case, close spatial and temporal relations exist for the extremely large volumes of felsic volcaniclastic material in the TAM and the mafic magmatites of the Ferrar Large Igneous Province. Therefore, also a genetic relationship between both is reasonable.

# 5 Diagenetic evolution of the Section Peak Formation

## 5.1 Introduction

Authigenic phases and the timing of diagenetic mineral reactions are important to decipher the diagenetic and burial history of sediments (e.g. Merino et al. 1997). In case of the SPF, the next younger sediments documented are related to the rifting of the Ross Sea in the Eocene. Therefore, the time span between the effusion of the Ferrar lavas at around 184 Ma (Encarnación et al. 1996; Minor and Mukasa 1997) and the opening of the Ross Sea at about 50 Ma (Rossetti et al. 2003b; Siddoway 2007) is relatively poorly constrained with evidence for post-Beacon evolution coming mainly from structural observations, mineral dating (apophyllite) and apatite fission track (AFT) data (e.g. Lisker et al. 2006; Molzahn et al. 1999; Rossetti et al. 2003b). The latter are the most substantial arguments for the proposed existence of a Cretaceous Antarctic-Australian Victoria basin, and maximum burial depths of 3 to more than 5 km for the SPF (Lisker and Läufer 2007, see also Fig. 5.1).

For NVL, various post-depositional thermal events are reported (see also Sect. 1). The first is related to emplacement of Ferrar effusive and intrusive rocks at about 184 Ma (Encarnación et al. 1996; Minor and Mukasa 1997), shortly after deposition of SPF and SHF. This event led to a significant increase of maturity of organic matter and of vitrinite reflectance in the contact aureole of the sills (Berner et al. 2009b). In SVL, an influence of sill intrusion on sediment diagenesis has been shown (Bernet and Gaupp 2005).

Other thermal events are most likely related to break-up processes of Gondwana during the mid-Cretaceous. From this time (between 130 and 96 Ma), events with temperatures of more than 300°C have been reported (Molzahn et al. 1999). The extension, leading to the formation of the Ross Sea as part of the West Antarctic Rift System (Rossetti et al. 2003b; Siddoway 2007), may also have been accompanied by a thermal event.

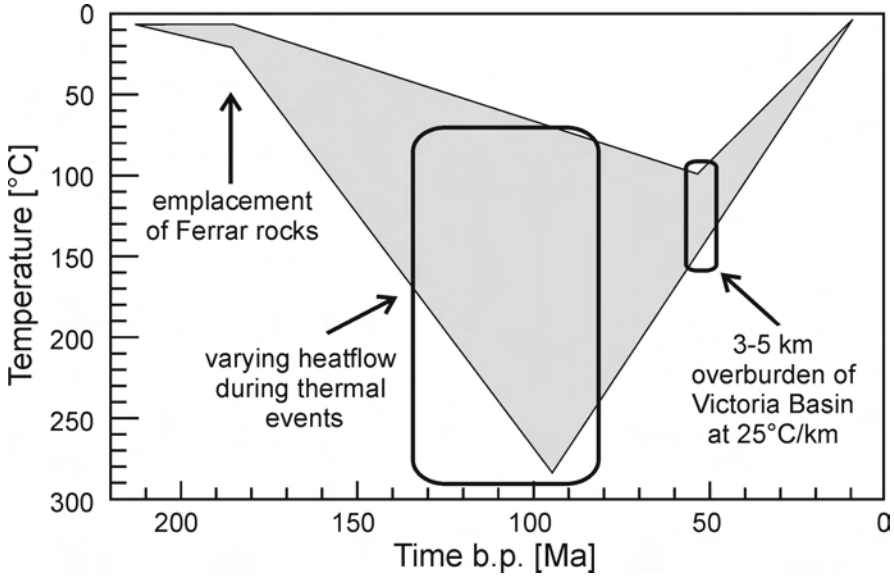


Fig. 5.1: Thermal history of the Beacon Supergroup in northern NVL as deduced from AFT data (redrawn after Lisker and Läufer 2007). A burial of 3 km to more than 5 km is proposed by these authors for the end of the Cretaceous.

In this section, diagenetic phases and mineral reactions within the SPF were analysed (1) to determine the maximal burial temperature and possible spatial temperature variations in NVL, (2) to find evidences for or against the existence of a Cretaceous basin, and (3) to detect possible mineralogical evidence for the influence of thermal events, especially of the Ferrar

sills. Therefore, this study emphasizes on temperature sensitive minerals and mineral reactions, although all other diagenetic minerals and features are equally described.

Besides optical microscopy, XRD measurements were performed using the fraction < 2 µm of carefully crushed mudstones and sandstones to determine clay mineral content and zeolite mineralogy. Electron microprobe analysis (EMP) was used to determine zeolite and feldspar composition. The methods are described in detail in Sect. 3.

## 5.2 Authigenic phases and mineral reactions in the SPF

### 5.2.1 Quartz

Minor syntaxial quartz overgrowths occur in some of the lithoclast-poorer samples throughout the working area (e.g. sections AN and SHS). However, they are frequent only in the very mature samples from the Stewart Heights (ST05, ST09), with a fraction of about 10 vol%. Here, the quartz-cements occur together with later stage kaolinite and calcite (the latter only in sample ST09). In other samples, quartz pre-dates zeolites (see also Di Giulio et al. 1997).

In samples from the northern parts of the working area, quartz cements have been found as about 5 µm large, pore-lining crystals (microquartz) in combination with chlorite.

Quartz cementation has been described to be significant only at temperatures greater than about 70-80°C (Giles et al. 2000), but may form already at much lower temperatures (R. Gaupp 2009, pers. comm.) and is therefore not suitable to determine burial temperatures. Clean quartz grain surfaces favour quartz overgrowth, while they may be inhibited by authigenic clay coatings. Section ST, in contrast to all other sections in NVL, comprises very mature quartz arenites, and no clay minerals are pre-dating the quartz cements.

### 5.2.2 Feldspar

#### 5.2.2.1 Authigenic feldspar

Authigenic feldspar occurs locally in a few samples, mostly as syntaxial overgrowths but also as euhedral crystals in pores. Due to their rare occurrences they were not investigated in detail. Dissolved volcanic detritus is a possible source of authigenic feldspar. A formation temperature of a similar range as for albitization (described below) can be expected, although it also has been found in eodiagenetic environments at much lower temperatures (Schöner 2006, and references therein).

#### 5.2.2.2 Albitization

Albitization of plagioclase has been observed in a sample from Skinner Ridge (SR03) and – more frequently – in samples from the section Chisholm Hills West (CHW). Albitization is restricted to plagioclase in all cases, whereas K-feldspar is not affected. In sample SR03 besides almost pure albites ($An_{0-1}$) some 'impure' albites ($An_{2-10}$) and a considerable amount of oligoclase is present (maximal $An_{23}$). In the samples from section CHW, a higher percentage of plagioclases are albitised, and less oligoclase is present. The results of microprobe analyses are shown in Fig. 5.2, and can be found in detail in the appendix.

Albitization of plagioclase is thought to occur by dissolution-precipitation processes at about 75-100°C (Morad et al. 1990), while albitization of K-feldspar requires higher temperatures of about 120-150°C (Baccar et al. 1993). Albitization of K-feldspar at lower temperatures (above 65°C) has also been reported (Saigal et al. 1988), but this seems to be exceptional, as K-Feldspar dissolution is usually faster than albite precipitation at this temperature (Aargaard et al. 1990).

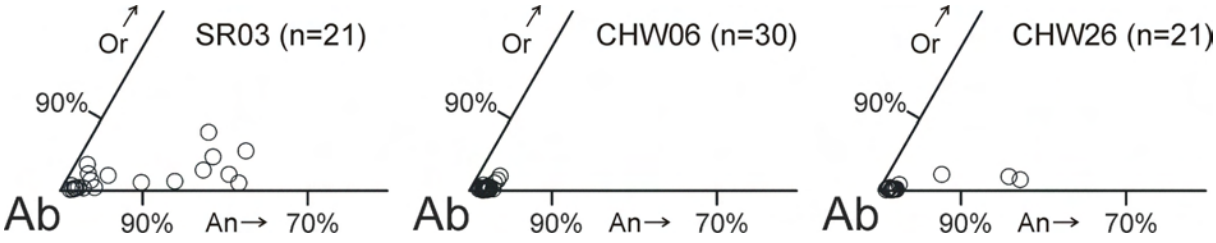


Fig. 5.2: Microprobe analyses of plagioclases from three samples (SR03, CHW06, CHW26) drawn in a detail of the ternary feldspar diagram. In both CHW samples the fraction of albitised plagioclases is higher than in sample SR03, possibly indicating higher temperatures.

#### 5.2.2.3 Dissolution of feldspar

Dissolution of feldspar is common in sections CHW and SR, resulting in a notable proportion of intra-granular porosity (up to 4 %), while in all other sections feldspar is less affected. It is not possible to give a certain temperature range for dissolution of feldspar. Above 145°C, albitization of K-Feldspar is presumed to be more likely than its dissolution (Aargaard et al. 1990). Therefore feldspar dissolution is also possible during eodiagenesis or telodiagenesis.

### 5.2.3 Calcite

Calcite cement has been found in many samples, and in nearly all cases it occurs close to a dolerite sill or to the basement (Tab. 5.1). It appears as patchy pore filling cement, but often shows corrosive growth and replacement of detrital grains. It occurs predominantly in zones of higher permeability, post-dating – where observable – hematite cements. Authigenic calcite accounts for up to 12 vol%, but considering replacement of dissolved grains, the intergranular calcite volume is usually below 3 vol%. As the intergranular volume (IGV) of the samples containing calcite is mostly very low, it is considered as a later stage precipitate after compaction.

| Sample | Calcite [%] | Distance to next sill | Distance to basement |
|---|---|---|---|
| RB01 | n/a | 28 m | 2 m |
| TI01 | 5.4% | 1 m | n/a |
| TI18 | 2.9% | 35 m | n/a |
| AN16-RS13 | 0.3% | 6 m | 59 m |
| AN18-RS14 | 12.2% | 2 m | 63 m |
| SHS01-RS02 | 6.5% | 30 m | 2 m |
| PT02-RS02 | 1.2% | 21 m | 4 m |
| PT05-RS05 | 1.6% | 5 m | 20 m |
| ST09 | 0.3% | 2 m | 13 m |

Tab. 5.1: Samples showing calcite cementation, the proportion given by point counting, and the distance to the next sill and to the basement. Apart from sample TI18, either a sill or the basement is close.

Due to the regional relationship of calcite to Ferrar sills, an influence of the sills on calcite precipitation was inferred, e.g. by the magma acting as a $CO_2$ source. The results of a $\delta^{18}O/\delta^{13}C$ -study were rather indefinite, and a hybridization of volcanic $CO_2$ with plant related $CO_2$ was suggested (Di Giulio et al. 1997). Also, these authors failed to consider the spatial correlation of calcite cements with the basement, making a control of calcite precipitation solely by magmatic activity unlikely. Instead, differences in the hydrodynamic of fluid flow close to baffles or barriers (as are both the sills and the basement) are more likely. The occurrence of calcite cements in sample TI18 far away from both, a sill and the basement, may be caused by the pelitic interbeds in section TI.

Calcite cements may already form at relatively low temperatures (e.g., Bjørlykke et al. 1989; Solano-Acosta et al. 2008), thus they cannot be considered as reliable tracers for definition of maximum burial temperatures. As precursor material in this case instable volcanic grains or plagioclase is possible (Bjørlykke et al. 1989).

### 5.2.4 Zeolites

Zeolites are frequently found not only in tuffaceous sandstones, where they replace vitric shards, but also as authigenic phases in sandstones, and in mudstones. Zeolites are especially useful to estimate palaeotemperatures during diagenesis, as the formation of the different zeolite types is temperature sensitive (e.g. Utada 2001a). Point-count data of zeolites vary between 0 and 17 vol%.

The 2 µm fraction of carefully crushed sandstone was separated and analysed by XRD (for methods, see Sect. 3). In a few polished thin sections chemical analyses have been carried out by EMP. Due to their mobility and the open framework structure of zeolites, determination of alkali and earth alkaline metals, in particular Ca, Na and K, is problematic. A distinction between framework and extra-framework cations is impossible. Therefore, zeolites were identified by proportions of atoms p.f.u. instead of their absolute numbers, with the Si:A ratio being especially useful. In Tab. 5.2, the zeolites found in the SPF are listed, including their chemical properties useful for identification by EMP, possible host rocks and typical temperature ranges of formation.

| Zeolite | Ideal chemical formula | DEC | R | Host rock | Temp. range |
|---|---|---|---|---|---|
| Clinoptilolite | $(Na,K,Ca_{0.5})_7[Al_7Si_{29}O_{72}] \bullet 22H_2O$ | Ca, Na, K | 0.80-0.85 | Felsic | 50–90°C |
| Heulandite | $(Na,K,Ca_{0.5})_7[Al_7Si_{29}O_{72}] \bullet 22H_2O$ | Ca, Na, K | 0.73-0.80 | Felsic / mafic | 90–120°C |
| Analcime | $Na_{16}[Al_{16}Si_{32}O_{96}] \bullet 16H_2O$ | Na | 0.60-0.74 | Felsic / mafic | 90–125°C[1] |
| Laumontite | $Ca_4[Al_8Si_{16}O_{48}] \bullet 16H_2O$ | Ca | 0.65-0.69 | Felsic / mafic | >90°C[2] |

Tab. 5.2: Summary of the chemical properties of the zeolites present in the SPF and their formation conditions. DEC: dominant extra-framework cation; R: approximate range of Si/(Si+Al) (modified after Passaglia and Sheppard 2001); Type of host rock is related to volcaniclastic rocks (Hay and Sheppard 2001); temperature ranges (Utada 2001a) modified after Gatta (pers. comm. 2007).
[1]In presence of alkaline brines, analcime may precipitate at surface temperatures (e.g. English 2001; Remy and Ferrell 1985).
[2] Only in cases with contemporaneous albitization (Noh and Boles 1993), otherwise >120°C (Utada 2001a).

Clinoptilolite and heulandite were distinguished chemically only by their proportion of Si:Al (see Fig. 5.3). According to the International Mineralogical Association (IMA), clinoptilolite is considered Si-rich with a Si:Al ration of 4 or more, while heulandite is Si-poor, with an Si:Al ration of less than 4 (Coombs et al. 1998). Laumontite can be identified chemically by its Si:(Si+Al) -, or by its Si:Al ratio, and the dominance of Ca over Na and K in combination with the absence of Mg, Sr and Ba (Passaglia and Sheppard 2001).

Major zeolite precipitation occurred in sections SHA, SHB, SR, MA, SP, SPP, CHW, and CE, while they are absent or only subordinate in the other sections. As precursor material, the vitric shards are obvious in case of the tuffaceous sandstones of sections SHA and SHC. Here, the glassy material has been replaced completely, but the shape of the shards is still preserved. In sandstones without glass shards, zeolites occur in inter-granular as well as intra-granular pores (mainly in dissolved feldspar) as pore-filling or, rarely, as pore-lining cements. Feldspar or volcanic lithoclasts of mafic or felsic composition can be inferred as likely precursor material. Table 5.3 lists samples containing authigenic zeolites, the methods applied and the zeolites identified.

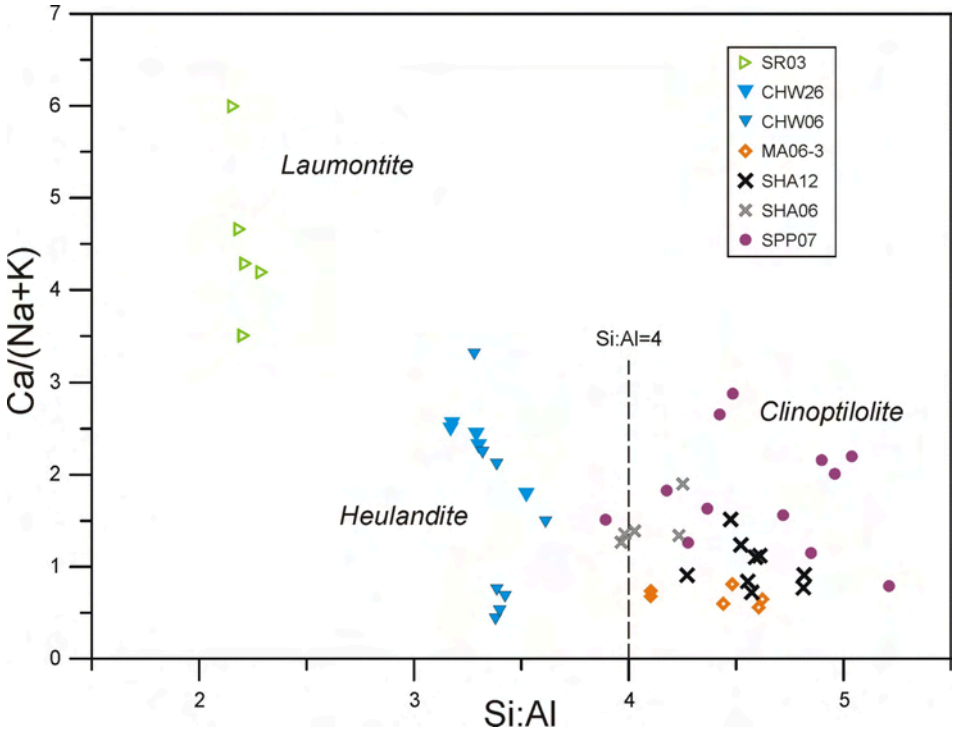


Fig. 5.3: Chemical composition of zeolites in the Si:Al versus Ca/(Na+K) diagram, determined by EMP. Laumontite has a higher Ca:(Na+K) ratio as well as a higher amount of Al than heulandite and clinoptilolite. The latter are separated at a Si:Al ratio of four by definition (Coombs et al. 1998).

| Section | Sample | Form. | Lithology | Occurrence | Dist. | PC | EMP | Zeolite |
|---|---|---|---|---|---|---|---|---|
| MA | MA02 | SPF | Sandstone | Cement | 6 m | 6.9 % | | n/a |
| | MA06-3 | SPF | Sandstone | Cement | 100 m | 17.5 % | x | Clin |
| CHW | CHW06 | SPF | Sandstone | Cement | 14 m | n/a | x | Heu |
| | CHW10 | SPF | Sandstone | Cement | 29 m | n/a | | Heu |
| | CHW26 | SPF | Sandstone | Cement | 3 m | 5.5 % | x | Heu |
| SP | SP-L1.1 | SPF | Mudstone | n/a | 5 m | n.d. | | Ana |
| SPP | SPP07 | SPF | Sandstone | Cement | 10 m | 23 % [1] | x | Clin |
| SR | SR01 | SPF | Sandstone | Cement | 10 m | 2.7 % | | n/a |
| | SR03 | SPF | Sandstone | Cement | 6 m | 5.7 % | x | Lau |
| SHA | SHA06 | SPF | Tuff. Sst. | Repl. shards | 5 m | n/a | x | Clin |
| | SHA08 | SPF | Mudstone | n/a | 11 m | n/a | | Clin/Heu |
| | SHA09 | SPF | Tuff. Sst. | Repl. shards | 15 m | n/a | | n/a |
| | SHA12 | SPF | Tuff. Sst. | Repl. shards | 16 m | n/a | x | Clin |
| | SHA14 | SPF | Tuff. Sst. | Repl. shards | 18 m | n/a | | n/a |
| SHB | SHB02 | EHT | Mudstone | n/a | 24 m | n/a | | Clin/Heu |
| | SHB07 | EHT | Mudstone | n/a | 29 m | n/a | | Clin/Heu |
| SHC | SHC29 | SHF | Mudstone | n/a | 11 m | n/a | | Clin/Heu |
| | SHC36 | SHF | Mudstone | n/a | 9 m | n/a | | Clin/Heu |

Tab. 5.3: Samples showing authigenic zeolites. Dist: approximate distance to the next sill/dyke; PC: Proportion of zeolites by point counting; EMP: samples on which EMP measurements were performed (detailed results in the appendix); Clin: Clinoptilolite; Heu: Heulandite; Lau: Laumontite; Ana: Analcime. The SHC samples are from the SHF and shown for comparison. [1] Estimation, based on point-count result of nearby sample SPP05.

The process of zeolitisation is influenced or even controlled by hydrothermal fluids (Hay 1966; Utada 2001b). In this case, these fluids may be related to the intrusion of Ferrar dolerites. This assumption is supported by the usually relatively short distance of the zeolite-bearing samples to the closest sill (see Tab. 5.3). However, in some cases the distance

is very high, for instance, 100 m for sample MA06-03. Especially in these samples, zeolitisation may be related to the EHT-deposits. Breccia-filled diatremes or vents are known to be possible pathways for hydrothermal fluids that may cause zeolitisation also within the adjoining sandstones (Svensen et al. 2006).

In NVL, possible zeolite forming hydrothermal events are recorded from the middle Cretaceous at around 130 – 96 Ma (Molzahn et al. 1999). However, zeolites indicating a temperature higher than 120°C (e.g. laumontite without contemporaneous albitization of plagioclases) are lacking, although temperatures of more than 300°C have been reported from theses events (Molzahn et al. 1999).

Besides suitable precursor material and the distance to a source (e.g. a sill) or pathway of hydrothermal fluids (e.g. an EHT-diatreme), other controlling mechanisms of zeolite formation are necessary, as in some volcaniclastic-rich sandstones close to a sill zeolites are very rare or absent. The simplest explanation is the reduced porosity and permeability within the sandstone itself due to strong and presumably rapid compaction (see Sect. 5.3), inhibiting fluid flow and thus preventing zeolite cementation.

### 5.2.5 Ca-sulphate

A Ca-sulphate has been found in sample MA06-1 of the Mount Adamson section, where it accounts for 18 % of the rock volume (point counting data). This sample was taken in very close distance to a small dike offsetting from a sill, and the Ca-sulphate is practically absent a few decimetres away. Therefore, this mineral is not of regional significance. EDX measurements suggest a chemical formula of $CaSO_4 \bullet H_2O$ and thus more water than normally found in bassanite ($CaSO_4 \bullet 0.5\ H_2O$), but less than in gypsum ($CaSO_4 \bullet 2\ H_2O$). However, the precise determination of $H_2O$ by means of this method is prone to errors. Microprobe BSE imaging revealed a higher density of the Ca-sulphate compared to normal rock forming minerals quartz and feldspar, thus pointing towards bassanite (2.7 g/cm$^3$) instead of gypsum (2.3 g/cm$^3$). In samples AN15 (Archambault Ridge North) and PT05 (Point 3350), Ca-sulphates occur as traces only; they have not been investigated in detail in these samples.

In general, bassanite is a relatively rare mineral, because it may hydrate in a humid atmosphere to the fully hydrated $CaSO_4$ modification gypsum ($CaSO_4 \bullet 2\ H_2O$), or, at elevated temperatures, dehydrate to the anhydrous anhydrite ($CaSO_4$). The stability of bassanite is temperature and – to a lesser extent – pressure dependent (McConnell et al. 1987; Yamamoto and Kennedy 1969). A temperature of more than about 105°C is required for bassanite formation at a pressure of about 350 bar (see Fig. 5.4), which is a plausible assumption for the SPF (see Sect. 5.3 for a pressure estimation).

Field evidence suggest a humid climate during deposition of the SPF (see Sect. 1), thus bassanite cementation can not be related to an arid climate, for example by dehydration of earlier gypsum cements. An IGV of 20 % in sample MA06-1 also argues against a very early formation. Instead, a precipitation from hot fluids related to intrusion of Ferrar dolerites is most likely, even more if the close distance to the dike is taken into account. The temperature of more than about 105°C may resemble local conditions close to the dike. The origin of sulphur required for bassanite formation is unknown, but may be magmatic and derived from the intruding dolerites. Especially favourable pathways for the fluids may have been opened by the formation of the EHT-diatreme in section MA.

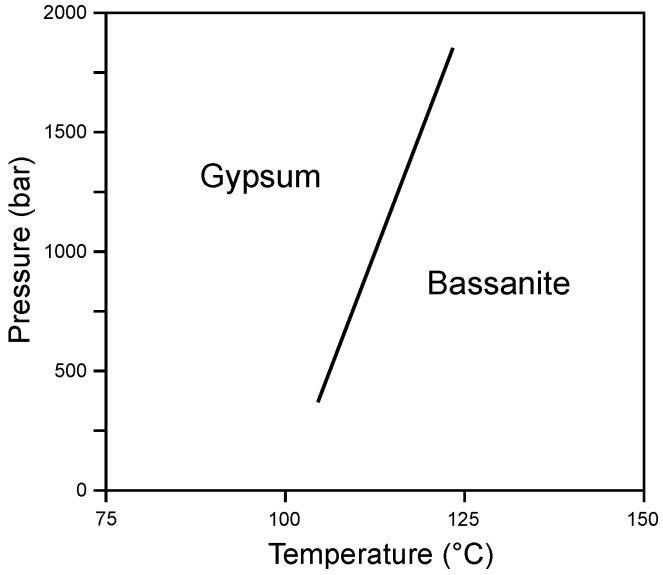


Fig. 5.4: An experimentally determined univariant pressure-temperature plot for the co-existence of gypsum and the hemi-hydrate bassanite (modified from McConnell et al. 1987).

## 5.2.6 Jarosite

Jarosite ($KFe_3(SO_4)_2(OH)_6$) has been found only in sample MA06-1, which contains also bassanite. It was probed by EMP (EDX) measurements, resembling closely the ideal chemical composition. Sodium has not been detected.

Jarosite precipitated mainly in zones free of bassanite or along the boundary zone of bassanite cementation. The geometric relationships indicate that jarosite formed contemporaneously to bassanite. Average point counting data of 0.5 vol% are misleading, as in some parts of the sample jarosite is completely absent, whereas it is much more frequent in other parts. As stated for bassanite, the precipitation of jarosite is most likely related to the intrusion of Ferrar dolerites.

## 5.2.7 Clay minerals

### 5.2.7.1 Kaolinite

Kaolinite is present as pore filling cement in the mature quartz arenites of section ST (5 - 6 vol%), where it post-dates quartz overgrowths, and from the southern part of the working area (sections TP, AG, ER). In sample AN15, kaolinite post-dates chloritic grain coatings. Additionally, in some samples traces of kaolinite have been found, possibly as alteration product of volcanic lithoclasts.

Kaolinite formation from oxygenated pore fluids is thought to occur at temperatures above about 100°C (e.g. Morad et al. 1990 and references therein), but kaolinite may form at much lower temperatures, especially when pH is low (Bjørlykke 1983; Bjørlykke and Brendsdal 1986; Bjørlykke et al. 1989; Solano-Acosta et al. 2008). However, an upper stability limit of kaolinite is given by various reactions. Dissolution of kaolinite and reprecipitation as dickite may take place already at temperatures of 90-130°C (Worden and Burley 2003). The presence of $K^+$ in the pore water may lead to illitisation above usually 120 to 125°C (Aargaard et al. 1990; Morad et al. 1990), although, under special conditions, illitisation of kaolinite has been reported at about 100°C (Ehrenberg 1993; Worden and Burley 2003). K is usually derived from contemporaneous dissolution of K-feldspar, however, in absence of K, illitisation is not possible and kaolinite can be stable to up to 200°C and transform to pyrophyllite at this temperature (Bjørlykke et al. 1989).

Another possible diagenetic reaction of kaolinite to chlorite requires $Fe^{2+}$ and $Mg^{2+}$ (Hower et al. 1976). These ions may be originate from increasing illitisation of smectite, thus this reaction can take place at a wider range of temperatures between about 60°C and possibly more than 120°C.

While in the lower part of section ST and in the sections TP, AG, and ER the kaolinite appears to be unaltered, in the upper part of section ST illite/chlorite forming pseudomorphoses after kaolinite booklets were observed in few cases, indicating that the reactions stated above have been taken place locally. The local occurrence beside unaltered kaolinite in a single thin section possibly shows that the alteration reaction was controlled by fluid chemistry rather than by temperature, thus a burial temperature cannot be deduced.

#### 5.2.7.2 Chlorite and chloritic mineral paragenesis

Chlorite has been found occasionally as grain coating rim (e.g. samples AN15, PT05). In sample AN15 it predates kaolinite. Radial, pore-filling chlorite characteristic for deeper burial has not been observed. However, chlorite is rare and irregularly distributed, and no further attempt was made for analyses.

In samples from central and northern parts of the working area (sections AN, SP, SPP, RB), a chlorite-like mineral occurs as grain-coating cement in paragenesis with other (clay) minerals. The constituents of the paragenesis and their fractions vary from section to section and even from sample to sample within a single section. In some samples, the paragenesis pre-dates feldspar dissolution and zeolite precipitation, while it is overgrown by small quartz crystals in other samples.

EDX analysis resulted in Si, Al, Fe, Mg and minor Ca or Na for its chemical composition. These elements match chlorite composition apart from Ca and Na, indicating intergrowth with other minerals, possibly smectite. Optically, this could not be determined. As K is absent, illite is unlikely to be an important constituent. In one sample, a post-dating of quartz cement has been observed. Feldspar was dissolved later, thus these coatings are a relatively early precipitates.

In some samples from section CHW, grains are rimmed by a greenish-brownish mixture of minerals, accounting for 3 - 4 vol% (point-counting result). It appears to consist of clay minerals (probably chlorite, smectite) and, in contrast to the paragenesis described above, it additionally contains iron oxides or hydroxides. This paragenesis usually pre-dates zeolite formation and feldspar dissolution, suggesting early formation similar to the paragenesis described above. However, it is in some samples also post-dated by zeolite precipitation.

#### 5.2.7.3 Smectite and mixed layer illite/smectite minerals (I/S)

The clay mineralogy of mudstones is usually related to source lithology and climate (Sect. 3.6). However, as the presence of expandable clay minerals may give important information about maximal burial temperatures, these minerals are included here.

Smectite or expandable smectite layers in I/S mixed layers have been identified by XRD in intercalated mudstones. Smectite is present in all mudstones apart from one sample (section AG), in which its absence is most likely primarily due to different source lithologies (see Sect. 3). Comparison with experimental and calculated diffraction profiles (Hower 1981; Środoń 1980) suggests a smectite content between about 30 and 70 %.

The presence of smectite indicates temperatures of less than about 65-90°C (Aargaard et al. 1990; Boles and Franks 1979; McKinley et al. 2003). With increasing temperature, irregularly stratified I/S mixed-layers are formed, transforming into regularly stratified I/S mixed-layers and finally to illite. The onset of the invariable ordering is thought to start at about 80 - 100°C (Dypvik 1983; Pearson et al. 1983) at a smectite content of about 35 - 40%

(Johns and Kurzweil 1979; Perry and Hower 1972). Above 80 % illite layers in I/S minerals, illitisation reaction slows down considerably and the proportions seem to reach a range of stability (Bruvoll et al. 2004; Perry and Hower 1972; Smart and Clayton 1985). However, at these proportions, the expandable component is difficult to detect with conventional XRD measurements (Shata et al. 2003).

The use of smectite in I/S mixed layers as a palaeogeothermometer was firstly proposed in 1979 (Hoffman and Hower). The conversion process with increasing illite proportion accompanied by increasing regularity of ordering is not only a function of temperature and time (Hower et al. 1976; Perry and Hower 1972), but is also controlled by fluid flow and fluid chemistry (Abid et al. 2004; Meunier and Velde 2004). As the latter parameters are unknown for most of the time of a basins history, temperatures or temperature ranges are difficult to assign to certain smectite fractions in I/S minerals.

Even if exact temperatures are difficult to assign, a maximum temperature for the existence of expandable layers in I/S mixed layers during burial diagenesis can be assumed. This is commonly thought to lie between 125 and 160°C (Perry and Hower 1972), although other authors suggest temperatures of only 100°C (see Bjørlykke et al. 1989 for references). However, smectite as product of hydrothermal alteration has been reported from temperatures of more than 200°C (e.g. Horton 1985).

## 5.2.8 Fe-Oxides and Fe-Hydroxides

### 5.2.8.1 Hematite

Hematite cements occur in a few samples throughout the working area (e.g. AN01, AN16, TP05, SP01, and PT05). Their abundance is usually below 3 vol%, and they often appear as traces only. However, in few samples, they reach 6 – 16 % of rock volume (point counting data), filling pores and forming thick crusts around detrital grains. Illite, as a frequently embedded mineral within hematite cements (Schöner 2006), has not been found in this case.

In the SPF, hematite cements are more frequent in stratigraphic lower parts. The IGV of these samples is relatively high (up to 18 %) indicating a relatively early formation of hematite close to the deposition surface.

For hematite cements, a variety of origins have been proposed, for example in situ formation of red hematitic soil, aging of amorphous limonite, and dehydration of crystalline goethite (Goss 1987; Gualtieri and Venturelli 1999; Walker 1967; Walker 1976). Hematite is stable during diagenesis until it recrystallizes as magnetite under low grade metamorphic conditions.

### 5.2.8.2 Fe-hydroxides

Laminated Fe-hydroxide cements occur in sample SHS04 only (17.5 %), pre-dating compaction. Their appearance implies formation from a gel-like state (A. Kronz 2007, pers. comm.). An intergrowth with clay minerals has been confirmed by EMP analysis.

Fe-hydroxides may dehydrate to form hematite at elevated temperatures, with particle size controlling the kinetics (Berner 1969). A maximal stability temperature of 105°C is reported for an example of the Triassic in Denmark (Weibel and Grobety 1999). Experimental studies under varying reducing conditions suggest temperatures of possibly less than 80°C (Brown et al. 1998), or between 200 and 270°C at oxic conditions (Gualtieri and Venturelli 1999) for dehydration of Fe-hydroxides.

## 5.3 Compaction

Besides cementation, compaction and the related reduction of porosity is an important process during sandstone diagenesis (e.g. Ehrenberg 1989; Houseknecht 1987; Lundegard 1992; Paxton et al. 2002). In the SPF, porosity is often very low (Fig. 5.5, left panel). The IGV is highly variable due to the different amounts of ductile lithoclasts, the various cements, and their different timing related to compaction, respectively (Fig. 5.5, right panel).

Due to the generally moderate to poor sorting of the sandstones, an initial porosity of about 30-35 % can be assumed (Beard and Weyl 1973). The reduction of porosity by compaction starts with mechanical compaction, thus with repacking of loose grains by rotation, slippage and fracturing of brittle grains. A reduction to a porosity of zero even with predominating ductile grains is thought to require a load of at least 2 km sediments (Worden and Burley 2003, see also Fig. 5.8). As the Beacon sediments are overlain not by sediments (initially around 1.7 g/cm$^3$ at 35 % porosity) but by the Ferrar Group Kirkpatrick basalts (2.9-3.1 g/cm$^3$, R. Hanemann 2009, pers. comm.), the required burial depth for destruction of pore space is much lower. The pressure related to the overlying igneous rocks is about 300 to 460 bar, if 1000 m of Kirkpatrick Basalts and 300 m Ferrar Dolerites are assumed in addition to the 250-300 m of SPF and SHF.

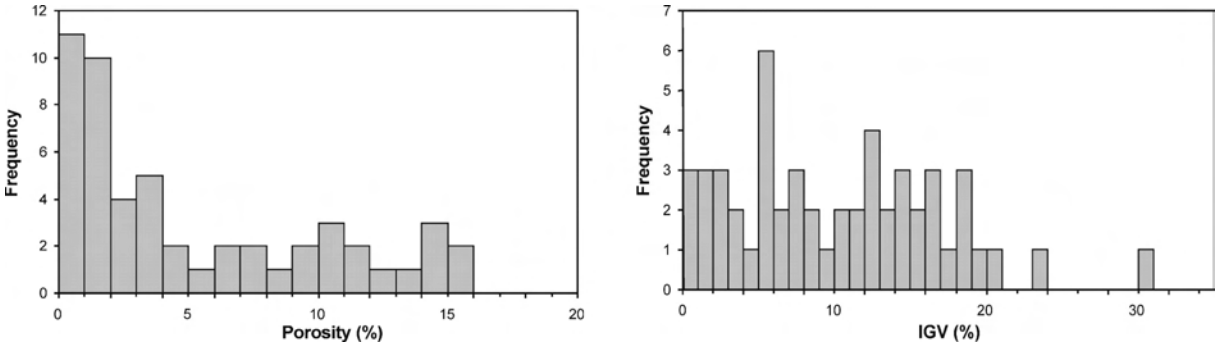


Fig. 5.5: Sample frequency of porosity and IGV in samples of the SPF. Porosity is usually below 15 %, with a maximum at values between 0 and 4 % (left panel). The IGV is irregularly distributed, possibly pointing towards a cementation at different stages of compaction.

Deformation of altered ductile grains and micas has been observed frequently in the SPF. Alteration of grains may have been favoured by emplacement of Ferrar dolerites, which was most likely associated by a hot fluid pulse. A major influence of compaction, usually prior to cementation, is indicated by the relationship of compaction to cementation. In Fig. 5.6, the relative amounts of compactional and cementational porosity losses are compared, showing that compactional processes were much more important for porosity loss than cementation.

IGV and porosity are difficult to compare between samples, because the amount of unstable lithic grains is highly variable (see Sect. 3), as is the distribution of early pore-filling cements. For the lithoclast-poorer samples (> 65 % rigid grains) with minor or no cementation (less than about 2 %) from sections SHS, PT, SHA, SP, SPP, and RB, porosity and IGV usually range from 8 % to 20 % (Fig. 5.7). Lithoclast-richer samples (< 60 % rigid grains) exhibit less porosity and IGV, both approaching 0 % in some samples. Rocks from southern parts of the working area (sections TP, AG, ER) also show low IGV of 3 - 6 %, despite the presence of more than 65 % rigid grains. As many of the frequent K-feldspar clasts in these rocks are partly or totally kaolinitised, they may possibly not be classified as ‘rigid’ clasts, as done in Fig. 5.7.

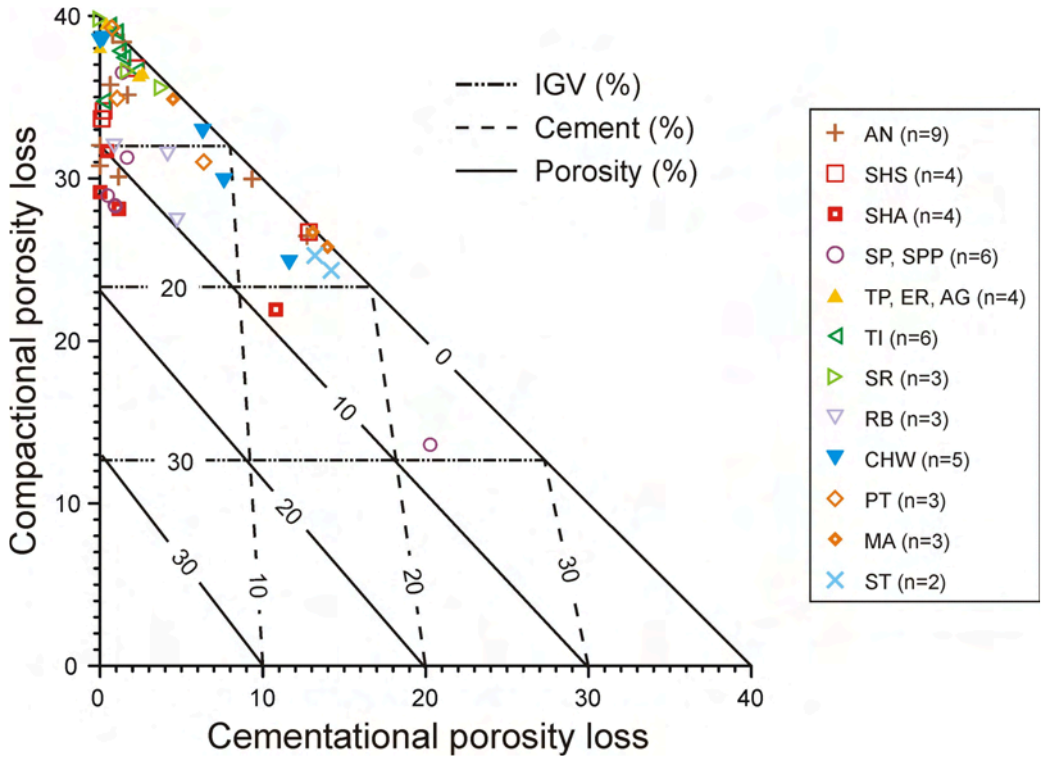


Fig. 5.6: Compactional versus cementational porosity loss diagram (after Lundegard 1992). Most of the porosity loss is related to compaction, whereas cementational porosity is less important. The initial porosity of 40 % in this diagram is higher than the assumed initial porosity of the moderately to poorly sorted sands of the SPF.

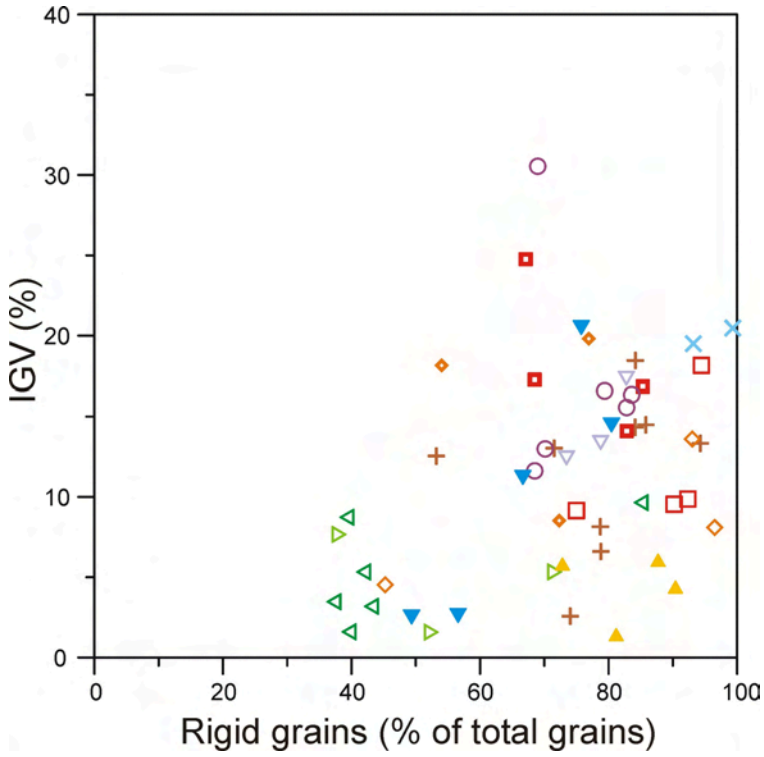


Fig. 5.7: Comparison of IGV with the relative amount of rigid grains (quartz including chert, feldspar, granitic rock fragments and heavy minerals). A lithoclast-richer group (around 40 % to 60 % rigid grains) with IGV up to 8 % can be distinguished from a lithoclast-poorer group (> 65 % rigid grains) with usually higher but strongly variable IGV. These two groups are identical to the quartz-poorer and quartz-richer group described in Sect. 3. In cases of a very high IGV (> 20 %), early cementation is pervasive. Legend as in Fig. 5.6.

Due to the relationship of compactionally induced volume reduction to the distribution of authigenic mineral phases (e.g. zeolites, see Tab. 5.4), it is possible to identify two phases of compaction. The first is most likely related to early sedimentary burial by higher stratigraphic parts of the SPF (and possibly the SHF). For the second phase, the emplacement of Ferrar igneous rocks is the most obvious argument.

The variation of IGV in uncemented or poorly cemented samples (e.g. clay minerals as grain coatings only) can therefore partially be explained by different portions of unstable clasts. However, even in samples with comparable proportions of rigid grains, the IGV varies strongly (Fig. 5.7). A determination of the maximal burial of the SPF using IGV is therefore difficult, but the common presence of IGV up to 20 % in relatively quartz-rich samples indicates that – apart from the known burial (Ferrar igneous rocks) – no additional major (sedimentary) load can be deduced (see also Di Giulio et al. 1997). The very low IGV (less than 8 %) in some quartz rich samples may result from a very rapid burial of the SPF due to the rapid intrusion and effusion of Ferrar rocks (780 m in 1 My or less, according to Heimann et al. 1994). Instead of a rearrangement of grains, a diffuse breaking and fracturing of quartz and feldspar grains took place (Di Giulio et al. 1997).

Figure 5.8 shows the relation of porosity to depth and pressure that is commonly assumed for sandstones with different proportions of rigid to unstable grains (Paxton et al. 2002; Worden and Burley 2003). The proposed path of SPF sandstones from an initial pore space of about 30-35 % to final values between 0 and 15 % at pressures between 300 and 460 bar is overplotted in the diagram.

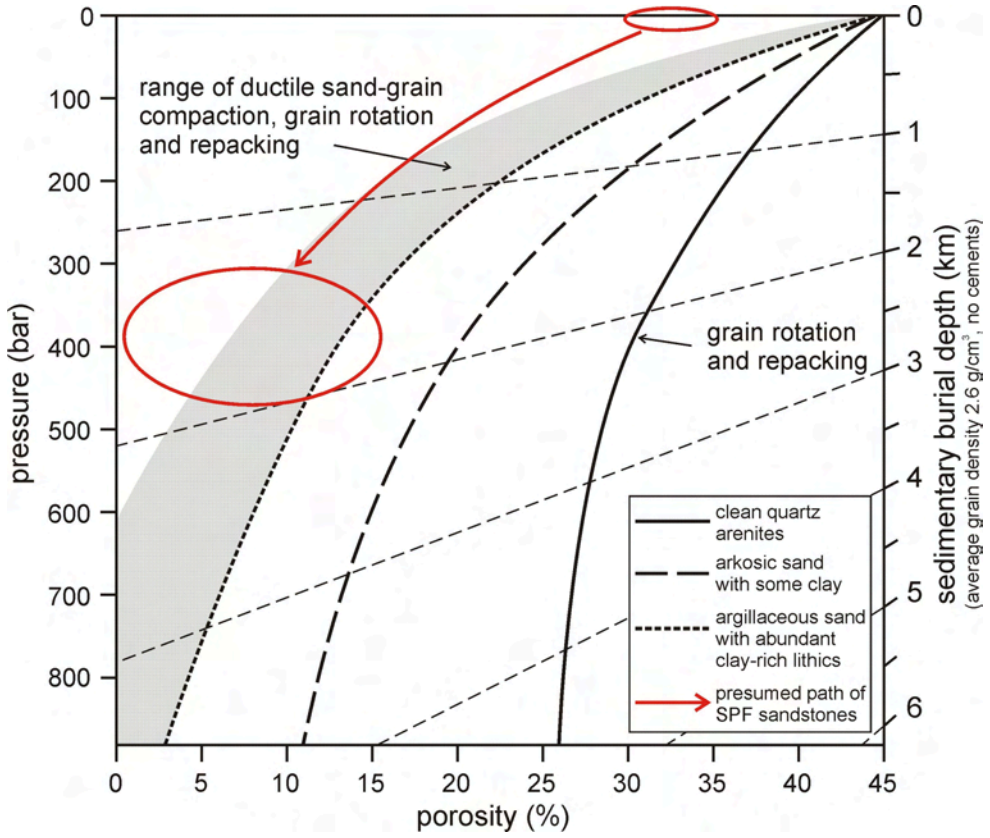


Fig. 5.8: Porosity versus pressure and depth diagram for sandstones of different compositions and moderately-well to well sorting and an initial pore volume of 45 % (modified after Worden and Burley 2003). An average grain density of 2.6 g/cm$^3$ and the absence of cementation and grain dissolution were assumed for the calculation of pressure. The SPF sandstones are thought to develop from an initial pore volume of 30-35 % to a pore volume of 0-15 %. The pressure of 300-460 bar is calculated from a burial by 1000 m effusive and 300 m intrusive Ferrar Group magmatites (2.9-3.1 g/cm$^3$) and the thickness of SPF (~250 m) and SHF (~50 m). The proposed evolutionary track of the SPF sandstones is shown in red.

## 5.4 Discussion: Diagenetic evolution and temperature development

None of the samples contains all of the authigenic minerals observed, and many precipitates and reactions have been found in a few samples only. Therefore, it is difficult to summarize the diagenesis of the SPF in a single paragenetic sequence.

However, in some samples relations of cements among each other and to compaction have been observed, as described above. The diagrams in Fig. 5.6 and 5.9 (after Ehrenberg 1989), show that compaction was generally more important for porosity loss than cementation.

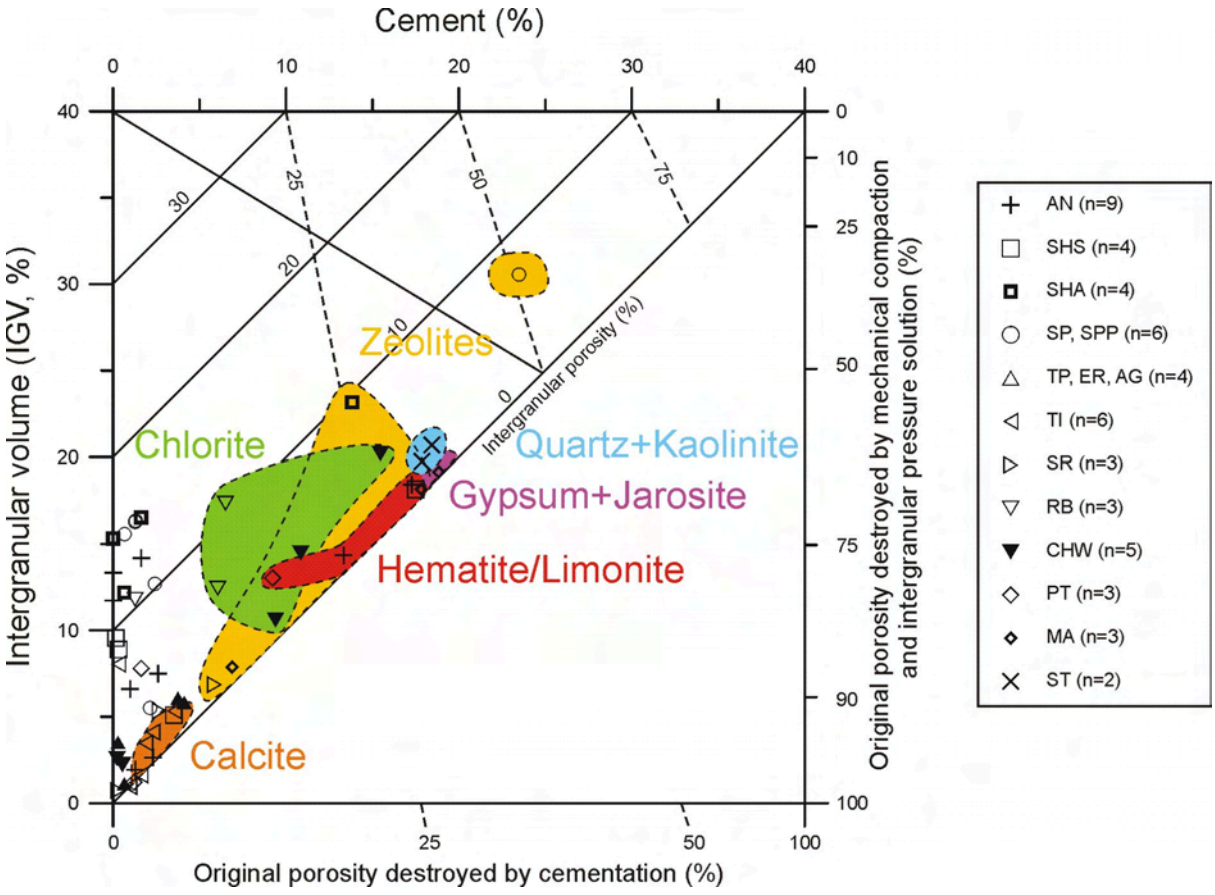


Fig. 5.9: Intergranular volume plotted versus proportion of cement (after Ehrenberg 1989). Cements are only listed if they contribute more than about 2 vol%). In most cases, compaction is more important than cementation for the reduction of porosity. 'Chlorite' refers also to different mineral parageneses containing chlorite.

All cements except the zeolites in samples SPP05 and SPP07 formed after a considerable compactionally induced porosity loss of about 50-90 % of the original pore space at time of deposition. Calcite formed even later. The relations of authigenic minerals, mineral reactions and compaction in the SPF, are summarized in Tab. 5.4, and Fig. 5.10 visualizes the paragenetic sequence derived from these information.

| Mineral/reaction | Pre-dating | Post-dating | Contemp. to | Selected samples |
|---|---|---|---|---|
| Quartz | Kaolinite, zeolite | Compaction | | ST05, ST09 |
| Fe-(Hydr)Oxides | Compaction 2 | Compaction 1 | | AN01, AN16 |
| | Calcite | | | PT05, AN16 |
| Zeolites | Compaction 2 | Compaction 1 | | CHW06, MA06-3 |
| | | K-Fsp. dissolution | | CHW06, CHW10 |
| | | | Albitis. of Plag. | SR03 |
| Zeolites, fan-like | Compaction | | | SPP05, SPP07 |
| Calcite | | Compaction | | AN18, SHS01 |
| | | Quartz, Kaolinite | | SHS01, ST09 |
| Bassanite | Compaction 2, Fsp-dissolution | Compaction 1, Fsp-dissolution | Jarosite | MA06-1 |
| Chloritic mineral paragenesis | Feldspar dissol. Zeolites, Compac. 2 | Compaction 1, Zeolites | Zeolites (?) | RB06, CHW06, CHW10 |

Tab. 5.4: Summary of the relations of the various authigenic minerals, mineral reactions and compaction. Some authigenic minerals indicate the presence of at least two phases of compaction.

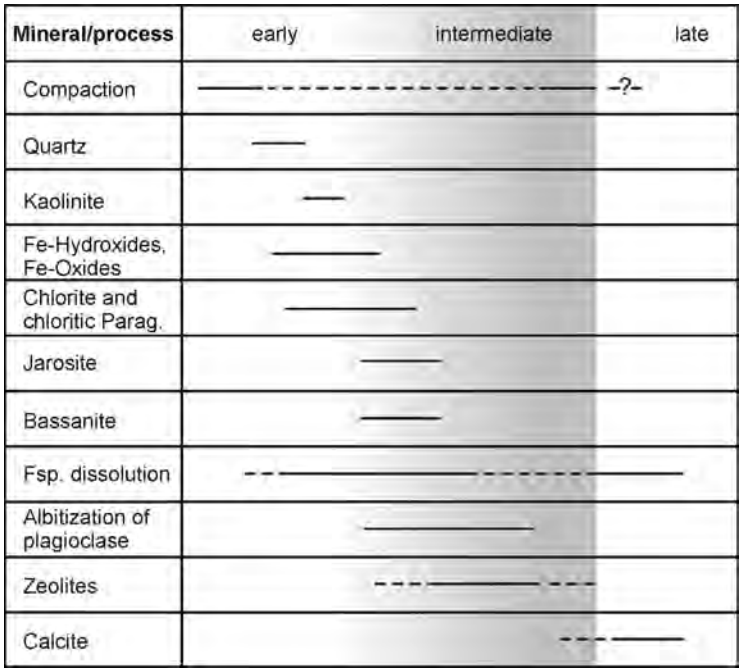


Fig. 5.10: Paragenetic sequence of diagenetic products and reactions in the SPF as derived from the observations listed in Tab. 5.4. The grey shaded area indicates the presumed time for the emplacement of the Ferrar igneous rocks.

Within the SPF, a great variety of authigenic minerals have been found, of which zeolites, some clay minerals, and the feldspar reactions can be used as indicators of palaeotemperature (Tab. 5.5, Fig. 5.11). Some of the mineral reactions provide only lower boundaries to the burial temperature. However, based on the available data, the maximum burial temperature in the southern parts of the working area south of the Priestley glacier were probably 90-100°C. This temperature is inferred from authigenic laumontite (> 90°C) and incompletely albitised plagioclase (< 100°C) in a sample from the Skinner Ridge (SR03). The occurrence of smectite (< 125°C) in a mudstone sample from the Timber Peak, and widespread kaolinite in sections TP, AG, and ER, support this conclusion.

In the Deep Freeze Range, indicators for palaeotemperature are more frequent. Clinoptilolite has been found in samples from the Shafer Peak and from Mt. Adamson, indicating a burial temperature of less than 90°C. This is in concordance with the abundance

of smectite in many mudstones from section SHA and SHB. The slightly more 'heulanditic' composition of zeolites in sample SHA06 at a distance of about 5 m to the next sill compared to the 'clinoptilolitic' composition of the zeolites in sample SHA12 about 16 m away, can be interpreted as a result of the thermal influence of the sills. The minimum of 105°C derived from the occurrence of bassanite in sample MA06-1 are related to a small dike; however, this does not stand in contrast to the maximum of 90°C in upper parts of the section.

In section CHW, clinoptilolite is lacking, and the occurring heulandite implies temperatures between 90 and 120°C. Although albitization of plagioclase is still incomplete, it is more widespread than in sample SR03. Expandable layers in I/S mixed layers and kaolinite are present in the nearby section ST (< 125°C).

Due to clinoptilolite in two samples a temperature below 90°C can be assumed for section SPP. In the neighbouring section SP, analcime gives a temperature between 90 and 125°C (supported by smectite in a pelite). Taking into account the maximal 90°C of the overlying section SPP, the maximal burial temperature of section SP was presumably closer to the lower end of the given range.

| Mineral / mineral reaction | Temperature range | Reference |
|---|---|---|
| Albitization of plagioclase | 60-100°C | (Morad et al. 1990) |
| Albitization of K-feldspar | 120-150°C<br><120°C | (Baccar et al. 1993)<br>(Saigal et al. 1988) |
| K-feldspar dissolution | <145°C | (Aargaard et al. 1990) |
| Clinoptilolite | 50-90°C | (Utada 2001a) |
| Heulandite | 90-120°C | (Utada 2001a) |
| Analcime | 90-125°C | (Utada 2001a) |
| Laumontite | >90° | (Noh and Boles 1993) |
| Expandable I/S mixed layers | <125°C<br><100°C | (Perry and Hower 1972)<br>(Bjørlykke et al. 1989) |
| Kaolinite | <125°C | (Aargaard et al. 1990) |
| Bassanite | c. 105°C | (McConnell et al. 1987) |

Tab. 5.5: Temperature sensitive authigenic minerals or mineral reactions, and their temperature range of formation or reaction assumed for this study.

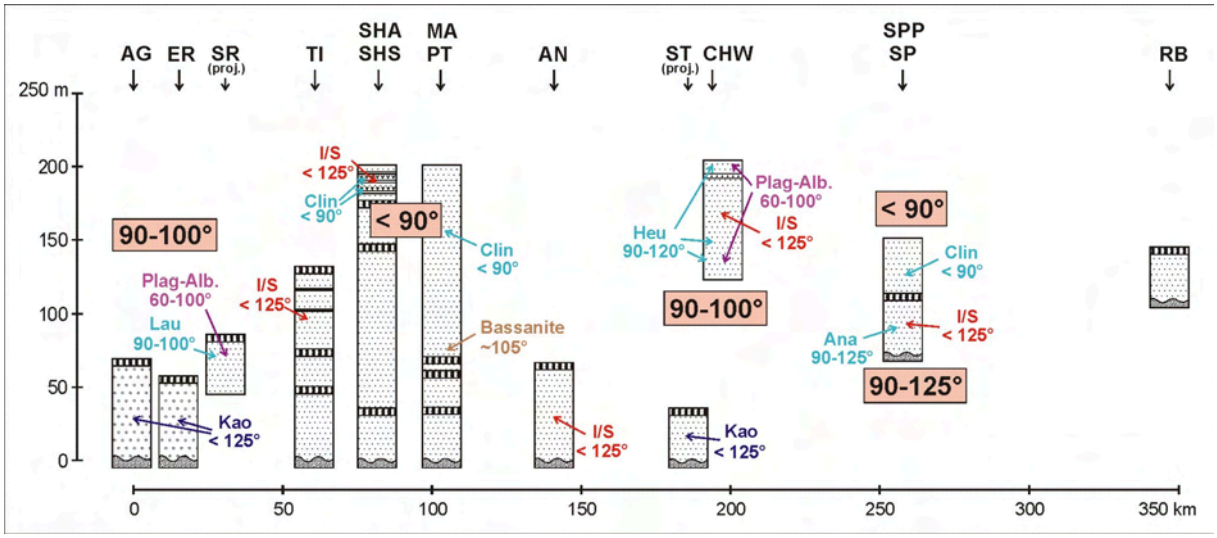


Fig. 5.11: Cross section along the analysed sections showing a selection of temperature sensitive authigenic minerals and mineral reactions in the SPF and the presumed maximum temperatures during diagenesis. See Fig. 1.3 for the trace of the cross section, and Fig. 1.8 for legend. Plag-Alb: Albitisation of Plagioclases; Ana: Analcime; Clin: Clinoptilolite; I/S: Illite/Smectite mixed layer minerals or Smectite; Kao: Kaolinite; Lau: Laumontite.

Apart from minor changes in chemical composition of zeolites in section SHA, it was not possible to prove the influence of the Ferrar sills, as shown for the maturity of organic matter (Berner et al. 2009b) and as reported from South Victoria Land (Bernet and Gaupp 2005). In most cases, sampling distance to the next sill was greater than for the study in SVL, and probably too large to detect possible thermal influences. Also, samples were not taken in order to investigate the thermal influence of sills. Therefore, the temperatures between < 90°C and < 120°C can be regarded as plausible maximum temperatures during burial diagenesis. This temperature agrees with the lowest vitrinite reflectance values of about 0.4 %Ro, measured on detrital organic matter in the SPF (Berner et al. 2009a). Higher temperatures were present in contact aureoles close to the Ferrar sills (Berner et al. 2009a; Berner et al. 2009b), but certainly not extending over a long time (maximal by thousand years, depending on sill thickness; L. Viereck-Götte 2009, pers. comm.). This was obviously not enough to produce significant mineralogical changes, but led to a significant increase of maturity of organic matter, highlighting the different response times of organic and anorganic geothermometry (see also Smart and Clayton 1985).

A minimal burial pressure can be derived from the known overburden of Ferrar group igneous rocks, consisting of about 1000 m effusive Kirkpatrick basalts and about 300-350 m intrusive Ferrar dolerite sills (Sect. 5.3). Their high density of 2.9 - 3.1 g/cm$^3$ (R. Hanemann 2009, pers. comm.) lead to burial pressures between about 300 and 460 bar, depending on the stratigraphic position within the SPF.

For the entire TAM, a geothermal gradient of 25 ± 8°/km has been suggested (Fitzgerald 1994; Lisker et al. 2006). However, during intrusion and effusion of Ferrar Group magmatites, NVL was part of a large igneous province and much higher temperatures must be expected, especially if an extensional tectonic setting is assumed (Elliot 1992; Schmidt and Rowley 1986). An envelope for possible p-T paths of the SPF sandstones during and after deposition is shown in Fig. 5.12.

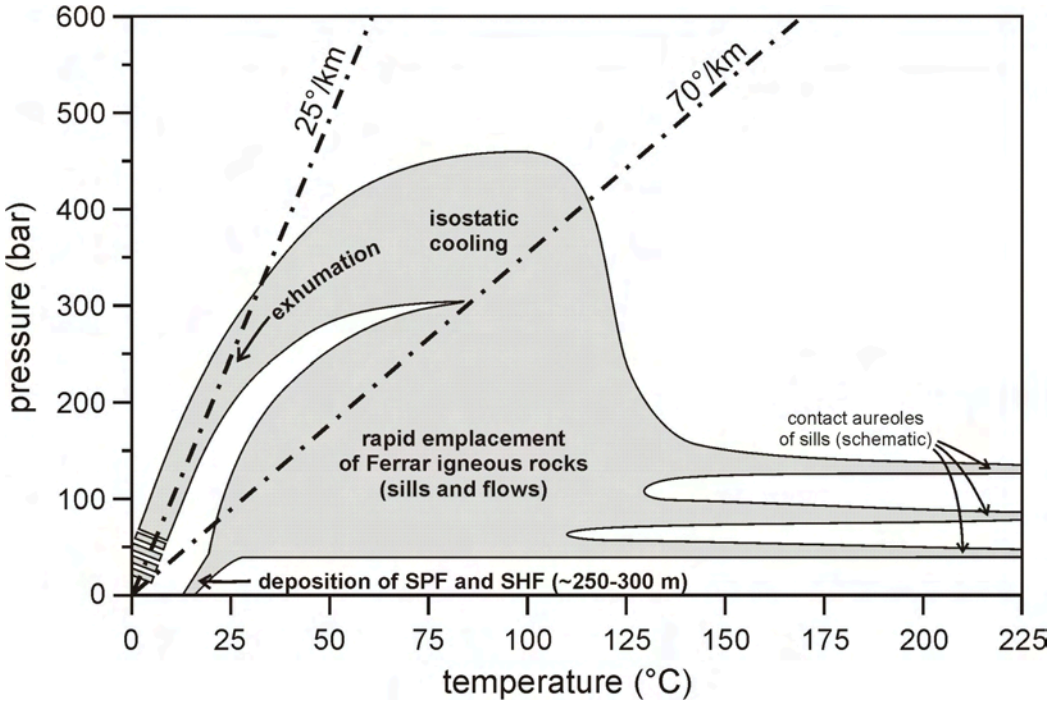


Fig. 5.12: Envelope of possible pressure-temperature-paths for the SPF during and after deposition. Intrusion and effusion of Ferrar magmatites were assumed to follow directly upon each other. The geothermal gradients of 25 and 70°C/km are shown for comparison. Many diagenetic processes took place most likely during emplacement of the Ferrar rocks and during the time indicated as 'isostatic cooling', when a smaller geothermal gradient was (re-)established.

The relatively large temperature variation in Fig. 5.12 is related to the pressure difference from base to top SPF, enhanced due to the Ferrar sills, and the temperature differences related to intrusive sill contacts. The proposed temperature range of < 90 to maximal 120°C derived from temperature sensitive authigenic minerals and mineral reactions most likely represents the time of isostatic cooling after effusion of Ferrar Group lava and the (re-)establishment of a smaller geothermal gradient.

From temperature sensitive authigenic minerals, there is no evidence for an additional overburden younger than the Ferrar Group. The compaction of the sandstones as concluded from their IGV is inconsistent, but this can be related to different sandstone compositions (rigid versus instable grains), and to the abrupt burial due to the rapid emplacement of Ferrar igneous rocks. An earlier phase of compaction most likely took place during sedimentary burial. In combination with the results of organic geochemistry and vitrinite reflectance, a Cretaceous basin (as proposed by Lisker and Läufer 2007) is unlikely for the analysed area in southern NVL. The temperature development of the SPF since its deposition as proposed by the results of this study, is shown in Fig. 5.13. Indications for thermal events (Molzahn et al. 1999) shown in this diagram have not been found within the sandstones directly, but radiometric K-Ar ages of the Ferrar igneous rocks in NVL are mostly younger than their proposed 184 Ma (Encarnación et al. 1996; Minor and Mukasa 1997) and show considerable variations (Brotzu et al. 1988; Di Giulio et al. 1997). A (partial) resetting of these ages by one or more thermal events may be a possible explanation.

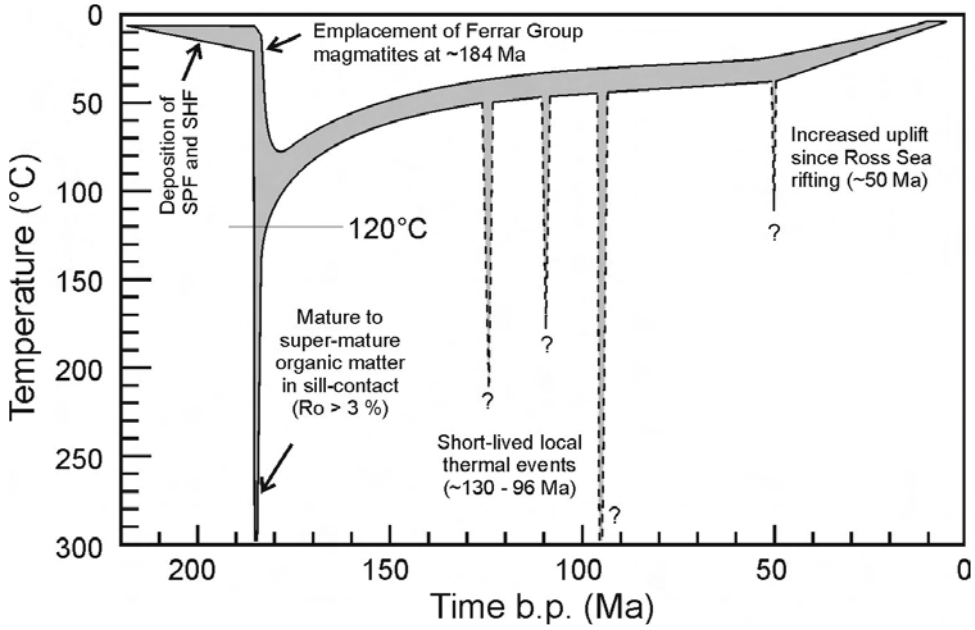


Fig. 5.13: Temperature-time burial model for the SPF. The mid-Cretaceous thermal events between 130 and 96 Ma are related to break-up processes of Gondwana (Molzahn et al. 1999, and references therein). The 55 Ma event is uncertain and only suggested for the beginning of Ross Sea rifting to explain AFT data (Lisker and Läufer 2007).

# 6 Conclusions

Composition, provenance, and diagenesis of the 'Beacon sandstone' in NVL have been analysed comprehensively, leading to new findings about shape, setting, and evolution of the Transantarctic Basin. In addition, the structural geology of NVL was studied by modelling the sub-Beacon unconformity. The most important results of this thesis are listed in what follows.

### Structural geology

(1) The displacement of the modelled sub-Beacon unconformity in NVL is in agreement with the dextral strike-slip system assumed by previous authors (e.g. Rossetti et al. 2003b). However, based on the model, NW-SE trending faults were interpreted as possible thrusts.

(2) The fault pattern can be explained to be the result of the same tectonic regime. A stress field in NNE-SSW direction may have lead to the formation of normal and reverse faults side by side. However, a slight rotation of the stress field and formation of faults during two separate events may provide a better explanation for the situation. This scenario has been previously assumed on a larger scale, from E-W extension in an early phase of Ross Sea rifting to a NW-SE extension lateron. Many if not most of the tectonic displacement took place along structures predefined during the Early Palaeozoic Ross Orogeny.

(3) No evidence for syn-sedimentary faulting during the Triassic to Early Jurassic was found. Accordingly, significant tectonic movements at faults considered in this study must at least be younger than the deposition of the Section Peak Formation. However, during deposition of Permian sediments in northern NVL syn-sedimentary faulting may have been active.

### Provenance of the Section Peak Formation

(4) Within the SPF, six different sandstone types have been identified by petrographic analyses. This result is supported by the evaluation of geochemical, mineralogical, and isotope data. Five of the sandstone types represent local inputs into the Transantarctic Basin from sources within NVL, or from regions located close to NVL at the time of deposition. The most frequent sandstone type is interpreted as longitudinally transported along the basin from sources outside NVL, possibly from SVL, or from the CTM.

(5) Quartz-rich sandstones within the SPF were not necessarily shed from the western, continental side of the Transantarctic Basin (Collinson et al. 1994). Local sources in NVL were also capable of producing quarz-rich debris despite lying on the eastern, arc side of the basin. The same must be assumed for other parts of the Transantarctic Basin.

(6) Detritus of a syn-sedimentary active magmatic arc along the active margin of Gondwana is present in some of the locally sourced sandstone types and in the axially transported sandstones. During basin evolution, arc derived material becomes increasingly more frequent within the axial flow.

(7) The conglomerates in the southern Eisenhower Range originate from a deeply weathered, local source within the Wilson terrane. A tectonic uplift is assumed to have resulted in the relief necessary for providing the coarse material. This uplift points towards a tectonic activity of the Ross High Foreswell until the Late Triassic, at least in parts of the NVL sector of the Transantarctic Basin.

### Regional geology of Antarctica

(8) Detrital zircons of the SPF with pan-African ages relatively frequently exhibit cores of Grenvillian age. This indicates a spatial relation of the zircon forming events from these times, previously interpreted as zones of rejuvenation (Yoshida et al. 2003).

(9) The 500-700 Ma old (pan-African) detrital zircons from the SPF present in axially transported material (type C sandstone) may originate from the ice-covered area below the polar plateau. The occurrence of this zircon age cluster correlates with an extremely garnet-rich heavy mineral assemblage. Garnet chemistry points toward a source of metasediments/granulites and basic gneisses/eclogites.

### Shape, setting, and evolution of the Transantarctic Basin

(10) The axis of the Transantarctic Basin followed roughly about the N-S oriented outcrops (coast parallel) in NVL. However, the basin axes shifted while the basin enlarged, and a sedimentary onlap developed on both the continental and the arc side of the basin. The maximum width of the basin was about 250 km shortly before the end of sedimentation caused by emplacement of Ferrar magmatites in the late Early Jurassic (184 Ma).

(11) Although a (retro-arc) foreland setting is assumed for the Transantarctic Basin (Collinson et al. 1994), in NVL the generally low sedimentation rate (6-15 m/Ma), the fining upward trend in some sections, the retrogradation, and the missing sedimentary recycling (‘cannibalism’) strongly argue against this hypothesis. Instead, an epicratonic setting is much more likely for the NVL sector of the basin. However, a (retro-arc) foreland setting may have been present in other parts of the basin, for instance in the CTM.

(12) The differences in setting along the strike of the Transantarctic Basin may be related to a varying subduction angle of the Proto-Pacific (Panthalassan) plate underneath Gondwana. Early precursors of sub-crustal processes finally leading to generation of the enormous magma volumes of the Ferrar Large Igneous Province may have also contributed to basin formation and evolution.

### Composition, provenance, and age of the tuffaceous sandstones in the uppermost Section Peak Formation and in the Shafer Peak Formation

(13) The tuffaceous sandstones building up most of the SHF and forming single layers within the upper SPF in the Deep Freeze Range form a mixing range between juvenile and epiclastic material with varying proportions. The juvenile magmatic material is of (?soda-)rhyodacitic composition, and the epiclastic material is compositionally similar to the axially transported sandstones from the uppermost SPF. Vitric shards are characteristic petrographic constituents of the tuffaceous sandstones. Although they are completely altered to authigenic zeolites, their shape is still preserved.

(14) A single juvenile tuff layer lacking epiclastic material has been identified within the upper SPF. This sample yielded a U-Pb (Shrimp) age of 188.2 ± 2.2 Ma. This result proves that deposition of the SPF persisted until the Early Jurassic (Pliensbachian). As a minimum age of 183.6 ± 2.1 Ma for the SHF is imposed by the age of the overlying Ferrar lavas, the depositional age of this formation is fairly well bracketed and can be confirmed as Early Jurassic (Pliensbachian).

(15) The SHF can be correlated lithologically and stratigraphically with the upper Hanson Formation in the CTM over more than 2000 km along the TAM. Similar deposits may also be present in SVL.

(16) The magmatic arc along the active margin of Gondwana is the most likely source for the juvenile material. Distal, ultra-plinian eruptions in a major volcanic province were necessary to generate the large volumes of pyroclastic material found at different locations along the TAM. The exact position of the source is unknown, but it may be located in the Chon Aike Volcanic Province in Patagonia or on the Antarctic Peninsula. However, due to palaeogeographic relationships, the Campbell Plateau, which is covered with sediments today, may also be a possible location for yet unknown volcanic eruption centres.

## Diagenesis of the Section Peak Formation

(17) The maximal burial temperature of the SPF derived from temperature sensitive authigenic minerals or mineral reactions (e.g. zeolites, albitization of feldspar) was below 120°C, for some parts of the higher SPF even less than 90°C. This temperature range was reached during emplacement of the Ferrar magmatites (Ferrar dolerites and Kirkpatrick basalts) shortly after deposition of SPF and SHF. Regarding an enhanced geothermal gradient in NVL as part of the Ferrar Large Igneous Province during the late Early Jurassic, the known overburden of SPF and SHF was sufficient to produce these temperatures. The existence of a Victoria Basin in the Cretaceous with 3 to 5 km of sediments (Lisker and Läufer 2007) is therefore unlikely for southern NVL.

(18) Most of the authigenic minerals and mineral reactions found in the SPF are related to a phase of isostatic cooling after emplacement of Ferrar magmatites and during (re-)establishment of a normal geothermal gradient.

(19) The composition of authigenic zeolites within the sandstones points toward a thermal influence of the sills, as is shown for SVL (Bernet and Gaupp 2005).

(20) For the porosity loss of sandstones, compaction was generally more important than cementation. A minimal burial pressure between about 300 and 460 bar (depending on the stratigraphic position within the SPF) can be derived from the known overburden of Ferrar group igneous rocks. Most of the cements formed after a considerable compactionally induced porosity loss of about 50-90 % of the original pore space at time of deposition. Two phases of compaction can be distinguished from the geometric relation of authigenic minerals: the first is related to burial by sedimentary overburden, the stronger second phase took place during rapid emplacement of Ferrar magmatites.

# 7 References

AARGAARD, P., EGEBERG, P.K., SAIGAL, G.C., MORAD, S., and BJØRLYKKE, K., 1990, Diagenetic albitization of detrital K-Feldspar in Jurassic, Lower Cretaceous and Tertiary clastic reservoir rocks from offshore Norway, II: Formation water chemistry and kinetic considerations: Journal of Sedimentary Petrology, v. 60, p. 575-581.

ABID, I.A., HESSE, R., and HARPER, J.D., 2004, Variations in mixed-layer illite/smectite diagenesis in the rift and post-rift sediments of the Jeanne d'Arc Basin, Grand Banks offshore Newfoundland, Canada: Canadian Journal of Earth Sciences, v. 41, p. 401-429.

ADAMS, C.J., SEWARD, D., and WEAVER, S.D., 1995, Geochronology of Cretaceous granites and metasedimentary basement on Edward VII Peninsula, Marie Byrd Land, West Antarctica: Antarct. Sci., v. 7, p. 265-277.

ADAMS, C.J., WHITLA, P.F., FINDLAY, R.H., and FIELD, B.F., 1986, Age of the Black Prince Volcanics in the central Admiralty Mountains and possibly related hypabyssal rocks in the Millen Range, *in* Stump, E., ed., Geological investigations in northern Victoria Land: Washington, D.C., Antarctic Research Series, American Geophysical Union, p. 203-210.

ARMIENTI, P., GHEZZO, C., INNOCENTI, F., MANETTI, P., ROCCHI, S., and TONARINI, S., 1990, Isotope geochemistry of granitoid suites from Granite Harbour Intrusives of the Wilson Terrane, North Victoria Land, Antarctica: European Journal of Mineralogy, v. 2, p. 103-123.

ARMSTRONG-ALTRIN, J.S., and VERMA, S.P., 2005, Critical evaluation of six tectonic setting discrimination diagrams using geochemical data of Neogene sediments from known tectonic settings: Sediment. Geol., v. 177, p. 115-129.

ARNDT, N.T., and GOLDSTEIN, S.L., 1987, Use and abuse of crust-formation ages: Geology, v. 15, p. 893-895.

BACCAR, M.B., FRITZ, B., and MADÉ, B., 1993, Diagenetic Albitization of K-Feldspar and Plagioclase in Sandstone Reservoirs: Thermodynamic and Kinetic Modeling: Journal of Sedimentary Petrology, v. 63, p. 1100-1109.

BACON, C.A., CALVER, C.R., BOREHAM, C.J., LEAMAN, D.E., MORRISON, K.C., REVILL, A.T., and VOLKMAN, J.K., 2000, The petroleum potential of onshore Tasmania: a review: Mineral Resources of Tasmania, Geological Survey Bulletin, v. 71, p. 1-93.

BACON, C.A., and EVERARD, J.L., 1981, Pyroclastics in the Upper Parmeener Super-Group, near Bicheno, eastern Tasmania: Papers and Proceedings Royal Society Tasmania, v. 115, p. 29–36.

BANKS, M.R., 1981, Late Paleozoic tillites of Tasmania, *in* Hambrey, M.J., and Harland, W.B., eds., Earth's Pre-Pleistocene Glacial Record: Cambridge, Cambridge University Press, p. 495-501.

BARRETT, P.J., 1991, The Devonian to Jurassic Beacon Supergroup of the Transantarctic Mountains and correlatives in other parts of Antarctica, *in* Tingey, R.J., ed., The geology of Antarctica: Oxford, Oxford University Press, p. 121-152.

BARRETT, P.J., ELLIOT, D.H., and LINDSAY, J.F., 1986, The Beacon Supergroup (Devonian-Triassic) and Ferrar Group (Jurassic) in the Beardmore Glacier area, Antarctica, *in* Turner, M.D., and Splettstoesser, J.F., eds., Geology of the central Transantarctic Mountains: Antarctic Research Series: Washington, D.C., American Geophysical Union, p. 339-453.

BARRETT, P.J., and FITZGERALD, P.G., 1985, Deposition of the Lower Feather Conglomerate, a Permian Braided River Deposit in Southern Victoria-Land, Antarctica, with Notes on the Regional Paleogeography: Sedimentary Geology, v. 45, p. 189-208.

BASILE, L., GROUSSET, F.E., REVEL, M., PETIT, J.R., BISCAYE, P.E., and BARKOV, N.I., 1997, Patagonian origin of glacial dust deposited in East Antarctica (Vostok and Dome C) during glacial stages 2, 4 and 6: Earth and Panetary Science Letters, v. 146, p. 573-589.

BASU, A., YOUNG, S.W., SUTTNER, L.J., JAMES, W.C., and MACK, G.H., 1975, Re-evaluation of the use of undulatory extinction and polycrystallinity in detrital quartz for provenance interpretation: Journal of Sedimentary Petrology, v. 45, p. 873-882.

BEARD, D.C., and WEYL, P.K., 1973, Influence of texture on porosity and permeability of unconsolidated sand: AAPG Bulletin, v. 57, p. 349-369.

BEHRENDT, J.C., LEMASURIER, W.E., COOPER, A.K., TESSENSOHN, F., TREHU, A., and DAMASKE, D., 1991, Geophysical studies of the West Antarctic rift system: Tectonics, v. 10, p. 1257-1273.

BENTLEY, C.R., 1983, Crustal structure of Antarctica from geophysical evidence - A review, *in* Oliver, R.L., James, P.R., and Jago, J.B., eds., Antarctic Earth Science: Cambridge, Cambridge University Press, p. 491-497.

BERNER, R.A., 1969, Goethite stability and the origin of red beds: Geochimica et Cosmochimica Acta, v. 33, p. 267-273.

BERNER, U., KUS, J., SCHEEDER, G., SCHNEIDER, J., SCHÖNER, R., and VIERECK-GÖTTE, L., 2009a, Influence of Jurassic Sill Intrusions on the Organic Matter of Upper Triassic Lacustrine and Fluvial Sediments of North Victoria Land (Antarctica), EGU: Wien, Geophysical Research Abstracts, Vol. 11.

BERNER, U., SCHEEDER, G., KUS, J., SCHNEIDER, J., and SCHÖNER, R., 2009b, Influence of Sill Intrusions on the Organic Geochemistry of Upper Triassic Lacustrine and Fluvial Sediments at Timber Peak (Antarctica), IMOG: Bremen.

BERNET, M., and GAUPP, R., 2005, Diagenetic history of Triassic sandstone from the Beacon Supergroup in central Victoria Land, Antarctica: New Zealand J. of Geology and Geophysics, v. 48, p. 447-458.

BHATIA, M.R., 1983, Plate tectonics and geochemical composition of sandstones: Journal of Geology, v. 91, p. 611-627.

BHATIA, M.R., and CROOK, K.A.W., 1986, Trace element characteristics of greywackes and tectonic setting discrimination of sedimentary basins: Contributions to Mineralogy and Petrology, v. 92, p. 181-193.

BIAGINI, R., DI VINCENZO, G., and GHEZZO, C., 1991, Petrology and geochemistry of peraluminous granitoids from Priestley and Aviator Glacier region, Northern Victoria Land, Antarctica.: Mem. Soc. Geol. It., v. 46, p. 205-230.

BJØRLYKKE, K., 1983, Diagenetic reactions in sandstones, *in* Parker, A., and Sellwood, B.W., eds., Sediment Diagenesis: Dordrecht, Boston, Lancaster, Reidel, p. 169-213.

BJØRLYKKE, K., and BRENDSDAL, A., 1986, Diagenesis of the Brent Sandstone in the Statfjord Field, North Sea, *in* Gautier, D.L., ed., Roles of Organic Matter in Sediment Diagenesis: Tulsa, p. 157-167.

BJØRLYKKE, K., RAMM, M., and SAIGAL, G.C., 1989, Sandstone diagenesis and porosity modification during basin evolution: Geologische Rundschau, v. 78, p. 243-268.

BLACK, L.P., KAMO, S.L., ALLEN, C.M., ALEINIKOFF, J.N., DAVIS, D.W., KORSCH, R.J., and FOUDOULIS, C., 2003, TEMORA 1: a new zircon standard for Phanerozoic U-Pb geochronology: Chem. Geol., v. 200, p. 155-170.

BOENIGK, W., 1983, Die Schwermineralanalyse: Stuttgart, Thieme, 158 p.

BOLES, J.R., and FRANKS, S.G., 1979, Clay diagenesis in Wilcox sandstones of southwest Texas: implications of smectite diagenesis on sandstone cementation: Journal of Sedimentary Petrology, v. 49, p. 55-70.

BOMFLEUR, B., SCHNEIDER, J., SCHÖNER, R., VIERECK-GOETTE, L., and KERP, H., 2007, Exceptionally well-preserved Triassic and Early Jurassic floras from North Victoria Land, Antarctica, *in* Cooper, A.K., and Raymond, C.R., eds., Antarctica: A Keystone in a Changing World - Online Proceedings of the 10th ISAES: USGS Open-File Report 2007-1047, Extended Abstract, p. 1-4.

BOMFLEUR, B., SCHNEIDER, J., SCHÖNER, R., VIERECK-GÖTTE, L., and KERP, H., in review, Fossil sites in the continental Victoria and Ferrar groups (Triassic–Jurassic) of North Victoria Land, Antarctica: Polarforschung.

BORG, S.G., DE PAOLO, D.J., and SMITH, B.M., 1990, Isotopic structure and tectonics of the Central Transantarctic Mountains: J. of Geophysical Research, v. 95, p. 6647-6667.

BORG, S.G., STUMP, E., CHAPPELL, B.W., MCCULLOCH, M.T., WYBORN, D., ARMSTRONG, R.L., and HOLLOWAY, J.R., 1987, Granitoids of northern Victoria Land, Antarctica: Implications of chemical and isotopic variations to regional crustal structure and tectonics: Am. J. Sci., v. 287, p. 127-169.

BORG, S.G., STUMP, E., and HOLLOWAY, J.R., 1986, Granitoids of northern Victoria Land, Antarctica: A reconnaissance study of field relations, petrography and geochemistry, *in* Stump, E., ed., Geologic investigations in northern Victoria Land: Washington, D.C., Antarctic Research Series, American Geophysical Union, p. 115-188.

BRADSHAW, J.D., 2007, The Ross Orogen and Lachlan Fold Belt in Marie Byrd Land, Northern Victoria Land and New Zealand: Implication for the tectonic setting of the Lachlan Fold Belt in Antarctica, *in* Cooper, A.K., Raymond, C.R., and others, eds., Antarctica: A Keystone in a Changing World – Online Proceedings of the 10th ISAES: Washington, DC, The National Academies Press.

BRADSHAW, M.A., 1987, Additional field interpretation of the Jurassic sequence at Carapace Nunatak and Coombs Hills, South Victoria Land, Antarctica: New Zealand Journal of Geology and Geophysics, v. 30, p. 37-49.

BREZA, J.R., and WISE, S.W.J., 1992, Lower Oligocene ice-rafted debris on the Kerguelen Plateau: Evidence for East Antarctic continental glaciation, *in* Wise, S.W.J., and Schlich, R., eds., Proceedings of the Ocean Drilling Program, Scientific Results, vol. 120, College Station, p. 161-178.

BRIGATTI, M.F., FRIGIERI, G., GHEZZO, C., and POPPI, L., 2000, Crystal chemistry of Al-rich biotites coexisting with muscovites in peraluminous granites: American Mineralogist, v. 85, p. 436-448.

BROMFIELD, K.E., 2004, Palaeoenvironmental Reconstruction of the Jurassic, using Plant Macrofossils from a site at Lune River, Southeast Tasmania: Hobart, University of Tasmania (B.Sc. thesis, unpubl.).

BROTZU, P., CAPALDI, G., CIVETTA, L., MELLUSO, L., and ORSI, G., 1988, Jurassic Ferrar dolerites and Kirkpatrick basalts in northern Victoria Land (Antarctica): Stratigraphy, Geochronology and Petrology: Mem. Soc. Geol. It., v. 43, p. 97-116.

BROWN, B., GAINA, C., and MULLER, R.D., 2006, Circum-Antarctic palaeobathymetry: Illustrated examples from Cenozoic to recent times: Palaeogeography, Palaeoclimatology, Palaeoecology, v. 231, p. 158-168.

BROWN, D.A., SAWICKI, J.A., and SHERRIFF, B.L., 1998, Alteration of microbially precipitated iron oxides and hydroxides: American Mineralogist, v. 83, p. 1418-1425.

BRUVOLL, M., JAHREN, J.S., and AAGAARD, P., 2004, Smectite illitization in organic rich shale offshore Mid-Norway: Clay Minerals Society 41st Annual Meeting, Richland, WA, June 19-24, 2004 (Abstract).

BRYAN, S.E., RILEY, T.R., JERRAM, D.A., STEPHENS, C.J., and LEAT, P.T., 2002, Silicic volcanism: An undervalued component of large igneous provinces and volcanic rifted margins, *in* Menzies, M.A., Klemperer, S.L., Ebinger, C.J., and Baker, J., eds., Volcanic rifted margins. Geol. Soc. America Sp. Paper 362: Boulder Geol. Soc. America, p. 99-120.

CAPPONI, G., MESSIGA, B., PICCARDO, G.B., SCAMBELLURI, M., TRAVERSO, G., and VANNUCCI, R., 1988, Metamorphic assemblages in layered amphibolites and micashists from the Dessent Formation (Mountaineer Range - Antarctica): Mem. Soc. Geol. It., v. 43, p. 87-95.

CASNEDI, R., and DI GIULIO, A., 1999, Sedimentology of the Section Peak Formation (Jurassic) northern Victoria Land, Antarctica: Spec. Publs. int. Ass. Sediment., v. 28, p. 435-448.

CLARKE, M.J., FORSYTH, S.M., BACON, C.A., BANKS, M.R., CALVER, C.R., and EVERARD, J.L., 1989, Late Carboniferous - Triassic, *in* Burrett, C.F., and Martin, E.L., eds., Geology and Mineral Resources of Tasmania, Geological Society of Australia, Special Publication, 15, p. 293-338.

CLEMENS, K.E., and KOMAR, P.D., 1988, Oregon beach-sand compositions produced by the mixing of sediments under a transgressing sea: J. Sediment. Petrol., v. 58, p. 519-529.

COLLINSON, J.W., ISBELL, J.L., ELLIOT, D.H., MILLER, M.F., MILLER, J.M.G., and VEEVERS, J.J., 1994, Permian-Triassic Transantarctic basin, *in* Veevers, J.J., and Powell, C.M., eds., Permian-Triassic Pangean Basins and Foldbelts along the Panthalassan Margin of Gondwanaland: Geological Society of America Memoir: Boulder, Colorado, p. 173-222.

COLLINSON, J.W., and KEMP, N.R., 1983, Permian-Triassic sedimentary sequence in northern Victoria Land, Antarctica, *in* Oliver, R.L., James, P.R., and Jago, J.B., eds., Antarctic Earth Science: Canberra, Australian Academy of Science, p. 221-225.

COLLINSON, J.W., PENNINGTON, C.D., and KEMP, N.R., 1983, Sedimentary petrology of Permian-Triassic fluvial rocks in the Allan Hills, central Victoria Land: Antarctic Journal of the Unites States, v. 18, p. 20-22.

COLLINSON, J.W., PENNINGTON, C.D., and KEMP, N.R., 1986, Stratigraphy and Petrology of Permian and Triassic fluvial deposits in northern Victoria Land, Antarctica, *in* Stump, E., ed., Geological Investigations in Northern Victoria Land, Antarctic Research Series, p. 211-242.

COLOMBI, A., 1988, Metamorphisme et geochimie des roches mafiques des Alpes Ouest-Centrales(Geoprofil Viege-Domodossola-Locarno): Dissertaton, Lausanne (unpubl.).

COOMBS, D.S., ALBERTI, A., ARMBRUSTER, T., ARTIOLI, G., COLELLA, C., GALLI, E., GRICE, J.D., LIEBAU, F., MANDARINO, J.A., MINATO, H., NICKEL, E.H., PASSAGLIA, E., PEACOR, D.H., QUARTIERI, S., RINALDI, R., ROSS, M., SHEPPARD, R.A., TILLMANNS, E., and VEZZALINI, G., 1998, Recommended nomenclature for zeolite minerals: Report of the subcommittee on zeolites of the International Mineralogical Association; Commission on New Minerals and Mineral Names: Am. Mineral Special Feature, p. 28.

CORFU, F., HANCHAR, J.M., HOSKIN, P.W.O., and KINNY, P., 2003, Atlas of Zircon Textures, *in* Hanchar, J.M., and Hoskin, P.W.O., eds., Zircon: Washington D.C., Min. Soc. Am., p. 469-500.

CROWELL, J.C., and FRAKES, L.A., 1971, Late Paleozoic Glaciation: Part IV, Australia: Geological Society of America Bulletin, v. 82, p. 2515-2540.

DALZIEL, I.W.D., and ELLIOT, D.H., 1982, West Antarctica - Problem Child of Gondwanaland: Tectonics, v. 1, p. 3-19.

DE PAOLO, D.J., and WASSERBURG, G.J., 1976, Nd isotopic variations and petrogenic models: Geophys. Res. Letters, v. 3, p. 249-252.

DEER, W.A., HOWIE, R.A., and ZUSSMAN, J., 1982, Orthosilicates: Rock-forming minerals, v. 1a: London, Longman, 919 p.

DEER, W.A., HOWIE, R.A., and ZUSSMAN, J., 1992, An introduction to rock forming minerals: Harlow, Longman, 696 p.

DEER, W.A., HOWIE, R.A., and ZUSSMAN, J., 1997, Double-chain silicates, *in* Deer, W.A., Howie, R.A., and Zussman, J., eds., Rock-forming minerals: London, Geol. Soc. London, p. 764.

DI GIULIO, A., CASNEDI, R., CERIANI, A., ORTENZI, A., and ROSSI, A., 1997, Sandstone Composition of the Section Peak Formation (Beacon Supergroup, Northern Victoria Land, Antarctica) and Relations with the Ferrar Group Volcanics, *in* Ricci, C.A., ed., The Antarctic Region: Geological Evolution and Processes, Proceedings of the VII International Symposium on Antarctic Earth Sciences: Siena, p. 297-304.

DI GIULIO, A., TRIBUZIO, R., CERIANI, A., and RICCARDI, M.P., 1999, Integrated analyses constraining the provenance of sandstones, a case study: the Section Peak Formation (Beacon Supergroup, Antarctica): Sediment. Geol., v. 124, p. 169-183.

DICK, H.J.B., and BULLEN, T., 1984, Chromian spinel as a petrogenetic indicator in abyssal and alpine-type peridotites and spatially associated lavas: Contrib. Mineral. Petrol., v. 86, p. 54-76.

DICKINSON, W.R., 1985, Interpreting Provenance Relations from Detrital Modes of Sandstones, *in* Zuffa, G.G., ed., Provenance of Arenites: Dordrecht, Reidel, p. 333-361.

DOW, J.A.S., and NEALL, V.E., 1974, Geology of the lower Rennick Glacier, northern Victoria Land, Antarctica: New Zealand J. of Geology and Geophysics, v. 17, p. 659-714.

DYPVIK, H., 1983, Clay mineral transformations in Tertiary and. Mesozoic sediments from the North Sea: AAPG Bulletin, v. 67, p. 160-165.

EHRENBERG, S.N., 1993, Preservation of anomalously high porosity in deeply buried sandstones by grain coating chlorite: examples from the Norwegian continental shelf: AAPG Bulletin, v. 77, p. 1260-1286.

EINSELE, G., 2000, Sedimentary Basins: Evolution, Facies and Sediment Budget: Berlin, Heidelberg, Springer, 792 p.

ELLIOT, D.H., 1975, Tectonics of Antarctica; a review: Am. J. Sci., v. 275-A, p. 45-106.

ELLIOT, D.H., 1992, Jurassic magmatism and tectonism associated with Gondwanaland break-up: an Antarctic perspective, *in* Storey, B.C., Alabaster, T., and Pankhurst, R.J., eds., Magmatism and the Causes of Continental Break-up: Geol. Soc. Spec. Publ.: London, p. 165-184.

ELLIOT, D.H., 1996, The Hanson Formation: a new stratigraphical unit in the Transantarctic Mountains, Antarctica: Antarct. Sci., v. 8, p. 389-394.

ELLIOT, D.H., 2000, Stratigraphy of Jurassic pyroclastic rocks in the Transantarctic Mountains: Journal of African Earth Sciences, v. 31, p. 77-89.

ELLIOT, D.H., and FANNING, C.M., 2008, Detrital zircons from upper Permian and lower Triassic Victoria Group sandstones, Shackleton Glacier region, Antarctica: Evidence for multiple sources along the Gondwana plate margin: Gondwana Research, v. 13, p. 259-274.

ELLIOT, D.H., FLEMING, T.H., FOLAND, K.A., and FANNING, C.M., 2007, Jurassic silicic volcanism in the Transantarctic Mountains: Was it related to plate margin processes or to Ferrar magmatism?, *in* Cooper, A.K., Raymond, C.R., and others, eds., Antarctica: A Keystone in a Changing World - Online Proceedings of the 10th ISAES: Washington, DC, The National Academies Press.

ELLIOT, D.H., and FOLAND, K.A., 1986, Potassium-Argon age determinations of the Kirkpatrick Basalt, Mesa Range: Geol. Investigations in Northern Victoria Land, v. 46, p. 279-288.

ELLIOT, D.H., HABAN, M.A., and SIDERS, M.A., 1986, The Exposure Hill Formation, Mesa Range, *in* Stump, E., ed., Geological Investigations in Northern Victoria Land: AGU Antarctic Research Series, p. 267-278.

ELLIOT, D.H., and LARSEN, D., 1993, Mesozoic volcanism in the central Transantarctic Mountains, Antarctica: Depositional environment and tectonic setting, *in* Findlay, R.H., Unrug, R., Banks, M.R., and Veevers, J.J., eds., Gondwana Eight: Assembly, Evolution and Dispersal: Balkema, Rotterdam, p. 397-410.

ENCARNACIÓN, J., FLEMING, T.H., ELLIOT, D.H., and EALES, H.V., 1996, Synchronous emplacement of Ferrar and Karoo dolerites and the early breakup of Gondwana: Geology, v. 24, p. 535-538.

ENCARNACIÓN, J., and GRUNOW, A., 1996, Changing magmatic and tectonic styles along the paleo-Pacific margin of Gondwana and the onset of early Paleozoic magmatism in Antarctica: Tectonics, v. 15, p. 1325-1342.

ENGEL, S., 1987, Contact Metamorphism by the Layered Gabbro at Spatulate Ridge and Apostrophe Island, North Victoria Land, Antarctica: Geol. Jb. B, v. B66, p. 275-302.

ENGLISH, P.M., 2001, Formation of analcime and moganite at Lake Lewis, central Australia: significance of groundwater evolution in diagenesis: Sedimentary Geology, v. 143, p. 219-244.

FANNING, C.M., MOORE, D.H., BENNETT, V.C., and DALY, S.J., 1996, The "Mawson Continent": Archaean to Proterozoic crust in East Antarctica and the Gawler Craton, Australia: A cornerstone in Rodinia and Gondwana: Geological Society of Australia, Abstracts 41, p. 135.

FAUPL, P., PAVLOPOULOS, A., KLÖTZLI, U., and PETRAKAKIS, K., 2006, On the provenance of mid-Cretaceous turbidites of the Pindos zone (Greece): implications from heavy mineral distribution, detrital zircon ages, and chrome spinel chemistry: Geol. Mag., v. 143, p. 329-342.

FAUPL, P., PETRAKAKIS, K., MIGIROS, G., and PAVLOPOULOS, A., 2002, Detrital blue amphibole from the western Othrys Mountain and their relationship to the blueshist terrains of the Hellenides (Greece): Int. J. Earth Sci., v. 91, p. 433-444.

FAURE, G., 1986, Principles of Isotope Geology: New York, Wiley, 589 p.

FAURE, G., and HILL, R.L., 1973, The age of the Falla Formation (Triassic), Queen Alexandra Range: Antarctic Journal of the United States, v. 8, p. 264-266.

FEDERICO, L., CAPPONI, G., and CRISPINI, L., 2006, The Ross orogeny of the transantarctic mountains: a northern Victoria Land perspective: International Journal of Earth Sciences, v. 95, p. 759-770.

FEDO, C.M., ERIKSSON, K.A., and KROGSTAD, E.J., 1996, Geochemistry of shales from the Archean (~3.0 Ga) Buhwa Greenstone Belt, Zimbambwe: implication for provenance and source-area weathering: Geochimica et Cosmochimica Acta, v. 60, p. 1751-1763.

FEDO, C.M., NESBITT, H.W., and YOUNG, G.M., 1995, Unraveling the effects of potassium metasomatism in sedimentary rocks and paleosols, with implications for paleoweathering conditions and provenance: Geology, v. 23, p. 921-924.

FERRACCIOLI, F., and BOZZO, E., 1999, Inherited crustal features and tectonic blocks of the Transantarctic Mountains: An aeromagnetic perspective (Victoria Land, Antarctica): Journal of Geophysical Research, v. 104, p. 25,297-25,319.

FIAMENI, S., 2007, Petrology and U-Pb geochronology of the mafic-ultramafic sequence and associated quartz-feldspathic rocks from Niagara Icefalls (northern Victoria land, Antarctica): Scientifica Acta, v. 1, p. 35-38.

FISHER, R.V., and SCHMINCKE, H.-U., 1984, Pyroclastic Rocks: Berlin, Springer, 472 p.

FITZGERALD, P.G., 1994, Thermochronologic constraints on post-Paleozoic tectonic evolution of the central Transantarctic Mountains, Antarctica: Tectonics, v. 13.

FITZGERALD, P.G., 2002, Tectonics and landscape evolution of the Antarctic plate since the breakup of Gondwana, with an emphasis on the West Antarctic Rift System and the Transantarctic Mountains, *in* Gamble, J.A., Skinner, D.N.B., and Henrys, S., eds., Antarctica at the close of the millennium, Proceedings of the 8th International Symposium on Antarctic Earth Sciences, Wellington, 1999: Royal Society of New Zealand Bulletin, p. 453-469.

FITZSIMONS, I.C.W., 2000, A review of tectonic events in the East Antarctic Shield and their implications for Gondwana and earlier supercontinents: Journal of African Earth Sciences, v. 31, p. 3-23.

FITZSIMONS, I.C.W., 2003, Proterozoic basement provinces of southern and southwestern Australia, and their correlation with Antarctica, *in* Yoshida, M., Windley, B.F., and Dasgupta, S., eds., Proterozoic East Gondwana: Supercontinent Assembly and Breakup, Geological Society London Special Publications, p. 93-130.

FLEET, M.E., 2003, Sheet silicates: Micas, *in* Deer, W.A., Howie, R.A., and Zussman, J., eds., Rock-forming minerals: London, Longman, p. 758.

FLEMINGS, T.D., and JORDAN, T.E., 1990, Stratigraphic modelling of foreland basins: interpreting thrust deformation and lithospheric rheology: Geology, v. 18, p. 430-435.

FLOYD, P.A., LEVERBRIDGE, B.E., FRANKE, W., SHAIL, R., and DÖRR, W., 1990, Provenance and depositional environment of Rhenohercynian synorogenic greywackes from the Giessen Nappe, Germany: Geol. Rundschau, v. 79, p. 611-626.

FOLK, R.L., 1968, Petrology of sedimentary rocks: Austin, The University of Texas.

FORCE, E.R., 1980, The provenance of rutile: Journal of Sedimentary Petrology, v. 50, p. 485-488.

FOSTER, D.A., and GRAY, D.R., 2000, Evolution and structure of the Lachlan Fold Belt (orogen) of eastern Australia: Annu. Rev. Earth Planet. Sci., v. 28, p. 47-80.

FRINGS, R.M., 2008, Downstream fining in large sand-bed rivers: Earth-Science Reviews, v. 87, p. 39-60.

FÜCHTBAUER, H., 1988, Sedimente und Sedimentgesteine: Stuttgart, Schweizerbart, p. 1141.

GAIR, H.S., NORRIS, G., and RICKER, J., 1965, Early Mesozoic microfloras from Antarctica: New Zealand J. of Geology and Geophysics, v. 8, p. 231-235.

GANOVEX-TEAM, 1987a, Geological Map of North Victoria Land, Antarctica, 1:500 000: Bundesanstalt für Geowissenschaften und Rohstoffe, Hannover.

GANOVEX-TEAM, 1987b, Geological Map of North Victoria Land, Antarctica, 1:500 000 - Explanatory Notes: Geol. Jb., v. B 66, p. 7-79.

GARVER, J.I., ROYCE, P.R., and SMICK, T.A., 1996, Chromium and nickel in shales of the taconic foreland: a case study for the provenance of fine grained sediments with an ultramafic source: Journal of Sedimentary Research, v. 66, p. 100-106.

GERDES, A., and ZEH, A., 2006, Combined U-Pb and Hf isotope LA-(MS-)ICP-MS analyses of detrital zircons: Comparison with SHRIMP and new constraints for the provenance and age of an Armorican metasediment in central Germany: Earth and Planetary Science Letters, v. 249, p. 47-62.

GHIRIBELLI, B., FREZZOTTI, M., and PALMIERI, R., 2001, Coesites in eclogites of the Lanterman Range (Antarctica): evidence from textural and raman spectroscopic studies: European Journal of Mineralogy, v. 14, p. 355-360.

GILES, M.R., INDRELID, S.L., BEYNON, G.V., and AMTHOR, J., 2000, The origin of large scale quartz cementation: evidence from large datasets and coupled heat-fluid mass transport modelling, *in* Worden, R.H., and Morad, S., eds., Quartz Cementation in Sandstones: Oxford, Special Publication of the International Association of Sedimentologists No. 29.

GOODGE, J.W., and FANNING, C.M., 2010, Composition and age of the East Antarctic Shield in eastern Wilkes Land determined by proxy from Oligocene-Pleistocene glaciomarine sediment and Beacon Supergroup sandstones, Antarctica: Geol. Society of America Bulletin, v. 122, p. 1135–1159.

GOODGE, J.W., MYROW, P., WILLIAMS, I.S., and BOWRING, S.A., 2002, Age and Provenance of the Beardmore Group, Antarctica: Constraints on Rodinia Supercontinent Breakup: J. Geol., v. 110, p. 393-406.

GOODGE, J.W., WILLIAMS, I.S., and MYROW, P., 2004, Provenance of Neoproterozoic and lower Paleozoic siliciclastic rocks of the central Ross orogen, Antarctica: Detrital record of rift-, passive-, and active margin sedimentation: Geol. Society of America Bulletin, v. 116, p. 1253-1279.

GOSS, C.J., 1987, The kinetics and reaction mechanism of the goethite to hematite tranformation: Mineralogical Magazine, v. 51, p. 437-451.

GRIGSBY, J.D., 1990, Detrital magnetite as provenance indicator: Journal of Sedimentary Petrology, v. 60, p. 940-951.

GRINDLEY, G.W., and OLIVER, P.J., 1983, Post-Ross orogeny cratonization of northern Victoria Land, *in* Oliver, R.L., James, P.R., and Jago, J.B., eds., Antarctic Earth Science: Canberra, Australian Academy of Science, p. 133-139.

GRUNOW, A.M., 1999, Gondwana events and palaeogeography: a palaeomagnetic review: Journal of African Earth Sciences, v. 28, p. 53-69.

GUALTIERI, A.F., and VENTURELLI, P., 1999, In situ study of the goethite-hematite phase transformation by real time synchrotron powder diffraction: American Mineralogist, v. 84, p. 895-904.

GUPTA, M.C., and MACFARLANE, R.D., 1970, The natural radioactivity of samarium: J. Inorg. Nucl. Chem. , v. 32, p. 3425.

HAMMER, W.R., HICKERSON, W.J., and SLAUGHTER, R.W., 1994, A dinosaur assemblage from the Transantarctic Mountains: Antarctic Journal of the United States, v. 29, p. 31-33.

HAND, S.J., 1993, Palaeogeography of Tasmania's Permo-Carboniferous glacigenic sediments, *in* Findlay, R.H., Unrug, R., Banks, M.R., and Veevers, J.J., eds., Gondwana Eight: Assembly, Evolution and Dispersal: Rotterdam, Balkema, p. 459-469.

HARNOIS, L., 1988, The CIW index: A new chemical index of weathering: Sediment. Geol., v. 55, p. 319-322.

HAWTHORNE, F.C., and OBERTI, R., 2006, On the classification of amphiboles: Can. Min., v. 44, p. 1-21.

HAY, R.L., 1966, Zeolites and zeolite reactions in sedimentary rocks, v. 85, Geol. Soc. Am. Special Publication, 130 p.

HAY, R.L., and SHEPPARD, R.A., 2001, Occurrence of Zeolites in Sedimentary Rocks: An Overview, *in* Bish, D.L., and Ming, D.W., eds., Natural Zeolites: Occurrence, Properties, Applications: Washington, D.C., The Mineralogical Society of America, p. 217-234.

HEIMANN, A., FLEMING, T.H., ELLIOT, D.H., and FOLAND, K.A., 1994, A short interval of Jurassic continental flood basalt volcanism in Antarctica as demonstrated by 40Ar/39Ar geochronology: Earth and Planetary Science Letters, v. 121, p. 19-41.

HENJES-KUNST, F., and KREUZER, H., 2003, Mid-Paleozoic Igneous Activity in Northern Victoria Land, Antarctica: Implications of New Geochronological Data: Geol. Jb., v. B 85, p. 271-302.

HENRY, D.J., and DUTROW, B.L., 1992, Tourmaline in a low grade clastic metasedimentary rock: an example of the petrogenetic potential of tourmaline: Contributions to Mineralogy and Petrology, v. 112, p. 203-218.

HENRY, D.J., and GUIDOTTI, C.V., 1985, Tourmaline as a petrogenetic indicator mineral: an example from the staurolite-grade metapelites of NW Maine: American Mineralogist, v. 70, p. 1-15.

HERGT, J.M., MCDOUGALL, I., BANKS, M.R., and GREEN, D.H., 1989, Jurassic dolerite, *in* Burrett, C.F., and Martin, E.L., eds., Geology and Mineral Resources of Tasmania Special Publication Geological Society of Australia, 15, p. 375–381.

HERRON, M.M., 1988, Geochemical classification of terrigenous sands and shales from core or log data: Journal of Sedimentary Petrology, v. 58, p. 820-829.

HOFFMAN, J., and HOWER, J., 1979, Clay mineral assemblages as low grade metamorphic geothermometers: application to the thrust faulted disturbed belt of Montana, USA, *in* Scholle, P.A., and Schluger, P.R., eds., Aspects of Diagenesis: Tulsa, Society of Economic Paleontologists and Mineralogists, Special Publications 26, p. 55-79.

HOPPE, G., 1962, Petrogenetische auswertbare morphologische Erscheinungen an akzessorischen Zirkonen: N. Jb. Mineral. Abh., v. 98, p. 35-50.

HORNIG, I., and WÖRNER, G., 2003, Cenozoic Volcanics from Coulman Island, Mandible Cirque, Malta Plateau and Navigator Nunatak, Victoria Land, Antarctica: Geol. Jb., v. B85, p. 373-406.

HORTON, D.G., 1985, Mixed-layer illite/smectite as a paleotemperature indicator. in the Amethyst vein system, Creede district, Colorado, USA: Contributions to Mineralogy and Petrology, v. 91, p. 171-179.

HOUSEKNECHT, D.W., 1987, Assessing the relative importance of compaction processes and cementation to reduction of porosity in sandstones: AAPG Bulletin, v. 71, p. 633-642.

HOWER, J., 1981, Shale diagenesis, *in* Longstaffe, F., ed., Short course in clays and the resource geologist: Calgary, Mineral Assoc Can, p. 60-77.

HOWER, J., ESLINGER, E.V., HOWER, M.E., and PERRY, E.A., 1976, Mechanism of burial metamorphism of argillaceous sediment: 1. Mineralogical and chemical evidence: Geological Society of America Bulletin, v. 87, p. 725-737.

HUBERT, J.F., 1962, A zircon-tourmaline-rutile maturity index and the interdependence of the composition of the heavy mineral assemblage with the gross composition and texture of sandstones: Journal of Sedimentary Petrology, v. 32, p. 440-450.

HUNTER, M.A., RILEY, T.R., CANTRILL, D.J., FLOWERDEW, M.J., and MILLAR, I.L., 2006, A new stratigraphy for the Latady Basin, Antarctic Peninsula: Part 1, Ellsworth Land Volcanic Group: Geological Magazine, v. 143, p. 777-796.

INGERSOLL, R.V., and BUSBY, C.J., 1995, Tectonics of Sedimentary Basins, *in* Busby, C.J., and Ingersoll, R.V., eds., Tectonics of Sedimentary Basins: Oxford, Blackwell, p. 1-52.

IRELAND, T.R., BRADSHAW, J.D., MUIR, R., WEAVER, S., and ADAMS, C., 1994, Zircon age distributions in granites, greywackes, and gneisses from the southwest Pacific–Gondwana region. Eighth International

Conference on Geochronology, Cosmochronology and Isotope Geology (Abstracts): U.S. Geological Survey Bulletin, v. 1107, p. 151.

ISBELL, J.L., 1991, Evidence for a low-gradient alluvial fan from the palaeo-Pacific margin in the upper Permian Buckley Formation, Beardmore Glacier area, Antarctica, *in* Thomson, M.R.A., Crame, J.A., and Thomson, J.W., eds., Geological evolution of Antarctica: Cambridge, Cambridge University Press, p. 215–217.

ISBELL, J.L., 1999, The Kukri Erosion Surface; a reassessment of its relationship to the rocks of the Beacon Supergroup in the central Transantarctic Mountains, Antarctica: Antarctic Science, v. 11, p. 228-238.

ISBELL, J.L., and CÚNEO, N.R., 1996, Depositional framework of Permian coal-bearing strata, southern Victoria Land, Antarctica: Palaeogeography, Palaeoclimatology, Palaeoecology, v. 125, p. 217-238.

JAGO, J.B., 1980, Late Precambrian - Early Paleozoic geological relationship between Tasmania and northern Victoria Land, *in* Creswell, M.M., and Vella, P., eds., Gondwana five: Rotterdam, Balkema, p. 199-204.

JAKES, P., and WHITE, A.J.R., 1972, Hornblendes from calc-alkaline rocks of Island Arcs and continental margins: Amer. Min., v. 57, p. 887-902.

JAMES, P.R., and TINGEY, R.J., 1983, The Precambrian evolution of the East Antarctic metamorphic shield - a review, *in* Oliver, R.L., James, P.R., and Jago, J.B., eds., Antarctic Earth Science: Canberra, Australian Academy of Science, p. 5-10.

JANOUŠEK, V., GERDES, A., VRÁNA, S., FINGER, F., ERBAN, V., FRIEDL, G., and BRAITHWAITE, C.J.R., 2006, Low-pressure Granulites of the Liúov Massif, southern Bohemia: Viséan metamorphism of Late Devonian plutonic arc rocks: Journal of Petrology, v. 47, p. 705-744.

JOHNS, W.D., and KURZWEIL, H., 1979, Quantitative estimation of Illite-Smectite Mixed-Phases formed during burial diagenesis: TMPM, v. 26, p. 203-215.

JORDAN, H., MÜLLER, P., TESSENSOHN, F., and DAMASKE, D., 2003, The Cenozoic Meander Intrusives of No Ridge and Cape King and their tectonic setting: Geol. Jb., v. B85, p. 335-369.

JORDAN, T.E., 1995, Retroarc Foreland and Related Basins, *in* Busby, C.J., and Ingersoll, R.V., eds., Tectonics of Sedimentary Basins: Oxford, Blackwell, p. 331-362.

KAMENETZKY, V.S., CRAWFORD, A.J., and MEFFRE, S., 2001, Factors controlling chemistry of magmatic spinel: an empirical study of associated olivine, Cr-spinel and melt inclusions from primitive rocks: Journal of Petrology, v. 42, p. 655-671.

KERP, H., 2000, The modernization of landscape during the Late Paleozoic-Early Mesozoic, *in* Gastoldo, R.A., and Dimichele, W.A., eds., Phanerozoic Terrestrial Ecosystems - The Paleontological Society Papers, 6, p. 79-113.

KIDDER, D.L., and WORSLEY, T.R., 2004, Causes and consequences of extreme Permo-Triassic warming to globally equable climate and relation to the Permo-Triassic extinction and recovery: Palaeogeogr. Palaeoclimatol. Palaeoecol., v. 203, p. 207-237.

KIMINAMI, K., and FUJII, K., 2007, The relationship between major element concentration and grain size within sandstones from four turbidite sequences in Japan: Sediment. Geol., v. 195, p. 203-215.

KINTER, E.B., and DIAMOND, S., 1956, A new method for preparation and treatment of oriented-aggregate specimens of soil clays for X-ray diffraction analysis: Soil Sci., v. 81, p. 111-120.

KLEINSCHMIDT, G., ROLAND, N.W., and SCHUBERT, W., 1984, The metamorphic basement in the Mountaineer Range, North Victoria Land, Antarctica: Geol. Jb. B, v. 60, p. 213-251.

KLEINSCHMIDT, G., SCHUBERT, W., OLESCH, M., and RETTMANN, E., 1987, Ultramafic Rocks of the Lanterman Range in North Victoria Land, Antarctica. Petrology, Geochemistry and Geodynamic Implications: Geol. Jb., v. B66, p. 231-273.

KLEINSCHMIDT, G., and SKINNER, D.N.B., 1981, Deformation styles in the basement rocks of North Victoria Land, Antarctica: Geol. Jb., v. B41, p. 155-199.

KLEINSCHMIDT, G., and TESSENSOHN, F., 1987, Early Paleozoic Westward directed Subduction at the Pacific Margin of Antarctica, *in* McKenzie, G.D., ed., Gondwana Six: Structure, Tectonics and Geophysics - Geophys. Monogr., 40: Washington, American Geophysical Union, p. 89-104.

KRETZSCHMAR, R., ROBARGEB, W.P., AMOOZEGARB, A., and VEPRASKASB, M.J., 1997, Biotite alteration to halloysite and kaolinite in soil-saprolite profiles developed from mica schist and granite gneiss: Geoderma, v. 75, p. 155-170.

LAIRD, M.G., and BRADSHAW, J.D., 1981, Permian tillites of North Victoria Land, Antarctica, *in* Hambrey, M.J., and Harland, W.B., eds., Earth's pre-Pleistocene glacial record: London, Cambridge University Press, p. 237-240.

LAIRD, M.G., BRADSHAW, J.D., and WODZICKY, A., 1982, Stratigraphy of the late Precambrian and early Paleozoic Bowers Supergroup, northern Victoria Land, Antarctica, *in* Craddock, C., ed., Antarctic Geoscience: Madison, Univ. Wisconsin Press, p. 535-542.

LARSEN, L.H., and POLDERVAART, A., 1957, Measurement and distribution of zircons in some granitic rocks of magmatic origin: Min. Mag., v. 31, p. 544-564.

LAWVER, L.A., GAHAGAN, L.M., and COFFIN, M.V., 1992, The development of palaeoseaways around Antarctica: The Antarctic palaeoenvironment: a perspective on global change. Antarctic Research Series, v. 56, p. 7-30: Washington DC, American Geophysical Union.

LE MAITRE, R.W., 1984, A proposal by the IUGS subcommission on the systematics of igneous rocks for a chemical classification of volcanic rocks based on the total alkali silica (TAS) diagram: Australian Journal of Earth Sciences, v. 31, p. 243-255.

LE MAITRE, R.W., 2002, Igneous Rocks. A Classification and Glossary of Terms. Recommendations of the International Union of Geological Sciences, Subcommission on the Systematics of Igneous Rocks: Cambridge, University Press, p. 236.

LEAKE, B.E., WOOLEY, A.R., ARPS, C.E.S., BIRCH, W.D., GILBERT, M.C., GRICE, J.D., HAWTHORNE, F.C., KATO, A., KISCH, H.J., KRIVOVICHEV, V.G., LINTHOUT, K., LAIRD, J., MANDARINO, J.A., MARESCH, W.V., NICKEL, E.H., ROCK, N.M.S., SCHUMACHER, J.C., SMITH, D.C., STEPHENSON, N.C.N., UNGARETTI, L., WHITTAKER, E.J.W., and YOUZHI, G., 1997, Nomenclature of amphiboles: Report of the subcommitee on amphiboles of the International Mineralogical Association, commission on new minerals and mineral names: Can. Min., v. 35, p. 219-246.

LEAKE, B.E., WOOLLEY, A.R., BIRCH, W.D., BURKE, E.A.J., FERRARIS, G., GRICE, J.D., HAWTHORNE, F.C., KISCH, H.J., KRIVOVICHEV, V.G., SCHUMACHER, J.C., STEPHENSON, N.C.N., and WHITTAKER, E.J.W., 2004, Nomenclature of amphiboles: Additions and revisions to the International Mineralogical Association´s amphibole nomenclature: American Mineralogist, v. 89, p. 883-887.

LEMCKE, K., 1988, Das bayerische Alpenvorland vor der Eiszeit: Stuttgart, Schweizerbart, 175 p.

LENAZ, D., KAMENETZKY, V.S., CRAWFORD, A.J., and PRINCIVALLE, F., 2000, Melt inclusions in detrital spinel from SE Alps (Italy-Slovenia): a new approach to provenance studies of sedimentary basins: Contributions to Mineralogy and Petrology, v. 139, p. 748-758.

LINDSTROM, S., and MCLOUGHLIN, S., 2007, Synchronous palynofloristic extinction and recovery after the end-Permian event in the Prince Charles Mountains, Antarctica: Implications for palynofloristic turnover across Gondwana: Review of Palaeobotany and Palynology, v. 145, p. 89-122.

LINNEMANN, U., GERDES, A., DROST, K., and BUSCHMANN, B., 2007, The continuum between Cadomian orogenesis and opening of the Rheic Ocean: Constraints from LA-ICP-MS U-Pb zircon dating and analysis of pate tectonic setting (Saxo-Thuringian zone, northeastern Bohemian Massif, Germany), *in* Linnemann, U., Nance, R., Kraft, P., and Zulauf, G., eds., The evolution of the Reic Ocean: From Avalonian-Cadomian active margin to Alleghenian-Variscan collision, Geological Society of America Special Paper 423, p. 61-96.

LISKER, F., and LÄUFER, A.L., 2007, A Cretaceous Victoria Basin between Australia and Antarctica inferred from volcanoclastic deposits, thermal indications and thermochronological data, *in* Cooper, A.K., Raymond, C.R., and others, eds., Antarctica: A Keystone in a Changing World – Online Proceedings of the 10th ISAES: Washington, DC The National Academies Press, p. 211-213.

LISKER, F., LÄUFER, A.L., OLESCH, M., ROSSETTI, F., and SCHÄFER, T., 2006, Transantarctic Basin: new insights from fission track and structural data from the USARP Mountains and adjacent areas (Northern Victoria Land, Antarctica): Basin Research, v. 18, p. 497-520.

LOCK, B.E., 1980, Flat-plate subduction and the Cape Fold Belt of South Africa: Geology, v. 8, p. 35-39.

LUDWIG, K.R., 1999, User 's manual for Isoplot/Ex, Version 2.10, A geochronological toolkit for Microsoft Excel: Berkeley Geochronology Center Special Publication,1a: Berkeley.

LUDWIG, K.R., 2000, SQUID 1.00, A User's Manual: Berkeley Geochronology Center Special Publication, 2: Berkeley.

LUNDEGARD, P.D., 1992, Sandstone porosity loss—a ‘‘big picture’’ view of the importance of compaction: Journal of Sedimentary Research, v. 62, p. 250-260.

LUŽAR-OBERITER, B., MIKES, T., VON EYNATTEN, H., and BABIĆ, L., 2009, Ophiolitic detritus in Cretaceous clastic formations of the Dinarides (NW Croatia): evidence from Cr-spinel chemistry: International Journal of Earth Sciences, v. 98, p. 1097-1108.

MANGE-RAJETZKY, M.A., and OBERHÄNSLI, R., 1982, Detrital lawsonite and blue sodic amphibole in the Molasse of Savoy, France, and their significance in assessing Alpine evolution: Schweiz. Mineral. Petrogr. Mitt., v. 62, p. 415-436.

MANGE, M.A., and MAURER, H.F.W., 1991, Schwerminerale in Farbe: Stuttgart, Ferdinand Enke, 148 p.

MARTINI, I.P., and BANKS, M.R., 1989, Sedimentology of the Cold-Climate, Coal-Bearing, Lower Permian Lower Fresh-Water Sequence of Tasmania: Sedimentary Geology, v. 64, p. 25-41.

MASSONNE, H.-J., 1991, High-pressure, low temperature metamorphism of pelitic and other protoliths based on experiments in the system $K_2O$-MgO-$Al_2O_3$-$SiO_2$-$H_2O$: Habilitationsschrift, Ruhr-Universität Bochum (unpubl.), 172 p.

MASSONNE, H.-J., and SCHREYER, W., 1987, Phengite geobarometry based on the limiting assemblage with K-feldspar, phlogopite and quartz: Contrib. Mineral. Petrol., v. 96, p. 212-224.

MCBRIDE, E.F., 1963, A classification of common sandstones: J. Sediment. Petrol., v. 33, p. 664-669.

MCBRIDE, E.F., and PICARD, M.D., 1987, Downstream changes in sand composition, roundness, and gravel size in a short-headed, high-gradient stream, northwestern Italy: J. Sediment. Petrol., v. 57, p. 1018-1026.

MCCANN, T., 1991, Petrological and geochemical determination of provenance in the southern Welsh Basin, *in* Morton, A.C., Todd, S.P., and Haughton, P.D.W., eds., Developments in Sedimentary Provenance Studies, Geological Society Special Publication, 57, p. 1-11.

MCCONNELL, J.D.C., ASTILL, D.M., and HALL, P.L., 1987, The pressure dependence of the dehydration of gypsum to bassanite: Mineralogical Magazine, v. 51, p. 453-457.

MCELHINNY, M.W., POWELL, C.M., and PISAREVSKY, S.A., 2003, Paleozoic terranes of eastern Australia and the drift history of Gondwana: Tectonophysics, v. 362, p. 41-65.

MCKELVEY, B.C., and WALKER, B.C., 1983, Late Palaeozoic glacigene strata in northern Victoria Land, *in* Oliver, R.L., James, P.R., and Jago, J.B., eds., Antarctic Earth Science 226: Canberra, Australian Academy of Science.

MCKINLEY, J.M., WORDEN, R.H., and RUFFELL, A.H., 2003, Smectite in sandstones: a review of the controls on occurrence and behaviour during diagenesis, *in* Worden, R.H., and Morad, S., eds., Clay Mineral Cements in Sandstones: Oxford, Spec. Publs int. Ass. Sediment. No. 34, p. 109-128.

MCLENNAN, S.M., HEMMING, S., MCDANIEL, D.K., and HANSON, G.N., 1993, Geochemical approaches to sedimentation, provenance and tectonics, *in* Johnsson, M.J., and Basu, A., eds., Processes controlling the composition of clastic sediments, Geological Society of America, Special Paper 284, p. 21-40.

MCLENNAN, S.M., TAYLOR, E.L., MCCULLOCH, M.T., and MAYNARD, J.B., 1990, Geochemical and Nd-Sr isotopic composition of deep-sea turbidites: crustal evolution and plat tectonic associations: Geochimica et Cosmochimica Acta, v. 54, p. 2015-2050.

MCLOUGHLIN, S., LINDSTROM, S., and DRINNAN, A.N., 1997, Gondwanan floristic and sedimentological trends during the Permian-Triassic transition: new evidence from the Amery Group, northern Prince Charles Mountains, East Antarctica: Antarctic Science, v. 9, p. 281-298.

MECCHERI, M., PERTUSATI, P.C., and TESSENSOHN, F., 2003, Explanatory Notes to the Geological and Structural Map of the Area between the Aviator Glacier and Victory Mountains, Northern Victoria Land, Antarctica: Geol. Jb., v. B85, p. 9-33.

MERINO, E., GIRARD, J.-P., MAY, M.T., and RANGANATHAN, V., 1997, Diagenetic mineralogy, geochemistry, and dynamics of mesozoic arcoses, Hartford rift basin, Connecticut, U.S.A.: Journal of Sedimentary Research, v. 67, p. 212-224.

MEUNIER, A., and VELDE, B., 2004, Illite - origins, evolution and metamorphism: Berlin, Springer, 286 p.

MEZGER, K., and KROGSTADT, E.J., 1997, Interpretation of discordant U-Pb zircon ages: An evaluation: J. metamorphic Geol., v. 15, p. 127-140.

MIALL, A.D., 1995, Collision-Related Foreland Basins, *in* Busby, C.J., and Ingersoll, R.V., eds., Tectonics of Sedimentary Basins: Oxford, Blackwell, p. 393-424.

MICHARD, A., GURRIET, P., SOUDANT, M., and ALBAREDE, F., 1985, Nd isotopes in French phanerozoic shales: external vs. internal aspects of crustal evolution: Geochim. Cosmochim. Acta, v. 49, p. 601-610.

MILLER, J.M.G., and WAUGH, B.J., 1987, Paleotectonic implications of the Permo-Carboniferous Pagoda Formation, Beardmore Glacier area: Antarctic Journal of the United States, Review, v. 22, p. 19-21.

MILLER, J.M.G., and WAUGH, B.J., 1991, Permo-carboniferous glacial sedimentation in the central Transantarctic Mountains and its palaeotectonic implications, *in* Thomson, M.R.A., Crame, J.A., and Thomson, J.W., eds., Geological evolution of Antarctica: Cambridge, Cambridge University press, p. 205-208.

MILLER, K.G., WRIGHT, J.D., KATZ, M.E., BROWNING, J.V., CRAMER, B.S., WADE, B.S., and MIZINTSEVA, S.F., 2007, A View of Antarctic Ice-Sheet Evolution from Sea-Level and Deep-Sea Isotope Changes During the Late Cretaceous-Cenozoic, *in* Cooper, A.K., Raymond, C.R., and Others, eds., Antarctica: A Keystone in a Changing World – Online Proceedings of the 10th ISAES.

MINOR, D.R., and MUKASA, S.B., 1997, Zircon U-Pb and hornblende 40Ar-39Ar ages for the Dufek layered mafic intrusion, Antarctica: Implications for the age of the Ferrar large igneous province: Geochim. Cosmochim. Acta, v. 61, p. 2497-2504.

MOLZAHN, M., WILHELM, S., and WÖRNER, G., 1996, Evidence for Arc-Related Magmatism Associated with the Ross Orogeny at the Walker Rock Nunataks, Northern Victoria Land, Antarctica, Geol. Jahrbuch: Hannover, p. 73-96.

MOLZAHN, M., WÖRNER, G., HENJES-KUNST, F., and ROCHOLL, A., 1999, Constraints on the Cretaceous thermal event in the Transantarctic Mountains from alteration processes in Ferrar flood basalts: Global and Planetary Change, v. 23, p. 45-60.

MOORE, D.M., and REYNOLDS, R.C., 1989, X-ray Diffraction and the Identification and Analysis of Clay Minerals: Oxford, New York, Oxford University Press, 332 p.

MORAD, S., BERGAN, M., KNARUD, R., and NYSTUEN, J.P., 1990, Albitization of Detrital Plagioclase in Triassic Reservoir Sandstones from the Snorre Field, Norwegian North Sea: Journal of Sedimentary Petrology, v. 60, p. 411-425.

MORTON, A.C., 1985, A new approach to provenance studies: electron microprobe analysis of detrital garnets from Middle Jurassic sandstones of the northern North Sea: Sedimentology, v. 32, p. 553-566.

MORTON, A.C., 1987, Influences of provenance and diagenesis on detrital garnet suites in the Forties sandstone, Paleocene, central North Sea: J. Sediment. Petrol., v. 57, p. 1027-1032.

MORTON, A.C., and HALLSWORTH, C.R., 1999, Processes controlling the composition of heavy mineral assemblages in sandstones: Sediment. Geol., v. 124, p. 3-29.

MORTON, A.C., WHITHAM, A.G., and FANNING, C.M., 2005, Provenance of Late Cretaceous to Paleocene submarine fan sandstones in the Norwegian Sea: Integration of heavy mineral, mineral chemical and zircon age data: Sediment. Geol., v. 182, p. 3-28.

MUKASA, S.B., and DALZIEL, I.W.D., 2000, Marie Byrd Land, West Antarctica: Evolution of Gondwana's Pacific margin constrained by zircon U–Pb geochronology and feldspar common-Pb isotopic compositions: Geological Society of America Bulletin, v. 112, p. 611-627.

MUSUMECI, G., PERTUSATI, P.C., RIBECAI, C., and MECCHERI, M., 2006, Early Jurassic Fossiliferous Black Shales in the Exposure Hill Formation, Ferrar Group of Northern Victoria Land, Antarctica: Terra Antarctica Reports, v. 12, p. 91-98.

NELSON, B.K., and DE PAOLO, D.J., 1988, Comparison of isotopic and petrographic provenance indicators in sediments from tertiary continental basins of New Mexico: Journal of Sedimentary Petrology, v. 58, p. 348-357.

NESBITT, H.W., and YOUNG, G.M., 1982, Early Proterozoic climates and plate motions inferred from major element chemistry of lutites: Nature, v. 299, p. 715-717.

NESBITT, H.W., and YOUNG, G.M., 1984, Prediction of some weathering trends of plutonic and volcanic rocks based on thermodynamic and kinetic considerations: Geochimica et Cosmochimica Acta, v. 48, p. 1523-1534.

NESBITT, H.W., and YOUNG, G.M., 1989, Formation and diagenesis of weathering profiles: Journal of Geology, v. 97, p. 129-147.

NOH, J.H., and BOLES, J.R., 1993, Origin of zeolite cements in the Miocene sandstones, North Tejon oil fields, California: Journal of Sedimentary Petrology, v. 63, p. 248-260.

NORRIS, G., 1965, Triassic and Jurassic miospores and acritarchs from the Beacon and Ferrar groups, Victoria Land, Antarctica: New Zealand J. of Geology and Geophysics, v. 8, p. 236-277.

PALMIERI, R., GHIRIBELLI, B., TALARICO, F., and RICCI, C.A., 2003, Ultra-high pressure metamorphism in felsic rocks: the garnet-phengite gneisses and quartzites from the Lanterman Range, Antarctica: European Journal of Mineralogy, v. 15, p. 513-525.

PALMIERI, R., and TALARICO, F., 1988, Contrasting petrological features between garnet-cordierite-biotite paragneisses from Black Ridge and from Cape Sastrugi, Deep Freeze Range (North Victoria Land, Antarctica): Mem. Soc. Geol. It., v. 43, p. 33-48.

PANKHURST, R.J., MILLAR, I.L., GRUNOW, A.M., and STOREY, B.C., 1993, The pre-Cenozoic magmatic history of the Thurston Island crustal block, West Antarctica: Journal of Geophysical Research, v. 98, p. 11835-11850.

PARKER, A., 1970, An index of weathering for silicate rocks: Geological Magazine, v. 107, p. 501-504.

PASSAGLIA, E., and SHEPPARD, R.A., 2001, The Crystal Chemistry of Zeolites, *in* Bish, D.L., and Ming, D.W., eds., Natural Zeolites: Occurrence, Properties, Applications: Washington, D.C., The Mineralogical Society of America, p. 69-116.

PAXTON, S.T., SZABO, J.O., AJDUKIEWICZ, J.M., and KLIMENTIDIS, R.E., 2002, Construction of an Intergranular Volume Compaction Curve for Evaluating and Predicting Compaction and Porosity Loss in Rigid-Grain Sandstone Reservoirs: AAPG Bulletin, v. 86, p. 2047-2067.

PEARCE, J.A., 1996, Sources and settings of granitic rocks: Episodes, v. 19, p. 120-125.

PEARCE, J.A., HARRIS, N.B.W., and TINDLE, A.G., 1984, Trace element discrimination diagrams for the tectonic interpretation of granitic rocks: Journal of Petrology, v. 25, p. 956-983.

PEARSON, M.J., WATKINS, D., PITTION, J.L., CASTON, D., and SMALL, J.S., 1983, Aspects of burial diagenesis, organic maturation and palaeothermal history of an area in the South Viking Graben, North Sea, *in* Brooks, J., ed., Petroleum Geochemistry and Exploration of Europe: Oxford, Geological Society Special Publication 12, p. 161-173.

PERRY, E.A., and HOWER, J., 1972, Late-stage dehydration in deeply buried pelitic sediments: AAPG Bulletin, v. 56, p. 2013-2021.

PERTUSATI, P.C., RIBECAI, C., CAROSI, R., and MECCHERI, M., 2006, Early Jurassic Age for Youngest Beacon Supergroup Strata Based on Palynomorphs from Section Peak, Northern Victoria Land, Antarctica: Terra Antarctica Reports, v. 12, p. 99-104.

PETRI, A., SALVINI, F., and STORTI, F., 1997, Geology of the Ferrar Supergroup in the Mesa Range, Northern Victoria Land, Antarctica: A Photogeological Study: The Antarctic Region: Geological Evolution and Processes, p. 305-312.

PETSCHICK, R., 2002, Röntgendiffraktometrie in der Sedimentologie: Schriftenr. dt. geol. Ges., v. 18, p. 99-118.

PETTIJOHN, F.J., POTTER, P.E., and SIEVER, R., 1972, Sand and Sandstone: New York, Springer Verlag, 618 p.

POBER, E., and FAUPL, P., 1988, The chemistry of detrital chromian spinels and its implications for the geodynamic evolution of the Eastern Alps: Geol. Rundschau, v. 77, p. 641-670.

POLDERVAART, A., 1950, Statistical studies of zircon as a criterion in granitisation: Nature, v. 165, p. 574-575.

POTTER, P.E., MAYNARD, J.B., and DEPETRIS, P.J., 2005, Mud and mudstone: Berlin, Springer, 297 p.

PRICE, J.R., and VELBEL, M.A., 2003, Chemical weathering indices applied to weathering profiles developed on heterogeneous felsic metamorphic parent rocks: Chemical Geology, v. 202, p. 397-416.

PUPIN, J.P., 1980, Zircon and granite petrology: Contributions to Mineralogy and Petrology, v. 73, p. 207-220.

REES, P.M., GIBBS, M.T., ZIEGLER, A.N., KUTZBACH, J.E., and BEHLING, P.J., 1999, Permian climates: Evaluating model predictions using global paleobotanical data: Geology, v. 27, p. 891-894.

REMY, R.R., and FERRELL, R.E., 1985, Distribution and Origin of Analcime in Marginal Lacustrine Mudstones of the Green River Formation, South-Central Uinta Basin, Utah: Clays and Clay Minerals, v. 37, p. 419-432.

RICCI, C.A., TALARICO, F., PALMIERI, R., DI VINCENZO, G., and PERTUSATI, P.C., 1996, Eclogite at the Antarctic palaeo-Pacific active margin of Gondwana (Lanterman Range, northern Victoria Land, Antarctica): Antarctic Science, v. 8, p. 277-280.

RICHARD, P., SHIMIZU, N., and ALLÈGRE, C.J., 1976, $^{143}Nd/^{146}Nd$, a natural tracer: An application to oceanic basalts: Earth and Panetary Science Letters, v. 31, p. 269-278.

RILEY, T.R., LEAT, P.T., PANKHURST, R.J., and HARRIS, C., 2001, Origins of Large Volume Rhyolitic Volcanism in the Antarctic Peninsula and Patagonia by Crustal Melting: Journal of Petrology, v. 42, p. 1043-1065.

ROLAND, N.W., LÄUFER, A.L., and ROSSETTI, F., 2004, Revision of the Terrane Model of Northern Victoria Land (Antarctica): Terra Antarctica, v. 11, p. 55-65.

ROLAND, N.W., OLESCH, M., and SCHUBERT, W., 1989, Geology and Petrology of the Western Border of the Transantarctic Mountains between the Outback Nunataks and Reeve Glacier, Northern Victoria Land, Antarctica, Geol. Jahrbuch: Hannover, p. 119-141.

ROLAND, N.W., and TESSENSOHN, F., 1987, Rennick Faulting - an Early Phase of Ross Sea Rifting: Geol. Jb., v. B66, p. 203-229.

ROLLINSON, H.R., 1993, Using geochemical data: evaluation, presentation, interpretation: Harlow, Longman, 352 p.

ROSER, B.P., 2000, Whole rock geochemical studies of clastic sedimentary suites: Geological Society of Japan, Memoirs, v. 57, p. 73-89.

ROSER, B.P., and KORSCH, R.J., 1986, Determination of tectonic setting of sandstone-mudstone suites using $SiO_2$ content and $K_2O/Na_2O$ ratio: J. Geol., v. 94, p. 635-650.

ROSER, B.P., and KORSCH, R.J., 1988, Provenance signatures of sandstone mudstone suites determined using discriminant function analysis of major element data Chem. Geol., v. 67, p. 119-139.

ROSER, B.P., and KORSCH, R.J., 1999a, Geochemical characterisation, evolution and source of a Mesozoic accretionary wedge: the Torlesse terrane, New Zealand: Geological Magazine, v. 136, p. 493-512.

ROSER, B.P., and KORSCH, R.J., 1999b, Geochemical characterization, evolution and source of a Mesozoic accretionary wedge: the Torlesse terrane, New Zealand: Geol. Mag., v. 136, p. 493-512.

ROSSETTI, F., LÄUFER, A.L., and STORTI, F., 2003a, Structural Architecture and tectonic Evolution of the Rennick Glacier Area (Northern Victoria Land, Antarctica) - Insights for the Cenozoic Tectonic Evolution of the Ross Sea Region: Terra Antarctica, v. 10, p. 141-156.

ROSSETTI, F., LISKER, F., STORTI, F., and LÄUFER, A.L., 2003b, Tectonic and denudational history of the Rennick Graben (North Victoria Land): Implications for the evolution of rifting between East and West Antarctica: Tectonics, v. 22, p. 11-1 - 11-18.

RUXTON, B.P., 1968, Measures of the degree of chemical weathering of rocks: J. Geol., v. 76, p. 518-527.

RYAN, K.M., and WILLIAMS, D.M., 2007, Testing the reliability of discrimination diagrams for determining the tectonic environment of ancient sedimentary basins: Chem. Geol., v. 242, p. 103-125.

SAIGAL, G.C., MORAD, S., BJØRLYKKE, K., EGEBERG, P.K., and AARGAARD, P., 1988, Diagenetic albitization of detrital K-Feldspar in Jurassic, Lower Cretaceous and Tertiary clastic reservoir rocks from offshore Norway, I: Textures and origin: Journal of Sedimentary Petrology, v. 58, p. 1003-1013.

SALEEMI, A.A., and AHMED, Z., 2000, Mineral and chemical composition of Karak mudstone, Kohat Plateau, Pakistan: implications for smectite-illitization and provenance: Sediment. Geol., v. 130, p. 229-247.

SALVINI, F., BRANCOLINI, G., BUSETTI, M., STORTI, F., MAZZARINI, F., and COREN, F., 1997, Cenozoic geodynamics of the Ross Sea region, Antarctica: Crustal extension, intraplate strike-slip faulting, and tectonic inheritance: Journal of Geophysical Research, v. 102, p. 24669-24696.

SALVINI, F., and STORTI, F., 1999, Cenozoic tectonic lineaments of the Terra Nova Bay region, Ross Embayment, Antarctica: Global and Planetary Change, v. 23, p. 129-144.

SCHMIDT, D.L., and ROWLEY, P.D., 1986, Continental rifting and transform faulting along the Jurassic Transantarctic Rift, Antarctica: Tectonics, v. 5, p. 279-291.

SCHNEIDER, J., BOMFLEUR, B., KERP, H., SCHÖNER, R., VIERECK-GÖTTE, L., and GAUPP, R., 2006, Biota of Late Triassic/Early Jurassic floodplains and lakes of North Victoria Land, Antarctica – implications on

environment and climate: Ancient Life and Modern Approaches, Abstracts of the 2nd International Palaeontological Congress 2006, p. 212-213.

SCHÖNER, R., 2006, Comparison of Rotliegend sandstone diagenesis from the northern and southern margin of the North German Basin, and implications for the importance of organic maturation and migration: Friedrich-Schiller-Universität Jena, PhD-Thesis, 160 p.

SCHÖNER, R., SCHNEIDER, J., BOMFLEUR, B., and VIERECK-GÖTTE, L., in review, The Triassic to Early Jurassic Section Peak Formation in North Victoria Land (Antarctica) revisited: Polarforschung.

SCHÖNER, R., SCHNEIDER, J., ELSNER, M., and GAUPP, R., 2008, Fluvial architecture of the Beacon Supergroup (Triassic-Jurassic) in North Victoria Land, Antarctica: Schriftenr. dt. geol. Ges., v. 58, p. 249.

SCHÖNER, R., VIERECK-GOETTE, L., SCHNEIDER, J., and BOMFLEUR, B., 2007, Triassic-Jurassic sediments and multiple volcanic events in North Victoria Land, Antarctica: A revised stratigraphic model, *in* Cooper, A.K., Raymond, C.R., and others, eds., Antarctica: A Keystone in a Changing World – Online Proceedings of the 10th ISAES: Washington, DC The National Academies Press.

SCHUBERT, W., OLESCH, M., and SCHMIDT, K., 1984, Paragneiss-orthogneiss relationships in the Kavrayskiy Hills, North Victoria Land, Antarctica: Geol. Jb. B, v. 60, p. 187-211.

SCHUMACHER, J.C., 1997, Appendix 2: The estimation of the proportion of ferric iron in the electron microprobe analysis of amphiboles, *in* Leake, B.E., Wooley, A.R., Arps, C.E.S., Birch, W.D., Gilbert, M.C., Grice, J.D., Hawthorne, F.C., Kato, A., Kisch, H.J., Krivovichev, V.G., Linthout, K., Laird, J., Mandarino, J.A., Maresch, W.V., Nickel, E.H., Rock, N.M.S., Schumacher, J.C., Smith, D.C., Stephenson, N.C.N., Ungaretti, L., Whittaker, E.J.W., and Youzhi, G., eds., Nomenclature of amphiboles: Report of the subcommitee on amphiboles of the International Mineralogical Association, commission on new minerals and mineral names, Can. Min., 35, 219-246.

SCHUMACHER, J.C., 2007, Metamorphic amphiboles: Composition and coexistence, *in* Hawthorne, F.C., Oberti, R., Della Ventura, G., and Mottana, A., eds., Amphiboles: Crystal chemistry, occurrence and health issue: Reviews in Mineralogy and Geochemistry, 67, p. 359-416.

SHATA, S., HESSE, R., MARTIN, R.F., and VALI, H., 2003, Expandability of anchizonal illite and chlorite: Significance for crystallinity development in the transition from diagenesis to metamorphism: American Mineralogist, v. 88, p. 748-762.

SHAW, H.F., 1972, The preparation of orientated clay mineral specimens for X-ray diffraction analysis by a suction-onto-ceramic tile method: Clay Minerals, v. 9, p. 349-350.

SIDDOWAY, C.S., 2007, Tectonics of the West Antarctic Rift System: New Light on the History and Dynamics of Distributed Intracontinental Extension, *in* Cooper, A.K., Raymond, C.R., and Others, eds., Antarctica: A Keystone in a Changing World – Proceedings of the 10th International Symposium on Antarctic Earth Sciences.: Washington, DC, The National Academies Press.

SIRCOMBE, K.N., 1999, Tracing provenance through the isotope ages of littoral and sedimentary detrital zircon, eastern Australia: Sediment. Geol., v. 124, p. 47-67.

SIRCOMBE, K.N., 2004, AgeDisplay: An Excel workbook to evaluate and display univariate geochronogical data using binned frequency histograms and probability density distributions: Computers and Geoscience, v. 30, p. 21-31.

SIRCOMBE, K.N., and STERN, R.A., 2002, An investigation of artificial biasing in detrital zircon U-Pb geochronology due to magnetic separation in sample preparation: Geochim. Cosmochim. Acta, v. 66, p. 2379-2397.

SKINNER, D.N.B., 1981, Possible Permian glaciation in north Victoria Land, Antarctica: Geologisches Jahrbuch B, v. B 41, p. 261-266.

SMART, G., and CLAYTON, T., 1985, The progressive illitization of interstratified Illite-Smectite from carboniferous sediments of northern England and its relationship to organic maturity indicators: Clay Minerals, v. 20, p. 455-466.

SMITH, C.H., 1996, Migmatites of the Alexandra Mountains, West Antarctica: Pressure-Temperature conditions of formation and regional context: Geologisches Jahrbuch B, v. 52, p. 169-178.

SOLANO-ACOSTA, W., SCHIMMELMANN, A., MASTALERZ, M., and ARANGO, I., 2008, Diagenetic mineralization in Pennsylvanian coals from Indiana, USA: $^{13}C/^{12}C$ and $^{18}O/^{16}O$ implications for cleat origin and coalbed methane generation: International Journal of Coal Geology, v. 73, p. 219-236.

SPEARS, D.A., KANARIS-SOTIRIOU, R., RILEY, N., and KRAUSE, P., 1999, Namurian bentonites in the Pennine Basin, UK - origin and magmatic affinities: Sedimentology, v. 46, p. 385-401.

ŚRODOŃ, J., 1980, Precise identification of illite/smectite interstratifications by X-ray powder diffraction: Clays and Clay Minerals, v. 28, p. 401-411.

STACEY, J.S., and KRAMERS, J.D., 1975, Approximation of terrestrial lead isotope evolution by a two-stage model: Earth and Panetary Science Letters, v. 26, p. 207-221.

STORTI, F., ROSSETTI, F., and SALVINI, F., 2001, Structural architecture and displacement accommodation mechanisms at the termination of the Priestley Fault, northern Victoria Land, Antarctica: Tectonophysics, v. 341, p. 141-161.

STUMP, E., WHITE, A.J.R., and BORG, S.G., 1986, Reconstruction of Australia and Antarctica: evidence from granites and recent mapping: Earth and Planetary Science Letters, v. 79, p. 348-360.

STURM, A., and CARRYER, S.J., 1970, Geology of the Region between Matusevich and Tucker Glaciers, North Victoria Land, Antarctica.: New Zealand Journal of Geology and Geophysics, v. 13, p. 408-435.

SVENSEN, H., JAMTVEIT, B., PLANKE, S., and CHELIER, L., 2006, Structure and evolution of hydrothermal vent complexes in the Karoo Basin: Journal of the Geological Society, London, v. 163, p. 671-682.

TALARICO, F., MEMMI, L., LOMBARDO, B., and RICCI, C.A., 1987, Thermo-barometry of granulite rocks from the Deep Freeze Range, North Victoria Land, Antarctica: Mem. Soc. Geol. It., v. 33, p. 131-141.

TAYLOR, E.L., BOUCHER, L.D., and TAYLOR, T.N., 1992, Dicroidium foliage from Mount Falla, central Transantarctic Mountains: Antarctic Journal of the United States, Review, p. 2-3.

TESSENSOHN, F., and HENJES-KUNST, F., 2005, Northern Victoria Land terranes, Antarctica: far-travelled or local products?, *in* Vaughan, A.P.M., Leat, P.T., and Pankhurst, R.J., eds., Terrane Processes at the Margins of Gondwana, Geol. Soc. London, p. 275-291.

TESSENSOHN, F., and MÄDLER, K., 1987, Triassic Plant Fossils from North Victoria Land, Antarctica: Geol. J., v. B 66, p. 187-201.

TILL, A.B., 1992, Detrital blueshist-facies mineral assemblages in Early Cretaceous sediments of the foreland basin of the Brooks Range, Alaska, and implications for orogenic evolution: Tectonics, v. 11, p. 1207-1223.

TONARINI, S., and ROCCHI, S., 1994, Geochronology of Cambro-Ordovician intrusives in northern Victoria Land: a review: Terra Antarctica, v. 1, p. 46-50.

TORSVIK, T.H., GAINA, C., and REDFIELD, T.F., 2008, Antarctica and Global Paleogeography: From Rodinia, Through Gondwanaland and Pangea, to the Birth of the Southern Ocean and the Opening of Gateways, *in* Cooper, A.K., Barrett, P.J., Stagg, H., Storey, B., Stump, E., Wise, W., and others, eds., Antarctica: A Keystone in a Changing World. Proceedings of the 10th International Symposium on Antarctic Earth Sciences: Washington, DC, The National Academies Press.

TRIEBOLD, S., VON EYNATTEN, H., LUVIZOTTO, G.L., and ZACK, T., 2007, Deducing source rock lithology from detrital rutile geochemistry: An example from the Erzgebirge, Germany: Chemical Geology, v. 244, p. 421-436.

ULITZKA, S., 1987, Petrology and Geochemistry of the Migmatites from Thompson Spur, Daniels Range, North Victoria Land, Antarctica: Geol. Jb., v. B 66, p. 81-130.

USGS/EROS, NASA, UNEP/GRID, USAID, INEGI/MEXICO, GSI/JAPAN, MWLR/NEW.ZEALAND, and SCAR, 1996, GTOPO30 (http://edc.usgs.gov/products/elevation/gtopo30/gtopo30.html).

UTADA, M., 2001a, Zeolites in Burial Diagenesis and Low-grade Metamorphic Rocks, *in* Bish, D.L., and Ming, D.W., eds., Natural Zeolites: Occurrence, Properties, Applications: Washington, D.C., The Mineralogical Society of America, p. 277-304.

UTADA, M., 2001b, Zeolites in Hydrothermally Altered Rocks, *in* Bish, D.L., and Ming, D.W., eds., Natural Zeolites: Occurrence, Properties, Applications: Washington, D.C., The Mineralogical Society of America, p. 305-322.

VAN DER PLAS, L., and TOBI, A.C., 1965, A chart for judging the reliability of point counting results: Am. J. Sci., v. 263, p. 87-90.

VAUGHAN, A.P.M., and PANKHURST, R.J., 2008, Tectonic overview of the West Gondwana margin: Gondwana Research, v. 13, p. 150-162.

VAVRA, C.L., STANLEY, K.O., and COLLINSON, J.W., 1981, Provenance and alteration of Triassic Fremouw Formation, central Transantarctic Mountains, *in* Creswell, M.M., and Vella, P., eds., Gondwana Five: Amsterdam, Balkema, p. 149–153.

VAVRA, G., 1990, On the kinematics of zircon growth and its petrogenetic significance: a cathodoluminescence study: Contributions to Mineralogy and Petrology, v. 106, p. 90-99.

VAVRA, G., SCHMID, R., and GEBAUER, D., 1999, Internal morphology, habit and U-Th-Pb microanalysis of amphibole to granulite facies zircon: geochronology of the Ivrea Zone (Southern Alps): Contributions to Mineralogy and Petrology, v. 134, p. 380-404.

VEEVERS, J.J., 2004, Gondwanaland from 650–500 Ma assembly through 320 Ma merger in Pangea to 185–100 Ma breakup: supercontinental tectonics via stratigraphy and radiometric dating: Earth-Science Reviews, v. 68, p. 1 –132.

VEEVERS, J.J., BELOUSOVA, E.A., SAEED, A., SIRCOMBE, K.N., COOPER, A.F., and READ, S.E., 2006, Pan-Gondwanaland detrital zircons from Australia analysed for Hf-isotopes and trace elements reflect an ice-covered Antarctic provenance of 700–500 Ma age, $T_{DM}$ of 2.0–1.0 Ga, and alkaline affinity: Earth-Science Reviews, v. 76, p. 135–174.

VEEVERS, J.J., SAEED, A., BELOUSOVA, E.A., and GRIFFIN, W.L., 2005, U–Pb ages and source composition of detrital zircons in Permian sandstone and modern sand from southwestern Australia and a review of the paleogeographical and denudational history of the Yilgarn Craton: Earth-Science Reviews, v. 68, p. 245-279.

VERMEESCH, P., 2004, How many grains are needed for a provenance study?: Earth and Planetary Science Letters, v. 224, p. 441–451.

VIERECK-GÖTTE, L., SCHÖNER, R., BOMFLEUR, B., and SCHNEIDER, J., 2007, Multiple shallow level sill intrusions coupled with hydromagmatic explosive eruptions marked the initial phase of Ferrar large igneous province magmatism in northern Victoria Land, Antarctica, *in* Cooper, A.K., Raymond, C.R., and others, eds., Antarctica: A Keystone in a Changing World – Online Proceedings of the 10th ISAES: Washington, DC, The National Academies Press.

VOGT, T., 1927, Sulitjelmafeltets geologi og petrografi: Norges Geologiske Undersokelse, 121: Oslo, 560 p.

VON EYNATTEN, H., 1996, Provenanzanalyse kretazischer Siliziklastika aus den Nördlichen Kalkalpen: Petrographie, Mineralchemie und Geochronologie des frühalpidisch umgelagerten Detritus: Ph.D.-Thesis, Johannes-Gutenberg-Universität Mainz, 145 p.

VON EYNATTEN, H., and GAUPP, R., 1999, Provenance of Cretaceous synorogenic sandstones in the Eastern Alps: constraints from framework petrography, heavy mineral analysis and mineral chemistry: Sediment. Geol., v. 124, p. 81-111.

WAGREICH, M., and MARSCHALKO, R., 1995, Late Cretaceous to Early Tertiary palaeogeography of the Western Carpathians (Slovakia) and the Eastern Alps (Austria): implications from heavy minerals: Geol. Rundschau, v. 84, p. 187-199.

WALKER, B.C., 1983, The Beacon Supergroup of Northern Victoria Land, Antarctica, *in* Oliver, R.L., James, P.R., and Jago, J.B., eds., Antarctic Earth Science: Canberra, p. 211-214.

WALKER, T.R., 1967, Formation of Red Beds in Modern and Ancient Deserts: Geol. Society of America Bulletin, v. 78, p. 353-368.

WALKER, T.R., 1976, Diagenetic origin of continental red beds, *in* Falke, H., ed., The continental Permian in Central, West and South Europe: Dordrecht, Reidel, p. 240-282.

WALTER, H.J., HEGNER, E., DIEKMANN, B., KUHN, G., and RUTGERS VAN DER LOEFF, M.M., 2000, Provenance and transport of terrigenous sediment in the South Atlantic Ocean and their relations to glacial and interglacial cycles: Nd and Sr isotopic evidence: Geochim. Cosmochim. Acta, v. 64, p. 3813-3827.

WAREHAM, C.D., PANKHURST, R.J., THOMAS, R.J., STOREY, B.C., GRANTHAM, G.H., JACOBS, J., and EGLINGTON, B.M., 1998, Pb, Nd and Sr isotope mapping of Grenville-age crustal provinces in Rodinia-age crustal Provinces in Rodinia: J. Geol., v. 106.

WEIBEL, R., and GROBETY, B., 1999, Pseudomorphous transformation of goethite needles into hematite in sediments of the Triassic Skagerrak Formation, Denmark: Clay Minerals, v. 34, p. 657-660.

WETHERILL, G.W., 1956, Discordant uranium-lead ages: Trans. Amer. Geophys. Union, v. 37, p. 320-326.

WHITEHEAD, J.M., P.G., Q., MCKELVEY, B.C., and O'BRIEN, P.E., 2006, A review of the Cenozoic stratigraphy and glacial history of the Lambert Graben - Prydz Bay region, Antarctica: Antarct. Sci., v. 18, p. 83-99.

WILLAN, R.C.R., 2003, Provenance of triassic-cretaceous sandstones in the Antarctic Peninsula: implications for terrane models during Gondwana breakup: Journal of Sedimentary Research, v. 73, p. 1062-1077.

WILLIAMS, I.S., 1998, U-Th-Pb Geochronology by Ion Microprobe, *in* McKibben, M.A., Shanks, W.C.I., and Ridley, W.I., eds., Applications of microanalytical techniques to understanding mineralizing processes. Reviews in Economic Geology, 7, p. 1-35.

WILLSCHER, B., 2004, Die kalkalpinen Tratenbach-Schichten (Oberkreide - Paläogen, Oberbayern) - Gesamtgesteinsanalysen und petrographische Untersuchungen zur stratigraphischen Stellung und geodynamischen Bedeutung: PhD-thesis, Friedrich-Schiller-Universität Jena, 129 p.

WIMMENAUER, W., 1985, Petrographie der magmatischen und metamorphen Gesteine: Stuttgart, Enke-Verlag, 382 p.

WINCHESTER, J.A., and FLOYD, P.A., 1977, Geochemical discrimination of different magma series and their differentiation products using immobile elements: Chem. Geol., v. 20, p. 325-343.

WINKLER, W., and BERNOULLI, D., 1986, Detrital high-pressure/low-temperature minerals in a late Turonian flysch sequence of the eastern Alps (western Austria): Implications for early Alpine tectonics: Geology, v. 14, p. 598-601.

WONES, D.R., and GILBERT, M.C., 1982, Amphiboles in the igneous environment, *in* Veblen, B.R., and Ribbe, P.H., eds., Amphiboles: petrology and experimental phase relations: Reviews in Mineralogy, 9B, p. 355-385.

WORDEN, R.H., and BURLEY, S.D., 2003, Sandstone diagenesis: the evolution of sand to stone, *in* Worden, R.H., and Burley, S.D., eds., Sandstone Diagenesis: Recent and Ancient: Oxford, Reprint Series vol. 4 of the Int. Ass. Sediment., p. 3-44.

WRIGHT, T.O., and BRODIE, C., 1986, The Handler Formation, a new unit of the Robertson Bay Group, northern Victoria Land, Antarctica, *in* McKenzie, G.D., ed., Gondwana Six: Structure, Tectonics, Geophysics - Geophys. Monogr., 40, Amer. Geophys. Union, p. 25-30.

WU, Y., and ZHENG, Y., 2004, Genesis of zircon and its constraints on interpretation of U-Pb age: Chinese Science Bulletin, v. 49, p. 1554-1469.

YAMAMOTO, H., and KENNEDY, G.C., 1969, Stability relations in the system $CaSO_4$-$H_20$ at high temperatures and pressures: American Journal of Science, v. 267-A, p. 550-557.

YOSHIDA, M., JACOBS, J., SANTOSH, M., and RAJESH, H.M., 2003, Role of Pan-African events in the Circum-East Antarctic Orogen of East Gondwana: a critical overview, *in* Yoshida, M., Windley, B.F., and Dasgupta, S., eds., Proterozoic East Gondwana: Supercontinent Assembly and Breakup: London, Geological Society, Special Publication 206, p. 57-75.

YOUNG, G.M., 1999, Some aspects of the geochemistry, provenance and palaeoclimatology of the Torridonian of NW scotland: Journal of the Geological Society, London, v. 156, p. 1097-1111.

ZACK, T., MORAES, R., and KRONZ, A., 2004a, Temperature dependence of Zr in rutile: empirical calibration of a rutile thermometer: Contributions to Mineralogy and Petrology, v. 148, p. 471-488.

ZACK, T., VON EYNATTEN, H., and KRONZ, A., 2004b, Rutile geochemistry and its potential use in quantitative provenance studies: Sediment. Geol., v. 171, p. 37-58.

ZEIL, W., 1986, Südamerika: Geologie der Erde: Stuttgart, Enke Verlag, 160 p.

ZIMMERLE, W., 1984, The geotectonic significance of detrital brown spinel in sediments: Mitt. Geol.-Paläont. Inst. Univ. Hamburg, v. 56, p. 337-360.

ZUFFA, G.G., 1985, Optical analyses of arenites: influence of methodology on compositional results, *in* Zuffa, G.G., ed., Provenance of arenites: Dordrecht, Reidel, p. 165-189.

## Appendix

# Appendix 1

Samples and applied methods

## Thern Promontory (TP)

Succession on top of basement — Southern Eisenhower Range — 161°59.876 East — 74°23.745 South — 1510 m above sea level (outcrop base)

| Sample | Strat. | Lithology | Light mineralogy | | Heavy mineralogy | RFA (whole rock) | EMP | XRD | U-Pb ages of Zircons | Sm, Nd, Sr isotopes |
|---|---|---|---|---|---|---|---|---|---|---|
| | | | qualit. | quantit. | | | | | | |
| TP02-RS03 | SPF | conglomerate | x | | | | | | | |
| TP03-RS05 | SPF | sandstone | x | | x | x | x | | | |
| TP04-RS07 | SPF | sandstone | x | | | x | | | | |
| TP05-RS08 | SPF | conglomerate | x | x | | | | | | |

## Anderton Glacier (AG)

Succession on top of basement — Southern Eisenhower Range — 162°14.719 East — 74°34.714 South — 1820 m above sea level (outcrop base)

| Sample | Strat. | Lithology | Light mineralogy | | Heavy mineralogy | RFA (whole rock) | EMP | XRD | U-Pb ages of Zircons | Sm, Nd, Sr isotopes |
|---|---|---|---|---|---|---|---|---|---|---|
| | | | qualit. | quantit. | | | | | | |
| AG08-JS | SPF | siltstone | | | | | | x | | |
| AG08-RS21 | SPF | siltstone | x | | | | | | | |
| AG09-RS22 | SPF | sandstone | x | x | | | | | | |

## Eisenhower Range (ER)

E-cliff — Southern Eisenhower Range — 162°31.407 East — 74°27.890 South — 2275 m above sea level (outcrop base)

| Sample | Strat. | Lithology | Light mineralogy | | Heavy mineralogy | RFA (whole rock) | EMP | XRD | U-Pb ages of Zircons | Sm, Nd, Sr isotopes |
|---|---|---|---|---|---|---|---|---|---|---|
| | | | qualit. | quantit. | | | | | | |
| ER03-JS01 | SPF | conglomerate | x | | | | | | | |
| ER04-RS03 | SPF | sandstone | x | x | x | | x | | LA-ICP-MS | |
| ER07-RS07 | SPF | sandstone | x | x | x | | | | | |
| ER08-RS09 | SPF | sand-siltstone | x | | | | | | | |
| ER09-RS10 | SPF | conglomerate | x | | | | | | | |

## Skinner Ridge (SR)

Sandstone succession between sills — Southern Eisenhower Range — 161°51.252 East — 74°21.747 South — ~2000 m above sea level (outcrop base)

| Sample | Strat. | Lithology | Light mineralogy | | Heavy mineralogy | RFA (whole rock) | EMP | XRD | U-Pb ages of Zircons | Sm, Nd, Sr isotopes |
|---|---|---|---|---|---|---|---|---|---|---|
| | | | qualit. | quantit. | | | | | | |
| SR01-RS03 | SPF | sandstone | x | x | | | | | | |
| SR03-RS07 | SPF | sandstone | x | x | | x | x | | | |
| SR03-RS09 | SPF | sandstone | x | x | | | | | | |

## Timber Peak (TI)

Sandstone/mudstone/coal succession between sills — Northern Eisenhower Range — 162°23.122 East — 74°10.504 South — 2840 m above sea level (outcrop base)

| Sample | Strat. | Lithology | Light mineralogy | | Heavy mineralogy | RFA (whole rock) | EMP | XRD | U-Pb ages of Zircons | Sm, Nd, Sr isotopes |
|---|---|---|---|---|---|---|---|---|---|---|
| | | | qualit. | quantit. | | | | | | |
| TI01-RS08 | SPF | sandstone | x | x | | | | | | |
| TI03-RS10 | SPF | sandstone | x | x | x | | | | | |
| TI04-RS11 | SPF | sandstone | x | | | x | | | | |
| TI11-RS17 | SPF | sandstone | x | x | | x | | | | |
| TI13-RS14 | SPF | sandstone, grey | x | | | | | | | |
| TI13-RS15 | SPF | siltstone, grey | | | | | | | | x |
| TI14-RS17 | SPF | sandstone | x | x | x | | x | | LA-ICP-MS | |
| TI16-RS20 | SPF | sandstone | x | | | x | | | | |
| TI18-RS22 | SPF | sandstone | x | x | x | | | | | |
| TI19-RS25 | SPF | sandstone | x | | | x | | | | |
| TI23-RS04 | SPF | sandstone | x | x | x | | | | | |

## Shafer Peak South (SHS)

Shafer Peak S-Ridge — Southern Deep Freeze Range — 162°37.310 East — 74°02.367 South — ~ 3000 m above sea level (outcrop base)

| Sample | Strat. | Lithology | Light mineralogy | | Heavy mineralogy | RFA (whole rock) | EMP | XRD | U-Pb ages of Zircons | Sm, Nd, Sr isotopes |
|---|---|---|---|---|---|---|---|---|---|---|
| | | | qualit. | quantit. | | | | | | |
| SHS01-RS02 | SPF | sandstone-conglomerate | x | x | x | x | | | | |
| SHS03-RS12 | SPF | sandstone | x | x | x | x | | | LA-ICP-MS | |
| SHS04-RS15 | SPF | sandstone, brown horizon | x | x | | | x | | | |
| SHS04-RS16 | SPF | sandstone | x | x | | x | | | | |

## Shafer Peak A (SHA)

Shafer Peak N-Ridge — Southern Deep Freeze Range — 162°36.266 East — 73°59.750 South — 3100 m above sea level (outcrop base)

| Sample | Strat. | Lithology | Light mineralogy | | Heavy mineralogy | RFA (whole rock) | EMP | XRD | U-Pb ages of Zircons | Sm, Nd, Sr isotopes |
|---|---|---|---|---|---|---|---|---|---|---|
| | | | qualit. | quantit. | | | | | | |
| SHA03-RS02 | SPF | sandstone | x | x | | x | | | | |
| SHA05-RS03 | SPF | sandstone | x | x | | x | x | | | |
| SHA06-RS04 | SPF | tuffite | x | x | | | x | | | |
| SHA06-RS05 | SPF | pelite | | | | | | x | | |
| SHA07-RS06 | SPF | sandstone | x | x | x | x | | | LA-ICP-MS | |
| SHA08-BB01 | SPF | pelite | | | | | | x | | |
| SHA09-RS09 | SPF | tuffite | x | x | | x | | | | |
| SHA11-RS12 | SPF | siltstone | | | | | | | | x |
| SHA12-RS14 | SPF | tuffite | x | x | | | x | x | | |
| SHA14-RS15 | SPF | tuffite | x | x | | x | | | SHRIMP | |
| SHA16-RS16 | SPF | tuffite | x | x | | | | | | |
| SHA17-RS17 | SPF | sandstone | x | x | x | x | | | | |

## Shafer Peak B (SHB)

Shafer Peak N-Ridge — Southern Deep Freeze Range — following on top of section Shafer Peak A

| Sample | Strat. | Lithology | Light mineralogy | | Heavy mineralogy | RFA (whole rock) | EMP | XRD | U-Pb ages of Zircons | Sm, Nd, Sr isotopes |
|---|---|---|---|---|---|---|---|---|---|---|
| | | | qualit. | quantit. | | | | | | |
| SHB02-RS20 | SPF (EHT) | pelite | | | | | | x | | |
| SHB07-RS26 | SPF (EHT) | pelite, dark grey | | | | | | x | | |

## Shafer Peak C (SHC)

Shafer Peak N-Ridge — Southern Deep Freeze Range — following on top of section Shafer Peak B

| Sample | Strat. | Lithology | Light mineralogy | | Heavy mineralogy | RFA (whole rock) | EMP | XRD | U-Pb ages of Zircons | Sm, Nd, Sr isotopes |
|---|---|---|---|---|---|---|---|---|---|---|
| | | | qualit. | quantit. | | | | | | |
| SHC02-JS01 | SHF | tuffaceous sandstone | | | | | | | SHRIMP | |
| SHC02-JS02 | SHF | tuffaceous sandstone | x | x | x | x | | | | |
| SHC03-JS02 | SHF | tuffaceous sandstone | x | x | | | | | | |
| SHC04-JS01 | SHF | tuffaceous sandstone | x | x | | | | | | |
| SHC06-JS01 | SHF | tuffaceous sandstone | x | x | | | | | | |
| SHC08-JS01 | SHF | tuffaceous sandstone | x | | | x | | | | |
| SHC11-RS27 | SHF | tuffaceous sandstone | x | | | | | | | |
| SHC16-RS29 | SHF | tuffaceous sandstone | x | x | | | | | | |
| SHC23-RS30 | SHF | tuffaceous sandstone | | | | | | x | | |
| SHC25-RS31 | SHF | sandstone | x | | x | x | x | | | |
| SHC29-RS34 | SHF | pelite | | | | | | x | | x |
| SHC33-RS36 | SHF | tuffaceous sandstone | x | x | | | x | | | |
| SHC33-RS46 | SHF | tuffaceous sandstone | | | | | | | SHRIMP | |
| SHC36-RS38 | SHF | pelite | | | | | | x | | |
| SHC39-RS39 | SHF | tuffaceous sandstone | x | x | | x | | | | |
| SHC41-RS40 | SHF | tuffaceous sst., mafic fragments | x | | | | | | | |
| SHC42-RS44 | SHF | tuffaceous sandstone, altered | x | | | | | | | |

## Priestley-S-cliff (PR)

Cliff towards Priestley Glacier NE of Shafer Pk. — Southern Deep Freeze Range — 162°26.833 East — 74°00.833 South — ~ 2800 m above sea level (outcrop top)

| Sample | Strat. | Lithology | Light mineralogy | | Heavy mineralogy | RFA (whole rock) | EMP | XRD | U-Pb ages of Zircons | Sm, Nd, Sr isotopes |
|---|---|---|---|---|---|---|---|---|---|---|
| | | | qualit. | quantit. | | | | | | |
| PR05-RS05 | SPF | sand-siltstone, grey | x | | | | | | | |

## Pt. 3350 (PT)

Succession on top of basement — Southern Deep Freeze Range — 162°58.142 East — 73°58.422 South — ~ 2615 m above sea level (outcrop base)

| Sample | Strat. | Lithology | Light mineralogy | | Heavy mineralogy | RFA (whole rock) | EMP | XRD | U-Pb ages of Zircons | Sm, Nd, Sr isotopes |
|---|---|---|---|---|---|---|---|---|---|---|
| | | | qualit. | quantit. | | | | | | |
| PT02-RS02 | SPF | sandstone | x | x | | | | | | |
| PT03-RS03 | SPF | sandstone | x | x | | | x | | | |
| PT05-RS05 | SPF | sandstone | x | x | | | | | | |

## Mt. Adamson (MA)

E-cliff and ridge — Southern Deep Freeze Range — 163°00.343 East — 73°56.418 South — ~ 2700 m above sea level (outcrop base)

| Sample | Strat. | Lithology | Light mineralogy | | Heavy mineralogy | RFA (whole rock) | EMP | XRD | U-Pb ages of Zircons | Sm, Nd, Sr isotopes |
|---|---|---|---|---|---|---|---|---|---|---|
| | | | qualit. | quantit. | | | | | | |
| MA02-RS15 | SPF | sandstone | x | x | | | | | | |
| MA06-1-RS13 | SPF | sandstone | x | x | | | x | x | | |
| MA06-2-RS11 | SPF | sandstone | x | | | | | | | |
| MA06-3-RS10 | SPF | sandstone | x | x | | | x | x | | |
| MA06-4-RS06 | SPF | sandstone | x | | | | | | | |
| MA06-4-RS07 | SPF | sandstone | | | | x | | | | |
| MA10-RS02 | SPF | volcaniclast. sst. | x | | | | | | | |

## Archambault Plateau N (AN)

Plateau N' Archambault Ridge — Northern Deep Freeze Range — 162°45.063 East — 73°41.310 South — ~ 2670 m above sea level (top of ridge)

| Sample | Strat. | Lithology | Light mineralogy | | Heavy mineralogy | RFA (whole rock) | EMP | XRD | U-Pb ages of Zircons | Sm, Nd, Sr isotopes |
|---|---|---|---|---|---|---|---|---|---|---|
| | | | qualit. | quantit. | | | | | | |
| AN01-RS01a | SPF | sandstone | x | x | x | x | x | x | | |
| AN01-RS01b | SPF | siltone-clast | x | | | | | | | |
| AN01-RS02 | SPF | sandstone | x | x | | | | | | |
| AN02-RS03 | SPF | sandstone | x | | x | x | | x | | |
| AN03-RS04 | SPF | sandstone | x | x | | | | | | |
| AN03-RS05a | SPF | clast | x | | | | | | | |
| AN03-RS05b | SPF | clast | x | | | | | | | |
| AN03-RS05c | SPF | clast | x | | | | | | | |
| AN03-RS06 | SPF | sandstone | x | | x | x | | x | | |
| AN03-RS06-O | SPF | sandstone | | | | x | | | | |
| AN05-RS08 | SPF | mudstone | x | | | x | | x | | |
| AN08-RS09 | SPF | sandstone | x | x | x | x | | x | | |
| AN09-RS10 | SPF | sandstone | x | x | | x | | | | |
| AN11-RS11 | SPF | sandstone | | | x | x | | x | | |
| AN15-RS12 | SPF | sandstone | x | x | | x | x | | | |
| AN16-RS13 | SPF | sandstone | x | x | x | x | | x | | |
| AN18-RS14 | SPF | sandstone | x | x | | x | | | | |

## Chisholm Hills W-Ridge (CHW)

Section on top of steep basalt cliff — Southern Cross Mountains — 163°18.586 East — 73°26.820 South — 2525 m above sea level (outcrop base)

| Sample | Strat. | Lithology | Light mineralogy | | Heavy mineralogy | RFA (whole rock) | EMP | XRD | U-Pb ages of Zircons | Sm, Nd, Sr isotopes |
|---|---|---|---|---|---|---|---|---|---|---|
| | | | qualit. | quantit. | | | | | | |
| CHW02-RS02 | SPF | sandstone | x | | | | | | | |
| CHW02-RS03 | SPF | sandstone | x | | | | | | | |
| CHW03-RS04 | SPF | sandstone | x | | | x | | | | |
| CHW04-RS05 | SPF | sandstone | x | x | | | | | | |
| CHW05-RS06 | SPF | mudstone | x | | | | | | | |
| CHW06-RS08 | SPF | sandstone | x | x | | | x | x | | |
| CHW07-RS10 | SPF | sandstone | x | | x | x | | | LA-ICP-MS | |
| CHW08-RS11 | SPF | mudstone | x | | | x | | | | |
| CHW10-RS14 | SPF | sandstone | x | x | | x | | x | | |
| CHW11-RS16 | SPF | sandstone | x | | | | | | | |
| CHW11-RS18 | SPF | sandstone | x | | x | | | | | |
| CHW12-RS20 | SPF | sandstone | x | | | | | | | |
| CHW14-RS22 | SPF | sandstone | x | | x | x | | | | |
| CHW15-RS24 | SPF | mudstone, black | | | | | | | | x |
| CHW18-RS32 | SPF | siltstone | x | | | | | | | |
| CHW22-RS37 | SPF | sandstone | x | | | | | | | |
| CHW23-RS38 | SPF | sandstone ('gres nougat') | x | | | | | | | |
| CHW25-RS40 | SPF | sandstone | x | | | | | | | |
| CHW26-RS41 | SPF | sandstone | x | x | x | x | x | x | LA-ICP-MS | |
| CHW27-RS65 | SPF | siltstone, coaly | x | | | | | | | |
| CHW61-RS59 | SPF | sandstone | x | | | | | | | |
| CHW67-RS62 | SPF | Siltstone | x | | | | | | | |

## Mt. Carson E-Ridge (CE)

Tuffaceous sandstones to pillows, SHF — Southern Cross Mountains — 163°12.100 East — 73°27.100 South — 2520 m above sea level (outcrop base)

| Sample | Strat. | Lithology | Light mineralogy | | Heavy mineralogy | RFA (whole rock) | EMP | XRD | U-Pb ages of Zircons | Sm, Nd, Sr isotopes |
|---|---|---|---|---|---|---|---|---|---|---|
| | | | qualit. | quantit. | | | | | | |
| CE02-RS26 | SHF | tuffaceous sandstone | x | x | | | | | | |
| CE09-RS01 | SHF | tuffaceous sandstone | x | x | | x | | | | |
| CE15-RS03 | SHF | intraclast-horizon | | | | | x | | | |
| CE19-RS05 | SHF | tuffaceous sandstone | x | x | | x | | | | |
| CE26-RS07 | SHF | tuffaceous sandstone | x | x | | | | | | |
| CE41-RS09 | SHF | tuffaceous sandstone | x | x | | x | | | | |
| CE55-RS14 | SHF | tuffaceous sandstone | x | x | | x | | | | |
| CE56-RS15 | SHF | mudstone | x | | | | | x | | |
| CE67-RS17 | SHF | mudstone | x | | | | | x | | |
| CE68-RS19 | SHF | tuffaceous sandstone | x | | | | | | | |
| CE77-RS20 | SHF | tuffaceous sandstone | x | x | | x | x | | | |
| CE90-RS24 | SHF (EHT) | debris flow | x | | | | x | | | |
| CE91-RS25 | SHF (EHT) | debris flow | x | | | | | | | |
| CE10-JS07 | SHF (EHT) | volcaniclast. sandstone | x | | | | | | | |

## Stewart Heights (ST)

Succession between basement and sill — Southern Cross Mountains — 163°54.682 East — 73°29.472 South — 2650 m above sea level (outcrop base)

| Sample | Strat. | Lithology | Light mineralogy | | Heavy mineralogy | RFA (whole rock) | EMP | XRD | U-Pb ages of Zircons | Sm, Nd, Sr isotopes |
|---|---|---|---|---|---|---|---|---|---|---|
| | | | qualit. | quantit. | | | | | | |
| ST01-RS01 | SPF | conglomerate | x | | | | | | | |
| ST05-RS03 | SPF | sandstone | x | x | | | | | | |
| ST09-RS05 | SPF | sandstone | x | x | | | | | | |

## Section Peak (SP)

Succession on top of basement — Upper Rennick Glacier — 161°56.105 East — 73°14.273 South — ~ 2250 m above sea level (outcrop base)

| Sample | Strat. | Lithology | Light mineralogy | | Heavy mineralogy | RFA (whole rock) | EMP | XRD | U-Pb ages of Zircons | Sm, Nd, Sr isotopes |
|---|---|---|---|---|---|---|---|---|---|---|
| | | | qualit. | quantit. | | | | | | |
| SP01-RS02 | SPF | sandstone | x | | | | x | | | |
| SP01-RS03 | SPF | sandstone | x | | | | | | | |
| SP05-RS05 | SPF | sandstone | x | x | x | x | | | | |
| SP08a-RS07 | SPF | sandstone | x | | | | | | | |
| SP08-RS06 | SPF | sandstone | | | x | x | x | | LA-ICP-MS | |
| SP11-RS08 | SPF | sandstone | x | x | | x | | | | |

## Section Peak Plateau (SPP)

Upper part (plateau) — Upper Rennick Glacier — 161°55.145 East — 73°14.454 South — 2400 m above sea level (outcrop base)

| Sample | Strat. | Lithology | Light mineralogy | | Heavy mineralogy | RFA (whole rock) | EMP | XRD | U-Pb ages of Zircons | Sm, Nd, Sr isotopes |
|---|---|---|---|---|---|---|---|---|---|---|
| | | | qualit. | quantit. | | | | | | |
| SPP02-JS | SPF | siltstone | | | | | | | | x |
| SPP05-RS17 | SPF | sandstone | x | x | | x | | | | |
| SPP07-RS19 | SPF | sandstone | x | | | | x | | | |
| SPP10-RS23 | SPF | sandstone | x | x | | | | | | |
| SPP17-RS29 | SPF | sandstone | x | | x | x | | | | |
| SPP20-RS03 | SPF | sandstone | x | x | | | | | | |
| SPP23-RS04 | SPF | sandstone | x | | | x | | | | |
| SPP31-RS07 | SPF | sandstone | x | x | | | x | | | |
| SPP36-RS14 | SPF | sandstone | x | | x | x | | | LA-ICP-MS | |

# Roberts Butte (RB)

Succession between basement and sill | Upper Rennick Glacier / Outback Nunatak | 160°08 East | 72°39 South | ~ 2800 m above sea level (outcrop base)

| Sample | Strat. | Lithology | Light mineralogy | | Heavy mineralogy | RFA (whole rock) | EMP | XRD | U-Pb ages of Zircons | Sm, Nd, Sr isotopes |
|---|---|---|---|---|---|---|---|---|---|---|
| | | | qualit. | quantit. | | | | | | |
| RB01 | SPF | sandstone | x | | | | | | | |
| RB02 | SPF | sandstone / conglomerate | x | | | | | | | |
| RB04 | SPF | sandstone | x | x | x | | x | | | |
| RB06 | SPF | sandstone, coaly layers | x | x | | | | | | |
| RB07 | SPF | sandstone, silicified wood | x | | | | | | | |
| RB08 | SPF | sandstone | x | | | x | | | | |
| RB11 | SPF | sandstone, coaly layers | x | x | x | | | | | |

# Appendix 2

Petrographic (point-counting) data of sandstones
and tuffaceous sandstones (light and heavy mineralogy)

## Light mineralogy of sandstones

| | Minerals | | | | | | | | Rock fragments | | | | | | | | | | | | Authigenic minerals | | | | | | | | | Pore space | |
|---|---|---|---|---|---|---|---|---|---|---|---|---|---|---|---|---|---|---|---|---|---|---|---|---|---|---|---|---|---|---|---|
| **Sample** | **Qm** | **Pl** | **Kf** | **Mi** | **Mu** | **Bi** | **Opq** | **HM** | **$Qp_{2-3}$** | **$Qp_{>3}$** | **Qc** | **Lvf** | **Lvm** | **Lvv** | **Ls** | **Lmq** | **Lmm** | **Lgr** | **Li** | **Luq** | **Lu** | **Qtz** | **Cc** | **Hem** | **Zeo** | **Bas** | **Jar** | **Ill** | **Kao** | **Chl** | **FeH** | **Intragr.** | **tot.** |
| TP05 | 31.6 | | 22.5 | 0.9 | 0.6 | 16.5 | | 0.6 | 6.3 | 2.2 | | 0.3 | | | | 1.9 | 2.2 | 4.4 | | 0.6 | 3.5 | | | 2.2 | | | | | 1.9 | | | | 1.6 |
| AG09-RS22 | 48.2 | | 20.2 | | 0.3 | 12.1 | | 0.3 | 6.5 | 0.7 | | 1.3 | | | | 0.7 | 2.6 | 4.2 | | | 1.6 | | | 0.7 | | | | | | 0.3 | | 0.3 |
| ER04 | 55.7 | | 10.8 | 0.7 | 0.3 | 3.6 | | | 11.5 | 3.3 | | 3.9 | | | | 0.3 | | 4.6 | | | 1.0 | | | | | | | | | 1.0 | | 3.3 |
| ER07 | 50.9 | | 16.6 | 0.3 | 0.6 | 4.7 | | | 7.2 | 1.3 | | 1.3 | | | | 1.6 | 0.9 | 6.3 | | 0.6 | 1.9 | | | 0.3 | | | | | 3.4 | | | | 2.2 |
| SR01-RS03 | 43.3 | | 14.7 | | | 1.0 | 0.3 | | 5.7 | 0.7 | | 17.3 | 0.7 | | 0.3 | 2.7 | 4.0 | 4.3 | | | 1.3 | | | | 2.7 | | | | | | | 1.7 | 2.7 |
| SR03-RS07 | 16.1 | 0.7 | 10.6 | | 0.3 | 2.6 | 1.3 | | 2.0 | 1.0 | 0.3 | 40.7 | 1.5 | | 1.1 | 2.8 | 5.2 | 3.4 | 0.2 | | 3.1 | | | | 5.7 | | | 0.2 | | | 0.8 | 0.3 | 1.0 |
| SR03-RS09 | 23.4 | | 19.9 | | 0.9 | 7.6 | 0.6 | | 1.3 | | 0.6 | 23.7 | 2.2 | | 0.6 | 3.2 | 4.1 | 5.7 | 0.6 | | 3.8 | | | | | | | | | | 1.3 | | 0.3 |
| TI01-RS08 | 16.9 | 1.8 | 10.8 | | | 0.9 | 0.6 | | 3.0 | 0.3 | 0.9 | 34.0 | 12.0 | 1.2 | 0.6 | 1.5 | 1.2 | 1.5 | | | 3.9 | | 5.4 | | | | | | | | 1.5 | | 1.8 |
| TI03-RS10 | 21.6 | 1.8 | 5.9 | 0.9 | | 0.6 | 0.3 | | 1.2 | 0.9 | 1.8 | 18.3 | 13.9 | | 0.3 | 9.5 | 8.3 | 5.3 | | | 4.1 | | | | | | | | 3.6 | | | | 1.8 |
| TI11-RS17 | 24.0 | 1.0 | 6.1 | | | 4.8 | 1.3 | | 0.6 | | 1.3 | 31.0 | 4.8 | | | 4.2 | 9.3 | 4.8 | | | 5.4 | | | 1.0 | | | | | | | 0.6 | | 0.0 |
| TI14-RS17 | 17.7 | 1.9 | 5.0 | 1.3 | | 0.9 | 0.3 | 0.3 | 0.9 | 1.6 | 1.3 | 8.8 | 19.2 | 0.6 | | 15.5 | 5.0 | 5.7 | | 4.7 | 5.7 | | | | | | | 1.9 | | | | 1.6 |
| TI18-RS22 | 17.5 | 3.8 | 15.3 | | | 1.0 | 0.6 | | 1.0 | | 0.6 | 30.6 | 13.4 | | | 3.2 | 2.5 | 2.9 | | | 4.5 | | 2.9 | 0.3 | | | | | | | | | 0.0 |
| TI23-RS04 | 54.0 | 0.3 | 9.3 | 0.6 | 0.3 | 0.6 | | | 4.8 | 1.6 | 0.3 | 4.5 | 1.3 | | 0.3 | 1.6 | 2.6 | 5.8 | | 0.0 | 2.3 | | | | | | | 0.3 | | | 1.6 | | 7.7 |
| SHS01-RS02 | 35.6 | | 7.3 | 0.6 | 0.3 | 0.3 | 0.6 | 0.3 | 19.2 | | 3.2 | 7.9 | 5.0 | | 2.5 | 1.6 | 0.6 | 1.3 | | 2.5 | 1.9 | 0.3 | 6.6 | | | | | | | | 0.6 | | 1.6 |
| SHS03-RS12 | 58.6 | 0.3 | 6.9 | 0.7 | 0.7 | | | | 12.2 | 2.3 | 0.3 | 2.3 | 1.6 | | 0.3 | 1.0 | 0.7 | 2.0 | | 0.3 | | | | | | | | 0.3 | | | 1.0 | | 8.6 |
| SHS04-RS15 | 58.1 | | 4.9 | 1.0 | | | 0.3 | 0.3 | 9.4 | 2.6 | 0.6 | 1.6 | | | | 0.3 | | | 0.3 | 0.0 | 2.3 | | | | | | | | | | 17.5 | | 0.6 |
| SHS04-RS16 | 55.5 | 0.2 | 11.0 | 1.5 | | 0.3 | 0.2 | 0.5 | 9.4 | 1.3 | 0.8 | 3.4 | 0.7 | 0.3 | 1.3 | 1.2 | 0.7 | 1.3 | 0.2 | 0.2 | 0.7 | 0.2 | | | | | | | | | | | 9.4 |
| SHA03-RS02 | 47.1 | 1.3 | 8.0 | 1.6 | | | 0.6 | 1.0 | 7.1 | 1.9 | 1.3 | 6.1 | 4.2 | 0.3 | | 3.2 | | 1.3 | | 0.0 | 1.0 | | | | | | | 0.6 | | | 1.9 | | 11.5 |
| SHA05-RS03 | 50.7 | 1.0 | 7.4 | 1.9 | | | 0.6 | 0.2 | 5.0 | 2.4 | 0.8 | 5.8 | 2.4 | 0.2 | 0.8 | 1.0 | 0.6 | 0.8 | | | 1.5 | 0.6 | | 0.3 | | | | 0.6 | | | 0.3 | | 14.9 |
| SHA07-RS06 | 32.8 | 1.0 | 5.1 | 1.0 | | 0.3 | 1.6 | 0.3 | 2.9 | 1.6 | 2.9 | 9.6 | 4.2 | | 0.6 | 5.8 | 2.3 | 1.3 | | 1.0 | 1.0 | | | | 13.8 | | | | | | 1.6 | | 9.3 |
| SHA17-RS17 | 42.3 | 2.3 | 3.6 | 1.6 | 0.3 | 0.3 | | 1.0 | 2.0 | 1.3 | 2.0 | 5.9 | 4.9 | | 1.6 | 5.9 | 2.0 | 0.7 | 0.7 | 0.3 | 4.2 | | | | | | | | | | 2.0 | | 15.3 |
| PT02-RS02 | 23.3 | 1.5 | 7.3 | | 0.3 | 0.6 | 3.0 | | 1.8 | 0.6 | 2.1 | 23.9 | 7.9 | 0.6 | 0.9 | 10.6 | 2.1 | 3.6 | 0.6 | 1.5 | 3.3 | | 1.2 | | | | | | | 0.6 | 2.7 | | 0.0 |
| PT03-RS03 | 61.7 | | 6.2 | 1.0 | | | | 1.3 | 12.3 | 2.6 | | 1.0 | | | | 0.3 | | 3.6 | | | 1.9 | | | | 0.6 | | | 1.0 | | | 0.3 | | 6.2 |
| PT05-RS05 | 45.3 | 0.3 | 16.1 | 1.3 | | | 0.3 | 0.6 | 12.0 | 0.9 | 0.3 | 3.5 | | | | 0.6 | 0.3 | 3.2 | 0.3 | | 1.3 | | 1.6 | 6.6 | | | | 0.3 | | 1.3 | | | 3.8 |
| MA02-RS15 | 33.1 | | 24.3 | | | 2.0 | 1.0 | 0.7 | 3.6 | 0.7 | | 18.7 | 0.7 | | 0.7 | 1.0 | 1.0 | 3.6 | | | 1.6 | | | | 6.9 | | | | | | 0.7 | | 1.0 |
| MA06-1-RS13 | 41.2 | | 8.4 | 0.6 | 1.3 | 0.3 | 0.3 | 0.3 | 3.9 | 1.3 | 1.6 | 7.5 | | | 2.6 | 2.3 | 1.9 | 3.9 | 0.3 | | 2.3 | | | | | 18.1 | 0.5 | 0.3 | | 0.3 | 0.3 | | 0.3 |
| MA06-3-RS10 | 30.0 | 1.0 | 6.9 | 0.3 | 1.7 | 2.3 | 1.0 | | 1.0 | | | 23.8 | 0.7 | | 0.3 | 4.3 | 3.3 | 4.0 | | 0.3 | 1.0 | | | 0.3 | 17.5 | | | | | | | | 0.3 |
| AN01-RS01a | 58.5 | | 1.9 | | 0.3 | 4.2 | 1.3 | | 7.7 | 2.9 | | 12.9 | 1.9 | | 3.5 | | | | 0.6 | | 1.6 | 1.3 | | | | | | | | | 0.6 | | 0.6 |
| AN01-RS02 | 49.3 | | 2.7 | 1.7 | 0.3 | | | 2.3 | 10.3 | 6.0 | | 6.3 | 2.0 | 1.0 | 1.0 | | | | 0.3 | 1.3 | 1.0 | | | 13.3 | | | | | | | | | 1.0 |
| AN03-RS04 | 46.9 | | 5.5 | 1.6 | 0.7 | 1.0 | 1.0 | 0.3 | 5.2 | 1.6 | | 11.4 | 1.0 | 2.0 | 2.0 | 1.3 | | | 1.6 | 2.0 | 2.0 | | | | | | | | | | 1.3 | | 11.7 |
| AN03-RS06 | 61.7 | | 6.3 | 1.3 | 0.7 | 0.7 | | 0.3 | 2.3 | 1.7 | | 6.3 | 3.0 | 1.0 | 2.0 | 1.3 | | | 1.0 | 2.3 | 1.7 | 1.0 | | | | | | | | | | | 5.6 |
| AN08-RS09 | 63.0 | | 2.0 | 2.3 | | 0.3 | 1.3 | | 8.7 | 4.7 | | 0.7 | 0.3 | | 1.0 | | | | 0.3 | 0.3 | 1.7 | | | | | | | | | | | | 13.3 |
| AN09-RS10 | 56.8 | | 5.2 | 1.3 | | | 1.6 | | 5.9 | 1.9 | | 5.8 | 1.0 | | 2.6 | | | 0.6 | | 1.0 | 1.6 | 1.6 | | | | | | | | | 0.3 | | 12.7 |
| AN15-RS12 | 55.4 | 1.3 | 6.2 | 1.3 | 1.0 | 0.3 | 1.6 | 0.3 | 4.6 | 1.6 | | 5.9 | 1.3 | | 4.9 | 2.3 | | | 0.7 | 0.3 | 2.9 | 1.6 | | 1.0 | | | | | | | 0.7 | | 4.9 |
| AN16-RS13 | 51.5 | 0.5 | 6.9 | 0.5 | 0.5 | 0.8 | | 0.7 | 5.7 | 1.0 | 1.6 | 4.8 | 1.0 | 0.3 | 1.3 | 0.2 | 1.6 | 0.3 | | 0.8 | 1.6 | 0.8 | 0.3 | 16.2 | | | | | | | | | 1.1 |
| AN18-RS14 | 36.0 | 1.0 | 4.6 | | | | 0.3 | | 2.0 | 2.0 | | 8.6 | 3.0 | | 7.6 | 4.0 | | 0.7 | | 12.5 | 5.3 | | 12.2 | | | | | | | | | | 0.3 |
| CHW04-RS05 | 31.0 | | 21.2 | | | 2.0 | | | 1.0 | 0.3 | 0.7 | 33.7 | 2.9 | | | 0.3 | 1.3 | 2.0 | | | 2.9 | | | 0.3 | | | | | | | 0.3 | 2.0 | 2.0 |
| CHW06-RS08 | 23.3 | 0.3 | 32.5 | | | | | | 2.5 | 0.6 | 0.3 | 14.8 | 2.5 | | | 0.6 | 0.3 | 3.5 | | | 1.9 | 0.3 | | | 12.0 | | | | | 3.2 | 0.3 | 3.8 | 4.7 |
| CHW10-RS14 | 29.9 | 0.3 | 33.2 | | | | | | 3.3 | 0.0 | 0.7 | 12.5 | 1.6 | | | 1.0 | 0.3 | 3.0 | | | 1.6 | | | | 6.9 | | | | | 3.9 | | 2.0 | 3.6 |
| CHW14-RS22 | 21.7 | | 22.0 | | | 1.6 | | | 0.6 | 0.0 | 0.3 | 36.2 | 2.8 | 0.6 | | 3.5 | 2.8 | 3.5 | | | 1.9 | | | | | | | | | | | | 2.5 |
| CHW26-RS41 | 30.3 | | 22.1 | | | 0.9 | 0.3 | 0.3 | 3.3 | 1.2 | | 16.7 | 3.9 | 1.8 | | 1.5 | 3.0 | 2.4 | | | 2.1 | | | | 5.5 | | | | | 3.9 | 0.6 | 1.2 | 1.2 |

## Light mineralogy of sandstones (continuation)

| | Minerals | | | | | | | | Rock fragments | | | | | | | | | | | | Authigenic minerals | | | | | | | | Pore space | |
|---|---|---|---|---|---|---|---|---|---|---|---|---|---|---|---|---|---|---|---|---|---|---|---|---|---|---|---|---|---|---|
| **Sample** | **Qm** | **Pl** | **Kf** | **Mi** | **Mu** | **Bi** | **Opq** | **HM** | **$Qp_{2-3}$** | **$Qp_{>3}$** | **Qc** | **Lvf** | **Lvm** | **Lvv** | **Ls** | **Lmq** | **Lmm** | **Lgr** | **Li** | **Luq** | **Lu** | **Qtz** | **Cc** | **Hem** | **Zeo** | **Bas** | **Jar** | **Ill** | **Kao** | **Chl** | **FeH** | **Intragr.** | **tot.** |
| ST05-03 | 59.2 | | | | | | | 0.2 | 17.6 | 1.6 | | | | | | | | 1.6 | | | | 12.7 | | | | | | | 5.4 | | | | 1.6 |
| ST09-05 | 51.3 | 0.3 | 0.6 | | | 1.3 | 0.6 | | 18.3 | 0.3 | | 0.6 | | | | | 0.6 | 2.0 | | | 3.4 | 11.3 | 0.3 | 1.3 | | | | | 5.6 | | | | 2.1 |
| SP05-RS05 | 39.1 | | 13.1 | | 0.6 | 1.5 | 1.2 | 0.3 | 2.8 | 0.6 | 0.3 | 10.7 | | 0.6 | 0.6 | 4.9 | 3.7 | 3.1 | | 1.2 | 4.0 | | | | | | | 0.3 | | 1.8 | 6.1 | | 3.4 |
| SP11-RS08 | 37.6 | 0.3 | 18.6 | 1.0 | | 0.0 | | 0.3 | 5.9 | 3.9 | 0.3 | 10.1 | 0.3 | 2.0 | | 0.7 | | 2.0 | | | 0.7 | | | | | | | 0.7 | | 0.7 | | | 15.0 |
| SPP05-RS17 | 36.0 | 1.0 | 6.4 | | | 1.6 | 0.6 | | 1.9 | 0.6 | | 8.7 | | | 0.3 | 3.2 | 4.2 | 1.3 | 1.3 | | 2.3 | | | | 23.5 | | | | | | | | 7.1 |
| SPP10-RS23 | 39.2 | 1.0 | 10.5 | 0.6 | | 0.3 | 0.3 | 5.7 | 6.7 | 0.6 | 0.3 | 9.6 | 0.6 | | 0.3 | 1.6 | 1.3 | 1.3 | 0.6 | 0.3 | 2.5 | | | | 0.6 | | | | | 0.6 | 0.3 | | 15.0 |
| SPP20-RS03 | 47.2 | 1.0 | 11.2 | 0.3 | 0.3 | 0.0 | | 1.0 | 5.0 | 0.7 | 0.3 | 9.2 | 0.3 | | 0.7 | 2.0 | 1.7 | 3.3 | | | 0.3 | | | 0.3 | | | | 0.3 | | | | | 14.9 |
| SPP31-RS07 | 39.3 | 1.5 | 12.7 | 0.6 | 0.3 | 1.5 | | 0.3 | 2.4 | 0.6 | 0.3 | 11.2 | 0.6 | | 1.2 | 2.4 | 4.8 | 3.3 | 1.2 | | 2.7 | | | | | | | 1.2 | | 1.2 | 0.3 | | 10.3 |
| RB04 | 41.5 | 1.9 | 12.7 | 1.0 | | 0.3 | 0.3 | 1.9 | 1.9 | 0.6 | 0.3 | 6.1 | 1.3 | | 0.3 | 6.4 | 1.3 | 6.1 | | 0.6 | 2.2 | | | | | | | 1.3 | | | 1.6 | | 10.5 |
| RB06 | 44.6 | 0.6 | 12.1 | 0.6 | 0.3 | | | | 2.2 | 0.6 | 1.3 | 8.6 | 1.6 | 1.0 | 1.0 | 6.4 | 1.9 | 2.2 | 0.3 | 0.3 | 1.9 | | | | | | | | | 6.1 | | | 6.4 |
| RB11 | 46.7 | 1.2 | 13.9 | 0.9 | | | | 0.6 | 2.5 | 0.3 | 0.3 | 3.4 | 0.9 | 0.6 | 0.9 | 5.3 | 1.5 | 1.9 | | | 1.5 | | | | | | | 1.2 | | 5.3 | | | 10.8 |

all data given in vol%

Abbreviations:
Qm: Monoquartz; Pl: Plagioclase; Kf: Kalifeldspar; Mi: Microkline; Mu: Muscovite/di-octahdral Mica; Bi: Biotite/tri-octahedral Mica; Opq: Opaque mineral; HM: Heavy mineral; Qp2-3: Polyquartz with 2-3 subgrains; Qp>3: Polyquartz with more than 3 subgrains; Qc: Chert; Lvf: Felsic volcanic lithoclast; Lvm: Mafic volcanic lithoclast; Lvv: Vitreous volcanic lithoclast; Ls: Sedimentary lithoclast; Lmq: Metamorphic lithoclast, quartz-rich; Lmm: Metamorphic lithoclast, mica-rich; Lgr: Ganitic lithoclast; Li: Illitic lithoclast; Luq: Unknown lithoclast, quartz-rich; Lu: Unknown lithoclast; Qtz: Quartz; Cc: Calcite; Hem: Hematite; Zeo: Zeolite; Bas: Bassanite; Jar: Jarosite; Ill: Illite; Kao: Kaolinite; Chl: Chloritic mineral paragenesis; FeH: Iron hydroxide; Intragr.: Intragranular; tot: total

## Heavy mineralogy of sandstones

| Sample | n (tra) | n (tot) | Opq | Zrn | Rtl | Tou | Grt | Apa cl | Apa alt. | Apa tot. | Epi | Am gr/br | Am cl | Am tot. | Chr* | other | Unk., Alt. | sum | ZTR | grt: ZTR |
|---|---|---|---|---|---|---|---|---|---|---|---|---|---|---|---|---|---|---|---|---|
| | | | [%] | [%] | [%] | [%] | [%] | [%] | [%] | [%] | [%] | [%] | [%] | [%] | [%] | [%] | [%] | [%] | [%] | |
| TP03 | 312 | 430 | 27 | 36 | 0 | 22 | 0 | 3 | 24 | 27 | 5 | 0 | 0 | 0 | 0 | 0 | 9 | 100 | 59 | 0.00 |
| ER04 | 317 | 458 | 31 | 12 | 5 | 33 | 3 | 8 | 22 | 31 | 1 | 0 | 0 | 0 | 1 | 0 | 13 | 100 | 51 | 0.06 |
| ER07 | 307 | 448 | 31 | 7 | 5 | 35 | 5 | 5 | 29 | 33 | 1 | 0 | 0 | 0 | 0 | 0 | 15 | 100 | 46 | 0.11 |
| TI03 | 233 | 319 | 27 | 12 | 0 | 3 | 1 | 10 | 29 | 39 | 6 | 0 | 0 | 0 | 0 | 5 | 33 | 100 | 15 | 0.06 |
| TI14 | 241 | 968 | 75 | 14 | 1 | 2 | 9 | 45 | 16 | 61 | 1 | 0 | 0 | 0 | 5 | 0 | 7 | 100 | 17 | 0.51 |
| TI18 | 203 | 621 | 67 | 6 | 1 | 0 | 3 | 63 | 19 | 82 | 1 | 0 | 0 | 0 | 0 | 0 | 5 | 100 | 8 | 0.38 |
| TI23 | 358 | 473 | 24 | 10 | 6 | 1 | 66 | 1 | 6 | 7 | 3 | 0 | 0 | 0 | 0 | 1 | 7 | 100 | 17 | 3.85 |
| SHS01 | 305 | 1147 | 73 | 17 | 0 | 14 | 6 | 26 | 17 | 42 | 2 | 0 | 1 | 1 | 0 | 1 | 17 | 100 | 31 | 0.19 |
| SHS03 | 442 | 687 | 36 | 4 | 5 | 1 | 84 | 2 | 0 | 2 | 0 | 0 | 0 | 0 | 0 | 1 | 3 | 100 | 10 | 8.04 |
| SHA07 | 226 | 437 | 48 | 5 | 2 | 3 | 69 | 8 | 4 | 12 | 0 | 3 | 2 | 4 | 0 | 0 | 4 | 100 | 10 | 6.74 |
| SHA17 | 369 | 494 | 25 | 9 | 1 | 4 | 58 | 10 | 1 | 12 | 2 | 8 | 0 | 8 | 0 | 1 | 7 | 100 | 13 | 4.37 |
| MA06-4 | 151 | 279 | 46 | 12 | 1 | 17 | 16 | 13 | 5 | 18 | 2 | 17 | 0 | 17 | 0 | 3 | 14 | 100 | 30 | 0.52 |
| AN03 | 370 | 690 | 46 | 5 | 11 | 2 | 73 | 1 | 0 | 1 | 4 | 0 | 0 | 0 | 0 | 1 | 4 | 100 | 18 | 4.15 |
| AN08 | 385 | 1292 | 70 | 24 | 16 | 1 | 2 | 25 | 0 | 25 | 3 | 0 | 0 | 0 | 0 | 2 | 27 | 100 | 41 | 0.06 |
| SP05 | 394 | 622 | 37 | 9 | 4 | 1 | 72 | 4 | 0 | 4 | 3 | 0 | 0 | 0 | 0 | 0 | 7 | 100 | 14 | 5.28 |
| SP08 | 392 | 684 | 43 | 10 | 0 | 1 | 71 | 10 | 0 | 10 | 2 | 0 | 0 | 0 | 0 | 1 | 5 | 100 | 11 | 6.18 |
| SPP17 | 364 | 644 | 43 | 7 | 4 | 2 | 61 | 11 | 0 | 11 | 2 | 1 | 2 | 3 | 0 | 1 | 9 | 100 | 13 | 4.63 |
| SPP36 | 502 | 896 | 44 | 7 | 0 | 0 | 77 | 8 | 0 | 8 | 0 | 0 | 0 | 0 | 0 | 0 | 7 | 100 | 7 | 10.46 |
| RB04 | 413 | 529 | 22 | 4 | 0 | 0 | 89 | 2 | 1 | 3 | 1 | 0 | 0 | 0 | 0 | 0 | 2 | 100 | 5 | 17.52 |
| RB11 | 340 | 418 | 19 | 3 | 1 | 4 | 83 | 4 | 1 | 4 | 1 | 0 | 0 | 0 | 0 | 0 | 3 | 100 | 8 | 10.11 |
| CHW07 | 442 | 544 | 19 | 8 | 0 | 0 | 74 | 7 | 0 | 7 | 2 | 0 | 0 | 0 | 0 | 0 | 8 | 100 | 8 | 8.84 |
| CHW14 | 335 | 477 | 30 | 4 | 2 | 0 | 53 | 16 | 0 | 16 | 6 | 2 | 0 | 2 | 0 | 4 | 14 | 100 | 6 | 8.38 |
| CHW26 | 376 | 706 | 47 | 2 | 1 | 0 | 78 | 5 | 0 | 5 | 3 | 1 | 0 | 1 | 0 | 1 | 9 | 100 | 2 | 32.78 |
| ST09 | 200 | 456 | 56 | 11 | 1 | 76 | 1 | 3 | 0 | 3 | 2 | 0 | 2 | 2 | 0 | 0 | 6 | 100 | 87 | 0.01 |

* estimated from polished heavy mineral mount

Abbreviations:

Alt: altered; Am: Amphibole; Apa: Apatite; Chr: Chromian Spinel; cl: clear; Epi: Epidote; gr/br: greenish/brownish; Grt: Garnet; Opq: Opaque mineral; Rtl: Rutile; tot: total; Tou: Tourmaline; tra: translucent; Unk: Unknown mineral; Zrn: Zircon; unk: unknown; ZTR: Zircon+Tourmaline+Rutile

Point counts of tuffaceous sandstones

| Sample | Minerals | Vitrics | Lithics | Cements, pores |
|---|---|---|---|---|
| SHA06 | 17.0 | 36.1 | | 14.5 |
| SHA09 | 12.0 | 36.7 | | 16.0 |
| SHA12 | 9.0 | 35.6 | | 18.7 |
| SHA14 | 28.0 | 32.0 | 2.6 | 12.3 |
| SHA16 | 8.5 | 37.9 | | 16.0 |
| SHC02 | 52.0 | 24.7 | 1.8 | 8.7 |
| SHC03 | 26.0 | 29.3 | 2.4 | 16.7 |
| SHC04 | 30.5 | 31.9 | 1.3 | 12.3 |
| SHC06 | 36.0 | 29.9 | 2.2 | 11.1 |
| SHC16 | 54.0 | 24.0 | 1.8 | 8.3 |
| SHC33 | 47.5 | 25.6 | 2.2 | 9.9 |
| SHC39 | 35.5 | 31.0 | 0.4 | 11.5 |
| CE02 | 55.0 | 24.5 | | 8.7 |
| CE09 | 51.5 | 25.9 | | 9.1 |
| CE19 | 50.5 | 26.4 | | 9.1 |
| CE26 | 40.5 | 29.8 | | 10.7 |
| CE41 | 43.0 | 29.0 | | 10.3 |
| CE55 | 47.0 | 27.5 | | 9.9 |
| CE77 | 48.0 | 27.3 | | 9.5 |

all data given in vol%

# Appendix 3

Photographies of thin sections
and heavy mineral mounts

# Petrography (1/4): Sandstone types A and B

a) Sandstones of type A consist predominantly of quartz (Qz) and K-feldspar (Kf). The latter is often altered to kaolinite or leached. Lithoclasts apart from granitic rock fragments are exceptional. A typical constituent is pale yellowish to brownish coloured biotite (Bi), which is altered to kaolinite/halloysite. Sorting and rounding of this sandstone type is mostly poor. Porosity is relatively low, as compaction squeezed the altered K-feldspars. However, dissolution of K-feldspar (possibly contemporaneous to its alteration) formed inter-granular porosity. Sample AG09, parallel Nichols.

b) As (a), crossed Nichols.

c) Another example of sandstone type A, showing less biotite than the sample in (a/b). Fe-oxides (black patches) and Fe- hydroxides (brown patches) precipitated as authigenic minerals during diagenesis. Sample TP05, parallel Nichols.

d) As (c), crossed Nichols.

e) Contrary to type A, in type B sandstones, lithoclasts are very abundant. Among these, felsic volcanics are the most frequent, mafic volcanic and metamorphic lithoclasts are less abundant. Sedimentary rock fragments are very rare, although in some samples rip-up lasts are frequent.. Mafic volcanic lithoclasts may show plagioclase laths in oriented (flow) texture (red arrow). Quartz and feldspar are far less abundant than in sandstone type A, however, plagioclase is present. Porosity is extremely low or virtually absent in sandstones of this type, as compaction squeezed the unstable lithic grains to form pseudomatrix. SampleTI14, parallel Nichols.

f) As (e), crossed Nichols.

g) Another example of sandstone type B. As in (e/f) volcanic lithoclasts are most abundant and porosity is virtually absent. Sample PT02, parallel Nichols.

h) As (g), crossed Nichols.

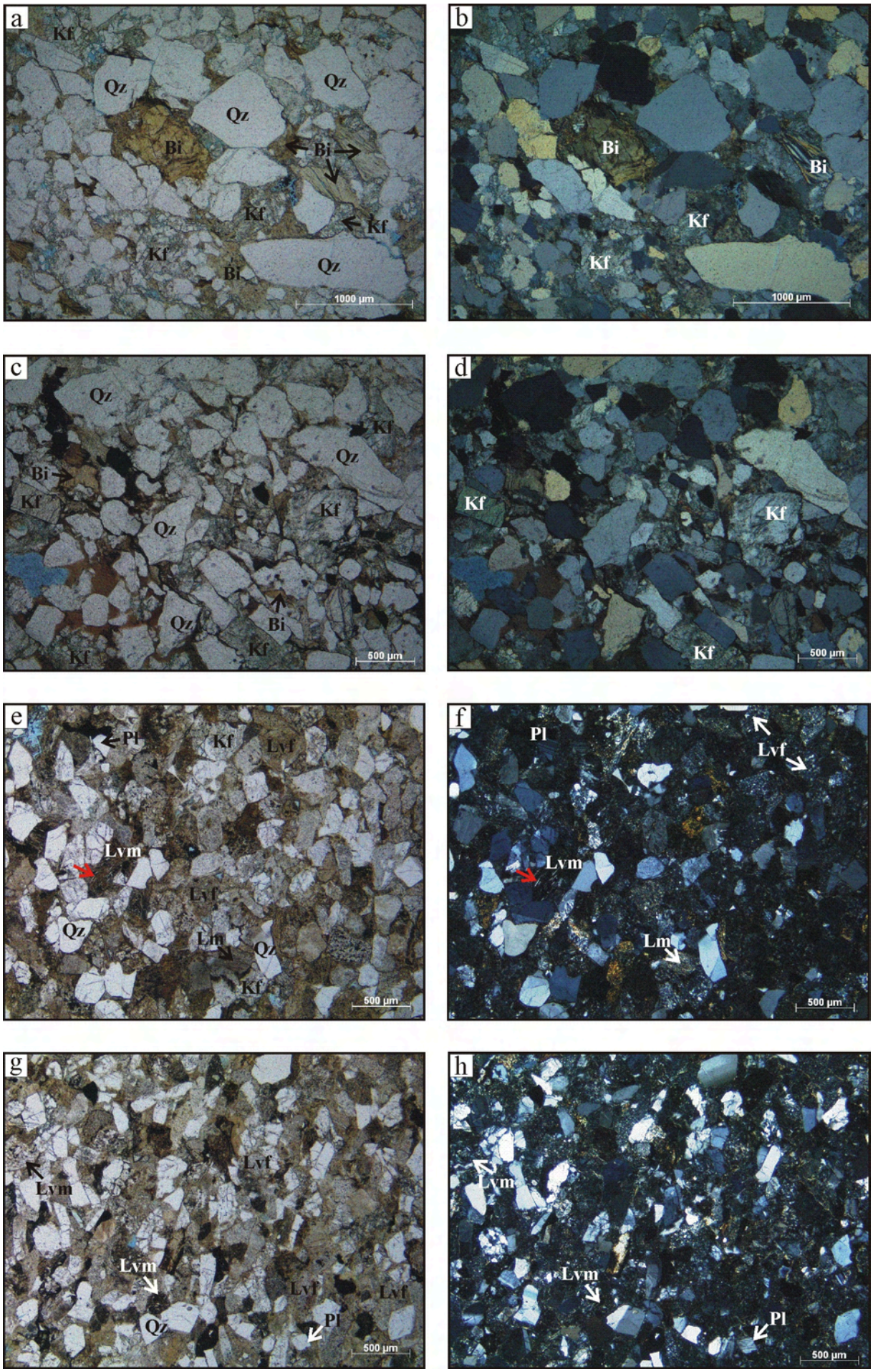
a
Kf
Qz
Qz
Qz
Bi
Bi
Kf
Kf
Kf
Bi
Qz
1000 µm
b
Bi
Bi
Kf
Kf
1000 µm
c
Qz
Kf
Qz
Bi
Kf
Kf
Qz
Bi
Qz
Kf
Kf
500 µm
d
Kf
Kf
Kf
500 µm
e
Pl
Kf
Lvf
Lvm
Lvf
Qz
Lm
Qz
Kf
500 µm
f
Pl
Lvf
Lvm
Lm
500 µm
g
Lvf
Lvm
Lvm
Lvf
Lvf
Qz
Pl
500 µm
h
Lvm
Lvm
Pl
500 µm

## Petrography (2/4): Sandstone types C and D

a) In sandstones of type C rounding is poor to moderate and sorting is moderate. Quartz (Qz; Qp: polyquartz) and K-feldspar are more frequent than in type B sandstones. On the other hand, lithoclasts are less abundant. However, as in type B, felsic (Lvf) are more frequent than mafic volcanic lithoclasts, and metamorphic and sedimentary rock fragments are rarer. Plagioclas is present in samples from higher stratigraphic position. Due to the higher fraction of stable grains (Qz, Kf) compactionally induced porosity loss was not complete. However, instable lithic grains are squeezed to pseudomatrix (red arrow points to an illitic rock fragment). Sample SHA03, parallel Nichols.

b) As (a), crossed Nichols.

c) Another example from sandstone type C, showing a similar composition as (a/b). Microcline (Mi) is generally a rare phase among the alkali feldspars. Sample SPP20, parallel Nichols.

d) As (c), crossed Nichols.

e) As type B, sandstones of type D are rich in felsic volcanic lithoclasts (Lvf), but feldspar (Kf, Pl) is much more abundant. The low porosity of type D sandstones is not only due to compaction of unstable lithic grains as in type B; often zeolites precipitated as authigenic minerals (red arrows). Sample CHW03, parallel Nichols.

f) As (e), crossed Nichols.

g) Another example of type D sandstones. As in sandstone type A and C, mafic volcanic lithoclasts are less abundant than felsic (Lvf), and plagioclase (Pl) less abundant than K-felspar (Kf). As precursor material for the authigenic zeolites K- feldspar is likely, as it often shows extensive dissolution features (red arrows). Sample CHW10, parallel Nichols.

h) As (g), crossed Nichols.

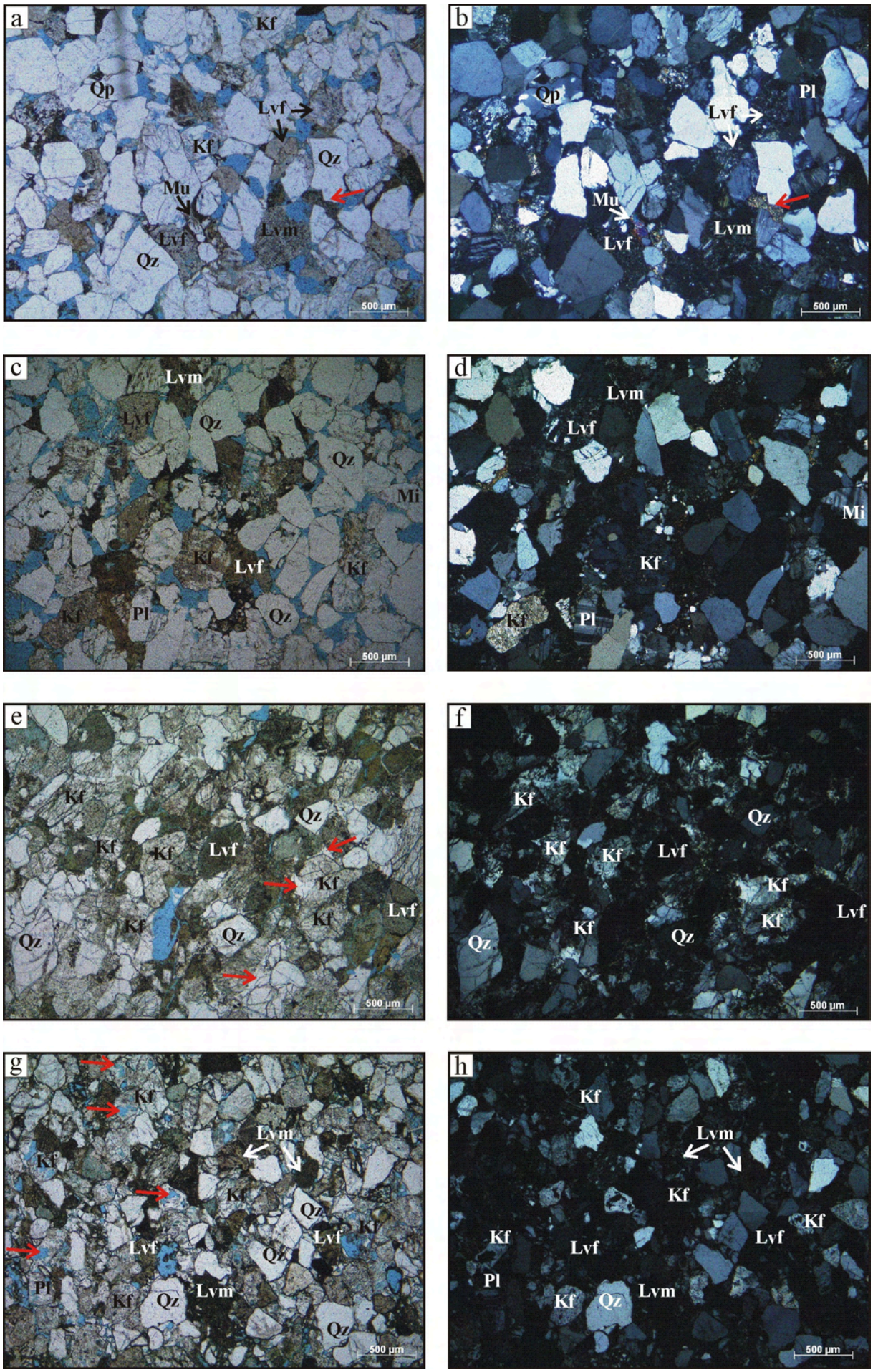
a
Kf
Qp
Lvf
Kf
Qz
Mu
Lvf
Lvm
Qz
500 µm
b
Qp
Pl
Lvf
Mu
Lvf
Lvm
500 µm
c
Lvm
Lvf
Qz
Qz
Mi
Kf
Lvf
Kf
Kf
Pl
Qz
500 µm
d
Lvm
Lvf
Mi
Kf
Kf
Pl
500 µm
e
Kf
Qz
Kf
Kf
Lvf
Kf
Kf
Lvf
Qz
Kf
Qz
500 µm
f
Kf
Qz
Kf
Kf
Lvf
Kf
Kf
Lvf
Qz
Kf
Qz
500 µm
g
Kf
Kf
Lvm
Kf
Qz
Kf
Lvf
Lvf
Qz
Pl
Kf
Qz
Lvm
Qz
500 µm
h
Kf
Lvm
Kf
Kf
Kf
Lvf
Lvf
Pl
Kf
Qz
Lvm
500 µm

## Petrography (3/4): Sandstone types E and F, and mixed samples

a) Sandstones of type E (section ST) are the only arenites found in the SPF. Feldspar and lithic grains are rare, but their fraction increases in samples from higher stratigraphic parts of the section. Kaolinite (Kao) is a frequent authigenic phase in this sandstone type. Quartz overgrowth (arrow) are also frequent. Opq is an opaque mineral. The grain on the left image boundary may be an altered K-feldspar. Sample ST05, parallel Nichols.

b) As (a), crossed Nichols.

c) Sandstone type F is represented by a single sample only. Its light mineralogy is similar to type C from the same stratigraphic level, thus very quartz-rich. Feldspar and lithoclasts are rare. Sample AN08, parallel Nichols.

d) As (c), crossed Nichols.

e) This sample exhibits a bimodal composition. A finer grained portion resembles the composition of type B (lithoclast rich, quartz-poor), but in addition larger quartz grains are found. Due to this observation and its heavy mineral assemblage, this sample is interpreted as a mixture of sandstone type A and B. Sample SHS01, parallel Nichols.

f) As (e), crossed Nichols.

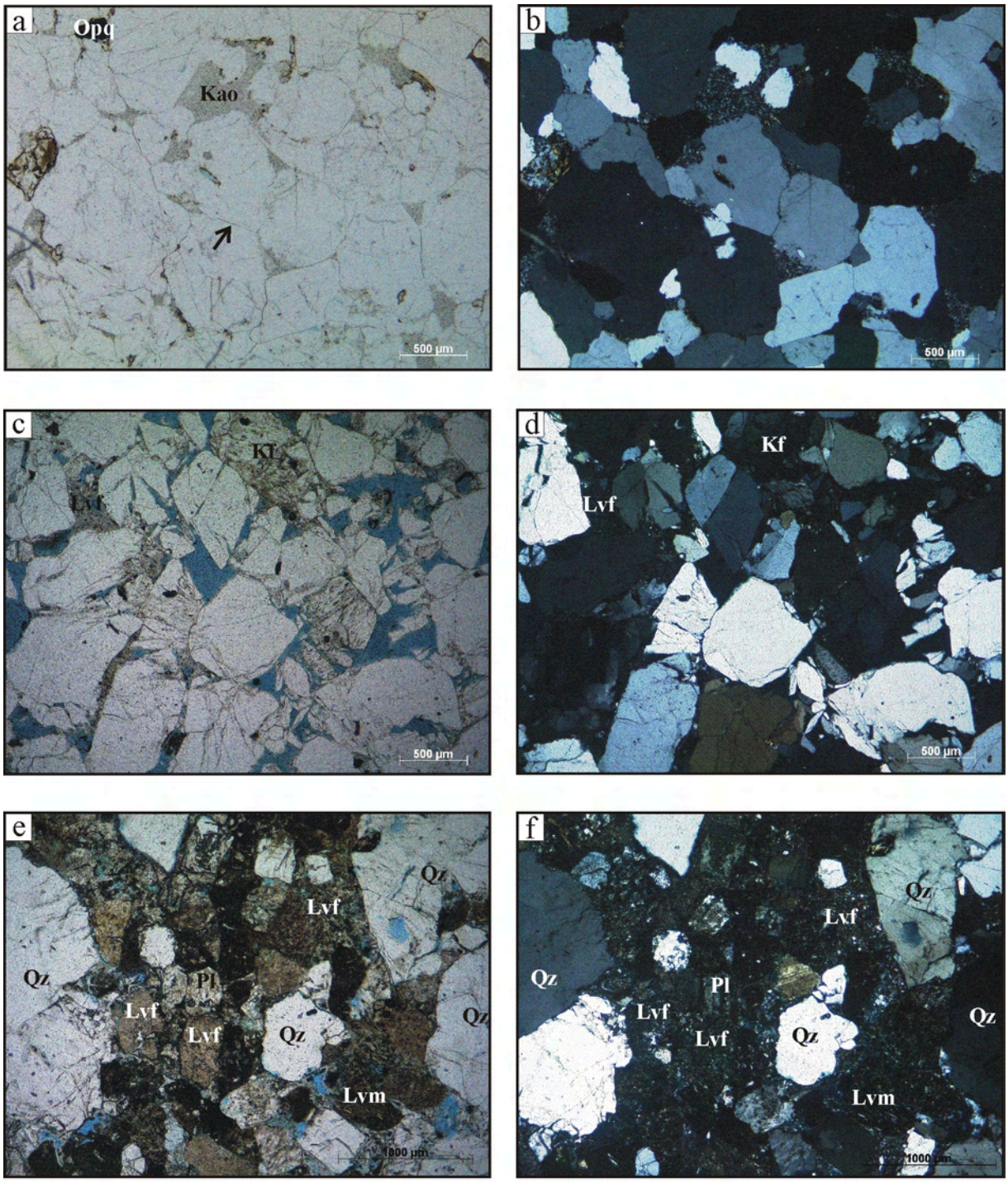
a
Opq
Kao
500 µm
b
500 µm
c
Kf
Lvf
500 µm
d
Kf
Lvf
500 µm
e
Qz
Lvf
Qz
Pl
Lvf
Lvf
Qz
Qz
Lvm
1000 µm
f
Qz
Lvf
Qz
Pl
Lvf
Lvf
Qz
Qz
Lvm
1000 µm

## Petrography (4/4): Tuffaceous sandstones and vitreous fragments

a) Tuffaceous sandstone from the SPF with cuspate and elongated shards. The dark color is caused by finely dispersed organic matter. A long fluvial transport seems unlikely regarding the shape of the shards. Minerals or mineral fragments are relatively rare. Sample SHA14, parallel Nichols.

b) Tuffaceous sandstone from the SPF, similar to (a). Most of the minerals or mineral fragments are Plagioclase in this case. The rectangle marks the area enlarged in (c) and (d).Sample SHA12, parallel Nichols.

c) Few shards are not dispersed completely. The large shard on the right includes a bubble. The vitric material has been replaced completely by Zeolites (Clinoptilolite/Heulandite). The original shape of the shards is outlined by a rim of smaller Zeolite crystals, while the crystals in the interior of the shards are larger, and colored differently (reddish) in some cases. Sample SHA12, parallel Nichols.

d) As (c), crossed Nichols.

e) A tuffaceous sandstone from the SHF. Shards are less abundant than in (a) and (b). In this case the alteration products (Zeolites) are slightly reddish colored as in (c). Sample CE90, parallel Nichols.

f) As (e), crossed Nichols.

g) Vitreous fragment within the SPF, showing a yellowish colour (alteration, palagonitization?). Shape and size is very different from the shards described in (a) to (f). In this case, formation of the vitreous fragment can be related to an EHT event. Sample CHW23, parallel Nichols.

h) Sample CHW23, crossed Nichols.

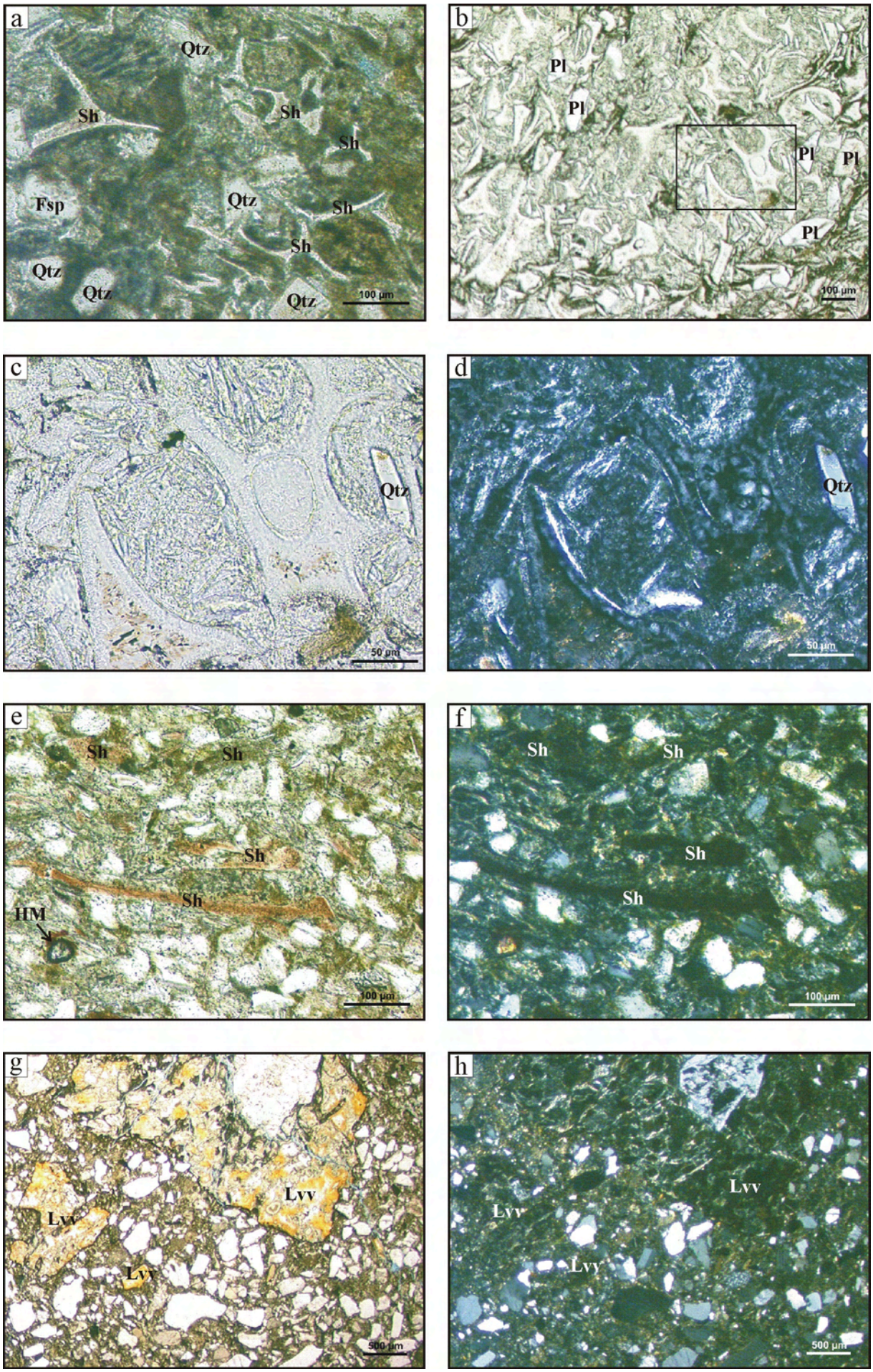
a
Qtz
Sh
Sh
Sh
Fsp
Qtz
Sh
Sh
Qtz
Qtz
Qtz
100 µm
b
Pl
Pl
Pl
Pl
Pl
100 µm
c
Qtz
50 µm
d
Qtz
50 µm
e
Sh
Sh
Sh
Sh
HM
100 µm
f
Sh
Sh
Sh
Sh
100 µm
g
Lvv
Lvv
Lvv
500 µm
h
Lvv
Lvv
Lvv
500 µm

# Diagenesis (1/2)

a) Grain-coating chloritic mineral paragenesis (Chl.P.: Quartz, Fe-oxides or -hydroxides, chlorite and other clay minerals in varying fractions) and zeolite cementation (Zeo: Clinoptilolite/Heulandite) occurred after dissolution of K-feldspar (KF). Some degree of compaction was prior to formation of authigenic rims, as shown by grain contacts free of authigenic minerals (red arrows). Sample CHW26, parallel Nichols.

b) Detail from (a), parallel Nichols.

c) Very early, radial, fan-like clinoptilolite has been found in section SPP only. The IGV of these samples are among the highest within the SPF (up to 24%), possibly because this area hosted a major feeder-system of the Ferrar dolerites. Sample SPP07, parallel Nichols.

d) Grain-coating chloritic mineral paragenesis, missing on grain contacts (red arrows). Blocky micro-quartz is a major constituent, as revealed by EMP. Zeolites as in (a) did not form here. Sample RB02, parallel Nichols.

e) Hematite was precipitated after compaction, as it is missing at grain contacts. The volcanic lithoclast (Lv) on the left has been squeezed by compaction, forming pseudomatrix. Sample AN02, parallel Nichols.

f) Fe-hydroxides and clay minerals form the authgenic paragenesis in sample SHS04-RS15, unique within the SPF. The minerals have possibly been precipitated from a gel-like state.

g) Bassanite cements have formed after feldspar-dissolution and within lithoclasts. However, feldspar dissolution also took place after bassanite formation, as some intra-granular pores in feldspar are free of any cement. Sample MA06-1, parallel Nichols.

h) In areas without massive bassanite cements greenish-brownish jarosite has been precipitated. This may be result of dissolution of earlier bassanite cements, but as geometric relations sometimes indicate jarosite formation after bassanite precipitation (EMP imagery), jarosite formed either more or less contemporaneous to bassanite, or its formation was in two phases. Sample MA06-1, parallel Nichols.

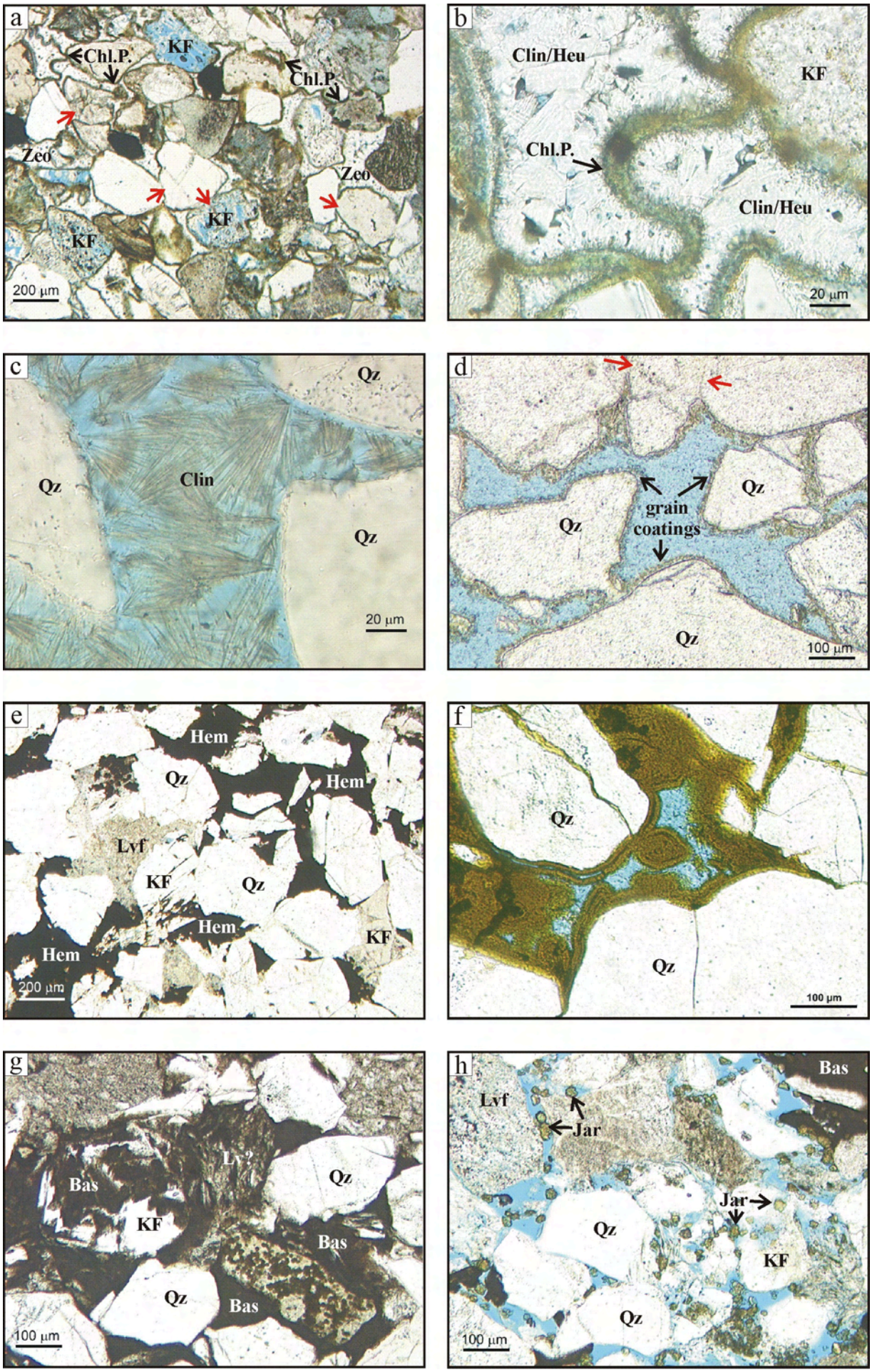
a
Chl.P.
KF
Chl.P.
Zeo
Zeo
KF
KF
200 µm
b
Clin/Heu
KF
Chl.P.
Clin/Heu
20 µm
c
Qz
Qz
Clin
Qz
20 µm
d
Qz
grain
coatings
Qz
Qz
100 µm
e
Hem
Qz
Hem
Lvf
KF
Qz
Hem
KF
Hem
200 µm
f
Qz
Qz
100 µm
g
Lv?
Qz
Bas
KF
Bas
Qz
Bas
100 µm
h
Bas
Lvf
Jar
Jar
Qz
KF
Qz
100 µm

## Diagenesis (2/2)

a) Notched overgrowth of K-feldspar on plagioclase. Sample SHA05, parallel Nichols.

b) Overgrowth of K-feldspar on K-feldspar. Sample SHA05, crossed Nichols.

c) Syntaxial quartz overgrowth formed prior to kaolinite and calcite. Sample ST09, crossed Nichols.

d) The unusual interference colors of the kaolinite booklets in this case point toward a later illitization or choritization. Sample ST09, crossed Nichols.

e) Patchy calcite-cements (Cc) formed not only in pores, but is also replacing detrital grains. In this case, a quartz grain (Qz) has been corroded resulting in rectangular grain boundaries. Sample AN18, crossed Nichols.

f) Compaction resulted commonly in squeezing of instable lithoclasts (Lvf: felsic volcanic lithoclasts; Lvm: mafic volcanic lithoclasts), and kinked mica (Bi). Sample AN15, parallel Nichols.

g) Compactionally induced fracture of feldspar (Fsp). Authigenic minerals (Chl.P.: chloritic mineral paragenesis; Zeo: clinoptilolite/heulandite) formed after the breakage. Sample CHW26, parallel Nichols.

h) A broken quartz grain (Qz) indicating a heavy degree of compaction. Along the surfaces of the open fracture an authigenic mineral formed, most likely illite. Sample SHA03, parallel Nichols.

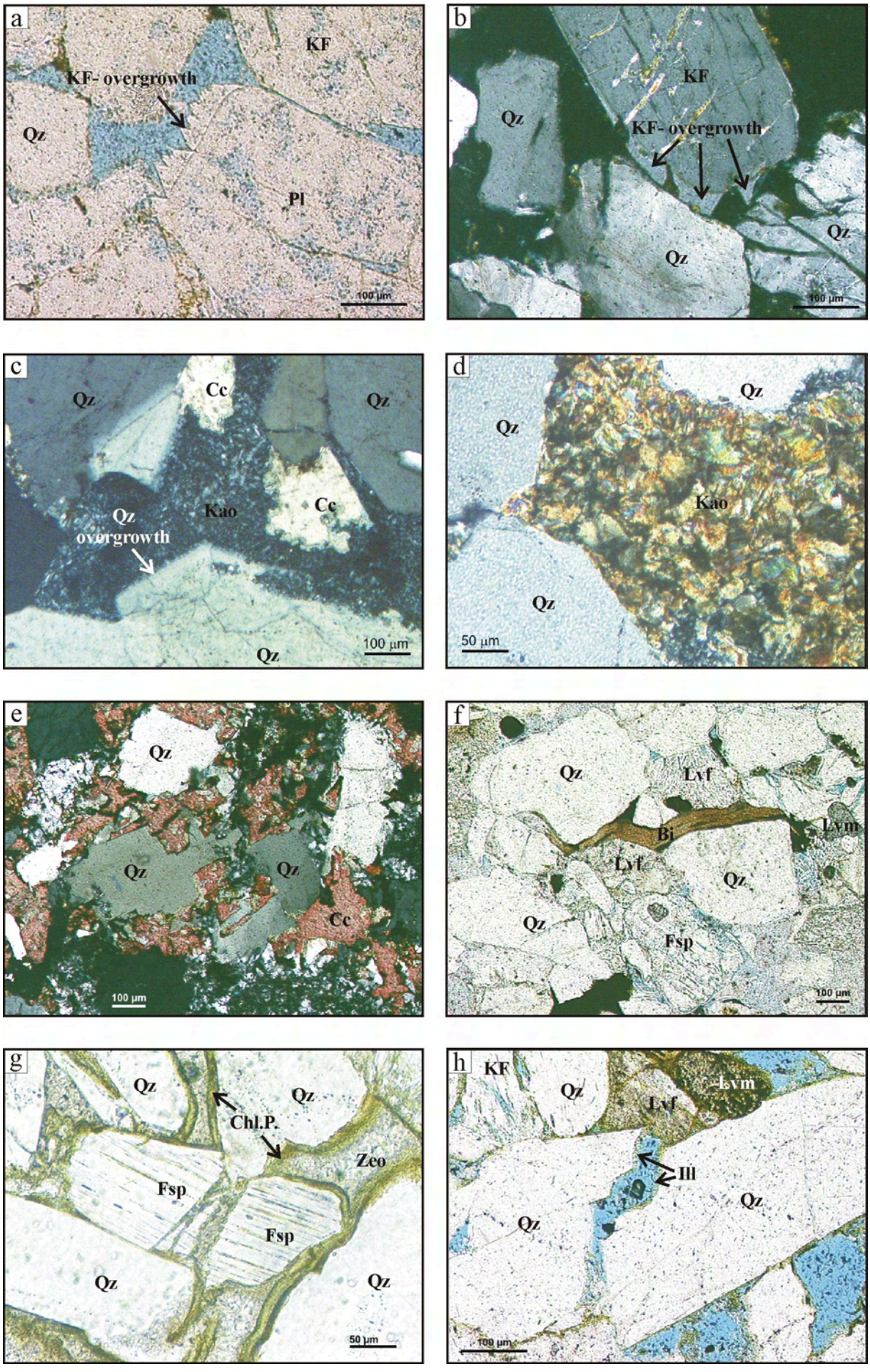
a
KF
KF- overgrowth
Qz
Pl
100 µm
b
KF
Qz
KF- overgrowth
Qz
Qz
100 µm
c
Qz
Cc
Qz
Qz
overgrowth
Kao
Cc
Qz
100 µm
d
Qz
Qz
Kao
Qz
50 µm
e
Qz
Qz
Qz
Cc
100 µm
f
Qz
Lvf
Lvm
Bi
Lvf
Qz
Qz
Fsp
100 µm
g
Qz
Qz
Chl.P.
Zeo
Fsp
Fsp
Qz
Qz
50 µm
h
KF
Qz
Lvm
Lvf
Ill
Qz
Qz
100 µm

# Heavy mineralogy (1/3): Sandstone types A, B, and C

a) The heavy mineral assemblage of sandstone type A is dominated by zircon (Zrn), tourmaline (Tou), and apatite (Apa). In contrast to the following images, this photography has been made from a polished heavy mineral mount. Sample TP03, parallel Nichols.

b) As (a), crossed Nichols.

c) In type B sandstones heavy minerals are relatively rare compared to the other sandstone types, and in addition the fraction of opaque heavy minerals is high. From the translucent heavy minerals, apatite is most frequent. Sample TI03, parallel Nichols.

d) As (c), crossed Nichols.

e) In type C sandstones garnet (grt) is the most abundant heavy mineral. In samples from higher stratigraphic position, greenish-brownish amphiboles are present (Am). Sample SHA07, parallel Nichols.

f) As (e), crossed Nichols.

g) Another example for the garnet-dominated heavy mineral assemblage of type C sandstones. Sample SPP17, parallel Nichols.

h) As (g), crossed Nichols.

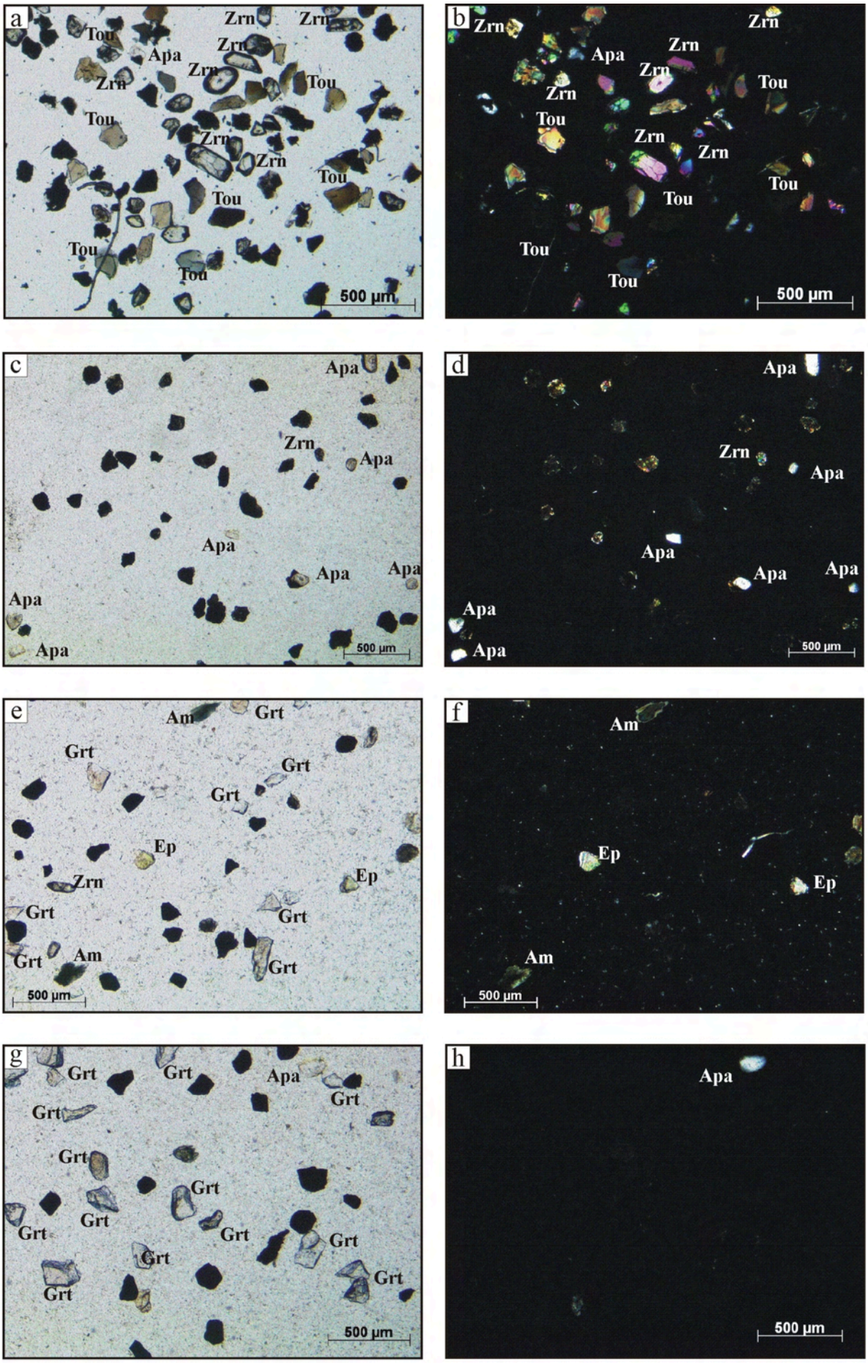
a
Zrn
Zrn
Tou
Apa
Zrn
Zrn
Zrn
Tou
Tou
Zrn
Zrn
Tou
Tou
Tou
Tou
500 µm
b
Zrn
Zrn
Apa
Zrn
Zrn
Zrn
Tou
Tou
Zrn
Zrn
Tou
Tou
Tou
Tou
500 µm
c
Apa
Zrn
Apa
Apa
Apa
Apa
Apa
Apa
500 µm
d
Apa
Zrn
Apa
Apa
Apa
Apa
Apa
Apa
500 µm
e
Am
Grt
Grt
Grt
Grt
Ep
Zrn
Ep
Grt
Grt
Grt
Am
Grt
500 µm
f
Am
Ep
Ep
Am
500 µm
g
Grt
Grt
Apa
Grt
Grt
Grt
Grt
Grt
Grt
Grt
Grt
Grt
Grt
Grt
500 µm
h
Apa
500 µm

## Heavy mineralogy (2/3): Sandstone types D, E, F, and mixed samples

a) The heavy mineral assemblage of type D sandstones is dominated by garnet, apatite (Apa) and zircon (zrn) are rare. It cannot be distinguished from the composition of type C sandstones. Sample CHW07, parallel Nichols.

b) As (a), crossed Nichols.

c) In type E sandstones tourmaline (Tou) is by far the most abundant heavy mineral, zircon (Zrn) is rare. Sample ST09, parallel Nichols.

d) As (c), crossed Nichols.

e) The type F sample is relatively rich in rutile (rtl). However, zircon (Zrn) and apatite (Apa) are even more frequent. Sample AN08, parallel Nichols.

f) As (e), crossed Nichols.

g) In this sample garnet (Grt, typically type C/D) and tourmaline (Tou, typically type A/E) are present in similar fractions. For their light mineralogy and for geographic constraints, this sample is interpreted as mixture of type C and A. Sample MA06-4, parallel Nichols.

h) As (g), crossed Nichols.

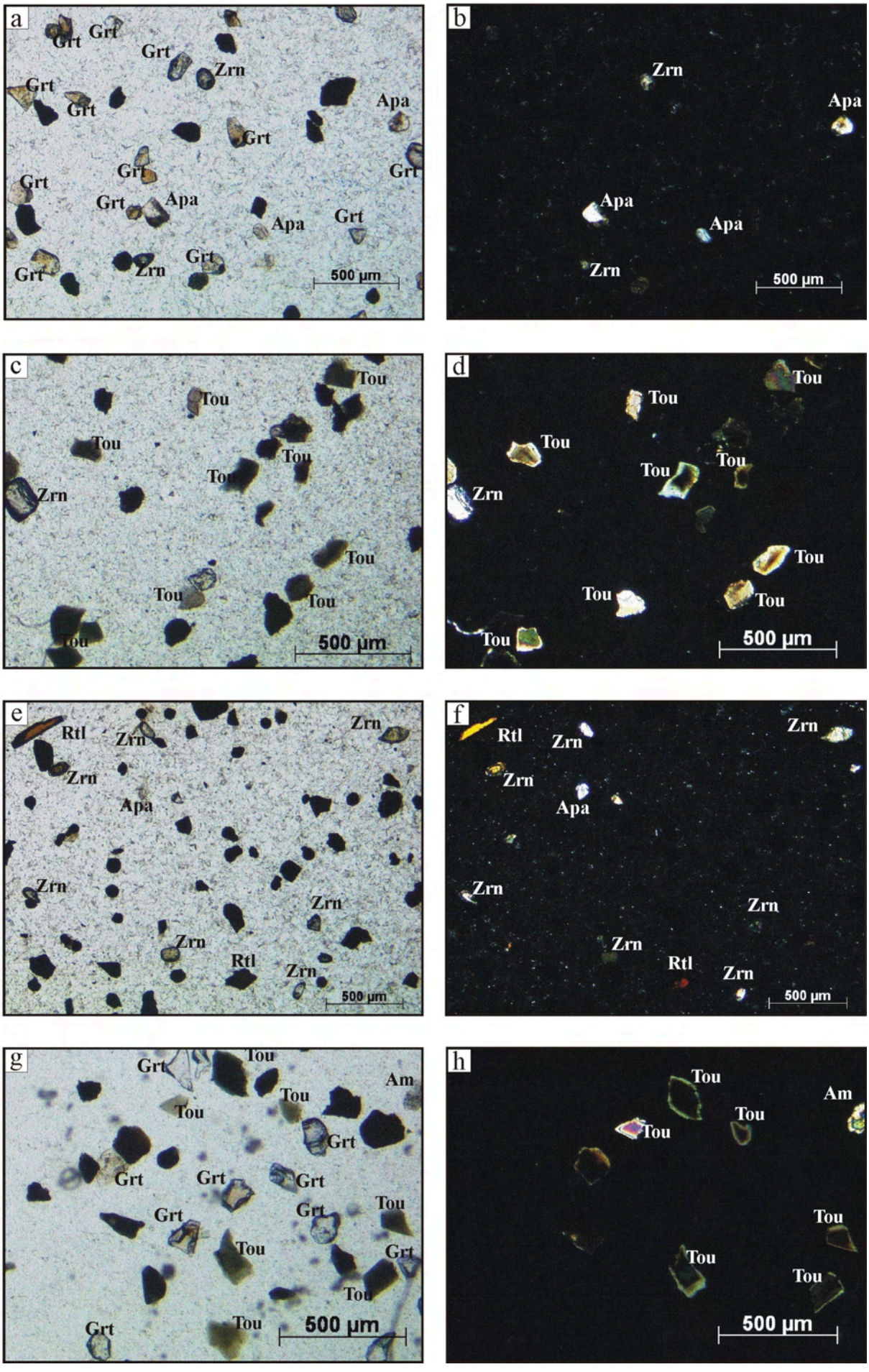
a
Grt
Grt
Grt
Zrn
Grt
Grt
Apa
Grt
Grt
Grt
Grt
Grt
Apa
Apa
Grt
Grt
Zrn
Grt
500 µm
b
Zrn
Apa
Apa
Apa
Zrn
500 µm
c
Tou
Tou
Tou
Tou
Tou
Zrn
Tou
Tou
Tou
500 µm
d
Tou
Tou
Tou
Tou
Tou
Zrn
Tou
Tou
Tou
Tou
500 µm
e
Rtl
Zrn
Zrn
Zrn
Apa
Zrn
Zrn
Zrn
Zrn
Rtl
Zrn
500 µm
f
Rtl
Zrn
Zrn
Zrn
Apa
Zrn
Zrn
Zrn
Rtl
Zrn
500 µm
g
Grt
Tou
Am
Tou
Tou
Grt
Grt
Grt
Grt
Grt
Grt
Tou
Tou
Grt
Tou
Grt
Tou
500 µm
h
Tou
Am
Tou
Tou
Tou
Tou
Tou
Tou
500 µm

## Heavy mineralogy (3/3)

a) Garnet (Grt) is the most abundant heavy mineral within the SPF, although it is not present in all sandstone types. Most garnets are free of inclusions, but this example shows rutile needles (arrows). Sample CHW06, parallel Nichols.

b) As (a), crossed Nichols.

c) Brownish-green amphiboles (Am) are present within samples from higher stratigraphic parts of type C sandstones only. Their fraction increases with the stratigraphic position. They indicate erosion of andesitic rocks within the source area, possibly andesitic lava flows contemporaneous to sedimentation of the SPF. Sample SHA05, parallel Nichols.

d) As (c), crossed Nichols.

e) A pyroxene within a mafic volcanic lithoclast, showing plagioclase. In general, pyroxenes are extremely rare within the SPF, and this example is also already altered. Sample TI14, parallel Nichols.

f) As (e), crossed Nichols.

g) Reddish brown Cr-spinel is very rare within the SPF. However, at it is diagnostic for certain source rocks, it provides very important information. Unlike the images shown above, this photo is from a polished heavy mineral mount. Sample TI14, parallel Nichols.

h) As (g), crossed Nichols.

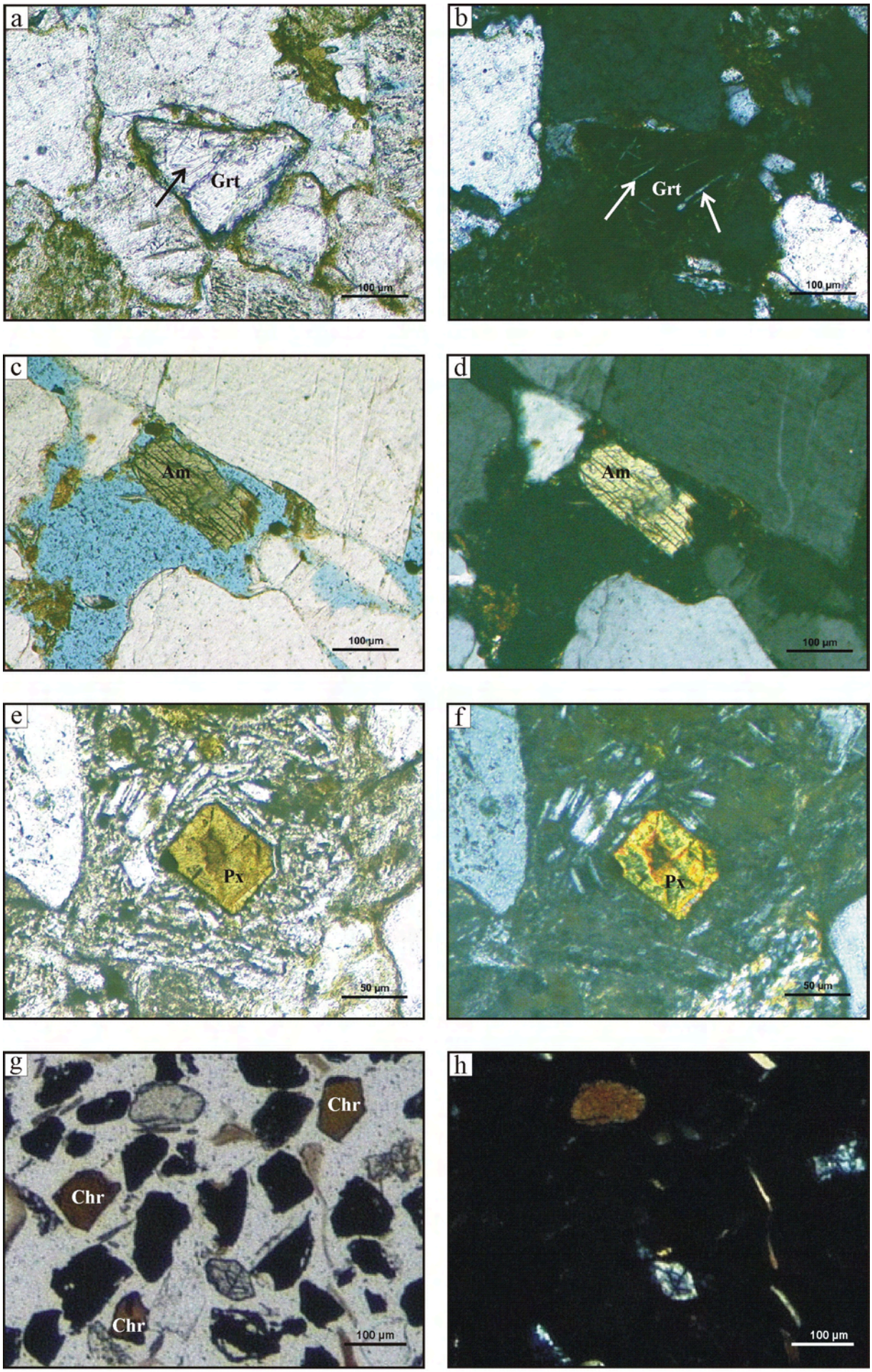
a
Grt
100 µm
b
Grt
100 µm
c
Am
100 µm
d
Am
100 µm
e
Px
50 µm
f
Px
50 µm
g
Chr
Chr
Chr
100 µm
h
100 µm

# Appendix 4

Whole-rock geochemical analyses (XRF)

Major elements (as weight% of oxides)

Section Peak Formation (SPF)

| Sample name | type | LOI | $SO_3$ | $P_2O_5$ | $K_2O$ | $Na_2O$ | CaO | MgO | MnO | $Fe_2O_3$ | $Al_2O_3$ | $TiO_2$ | $SiO_2$ | Sum |
|---|---|---|---|---|---|---|---|---|---|---|---|---|---|---|
| AN 01 RS 01 a | Sst. | 10.85 | <d.l. | 0.03 | 0.98 | 0.32 | 0.14 | 0.08 | 0.05 | 2.39 | 6.72 | 0.31 | 89.23 | 100.25 |
| AN 02 RS 03 | Sst. | 9.38 | <d.l. | 0.03 | 1.57 | 0.33 | 0.30 | 0.15 | 0.03 | 4.18 | 5.60 | 0.66 | 85.88 | 98.73 |
| AN 03 RS 06 | Sst. | 9.51 | <d.l. | 0.03 | 1.95 | 0.37 | 0.12 | 0.14 | 0.01 | 0.82 | 7.45 | 0.44 | 88.54 | 99.87 |
| AN 08 RS 09 | Sst. | 9.33 | <d.l. | 0.01 | 1.21 | 0.18 | 0.04 | 0.07 | 0.00 | 0.13 | 2.94 | 0.07 | 95.28 | 99.93 |
| AN 09 RS 10 | Sst. | 9.91 | <d.l. | 0.02 | 1.82 | 0.25 | 0.19 | 0.09 | 0.01 | 0.80 | 6.05 | 0.73 | 89.91 | 99.87 |
| AN 11 RS 11 | Sst. | 8.78 | <d.l. | 0.01 | 1.74 | 0.23 | 0.30 | 0.06 | 0.07 | 2.36 | 6.06 | 0.11 | 88.61 | 99.55 |
| AN 15 RS 12 | Sst. | 8.05 | <d.l. | 0.04 | 2.29 | 1.52 | 0.52 | 0.44 | 0.04 | 1.35 | 9.46 | 0.31 | 84.06 | 100.03 |
| AN 16 RS 13 | Sst. | 9.53 | 0.02 | 0.04 | 1.97 | 1.23 | 1.14 | 0.44 | 0.70 | 9.19 | 8.45 | 0.32 | 75.44 | 98.94 |
| AN 18 RS 14 | Sst. | 8.90 | 0.23 | 0.05 | 3.93 | 2.39 | 8.72 | 0.53 | 0.18 | 2.36 | 13.13 | 0.24 | 68.23 | 99.99 |
| SHS 01 RS 02 | Sst. | 2.51 | 0.09 | 0.08 | 2.25 | 1.78 | 2.15 | 0.42 | 0.08 | 1.81 | 9.15 | 0.43 | 81.70 | 99.94 |
| SHS 03 RS 12 | Sst. | 0.75 | <d.l. | 0.02 | 1.65 | 0.61 | 0.19 | 0.10 | 0.01 | 0.67 | 4.73 | 0.19 | 91.67 | 99.84 |
| SHS 04 RS 16 | Sst. | 0.73 | <d.l. | 0.02 | 1.93 | 1.02 | 0.23 | 0.07 | 0.01 | 0.68 | 6.17 | 0.15 | 89.58 | 99.86 |
| SHA 03 RS 02 | Sst. | 1.22 | <d.l. | 0.04 | 2.78 | 2.00 | 1.06 | 0.47 | 0.03 | 2.11 | 10.31 | 0.41 | 80.00 | 99.21 |
| SHA 05 RS 03 | Sst. | 0.94 | <d.l. | 0.04 | 3.39 | 1.71 | 0.79 | 0.14 | 0.01 | 1.10 | 9.57 | 0.18 | 83.01 | 99.94 |
| SHA 07 RS 06 | Sst. | 2.67 | 0.09 | 0.09 | 2.96 | 2.59 | 1.76 | 0.44 | 0.04 | 2.08 | 12.91 | 0.55 | 76.39 | 99.81 |
| SHA 09 RS 09 | Tf. sst. | 7.66 | 0.07 | 0.09 | 1.92 | 2.06 | 3.10 | 0.63 | 0.02 | 2.51 | 16.52 | 0.42 | 72.49 | 99.76 |
| SHA 12-RS 13 | Tf. sst. | 8.26 | 0.02 | 0.17 | 1.01 | 2.86 | 3.92 | 0.29 | 0.02 | 1.60 | 15.62 | 0.21 | 74.03 | 99.75 |
| SHA14-RS15 | Tf. sst. | 4.79 | <d.l. | 0.08 | 2.29 | 2.49 | 2.73 | 0.58 | 0.01 | 2.22 | 15.58 | 0.45 | 73.67 | 100.10 |
| SHA 17 RS 17 | Sst. | 3.71 | 0.06 | 0.10 | 2.39 | 2.34 | 2.31 | 0.40 | 0.02 | 1.85 | 13.40 | 0.57 | 76.36 | 99.80 |
| SP 05-RS05 | Sst. | 4.76 | <d.l. | 0.05 | 2.49 | 1.80 | 1.03 | 0.89 | 0.06 | 2.93 | 13.52 | 0.50 | 76.15 | 99.42 |
| SP 08-RS06 | Sst. | 3.64 | <d.l. | 0.07 | 4.54 | 2.34 | 1.14 | 0.89 | 0.05 | 2.23 | 14.83 | 0.64 | 72.05 | 98.78 |
| SP-L1.1 | Mst. | 8.76 | <d.l. | 0.06 | 2.44 | 0.77 | 1.53 | 1.63 | 0.01 | 4.22 | 23.50 | 0.86 | 65.24 | 100.26 |
| SP 11-RS08 | Sst. | 1.81 | <d.l. | 0.03 | 2.64 | 1.73 | 1.25 | 0.15 | 0.02 | 0.79 | 7.96 | 0.16 | 84.95 | 99.68 |
| SP 23-RS04 | Sst. | 2.48 | <d.l. | 0.04 | 2.86 | 2.26 | 1.23 | 0.45 | 0.02 | 1.44 | 11.92 | 0.35 | 78.89 | 99.46 |
| SPP 05-RS17 | Sst. | 3.5 | <d.l. | 0.04 | 3.29 | 2.76 | 1.66 | 0.57 | 0.02 | 1.62 | 15.96 | 0.34 | 74.27 | 100.53 |
| SPP 17-RS29 | Sst. | 2.36 | <d.l. | 0.05 | 2.58 | 2.23 | 1.26 | 0.39 | 0.01 | 1.31 | 11.27 | 0.38 | 80.19 | 99.67 |
| SPP 36-RS14 | Sst. | 1.34 | <d.l. | 0.04 | 3.63 | 2.07 | 0.89 | 0.36 | 0.04 | 1.68 | 10.98 | 0.37 | 78.92 | 98.98 |
| MA02-RS15 | Sst. | 3.62 | <d.l. | 0.06 | 3.12 | 2.84 | 1.58 | 0.55 | 0.04 | 1.95 | 12.23 | 0.50 | 77.02 | 99.89 |
| MA06-2-RS11 | Sst. | 10.26 | 0.09 | 0.02 | 1.52 | 1.26 | 1.50 | 0.59 | 0.02 | 2.60 | 17.55 | 0.58 | 74.36 | 100.09 |
| MA06-4-RS07 | Sst. | 1.99 | <d.l. | 0.05 | 2.50 | 2.17 | 1.44 | 0.45 | 0.02 | 1.92 | 10.39 | 0.32 | 80.48 | 99.74 |
| RB 02 | Sst. | 2.22 | 0.03 | 0.09 | 1.99 | 1.85 | 1.32 | 0.68 | 0.05 | 2.34 | 9.74 | 0.94 | 80.61 | 99.64 |
| RB 08 | Sst. | 4.02 | <d.l. | 0.04 | 2.57 | 2.60 | 1.64 | 0.81 | 0.01 | 1.32 | 13.08 | 0.28 | 77.39 | 99.74 |

Section Peak Formation (SPF, continuation)

| Sample name | type | LOI | $SO_3$ | $P_2O_5$ | $K_2O$ | $Na_2O$ | CaO | MgO | MnO | $Fe_2O_3$ | $Al_2O_3$ | $TiO_2$ | $SiO_2$ | Sum |
|---|---|---|---|---|---|---|---|---|---|---|---|---|---|---|
| TP 03-RS05 | Sst. | 3.41 | <d.l. | 0.03 | 2.50 | 0.18 | 0.03 | 0.03 | <d.l. | 0.41 | 11.51 | 0.82 | 84.18 | 99.69 |
| TP 04-RS07 | Sst. | 2.76 | <d.l. | 0.02 | 2.48 | 0.14 | 0.01 | 0.02 | <d.l. | 0.30 | 10.44 | 0.62 | 85.57 | 99.60 |
| CHW 03-RS04 | Sst. | 5.63 | <d.l. | 0.03 | 2.46 | 1.87 | 4.25 | 0.14 | 0.02 | 1.60 | 15.52 | 0.53 | 72.81 | 99.23 |
| CHW 06-RS08 | Sst. | 3.83 | <d.l. | 0.05 | 2.63 | 3.37 | 1.19 | 0.49 | 0.03 | 1.75 | 12.27 | 0.26 | 77.54 | 99.58 |
| CHW 07-RS10 | Sst. | 4.48 | 0.01 | 0.06 | 3.59 | 3.86 | 1.31 | 0.48 | 0.04 | 2.45 | 14.40 | 0.44 | 72.82 | 99.46 |
| CHW 08-RS11 | Sst. | 3.63 | <d.l. | 0.06 | 6.76 | 2.31 | 0.60 | 1.09 | 0.04 | 3.49 | 17.26 | 0.57 | 67.63 | 99.81 |
| CHW 10-RS14 | Sst. | 3.31 | <d.l. | 0.05 | 3.34 | 3.53 | 1.01 | 0.37 | 0.02 | 2.06 | 12.68 | 0.45 | 75.31 | 98.82 |
| CHW 14-RS22 | Sst. | 5.57 | 0.01 | 0.09 | 2.51 | 2.30 | 1.77 | 1.01 | 0.06 | 2.36 | 15.66 | 0.43 | 74.30 | 100.50 |
| CHW15-RS24 | Mst. | 5.49 | <d.l. | 0.06 | 2.09 | 1.53 | 2.10 | 1.35 | 0.05 | 3.76 | 17.47 | 0.55 | 71.31 | 100.27 |
| CHW 26-RS41 | Sst. | 2.95 | <d.l. | 0.06 | 2.41 | 2.79 | 1.19 | 0.45 | 0.07 | 2.60 | 11.27 | 0.58 | 77.72 | 99.14 |
| TI 04-RS11 | Sst. | 4.51 | <d.l. | 0.09 | 2.83 | 3.32 | 1.84 | 0.97 | 0.06 | 2.74 | 16.59 | 0.57 | 71.03 | 100.04 |
| TI 11-RS17 | Sst. | 4.87 | <d.l. | 0.07 | 2.55 | 3.15 | 1.63 | 0.75 | 0.04 | 2.44 | 18.32 | 0.73 | 69.92 | 99.60 |
| TI13-RS15 | Mst. | 7.31 | <d.l. | 0.04 | 2.08 | 1.40 | 0.94 | 0.70 | 0.03 | 3.34 | 21.55 | 1.05 | 69.22 | 100.35 |
| TI 16-RS20 | Sst. | 3.26 | <d.l. | 0.10 | 2.04 | 3.74 | 2.41 | 0.39 | 0.05 | 2.10 | 16.05 | 0.55 | 72.12 | 99.55 |
| TI 19-RS25 | Sst. | 6.51 | <d.l. | 0.08 | 2.72 | 2.93 | 2.20 | 0.67 | 0.04 | 2.54 | 19.03 | 0.60 | 69.01 | 99.82 |
| SR 03-RS07 | Sst. | 5.08 | <d.l. | 0.08 | 2.35 | 3.51 | 1.53 | 0.97 | 0.05 | 3.10 | 15.79 | 0.63 | 71.17 | 99.18 |

Shafer Peak Formation (SHF)

| Sample name | type | LOI | $SO_3$ | $P_2O_5$ | $K_2O$ | $Na_2O$ | CaO | MgO | MnO | $Fe_2O_3$ | $Al_2O_3$ | $TiO_2$ | $SiO_2$ | Sum |
|---|---|---|---|---|---|---|---|---|---|---|---|---|---|---|
| SHC 02 JS 02 | Tf. sst. | 3.17 | 0.03 | 0.04 | 2.51 | 2.19 | 1.51 | 0.55 | 0.02 | 1.64 | 12.14 | 0.41 | 79.02 | 100.06 |
| SHC08-JS01 | Tf. sst. | 2.99 | <d.l. | 0.02 | 3.41 | 1.96 | 1.58 | 0.48 | 0.02 | 1.47 | 11.55 | 0.38 | 78.85 | 99.72 |
| SHC 25 RS 31 | Sst. | 2.39 | <d.l. | 0.03 | 4.58 | 1.92 | 0.89 | 0.43 | 0.02 | 1.54 | 11.53 | 0.45 | 78.48 | 99.87 |
| SHC39-RS39 | Tf. sst. | 6.28 | <d.l. | 0.04 | 2.41 | 1.68 | 2.60 | 0.58 | 0.02 | 1.53 | 13.53 | 0.39 | 77.13 | 99.91 |
| CE09-RS01 | Tf. sst. | 3.50 | <d.l. | 0.04 | 3.26 | 1.97 | 1.07 | 0.55 | 0.03 | 1.82 | 10.46 | 0.53 | 79.01 | 98.74 |
| CE19-RS05 | Tf. sst. | 4.14 | <d.l. | 0.04 | 2.57 | 1.81 | 1.42 | 0.25 | 0.02 | 1.23 | 10.34 | 0.42 | 81.03 | 99.13 |
| CE41-RS09 | Tf. sst. | 5.16 | <d.l. | 0.03 | 2.81 | 1.88 | 1.43 | 0.28 | 0.02 | 1.16 | 10.95 | 0.41 | 79.67 | 98.64 |
| CE55-RS14 | Tf. sst. | 7.14 | <d.l. | 0.03 | 2.67 | 1.96 | 2.10 | 0.46 | 0.01 | 1.62 | 12.36 | 0.38 | 77.19 | 98.78 |
| CE77-RS20 | Tf. sst. | 7.79 | <d.l. | 0.05 | 2.45 | 2.33 | 2.36 | 0.51 | 0.03 | 2.00 | 12.26 | 0.39 | 76.66 | 99.04 |

Sst.: sandstone; Mst.: mudstone; Tf. Sst.: Tuffaceous sandstone; LOI: loss on ignition; d.l.: detection limit

## Trace elements (as ppm)

### Section Peak Formation (SPF)

| Sample name | type | V | Cr | Co | Ni | Cu | Zn | Rb | Sr | Y | Zr | Nb | Ba | Pb | U | S | Cl | Ce | La | Th | Sc | Ga | sum (%) |
|---|---|---|---|---|---|---|---|---|---|---|---|---|---|---|---|---|---|---|---|---|---|---|---|
| AN 01 RS 01 a | Sst. | 38 | 14 | 9 | 29 | 7 | 40 | 53 | 56 | 15 | 144 | 7 | 254 | 13 | <d.l. | 356 | <d.l. | 26 | 11 | 7 | 6 | n.d. | 0.099 |
| AN 02 RS 03 | Sst. | 47 | 16 | 9 | 24 | <d.l. | 11 | 57 | 97 | 16 | 337 | 13 | 436 | 27 | <d.l. | 3116 | <d.l. | 60 | 27 | 18 | 4 | n.d. | 0.415 |
| AN 03 RS 06 | Sst. | 42 | 18 | <d.l. | 24 | 3 | 7 | 79 | 110 | 19 | 318 | 10 | 514 | 15 | <d.l. | 652 | <d.l. | 41 | 19 | 11 | 6 | n.d. | 0.175 |
| AN 08 RS 09 | Sst. | 10 | 3 | <d.l. | 24 | 5 | <d.l. | 43 | 83 | 9 | 135 | 4 | 301 | 10 | <d.l. | 3316 | <d.l. | 21 | 9 | 4 | 4 | n.d. | 0.386 |
| AN 09 RS 10 | Sst. | 45 | 15 | <d.l. | 24 | 4 | 20 | 70 | 97 | 22 | 408 | 14 | 456 | 11 | 2 | 1325 | <d.l. | 51 | 22 | 15 | 6 | n.d. | 0.246 |
| AN 11 RS 11 | Sst. | 40 | 8 | 6 | 28 | 8 | 24 | 69 | 113 | 20 | 163 | 3 | 488 | 9 | 1 | 3376 | <d.l. | 34 | 16 | 5 | 6 | n.d. | 0.428 |
| AN 15 RS 12 | Sst. | 33 | 12 | 4 | 27 | 9 | 32 | 98 | 188 | 25 | 225 | 9 | 587 | 16 | <d.l. | 1104 | 85 | 46 | 21 | 7 | 7 | n.d. | 0.245 |
| AN 16 RS 13 | Sst. | 50 | 16 | 48 | 43 | 2 | 104 | 59 | 143 | 38 | 196 | 5 | 527 | 10 | 2 | 357 | 138 | 90 | 46 | 10 | 7 | n.d. | 0.174 |
| AN 18 RS 14 | Sst. | 45 | 9 | 7 | 27 | 2 | 58 | 124 | 473 | 23 | 147 | 8 | 818 | 15 | <d.l. | 1286 | 552 | 55 | 26 | 11 | 6 | n.d. | 0.360 |
| SHS 01 RS 02 | Sst. | 57 | 9 | 7 | 30 | 9 | 73 | 93 | 170 | 25 | 175 | 7 | 546 | 12 | <d.l. | 743 | 73 | n.d. | n.d. | n.d. | n.d. | n.d. | 0.203 |
| SHS 03 RS 12 | Sst. | 22 | <d.l. | 1 | 26 | 17 | 7 | 63 | 106 | 10 | 175 | 7 | 412 | 12 | <d.l. | 264 | <d.l. | n.d. | n.d. | n.d. | n.d. | n.d. | 0.106 |
| SHS 04 RS 16 | Sst. | 23 | 5 | <d.l. | 25 | 6 | 9 | 74 | 155 | 13 | 169 | 5 | 487 | 11 | <d.l. | <d.l. | <d.l. | n.d. | n.d. | n.d. | n.d. | n.d. | 0.860 |
| SHA 03 RS 02 | Sst. | 49 | 15 | 5 | 27 | 10 | 31 | 99 | 267 | 22 | 189 | 10 | 620 | 19 | <d.l. | 2886 | <d.l. | n.d. | n.d. | n.d. | n.d. | n.d. | 0.417 |
| SHA 05 RS 03 | Sst. | 24 | <d.l. | 2 | 25 | 8 | 10 | 133 | 259 | 9 | 140 | 4 | 637 | 17 | 3 | 1828 | <d.l. | n.d. | n.d. | n.d. | n.d. | n.d. | 0.303 |
| SHA 07 RS 06 | Sst. | 56 | 19 | 7 | 37 | 8 | 47 | 119 | 395 | 32 | 260 | 12 | 829 | 22 | 2 | 7877 | <d.l. | n.d. | n.d. | n.d. | n.d. | n.d. | 0.966 |
| SHA 09 RS 09 | Tf.Sst. | 48 | 8 | 4 | 30 | 22 | 84 | 97 | 313 | 41 | 265 | 14 | 954 | 20 | 4 | 937 | <d.l. | n.d. | n.d. | n.d. | n.d. | n.d. | 0.280 |
| SHA 12-RS 13 | Tf.Sst. | 20 | <d.l. | <d.l. | 24 | 9 | 30 | 43 | 397 | 19 | 177 | 8 | 1082 | 17 | 5 | 414 | 7 | 23 | 13 | 24 | 5 | 13 | 0.225 |
| SHA14-RS15 | Tf.Sst. | 47 | 18 | 3 | 29 | 11 | 68 | 117 | 356 | 45 | 323 | 14 | 843 | 19 | 1 | 463 | 98 | n.d. | n.d. | n.d. | n.d. | n.d. | 0.245 |
| SHA 17 RS 17 | Sst. | 54 | 21 | 3 | 27 | 7 | 59 | 97 | 375 | 25 | 492 | 12 | 633 | 17 | 3 | 3872 | <d.l. | n.d. | n.d. | n.d. | n.d. | n.d. | 0.565 |
| SP 05-RS05 | Sst. | 74 | 30 | 11 | 34 | 8 | 87 | 105 | 241 | 30 | 291 | 11 | 628 | 19 | 5 | 365 | 129 | 38 | 18 | 6 | 7 | n.d. | 0.207 |
| SP 08-RS06 | Sst. | 90 | 30 | 19 | 68 | 7 | 114 | 186 | 268 | 33 | 475 | 16 | 867 | 35 | 5 | 424 | <d.l. | 68 | 33 | 16 | 8 | n.d. | 0.263 |
| SP-L1.1 | Mst. | 124 | 50 | 20 | 54 | 48 | 122 | 210 | 50 | 57 | 305 | 18 | 400 | 19 | 8 | 168 | 125 | n.d. | n.d. | n.d. | n.d. | n.d. | 0.165 |
| SP 11-RS08 | Sst. | 22 | 7 | 3 | 32 | 8 | 14 | 106 | 247 | 16 | 156 | 4 | 629 | 17 | 2 | 5879 | <d.l. | 77 | 33 | 19 | 6 | n.d. | 0.709 |
| SP 23-RS04 | Sst. | 52 | 19 | 6 | 30 | 14 | 57 | 140 | 288 | 19 | 232 | 11 | 654 | 16 | 1 | 140 | <d.l. | 51 | 23 | 12 | 6 | n.d. | 0.166 |
| SPP 05-RS17 | Sst. | 61 | 20 | 5 | 31 | 13 | 59 | 146 | 352 | 21 | 201 | 9 | 782 | 18 | 5 | 688 | <d.l. | 54 | 29 | 12 | 7 | n.d. | 0.240 |
| SPP 17-RS29 | Sst. | 65 | 18 | 3 | 26 | 9 | 43 | 116 | 283 | 18 | 255 | 9 | 594 | 16 | 2 | 937 | <d.l. | 47 | 22 | 8 | 7 | n.d. | 0.237 |
| SPP 36-RS14 | Sst. | 42 | 10 | 3 | 29 | 10 | 48 | 172 | 222 | 18 | 269 | 9 | 652 | 16 | 4 | 475 | 29 | 43 | 18 | 12 | 8 | n.d. | 0.201 |
| MA02-RS15 | Sst. | 49 | 23 | 4 | 32 | 10 | 47 | 117 | 936 | 22 | 299 | 12 | 789 | 14 | <d.l. | 1100 | 55 | 46 | 24 | 11 | 6 | n.d. | 0.351 |
| MA06-2-RS11 | Sst. | 69 | 31 | 10 | 35 | 20 | 187 | 88 | 283 | 34 | 428 | 18 | 1038 | 26 | 1 | 2613 | <d.l. | 41 | 21 | 15 | 8 | n.d. | 0.486 |
| MA06-4-RS07 | Sst. | 40 | 17 | 3 | 28 | 3 | 31 | 96 | 327 | 20 | 181 | 6 | 618 | 16 | 3 | 1617 | <d.l. | 44 | 20 | 7 | 6 | n.d. | 0.295 |
| RB 02 | Sst. | 75 | 24 | 10 | 27 | 11 | 39 | 79 | 289 | 34 | 280 | 14 | 557 | 12 | 3 | 1293 | <d.l. | 41 | 17 | 11 | 9 | n.d. | 0.272 |
| RB 08 | Sst. | 105 | 49 | 14 | 39 | 13 | 87 | 107 | 473 | 28 | 220 | 9 | 631 | 11 | 2 | 293 | 156 | 36 | 18 | 8 | 6 | n.d. | 0.323 |

Section Peak Formation (SPF, continuation)

| Sample name | type | V | Cr | Co | Ni | Cu | Zn | Rb | Sr | Y | Zr | Nb | Ba | Pb | U | S | Cl | Ce | La | Th | Sc | Ga | sum (%) |
|---|---|---|---|---|---|---|---|---|---|---|---|---|---|---|---|---|---|---|---|---|---|---|---|
| TP 03-RS05 | Sst. | 41 | 4 | <d.l. | 25 | 6 | 19 | 100 | 75 | 26 | 568 | 27 | 448 | 21 | 6 | 904 | <d.l. | 35 | 14 | 12 | 7 | n.d. | 0.220 |
| TP 04-RS07 | Sst. | 25 | 4 | <d.l. | 24 | 8 | 4 | 106 | 67 | 14 | 324 | 22 | 388 | 18 | 3 | 138 | <d.l. | 30 | 12 | 9 | 12 | n.d. | 0.108 |
| CHW 03-RS04 | Sst. | 37 | 13 | 2 | 24 | 4 | 93 | 84 | 90 | 18 | 267 | 14 | 667 | 18 | <d.l. | 1567 | <d.l. | 47 | 22 | 14 | 10 | n.d. | 0.285 |
| CHW 06-RS08 | Sst. | 38 | 15 | 7 | 29 | 5 | 43 | 95 | 678 | 26 | 175 | 7 | 621 | 16 | 2 | 3414 | <d.l. | 50 | 24 | 7 | 7 | n.d. | 0.515 |
| CHW 07-RS10 | Sst. | 54 | 21 | 7 | 31 | 6 | 58 | 140 | 872 | 21 | 280 | 11 | 812 | 18 | 3 | 6961 | <d.l. | 46 | 24 | 12 | 5 | n.d. | 0.921 |
| CHW 08-RS11 | Sst. | 85 | 27 | 9 | 34 | 30 | 87 | 244 | 117 | 37 | 217 | 13 | 959 | 23 | 7 | 35 | <d.l. | 48 | 26 | 18 | 7 | n.d. | 0.187 |
| CHW 10-RS14 | Sst. | 49 | 14 | 7 | 30 | 7 | 53 | 122 | 816 | 19 | 225 | 9 | 819 | 16 | 1 | 3406 | 14 | 41 | 21 | 8 | 7 | n.d. | 0.561 |
| CHW 14-RS22 | Sst. | 53 | 17 | 7 | 31 | 10 | 74 | 96 | 485 | 25 | 267 | 12 | 672 | 18 | 3 | 291 | 19 | 45 | 21 | 13 | 7 | n.d. | 0.208 |
| CHW15-RS24 | Mst. | 76 | 25 | 9 | 34 | 25 | 90 | 104 | 219 | 40 | 314 | 17 | 428 | 27 | 3 | 210 | 141 | n.d. | n.d. | n.d. | n.d. | n.d. | 0.162 |
| CHW 26-RS41 | Sst. | 56 | 23 | 8 | 30 | 5 | 49 | 85 | 548 | 21 | 275 | 10 | 858 | 20 | 4 | 883 | <d.l. | 46 | 24 | 11 | 9 | n.d. | 0.285 |
| TI 04-RS11 | Sst. | 104 | 26 | 14 | 35 | 14 | 90 | 116 | 495 | 35 | 233 | 8 | 752 | 18 | 3 | 684 | 179 | 57 | 28 | 10 | 9 | n.d. | 0.281 |
| TI 11-RS17 | Sst. | 95 | 36 | 7 | 37 | 12 | 144 | 120 | 352 | 32 | 344 | 12 | 558 | 15 | <d.l. | 116 | <d.l. | 40 | 19 | 12 | 12 | n.d. | 0.186 |
| TI13-RS15 | Mst. | 181 | 65 | 7 | 36 | 44 | 106 | 138 | 142 | 45 | 337 | 13 | 401 | 31 | 4 | 329 | <d.l. | n.d. | n.d. | n.d. | n.d. | n.d. | 0.188 |
| TI 16-RS20 | Sst. | 76 | 15 | 9 | 33 | 9 | 90 | 80 | 1099 | 35 | 226 | 6 | 1275 | 18 | 4 | 503 | <d.l. | 44 | 21 | 8 | 5 | n.d. | 0.344 |
| TI 19-RS25 | Sst. | 93 | 16 | 9 | 34 | 11 | 113 | 113 | 912 | 30 | 312 | 11 | 1358 | 20 | <d.l. | 445 | 11 | 44 | 26 | 13 | 9 | n.d. | 0.349 |
| SR 03-RS07 | Sst. | 42 | 19 | 2 | 28 | 6 | 38 | 105 | 471 | 18 | 194 | 9 | 633 | 15 | 1 | 1592 | 55 | 42 | 19 | 9 | 11 | n.d. | 0.224 |

Shafer Peak Formation (SHF)

| Sample name | type | V | Cr | Co | Ni | Cu | Zn | Rb | Sr | Y | Zr | Nb | Ba | Pb | U | S | Cl | Ce | La | Th | Sc | Ga | sum (%) |
|---|---|---|---|---|---|---|---|---|---|---|---|---|---|---|---|---|---|---|---|---|---|---|---|
| SHC 02 JS 02 | Tf. sst. | 42 | 13 | 2 | 27 | 15 | 33 | 109 | 251 | 20 | 556 | 13 | 540 | 23 | 4 | 3284 | <d.l. | n.d. | n.d. | n.d. | n.d. | n.d. | 0.486 |
| SHC08-JS01 | Tf. sst. | 36 | 11 | 1 | 29 | 17 | 34 | 147 | 242 | 21 | 389 | 11 | 639 | 14 | 5 | 792 | 271 | n.d. | n.d. | n.d. | n.d. | n.d. | 0.266 |
| SHC 25 RS 31 | Sst. | 38 | 19 | 2 | 29 | 15 | 34 | 160 | 328 | 29 | 614 | 13 | 779 | 16 | 2 | 1166 | <d.l. | n.d. | n.d. | n.d. | n.d. | n.d. | 0.319 |
| SHC39-RS 39 | Tf. sst. | 42 | 14 | 1 | 30 | 22 | 57 | 108 | 297 | 31 | 367 | 17 | 712 | 19 | <d.l. | 1868 | 14 | n.d. | n.d. | n.d. | n.d. | n.d. | 0.36 |
| CE09-RS01 | Tf. sst. | 38 | 14 | 2 | 30 | 15 | 39 | 121 | 160 | 35 | 862 | 15 | 555 | 15 | 3 | 165 | <d.l. | 49 | 23 | 13 | 7 | 14 | 0.206 |
| CE19-RS05 | Tf. sst. | 37 | 11 | 1 | 27 | 16 | 18 | 100 | 306 | 27 | 641 | 14 | 687 | 14 | <d.l. | 273 | <d.l. | 35 | 18 | 9 | 5 | 7 | 0.212 |
| CE41-RS09 | Tf. sst. | 31 | 18 | 1 | 29 | 13 | 33 | 112 | 287 | 27 | 653 | 13 | 673 | 16 | 3 | 1542 | <d.l. | 37 | 19 | 11 | 10 | 25 | 0.336 |
| CE55-RS14 | Tf. sst. | 40 | 10 | 0 | 30 | 19 | 44 | 121 | 302 | 24 | 311 | 14 | 648 | 16 | 2 | 1286 | <d.l. | 37 | 19 | 12 | 8 | 14 | 0.282 |
| CE77-RS20 | Tf. sst. | 40 | 12 | 7 | 34 | 18 | 50 | 118 | 341 | 29 | 453 | 14 | 739 | 16 | 4 | 100 | 51 | 40 | 20 | 14 | 7 | 13 | 0.202 |
| detection limit | | 1.6 | 2.8 | 1.0 | 1.4 | 0.9 | 1.1 | 0.8 | 1.0 | 0.5 | 0.7 | 0.9 | 8.4 | 1.1 | 0.8 | 1.3 | 1.9 | 1.3 | 1.6 | 1.5 | 1.6 | 1.8 | |

Sst.: sandstone; Mst.: mudstone; Tf. Sst.: Tuffaceous sandstone; LOI: loss on ignition; d.l.: detection limit

# Appendix 5

Mineral chemical analyses (EMP)

# Analyses of feldspar from sandstones

| Sample / No. | $SiO_2$ | $Na_2O$ | $K_2O$ | CaO | FeO | $Al_2O_3$ | MgO | SrO | $TiO_2$ | MnO | BaO | wt-total | Si_at | Na_at | K_at | Ca_at | Fe_at | Al_at | Mg_at | Sr_at | Ti_at | Mn_at | Ba_at | at-total |
|---|---|---|---|---|---|---|---|---|---|---|---|---|---|---|---|---|---|---|---|---|---|---|---|---|
| AN01a_Fsp11 | 65.85 | 10.16 | 0.52 | 2.40 | 0.13 | 21.16 | 0.00 | 0.00 | 0.00 | 0.01 | 0.02 | 100.24 | 8.684 | 2.599 | 0.087 | 0.338 | 0.014 | 3.289 | 0.000 | 0.000 | 0.000 | 0.001 | 0.001 | 15.014 |
| AN01a_Fsp12 | 64.00 | 0.64 | 15.55 | 0.00 | 0.09 | 18.54 | 0.00 | 0.00 | 0.02 | 0.03 | 0.67 | 99.53 | 8.946 | 0.174 | 2.773 | 0.000 | 0.010 | 3.054 | 0.000 | 0.000 | 0.002 | 0.003 | 0.037 | 14.999 |
| AN01a_Fsp13 | 65.68 | 1.52 | 14.73 | 0.01 | 0.02 | 18.69 | 0.00 | 0.00 | 0.00 | 0.01 | 0.10 | 100.76 | 8.989 | 0.403 | 2.572 | 0.002 | 0.002 | 3.015 | 0.000 | 0.000 | 0.000 | 0.002 | 0.005 | 14.991 |
| AN01a_Fsp14 | 65.50 | 1.42 | 14.77 | 0.03 | 0.02 | 18.61 | 0.02 | 0.06 | 0.02 | 0.00 | 0.05 | 100.49 | 8.990 | 0.378 | 2.587 | 0.004 | 0.002 | 3.011 | 0.004 | 0.004 | 0.002 | 0.000 | 0.003 | 14.985 |
| AN01a_Fsp15 | 64.29 | 0.96 | 14.96 | 0.05 | 0.01 | 18.63 | 0.00 | 0.06 | 0.01 | 0.00 | 0.17 | 99.15 | 8.962 | 0.259 | 2.660 | 0.008 | 0.001 | 3.061 | 0.000 | 0.005 | 0.001 | 0.000 | 0.009 | 14.967 |
| AN01a_Fsp16 | 64.41 | 1.07 | 14.98 | 0.03 | 0.00 | 18.51 | 0.01 | 0.00 | 0.00 | 0.00 | 0.04 | 99.05 | 8.977 | 0.290 | 2.664 | 0.004 | 0.000 | 3.040 | 0.002 | 0.000 | 0.000 | 0.000 | 0.002 | 14.980 |
| AN01a_Fsp20 | 65.05 | 0.98 | 15.32 | 0.00 | 0.00 | 18.65 | 0.01 | 0.03 | 0.01 | 0.03 | 0.31 | 100.38 | 8.973 | 0.263 | 2.695 | 0.000 | 0.000 | 3.032 | 0.002 | 0.003 | 0.001 | 0.003 | 0.017 | 14.989 |
| AN15_Fsp01 | 65.29 | 0.73 | 15.68 | 0.01 | 0.02 | 18.68 | 0.00 | 0.03 | 0.01 | 0.03 | 0.41 | 100.90 | 8.977 | 0.194 | 2.750 | 0.002 | 0.002 | 3.027 | 0.001 | 0.002 | 0.001 | 0.004 | 0.022 | 14.981 |
| AN15_Fsp02 | 65.42 | 1.21 | 14.81 | 0.02 | 0.05 | 18.68 | 0.02 | 0.03 | 0.04 | 0.00 | 0.37 | 100.65 | 8.982 | 0.323 | 2.594 | 0.003 | 0.006 | 3.023 | 0.005 | 0.003 | 0.004 | 0.000 | 0.020 | 14.961 |
| AN15_Fsp03 | 65.50 | 0.97 | 15.50 | 0.00 | 0.06 | 18.62 | 0.01 | 0.10 | 0.00 | 0.02 | 0.09 | 100.87 | 8.987 | 0.259 | 2.713 | 0.000 | 0.007 | 3.011 | 0.001 | 0.008 | 0.000 | 0.002 | 0.005 | 14.993 |
| AN15_Fsp04 | 62.33 | 8.49 | 0.36 | 5.06 | 0.08 | 23.77 | 0.00 | 0.17 | 0.00 | 0.01 | 0.01 | 100.27 | 8.277 | 2.186 | 0.060 | 0.720 | 0.008 | 3.720 | 0.000 | 0.013 | 0.000 | 0.001 | 0.001 | 14.987 |
| AN15_Fsp05 | 64.78 | 0.97 | 15.01 | 0.00 | 0.03 | 18.71 | 0.01 | 0.11 | 0.04 | 0.01 | 0.70 | 100.36 | 8.956 | 0.259 | 2.648 | 0.000 | 0.003 | 3.049 | 0.001 | 0.009 | 0.004 | 0.001 | 0.038 | 14.968 |
| AN15_Fsp06 | 62.57 | 8.58 | 0.27 | 4.93 | 0.07 | 23.83 | 0.00 | 0.07 | 0.00 | 0.00 | 0.01 | 100.33 | 8.289 | 2.204 | 0.046 | 0.700 | 0.007 | 3.722 | 0.000 | 0.006 | 0.000 | 0.000 | 0.001 | 14.975 |
| AN15_Fsp07 | 60.84 | 7.96 | 0.36 | 6.15 | 0.01 | 24.63 | 0.00 | 0.07 | 0.00 | 0.01 | 0.02 | 100.06 | 8.119 | 2.061 | 0.061 | 0.880 | 0.001 | 3.874 | 0.000 | 0.005 | 0.000 | 0.001 | 0.001 | 15.004 |
| AN15_Fsp08 | 63.81 | 9.23 | 0.31 | 3.90 | 0.11 | 22.80 | 0.01 | 0.09 | 0.00 | 0.02 | 0.02 | 100.29 | 8.440 | 2.366 | 0.052 | 0.553 | 0.012 | 3.555 | 0.003 | 0.007 | 0.000 | 0.002 | 0.001 | 14.991 |
| AN15_Fsp11 | 65.24 | 0.72 | 15.72 | 0.00 | 0.06 | 18.58 | 0.01 | 0.02 | 0.00 | 0.03 | 0.22 | 100.61 | 8.985 | 0.193 | 2.763 | 0.000 | 0.007 | 3.017 | 0.003 | 0.002 | 0.000 | 0.003 | 0.012 | 14.984 |
| AN15_Fsp12 | 62.53 | 8.45 | 0.37 | 5.37 | 0.09 | 23.84 | 0.00 | 0.05 | 0.00 | 0.00 | 0.00 | 100.70 | 8.269 | 2.166 | 0.063 | 0.761 | 0.010 | 3.716 | 0.000 | 0.004 | 0.000 | 0.000 | 0.000 | 14.988 |
| AN15_Fsp13 | 63.24 | 8.73 | 0.57 | 4.44 | 0.10 | 22.92 | 0.01 | 0.02 | 0.01 | 0.00 | 0.00 | 100.04 | 8.399 | 2.249 | 0.097 | 0.632 | 0.011 | 3.588 | 0.002 | 0.002 | 0.001 | 0.000 | 0.000 | 14.979 |
| AN15_Fsp14 | 65.05 | 0.82 | 15.41 | 0.01 | 0.02 | 18.82 | 0.00 | 0.10 | 0.02 | 0.01 | 0.51 | 100.78 | 8.956 | 0.220 | 2.707 | 0.001 | 0.002 | 3.054 | 0.000 | 0.008 | 0.002 | 0.002 | 0.028 | 14.979 |
| AN15_Fsp15 | 64.93 | 1.08 | 14.81 | 0.01 | 0.00 | 18.72 | 0.00 | 0.00 | 0.04 | 0.00 | 1.06 | 100.66 | 8.959 | 0.290 | 2.608 | 0.002 | 0.000 | 3.045 | 0.000 | 0.000 | 0.004 | 0.000 | 0.057 | 14.964 |
| AN15_Fsp16 | 65.80 | 3.24 | 12.03 | 0.23 | 0.01 | 18.92 | 0.00 | 0.03 | 0.01 | 0.00 | 0.13 | 100.42 | 8.962 | 0.856 | 2.091 | 0.034 | 0.002 | 3.037 | 0.000 | 0.002 | 0.001 | 0.000 | 0.007 | 14.992 |
| AN15_Fsp17 | 61.83 | 8.45 | 0.35 | 5.26 | 0.00 | 24.07 | 0.01 | 0.05 | 0.02 | 0.00 | 0.04 | 100.08 | 8.228 | 2.181 | 0.059 | 0.749 | 0.000 | 3.775 | 0.002 | 0.004 | 0.002 | 0.000 | 0.002 | 15.003 |
| AN15_Fsp18 | 64.89 | 9.75 | 0.26 | 3.28 | 0.07 | 21.94 | 0.00 | 0.09 | 0.00 | 0.00 | 0.01 | 100.28 | 8.566 | 2.496 | 0.044 | 0.464 | 0.007 | 3.414 | 0.000 | 0.007 | 0.000 | 0.000 | 0.000 | 14.998 |
| AN15_Fsp19 | 65.00 | 9.67 | 0.27 | 3.12 | 0.05 | 22.06 | 0.00 | 0.01 | 0.00 | 0.00 | 0.01 | 100.18 | 8.575 | 2.473 | 0.045 | 0.441 | 0.005 | 3.430 | 0.000 | 0.001 | 0.000 | 0.000 | 0.001 | 14.969 |
| AN15_Fsp20 | 65.16 | 0.61 | 15.99 | 0.00 | 0.05 | 18.35 | 0.00 | 0.00 | 0.00 | 0.01 | 0.08 | 100.25 | 9.006 | 0.163 | 2.820 | 0.000 | 0.006 | 2.990 | 0.000 | 0.000 | 0.000 | 0.002 | 0.004 | 14.991 |
| AN15_Fsp21 | 62.52 | 8.71 | 0.73 | 4.75 | 0.08 | 23.34 | 0.00 | 0.00 | 0.00 | 0.01 | 0.04 | 100.19 | 8.318 | 2.246 | 0.125 | 0.677 | 0.009 | 3.661 | 0.000 | 0.000 | 0.000 | 0.001 | 0.002 | 15.037 |
| AN15_Fsp22 | 61.92 | 8.74 | 0.17 | 4.76 | 0.00 | 23.95 | 0.00 | 0.05 | 0.05 | 0.00 | 0.00 | 99.65 | 8.257 | 2.259 | 0.029 | 0.681 | 0.000 | 3.765 | 0.000 | 0.004 | 0.005 | 0.000 | 0.000 | 15.000 |
| AN15_Fsp23 | 64.91 | 1.61 | 14.64 | 0.03 | 0.04 | 18.70 | 0.03 | 0.03 | 0.01 | 0.00 | 0.09 | 100.08 | 8.956 | 0.429 | 2.577 | 0.004 | 0.004 | 3.042 | 0.005 | 0.002 | 0.001 | 0.000 | 0.005 | 15.026 |
| AN15_Fsp24 | 62.38 | 8.36 | 0.58 | 5.18 | 0.06 | 23.55 | 0.00 | 0.05 | 0.00 | 0.01 | 0.06 | 100.22 | 8.293 | 2.154 | 0.099 | 0.737 | 0.007 | 3.690 | 0.000 | 0.004 | 0.000 | 0.001 | 0.003 | 14.988 |
| AN15_Fsp25 | 64.93 | 0.86 | 15.46 | 0.01 | 0.04 | 18.43 | 0.02 | 0.00 | 0.03 | 0.00 | 0.44 | 100.22 | 8.986 | 0.231 | 2.730 | 0.001 | 0.005 | 3.006 | 0.003 | 0.000 | 0.003 | 0.000 | 0.024 | 14.989 |
| AN15_Fsp26 | 62.56 | 8.54 | 0.27 | 5.06 | 0.10 | 23.64 | 0.00 | 0.14 | 0.01 | 0.01 | 0.00 | 100.34 | 8.296 | 2.196 | 0.046 | 0.718 | 0.012 | 3.695 | 0.001 | 0.011 | 0.001 | 0.001 | 0.000 | 14.977 |
| AN15_Fsp27 | 64.88 | 9.78 | 0.19 | 3.29 | 0.03 | 22.34 | 0.00 | 0.10 | 0.01 | 0.02 | 0.01 | 100.65 | 8.532 | 2.493 | 0.032 | 0.464 | 0.003 | 3.463 | 0.000 | 0.008 | 0.001 | 0.003 | 0.001 | 14.999 |
| AN15_Fsp28 | 61.48 | 8.29 | 0.41 | 5.51 | 0.05 | 24.13 | 0.00 | 0.05 | 0.01 | 0.00 | 0.04 | 99.98 | 8.200 | 2.145 | 0.069 | 0.788 | 0.005 | 3.794 | 0.000 | 0.004 | 0.001 | 0.000 | 0.002 | 15.008 |
| AN15_Fsp29 | 62.28 | 8.57 | 0.27 | 5.26 | 0.07 | 24.00 | 0.01 | 0.04 | 0.00 | 0.01 | 0.00 | 100.50 | 8.249 | 2.200 | 0.045 | 0.746 | 0.008 | 3.746 | 0.003 | 0.003 | 0.000 | 0.001 | 0.000 | 15.001 |
| SHS04_Fsp01 | 64.77 | 0.95 | 15.32 | 0.00 | 0.05 | 18.76 | 0.01 | 0.10 | 0.01 | 0.00 | 0.27 | 100.25 | 8.952 | 0.255 | 2.701 | 0.001 | 0.006 | 3.057 | 0.003 | 0.008 | 0.001 | 0.000 | 0.015 | 14.997 |
| SHS04_Fsp02 | 64.90 | 0.98 | 15.24 | 0.01 | 0.01 | 18.68 | 0.01 | 0.02 | 0.00 | 0.00 | 0.50 | 100.35 | 8.965 | 0.263 | 2.685 | 0.002 | 0.001 | 3.041 | 0.002 | 0.002 | 0.000 | 0.000 | 0.027 | 14.988 |
| SHS04_Fsp03 | 65.57 | 0.96 | 15.44 | 0.00 | 0.08 | 18.64 | 0.00 | 0.00 | 0.02 | 0.00 | 0.09 | 100.80 | 8.992 | 0.254 | 2.702 | 0.000 | 0.009 | 3.012 | 0.000 | 0.000 | 0.002 | 0.000 | 0.005 | 14.977 |
| SHS04_Fsp05 | 64.48 | 1.43 | 14.39 | 0.06 | 0.09 | 18.92 | 0.00 | 0.18 | 0.00 | 0.01 | 0.29 | 99.85 | 8.927 | 0.383 | 2.542 | 0.009 | 0.011 | 3.088 | 0.001 | 0.015 | 0.000 | 0.001 | 0.016 | 14.992 |
| SHS04_Fsp07 | 65.47 | 3.14 | 12.01 | 0.11 | 0.04 | 19.10 | 0.01 | 0.07 | 0.03 | 0.02 | 0.47 | 100.47 | 8.934 | 0.830 | 2.091 | 0.016 | 0.004 | 3.072 | 0.003 | 0.005 | 0.003 | 0.002 | 0.025 | 14.987 |
| SHS04_Fsp08 | 64.53 | 2.14 | 13.27 | 0.06 | 0.12 | 19.03 | 0.00 | 0.20 | 0.04 | 0.02 | 0.72 | 100.12 | 8.907 | 0.573 | 2.336 | 0.009 | 0.013 | 3.095 | 0.000 | 0.016 | 0.005 | 0.002 | 0.039 | 14.995 |
| SHS04_Fsp10 | 65.36 | 0.97 | 15.14 | 0.01 | 0.03 | 18.85 | 0.00 | 0.03 | 0.00 | 0.02 | 0.00 | 100.41 | 8.978 | 0.259 | 2.653 | 0.002 | 0.004 | 3.051 | 0.000 | 0.002 | 0.000 | 0.003 | 0.000 | 14.952 |
| SHS04_Fsp11 | 64.68 | 0.81 | 15.50 | 0.01 | 0.18 | 18.87 | 0.04 | 0.09 | 0.00 | 0.04 | 0.20 | 100.43 | 8.932 | 0.217 | 2.732 | 0.002 | 0.021 | 3.072 | 0.008 | 0.007 | 0.000 | 0.005 | 0.011 | 15.006 |
| SHS04_Fsp12 | 64.94 | 0.75 | 15.31 | 0.04 | 0.00 | 18.58 | 0.00 | 0.03 | 0.03 | 0.03 | 0.12 | 99.83 | 8.988 | 0.202 | 2.703 | 0.006 | 0.000 | 3.032 | 0.000 | 0.003 | 0.003 | 0.003 | 0.007 | 14.946 |
| SHS04_Fsp13 | 65.04 | 1.54 | 14.09 | 0.04 | 0.04 | 18.95 | 0.01 | 0.00 | 0.02 | 0.02 | 0.19 | 99.94 | 8.956 | 0.412 | 2.475 | 0.006 | 0.004 | 3.076 | 0.002 | 0.000 | 0.003 | 0.003 | 0.010 | 14.947 |
| SHS04_Fsp14 | 63.75 | 0.67 | 15.29 | 0.00 | 0.05 | 18.33 | 0.00 | 0.00 | 0.01 | 0.01 | 0.10 | 98.21 | 8.978 | 0.182 | 2.748 | 0.000 | 0.005 | 3.043 | 0.000 | 0.000 | 0.001 | 0.002 | 0.006 | 14.964 |
| SHS04_Fsp15 | 64.52 | 0.55 | 15.62 | 0.00 | 0.15 | 18.70 | 0.00 | 0.03 | 0.00 | 0.00 | 0.29 | 99.86 | 8.958 | 0.148 | 2.766 | 0.000 | 0.017 | 3.061 | 0.000 | 0.002 | 0.000 | 0.000 | 0.016 | 14.968 |
| SHS04_Fsp16 | 65.09 | 1.01 | 14.71 | 0.03 | 0.11 | 18.64 | 0.01 | 0.03 | 0.03 | 0.02 | 0.48 | 100.15 | 8.983 | 0.270 | 2.591 | 0.004 | 0.012 | 3.032 | 0.002 | 0.003 | 0.003 | 0.002 | 0.026 | 14.928 |
| SHS04_Fsp17 | 65.13 | 1.38 | 14.42 | 0.10 | 0.10 | 19.07 | 0.01 | 0.02 | 0.01 | 0.00 | 0.46 | 100.69 | 8.936 | 0.368 | 2.525 | 0.015 | 0.012 | 3.083 | 0.001 | 0.002 | 0.001 | 0.000 | 0.025 | 14.967 |
| SHS04_Fsp18 | 65.23 | 0.47 | 15.88 | 0.00 | 0.06 | 18.51 | 0.01 | 0.00 | 0.00 | 0.00 | 0.14 | 100.29 | 9.003 | 0.126 | 2.796 | 0.000 | 0.006 | 3.011 | 0.001 | 0.000 | 0.000 | 0.000 | 0.007 | 14.952 |
| SHS04_Fsp19 | 64.99 | 1.07 | 14.91 | 0.03 | 0.01 | 18.86 | 0.01 | 0.00 | 0.03 | 0.00 | 0.25 | 100.16 | 8.960 | 0.285 | 2.623 | 0.005 | 0.001 | 3.065 | 0.002 | 0.000 | 0.003 | 0.000 | 0.014 | 14.958 |
| SHS04_Fsp20 | 65.42 | 1.21 | 14.95 | 0.00 | 0.01 | 18.85 | 0.01 | 0.01 | 0.01 | 0.00 | 0.14 | 100.61 | 8.973 | 0.323 | 2.616 | 0.000 | 0.002 | 3.047 | 0.003 | 0.000 | 0.001 | 0.000 | 0.008 | 14.972 |
| SHS04_Fsp21 | 64.90 | 1.12 | 14.85 | 0.07 | 0.09 | 18.54 | 0.01 | 0.02 | 0.00 | 0.00 | 0.15 | 99.76 | 8.984 | 0.301 | 2.623 | 0.010 | 0.010 | 3.025 | 0.002 | 0.002 | 0.000 | 0.000 | 0.008 | 14.965 |

| Sample / No. | $SiO_2$ | $Na_2O$ | $K_2O$ | CaO | FeO | $Al_2O_3$ | MgO | SrO | $TiO_2$ | MnO | BaO | wt-total | Si_at | Na_at | K_at | Ca_at | Fe_at | Al_at | Mg_at | Sr_at | Ti_at | Mn_at | Ba_at | at-total |
|---|---|---|---|---|---|---|---|---|---|---|---|---|---|---|---|---|---|---|---|---|---|---|---|---|
| SHS04_Fsp22 | 65.19 | 1.03 | 14.99 | 0.01 | 0.09 | 18.69 | 0.02 | 0.04 | 0.00 | 0.00 | 0.21 | 100.28 | 8.981 | 0.275 | 2.634 | 0.001 | 0.011 | 3.035 | 0.004 | 0.003 | 0.000 | 0.000 | 0.011 | 14.957 |
| SHS04_Fsp33 | 65.26 | 9.74 | 0.36 | 2.96 | 0.17 | 21.73 | 0.00 | 0.00 | 0.04 | 0.02 | 0.00 | 100.27 | 8.606 | 2.489 | 0.060 | 0.418 | 0.019 | 3.378 | 0.000 | 0.000 | 0.004 | 0.002 | 0.000 | 14.976 |
| SHA05_Fsp01 | 59.27 | 7.14 | 0.49 | 7.43 | 0.03 | 25.99 | 0.01 | 0.06 | 0.00 | 0.01 | 0.02 | 100.47 | 7.911 | 1.849 | 0.084 | 1.063 | 0.004 | 4.090 | 0.002 | 0.005 | 0.000 | 0.001 | 0.001 | 15.010 |
| SHA05_Fsp02 | 57.67 | 6.36 | 0.32 | 8.72 | 0.12 | 26.67 | 0.00 | 0.12 | 0.01 | 0.02 | 0.02 | 100.04 | 7.757 | 1.659 | 0.055 | 1.257 | 0.014 | 4.228 | 0.001 | 0.010 | 0.001 | 0.002 | 0.001 | 14.985 |
| SHA05_Fsp06 | 66.90 | 0.09 | 15.45 | 0.02 | 0.11 | 17.54 | 0.02 | 0.04 | 0.01 | 0.01 | 0.00 | 100.19 | 9.177 | 0.024 | 2.704 | 0.002 | 0.013 | 2.837 | 0.004 | 0.003 | 0.001 | 0.002 | 0.000 | 14.767 |
| SHA05_Fsp08 | 67.20 | 2.47 | 12.17 | 0.18 | 0.12 | 17.78 | 0.01 | 0.00 | 0.03 | 0.00 | 0.09 | 100.05 | 9.144 | 0.651 | 2.112 | 0.026 | 0.014 | 2.852 | 0.003 | 0.000 | 0.003 | 0.000 | 0.005 | 14.809 |
| SHA05_Fsp09 | 64.33 | 9.36 | 0.36 | 3.59 | 0.09 | 22.50 | 0.00 | 0.01 | 0.00 | 0.01 | 0.02 | 100.26 | 8.498 | 2.397 | 0.061 | 0.508 | 0.010 | 3.503 | 0.000 | 0.001 | 0.000 | 0.001 | 0.001 | 14.980 |
| SHA05_Fsp10 | 56.75 | 6.24 | 0.13 | 9.08 | 0.13 | 27.47 | 0.01 | 0.06 | 0.04 | 0.00 | 0.01 | 99.91 | 7.645 | 1.629 | 0.022 | 1.311 | 0.014 | 4.362 | 0.003 | 0.005 | 0.004 | 0.000 | 0.001 | 14.995 |
| SHA05_Fsp12 | 58.81 | 6.94 | 0.39 | 7.78 | 0.04 | 26.14 | 0.00 | 0.09 | 0.02 | 0.00 | 0.00 | 100.21 | 7.873 | 1.802 | 0.067 | 1.116 | 0.004 | 4.125 | 0.000 | 0.007 | 0.002 | 0.001 | 0.000 | 14.997 |
| SHA05_Fsp13 | 56.76 | 6.20 | 0.07 | 9.52 | 0.02 | 27.71 | 0.01 | 0.06 | 0.01 | 0.01 | 0.00 | 100.36 | 7.616 | 1.614 | 0.011 | 1.368 | 0.002 | 4.383 | 0.001 | 0.004 | 0.001 | 0.001 | 0.000 | 15.003 |
| SHA05_Fsp14 | 62.21 | 7.88 | 0.83 | 5.34 | 0.19 | 23.79 | 0.01 | 0.05 | 0.03 | 0.00 | 0.09 | 100.41 | 8.265 | 2.030 | 0.140 | 0.760 | 0.022 | 3.725 | 0.001 | 0.004 | 0.003 | 0.000 | 0.005 | 14.955 |
| SHA05_Fsp15 | 60.45 | 7.74 | 0.34 | 6.37 | 0.12 | 24.68 | 0.01 | 0.22 | 0.00 | 0.00 | 0.06 | 99.99 | 8.089 | 2.009 | 0.058 | 0.913 | 0.014 | 3.893 | 0.001 | 0.017 | 0.000 | 0.000 | 0.003 | 14.998 |
| SHA05_Fsp16 | 60.97 | 7.89 | 0.91 | 5.65 | 0.33 | 23.70 | 0.02 | 0.14 | 0.02 | 0.00 | 0.15 | 99.78 | 8.193 | 2.057 | 0.156 | 0.813 | 0.037 | 3.753 | 0.004 | 0.011 | 0.002 | 0.000 | 0.008 | 15.034 |
| SHA05_Fsp17 | 66.01 | 3.56 | 11.20 | 0.13 | 0.08 | 18.65 | 0.00 | 0.03 | 0.02 | 0.00 | 0.13 | 99.81 | 9.007 | 0.942 | 1.951 | 0.018 | 0.010 | 2.999 | 0.000 | 0.002 | 0.002 | 0.000 | 0.007 | 14.938 |
| SHA05_Fsp18 | 59.18 | 7.24 | 0.16 | 7.55 | 0.01 | 25.66 | 0.00 | 0.07 | 0.00 | 0.00 | 0.04 | 99.92 | 7.934 | 1.882 | 0.027 | 1.084 | 0.001 | 4.056 | 0.001 | 0.006 | 0.000 | 0.000 | 0.002 | 14.993 |
| SHA05_Fsp19 | 58.81 | 6.93 | 0.33 | 7.71 | 0.03 | 25.74 | 0.00 | 0.06 | 0.04 | 0.00 | 0.00 | 99.66 | 7.909 | 1.808 | 0.057 | 1.112 | 0.004 | 4.080 | 0.001 | 0.005 | 0.004 | 0.000 | 0.000 | 14.979 |
| SHA05_Fsp20 | 65.14 | 0.98 | 15.21 | 0.00 | 0.04 | 18.56 | 0.01 | 0.03 | 0.00 | 0.00 | 0.21 | 100.19 | 8.990 | 0.262 | 2.679 | 0.000 | 0.005 | 3.019 | 0.003 | 0.002 | 0.000 | 0.000 | 0.011 | 14.971 |
| SHA05_Fsp21 | 58.54 | 6.69 | 0.40 | 8.04 | 0.07 | 26.52 | 0.00 | 0.18 | 0.01 | 0.00 | 0.00 | 100.45 | 7.827 | 1.735 | 0.068 | 1.151 | 0.008 | 4.179 | 0.001 | 0.014 | 0.001 | 0.000 | 0.000 | 14.984 |
| SHA05_Fsp22 | 64.40 | 1.30 | 14.55 | 0.01 | 0.01 | 18.61 | 0.00 | 0.00 | 0.01 | 0.00 | 0.06 | 98.96 | 8.970 | 0.352 | 2.586 | 0.002 | 0.001 | 3.056 | 0.000 | 0.000 | 0.001 | 0.000 | 0.003 | 14.970 |
| SHA05_Fsp23 | 62.17 | 7.99 | 0.90 | 4.95 | 0.14 | 23.29 | 0.00 | 0.06 | 0.00 | 0.00 | 0.07 | 99.58 | 8.320 | 2.075 | 0.154 | 0.710 | 0.016 | 3.674 | 0.000 | 0.005 | 0.000 | 0.000 | 0.004 | 14.957 |
| SHA05_Fsp24 | 65.21 | 1.32 | 14.76 | 0.00 | 0.00 | 18.70 | 0.00 | 0.11 | 0.03 | 0.00 | 0.23 | 100.35 | 8.975 | 0.352 | 2.593 | 0.000 | 0.000 | 3.034 | 0.000 | 0.009 | 0.003 | 0.000 | 0.012 | 14.977 |
| SHA05_Fsp25 | 64.74 | 0.89 | 15.48 | 0.02 | 0.00 | 18.47 | 0.00 | 0.00 | 0.00 | 0.02 | 0.07 | 99.69 | 8.984 | 0.239 | 2.741 | 0.004 | 0.000 | 3.022 | 0.000 | 0.000 | 0.000 | 0.002 | 0.004 | 14.995 |
| SHA05_Fsp26 | 61.17 | 7.77 | 0.54 | 6.18 | 0.12 | 24.57 | 0.00 | 0.07 | 0.01 | 0.01 | 0.01 | 100.45 | 8.135 | 2.004 | 0.092 | 0.881 | 0.013 | 3.852 | 0.000 | 0.005 | 0.001 | 0.002 | 0.000 | 14.986 |
| SHA05_Fsp27 | 61.51 | 8.23 | 0.29 | 5.76 | 0.02 | 24.54 | 0.00 | 0.12 | 0.00 | 0.00 | 0.00 | 100.47 | 8.163 | 2.119 | 0.050 | 0.819 | 0.002 | 3.839 | 0.000 | 0.009 | 0.000 | 0.000 | 0.000 | 15.001 |
| SHA05_Fsp28 | 65.11 | 1.04 | 15.05 | 0.05 | 0.04 | 18.58 | 0.00 | 0.02 | 0.00 | 0.00 | 0.18 | 100.07 | 8.989 | 0.279 | 2.650 | 0.007 | 0.005 | 3.023 | 0.001 | 0.002 | 0.000 | 0.000 | 0.010 | 14.965 |
| SHA05_Fsp51 | 64.22 | 0.03 | 15.28 | 0.00 | 0.01 | 18.43 | 0.00 | 0.00 | 0.00 | 0.00 | 0.36 | 98.32 | 9.016 | 0.008 | 2.737 | 0.000 | 0.001 | 3.050 | 0.000 | 0.000 | 0.000 | 0.000 | 0.020 | 14.832 |
| SHC25_Fsp01 | 63.21 | 9.18 | 0.29 | 4.04 | 0.05 | 22.97 | 0.00 | 0.08 | 0.00 | 0.00 | 0.00 | 99.82 | 8.403 | 2.367 | 0.050 | 0.576 | 0.005 | 3.599 | 0.000 | 0.006 | 0.000 | 0.000 | 0.000 | 15.006 |
| SHC25_Fsp03 | 61.40 | 8.26 | 0.23 | 5.84 | 0.02 | 24.51 | 0.00 | 0.03 | 0.03 | 0.01 | 0.01 | 100.35 | 8.158 | 2.127 | 0.040 | 0.831 | 0.002 | 3.838 | 0.000 | 0.002 | 0.003 | 0.001 | 0.001 | 15.004 |
| SHC25_Fsp04 | 60.24 | 7.81 | 0.15 | 6.71 | 0.05 | 25.10 | 0.00 | 0.11 | 0.00 | 0.00 | 0.02 | 100.20 | 8.038 | 2.021 | 0.026 | 0.960 | 0.006 | 3.949 | 0.001 | 0.009 | 0.000 | 0.000 | 0.001 | 15.011 |
| SHC25_Fsp06 | 65.26 | 0.52 | 16.28 | 0.00 | 0.08 | 18.56 | 0.00 | 0.00 | 0.00 | 0.00 | 0.03 | 100.73 | 8.986 | 0.139 | 2.860 | 0.000 | 0.009 | 3.012 | 0.000 | 0.000 | 0.000 | 0.000 | 0.002 | 15.008 |
| SHC25_Fsp08 | 64.61 | 9.81 | 0.23 | 3.08 | 0.01 | 22.03 | 0.00 | 0.00 | 0.02 | 0.01 | 0.00 | 99.81 | 8.558 | 2.519 | 0.040 | 0.437 | 0.001 | 3.440 | 0.000 | 0.000 | 0.002 | 0.001 | 0.000 | 14.999 |
| SHC25_Fsp10 | 59.84 | 7.29 | 0.43 | 7.16 | 0.05 | 25.23 | 0.00 | 0.06 | 0.00 | 0.02 | 0.02 | 100.11 | 8.005 | 1.891 | 0.074 | 1.026 | 0.006 | 3.978 | 0.001 | 0.005 | 0.000 | 0.002 | 0.001 | 14.988 |
| SHC25_Fsp11 | 65.53 | 9.88 | 0.33 | 2.63 | 0.03 | 21.61 | 0.00 | 0.05 | 0.00 | 0.00 | 0.00 | 100.06 | 8.644 | 2.527 | 0.055 | 0.372 | 0.003 | 3.361 | 0.000 | 0.004 | 0.000 | 0.000 | 0.000 | 14.967 |
| SHC25_Fsp12 | 60.74 | 7.96 | 0.34 | 6.32 | 0.09 | 24.49 | 0.00 | 0.01 | 0.03 | 0.00 | 0.00 | 99.96 | 8.117 | 2.062 | 0.059 | 0.904 | 0.010 | 3.857 | 0.000 | 0.001 | 0.003 | 0.000 | 0.000 | 15.012 |
| SHC25_Fsp14 | 65.22 | 0.73 | 15.77 | 0.00 | 0.00 | 18.85 | 0.00 | 0.04 | 0.00 | 0.01 | 0.12 | 100.74 | 8.964 | 0.196 | 2.765 | 0.000 | 0.000 | 3.054 | 0.000 | 0.003 | 0.000 | 0.001 | 0.007 | 14.989 |
| SHC25_Fsp18 | 65.20 | 0.62 | 15.93 | 0.00 | 0.04 | 18.56 | 0.00 | 0.00 | 0.00 | 0.01 | 0.21 | 100.56 | 8.988 | 0.167 | 2.802 | 0.000 | 0.004 | 3.015 | 0.000 | 0.000 | 0.000 | 0.001 | 0.012 | 14.988 |
| SHC25_Fsp26 | 64.84 | 0.57 | 16.00 | 0.00 | 0.03 | 18.86 | 0.00 | 0.05 | 0.03 | 0.00 | 0.75 | 101.13 | 8.935 | 0.153 | 2.812 | 0.000 | 0.004 | 3.063 | 0.000 | 0.004 | 0.003 | 0.000 | 0.041 | 15.014 |
| SHC25_Fsp30 | 65.03 | 0.52 | 15.93 | 0.00 | 0.05 | 18.78 | 0.00 | 0.01 | 0.00 | 0.01 | 0.38 | 100.72 | 8.962 | 0.140 | 2.802 | 0.000 | 0.005 | 3.051 | 0.001 | 0.001 | 0.000 | 0.001 | 0.021 | 14.983 |
| SHC25_Fsp31 | 63.11 | 9.32 | 0.12 | 4.20 | 0.14 | 23.07 | 0.00 | 0.05 | 0.03 | 0.00 | 0.02 | 100.06 | 8.376 | 2.398 | 0.021 | 0.597 | 0.016 | 3.610 | 0.001 | 0.004 | 0.003 | 0.000 | 0.001 | 15.026 |
| SHC25_Fsp32 | 63.63 | 9.44 | 0.21 | 4.13 | 0.08 | 22.88 | 0.01 | 0.02 | 0.04 | 0.02 | 0.04 | 100.49 | 8.409 | 2.420 | 0.036 | 0.585 | 0.009 | 3.564 | 0.001 | 0.001 | 0.004 | 0.002 | 0.002 | 15.033 |
| SP08_Fsp01 | 65.63 | 2.03 | 13.50 | 0.00 | 0.05 | 18.71 | 0.01 | 0.03 | 0.00 | 0.00 | 0.17 | 100.12 | 8.998 | 0.539 | 2.361 | 0.000 | 0.005 | 3.023 | 0.002 | 0.002 | 0.000 | 0.000 | 0.009 | 14.940 |
| SP08_Fsp02 | 60.67 | 7.77 | 0.54 | 6.06 | 0.11 | 24.64 | 0.00 | 0.08 | 0.00 | 0.03 | 0.00 | 99.90 | 8.115 | 2.015 | 0.093 | 0.868 | 0.012 | 3.884 | 0.000 | 0.006 | 0.000 | 0.003 | 0.000 | 14.997 |
| SP08_Fsp04 | 63.99 | 1.37 | 14.07 | 0.00 | 0.01 | 18.99 | 0.00 | 0.09 | 0.02 | 0.01 | 0.93 | 99.50 | 8.911 | 0.371 | 2.500 | 0.000 | 0.001 | 3.118 | 0.000 | 0.007 | 0.003 | 0.001 | 0.051 | 14.963 |
| SP08_Fsp05 | 59.16 | 7.02 | 0.82 | 6.95 | 0.36 | 25.16 | 0.01 | 0.17 | 0.05 | 0.02 | 0.11 | 99.83 | 7.970 | 1.833 | 0.141 | 1.003 | 0.041 | 3.996 | 0.003 | 0.013 | 0.005 | 0.002 | 0.006 | 15.014 |
| SP08_Fsp07 | 64.91 | 1.70 | 13.77 | 0.03 | 0.03 | 18.73 | 0.00 | 0.01 | 0.00 | 0.00 | 0.22 | 99.41 | 8.977 | 0.457 | 2.431 | 0.004 | 0.004 | 3.053 | 0.000 | 0.001 | 0.000 | 0.000 | 0.012 | 14.939 |
| SP08_Fsp08 | 57.36 | 6.53 | 0.28 | 8.63 | 0.04 | 26.80 | 0.01 | 0.01 | 0.02 | 0.01 | 0.00 | 99.68 | 7.737 | 1.709 | 0.048 | 1.247 | 0.005 | 4.260 | 0.001 | 0.001 | 0.002 | 0.001 | 0.000 | 15.010 |
| SP08_Fsp09 | 59.90 | 7.68 | 0.34 | 6.79 | 0.02 | 24.93 | 0.00 | 0.10 | 0.00 | 0.00 | 0.00 | 99.77 | 8.036 | 1.997 | 0.058 | 0.977 | 0.002 | 3.942 | 0.001 | 0.008 | 0.000 | 0.000 | 0.000 | 15.021 |
| SP08_Fsp10 | 59.39 | 7.31 | 0.20 | 7.10 | 0.08 | 25.44 | 0.00 | 0.02 | 0.00 | 0.00 | 0.00 | 99.55 | 7.977 | 1.903 | 0.035 | 1.022 | 0.009 | 4.028 | 0.000 | 0.002 | 0.000 | 0.000 | 0.000 | 14.978 |
| SP08_Fsp11 | 61.10 | 7.54 | 0.98 | 5.72 | 0.23 | 23.74 | 0.01 | 0.11 | 0.01 | 0.00 | 0.06 | 99.50 | 8.213 | 1.964 | 0.168 | 0.824 | 0.026 | 3.761 | 0.003 | 0.008 | 0.001 | 0.000 | 0.003 | 14.972 |
| SP08_Fsp14 | 59.64 | 7.15 | 0.72 | 6.88 | 0.26 | 24.98 | 0.01 | 0.11 | 0.00 | 0.00 | 0.01 | 99.76 | 8.018 | 1.865 | 0.123 | 0.990 | 0.030 | 3.959 | 0.002 | 0.008 | 0.000 | 0.000 | 0.001 | 14.996 |
| SP08_Fsp15 | 64.20 | 1.61 | 13.66 | 0.14 | 0.02 | 19.17 | 0.01 | 0.09 | 0.04 | 0.02 | 0.64 | 99.61 | 8.899 | 0.433 | 2.416 | 0.020 | 0.003 | 3.133 | 0.001 | 0.007 | 0.004 | 0.003 | 0.035 | 14.955 |
| SP08_Fsp17 | 64.96 | 0.68 | 15.54 | 0.00 | 0.03 | 18.70 | 0.00 | 0.01 | 0.02 | 0.03 | 0.07 | 100.05 | 8.977 | 0.182 | 2.739 | 0.000 | 0.003 | 3.046 | 0.000 | 0.001 | 0.002 | 0.004 | 0.004 | 14.959 |
| SP08_Fsp18 | 58.01 | 6.75 | 0.29 | 8.32 | 0.07 | 26.34 | 0.00 | 0.05 | 0.00 | 0.00 | 0.00 | 99.83 | 7.807 | 1.763 | 0.049 | 1.200 | 0.007 | 4.179 | 0.000 | 0.004 | 0.000 | 0.000 | 0.000 | 15.009 |

# Analyses of feldspar from sandstones (continuation)

| Sample / No. | $SiO_2$ | $Na_2O$ | $K_2O$ | CaO | FeO | $Al_2O_3$ | MgO | SrO | $TiO_2$ | MnO | BaO | wt-total | Si_at | Na_at | K_at | Ca_at | Fe_at | Al_at | Mg_at | Sr_at | Ti_at | Mn_at | Ba_at | at-total |
|---|---|---|---|---|---|---|---|---|---|---|---|---|---|---|---|---|---|---|---|---|---|---|---|---|
| SP08_Fsp19 | 64.27 | 9.04 | 1.12 | 3.00 | 0.17 | 21.78 | 0.00 | 0.00 | 0.01 | 0.01 | 0.00 | 99.40 | 8.574 | 2.338 | 0.190 | 0.428 | 0.019 | 3.424 | 0.000 | 0.000 | 0.001 | 0.001 | 0.000 | 14.977 |
| SP08_Fsp20 | 62.13 | 8.63 | 0.31 | 5.06 | 0.10 | 23.69 | 0.00 | 0.02 | 0.01 | 0.00 | 0.01 | 99.96 | 8.273 | 2.229 | 0.053 | 0.722 | 0.011 | 3.718 | 0.000 | 0.002 | 0.001 | 0.000 | 0.000 | 15.009 |
| SP08_Fsp23 | 62.10 | 8.59 | 0.32 | 5.24 | 0.08 | 23.66 | 0.00 | 0.12 | 0.00 | 0.02 | 0.05 | 100.18 | 8.264 | 2.217 | 0.054 | 0.747 | 0.009 | 3.711 | 0.000 | 0.009 | 0.000 | 0.002 | 0.003 | 15.016 |
| SP08_Fsp25 | 65.17 | 1.62 | 13.95 | 0.00 | 0.04 | 18.71 | 0.00 | 0.10 | 0.00 | 0.00 | 0.26 | 99.85 | 8.984 | 0.434 | 2.453 | 0.000 | 0.005 | 3.040 | 0.000 | 0.008 | 0.000 | 0.000 | 0.014 | 14.939 |
| SP08_Fsp26 | 59.12 | 7.59 | 0.20 | 7.18 | 0.05 | 25.32 | 0.00 | 0.04 | 0.01 | 0.01 | 0.03 | 99.55 | 7.958 | 1.982 | 0.034 | 1.036 | 0.005 | 4.017 | 0.001 | 0.003 | 0.001 | 0.001 | 0.001 | 15.040 |
| SP08_Fsp27 | 65.04 | 0.91 | 14.76 | 0.00 | 0.02 | 18.66 | 0.00 | 0.01 | 0.01 | 0.00 | 0.32 | 99.74 | 8.995 | 0.245 | 2.603 | 0.000 | 0.002 | 3.042 | 0.000 | 0.001 | 0.001 | 0.000 | 0.017 | 14.907 |
| SPP31_Fsp02 | 64.19 | 1.06 | 15.52 | 0.00 | 0.01 | 19.02 | 0.01 | 0.00 | 0.01 | 0.00 | 0.00 | 99.82 | 8.906 | 0.284 | 2.748 | 0.000 | 0.002 | 3.111 | 0.001 | 0.000 | 0.001 | 0.000 | 0.000 | 15.053 |
| SPP31_Fsp03 | 64.87 | 0.75 | 15.91 | 0.00 | 0.02 | 18.48 | 0.01 | 0.03 | 0.00 | 0.01 | 0.15 | 100.23 | 8.978 | 0.200 | 2.808 | 0.000 | 0.002 | 3.015 | 0.002 | 0.002 | 0.000 | 0.001 | 0.008 | 15.018 |
| SPP31_Fsp04 | 60.34 | 7.63 | 0.45 | 6.49 | 0.30 | 24.87 | 0.01 | 0.28 | 0.02 | 0.01 | 0.07 | 100.48 | 8.055 | 1.976 | 0.077 | 0.928 | 0.033 | 3.913 | 0.003 | 0.022 | 0.002 | 0.001 | 0.004 | 15.013 |
| SPP31_Fsp05 | 64.74 | 0.98 | 15.32 | 0.06 | 0.00 | 18.74 | 0.01 | 0.08 | 0.03 | 0.00 | 0.51 | 100.47 | 8.945 | 0.263 | 2.701 | 0.008 | 0.001 | 3.052 | 0.002 | 0.007 | 0.003 | 0.000 | 0.028 | 15.009 |
| SPP31_Fsp06 | 59.45 | 7.04 | 0.51 | 7.31 | 0.11 | 25.56 | 0.00 | 0.04 | 0.02 | 0.00 | 0.04 | 100.08 | 7.960 | 1.828 | 0.087 | 1.049 | 0.013 | 4.034 | 0.001 | 0.003 | 0.002 | 0.000 | 0.002 | 14.979 |
| SPP31_Fsp07 | 58.53 | 6.52 | 0.63 | 7.75 | 0.37 | 25.66 | 0.03 | 0.15 | 0.03 | 0.02 | 0.07 | 99.76 | 7.892 | 1.705 | 0.109 | 1.120 | 0.042 | 4.079 | 0.005 | 0.012 | 0.003 | 0.002 | 0.004 | 14.972 |
| SPP31_Fsp08 | 66.32 | 8.78 | 3.30 | 1.22 | 0.19 | 20.11 | 0.00 | 0.00 | 0.02 | 0.01 | 0.45 | 100.40 | 8.818 | 2.264 | 0.559 | 0.173 | 0.021 | 3.153 | 0.000 | 0.000 | 0.002 | 0.001 | 0.023 | 15.015 |
| SPP31_Fsp10 | 65.31 | 0.98 | 15.43 | 0.02 | 0.04 | 18.45 | 0.01 | 0.00 | 0.01 | 0.01 | 0.27 | 100.53 | 8.996 | 0.262 | 2.711 | 0.003 | 0.004 | 2.996 | 0.002 | 0.000 | 0.002 | 0.001 | 0.015 | 14.991 |
| SPP31_Fsp11 | 61.45 | 7.88 | 0.83 | 5.55 | 0.26 | 24.02 | 0.01 | 0.10 | 0.01 | 0.00 | 0.12 | 100.23 | 8.201 | 2.040 | 0.141 | 0.794 | 0.030 | 3.778 | 0.002 | 0.008 | 0.001 | 0.000 | 0.006 | 15.000 |
| SPP31_Fsp13 | 65.98 | 6.25 | 7.25 | 0.59 | 0.23 | 19.45 | 0.04 | 0.03 | 0.03 | 0.00 | 0.03 | 99.88 | 8.897 | 1.633 | 1.247 | 0.086 | 0.026 | 3.092 | 0.007 | 0.003 | 0.003 | 0.001 | 0.002 | 14.994 |
| SPP31_Fsp14 | 64.96 | 0.82 | 15.72 | 0.00 | 0.09 | 18.37 | 0.00 | 0.04 | 0.00 | 0.03 | 0.00 | 100.01 | 8.994 | 0.219 | 2.776 | 0.000 | 0.011 | 2.998 | 0.000 | 0.003 | 0.000 | 0.003 | 0.000 | 15.005 |
| SPP31_Fsp18 | 60.25 | 7.63 | 0.24 | 7.04 | 0.00 | 25.29 | 0.00 | 0.09 | 0.00 | 0.01 | 0.04 | 100.59 | 8.016 | 1.969 | 0.041 | 1.003 | 0.000 | 3.966 | 0.001 | 0.007 | 0.000 | 0.001 | 0.002 | 15.006 |
| SPP31_Fsp19 | 67.89 | 11.36 | 0.33 | 0.40 | 0.10 | 20.04 | 0.03 | 0.08 | 0.02 | 0.01 | 0.00 | 100.26 | 8.900 | 2.888 | 0.055 | 0.056 | 0.011 | 3.096 | 0.006 | 0.006 | 0.002 | 0.001 | 0.000 | 15.021 |
| SPP31_Fsp20 | 59.26 | 7.08 | 0.58 | 7.17 | 0.25 | 25.23 | 0.02 | 0.15 | 0.04 | 0.02 | 0.00 | 99.79 | 7.970 | 1.847 | 0.100 | 1.033 | 0.028 | 4.000 | 0.004 | 0.012 | 0.004 | 0.002 | 0.000 | 14.999 |
| SPP31_Fsp21 | 64.76 | 0.87 | 15.35 | 0.00 | 0.01 | 18.71 | 0.00 | 0.00 | 0.03 | 0.00 | 0.50 | 100.21 | 8.960 | 0.233 | 2.709 | 0.000 | 0.001 | 3.051 | 0.000 | 0.000 | 0.003 | 0.000 | 0.027 | 14.983 |
| SPP31_Fsp22 | 58.24 | 6.70 | 0.48 | 8.16 | 0.04 | 26.18 | 0.00 | 0.09 | 0.02 | 0.00 | 0.06 | 99.97 | 7.832 | 1.747 | 0.083 | 1.176 | 0.004 | 4.151 | 0.000 | 0.007 | 0.002 | 0.000 | 0.003 | 15.005 |
| SPP31_Fsp26 | 63.62 | 8.64 | 1.28 | 3.71 | 0.27 | 22.51 | 0.01 | 0.09 | 0.04 | 0.02 | 0.17 | 100.35 | 8.453 | 2.226 | 0.218 | 0.528 | 0.030 | 3.525 | 0.001 | 0.007 | 0.004 | 0.002 | 0.009 | 15.002 |
| SPP31_Fsp27 | 64.66 | 0.65 | 16.05 | 0.00 | 0.02 | 18.73 | 0.00 | 0.02 | 0.00 | 0.00 | 0.09 | 100.23 | 8.951 | 0.175 | 2.834 | 0.000 | 0.003 | 3.056 | 0.000 | 0.001 | 0.000 | 0.000 | 0.005 | 15.025 |
| SPP31_Fsp28 | 63.58 | 0.98 | 15.46 | 0.00 | 0.03 | 18.93 | 0.00 | 0.00 | 0.01 | 0.00 | 0.59 | 99.59 | 8.887 | 0.265 | 2.757 | 0.000 | 0.004 | 3.118 | 0.000 | 0.000 | 0.001 | 0.000 | 0.032 | 15.064 |
| RB06_001-Fsp | 61.32 | 7.98 | 0.28 | 5.72 | 0.07 | 24.59 | 0.01 | 0.01 | 0.02 | 0.04 | 0.04 | 100.12 | 8.159 | 2.060 | 0.048 | 0.816 | 0.008 | 3.857 | 0.003 | 0.001 | 0.002 | 0.004 | 0.002 | 14.963 |
| RB06_002-Fsp | 59.50 | 7.69 | 0.29 | 6.85 | 0.06 | 25.51 | 0.00 | 0.11 | 0.01 | 0.00 | 0.00 | 100.04 | 7.967 | 1.997 | 0.050 | 0.983 | 0.007 | 4.026 | 0.000 | 0.008 | 0.001 | 0.001 | 0.000 | 15.041 |
| RB06_003-Fsp | 62.76 | 8.58 | 0.48 | 4.68 | 0.13 | 23.40 | 0.00 | 0.02 | 0.00 | 0.02 | 0.03 | 100.12 | 8.336 | 2.211 | 0.081 | 0.665 | 0.015 | 3.664 | 0.000 | 0.002 | 0.000 | 0.002 | 0.002 | 14.978 |
| RB06_004-Fsp | 59.61 | 7.54 | 0.49 | 6.90 | 0.07 | 25.41 | 0.00 | 0.04 | 0.00 | 0.01 | 0.03 | 100.11 | 7.980 | 1.957 | 0.084 | 0.990 | 0.008 | 4.010 | 0.001 | 0.003 | 0.000 | 0.001 | 0.001 | 15.035 |
| RB06_005-Fsp | 55.00 | 5.23 | 0.29 | 10.57 | 0.05 | 28.21 | 0.01 | 0.11 | 0.04 | 0.02 | 0.00 | 99.56 | 7.471 | 1.378 | 0.051 | 1.538 | 0.005 | 4.517 | 0.001 | 0.009 | 0.004 | 0.002 | 0.000 | 14.979 |
| RB06_005-Fsp | 59.83 | 7.32 | 0.42 | 7.03 | 0.12 | 25.06 | 0.00 | 0.00 | 0.00 | 0.00 | 0.02 | 99.81 | 8.023 | 1.904 | 0.072 | 1.010 | 0.014 | 3.961 | 0.000 | 0.000 | 0.000 | 0.000 | 0.001 | 14.985 |
| RB06_006-Fsp | 56.82 | 6.29 | 0.22 | 9.13 | 0.05 | 27.18 | 0.02 | 0.17 | 0.00 | 0.00 | 0.00 | 99.90 | 7.665 | 1.645 | 0.038 | 1.320 | 0.005 | 4.322 | 0.004 | 0.013 | 0.000 | 0.000 | 0.000 | 15.015 |
| RB06_007-Fsp | 60.45 | 7.91 | 0.39 | 6.09 | 0.07 | 24.68 | 0.00 | 0.06 | 0.00 | 0.00 | 0.05 | 99.69 | 8.101 | 2.054 | 0.066 | 0.875 | 0.008 | 3.899 | 0.000 | 0.005 | 0.000 | 0.000 | 0.003 | 15.010 |
| RB06_008-Fsp | 60.38 | 7.70 | 0.30 | 6.59 | 0.08 | 24.83 | 0.01 | 0.07 | 0.00 | 0.01 | 0.00 | 99.98 | 8.072 | 1.995 | 0.050 | 0.944 | 0.009 | 3.913 | 0.001 | 0.006 | 0.000 | 0.001 | 0.000 | 14.993 |
| RB06_009-Fsp | 65.11 | 0.62 | 15.81 | 0.00 | 0.00 | 18.44 | 0.00 | 0.11 | 0.00 | 0.02 | 0.43 | 100.54 | 8.993 | 0.166 | 2.786 | 0.000 | 0.000 | 3.002 | 0.000 | 0.009 | 0.000 | 0.002 | 0.023 | 14.982 |
| RB06_011-Fsp | 58.56 | 6.73 | 0.39 | 7.94 | 0.20 | 25.97 | 0.02 | 0.15 | 0.00 | 0.03 | 0.07 | 100.05 | 7.867 | 1.752 | 0.067 | 1.143 | 0.022 | 4.112 | 0.004 | 0.011 | 0.000 | 0.004 | 0.004 | 14.986 |
| RB06_012-Fsp | 59.86 | 7.28 | 0.48 | 6.77 | 0.18 | 25.05 | 0.00 | 0.05 | 0.01 | 0.03 | 0.03 | 99.73 | 8.033 | 1.893 | 0.082 | 0.973 | 0.020 | 3.963 | 0.000 | 0.004 | 0.001 | 0.004 | 0.001 | 14.973 |
| RB06_013-Fsp | 65.42 | 1.30 | 15.07 | 0.05 | 0.05 | 18.49 | 0.02 | 0.01 | 0.05 | 0.00 | 0.18 | 100.64 | 8.988 | 0.346 | 2.641 | 0.008 | 0.005 | 2.994 | 0.004 | 0.001 | 0.005 | 0.000 | 0.009 | 15.003 |
| RB06_014-Fsp | 60.11 | 7.46 | 0.42 | 6.88 | 0.11 | 24.94 | 0.01 | 0.09 | 0.02 | 0.03 | 0.02 | 100.09 | 8.041 | 1.935 | 0.072 | 0.987 | 0.012 | 3.932 | 0.003 | 0.007 | 0.002 | 0.004 | 0.001 | 14.995 |
| RB06_015-Fsp | 60.63 | 7.67 | 0.56 | 6.19 | 0.00 | 24.45 | 0.00 | 0.01 | 0.01 | 0.01 | 0.00 | 99.55 | 8.131 | 1.993 | 0.096 | 0.890 | 0.000 | 3.865 | 0.000 | 0.001 | 0.001 | 0.001 | 0.000 | 14.980 |
| RB06_032-Fsp | 64.64 | 1.59 | 14.54 | 0.08 | 0.07 | 18.83 | 0.00 | 0.08 | 0.00 | 0.00 | 0.24 | 100.08 | 8.932 | 0.426 | 2.564 | 0.012 | 0.008 | 3.067 | 0.000 | 0.007 | 0.000 | 0.000 | 0.013 | 15.029 |
| RB06_033-Fsp | 62.71 | 6.73 | 3.09 | 4.19 | 0.01 | 22.30 | 0.01 | 0.06 | 0.00 | 0.02 | 0.05 | 99.18 | 8.458 | 1.760 | 0.532 | 0.606 | 0.001 | 3.545 | 0.001 | 0.005 | 0.000 | 0.003 | 0.002 | 14.914 |
| RB06_034-Fsp | 64.97 | 1.48 | 14.48 | 0.05 | 0.05 | 18.80 | 0.01 | 0.13 | 0.03 | 0.02 | 0.22 | 100.25 | 8.952 | 0.396 | 2.546 | 0.007 | 0.005 | 3.053 | 0.003 | 0.011 | 0.003 | 0.002 | 0.012 | 14.990 |
| RB06_035-Fsp | 64.29 | 0.98 | 15.03 | 0.20 | 0.01 | 19.00 | 0.01 | 0.14 | 0.03 | 0.00 | 0.75 | 100.45 | 8.900 | 0.264 | 2.655 | 0.029 | 0.001 | 3.101 | 0.002 | 0.011 | 0.003 | 0.000 | 0.041 | 15.006 |
| RB06_036-Fsp | 64.90 | 1.61 | 14.14 | 0.06 | 0.00 | 18.92 | 0.02 | 0.09 | 0.04 | 0.00 | 0.90 | 100.70 | 8.930 | 0.430 | 2.483 | 0.009 | 0.000 | 3.069 | 0.005 | 0.008 | 0.004 | 0.000 | 0.048 | 14.988 |
| RB06_037-Fsp | 60.89 | 8.01 | 0.08 | 6.25 | 0.05 | 25.00 | 0.03 | 0.15 | 0.00 | 0.02 | 0.07 | 100.54 | 8.087 | 2.064 | 0.014 | 0.889 | 0.005 | 3.913 | 0.005 | 0.011 | 0.000 | 0.002 | 0.004 | 14.995 |
| RB06_038-Fsp | 64.46 | 0.60 | 15.97 | 0.00 | 0.05 | 18.02 | 0.01 | 0.00 | 0.03 | 0.03 | 0.26 | 99.46 | 9.005 | 0.163 | 2.845 | 0.000 | 0.006 | 2.967 | 0.003 | 0.000 | 0.004 | 0.004 | 0.014 | 15.012 |
| RB06_040-Fsp | 64.97 | 1.01 | 15.14 | 0.04 | 0.04 | 18.61 | 0.00 | 0.05 | 0.01 | 0.03 | 0.37 | 100.28 | 8.973 | 0.272 | 2.667 | 0.006 | 0.005 | 3.029 | 0.000 | 0.004 | 0.001 | 0.004 | 0.020 | 14.981 |
| RB06_041-Fsp | 64.84 | 1.67 | 14.45 | 0.01 | 0.04 | 18.45 | 0.00 | 0.10 | 0.02 | 0.00 | 0.28 | 99.86 | 8.975 | 0.449 | 2.552 | 0.002 | 0.004 | 3.011 | 0.001 | 0.008 | 0.002 | 0.000 | 0.015 | 15.018 |
| TI14_070-Fsp | 62.68 | 8.40 | 0.88 | 4.51 | 0.18 | 22.44 | 0.02 | 0.07 | 0.03 | 0.02 | 0.02 | 99.23 | 8.411 | 2.186 | 0.151 | 0.648 | 0.020 | 3.549 | 0.004 | 0.005 | 0.003 | 0.002 | 0.001 | 14.980 |
| TI14_071-Fsp | 56.64 | 6.14 | 0.26 | 9.19 | 0.41 | 27.06 | 0.03 | 0.17 | 0.05 | 0.04 | 0.00 | 100.01 | 7.649 | 1.609 | 0.044 | 1.330 | 0.047 | 4.308 | 0.007 | 0.014 | 0.006 | 0.005 | 0.000 | 15.018 |
| TI14_072-Fsp | 61.97 | 8.19 | 0.84 | 4.91 | 0.36 | 23.23 | 0.01 | 0.17 | 0.05 | 0.03 | 0.11 | 99.88 | 8.294 | 2.127 | 0.143 | 0.704 | 0.040 | 3.664 | 0.003 | 0.013 | 0.005 | 0.004 | 0.006 | 15.003 |

| Sample / No. | $SiO_2$ | $Na_2O$ | $K_2O$ | CaO | FeO | $Al_2O_3$ | MgO | SrO | $TiO_2$ | MnO | BaO | wt-total | Si_at | Na_at | K_at | Ca_at | Fe_at | Al_at | Mg_at | Sr_at | Ti_at | Mn_at | Ba_at | at-total |
|---|---|---|---|---|---|---|---|---|---|---|---|---|---|---|---|---|---|---|---|---|---|---|---|---|
| TI14_073-Fsp | 66.37 | 9.68 | 1.46 | 1.58 | 0.08 | 20.61 | 0.00 | 0.00 | 0.02 | 0.00 | 0.01 | 99.82 | 8.786 | 2.485 | 0.246 | 0.225 | 0.009 | 3.216 | 0.000 | 0.000 | 0.002 | 0.000 | 0.001 | 14.970 |
| TI14_074-Fsp | 58.68 | 6.73 | 0.41 | 7.59 | 0.35 | 25.45 | 0.02 | 0.15 | 0.06 | 0.00 | 0.10 | 99.55 | 7.919 | 1.760 | 0.070 | 1.098 | 0.040 | 4.049 | 0.004 | 0.011 | 0.006 | 0.000 | 0.005 | 14.965 |
| TI14_075-Fsp | 56.60 | 6.08 | 0.50 | 9.28 | 0.20 | 26.91 | 0.00 | 0.12 | 0.04 | 0.04 | 0.01 | 99.78 | 7.662 | 1.595 | 0.086 | 1.347 | 0.022 | 4.294 | 0.000 | 0.009 | 0.004 | 0.004 | 0.000 | 15.027 |
| TI14_076-Fsp | 59.00 | 6.44 | 0.86 | 7.58 | 0.36 | 25.24 | 0.01 | 0.19 | 0.05 | 0.00 | 0.03 | 99.77 | 7.952 | 1.683 | 0.148 | 1.095 | 0.040 | 4.010 | 0.003 | 0.015 | 0.006 | 0.000 | 0.001 | 14.953 |
| TI14_077-Fsp | 61.76 | 7.99 | 0.79 | 5.24 | 0.14 | 23.69 | 0.00 | 0.11 | 0.00 | 0.00 | 0.00 | 99.72 | 8.259 | 2.072 | 0.134 | 0.751 | 0.016 | 3.734 | 0.000 | 0.008 | 0.001 | 0.000 | 0.000 | 14.976 |
| TI14_078-Fsp | 62.08 | 7.81 | 1.01 | 5.10 | 0.25 | 23.47 | 0.02 | 0.11 | 0.00 | 0.00 | 0.06 | 99.91 | 8.293 | 2.022 | 0.171 | 0.730 | 0.028 | 3.695 | 0.004 | 0.008 | 0.000 | 0.000 | 0.003 | 14.956 |
| TI14_079-Fsp | 63.69 | 8.80 | 1.23 | 3.64 | 0.23 | 22.44 | 0.01 | 0.12 | 0.03 | 0.06 | 0.19 | 100.47 | 8.457 | 2.265 | 0.209 | 0.518 | 0.025 | 3.512 | 0.002 | 0.009 | 0.003 | 0.007 | 0.010 | 15.019 |
| TI14_080-Fsp | 60.03 | 7.16 | 0.79 | 6.60 | 0.37 | 24.68 | 0.01 | 0.13 | 0.03 | 0.02 | 0.05 | 99.87 | 8.063 | 1.865 | 0.136 | 0.950 | 0.042 | 3.907 | 0.002 | 0.010 | 0.003 | 0.003 | 0.003 | 14.981 |
| TI14_081-Fsp | 64.15 | 8.81 | 1.42 | 3.31 | 0.22 | 21.86 | 0.00 | 0.10 | 0.03 | 0.01 | 0.19 | 100.10 | 8.539 | 2.274 | 0.242 | 0.471 | 0.025 | 3.430 | 0.000 | 0.008 | 0.003 | 0.001 | 0.010 | 15.002 |
| TI14_082-Fsp | 63.62 | 8.59 | 1.25 | 3.46 | 0.20 | 22.20 | 0.00 | 0.11 | 0.01 | 0.00 | 0.14 | 99.58 | 8.500 | 2.225 | 0.212 | 0.496 | 0.022 | 3.497 | 0.000 | 0.009 | 0.002 | 0.000 | 0.007 | 14.969 |
| TI14_083-Fsp | 62.17 | 8.02 | 0.96 | 5.04 | 0.18 | 23.26 | 0.01 | 0.19 | 0.00 | 0.02 | 0.08 | 99.93 | 8.308 | 2.078 | 0.163 | 0.722 | 0.020 | 3.665 | 0.001 | 0.015 | 0.000 | 0.002 | 0.004 | 14.980 |
| TI14_085-Fsp | 56.13 | 5.62 | 0.40 | 9.71 | 0.64 | 26.83 | 0.07 | 0.02 | 0.10 | 0.01 | 0.01 | 99.55 | 7.627 | 1.482 | 0.069 | 1.413 | 0.073 | 4.297 | 0.014 | 0.002 | 0.011 | 0.001 | 0.001 | 14.989 |
| TI14_086-Fsp | 58.46 | 6.61 | 0.34 | 8.10 | 0.22 | 25.85 | 0.00 | 0.12 | 0.00 | 0.03 | 0.02 | 99.75 | 7.872 | 1.726 | 0.058 | 1.169 | 0.024 | 4.103 | 0.001 | 0.009 | 0.000 | 0.004 | 0.001 | 14.968 |
| TI14_087-Fsp | 62.38 | 8.55 | 0.51 | 4.83 | 0.08 | 22.99 | 0.00 | 0.00 | 0.00 | 0.02 | 0.00 | 99.37 | 8.351 | 2.220 | 0.087 | 0.692 | 0.009 | 3.627 | 0.000 | 0.000 | 0.000 | 0.002 | 0.000 | 14.989 |
| TI14_088-Fsp | 61.17 | 7.87 | 0.52 | 5.71 | 0.29 | 23.86 | 0.01 | 0.03 | 0.02 | 0.00 | 0.12 | 99.61 | 8.203 | 2.046 | 0.089 | 0.820 | 0.032 | 3.771 | 0.002 | 0.003 | 0.002 | 0.000 | 0.006 | 14.976 |
| TI14_114-Fsp | 65.57 | 1.08 | 15.22 | 0.00 | 0.04 | 18.30 | 0.01 | 0.08 | 0.00 | 0.01 | 0.11 | 100.42 | 9.023 | 0.288 | 2.672 | 0.000 | 0.005 | 2.969 | 0.001 | 0.006 | 0.000 | 0.001 | 0.006 | 14.972 |
| TI14_117-Fsp | 64.63 | 1.65 | 14.00 | 0.07 | 0.12 | 18.38 | 0.00 | 0.02 | 0.01 | 0.00 | 0.14 | 99.04 | 8.988 | 0.445 | 2.484 | 0.010 | 0.014 | 3.013 | 0.001 | 0.002 | 0.001 | 0.001 | 0.008 | 14.968 |
| TI14_119-Fsp | 64.44 | 2.12 | 13.10 | 0.04 | 0.09 | 19.02 | 0.00 | 0.04 | 0.06 | 0.02 | 1.56 | 100.49 | 8.900 | 0.567 | 2.307 | 0.006 | 0.011 | 3.097 | 0.000 | 0.003 | 0.006 | 0.003 | 0.085 | 14.983 |
| TI14_120-Fsp | 64.74 | 0.34 | 16.32 | 0.01 | 0.00 | 18.27 | 0.02 | 0.02 | 0.02 | 0.00 | 0.00 | 99.74 | 9.002 | 0.091 | 2.895 | 0.001 | 0.000 | 2.995 | 0.005 | 0.002 | 0.002 | 0.000 | 0.000 | 14.992 |
| SR03_002-Fsp | 68.73 | 11.62 | 0.06 | 0.29 | 0.01 | 19.69 | 0.01 | 0.05 | 0.01 | 0.00 | 0.00 | 100.47 | 8.967 | 2.939 | 0.010 | 0.041 | 0.001 | 3.028 | 0.002 | 0.004 | 0.001 | 0.000 | 0.000 | 14.993 |
| SR03_003-Fsp | 68.09 | 11.12 | 0.26 | 0.58 | 0.05 | 19.63 | 0.01 | 0.03 | 0.00 | 0.00 | 0.00 | 99.77 | 8.953 | 2.835 | 0.043 | 0.082 | 0.006 | 3.042 | 0.001 | 0.003 | 0.000 | 0.000 | 0.000 | 14.965 |
| SR03_004-Fsp | 66.73 | 10.87 | 0.41 | 0.41 | 0.11 | 19.70 | 0.06 | 0.03 | 0.04 | 0.01 | 0.01 | 98.39 | 8.906 | 2.815 | 0.070 | 0.059 | 0.013 | 3.100 | 0.012 | 0.003 | 0.004 | 0.001 | 0.000 | 14.982 |
| SR03_005-Fsp | 65.06 | 8.82 | 1.36 | 2.80 | 0.14 | 21.41 | 0.01 | 0.04 | 0.03 | 0.01 | 0.16 | 99.84 | 8.643 | 2.272 | 0.230 | 0.399 | 0.016 | 3.353 | 0.001 | 0.003 | 0.003 | 0.001 | 0.008 | 14.929 |
| SR03_007-Fsp | 65.62 | 5.49 | 8.38 | 0.59 | 0.21 | 18.91 | 0.00 | 0.07 | 0.09 | 0.03 | 0.25 | 99.67 | 8.923 | 1.449 | 1.454 | 0.086 | 0.024 | 3.031 | 0.000 | 0.005 | 0.009 | 0.004 | 0.013 | 15.002 |
| SR03_008-Fsp | 68.24 | 11.20 | 0.06 | 0.37 | 0.08 | 19.55 | 0.01 | 0.03 | 0.00 | 0.00 | 0.04 | 99.57 | 8.977 | 2.856 | 0.011 | 0.052 | 0.008 | 3.031 | 0.002 | 0.002 | 0.000 | 0.000 | 0.002 | 14.941 |
| SR03_009-Fsp | 65.20 | 10.00 | 0.23 | 2.75 | 0.03 | 21.25 | 0.01 | 0.00 | 0.01 | 0.00 | 0.00 | 99.47 | 8.655 | 2.573 | 0.040 | 0.392 | 0.003 | 3.324 | 0.002 | 0.000 | 0.001 | 0.000 | 0.000 | 14.988 |
| SR03_011-Fsp | 67.14 | 10.82 | 0.37 | 0.95 | 0.06 | 19.93 | 0.00 | 0.02 | 0.00 | 0.00 | 0.03 | 99.32 | 8.886 | 2.776 | 0.062 | 0.135 | 0.007 | 3.109 | 0.000 | 0.002 | 0.000 | 0.000 | 0.002 | 14.978 |
| SR03_012-Fsp | 64.17 | 9.06 | 0.80 | 3.31 | 0.17 | 21.88 | 0.02 | 0.00 | 0.00 | 0.00 | 0.09 | 99.51 | 8.552 | 2.342 | 0.136 | 0.472 | 0.018 | 3.438 | 0.003 | 0.000 | 0.000 | 0.000 | 0.005 | 14.967 |
| SR03_013-Fsp | 64.47 | 9.40 | 0.49 | 3.29 | 0.13 | 21.99 | 0.03 | 0.02 | 0.01 | 0.00 | 0.04 | 99.88 | 8.550 | 2.418 | 0.084 | 0.467 | 0.015 | 3.437 | 0.006 | 0.001 | 0.001 | 0.000 | 0.002 | 14.981 |
| SR03_014-Fsp | 65.48 | 0.16 | 16.14 | 0.01 | 0.04 | 18.33 | 0.00 | 0.00 | 0.00 | 0.00 | 0.27 | 100.44 | 9.032 | 0.042 | 2.840 | 0.002 | 0.004 | 2.981 | 0.001 | 0.000 | 0.000 | 0.000 | 0.015 | 14.917 |
| SR03_015-Fsp | 67.14 | 10.82 | 0.63 | 0.26 | 0.19 | 20.17 | 0.06 | 0.04 | 0.01 | 0.00 | 0.04 | 99.35 | 8.883 | 2.777 | 0.106 | 0.036 | 0.021 | 3.145 | 0.012 | 0.003 | 0.001 | 0.000 | 0.002 | 14.985 |
| SR03_016-Fsp | 68.75 | 11.57 | 0.05 | 0.31 | 0.02 | 19.35 | 0.00 | 0.06 | 0.01 | 0.00 | 0.01 | 100.12 | 8.999 | 2.935 | 0.009 | 0.043 | 0.002 | 2.985 | 0.000 | 0.005 | 0.001 | 0.000 | 0.000 | 14.980 |
| SR03_018-Fsp | 67.85 | 11.51 | 0.07 | 0.52 | 0.05 | 19.54 | 0.02 | 0.00 | 0.00 | 0.00 | 0.00 | 99.56 | 8.943 | 2.942 | 0.011 | 0.073 | 0.006 | 3.036 | 0.004 | 0.000 | 0.000 | 0.000 | 0.000 | 15.015 |
| SR03_019-Fsp | 68.11 | 11.47 | 0.03 | 0.25 | 0.00 | 19.36 | 0.00 | 0.02 | 0.00 | 0.02 | 0.00 | 99.26 | 8.987 | 2.935 | 0.006 | 0.035 | 0.000 | 3.011 | 0.000 | 0.002 | 0.000 | 0.002 | 0.000 | 14.977 |
| SR03_021-Fsp | 65.22 | 0.99 | 15.42 | 0.05 | 0.03 | 18.25 | 0.01 | 0.02 | 0.00 | 0.04 | 0.11 | 100.15 | 9.012 | 0.266 | 2.718 | 0.007 | 0.004 | 2.973 | 0.001 | 0.002 | 0.000 | 0.005 | 0.006 | 14.993 |
| SR03_022-Fsp | 65.55 | 1.34 | 15.10 | 0.05 | 0.06 | 18.41 | 0.00 | 0.00 | 0.03 | 0.00 | 0.02 | 100.57 | 9.003 | 0.357 | 2.646 | 0.008 | 0.007 | 2.980 | 0.000 | 0.000 | 0.003 | 0.000 | 0.001 | 15.005 |
| SR03_025-Fsp | 63.45 | 8.62 | 0.96 | 4.07 | 0.21 | 22.63 | 0.02 | 0.09 | 0.00 | 0.01 | 0.04 | 100.14 | 8.433 | 2.221 | 0.163 | 0.580 | 0.023 | 3.545 | 0.003 | 0.007 | 0.000 | 0.002 | 0.002 | 14.984 |
| SR03_026-Fsp | 65.35 | 0.86 | 15.69 | 0.04 | 0.11 | 18.10 | 0.00 | 0.00 | 0.02 | 0.00 | 0.14 | 100.32 | 9.026 | 0.230 | 2.765 | 0.007 | 0.013 | 2.947 | 0.000 | 0.000 | 0.002 | 0.000 | 0.008 | 14.996 |
| SR03_034-Fsp | 63.02 | 9.00 | 0.19 | 4.37 | 0.01 | 23.25 | 0.00 | 0.03 | 0.00 | 0.00 | 0.00 | 99.91 | 8.368 | 2.318 | 0.032 | 0.622 | 0.002 | 3.639 | 0.000 | 0.003 | 0.000 | 0.000 | 0.000 | 14.987 |
| SR03_035-Fsp | 67.54 | 11.14 | 0.07 | 0.79 | 0.09 | 19.94 | 0.00 | 0.02 | 0.00 | 0.02 | 0.02 | 99.64 | 8.899 | 2.845 | 0.012 | 0.111 | 0.010 | 3.097 | 0.000 | 0.002 | 0.000 | 0.002 | 0.001 | 14.980 |
| SR03_038-Fsp | 67.20 | 11.49 | 0.06 | 0.32 | 0.10 | 19.15 | 0.03 | 0.07 | 0.03 | 0.03 | 0.00 | 98.51 | 8.958 | 2.969 | 0.010 | 0.046 | 0.011 | 3.009 | 0.007 | 0.005 | 0.003 | 0.003 | 0.000 | 15.024 |
| SR03_039-Fsp | 63.13 | 9.08 | 0.40 | 4.01 | 0.04 | 22.66 | 0.00 | 0.03 | 0.01 | 0.00 | 0.00 | 99.36 | 8.430 | 2.352 | 0.069 | 0.573 | 0.005 | 3.566 | 0.000 | 0.002 | 0.001 | 0.000 | 0.000 | 14.997 |
| SR03_040-Fsp | 64.91 | 0.87 | 15.32 | 0.03 | 0.05 | 18.38 | 0.00 | 0.04 | 0.06 | 0.01 | 0.41 | 100.07 | 8.990 | 0.234 | 2.707 | 0.004 | 0.006 | 3.000 | 0.000 | 0.003 | 0.006 | 0.002 | 0.022 | 14.974 |
| SR03_041-Fsp | 65.34 | 0.92 | 15.80 | 0.06 | 0.10 | 17.99 | 0.00 | 0.01 | 0.03 | 0.00 | 0.00 | 100.24 | 9.031 | 0.245 | 2.786 | 0.008 | 0.011 | 2.931 | 0.001 | 0.000 | 0.003 | 0.000 | 0.000 | 15.016 |
| SR03_043-Fsp | 65.12 | 1.34 | 14.96 | 0.02 | 0.16 | 18.22 | 0.01 | 0.00 | 0.01 | 0.02 | 0.01 | 99.87 | 9.008 | 0.360 | 2.641 | 0.003 | 0.018 | 2.970 | 0.003 | 0.000 | 0.001 | 0.002 | 0.000 | 15.006 |
| SR03_044-Fsp | 68.01 | 11.30 | 0.12 | 0.16 | 0.07 | 19.16 | 0.02 | 0.00 | 0.00 | 0.02 | 0.02 | 98.89 | 9.007 | 2.902 | 0.021 | 0.023 | 0.008 | 2.991 | 0.004 | 0.000 | 0.000 | 0.002 | 0.001 | 14.958 |
| SR03_046-Fsp | 65.29 | 1.24 | 14.75 | 0.00 | 0.10 | 18.70 | 0.00 | 0.00 | 0.01 | 0.01 | 0.49 | 100.59 | 8.977 | 0.332 | 2.587 | 0.000 | 0.011 | 3.031 | 0.000 | 0.000 | 0.001 | 0.002 | 0.027 | 14.966 |
| SR03_048-Fsp | 66.35 | 10.44 | 0.21 | 1.91 | 0.04 | 20.97 | 0.00 | 0.00 | 0.01 | 0.02 | 0.00 | 99.95 | 8.742 | 2.668 | 0.035 | 0.269 | 0.005 | 3.257 | 0.000 | 0.000 | 0.001 | 0.002 | 0.000 | 14.979 |
| SR03_049-Fsp | 68.33 | 11.40 | 0.03 | 0.19 | 0.01 | 19.21 | 0.00 | 0.08 | 0.00 | 0.02 | 0.01 | 99.27 | 9.012 | 2.914 | 0.004 | 0.027 | 0.001 | 2.987 | 0.000 | 0.006 | 0.000 | 0.003 | 0.001 | 14.954 |
| PT03_051-Fsp | 64.53 | 1.45 | 14.37 | 0.04 | 0.00 | 18.81 | 0.01 | 0.22 | 0.03 | 0.00 | 0.70 | 100.15 | 8.932 | 0.389 | 2.537 | 0.006 | 0.000 | 3.068 | 0.001 | 0.018 | 0.004 | 0.000 | 0.038 | 14.993 |
| PT03_052-Fsp | 64.76 | 0.59 | 15.34 | 0.00 | 0.00 | 18.43 | 0.00 | 0.01 | 0.03 | 0.00 | 0.23 | 99.39 | 9.005 | 0.158 | 2.722 | 0.000 | 0.000 | 3.021 | 0.000 | 0.001 | 0.003 | 0.000 | 0.012 | 14.922 |
| PT03_054-Fsp | 65.20 | 10.09 | 0.32 | 2.56 | 0.00 | 21.77 | 0.00 | 0.02 | 0.00 | 0.00 | 0.00 | 99.99 | 8.614 | 2.584 | 0.054 | 0.363 | 0.000 | 3.391 | 0.000 | 0.001 | 0.000 | 0.000 | 0.000 | 15.009 |
| PT03_056-Fsp | 64.59 | 1.31 | 14.90 | 0.05 | 0.01 | 18.80 | 0.00 | 0.02 | 0.00 | 0.01 | 0.25 | 99.95 | 8.941 | 0.352 | 2.632 | 0.008 | 0.002 | 3.068 | 0.000 | 0.001 | 0.000 | 0.001 | 0.013 | 15.017 |
| PT03_057-Fsp | 64.93 | 1.10 | 15.31 | 0.03 | 0.02 | 18.47 | 0.00 | 0.11 | 0.00 | 0.00 | 0.07 | 100.05 | 8.982 | 0.296 | 2.702 | 0.005 | 0.002 | 3.011 | 0.000 | 0.009 | 0.000 | 0.000 | 0.004 | 15.011 |

# Analyses of feldspar from sandstones (continuation)

| Sample / No. | $SiO_2$ | $Na_2O$ | $K_2O$ | CaO | FeO | $Al_2O_3$ | MgO | SrO | $TiO_2$ | MnO | BaO | wt-total | Si_at | Na_at | K_at | Ca_at | Fe_at | Al_at | Mg_at | Sr_at | Ti_at | Mn_at | Ba_at | at-total |
|---|---|---|---|---|---|---|---|---|---|---|---|---|---|---|---|---|---|---|---|---|---|---|---|---|
| PT03_058-Fsp | 63.82 | 9.44 | 0.25 | 3.45 | 0.06 | 21.87 | 0.01 | 0.02 | 0.02 | 0.00 | 0.00 | 98.98 | 8.535 | 2.448 | 0.043 | 0.494 | 0.006 | 3.448 | 0.002 | 0.001 | 0.002 | 0.000 | 0.000 | 14.983 |
| PT03_059-Fsp | 64.83 | 0.81 | 15.78 | 0.00 | 0.03 | 18.20 | 0.00 | 0.00 | 0.01 | 0.00 | 0.12 | 99.79 | 9.005 | 0.218 | 2.797 | 0.000 | 0.003 | 2.980 | 0.000 | 0.000 | 0.001 | 0.000 | 0.007 | 15.012 |
| PT03_060-Fsp | 64.49 | 0.97 | 15.24 | 0.01 | 0.02 | 18.51 | 0.01 | 0.07 | 0.03 | 0.00 | 0.46 | 99.80 | 8.963 | 0.261 | 2.702 | 0.002 | 0.003 | 3.033 | 0.002 | 0.006 | 0.003 | 0.000 | 0.025 | 14.999 |
| MA06-1_080-Fsp | 58.86 | 6.65 | 0.52 | 7.85 | 0.08 | 26.04 | 0.00 | 0.05 | 0.03 | 0.04 | 0.02 | 100.16 | 7.884 | 1.727 | 0.089 | 1.127 | 0.009 | 4.112 | 0.000 | 0.004 | 0.003 | 0.005 | 0.001 | 14.963 |
| MA06-1_081-Fsp | 58.66 | 6.82 | 0.32 | 8.07 | 0.29 | 25.99 | 0.02 | 0.11 | 0.00 | 0.00 | 0.04 | 100.31 | 7.862 | 1.772 | 0.055 | 1.159 | 0.033 | 4.105 | 0.003 | 0.009 | 0.000 | 0.000 | 0.002 | 14.999 |
| MA06-1_082-Fsp | 65.99 | 10.10 | 0.34 | 2.39 | 0.11 | 21.32 | 0.00 | 0.03 | 0.00 | 0.03 | 0.02 | 100.33 | 8.683 | 2.578 | 0.057 | 0.337 | 0.012 | 3.307 | 0.000 | 0.002 | 0.000 | 0.004 | 0.001 | 14.981 |
| MA06-1_083-Fsp | 58.43 | 6.78 | 0.36 | 8.05 | 0.12 | 26.20 | 0.00 | 0.05 | 0.00 | 0.02 | 0.01 | 100.02 | 7.845 | 1.766 | 0.061 | 1.158 | 0.014 | 4.146 | 0.000 | 0.004 | 0.000 | 0.003 | 0.000 | 14.996 |
| MA06-1_085-Fsp | 62.36 | 8.52 | 0.39 | 5.17 | 0.10 | 23.77 | 0.00 | 0.01 | 0.00 | 0.02 | 0.04 | 100.39 | 8.272 | 2.190 | 0.066 | 0.735 | 0.011 | 3.717 | 0.001 | 0.001 | 0.000 | 0.002 | 0.002 | 14.998 |
| MA06-1_086-Fsp | 60.61 | 7.80 | 0.25 | 6.29 | 0.00 | 24.81 | 0.00 | 0.03 | 0.00 | 0.00 | 0.00 | 99.80 | 8.101 | 2.021 | 0.043 | 0.901 | 0.000 | 3.908 | 0.000 | 0.002 | 0.000 | 0.000 | 0.000 | 14.977 |
| MA06-1_087-Fsp | 61.61 | 7.75 | 1.02 | 5.31 | 0.22 | 23.67 | 0.00 | 0.12 | 0.01 | 0.04 | 0.07 | 99.84 | 8.248 | 2.011 | 0.174 | 0.762 | 0.025 | 3.735 | 0.000 | 0.009 | 0.002 | 0.004 | 0.004 | 14.975 |
| MA06-1_088-Fsp | 58.36 | 6.78 | 0.50 | 7.76 | 0.07 | 26.00 | 0.00 | 0.02 | 0.02 | 0.00 | 0.03 | 99.53 | 7.869 | 1.774 | 0.087 | 1.122 | 0.007 | 4.131 | 0.000 | 0.001 | 0.002 | 0.000 | 0.001 | 14.994 |
| MA06-1_089-Fsp | 59.99 | 7.16 | 0.32 | 7.20 | 0.04 | 25.57 | 0.00 | 0.13 | 0.00 | 0.02 | 0.03 | 100.48 | 7.989 | 1.848 | 0.055 | 1.028 | 0.005 | 4.014 | 0.000 | 0.010 | 0.000 | 0.002 | 0.002 | 14.955 |
| MA06-1_090-Fsp | 64.77 | 9.39 | 1.30 | 2.73 | 0.18 | 21.59 | 0.01 | 0.00 | 0.00 | 0.00 | 0.03 | 100.01 | 8.600 | 2.417 | 0.220 | 0.388 | 0.020 | 3.378 | 0.001 | 0.000 | 0.000 | 0.000 | 0.002 | 15.028 |
| MA06-1_092-Fsp | 66.18 | 10.16 | 0.36 | 2.25 | 0.02 | 21.31 | 0.02 | 0.02 | 0.04 | 0.03 | 0.09 | 100.50 | 8.692 | 2.587 | 0.061 | 0.317 | 0.002 | 3.300 | 0.004 | 0.001 | 0.004 | 0.004 | 0.005 | 14.978 |
| MA06-1_093-Fsp | 61.04 | 7.92 | 0.41 | 6.08 | 0.11 | 24.49 | 0.03 | 0.00 | 0.00 | 0.02 | 0.01 | 100.13 | 8.138 | 2.047 | 0.069 | 0.869 | 0.013 | 3.849 | 0.006 | 0.000 | 0.000 | 0.002 | 0.001 | 14.994 |
| MA06-1_094-Fsp | 60.55 | 7.56 | 0.44 | 6.60 | 0.11 | 24.71 | 0.00 | 0.05 | 0.01 | 0.00 | 0.00 | 100.05 | 8.090 | 1.958 | 0.076 | 0.945 | 0.013 | 3.892 | 0.001 | 0.004 | 0.002 | 0.000 | 0.000 | 14.980 |
| MA06-1_095-Fsp | 59.54 | 7.16 | 0.59 | 6.88 | 0.06 | 25.48 | 0.00 | 0.22 | 0.01 | 0.01 | 0.04 | 99.98 | 7.981 | 1.860 | 0.101 | 0.989 | 0.007 | 4.027 | 0.000 | 0.017 | 0.001 | 0.001 | 0.002 | 14.985 |
| MA06-1_096-Fsp | 62.47 | 8.49 | 0.34 | 5.13 | 0.04 | 23.80 | 0.00 | 0.15 | 0.00 | 0.01 | 0.01 | 100.47 | 8.277 | 2.182 | 0.058 | 0.728 | 0.005 | 3.718 | 0.000 | 0.012 | 0.000 | 0.001 | 0.001 | 14.983 |
| MA06-1_097-Fsp | 65.33 | 0.52 | 15.86 | 0.00 | 0.02 | 18.58 | 0.01 | 0.02 | 0.00 | 0.00 | 0.32 | 100.67 | 8.995 | 0.139 | 2.787 | 0.000 | 0.002 | 3.015 | 0.002 | 0.002 | 0.000 | 0.000 | 0.017 | 14.960 |
| MA06-1_098-Fsp | 60.34 | 7.72 | 0.39 | 6.27 | 0.10 | 24.37 | 0.00 | 0.10 | 0.00 | 0.02 | 0.00 | 99.34 | 8.117 | 2.013 | 0.067 | 0.904 | 0.011 | 3.865 | 0.001 | 0.008 | 0.000 | 0.002 | 0.000 | 14.990 |
| MA06-1_099-Fsp | 61.88 | 8.21 | 0.43 | 5.50 | 0.03 | 24.09 | 0.00 | 0.02 | 0.00 | 0.00 | 0.02 | 100.19 | 8.226 | 2.116 | 0.073 | 0.784 | 0.003 | 3.775 | 0.000 | 0.001 | 0.000 | 0.000 | 0.001 | 14.980 |
| MA06-1_100-Fsp | 60.40 | 7.80 | 0.41 | 6.34 | 0.02 | 24.73 | 0.00 | 0.06 | 0.00 | 0.02 | 0.01 | 99.79 | 8.088 | 2.025 | 0.071 | 0.910 | 0.002 | 3.903 | 0.000 | 0.004 | 0.000 | 0.003 | 0.000 | 15.007 |
| MA06-1_102-Fsp | 66.13 | 3.83 | 11.19 | 0.14 | 0.05 | 18.57 | 0.00 | 0.00 | 0.02 | 0.02 | 0.00 | 99.95 | 9.009 | 1.012 | 1.944 | 0.021 | 0.006 | 2.982 | 0.000 | 0.000 | 0.002 | 0.002 | 0.000 | 14.977 |
| MA06-1_103-Fsp | 65.53 | 1.00 | 15.23 | 0.05 | 0.07 | 18.47 | 0.01 | 0.01 | 0.00 | 0.00 | 0.00 | 100.37 | 9.011 | 0.266 | 2.672 | 0.007 | 0.008 | 2.994 | 0.003 | 0.001 | 0.000 | 0.000 | 0.000 | 14.961 |
| MA06-1_105-Fsp | 61.95 | 8.41 | 0.41 | 4.98 | 0.21 | 23.46 | 0.01 | 0.27 | 0.00 | 0.01 | 0.00 | 99.73 | 8.283 | 2.180 | 0.070 | 0.713 | 0.024 | 3.698 | 0.001 | 0.021 | 0.000 | 0.001 | 0.000 | 14.993 |
| MA06-1_106-Fsp | 65.32 | 1.03 | 14.92 | 0.00 | 0.04 | 18.65 | 0.00 | 0.02 | 0.00 | 0.00 | 0.09 | 100.08 | 8.998 | 0.276 | 2.622 | 0.000 | 0.005 | 3.028 | 0.000 | 0.001 | 0.000 | 0.000 | 0.005 | 14.937 |
| MA06-1_107-Fsp | 65.20 | 0.76 | 15.58 | 0.01 | 0.01 | 18.69 | 0.00 | 0.01 | 0.00 | 0.04 | 0.24 | 100.58 | 8.977 | 0.203 | 2.737 | 0.002 | 0.001 | 3.034 | 0.000 | 0.001 | 0.000 | 0.005 | 0.013 | 14.975 |
| MA06-1_109-Fsp | 65.34 | 1.28 | 14.86 | 0.01 | 0.07 | 18.35 | 0.01 | 0.00 | 0.04 | 0.00 | 0.13 | 100.10 | 9.010 | 0.343 | 2.615 | 0.002 | 0.008 | 2.982 | 0.003 | 0.000 | 0.004 | 0.000 | 0.007 | 14.974 |
| MA06-1_110-Fsp | 65.33 | 1.50 | 14.33 | 0.02 | 0.00 | 18.95 | 0.00 | 0.05 | 0.04 | 0.01 | 0.52 | 100.77 | 8.954 | 0.398 | 2.506 | 0.003 | 0.001 | 3.062 | 0.000 | 0.004 | 0.004 | 0.001 | 0.028 | 14.962 |
| MA06-1_111-Fsp | 65.05 | 1.41 | 14.50 | 0.01 | 0.01 | 18.90 | 0.00 | 0.00 | 0.00 | 0.02 | 0.09 | 99.99 | 8.962 | 0.378 | 2.549 | 0.002 | 0.001 | 3.069 | 0.000 | 0.000 | 0.000 | 0.002 | 0.005 | 14.967 |
| MA06-1_112-Fsp | 67.61 | 7.11 | 6.61 | 0.11 | 0.29 | 18.75 | 0.01 | 0.00 | 0.01 | 0.01 | 0.00 | 100.51 | 9.020 | 1.838 | 1.125 | 0.016 | 0.033 | 2.949 | 0.001 | 0.000 | 0.001 | 0.001 | 0.000 | 14.985 |
| MA06-1_113-Fsp | 65.35 | 1.60 | 14.19 | 0.08 | 0.04 | 18.57 | 0.01 | 0.06 | 0.03 | 0.00 | 0.27 | 100.20 | 8.990 | 0.427 | 2.491 | 0.011 | 0.005 | 3.011 | 0.002 | 0.005 | 0.003 | 0.000 | 0.015 | 14.960 |
| MA06-1_115-Fsp | 64.37 | 1.14 | 14.57 | 0.28 | 0.02 | 18.90 | 0.00 | 0.06 | 0.05 | 0.04 | 0.53 | 99.95 | 8.919 | 0.306 | 2.576 | 0.042 | 0.002 | 3.087 | 0.000 | 0.005 | 0.005 | 0.005 | 0.029 | 14.974 |
| MA06-1_116-Fsp | 64.65 | 1.34 | 14.70 | 0.06 | 0.01 | 18.81 | 0.00 | 0.01 | 0.04 | 0.02 | 0.28 | 99.95 | 8.941 | 0.360 | 2.593 | 0.009 | 0.001 | 3.067 | 0.000 | 0.001 | 0.004 | 0.003 | 0.015 | 14.997 |
| MA06-1_117-Fsp | 65.42 | 1.93 | 13.88 | 0.08 | 0.05 | 18.91 | 0.00 | 0.09 | 0.06 | 0.03 | 0.34 | 100.78 | 8.950 | 0.513 | 2.422 | 0.012 | 0.005 | 3.049 | 0.000 | 0.007 | 0.007 | 0.003 | 0.018 | 14.987 |
| MA06-1_119-Fsp | 61.14 | 8.09 | 0.46 | 5.79 | 0.04 | 24.66 | 0.00 | 0.03 | 0.05 | 0.00 | 0.04 | 100.30 | 8.135 | 2.088 | 0.077 | 0.826 | 0.005 | 3.867 | 0.000 | 0.002 | 0.005 | 0.000 | 0.002 | 15.009 |
| MA06-1_120-Fsp | 65.19 | 0.65 | 15.70 | 0.01 | 0.02 | 18.63 | 0.00 | 0.01 | 0.00 | 0.00 | 0.44 | 100.67 | 8.983 | 0.173 | 2.760 | 0.001 | 0.003 | 3.026 | 0.000 | 0.001 | 0.000 | 0.000 | 0.024 | 14.971 |
| MA06-1_121-Fsp | 65.69 | 1.29 | 14.85 | 0.00 | 0.00 | 18.45 | 0.01 | 0.05 | 0.00 | 0.00 | 0.16 | 100.52 | 9.017 | 0.343 | 2.601 | 0.000 | 0.000 | 2.985 | 0.001 | 0.004 | 0.000 | 0.000 | 0.009 | 14.961 |
| MA06-1_123-Fsp | 64.95 | 0.96 | 15.02 | 0.00 | 0.04 | 18.44 | 0.01 | 0.00 | 0.06 | 0.00 | 0.29 | 99.77 | 8.997 | 0.259 | 2.655 | 0.000 | 0.005 | 3.010 | 0.002 | 0.000 | 0.006 | 0.000 | 0.016 | 14.949 |
| MA06-3_070-Fsp | 57.66 | 6.47 | 0.12 | 8.83 | 0.12 | 26.92 | 0.01 | 0.05 | 0.00 | 0.02 | 0.00 | 100.22 | 7.735 | 1.683 | 0.021 | 1.269 | 0.014 | 4.257 | 0.003 | 0.004 | 0.000 | 0.003 | 0.000 | 14.989 |
| MA06-3_072-Fsp | 63.11 | 8.23 | 1.01 | 4.37 | 0.17 | 23.13 | 0.01 | 0.02 | 0.01 | 0.00 | 0.03 | 100.09 | 8.386 | 2.121 | 0.171 | 0.622 | 0.019 | 3.623 | 0.001 | 0.002 | 0.001 | 0.000 | 0.002 | 14.948 |
| MA06-3_073-Fsp | 59.38 | 7.47 | 0.10 | 7.32 | 0.11 | 25.52 | 0.00 | 0.10 | 0.04 | 0.03 | 0.00 | 100.07 | 7.950 | 1.939 | 0.017 | 1.050 | 0.013 | 4.027 | 0.000 | 0.007 | 0.004 | 0.003 | 0.000 | 15.011 |
| MA06-3_074-Fsp | 59.75 | 7.10 | 0.62 | 6.93 | 0.19 | 25.24 | 0.01 | 0.23 | 0.01 | 0.00 | 0.02 | 100.09 | 8.005 | 1.844 | 0.106 | 0.994 | 0.021 | 3.986 | 0.001 | 0.018 | 0.001 | 0.000 | 0.001 | 14.977 |
| MA06-3_077-Fsp | 60.29 | 7.30 | 0.36 | 7.07 | 0.15 | 25.29 | 0.00 | 0.15 | 0.01 | 0.01 | 0.01 | 100.65 | 8.020 | 1.882 | 0.062 | 1.007 | 0.016 | 3.965 | 0.001 | 0.012 | 0.001 | 0.001 | 0.000 | 14.968 |
| MA06-3_078-Fsp | 61.86 | 8.62 | 0.20 | 5.38 | 0.00 | 24.36 | 0.00 | 0.09 | 0.01 | 0.02 | 0.00 | 100.54 | 8.197 | 2.216 | 0.035 | 0.763 | 0.000 | 3.805 | 0.000 | 0.007 | 0.001 | 0.002 | 0.000 | 15.025 |
| MA06-3_080-Fsp | 57.30 | 6.18 | 0.41 | 8.89 | 0.28 | 26.89 | 0.01 | 0.16 | 0.03 | 0.01 | 0.03 | 100.21 | 7.710 | 1.613 | 0.071 | 1.282 | 0.032 | 4.265 | 0.002 | 0.012 | 0.003 | 0.001 | 0.002 | 14.995 |
| MA06-3_081-Fsp | 60.42 | 8.08 | 0.20 | 6.03 | 0.05 | 24.84 | 0.00 | 0.10 | 0.00 | 0.00 | 0.00 | 99.74 | 8.087 | 2.098 | 0.034 | 0.865 | 0.006 | 3.919 | 0.000 | 0.008 | 0.000 | 0.000 | 0.000 | 15.019 |
| MA06-3_082-Fsp | 59.55 | 7.00 | 0.85 | 7.20 | 0.31 | 25.35 | 0.02 | 0.09 | 0.05 | 0.04 | 0.13 | 100.61 | 7.963 | 1.814 | 0.146 | 1.032 | 0.034 | 3.996 | 0.003 | 0.007 | 0.005 | 0.005 | 0.007 | 15.013 |
| MA06-3_083-Fsp | 65.86 | 10.55 | 0.18 | 1.95 | 0.04 | 21.26 | 0.00 | 0.00 | 0.00 | 0.00 | 0.00 | 99.85 | 8.695 | 2.701 | 0.030 | 0.276 | 0.004 | 3.308 | 0.000 | 0.000 | 0.000 | 0.001 | 0.000 | 15.015 |
| MA06-3_084-Fsp | 59.35 | 7.07 | 0.39 | 7.46 | 0.04 | 25.67 | 0.00 | 0.00 | 0.03 | 0.05 | 0.03 | 100.08 | 7.944 | 1.834 | 0.066 | 1.071 | 0.005 | 4.049 | 0.001 | 0.000 | 0.003 | 0.005 | 0.002 | 14.979 |
| MA06-3_085-Fsp | 59.85 | 7.24 | 0.34 | 7.04 | 0.05 | 25.39 | 0.00 | 0.21 | 0.00 | 0.01 | 0.05 | 100.19 | 7.999 | 1.877 | 0.059 | 1.009 | 0.005 | 3.999 | 0.000 | 0.017 | 0.000 | 0.001 | 0.002 | 14.968 |
| MA06-3_086-Fsp | 65.80 | 10.05 | 0.31 | 2.40 | 0.00 | 21.58 | 0.00 | 0.04 | 0.01 | 0.01 | 0.00 | 100.20 | 8.662 | 2.566 | 0.052 | 0.338 | 0.000 | 3.348 | 0.000 | 0.003 | 0.001 | 0.002 | 0.000 | 14.972 |

| Sample / No. | $SiO_2$ | $Na_2O$ | $K_2O$ | CaO | FeO | $Al_2O_3$ | MgO | SrO | $TiO_2$ | MnO | BaO | wt-total | Si_at | Na_at | K_at | Ca_at | Fe_at | Al_at | Mg_at | Sr_at | Ti_at | Mn_at | Ba_at | at-total |
|---|---|---|---|---|---|---|---|---|---|---|---|---|---|---|---|---|---|---|---|---|---|---|---|---|
| MA06-3_088-Fsp | 58.18 | 6.67 | 0.24 | 7.98 | 0.13 | 26.26 | 0.01 | 0.33 | 0.00 | 0.00 | 0.06 | 99.87 | 7.831 | 1.741 | 0.041 | 1.151 | 0.015 | 4.166 | 0.003 | 0.026 | 0.000 | 0.000 | 0.003 | 14.977 |
| MA06-3_089-Fsp | 55.54 | 5.30 | 0.46 | 10.16 | 0.62 | 27.59 | 0.04 | 0.28 | 0.02 | 0.02 | 0.00 | 100.04 | 7.532 | 1.394 | 0.080 | 1.477 | 0.071 | 4.409 | 0.009 | 0.022 | 0.002 | 0.002 | 0.000 | 14.998 |
| MA06-3_090-Fsp | 65.61 | 3.50 | 11.10 | 0.19 | 0.07 | 19.07 | 0.00 | 0.00 | 0.05 | 0.01 | 1.17 | 100.76 | 8.936 | 0.925 | 1.929 | 0.028 | 0.007 | 3.061 | 0.000 | 0.000 | 0.005 | 0.002 | 0.062 | 14.955 |
| MA06-3_092-Fsp | 58.13 | 6.58 | 0.27 | 8.33 | 0.06 | 26.70 | 0.00 | 0.18 | 0.02 | 0.02 | 0.03 | 100.31 | 7.788 | 1.708 | 0.046 | 1.196 | 0.007 | 4.216 | 0.000 | 0.014 | 0.002 | 0.002 | 0.002 | 14.979 |
| MA06-3_094-Fsp | 65.86 | 10.25 | 0.69 | 1.99 | 0.00 | 21.19 | 0.01 | 0.00 | 0.01 | 0.01 | 0.09 | 100.09 | 8.696 | 2.625 | 0.116 | 0.281 | 0.000 | 3.298 | 0.001 | 0.000 | 0.001 | 0.001 | 0.005 | 15.024 |
| MA06-3_095-Fsp | 59.76 | 6.99 | 0.53 | 7.14 | 0.16 | 25.43 | 0.00 | 0.11 | 0.00 | 0.00 | 0.00 | 100.12 | 7.992 | 1.812 | 0.090 | 1.023 | 0.018 | 4.009 | 0.000 | 0.008 | 0.000 | 0.000 | 0.000 | 14.953 |
| MA06-3_096-Fsp | 61.18 | 8.21 | 0.28 | 5.61 | 0.47 | 24.03 | 0.00 | 0.01 | 0.13 | 0.00 | 0.00 | 99.95 | 8.174 | 2.128 | 0.048 | 0.803 | 0.053 | 3.784 | 0.000 | 0.001 | 0.013 | 0.000 | 0.000 | 15.007 |
| MA06-3_148-Fsp | 61.86 | 8.47 | 0.18 | 5.40 | 0.08 | 23.96 | 0.00 | 0.23 | 0.00 | 0.00 | 0.02 | 100.20 | 8.229 | 2.184 | 0.031 | 0.769 | 0.009 | 3.757 | 0.000 | 0.018 | 0.000 | 0.000 | 0.001 | 14.999 |
| MA06-3_149-Fsp | 64.60 | 1.94 | 14.09 | 0.02 | 0.05 | 18.99 | 0.01 | 0.19 | 0.01 | 0.00 | 0.34 | 100.25 | 8.911 | 0.520 | 2.480 | 0.003 | 0.006 | 3.088 | 0.002 | 0.015 | 0.001 | 0.000 | 0.019 | 15.044 |
| MA06-3_150-Fsp | 58.67 | 7.18 | 0.23 | 7.77 | 0.02 | 26.39 | 0.00 | 0.08 | 0.00 | 0.00 | 0.00 | 100.34 | 7.845 | 1.862 | 0.038 | 1.113 | 0.003 | 4.159 | 0.000 | 0.006 | 0.000 | 0.000 | 0.000 | 15.026 |
| MA06-3_151-Fsp | 61.69 | 8.48 | 0.24 | 5.36 | 0.11 | 23.98 | 0.00 | 0.00 | 0.01 | 0.02 | 0.00 | 99.91 | 8.223 | 2.192 | 0.040 | 0.766 | 0.013 | 3.768 | 0.000 | 0.000 | 0.001 | 0.002 | 0.000 | 15.007 |
| MA06-3_152-Fsp | 60.38 | 7.72 | 1.12 | 5.34 | 0.30 | 23.86 | 0.02 | 0.17 | 0.04 | 0.00 | 0.20 | 99.17 | 8.168 | 2.026 | 0.193 | 0.774 | 0.034 | 3.805 | 0.005 | 0.013 | 0.004 | 0.001 | 0.011 | 15.034 |
| MA06-3_153-Fsp | 64.51 | 0.74 | 15.54 | 0.00 | 0.03 | 18.66 | 0.02 | 0.00 | 0.00 | 0.01 | 0.17 | 99.68 | 8.961 | 0.199 | 2.754 | 0.000 | 0.004 | 3.054 | 0.005 | 0.000 | 0.000 | 0.001 | 0.009 | 14.988 |
| MA06-3_154-Fsp | 60.39 | 8.29 | 0.28 | 5.51 | 0.07 | 24.25 | 0.02 | 0.14 | 0.02 | 0.00 | 0.00 | 98.98 | 8.144 | 2.167 | 0.048 | 0.797 | 0.008 | 3.854 | 0.004 | 0.011 | 0.002 | 0.000 | 0.000 | 15.035 |
| MA06-3_155-Fsp | 66.56 | 6.53 | 7.09 | 0.29 | 0.19 | 19.28 | 0.00 | 0.00 | 0.00 | 0.01 | 0.02 | 99.98 | 8.946 | 1.702 | 1.216 | 0.042 | 0.021 | 3.055 | 0.000 | 0.000 | 0.000 | 0.002 | 0.001 | 14.985 |
| MA06-3_156-Fsp | 64.62 | 1.60 | 14.50 | 0.05 | 0.05 | 18.62 | 0.00 | 0.00 | 0.04 | 0.03 | 0.05 | 99.58 | 8.955 | 0.429 | 2.564 | 0.007 | 0.006 | 3.042 | 0.000 | 0.000 | 0.004 | 0.004 | 0.003 | 15.015 |
| MA06-3_157-Fsp | 64.20 | 2.63 | 12.84 | 0.15 | 0.02 | 18.99 | 0.00 | 0.06 | 0.02 | 0.00 | 0.25 | 99.15 | 8.904 | 0.707 | 2.271 | 0.022 | 0.002 | 3.105 | 0.000 | 0.005 | 0.002 | 0.000 | 0.014 | 15.031 |
| MA06-3_158-Fsp | 64.97 | 0.75 | 15.71 | 0.00 | 0.00 | 18.78 | 0.00 | 0.00 | 0.01 | 0.00 | 0.08 | 100.29 | 8.965 | 0.200 | 2.766 | 0.000 | 0.000 | 3.054 | 0.000 | 0.000 | 0.001 | 0.000 | 0.004 | 14.991 |
| MA06-3_159-Fsp | 63.97 | 1.55 | 13.82 | 0.04 | 0.06 | 18.94 | 0.00 | 0.19 | 0.05 | 0.00 | 1.17 | 99.79 | 8.901 | 0.417 | 2.453 | 0.006 | 0.007 | 3.106 | 0.000 | 0.015 | 0.005 | 0.000 | 0.064 | 14.976 |
| MA06-3_160-Fsp | 60.44 | 7.81 | 0.58 | 6.03 | 0.09 | 24.53 | 0.02 | 0.08 | 0.00 | 0.03 | 0.01 | 99.61 | 8.112 | 2.032 | 0.099 | 0.866 | 0.011 | 3.880 | 0.003 | 0.007 | 0.000 | 0.003 | 0.000 | 15.014 |
| MA06-3_161-Fsp | 65.68 | 1.48 | 14.61 | 0.04 | 0.00 | 18.77 | 0.01 | 0.00 | 0.01 | 0.00 | 0.04 | 100.65 | 8.987 | 0.393 | 2.550 | 0.006 | 0.001 | 3.027 | 0.002 | 0.000 | 0.001 | 0.000 | 0.002 | 14.969 |
| MA06-3_162-Fsp | 57.13 | 6.72 | 0.23 | 8.38 | 0.20 | 26.46 | 0.00 | 0.00 | 0.00 | 0.00 | 0.01 | 99.14 | 7.752 | 1.768 | 0.040 | 1.218 | 0.023 | 4.232 | 0.000 | 0.000 | 0.000 | 0.000 | 0.001 | 15.035 |
| MA06-3_162-Fsp | 65.14 | 1.57 | 14.35 | 0.00 | 0.09 | 18.81 | 0.00 | 0.04 | 0.00 | 0.00 | 0.22 | 100.23 | 8.964 | 0.420 | 2.520 | 0.000 | 0.011 | 3.051 | 0.000 | 0.004 | 0.000 | 0.000 | 0.012 | 14.980 |
| MA06-3_163-Fsp | 64.12 | 1.14 | 14.86 | 0.08 | 0.06 | 18.95 | 0.01 | 0.02 | 0.02 | 0.00 | 0.69 | 99.96 | 8.905 | 0.308 | 2.634 | 0.012 | 0.007 | 3.102 | 0.001 | 0.002 | 0.002 | 0.000 | 0.038 | 15.012 |
| CHW26_200-Fsp | 68.77 | 11.65 | 0.05 | 0.30 | 0.05 | 19.75 | 0.00 | 0.01 | 0.00 | 0.00 | 0.00 | 100.60 | 8.961 | 2.944 | 0.008 | 0.042 | 0.006 | 3.033 | 0.000 | 0.001 | 0.000 | 0.000 | 0.000 | 14.997 |
| CHW26_201-Fsp | 68.58 | 11.59 | 0.06 | 0.20 | 0.01 | 19.71 | 0.01 | 0.00 | 0.05 | 0.00 | 0.05 | 100.29 | 8.962 | 2.937 | 0.010 | 0.028 | 0.001 | 3.036 | 0.001 | 0.000 | 0.005 | 0.000 | 0.003 | 14.987 |
| CHW26_202-Fsp | 68.58 | 11.47 | 0.04 | 0.38 | 0.02 | 19.72 | 0.01 | 0.01 | 0.03 | 0.00 | 0.00 | 100.26 | 8.962 | 2.905 | 0.007 | 0.054 | 0.003 | 3.037 | 0.002 | 0.000 | 0.003 | 0.000 | 0.000 | 14.973 |
| CHW26_203-Fsp | 68.68 | 11.69 | 0.03 | 0.30 | 0.06 | 19.83 | 0.00 | 0.00 | 0.01 | 0.00 | 0.00 | 100.60 | 8.950 | 2.954 | 0.004 | 0.042 | 0.007 | 3.046 | 0.000 | 0.000 | 0.001 | 0.000 | 0.000 | 15.005 |
| CHW26_213-Fsp | 68.01 | 11.54 | 0.04 | 0.39 | 0.02 | 19.79 | 0.00 | 0.00 | 0.00 | 0.01 | 0.00 | 99.79 | 8.936 | 2.940 | 0.007 | 0.054 | 0.002 | 3.065 | 0.000 | 0.000 | 0.000 | 0.001 | 0.000 | 15.005 |
| CHW26_214-Fsp | 68.52 | 11.72 | 0.03 | 0.28 | 0.06 | 19.71 | 0.00 | 0.00 | 0.00 | 0.02 | 0.05 | 100.39 | 8.954 | 2.969 | 0.004 | 0.039 | 0.007 | 3.036 | 0.000 | 0.000 | 0.000 | 0.002 | 0.003 | 15.014 |
| CHW26_215-Fsp | 67.38 | 11.46 | 0.05 | 0.34 | 0.00 | 19.60 | 0.00 | 0.05 | 0.00 | 0.00 | 0.00 | 98.90 | 8.936 | 2.947 | 0.008 | 0.049 | 0.000 | 3.063 | 0.000 | 0.004 | 0.000 | 0.000 | 0.000 | 15.009 |
| CHW26_216-Fsp | 68.96 | 11.88 | 0.05 | 0.19 | 0.04 | 19.63 | 0.01 | 0.00 | 0.00 | 0.01 | 0.00 | 100.78 | 8.973 | 2.997 | 0.008 | 0.026 | 0.005 | 3.011 | 0.001 | 0.000 | 0.000 | 0.001 | 0.000 | 15.023 |
| CHW26_217-Fsp | 65.93 | 0.05 | 15.81 | 0.00 | 0.15 | 18.32 | 0.00 | 0.00 | 0.04 | 0.02 | 0.04 | 100.37 | 9.062 | 0.015 | 2.772 | 0.000 | 0.017 | 2.967 | 0.001 | 0.000 | 0.004 | 0.002 | 0.002 | 14.843 |
| CHW26_220-Fsp | 67.04 | 10.75 | 0.41 | 1.34 | 0.12 | 20.41 | 0.00 | 0.00 | 0.05 | 0.00 | 0.00 | 100.15 | 8.817 | 2.742 | 0.068 | 0.190 | 0.014 | 3.164 | 0.000 | 0.000 | 0.005 | 0.000 | 0.000 | 15.000 |
| CHW26_221-Fsp | 65.13 | 1.03 | 15.28 | 0.05 | 0.06 | 18.84 | 0.00 | 0.02 | 0.00 | 0.00 | 0.41 | 100.82 | 8.953 | 0.275 | 2.679 | 0.007 | 0.007 | 3.052 | 0.001 | 0.002 | 0.000 | 0.000 | 0.022 | 14.998 |
| CHW26_222-Fsp | 68.05 | 11.60 | 0.02 | 0.30 | 0.01 | 19.73 | 0.00 | 0.07 | 0.00 | 0.00 | 0.00 | 99.80 | 8.943 | 2.957 | 0.003 | 0.042 | 0.001 | 3.056 | 0.000 | 0.005 | 0.000 | 0.000 | 0.000 | 15.009 |
| CHW26_224-Fsp | 61.30 | 1.95 | 11.82 | 0.03 | 0.06 | 20.30 | 0.00 | 0.67 | 0.13 | 0.03 | 4.72 | 101.01 | 8.631 | 0.533 | 2.123 | 0.005 | 0.007 | 3.368 | 0.000 | 0.055 | 0.014 | 0.004 | 0.261 | 14.999 |
| CHW26_226-Fsp | 64.72 | 2.18 | 13.52 | 0.29 | 0.00 | 19.08 | 0.00 | 0.03 | 0.03 | 0.00 | 0.20 | 100.06 | 8.908 | 0.582 | 2.373 | 0.043 | 0.001 | 3.096 | 0.000 | 0.002 | 0.003 | 0.000 | 0.011 | 15.019 |
| CHW26_227-Fsp | 64.34 | 0.97 | 15.41 | 0.02 | 0.05 | 18.73 | 0.00 | 0.01 | 0.00 | 0.01 | 0.05 | 99.60 | 8.943 | 0.262 | 2.732 | 0.003 | 0.006 | 3.069 | 0.000 | 0.001 | 0.000 | 0.001 | 0.003 | 15.020 |
| CHW26_228-Fsp | 65.54 | 2.28 | 13.55 | 0.26 | 0.04 | 19.01 | 0.00 | 0.01 | 0.00 | 0.00 | 0.22 | 100.93 | 8.939 | 0.603 | 2.358 | 0.038 | 0.005 | 3.057 | 0.000 | 0.001 | 0.000 | 0.000 | 0.012 | 15.012 |
| CHW26_229-Fsp | 66.10 | 3.47 | 11.81 | 0.18 | 0.01 | 19.10 | 0.02 | 0.00 | 0.06 | 0.03 | 0.17 | 100.95 | 8.949 | 0.911 | 2.040 | 0.025 | 0.001 | 3.048 | 0.003 | 0.000 | 0.006 | 0.004 | 0.009 | 14.997 |
| CHW26_230-Fsp | 65.24 | 1.69 | 14.51 | 0.08 | 0.02 | 18.79 | 0.00 | 0.00 | 0.03 | 0.00 | 0.25 | 100.62 | 8.955 | 0.451 | 2.541 | 0.011 | 0.003 | 3.040 | 0.000 | 0.000 | 0.003 | 0.000 | 0.014 | 15.018 |
| CHW26_231-Fsp | 64.18 | 0.96 | 15.14 | 0.05 | 0.00 | 18.90 | 0.01 | 0.06 | 0.00 | 0.00 | 0.70 | 100.00 | 8.917 | 0.258 | 2.683 | 0.007 | 0.000 | 3.095 | 0.002 | 0.005 | 0.000 | 0.000 | 0.038 | 15.006 |
| CHW26_232-Fsp | 63.59 | 1.75 | 14.04 | 0.00 | 0.07 | 18.96 | 0.02 | 0.21 | 0.04 | 0.00 | 0.93 | 99.62 | 8.873 | 0.474 | 2.498 | 0.001 | 0.008 | 3.119 | 0.005 | 0.017 | 0.004 | 0.000 | 0.051 | 15.049 |
| CHW26_233-Fsp | 68.35 | 11.80 | 0.02 | 0.27 | 0.02 | 19.75 | 0.00 | 0.01 | 0.02 | 0.00 | 0.00 | 100.25 | 8.943 | 2.992 | 0.003 | 0.038 | 0.003 | 3.046 | 0.000 | 0.001 | 0.002 | 0.000 | 0.000 | 15.029 |
| CHW26_234-Fsp | 65.06 | 1.40 | 14.79 | 0.07 | 0.00 | 18.79 | 0.00 | 0.07 | 0.02 | 0.03 | 0.39 | 100.62 | 8.950 | 0.374 | 2.596 | 0.010 | 0.000 | 3.047 | 0.000 | 0.006 | 0.002 | 0.004 | 0.021 | 15.009 |
| CHW26_235-Fsp | 65.06 | 1.29 | 14.94 | 0.05 | 0.06 | 18.74 | 0.01 | 0.05 | 0.02 | 0.01 | 0.75 | 100.99 | 8.947 | 0.345 | 2.621 | 0.008 | 0.007 | 3.038 | 0.001 | 0.004 | 0.002 | 0.001 | 0.041 | 15.015 |
| CHW26_236-Fsp | 68.31 | 11.39 | 0.15 | 0.39 | 0.01 | 19.93 | 0.01 | 0.05 | 0.00 | 0.00 | 0.01 | 100.24 | 8.936 | 2.888 | 0.025 | 0.055 | 0.001 | 3.073 | 0.001 | 0.004 | 0.000 | 0.000 | 0.000 | 14.984 |
| CHW26_237-Fsp | 65.06 | 1.18 | 15.05 | 0.01 | 0.01 | 18.71 | 0.00 | 0.00 | 0.03 | 0.00 | 0.38 | 100.42 | 8.965 | 0.314 | 2.647 | 0.001 | 0.001 | 3.040 | 0.000 | 0.000 | 0.003 | 0.000 | 0.021 | 14.992 |
| CHW26_238-Fsp | 64.54 | 1.20 | 15.01 | 0.04 | 0.00 | 18.98 | 0.00 | 0.05 | 0.02 | 0.00 | 0.48 | 100.32 | 8.919 | 0.323 | 2.646 | 0.006 | 0.000 | 3.091 | 0.000 | 0.004 | 0.002 | 0.000 | 0.026 | 15.018 |
| CHW26_239-Fsp | 68.28 | 11.32 | 0.03 | 0.28 | 0.00 | 19.92 | 0.00 | 0.00 | 0.00 | 0.00 | 0.04 | 99.87 | 8.950 | 2.878 | 0.005 | 0.039 | 0.000 | 3.078 | 0.000 | 0.000 | 0.000 | 0.000 | 0.002 | 14.952 |
| CHW26_240-Fsp | 64.39 | 0.70 | 15.81 | 0.00 | 0.00 | 18.62 | 0.00 | 0.04 | 0.00 | 0.00 | 0.00 | 99.56 | 8.959 | 0.188 | 2.806 | 0.000 | 0.000 | 3.054 | 0.000 | 0.003 | 0.000 | 0.000 | 0.000 | 15.011 |
| CHW26_241-Fsp | 65.46 | 2.37 | 13.29 | 0.17 | 0.03 | 18.86 | 0.00 | 0.01 | 0.05 | 0.00 | 0.18 | 100.41 | 8.957 | 0.628 | 2.321 | 0.026 | 0.003 | 3.042 | 0.000 | 0.000 | 0.005 | 0.000 | 0.010 | 14.991 |
| CHW26_242-Fsp | 64.71 | 0.64 | 15.89 | 0.00 | 0.00 | 18.56 | 0.00 | 0.00 | 0.00 | 0.01 | 0.06 | 99.87 | 8.975 | 0.173 | 2.813 | 0.000 | 0.000 | 3.035 | 0.000 | 0.000 | 0.000 | 0.001 | 0.003 | 15.000 |

# Analyses of feldspar from sandstones (continuation)

| Sample / No. | $SiO_2$ | $Na_2O$ | $K_2O$ | CaO | FeO | $Al_2O_3$ | MgO | SrO | $TiO_2$ | MnO | BaO | wt-total | Si_at | Na_at | K_at | Ca_at | Fe_at | Al_at | Mg_at | Sr_at | Ti_at | Mn_at | Ba_at | at-total |
|---|---|---|---|---|---|---|---|---|---|---|---|---|---|---|---|---|---|---|---|---|---|---|---|---|
| CHW26_243-Fsp | 68.53 | 11.57 | 0.05 | 0.20 | 0.01 | 19.54 | 0.00 | 0.00 | 0.00 | 0.02 | 0.00 | 99.94 | 8.981 | 2.940 | 0.009 | 0.028 | 0.002 | 3.018 | 0.000 | 0.000 | 0.000 | 0.002 | 0.000 | 14.983 |
| CHW26_244-Fsp | 68.41 | 11.64 | 0.05 | 0.15 | 0.05 | 19.59 | 0.01 | 0.09 | 0.04 | 0.00 | 0.03 | 100.06 | 8.966 | 2.958 | 0.009 | 0.021 | 0.006 | 3.026 | 0.001 | 0.007 | 0.004 | 0.000 | 0.001 | 15.000 |
| CHW26_245-Fsp | 63.73 | 9.77 | 0.35 | 3.10 | 0.01 | 22.55 | 0.00 | 0.00 | 0.00 | 0.00 | 0.01 | 99.52 | 8.481 | 2.521 | 0.060 | 0.442 | 0.002 | 3.537 | 0.000 | 0.000 | 0.000 | 0.000 | 0.000 | 15.041 |
| CHW26_246-Fsp | 68.02 | 11.75 | 0.04 | 0.29 | 0.03 | 19.72 | 0.00 | 0.01 | 0.00 | 0.00 | 0.01 | 99.91 | 8.934 | 2.991 | 0.007 | 0.041 | 0.003 | 3.053 | 0.000 | 0.001 | 0.000 | 0.000 | 0.001 | 15.036 |
| CHW26_247-Fsp | 64.57 | 1.81 | 13.96 | 0.25 | 0.01 | 19.11 | 0.00 | 0.03 | 0.01 | 0.02 | 0.25 | 100.02 | 8.905 | 0.485 | 2.457 | 0.037 | 0.002 | 3.106 | 0.000 | 0.002 | 0.001 | 0.002 | 0.014 | 15.011 |
| CHW26_248-Fsp | 68.57 | 11.63 | 0.03 | 0.40 | 0.00 | 19.88 | 0.00 | 0.03 | 0.00 | 0.01 | 0.00 | 100.56 | 8.941 | 2.941 | 0.006 | 0.056 | 0.000 | 3.056 | 0.000 | 0.003 | 0.000 | 0.001 | 0.000 | 15.004 |
| CHW26_249-Fsp | 68.44 | 11.55 | 0.05 | 0.31 | 0.00 | 19.75 | 0.00 | 0.02 | 0.00 | 0.03 | 0.00 | 100.16 | 8.956 | 2.930 | 0.008 | 0.043 | 0.000 | 3.046 | 0.000 | 0.002 | 0.000 | 0.004 | 0.000 | 14.989 |
| CHW26_250-Fsp | 63.81 | 9.52 | 0.26 | 3.40 | 0.14 | 22.21 | 0.00 | 0.04 | 0.03 | 0.02 | 0.04 | 99.48 | 8.501 | 2.459 | 0.044 | 0.485 | 0.016 | 3.488 | 0.000 | 0.003 | 0.003 | 0.003 | 0.002 | 15.004 |
| CHW26_254-Fsp | 68.41 | 11.89 | 0.02 | 0.14 | 0.01 | 19.69 | 0.00 | 0.06 | 0.00 | 0.00 | 0.00 | 100.22 | 8.953 | 3.018 | 0.004 | 0.020 | 0.001 | 3.038 | 0.000 | 0.004 | 0.000 | 0.000 | 0.000 | 15.038 |
| CHW06_001-Fsp | 64.68 | 0.40 | 15.96 | 0.01 | 0.04 | 18.43 | 0.04 | 0.00 | 0.00 | 0.00 | 0.32 | 99.87 | 8.986 | 0.108 | 2.828 | 0.001 | 0.004 | 3.019 | 0.008 | 0.000 | 0.000 | 0.000 | 0.017 | 14.973 |
| CHW06_002-Fsp | 68.77 | 11.49 | 0.14 | 0.23 | 0.00 | 19.69 | 0.00 | 0.00 | 0.03 | 0.01 | 0.03 | 100.38 | 8.975 | 2.909 | 0.023 | 0.033 | 0.000 | 3.029 | 0.000 | 0.000 | 0.003 | 0.001 | 0.001 | 14.973 |
| CHW06_003-Fsp | 66.08 | 3.20 | 12.02 | 0.23 | 0.03 | 18.78 | 0.00 | 0.03 | 0.02 | 0.03 | 0.06 | 100.47 | 8.986 | 0.843 | 2.085 | 0.034 | 0.003 | 3.010 | 0.000 | 0.003 | 0.002 | 0.003 | 0.003 | 14.972 |
| CHW06_004-Fsp | 64.89 | 0.22 | 16.33 | 0.00 | 0.00 | 18.52 | 0.01 | 0.02 | 0.01 | 0.00 | 0.50 | 100.49 | 8.982 | 0.058 | 2.883 | 0.000 | 0.000 | 3.021 | 0.002 | 0.001 | 0.001 | 0.000 | 0.027 | 14.977 |
| CHW06_005-Fsp | 64.80 | 0.40 | 15.91 | 0.02 | 0.01 | 18.57 | 0.06 | 0.00 | 0.00 | 0.01 | 0.48 | 100.26 | 8.975 | 0.108 | 2.812 | 0.003 | 0.001 | 3.032 | 0.012 | 0.000 | 0.000 | 0.001 | 0.026 | 14.969 |
| CHW06_006-Fsp | 68.85 | 11.47 | 0.02 | 0.18 | 0.04 | 19.45 | 0.02 | 0.00 | 0.00 | 0.02 | 0.06 | 100.12 | 9.003 | 2.909 | 0.004 | 0.025 | 0.005 | 2.998 | 0.004 | 0.000 | 0.000 | 0.002 | 0.003 | 14.954 |
| CHW06_007-Fsp | 65.88 | 4.55 | 10.26 | 0.20 | 0.04 | 19.00 | 0.02 | 0.04 | 0.02 | 0.03 | 0.03 | 100.07 | 8.949 | 1.198 | 1.779 | 0.029 | 0.005 | 3.042 | 0.005 | 0.004 | 0.002 | 0.003 | 0.002 | 15.016 |
| CHW06_008-Fsp | 64.66 | 0.18 | 16.02 | 0.00 | 0.00 | 18.69 | 0.01 | 0.00 | 0.04 | 0.00 | 0.70 | 100.29 | 8.965 | 0.047 | 2.833 | 0.000 | 0.000 | 3.054 | 0.002 | 0.000 | 0.005 | 0.000 | 0.038 | 14.943 |
| CHW06_009-Fsp | 64.03 | 0.20 | 16.39 | 0.00 | 0.02 | 18.27 | 0.01 | 0.00 | 0.00 | 0.00 | 0.51 | 99.43 | 8.974 | 0.056 | 2.930 | 0.000 | 0.003 | 3.018 | 0.002 | 0.000 | 0.000 | 0.000 | 0.028 | 15.010 |
| CHW06_010-Fsp | 66.07 | 3.33 | 11.84 | 0.19 | 0.04 | 18.98 | 0.02 | 0.01 | 0.03 | 0.00 | 0.13 | 100.63 | 8.967 | 0.875 | 2.050 | 0.027 | 0.005 | 3.036 | 0.004 | 0.001 | 0.003 | 0.000 | 0.007 | 14.975 |
| CHW06_011-Fsp | 64.70 | 0.31 | 16.17 | 0.03 | 0.01 | 18.55 | 0.05 | 0.00 | 0.04 | 0.03 | 0.50 | 100.38 | 8.965 | 0.084 | 2.858 | 0.005 | 0.001 | 3.030 | 0.011 | 0.000 | 0.004 | 0.003 | 0.027 | 14.987 |
| CHW06_012-Fsp | 65.19 | 0.32 | 16.03 | 0.00 | 0.00 | 18.47 | 0.00 | 0.00 | 0.04 | 0.00 | 0.45 | 100.50 | 9.002 | 0.086 | 2.824 | 0.000 | 0.000 | 3.006 | 0.000 | 0.000 | 0.004 | 0.000 | 0.024 | 14.946 |
| CHW06_013-Fsp | 64.60 | 0.24 | 16.10 | 0.01 | 0.04 | 18.56 | 0.02 | 0.01 | 0.01 | 0.01 | 0.67 | 100.30 | 8.966 | 0.066 | 2.851 | 0.002 | 0.005 | 3.036 | 0.004 | 0.001 | 0.001 | 0.002 | 0.037 | 14.972 |
| CHW06_014-Fsp | 64.75 | 0.38 | 15.69 | 0.03 | 0.05 | 18.42 | 0.01 | 0.00 | 0.01 | 0.00 | 0.44 | 99.78 | 8.997 | 0.104 | 2.782 | 0.004 | 0.006 | 3.016 | 0.002 | 0.000 | 0.001 | 0.000 | 0.024 | 14.937 |
| CHW06_015-Fsp | 66.16 | 4.13 | 10.86 | 0.06 | 0.03 | 18.84 | 0.00 | 0.08 | 0.03 | 0.01 | 0.36 | 100.56 | 8.977 | 1.086 | 1.880 | 0.009 | 0.003 | 3.012 | 0.000 | 0.007 | 0.003 | 0.001 | 0.019 | 14.997 |
| CHW06_016-Fsp | 65.11 | 0.10 | 16.44 | 0.00 | 0.00 | 18.49 | 0.02 | 0.00 | 0.00 | 0.01 | 0.29 | 100.47 | 8.998 | 0.026 | 2.898 | 0.000 | 0.000 | 3.012 | 0.004 | 0.000 | 0.000 | 0.001 | 0.016 | 14.957 |
| CHW06_017-Fsp | 64.25 | 0.47 | 15.80 | 0.00 | 0.05 | 18.34 | 0.06 | 0.00 | 0.00 | 0.18 | 0.33 | 99.48 | 8.971 | 0.128 | 2.814 | 0.000 | 0.005 | 3.018 | 0.013 | 0.000 | 0.000 | 0.022 | 0.018 | 14.991 |
| CHW06_018-Fsp | 64.87 | 0.36 | 15.99 | 0.00 | 0.01 | 18.41 | 0.04 | 0.03 | 0.00 | 0.01 | 0.28 | 99.99 | 8.998 | 0.097 | 2.829 | 0.000 | 0.002 | 3.009 | 0.008 | 0.002 | 0.000 | 0.001 | 0.015 | 14.961 |
| CHW06_019-Fsp | 65.33 | 0.16 | 16.40 | 0.00 | 0.02 | 18.63 | 0.00 | 0.00 | 0.04 | 0.00 | 0.43 | 101.01 | 8.987 | 0.042 | 2.878 | 0.000 | 0.002 | 3.021 | 0.001 | 0.000 | 0.004 | 0.000 | 0.023 | 14.958 |
| CHW06_020-Fsp | 65.20 | 0.13 | 16.54 | 0.00 | 0.03 | 18.48 | 0.00 | 0.00 | 0.01 | 0.00 | 0.35 | 100.77 | 8.995 | 0.036 | 2.911 | 0.000 | 0.004 | 3.006 | 0.000 | 0.000 | 0.001 | 0.000 | 0.019 | 14.973 |
| CHW06_021-Fsp | 64.77 | 0.23 | 16.08 | 0.00 | 0.01 | 18.45 | 0.03 | 0.00 | 0.03 | 0.00 | 0.42 | 100.03 | 8.991 | 0.061 | 2.848 | 0.000 | 0.002 | 3.019 | 0.005 | 0.000 | 0.003 | 0.000 | 0.023 | 14.951 |
| CHW06_022-Fsp | 64.87 | 0.25 | 16.18 | 0.00 | 0.00 | 18.50 | 0.00 | 0.06 | 0.00 | 0.00 | 0.56 | 100.43 | 8.984 | 0.067 | 2.859 | 0.000 | 0.000 | 3.021 | 0.000 | 0.005 | 0.000 | 0.000 | 0.030 | 14.967 |
| CHW06_023-Fsp | 64.74 | 0.34 | 16.10 | 0.05 | 0.05 | 18.53 | 0.03 | 0.00 | 0.04 | 0.00 | 0.47 | 100.37 | 8.968 | 0.092 | 2.845 | 0.007 | 0.006 | 3.026 | 0.006 | 0.000 | 0.004 | 0.000 | 0.026 | 14.982 |
| CHW06_024-Fsp | 64.42 | 0.24 | 15.97 | 0.26 | 0.00 | 18.53 | 0.03 | 0.05 | 0.01 | 0.00 | 0.64 | 100.17 | 8.954 | 0.065 | 2.831 | 0.039 | 0.000 | 3.036 | 0.006 | 0.004 | 0.001 | 0.000 | 0.035 | 14.974 |
| CHW06_025-Fsp | 64.68 | 0.34 | 15.86 | 0.01 | 0.05 | 18.40 | 0.02 | 0.00 | 0.01 | 0.00 | 0.40 | 99.77 | 8.994 | 0.093 | 2.815 | 0.002 | 0.005 | 3.015 | 0.005 | 0.000 | 0.001 | 0.000 | 0.022 | 14.951 |
| CHW06_026-Fsp | 66.64 | 4.47 | 9.68 | 0.37 | 0.07 | 19.02 | 0.01 | 0.01 | 0.00 | 0.02 | 0.18 | 100.48 | 8.986 | 1.170 | 1.665 | 0.054 | 0.008 | 3.023 | 0.002 | 0.001 | 0.000 | 0.003 | 0.009 | 14.920 |
| CHW06_027-Fsp | 67.44 | 11.00 | 0.09 | 0.41 | 0.12 | 19.95 | 0.11 | 0.00 | 0.00 | 0.00 | 0.00 | 99.13 | 8.913 | 2.820 | 0.015 | 0.059 | 0.013 | 3.108 | 0.022 | 0.000 | 0.000 | 0.000 | 0.000 | 14.950 |
| CHW06_028-Fsp | 67.69 | 11.19 | 0.19 | 0.48 | 0.07 | 20.00 | 0.08 | 0.04 | 0.00 | 0.00 | 0.00 | 99.75 | 8.905 | 2.855 | 0.032 | 0.068 | 0.008 | 3.102 | 0.015 | 0.003 | 0.000 | 0.000 | 0.000 | 14.988 |
| CHW06_029-Fsp | 68.21 | 11.21 | 0.26 | 0.52 | 0.11 | 19.79 | 0.05 | 0.00 | 0.02 | 0.02 | 0.00 | 100.20 | 8.935 | 2.846 | 0.044 | 0.074 | 0.012 | 3.055 | 0.010 | 0.000 | 0.002 | 0.002 | 0.000 | 14.980 |
| CHW06_030-Fsp | 68.71 | 11.60 | 0.04 | 0.37 | 0.01 | 19.81 | 0.00 | 0.04 | 0.06 | 0.01 | 0.00 | 100.66 | 8.950 | 2.929 | 0.007 | 0.051 | 0.001 | 3.042 | 0.000 | 0.003 | 0.006 | 0.001 | 0.000 | 14.991 |
| CHW06_031-Fsp | 67.24 | 11.01 | 0.35 | 0.52 | 0.04 | 20.31 | 0.09 | 0.03 | 0.04 | 0.00 | 0.02 | 99.65 | 8.862 | 2.814 | 0.060 | 0.074 | 0.004 | 3.155 | 0.018 | 0.002 | 0.004 | 0.000 | 0.001 | 14.994 |
| CHW06_032-Fsp | 68.45 | 11.44 | 0.04 | 0.46 | 0.05 | 19.79 | 0.01 | 0.00 | 0.03 | 0.02 | 0.00 | 100.32 | 8.945 | 2.900 | 0.006 | 0.064 | 0.006 | 3.049 | 0.002 | 0.000 | 0.003 | 0.003 | 0.000 | 14.979 |
| CHW06_033-Fsp | 68.44 | 11.47 | 0.04 | 0.37 | 0.05 | 19.79 | 0.00 | 0.03 | 0.01 | 0.02 | 0.00 | 100.22 | 8.951 | 2.910 | 0.006 | 0.052 | 0.006 | 3.051 | 0.000 | 0.002 | 0.001 | 0.002 | 0.000 | 14.980 |
| CHW06_034-Fsp | 68.25 | 11.24 | 0.06 | 0.44 | 0.04 | 19.79 | 0.01 | 0.00 | 0.01 | 0.02 | 0.00 | 99.86 | 8.952 | 2.858 | 0.009 | 0.062 | 0.005 | 3.060 | 0.002 | 0.000 | 0.001 | 0.002 | 0.000 | 14.951 |
| CHW06_035-Fsp | 68.65 | 11.66 | 0.06 | 0.37 | 0.04 | 19.58 | 0.00 | 0.00 | 0.02 | 0.01 | 0.01 | 100.41 | 8.967 | 2.953 | 0.010 | 0.052 | 0.004 | 3.014 | 0.000 | 0.000 | 0.002 | 0.001 | 0.000 | 15.005 |
| CHW06_036-Fsp | 68.25 | 11.54 | 0.04 | 0.37 | 0.04 | 19.80 | 0.00 | 0.03 | 0.00 | 0.00 | 0.00 | 100.07 | 8.943 | 2.933 | 0.006 | 0.052 | 0.004 | 3.057 | 0.000 | 0.002 | 0.000 | 0.000 | 0.000 | 14.998 |
| CHW06_037-Fsp | 68.65 | 11.38 | 0.02 | 0.54 | 0.00 | 20.03 | 0.01 | 0.01 | 0.01 | 0.00 | 0.07 | 100.71 | 8.935 | 2.873 | 0.004 | 0.076 | 0.000 | 3.072 | 0.001 | 0.001 | 0.001 | 0.000 | 0.003 | 14.967 |
| CHW06_038-Fsp | 68.41 | 11.54 | 0.03 | 0.38 | 0.05 | 19.77 | 0.01 | 0.00 | 0.00 | 0.00 | 0.00 | 100.19 | 8.950 | 2.928 | 0.006 | 0.053 | 0.006 | 3.049 | 0.002 | 0.000 | 0.000 | 0.000 | 0.000 | 14.992 |
| CHW06_039-Fsp | 68.72 | 11.53 | 0.04 | 0.34 | 0.00 | 19.88 | 0.00 | 0.00 | 0.02 | 0.00 | 0.00 | 100.53 | 8.954 | 2.913 | 0.006 | 0.047 | 0.000 | 3.053 | 0.000 | 0.000 | 0.002 | 0.000 | 0.000 | 14.976 |
| CHW06_040-Fsp | 68.67 | 11.52 | 0.05 | 0.28 | 0.02 | 19.67 | 0.00 | 0.00 | 0.01 | 0.00 | 0.04 | 100.25 | 8.974 | 2.918 | 0.008 | 0.039 | 0.002 | 3.030 | 0.000 | 0.000 | 0.001 | 0.000 | 0.002 | 14.973 |
| CHW06_041-Fsp | 68.36 | 11.46 | 0.03 | 0.43 | 0.03 | 19.71 | 0.01 | 0.00 | 0.00 | 0.00 | 0.02 | 100.04 | 8.955 | 2.910 | 0.005 | 0.060 | 0.003 | 3.044 | 0.003 | 0.000 | 0.000 | 0.000 | 0.001 | 14.980 |
| CHW06_042-Fsp | 68.75 | 11.43 | 0.05 | 0.31 | 0.00 | 19.80 | 0.01 | 0.06 | 0.00 | 0.02 | 0.06 | 100.50 | 8.965 | 2.891 | 0.009 | 0.044 | 0.000 | 3.044 | 0.001 | 0.005 | 0.000 | 0.003 | 0.003 | 14.963 |
| CHW06_043-Fsp | 68.63 | 11.39 | 0.02 | 0.39 | 0.00 | 19.70 | 0.02 | 0.02 | 0.02 | 0.00 | 0.01 | 100.20 | 8.969 | 2.887 | 0.003 | 0.054 | 0.000 | 3.035 | 0.004 | 0.002 | 0.002 | 0.000 | 0.000 | 14.956 |

| Sample / No. | $SiO_2$ | $Na_2O$ | $K_2O$ | CaO | FeO | $Al_2O_3$ | MgO | SrO | $TiO_2$ | MnO | BaO | wt-total | Si_at | Na_at | K_at | Ca_at | Fe_at | Al_at | Mg_at | Sr_at | Ti_at | Mn_at | Ba_at | at-total |
|---|---|---|---|---|---|---|---|---|---|---|---|---|---|---|---|---|---|---|---|---|---|---|---|---|
| CHW06_044-Fsp | 68.24 | 11.44 | 0.04 | 0.43 | 0.04 | 19.86 | 0.00 | 0.00 | 0.01 | 0.01 | 0.00 | 100.07 | 8.939 | 2.906 | 0.006 | 0.060 | 0.005 | 3.067 | 0.000 | 0.000 | 0.001 | 0.001 | 0.000 | 14.983 |
| CHW06_045-Fsp | 68.80 | 11.65 | 0.05 | 0.24 | 0.01 | 19.63 | 0.01 | 0.02 | 0.00 | 0.00 | 0.00 | 100.43 | 8.976 | 2.948 | 0.009 | 0.033 | 0.001 | 3.019 | 0.001 | 0.002 | 0.000 | 0.000 | 0.000 | 14.991 |
| CHW06_046-Fsp | 68.27 | 11.54 | 0.09 | 0.37 | 0.03 | 19.95 | 0.00 | 0.01 | 0.01 | 0.00 | 0.02 | 100.29 | 8.929 | 2.928 | 0.015 | 0.052 | 0.003 | 3.075 | 0.000 | 0.001 | 0.001 | 0.000 | 0.001 | 15.004 |
| CHW06_047-Fsp | 68.25 | 11.57 | 0.11 | 0.38 | 0.06 | 19.68 | 0.02 | 0.00 | 0.03 | 0.00 | 0.00 | 100.11 | 8.945 | 2.940 | 0.018 | 0.053 | 0.006 | 3.039 | 0.003 | 0.000 | 0.003 | 0.000 | 0.000 | 15.011 |
| CHW06_048-Fsp | 68.67 | 11.37 | 0.01 | 0.29 | 0.00 | 19.69 | 0.00 | 0.00 | 0.02 | 0.03 | 0.00 | 100.08 | 8.978 | 2.883 | 0.002 | 0.041 | 0.000 | 3.035 | 0.001 | 0.000 | 0.002 | 0.003 | 0.000 | 14.945 |
| CHW06_049-Fsp | 68.60 | 11.47 | 0.05 | 0.39 | 0.03 | 19.83 | 0.00 | 0.00 | 0.00 | 0.00 | 0.00 | 100.37 | 8.955 | 2.903 | 0.008 | 0.055 | 0.004 | 3.051 | 0.000 | 0.000 | 0.000 | 0.000 | 0.000 | 14.975 |
| CHW06_050-Fsp | 68.61 | 11.47 | 0.04 | 0.32 | 0.00 | 19.67 | 0.00 | 0.05 | 0.04 | 0.03 | 0.00 | 100.23 | 8.968 | 2.907 | 0.007 | 0.044 | 0.000 | 3.031 | 0.000 | 0.004 | 0.004 | 0.003 | 0.000 | 14.968 |
| CHW06_051-Fsp | 68.70 | 11.50 | 0.03 | 0.37 | 0.01 | 19.77 | 0.00 | 0.02 | 0.03 | 0.00 | 0.00 | 100.44 | 8.962 | 2.910 | 0.006 | 0.052 | 0.002 | 3.039 | 0.000 | 0.002 | 0.003 | 0.000 | 0.000 | 14.974 |
| CHW06_052-Fsp | 68.23 | 11.48 | 0.03 | 0.31 | 0.00 | 19.74 | 0.00 | 0.00 | 0.03 | 0.01 | 0.00 | 99.83 | 8.953 | 2.921 | 0.005 | 0.044 | 0.000 | 3.053 | 0.000 | 0.000 | 0.003 | 0.001 | 0.000 | 14.980 |
| CHW06_053-Fsp | 68.54 | 11.70 | 0.05 | 0.34 | 0.01 | 19.57 | 0.01 | 0.00 | 0.01 | 0.01 | 0.00 | 100.25 | 8.965 | 2.968 | 0.008 | 0.047 | 0.001 | 3.017 | 0.002 | 0.000 | 0.001 | 0.001 | 0.000 | 15.012 |
| CHW06_055-Fsp | 68.58 | 11.62 | 0.07 | 0.19 | 0.02 | 19.54 | 0.01 | 0.00 | 0.00 | 0.03 | 0.02 | 100.06 | 8.981 | 2.950 | 0.011 | 0.026 | 0.003 | 3.016 | 0.001 | 0.000 | 0.000 | 0.003 | 0.001 | 14.991 |
| TP03_Fsp01 | 64.06 | 0.97 | 14.74 | 0.00 | 0.04 | 18.80 | 0.01 | 0.05 | 0.02 | 0.00 | 0.69 | 99.37 | 8.935 | 0.263 | 2.623 | 0.000 | 0.004 | 3.091 | 0.001 | 0.004 | 0.002 | 0.000 | 0.038 | 14.960 |
| TP03_Fsp02 | 65.08 | 1.03 | 14.97 | 0.04 | 0.01 | 18.68 | 0.02 | 0.00 | 0.03 | 0.01 | 0.13 | 99.99 | 8.981 | 0.275 | 2.635 | 0.005 | 0.001 | 3.039 | 0.003 | 0.000 | 0.003 | 0.001 | 0.007 | 14.952 |
| TP03_Fsp03 | 64.10 | 1.31 | 14.36 | 0.05 | 0.02 | 18.70 | 0.00 | 0.08 | 0.03 | 0.00 | 0.25 | 98.90 | 8.947 | 0.356 | 2.558 | 0.007 | 0.002 | 3.076 | 0.000 | 0.007 | 0.003 | 0.000 | 0.014 | 14.969 |
| TP03_Fsp04 | 64.34 | 0.94 | 14.98 | 0.00 | 0.02 | 18.81 | 0.00 | 0.04 | 0.03 | 0.00 | 0.46 | 99.61 | 8.943 | 0.254 | 2.656 | 0.000 | 0.002 | 3.081 | 0.000 | 0.003 | 0.003 | 0.000 | 0.025 | 14.968 |
| TP03_Fsp05 | 64.72 | 0.95 | 14.96 | 0.04 | 0.05 | 18.65 | 0.00 | 0.04 | 0.04 | 0.03 | 0.13 | 99.60 | 8.973 | 0.255 | 2.646 | 0.006 | 0.006 | 3.048 | 0.000 | 0.003 | 0.004 | 0.003 | 0.007 | 14.950 |
| TP03_Fsp06 | 63.02 | 0.91 | 14.65 | 0.05 | 0.03 | 18.26 | 0.01 | 0.05 | 0.01 | 0.00 | 0.23 | 97.22 | 8.961 | 0.251 | 2.657 | 0.008 | 0.003 | 3.060 | 0.003 | 0.004 | 0.001 | 0.000 | 0.013 | 14.962 |
| TP03_Fsp07 | 63.92 | 0.95 | 15.00 | 0.00 | 0.01 | 18.39 | 0.00 | 0.00 | 0.00 | 0.00 | 0.10 | 98.38 | 8.977 | 0.259 | 2.687 | 0.000 | 0.002 | 3.044 | 0.001 | 0.000 | 0.000 | 0.000 | 0.006 | 14.974 |
| TP03_Fsp08 | 63.71 | 1.11 | 14.66 | 0.00 | 0.01 | 18.55 | 0.00 | 0.01 | 0.00 | 0.01 | 0.03 | 98.09 | 8.958 | 0.302 | 2.630 | 0.000 | 0.001 | 3.075 | 0.000 | 0.001 | 0.000 | 0.002 | 0.002 | 14.970 |
| TP03_Fsp09 | 64.14 | 0.97 | 14.67 | 0.01 | 0.00 | 18.47 | 0.00 | 0.02 | 0.02 | 0.00 | 0.17 | 98.47 | 8.984 | 0.263 | 2.622 | 0.001 | 0.000 | 3.049 | 0.000 | 0.002 | 0.002 | 0.000 | 0.010 | 14.932 |
| TP03_Fsp10 | 65.03 | 1.07 | 14.57 | 0.00 | 0.04 | 18.45 | 0.00 | 0.00 | 0.00 | 0.01 | 0.02 | 99.20 | 9.018 | 0.287 | 2.578 | 0.000 | 0.005 | 3.016 | 0.000 | 0.000 | 0.000 | 0.001 | 0.001 | 14.906 |
| TP03_Fsp11 | 64.79 | 1.39 | 14.10 | 0.05 | 0.00 | 18.62 | 0.00 | 0.07 | 0.05 | 0.01 | 0.20 | 99.28 | 8.983 | 0.374 | 2.495 | 0.007 | 0.000 | 3.043 | 0.000 | 0.005 | 0.005 | 0.001 | 0.011 | 14.925 |
| TP03_Fsp12 | 64.75 | 0.68 | 15.13 | 0.00 | 0.00 | 18.84 | 0.00 | 0.00 | 0.02 | 0.01 | 0.19 | 99.61 | 8.971 | 0.182 | 2.675 | 0.000 | 0.000 | 3.077 | 0.000 | 0.000 | 0.002 | 0.001 | 0.010 | 14.917 |
| TP03_Fsp13 | 64.45 | 0.84 | 15.04 | 0.00 | 0.01 | 18.66 | 0.00 | 0.00 | 0.02 | 0.00 | 0.14 | 99.16 | 8.973 | 0.226 | 2.671 | 0.000 | 0.001 | 3.062 | 0.000 | 0.000 | 0.003 | 0.000 | 0.008 | 14.942 |
| TP03_Fsp14 | 64.05 | 0.79 | 14.99 | 0.04 | 0.03 | 18.65 | 0.00 | 0.00 | 0.02 | 0.00 | 0.11 | 98.67 | 8.961 | 0.214 | 2.675 | 0.006 | 0.003 | 3.075 | 0.000 | 0.000 | 0.002 | 0.000 | 0.006 | 14.943 |
| TP03_Fsp16 | 64.46 | 0.85 | 14.84 | 0.00 | 0.00 | 18.65 | 0.00 | 0.04 | 0.02 | 0.00 | 0.52 | 99.38 | 8.971 | 0.230 | 2.635 | 0.000 | 0.000 | 3.059 | 0.000 | 0.003 | 0.003 | 0.000 | 0.028 | 14.929 |
| TP03_Fsp17 | 63.71 | 0.80 | 14.66 | 0.00 | 0.00 | 18.48 | 0.00 | 0.01 | 0.01 | 0.00 | 0.32 | 97.99 | 8.975 | 0.217 | 2.636 | 0.000 | 0.000 | 3.068 | 0.000 | 0.001 | 0.001 | 0.000 | 0.018 | 14.916 |
| TP03_Fsp19 | 65.04 | 1.01 | 14.81 | 0.00 | 0.02 | 18.49 | 0.01 | 0.06 | 0.00 | 0.00 | 0.26 | 99.71 | 9.003 | 0.270 | 2.616 | 0.000 | 0.003 | 3.018 | 0.002 | 0.005 | 0.001 | 0.000 | 0.014 | 14.931 |
| TP03_Fsp21 | 64.94 | 0.99 | 14.71 | 0.00 | 0.00 | 18.68 | 0.00 | 0.04 | 0.00 | 0.00 | 0.21 | 99.56 | 8.991 | 0.265 | 2.599 | 0.001 | 0.000 | 3.048 | 0.000 | 0.003 | 0.000 | 0.000 | 0.011 | 14.917 |
| TP03_Fsp22 | 63.49 | 1.08 | 14.64 | 0.00 | 0.02 | 18.60 | 0.00 | 0.01 | 0.02 | 0.01 | 0.12 | 97.99 | 8.945 | 0.294 | 2.631 | 0.000 | 0.003 | 3.089 | 0.000 | 0.001 | 0.002 | 0.001 | 0.007 | 14.972 |
| TP03_Fsp25 | 62.87 | 1.00 | 14.61 | 0.03 | 0.01 | 18.28 | 0.00 | 0.07 | 0.01 | 0.00 | 0.08 | 96.96 | 8.956 | 0.277 | 2.655 | 0.005 | 0.001 | 3.070 | 0.000 | 0.006 | 0.001 | 0.000 | 0.005 | 14.974 |
| TP03_Fsp26 | 64.02 | 1.07 | 14.55 | 0.01 | 0.03 | 18.60 | 0.00 | 0.02 | 0.02 | 0.00 | 0.07 | 98.38 | 8.968 | 0.290 | 2.600 | 0.002 | 0.004 | 3.070 | 0.000 | 0.002 | 0.002 | 0.000 | 0.004 | 14.940 |
| TP03_Fsp30 | 64.46 | 0.99 | 14.60 | 0.02 | 0.00 | 18.50 | 0.00 | 0.05 | 0.00 | 0.00 | 0.19 | 98.80 | 8.994 | 0.267 | 2.598 | 0.002 | 0.000 | 3.042 | 0.000 | 0.004 | 0.000 | 0.000 | 0.010 | 14.918 |
| ER04_223-Fsp | 65.49 | 0.69 | 15.91 | 0.00 | 0.05 | 18.58 | 0.00 | 0.00 | 0.02 | 0.01 | 0.16 | 100.92 | 8.991 | 0.184 | 2.788 | 0.000 | 0.006 | 3.007 | 0.000 | 0.000 | 0.002 | 0.001 | 0.008 | 14.989 |
| ER04_224-Fsp | 65.24 | 0.63 | 15.94 | 0.00 | 0.01 | 18.61 | 0.00 | 0.04 | 0.03 | 0.01 | 0.10 | 100.61 | 8.984 | 0.168 | 2.801 | 0.000 | 0.002 | 3.020 | 0.000 | 0.003 | 0.003 | 0.001 | 0.005 | 14.988 |
| ER04_225-Fsp | 65.30 | 0.54 | 15.88 | 0.00 | 0.00 | 18.77 | 0.00 | 0.00 | 0.04 | 0.00 | 0.19 | 100.73 | 8.977 | 0.144 | 2.785 | 0.000 | 0.000 | 3.041 | 0.000 | 0.000 | 0.004 | 0.000 | 0.010 | 14.962 |
| ER04_226-Fsp | 65.45 | 0.69 | 15.81 | 0.00 | 0.05 | 18.39 | 0.00 | 0.00 | 0.02 | 0.00 | 0.07 | 100.48 | 9.013 | 0.185 | 2.779 | 0.000 | 0.006 | 2.985 | 0.001 | 0.000 | 0.002 | 0.000 | 0.004 | 14.974 |
| ER04_227-Fsp | 64.66 | 0.91 | 14.91 | 0.00 | 0.01 | 18.84 | 0.00 | 0.14 | 0.05 | 0.04 | 1.20 | 100.77 | 8.934 | 0.244 | 2.628 | 0.000 | 0.001 | 3.068 | 0.000 | 0.011 | 0.006 | 0.005 | 0.065 | 14.962 |
| ER04_230-Fsp | 64.28 | 0.86 | 14.97 | 0.01 | 0.00 | 18.87 | 0.00 | 0.04 | 0.02 | 0.00 | 1.34 | 100.39 | 8.923 | 0.232 | 2.652 | 0.001 | 0.000 | 3.087 | 0.000 | 0.003 | 0.002 | 0.001 | 0.073 | 14.974 |
| ER04_231-Fsp | 65.71 | 0.81 | 15.76 | 0.02 | 0.03 | 18.66 | 0.01 | 0.04 | 0.03 | 0.00 | 0.06 | 101.14 | 8.990 | 0.216 | 2.750 | 0.004 | 0.004 | 3.010 | 0.002 | 0.003 | 0.003 | 0.000 | 0.003 | 14.985 |
| ER04_232-Fsp | 64.90 | 0.89 | 15.33 | 0.00 | 0.03 | 18.56 | 0.00 | 0.00 | 0.03 | 0.00 | 0.64 | 100.41 | 8.972 | 0.238 | 2.704 | 0.000 | 0.003 | 3.025 | 0.000 | 0.000 | 0.003 | 0.000 | 0.035 | 14.982 |
| ER04_233-Fsp | 65.01 | 0.75 | 15.89 | 0.00 | 0.00 | 18.49 | 0.00 | 0.06 | 0.01 | 0.00 | 0.41 | 100.62 | 8.978 | 0.200 | 2.800 | 0.000 | 0.000 | 3.010 | 0.000 | 0.005 | 0.001 | 0.000 | 0.022 | 15.016 |
| ER04_234-Fsp | 65.29 | 0.69 | 15.52 | 0.00 | 0.00 | 18.46 | 0.01 | 0.01 | 0.04 | 0.02 | 0.29 | 100.33 | 9.006 | 0.185 | 2.732 | 0.000 | 0.000 | 3.001 | 0.003 | 0.001 | 0.004 | 0.002 | 0.016 | 14.948 |
| ER04_234-Fsp | 63.93 | 0.98 | 15.09 | 0.06 | 0.03 | 18.34 | 0.00 | 0.05 | 0.04 | 0.00 | 0.58 | 99.10 | 8.959 | 0.265 | 2.699 | 0.009 | 0.003 | 3.030 | 0.000 | 0.004 | 0.005 | 0.000 | 0.032 | 15.004 |
| ER04_235-Fsp | 65.36 | 0.93 | 15.79 | 0.00 | 0.03 | 18.54 | 0.01 | 0.00 | 0.00 | 0.04 | 0.06 | 100.78 | 8.985 | 0.247 | 2.769 | 0.000 | 0.004 | 3.003 | 0.002 | 0.000 | 0.000 | 0.005 | 0.003 | 15.020 |
| ER04_236-Fsp | 65.26 | 1.00 | 15.34 | 0.00 | 0.01 | 18.62 | 0.00 | 0.00 | 0.04 | 0.04 | 0.36 | 100.67 | 8.979 | 0.266 | 2.692 | 0.000 | 0.002 | 3.020 | 0.000 | 0.000 | 0.004 | 0.005 | 0.019 | 14.987 |
| ER04_237-Fsp | 64.97 | 0.75 | 15.64 | 0.00 | 0.04 | 18.49 | 0.00 | 0.08 | 0.03 | 0.00 | 0.16 | 100.19 | 8.984 | 0.201 | 2.760 | 0.000 | 0.005 | 3.014 | 0.000 | 0.007 | 0.003 | 0.000 | 0.009 | 14.985 |
| ER04_240-Fsp | 64.26 | 0.78 | 15.11 | 0.01 | 0.00 | 18.85 | 0.01 | 0.08 | 0.03 | 0.00 | 1.33 | 100.45 | 8.921 | 0.210 | 2.676 | 0.002 | 0.000 | 3.084 | 0.002 | 0.006 | 0.003 | 0.000 | 0.072 | 14.976 |
| ER04_241-Fsp | 65.32 | 0.77 | 15.88 | 0.04 | 0.02 | 18.41 | 0.02 | 0.00 | 0.00 | 0.00 | 0.02 | 100.49 | 9.001 | 0.206 | 2.791 | 0.006 | 0.003 | 2.991 | 0.005 | 0.000 | 0.000 | 0.000 | 0.001 | 15.003 |

## Analyses of feldspar from volcanic lithoclasts within sandstones

| Sample / No. | $SiO_2$ | $Na_2O$ | $K_2O$ | CaO | FeO | $Al_2O_3$ | MgO | SrO | $TiO_2$ | MnO | BaO | wt-total | Si_at | Na_at | K_at | Ca_at | Fe_at | Al_at | Mg_at | Sr_at | Ti_at | Mn_at | Ba_at | at-total |
|---|---|---|---|---|---|---|---|---|---|---|---|---|---|---|---|---|---|---|---|---|---|---|---|---|
| RB06_046-VRF-Fsp | 60.44 | 6.97 | 2.27 | 4.74 | 1.05 | 22.56 | 0.07 | 0.09 | 0.90 | 0.03 | 0.13 | 99.26 | 8.218 | 1.837 | 0.394 | 0.690 | 0.119 | 3.616 | 0.015 | 0.007 | 0.092 | 0.004 | 0.007 | 15.00 |
| TI14_091-VRF-Fsp | 60.13 | 6.78 | 1.63 | 5.90 | 0.60 | 23.44 | 0.05 | 0.10 | 0.04 | 0.00 | 0.15 | 98.83 | 8.181 | 1.788 | 0.284 | 0.861 | 0.068 | 3.759 | 0.010 | 0.008 | 0.004 | 0.000 | 0.008 | 14.97 |
| TI14_094-VRF-Fsp | 57.84 | 6.57 | 0.37 | 8.23 | 0.59 | 25.98 | 0.05 | 0.17 | 0.06 | 0.02 | 0.09 | 99.98 | 7.804 | 1.718 | 0.063 | 1.190 | 0.066 | 4.133 | 0.011 | 0.014 | 0.006 | 0.002 | 0.005 | 15.01 |
| TI14_095-VRF-Fsp | 65.81 | 7.73 | 3.48 | 2.03 | 0.32 | 20.33 | 0.03 | 0.00 | 0.09 | 0.00 | 0.13 | 99.95 | 8.777 | 1.999 | 0.593 | 0.290 | 0.036 | 3.195 | 0.006 | 0.000 | 0.009 | 0.000 | 0.007 | 14.91 |
| TI14_096-VRF-Fsp | 59.34 | 5.61 | 2.97 | 5.64 | 0.70 | 23.07 | 0.13 | 0.05 | 0.14 | 0.04 | 0.10 | 97.81 | 8.187 | 1.500 | 0.522 | 0.834 | 0.081 | 3.751 | 0.027 | 0.004 | 0.015 | 0.005 | 0.005 | 14.93 |
| TI14_097-VRF-Fsp | 59.06 | 6.80 | 0.66 | 7.39 | 0.37 | 25.29 | 0.01 | 0.11 | 0.03 | 0.03 | 0.08 | 99.84 | 7.952 | 1.776 | 0.114 | 1.066 | 0.042 | 4.013 | 0.003 | 0.009 | 0.003 | 0.003 | 0.004 | 14.98 |
| TI14_099-VRF-Fsp | 64.76 | 8.33 | 2.94 | 1.97 | 0.73 | 20.21 | 0.02 | 0.02 | 0.09 | 0.00 | 0.14 | 99.20 | 8.725 | 2.175 | 0.506 | 0.284 | 0.083 | 3.209 | 0.004 | 0.001 | 0.009 | 0.000 | 0.008 | 15.00 |
| TI14_100-VRF-Fsp | 63.16 | 6.25 | 1.77 | 5.04 | 0.54 | 21.26 | 0.05 | 0.08 | 0.07 | 0.04 | 0.14 | 98.40 | 8.551 | 1.641 | 0.306 | 0.730 | 0.061 | 3.393 | 0.010 | 0.006 | 0.007 | 0.004 | 0.008 | 14.72 |
| SR03_028-VRF-Fsp | 65.23 | 9.92 | 0.33 | 1.78 | 0.24 | 20.13 | 0.02 | 0.08 | 0.03 | 0.01 | 0.05 | 97.83 | 8.788 | 2.591 | 0.057 | 0.257 | 0.028 | 3.197 | 0.005 | 0.006 | 0.003 | 0.001 | 0.003 | 14.94 |
| SR03_030-VRF-Fsp | 66.42 | 10.63 | 0.36 | 0.82 | 0.19 | 19.21 | 0.03 | 0.07 | 0.04 | 0.05 | 0.03 | 97.84 | 8.927 | 2.770 | 0.062 | 0.118 | 0.022 | 3.043 | 0.006 | 0.005 | 0.004 | 0.005 | 0.002 | 14.96 |
| SR03_031-VRF-Fsp | 67.33 | 10.00 | 1.86 | 0.48 | 0.12 | 19.33 | 0.02 | 0.03 | 0.00 | 0.00 | 0.11 | 99.29 | 8.956 | 2.578 | 0.316 | 0.068 | 0.013 | 3.030 | 0.004 | 0.003 | 0.000 | 0.000 | 0.006 | 14.98 |
| SR03_032-VRF-Fsp | 67.90 | 11.42 | 0.07 | 0.38 | 0.09 | 19.80 | 0.02 | 0.00 | 0.00 | 0.00 | 0.02 | 99.71 | 8.932 | 2.912 | 0.011 | 0.053 | 0.010 | 3.070 | 0.004 | 0.000 | 0.000 | 0.000 | 0.001 | 15.00 |
| SR03_045-VRF-Fsp | 67.93 | 10.71 | 0.63 | 0.62 | 0.09 | 19.66 | 0.02 | 0.04 | 0.08 | 0.00 | 0.07 | 99.85 | 8.941 | 2.733 | 0.105 | 0.087 | 0.010 | 3.050 | 0.003 | 0.003 | 0.008 | 0.000 | 0.004 | 14.94 |
| SR03_047-VRF-Fsp | 66.83 | 9.79 | 2.09 | 0.36 | 0.16 | 19.05 | 0.03 | 0.03 | 0.05 | 0.03 | 0.10 | 98.52 | 8.966 | 2.547 | 0.358 | 0.051 | 0.018 | 3.012 | 0.007 | 0.003 | 0.005 | 0.004 | 0.005 | 14.98 |
| SR03_052-VRF-Fsp | 65.55 | 10.57 | 0.33 | 0.70 | 0.87 | 19.74 | 0.23 | 0.07 | 0.73 | 0.02 | 0.00 | 98.82 | 8.767 | 2.741 | 0.057 | 0.100 | 0.097 | 3.112 | 0.045 | 0.005 | 0.074 | 0.002 | 0.000 | 15.00 |

## Analyses of feldspar from mafic pyroclastic deposits (EHT event)

| Sample / No. | $SiO_2$ | $Na_2O$ | $K_2O$ | CaO | FeO | $Al_2O_3$ | MgO | SrO | $TiO_2$ | MnO | BaO | wt-total | Si_at | Na_at | K_at | Ca_at | Fe_at | Al_at | Mg_at | Sr_at | Ti_at | Mn_at | Ba_at | at-total |
|---|---|---|---|---|---|---|---|---|---|---|---|---|---|---|---|---|---|---|---|---|---|---|---|---|
| CE90_Fsp01 | 67.05 | 0.95 | 0.22 | 6.46 | 0.22 | 14.13 | 0.01 | 0.03 | 0.01 | 0.00 | 0.03 | 89.10 | 9.619 | 0.265 | 0.040 | 0.992 | 0.027 | 2.389 | 0.001 | 0.002 | 0.001 | 0.000 | 0.002 | 13.338 |
| CE90_Fsp02 | 67.66 | 1.00 | 0.14 | 6.26 | 0.28 | 13.88 | 0.01 | 0.00 | 0.00 | 0.02 | 0.10 | 89.35 | 9.670 | 0.278 | 0.026 | 0.959 | 0.034 | 2.338 | 0.001 | 0.000 | 0.000 | 0.002 | 0.006 | 13.313 |
| CE90_Fsp03 | 66.96 | 0.60 | 0.17 | 6.39 | 0.26 | 14.26 | 0.00 | 0.10 | 0.00 | 0.02 | 0.06 | 88.82 | 9.624 | 0.168 | 0.030 | 0.984 | 0.031 | 2.416 | 0.000 | 0.008 | 0.000 | 0.002 | 0.003 | 13.268 |
| CE90_Fsp04 | 66.29 | 0.55 | 0.17 | 6.21 | 0.25 | 14.02 | 0.01 | 0.08 | 0.00 | 0.01 | 0.10 | 87.69 | 9.643 | 0.155 | 0.032 | 0.969 | 0.031 | 2.404 | 0.002 | 0.007 | 0.000 | 0.001 | 0.006 | 13.248 |
| CE90_Fsp06 | 69.60 | 0.52 | 0.17 | 6.01 | 0.09 | 13.58 | 0.00 | 0.02 | 0.01 | 0.00 | 0.04 | 90.05 | 9.803 | 0.141 | 0.030 | 0.907 | 0.011 | 2.255 | 0.000 | 0.002 | 0.001 | 0.000 | 0.002 | 13.153 |
| CE90_Fsp08 | 65.11 | 0.73 | 0.19 | 6.81 | 0.14 | 14.84 | 0.01 | 0.04 | 0.02 | 0.01 | 0.08 | 87.97 | 9.483 | 0.205 | 0.036 | 1.063 | 0.017 | 2.547 | 0.001 | 0.004 | 0.002 | 0.002 | 0.005 | 13.363 |

## Analyses of feldspar from tuffaceous sandstones

| Sample / No. | $SiO_2$ | $Na_2O$ | $K_2O$ | CaO | FeO | $Al_2O_3$ | MgO | SrO | $TiO_2$ | MnO | BaO | wt-total | Si_at | Na_at | K_at | Ca_at | Fe_at | Al_at | Mg_at | Sr_at | Ti_at | Mn_at | Ba_at | at-total |
|---|---|---|---|---|---|---|---|---|---|---|---|---|---|---|---|---|---|---|---|---|---|---|---|---|
| SHA06_Fsp26 | 57.70 | 6.20 | 0.55 | 8.88 | 0.32 | 26.55 | 0.03 | 0.14 | 0.05 | 0.00 | 0.13 | 100.55 | 7.747 | 1.613 | 0.095 | 1.278 | 0.036 | 4.203 | 0.006 | 0.011 | 0.005 | 0.000 | 0.007 | 15.000 |
| SHA06_Fsp27 | 67.86 | 11.26 | 0.37 | 0.19 | 0.08 | 20.11 | 0.03 | 0.00 | 0.01 | 0.01 | 0.01 | 99.95 | 8.910 | 2.867 | 0.062 | 0.027 | 0.009 | 3.112 | 0.007 | 0.000 | 0.001 | 0.001 | 0.001 | 14.997 |
| SHA06_Fsp30 | 68.52 | 1.88 | 0.38 | 5.19 | 0.06 | 14.82 | 0.12 | 0.00 | 0.01 | 0.00 | 0.15 | 91.12 | 9.607 | 0.510 | 0.069 | 0.780 | 0.007 | 2.450 | 0.025 | 0.000 | 0.001 | 0.000 | 0.009 | 13.456 |
| SHA06_Fsp32 | 58.91 | 7.05 | 0.41 | 7.67 | 0.12 | 25.96 | 0.00 | 0.08 | 0.01 | 0.01 | 0.00 | 100.21 | 7.890 | 1.832 | 0.069 | 1.100 | 0.013 | 4.098 | 0.000 | 0.006 | 0.001 | 0.002 | 0.000 | 15.011 |
| SHA06_Fsp33 | 66.36 | 4.21 | 9.49 | 0.44 | 0.26 | 18.47 | 0.00 | 0.04 | 0.04 | 0.00 | 0.08 | 99.39 | 9.033 | 1.111 | 1.648 | 0.064 | 0.030 | 2.963 | 0.000 | 0.003 | 0.004 | 0.000 | 0.004 | 14.861 |
| SHA06_Fsp34 | 68.86 | 11.59 | 0.17 | 0.17 | 0.05 | 19.67 | 0.00 | 0.04 | 0.00 | 0.01 | 0.00 | 100.55 | 8.977 | 2.929 | 0.029 | 0.023 | 0.006 | 3.022 | 0.000 | 0.003 | 0.000 | 0.001 | 0.000 | 14.990 |
| SHA06_Fsp35 | 57.49 | 6.52 | 0.33 | 8.53 | 0.15 | 26.57 | 0.01 | 0.14 | 0.03 | 0.01 | 0.03 | 99.81 | 7.755 | 1.705 | 0.058 | 1.233 | 0.017 | 4.226 | 0.001 | 0.011 | 0.003 | 0.001 | 0.002 | 15.010 |
| SHA06_Fsp37 | 61.34 | 7.75 | 0.80 | 5.77 | 0.22 | 23.99 | 0.01 | 0.04 | 0.00 | 0.02 | 0.03 | 99.96 | 8.199 | 2.009 | 0.136 | 0.826 | 0.025 | 3.780 | 0.003 | 0.003 | 0.000 | 0.002 | 0.001 | 14.984 |
| SHA06_Fsp38 | 65.02 | 0.47 | 16.07 | 0.00 | 0.06 | 18.65 | 0.00 | 0.02 | 0.02 | 0.00 | 0.49 | 100.80 | 8.968 | 0.125 | 2.828 | 0.000 | 0.007 | 3.033 | 0.000 | 0.002 | 0.002 | 0.000 | 0.027 | 14.990 |
| SHA06_Fsp43 | 58.78 | 7.17 | 0.12 | 7.83 | 0.14 | 26.08 | 0.00 | 0.19 | 0.00 | 0.00 | 0.04 | 100.35 | 7.866 | 1.860 | 0.020 | 1.123 | 0.016 | 4.114 | 0.000 | 0.015 | 0.000 | 0.000 | 0.002 | 15.017 |
| SHA06_Fsp40 | 63.29 | 8.91 | 0.45 | 4.09 | 0.18 | 22.67 | 0.03 | 0.07 | 0.02 | 0.00 | 0.00 | 99.69 | 8.428 | 2.300 | 0.076 | 0.583 | 0.020 | 3.559 | 0.006 | 0.006 | 0.002 | 0.000 | 0.000 | 14.978 |
| SHA12_Fsp17 | 61.31 | 7.62 | 0.85 | 5.73 | 0.22 | 24.05 | 0.02 | 0.10 | 0.00 | 0.00 | 0.09 | 100.00 | 8.196 | 1.976 | 0.145 | 0.821 | 0.025 | 3.790 | 0.004 | 0.008 | 0.000 | 0.000 | 0.005 | 14.969 |
| SHA12_Fsp18 | 61.99 | 7.98 | 1.04 | 5.08 | 0.22 | 23.17 | 0.00 | 0.04 | 0.01 | 0.01 | 0.02 | 99.57 | 8.309 | 2.074 | 0.178 | 0.730 | 0.025 | 3.662 | 0.001 | 0.003 | 0.001 | 0.001 | 0.001 | 14.985 |
| SHA12_Fsp19 | 62.20 | 7.82 | 0.97 | 5.34 | 0.19 | 23.64 | 0.01 | 0.07 | 0.00 | 0.01 | 0.07 | 100.32 | 8.276 | 2.019 | 0.165 | 0.761 | 0.022 | 3.707 | 0.002 | 0.006 | 0.000 | 0.001 | 0.004 | 14.962 |
| SHA12_Fsp21 | 61.39 | 7.88 | 0.96 | 5.48 | 0.20 | 23.83 | 0.01 | 0.17 | 0.02 | 0.00 | 0.06 | 100.00 | 8.214 | 2.045 | 0.163 | 0.785 | 0.023 | 3.759 | 0.002 | 0.013 | 0.002 | 0.000 | 0.003 | 15.009 |
| SHA12_Fsp22 | 61.54 | 8.00 | 1.06 | 5.12 | 0.19 | 23.49 | 0.01 | 0.13 | 0.01 | 0.00 | 0.10 | 99.66 | 8.259 | 2.083 | 0.182 | 0.736 | 0.021 | 3.716 | 0.001 | 0.010 | 0.001 | 0.000 | 0.005 | 15.014 |
| SHA12_Fsp24 | 61.83 | 7.66 | 1.03 | 5.56 | 0.22 | 23.77 | 0.00 | 0.06 | 0.00 | 0.00 | 0.06 | 100.19 | 8.245 | 1.980 | 0.176 | 0.795 | 0.024 | 3.736 | 0.001 | 0.005 | 0.000 | 0.000 | 0.003 | 14.964 |
| SHA12_Fsp25 | 61.49 | 7.71 | 0.91 | 5.61 | 0.25 | 23.85 | 0.00 | 0.06 | 0.01 | 0.00 | 0.09 | 99.98 | 8.221 | 2.000 | 0.155 | 0.804 | 0.028 | 3.758 | 0.000 | 0.005 | 0.001 | 0.000 | 0.005 | 14.976 |
| SHA12_Fsp27 | 61.09 | 7.72 | 0.83 | 5.96 | 0.19 | 24.16 | 0.01 | 0.10 | 0.01 | 0.00 | 0.08 | 100.14 | 8.165 | 2.002 | 0.141 | 0.853 | 0.021 | 3.806 | 0.002 | 0.008 | 0.001 | 0.000 | 0.004 | 15.003 |
| SHA12_Fsp30 | 62.05 | 7.92 | 1.02 | 5.49 | 0.24 | 23.51 | 0.01 | 0.12 | 0.01 | 0.00 | 0.05 | 100.42 | 8.265 | 2.045 | 0.174 | 0.784 | 0.026 | 3.690 | 0.002 | 0.010 | 0.001 | 0.000 | 0.003 | 14.999 |

# Analyses of sheet-silicates (mica) from sandstones

| Sample / No. | $SiO_2$ | $Na_2O$ | CaO | $K_2O$ | FeO | $Al_2O_3$ | MgO | $TiO_2$ | MnO | $Cr_2O_3$ | BaO | wt-total | Si_at | Na_at | Ca_at | K_at | Fe_at | Al_at | Mg_at | Ti_at | Mn_at | Cr_at | Ba_at | at-total |
|---|---|---|---|---|---|---|---|---|---|---|---|---|---|---|---|---|---|---|---|---|---|---|---|---|
| AN01a_Gl17 | 45.68 | 0.51 | 0.00 | 9.76 | 1.48 | 35.94 | 0.35 | 0.10 | 0.00 | n.d. | 0.00 | 93.81 | 6.705 | 0.144 | 0.000 | 1.827 | 0.182 | 6.217 | 0.076 | 0.011 | 0.000 | n.d. | 0.000 | 15.162 |
| AN01a_Gl18 | 45.98 | 0.46 | 0.00 | 10.56 | 1.09 | 34.52 | 0.83 | 0.87 | 0.00 | n.d. | 0.07 | 94.38 | 6.743 | 0.132 | 0.000 | 1.976 | 0.133 | 5.967 | 0.182 | 0.096 | 0.000 | n.d. | 0.004 | 15.232 |
| AN01a_Gl27 | 46.43 | 0.28 | 0.00 | 10.63 | 1.34 | 31.64 | 1.14 | 2.93 | 0.02 | n.d. | 0.19 | 94.61 | 6.829 | 0.080 | 0.000 | 1.995 | 0.165 | 5.485 | 0.251 | 0.324 | 0.003 | n.d. | 0.011 | 15.142 |
| AN15_Gl30 | 46.56 | 0.29 | 0.00 | 10.89 | 1.77 | 33.24 | 0.93 | 1.21 | 0.01 | n.d. | 0.10 | 95.05 | 6.819 | 0.083 | 0.000 | 2.034 | 0.217 | 5.737 | 0.204 | 0.133 | 0.002 | n.d. | 0.006 | 15.238 |
| AN15_Gl31 | 46.31 | 0.22 | 0.00 | 10.55 | 5.69 | 28.26 | 2.34 | 0.39 | 0.10 | n.d. | 0.06 | 93.93 | 7.013 | 0.065 | 0.000 | 2.039 | 0.721 | 5.045 | 0.527 | 0.044 | 0.012 | n.d. | 0.004 | 15.472 |
| AN15_Gl32 | 45.86 | 0.50 | 0.00 | 10.62 | 2.74 | 34.25 | 0.53 | 0.16 | 0.03 | n.d. | 0.00 | 94.69 | 6.757 | 0.142 | 0.000 | 1.996 | 0.338 | 5.949 | 0.116 | 0.018 | 0.004 | n.d. | 0.000 | 15.320 |
| AN15_Gl33 | 45.81 | 0.45 | 0.00 | 10.58 | 1.20 | 34.86 | 0.68 | 1.11 | 0.01 | n.d. | 0.20 | 94.92 | 6.695 | 0.126 | 0.000 | 1.974 | 0.147 | 6.005 | 0.147 | 0.122 | 0.002 | n.d. | 0.012 | 15.231 |
| AN15_Gl37 | 46.52 | 0.35 | 0.08 | 10.64 | 4.35 | 28.83 | 2.07 | 1.01 | 0.00 | n.d. | 0.35 | 94.20 | 6.995 | 0.102 | 0.013 | 2.041 | 0.547 | 5.111 | 0.463 | 0.115 | 0.000 | n.d. | 0.021 | 15.406 |
| AN15_Gl38 | 44.18 | 0.84 | 0.01 | 10.06 | 2.73 | 33.93 | 0.60 | 0.50 | 0.03 | n.d. | 0.15 | 93.03 | 6.643 | 0.246 | 0.001 | 1.931 | 0.344 | 6.014 | 0.134 | 0.056 | 0.004 | n.d. | 0.009 | 15.382 |
| AN15_Gl39 | 45.24 | 0.59 | 0.00 | 10.35 | 3.10 | 33.40 | 0.56 | 1.03 | 0.02 | n.d. | 0.02 | 94.34 | 6.713 | 0.170 | 0.000 | 1.960 | 0.385 | 5.842 | 0.124 | 0.115 | 0.002 | n.d. | 0.001 | 15.316 |
| AN15_Gl40 | 45.17 | 0.62 | 0.00 | 10.34 | 2.17 | 34.33 | 0.70 | 0.42 | 0.01 | n.d. | 0.08 | 93.83 | 6.702 | 0.178 | 0.000 | 1.957 | 0.269 | 6.004 | 0.154 | 0.047 | 0.001 | n.d. | 0.004 | 15.317 |
| TP03_Gl32 | 45.59 | 0.51 | 0.00 | 10.03 | 1.54 | 34.25 | 0.71 | 0.73 | 0.03 | n.d. | 0.04 | 93.43 | 6.749 | 0.146 | 0.000 | 1.893 | 0.191 | 5.977 | 0.157 | 0.081 | 0.004 | n.d. | 0.002 | 15.201 |
| TP03_Gl34 | 45.03 | 0.70 | 0.00 | 9.65 | 1.25 | 35.17 | 0.53 | 0.26 | 0.04 | n.d. | 0.00 | 92.63 | 6.698 | 0.203 | 0.000 | 1.832 | 0.155 | 6.166 | 0.118 | 0.030 | 0.005 | n.d. | 0.000 | 15.207 |
| TP03_Gl35 | 45.17 | 0.47 | 0.00 | 10.04 | 1.04 | 35.42 | 0.65 | 0.54 | 0.03 | n.d. | 0.12 | 93.48 | 6.669 | 0.133 | 0.000 | 1.892 | 0.129 | 6.165 | 0.142 | 0.060 | 0.004 | n.d. | 0.007 | 15.201 |
| TP03_Gl36 | 44.97 | 0.54 | 0.00 | 10.02 | 0.68 | 34.31 | 1.07 | 1.40 | 0.03 | n.d. | 0.16 | 93.16 | 6.668 | 0.154 | 0.000 | 1.895 | 0.084 | 5.997 | 0.236 | 0.156 | 0.003 | n.d. | 0.009 | 15.203 |
| TP03_Gl37 | 45.60 | 0.41 | 0.00 | 10.29 | 1.28 | 33.86 | 1.08 | 0.93 | 0.01 | n.d. | 0.26 | 93.71 | 6.747 | 0.117 | 0.000 | 1.942 | 0.158 | 5.905 | 0.239 | 0.103 | 0.001 | n.d. | 0.015 | 15.226 |
| TP03_Gl39 | 45.65 | 0.47 | 0.01 | 10.29 | 2.08 | 33.89 | 0.80 | 0.88 | 0.01 | n.d. | 0.05 | 94.12 | 6.741 | 0.135 | 0.001 | 1.938 | 0.257 | 5.898 | 0.176 | 0.097 | 0.001 | n.d. | 0.003 | 15.249 |
| TP03_Gl41 | 45.34 | 0.64 | 0.00 | 10.14 | 0.68 | 35.88 | 0.66 | 0.66 | 0.03 | n.d. | 0.01 | 94.07 | 6.643 | 0.183 | 0.000 | 1.896 | 0.083 | 6.197 | 0.144 | 0.072 | 0.003 | n.d. | 0.001 | 15.225 |
| TP03_Gl44 | 44.53 | 0.52 | 0.00 | 9.97 | 0.92 | 35.53 | 0.85 | 0.12 | 0.01 | n.d. | 0.04 | 92.48 | 6.638 | 0.151 | 0.000 | 1.897 | 0.115 | 6.244 | 0.189 | 0.013 | 0.002 | n.d. | 0.002 | 15.250 |
| TP03_Gl46 | 44.83 | 0.48 | 0.00 | 10.22 | 1.44 | 34.13 | 0.75 | 0.88 | 0.02 | n.d. | 0.09 | 92.83 | 6.696 | 0.139 | 0.000 | 1.947 | 0.180 | 6.009 | 0.167 | 0.099 | 0.002 | n.d. | 0.005 | 15.244 |
| SHA05_Gl55 | 44.89 | 0.50 | 0.00 | 10.44 | 2.36 | 34.04 | 0.69 | 0.63 | 0.01 | n.d. | 0.20 | 93.80 | 6.684 | 0.143 | 0.001 | 1.984 | 0.294 | 5.975 | 0.153 | 0.071 | 0.002 | n.d. | 0.012 | 15.321 |
| SHC25_Gl15 | 37.24 | 0.09 | 0.00 | 8.43 | 13.40 | 14.01 | 13.61 | 6.74 | 0.00 | 0.00 | 0.23 | 93.75 | 6.103 | 0.028 | 0.000 | 1.762 | 1.837 | 2.706 | 3.325 | 0.831 | 0.000 | 0.000 | 0.015 | 16.608 |
| SHC25_Gl20 | 44.86 | 0.74 | 0.00 | 10.28 | 3.19 | 33.58 | 0.65 | 0.52 | 0.02 | n.d. | 0.18 | 94.03 | 6.692 | 0.214 | 0.000 | 1.957 | 0.398 | 5.905 | 0.145 | 0.058 | 0.002 | n.d. | 0.011 | 15.383 |
| SHC25_Gl24 | 47.39 | 1.31 | 0.06 | 8.73 | 1.12 | 33.46 | 1.41 | 0.44 | 0.00 | n.d. | 0.21 | 94.13 | 6.909 | 0.369 | 0.010 | 1.625 | 0.136 | 5.749 | 0.307 | 0.048 | 0.000 | n.d. | 0.012 | 15.165 |
| SP08_Gl41 | 45.80 | 0.71 | 0.00 | 9.72 | 2.38 | 34.61 | 0.66 | 0.43 | 0.01 | n.d. | 0.18 | 94.50 | 6.728 | 0.203 | 0.000 | 1.822 | 0.292 | 5.992 | 0.145 | 0.047 | 0.001 | n.d. | 0.011 | 15.241 |
| SP08_Gl42 | 36.92 | 0.15 | 0.02 | 9.10 | 13.44 | 15.51 | 14.03 | 5.62 | 0.00 | 0.01 | 0.18 | 94.99 | 5.990 | 0.048 | 0.004 | 1.883 | 1.824 | 2.967 | 3.392 | 0.685 | 0.000 | 0.002 | 0.011 | 16.807 |
| SP08_Gl43 | 34.58 | 0.26 | 0.08 | 7.79 | 21.73 | 18.28 | 7.06 | 4.00 | 0.00 | 0.12 | 0.05 | 93.94 | 5.860 | 0.086 | 0.014 | 1.684 | 3.080 | 3.652 | 1.783 | 0.510 | 0.000 | 0.017 | 0.003 | 16.689 |
| SP08_Gl44 | 36.94 | 0.20 | 0.00 | 8.80 | 15.58 | 15.80 | 12.14 | 5.10 | 0.03 | 0.05 | 0.21 | 94.84 | 6.049 | 0.063 | 0.000 | 1.839 | 2.133 | 3.050 | 2.965 | 0.628 | 0.003 | 0.007 | 0.014 | 16.750 |
| SP08_Gl45 | 36.56 | 0.23 | 0.04 | 8.92 | 10.75 | 14.66 | 15.75 | 6.30 | 0.00 | 0.02 | 0.75 | 93.98 | 5.959 | 0.073 | 0.008 | 1.855 | 1.466 | 2.816 | 3.826 | 0.772 | 0.000 | 0.002 | 0.048 | 16.825 |
| SPP31_Gl32 | 37.45 | 0.17 | 0.33 | 7.68 | 12.08 | 14.48 | 11.62 | 6.56 | n.d. | 0.03 | 0.04 | 90.43 | 6.274 | 0.054 | 0.059 | 1.641 | 1.693 | 2.860 | 2.903 | 0.826 | n.d. | 0.005 | 0.003 | 16.317 |
| SPP31_Gl35 | 53.74 | 0.56 | 1.52 | 4.58 | 5.26 | 22.40 | 1.81 | 0.39 | 0.04 | n.d. | 0.03 | 90.34 | 8.07 | 0.164 | 0.244 | 0.876 | 0.661 | 3.962 | 0.406 | 0.044 | 0.005 | n.d. | 0.002 | 14.430 |
| SPP31_Gl37 | 42.37 | 0.48 | 0.62 | 5.24 | 7.86 | 14.89 | 15.75 | 3.55 | 0.04 | n.d. | 0.11 | 90.92 | 6.73 | 0.148 | 0.106 | 1.062 | 1.045 | 2.789 | 3.732 | 0.425 | 0.006 | n.d. | 0.007 | 16.052 |
| SPP31_Gl38 | 53.44 | 0.56 | 0.95 | 5.15 | 6.27 | 25.29 | 1.52 | 0.12 | 0.09 | n.d. | 0.04 | 93.45 | 7.81 | 0.159 | 0.149 | 0.960 | 0.766 | 4.356 | 0.330 | 0.013 | 0.011 | n.d. | 0.003 | 14.558 |
| SPP31_Gl39 | 48.16 | 0.62 | 1.04 | 4.38 | 6.70 | 21.54 | 4.14 | 4.49 | 0.05 | n.d. | 0.04 | 91.16 | 7.34 | 0.183 | 0.169 | 0.850 | 0.854 | 3.869 | 0.941 | 0.515 | 0.007 | n.d. | 0.002 | 14.729 |
| SPP31_Gl40 | 49.66 | 0.61 | 3.85 | 1.09 | 7.52 | 20.64 | 4.78 | 2.59 | 0.05 | n.d. | 0.01 | 90.79 | 7.57 | 0.182 | 0.749 | 0.177 | 0.959 | 3.711 | 1.088 | 0.296 | 0.007 | n.d. | 0.000 | 14.741 |
| SPP31_Gl41 | 45.32 | 0.75 | 0.01 | 10.00 | 3.79 | 32.79 | 0.90 | 0.53 | 0.02 | n.d. | 0.17 | 94.31 | 6.749 | 0.217 | 0.002 | 1.901 | 0.472 | 5.757 | 0.200 | 0.060 | 0.003 | n.d. | 0.010 | 15.371 |
| SPP31_Gl44 | 46.74 | 1.19 | 0.14 | 8.56 | 3.30 | 32.68 | 0.80 | 0.63 | 0.03 | n.d. | 0.14 | 94.19 | 6.882 | 0.340 | 0.022 | 1.608 | 0.406 | 5.671 | 0.176 | 0.070 | 0.004 | n.d. | 0.008 | 15.186 |
| SPP31_Gl63 | 53.04 | 0.46 | 1.07 | 4.12 | 9.98 | 21.79 | 2.15 | 0.32 | 0.06 | n.d. | 0.00 | 93.00 | 7.91 | 0.134 | 0.171 | 0.784 | 1.245 | 3.830 | 0.477 | 0.035 | 0.008 | n.d. | 0.000 | 14.598 |
| SPP31_Gl64 | 53.71 | 0.43 | 1.12 | 4.46 | 8.72 | 21.80 | 1.89 | 0.87 | 0.08 | n.d. | 0.03 | 93.11 | 7.96 | 0.124 | 0.177 | 0.843 | 1.081 | 3.808 | 0.417 | 0.097 | 0.010 | n.d. | 0.002 | 14.522 |
| SPP31_Gl70 | 54.03 | 0.58 | 1.16 | 4.51 | 10.39 | 21.01 | 1.99 | 0.46 | 0.05 | n.d. | 0.00 | 94.18 | 7.99 | 0.167 | 0.183 | 0.851 | 1.286 | 3.662 | 0.439 | 0.051 | 0.006 | n.d. | 0.000 | 14.637 |
| SPP31_Gl71 | 54.91 | 0.80 | 1.62 | 3.02 | 9.56 | 21.69 | 2.06 | 0.36 | 0.05 | n.d. | 0.05 | 94.15 | 8.02 | 0.226 | 0.254 | 0.563 | 1.167 | 3.735 | 0.449 | 0.040 | 0.006 | n.d. | 0.003 | 14.466 |
| SPP31_Gl72 | 53.92 | 0.62 | 1.44 | 3.92 | 9.82 | 21.46 | 1.99 | 0.51 | 0.04 | n.d. | 0.00 | 93.75 | 7.97 | 0.178 | 0.228 | 0.739 | 1.214 | 3.738 | 0.439 | 0.057 | 0.005 | n.d. | 0.000 | 14.566 |
| SPP31_Gl68 | 54.56 | 0.62 | 1.59 | 4.17 | 8.98 | 22.36 | 1.95 | 0.66 | 0.05 | n.d. | 0.00 | 94.95 | 7.93 | 0.176 | 0.248 | 0.774 | 1.092 | 3.832 | 0.422 | 0.072 | 0.007 | n.d. | 0.000 | 14.554 |
| TI14_106-Gl | 45.58 | 0.47 | 0.00 | 10.16 | 1.73 | 33.44 | 1.10 | 0.42 | 0.00 | 0.01 | 0.25 | 93.16 | 6.793 | 0.135 | 0.000 | 1.932 | 0.215 | 5.873 | 0.245 | 0.047 | 0.000 | 0.001 | 0.015 | 15.256 |
| TI14_108-Gl | 55.63 | 0.62 | 0.79 | 3.93 | 5.03 | 25.99 | 1.10 | 0.28 | 0.08 | 0.02 | 0.00 | 93.47 | 7.969 | 0.173 | 0.121 | 0.718 | 0.602 | 4.389 | 0.236 | 0.031 | 0.010 | 0.002 | 0.000 | 14.250 |
| TI14_110-Gl | 54.72 | 0.46 | 0.50 | 4.98 | 5.39 | 25.60 | 1.20 | 0.33 | 0.04 | 0.01 | 0.00 | 93.24 | 7.925 | 0.129 | 0.078 | 0.921 | 0.653 | 4.370 | 0.260 | 0.036 | 0.005 | 0.001 | 0.000 | 14.377 |
| TI14_121-Gl | 52.78 | 0.54 | 0.84 | 3.99 | 7.64 | 24.40 | 1.52 | 0.23 | 0.10 | 0.02 | 0.00 | 92.07 | 7.829 | 0.154 | 0.133 | 0.756 | 0.947 | 4.267 | 0.337 | 0.026 | 0.013 | 0.002 | 0.000 | 14.465 |
| TI14_123-Gl | 56.04 | 0.11 | 0.39 | 7.65 | 10.12 | 14.32 | 3.63 | 0.35 | 0.05 | 0.02 | 0.00 | 92.69 | 8.552 | 0.032 | 0.064 | 1.489 | 1.292 | 2.575 | 0.826 | 0.040 | 0.006 | 0.003 | 0.000 | 14.880 |

## Analyses of sheet-silicates (mica) from sandstones (continuation)

| Sample / No. | $SiO_2$ | $Na_2O$ | CaO | $K_2O$ | FeO | $Al_2O_3$ | MgO | $TiO_2$ | MnO | $Cr_2O_3$ | BaO | wt-total | Si_at | Na_at | Ca_at | K_at | Fe_at | Al_at | Mg_at | Ti_at | Mn_at | Cr_at | Ba_at | at-total |
|---|---|---|---|---|---|---|---|---|---|---|---|---|---|---|---|---|---|---|---|---|---|---|---|---|
| RB06_016-Gl | 45.16 | 0.44 | 0.05 | 10.43 | 2.61 | 33.42 | 0.61 | 1.08 | 0.00 | 0.05 | 0.13 | 94.00 | 6.716 | 0.126 | 0.008 | 1.978 | 0.324 | 5.859 | 0.136 | 0.120 | 0.000 | 0.006 | 0.007 | 15.283 |
| RB06_017-Gl | 43.45 | 0.45 | 1.46 | 10.27 | 2.39 | 32.71 | 0.65 | 0.91 | 0.01 | 0.01 | 0.12 | 92.45 | 6.613 | 0.133 | 0.238 | 1.994 | 0.304 | 5.868 | 0.146 | 0.104 | 0.001 | 0.001 | 0.007 | 15.412 |
| RB06_018-Gl | 44.46 | 0.66 | 0.65 | 9.96 | 1.07 | 35.21 | 0.66 | 0.02 | 0.03 | 0.01 | 0.13 | 92.87 | 6.634 | 0.192 | 0.104 | 1.895 | 0.134 | 6.192 | 0.146 | 0.002 | 0.003 | 0.001 | 0.008 | 15.311 |
| RB06_030-Gl | 50.05 | 0.16 | 0.28 | 10.48 | 3.07 | 26.66 | 2.92 | 0.26 | 0.03 | 0.02 | 0.12 | 94.05 | 7.425 | 0.045 | 0.044 | 1.983 | 0.381 | 4.662 | 0.646 | 0.029 | 0.004 | 0.003 | 0.007 | 15.228 |
| MA06-1_084-Gl | 49.85 | 0.81 | 0.08 | 9.14 | 1.82 | 29.87 | 1.64 | 0.03 | 0.11 | 0.00 | 0.45 | 93.82 | 7.317 | 0.230 | 0.013 | 1.712 | 0.223 | 5.167 | 0.360 | 0.003 | 0.014 | 0.000 | 0.026 | 15.067 |
| MA06-1_142-Gl | 46.03 | 0.29 | 0.01 | 10.30 | 3.04 | 32.02 | 1.03 | 0.95 | 0.00 | 0.05 | 0.03 | 93.75 | 6.857 | 0.084 | 0.001 | 1.958 | 0.379 | 5.622 | 0.228 | 0.106 | 0.000 | 0.006 | 0.002 | 15.243 |
| MA06-1_146-Gl | 44.66 | 0.53 | 0.01 | 10.40 | 3.37 | 33.05 | 0.66 | 1.00 | 0.00 | 0.04 | 0.14 | 93.87 | 6.686 | 0.153 | 0.002 | 1.986 | 0.421 | 5.832 | 0.146 | 0.113 | 0.000 | 0.005 | 0.008 | 15.352 |
| MA06-1_148-Gl | 46.66 | 0.31 | 0.03 | 9.28 | 3.49 | 31.03 | 0.80 | 0.37 | 0.04 | 0.02 | 0.08 | 92.11 | 7.034 | 0.092 | 0.006 | 1.785 | 0.440 | 5.515 | 0.179 | 0.042 | 0.006 | 0.002 | 0.005 | 15.104 |
| MA06-1_149-Gl | 46.51 | 0.29 | 0.00 | 10.25 | 2.10 | 33.33 | 1.43 | 0.15 | 0.03 | 0.02 | 0.37 | 94.49 | 6.845 | 0.083 | 0.000 | 1.925 | 0.259 | 5.781 | 0.314 | 0.016 | 0.004 | 0.002 | 0.021 | 15.251 |
| MA06-3_131-Gl | 46.38 | 0.22 | 0.00 | 10.74 | 3.35 | 32.26 | 1.44 | 0.25 | 0.03 | 0.00 | 0.17 | 94.85 | 6.859 | 0.064 | 0.000 | 2.026 | 0.414 | 5.623 | 0.318 | 0.028 | 0.004 | 0.000 | 0.010 | 15.347 |
| MA06-3_132-Gl | 45.96 | 0.28 | 0.01 | 10.95 | 2.56 | 32.66 | 0.93 | 1.20 | 0.01 | 0.03 | 0.36 | 94.94 | 6.790 | 0.079 | 0.002 | 2.064 | 0.316 | 5.688 | 0.205 | 0.133 | 0.002 | 0.004 | 0.021 | 15.303 |
| MA06-3_133-Gl | 46.59 | 1.25 | 0.00 | 9.49 | 0.97 | 34.77 | 0.91 | 0.58 | 0.02 | 0.00 | 0.09 | 94.68 | 6.776 | 0.352 | 0.000 | 1.761 | 0.118 | 5.960 | 0.198 | 0.064 | 0.003 | 0.000 | 0.005 | 15.237 |
| MA06-3_135-Gl | 38.65 | 0.08 | 0.01 | 9.46 | 9.63 | 13.69 | 17.03 | 5.26 | 0.48 | 0.02 | 0.54 | 94.89 | 6.192 | 0.025 | 0.002 | 1.934 | 1.291 | 2.585 | 4.068 | 0.634 | 0.060 | 0.002 | 0.034 | 16.831 |
| MA06-3_138-Gl | 45.46 | 0.75 | 0.00 | 10.27 | 3.22 | 33.41 | 0.77 | 0.76 | 0.01 | 0.03 | 0.17 | 94.86 | 6.719 | 0.216 | 0.000 | 1.936 | 0.398 | 5.821 | 0.171 | 0.085 | 0.001 | 0.004 | 0.010 | 15.360 |
| MA06-3_139-Gl | 40.68 | 0.27 | 0.00 | 10.01 | 3.96 | 13.68 | 24.29 | 0.56 | 0.01 | n.d. | 0.85 | 94.33 | 6.384 | 0.082 | 0.000 | 2.004 | 0.520 | 2.531 | 5.684 | 0.066 | 0.001 | n.d. | 0.052 | 17.327 |
| MA06-3_140-Gl | 45.08 | 0.30 | 0.00 | 10.78 | 2.86 | 33.05 | 0.96 | 0.50 | 0.02 | 0.00 | 0.03 | 93.60 | 6.746 | 0.088 | 0.001 | 2.058 | 0.358 | 5.830 | 0.215 | 0.057 | 0.002 | 0.000 | 0.002 | 15.356 |
| MA06-3_141-Gl | 35.50 | 0.23 | 0.24 | 5.66 | 18.95 | 14.70 | 10.08 | 4.77 | 0.06 | 0.10 | 0.00 | 90.30 | 6.117 | 0.077 | 0.045 | 1.245 | 2.731 | 2.985 | 2.589 | 0.618 | 0.008 | 0.014 | 0.000 | 16.430 |
| MA06-3_142-Gl | 45.34 | 0.86 | 0.00 | 10.07 | 2.01 | 35.30 | 0.42 | 0.69 | 0.00 | 0.04 | 0.20 | 94.93 | 6.642 | 0.244 | 0.000 | 1.883 | 0.246 | 6.095 | 0.093 | 0.076 | 0.000 | 0.005 | 0.012 | 15.295 |
| MA06-3_143-Gl | 35.35 | 0.52 | 0.03 | 8.52 | 24.35 | 14.10 | 7.93 | 4.13 | 0.00 | 0.35 | 0.71 | 95.99 | 6.034 | 0.173 | 0.006 | 1.856 | 3.477 | 2.837 | 2.019 | 0.531 | 0.000 | 0.051 | 0.047 | 17.030 |
| MA06-3_144-Gl | 45.62 | 1.03 | 0.00 | 9.83 | 0.97 | 35.91 | 0.61 | 0.74 | 0.00 | 0.04 | 0.20 | 94.97 | 6.637 | 0.291 | 0.000 | 1.824 | 0.118 | 6.157 | 0.133 | 0.081 | 0.001 | 0.004 | 0.011 | 15.258 |
| MA06-3_145-Gl | 45.56 | 0.86 | 0.00 | 10.14 | 2.37 | 34.54 | 0.55 | 0.73 | 0.04 | 0.01 | 0.11 | 94.91 | 6.689 | 0.244 | 0.001 | 1.899 | 0.292 | 5.976 | 0.120 | 0.081 | 0.005 | 0.001 | 0.006 | 15.314 |
| MA06-3_146-Gl | 45.26 | 0.50 | 0.00 | 10.80 | 3.42 | 33.50 | 0.77 | 0.63 | 0.05 | 0.06 | 0.06 | 95.05 | 6.697 | 0.143 | 0.000 | 2.039 | 0.423 | 5.842 | 0.169 | 0.071 | 0.006 | 0.007 | 0.004 | 15.399 |
| MA06-3_147-Gl | 45.48 | 1.16 | 0.00 | 9.82 | 0.92 | 36.15 | 0.48 | 0.58 | 0.01 | 0.02 | 0.40 | 95.09 | 6.621 | 0.326 | 0.000 | 1.823 | 0.112 | 6.204 | 0.105 | 0.063 | 0.001 | 0.003 | 0.023 | 15.288 |
| MA06-3_148-Gl | 36.07 | 0.49 | 0.09 | 7.42 | 18.24 | 13.70 | 12.39 | 5.02 | 0.01 | 0.22 | 0.55 | 94.19 | 6.039 | 0.161 | 0.015 | 1.584 | 2.553 | 2.704 | 3.091 | 0.632 | 0.001 | 0.031 | 0.036 | 16.848 |
| MA06-3_149-Gl | 36.52 | 0.08 | 0.00 | 9.77 | 17.15 | 16.72 | 10.08 | 4.87 | 0.07 | 0.02 | 0.00 | 95.28 | 6.016 | 0.025 | 0.000 | 2.052 | 2.363 | 3.246 | 2.475 | 0.603 | 0.009 | 0.003 | 0.000 | 16.793 |
| ER04_202-Gl | 45.95 | 0.79 | 0.04 | 10.13 | 1.01 | 34.89 | 0.89 | 0.95 | 0.01 | 0.02 | 0.08 | 94.79 | 6.702 | 0.225 | 0.007 | 1.884 | 0.123 | 5.999 | 0.193 | 0.104 | 0.001 | 0.002 | 0.005 | 15.248 |
| ER04_203-Gl | 45.64 | 0.76 | 0.08 | 9.93 | 0.76 | 35.25 | 0.63 | 0.68 | 0.04 | 0.02 | 0.15 | 93.95 | 6.700 | 0.218 | 0.013 | 1.859 | 0.093 | 6.100 | 0.138 | 0.075 | 0.005 | 0.002 | 0.009 | 15.212 |
| ER04_210-Gl | 46.10 | 0.93 | 0.00 | 9.89 | 1.60 | 33.90 | 1.53 | 0.52 | 0.01 | 0.01 | 0.50 | 95.02 | 6.748 | 0.264 | 0.000 | 1.847 | 0.196 | 5.848 | 0.333 | 0.057 | 0.001 | 0.001 | 0.029 | 15.326 |
| ER04_211-Gl | 46.03 | 0.77 | 0.25 | 8.88 | 1.24 | 32.92 | 1.53 | 0.48 | 0.02 | 0.01 | 0.53 | 92.67 | 6.852 | 0.222 | 0.040 | 1.687 | 0.154 | 5.777 | 0.340 | 0.054 | 0.003 | 0.002 | 0.031 | 15.159 |
| ER04_216-Gl | 46.23 | 0.79 | 0.00 | 9.88 | 0.91 | 35.82 | 0.59 | 0.52 | 0.00 | 0.03 | 0.15 | 94.96 | 6.708 | 0.222 | 0.000 | 1.829 | 0.110 | 6.126 | 0.129 | 0.057 | 0.000 | 0.004 | 0.009 | 15.196 |

## Analyses of sheet-silicates (mica) from tuffaceous sandstones

| Sample / No. | $SiO_2$ | $Na_2O$ | CaO | $K_2O$ | FeO | $Al_2O_3$ | MgO | $TiO_2$ | MnO | $Cr_2O_3$ | BaO | wt-total | Si_at | Na_at | Ca_at | K_at | Fe_at | Al_at | Mg_at | Ti_at | Mn_at | Cr_at | Ba_at | at-total |
|---|---|---|---|---|---|---|---|---|---|---|---|---|---|---|---|---|---|---|---|---|---|---|---|---|
| SHA06_Gl5 | 46.45 | 0.60 | 0.15 | 9.96 | 3.58 | 31.08 | 1.16 | 0.51 | 0.03 | n.d. | 0.28 | 93.81 | 6.942 | 0.174 | 0.024 | 1.899 | 0.448 | 5.476 | 0.259 | 0.058 | 0.004 | n.d. | 0.017 | 15.299 |
| SHA06_Gl41 | 45.74 | 0.43 | 0.01 | 10.70 | 4.57 | 31.56 | 0.96 | 0.20 | 0.08 | n.d. | 0.27 | 94.52 | 6.850 | 0.124 | 0.001 | 2.044 | 0.573 | 5.571 | 0.215 | 0.023 | 0.010 | n.d. | 0.016 | 15.426 |
| SHA12_Gl16 | 35.39 | 0.34 | 0.77 | 6.91 | 16.75 | 13.76 | 11.77 | 4.94 | 0.00 | 0.36 | 0.26 | 91.25 | 6.064 | 0.113 | 0.142 | 1.511 | 2.401 | 2.779 | 3.006 | 0.636 | 0.000 | 0.053 | 0.017 | 16.722 |
| SHA12_Gl20 | 36.66 | 0.49 | 0.19 | 7.55 | 17.92 | 13.40 | 11.87 | 5.29 | 0.00 | 0.36 | 0.37 | 94.09 | 6.128 | 0.160 | 0.034 | 1.609 | 2.505 | 2.640 | 2.957 | 0.665 | 0.000 | 0.051 | 0.024 | 16.771 |
| SHA12_Gl23 | 36.43 | 0.37 | 0.23 | 6.17 | 18.15 | 13.65 | 11.78 | 4.75 | 0.03 | 0.28 | 0.22 | 92.06 | 6.168 | 0.121 | 0.042 | 1.334 | 2.570 | 2.723 | 2.974 | 0.605 | 0.003 | 0.040 | 0.015 | 16.593 |
| SHA12_Gl26 | 36.89 | 0.39 | 0.10 | 8.17 | 17.45 | 13.38 | 12.41 | 4.79 | 0.00 | 0.35 | 0.31 | 94.23 | 6.155 | 0.128 | 0.018 | 1.739 | 2.435 | 2.631 | 3.086 | 0.601 | 0.000 | 0.050 | 0.020 | 16.862 |
| SHA12_Gl34 | 36.38 | 0.30 | 0.26 | 6.39 | 17.24 | 13.94 | 11.90 | 4.83 | 0.02 | 0.35 | 0.33 | 91.95 | 6.152 | 0.099 | 0.047 | 1.379 | 2.438 | 2.778 | 3.001 | 0.615 | 0.002 | 0.050 | 0.022 | 16.584 |

n.d.: not determined

# Analyses of tourmaline

| Sample / No. | $SiO_2$ | $Na_2O$ | $K_2O$ | CaO | FeO | $Al_2O_3$ | MgO | SrO | $TiO_2$ | MnO | BaO | wt-total | Si_at | Na_at | K_at | Ca_at | Fe_at | Al_at | Mg_at | Sr_at | Ti_at | Mn_at | Ba_at | at-total |
|---|---|---|---|---|---|---|---|---|---|---|---|---|---|---|---|---|---|---|---|---|---|---|---|---|
| AN15_Trm68 | 35.84 | 1.68 | 0.02 | 2.17 | 8.09 | 26.99 | 9.03 | 0.05 | 1.26 | 0.01 | 0.01 | 85.14 | 5.911 | 0.537 | 0.004 | 0.383 | 1.116 | 5.246 | 2.221 | 0.004 | 0.156 | 0.002 | 0.000 | 15.580 |
| SHA07_122-Trm | 36.78 | 2.06 | 0.07 | 1.50 | 5.03 | 30.69 | 8.50 | 0.09 | 0.79 | 0.05 | 0.00 | 85.65 | 5.895 | 0.640 | 0.014 | 0.257 | 0.674 | 5.798 | 2.032 | 0.009 | 0.095 | 0.006 | 0.000 | 15.432 |
| SP08_Trm69 | 36.24 | 1.78 | 0.04 | 1.87 | 2.71 | 30.91 | 10.54 | 0.02 | 1.12 | 0.03 | 0.00 | 100.00 | 5.894 | 0.560 | 0.009 | 0.326 | 0.369 | 5.926 | 2.556 | 0.002 | 0.137 | 0.004 | 0.000 | 21.929 |
| SP08_Trm70 | 34.62 | 1.68 | 0.09 | 2.23 | 10.12 | 26.67 | 8.44 | 0.01 | 1.21 | 0.12 | 0.02 | 100.00 | 5.845 | 0.551 | 0.018 | 0.404 | 1.429 | 5.308 | 2.124 | 0.001 | 0.154 | 0.017 | 0.001 | 22.248 |
| SPP17_202-Trm | 35.85 | 1.87 | 0.04 | 1.15 | 4.88 | 34.41 | 6.85 | 0.00 | 0.48 | 0.00 | 0.00 | 85.57 | 5.710 | 0.577 | 0.009 | 0.197 | 0.650 | 6.460 | 1.626 | 0.000 | 0.058 | 0.000 | 0.000 | 15.293 |
| SPP17_203-Trm | 36.81 | 1.64 | 0.04 | 1.29 | 6.11 | 33.02 | 7.09 | 0.04 | 0.91 | 0.07 | 0.04 | 87.05 | 5.807 | 0.501 | 0.008 | 0.218 | 0.806 | 6.139 | 1.668 | 0.003 | 0.108 | 0.010 | 0.002 | 15.270 |
| SPP17_204-Trm | 36.26 | 2.07 | 0.07 | 0.79 | 9.16 | 31.56 | 5.72 | 0.00 | 0.70 | 0.17 | 0.02 | 86.51 | 5.857 | 0.649 | 0.015 | 0.136 | 1.237 | 6.008 | 1.376 | 0.000 | 0.085 | 0.023 | 0.001 | 15.386 |
| SPP17_206-Trm | 36.76 | 1.58 | 0.04 | 1.52 | 6.40 | 32.06 | 7.25 | 0.01 | 0.67 | 0.04 | 0.02 | 86.34 | 5.858 | 0.490 | 0.008 | 0.260 | 0.853 | 6.022 | 1.721 | 0.001 | 0.080 | 0.005 | 0.001 | 15.299 |
| SPP17_207-Trm | 35.30 | 1.84 | 0.06 | 1.60 | 14.52 | 28.94 | 4.10 | 0.03 | 0.77 | 0.10 | 0.00 | 87.28 | 5.849 | 0.591 | 0.012 | 0.284 | 2.013 | 5.652 | 1.012 | 0.003 | 0.096 | 0.015 | 0.000 | 15.529 |
| SPP17_208-Trm | 36.14 | 1.71 | 0.07 | 1.67 | 7.79 | 30.17 | 7.73 | 0.00 | 0.62 | 0.07 | 0.00 | 86.04 | 5.851 | 0.536 | 0.014 | 0.290 | 1.055 | 5.757 | 1.867 | 0.000 | 0.076 | 0.010 | 0.000 | 15.465 |
| SPP17_209-Trm | 35.51 | 2.25 | 0.06 | 0.38 | 11.92 | 31.92 | 3.95 | 0.00 | 0.68 | 0.14 | 0.00 | 86.81 | 5.794 | 0.713 | 0.013 | 0.066 | 1.627 | 6.139 | 0.962 | 0.000 | 0.083 | 0.020 | 0.000 | 15.416 |
| SPP17_210-Trm | 35.35 | 2.40 | 0.09 | 0.38 | 13.52 | 30.67 | 3.21 | 0.02 | 0.92 | 0.11 | 0.00 | 86.69 | 5.839 | 0.767 | 0.020 | 0.067 | 1.867 | 5.970 | 0.789 | 0.002 | 0.115 | 0.015 | 0.000 | 15.454 |
| SPP17_224-Trm | 35.83 | 1.55 | 0.02 | 2.23 | 9.48 | 28.97 | 7.15 | 0.05 | 0.93 | 0.09 | 0.00 | 86.29 | 5.855 | 0.490 | 0.005 | 0.390 | 1.295 | 5.581 | 1.741 | 0.005 | 0.114 | 0.013 | 0.000 | 15.488 |
| SPP31_Trm66 | 37.08 | 2.10 | 0.07 | 1.09 | 2.49 | 32.83 | 9.10 | 0.02 | 1.45 | 0.09 | 0.01 | 86.32 | 5.802 | 0.637 | 0.015 | 0.182 | 0.326 | 6.056 | 2.122 | 0.002 | 0.170 | 0.011 | 0.001 | 15.325 |
| SPP31_Trm69 | 36.31 | 2.15 | 0.06 | 0.59 | 6.04 | 34.19 | 6.23 | 0.00 | 1.03 | 0.03 | 0.01 | 86.66 | 5.743 | 0.660 | 0.012 | 0.101 | 0.799 | 6.373 | 1.469 | 0.000 | 0.123 | 0.004 | 0.000 | 15.284 |
| TI14_303-Trm | 34.90 | 2.04 | 0.26 | 1.11 | 16.43 | 26.71 | 4.46 | 0.07 | 0.78 | 0.00 | 0.00 | 86.75 | 5.900 | 0.668 | 0.056 | 0.201 | 2.323 | 5.323 | 1.124 | 0.007 | 0.099 | 0.000 | 0.000 | 15.701 |
| TI14_304-Trm | 35.85 | 2.66 | 0.08 | 0.15 | 13.88 | 27.41 | 5.25 | 0.11 | 0.72 | 0.02 | 0.00 | 86.17 | 5.992 | 0.862 | 0.017 | 0.028 | 1.940 | 5.399 | 1.309 | 0.010 | 0.091 | 0.004 | 0.000 | 15.655 |
| TI14_309-Trm | 35.74 | 2.11 | 0.02 | 1.14 | 13.91 | 28.16 | 5.23 | 0.07 | 0.03 | 0.06 | 0.00 | 86.49 | 5.951 | 0.682 | 0.005 | 0.204 | 1.937 | 5.527 | 1.298 | 0.007 | 0.004 | 0.009 | 0.000 | 15.625 |
| TI14_321-Trm | 36.08 | 1.78 | 0.10 | 1.44 | 4.59 | 35.20 | 6.98 | 0.00 | 0.44 | 0.04 | 0.00 | 86.67 | 5.671 | 0.543 | 0.020 | 0.243 | 0.603 | 6.521 | 1.636 | 0.000 | 0.052 | 0.005 | 0.000 | 15.297 |
| TP03_Trm59 | 36.20 | 1.42 | 0.04 | 0.15 | 9.43 | 35.63 | 3.04 | 0.01 | 0.22 | 0.16 | 0.00 | 86.29 | 5.798 | 0.440 | 0.008 | 0.026 | 1.264 | 6.727 | 0.726 | 0.001 | 0.026 | 0.022 | 0.000 | 15.037 |
| TP03_Trm60 | 36.15 | 1.93 | 0.04 | 0.59 | 5.80 | 34.13 | 6.30 | 0.00 | 0.76 | 0.04 | 0.00 | 85.73 | 5.762 | 0.598 | 0.009 | 0.100 | 0.773 | 6.412 | 1.497 | 0.000 | 0.091 | 0.005 | 0.000 | 15.245 |
| TP03_Trm61 | 35.25 | 1.64 | 0.04 | 0.28 | 8.04 | 34.86 | 4.43 | 0.00 | 0.39 | 0.05 | 0.03 | 100.00 | 5.792 | 0.524 | 0.009 | 0.050 | 1.104 | 6.751 | 1.084 | 0.000 | 0.048 | 0.007 | 0.002 | 21.650 |
| TP03_Trm62 | 35.54 | 1.80 | 0.07 | 1.07 | 6.60 | 31.91 | 7.02 | 0.01 | 1.65 | 0.07 | 0.00 | 100.00 | 5.869 | 0.576 | 0.015 | 0.190 | 0.911 | 6.211 | 1.727 | 0.001 | 0.205 | 0.010 | 0.000 | 21.818 |
| TP03_Trm63 | 35.20 | 1.84 | 0.05 | 0.42 | 9.64 | 34.48 | 3.75 | 0.00 | 0.49 | 0.07 | 0.00 | 100.00 | 5.857 | 0.595 | 0.011 | 0.075 | 1.341 | 6.762 | 0.930 | 0.000 | 0.062 | 0.010 | 0.000 | 21.732 |
| TP03_Trm65 | 35.51 | 1.87 | 0.06 | 0.23 | 9.75 | 34.64 | 3.57 | 0.00 | 0.30 | 0.18 | 0.00 | 100.00 | 5.910 | 0.603 | 0.012 | 0.041 | 1.358 | 6.795 | 0.886 | 0.000 | 0.038 | 0.025 | 0.000 | 21.714 |
| TP03_Trm66 | 34.41 | 2.00 | 0.07 | 0.89 | 10.21 | 32.11 | 4.62 | 0.00 | 1.11 | 0.07 | 0.00 | 100.00 | 5.763 | 0.649 | 0.016 | 0.159 | 1.431 | 6.339 | 1.154 | 0.000 | 0.140 | 0.011 | 0.000 | 21.922 |
| TP03_Trm67 | 34.68 | 2.11 | 0.05 | 0.50 | 10.90 | 32.26 | 3.99 | 0.00 | 1.57 | 0.10 | 0.02 | 100.00 | 5.838 | 0.690 | 0.011 | 0.091 | 1.534 | 6.400 | 1.002 | 0.000 | 0.199 | 0.014 | 0.001 | 21.873 |
| TP03_Trm68 | 35.22 | 1.95 | 0.01 | 0.49 | 8.04 | 32.70 | 5.71 | 0.02 | 0.76 | 0.04 | 0.00 | 100.00 | 5.809 | 0.624 | 0.002 | 0.086 | 1.110 | 6.358 | 1.403 | 0.002 | 0.095 | 0.006 | 0.000 | 21.819 |
| TP03_Trm70 | 34.83 | 1.65 | 0.05 | 1.95 | 6.17 | 30.37 | 8.09 | 0.02 | 1.81 | 0.03 | 0.01 | 100.00 | 5.748 | 0.529 | 0.011 | 0.346 | 0.851 | 5.909 | 1.990 | 0.002 | 0.224 | 0.004 | 0.001 | 21.935 |
| TP03_Trm73 | 34.05 | 1.71 | 0.06 | 0.63 | 9.47 | 33.55 | 4.19 | 0.03 | 1.05 | 0.06 | 0.03 | 100.00 | 5.651 | 0.550 | 0.012 | 0.112 | 1.315 | 6.564 | 1.038 | 0.003 | 0.131 | 0.009 | 0.002 | 21.785 |
| TP03_Trm74 | 35.10 | 1.77 | 0.07 | 0.25 | 10.07 | 34.63 | 3.38 | 0.00 | 0.46 | 0.09 | 0.04 | 100.00 | 5.843 | 0.572 | 0.014 | 0.045 | 1.402 | 6.796 | 0.839 | 0.000 | 0.058 | 0.012 | 0.002 | 21.708 |
| TP03_Trm75 | 34.47 | 1.87 | 0.04 | 0.78 | 10.39 | 32.63 | 4.31 | 0.00 | 1.05 | 0.05 | 0.00 | 100.00 | 5.770 | 0.608 | 0.009 | 0.140 | 1.454 | 6.437 | 1.075 | 0.000 | 0.132 | 0.007 | 0.000 | 21.863 |
| TP03_Trm78 | 35.30 | 1.95 | 0.05 | 0.65 | 9.13 | 33.11 | 4.83 | 0.00 | 1.07 | 0.16 | 0.04 | 100.00 | 5.893 | 0.630 | 0.011 | 0.117 | 1.275 | 6.515 | 1.202 | 0.000 | 0.134 | 0.022 | 0.003 | 21.813 |
| ER04_207-Trm | 35.65 | 1.95 | 0.07 | 1.32 | 14.71 | 28.70 | 3.61 | 0.05 | 0.94 | 0.24 | 0.03 | 87.28 | 5.911 | 0.627 | 0.014 | 0.235 | 2.040 | 5.610 | 0.891 | 0.005 | 0.117 | 0.034 | 0.002 | 15.487 |
| ER04_208-Trm | 35.55 | 2.00 | 0.05 | 1.39 | 14.50 | 28.88 | 3.55 | 0.00 | 0.91 | 0.23 | 0.00 | 87.05 | 5.901 | 0.644 | 0.011 | 0.247 | 2.013 | 5.649 | 0.879 | 0.000 | 0.113 | 0.033 | 0.000 | 15.489 |
| ER04_209-Trm | 35.31 | 1.94 | 0.06 | 1.43 | 14.62 | 28.65 | 3.56 | 0.00 | 1.01 | 0.21 | 0.00 | 86.80 | 5.886 | 0.628 | 0.012 | 0.256 | 2.039 | 5.629 | 0.884 | 0.000 | 0.127 | 0.030 | 0.000 | 15.492 |
| ER04_212-Trm | 35.71 | 1.71 | 0.06 | 1.39 | 10.62 | 31.06 | 5.10 | 0.02 | 1.20 | 0.07 | 0.00 | 86.91 | 5.796 | 0.537 | 0.012 | 0.241 | 1.441 | 5.942 | 1.235 | 0.002 | 0.146 | 0.010 | 0.000 | 15.361 |
| ER04_213-Trm | 35.75 | 1.70 | 0.06 | 1.29 | 10.46 | 30.36 | 5.09 | 0.01 | 1.36 | 0.11 | 0.00 | 86.21 | 5.847 | 0.540 | 0.013 | 0.226 | 1.431 | 5.853 | 1.240 | 0.001 | 0.168 | 0.015 | 0.000 | 15.335 |
| ER04_214-Trm | 36.09 | 2.19 | 0.06 | 0.73 | 7.34 | 32.75 | 6.02 | 0.00 | 0.81 | 0.07 | 0.00 | 86.06 | 5.797 | 0.683 | 0.012 | 0.126 | 0.986 | 6.201 | 1.442 | 0.000 | 0.098 | 0.009 | 0.000 | 15.353 |
| ER04_215-Trm | 36.59 | 2.60 | 0.02 | 0.20 | 8.49 | 31.12 | 6.56 | 0.04 | 0.76 | 0.08 | 0.00 | 86.50 | 5.889 | 0.810 | 0.004 | 0.035 | 1.143 | 5.904 | 1.575 | 0.003 | 0.092 | 0.010 | 0.000 | 15.471 |
| ER04_228-Trm | 36.65 | 1.81 | 0.03 | 1.31 | 7.77 | 31.29 | 6.75 | 0.06 | 0.51 | 0.00 | 0.00 | 86.27 | 5.894 | 0.565 | 0.006 | 0.226 | 1.045 | 5.930 | 1.618 | 0.006 | 0.061 | 0.000 | 0.000 | 15.361 |
| ER04_229-Trm | 36.37 | 1.69 | 0.01 | 1.77 | 8.40 | 30.02 | 7.29 | 0.00 | 1.15 | 0.11 | 0.00 | 86.83 | 5.854 | 0.528 | 0.001 | 0.305 | 1.130 | 5.695 | 1.750 | 0.000 | 0.139 | 0.014 | 0.000 | 15.422 |

# Analyses of garnets

| Sample / No. | $SiO_2$ | $Na_2O$ | $Cr_2O_3$ | CaO | FeO | $Al_2O_3$ | MgO | $K_2O$ | $TiO_2$ | MnO | wt-total | Si_at | Na_at | Cr_at | Ca_at | Fe_at | Al_at | Mg_at | K_at | Ti_at | Mn_at | at-total |
|---|---|---|---|---|---|---|---|---|---|---|---|---|---|---|---|---|---|---|---|---|---|---|
| AN15_Grt41 | 39.02 | 0.00 | 0.01 | 1.77 | 26.20 | 22.08 | 10.08 | 0.00 | 0.05 | 0.43 | 99.64 | 5.989 | 0.000 | 0.001 | 0.291 | 3.362 | 3.995 | 2.307 | 0.000 | 0.005 | 0.056 | 16.007 |
| AN15_Grt42 | 38.75 | 0.00 | 0.04 | 2.44 | 29.44 | 21.85 | 6.95 | 0.00 | 0.01 | 0.92 | 100.40 | 6.017 | 0.000 | 0.005 | 0.406 | 3.823 | 3.998 | 1.609 | 0.000 | 0.001 | 0.121 | 15.980 |
| AN15_Grt44 | 38.74 | 0.03 | 0.08 | 0.39 | 30.19 | 21.69 | 7.83 | 0.01 | 0.04 | 1.65 | 100.64 | 6.008 | 0.008 | 0.010 | 0.065 | 3.916 | 3.964 | 1.811 | 0.002 | 0.005 | 0.216 | 16.006 |
| AN15_Grt45 | 38.82 | 0.02 | 0.09 | 2.14 | 28.93 | 21.69 | 7.89 | 0.00 | 0.08 | 0.56 | 100.22 | 6.013 | 0.005 | 0.011 | 0.356 | 3.747 | 3.960 | 1.821 | 0.000 | 0.009 | 0.073 | 15.995 |
| AN15_Grt46 | 39.16 | 0.04 | 0.04 | 1.80 | 27.84 | 22.03 | 9.14 | 0.00 | 0.01 | 0.38 | 100.43 | 6.005 | 0.011 | 0.005 | 0.296 | 3.570 | 3.981 | 2.089 | 0.001 | 0.001 | 0.049 | 16.007 |
| AN15_Grt47 | 39.66 | 0.00 | 0.00 | 1.52 | 25.95 | 22.09 | 10.79 | 0.01 | 0.07 | 0.29 | 100.39 | 6.018 | 0.000 | 0.000 | 0.248 | 3.293 | 3.951 | 2.442 | 0.001 | 0.008 | 0.038 | 15.999 |
| AN15_Grt48 | 39.40 | 0.01 | 0.04 | 1.45 | 26.44 | 22.58 | 10.77 | 0.00 | 0.06 | 0.35 | 101.09 | 5.952 | 0.002 | 0.005 | 0.234 | 3.340 | 4.020 | 2.425 | 0.001 | 0.007 | 0.045 | 16.030 |
| AN15_Grt49 | 38.02 | 0.00 | 0.08 | 2.55 | 32.11 | 21.31 | 4.96 | 0.00 | 0.01 | 1.24 | 100.29 | 6.008 | 0.000 | 0.010 | 0.432 | 4.243 | 3.970 | 1.169 | 0.000 | 0.002 | 0.166 | 16.000 |
| AN15_Grt50 | 38.12 | 0.02 | 0.05 | 3.90 | 24.29 | 21.36 | 4.69 | 0.01 | 0.04 | 8.00 | 100.48 | 6.003 | 0.007 | 0.006 | 0.658 | 3.199 | 3.965 | 1.101 | 0.001 | 0.005 | 1.068 | 16.011 |
| AN15_Grt51 | 38.11 | 0.05 | 0.01 | 11.91 | 26.10 | 21.18 | 2.26 | 0.00 | 0.06 | 0.82 | 100.49 | 5.999 | 0.015 | 0.001 | 2.009 | 3.436 | 3.929 | 0.531 | 0.000 | 0.007 | 0.109 | 16.036 |
| AN15_Grt52 | 38.94 | 0.00 | 0.05 | 2.62 | 27.12 | 22.06 | 8.89 | 0.00 | 0.10 | 0.61 | 100.39 | 5.977 | 0.000 | 0.007 | 0.430 | 3.482 | 3.991 | 2.034 | 0.000 | 0.012 | 0.080 | 16.013 |
| AN15_Grt53 | 39.17 | 0.00 | 0.08 | 1.64 | 28.07 | 22.09 | 9.23 | 0.00 | 0.02 | 0.41 | 100.71 | 5.992 | 0.000 | 0.010 | 0.269 | 3.591 | 3.984 | 2.105 | 0.000 | 0.003 | 0.054 | 16.008 |
| AN15_Grt54a | 38.57 | 0.01 | 0.05 | 0.86 | 30.25 | 21.87 | 8.37 | 0.00 | 0.02 | 0.60 | 100.60 | 5.968 | 0.002 | 0.006 | 0.143 | 3.915 | 3.989 | 1.931 | 0.000 | 0.002 | 0.078 | 16.034 |
| AN15_Grt55 | 38.53 | 0.01 | 0.04 | 2.54 | 30.80 | 21.71 | 6.46 | 0.00 | 0.06 | 0.75 | 100.90 | 5.992 | 0.002 | 0.005 | 0.422 | 4.006 | 3.979 | 1.498 | 0.000 | 0.007 | 0.099 | 16.010 |
| AN15_Grt56 | 38.18 | 0.03 | 0.04 | 2.76 | 30.25 | 21.67 | 6.37 | 0.00 | 0.03 | 0.75 | 100.06 | 5.982 | 0.008 | 0.005 | 0.463 | 3.964 | 4.002 | 1.487 | 0.000 | 0.003 | 0.100 | 16.015 |
| AN15_Grt57 | 38.93 | 0.00 | 0.04 | 2.47 | 26.15 | 21.96 | 9.66 | 0.02 | 0.04 | 0.86 | 100.13 | 5.972 | 0.000 | 0.005 | 0.407 | 3.355 | 3.971 | 2.208 | 0.004 | 0.005 | 0.111 | 16.037 |
| AN15_Grt58 | 39.12 | 0.01 | 0.01 | 2.59 | 26.23 | 22.00 | 9.76 | 0.00 | 0.06 | 0.81 | 100.58 | 5.973 | 0.002 | 0.001 | 0.423 | 3.350 | 3.960 | 2.221 | 0.000 | 0.006 | 0.105 | 16.041 |
| AN15_Grt59 | 38.82 | 0.01 | 0.04 | 2.00 | 28.79 | 21.85 | 8.34 | 0.02 | 0.07 | 0.65 | 100.60 | 5.986 | 0.002 | 0.005 | 0.331 | 3.712 | 3.971 | 1.917 | 0.004 | 0.008 | 0.085 | 16.021 |
| AN15_Grt60 | 40.02 | 0.00 | 0.15 | 6.57 | 19.03 | 22.27 | 11.69 | 0.01 | 0.04 | 0.47 | 100.25 | 5.987 | 0.000 | 0.018 | 1.053 | 2.381 | 3.926 | 2.607 | 0.003 | 0.004 | 0.060 | 16.039 |
| AN15_Grt61 | 38.82 | 0.02 | 0.02 | 1.76 | 29.34 | 21.95 | 8.06 | 0.00 | 0.02 | 0.63 | 100.61 | 5.993 | 0.005 | 0.002 | 0.292 | 3.788 | 3.993 | 1.854 | 0.000 | 0.002 | 0.082 | 16.010 |
| AN15_Grt62 | 38.27 | 0.00 | 0.04 | 0.97 | 31.36 | 21.84 | 7.05 | 0.00 | 0.06 | 0.83 | 100.42 | 5.973 | 0.000 | 0.005 | 0.162 | 4.094 | 4.018 | 1.639 | 0.000 | 0.007 | 0.110 | 16.008 |
| AN15_Grt63 | 39.04 | 0.00 | 0.08 | 0.93 | 27.23 | 22.27 | 10.40 | 0.02 | 0.05 | 0.41 | 100.42 | 5.959 | 0.000 | 0.009 | 0.152 | 3.475 | 4.006 | 2.365 | 0.004 | 0.006 | 0.053 | 16.029 |
| AN15_Grt64 | 37.67 | 0.02 | 0.02 | 3.21 | 32.15 | 21.20 | 2.95 | 0.01 | 0.05 | 3.22 | 100.51 | 6.011 | 0.008 | 0.003 | 0.549 | 4.291 | 3.987 | 0.703 | 0.001 | 0.006 | 0.435 | 15.993 |
| SHA05_Grt30 | 39.62 | 0.03 | 0.15 | 2.23 | 25.32 | 22.00 | 10.55 | 0.00 | 0.09 | 0.72 | 100.71 | 6.004 | 0.008 | 0.018 | 0.362 | 3.209 | 3.929 | 2.384 | 0.000 | 0.010 | 0.093 | 16.017 |
| SHA05_Grt31 | 40.05 | 0.00 | 0.01 | 1.88 | 23.23 | 22.69 | 12.58 | 0.00 | 0.03 | 0.44 | 100.90 | 5.977 | 0.000 | 0.002 | 0.301 | 2.899 | 3.990 | 2.798 | 0.000 | 0.003 | 0.055 | 16.024 |
| SHA05_Grt32 | 38.73 | 0.00 | 0.00 | 1.51 | 29.95 | 22.07 | 8.23 | 0.02 | 0.05 | 0.73 | 101.30 | 5.954 | 0.000 | 0.000 | 0.249 | 3.850 | 3.999 | 1.886 | 0.004 | 0.006 | 0.095 | 16.043 |
| SHA05_Grt33 | 38.52 | 0.00 | 0.05 | 1.03 | 32.16 | 21.94 | 7.13 | 0.00 | 0.03 | 0.38 | 101.24 | 5.969 | 0.000 | 0.006 | 0.171 | 4.168 | 4.007 | 1.647 | 0.000 | 0.003 | 0.050 | 16.022 |
| SHA05_Grt34 | 37.62 | 0.01 | 0.01 | 0.65 | 35.92 | 21.48 | 4.68 | 0.01 | 0.02 | 0.47 | 100.88 | 5.964 | 0.003 | 0.002 | 0.111 | 4.762 | 4.014 | 1.106 | 0.002 | 0.002 | 0.063 | 16.029 |
| SHA05_Grt35 | 37.90 | 0.00 | 0.00 | 1.46 | 33.17 | 21.48 | 4.66 | 0.00 | 0.02 | 2.32 | 101.01 | 5.983 | 0.000 | 0.001 | 0.246 | 4.380 | 3.997 | 1.097 | 0.001 | 0.002 | 0.311 | 16.017 |
| SHA05_Grt37 | 39.37 | 0.02 | 0.02 | 6.69 | 22.57 | 22.14 | 9.20 | 0.00 | 0.03 | 0.34 | 100.38 | 5.979 | 0.007 | 0.002 | 1.089 | 2.867 | 3.964 | 2.082 | 0.000 | 0.003 | 0.044 | 16.038 |
| SHA05_Grt39 | 39.81 | 0.00 | 0.00 | 0.83 | 24.73 | 22.53 | 12.61 | 0.01 | 0.02 | 0.26 | 100.81 | 5.969 | 0.001 | 0.000 | 0.134 | 3.101 | 3.981 | 2.817 | 0.003 | 0.002 | 0.033 | 16.040 |
| SHA05_Grt40 | 39.92 | 0.00 | 0.07 | 2.41 | 23.15 | 22.43 | 12.11 | 0.01 | 0.02 | 0.30 | 100.42 | 5.994 | 0.001 | 0.008 | 0.387 | 2.906 | 3.970 | 2.710 | 0.002 | 0.002 | 0.039 | 16.017 |
| SHA05_Grt41 | 38.83 | 0.00 | 0.03 | 1.48 | 29.29 | 22.18 | 8.55 | 0.00 | 0.04 | 0.43 | 100.84 | 5.967 | 0.000 | 0.004 | 0.244 | 3.765 | 4.018 | 1.958 | 0.001 | 0.005 | 0.056 | 16.017 |
| SHA07_130-Grt | 38.51 | 0.00 | 0.04 | 2.17 | 30.76 | 21.65 | 6.51 | 0.01 | 0.04 | 0.67 | 100.37 | 6.012 | 0.000 | 0.005 | 0.363 | 4.015 | 3.983 | 1.515 | 0.003 | 0.005 | 0.089 | 15.990 |
| SHA07_131-Grt | 38.96 | 0.02 | 0.13 | 6.27 | 25.77 | 21.60 | 6.38 | 0.00 | 0.15 | 1.03 | 100.34 | 6.026 | 0.005 | 0.016 | 1.039 | 3.333 | 3.938 | 1.470 | 0.000 | 0.018 | 0.134 | 15.982 |
| SHA07_132-Grt | 38.85 | 0.00 | 0.00 | 1.44 | 29.48 | 21.76 | 8.09 | 0.01 | 0.07 | 0.62 | 100.38 | 6.011 | 0.000 | 0.000 | 0.238 | 3.815 | 3.969 | 1.867 | 0.001 | 0.008 | 0.081 | 15.997 |
| SHA07_133-Grt | 38.90 | 0.00 | 0.05 | 2.07 | 28.57 | 22.07 | 8.40 | 0.00 | 0.00 | 0.47 | 100.52 | 5.988 | 0.000 | 0.006 | 0.341 | 3.679 | 4.004 | 1.927 | 0.000 | 0.000 | 0.061 | 16.007 |
| SHA07_134-Grt | 39.49 | 0.00 | 0.03 | 1.07 | 26.95 | 22.17 | 10.07 | 0.00 | 0.05 | 0.26 | 100.17 | 6.027 | 0.000 | 0.003 | 0.174 | 3.440 | 3.989 | 2.290 | 0.000 | 0.006 | 0.034 | 15.971 |
| SHA07_135-Grt | 38.34 | 0.01 | 0.02 | 1.27 | 32.01 | 21.70 | 5.96 | 0.00 | 0.04 | 1.50 | 100.86 | 5.997 | 0.002 | 0.002 | 0.213 | 4.188 | 4.001 | 1.390 | 0.000 | 0.004 | 0.198 | 15.998 |
| SHA07_136-Grt | 38.93 | 0.02 | 0.00 | 14.53 | 16.49 | 21.12 | 1.46 | 0.00 | 0.18 | 8.50 | 101.24 | 6.058 | 0.005 | 0.000 | 2.422 | 2.145 | 3.874 | 0.339 | 0.000 | 0.022 | 1.120 | 15.986 |
| SHA07_137-Grt | 39.77 | 0.02 | 0.04 | 1.01 | 27.44 | 22.29 | 9.91 | 0.00 | 0.00 | 0.46 | 100.96 | 6.033 | 0.007 | 0.005 | 0.164 | 3.481 | 3.986 | 2.240 | 0.000 | 0.000 | 0.059 | 15.975 |
| SHA07_138-Grt | 39.00 | 0.00 | 0.04 | 6.27 | 26.46 | 21.91 | 6.18 | 0.00 | 0.17 | 0.85 | 100.89 | 6.007 | 0.000 | 0.005 | 1.035 | 3.408 | 3.977 | 1.418 | 0.000 | 0.020 | 0.111 | 15.982 |
| SHA07_139-Grt | 38.87 | 0.00 | 0.02 | 2.38 | 29.68 | 21.81 | 6.66 | 0.01 | 0.06 | 1.08 | 100.59 | 6.033 | 0.000 | 0.003 | 0.396 | 3.853 | 3.990 | 1.540 | 0.001 | 0.008 | 0.142 | 15.964 |
| SHA07_140-Grt | 39.10 | 0.00 | 0.11 | 2.71 | 29.32 | 21.92 | 7.12 | 0.00 | 0.06 | 0.81 | 101.22 | 6.017 | 0.000 | 0.013 | 0.447 | 3.775 | 3.976 | 1.634 | 0.000 | 0.008 | 0.106 | 15.981 |
| SHA07_141-Grt | 39.37 | 0.01 | 0.02 | 34.65 | 7.64 | 17.91 | 0.36 | 0.01 | 0.53 | 0.42 | 100.93 | 6.070 | 0.004 | 0.002 | 5.725 | 0.986 | 3.255 | 0.083 | 0.003 | 0.061 | 0.055 | 16.243 |
| SHA07_143-Grt | 39.07 | 0.01 | 0.07 | 1.13 | 26.99 | 22.27 | 10.06 | 0.00 | 0.10 | 0.32 | 100.05 | 5.979 | 0.002 | 0.009 | 0.185 | 3.454 | 4.017 | 2.295 | 0.000 | 0.012 | 0.041 | 15.997 |
| SHA07_146-Grt | 39.13 | 0.00 | 0.02 | 1.29 | 29.55 | 22.33 | 8.42 | 0.00 | 0.06 | 0.34 | 101.16 | 5.989 | 0.000 | 0.002 | 0.212 | 3.783 | 4.029 | 1.920 | 0.000 | 0.007 | 0.045 | 15.989 |
| SHA07_147-Grt | 38.77 | 0.00 | 0.00 | 1.33 | 31.41 | 22.06 | 6.98 | 0.00 | 0.12 | 0.42 | 101.18 | 5.994 | 0.000 | 0.000 | 0.221 | 4.061 | 4.019 | 1.609 | 0.000 | 0.014 | 0.055 | 15.981 |
| SHA07_147-Grt | 39.50 | 0.00 | 0.00 | 1.39 | 26.74 | 22.50 | 9.69 | 0.00 | 0.14 | 0.99 | 100.96 | 5.995 | 0.000 | 0.000 | 0.227 | 3.393 | 4.025 | 2.192 | 0.001 | 0.016 | 0.128 | 15.977 |
| SHA07_148-Grt | 39.28 | 0.02 | 0.02 | 6.13 | 26.28 | 21.67 | 6.94 | 0.00 | 0.18 | 0.69 | 101.21 | 6.018 | 0.005 | 0.002 | 1.006 | 3.367 | 3.914 | 1.584 | 0.001 | 0.021 | 0.089 | 16.007 |
| SHA07_150-Grt | 38.64 | 0.00 | 0.05 | 0.91 | 31.09 | 21.94 | 7.66 | 0.00 | 0.07 | 0.34 | 100.69 | 5.986 | 0.000 | 0.006 | 0.151 | 4.028 | 4.007 | 1.769 | 0.000 | 0.008 | 0.045 | 16.000 |

| Sample / No. | $SiO_2$ | $Na_2O$ | $Cr_2O_3$ | CaO | FeO | $Al_2O_3$ | MgO | $K_2O$ | $TiO_2$ | MnO | wt-total | Si_at | Na_at | Cr_at | Ca_at | Fe_at | Al_at | Mg_at | K_at | Ti_at | Mn_at | at-total |
|---|---|---|---|---|---|---|---|---|---|---|---|---|---|---|---|---|---|---|---|---|---|---|
| SHA07_152-Grt | 39.19 | 0.03 | 0.05 | 1.29 | 29.28 | 22.20 | 8.46 | 0.00 | 0.04 | 0.55 | 101.09 | 6.001 | 0.010 | 0.006 | 0.212 | 3.750 | 4.007 | 1.931 | 0.000 | 0.004 | 0.072 | 15.993 |
| SHA07_153-Grt | 39.44 | 0.00 | 0.04 | 3.04 | 26.24 | 21.85 | 9.11 | 0.00 | 0.09 | 0.45 | 100.28 | 6.034 | 0.000 | 0.005 | 0.498 | 3.358 | 3.941 | 2.078 | 0.000 | 0.010 | 0.058 | 15.983 |
| SHA07_154-Grt | 38.37 | 0.00 | 0.02 | 1.40 | 34.41 | 21.58 | 4.60 | 0.00 | 0.09 | 0.87 | 101.38 | 6.021 | 0.000 | 0.002 | 0.235 | 4.516 | 3.991 | 1.076 | 0.001 | 0.011 | 0.116 | 15.972 |
| SHA07_155-Grt | 39.55 | 0.00 | 0.06 | 1.03 | 30.05 | 22.37 | 8.53 | 0.00 | 0.03 | 0.40 | 102.06 | 6.005 | 0.000 | 0.007 | 0.168 | 3.816 | 4.003 | 1.931 | 0.000 | 0.003 | 0.051 | 15.987 |
| SHC25_Grt29 | 39.66 | 0.03 | n.d. | 8.01 | 22.06 | 22.22 | 8.51 | 0.03 | 0.02 | 0.38 | 100.91 | 5.997 | 0.009 | n.d. | 1.298 | 2.790 | 3.961 | 1.918 | 0.005 | 0.002 | 0.049 | 16.028 |
| SP08_Grt48 | 38.34 | 0.06 | 0.02 | 2.11 | 30.52 | 21.81 | 6.86 | 0.00 | 0.03 | 0.81 | 100.55 | 5.973 | 0.017 | 0.003 | 0.352 | 3.976 | 4.004 | 1.594 | 0.000 | 0.003 | 0.107 | 16.029 |
| SP08_Grt49 | 38.78 | 0.00 | 0.11 | 2.29 | 27.82 | 21.84 | 8.37 | 0.01 | 0.04 | 1.07 | 100.33 | 5.987 | 0.000 | 0.014 | 0.378 | 3.592 | 3.973 | 1.926 | 0.002 | 0.004 | 0.140 | 16.016 |
| SP08_Grt50 | 38.80 | 0.02 | 0.02 | 1.32 | 29.39 | 22.09 | 8.49 | 0.00 | 0.06 | 0.73 | 100.91 | 5.967 | 0.005 | 0.003 | 0.218 | 3.780 | 4.004 | 1.947 | 0.000 | 0.007 | 0.095 | 16.025 |
| SP08_Grt51 | 39.20 | 0.00 | 0.02 | 1.29 | 26.89 | 22.35 | 10.39 | 0.01 | 0.05 | 0.39 | 100.59 | 5.966 | 0.000 | 0.002 | 0.211 | 3.423 | 4.008 | 2.357 | 0.002 | 0.006 | 0.051 | 16.025 |
| SP08_Grt55 | 39.68 | 0.04 | 0.05 | 1.88 | 23.36 | 22.56 | 12.13 | 0.02 | 0.04 | 0.51 | 100.27 | 5.971 | 0.012 | 0.006 | 0.303 | 2.939 | 4.002 | 2.721 | 0.004 | 0.005 | 0.065 | 16.028 |
| SP08_Grt56 | 38.16 | 0.01 | 0.01 | 1.60 | 31.66 | 21.67 | 6.12 | 0.01 | 0.02 | 0.82 | 100.08 | 5.998 | 0.003 | 0.001 | 0.270 | 4.161 | 4.015 | 1.434 | 0.003 | 0.002 | 0.109 | 15.995 |
| SP08_Grt58 | 38.46 | 0.00 | 0.06 | 7.51 | 27.19 | 21.74 | 5.39 | 0.01 | 0.05 | 0.76 | 101.16 | 5.957 | 0.000 | 0.008 | 1.246 | 3.522 | 3.968 | 1.244 | 0.001 | 0.006 | 0.099 | 16.050 |
| SP08_Grt59 | 38.53 | 0.02 | 0.09 | 0.94 | 32.10 | 21.84 | 6.84 | 0.01 | 0.06 | 0.54 | 100.97 | 5.990 | 0.005 | 0.011 | 0.157 | 4.173 | 4.001 | 1.584 | 0.001 | 0.007 | 0.071 | 16.000 |
| SP08_Grt60 | 38.55 | 0.04 | 0.03 | 2.86 | 29.09 | 21.87 | 6.91 | 0.00 | 0.05 | 1.13 | 100.52 | 5.986 | 0.012 | 0.003 | 0.476 | 3.778 | 4.003 | 1.599 | 0.000 | 0.006 | 0.148 | 16.011 |
| SP08_Grt61 | 37.85 | 0.04 | 0.07 | 2.49 | 32.46 | 21.41 | 4.79 | 0.01 | 0.04 | 1.04 | 100.19 | 5.993 | 0.012 | 0.008 | 0.422 | 4.298 | 3.996 | 1.131 | 0.002 | 0.005 | 0.139 | 16.006 |
| SP08_Grt62 | 38.16 | 0.00 | 0.00 | 2.47 | 33.32 | 21.59 | 4.80 | 0.00 | 0.02 | 0.81 | 101.17 | 5.991 | 0.000 | 0.000 | 0.415 | 4.375 | 3.996 | 1.123 | 0.000 | 0.002 | 0.108 | 16.010 |
| SP08_Grt63 | 38.46 | 0.00 | 0.09 | 0.88 | 31.63 | 21.76 | 7.13 | 0.00 | 0.03 | 0.52 | 100.50 | 5.994 | 0.000 | 0.011 | 0.147 | 4.122 | 3.997 | 1.655 | 0.000 | 0.003 | 0.069 | 15.999 |
| SPP31_Grt46 | 39.32 | 0.01 | 0.02 | 0.99 | 28.17 | 22.37 | 9.68 | 0.00 | 0.02 | 0.35 | 100.92 | 5.988 | 0.002 | 0.003 | 0.161 | 3.588 | 4.016 | 2.197 | 0.001 | 0.002 | 0.046 | 16.002 |
| SPP31_Grt47 | 38.81 | 0.00 | 0.07 | 1.13 | 29.66 | 22.19 | 8.68 | 0.01 | 0.03 | 0.39 | 100.97 | 5.960 | 0.000 | 0.009 | 0.185 | 3.809 | 4.017 | 1.988 | 0.003 | 0.003 | 0.051 | 16.025 |
| SPP31_Grt48 | 38.56 | 0.00 | 0.08 | 6.18 | 26.75 | 21.63 | 6.27 | 0.00 | 0.12 | 1.12 | 100.70 | 5.974 | 0.000 | 0.010 | 1.026 | 3.465 | 3.949 | 1.447 | 0.000 | 0.014 | 0.147 | 16.032 |
| SPP31_Grt49 | 38.10 | 0.00 | 0.05 | 2.47 | 33.26 | 21.61 | 4.90 | 0.01 | 0.05 | 0.82 | 101.27 | 5.975 | 0.000 | 0.007 | 0.416 | 4.363 | 3.995 | 1.147 | 0.001 | 0.006 | 0.109 | 16.018 |
| SPP31_Grt50 | 38.13 | 0.00 | 0.08 | 1.32 | 31.54 | 21.78 | 7.03 | 0.01 | 0.06 | 0.50 | 100.44 | 5.956 | 0.000 | 0.009 | 0.221 | 4.120 | 4.009 | 1.636 | 0.002 | 0.007 | 0.066 | 16.028 |
| SPP31_Grt51 | 38.33 | 0.00 | 0.00 | 1.21 | 32.01 | 21.74 | 6.50 | 0.01 | 0.06 | 0.97 | 100.81 | 5.983 | 0.000 | 0.000 | 0.202 | 4.178 | 4.000 | 1.512 | 0.001 | 0.007 | 0.128 | 16.011 |
| SPP31_Grt52 | 39.87 | 0.05 | 0.02 | 7.03 | 19.55 | 22.35 | 11.15 | 0.00 | 0.10 | 0.44 | 100.56 | 5.967 | 0.016 | 0.002 | 1.128 | 2.447 | 3.943 | 2.488 | 0.000 | 0.011 | 0.056 | 16.057 |
| SPP31_Grt53 | 38.73 | 0.00 | 0.24 | 6.86 | 25.30 | 21.80 | 6.88 | 0.00 | 0.02 | 0.83 | 100.66 | 5.966 | 0.000 | 0.029 | 1.132 | 3.260 | 3.959 | 1.581 | 0.000 | 0.002 | 0.108 | 16.038 |
| SPP31_Grt54 | 39.51 | 0.00 | 0.04 | 1.10 | 25.82 | 22.41 | 11.46 | 0.00 | 0.02 | 0.35 | 100.71 | 5.969 | 0.000 | 0.004 | 0.178 | 3.262 | 3.991 | 2.580 | 0.001 | 0.002 | 0.045 | 16.032 |
| SPP31_Grt55 | 38.98 | 0.03 | 0.04 | 0.99 | 28.37 | 22.37 | 9.88 | 0.01 | 0.06 | 0.33 | 101.07 | 5.940 | 0.009 | 0.005 | 0.162 | 3.615 | 4.018 | 2.244 | 0.001 | 0.007 | 0.043 | 16.046 |
| SPP17_225-Grt | 39.72 | 0.00 | 0.03 | 1.23 | 26.13 | 22.27 | 10.44 | 0.00 | 0.03 | 0.38 | 100.27 | 6.034 | 0.001 | 0.004 | 0.200 | 3.320 | 3.987 | 2.365 | 0.000 | 0.004 | 0.049 | 15.967 |
| SPP17_226-Grt | 39.22 | 0.02 | 0.01 | 1.00 | 27.66 | 22.15 | 9.38 | 0.02 | 0.13 | 0.64 | 100.26 | 6.012 | 0.005 | 0.001 | 0.164 | 3.545 | 4.001 | 2.144 | 0.005 | 0.015 | 0.083 | 15.977 |
| SPP17_232-Grt | 39.64 | 0.04 | 0.03 | 9.36 | 21.95 | 22.22 | 6.96 | 0.01 | 0.13 | 0.36 | 100.75 | 6.024 | 0.011 | 0.004 | 1.524 | 2.790 | 3.980 | 1.577 | 0.001 | 0.014 | 0.047 | 15.976 |
| SPP17_233-Grt | 39.59 | 0.01 | 0.05 | 2.89 | 26.79 | 22.31 | 8.08 | 0.01 | 0.02 | 1.46 | 101.23 | 6.032 | 0.003 | 0.006 | 0.472 | 3.414 | 4.007 | 1.834 | 0.002 | 0.003 | 0.189 | 15.962 |
| SPP17_234-Grt | 39.02 | 0.00 | 0.02 | 2.87 | 30.18 | 21.77 | 6.71 | 0.02 | 0.05 | 0.73 | 101.36 | 6.020 | 0.000 | 0.002 | 0.474 | 3.894 | 3.958 | 1.542 | 0.005 | 0.006 | 0.095 | 15.997 |
| SPP17_235-Grt | 38.64 | 0.01 | 0.01 | 1.02 | 30.95 | 22.18 | 7.34 | 0.00 | 0.05 | 0.51 | 100.72 | 5.985 | 0.002 | 0.002 | 0.169 | 4.009 | 4.050 | 1.695 | 0.000 | 0.006 | 0.067 | 15.985 |
| SPP17_236-Grt | 38.09 | 0.01 | 0.01 | 2.72 | 33.05 | 21.48 | 4.65 | 0.00 | 0.05 | 0.63 | 100.73 | 6.003 | 0.002 | 0.002 | 0.459 | 4.356 | 3.991 | 1.091 | 0.000 | 0.005 | 0.084 | 15.997 |
| SPP17_237-Grt | 39.17 | 0.04 | 0.08 | 0.99 | 29.28 | 21.96 | 8.75 | 0.00 | 0.02 | 0.30 | 100.64 | 6.019 | 0.013 | 0.010 | 0.164 | 3.763 | 3.976 | 2.004 | 0.000 | 0.002 | 0.039 | 15.992 |
| SPP17_238-Grt | 39.52 | 0.04 | 0.04 | 2.15 | 25.65 | 22.31 | 9.70 | 0.00 | 0.05 | 0.91 | 100.44 | 6.015 | 0.011 | 0.004 | 0.351 | 3.266 | 4.003 | 2.200 | 0.000 | 0.006 | 0.118 | 15.981 |
| SPP17_239-Grt | 38.95 | 0.01 | 0.03 | 0.87 | 31.44 | 21.98 | 7.34 | 0.00 | 0.04 | 0.62 | 101.29 | 6.009 | 0.003 | 0.004 | 0.144 | 4.056 | 3.997 | 1.687 | 0.000 | 0.005 | 0.082 | 15.987 |
| SPP17_240-Grt | 38.84 | 0.00 | 0.01 | 0.85 | 31.53 | 21.99 | 7.03 | 0.00 | 0.08 | 0.33 | 100.67 | 6.024 | 0.000 | 0.002 | 0.142 | 4.090 | 4.020 | 1.626 | 0.000 | 0.009 | 0.043 | 15.956 |
| SPP17_241-Grt | 39.79 | 0.02 | 0.00 | 1.52 | 25.57 | 22.50 | 10.58 | 0.01 | 0.06 | 0.55 | 100.61 | 6.015 | 0.006 | 0.000 | 0.246 | 3.233 | 4.010 | 2.385 | 0.002 | 0.007 | 0.071 | 15.976 |
| SPP17_242-Grt | 39.22 | 0.04 | 0.07 | 6.15 | 25.75 | 22.03 | 7.20 | 0.00 | 0.11 | 0.50 | 101.09 | 5.997 | 0.013 | 0.009 | 1.007 | 3.293 | 3.970 | 1.642 | 0.000 | 0.013 | 0.065 | 16.008 |
| SPP17_243-Grt | 39.60 | 0.01 | 0.02 | 13.34 | 23.79 | 21.72 | 3.04 | 0.01 | 0.02 | 0.52 | 102.10 | 6.059 | 0.004 | 0.002 | 2.187 | 3.045 | 3.917 | 0.694 | 0.002 | 0.002 | 0.067 | 15.982 |
| SPP17_244-Grt | 39.05 | 0.02 | 0.02 | 1.15 | 31.56 | 22.12 | 7.09 | 0.00 | 0.03 | 0.52 | 101.57 | 6.010 | 0.006 | 0.003 | 0.189 | 4.062 | 4.013 | 1.627 | 0.000 | 0.004 | 0.068 | 15.981 |
| SPP17_247-Grt | 40.38 | 0.02 | 0.00 | 1.12 | 22.81 | 22.78 | 12.15 | 0.01 | 0.05 | 1.43 | 100.77 | 6.029 | 0.005 | 0.000 | 0.179 | 2.849 | 4.009 | 2.705 | 0.002 | 0.005 | 0.181 | 15.965 |
| SPP17_249-Grt | 39.69 | 0.03 | 0.05 | 1.64 | 23.47 | 22.62 | 12.25 | 0.02 | 0.05 | 0.23 | 100.08 | 5.976 | 0.009 | 0.006 | 0.264 | 2.955 | 4.015 | 2.749 | 0.004 | 0.006 | 0.029 | 16.015 |
| SPP17_252-Grt | 38.70 | 0.02 | 0.04 | 2.17 | 29.06 | 21.74 | 7.71 | 0.00 | 0.10 | 0.71 | 100.30 | 6.000 | 0.005 | 0.004 | 0.360 | 3.768 | 3.973 | 1.782 | 0.000 | 0.012 | 0.093 | 16.002 |
| SPP17_254-Grt | 38.35 | 0.00 | 0.02 | 1.54 | 30.60 | 21.83 | 7.41 | 0.01 | 0.03 | 0.44 | 100.22 | 5.975 | 0.000 | 0.002 | 0.256 | 3.988 | 4.010 | 1.721 | 0.001 | 0.004 | 0.058 | 16.015 |
| SPP17_255-Grt | 38.71 | 0.00 | 0.01 | 9.30 | 24.18 | 21.36 | 5.74 | 0.00 | 0.02 | 0.61 | 99.93 | 6.014 | 0.001 | 0.002 | 1.547 | 3.141 | 3.911 | 1.330 | 0.000 | 0.002 | 0.080 | 16.028 |
| SPP17_257-Grt | 38.46 | 0.07 | 0.07 | 0.84 | 29.82 | 21.71 | 7.93 | 0.00 | 0.05 | 0.85 | 99.86 | 5.996 | 0.020 | 0.008 | 0.140 | 3.889 | 3.990 | 1.844 | 0.000 | 0.006 | 0.113 | 16.009 |

n.d.: not determined

Analyses of garnets (continuation)

| Sample / No. | $SiO_2$ | $Na_2O$ | $Cr_2O_3$ | CaO | FeO | $Al_2O_3$ | MgO | $K_2O$ | $TiO_2$ | MnO | wt-total | Si_at | Na_at | Cr_at | Ca_at | Fe_at | Al_at | Mg_at | K_at | Ti_at | Mn_at | at-total |
|---|---|---|---|---|---|---|---|---|---|---|---|---|---|---|---|---|---|---|---|---|---|---|
| RB06_141-Grt | 38.59 | 0.01 | 0.01 | 1.08 | 30.29 | 22.01 | 7.82 | 0.00 | 0.04 | 0.55 | 100.42 | 5.983 | 0.002 | 0.001 | 0.179 | 3.928 | 4.022 | 1.808 | 0.000 | 0.004 | 0.072 | 16.002 |
| RB06_142-Grt | 38.26 | 0.00 | 0.03 | 1.67 | 33.13 | 21.92 | 5.34 | 0.01 | 0.01 | 0.60 | 100.97 | 5.990 | 0.000 | 0.004 | 0.280 | 4.337 | 4.045 | 1.245 | 0.003 | 0.002 | 0.079 | 15.985 |
| RB06_143-Grt | 38.05 | 0.00 | 0.03 | 1.10 | 32.24 | 21.98 | 6.57 | 0.00 | 0.01 | 0.55 | 100.53 | 5.952 | 0.000 | 0.004 | 0.184 | 4.218 | 4.053 | 1.532 | 0.001 | 0.002 | 0.073 | 16.018 |
| RB06_144-Grt | 38.32 | 0.03 | 0.02 | 2.35 | 32.01 | 21.63 | 5.89 | 0.00 | 0.04 | 0.64 | 100.98 | 5.987 | 0.010 | 0.003 | 0.393 | 4.182 | 3.982 | 1.372 | 0.000 | 0.005 | 0.085 | 16.021 |
| RB06_145-Grt | 39.10 | 0.03 | 0.04 | 4.61 | 26.09 | 21.78 | 7.81 | 0.00 | 0.08 | 0.91 | 100.48 | 6.012 | 0.010 | 0.004 | 0.759 | 3.354 | 3.948 | 1.789 | 0.000 | 0.010 | 0.119 | 16.008 |
| RB06_146-Grt | 38.60 | 0.00 | 0.03 | 1.79 | 30.00 | 21.90 | 7.27 | 0.00 | 0.04 | 0.56 | 100.19 | 6.003 | 0.000 | 0.003 | 0.299 | 3.901 | 4.014 | 1.685 | 0.000 | 0.005 | 0.073 | 15.983 |
| RB06_147-Grt | 38.57 | 0.00 | 0.02 | 6.81 | 27.75 | 21.53 | 4.94 | 0.03 | 0.12 | 0.83 | 100.63 | 6.011 | 0.000 | 0.002 | 1.137 | 3.616 | 3.955 | 1.147 | 0.006 | 0.014 | 0.109 | 16.000 |
| RB06_148-Grt | 37.80 | 0.01 | 0.00 | 1.53 | 34.88 | 21.61 | 4.04 | 0.00 | 0.00 | 1.06 | 100.96 | 5.985 | 0.004 | 0.000 | 0.260 | 4.619 | 4.033 | 0.954 | 0.000 | 0.000 | 0.142 | 16.000 |
| RB06_149-Grt | 38.75 | 0.00 | 0.00 | 3.26 | 29.53 | 21.91 | 6.41 | 0.02 | 0.05 | 0.66 | 100.58 | 6.015 | 0.000 | 0.000 | 0.542 | 3.833 | 4.008 | 1.483 | 0.003 | 0.006 | 0.087 | 15.977 |
| RB06_150-Grt | 39.25 | 0.00 | 0.00 | 7.06 | 25.56 | 21.78 | 6.63 | 0.02 | 0.08 | 0.63 | 101.03 | 6.018 | 0.000 | 0.000 | 1.161 | 3.278 | 3.937 | 1.516 | 0.004 | 0.010 | 0.081 | 16.005 |
| RB06_151-Grt | 38.74 | 0.01 | 0.04 | 6.07 | 28.28 | 21.67 | 5.39 | 0.01 | 0.16 | 0.67 | 101.04 | 6.004 | 0.003 | 0.005 | 1.008 | 3.666 | 3.958 | 1.246 | 0.002 | 0.018 | 0.088 | 15.998 |
| RB06_152-Grt | 39.11 | 0.00 | 0.03 | 1.28 | 27.99 | 22.13 | 9.01 | 0.01 | 0.04 | 0.36 | 100.00 | 6.017 | 0.000 | 0.004 | 0.212 | 3.602 | 4.013 | 2.066 | 0.003 | 0.005 | 0.047 | 15.971 |
| RB06_153-Grt | 38.37 | 0.00 | 0.05 | 1.71 | 33.00 | 21.80 | 5.32 | 0.01 | 0.00 | 0.54 | 100.80 | 6.012 | 0.001 | 0.006 | 0.287 | 4.325 | 4.027 | 1.242 | 0.001 | 0.000 | 0.072 | 15.973 |
| RB06_154-Grt | 38.85 | 0.04 | 0.03 | 1.43 | 30.21 | 22.04 | 7.55 | 0.00 | 0.01 | 0.50 | 100.66 | 6.006 | 0.013 | 0.003 | 0.237 | 3.906 | 4.017 | 1.740 | 0.001 | 0.001 | 0.065 | 15.990 |
| TI14_314-Grt | 36.56 | 0.02 | 0.00 | 0.62 | 32.09 | 20.45 | 1.55 | 0.00 | 0.24 | 8.63 | 100.20 | 5.977 | 0.007 | 0.000 | 0.109 | 4.387 | 3.940 | 0.378 | 0.000 | 0.030 | 1.196 | 16.026 |
| TI14_315-Grt | 38.55 | 0.03 | 0.02 | 1.16 | 31.14 | 21.92 | 6.53 | 0.00 | 0.03 | 1.31 | 100.75 | 6.004 | 0.008 | 0.002 | 0.193 | 4.056 | 4.024 | 1.516 | 0.000 | 0.003 | 0.173 | 15.984 |
| TI14_316-Grt | 36.92 | 0.01 | 0.02 | 0.61 | 32.88 | 20.58 | 1.04 | 0.00 | 0.15 | 8.79 | 101.00 | 6.002 | 0.002 | 0.003 | 0.107 | 4.470 | 3.943 | 0.252 | 0.000 | 0.018 | 1.210 | 16.008 |
| TI14_317-Grt | 39.55 | 0.00 | 0.04 | 2.55 | 26.36 | 22.31 | 9.43 | 0.00 | 0.03 | 0.46 | 100.73 | 6.013 | 0.000 | 0.005 | 0.416 | 3.352 | 3.997 | 2.138 | 0.000 | 0.003 | 0.059 | 15.983 |
| TI14_318-Grt | 37.93 | 0.02 | 0.02 | 1.08 | 33.29 | 21.44 | 5.75 | 0.00 | 0.08 | 0.68 | 100.30 | 5.985 | 0.007 | 0.003 | 0.183 | 4.394 | 3.988 | 1.352 | 0.000 | 0.010 | 0.091 | 16.013 |
| TI14_319-Grt | 38.36 | 0.00 | 0.03 | 1.06 | 30.61 | 21.73 | 7.29 | 0.03 | 0.06 | 0.59 | 99.77 | 6.002 | 0.000 | 0.004 | 0.178 | 4.005 | 4.007 | 1.701 | 0.006 | 0.008 | 0.078 | 15.988 |
| TI14_320-Grt | 37.16 | 0.00 | 0.05 | 0.92 | 19.92 | 21.19 | 1.59 | 0.01 | 0.18 | 20.04 | 101.05 | 5.981 | 0.000 | 0.006 | 0.159 | 2.682 | 4.021 | 0.381 | 0.002 | 0.022 | 2.732 | 15.985 |
| PT03_125-Grt | 39.06 | 0.02 | 0.03 | 1.61 | 27.50 | 22.48 | 9.25 | 0.02 | 0.04 | 0.39 | 100.41 | 5.976 | 0.006 | 0.004 | 0.263 | 3.520 | 4.055 | 2.111 | 0.003 | 0.004 | 0.050 | 15.994 |
| PT03_126-Grt | 38.16 | 0.03 | 0.01 | 6.95 | 28.07 | 21.35 | 4.42 | 0.00 | 0.11 | 0.70 | 99.81 | 6.010 | 0.008 | 0.001 | 1.173 | 3.697 | 3.963 | 1.038 | 0.000 | 0.013 | 0.093 | 15.999 |
| PT03_127-Grt | 38.28 | 0.01 | 0.00 | 6.94 | 28.93 | 21.45 | 4.09 | 0.00 | 0.07 | 0.75 | 100.50 | 6.007 | 0.002 | 0.000 | 1.168 | 3.797 | 3.967 | 0.956 | 0.000 | 0.008 | 0.099 | 16.002 |
| PT03_128-Grt | 39.19 | 0.00 | 0.04 | 6.08 | 23.38 | 22.10 | 8.17 | 0.00 | 0.07 | 1.09 | 100.16 | 5.999 | 0.000 | 0.005 | 0.997 | 2.993 | 3.987 | 1.863 | 0.000 | 0.008 | 0.142 | 15.997 |
| PT03_129-Grt | 37.99 | 0.00 | 0.04 | 0.92 | 33.56 | 21.80 | 5.50 | 0.01 | 0.03 | 0.88 | 100.76 | 5.974 | 0.000 | 0.004 | 0.155 | 4.413 | 4.040 | 1.290 | 0.003 | 0.004 | 0.118 | 16.002 |
| PT03_130-Grt | 39.05 | 0.01 | 0.03 | 1.09 | 27.96 | 22.41 | 9.32 | 0.00 | 0.03 | 0.66 | 100.62 | 5.976 | 0.003 | 0.003 | 0.179 | 3.579 | 4.041 | 2.126 | 0.000 | 0.003 | 0.085 | 16.000 |
| PT03_131-Grt | 39.15 | 0.00 | 0.03 | 1.78 | 27.62 | 22.30 | 8.67 | 0.00 | 0.01 | 0.54 | 100.10 | 6.017 | 0.000 | 0.003 | 0.294 | 3.550 | 4.040 | 1.987 | 0.001 | 0.001 | 0.070 | 15.961 |
| PT03_132-Grt | 38.62 | 0.01 | 0.06 | 1.04 | 30.57 | 22.13 | 7.68 | 0.00 | 0.01 | 0.20 | 100.36 | 5.988 | 0.003 | 0.007 | 0.173 | 3.965 | 4.044 | 1.776 | 0.000 | 0.001 | 0.027 | 15.987 |
| PT03_133-Grt | 39.86 | 0.01 | 0.08 | 1.82 | 22.33 | 22.78 | 12.54 | 0.02 | 0.03 | 0.37 | 99.84 | 5.987 | 0.002 | 0.010 | 0.293 | 2.805 | 4.033 | 2.808 | 0.003 | 0.003 | 0.047 | 15.991 |
| PT03_134-Grt | 39.92 | 0.00 | 0.07 | 1.77 | 22.19 | 22.95 | 12.63 | 0.00 | 0.00 | 0.41 | 99.96 | 5.983 | 0.000 | 0.008 | 0.284 | 2.782 | 4.054 | 2.822 | 0.000 | 0.000 | 0.052 | 15.985 |
| PT03_135-Grt | 39.10 | 0.00 | 0.07 | 1.59 | 27.29 | 22.19 | 9.16 | 0.00 | 0.03 | 0.80 | 100.29 | 5.998 | 0.000 | 0.009 | 0.261 | 3.501 | 4.013 | 2.094 | 0.000 | 0.003 | 0.105 | 15.988 |
| PT03_136-Grt | 40.39 | 0.00 | 0.04 | 1.76 | 20.15 | 23.05 | 13.87 | 0.00 | 0.00 | 0.83 | 100.17 | 5.993 | 0.000 | 0.005 | 0.279 | 2.501 | 4.031 | 3.068 | 0.000 | 0.000 | 0.105 | 15.989 |
| PT03_137-Grt | 37.54 | 0.00 | 0.00 | 1.29 | 35.58 | 21.50 | 3.24 | 0.00 | 0.02 | 1.78 | 100.97 | 5.982 | 0.000 | 0.000 | 0.220 | 4.741 | 4.039 | 0.770 | 0.000 | 0.002 | 0.240 | 15.996 |
| PT03_138-Grt | 39.58 | 0.02 | 0.09 | 2.51 | 25.46 | 22.22 | 10.13 | 0.00 | 0.04 | 0.41 | 100.54 | 6.009 | 0.005 | 0.011 | 0.407 | 3.233 | 3.976 | 2.293 | 0.000 | 0.004 | 0.053 | 15.996 |
| PT03_139-Grt | 38.51 | 0.03 | 0.03 | 0.94 | 31.63 | 21.91 | 6.69 | 0.00 | 0.01 | 0.92 | 100.68 | 5.999 | 0.008 | 0.003 | 0.156 | 4.121 | 4.024 | 1.555 | 0.000 | 0.002 | 0.121 | 15.990 |
| PT03_140-Grt | 39.61 | 0.00 | 0.22 | 6.21 | 22.66 | 22.17 | 8.98 | 0.01 | 0.05 | 0.65 | 100.57 | 6.005 | 0.000 | 0.027 | 1.008 | 2.873 | 3.961 | 2.030 | 0.002 | 0.006 | 0.084 | 15.996 |
| MA06-1_091-Grt | 38.56 | 0.00 | 0.04 | 0.76 | 32.28 | 21.62 | 6.81 | 0.01 | 0.04 | 0.59 | 100.78 | 6.011 | 0.000 | 0.005 | 0.126 | 4.208 | 3.973 | 1.583 | 0.003 | 0.005 | 0.078 | 15.997 |
| MA06-1_133-Grt | 38.47 | 0.00 | 0.04 | 1.61 | 30.22 | 21.85 | 7.30 | 0.00 | 0.02 | 0.60 | 100.10 | 5.994 | 0.000 | 0.005 | 0.268 | 3.938 | 4.013 | 1.696 | 0.000 | 0.002 | 0.080 | 15.995 |
| MA06-1_134-Grt | 39.22 | 0.04 | 0.03 | 9.48 | 23.59 | 21.53 | 6.35 | 0.02 | 0.20 | 0.43 | 100.92 | 6.010 | 0.011 | 0.004 | 1.556 | 3.023 | 3.888 | 1.450 | 0.004 | 0.023 | 0.056 | 16.029 |
| MA06-1_135-Grt | 39.05 | 0.01 | 0.05 | 1.71 | 29.59 | 21.72 | 7.69 | 0.01 | 0.02 | 0.78 | 100.66 | 6.034 | 0.003 | 0.007 | 0.283 | 3.824 | 3.956 | 1.771 | 0.002 | 0.002 | 0.102 | 15.985 |
| MA06-1_136-Grt | 38.68 | 0.00 | 0.01 | 7.79 | 26.03 | 21.27 | 5.41 | 0.00 | 0.09 | 0.78 | 100.06 | 6.031 | 0.000 | 0.001 | 1.302 | 3.394 | 3.908 | 1.256 | 0.000 | 0.010 | 0.103 | 16.005 |
| MA06-1_137-Grt | 38.72 | 0.00 | 0.02 | 0.69 | 29.84 | 22.07 | 8.73 | 0.01 | 0.08 | 0.19 | 100.35 | 5.977 | 0.000 | 0.002 | 0.113 | 3.853 | 4.015 | 2.010 | 0.002 | 0.010 | 0.025 | 16.006 |
| MA06-1_138-Grt | 39.01 | 0.01 | 0.03 | 1.03 | 28.26 | 22.29 | 9.27 | 0.01 | 0.08 | 0.29 | 100.28 | 5.986 | 0.002 | 0.003 | 0.170 | 3.627 | 4.032 | 2.120 | 0.002 | 0.010 | 0.038 | 15.988 |
| MA06-1_139-Grt | 38.52 | 0.02 | 0.12 | 6.38 | 27.89 | 21.68 | 5.59 | 0.00 | 0.06 | 0.65 | 100.95 | 5.976 | 0.005 | 0.015 | 1.061 | 3.619 | 3.964 | 1.293 | 0.000 | 0.008 | 0.086 | 16.029 |
| MA06-1_140-Grt | 39.78 | 0.01 | 0.15 | 2.22 | 25.80 | 22.34 | 9.73 | 0.02 | 0.03 | 0.78 | 100.88 | 6.026 | 0.003 | 0.018 | 0.361 | 3.268 | 3.988 | 2.196 | 0.005 | 0.004 | 0.100 | 15.970 |
| MA06-1_147-Grt | 38.50 | 0.01 | 0.00 | 0.62 | 32.36 | 21.89 | 6.71 | 0.01 | 0.05 | 0.62 | 100.76 | 5.998 | 0.004 | 0.000 | 0.103 | 4.217 | 4.020 | 1.558 | 0.003 | 0.005 | 0.082 | 15.990 |

| Sample / No. | $SiO_2$ | $Na_2O$ | $Cr_2O_3$ | CaO | FeO | $Al_2O_3$ | MgO | $K_2O$ | $TiO_2$ | MnO | wt-total | Si_at | Na_at | Cr_at | Ca_at | Fe_at | Al_at | Mg_at | K_at | Ti_at | Mn_at | at-total |
|---|---|---|---|---|---|---|---|---|---|---|---|---|---|---|---|---|---|---|---|---|---|---|
| MA06-3_107-Grt | 38.85 | 0.04 | 0.05 | 0.87 | 29.70 | 22.36 | 8.63 | 0.01 | 0.00 | 0.52 | 101.04 | 5.961 | 0.011 | 0.007 | 0.144 | 3.811 | 4.044 | 1.975 | 0.002 | 0.000 | 0.067 | 16.021 |
| MA06-3_108-Grt | 38.83 | 0.00 | 0.00 | 1.83 | 29.52 | 22.05 | 7.34 | 0.01 | 0.01 | 1.18 | 100.77 | 6.003 | 0.001 | 0.000 | 0.302 | 3.817 | 4.017 | 1.691 | 0.001 | 0.001 | 0.154 | 15.989 |
| MA06-3_110-Grt | 40.21 | 0.01 | 0.05 | 2.99 | 24.15 | 22.43 | 10.65 | 0.02 | 0.03 | 0.26 | 100.81 | 6.043 | 0.003 | 0.006 | 0.481 | 3.036 | 3.973 | 2.386 | 0.003 | 0.003 | 0.034 | 15.968 |
| MA06-3_110-Grt | 39.24 | 0.00 | 0.02 | 0.76 | 27.16 | 22.16 | 9.73 | 0.00 | 0.07 | 0.87 | 100.03 | 6.015 | 0.000 | 0.003 | 0.125 | 3.482 | 4.005 | 2.223 | 0.000 | 0.008 | 0.113 | 15.973 |
| MA06-3_112-Grt | 39.12 | 0.00 | 0.03 | 2.64 | 29.11 | 22.05 | 7.13 | 0.00 | 0.06 | 0.63 | 100.79 | 6.030 | 0.000 | 0.004 | 0.436 | 3.753 | 4.007 | 1.637 | 0.000 | 0.007 | 0.082 | 15.957 |
| MA06-3_113-Grt | 39.02 | 0.00 | 0.01 | 1.14 | 28.69 | 22.27 | 8.84 | 0.02 | 0.06 | 0.26 | 100.33 | 5.997 | 0.000 | 0.001 | 0.188 | 3.687 | 4.034 | 2.026 | 0.003 | 0.007 | 0.034 | 15.980 |
| MA06-3_114-Grt | 38.56 | 0.02 | 0.02 | 1.77 | 30.43 | 21.71 | 6.86 | 0.01 | 0.02 | 0.60 | 100.01 | 6.022 | 0.006 | 0.002 | 0.296 | 3.975 | 3.997 | 1.598 | 0.002 | 0.003 | 0.080 | 15.980 |
| MA06-3_119-Grt | 38.67 | 0.00 | 0.10 | 1.87 | 31.47 | 21.74 | 6.36 | 0.00 | 0.04 | 0.39 | 100.66 | 6.023 | 0.000 | 0.012 | 0.312 | 4.099 | 3.990 | 1.476 | 0.001 | 0.005 | 0.052 | 15.971 |
| MA06-3_121-Grt | 39.70 | 0.00 | 0.17 | 2.38 | 22.54 | 22.19 | 11.70 | 0.01 | 0.03 | 0.39 | 99.10 | 6.028 | 0.000 | 0.020 | 0.387 | 2.863 | 3.971 | 2.649 | 0.002 | 0.003 | 0.050 | 15.974 |
| MA06-3_122-Grt | 39.06 | 0.04 | 0.00 | 8.30 | 24.13 | 21.67 | 6.50 | 0.01 | 0.15 | 0.54 | 100.41 | 6.011 | 0.012 | 0.000 | 1.369 | 3.106 | 3.932 | 1.492 | 0.002 | 0.018 | 0.071 | 16.012 |
| MA06-3_124-Grt | 39.22 | 0.00 | 0.07 | 0.99 | 27.30 | 22.39 | 9.83 | 0.00 | 0.03 | 0.48 | 100.30 | 5.991 | 0.000 | 0.009 | 0.162 | 3.487 | 4.031 | 2.240 | 0.000 | 0.003 | 0.062 | 15.985 |
| MA06-3_125-Grt | 39.53 | 0.00 | 0.09 | 0.90 | 27.87 | 22.09 | 9.53 | 0.00 | 0.03 | 0.34 | 100.38 | 6.042 | 0.000 | 0.011 | 0.147 | 3.563 | 3.979 | 2.171 | 0.000 | 0.003 | 0.044 | 15.960 |
| MA06-3_126-Grt | 37.47 | 0.02 | 0.00 | 7.09 | 32.31 | 20.63 | 1.74 | 0.01 | 0.08 | 0.85 | 100.19 | 6.015 | 0.006 | 0.000 | 1.220 | 4.339 | 3.903 | 0.416 | 0.001 | 0.010 | 0.116 | 16.026 |
| MA06-3_127-Grt | 39.59 | 0.03 | 0.04 | 1.59 | 26.21 | 22.38 | 10.27 | 0.01 | 0.03 | 0.19 | 100.32 | 6.015 | 0.008 | 0.005 | 0.259 | 3.331 | 4.008 | 2.326 | 0.001 | 0.003 | 0.024 | 15.980 |
| MA06-3_128-Grt | 39.28 | 0.00 | 0.00 | 1.04 | 29.58 | 22.24 | 8.16 | 0.00 | 0.05 | 0.39 | 100.75 | 6.031 | 0.001 | 0.000 | 0.171 | 3.798 | 4.025 | 1.868 | 0.000 | 0.006 | 0.051 | 15.951 |
| CHW26_252-Grt | 38.44 | 0.00 | 0.03 | 1.41 | 32.09 | 21.64 | 6.46 | 0.00 | 0.05 | 0.71 | 100.83 | 5.997 | 0.000 | 0.003 | 0.236 | 4.188 | 3.980 | 1.502 | 0.000 | 0.006 | 0.093 | 16.005 |
| CHW26_253-Grt | 38.82 | 0.02 | 0.10 | 3.74 | 28.79 | 21.66 | 6.59 | 0.01 | 0.06 | 0.81 | 100.64 | 6.020 | 0.005 | 0.013 | 0.621 | 3.734 | 3.958 | 1.523 | 0.001 | 0.006 | 0.106 | 15.991 |
| CHW26_255-Grt | 38.36 | 0.00 | 0.01 | 1.77 | 31.81 | 21.83 | 6.64 | 0.00 | 0.06 | 0.45 | 100.93 | 5.971 | 0.000 | 0.001 | 0.295 | 4.141 | 4.005 | 1.541 | 0.000 | 0.007 | 0.060 | 16.020 |
| CHW26_256-Grt | 38.31 | 0.00 | 0.00 | 3.57 | 31.15 | 21.47 | 4.69 | 0.02 | 0.07 | 1.90 | 101.20 | 6.002 | 0.000 | 0.000 | 0.599 | 4.082 | 3.965 | 1.095 | 0.004 | 0.008 | 0.252 | 16.009 |
| CHW26_257-Grt | 38.57 | 0.01 | 0.03 | 6.22 | 26.87 | 21.76 | 5.93 | 0.00 | 0.07 | 0.96 | 100.43 | 5.989 | 0.002 | 0.004 | 1.035 | 3.489 | 3.983 | 1.373 | 0.000 | 0.009 | 0.126 | 16.010 |
| CHW26_258-Grt | 37.79 | 0.03 | 0.14 | 6.20 | 30.28 | 21.23 | 3.66 | 0.00 | 0.00 | 0.84 | 100.16 | 5.989 | 0.010 | 0.017 | 1.053 | 4.014 | 3.965 | 0.864 | 0.000 | 0.000 | 0.112 | 16.024 |
| CHW26_259-Grt | 38.00 | 0.00 | 0.00 | 2.36 | 32.03 | 21.37 | 4.88 | 0.00 | 0.00 | 1.37 | 100.03 | 6.018 | 0.001 | 0.000 | 0.400 | 4.242 | 3.989 | 1.152 | 0.000 | 0.000 | 0.183 | 15.988 |
| CHW26_260-Grt | 38.25 | 0.03 | 0.08 | 2.52 | 31.18 | 21.32 | 6.10 | 0.00 | 0.05 | 0.96 | 100.49 | 5.997 | 0.009 | 0.010 | 0.423 | 4.089 | 3.940 | 1.425 | 0.000 | 0.006 | 0.127 | 16.026 |
| CHW26_261-Grt | 38.23 | 0.05 | 0.02 | 1.36 | 32.56 | 21.79 | 5.95 | 0.00 | 0.03 | 0.81 | 100.80 | 5.983 | 0.016 | 0.002 | 0.228 | 4.262 | 4.020 | 1.388 | 0.001 | 0.003 | 0.108 | 16.011 |
| CHW26_262-Grt | 37.71 | 0.00 | 0.01 | 2.73 | 33.56 | 21.14 | 3.56 | 0.01 | 0.03 | 1.84 | 100.65 | 6.004 | 0.000 | 0.002 | 0.466 | 4.469 | 3.968 | 0.844 | 0.002 | 0.003 | 0.248 | 16.009 |
| CHW26_263-Grt | 38.31 | 0.01 | 0.02 | 5.37 | 31.78 | 20.85 | 4.06 | 0.00 | 0.06 | 0.62 | 101.09 | 6.029 | 0.004 | 0.002 | 0.905 | 4.182 | 3.866 | 0.953 | 0.000 | 0.008 | 0.082 | 16.031 |
| CHW26_264-Grt | 40.48 | 0.00 | 0.00 | 6.57 | 18.44 | 22.60 | 12.13 | 0.00 | 0.08 | 0.21 | 100.53 | 6.005 | 0.000 | 0.000 | 1.045 | 2.288 | 3.952 | 2.682 | 0.000 | 0.009 | 0.027 | 16.010 |
| CHW26_265-Grt | 39.03 | 0.02 | 0.04 | 1.34 | 28.96 | 22.11 | 8.74 | 0.02 | 0.04 | 0.21 | 100.53 | 5.998 | 0.005 | 0.005 | 0.221 | 3.723 | 4.005 | 2.002 | 0.003 | 0.005 | 0.027 | 15.996 |
| CHW26_267-Grt | 36.54 | 0.04 | 0.02 | 0.86 | 22.15 | 19.86 | 0.98 | 0.00 | 0.10 | 19.59 | 100.19 | 6.009 | 0.011 | 0.002 | 0.151 | 3.047 | 3.850 | 0.241 | 0.000 | 0.013 | 2.729 | 16.058 |
| CHW26_268-Grt | 39.34 | 0.02 | 0.08 | 1.47 | 26.58 | 22.09 | 9.90 | 0.00 | 0.02 | 0.36 | 99.89 | 6.023 | 0.005 | 0.009 | 0.242 | 3.404 | 3.986 | 2.260 | 0.000 | 0.002 | 0.047 | 15.980 |
| CHW26_269-Grt | 39.16 | 0.02 | 0.04 | 5.64 | 24.76 | 21.39 | 8.12 | 0.01 | 0.12 | 1.10 | 100.44 | 6.016 | 0.005 | 0.005 | 0.929 | 3.181 | 3.874 | 1.860 | 0.003 | 0.014 | 0.143 | 16.035 |
| CHW26_270-Grt | 38.05 | 0.05 | 0.00 | 0.86 | 31.94 | 21.97 | 7.15 | 0.00 | 0.02 | 0.21 | 100.26 | 5.949 | 0.017 | 0.000 | 0.144 | 4.176 | 4.049 | 1.667 | 0.000 | 0.002 | 0.028 | 16.032 |
| CHW26_271-Grt | 38.44 | 0.02 | 0.05 | 5.75 | 22.66 | 21.22 | 6.96 | 0.00 | 0.07 | 4.26 | 99.48 | 6.002 | 0.005 | 0.006 | 0.963 | 2.960 | 3.905 | 1.621 | 0.000 | 0.008 | 0.564 | 16.037 |
| CHW26_272-Grt | 38.81 | 0.02 | 0.01 | 5.76 | 23.12 | 21.58 | 6.96 | 0.00 | 0.06 | 4.44 | 100.76 | 5.988 | 0.006 | 0.001 | 0.953 | 2.983 | 3.926 | 1.601 | 0.000 | 0.007 | 0.580 | 16.045 |
| CHW06_057-Grt | 39.43 | 0.00 | 0.07 | 2.77 | 27.00 | 22.02 | 8.78 | 0.00 | 0.07 | 0.94 | 101.10 | 6.012 | 0.000 | 0.009 | 0.452 | 3.443 | 3.956 | 1.996 | 0.001 | 0.008 | 0.121 | 15.998 |
| CHW06_058-Grt | 38.61 | 0.01 | 0.01 | 2.40 | 31.02 | 21.56 | 5.92 | 0.00 | 0.05 | 0.94 | 100.54 | 6.033 | 0.003 | 0.001 | 0.401 | 4.054 | 3.971 | 1.380 | 0.000 | 0.006 | 0.125 | 15.976 |
| CHW06_059-Grt | 39.04 | 0.05 | 0.06 | 1.38 | 28.30 | 22.25 | 8.85 | 0.01 | 0.08 | 0.63 | 100.70 | 5.985 | 0.016 | 0.007 | 0.226 | 3.628 | 4.019 | 2.022 | 0.002 | 0.010 | 0.082 | 16.001 |
| CHW06_061-Grt | 37.84 | 0.00 | 0.01 | 1.00 | 34.96 | 21.46 | 4.63 | 0.01 | 0.01 | 0.57 | 100.51 | 5.999 | 0.000 | 0.002 | 0.169 | 4.636 | 4.012 | 1.094 | 0.001 | 0.002 | 0.077 | 15.993 |
| CHW06_063-Grt | 38.83 | 0.06 | 0.07 | 1.19 | 29.47 | 21.80 | 8.16 | 0.01 | 0.02 | 0.59 | 100.19 | 6.014 | 0.017 | 0.009 | 0.198 | 3.817 | 3.980 | 1.885 | 0.002 | 0.002 | 0.077 | 16.000 |
| CHW06_064-Grt | 39.21 | 0.01 | 0.06 | 2.50 | 28.13 | 22.10 | 8.02 | 0.02 | 0.07 | 0.59 | 100.73 | 6.019 | 0.003 | 0.007 | 0.412 | 3.611 | 3.998 | 1.834 | 0.004 | 0.008 | 0.077 | 15.975 |
| CHW06_066-Grt | 39.36 | 0.04 | 0.06 | 1.94 | 27.01 | 22.27 | 9.33 | 0.02 | 0.07 | 0.80 | 100.93 | 5.994 | 0.011 | 0.007 | 0.316 | 3.441 | 3.998 | 2.117 | 0.003 | 0.008 | 0.103 | 16.002 |
| CHW06_067-Grt | 38.39 | 0.02 | 0.04 | 6.22 | 23.56 | 20.85 | 4.79 | 0.00 | 0.12 | 6.32 | 100.34 | 6.031 | 0.007 | 0.005 | 1.047 | 3.095 | 3.861 | 1.122 | 0.000 | 0.014 | 0.840 | 16.025 |
| CHW06_068-Grt | 38.69 | 0.00 | 0.06 | 2.65 | 30.35 | 21.71 | 6.25 | 0.01 | 0.04 | 0.92 | 100.68 | 6.021 | 0.000 | 0.008 | 0.442 | 3.950 | 3.982 | 1.449 | 0.001 | 0.004 | 0.122 | 15.980 |
| CHW06_069-Grt | 39.00 | 0.01 | 0.01 | 1.40 | 28.93 | 22.08 | 8.12 | 0.00 | 0.00 | 0.59 | 100.19 | 6.023 | 0.004 | 0.001 | 0.231 | 3.737 | 4.021 | 1.869 | 0.000 | 0.000 | 0.078 | 15.968 |
| CHW06_070-Grt | 39.42 | 0.00 | 0.05 | 5.97 | 24.65 | 21.96 | 7.40 | 0.00 | 0.06 | 1.60 | 101.20 | 6.016 | 0.000 | 0.006 | 0.977 | 3.146 | 3.950 | 1.685 | 0.000 | 0.006 | 0.207 | 16.000 |
| CHW06_076-Grt | 38.86 | 0.02 | 0.09 | 1.51 | 27.68 | 21.82 | 8.51 | 0.00 | 0.04 | 1.07 | 99.60 | 6.023 | 0.006 | 0.011 | 0.251 | 3.588 | 3.986 | 1.966 | 0.000 | 0.005 | 0.141 | 15.977 |
| ER04_201-Grt | 38.10 | 0.05 | 0.01 | 4.13 | 29.37 | 21.41 | 3.68 | 0.01 | 0.13 | 3.93 | 100.82 | 6.011 | 0.016 | 0.001 | 0.697 | 3.875 | 3.982 | 0.865 | 0.003 | 0.016 | 0.525 | 15.992 |
| ER04_219-Grt | 39.87 | 0.00 | 0.01 | 32.17 | 7.03 | 20.98 | 0.09 | 0.02 | 0.19 | 0.56 | 100.95 | 6.052 | 0.000 | 0.001 | 5.232 | 0.892 | 3.754 | 0.020 | 0.003 | 0.021 | 0.072 | 16.051 |
| ER04_220-Grt | 39.64 | 0.00 | 0.01 | 32.67 | 7.12 | 20.56 | 0.08 | 0.00 | 0.24 | 0.55 | 100.89 | 6.039 | 0.000 | 0.001 | 5.332 | 0.907 | 3.691 | 0.018 | 0.000 | 0.028 | 0.070 | 16.088 |
| ER04_221-Grt | 39.58 | 0.00 | 0.03 | 32.52 | 7.08 | 20.59 | 0.08 | 0.01 | 0.31 | 0.55 | 100.74 | 6.035 | 0.000 | 0.004 | 5.313 | 0.902 | 3.699 | 0.017 | 0.002 | 0.035 | 0.072 | 16.080 |

# Analyses of amphiboles

| Sample / No. | $SiO_2$ | $Na_2O$ | $K_2O$ | CaO | FeO | $Al_2O_3$ | MgO | SrO | $TiO_2$ | MnO | BaO | wt-total | Si_at | Na_at | K_at | Ca_at | $Fe^{3+}$_at | $Fe^{2+}$_at | Al_at | Mg_at | Sr_at | Ti_at | Mn_at | Ba_at | at-total | O_at |
|---|---|---|---|---|---|---|---|---|---|---|---|---|---|---|---|---|---|---|---|---|---|---|---|---|---|---|
| SHA05_Hbl43 | 41.96 | 1.50 | 1.94 | 11.41 | 17.74 | 11.51 | 9.15 | 0.05 | 2.63 | 0.14 | 0.00 | 98.01 | 6.287 | 0.438 | 0.371 | 1.832 | 0.521 | 1.702 | 2.033 | 2.044 | 0.004 | 0.296 | 0.017 | 0.000 | 15.545 | 22.740 |
| SHA05_Hbl44 | 41.77 | 1.53 | 1.87 | 11.36 | 17.59 | 11.64 | 9.14 | 0.00 | 2.64 | 0.14 | 0.02 | 97.69 | 6.271 | 0.448 | 0.358 | 1.828 | 0.534 | 1.675 | 2.060 | 2.046 | 0.000 | 0.298 | 0.017 | 0.001 | 15.536 | 22.733 |
| SHA05_Hbl45 | 43.02 | 1.60 | 1.63 | 11.54 | 14.17 | 10.32 | 12.21 | 0.00 | 1.97 | 0.23 | 0.05 | 96.75 | 6.395 | 0.463 | 0.309 | 1.838 | 0.668 | 1.094 | 1.808 | 2.706 | 0.000 | 0.220 | 0.029 | 0.003 | 15.533 | 22.666 |
| SHA05_Hbl47 | 43.57 | 1.64 | 1.34 | 10.96 | 15.87 | 10.04 | 11.13 | 0.01 | 1.65 | 0.14 | 0.00 | 96.34 | 6.523 | 0.478 | 0.256 | 1.758 | 0.619 | 1.368 | 1.772 | 2.485 | 0.001 | 0.186 | 0.018 | 0.000 | 15.463 | 22.691 |
| SHA05_Hbl48 | 41.91 | 1.79 | 1.23 | 11.17 | 17.94 | 11.86 | 9.18 | 0.00 | 2.30 | 0.18 | 0.04 | 97.60 | 6.263 | 0.521 | 0.235 | 1.788 | 0.691 | 1.551 | 2.089 | 2.045 | 0.000 | 0.258 | 0.023 | 0.002 | 15.467 | 22.654 |
| SHA05_Hbl50 | 42.44 | 1.44 | 1.94 | 11.84 | 12.00 | 12.79 | 12.57 | 0.00 | 1.98 | 0.12 | 0.00 | 97.11 | 6.234 | 0.412 | 0.364 | 1.864 | 0.556 | 0.918 | 2.215 | 2.753 | 0.000 | 0.219 | 0.014 | 0.000 | 15.549 | 22.722 |
| SHA05_Hbl51 | 42.77 | 1.48 | 1.96 | 11.86 | 11.60 | 12.56 | 12.70 | 0.00 | 2.15 | 0.12 | 0.00 | 97.20 | 6.269 | 0.423 | 0.367 | 1.863 | 0.524 | 0.898 | 2.170 | 2.776 | 0.000 | 0.237 | 0.015 | 0.000 | 15.541 | 22.738 |
| SHA05_Hbl52r | 43.82 | 1.48 | 1.30 | 11.80 | 15.72 | 9.92 | 10.95 | 0.00 | 1.08 | 0.50 | 0.00 | 97.38 | 6.515 | 0.428 | 0.246 | 1.880 | 0.738 | 1.307 | 1.738 | 2.427 | 0.000 | 0.121 | 0.063 | 0.000 | 15.464 | 22.631 |
| SHA05_Hbl53r | 43.41 | 1.74 | 1.28 | 11.72 | 13.38 | 11.30 | 12.72 | 0.00 | 1.62 | 0.30 | 0.06 | 97.57 | 6.344 | 0.496 | 0.239 | 1.835 | 0.758 | 0.883 | 1.947 | 2.772 | 0.000 | 0.178 | 0.037 | 0.004 | 15.492 | 22.621 |
| SHA07_101-Hbl | 46.62 | 0.93 | 0.83 | 11.59 | 15.46 | 8.45 | 11.97 | 0.00 | 1.68 | 0.39 | 0.00 | 97.91 | 6.840 | 0.264 | 0.156 | 1.821 | 0.332 | 1.566 | 1.461 | 2.616 | 0.000 | 0.185 | 0.049 | 0.000 | 15.289 | 22.834 |
| SHA07_102-Hbl | 44.12 | 1.29 | 0.98 | 11.80 | 15.21 | 11.18 | 11.26 | 0.00 | 1.01 | 0.33 | 0.00 | 97.24 | 6.506 | 0.370 | 0.185 | 1.865 | 0.632 | 1.243 | 1.943 | 2.475 | 0.000 | 0.112 | 0.041 | 0.000 | 15.372 | 22.684 |
| SHA07_103-Hbl | 43.19 | 1.40 | 0.84 | 11.84 | 16.77 | 12.01 | 10.17 | 0.02 | 1.02 | 0.31 | 0.00 | 97.59 | 6.377 | 0.400 | 0.159 | 1.874 | 0.764 | 1.307 | 2.090 | 2.239 | 0.002 | 0.113 | 0.039 | 0.000 | 15.363 | 22.618 |
| SHA07_104-Hbl | 42.12 | 1.55 | 1.69 | 11.38 | 13.02 | 13.01 | 11.85 | 0.00 | 2.17 | 0.13 | 0.00 | 97.27 | 6.229 | 0.444 | 0.319 | 1.803 | 0.466 | 1.144 | 2.268 | 2.613 | 0.000 | 0.242 | 0.016 | 0.000 | 15.544 | 22.767 |
| SHA07_105-Hbl | 42.05 | 1.56 | 2.19 | 11.34 | 17.52 | 11.55 | 9.61 | 0.04 | 1.32 | 0.37 | 0.00 | 97.56 | 6.332 | 0.457 | 0.420 | 1.830 | 0.557 | 1.649 | 2.050 | 2.159 | 0.003 | 0.149 | 0.047 | 0.000 | 15.654 | 22.721 |
| SHA07_106-Hbl | 44.72 | 1.26 | 0.98 | 11.29 | 11.99 | 11.47 | 13.78 | 0.02 | 1.09 | 0.59 | 0.01 | 97.24 | 6.485 | 0.353 | 0.181 | 1.754 | 0.642 | 0.812 | 1.961 | 2.978 | 0.002 | 0.119 | 0.072 | 0.000 | 15.361 | 22.679 |
| SHA07_107-Hbl | 44.98 | 1.40 | 1.24 | 11.83 | 11.15 | 10.72 | 13.56 | 0.07 | 1.95 | 0.14 | 0.00 | 97.41 | 6.564 | 0.397 | 0.232 | 1.850 | 0.357 | 1.004 | 1.845 | 2.951 | 0.006 | 0.214 | 0.017 | 0.000 | 15.436 | 22.822 |
| SHA07_108-Hbl | 42.02 | 1.77 | 1.63 | 11.00 | 18.07 | 11.34 | 9.13 | 0.02 | 1.83 | 0.40 | 0.00 | 97.23 | 6.347 | 0.520 | 0.314 | 1.780 | 0.548 | 1.735 | 2.019 | 2.056 | 0.002 | 0.207 | 0.051 | 0.000 | 15.579 | 22.726 |
| SHA07_109-Hbl | 43.33 | 2.39 | 0.63 | 11.74 | 8.30 | 12.59 | 15.88 | 0.00 | 1.78 | 0.15 | 0.00 | 96.93 | 6.185 | 0.662 | 0.114 | 1.795 | 0.991 | 0.000 | 2.118 | 3.378 | 0.000 | 0.191 | 0.018 | 0.000 | 15.452 | 22.499 |
| SHA07_110-Hbl | 43.85 | 2.25 | 1.21 | 11.18 | 11.98 | 11.86 | 13.63 | 0.00 | 0.86 | 0.12 | 0.00 | 97.14 | 6.384 | 0.634 | 0.226 | 1.744 | 0.770 | 0.689 | 2.036 | 2.958 | 0.000 | 0.094 | 0.015 | 0.000 | 15.549 | 22.615 |
| SHA07_111-Hbl | 43.17 | 1.61 | 1.48 | 11.47 | 16.25 | 10.51 | 10.66 | 0.00 | 1.86 | 0.37 | 0.00 | 97.37 | 6.440 | 0.465 | 0.282 | 1.834 | 0.567 | 1.459 | 1.848 | 2.369 | 0.000 | 0.208 | 0.046 | 0.000 | 15.518 | 22.716 |
| SHA07_112-Hbl | 44.29 | 0.98 | 0.81 | 11.63 | 17.52 | 9.60 | 10.02 | 0.03 | 1.28 | 0.52 | 0.00 | 96.71 | 6.642 | 0.285 | 0.156 | 1.870 | 0.567 | 1.631 | 1.697 | 2.240 | 0.002 | 0.145 | 0.066 | 0.000 | 15.301 | 22.716 |
| SHA07_113-Hbl | 42.97 | 1.58 | 1.75 | 11.40 | 15.48 | 11.53 | 10.70 | 0.00 | 1.68 | 0.27 | 0.00 | 97.45 | 6.401 | 0.456 | 0.331 | 1.820 | 0.456 | 1.472 | 2.025 | 2.377 | 0.000 | 0.189 | 0.035 | 0.000 | 15.563 | 22.772 |
| SHA07_114-Hbl | 45.25 | 1.19 | 0.88 | 11.77 | 12.73 | 9.77 | 13.01 | 0.00 | 2.07 | 0.21 | 0.00 | 96.89 | 6.635 | 0.339 | 0.165 | 1.849 | 0.415 | 1.146 | 1.690 | 2.844 | 0.000 | 0.228 | 0.026 | 0.000 | 15.336 | 22.792 |
| SHA07_115-Hbl | 40.85 | 1.67 | 1.84 | 10.99 | 16.90 | 13.28 | 9.58 | 0.01 | 1.86 | 0.21 | 0.06 | 97.36 | 6.136 | 0.486 | 0.352 | 1.769 | 0.593 | 1.530 | 2.351 | 2.144 | 0.001 | 0.209 | 0.027 | 0.004 | 15.602 | 22.704 |
| SHC25_Hbl19 | 40.65 | 1.78 | 1.84 | 11.34 | 17.97 | 12.29 | 8.89 | 0.02 | 2.70 | 0.10 | 0.07 | 97.65 | 6.118 | 0.522 | 0.353 | 1.829 | 0.683 | 1.579 | 2.180 | 1.995 | 0.002 | 0.306 | 0.012 | 0.004 | 15.583 | 22.659 |
| SHC25_Hbl21 | 43.32 | 1.46 | 1.50 | 11.64 | 15.79 | 11.24 | 10.83 | 0.02 | 1.64 | 0.17 | 0.02 | 97.62 | 6.414 | 0.421 | 0.283 | 1.847 | 0.589 | 1.367 | 1.962 | 2.391 | 0.001 | 0.182 | 0.022 | 0.001 | 15.480 | 22.706 |
| SHC25_Hbl22r | 42.88 | 1.16 | 1.37 | 11.92 | 15.62 | 10.33 | 10.09 | 0.00 | 1.32 | 0.48 | 0.02 | 97.36 | 6.426 | 0.339 | 0.261 | 1.915 | 0.761 | 1.441 | 1.824 | 2.254 | 0.000 | 0.148 | 0.062 | 0.001 | 15.434 | 22.619 |
| SHC25_Hbl23r | 44.50 | 1.34 | 0.98 | 11.49 | 14.72 | 10.01 | 11.88 | 0.03 | 1.15 | 0.30 | 0.04 | 97.14 | 6.571 | 0.385 | 0.185 | 1.818 | 0.665 | 1.229 | 1.743 | 2.616 | 0.002 | 0.128 | 0.038 | 0.002 | 15.382 | 22.668 |
| SHC25_Hbl28r | 39.70 | 1.20 | 2.04 | 11.57 | 21.43 | 13.58 | 5.79 | 0.02 | 1.30 | 0.34 | 0.04 | 97.66 | 6.102 | 0.359 | 0.400 | 1.906 | 0.628 | 2.204 | 2.461 | 1.326 | 0.001 | 0.150 | 0.044 | 0.002 | 15.584 | 22.686 |
| MA06-3_071-Hbl | 42.31 | 1.72 | 2.03 | 11.13 | 17.91 | 11.15 | 9.37 | 0.05 | 1.96 | 0.16 | 0.00 | 97.84 | 6.373 | 0.503 | 0.390 | 1.796 | 0.427 | 1.829 | 1.980 | 2.103 | 0.004 | 0.221 | 0.020 | 0.000 | 15.649 | 22.787 |
| MA06-3_075-Hbl | 44.08 | 1.47 | 0.95 | 11.77 | 14.63 | 11.57 | 11.16 | 0.00 | 1.07 | 0.33 | 0.00 | 97.09 | 6.502 | 0.421 | 0.179 | 1.860 | 0.560 | 1.244 | 2.012 | 2.454 | 0.000 | 0.119 | 0.041 | 0.000 | 15.393 | 22.720 |
| MA06-3_076-Hbl | 43.60 | 1.56 | 1.09 | 11.67 | 14.82 | 12.14 | 11.11 | 0.00 | 1.15 | 0.35 | 0.00 | 97.57 | 6.412 | 0.444 | 0.204 | 1.838 | 0.608 | 1.215 | 2.103 | 2.435 | 0.000 | 0.127 | 0.044 | 0.000 | 15.429 | 22.696 |
| MA06-3_087-Hbl | 41.72 | 1.72 | 2.00 | 11.52 | 14.03 | 13.33 | 10.34 | 0.06 | 3.09 | 0.07 | 0.00 | 97.91 | 6.198 | 0.494 | 0.380 | 1.834 | 0.186 | 1.557 | 2.334 | 2.291 | 0.006 | 0.345 | 0.009 | 0.000 | 15.634 | 22.907 |
| MA06-3_091-Hbl | 42.78 | 2.08 | 0.37 | 10.77 | 13.15 | 13.41 | 12.07 | 0.00 | 0.78 | 0.52 | 0.00 | 95.96 | 6.284 | 0.594 | 0.069 | 1.694 | 0.857 | 0.759 | 2.323 | 2.642 | 0.000 | 0.086 | 0.065 | 0.000 | 15.372 | 22.572 |
| MA06-3_093-Hbl | 44.18 | 1.45 | 1.24 | 11.50 | 16.86 | 9.51 | 10.58 | 0.00 | 1.51 | 0.55 | 0.00 | 97.41 | 6.589 | 0.419 | 0.237 | 1.838 | 0.568 | 1.536 | 1.671 | 2.353 | 0.000 | 0.170 | 0.069 | 0.000 | 15.449 | 22.716 |
| MA06-3_097-Hbl | 43.46 | 1.53 | 1.38 | 11.39 | 18.32 | 9.79 | 9.45 | 0.06 | 1.70 | 0.48 | 0.00 | 97.60 | 6.535 | 0.445 | 0.265 | 1.835 | 0.534 | 1.769 | 1.734 | 2.118 | 0.005 | 0.192 | 0.061 | 0.000 | 15.494 | 22.733 |
| MA06-3_098-Hbl | 43.52 | 1.35 | 1.36 | 11.70 | 18.05 | 9.28 | 9.76 | 0.02 | 1.75 | 0.55 | 0.00 | 97.36 | 6.547 | 0.395 | 0.261 | 1.885 | 0.598 | 1.674 | 1.645 | 2.188 | 0.002 | 0.198 | 0.070 | 0.000 | 15.462 | 22.701 |
| MA06-3_099-Hbl | 40.98 | 1.42 | 1.98 | 11.38 | 19.85 | 12.12 | 7.70 | 0.00 | 2.07 | 0.20 | 0.00 | 97.75 | 6.232 | 0.420 | 0.385 | 1.854 | 0.496 | 2.029 | 2.174 | 1.745 | 0.000 | 0.237 | 0.025 | 0.000 | 15.598 | 22.752 |
| MA06-3_100-Hbl | 42.94 | 1.35 | 1.45 | 11.28 | 18.75 | 10.68 | 9.14 | 0.00 | 1.90 | 0.18 | 0.00 | 97.68 | 6.455 | 0.392 | 0.279 | 1.818 | 0.485 | 1.872 | 1.892 | 2.048 | 0.000 | 0.215 | 0.023 | 0.000 | 15.478 | 22.758 |
| MA06-3_101-Hbl | 47.00 | 1.29 | 0.79 | 11.68 | 12.38 | 8.06 | 14.04 | 0.00 | 0.61 | 0.19 | 0.03 | 96.20 | 6.901 | 0.367 | 0.149 | 1.838 | 0.513 | 1.007 | 1.395 | 3.073 | 0.000 | 0.068 | 0.024 | 0.001 | 15.335 | 22.744 |
| MA06-3_102-Hbl | 47.31 | 1.19 | 0.76 | 11.46 | 15.23 | 7.07 | 12.45 | 0.00 | 1.75 | 0.53 | 0.00 | 97.75 | 6.949 | 0.338 | 0.142 | 1.804 | 0.345 | 1.525 | 1.225 | 2.726 | 0.000 | 0.193 | 0.066 | 0.000 | 15.313 | 22.827 |
| MA06-3_103-Hbl | 42.44 | 1.41 | 1.79 | 11.41 | 17.67 | 10.99 | 9.74 | 0.01 | 1.76 | 0.15 | 0.00 | 97.41 | 6.384 | 0.411 | 0.343 | 1.839 | 0.536 | 1.688 | 1.949 | 2.184 | 0.001 | 0.199 | 0.019 | 0.000 | 15.552 | 22.732 |
| MA06-3_106-Hbl | 42.57 | 1.62 | 1.47 | 11.06 | 18.41 | 11.39 | 8.65 | 0.04 | 2.14 | 0.24 | 0.00 | 97.64 | 6.417 | 0.475 | 0.283 | 1.786 | 0.363 | 1.959 | 2.023 | 1.943 | 0.003 | 0.243 | 0.031 | 0.000 | 15.526 | 22.819 |
| MA06-3_120-Hbl | 45.94 | 1.61 | 0.81 | 11.28 | 12.34 | 8.19 | 13.99 | 0.04 | 2.10 | 0.20 | 0.00 | 96.57 | 6.746 | 0.459 | 0.152 | 1.774 | 0.463 | 1.052 | 1.418 | 3.062 | 0.004 | 0.233 | 0.025 | 0.000 | 15.387 | 22.768 |
| MA06-3_129-Hbl | 42.37 | 1.59 | 2.02 | 11.56 | 13.32 | 11.00 | 12.15 | 0.02 | 2.02 | 0.17 | 0.01 | 96.68 | 6.344 | 0.461 | 0.385 | 1.856 | 0.521 | 1.147 | 1.942 | 2.713 | 0.002 | 0.227 | 0.022 | 0.000 | 15.620 | 22.740 |

$Fe^{2+}$ and $Fe^{3+}$ calculated after Schumacher (1997)

## Analyses of epidote from sandstones

| Sample / No. | $SiO_2$ | $Na_2O$ | $K_2O$ | CaO | FeO | $Al_2O_3$ | MgO | SrO | $TiO_2$ | MnO | BaO | wt-total | Si_at | Na_at | K_at | Ca_at | Fe_at | Al_at | Mg_at | Sr_at | Ti_at | Mn_at | Ba_at | at-total |
|---|---|---|---|---|---|---|---|---|---|---|---|---|---|---|---|---|---|---|---|---|---|---|---|---|
| SHA07_117-Ep | 38.40 | 0.01 | 0.00 | 23.13 | 10.51 | 24.99 | 0.03 | 0.12 | 0.15 | 0.17 | 0.02 | 97.54 | 5.943 | 0.002 | 0.000 | 3.836 | 1.361 | 4.559 | 0.006 | 0.011 | 0.018 | 0.023 | 0.001 | 15.761 |
| SHA07_142-Ep | 38.53 | 0.01 | 0.00 | 23.80 | 7.95 | 26.71 | 0.05 | 0.10 | 0.06 | 0.03 | 0.00 | 97.27 | 5.900 | 0.003 | 0.000 | 3.905 | 1.019 | 4.821 | 0.013 | 0.009 | 0.007 | 0.004 | 0.000 | 15.682 |
| SHC25_Ep27 | 38.30 | 0.00 | 0.01 | 23.61 | 10.30 | 24.87 | 0.02 | 0.07 | 0.14 | 0.24 | 0.00 | 97.55 | 5.932 | 0.000 | 0.001 | 3.918 | 1.334 | 4.540 | 0.005 | 0.006 | 0.016 | 0.031 | 0.000 | 15.783 |
| SP08_Ep71 | 38.24 | 0.03 | 0.00 | 23.23 | 9.21 | 26.11 | 0.17 | 0.19 | 0.08 | 0.20 | 0.00 | 97.47 | 5.886 | 0.010 | 0.000 | 3.832 | 1.186 | 4.737 | 0.038 | 0.017 | 0.009 | 0.026 | 0.000 | 15.741 |
| SP08_Ep72 | 38.15 | 0.03 | 0.01 | 23.60 | 11.19 | 23.94 | 0.01 | 0.06 | 0.13 | 0.25 | 0.00 | 97.35 | 5.955 | 0.008 | 0.002 | 3.947 | 1.461 | 4.405 | 0.002 | 0.005 | 0.015 | 0.033 | 0.000 | 15.832 |
| SP08_Ep73 | 37.49 | 0.00 | 0.00 | 23.40 | 10.98 | 23.80 | 0.04 | 0.05 | 0.30 | 0.23 | 0.01 | 96.30 | 5.917 | 0.000 | 0.001 | 3.958 | 1.449 | 4.428 | 0.009 | 0.005 | 0.036 | 0.030 | 0.000 | 15.833 |
| SPP17_201-Ep | 37.92 | 0.00 | 0.00 | 22.83 | 12.14 | 23.56 | 0.06 | 0.50 | 0.02 | 0.36 | 0.00 | 97.39 | 5.955 | 0.000 | 0.000 | 3.842 | 1.595 | 4.361 | 0.013 | 0.046 | 0.002 | 0.049 | 0.000 | 15.862 |
| SPP17_215-Ep | 38.57 | 0.01 | 0.01 | 23.41 | 11.01 | 24.63 | 0.02 | 0.12 | 0.06 | 0.09 | 0.04 | 97.99 | 5.961 | 0.002 | 0.003 | 3.876 | 1.424 | 4.486 | 0.004 | 0.010 | 0.007 | 0.012 | 0.002 | 15.790 |
| SPP17_230-Ep | 38.07 | 0.03 | 0.01 | 23.31 | 11.40 | 24.16 | 0.03 | 0.08 | 0.00 | 0.13 | 0.03 | 97.25 | 5.947 | 0.009 | 0.001 | 3.902 | 1.490 | 4.450 | 0.008 | 0.008 | 0.000 | 0.017 | 0.002 | 15.833 |
| SPP17_231-Ep | 37.98 | 0.00 | 0.00 | 23.18 | 12.99 | 22.60 | 0.03 | 0.05 | 0.10 | 0.25 | 0.02 | 97.20 | 5.994 | 0.000 | 0.000 | 3.920 | 1.715 | 4.204 | 0.007 | 0.005 | 0.012 | 0.033 | 0.001 | 15.891 |
| SPP17_248-Ep | 37.27 | 0.01 | 0.01 | 22.84 | 12.73 | 22.74 | 0.00 | 0.06 | 0.14 | 0.32 | 0.03 | 96.20 | 5.944 | 0.003 | 0.002 | 3.904 | 1.699 | 4.276 | 0.001 | 0.006 | 0.017 | 0.043 | 0.002 | 15.901 |
| SPP17_258-Ep | 38.16 | 0.00 | 0.02 | 22.91 | 9.17 | 25.93 | 0.04 | 0.19 | 0.15 | 0.19 | 0.02 | 96.78 | 5.910 | 0.000 | 0.004 | 3.802 | 1.188 | 4.734 | 0.009 | 0.017 | 0.018 | 0.025 | 0.001 | 15.707 |
| TI14_307-Ep | 38.10 | 0.02 | 0.00 | 22.97 | 12.58 | 23.09 | 0.06 | 0.13 | 0.03 | 0.23 | 0.01 | 97.22 | 5.993 | 0.006 | 0.000 | 3.871 | 1.655 | 4.280 | 0.014 | 0.012 | 0.003 | 0.031 | 0.001 | 15.866 |
| TI14_308-Ep | 37.85 | 0.00 | 0.00 | 23.05 | 11.48 | 23.82 | 0.02 | 0.10 | 0.11 | 0.16 | 0.03 | 96.63 | 5.956 | 0.000 | 0.001 | 3.887 | 1.511 | 4.417 | 0.005 | 0.010 | 0.013 | 0.021 | 0.002 | 15.823 |
| TI14_325-Ep | 37.92 | 0.00 | 0.02 | 23.34 | 11.99 | 23.23 | 0.02 | 0.15 | 0.19 | 0.09 | 0.00 | 96.95 | 5.970 | 0.000 | 0.004 | 3.938 | 1.578 | 4.310 | 0.005 | 0.014 | 0.023 | 0.012 | 0.000 | 15.854 |
| TI14_326-Ep | 37.80 | 0.02 | 0.00 | 22.98 | 14.00 | 21.17 | 0.09 | 0.09 | 0.04 | 0.07 | 0.01 | 96.30 | 6.059 | 0.008 | 0.001 | 3.947 | 1.877 | 4.000 | 0.021 | 0.008 | 0.005 | 0.010 | 0.001 | 15.938 |
| MA06-3_118Ep | 37.95 | 0.03 | 0.03 | 23.07 | 12.30 | 23.36 | 0.00 | 0.16 | 0.03 | 0.21 | 0.00 | 97.16 | 5.969 | 0.010 | 0.006 | 3.888 | 1.618 | 4.331 | 0.000 | 0.014 | 0.004 | 0.028 | 0.000 | 15.870 |

## Analyses of epidote from tuffaceous sandstones

| Sample / No. | $SiO_2$ | $Na_2O$ | $K_2O$ | CaO | FeO | $Al_2O_3$ | MgO | SrO | $TiO_2$ | MnO | BaO | wt-total | Si_at | Na_at | K_at | Ca_at | Fe_at | Al_at | Mg_at | Sr_at | Ti_at | Mn_at | Ba_at | at-total |
|---|---|---|---|---|---|---|---|---|---|---|---|---|---|---|---|---|---|---|---|---|---|---|---|---|
| SHA06_Ep23 | 37.72 | 0.00 | 0.36 | 22.45 | 12.78 | 22.29 | 0.52 | 0.38 | 0.23 | 0.16 | 0.00 | 96.88 | 5.984 | 0.000 | 0.073 | 3.816 | 1.695 | 4.168 | 0.122 | 0.035 | 0.028 | 0.021 | 0.000 | 15.941 |
| SHA06_Ep28 | 37.85 | 0.00 | 0.02 | 23.18 | 10.71 | 24.35 | 0.08 | 0.10 | 0.11 | 0.22 | 0.00 | 96.64 | 5.933 | 0.000 | 0.005 | 3.893 | 1.404 | 4.500 | 0.019 | 0.009 | 0.013 | 0.030 | 0.000 | 15.806 |
| SHA06_Ep44 | 38.04 | 0.00 | 0.01 | 23.38 | 12.52 | 23.04 | 0.01 | 0.04 | 0.02 | 0.18 | 0.00 | 97.22 | 5.985 | 0.000 | 0.002 | 3.941 | 1.647 | 4.272 | 0.002 | 0.003 | 0.002 | 0.024 | 0.000 | 15.878 |

## Analyses of pyroxenes from mafic pyroclastic deposits (EHT event)

| Sample / No. | $SiO_2$ | $Na_2O$ | $K_2O$ | CaO | FeO | $Al_2O_3$ | MgO | SrO | $TiO_2$ | MnO | BaO | wt-total | Si_at | Na_at | K_at | Ca_at | Fe_at | Al_at | Mg_at | Sr_at | Ti_at | Mn_at | Ba_at | at-total |
|---|---|---|---|---|---|---|---|---|---|---|---|---|---|---|---|---|---|---|---|---|---|---|---|---|
| CE90_SM07 | 53.32 | 0.09 | 0.00 | 18.33 | 9.14 | 1.25 | 17.60 | 0.00 | 0.22 | 0.27 | 0.05 | 100.27 | 7.849 | 0.027 | 0.000 | 2.892 | 1.125 | 0.216 | 3.862 | 0.000 | 0.025 | 0.034 | 0.003 | 16.032 |
| CE90_SM10 | 52.73 | 0.11 | 0.01 | 19.38 | 10.09 | 1.65 | 15.82 | 0.00 | 0.39 | 0.27 | 0.00 | 100.45 | 7.807 | 0.032 | 0.003 | 3.075 | 1.249 | 0.288 | 3.493 | 0.000 | 0.044 | 0.034 | 0.000 | 16.023 |
| CE90_SM11 | 53.44 | 0.14 | 0.00 | 18.82 | 9.05 | 1.47 | 17.00 | 0.02 | 0.28 | 0.26 | 0.00 | 100.47 | 7.852 | 0.039 | 0.000 | 2.964 | 1.112 | 0.254 | 3.725 | 0.002 | 0.030 | 0.032 | 0.000 | 16.010 |
| CE90_SM12 | 53.50 | 0.10 | 0.00 | 18.10 | 9.61 | 1.15 | 17.30 | 0.03 | 0.23 | 0.27 | 0.00 | 100.28 | 7.880 | 0.029 | 0.001 | 2.857 | 1.184 | 0.199 | 3.799 | 0.003 | 0.025 | 0.034 | 0.000 | 16.010 |
| CE90_SM13 | 53.54 | 0.11 | 0.02 | 18.22 | 9.06 | 1.26 | 17.71 | 0.00 | 0.22 | 0.25 | 0.00 | 100.38 | 7.861 | 0.032 | 0.003 | 2.867 | 1.112 | 0.217 | 3.877 | 0.000 | 0.024 | 0.032 | 0.000 | 16.025 |

## Analyses of Cr-spinel

| Sample / No. | $SiO_2$ | $Na_2O$ | $K_2O$ | CaO | FeO | $Al_2O_3$ | MgO | SrO | $TiO_2$ | MnO | $Cr_2O_3$ | BaO | wt-total | Si_at | Na_at | K_at | Ca_at | Fe_at | Al_at | Mg_at | Sr_at | Ti_at | Mn_at | Cr_at | Ba_at | at-total |
|---|---|---|---|---|---|---|---|---|---|---|---|---|---|---|---|---|---|---|---|---|---|---|---|---|---|---|
| TI14_310-Chr | 0.04 | 0.01 | 0.01 | 0.07 | 20.40 | 23.50 | 11.91 | 0.04 | 0.08 | 0.30 | 43.27 | 0.01 | 99.62 | 0.007 | 0.002 | 0.002 | 0.013 | 3.194 | 5.184 | 3.322 | 0.004 | 0.011 | 0.047 | 6.404 | 0.001 | 18.191 |
| TI14_311-Chr | 0.01 | 0.00 | 0.00 | 0.03 | 19.56 | 20.61 | 11.41 | 0.05 | 0.15 | 0.27 | 47.76 | 0.01 | 99.87 | 0.002 | 0.001 | 0.000 | 0.007 | 3.092 | 4.591 | 3.215 | 0.005 | 0.021 | 0.043 | 7.136 | 0.001 | 18.114 |
| TI14_312-Chr | 0.00 | 0.01 | 0.01 | 0.05 | 19.61 | 17.74 | 10.91 | 0.07 | 0.08 | 0.33 | 50.70 | 0.00 | 99.49 | 0.000 | 0.002 | 0.002 | 0.011 | 3.157 | 4.025 | 3.131 | 0.008 | 0.012 | 0.053 | 7.718 | 0.000 | 18.119 |
| TI14_313-Chr | 0.04 | 0.04 | 0.01 | 0.02 | 18.20 | 28.70 | 12.66 | 0.02 | 0.25 | 0.24 | 39.06 | 0.03 | 99.28 | 0.008 | 0.013 | 0.001 | 0.005 | 2.769 | 6.154 | 3.433 | 0.002 | 0.035 | 0.037 | 5.619 | 0.002 | 18.078 |
| TI14_323-Chr | 0.03 | 0.00 | 0.03 | 0.03 | 19.72 | 12.83 | 9.80 | 0.00 | 0.12 | 0.29 | 56.40 | 0.00 | 99.24 | 0.006 | 0.000 | 0.006 | 0.006 | 3.266 | 2.994 | 2.893 | 0.000 | 0.017 | 0.049 | 8.830 | 0.000 | 18.068 |
| TI14_324-Chr | 0.02 | 0.00 | 0.02 | 0.05 | 20.90 | 8.89 | 10.11 | 0.02 | 0.25 | 0.41 | 58.37 | 0.05 | 99.09 | 0.004 | 0.000 | 0.005 | 0.012 | 3.544 | 2.125 | 3.057 | 0.003 | 0.038 | 0.070 | 9.359 | 0.004 | 18.219 |
| ER04_222-Chr | 0.05 | 0.02 | 0.01 | 0.01 | 21.58 | 12.89 | 8.85 | 0.04 | 0.07 | 0.34 | 55.55 | 0.00 | 99.40 | 0.010 | 0.006 | 0.003 | 0.002 | 3.596 | 3.026 | 2.629 | 0.005 | 0.010 | 0.057 | 8.751 | 0.000 | 18.095 |

# Analyses of zeolites from sandstones

| Sample / No. | $SiO_2$ | $Na_2O$ | $K_2O$ | CaO | FeO | $Al_2O_3$ | MgO | SrO | $TiO_2$ | MnO | BaO | wt-total | Si_at | Na_at | K_at | Ca_at | Fe_at | Al_at | Mg_at | Sr_at | Ti_at | Mn_at | Ba_at | at-total |
|---|---|---|---|---|---|---|---|---|---|---|---|---|---|---|---|---|---|---|---|---|---|---|---|---|
| SPP07_Ze02 | 68.63 | 0.15 | 0.57 | 2.75 | 1.41 | 12.99 | 0.34 | n.d. | 0.00 | 0.00 | n.d. | 86.84 | 5.810 | 0.025 | 0.061 | 0.249 | 0.100 | 1.296 | 0.042 | n.d. | 0.000 | 0.000 | n.d. | 7.585 |
| SPP07_Ze03 | 66.58 | 0.27 | 0.57 | 3.09 | 0.87 | 12.79 | 0.25 | n.d. | 0.01 | 0.00 | n.d. | 84.42 | 5.797 | 0.045 | 0.063 | 0.289 | 0.063 | 1.312 | 0.032 | n.d. | 0.001 | 0.000 | n.d. | 7.602 |
| SPP07_Ze04 | 67.13 | 0.47 | 1.03 | 2.61 | 1.37 | 13.34 | 0.43 | n.d. | 0.02 | 0.02 | n.d. | 86.42 | 5.746 | 0.077 | 0.113 | 0.239 | 0.098 | 1.346 | 0.055 | n.d. | 0.002 | 0.002 | n.d. | 7.679 |
| SPP07_Ze05 | 70.19 | 0.98 | 0.32 | 4.66 | 0.20 | 12.16 | 0.02 | n.d. | 0.02 | 0.01 | n.d. | 88.55 | 5.842 | 0.158 | 0.034 | 0.416 | 0.014 | 1.192 | 0.002 | n.d. | 0.002 | 0.001 | n.d. | 7.660 |
| SPP07_Ze06 | 68.64 | 0.43 | 0.71 | 2.67 | 1.15 | 13.36 | 0.45 | n.d. | 0.02 | 0.00 | n.d. | 87.41 | 5.780 | 0.071 | 0.076 | 0.241 | 0.081 | 1.326 | 0.057 | n.d. | 0.002 | 0.000 | n.d. | 7.632 |
| SPP07_Ze07 | 71.15 | 0.74 | 0.44 | 2.92 | 0.83 | 12.81 | 0.23 | n.d. | 0.03 | 0.01 | n.d. | 89.16 | 5.856 | 0.118 | 0.047 | 0.258 | 0.057 | 1.242 | 0.029 | n.d. | 0.003 | 0.000 | n.d. | 7.609 |
| SPP07_Ze08 | 65.38 | 0.38 | 0.96 | 2.75 | 2.09 | 14.27 | 0.69 | n.d. | 0.01 | 0.03 | n.d. | 86.56 | 5.625 | 0.063 | 0.106 | 0.254 | 0.150 | 1.447 | 0.089 | n.d. | 0.001 | 0.002 | n.d. | 7.737 |
| SPP07_Ze09 | 68.88 | 1.17 | 0.25 | 2.75 | 0.50 | 12.07 | 0.11 | n.d. | 0.01 | 0.05 | n.d. | 85.78 | 5.881 | 0.193 | 0.027 | 0.252 | 0.036 | 1.215 | 0.014 | n.d. | 0.001 | 0.003 | n.d. | 7.622 |
| SPP07_Ze11 | 71.18 | 1.95 | 0.26 | 3.02 | 0.05 | 11.60 | 0.00 | n.d. | 0.01 | 0.01 | n.d. | 88.09 | 5.924 | 0.314 | 0.028 | 0.269 | 0.004 | 1.138 | 0.001 | n.d. | 0.001 | 0.001 | n.d. | 7.679 |
| SPP07_Ze12 | 62.88 | 0.41 | 0.85 | 3.22 | 1.71 | 12.79 | 0.52 | n.d. | 0.03 | 0.03 | n.d. | 82.44 | 5.680 | 0.072 | 0.098 | 0.312 | 0.129 | 1.362 | 0.070 | n.d. | 0.004 | 0.002 | n.d. | 7.728 |
| SPP07_Ze13 | 68.09 | 0.66 | 0.27 | 3.36 | 0.43 | 11.49 | 0.10 | n.d. | 0.04 | 0.02 | n.d. | 84.47 | 5.905 | 0.111 | 0.030 | 0.312 | 0.031 | 1.174 | 0.014 | n.d. | 0.005 | 0.001 | n.d. | 7.583 |
| SPP07_Ze14 | 70.90 | 0.62 | 0.24 | 2.83 | 0.29 | 12.14 | 0.06 | n.d. | 0.02 | 0.00 | n.d. | 87.10 | 5.930 | 0.100 | 0.026 | 0.254 | 0.020 | 1.197 | 0.007 | n.d. | 0.002 | 0.000 | n.d. | 7.537 |
| SR03_057-Ze | 54.20 | 0.89 | 0.64 | 10.17 | 0.00 | 20.75 | 0.00 | 0.01 | 0.02 | 0.00 | 0.00 | 86.68 | 8.270 | 0.264 | 0.124 | 1.663 | 0.000 | 3.732 | 0.000 | 0.001 | 0.002 | 0.000 | 0.000 | 14.056 |
| SR03_058-Ze | 54.23 | 0.76 | 0.65 | 9.97 | 0.02 | 21.02 | 0.01 | 0.13 | 0.00 | 0.01 | 0.00 | 86.80 | 8.259 | 0.224 | 0.126 | 1.627 | 0.002 | 3.774 | 0.001 | 0.011 | 0.000 | 0.002 | 0.000 | 14.027 |
| SR03_059-Ze | 55.03 | 0.75 | 0.78 | 9.60 | 0.00 | 20.38 | 0.00 | 0.03 | 0.00 | 0.00 | 0.02 | 86.59 | 8.379 | 0.222 | 0.151 | 1.566 | 0.000 | 3.657 | 0.001 | 0.002 | 0.000 | 0.000 | 0.001 | 13.979 |
| SR03_060-Ze | 55.09 | 1.13 | 0.68 | 9.99 | 0.03 | 21.18 | 0.00 | 0.06 | 0.00 | 0.00 | 0.03 | 88.20 | 8.267 | 0.329 | 0.129 | 1.607 | 0.004 | 3.745 | 0.000 | 0.005 | 0.000 | 0.000 | 0.002 | 14.089 |
| SR03_061-Ze | 54.39 | 0.58 | 0.57 | 10.35 | 0.01 | 21.37 | 0.01 | 0.03 | 0.00 | 0.00 | 0.00 | 87.32 | 8.229 | 0.171 | 0.109 | 1.677 | 0.002 | 3.812 | 0.003 | 0.003 | 0.000 | 0.000 | 0.000 | 14.005 |
| MA06-3_164-Ze | 69.48 | 2.38 | 0.89 | 3.65 | 0.52 | 14.37 | 0.28 | 0.03 | 0.00 | 0.00 | 0.18 | 91.78 | 9.689 | 0.644 | 0.158 | 0.545 | 0.060 | 2.362 | 0.058 | 0.002 | 0.000 | 0.000 | 0.010 | 13.530 |
| MA06-3_165-Ze | 70.50 | 2.37 | 0.91 | 3.00 | 0.36 | 12.99 | 0.62 | 0.01 | 0.00 | 0.01 | 0.00 | 90.76 | 9.878 | 0.644 | 0.162 | 0.450 | 0.042 | 2.145 | 0.129 | 0.001 | 0.000 | 0.001 | 0.000 | 13.453 |
| MA06-3_166-Ze | 69.77 | 2.15 | 0.95 | 3.01 | 0.34 | 13.33 | 0.49 | 0.00 | 0.01 | 0.01 | 0.06 | 90.12 | 9.845 | 0.588 | 0.172 | 0.455 | 0.040 | 2.217 | 0.103 | 0.000 | 0.001 | 0.001 | 0.004 | 13.425 |
| MA06-3_167-Ze | 68.84 | 2.04 | 0.95 | 3.56 | 0.56 | 14.23 | 0.16 | 0.11 | 0.05 | 0.00 | 0.23 | 90.76 | 9.706 | 0.559 | 0.170 | 0.537 | 0.066 | 2.366 | 0.034 | 0.009 | 0.005 | 0.000 | 0.013 | 13.469 |
| MA06-3_168-Ze | 69.09 | 1.72 | 0.79 | 3.29 | 0.43 | 13.08 | 0.37 | 0.07 | 0.00 | 0.00 | 0.06 | 88.91 | 9.871 | 0.477 | 0.144 | 0.504 | 0.051 | 2.202 | 0.080 | 0.005 | 0.000 | 0.000 | 0.003 | 13.338 |
| MA06-3_169-Ze | 72.93 | 2.02 | 0.89 | 3.05 | 0.35 | 13.39 | 0.50 | 0.00 | 0.00 | 0.02 | 0.00 | 93.17 | 9.923 | 0.534 | 0.154 | 0.445 | 0.040 | 2.147 | 0.101 | 0.000 | 0.000 | 0.003 | 0.000 | 13.347 |
| CHW26_210-Ze | 63.57 | 1.33 | 0.31 | 7.09 | 0.08 | 16.97 | 0.04 | 0.42 | 0.01 | 0.02 | 0.48 | 90.34 | 9.145 | 0.372 | 0.057 | 1.092 | 0.010 | 2.878 | 0.008 | 0.035 | 0.001 | 0.003 | 0.027 | 13.629 |
| CHW26_211-Ze | 63.88 | 1.55 | 0.22 | 7.08 | 0.05 | 16.42 | 0.01 | 0.25 | 0.02 | 0.01 | 0.42 | 89.90 | 9.213 | 0.434 | 0.041 | 1.094 | 0.006 | 2.791 | 0.003 | 0.021 | 0.002 | 0.001 | 0.024 | 13.627 |
| CHW26_212-Ze | 63.31 | 1.38 | 0.28 | 7.04 | 0.06 | 16.94 | 0.04 | 0.43 | 0.04 | 0.04 | 0.44 | 89.99 | 9.140 | 0.386 | 0.051 | 1.089 | 0.007 | 2.883 | 0.008 | 0.036 | 0.004 | 0.005 | 0.025 | 13.634 |
| CHW26_251-Ze | 65.89 | 1.62 | 0.34 | 5.93 | 0.05 | 15.87 | 0.00 | 0.31 | 0.01 | 0.00 | 0.22 | 90.24 | 9.396 | 0.448 | 0.062 | 0.906 | 0.006 | 2.667 | 0.000 | 0.026 | 0.001 | 0.000 | 0.013 | 13.524 |
| CHW26_273-Ze | 64.74 | 1.42 | 0.27 | 7.05 | 0.04 | 16.70 | 0.01 | 0.29 | 0.00 | 0.01 | 0.47 | 91.02 | 9.219 | 0.393 | 0.050 | 1.076 | 0.005 | 2.802 | 0.002 | 0.024 | 0.000 | 0.001 | 0.026 | 13.600 |
| CHW06_071-Ze | 64.33 | 2.59 | 0.06 | 2.04 | 0.00 | 16.15 | 2.38 | 0.00 | 0.02 | 0.00 | 0.00 | 87.58 | 9.327 | 0.728 | 0.012 | 0.317 | 0.001 | 2.760 | 0.514 | 0.000 | 0.002 | 0.000 | 0.000 | 13.660 |
| CHW06_072-Ze | 64.78 | 1.49 | 0.18 | 6.15 | 0.04 | 16.24 | 0.04 | 0.50 | 0.02 | 0.01 | 0.14 | 89.60 | 9.316 | 0.416 | 0.033 | 0.947 | 0.005 | 2.752 | 0.009 | 0.042 | 0.002 | 0.001 | 0.008 | 13.531 |
| CHW06_073-Ze | 62.47 | 0.97 | 0.16 | 6.41 | 0.01 | 16.16 | 0.06 | 0.73 | 0.04 | 0.05 | 0.16 | 87.22 | 9.248 | 0.278 | 0.030 | 1.016 | 0.001 | 2.819 | 0.013 | 0.063 | 0.004 | 0.006 | 0.009 | 13.490 |
| CHW06_074-Ze | 65.81 | 3.72 | 0.09 | 4.60 | 0.00 | 16.31 | 0.14 | 0.02 | 0.03 | 0.00 | 0.07 | 90.79 | 9.327 | 1.021 | 0.017 | 0.699 | 0.000 | 2.724 | 0.029 | 0.001 | 0.003 | 0.000 | 0.004 | 13.827 |
| CHW06_075-Ze | 64.67 | 3.62 | 0.08 | 3.43 | 0.00 | 16.14 | 0.78 | 0.00 | 0.00 | 0.00 | 0.02 | 88.74 | 9.333 | 1.013 | 0.015 | 0.531 | 0.000 | 2.746 | 0.168 | 0.000 | 0.000 | 0.000 | 0.001 | 13.808 |
| CHW06_077-Ze | 65.91 | 2.00 | 0.21 | 5.74 | 0.19 | 15.48 | 0.07 | 0.26 | 0.00 | 0.01 | 0.13 | 90.00 | 9.421 | 0.555 | 0.037 | 0.879 | 0.022 | 2.608 | 0.016 | 0.021 | 0.000 | 0.001 | 0.007 | 13.570 |
| CHW06_078-Ze | 64.11 | 1.51 | 0.14 | 6.46 | 0.08 | 16.38 | 0.06 | 0.52 | 0.00 | 0.00 | 0.19 | 89.45 | 9.258 | 0.422 | 0.025 | 1.000 | 0.009 | 2.789 | 0.013 | 0.044 | 0.000 | 0.000 | 0.011 | 13.571 |
| CHW06_079-Ze | 66.64 | 3.24 | 0.10 | 4.47 | 0.01 | 16.70 | 0.74 | 0.01 | 0.00 | 0.02 | 0.06 | 92.00 | 9.300 | 0.877 | 0.018 | 0.668 | 0.001 | 2.747 | 0.154 | 0.001 | 0.000 | 0.002 | 0.003 | 13.773 |

n.d.: not determined

Analyses of zeolites from tuffaceous sandstones

| Sample / No. | $SiO_2$ | $Na_2O$ | $K_2O$ | CaO | FeO | $Al_2O_3$ | MgO | SrO | $TiO_2$ | MnO | BaO | wt-total | Si_at | Na_at | K_at | Ca_at | Fe_at | Al_at | Mg_at | Sr_at | Ti_at | Mn_at | Ba_at | at-total |
|---|---|---|---|---|---|---|---|---|---|---|---|---|---|---|---|---|---|---|---|---|---|---|---|---|
| SHA06_Ze14 | 68.61 | 1.94 | 0.38 | 5.02 | 0.04 | 14.68 | 0.09 | 0.06 | 0.00 | 0.03 | 0.14 | 91.00 | 9.631 | 0.529 | 0.068 | 0.756 | 0.005 | 2.429 | 0.019 | 0.005 | 0.000 | 0.003 | 0.008 | 13.453 |
| SHA06_Ze15 | 68.97 | 1.87 | 0.37 | 5.18 | 0.04 | 14.70 | 0.10 | 0.02 | 0.00 | 0.00 | 0.06 | 91.31 | 9.638 | 0.507 | 0.066 | 0.776 | 0.005 | 2.421 | 0.021 | 0.002 | 0.000 | 0.000 | 0.004 | 13.438 |
| SHA06_Ze16 | 68.05 | 1.76 | 0.39 | 5.07 | 0.08 | 14.34 | 0.09 | 0.02 | 0.02 | 0.01 | 0.13 | 89.95 | 9.657 | 0.485 | 0.070 | 0.771 | 0.010 | 2.398 | 0.018 | 0.002 | 0.002 | 0.001 | 0.008 | 13.420 |
| SHA06_Ze17 | 70.49 | 1.17 | 0.40 | 4.91 | 0.11 | 14.07 | 0.08 | 0.05 | 0.02 | 0.01 | 0.05 | 91.34 | 9.791 | 0.315 | 0.070 | 0.731 | 0.013 | 2.303 | 0.016 | 0.004 | 0.002 | 0.001 | 0.003 | 13.248 |
| SHA06_Ze18 | 70.07 | 1.77 | 0.40 | 4.94 | 0.10 | 14.04 | 0.09 | 0.02 | 0.00 | 0.00 | 0.06 | 91.49 | 9.750 | 0.478 | 0.071 | 0.736 | 0.012 | 2.303 | 0.018 | 0.001 | 0.000 | 0.000 | 0.004 | 13.373 |
| SHA12_Ze01 | 70.33 | 1.35 | 0.48 | 4.57 | 0.12 | 13.34 | 0.06 | 0.06 | 0.01 | 0.00 | 0.07 | 90.38 | 9.870 | 0.368 | 0.086 | 0.687 | 0.015 | 2.206 | 0.012 | 0.005 | 0.001 | 0.000 | 0.004 | 13.253 |
| SHA12_Ze02 | 72.97 | 1.84 | 0.71 | 3.80 | 0.14 | 12.85 | 0.04 | 0.05 | 0.01 | 0.00 | 0.05 | 92.45 | 9.995 | 0.488 | 0.125 | 0.558 | 0.016 | 2.075 | 0.008 | 0.004 | 0.001 | 0.000 | 0.003 | 13.272 |
| SHA12_Ze03 | 72.16 | 2.41 | 0.68 | 3.73 | 0.04 | 13.39 | 0.04 | 0.04 | 0.00 | 0.01 | 0.13 | 92.63 | 9.900 | 0.641 | 0.119 | 0.549 | 0.005 | 2.165 | 0.008 | 0.003 | 0.000 | 0.001 | 0.007 | 13.398 |
| SHA12_Ze04 | 70.94 | 1.61 | 0.63 | 4.05 | 0.08 | 13.11 | 0.05 | 0.03 | 0.00 | 0.01 | 0.04 | 90.54 | 9.925 | 0.438 | 0.112 | 0.607 | 0.010 | 2.162 | 0.010 | 0.003 | 0.000 | 0.001 | 0.002 | 13.269 |
| SHA12_Ze05 | 71.65 | 1.70 | 0.54 | 4.60 | 0.07 | 13.44 | 0.04 | 0.05 | 0.02 | 0.00 | 0.06 | 92.17 | 9.872 | 0.454 | 0.095 | 0.679 | 0.008 | 2.183 | 0.007 | 0.004 | 0.003 | 0.000 | 0.003 | 13.309 |
| SHA12_Ze06 | 73.83 | 2.11 | 0.73 | 3.62 | 0.09 | 13.01 | 0.06 | 0.00 | 0.00 | 0.00 | 0.06 | 93.52 | 9.997 | 0.554 | 0.126 | 0.525 | 0.010 | 2.077 | 0.012 | 0.000 | 0.000 | 0.000 | 0.003 | 13.305 |
| SHA12_Ze07 | 72.43 | 1.70 | 0.55 | 4.17 | 0.12 | 13.33 | 0.05 | 0.03 | 0.01 | 0.02 | 0.05 | 92.45 | 9.926 | 0.451 | 0.096 | 0.613 | 0.013 | 2.153 | 0.009 | 0.002 | 0.001 | 0.003 | 0.003 | 13.270 |
| SHA12_Ze11 | 71.18 | 2.20 | 0.63 | 3.98 | 0.09 | 13.26 | 0.06 | 0.02 | 0.00 | 0.00 | 0.03 | 91.45 | 9.887 | 0.593 | 0.111 | 0.592 | 0.011 | 2.171 | 0.011 | 0.002 | 0.000 | 0.000 | 0.002 | 13.380 |
| SHA12_Ze13 | 69.67 | 2.23 | 0.52 | 4.23 | 0.71 | 13.84 | 0.03 | 0.02 | 0.01 | 0.00 | 0.08 | 91.35 | 9.748 | 0.605 | 0.093 | 0.634 | 0.083 | 2.282 | 0.007 | 0.002 | 0.001 | 0.000 | 0.005 | 13.459 |

# Appendix 6

EMP photographies (BSE) and element mappings

# EMP (BSE) photographies 1

a) Hematite cements (Hem) formed after compaction. Kaolinite (Kao) fills the remaining pore space. Qz: Quartz; KF: K-feldspar. Sample AN01a.

b) Chlorite rim (Chl) on grain surfaces pre-dating kaolinite formation. Pore throats are free of kaolinite. Sample AN15.

c) Kaolinite booklets are the only authigenic phases in sample ER04.

d) Ca-sulphate precipitation (most likely bassanit, Bas) post-dating Jarosite (Jar, red arrows). Dissolution of plagioclase (Pl) occured most likely prior to jarosite formation (blue arrow). Sample MA06-1.

e) Chlorite partially lines the grain surfaces. Later authigenic Fe-oxides are of unknown origin. Sample PT05.

f) In sandstones with abundant lithoclasts the IGV is often very low. Compaction was early and strong enough to squeeze instable rock fragments, in this case mafic (Lvm) and felsic (Lvf) volcanic lithoclasts, and biotite (Bi). Sample TI14.

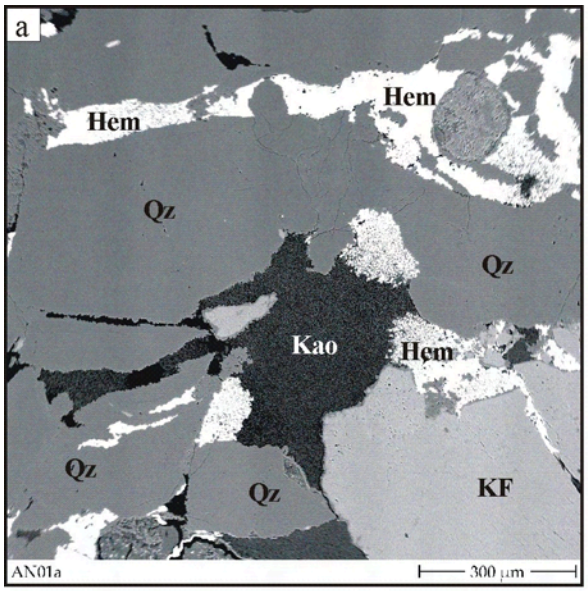
a
Hem
Hem
Qz
Qz
Kao
Hem
Qz
Qz
KF
AN01a
300 µm

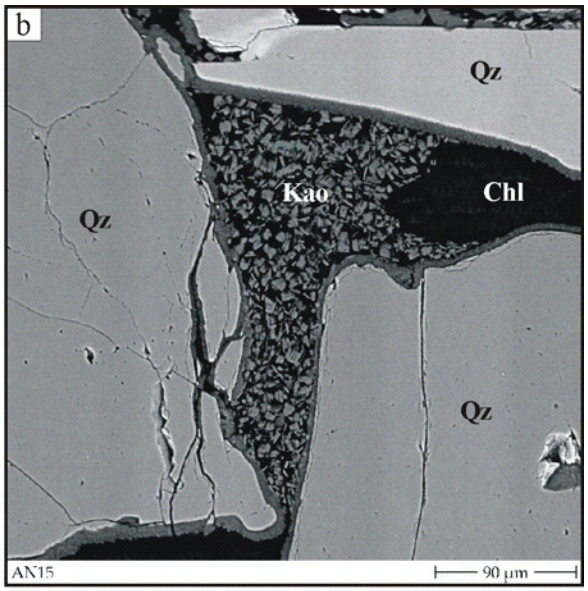
b
Qz
Kao
Chl
Qz
Qz
AN15
90 µm

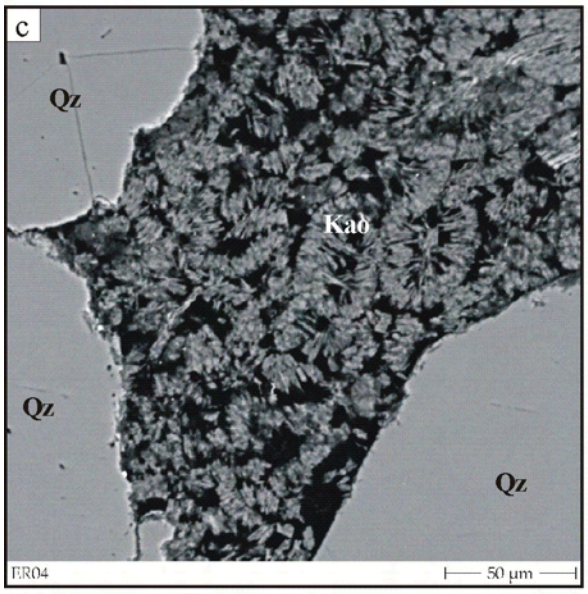
c
Qz
Kao
Qz
Qz
ER04
50 µm

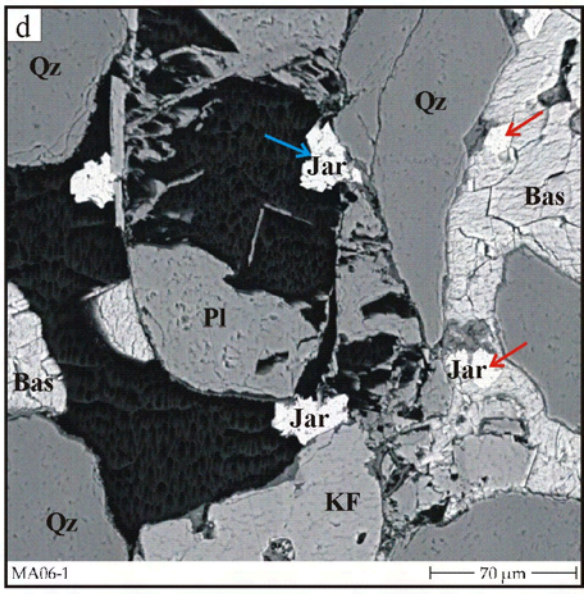
d
Qz
Qz
Jar
Bas
Pl
Bas
Jar
Jar
KF
Qz
MA06-1
70 µm

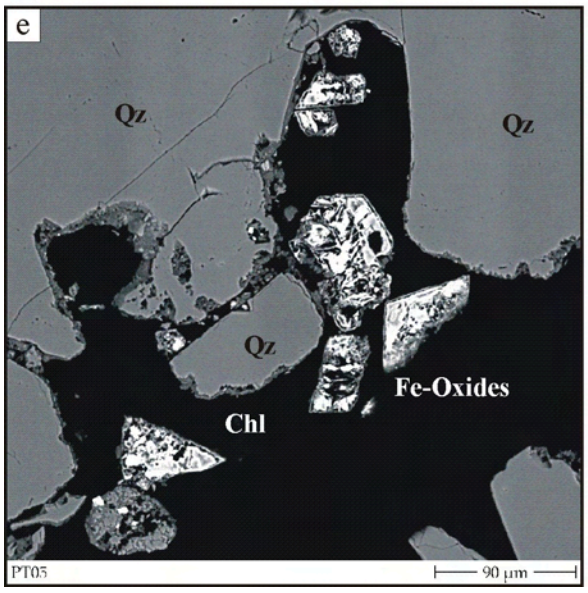
e
Qz
Qz
Qz
Fe-Oxides
Chl
PT05
90 µm

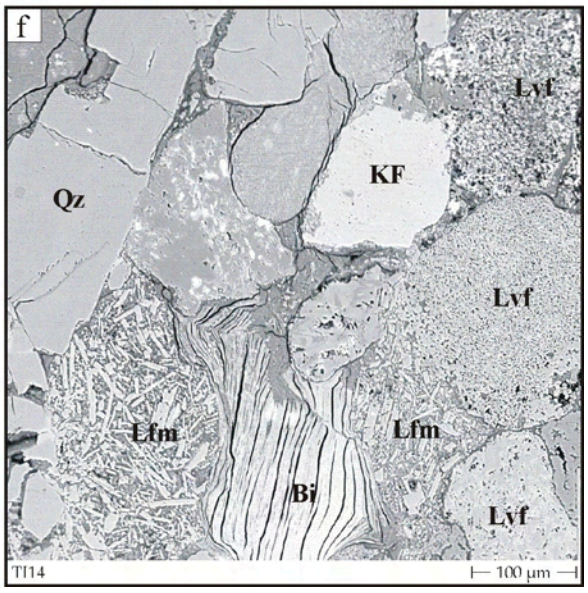
f
Lvf
KF
Qz
Lvf
Lfm
Lfm
Bi
Lvf
TI14
100 µm

# EMP (BSE) photographies 2

a) Notched K-feldspar (KF) overgrowth on plagioclase (Pl). Quartz grains (Qz) are free of overgrowths. Sample SHA05.

b) Zeolite formation (Zeo) may have occurred in two phases, as shown by the rim of chlorite (Chl) in between zeolites. However, in many other cases chlorite precipitation clearly pre-dates zeolite formation. Sample CHW06.

c) Chloritic mineral paragenesis (Chl.P.) on grain surfaces. In the center a grain (most likely feldspar) has been dissolved completey later. Overgrowths can partially be found also along grain contacts, indicating that some compaction occurred also after precipitation of the authigenic minerals. Sample RB06.

d) Enlarged part of (c). The chloritic mineral paragenesis in this case is formed by chlorite and blocky microquartz. Sample RB06.

e) Auhigenic Fe-hydroxide (limonite) is presumably intergrown or interdigitating with clay minerals (illite or smectite). Variable chemical compositions are shown by the different color intensity. Sample SHA04.

f) Shards (Sh) and minerals or mineral fragments (in this case plagioclases, Pl) in a tuffaceous sandstone. The shards are replaced completely by zeolites (clinoptilolite/heulandite), with a rim of smaller crystals and larger crystals in the interior. Sample SHA12.

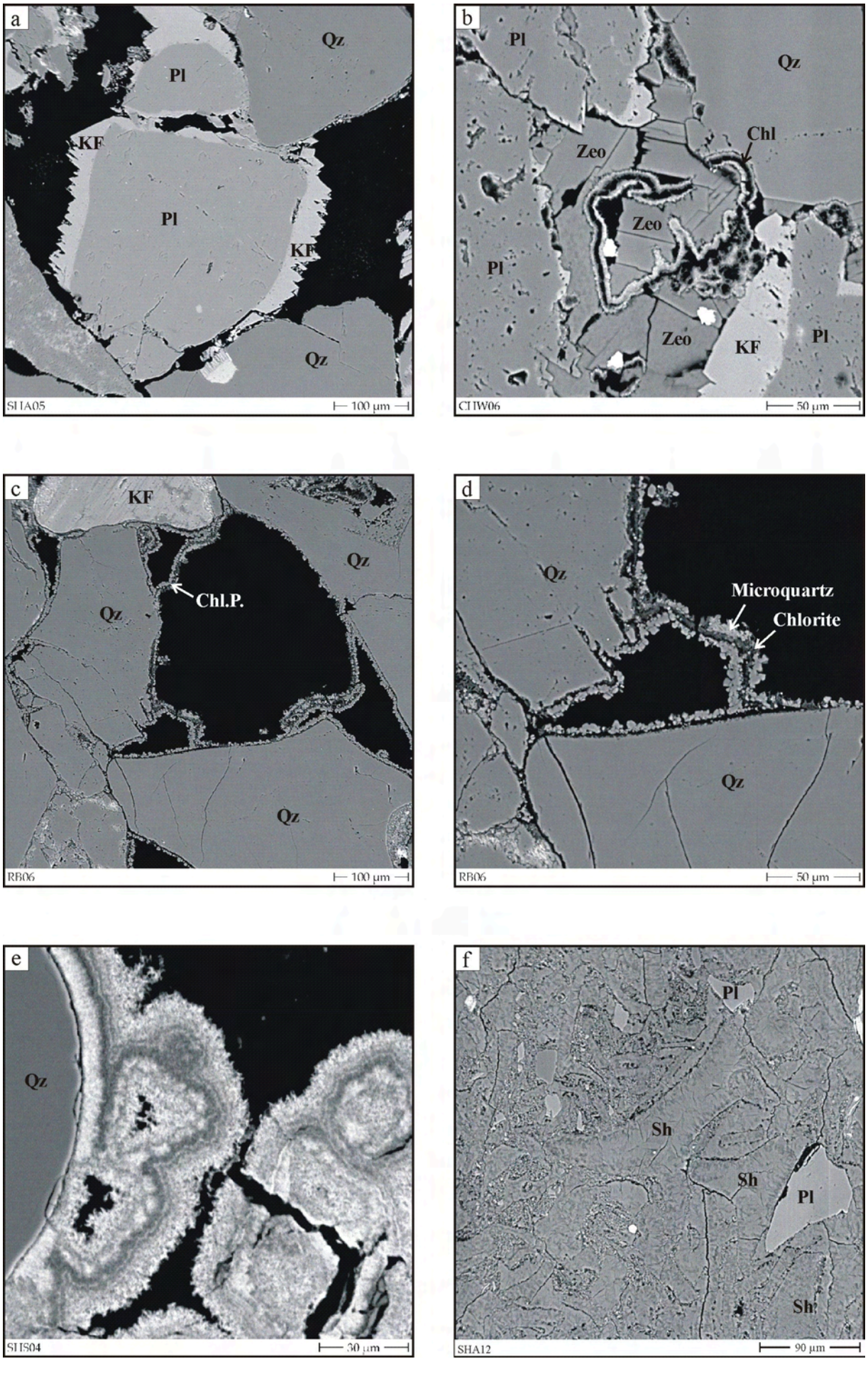
a
Qz
Pl
KF
Pl
KF
Qz
SHA05
100 µm
b
Pl
Qz
Chl
Zeo
Zeo
Pl
Zeo
KF
Pl
CHW06
50 µm
c
KF
Qz
Chl.P.
Qz
Qz
RB06
100 µm
d
Qz
Microquartz
Chlorite
Qz
RB06
50 µm
e
Qz
SHS04
30 µm
f
Pl
Sh
Sh
Pl
Sh
SHA12
90 µm

# EMP element mapping 1

Element-mapping of the tuffaceous sandstone sample SHA12 (SPF), recording the elements Si, Al, Ca, Na, K, Fe, and Ti. The colour intensity represent the abundance of the element. In the upper left a BSE image. For orientation, the outline of a shard has been drawn in all images in red.

The zeolites (clinoptilolite/ceulandite) replacing the shards (Sh) are of different grain size (rim: smaller, interior: larger), but their chemical composition is very similar. However, in comparison, the zeolites filling the pore space contain distinctly less Ca and Na and slightly less Al, but more Fe and Si. The K-content of both zeolite types is similar. Plagioclase (Pl) can be found as mineral constituent of the tuffaceous sandstone.

In Ti-phases (lower right image) also sulphur is an important constituent. Possibly authigenic Ti-minerals have precipitated preferentially on organic material.

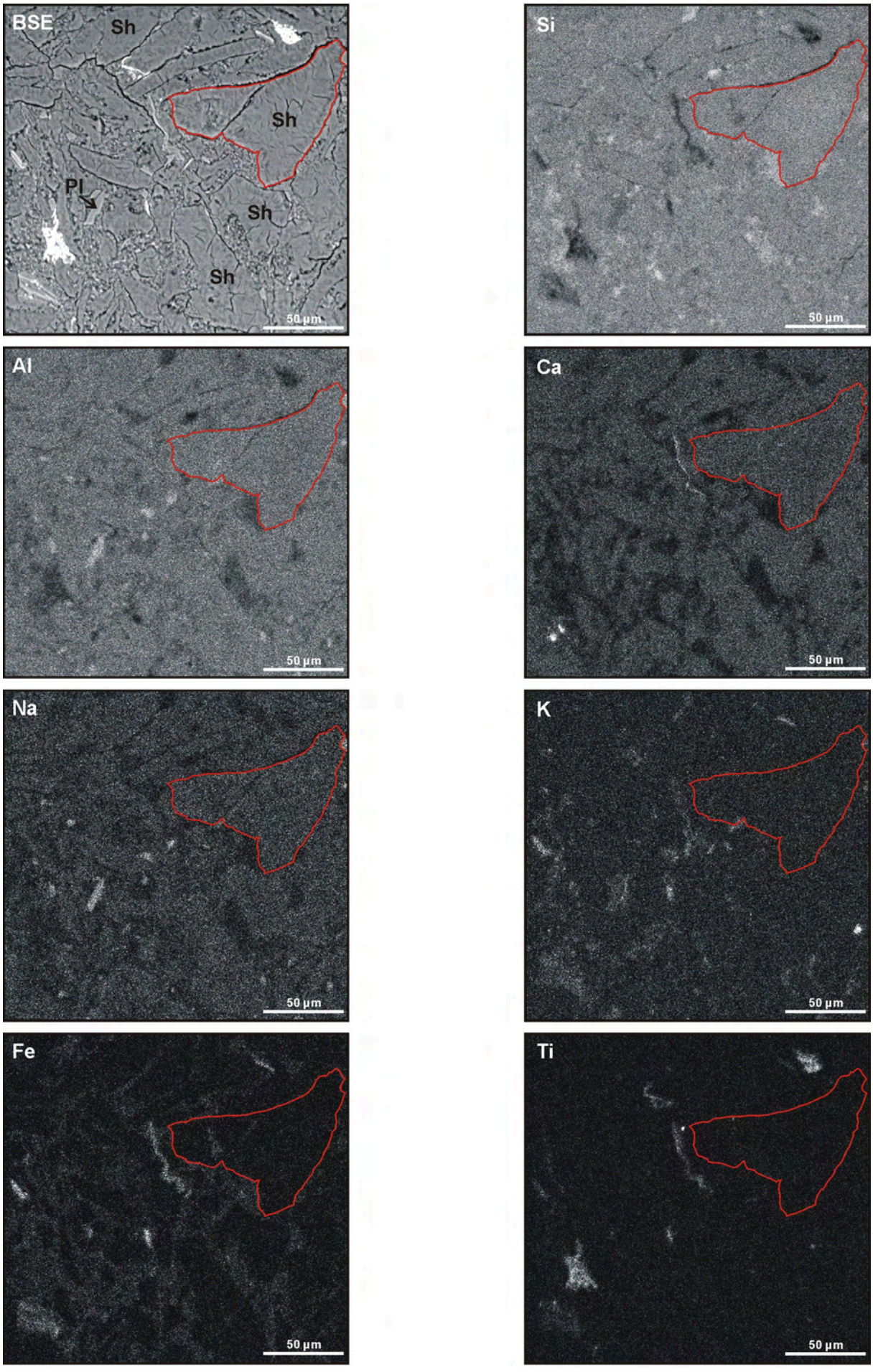
BSE
Sh
Sh
Pl
Sh
Sh
50 µm
Si
50 µm
Al
50 µm
Ca
50 µm
Na
50 µm
K
50 µm
Fe
50 µm
Ti
50 µm

# EMP element mapping 2

Element-mapping of sample CE77 (SHF), recording the elements Si, Al, Ca, Na, K, Fe, and Mg. The colour intensity represent the abundance of the element. In the upper left a BSE image. For orientation, the outline of a shard has been drawn in all images in red.

Shards (Sh) are replaced completely by zeolites. Also, the pores are filled completely by Zeolites. In comparison, the zeolites replacing the shards contain less Ca, but more Fe and K than the zeolites within the pores.

Quartz (Qtz), K-feldspar (KF) and albite (Ab) are frequent mineral constituents. Albite has most likely formed by diagenetic albitization of plagioclase.

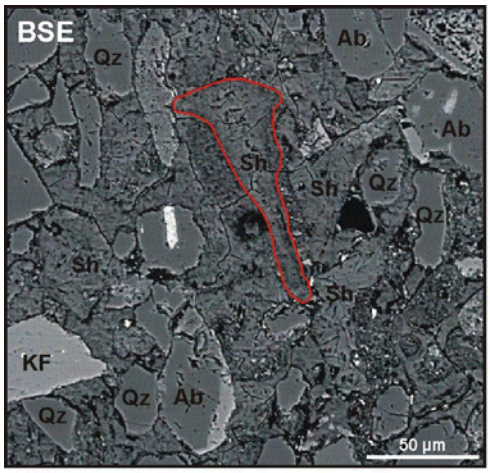
BSE
Qz
Ab
Ab
Sh
Sh
Qz
Qz
Sh
Sh
KF
Qz
Ab
Qz
50 µm

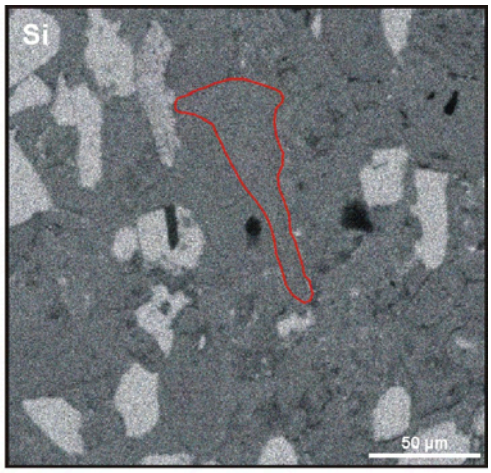
Si
50 µm

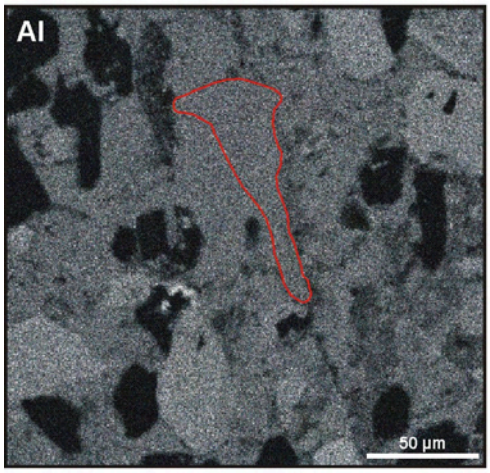
Al
50 µm

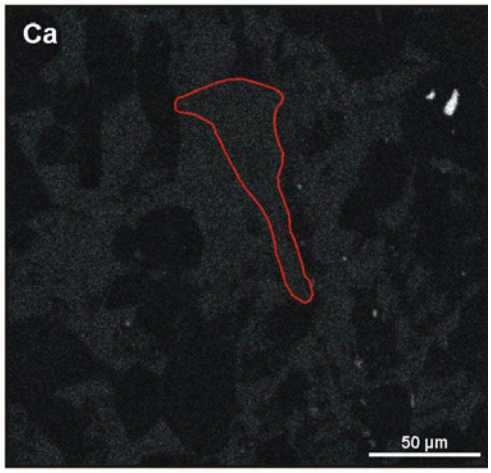
Ca
50 µm

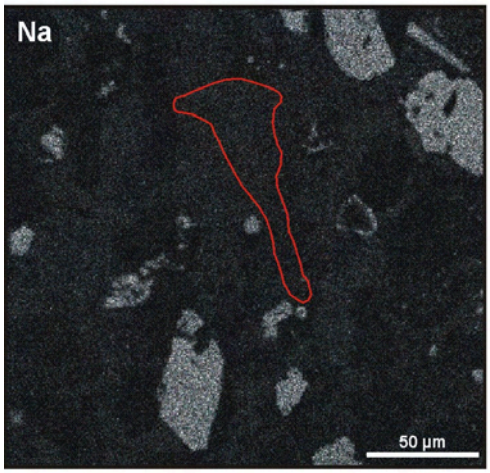
Na
50 µm

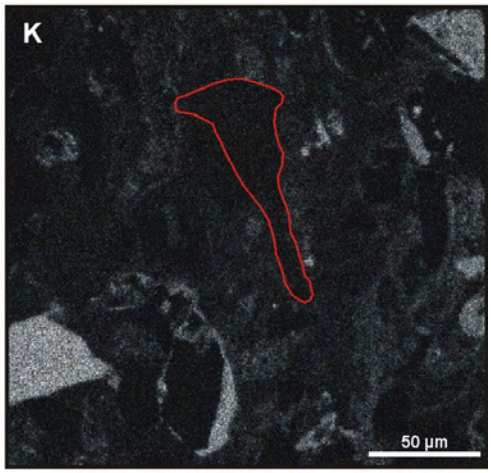
K
50 µm

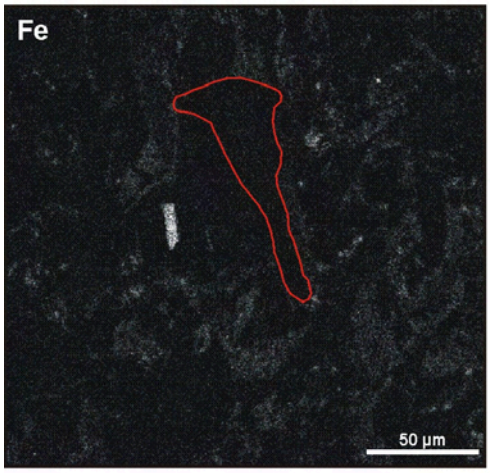
Fe
50 µm

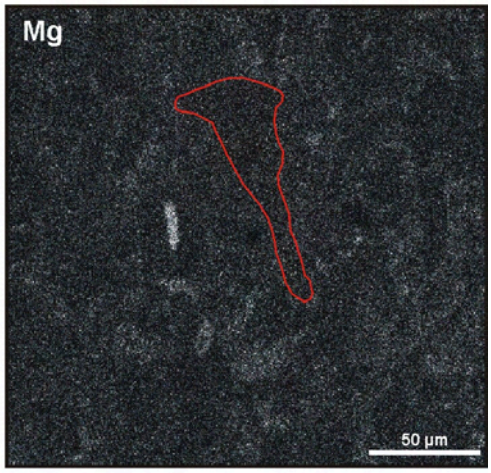
Mg
50 µm

# Appendix 7.1

U-Pb (LA-ICPMS) isotope data
and ages of detrital zircons from the SPF

# Results of U-Th-Pb LA-ICPMS analyses of zircons from sample ER04

| Spot | Seq. | No. | $^{207}Pb$ [a] (cps) | U [b] (ppm) | Pb [b] (ppm) | Th/U [b] | $^{206}Pb/^{204}Pb$ | $^{206}Pb/^{238}U$ [c] | ±2s (%) | $^{207}Pb/^{235}U$ [c] | ±2s (%) | $^{207}Pb/^{206}Pb$ [c] | ±2s (%) | Rho [d] | Age (Ma) $^{206}Pb/^{238}U$ | ±2s | Age (Ma) $^{207}Pb/^{235}U$ | ±2s | Age (Ma) $^{207}Pb/^{206}Pb$ [c] | ±2s | conc [e] (%) | Origin [f] |
|---|---|---|---|---|---|---|---|---|---|---|---|---|---|---|---|---|---|---|---|---|---|---|
| ER04-1 | 3 | a1 | 736 | 46 | 4 | 0.42 | 1198 | 0.0801 | 5.1 | 0.70 | 9.5 | 0.0634 | 8.0 | 0.54 | 497 | 25 | 539 | 41 | 723 | 171 | 69 | met. |
| ER04-2 | 3 | a2 | 481 | 16 | 3 | 1.18 | 687 | 0.1835 | 5.6 | 1.86 | 12.2 | 0.0734 | 10.8 | 0.46 | 1086 | 56 | 1066 | 84 | 1024 | 219 | 106 | mag. |
| ER04-3 | 3 | a3 | 6528 | 552 | 52 | 0.04 | 608 | 0.1000 | 3.5 | 0.83 | 8.1 | 0.0601 | 7.2 | 0.44 | 614 | 21 | 613 | 38 | 607 | 157 | 101 | met. |
| ER04-4 | 3 | a4 | 486 | 44 | 4 | 1.04 | 856 | 0.0823 | 2.9 | 0.65 | 9.6 | 0.0571 | 9.1 | 0.30 | 510 | 14 | 507 | 39 | 496 | 201 | 103 | mag. |
| ER04-5 | 3 | a5 | 687 | 60 | 6 | 0.65 | 1190 | 0.0875 | 3.4 | 0.70 | 7.7 | 0.0582 | 6.9 | 0.44 | 541 | 17 | 540 | 33 | 536 | 152 | 101 | mag. |
| ER04-6m | 3 | a6 | 235 | 64 | 2 | 0.94 | 476 | 0.0339 | 3.6 | 0.24 | 13.1 | 0.0503 | 12.6 | 0.28 | 215 | 8 | 215 | 26 | 210 | 292 | 103 | mag. |
| ER04-7c | 3 | a7 | 709 | 66 | 8 | 1.31 | 1188 | 0.1030 | 2.7 | 0.85 | 7.9 | 0.0595 | 7.4 | 0.34 | 632 | 16 | 622 | 38 | 586 | 161 | 108 | mag. |
| ER04-8r | 3 | a8 | 2962 | 233 | 22 | 0.41 | 2654 | 0.0925 | 2.6 | 0.78 | 3.9 | 0.0609 | 2.9 | 0.66 | 571 | 14 | 584 | 18 | 635 | 63 | 90 | mag. |
| ER04-9c | 3 | a9 | 1723 | 164 | 13 | 0.62 | 3149 | 0.0745 | 4.6 | 0.59 | 10.3 | 0.0571 | 9.3 | 0.44 | 463 | 21 | 469 | 40 | 494 | 204 | 94 | mag. |
| ER04-9r | 3 | a10 | 2013 | 185 | 18 | 0.46 | 2120 | 0.0980 | 3.0 | 0.79 | 6.6 | 0.0588 | 5.9 | 0.45 | 603 | 17 | 594 | 30 | 559 | 128 | 108 | mag. |
| ER04-10r | 3 | a11 | 2436 | 192 | 19 | 0.19 | 2403 | 0.1041 | 3.5 | 0.86 | 9.0 | 0.0603 | 8.3 | 0.39 | 638 | 22 | 633 | 43 | 613 | 180 | 104 | met. |
| ER04-11 | 3 | a12 | 8659 | 266 | 60 | 0.37 | 1265 | 0.2186 | 5.3 | 2.56 | 7.1 | 0.0851 | 4.8 | 0.74 | 1275 | 62 | 1290 | 53 | 1317 | 93 | 97 | mag. |
| ER04-12r | 3 | a13 | 2349 | 162 | 16 | 0.20 | 358 | 0.0975 | 2.5 | 1.12 | 7.5 | 0.0833 | 7.1 | 0.34 | 599 | 14 | 763 | 41 | 1276 | 138 | 47 | mag. |
| ER04-13 | 3 | a14 | 1827 | 165 | 17 | 1.14 | 1747 | 0.0891 | 3.2 | 0.73 | 7.6 | 0.0592 | 6.9 | 0.43 | 550 | 17 | 555 | 33 | 574 | 150 | 96 | mag. |
| ER04-14r | 3 | a15 | 1628 | 138 | 12 | 0.16 | 2738 | 0.0871 | 3.8 | 0.72 | 5.6 | 0.0595 | 4.1 | 0.68 | 538 | 20 | 548 | 24 | 587 | 90 | 92 | mag. |
| ER04-14c | 3 | a16 | 671 | 64 | 6 | 0.45 | 1190 | 0.0928 | 4.0 | 0.77 | 8.9 | 0.0602 | 8.0 | 0.45 | 572 | 22 | 579 | 40 | 609 | 172 | 94 | mag. |
| ER04-15r | 3 | a17 | 1421 | 93 | 11 | 0.07 | 2170 | 0.1208 | 3.2 | 1.10 | 6.2 | 0.0659 | 5.3 | 0.51 | 735 | 22 | 753 | 33 | 804 | 111 | 92 | met. |
| ER04-15c | 3 | a18 | 8478 | 308 | 59 | 0.43 | 7544 | 0.1859 | 4.2 | 1.95 | 6.2 | 0.0760 | 4.5 | 0.69 | 1099 | 43 | 1098 | 42 | 1095 | 90 | 100 | mag. |
| ER04-16 | 3 | a19 | 9237 | 333 | 55 | 0.29 | 470 | 0.1582 | 3.3 | 1.55 | 5.9 | 0.0712 | 4.9 | 0.56 | 947 | 29 | 952 | 37 | 965 | 100 | 98 | met. |
| ER04-18 | 3 | a21 | 470 | 40 | 5 | 1.56 | 789 | 0.0910 | 8.9 | 0.75 | 14.9 | 0.0600 | 12.0 | 0.60 | 561 | 48 | 570 | 67 | 602 | 259 | 93 | mag. |
| ER04-19 | 3 | a22 | 1302 | 150 | 18 | 1.04 | 2460 | 0.1083 | 14.2 | 0.89 | 15.9 | 0.0598 | 7.2 | 0.89 | 663 | 90 | 648 | 79 | 596 | 156 | 111 | mag. |
| ER04-21r | 3 | a24 | 1076 | 95 | 10 | 0.38 | 1635 | 0.1075 | 2.1 | 1.00 | 5.6 | 0.0671 | 5.2 | 0.38 | 658 | 13 | 701 | 29 | 842 | 108 | 78 | mag. |
| ER04-21c | 3 | a25 | 1076 | 105 | 10 | 0.76 | 827 | 0.0879 | 4.4 | 0.70 | 8.1 | 0.0576 | 6.8 | 0.54 | 543 | 23 | 538 | 34 | 516 | 149 | 105 | mag. |
| ER04-22r | 3 | a26 | 674 | 170 | 8 | 0.65 | 1296 | 0.0421 | 3.6 | 0.30 | 7.9 | 0.0522 | 7.1 | 0.46 | 266 | 9 | 269 | 19 | 295 | 161 | 90 | mag. |
| ER04-23r | 3 | a27 | 2155 | 170 | 19 | 1.25 | 1441 | 0.0919 | 3.3 | 0.75 | 5.7 | 0.0593 | 4.6 | 0.58 | 567 | 18 | 569 | 25 | 578 | 101 | 98 | mag. |
| ER04-24r | 3 | a28 | 1227 | 110 | 10 | 0.60 | 1709 | 0.0896 | 2.4 | 0.74 | 7.3 | 0.0602 | 6.9 | 0.33 | 553 | 13 | 564 | 32 | 610 | 150 | 91 | mag. |
| ER04-25 | 3 | a29 | 1925 | 157 | 13 | 0.58 | 551 | 0.0759 | 5.7 | 0.64 | 8.3 | 0.0611 | 6.1 | 0.69 | 472 | 26 | 502 | 34 | 642 | 130 | 74 | mag. |
| ER04-26r | 3 | a30 | 1010 | 104 | 33 | 12.53 | 1673 | 0.0968 | 3.6 | 0.81 | 7.0 | 0.0608 | 6.0 | 0.51 | 596 | 20 | 603 | 32 | 632 | 129 | 94 | mag. |
| ER04-28 | 3 | a32 | 1553 | 175 | 17 | 0.81 | 2661 | 0.0897 | 2.5 | 0.73 | 5.6 | 0.0590 | 5.0 | 0.45 | 554 | 13 | 556 | 24 | 566 | 108 | 98 | mag. |
| ER04-29 | 3 | a33 | 1088 | 130 | 12 | 0.88 | 1903 | 0.0854 | 2.0 | 0.68 | 6.8 | 0.0577 | 6.5 | 0.30 | 529 | 10 | 527 | 28 | 519 | 143 | 102 | mag. |
| ER04-30 | 3 | a34 | 670 | 79 | 6 | 0.77 | 1204 | 0.0741 | 3.9 | 0.58 | 9.0 | 0.0563 | 8.2 | 0.43 | 461 | 17 | 462 | 34 | 464 | 181 | 99 | mag. |
| ER04-31r | 3 | a35 | 471 | 73 | 6 | 0.84 | 830 | 0.0830 | 3.3 | 0.67 | 11.1 | 0.0582 | 10.6 | 0.30 | 514 | 16 | 518 | 46 | 538 | 231 | 96 | mag. |
| ER04-31c | 3 | a36 | 472 | 77 | 6 | 1.37 | 868 | 0.0651 | 3.8 | 0.49 | 11.7 | 0.0543 | 11.1 | 0.32 | 406 | 15 | 403 | 40 | 385 | 250 | 106 | mag. |
| ER04-32 | 3 | a37 | 5337 | 211 | 71 | 4.06 | 7101 | 0.1812 | 2.6 | 1.88 | 4.2 | 0.0754 | 3.3 | 0.63 | 1074 | 26 | 1075 | 28 | 1078 | 66 | 100 | mag. |
| ER04-33m | 3 | a38 | 1536 | 189 | 16 | 0.43 | 2648 | 0.0811 | 3.0 | 0.66 | 6.3 | 0.0586 | 5.5 | 0.48 | 502 | 15 | 512 | 26 | 553 | 120 | 91 | mag. |
| ER04-33c | 3 | a39 | 5316 | 585 | 52 | 0.34 | 2190 | 0.0898 | 3.4 | 0.73 | 5.9 | 0.0591 | 4.8 | 0.58 | 555 | 18 | 558 | 26 | 571 | 104 | 97 | mag. |
| ER04-34r | 3 | a40 | 1910 | 231 | 22 | 0.69 | 3295 | 0.0889 | 2.8 | 0.72 | 5.4 | 0.0587 | 4.6 | 0.52 | 549 | 15 | 550 | 23 | 555 | 101 | 99 | mag. |
| ER04-34c | 3 | a41 | 2314 | 230 | 29 | 1.32 | 3807 | 0.1062 | 3.2 | 0.90 | 8.7 | 0.0616 | 8.1 | 0.37 | 650 | 20 | 653 | 43 | 660 | 173 | 98 | mag. |
| ER04-35 | 3 | a42 | 1293 | 116 | 12 | 0.69 | 2265 | 0.0966 | 6.6 | 0.80 | 13.0 | 0.0599 | 11.2 | 0.51 | 595 | 37 | 596 | 60 | 602 | 242 | 99 | mag. |
| ER04-36 | 3 | a43 | 3018 | 152 | 53 | 0.96 | 578 | 0.3231 | 3.2 | 4.94 | 5.5 | 0.1109 | 4.5 | 0.58 | 1805 | 50 | 1809 | 47 | 1814 | 81 | 100 | mag. |
| ER04-37 | 3 | a44 | 2462 | 84 | 22 | 1.03 | 1110 | 0.2280 | 3.5 | 2.55 | 4.7 | 0.0812 | 3.2 | 0.73 | 1324 | 41 | 1287 | 35 | 1225 | 63 | 108 | mag. |
| ER04-38 | 3 | a45 | 3657 | 412 | 42 | 0.89 | 6353 | 0.0928 | 4.6 | 0.74 | 6.0 | 0.0580 | 3.9 | 0.76 | 572 | 25 | 564 | 26 | 529 | 85 | 108 | mag. |
| ER04-39 | 3 | a46 | 1399 | 177 | 16 | 0.90 | 2439 | 0.0811 | 4.4 | 0.65 | 6.9 | 0.0581 | 5.3 | 0.64 | 503 | 21 | 508 | 28 | 532 | 116 | 94 | mag. |
| ER04-40 | 3 | a47 | 3652 | 393 | 39 | 0.67 | 6272 | 0.0930 | 4.3 | 0.75 | 5.9 | 0.0586 | 4.0 | 0.73 | 573 | 24 | 569 | 26 | 552 | 87 | 104 | unc. |
| ER04-41 | 3 | a48 | 3193 | 392 | 37 | 0.90 | 3465 | 0.0847 | 8.0 | 0.67 | 10.6 | 0.0572 | 7.0 | 0.75 | 524 | 40 | 519 | 44 | 499 | 154 | 105 | mag. |
| ER04-42 | 3 | a49 | 6190 | 299 | 45 | 0.25 | 3813 | 0.1501 | 6.1 | 1.49 | 7.2 | 0.0719 | 3.7 | 0.85 | 902 | 52 | 925 | 45 | 982 | 76 | 92 | met. |
| ER04-43 | 3 | a50 | 1678 | 222 | 20 | 0.76 | 866 | 0.0827 | 5.6 | 0.67 | 8.6 | 0.0587 | 6.5 | 0.65 | 512 | 28 | 520 | 36 | 554 | 143 | 92 | mag. |
| ER04-44c | 3 | a51 | 385 | 41 | 4 | 1.17 | 608 | 0.0859 | 6.3 | 0.77 | 11.6 | 0.0654 | 9.8 | 0.54 | 531 | 32 | 582 | 53 | 789 | 205 | 67 | mag. |
| ER04-45 | 3 | a52 | 4071 | 521 | 42 | 0.37 | 3018 | 0.0808 | 5.2 | 0.65 | 7.2 | 0.0586 | 5.0 | 0.72 | 501 | 25 | 510 | 29 | 552 | 109 | 91 | met. |
| ER04-46r | 3 | a53 | 4983 | 486 | 43 | 0.51 | 557 | 0.0829 | 4.9 | 0.66 | 7.0 | 0.0580 | 5.0 | 0.70 | 514 | 24 | 516 | 29 | 528 | 109 | 97 | unc. |
| ER04-46c | 3 | a54 | 1709 | 196 | 20 | 0.85 | 2835 | 0.0905 | 4.7 | 0.73 | 8.0 | 0.0583 | 6.4 | 0.59 | 559 | 25 | 555 | 35 | 540 | 140 | 103 | unc. |
| ER04-47 | 3 | a55 | 1866 | 213 | 22 | 0.70 | 3130 | 0.0943 | 3.1 | 0.79 | 5.5 | 0.0605 | 4.6 | 0.56 | 581 | 17 | 589 | 25 | 621 | 98 | 94 | mag. |
| ER04-48r | 4 | a1 | 3671 | 260 | 23 | 0.38 | 4979 | 0.0855 | 2.7 | 0.69 | 3.4 | 0.0582 | 2.0 | 0.80 | 529 | 14 | 530 | 14 | 537 | 45 | 98 | mag. |
| ER04-48c | 4 | a2 | 1407 | 110 | 10 | 0.69 | 4930 | 0.0857 | 2.4 | 0.67 | 4.6 | 0.0571 | 3.9 | 0.53 | 530 | 12 | 524 | 19 | 496 | 87 | 107 | mag. |
| ER04-49 | 4 | a3 | 3248 | 224 | 21 | 0.68 | 10920 | 0.0852 | 2.3 | 0.68 | 4.5 | 0.0581 | 3.9 | 0.51 | 527 | 12 | 528 | 19 | 533 | 84 | 99 | mag. |
| ER04-50c | 4 | a4 | 2102 | 75 | 8 | 0.65 | 3777 | 0.0911 | 2.7 | 0.73 | 5.1 | 0.0580 | 4.3 | 0.53 | 562 | 15 | 556 | 22 | 531 | 95 | 106 | mag. |
| ER04-51 | 4 | a5 | 3280 | 262 | 23 | 0.28 | 1741 | 0.0881 | 2.7 | 0.71 | 3.7 | 0.0587 | 2.4 | 0.75 | 544 | 14 | 547 | 16 | 558 | 53 | 98 | met. |
| ER04-52 | 4 | a6 | 6863 | 594 | 63 | 0.90 | 23304 | 0.0917 | 2.7 | 0.74 | 3.9 | 0.0586 | 2.8 | 0.70 | 565 | 15 | 563 | 17 | 552 | 61 | 103 | mag. |
| ER04-53 | 4 | a7 | 2080 | 151 | 16 | 0.62 | 2055 | 0.1000 | 2.0 | 0.83 | 4.2 | 0.0601 | 3.7 | 0.47 | 614 | 12 | 613 | 20 | 609 | 81 | 101 | mag. |
| ER04-54 | 4 | a8 | 3379 | 193 | 21 | 1.50 | 1770 | 0.0838 | 3.5 | 0.66 | 5.0 | 0.0575 | 3.6 | 0.70 | 519 | 18 | 517 | 21 | 511 | 80 | 101 | mag. |
| ER04-55r | 4 | a9 | 2828 | 269 | 25 | 0.71 | 9914 | 0.0819 | 2.5 | 0.64 | 3.8 | 0.0569 | 2.9 | 0.65 | 507 | 12 | 504 | 15 | 489 | 63 | 104 | mag. |
| ER04-55c | 4 | a10 | 3144 | 292 | 28 | 0.99 | 10895 | 0.0810 | 2.9 | 0.64 | 3.8 | 0.0575 | 2.4 | 0.77 | 502 | 14 | 504 | 15 | 512 | 54 | 98 | mag. |
| ER04-56 | 4 | a11 | 20246 | 84 | 53 | 0.57 | 5513 | 0.5608 | 2.4 | 15.32 | 2.7 | 0.1981 | 1.2 | 0.90 | 2870 | 56 | 2835 | 26 | 2811 | 19 | 102 | mag. |
| ER04-57 | 4 | a12 | 2986 | 166 | 17 | 0.57 | 6649 | 0.0943 | 2.5 | 0.78 | 4.4 | 0.0597 | 3.6 | 0.56 | 581 | 14 | 584 | 20 | 593 | 79 | 98 | mag. |
| ER04-6c | 4 | a13 | 2201 | 114 | 10 | 0.69 | 2277 | 0.0788 | 2.4 | 0.61 | 3.8 | 0.0558 | 3.0 | 0.63 | 489 | 11 | 482 | 15 | 445 | 66 | 110 | mag. |
| ER04-8c | 4 | a14 | 1870 | 61 | 6 | 0.86 | 2902 | 0.0898 | 2.7 | 0.72 | 4.5 | 0.0582 | 3.6 | 0.59 | 555 | 14 | 551 | 19 | 536 | 79 | 103 | mag. |
| ER04-23c | 4 | a15 | 3374 | 214 | 21 | 0.98 | 3412 | 0.0835 | 2.7 | 0.66 | 4.0 | 0.0578 | 2.9 | 0.69 | 517 | 14 | 518 | 16 | 521 | 63 | 99 | mag. |
| ER04-26c | 4 | a16 | 1433 | 39 | 3 | 0.76 | 3466 | 0.0782 | 2.8 | 0.62 | 6.2 | 0.0574 | 5.5 | 0.46 | 485 | 13 | 489 | 24 | 508 | 121 | 96 | mag. |

# Results of U-Th-Pb LA-ICPMS analyses of zircons from sample TI14

| Spot | Seq. | No. | $^{207}Pb$ [a] (cps) | U [b] (ppm) | Pb [b] (ppm) | Th/U [b] | $^{206}Pb/^{204}Pb$ | $^{206}Pb/^{238}U$ [c] | ±2s (%) | $^{207}Pb/^{235}U$ [c] | ±2s (%) | $^{207}Pb/^{206}Pb$ [c] | ±2s (%) | Rho [d] | Age (Ma) $^{206}Pb/^{238}U$ | ±2s | Age (Ma) $^{207}Pb/^{235}U$ | ±2s | Age (Ma) $^{207}Pb/^{206}Pb$ [c] | ±2s | conc [e] (%) | Origin [f] |
|---|---|---|---|---|---|---|---|---|---|---|---|---|---|---|---|---|---|---|---|---|---|---|
| TI14-1 | 9 | a1 | 1350 | 70 | 4 | 2.30 | 1389 | 0.0351 | 3.9 | 0.25 | 9.9 | 0.0509 | 9.1 | 0.39 | 222 | 9 | 224 | 20 | 238 | 211 | 93 | mag. |
| TI14-2r | 9 | a2 | 11586 | 99 | 10 | 1.31 | 3658 | 0.0849 | 5.3 | 0.71 | 7.1 | 0.0604 | 4.7 | 0.75 | 525 | 27 | 543 | 30 | 619 | 102 | 85 | mag. |
| TI14-2c | 9 | a3 | 11747 | 124 | 12 | 1.23 | 3277 | 0.0842 | 7.1 | 0.68 | 8.5 | 0.0584 | 4.7 | 0.83 | 521 | 36 | 525 | 36 | 544 | 103 | 96 | mag. |
| TI14-3 | 9 | a4 | 1380 | 80 | 3 | 0.98 | 1544 | 0.0327 | 3.9 | 0.23 | 9.3 | 0.0503 | 8.4 | 0.42 | 208 | 8 | 208 | 18 | 210 | 194 | 99 | mag. |
| TI14-4 | 9 | a5 | 1783 | 125 | 6 | 0.53 | 3042 | 0.0449 | 2.4 | 0.32 | 6.7 | 0.0521 | 6.3 | 0.35 | 283 | 7 | 284 | 17 | 289 | 144 | 98 | mag. |
| TI14-5 | 9 | a7 | 11097 | 143 | 10 | 1.43 | 4081 | 0.0553 | 3.4 | 0.40 | 6.1 | 0.0524 | 5.1 | 0.55 | 347 | 11 | 341 | 18 | 303 | 116 | 114 | mag. |
| TI14-6r | 9 | a9 | 1107 | 25 | 1 | 0.86 | 2447 | 0.0351 | 4.3 | 0.23 | 12.3 | 0.0485 | 11.5 | 0.35 | 223 | 9 | 214 | 24 | 125 | 271 | 178 | mag. |
| TI14-6c | 9 | a10 | 1488 | 114 | 4 | 0.69 | 3924 | 0.0345 | 3.8 | 0.24 | 8.3 | 0.0508 | 7.3 | 0.46 | 219 | 8 | 220 | 17 | 233 | 169 | 94 | mag. |
| TI14-8 | 9 | a12 | 12239 | 148 | 15 | 0.91 | 7537 | 0.0883 | 2.9 | 0.73 | 5.4 | 0.0596 | 4.6 | 0.54 | 545 | 15 | 554 | 23 | 590 | 99 | 92 | mag. |
| TI14-9c | 9 | a13 | 1478 | 78 | 4 | 0.68 | 3887 | 0.0453 | 3.8 | 0.32 | 9.6 | 0.0517 | 8.9 | 0.39 | 286 | 11 | 284 | 24 | 272 | 203 | 105 | mag. |
| TI14-10r | 9 | a14 | 1234 | 47 | 2 | 1.20 | 2865 | 0.0317 | 5.0 | 0.22 | 7.3 | 0.0506 | 5.3 | 0.68 | 201 | 10 | 203 | 13 | 221 | 123 | 91 | mag. |
| TI14-10c | 9 | a15 | 1162 | 38 | 1 | 0.72 | 2646 | 0.0319 | 6.9 | 0.22 | 15.8 | 0.0501 | 14.2 | 0.44 | 202 | 14 | 202 | 29 | 200 | 329 | 101 | mag. |
| TI14-11 | 9 | a16 | 11457 | 279 | 11 | 0.79 | 5557 | 0.0347 | 3.2 | 0.25 | 4.8 | 0.0516 | 3.6 | 0.66 | 220 | 7 | 224 | 10 | 267 | 82 | 82 | mag. |
| TI14-12 | 9 | a17 | 5359 | 179 | 32 | 0.44 | 14423 | 0.1743 | 3.7 | 1.79 | 4.9 | 0.0747 | 3.1 | 0.77 | 1036 | 36 | 1043 | 32 | 1059 | 63 | 98 | unc. |
| TI14-13 | 9 | a18 | 11165 | 259 | 10 | 0.59 | 4619 | 0.0358 | 3.8 | 0.25 | 7.6 | 0.0510 | 6.5 | 0.50 | 227 | 9 | 228 | 16 | 239 | 151 | 95 | mag. |
| TI14-14r | 9 | a19 | 1658 | 92 | 5 | 0.48 | 404 | 0.0534 | 4.0 | 0.39 | 8.2 | 0.0535 | 7.1 | 0.49 | 335 | 13 | 337 | 24 | 350 | 161 | 96 | mag. |
| TI14-14c | 9 | a20 | 1683 | 99 | 6 | 0.36 | 2584 | 0.0563 | 3.2 | 0.41 | 7.6 | 0.0534 | 6.8 | 0.43 | 353 | 11 | 352 | 23 | 345 | 155 | 102 | mag. |
| TI14-15r | 9 | a21 | 153 | 17 | 1 | 1.27 | 1354 | 0.0312 | 6.8 | 0.22 | 10.2 | 0.0501 | 7.6 | 0.66 | 198 | 13 | 198 | 19 | 201 | 177 | 98 | mag. |
| TI14-15c | 9 | a22 | 1321 | 68 | 3 | 1.25 | 3213 | 0.0330 | 4.1 | 0.23 | 16.7 | 0.0506 | 16.1 | 0.25 | 209 | 9 | 210 | 32 | 221 | 374 | 95 | mag. |
| TI14-16c | 9 | a23 | 1656 | 68 | 6 | 0.83 | 2403 | 0.0850 | 4.1 | 0.67 | 8.0 | 0.0570 | 6.8 | 0.52 | 526 | 21 | 519 | 33 | 492 | 150 | 107 | mag. |
| TI14-17 | 9 | a24 | 172 | 19 | 1 | 1.49 | 2288 | 0.0369 | 4.6 | 0.26 | 22.5 | 0.0511 | 22.0 | 0.20 | 234 | 11 | 235 | 48 | 247 | 507 | 95 | mag. |
| TI14-18c | 9 | a25 | 1328 | 88 | 4 | 1.60 | 3338 | 0.0339 | 4.2 | 0.24 | 10.2 | 0.0505 | 9.3 | 0.41 | 215 | 9 | 215 | 20 | 216 | 216 | 99 | mag. |
| TI14-19c | 9 | a26 | 1200 | 57 | 3 | 1.36 | 2878 | 0.0335 | 7.3 | 0.22 | 15.5 | 0.0475 | 13.6 | 0.47 | 213 | 15 | 202 | 29 | 76 | 324 | 279 | mag. |
| TI14-20 | 9 | a27 | 1394 | 101 | 5 | 1.51 | 1608 | 0.0393 | 4.2 | 0.27 | 9.6 | 0.0508 | 8.7 | 0.43 | 248 | 10 | 247 | 21 | 232 | 201 | 107 | mag. |
| TI14-21 | 9 | a28 | 1205 | 56 | 3 | 1.49 | 2828 | 0.0338 | 5.4 | 0.23 | 11.6 | 0.0503 | 10.2 | 0.47 | 215 | 11 | 214 | 23 | 208 | 236 | 103 | mag. |
| TI14-22r | 9 | a29 | 11593 | 151 | 6 | 0.67 | 2342 | 0.0358 | 3.7 | 0.25 | 7.8 | 0.0506 | 6.9 | 0.47 | 227 | 8 | 227 | 16 | 224 | 160 | 101 | mag. |
| TI14-23r | 9 | a30 | 1877 | 237 | 9 | 0.68 | 3573 | 0.0336 | 4.2 | 0.24 | 8.0 | 0.0507 | 6.7 | 0.53 | 213 | 9 | 214 | 15 | 229 | 156 | 93 | mag. |
| TI14-24r | 9 | a31 | 1548 | 149 | 6 | 1.06 | 2176 | 0.0357 | 4.2 | 0.25 | 8.1 | 0.0508 | 6.9 | 0.52 | 226 | 9 | 226 | 17 | 232 | 160 | 97 | mag. |
| TI14-24c | 9 | a32 | 1698 | 146 | 7 | 2.42 | 2695 | 0.0318 | 2.2 | 0.23 | 6.9 | 0.0513 | 6.5 | 0.32 | 202 | 4 | 206 | 13 | 256 | 149 | 79 | mag. |
| TI14-25 | 9 | a33 | 1304 | 92 | 4 | 1.49 | 1049 | 0.0336 | 2.7 | 0.24 | 8.1 | 0.0510 | 7.6 | 0.33 | 213 | 6 | 215 | 16 | 241 | 176 | 88 | mag. |
| TI14-26r | 9 | a34 | 11756 | 205 | 16 | 0.42 | 6089 | 0.0761 | 3.4 | 0.60 | 5.5 | 0.0575 | 4.3 | 0.62 | 473 | 15 | 479 | 21 | 512 | 94 | 92 | mag. |
| TI14-26c | 9 | a35 | 1664 | 80 | 8 | 1.08 | 2456 | 0.0852 | 3.1 | 0.66 | 5.6 | 0.0565 | 4.7 | 0.55 | 527 | 16 | 517 | 23 | 474 | 103 | 111 | mag. |
| TI14-28r | 9 | a37 | 1155 | 48 | 2 | 1.98 | 614 | 0.0366 | 6.4 | 0.25 | 18.0 | 0.0505 | 16.9 | 0.35 | 231 | 15 | 230 | 38 | 218 | 391 | 106 | mag. |
| TI14-29r | 9 | a38 | 11772 | 73 | 14 | 0.74 | 4936 | 0.1844 | 7.4 | 1.90 | 8.0 | 0.0749 | 3.0 | 0.92 | 1091 | 74 | 1083 | 54 | 1065 | 61 | 102 | unc. |
| TI14-30 | 9 | a39 | 16711 | 167 | 53 | 1.62 | 9691 | 0.2488 | 8.8 | 3.09 | 10.2 | 0.0902 | 5.2 | 0.86 | 1432 | 114 | 1431 | 82 | 1429 | 99 | 100 | mag. |
| TI14-31c | 9 | a40 | 1161 | 52 | 2 | 1.71 | 647 | 0.0366 | 4.8 | 0.26 | 13.2 | 0.0512 | 12.4 | 0.36 | 232 | 11 | 234 | 28 | 250 | 284 | 93 | mag. |
| TI14-32m | 9 | a41 | 1420 | 135 | 5 | 0.77 | 1685 | 0.0360 | 6.4 | 0.25 | 10.3 | 0.0506 | 8.0 | 0.62 | 228 | 14 | 228 | 21 | 222 | 186 | 103 | mag. |
| TI14-33 | 9 | a42 | 1699 | 224 | 9 | 0.94 | 2758 | 0.0367 | 5.0 | 0.26 | 7.3 | 0.0511 | 5.3 | 0.68 | 233 | 11 | 234 | 15 | 247 | 123 | 94 | mag. |
| TI14-34 | 9 | a43 | 11235 | 418 | 18 | 1.43 | 4826 | 0.0360 | 3.4 | 0.25 | 5.4 | 0.0505 | 4.2 | 0.64 | 228 | 8 | 227 | 11 | 217 | 96 | 105 | mag. |
| TI14-35r | 9 | a44 | 1395 | 129 | 4 | 0.82 | 1616 | 0.0311 | 4.8 | 0.21 | 9.3 | 0.0492 | 7.9 | 0.52 | 197 | 9 | 194 | 16 | 159 | 185 | 124 | mag. |
| TI14-36 | 9 | a45 | 1481 | 161 | 6 | 0.75 | 1850 | 0.0366 | 3.9 | 0.26 | 8.7 | 0.0512 | 7.7 | 0.45 | 232 | 9 | 233 | 18 | 248 | 178 | 93 | mag. |
| TI14-37 | 9 | a46 | 1380 | 134 | 5 | 0.66 | 1523 | 0.0338 | 3.4 | 0.23 | 8.2 | 0.0502 | 7.4 | 0.42 | 214 | 7 | 213 | 16 | 204 | 172 | 105 | mag. |
| TI14-38r | 9 | a47 | 1742 | 260 | 10 | 0.79 | 1099 | 0.0361 | 2.9 | 0.25 | 5.9 | 0.0503 | 5.1 | 0.48 | 229 | 6 | 227 | 12 | 211 | 119 | 108 | mag. |
| TI14-38c | 9 | a48 | 198 | 37 | 1 | 0.96 | 420 | 0.0343 | 4.8 | 0.23 | 14.4 | 0.0490 | 13.6 | 0.33 | 217 | 10 | 212 | 28 | 147 | 319 | 148 | mag. |
| TI14-39r | 9 | a49 | 1409 | 125 | 5 | 0.82 | 1351 | 0.0343 | 4.5 | 0.29 | 13.2 | 0.0615 | 12.4 | 0.34 | 218 | 10 | 259 | 31 | 657 | 267 | 33 | mag. |
| TI14-39c | 9 | a50 | 1511 | 221 | 10 | 1.92 | 2040 | 0.0336 | 3.8 | 0.23 | 8.6 | 0.0491 | 7.7 | 0.45 | 213 | 8 | 208 | 16 | 153 | 180 | 139 | mag. |
| TI14-40c | 9 | a51 | 17461 | 134 | 51 | 0.80 | 2338 | 0.3344 | 3.8 | 5.18 | 5.7 | 0.1124 | 4.2 | 0.67 | 1860 | 62 | 1849 | 50 | 1838 | 76 | 101 | mag. |
| TI14-41r | 9 | a52 | 11067 | 55 | 11 | 1.01 | 2687 | 0.1890 | 4.9 | 2.10 | 6.9 | 0.0805 | 4.8 | 0.72 | 1116 | 51 | 1148 | 48 | 1210 | 94 | 92 | mag. |
| TI14-42c | 9 | a53 | 1498 | 214 | 9 | 1.22 | 2042 | 0.0366 | 4.3 | 0.25 | 8.9 | 0.0496 | 7.7 | 0.49 | 232 | 10 | 227 | 18 | 176 | 181 | 132 | mag. |
| TI14-43 | 9 | a54 | 1495 | 192 | 8 | 0.74 | 1941 | 0.0362 | 3.8 | 0.26 | 7.5 | 0.0513 | 6.5 | 0.50 | 229 | 8 | 232 | 16 | 255 | 149 | 90 | mag. |
| TI14-44 | 9 | a55 | 1104 | 47 | 2 | 1.45 | 414 | 0.0337 | 5.5 | 0.23 | 16.7 | 0.0501 | 15.8 | 0.33 | 214 | 12 | 213 | 33 | 200 | 366 | 107 | mag. |
| TI14-45c | 10 | a1 | 3679 | 600 | 29 | 1.70 | 7766 | 0.0362 | 2.1 | 0.25 | 3.4 | 0.0500 | 2.6 | 0.62 | 229 | 5 | 226 | 7 | 193 | 62 | 119 | mag. |
| TI14-46 | 10 | a2 | 2177 | 335 | 14 | 0.91 | 5258 | 0.0357 | 2.9 | 0.25 | 4.6 | 0.0507 | 3.6 | 0.62 | 226 | 6 | 226 | 9 | 227 | 83 | 100 | mag. |
| TI14-47 | 10 | a3 | 1527 | 355 | 12 | 0.49 | 22112 | 0.0317 | 6.2 | 0.22 | 13.7 | 0.0503 | 12.2 | 0.45 | 201 | 12 | 202 | 25 | 208 | 283 | 97 | unc. |
| TI14-48 | 10 | a4 | 2142 | 152 | 7 | 0.82 | 1657 | 0.0398 | 3.2 | 0.28 | 6.3 | 0.0515 | 5.4 | 0.51 | 251 | 8 | 253 | 14 | 263 | 124 | 96 | mag. |
| TI14-49r | 10 | a5 | 1250 | 134 | 7 | 0.44 | 1330 | 0.0542 | 2.3 | 0.40 | 6.1 | 0.0530 | 5.6 | 0.38 | 340 | 8 | 339 | 18 | 328 | 127 | 104 | unc. |
| TI14-49c | 10 | a6 | 2281 | 235 | 13 | 0.61 | 8617 | 0.0532 | 4.0 | 0.39 | 6.3 | 0.0533 | 4.8 | 0.64 | 334 | 13 | 335 | 18 | 343 | 109 | 97 | mag. |
| TI14-50c | 10 | a7 | 955 | 126 | 5 | 1.03 | 3136 | 0.0319 | 2.7 | 0.23 | 9.3 | 0.0527 | 8.9 | 0.29 | 202 | 5 | 212 | 18 | 317 | 202 | 64 | mag. |
| TI14-52m | 10 | a9 | 681 | 83 | 3 | 1.05 | 1850 | 0.0339 | 3.6 | 0.24 | 8.9 | 0.0524 | 8.1 | 0.41 | 215 | 8 | 222 | 18 | 301 | 186 | 71 | mag. |
| TI14-53 | 10 | a10 | 635 | 113 | 4 | 0.69 | 2495 | 0.0356 | 3.0 | 0.25 | 7.3 | 0.0507 | 6.7 | 0.41 | 225 | 7 | 226 | 15 | 227 | 155 | 99 | mag. |
| TI14-54 | 10 | a11 | 900 | 103 | 4 | 0.97 | 2375 | 0.0347 | 3.2 | 0.24 | 6.6 | 0.0506 | 5.7 | 0.49 | 220 | 7 | 220 | 13 | 224 | 132 | 98 | unc. |
| TI14-55c | 10 | a12 | 2176 | 392 | 17 | 1.73 | 1489 | 0.0331 | 3.7 | 0.23 | 10.0 | 0.0504 | 9.3 | 0.37 | 210 | 8 | 210 | 19 | 213 | 215 | 99 | mag. |
| TI14-56r | 10 | a13 | 552 | 100 | 4 | 0.45 | 2212 | 0.0356 | 2.9 | 0.25 | 8.3 | 0.0502 | 7.7 | 0.35 | 225 | 6 | 224 | 17 | 206 | 180 | 109 | unc. |
| TI14-56c | 10 | a14 | 938 | 162 | 6 | 0.61 | 3691 | 0.0365 | 2.5 | 0.26 | 7.1 | 0.0508 | 6.6 | 0.36 | 231 | 6 | 231 | 15 | 232 | 152 | 100 | mag. |
| TI14-57 | 10 | a15 | 536 | 59 | 2 | 0.79 | 1259 | 0.0352 | 2.7 | 0.27 | 10.5 | 0.0547 | 10.1 | 0.26 | 223 | 6 | 239 | 23 | 402 | 227 | 56 | mag. |
| TI14-58r | 10 | a16 | 1623 | 182 | 12 | 1.03 | 5997 | 0.0558 | 2.8 | 0.42 | 5.3 | 0.0542 | 4.5 | 0.52 | 350 | 9 | 354 | 16 | 378 | 101 | 93 | mag. |
| TI14-58c | 10 | a17 | 3991 | 394 | 32 | 1.85 | 5521 | 0.0630 | 3.7 | 0.48 | 4.5 | 0.0551 | 2.5 | 0.83 | 394 | 14 | 397 | 15 | 418 | 56 | 94 | mag. |
| TI14-59 | 10 | a18 | 778 | 66 | 4 | 0.54 | 2499 | 0.0627 | 2.9 | 0.47 | 7.0 | 0.0538 | 6.3 | 0.41 | 392 | 11 | 388 | 23 | 364 | 143 | 108 | mag. |
| TI14-60r | 10 | a19 | 1906 | 341 | 15 | 1.38 | 3998 | 0.0348 | 5.0 | 0.27 | 6.3 | 0.0562 | 3.8 | 0.80 | 221 | 11 | 243 | 14 | 460 | 83 | 48 | mag. |
| TI14-60c | 10 | a20 | 1494 | 194 | 11 | 1.53 | 1181 | 0.0424 | 3.2 | 0.37 | 6.6 | 0.0634 | 5.8 | 0.48 | 267 | 8 | 320 | 18 | 721 | 122 | 37 | mag. |

# Results of U-Th-Pb LA-ICPMS analyses of zircons from sample SHS03

| Spot | Seq. | No. | $^{207}Pb$ [a] (cps) | U [b] (ppm) | Pb [b] (ppm) | Th [b] U | $^{206}Pb/^{204}Pb$ | $^{206}Pb/^{238}U$ [c] | ±2s (%) | $^{207}Pb/^{235}U$ [c] | ±2s (%) | $^{207}Pb/^{206}Pb$ [c] | ±2s (%) | Rho [d] | Age (Ma) $^{206}Pb/^{238}U$ | ±2s | $^{207}Pb/^{235}U$ | ±2s | $^{207}Pb/^{206}Pb$ [c] | ±2s | conc [e] (%) | Origin [f] |
|---|---|---|---|---|---|---|---|---|---|---|---|---|---|---|---|---|---|---|---|---|---|---|
| SHS03-1c | 10 | a21 | 14094 | 377 | 74 | 0.66 | 38281 | 0.1822 | 3.2 | 1.85 | 3.8 | 0.0737 | 2.0 | 0.85 | 1079 | 32 | 1064 | 25 | 1032 | 40 | 105 | mag. |
| SHS03-1r | 10 | a22 | 2280 | 120 | 13 | 0.65 | 7454 | 0.1044 | 3.4 | 0.89 | 5.3 | 0.0615 | 4.1 | 0.63 | 640 | 21 | 644 | 26 | 658 | 88 | 97 | mag. |
| SHS03-2 | 10 | a23 | 1372 | 81 | 8 | 0.64 | 4559 | 0.0946 | 3.7 | 0.79 | 5.9 | 0.0603 | 4.6 | 0.63 | 583 | 21 | 589 | 27 | 615 | 98 | 95 | mag. |
| SHS03-3 | 10 | a24 | 2213 | 141 | 13 | 0.50 | 7537 | 0.0915 | 3.5 | 0.74 | 4.9 | 0.0584 | 3.4 | 0.71 | 565 | 19 | 561 | 21 | 544 | 75 | 104 | mag. |
| SHS03-4r | 10 | a25 | 3760 | 247 | 20 | 0.01 | 12749 | 0.0897 | 3.4 | 0.73 | 4.6 | 0.0592 | 3.2 | 0.73 | 554 | 18 | 558 | 20 | 574 | 69 | 96 | met. |
| SHS03-4c | 10 | a26 | 3556 | 126 | 19 | 0.14 | 2484 | 0.1554 | 3.2 | 1.47 | 4.6 | 0.0687 | 3.3 | 0.69 | 931 | 28 | 919 | 28 | 889 | 68 | 105 | mag. |
| SHS03-5 | 10 | a27 | 10605 | 306 | 60 | 0.95 | 28951 | 0.1704 | 4.1 | 1.74 | 5.0 | 0.0740 | 2.8 | 0.82 | 1015 | 39 | 1023 | 32 | 1040 | 57 | 98 | mag. |
| SHS03-6 | 10 | a28 | 992 | 44 | 4 | 0.48 | 2324 | 0.0997 | 3.7 | 0.83 | 8.0 | 0.0601 | 7.1 | 0.46 | 613 | 22 | 612 | 38 | 608 | 154 | 101 | met. |
| SHS03-7r | 10 | a29 | 2397 | 126 | 13 | 1.64 | 1526 | 0.0877 | 3.6 | 0.73 | 5.9 | 0.0601 | 4.6 | 0.62 | 542 | 19 | 554 | 26 | 606 | 100 | 89 | mag. |
| SHS03-8r | 10 | a30 | 834 | 42 | 4 | 0.75 | 2712 | 0.0978 | 4.7 | 0.82 | 6.8 | 0.0607 | 4.9 | 0.69 | 602 | 27 | 607 | 32 | 627 | 106 | 96 | mag. |
| SHS03-8c | 10 | a31 | 4522 | 254 | 27 | 0.42 | 4433 | 0.1064 | 3.8 | 0.92 | 5.5 | 0.0625 | 4.1 | 0.68 | 652 | 24 | 661 | 27 | 693 | 86 | 94 | mag. |
| SHS03-9 | 10 | a32 | 6739 | 192 | 35 | 0.37 | 17936 | 0.1786 | 4.1 | 1.85 | 5.4 | 0.0753 | 3.5 | 0.75 | 1059 | 40 | 1064 | 36 | 1075 | 71 | 99 | mag. |
| SHS03-10r | 10 | a33 | 7076 | 265 | 40 | 0.58 | 20666 | 0.1437 | 3.2 | 1.36 | 4.2 | 0.0688 | 2.8 | 0.76 | 866 | 26 | 874 | 25 | 893 | 57 | 97 | mag. |
| SHS03-11 | 10 | a34 | 3934 | 125 | 23 | 0.21 | 10559 | 0.1870 | 4.7 | 1.93 | 5.6 | 0.0749 | 3.0 | 0.84 | 1105 | 48 | 1092 | 38 | 1065 | 61 | 104 | met. |
| SHS03-12r | 10 | a35 | 7579 | 61 | 14 | 1.62 | 1312 | 0.1029 | 5.0 | 0.91 | 10.9 | 0.0645 | 9.7 | 0.46 | 631 | 30 | 659 | 54 | 758 | 205 | 83 | mag. |
| SHS03-13c | 10 | a36 | 1135 | 267 | 13 | 2.20 | 3763 | 0.0349 | 3.9 | 0.24 | 6.8 | 0.0502 | 5.6 | 0.57 | 221 | 8 | 219 | 14 | 202 | 131 | 109 | mag. |
| SHS03-14r | 10 | a37 | 3029 | 196 | 21 | 0.49 | 10231 | 0.1026 | 2.7 | 0.85 | 4.2 | 0.0598 | 3.2 | 0.65 | 629 | 16 | 622 | 20 | 595 | 69 | 106 | met. |
| SHS03-15 | 10 | a38 | 1780 | 110 | 12 | 0.83 | 5846 | 0.0988 | 5.4 | 0.82 | 8.0 | 0.0605 | 5.8 | 0.68 | 608 | 32 | 610 | 37 | 620 | 126 | 98 | met. |
| SHS03-16r | 10 | a39 | 816 | 141 | 6 | 1.00 | 2859 | 0.0377 | 4.3 | 0.26 | 8.2 | 0.0506 | 6.9 | 0.53 | 239 | 10 | 237 | 17 | 221 | 161 | 108 | mag. |
| SHS03-16c | 10 | a40 | 11927 | 384 | 67 | 0.26 | 32139 | 0.1761 | 3.9 | 1.80 | 4.4 | 0.0741 | 2.2 | 0.87 | 1046 | 37 | 1045 | 29 | 1044 | 45 | 100 | mag. |
| SHS03-17r | 10 | a41 | 1864 | 140 | 14 | 0.62 | 6401 | 0.0927 | 3.9 | 0.74 | 5.4 | 0.0579 | 3.8 | 0.71 | 571 | 21 | 562 | 24 | 526 | 84 | 109 | mag. |
| SHS03-18r | 10 | a42 | 6850 | 499 | 46 | 0.23 | 23372 | 0.0953 | 4.4 | 0.77 | 5.3 | 0.0588 | 3.0 | 0.82 | 587 | 25 | 582 | 24 | 561 | 66 | 105 | mag. |
| SHS03-19 | 10 | a43 | 864 | 52 | 5 | 0.78 | 1771 | 0.0897 | 2.9 | 0.73 | 7.5 | 0.0590 | 6.9 | 0.39 | 554 | 16 | 557 | 33 | 568 | 150 | 98 | mag. |
| SHS03-20r | 10 | a44 | 4958 | 310 | 31 | 0.11 | 16434 | 0.1074 | 3.8 | 0.90 | 5.4 | 0.0607 | 3.9 | 0.69 | 657 | 24 | 651 | 26 | 630 | 85 | 104 | mag. |
| SHS03-21r | 10 | a45 | 1755 | 123 | 12 | 0.30 | 1222 | 0.0956 | 3.1 | 0.79 | 4.8 | 0.0600 | 3.6 | 0.65 | 589 | 18 | 592 | 22 | 603 | 78 | 98 | mag. |
| SHS03-21c | 10 | a46 | 19466 | 207 | 54 | 0.28 | 25443 | 0.2435 | 3.5 | 5.17 | 4.4 | 0.1539 | 2.8 | 0.78 | 1405 | 44 | 1847 | 38 | 2390 | 47 | 59 | mag. |
| SHS03-22r | 10 | a47 | 1575 | 391 | 14 | 0.73 | 6184 | 0.0337 | 3.8 | 0.24 | 6.0 | 0.0514 | 4.7 | 0.63 | 214 | 8 | 217 | 12 | 258 | 107 | 83 | mag. |
| SHS03-22c | 10 | a48 | 1340 | 328 | 13 | 0.67 | 5339 | 0.0368 | 4.2 | 0.26 | 7.1 | 0.0505 | 5.8 | 0.59 | 233 | 10 | 232 | 15 | 218 | 134 | 107 | mag. |
| SHS03-23r | 10 | a49 | 1370 | 105 | 11 | 0.71 | 4656 | 0.0958 | 4.0 | 0.79 | 7.5 | 0.0594 | 6.4 | 0.53 | 590 | 23 | 588 | 34 | 584 | 139 | 101 | mag. |
| SHS03-24c | 10 | a50 | 3172 | 96 | 19 | 0.52 | 8218 | 0.1849 | 5.0 | 1.97 | 6.0 | 0.0774 | 3.4 | 0.83 | 1094 | 50 | 1106 | 41 | 1131 | 67 | 97 | mag. |
| SHS03-25 | 10 | a51 | 1158 | 44 | 8 | 0.57 | 3245 | 0.1772 | 4.4 | 1.77 | 6.5 | 0.0725 | 4.8 | 0.67 | 1051 | 42 | 1035 | 43 | 999 | 98 | 105 | mag. |
| SHS03-26r | 10 | a52 | 871 | 66 | 8 | 1.45 | 2956 | 0.0993 | 3.1 | 0.82 | 6.8 | 0.0596 | 6.1 | 0.46 | 610 | 18 | 606 | 32 | 589 | 132 | 104 | mag. |
| SHS03-27 | 10 | a53 | 5505 | 165 | 33 | 0.71 | 14643 | 0.1831 | 3.9 | 1.90 | 4.8 | 0.0754 | 2.8 | 0.81 | 1084 | 39 | 1082 | 33 | 1078 | 57 | 101 | mag. |
| SHS03-28 | 10 | a54 | 6486 | 209 | 41 | 0.68 | 10737 | 0.1820 | 3.9 | 1.90 | 5.4 | 0.0756 | 3.8 | 0.71 | 1078 | 38 | 1080 | 37 | 1085 | 76 | 99 | mag. |
| SHS03-29 | 10 | a55 | 1179 | 108 | 11 | 0.98 | 4063 | 0.0868 | 3.6 | 0.70 | 7.0 | 0.0584 | 6.0 | 0.51 | 537 | 19 | 538 | 30 | 545 | 132 | 99 | mag. |
| SHS03-30r | 11 | a1 | 659 | 58 | 7 | 1.27 | 2266 | 0.0960 | 3.7 | 0.78 | 5.8 | 0.0588 | 4.5 | 0.63 | 591 | 21 | 584 | 26 | 558 | 99 | 106 | mag. |
| SHS03-31 | 11 | a2 | 2038 | 165 | 16 | 0.27 | 6746 | 0.1004 | 4.1 | 0.84 | 5.3 | 0.0609 | 3.3 | 0.78 | 616 | 24 | 621 | 25 | 636 | 72 | 97 | mag. |
| SHS03-32r | 11 | a3 | 4816 | 31 | 14 | 0.18 | 2077 | 0.4422 | 4.0 | 10.68 | 5.2 | 0.1751 | 3.4 | 0.76 | 2360 | 79 | 2495 | 50 | 2607 | 57 | 91 | mag. |
| SHS03-33c | 11 | a4 | 593 | 166 | 7 | 1.33 | 2357 | 0.0335 | 3.8 | 0.23 | 6.1 | 0.0508 | 4.8 | 0.62 | 212 | 8 | 214 | 12 | 233 | 112 | 91 | mag. |
| SHS03-34 | 11 | a5 | 3615 | 329 | 29 | 0.19 | 12305 | 0.0928 | 4.3 | 0.76 | 5.6 | 0.0591 | 3.6 | 0.77 | 572 | 24 | 572 | 25 | 571 | 77 | 100 | mag. |
| SHS03-35r | 11 | a6 | 3612 | 324 | 33 | 0.57 | 12356 | 0.0973 | 3.4 | 0.79 | 4.8 | 0.0585 | 3.5 | 0.70 | 599 | 19 | 588 | 22 | 549 | 76 | 109 | mag. |
| SHS03-35c | 11 | a7 | 4915 | 440 | 50 | 1.01 | 16646 | 0.0977 | 3.5 | 0.79 | 5.3 | 0.0588 | 3.9 | 0.67 | 601 | 20 | 592 | 24 | 560 | 85 | 107 | mag. |
| SHS03-36 | 11 | a8 | 3913 | 370 | 32 | 0.46 | 8867 | 0.0852 | 3.3 | 0.68 | 4.9 | 0.0581 | 3.6 | 0.67 | 527 | 17 | 528 | 20 | 533 | 80 | 99 | mag. |
| SHS03-37 | 11 | a9 | 4372 | 168 | 35 | 1.57 | 11769 | 0.1637 | 3.1 | 1.68 | 4.3 | 0.0744 | 3.1 | 0.71 | 977 | 28 | 1001 | 28 | 1052 | 62 | 93 | mag. |
| SHS03-38r | 11 | a10 | 1320 | 159 | 15 | 0.80 | 5105 | 0.0833 | 4.3 | 0.67 | 5.9 | 0.0583 | 4.1 | 0.73 | 516 | 21 | 521 | 24 | 543 | 89 | 95 | mag. |
| SHS03-38c | 11 | a11 | 3587 | 318 | 43 | 2.34 | 12034 | 0.0940 | 3.9 | 0.77 | 6.0 | 0.0595 | 4.6 | 0.65 | 579 | 22 | 581 | 27 | 587 | 99 | 99 | mag. |
| SHS03-39 | 11 | a12 | 1668 | 140 | 15 | 0.81 | 3098 | 0.1009 | 3.4 | 0.82 | 5.2 | 0.0591 | 4.0 | 0.65 | 619 | 20 | 609 | 24 | 571 | 87 | 108 | mag. |
| SHS03-40 | 11 | a13 | 1983 | 149 | 16 | 0.36 | 6550 | 0.1101 | 4.5 | 0.92 | 6.3 | 0.0604 | 4.5 | 0.71 | 673 | 29 | 661 | 31 | 619 | 97 | 109 | mag. |
| SHS03-41 | 11 | a14 | 1556 | 155 | 14 | 0.69 | 5378 | 0.0832 | 3.7 | 0.66 | 5.3 | 0.0579 | 3.7 | 0.71 | 515 | 19 | 517 | 22 | 525 | 82 | 98 | mag. |
| SHS03-42 | 11 | a15 | 3172 | 293 | 26 | 0.15 | 10922 | 0.0912 | 3.6 | 0.73 | 5.7 | 0.0580 | 4.5 | 0.63 | 562 | 20 | 556 | 25 | 529 | 98 | 106 | mag. |
| SHS03-43c | 11 | a16 | 1993 | 173 | 23 | 1.99 | 2678 | 0.0959 | 3.4 | 0.78 | 5.8 | 0.0593 | 4.7 | 0.59 | 591 | 19 | 588 | 26 | 577 | 101 | 102 | mag. |
| SHS03-44m | 11 | a17 | 3207 | 252 | 28 | 0.51 | 10752 | 0.1051 | 4.1 | 0.86 | 5.2 | 0.0595 | 3.3 | 0.78 | 645 | 25 | 632 | 25 | 586 | 71 | 110 | mag. |
| SHS03-45 | 11 | a18 | 946 | 86 | 8 | 0.27 | 3340 | 0.0904 | 3.6 | 0.72 | 7.0 | 0.0575 | 6.0 | 0.52 | 558 | 19 | 549 | 30 | 511 | 132 | 109 | mag. |
| SHS03-46r | 11 | a19 | 3254 | 326 | 26 | 0.07 | 6867 | 0.0846 | 4.5 | 0.67 | 6.0 | 0.0578 | 4.0 | 0.75 | 524 | 23 | 524 | 25 | 523 | 88 | 100 | met. |
| SHS03-46c | 11 | a20 | 4631 | 33 | 22 | 1.41 | 5419 | 0.4984 | 4.2 | 11.93 | 5.5 | 0.1736 | 3.5 | 0.77 | 2607 | 91 | 2599 | 53 | 2593 | 59 | 101 | mag. |
| SHS03-47 | 11 | a21 | 897 | 84 | 8 | 0.47 | 3095 | 0.0915 | 4.7 | 0.74 | 6.5 | 0.0583 | 4.5 | 0.72 | 564 | 25 | 560 | 28 | 541 | 99 | 104 | unc. |
| SHS03-48m | 11 | a22 | 1782 | 57 | 11 | 0.62 | 4766 | 0.1713 | 5.3 | 1.80 | 6.6 | 0.0764 | 4.0 | 0.80 | 1019 | 50 | 1047 | 44 | 1105 | 79 | 92 | mag. |
| SHS03-49r | 11 | a23 | 1082 | 96 | 9 | 0.31 | 3638 | 0.0887 | 3.2 | 0.73 | 5.8 | 0.0597 | 4.8 | 0.55 | 548 | 17 | 557 | 25 | 594 | 105 | 92 | mag. |
| SHS03-50m | 11 | a24 | 1690 | 158 | 13 | 0.33 | 5829 | 0.0835 | 2.7 | 0.67 | 5.9 | 0.0583 | 5.2 | 0.46 | 517 | 14 | 521 | 24 | 541 | 113 | 95 | mag. |
| SHS03-51 | 11 | a25 | 2208 | 174 | 16 | 0.36 | 7391 | 0.0913 | 3.1 | 0.75 | 5.5 | 0.0595 | 4.5 | 0.56 | 563 | 17 | 568 | 24 | 585 | 99 | 96 | unc. |
| SHS03-52r | 11 | a26 | 1200 | 110 | 11 | 0.79 | 4077 | 0.0911 | 2.6 | 0.74 | 5.9 | 0.0589 | 5.3 | 0.45 | 562 | 14 | 562 | 26 | 563 | 115 | 100 | mag. |
| SHS03-52c | 11 | a27 | 8174 | 333 | 50 | 0.48 | 8171 | 0.1462 | 5.0 | 1.40 | 6.9 | 0.0693 | 4.7 | 0.73 | 880 | 41 | 888 | 42 | 909 | 97 | 97 | mag. |
| SHS03-53 | 11 | a28 | 490 | 75 | 5 | 0.61 | 1816 | 0.0596 | 4.2 | 0.45 | 7.9 | 0.0543 | 6.7 | 0.53 | 373 | 15 | 375 | 25 | 385 | 150 | 97 | mag. |
| SHS03-54 | 11 | a29 | 7109 | 572 | 56 | 0.35 | 18608 | 0.0979 | 3.6 | 0.82 | 5.5 | 0.0607 | 4.2 | 0.65 | 602 | 21 | 608 | 25 | 630 | 89 | 96 | mag. |
| SHS03-55r | 11 | a30 | 6058 | 457 | 43 | 0.14 | 10205 | 0.0979 | 2.8 | 0.81 | 4.0 | 0.0603 | 2.8 | 0.71 | 602 | 16 | 605 | 18 | 615 | 60 | 98 | mag. |
| SHS03-56c | 11 | a31 | 2639 | 98 | 18 | 0.49 | 7169 | 0.1759 | 3.5 | 1.80 | 5.6 | 0.0741 | 4.4 | 0.62 | 1044 | 34 | 1045 | 37 | 1045 | 89 | 100 | mag. |
| SHS03-57 | 11 | a32 | 10701 | 219 | 70 | 0.16 | 16808 | 0.3150 | 3.1 | 4.95 | 12.8 | 0.1139 | 12.4 | 0.24 | 1765 | 48 | 1811 | 114 | 1863 | 224 | 95 | mag. |
| SHS03-58c | 11 | a33 | 2134 | 76 | 15 | 0.89 | 2769 | 0.1721 | 3.9 | 1.74 | 5.4 | 0.0735 | 3.7 | 0.72 | 1024 | 37 | 1025 | 35 | 1027 | 76 | 100 | mag. |
| SHS03-59 | 11 | a34 | 1851 | 388 | 13 | 0.22 | 3208 | 0.0348 | 4.1 | 0.24 | 9.0 | 0.0510 | 8.0 | 0.45 | 220 | 9 | 222 | 18 | 240 | 186 | 92 | mag. |
| SHS03-60c | 11 | a35 | 8079 | 683 | 66 | 0.38 | 27360 | 0.0971 | 4.3 | 0.79 | 5.5 | 0.0590 | 3.5 | 0.77 | 598 | 24 | 592 | 25 | 569 | 76 | 105 | mag. |
| SHS03-61 | 11 | a36 | 2963 | 521 | 975 | 2.60 | 1995 | 0.0935 | 3.0 | 0.77 | 5.6 | 0.0600 | 4.8 | 0.54 | 576 | 17 | 582 | 25 | 604 | 103 | 95 | mag. |
| SHS03-62 | 11 | a37 | 779 | 62 | 7 | 0.96 | 2542 | 0.1006 | 4.4 | 0.85 | 8.1 | 0.0614 | 6.8 | 0.54 | 618 | 26 | 626 | 39 | 654 | 147 | 94 | mag. |
| SHS03-63r | 11 | a38 | 970 | 90 | 7 | 0.22 | 2543 | 0.0853 | 4.5 | 0.67 | 9.0 | 0.0572 | 7.8 | 0.50 | 528 | 23 | 522 | 38 | 500 | 172 | 105 | mag. |
| SHS03-64r | 11 | a39 | 473 | 42 | 4 | 0.77 | 1658 | 0.0859 | 5.1 | 0.68 | 9.0 | 0.0573 | 7.4 | 0.57 | 532 | 26 | 526 | 37 | 504 | 162 | 106 | mag. |
| SHS03-65m | 11 | a40 | 1240 | 113 | 11 | 0.59 | 1750 | 0.0911 | 4.8 | 0.74 | 6.1 | 0.0586 | 3.8 | 0.78 | 562 | 26 | 560 | 27 | 554 | 83 | 102 | mag. |

# Results of U-Th-Pb LA-ICPMS analyses of zircons from sample SHS03 (continuation)

| Spot | Seq. | No. | $^{207}Pb$ [a] (cps) | U [b] (ppm) | Pb [b] (ppm) | Th/U [b] | $^{206}Pb/^{204}Pb$ | $^{206}Pb/^{238}U$ [c] | ±2s (%) | $^{207}Pb/^{235}U$ [c] | ±2s (%) | $^{207}Pb/^{206}Pb$ [c] | ±2s (%) | Rho [d] | Age (Ma) $^{206}Pb/^{238}U$ | ±2s | $^{207}Pb/^{235}U$ | ±2s | $^{207}Pb/^{206}Pb$ [c] | ±2s | conc [e] (%) | Origin [f] |
|---|---|---|---|---|---|---|---|---|---|---|---|---|---|---|---|---|---|---|---|---|---|---|
| SHS03-66m | 11 | a41 | 13122 | 1016 | 111 | 0.33 | 4206 | 0.1142 | 2.7 | 0.97 | 4.0 | 0.0619 | 3.0 | 0.67 | 697 | 18 | 691 | 20 | 671 | 64 | 104 | mag. |
| SHS03-67c | 11 | a42 | 9963 | 792 | 77 | 0.12 | 33103 | 0.1029 | 3.4 | 0.86 | 4.5 | 0.0607 | 2.9 | 0.76 | 631 | 20 | 631 | 21 | 629 | 62 | 100 | mag. |
| SHS03-68c | 11 | a43 | 5778 | 254 | 46 | 0.54 | 8079 | 0.1742 | 4.0 | 1.70 | 5.0 | 0.0706 | 2.9 | 0.81 | 1035 | 39 | 1007 | 33 | 945 | 60 | 110 | mag. |
| SHS03-69 | 11 | a44 | 2094 | 81 | 16 | 0.72 | 5630 | 0.1846 | 4.5 | 1.90 | 6.6 | 0.0748 | 4.9 | 0.68 | 1092 | 45 | 1083 | 45 | 1064 | 98 | 103 | mag. |
| SHS03-70 | 11 | a45 | 623 | 35 | 4 | 0.18 | 1905 | 0.1266 | 6.0 | 1.16 | 8.5 | 0.0666 | 6.0 | 0.70 | 768 | 43 | 783 | 47 | 825 | 126 | 93 | met. |
| SHS03-71 | 11 | a46 | 3761 | 396 | 47 | 1.34 | 2375 | 0.0926 | 4.7 | 0.76 | 6.2 | 0.0596 | 4.1 | 0.76 | 571 | 26 | 575 | 28 | 590 | 88 | 97 | mag. |
| SHS03-72r | 11 | a47 | 849 | 293 | 25 | 0.03 | 1974 | 0.0928 | 4.7 | 0.74 | 6.3 | 0.0581 | 4.2 | 0.74 | 572 | 26 | 564 | 28 | 532 | 93 | 107 | met. |
| SHS03-72c | 11 | a48 | 524 | 45 | 4 | 0.05 | 1792 | 0.0983 | 4.3 | 0.81 | 8.1 | 0.0598 | 6.9 | 0.53 | 604 | 25 | 603 | 38 | 596 | 149 | 101 | met. |
| SHS03-73 | 11 | a49 | 340 | 29 | 3 | 0.41 | 1175 | 0.0908 | 5.9 | 0.72 | 8.8 | 0.0577 | 6.4 | 0.68 | 561 | 32 | 552 | 38 | 518 | 141 | 108 | met. |
| SHS03-74r | 11 | a50 | 2019 | 179 | 18 | 0.61 | 3380 | 0.0954 | 4.0 | 0.77 | 6.4 | 0.0583 | 5.0 | 0.63 | 587 | 23 | 578 | 29 | 543 | 109 | 108 | mag. |
| SHS03-75 | 11 | a51 | 1206 | 163 | 18 | 0.02 | 2580 | 0.1199 | 5.6 | 1.30 | 13.5 | 0.0785 | 12.2 | 0.42 | 730 | 39 | 845 | 80 | 1159 | 242 | 63 | met. |
| SHS03-76m | 11 | a52 | 2155 | 200 | 17 | 0.18 | 7343 | 0.0881 | 3.4 | 0.71 | 5.4 | 0.0581 | 4.2 | 0.63 | 545 | 18 | 542 | 23 | 533 | 93 | 102 | mag. |
| SHS03-77 | 11 | a53 | 2547 | 222 | 22 | 0.44 | 8643 | 0.0976 | 3.6 | 0.80 | 5.5 | 0.0592 | 4.1 | 0.66 | 600 | 21 | 595 | 25 | 576 | 90 | 104 | met. |
| SHS03-78r | 11 | a54 | 4296 | 355 | 33 | 0.17 | 14502 | 0.0972 | 3.7 | 0.79 | 5.1 | 0.0589 | 3.6 | 0.72 | 598 | 21 | 591 | 23 | 562 | 78 | 106 | met. |
| SHS03-78c | 11 | a55 | 10476 | 198 | 61 | 0.71 | 22049 | 0.2791 | 4.5 | 3.68 | 5.6 | 0.0956 | 3.3 | 0.81 | 1587 | 63 | 1567 | 45 | 1541 | 62 | 103 | mag. |
| SHS03-79 | 12 | a1 | 934 | 90 | 7 | 0.15 | 3170 | 0.0850 | 4.7 | 0.67 | 10.8 | 0.0575 | 9.8 | 0.43 | 526 | 24 | 523 | 45 | 510 | 215 | 103 | met. |
| SHS03-80 | 12 | a2 | 17627 | 198 | 78 | 0.58 | 12661 | 0.3560 | 4.3 | 5.87 | 5.0 | 0.1196 | 2.4 | 0.87 | 1963 | 74 | 1957 | 44 | 1950 | 43 | 101 | mag. |
| SHS03-81 | 12 | a3 | 573 | 52 | 5 | 1.00 | 1990 | 0.0847 | 6.0 | 0.69 | 10.5 | 0.0590 | 8.6 | 0.57 | 524 | 30 | 533 | 45 | 568 | 188 | 92 | mag. |
| SHS03-82r | 12 | a4 | 3615 | 308 | 29 | 0.24 | 8692 | 0.0965 | 3.8 | 0.80 | 5.5 | 0.0597 | 3.9 | 0.70 | 594 | 22 | 594 | 25 | 594 | 85 | 100 | mag. |
| SHS03-82c | 12 | a5 | 2325 | 104 | 12 | 0.96 | 4492 | 0.0976 | 2.9 | 0.80 | 5.4 | 0.0597 | 4.6 | 0.54 | 600 | 17 | 599 | 25 | 594 | 99 | 101 | mag. |
| SHS03-83 | 12 | a6 | 2420 | 121 | 11 | 0.41 | 8855 | 0.0876 | 3.4 | 0.71 | 6.1 | 0.0592 | 5.1 | 0.55 | 541 | 18 | 547 | 26 | 573 | 111 | 95 | mag. |
| SHS03-84 | 12 | a7 | 3196 | 199 | 18 | 0.37 | 7627 | 0.0883 | 2.8 | 0.71 | 5.4 | 0.0581 | 4.7 | 0.51 | 545 | 15 | 543 | 23 | 532 | 102 | 103 | mag. |
| SHS03-85 | 12 | a8 | 2802 | 193 | 22 | 1.03 | 9285 | 0.0976 | 2.8 | 0.82 | 4.3 | 0.0607 | 3.3 | 0.65 | 600 | 16 | 606 | 20 | 629 | 70 | 95 | mag. |
| SHS03-86 | 12 | a9 | 8051 | 684 | 63 | 0.03 | 26871 | 0.0988 | 3.6 | 0.82 | 4.6 | 0.0605 | 2.9 | 0.78 | 607 | 21 | 610 | 21 | 620 | 62 | 98 | mag. |
| SHS03-87 | 12 | a10 | 3075 | 246 | 24 | 0.47 | 8951 | 0.0934 | 3.5 | 0.75 | 4.6 | 0.0579 | 3.1 | 0.75 | 576 | 19 | 566 | 20 | 525 | 68 | 110 | mag. |
| SHS03-88 | 12 | a11 | 157147 | 683 | 446 | 0.40 | 140263 | 0.5702 | 3.0 | 17.74 | 4.0 | 0.2257 | 2.7 | 0.74 | 2909 | 70 | 2976 | 39 | 3021 | 43 | 96 | mag. |
| SHS03-89r | 16 | a39 | 493 | 23 | 2 | 0.96 | 1382 | 0.0889 | 4.4 | 0.73 | 7.6 | 0.0593 | 6.2 | 0.58 | 549 | 23 | 555 | 33 | 576 | 134 | 95 | mag. |
| SHS03-89c | 16 | a40 | 3349 | 77 | 13 | 0.63 | 7814 | 0.1506 | 2.9 | 1.48 | 4.3 | 0.0711 | 3.2 | 0.67 | 904 | 25 | 921 | 27 | 961 | 65 | 94 | mag. |
| SHS03-90 | 16 | a41 | 3551 | 582 | 23 | 0.84 | 11741 | 0.0352 | 4.0 | 0.24 | 5.5 | 0.0503 | 3.8 | 0.73 | 223 | 9 | 222 | 11 | 208 | 88 | 107 | mag. |
| SHS03-91 | 16 | a42 | 6016 | 282 | 32 | 1.04 | 4718 | 0.0987 | 3.7 | 0.81 | 4.4 | 0.0593 | 2.4 | 0.84 | 607 | 21 | 601 | 20 | 579 | 51 | 105 | mag. |
| SHS03-92r | 16 | a43 | 7948 | 151 | 27 | 0.34 | 17238 | 0.1769 | 3.2 | 1.86 | 4.0 | 0.0763 | 2.4 | 0.80 | 1050 | 31 | 1067 | 27 | 1104 | 48 | 95 | mag. |
| SHS03-93 | 16 | a44 | 5897 | 330 | 29 | 0.03 | 16688 | 0.0963 | 2.9 | 0.78 | 4.1 | 0.0587 | 2.9 | 0.71 | 593 | 17 | 585 | 18 | 556 | 63 | 107 | mag. |
| SHS03-94r | 16 | a45 | 1485 | 74 | 7 | 0.91 | 4316 | 0.0881 | 3.5 | 0.70 | 6.2 | 0.0579 | 5.2 | 0.56 | 544 | 18 | 541 | 27 | 527 | 114 | 103 | mag. |
| SHS03-97r | 16 | a48 | 4416 | 226 | 22 | 0.80 | 12683 | 0.0880 | 2.7 | 0.70 | 3.7 | 0.0579 | 2.6 | 0.73 | 543 | 14 | 540 | 16 | 526 | 56 | 103 | mag. |
| SHS03-99 | 16 | a50 | 6528 | 238 | 27 | 0.56 | 10057 | 0.1107 | 2.6 | 0.95 | 4.3 | 0.0624 | 3.4 | 0.60 | 677 | 17 | 680 | 21 | 688 | 73 | 98 | mag. |
| SHS03-100c | 16 | a51 | 2348 | 104 | 12 | 1.19 | 6519 | 0.0975 | 3.0 | 0.80 | 4.4 | 0.0599 | 3.2 | 0.69 | 600 | 17 | 599 | 20 | 598 | 69 | 100 | mag. |
| SHS03-101c | 16 | a52 | 5475 | 125 | 19 | 0.17 | 13514 | 0.1544 | 2.5 | 1.45 | 6.8 | 0.0682 | 6.3 | 0.37 | 925 | 22 | 910 | 42 | 874 | 131 | 106 | mag. |
| SHS03-102r | 16 | a53 | 1059 | 46 | 5 | 0.72 | 5707 | 0.0916 | 2.8 | 0.76 | 6.9 | 0.0598 | 6.3 | 0.41 | 565 | 15 | 572 | 31 | 598 | 136 | 95 | mag. |
| SHS03-103m | 16 | a54 | 1150 | 53 | 7 | 2.48 | 6845 | 0.0839 | 3.4 | 0.68 | 8.1 | 0.0588 | 7.3 | 0.42 | 519 | 17 | 526 | 34 | 558 | 160 | 93 | mag. |

# Results of U-Th-Pb LA-ICPMS analyses of zircons from sample SHA07

| Spot | Seq. | No. | $^{207}Pb$ [a] (cps) | U [b] (ppm) | Pb [b] (ppm) | Th/U [b] | $^{206}Pb/^{204}Pb$ | $^{206}Pb/^{238}U$ [c] | ±2s (%) | $^{207}Pb/^{235}U$ [c] | ±2s (%) | $^{207}Pb/^{206}Pb$ [c] | ±2s (%) | Rho [d] | Age (Ma) $^{206}Pb/^{238}U$ | ±2s | Age (Ma) $^{207}Pb/^{235}U$ | ±2s | Age (Ma) $^{207}Pb/^{206}Pb$ [c] | ±2s | conc [e] (%) | Origin [f] |
|---|---|---|---|---|---|---|---|---|---|---|---|---|---|---|---|---|---|---|---|---|---|---|
| SHA07-1r | 12 | a12 | 1816 | 107 | 4 | 1.21 | 5853 | 0.0344 | 3.3 | 0.24 | 6.4 | 0.0507 | 5.5 | 0.51 | 218 | 7 | 219 | 13 | 229 | 128 | 95 | mag. |
| SHA07-2r | 12 | a13 | 1864 | 64 | 7 | 1.06 | 8873 | 0.0984 | 2.9 | 0.82 | 5.1 | 0.0602 | 4.2 | 0.57 | 605 | 17 | 606 | 24 | 609 | 91 | 99 | mag. |
| SHA07-3 | 12 | a14 | 2142 | 314 | 13 | 1.07 | 8584 | 0.0341 | 3.7 | 0.24 | 6.0 | 0.0501 | 4.7 | 0.62 | 216 | 8 | 215 | 12 | 201 | 110 | 107 | mag. |
| SHA07-4 | 12 | a15 | 1224 | 115 | 4 | 1.01 | 2763 | 0.0304 | 3.3 | 0.26 | 12.7 | 0.0610 | 12.2 | 0.26 | 193 | 6 | 231 | 27 | 640 | 263 | 30 | mag. |
| SHA07-5c | 12 | a16 | 3105 | 102 | 10 | 0.81 | 5827 | 0.0838 | 3.9 | 0.68 | 5.4 | 0.0589 | 3.7 | 0.73 | 519 | 20 | 527 | 23 | 562 | 81 | 92 | mag. |
| SHA07-6 | 12 | a17 | 2210 | 103 | 10 | 0.88 | 3051 | 0.0843 | 4.2 | 0.66 | 5.2 | 0.0571 | 3.1 | 0.81 | 522 | 21 | 517 | 21 | 496 | 68 | 105 | mag. |
| SHA07-7 | 12 | a18 | 2910 | 111 | 21 | 0.98 | 9420 | 0.1628 | 3.4 | 1.60 | 4.6 | 0.0714 | 3.0 | 0.75 | 972 | 31 | 971 | 29 | 969 | 61 | 100 | mag. |
| SHA07-8 | 12 | a19 | 8962 | 908 | 79 | 0.11 | 6852 | 0.0922 | 3.4 | 0.75 | 5.4 | 0.0589 | 4.2 | 0.63 | 569 | 18 | 567 | 24 | 562 | 92 | 101 | unc. |
| SHA07-9c | 12 | a20 | 1054 | 316 | 11 | 0.89 | 4256 | 0.0303 | 4.2 | 0.21 | 7.1 | 0.0504 | 5.7 | 0.59 | 193 | 8 | 194 | 13 | 211 | 133 | 91 | mag. |
| SHA07-10 | 12 | a21 | 1825 | 130 | 18 | 1.72 | 1914 | 0.1022 | 4.0 | 0.86 | 6.3 | 0.0609 | 4.8 | 0.64 | 627 | 24 | 629 | 30 | 635 | 104 | 99 | mag. |
| SHA07-11 | 12 | a22 | 1022 | 78 | 9 | 1.40 | 3493 | 0.0956 | 4.2 | 0.77 | 5.8 | 0.0586 | 4.0 | 0.72 | 588 | 24 | 581 | 26 | 553 | 87 | 106 | mag. |
| SHA07-12 | 12 | a23 | 1010 | 307 | 11 | 0.91 | 4092 | 0.0307 | 4.5 | 0.21 | 7.1 | 0.0500 | 5.5 | 0.63 | 195 | 9 | 195 | 13 | 194 | 128 | 100 | mag. |
| SHA07-13 | 12 | a24 | 1355 | 30 | 3 | 0.34 | 3220 | 0.0865 | 3.4 | 0.70 | 7.6 | 0.0585 | 6.7 | 0.45 | 535 | 18 | 537 | 32 | 548 | 147 | 98 | met. |
| SHA07-14 | 12 | a25 | 3348 | 208 | 19 | 0.35 | 7297 | 0.0926 | 3.4 | 0.74 | 5.6 | 0.0582 | 4.5 | 0.61 | 571 | 19 | 564 | 25 | 536 | 98 | 107 | mag. |
| SHA07-15r | 12 | a26 | 2147 | 336 | 15 | 1.74 | 2060 | 0.0329 | 3.3 | 0.23 | 5.5 | 0.0500 | 4.4 | 0.59 | 209 | 7 | 208 | 10 | 195 | 103 | 107 | mag. |
| SHA07-15c | 12 | a27 | 1208 | 62 | 2 | 1.19 | 2828 | 0.0336 | 3.3 | 0.23 | 5.0 | 0.0500 | 3.8 | 0.65 | 213 | 7 | 211 | 10 | 194 | 89 | 110 | mag. |
| SHA07-16 | 12 | a28 | 1472 | 43 | 4 | 1.06 | 1845 | 0.0863 | 2.9 | 0.68 | 5.7 | 0.0575 | 4.9 | 0.51 | 534 | 15 | 529 | 24 | 510 | 108 | 105 | mag. |
| SHA07-17r | 12 | a29 | 1581 | 155 | 7 | 1.60 | 2079 | 0.0397 | 2.8 | 0.28 | 5.5 | 0.0513 | 4.8 | 0.50 | 251 | 7 | 251 | 12 | 254 | 110 | 99 | mag. |
| SHA07-18 | 12 | a30 | 233 | 58 | 2 | 1.29 | 922 | 0.0313 | 5.3 | 0.22 | 8.9 | 0.0510 | 7.2 | 0.59 | 199 | 10 | 202 | 16 | 240 | 167 | 83 | mag. |
| SHA07-19 | 12 | a31 | 1768 | 181 | 8 | 0.98 | 3786 | 0.0399 | 4.5 | 0.28 | 6.2 | 0.0511 | 4.3 | 0.72 | 252 | 11 | 251 | 14 | 243 | 98 | 104 | mag. |
| SHA07-20 | 12 | a32 | 1235 | 34 | 2 | 0.56 | 2876 | 0.0601 | 2.6 | 0.44 | 5.6 | 0.0534 | 4.9 | 0.47 | 376 | 10 | 372 | 18 | 348 | 111 | 108 | mag. |
| SHA07-21 | 12 | a33 | 1708 | 72 | 7 | 0.82 | 3395 | 0.0823 | 3.2 | 0.65 | 7.1 | 0.0573 | 6.3 | 0.45 | 510 | 16 | 508 | 29 | 503 | 139 | 101 | mag. |
| SHA07-22 | 12 | a34 | 2760 | 139 | 14 | 0.63 | 5727 | 0.0927 | 3.9 | 0.76 | 6.4 | 0.0593 | 5.0 | 0.62 | 571 | 22 | 573 | 28 | 578 | 109 | 99 | mag. |
| SHA07-23 | 12 | a35 | 963 | 294 | 13 | 1.73 | 1511 | 0.0332 | 4.0 | 0.23 | 8.4 | 0.0503 | 7.3 | 0.48 | 211 | 8 | 211 | 16 | 209 | 170 | 101 | mag. |
| SHA07-24 | 12 | a36 | 2990 | 147 | 15 | 0.47 | 4913 | 0.0993 | 3.4 | 0.81 | 5.3 | 0.0594 | 4.0 | 0.65 | 611 | 20 | 604 | 24 | 582 | 87 | 105 | unc. |
| SHA07-25r | 12 | a37 | 2160 | 40 | 2 | 2.15 | 4650 | 0.0401 | 3.2 | 0.28 | 8.5 | 0.0508 | 7.9 | 0.38 | 254 | 8 | 252 | 19 | 231 | 183 | 110 | mag. |
| SHA07-26 | 12 | a38 | 2333 | 104 | 4 | 1.97 | 5409 | 0.0309 | 3.8 | 0.21 | 7.3 | 0.0491 | 6.2 | 0.52 | 196 | 7 | 193 | 13 | 155 | 145 | 127 | mag. |
| SHA07-27 | 12 | a39 | 785 | 80 | 4 | 0.48 | 8329 | 0.0454 | 6.2 | 0.33 | 17.1 | 0.0523 | 15.9 | 0.36 | 286 | 17 | 287 | 44 | 297 | 364 | 96 | unc. |
| SHA07-28 | 12 | a40 | 3669 | 247 | 22 | 0.51 | 9553 | 0.0867 | 3.0 | 0.70 | 4.4 | 0.0587 | 3.1 | 0.70 | 536 | 16 | 540 | 18 | 557 | 68 | 96 | mag. |
| SHA07-29 | 12 | a41 | 14745 | 707 | 89 | 0.17 | 33347 | 0.1313 | 3.3 | 1.17 | 4.2 | 0.0647 | 2.7 | 0.77 | 796 | 24 | 787 | 23 | 765 | 57 | 104 | mag. |
| SHA07-30r | 12 | a42 | 1585 | 52 | 5 | 1.01 | 4034 | 0.0886 | 4.1 | 0.71 | 5.9 | 0.0579 | 4.2 | 0.70 | 547 | 22 | 543 | 25 | 528 | 93 | 104 | mag. |
| SHA07-30c | 12 | a43 | 6455 | 192 | 44 | 1.54 | 15879 | 0.1775 | 3.2 | 1.86 | 4.8 | 0.0760 | 3.6 | 0.66 | 1053 | 31 | 1067 | 32 | 1095 | 72 | 96 | mag. |
| SHA07-31 | 12 | a44 | 1668 | 214 | 8 | 0.97 | 4685 | 0.0310 | 4.2 | 0.22 | 6.7 | 0.0503 | 5.2 | 0.63 | 197 | 8 | 198 | 12 | 210 | 120 | 94 | mag. |
| SHA07-32 | 12 | a45 | 1678 | 55 | 6 | 0.74 | 3802 | 0.0989 | 3.6 | 0.82 | 6.7 | 0.0599 | 5.6 | 0.54 | 608 | 21 | 606 | 31 | 599 | 121 | 101 | mag. |
| SHA07-33 | 12 | a46 | 2620 | 143 | 16 | 0.77 | 4684 | 0.0986 | 3.6 | 0.82 | 5.9 | 0.0605 | 4.7 | 0.61 | 606 | 21 | 610 | 28 | 623 | 101 | 97 | mag. |
| SHA07-34 | 12 | a47 | 596 | 169 | 6 | 0.62 | 2358 | 0.0350 | 3.7 | 0.25 | 8.3 | 0.0511 | 7.4 | 0.44 | 222 | 8 | 224 | 17 | 244 | 172 | 91 | mag. |
| SHA07-35c | 12 | a48 | 2016 | 84 | 10 | 1.04 | 5389 | 0.1032 | 3.7 | 0.87 | 6.9 | 0.0609 | 5.8 | 0.54 | 633 | 22 | 634 | 33 | 634 | 124 | 100 | mag. |
| SHA07-36 | 12 | a49 | 6755 | 431 | 45 | 0.24 | 29172 | 0.1065 | 3.3 | 0.89 | 4.2 | 0.0603 | 2.5 | 0.80 | 653 | 21 | 644 | 20 | 614 | 54 | 106 | unc. |
| SHA07-37r | 12 | a50 | 1472 | 110 | 8 | 0.32 | 3324 | 0.0736 | 5.8 | 0.72 | 8.2 | 0.0708 | 5.7 | 0.71 | 458 | 26 | 549 | 35 | 951 | 117 | 48 | mag. |
| SHA07-37c | 12 | a51 | 3955 | 236 | 27 | 0.67 | 9718 | 0.1071 | 2.5 | 0.90 | 4.9 | 0.0612 | 4.2 | 0.51 | 656 | 15 | 654 | 24 | 648 | 90 | 101 | mag. |
| SHA07-38c | 12 | a52 | 4547 | 254 | 28 | 0.46 | 10044 | 0.1075 | 4.6 | 0.91 | 6.6 | 0.0615 | 4.8 | 0.69 | 658 | 29 | 658 | 32 | 657 | 102 | 100 | unc. |
| SHA07-39 | 12 | a53 | 2267 | 378 | 17 | 1.82 | 4505 | 0.0335 | 4.0 | 0.23 | 5.7 | 0.0503 | 4.1 | 0.70 | 212 | 8 | 212 | 11 | 209 | 95 | 101 | mag. |
| SHA07-40 | 12 | a54 | 2451 | 42 | 5 | 1.37 | 3508 | 0.0958 | 3.1 | 0.79 | 5.6 | 0.0601 | 4.7 | 0.55 | 590 | 17 | 593 | 26 | 607 | 101 | 97 | mag. |
| SHA07-41 | 12 | a55 | 232 | 74 | 3 | 1.08 | 943 | 0.0332 | 5.0 | 0.23 | 14.6 | 0.0507 | 13.8 | 0.34 | 211 | 10 | 212 | 28 | 228 | 318 | 92 | mag. |
| SHA07-42 | 13 | a1 | 9687 | 71 | 34 | 1.28 | 15458 | 0.3745 | 2.3 | 6.45 | 2.8 | 0.1249 | 1.5 | 0.83 | 2051 | 40 | 2039 | 24 | 2028 | 27 | 101 | mag. |
| SHA07-43 | 13 | a2 | 137447 | 403 | 256 | 0.54 | 15648 | 0.5412 | 2.0 | 16.87 | 2.2 | 0.2261 | 0.8 | 0.92 | 2788 | 45 | 2928 | 21 | 3025 | 13 | 92 | mag. |
| SHA07-44 | 13 | a3 | 1803 | 434 | 16 | 1.32 | 2614 | 0.0303 | 2.1 | 0.21 | 4.1 | 0.0503 | 3.5 | 0.52 | 192 | 4 | 194 | 7 | 210 | 81 | 92 | mag. |
| SHA07-45c | 13 | a4 | 1679 | 82 | 10 | 0.44 | 5403 | 0.1143 | 2.5 | 0.97 | 4.7 | 0.0616 | 4.0 | 0.52 | 698 | 16 | 689 | 24 | 661 | 86 | 106 | mag. |
| SHA07-46 | 13 | a5 | 2044 | 403 | 16 | 0.75 | 8151 | 0.0372 | 2.2 | 0.26 | 3.8 | 0.0500 | 3.0 | 0.59 | 236 | 5 | 232 | 8 | 193 | 71 | 122 | mag. |
| SHA07-47 | 13 | a6 | 1557 | 350 | 13 | 1.01 | 1924 | 0.0309 | 2.4 | 0.22 | 4.1 | 0.0505 | 3.4 | 0.59 | 196 | 5 | 198 | 7 | 217 | 78 | 90 | mag. |
| SHA07-48 | 13 | a7 | 1540 | 291 | 11 | 0.88 | 6036 | 0.0348 | 2.4 | 0.24 | 4.3 | 0.0507 | 3.6 | 0.55 | 221 | 5 | 221 | 9 | 228 | 84 | 97 | mag. |
| SHA07-49 | 13 | a8 | 1727 | 97 | 12 | 1.08 | 5672 | 0.1035 | 2.4 | 0.87 | 3.9 | 0.0607 | 3.1 | 0.61 | 635 | 14 | 633 | 19 | 627 | 67 | 101 | mag. |
| SHA07-50 | 13 | a9 | 3013 | 177 | 18 | 0.51 | 4209 | 0.0991 | 2.5 | 0.81 | 4.1 | 0.0590 | 3.2 | 0.61 | 609 | 14 | 600 | 19 | 566 | 70 | 108 | mag. |
| SHA07-51 | 13 | a10 | 1356 | 300 | 11 | 0.93 | 5282 | 0.0311 | 2.6 | 0.22 | 4.5 | 0.0510 | 3.7 | 0.56 | 197 | 5 | 201 | 8 | 241 | 86 | 82 | mag. |
| SHA07-52 | 13 | a11 | 8085 | 505 | 63 | 1.27 | 6167 | 0.1019 | 2.5 | 0.83 | 3.1 | 0.0593 | 1.9 | 0.80 | 625 | 15 | 615 | 15 | 577 | 41 | 108 | mag. |
| SHA07-53c | 13 | a12 | 6642 | 242 | 37 | 0.36 | 19184 | 0.1526 | 2.5 | 1.45 | 3.1 | 0.0689 | 1.9 | 0.80 | 916 | 21 | 910 | 19 | 895 | 38 | 102 | met. |
| SHA07-54 | 13 | a13 | 1555 | 294 | 12 | 2.12 | 4121 | 0.0305 | 2.8 | 0.21 | 4.2 | 0.0509 | 3.1 | 0.67 | 194 | 5 | 197 | 8 | 235 | 72 | 82 | mag. |
| SHA07-55r | 13 | a14 | 44820 | 187 | 88 | 0.23 | 50030 | 0.4397 | 2.9 | 10.60 | 3.2 | 0.1749 | 1.3 | 0.91 | 2349 | 57 | 2489 | 30 | 2605 | 22 | 90 | mag. |
| SHA07-56r | 13 | a15 | 1501 | 28 | 3 | 0.00 | 1689 | 0.0993 | 4.0 | 0.82 | 6.7 | 0.0597 | 5.4 | 0.59 | 610 | 23 | 607 | 31 | 593 | 117 | 103 | met. |
| SHA07-56c | 13 | a16 | 30955 | 53 | 43 | 1.00 | 21588 | 0.6091 | 2.5 | 24.14 | 2.8 | 0.2875 | 1.2 | 0.91 | 3066 | 62 | 3274 | 28 | 3404 | 18 | 90 | mag. |
| SHA07-57 | 13 | a17 | 1393 | 78 | 8 | 0.32 | 4569 | 0.0970 | 2.4 | 0.80 | 4.6 | 0.0602 | 3.9 | 0.52 | 597 | 14 | 599 | 21 | 609 | 85 | 98 | met. |
| SHA07-58c | 13 | a18 | 3928 | 98 | 18 | 0.66 | 10390 | 0.1705 | 2.3 | 1.77 | 3.8 | 0.0754 | 3.0 | 0.61 | 1015 | 22 | 1035 | 25 | 1078 | 60 | 94 | mag. |
| SHA07-59 | 13 | a19 | 2221 | 123 | 13 | 0.78 | 7126 | 0.0958 | 3.1 | 0.80 | 4.7 | 0.0609 | 3.5 | 0.66 | 590 | 17 | 599 | 21 | 635 | 75 | 93 | mag. |
| SHA07-60 | 13 | a20 | 3242 | 217 | 19 | 0.39 | 2159 | 0.0875 | 2.5 | 0.69 | 3.8 | 0.0575 | 2.9 | 0.65 | 541 | 13 | 535 | 16 | 511 | 64 | 106 | mag. |
| SHA07-61c | 13 | a21 | 3309 | 76 | 15 | 0.84 | 4690 | 0.1755 | 1.8 | 1.82 | 4.0 | 0.0752 | 3.6 | 0.45 | 1042 | 18 | 1053 | 27 | 1074 | 72 | 97 | mag. |
| SHA07-62 | 13 | a22 | 4929 | 123 | 24 | 0.41 | 13073 | 0.1863 | 2.2 | 1.93 | 3.5 | 0.0751 | 2.7 | 0.63 | 1101 | 23 | 1091 | 24 | 1072 | 55 | 103 | mag. |
| SHA07-63 | 13 | a23 | 1432 | 90 | 3 | 0.57 | 3717 | 0.0305 | 2.0 | 0.21 | 5.4 | 0.0498 | 5.0 | 0.38 | 194 | 4 | 193 | 9 | 186 | 115 | 104 | mag. |
| SHA07-64 | 13 | a24 | 524 | 116 | 6 | 1.92 | 4036 | 0.0312 | 2.9 | 0.22 | 8.3 | 0.0505 | 7.8 | 0.35 | 198 | 6 | 200 | 15 | 220 | 179 | 90 | mag. |
| SHA07-65c | 13 | a25 | 1219 | 256 | 8 | 0.64 | 2665 | 0.0304 | 3.1 | 0.21 | 6.0 | 0.0503 | 5.2 | 0.51 | 193 | 6 | 195 | 11 | 209 | 120 | 92 | mag. |
| SHA07-66 | 13 | a26 | 1149 | 74 | 7 | 1.23 | 2369 | 0.0813 | 4.3 | 0.64 | 6.1 | 0.0575 | 4.4 | 0.70 | 504 | 21 | 505 | 25 | 510 | 97 | 99 | mag. |
| SHA07-67 | 13 | a27 | 1242 | 82 | 3 | 1.26 | 2816 | 0.0315 | 4.6 | 0.22 | 6.2 | 0.0508 | 4.1 | 0.75 | 200 | 9 | 203 | 11 | 231 | 94 | 87 | mag. |
| SHA07-68r | 13 | a28 | 1523 | 112 | 4 | 1.12 | 4112 | 0.0301 | 2.6 | 0.21 | 5.9 | 0.0496 | 5.3 | 0.44 | 191 | 5 | 190 | 10 | 178 | 124 | 108 | mag. |
| SHA07-68c | 13 | a29 | 980 | 157 | 7 | 2.26 | 2616 | 0.0305 | 3.6 | 0.21 | 6.3 | 0.0505 | 5.2 | 0.57 | 194 | 7 | 195 | 11 | 216 | 120 | 89 | mag. |
| SHA07-69 | 13 | a30 | 8793 | 530 | 52 | 0.49 | 29748 | 0.0941 | 4.8 | 0.76 | 5.5 | 0.0587 | 2.8 | 0.86 | 580 | 27 | 575 | 25 | 557 | 61 | 104 | mag. |
| SHA07-70 | 13 | a31 | 929 | 29 | 1 | 0.65 | 540 | 0.0302 | 4.8 | 0.21 | 6.3 | 0.0497 | 4.1 | 0.76 | 192 | 9 | 191 | 11 | 179 | 96 | 107 | mag. |

# Results of U-Th-Pb LA-ICPMS analyses of zircons from sample SHA07 (continuation)

| Spot | Seq. | No. | $^{207}Pb$ [a] (cps) | U [b] (ppm) | Pb [b] (ppm) | Th/U [b] | $^{206}Pb/^{204}Pb$ | $^{206}Pb/^{238}U$ [c] | ±2s (%) | $^{207}Pb/^{235}U$ [c] | ±2s (%) | $^{207}Pb/^{206}Pb$ [c] | ±2s (%) | Rho [d] | Age (Ma) $^{206}Pb/^{238}U$ | ±2s | Age (Ma) $^{207}Pb/^{235}U$ | ±2s | Age (Ma) $^{207}Pb/^{206}Pb$ [c] | ±2s | conc [e] (%) | Origin [f] |
|---|---|---|---|---|---|---|---|---|---|---|---|---|---|---|---|---|---|---|---|---|---|---|
| SHA07-71r | 13 | a32 | 3538 | 216 | 19 | 0.51 | 12130 | 0.0815 | 3.2 | 0.66 | 4.3 | 0.0583 | 2.8 | 0.76 | 505 | 16 | 512 | 17 | 543 | 60 | 93 | mag. |
| SHA07-71c | 13 | a33 | 1448 | 90 | 8 | 0.61 | 5013 | 0.0785 | 3.0 | 0.62 | 4.6 | 0.0575 | 3.6 | 0.64 | 487 | 14 | 492 | 18 | 512 | 78 | 95 | mag. |
| SHA07-72r | 13 | a34 | 2502 | 134 | 12 | 0.24 | 8309 | 0.0902 | 2.9 | 0.73 | 4.5 | 0.0589 | 3.5 | 0.63 | 557 | 15 | 559 | 20 | 565 | 76 | 99 | mag. |
| SHA07-72c | 13 | a35 | 9438 | 251 | 44 | 0.47 | 14192 | 0.1672 | 2.3 | 1.63 | 3.6 | 0.0707 | 2.8 | 0.63 | 997 | 21 | 982 | 23 | 950 | 57 | 105 | mag. |
| SHA07-73 | 13 | a36 | 1978 | 53 | 6 | 1.35 | 7205 | 0.0931 | 2.8 | 0.77 | 5.6 | 0.0596 | 4.9 | 0.49 | 574 | 15 | 577 | 25 | 590 | 106 | 97 | mag. |
| SHA07-74c | 13 | a37 | 7759 | 251 | 36 | 0.25 | 11738 | 0.1471 | 3.2 | 1.40 | 3.6 | 0.0689 | 1.7 | 0.88 | 885 | 26 | 888 | 22 | 895 | 36 | 99 | mag. |
| SHA07-75 | 13 | a38 | 3202 | 213 | 19 | 0.58 | 4825 | 0.0830 | 3.7 | 0.65 | 4.7 | 0.0565 | 2.9 | 0.79 | 514 | 18 | 506 | 19 | 471 | 63 | 109 | mag. |
| SHA07-76r | 13 | a39 | 884 | 159 | 6 | 0.98 | 3487 | 0.0332 | 2.8 | 0.23 | 5.7 | 0.0504 | 5.0 | 0.49 | 211 | 6 | 211 | 11 | 212 | 115 | 99 | mag. |
| SHA07-77 | 13 | a40 | 1344 | 275 | 9 | 0.64 | 5483 | 0.0303 | 3.0 | 0.21 | 4.8 | 0.0491 | 3.7 | 0.63 | 193 | 6 | 189 | 8 | 151 | 87 | 128 | mag. |
| SHA07-78r | 13 | a41 | 19566 | 479 | 83 | 0.07 | 53126 | 0.1828 | 2.4 | 1.85 | 2.7 | 0.0734 | 1.3 | 0.88 | 1082 | 24 | 1064 | 18 | 1026 | 26 | 105 | mag. |
| SHA07-79r | 13 | a42 | 4755 | 235 | 23 | 0.09 | 15658 | 0.1060 | 2.6 | 0.88 | 4.0 | 0.0601 | 3.1 | 0.64 | 650 | 16 | 640 | 19 | 605 | 67 | 107 | unc. |
| SHA07-79c | 13 | a43 | 1670 | 65 | 8 | 0.56 | 2811 | 0.1103 | 2.4 | 0.97 | 4.7 | 0.0635 | 4.1 | 0.50 | 674 | 15 | 686 | 24 | 726 | 87 | 93 | mag. |
| SHA07-80r | 13 | a44 | 1628 | 334 | 11 | 0.73 | 6477 | 0.0307 | 2.2 | 0.21 | 5.6 | 0.0499 | 5.1 | 0.40 | 195 | 4 | 195 | 10 | 190 | 119 | 103 | mag. |
| SHA07-81r | 13 | a45 | 2831 | 138 | 15 | 0.68 | 9256 | 0.1009 | 2.6 | 0.85 | 4.2 | 0.0611 | 3.4 | 0.61 | 620 | 15 | 625 | 20 | 642 | 73 | 97 | mag. |
| SHA07-82r | 13 | a46 | 699 | 40 | 5 | 1.44 | 1170 | 0.0907 | 2.7 | 0.75 | 5.7 | 0.0596 | 5.0 | 0.48 | 560 | 15 | 565 | 25 | 588 | 108 | 95 | mag. |
| SHA07-82c | 13 | a47 | 2497 | 66 | 12 | 0.69 | 1632 | 0.1663 | 1.9 | 1.65 | 3.7 | 0.0718 | 3.2 | 0.52 | 991 | 18 | 988 | 24 | 981 | 65 | 101 | mag. |
| SHA07-83 | 13 | a48 | 4079 | 189 | 20 | 0.35 | 3403 | 0.1074 | 2.2 | 0.91 | 3.5 | 0.0613 | 2.7 | 0.63 | 657 | 14 | 656 | 17 | 651 | 58 | 101 | mag. |
| SHA07-84 | 13 | a49 | 4282 | 846 | 37 | 1.82 | 17010 | 0.0330 | 2.1 | 0.23 | 3.6 | 0.0502 | 2.9 | 0.58 | 210 | 4 | 209 | 7 | 205 | 68 | 102 | mag. |
| SHA07-85r | 13 | a50 | 909 | 104 | 5 | 1.50 | 1610 | 0.0359 | 2.6 | 0.25 | 6.3 | 0.0508 | 5.8 | 0.41 | 228 | 6 | 228 | 13 | 230 | 133 | 99 | mag. |
| SHA07-86m | 13 | a51 | 4255 | 116 | 19 | 0.32 | 12181 | 0.1692 | 2.7 | 1.63 | 3.8 | 0.0699 | 2.7 | 0.71 | 1008 | 25 | 982 | 24 | 925 | 55 | 109 | unc. |
| SHA07-86c | 13 | a52 | 2486 | 75 | 12 | 0.55 | 1990 | 0.1493 | 2.3 | 1.43 | 4.3 | 0.0693 | 3.7 | 0.53 | 897 | 19 | 900 | 26 | 907 | 76 | 99 | mag. |
| SHA07-87r | 13 | a53 | 5889 | 23 | 12 | 1.34 | 6689 | 0.3941 | 4.5 | 9.62 | 5.0 | 0.1770 | 2.2 | 0.90 | 2142 | 82 | 2399 | 47 | 2625 | 36 | 82 | mag. |
| SHA07-87c | 13 | a54 | 73336 | 137 | 112 | 1.56 | 14329 | 0.5747 | 1.9 | 22.70 | 2.2 | 0.2865 | 1.2 | 0.86 | 2927 | 45 | 3214 | 22 | 3399 | 18 | 86 | mag. |
| SHA07-88 | 13 | a55 | 278 | 50 | 2 | 1.31 | 1122 | 0.0306 | 2.6 | 0.21 | 6.7 | 0.0495 | 6.2 | 0.38 | 194 | 5 | 193 | 12 | 171 | 145 | 114 | mag. |
| SHA07-89c | 14 | a1 | 3467 | 185 | 20 | 0.70 | 3378 | 0.1002 | 2.6 | 0.83 | 4.3 | 0.0600 | 3.5 | 0.61 | 616 | 15 | 613 | 20 | 602 | 75 | 102 | mag. |
| SHA07-90 | 14 | a2 | 2940 | 148 | 14 | 0.25 | 9703 | 0.0981 | 3.3 | 0.81 | 4.6 | 0.0602 | 3.3 | 0.70 | 603 | 19 | 605 | 21 | 611 | 71 | 99 | met. |
| SHA07-91 | 14 | a3 | 1740 | 126 | 13 | 1.43 | 6055 | 0.0770 | 2.5 | 0.60 | 4.9 | 0.0570 | 4.2 | 0.51 | 478 | 11 | 480 | 19 | 492 | 92 | 97 | mag. |
| SHA07-92 | 14 | a4 | 1572 | 37 | 7 | 0.74 | 4210 | 0.1817 | 3.2 | 1.85 | 5.0 | 0.0738 | 3.9 | 0.63 | 1076 | 32 | 1063 | 34 | 1037 | 79 | 104 | mag. |
| SHA07-93 | 14 | a5 | 333 | 59 | 2 | 0.96 | 1070 | 0.0330 | 3.0 | 0.23 | 6.9 | 0.0513 | 6.2 | 0.44 | 209 | 6 | 213 | 13 | 253 | 142 | 83 | mag. |
| SHA07-94c | 14 | a6 | 693 | 133 | 7 | 2.83 | 2040 | 0.0315 | 2.9 | 0.22 | 6.8 | 0.0505 | 6.2 | 0.43 | 200 | 6 | 201 | 13 | 217 | 143 | 92 | mag. |
| SHA07-95r | 14 | a7 | 2013 | 133 | 13 | 0.71 | 931 | 0.0880 | 2.6 | 0.70 | 4.8 | 0.0577 | 4.0 | 0.55 | 544 | 14 | 539 | 20 | 518 | 88 | 105 | mag. |
| SHA07-95c | 14 | a8 | 2013 | 133 | 13 | 0.71 | 931 | 0.0865 | 3.2 | 0.69 | 5.1 | 0.0577 | 4.0 | 0.63 | 535 | 17 | 531 | 22 | 518 | 88 | 103 | mag. |
| SHA07-96 | 14 | a9 | 1607 | 102 | 11 | 1.33 | 5491 | 0.0885 | 3.6 | 0.72 | 5.3 | 0.0590 | 3.9 | 0.68 | 546 | 19 | 550 | 23 | 566 | 84 | 96 | mag. |
| SHA07-97 | 14 | a10 | 2456 | 130 | 13 | 0.53 | 1710 | 0.0939 | 2.6 | 0.76 | 4.8 | 0.0589 | 4.0 | 0.54 | 578 | 14 | 576 | 21 | 565 | 87 | 102 | mag. |
| SHA07-98 | 14 | a11 | 1528 | 82 | 9 | 0.96 | 5111 | 0.0943 | 2.9 | 0.77 | 6.2 | 0.0595 | 5.5 | 0.46 | 581 | 16 | 581 | 28 | 584 | 120 | 99 | mag. |
| SHA07-99r | 14 | a12 | 1483 | 86 | 9 | 0.89 | 4981 | 0.0972 | 2.6 | 0.79 | 5.9 | 0.0591 | 5.3 | 0.44 | 598 | 15 | 592 | 27 | 569 | 116 | 105 | mag. |
| SHA07-100r | 14 | a13 | 3388 | 189 | 18 | 0.30 | 11237 | 0.0983 | 3.5 | 0.81 | 4.6 | 0.0599 | 3.0 | 0.77 | 604 | 20 | 604 | 21 | 602 | 64 | 100 | mag. |
| SHA07-101r | 14 | a14 | 781 | 171 | 6 | 1.14 | 3075 | 0.0307 | 2.9 | 0.21 | 6.7 | 0.0500 | 6.0 | 0.43 | 195 | 6 | 195 | 12 | 196 | 140 | 99 | mag. |
| SHA07-102 | 14 | a15 | 6608 | 236 | 37 | 0.29 | 19120 | 0.1585 | 2.4 | 1.50 | 3.8 | 0.0685 | 2.9 | 0.64 | 948 | 21 | 929 | 23 | 884 | 60 | 107 | mag. |
| SHA07-103 | 14 | a16 | 1145 | 31 | 1 | 0.70 | 2526 | 0.0319 | 5.1 | 0.22 | 7.5 | 0.0510 | 5.5 | 0.68 | 202 | 10 | 205 | 14 | 241 | 127 | 84 | mag. |
| SHA07-104r | 14 | a17 | 5808 | 355 | 30 | 0.11 | 19495 | 0.0903 | 2.5 | 0.74 | 3.5 | 0.0591 | 2.4 | 0.73 | 557 | 13 | 560 | 15 | 571 | 52 | 98 | mag. |
| SHA07-104c | 14 | a18 | 6300 | 275 | 34 | 0.27 | 19091 | 0.1233 | 5.4 | 1.12 | 5.7 | 0.0658 | 1.9 | 0.94 | 749 | 38 | 762 | 31 | 799 | 39 | 94 | mag. |
| SHA07-105r | 14 | a19 | 1061 | 226 | 9 | 1.28 | 4057 | 0.0318 | 3.2 | 0.22 | 5.6 | 0.0510 | 4.6 | 0.58 | 202 | 6 | 205 | 11 | 241 | 106 | 84 | mag. |
| SHA07-106 | 14 | a20 | 1565 | 128 | 5 | 1.32 | 22140 | 0.0310 | 2.4 | 0.22 | 4.5 | 0.0516 | 3.8 | 0.53 | 197 | 5 | 202 | 8 | 266 | 88 | 74 | mag. |
| SHA07-107r | 14 | a21 | 4755 | 750 | 32 | 0.53 | 18277 | 0.0405 | 3.0 | 0.29 | 3.8 | 0.0518 | 2.3 | 0.79 | 256 | 8 | 258 | 9 | 275 | 53 | 93 | mag. |
| SHA07-108 | 14 | a22 | 2430 | 146 | 15 | 0.58 | 2229 | 0.0985 | 2.9 | 0.80 | 4.3 | 0.0592 | 3.2 | 0.67 | 605 | 17 | 599 | 20 | 576 | 69 | 105 | met. |
| SHA07-110r | 14 | a24 | 1345 | 167 | 5 | 0.29 | 3370 | 0.0328 | 3.0 | 0.23 | 10.9 | 0.0505 | 10.5 | 0.28 | 208 | 6 | 209 | 21 | 220 | 242 | 95 | unc. |
| SHA07-110c | 14 | a25 | 1434 | 326 | 11 | 0.94 | 5718 | 0.0301 | 2.5 | 0.21 | 5.5 | 0.0500 | 4.9 | 0.45 | 191 | 5 | 191 | 10 | 195 | 114 | 98 | mag. |
| SHA07-111 | 14 | a26 | 1262 | 87 | 8 | 0.32 | 743 | 0.0866 | 2.6 | 0.72 | 5.1 | 0.0599 | 4.3 | 0.51 | 536 | 13 | 548 | 22 | 598 | 94 | 90 | met. |
| SHA07-112r | 14 | a27 | 6429 | 428 | 38 | 0.25 | 21830 | 0.0910 | 2.5 | 0.73 | 3.3 | 0.0586 | 2.1 | 0.77 | 561 | 14 | 559 | 14 | 552 | 46 | 102 | unc. |
| SHA07-112c | 14 | a28 | 1718 | 111 | 11 | 0.79 | 5793 | 0.0929 | 3.0 | 0.75 | 4.8 | 0.0584 | 3.8 | 0.62 | 573 | 16 | 567 | 21 | 546 | 83 | 105 | mag. |
| SHA07-113 | 14 | a29 | 7249 | 395 | 48 | 0.89 | 23795 | 0.1065 | 2.5 | 0.89 | 3.6 | 0.0607 | 2.5 | 0.70 | 653 | 15 | 647 | 17 | 629 | 55 | 104 | mag. |
| SHA07-114r | 14 | a30 | 11668 | 528 | 61 | 0.28 | 21384 | 0.1142 | 3.6 | 1.01 | 4.1 | 0.0644 | 1.9 | 0.89 | 697 | 24 | 710 | 21 | 753 | 40 | 93 | mag. |
| SHA07-114c | 14 | a31 | 3792 | 124 | 24 | 0.59 | 10566 | 0.1734 | 3.1 | 1.71 | 4.4 | 0.0713 | 3.2 | 0.70 | 1031 | 29 | 1011 | 29 | 967 | 64 | 107 | mag. |
| SHA07-115 | 14 | a32 | 3431 | 192 | 21 | 0.55 | 2783 | 0.1020 | 2.6 | 0.85 | 4.2 | 0.0603 | 3.2 | 0.64 | 626 | 16 | 624 | 20 | 614 | 69 | 102 | mag. |
| SHA07-116 | 14 | a33 | 1716 | 97 | 11 | 0.67 | 5637 | 0.1098 | 2.7 | 0.91 | 4.5 | 0.0604 | 3.6 | 0.61 | 671 | 18 | 659 | 22 | 618 | 77 | 109 | mag. |
| SHA07-117r | 14 | a34 | 22429 | 978 | 95 | 0.06 | 23829 | 0.1045 | 3.0 | 0.86 | 3.3 | 0.0597 | 1.3 | 0.92 | 641 | 18 | 630 | 15 | 592 | 28 | 108 | met. |
| SHA07-117c | 14 | a35 | 4304 | 179 | 26 | 0.60 | 12804 | 0.1352 | 2.6 | 1.21 | 4.1 | 0.0651 | 3.2 | 0.63 | 818 | 20 | 807 | 23 | 776 | 67 | 105 | mag. |

# Results of U-Th-Pb LA-ICPMS analyses of zircons from sample SP08

| Spot | Seq. | No. | $^{207}Pb$ [a] (cps) | U [b] (ppm) | Pb [b] (ppm) | Th [b] U | $^{206}Pb$ / $^{204}Pb$ | $^{206}Pb$ [c] / $^{238}U$ | ±2s (%) | $^{207}Pb$ [c] / $^{235}U$ | ±2s (%) | $^{207}Pb$ [c] / $^{206}Pb$ | ±2s (%) | Rho [d] | Age (Ma) $^{206}Pb$ / $^{238}U$ | ±2s | Age (Ma) $^{207}Pb$ / $^{235}U$ | ±2s | Age (Ma) $^{207}Pb$ [c] / $^{206}Pb$ | ±2s | conc [e] (%) | Origin [f] |
|---|---|---|---|---|---|---|---|---|---|---|---|---|---|---|---|---|---|---|---|---|---|---|
| SP08-1r | 1 | a1 | 5693 | 496 | 41 | 0.20 | 9629 | 0.0878 | 2.5 | 0.72 | 3.7 | 0.0595 | 2.7 | 0.68 | 542 | 13 | 551 | 16 | 587 | 59 | 92 | met. |
| SP08-1m | 1 | a2 | 1324 | 114 | 10 | 0.53 | 2322 | 0.0827 | 3.5 | 0.66 | 7.1 | 0.0579 | 6.2 | 0.49 | 512 | 17 | 515 | 29 | 527 | 135 | 97 | mag. |
| SP08-1c | 1 | a3 | 10216 | 333 | 58 | 0.35 | 4386 | 0.1722 | 2.8 | 1.76 | 3.8 | 0.0743 | 2.5 | 0.75 | 1024 | 27 | 1032 | 25 | 1049 | 50 | 98 | mag. |
| SP08-2m | 1 | a4 | 496 | 43 | 4 | 1.06 | 848 | 0.0837 | 3.8 | 0.68 | 9.3 | 0.0589 | 8.4 | 0.41 | 518 | 19 | 526 | 39 | 563 | 184 | 92 | mag. |
| SP08-2r | 1 | a5 | 684 | 59 | 6 | 0.66 | 1183 | 0.0867 | 3.9 | 0.70 | 8.8 | 0.0585 | 7.9 | 0.44 | 536 | 20 | 538 | 38 | 548 | 173 | 98 | mag. |
| SP08-3 | 1 | a6 | 238 | 62 | 2 | 0.95 | 481 | 0.0326 | 4.4 | 0.23 | 14.1 | 0.0505 | 13.4 | 0.31 | 207 | 9 | 208 | 27 | 216 | 311 | 96 | mag. |
| SP08-4 | 1 | a7 | 1627 | 122 | 12 | 0.47 | 898 | 0.1018 | 2.8 | 0.87 | 5.6 | 0.0621 | 4.8 | 0.50 | 625 | 17 | 636 | 27 | 676 | 103 | 92 | mag. |
| SP08-5 | 1 | a8 | 2904 | 229 | 22 | 0.41 | 3355 | 0.0929 | 3.2 | 0.77 | 4.7 | 0.0603 | 3.4 | 0.68 | 572 | 17 | 581 | 21 | 613 | 74 | 93 | met. |
| SP08-6r | 1 | a9 | 3006 | 430 | 26 | 0.36 | 2727 | 0.0598 | 3.1 | 0.45 | 4.6 | 0.0545 | 3.4 | 0.67 | 375 | 11 | 377 | 15 | 391 | 76 | 96 | mag. |
| SP08-6c | 1 | a10 | 5295 | 363 | 49 | 0.74 | 8514 | 0.1247 | 2.4 | 1.08 | 3.8 | 0.0627 | 3.0 | 0.63 | 758 | 17 | 742 | 20 | 697 | 63 | 109 | mag. |
| SP08-7r | 1 | a11 | 3727 | 286 | 29 | 0.55 | 6172 | 0.0969 | 3.1 | 0.81 | 4.5 | 0.0607 | 3.2 | 0.69 | 596 | 18 | 603 | 21 | 630 | 69 | 95 | mag. |
| SP08-7m | 1 | a12 | 3073 | 245 | 33 | 1.87 | 4958 | 0.0999 | 2.7 | 0.86 | 4.5 | 0.0621 | 3.6 | 0.61 | 614 | 16 | 628 | 21 | 678 | 77 | 91 | mag. |
| SP08-8 | 1 | a13 | 3881 | 213 | 36 | 0.73 | 2035 | 0.1593 | 2.7 | 1.53 | 4.8 | 0.0696 | 4.0 | 0.57 | 953 | 24 | 942 | 30 | 917 | 82 | 104 | mag. |
| SP08-9 | 1 | a14 | 3670 | 276 | 30 | 0.54 | 5930 | 0.1018 | 2.8 | 0.88 | 4.5 | 0.0625 | 3.5 | 0.63 | 625 | 17 | 640 | 21 | 692 | 74 | 90 | mag. |
| SP08-10 | 1 | a15 | 2039 | 47 | 13 | 1.13 | 2197 | 0.2381 | 2.8 | 3.08 | 5.0 | 0.0938 | 4.1 | 0.56 | 1377 | 35 | 1427 | 39 | 1503 | 78 | 92 | mag. |
| SP08-11 | 1 | a16 | 15621 | 438 | 91 | 0.41 | 7038 | 0.1999 | 2.7 | 2.20 | 3.3 | 0.0799 | 2.0 | 0.79 | 1175 | 29 | 1181 | 24 | 1194 | 40 | 98 | mag. |
| SP08-12 | 1 | a17 | 6760 | 236 | 43 | 0.16 | 9012 | 0.1859 | 2.6 | 1.94 | 3.9 | 0.0757 | 2.9 | 0.66 | 1099 | 26 | 1095 | 27 | 1087 | 59 | 101 | mag. |
| SP08-13r | 1 | a18 | 2116 | 90 | 14 | 0.36 | 2944 | 0.1501 | 3.2 | 1.50 | 5.6 | 0.0726 | 4.7 | 0.56 | 902 | 27 | 932 | 35 | 1004 | 94 | 90 | mag. |
| SP08-13c | 1 | a19 | 1336 | 59 | 10 | 0.54 | 1915 | 0.1595 | 2.7 | 1.54 | 5.9 | 0.0701 | 5.3 | 0.46 | 954 | 24 | 947 | 37 | 932 | 108 | 102 | mag. |
| SP08-15 | 1 | a21 | 12115 | 165 | 58 | 1.03 | 11928 | 0.2997 | 2.6 | 4.23 | 3.3 | 0.1023 | 2.1 | 0.77 | 1690 | 38 | 1680 | 28 | 1667 | 39 | 101 | mag. |
| SP08-16 | 1 | a22 | 2266 | 198 | 17 | 0.58 | 4053 | 0.0832 | 3.0 | 0.65 | 5.1 | 0.0566 | 4.1 | 0.59 | 515 | 15 | 508 | 21 | 476 | 91 | 108 | mag. |
| SP08-17 | 1 | a23 | 1322 | 128 | 12 | 0.53 | 2261 | 0.0925 | 3.5 | 0.75 | 7.6 | 0.0591 | 6.7 | 0.46 | 570 | 19 | 570 | 34 | 571 | 146 | 100 | mag. |
| SP08-18r | 1 | a24 | 2044 | 213 | 19 | 0.41 | 953 | 0.0898 | 3.3 | 0.75 | 5.5 | 0.0603 | 4.4 | 0.61 | 554 | 18 | 566 | 24 | 613 | 94 | 90 | met. |
| SP08-18c | 1 | a25 | 1368 | 146 | 13 | 0.54 | 2394 | 0.0892 | 4.2 | 0.71 | 6.5 | 0.0577 | 5.0 | 0.65 | 551 | 22 | 545 | 28 | 520 | 109 | 106 | mag. |
| SP08-19r | 1 | a26 | 1394 | 141 | 17 | 2.05 | 2407 | 0.0928 | 2.9 | 0.75 | 5.4 | 0.0584 | 4.6 | 0.53 | 572 | 16 | 567 | 24 | 545 | 101 | 105 | mag. |
| SP08-19c | 1 | a27 | 6324 | 335 | 52 | 0.65 | 8883 | 0.1455 | 4.6 | 1.44 | 5.3 | 0.0716 | 2.6 | 0.87 | 876 | 38 | 904 | 32 | 974 | 53 | 90 | mag. |
| SP08-20 | 1 | a28 | 1440 | 151 | 15 | 0.70 | 2464 | 0.0945 | 2.5 | 0.77 | 5.2 | 0.0590 | 4.6 | 0.48 | 582 | 14 | 579 | 23 | 568 | 100 | 103 | mag. |
| SP08-21c | 1 | a29 | 2194 | 119 | 18 | 0.96 | 3262 | 0.1336 | 3.0 | 1.24 | 4.7 | 0.0672 | 3.7 | 0.63 | 809 | 23 | 818 | 27 | 845 | 77 | 96 | mag. |
| SP08-22 | 1 | a30 | 1087 | 109 | 10 | 0.80 | 1831 | 0.0909 | 3.7 | 0.75 | 7.4 | 0.0600 | 6.4 | 0.50 | 561 | 20 | 569 | 33 | 603 | 139 | 93 | mag. |
| SP08-23 | 1 | a31 | 1602 | 156 | 16 | 0.87 | 2733 | 0.0942 | 5.8 | 0.77 | 9.5 | 0.0595 | 7.5 | 0.61 | 581 | 32 | 581 | 43 | 584 | 163 | 99 | mag. |
| SP08-24 | 1 | a32 | 374 | 39 | 4 | 0.94 | 683 | 0.0977 | 4.4 | 0.76 | 12.1 | 0.0568 | 11.3 | 0.37 | 601 | 26 | 577 | 55 | 483 | 249 | 124 | mag. |
| SP08-25 | 1 | a33 | 3293 | 323 | 32 | 0.66 | 5624 | 0.0922 | 4.4 | 0.75 | 5.9 | 0.0590 | 3.9 | 0.75 | 569 | 24 | 568 | 26 | 568 | 84 | 100 | mag. |
| SP08-26r | 1 | a34 | 962 | 78 | 9 | 0.35 | 1541 | 0.1098 | 4.8 | 0.96 | 8.0 | 0.0633 | 6.5 | 0.59 | 672 | 31 | 683 | 41 | 719 | 138 | 93 | mag. |
| SP08-26c | 1 | a35 | 2825 | 235 | 30 | 0.45 | 4481 | 0.1252 | 5.3 | 1.10 | 7.3 | 0.0637 | 5.0 | 0.72 | 760 | 38 | 753 | 39 | 732 | 106 | 104 | mag. |
| SP08-27c | 1 | a36 | 5110 | 240 | 38 | 0.23 | 6931 | 0.1647 | 3.8 | 1.69 | 5.3 | 0.0742 | 3.8 | 0.71 | 983 | 35 | 1003 | 35 | 1048 | 76 | 94 | mag. |
| SP08-27r | 1 | a37 | 3481 | 376 | 33 | 0.28 | 5989 | 0.0912 | 3.2 | 0.74 | 4.5 | 0.0587 | 3.2 | 0.70 | 563 | 17 | 562 | 20 | 557 | 71 | 101 | mag. |
| SP08-28r | 1 | a38 | 7751 | 766 | 71 | 0.06 | 12675 | 0.1002 | 4.0 | 0.84 | 4.8 | 0.0609 | 2.7 | 0.82 | 616 | 23 | 620 | 22 | 634 | 58 | 97 | met. |
| SP08-29r | 1 | a39 | 44289 | 243 | 140 | 0.11 | 20835 | 0.5439 | 2.8 | 15.06 | 3.4 | 0.2008 | 1.9 | 0.83 | 2800 | 65 | 2819 | 33 | 2833 | 31 | 99 | mag. |
| SP08-29c | 1 | a40 | 12927 | 37 | 40 | 1.25 | 1565 | 0.8126 | 3.1 | 34.21 | 4.5 | 0.3053 | 3.3 | 0.69 | 3834 | 90 | 3616 | 46 | 3497 | 51 | 110 | mag. |
| SP08-30 | 1 | a41 | 1032 | 133 | 13 | 0.83 | 1722 | 0.0973 | 3.6 | 0.81 | 7.3 | 0.0607 | 6.3 | 0.50 | 598 | 21 | 605 | 34 | 630 | 136 | 95 | mag. |
| SP08-31 | 1 | a42 | 359 | 140 | 5 | 0.87 | 724 | 0.0329 | 5.6 | 0.23 | 12.4 | 0.0504 | 11.1 | 0.45 | 209 | 12 | 209 | 24 | 215 | 256 | 97 | mag. |
| SP08-32 | 1 | a43 | 2220 | 262 | 23 | 0.34 | 3851 | 0.0890 | 3.5 | 0.72 | 5.4 | 0.0584 | 4.1 | 0.65 | 550 | 18 | 549 | 23 | 545 | 90 | 101 | mag. |
| SP08-33 | 1 | a44 | 5039 | 481 | 54 | 0.39 | 8311 | 0.1114 | 2.9 | 0.94 | 4.2 | 0.0612 | 3.1 | 0.68 | 681 | 18 | 672 | 21 | 645 | 66 | 106 | unc. |
| SP08-34 | 1 | a45 | 5072 | 253 | 45 | 0.30 | 6955 | 0.1792 | 3.2 | 1.82 | 5.0 | 0.0735 | 3.8 | 0.64 | 1062 | 32 | 1051 | 33 | 1028 | 77 | 103 | mag. |
| SP08-35r | 1 | a46 | 608 | 68 | 8 | 0.96 | 1021 | 0.0990 | 3.7 | 0.82 | 8.1 | 0.0604 | 7.2 | 0.46 | 608 | 21 | 611 | 38 | 619 | 156 | 98 | mag. |
| SP08-35m | 1 | a47 | 34808 | 774 | 177 | 0.11 | 11912 | 0.2323 | 3.3 | 4.01 | 4.0 | 0.1251 | 2.2 | 0.84 | 1346 | 40 | 1636 | 33 | 2030 | 38 | 66 | mag. |
| SP08-35c | 1 | a48 | 43423 | 1086 | 226 | 0.45 | 11189 | 0.1945 | 3.4 | 3.35 | 4.0 | 0.1250 | 2.2 | 0.84 | 1146 | 36 | 1493 | 32 | 2029 | 39 | 56 | mag. |
| SP08-36r | 1 | a49 | 12504 | 829 | 126 | 0.19 | 18418 | 0.1582 | 3.1 | 1.49 | 4.5 | 0.0685 | 3.3 | 0.68 | 947 | 27 | 928 | 28 | 884 | 67 | 107 | mag. |
| SP08-36m | 1 | a50 | 4970 | 257 | 47 | 0.71 | 1148 | 0.1726 | 3.6 | 1.82 | 4.8 | 0.0764 | 3.1 | 0.76 | 1027 | 35 | 1053 | 32 | 1107 | 61 | 93 | mag. |
| SP08-37r | 1 | a51 | 1146 | 162 | 15 | 1.03 | 1964 | 0.0941 | 3.4 | 0.77 | 5.8 | 0.0590 | 4.7 | 0.59 | 580 | 19 | 577 | 26 | 567 | 102 | 102 | mag. |
| SP08-38 | 1 | a52 | 1371 | 572 | 25 | 1.94 | 2763 | 0.0341 | 2.6 | 0.24 | 6.8 | 0.0502 | 6.3 | 0.37 | 216 | 5 | 215 | 13 | 202 | 147 | 107 | mag. |
| SP08-39 | 1 | a53 | 1440 | 79 | 15 | 0.75 | 2003 | 0.1725 | 4.0 | 1.73 | 6.4 | 0.0727 | 5.1 | 0.62 | 1026 | 38 | 1019 | 42 | 1006 | 103 | 102 | mag. |
| SP08-40m | 1 | a54 | 3928 | 456 | 44 | 0.11 | 4586 | 0.1019 | 2.7 | 0.85 | 4.8 | 0.0603 | 3.9 | 0.56 | 626 | 16 | 624 | 22 | 616 | 85 | 102 | mag. |
| SP08-40c | 1 | a55 | 1518 | 93 | 15 | 0.39 | 2150 | 0.1611 | 3.7 | 1.59 | 5.8 | 0.0714 | 4.5 | 0.63 | 963 | 33 | 965 | 37 | 968 | 92 | 100 | mag. |
| SP08-41 | 2 | a1 | 8391 | 666 | 59 | 0.09 | 11427 | 0.0936 | 4.0 | 0.75 | 5.1 | 0.0581 | 3.2 | 0.77 | 577 | 22 | 569 | 23 | 535 | 71 | 108 | met. |
| SP08-42r | 2 | a2 | 722 | 195 | 8 | 1.68 | 1431 | 0.0338 | 3.4 | 0.24 | 7.6 | 0.0508 | 6.8 | 0.45 | 215 | 7 | 216 | 15 | 230 | 157 | 93 | mag. |
| SP08-43 | 2 | a3 | 2467 | 184 | 19 | 0.44 | 4183 | 0.0996 | 3.7 | 0.82 | 6.0 | 0.0595 | 4.7 | 0.62 | 612 | 22 | 606 | 28 | 584 | 102 | 105 | mag. |
| SP08-44 | 2 | a4 | 1225 | 330 | 12 | 0.53 | 2375 | 0.0347 | 3.0 | 0.24 | 5.4 | 0.0508 | 4.4 | 0.57 | 220 | 7 | 221 | 11 | 233 | 102 | 95 | mag. |
| SP08-45 | 2 | a5 | 1966 | 184 | 14 | 0.17 | 3428 | 0.0783 | 3.9 | 0.62 | 5.7 | 0.0575 | 4.1 | 0.69 | 486 | 18 | 490 | 22 | 511 | 91 | 95 | mag. |
| SP08-46r | 2 | a6 | 217 | 13 | 2 | 0.33 | 364 | 0.1209 | 10.3 | 0.89 | 23.0 | 0.0533 | 20.6 | 0.45 | 736 | 72 | 645 | 116 | 340 | 467 | 217 | unc. |
| SP08-46c | 2 | a7 | 5085 | 461 | 38 | 0.16 | 8698 | 0.0866 | 3.6 | 0.70 | 4.9 | 0.0587 | 3.3 | 0.74 | 535 | 19 | 539 | 21 | 556 | 72 | 96 | met. |
| SP08-47 | 2 | a8 | 14925 | 779 | 103 | 0.11 | 24905 | 0.1413 | 6.1 | 1.20 | 9.3 | 0.0616 | 7.0 | 0.66 | 852 | 49 | 801 | 53 | 661 | 149 | 129 | met. |
| SP08-48c | 2 | a9 | 1573 | 146 | 15 | 1.10 | 2645 | 0.0872 | 3.8 | 0.71 | 5.8 | 0.0594 | 4.4 | 0.65 | 539 | 20 | 548 | 25 | 583 | 96 | 92 | mag. |
| SP08-49 | 2 | a10 | 2970 | 214 | 26 | 0.74 | 4855 | 0.1094 | 3.0 | 0.94 | 5.2 | 0.0621 | 4.2 | 0.58 | 669 | 19 | 671 | 26 | 678 | 90 | 99 | mag. |
| SP08-50 | 2 | a11 | 4392 | 305 | 31 | 0.37 | 2201 | 0.0997 | 4.6 | 0.84 | 7.2 | 0.0610 | 5.6 | 0.63 | 613 | 27 | 618 | 34 | 639 | 120 | 96 | mag. |
| SP08-51 | 2 | a12 | 1416 | 69 | 11 | 0.81 | 603 | 0.1409 | 2.9 | 1.32 | 5.9 | 0.0681 | 5.2 | 0.50 | 850 | 23 | 856 | 35 | 873 | 107 | 97 | mag. |
| SP08-52 | 2 | a13 | 71 | 22 | 1 | 1.65 | 144 | 0.0317 | 5.8 | 0.22 | 15.1 | 0.0504 | 14.0 | 0.39 | 201 | 12 | 202 | 28 | 214 | 323 | 94 | mag. |
| SP08-53 | 2 | a14 | 2128 | 141 | 17 | 0.47 | 3365 | 0.1169 | 3.3 | 1.03 | 5.5 | 0.0637 | 4.4 | 0.60 | 713 | 22 | 718 | 29 | 733 | 93 | 97 | mag. |
| SP08-54 | 2 | a15 | 2756 | 228 | 22 | 0.33 | 2335 | 0.0968 | 3.2 | 0.80 | 4.9 | 0.0600 | 3.7 | 0.65 | 595 | 18 | 597 | 22 | 603 | 81 | 99 | mag. |
| SP08-55r | 2 | a16 | 16513 | 565 | 109 | 0.11 | 21843 | 0.2017 | 3.1 | 2.11 | 3.9 | 0.0757 | 2.5 | 0.78 | 1185 | 33 | 1151 | 27 | 1087 | 50 | 109 | met. |
| SP08-56r | 2 | a17 | 6208 | 515 | 48 | 0.22 | 7800 | 0.0949 | 3.6 | 0.78 | 6.2 | 0.0598 | 5.1 | 0.57 | 585 | 20 | 587 | 28 | 596 | 110 | 98 | met. |
| SP08-56c | 2 | a18 | 1882 | 132 | 16 | 0.53 | 990 | 0.1142 | 3.6 | 0.98 | 5.8 | 0.0623 | 4.5 | 0.63 | 697 | 24 | 694 | 29 | 684 | 96 | 102 | mag. |
| SP08-57 | 2 | a19 | 1572 | 415 | 18 | 0.58 | 1956 | 0.0410 | 5.0 | 0.29 | 7.9 | 0.0516 | 6.1 | 0.64 | 259 | 13 | 260 | 18 | 268 | 140 | 97 | mag. |
| SP08-59 | 2 | a21 | 5570 | 896 | 53 | 0.75 | 10430 | 0.0540 | 2.7 | 0.40 | 4.4 | 0.0537 | 3.5 | 0.61 | 339 | 9 | 341 | 13 | 359 | 79 | 94 | mag. |
| SP08-60r | 2 | a22 | 1909 | 229 | 18 | 0.18 | 3245 | 0.0828 | 3.4 | 0.67 | 6.5 | 0.0587 | 5.6 | 0.52 | 513 | 17 | 521 | 27 | 556 | 122 | 92 | met. |

# Results of U-Th-Pb LA-ICPMS analyses of zircons from sample SP08 (continuation)

| Spot | Seq. | No. | $^{207}Pb$ [a] (cps) | U [b] (ppm) | Pb [b] (ppm) | Th/U [b] | $^{206}Pb/^{204}Pb$ | $^{206}Pb/^{238}U$ [c] | ±2s (%) | $^{207}Pb/^{235}U$ [c] | ±2s (%) | $^{207}Pb/^{206}Pb$ [c] | ±2s (%) | Rho [d] | Age (Ma) $^{206}Pb/^{238}U$ | ±2s | $^{207}Pb/^{235}U$ | ±2s | $^{207}Pb/^{206}Pb$ [c] | ±2s | conc [e] (%) | Origin [f] |
|---|---|---|---|---|---|---|---|---|---|---|---|---|---|---|---|---|---|---|---|---|---|---|
| SP08-61 | 2 | a23 | 673 | 58 | 6 | 0.33 | 1008 | 0.1140 | 8.1 | 1.00 | 16.0 | 0.0635 | 13.8 | 0.51 | 696 | 54 | 703 | 85 | 725 | 292 | 96 | mag. |
| SP08-62r | 2 | a24 | 915 | 57 | 10 | 1.01 | 1511 | 0.1557 | 3.9 | 1.23 | 6.9 | 0.0571 | 5.7 | 0.56 | 933 | 34 | 813 | 39 | 497 | 125 | 188 | mag. |
| SP08-62c | 2 | a25 | 532 | 46 | 5 | 0.91 | 869 | 0.1011 | 3.6 | 0.85 | 9.3 | 0.0610 | 8.6 | 0.39 | 621 | 21 | 625 | 44 | 638 | 184 | 97 | mag. |
| SP08-63r | 2 | a26 | 198 | 61 | 2 | 0.35 | 385 | 0.0363 | 3.7 | 0.26 | 14.0 | 0.0511 | 13.5 | 0.26 | 230 | 8 | 231 | 29 | 247 | 311 | 93 | mag. |
| SP08-63c | 2 | a27 | 2476 | 695 | 29 | 0.92 | 4922 | 0.0363 | 2.9 | 0.25 | 5.3 | 0.0506 | 4.5 | 0.54 | 230 | 7 | 230 | 11 | 225 | 103 | 102 | mag. |
| SP08-64 | 2 | a28 | 2508 | 261 | 20 | 0.07 | 3533 | 0.0837 | 2.7 | 0.67 | 4.5 | 0.0585 | 3.6 | 0.60 | 518 | 14 | 523 | 19 | 547 | 79 | 95 | met. |
| SP08-65 | 2 | a29 | 491 | 153 | 6 | 1.28 | 963 | 0.0343 | 3.5 | 0.24 | 8.8 | 0.0508 | 8.1 | 0.40 | 217 | 7 | 218 | 18 | 230 | 188 | 95 | mag. |
| SP08-66c | 2 | a30 | 2012 | 182 | 22 | 0.96 | 3328 | 0.1054 | 3.1 | 0.88 | 6.6 | 0.0605 | 5.8 | 0.47 | 646 | 19 | 641 | 32 | 623 | 126 | 104 | mag. |
| SP08-67 | 2 | a31 | 811 | 220 | 10 | 1.13 | 1576 | 0.0372 | 3.3 | 0.26 | 7.5 | 0.0509 | 6.7 | 0.44 | 236 | 8 | 236 | 16 | 236 | 155 | 100 | mag. |
| SP08-68 | 2 | a32 | 927 | 111 | 10 | 0.66 | 1624 | 0.0795 | 3.3 | 0.63 | 7.2 | 0.0576 | 6.3 | 0.47 | 493 | 16 | 497 | 29 | 513 | 139 | 96 | mag. |
| SP08-69r | 2 | a33 | 2061 | 240 | 23 | 0.78 | 3568 | 0.0900 | 3.0 | 0.73 | 6.0 | 0.0586 | 5.2 | 0.50 | 556 | 16 | 555 | 26 | 552 | 113 | 101 | mag. |
| SP08-69c | 2 | a34 | 716 | 76 | 8 | 0.62 | 1229 | 0.0919 | 2.8 | 0.75 | 8.6 | 0.0593 | 8.1 | 0.33 | 567 | 15 | 569 | 38 | 578 | 176 | 98 | mag. |
| SP08-70 | 2 | a35 | 86 | 28 | 1 | 1.80 | 174 | 0.0351 | 7.1 | 0.25 | 23.1 | 0.0511 | 22.0 | 0.31 | 222 | 15 | 224 | 48 | 245 | 507 | 91 | mag. |
| SP08-71c | 2 | a36 | 1052 | 112 | 10 | 0.40 | 938 | 0.0902 | 3.5 | 0.72 | 6.9 | 0.0580 | 5.9 | 0.51 | 557 | 19 | 552 | 30 | 530 | 130 | 105 | met. |
| SP08-72 | 2 | a37 | 4375 | 368 | 37 | 0.20 | 7130 | 0.1048 | 3.1 | 0.89 | 5.0 | 0.0616 | 4.0 | 0.61 | 643 | 19 | 646 | 24 | 659 | 85 | 98 | met. |
| SP08-73 | 2 | a38 | 2122 | 159 | 19 | 0.38 | 3247 | 0.1203 | 2.8 | 1.07 | 5.1 | 0.0648 | 4.2 | 0.55 | 732 | 19 | 741 | 27 | 766 | 89 | 96 | mag. |
| SP08-74 | 2 | a39 | 1004 | 355 | 16 | 1.95 | 2001 | 0.0333 | 3.8 | 0.23 | 7.3 | 0.0504 | 6.2 | 0.52 | 211 | 8 | 211 | 14 | 212 | 145 | 100 | mag. |
| SP08-75 | 2 | a40 | 741 | 254 | 9 | 0.87 | 1447 | 0.0334 | 3.8 | 0.23 | 8.0 | 0.0504 | 7.0 | 0.47 | 212 | 8 | 212 | 15 | 214 | 163 | 99 | mag. |
| SP08-76 | 2 | a41 | 9639 | 779 | 80 | 0.13 | 15305 | 0.1076 | 4.4 | 0.92 | 5.2 | 0.0622 | 2.7 | 0.85 | 659 | 27 | 664 | 25 | 681 | 59 | 97 | mag. |
| SP08-77r | 2 | a42 | 1748 | 182 | 20 | 0.85 | 2964 | 0.1010 | 3.6 | 0.82 | 6.8 | 0.0591 | 5.7 | 0.53 | 620 | 21 | 610 | 32 | 572 | 125 | 108 | mag. |
| SP08-78 | 2 | a43 | 5202 | 153 | 40 | 0.81 | 5840 | 0.2310 | 3.1 | 2.83 | 4.5 | 0.0890 | 3.2 | 0.69 | 1339 | 38 | 1365 | 34 | 1404 | 62 | 95 | mag. |
| SP08-79c | 2 | a44 | 1905 | 208 | 20 | 0.32 | 1055 | 0.1013 | 3.3 | 0.83 | 5.8 | 0.0592 | 4.8 | 0.56 | 622 | 19 | 612 | 27 | 574 | 105 | 108 | mag. |
| SP08-79r | 2 | a45 | 15473 | 1418 | 142 | 0.04 | 25531 | 0.1078 | 3.2 | 0.91 | 4.1 | 0.0609 | 2.5 | 0.79 | 660 | 20 | 655 | 20 | 637 | 53 | 104 | met. |
| SP08-80r | 2 | a46 | 6387 | 436 | 61 | 0.23 | 9268 | 0.1440 | 2.9 | 1.37 | 3.7 | 0.0691 | 2.3 | 0.78 | 867 | 24 | 877 | 22 | 903 | 47 | 96 | met. |
| SP08-80c | 2 | a47 | 2779 | 160 | 27 | 0.72 | 3941 | 0.1573 | 2.9 | 1.53 | 4.9 | 0.0704 | 3.9 | 0.60 | 942 | 26 | 941 | 31 | 940 | 81 | 100 | mag. |
| SP08-81c | 2 | a48 | 6590 | 285 | 63 | 0.51 | 8474 | 0.2107 | 3.2 | 2.25 | 4.2 | 0.0774 | 2.8 | 0.75 | 1233 | 36 | 1197 | 30 | 1132 | 55 | 109 | mag. |
| SP08-82 | 2 | a49 | 779 | 245 | 10 | 0.72 | 1523 | 0.0398 | 3.0 | 0.28 | 7.5 | 0.0515 | 6.9 | 0.39 | 252 | 7 | 253 | 17 | 263 | 159 | 96 | mag. |
| SP08-83 | 2 | a50 | 3740 | 224 | 36 | 0.59 | 5299 | 0.1524 | 3.5 | 1.49 | 5.5 | 0.0707 | 4.2 | 0.63 | 914 | 30 | 925 | 34 | 949 | 87 | 96 | unc. |
| SP08-84r | 2 | a51 | 4901 | 527 | 53 | 0.26 | 2551 | 0.1017 | 3.7 | 0.84 | 5.1 | 0.0603 | 3.5 | 0.73 | 624 | 22 | 622 | 24 | 613 | 76 | 102 | mag. |
| SP08-84c | 2 | a52 | 13284 | 919 | 134 | 0.06 | 19003 | 0.1557 | 2.6 | 1.48 | 3.7 | 0.0688 | 2.5 | 0.72 | 933 | 23 | 921 | 22 | 893 | 53 | 105 | unc. |
| SP08-85r | 2 | a53 | 1113 | 134 | 13 | 0.37 | 1791 | 0.1016 | 3.9 | 0.85 | 7.1 | 0.0610 | 5.9 | 0.56 | 624 | 23 | 627 | 34 | 640 | 126 | 98 | mag. |
| SP08-85c | 2 | a54 | 2249 | 280 | 25 | 0.23 | 817 | 0.0908 | 4.3 | 0.73 | 6.2 | 0.0584 | 4.4 | 0.70 | 560 | 23 | 557 | 27 | 545 | 97 | 103 | met. |
| SP08-40r | 2 | a55 | 1010 | 122 | 13 | 0.99 | 1645 | 0.0995 | 4.4 | 0.85 | 7.9 | 0.0617 | 6.6 | 0.56 | 611 | 26 | 623 | 38 | 663 | 141 | 92 | mag. |

# Results of U-Th-Pb LA-ICPMS analyses of zircons from sample SPP36

| Spot | Seq. | No. | $^{207}Pb$ [a] (cps) | U [b] (ppm) | Pb [b] (ppm) | Th [b] U | $^{206}Pb/^{204}Pb$ | $^{206}Pb^{c}/^{238}U$ | ±2s (%) | $^{207}Pb^{c}/^{235}U$ | ±2s (%) | $^{207}Pb^{c}/^{206}Pb$ | ±2s (%) | Rho [d] | Age (Ma) $^{206}Pb/^{238}U$ | ±2s | $^{207}Pb/^{235}U$ | ±2s | $^{207}Pb^{c}/^{206}Pb$ | ±2s | conc [e] (%) | Origin [f] |
|---|---|---|---|---|---|---|---|---|---|---|---|---|---|---|---|---|---|---|---|---|---|---|
| SPP36-1c | 14 | a36 | 13719 | 377 | 71 | 0.53 | 36554 | 0.1780 | 2.7 | 1.83 | 3.2 | 0.0744 | 1.8 | 0.83 | 1056 | 26 | 1055 | 21 | 1053 | 36 | 100 | mag. |
| SPP36-2r | 14 | a37 | 918 | 55 | 5 | 0.90 | 2520 | 0.0835 | 3.2 | 0.66 | 7.6 | 0.0571 | 6.9 | 0.42 | 517 | 16 | 513 | 31 | 494 | 152 | 105 | mag. |
| SPP36-2c | 14 | a38 | 899 | 74 | 6 | 0.72 | 3036 | 0.0792 | 3.2 | 0.62 | 6.1 | 0.0572 | 5.3 | 0.51 | 491 | 15 | 493 | 24 | 500 | 116 | 98 | mag. |
| SPP36-3 | 14 | a39 | 5802 | 149 | 29 | 0.58 | 15283 | 0.1826 | 2.3 | 1.90 | 3.2 | 0.0756 | 2.3 | 0.70 | 1081 | 23 | 1082 | 22 | 1083 | 46 | 100 | mag. |
| SPP36-4 | 14 | a40 | 1713 | 281 | 13 | 0.73 | 6450 | 0.0417 | 3.2 | 0.30 | 5.4 | 0.0519 | 4.3 | 0.59 | 263 | 8 | 265 | 13 | 279 | 99 | 94 | mag. |
| SPP36-5 | 14 | a41 | 141622 | 652 | 171 | 1.86 | 357126 | 0.2016 | 2.9 | 2.17 | 3.2 | 0.0783 | 1.2 | 0.92 | 1184 | 32 | 1173 | 22 | 1153 | 24 | 103 | mag. |
| SPP36-6r | 14 | a42 | 3986 | 283 | 28 | 0.46 | 13262 | 0.0966 | 2.7 | 0.78 | 3.7 | 0.0586 | 2.6 | 0.72 | 595 | 15 | 586 | 17 | 551 | 57 | 108 | mag. |
| SPP36-7r | 14 | a43 | 2995 | 215 | 18 | 0.12 | 2254 | 0.0875 | 2.5 | 0.71 | 4.1 | 0.0586 | 3.2 | 0.62 | 541 | 13 | 543 | 17 | 552 | 69 | 98 | met. |
| SPP36-8 | 14 | a44 | 12259 | 388 | 67 | 0.54 | 7258 | 0.1636 | 3.3 | 1.64 | 3.8 | 0.0728 | 2.0 | 0.86 | 977 | 30 | 987 | 25 | 1009 | 40 | 97 | mag. |
| SPP36-9 | 14 | a45 | 1741 | 618 | 21 | 0.21 | 2882 | 0.0351 | 2.3 | 0.25 | 5.5 | 0.0511 | 4.9 | 0.43 | 222 | 5 | 224 | 11 | 244 | 113 | 91 | mag. |
| SPP36-10r | 14 | a46 | 1841 | 300 | 15 | 0.81 | 3972 | 0.0454 | 2.7 | 0.32 | 5.3 | 0.0515 | 4.5 | 0.52 | 286 | 8 | 284 | 13 | 265 | 103 | 108 | mag. |
| SPP36-11 | 14 | a47 | 2960 | 180 | 19 | 0.34 | 5312 | 0.1039 | 3.0 | 0.86 | 4.4 | 0.0597 | 3.2 | 0.68 | 637 | 18 | 628 | 21 | 592 | 70 | 108 | met. |
| SPP36-12 | 14 | a48 | 735 | 183 | 7 | 0.80 | 2875 | 0.0324 | 2.7 | 0.22 | 7.1 | 0.0501 | 6.6 | 0.37 | 205 | 5 | 205 | 13 | 201 | 152 | 102 | mag. |
| SPP36-13 | 14 | a49 | 936 | 175 | 7 | 1.18 | 2917 | 0.0332 | 2.6 | 0.23 | 7.7 | 0.0505 | 7.2 | 0.34 | 210 | 5 | 211 | 15 | 219 | 167 | 96 | mag. |
| SPP36-14 | 14 | a50 | 2217 | 175 | 15 | 0.56 | 7705 | 0.0818 | 2.7 | 0.65 | 5.1 | 0.0574 | 4.4 | 0.52 | 507 | 13 | 507 | 21 | 509 | 96 | 100 | mag. |
| SPP36-15c | 14 | a51 | 1599 | 125 | 5 | 1.33 | 2366 | 0.0338 | 2.8 | 0.24 | 7.0 | 0.0505 | 6.4 | 0.41 | 214 | 6 | 214 | 14 | 216 | 147 | 99 | mag. |
| SPP36-16 | 14 | a52 | 1741 | 906 | 36 | 1.47 | 6957 | 0.0309 | 2.8 | 0.21 | 4.9 | 0.0495 | 4.0 | 0.57 | 196 | 5 | 194 | 9 | 172 | 93 | 114 | mag. |
| SPP36-17r | 14 | a53 | 3195 | 183 | 20 | 0.59 | 3120 | 0.1018 | 2.5 | 0.85 | 4.0 | 0.0606 | 3.1 | 0.62 | 625 | 15 | 625 | 19 | 626 | 67 | 100 | mag. |
| SPP36-17c | 14 | a54 | 3280 | 220 | 23 | 0.53 | 10501 | 0.1058 | 2.7 | 0.91 | 4.0 | 0.0627 | 3.0 | 0.66 | 648 | 16 | 659 | 20 | 699 | 64 | 93 | mag. |
| SPP36-18 | 14 | a55 | 540 | 127 | 5 | 1.23 | 2149 | 0.0315 | 3.5 | 0.22 | 7.5 | 0.0502 | 6.6 | 0.47 | 200 | 7 | 200 | 14 | 204 | 154 | 98 | mag. |
| SPP36-19 | 15 | a1 | 24770 | 1489 | 150 | 0.04 | 39719 | 0.1090 | 2.5 | 0.91 | 2.9 | 0.0604 | 1.5 | 0.85 | 667 | 16 | 656 | 14 | 617 | 33 | 108 | met. |
| SPP36-20 | 15 | a2 | 2378 | 205 | 19 | 0.44 | 4043 | 0.0884 | 2.2 | 0.71 | 3.9 | 0.0584 | 3.2 | 0.56 | 546 | 12 | 546 | 17 | 543 | 71 | 100 | mag. |
| SPP36-21 | 15 | a3 | 764 | 208 | 9 | 1.40 | 903 | 0.0323 | 2.7 | 0.22 | 7.9 | 0.0502 | 7.4 | 0.34 | 205 | 5 | 205 | 15 | 204 | 172 | 101 | mag. |
| SPP36-22 | 15 | a4 | 1113 | 306 | 13 | 1.55 | 2226 | 0.0320 | 2.9 | 0.22 | 6.4 | 0.0501 | 5.8 | 0.45 | 203 | 6 | 203 | 12 | 200 | 134 | 102 | mag. |
| SPP36-23 | 15 | a5 | 907 | 131 | 5 | 1.12 | 1596 | 0.0335 | 7.8 | 0.24 | 9.5 | 0.0510 | 5.4 | 0.82 | 212 | 16 | 215 | 19 | 242 | 125 | 88 | mag. |
| SPP36-24 | 15 | a6 | 22406 | 342 | 106 | 0.25 | 21495 | 0.3053 | 2.8 | 4.35 | 3.2 | 0.1034 | 1.4 | 0.89 | 1718 | 43 | 1703 | 27 | 1686 | 27 | 102 | met. |
| SPP36-25 | 15 | a7 | 1365 | 485 | 17 | 0.51 | 1723 | 0.0333 | 3.3 | 0.23 | 9.2 | 0.0505 | 8.6 | 0.36 | 211 | 7 | 212 | 18 | 217 | 199 | 97 | mag. |
| SPP36-26 | 15 | a8 | 1049 | 266 | 12 | 1.30 | 2068 | 0.0362 | 2.6 | 0.25 | 8.3 | 0.0507 | 7.9 | 0.32 | 229 | 6 | 229 | 17 | 226 | 183 | 102 | mag. |
| SPP36-27 | 15 | a9 | 1050 | 284 | 11 | 1.20 | 2092 | 0.0324 | 3.2 | 0.22 | 6.0 | 0.0500 | 5.1 | 0.53 | 206 | 6 | 205 | 11 | 196 | 118 | 105 | mag. |
| SPP36-28r | 15 | a10 | 7128 | 564 | 51 | 0.05 | 4428 | 0.0969 | 2.3 | 0.80 | 3.2 | 0.0600 | 2.3 | 0.70 | 596 | 13 | 597 | 15 | 602 | 50 | 99 | met. |
| SPP36-28c | 15 | a11 | 24128 | 64 | 59 | 1.88 | 4741 | 0.6189 | 3.0 | 21.66 | 3.3 | 0.2538 | 1.2 | 0.93 | 3106 | 75 | 3169 | 32 | 3209 | 19 | 97 | mag. |
| SPP36-29r | 15 | a12 | 5262 | 366 | 35 | 0.07 | 8585 | 0.1035 | 2.9 | 0.87 | 3.7 | 0.0610 | 2.4 | 0.77 | 635 | 17 | 636 | 18 | 638 | 51 | 100 | met. |
| SPP36-30 | 15 | a13 | 3237 | 256 | 29 | 1.00 | 5288 | 0.0981 | 3.0 | 0.80 | 5.2 | 0.0590 | 4.3 | 0.57 | 603 | 17 | 596 | 24 | 568 | 93 | 106 | mag. |
| SPP36-31 | 15 | a14 | 14091 | 510 | 91 | 0.52 | 10986 | 0.1698 | 3.4 | 1.69 | 4.0 | 0.0722 | 2.1 | 0.86 | 1011 | 32 | 1005 | 26 | 992 | 42 | 102 | mag. |
| SPP36-32r | 15 | a15 | 4223 | 1273 | 40 | 0.89 | 1593 | 0.0315 | 3.0 | 0.23 | 9.1 | 0.0524 | 8.6 | 0.33 | 200 | 6 | 208 | 17 | 304 | 196 | 66 | mag. |
| SPP36-33 | 15 | a16 | 2765 | 217 | 19 | 0.08 | 4541 | 0.0918 | 3.0 | 0.73 | 5.0 | 0.0577 | 4.0 | 0.61 | 566 | 16 | 557 | 22 | 518 | 87 | 109 | met. |
| SPP36-34 | 15 | a17 | 2494 | 193 | 19 | 0.47 | 4175 | 0.0939 | 3.0 | 0.77 | 5.2 | 0.0596 | 4.2 | 0.58 | 579 | 17 | 581 | 23 | 588 | 92 | 98 | mag. |
| SPP36-35 | 15 | a18 | 927 | 356 | 11 | 0.20 | 1655 | 0.0319 | 4.4 | 0.22 | 10.3 | 0.0502 | 9.3 | 0.43 | 202 | 9 | 203 | 19 | 205 | 215 | 99 | mag. |
| SPP36-36c | 15 | a19 | 2931 | 280 | 26 | 0.95 | 5032 | 0.0809 | 2.8 | 0.64 | 4.6 | 0.0577 | 3.7 | 0.59 | 501 | 13 | 505 | 19 | 519 | 82 | 97 | mag. |
| SPP36-37 | 15 | a20 | 7791 | 446 | 53 | 0.58 | 7460 | 0.1177 | 3.6 | 1.03 | 3.9 | 0.0636 | 1.5 | 0.92 | 717 | 24 | 720 | 20 | 729 | 32 | 98 | mag. |
| SPP36-38 | 15 | a21 | 1463 | 649 | 21 | 0.28 | 5916 | 0.0327 | 3.4 | 0.23 | 7.7 | 0.0500 | 6.9 | 0.44 | 208 | 7 | 207 | 14 | 195 | 160 | 106 | mag. |
| SPP36-39m | 15 | a22 | 8085 | 523 | 55 | 0.30 | 9716 | 0.1068 | 2.8 | 0.89 | 4.1 | 0.0604 | 2.9 | 0.69 | 654 | 17 | 646 | 20 | 617 | 63 | 106 | mag. |
| SPP36-40 | 15 | a23 | 908 | 207 | 8 | 0.53 | 1791 | 0.0368 | 3.8 | 0.26 | 6.5 | 0.0504 | 5.3 | 0.58 | 233 | 9 | 231 | 14 | 214 | 123 | 109 | mag. |
| SPP36-41 | 15 | a24 | 3090 | 655 | 31 | 1.03 | 5039 | 0.0418 | 3.6 | 0.30 | 5.0 | 0.0513 | 3.5 | 0.72 | 264 | 9 | 263 | 12 | 255 | 81 | 103 | mag. |
| SPP36-42 | 15 | a25 | 1638 | 395 | 16 | 0.81 | 3268 | 0.0370 | 2.7 | 0.26 | 5.7 | 0.0508 | 5.0 | 0.48 | 234 | 6 | 234 | 12 | 233 | 117 | 101 | mag. |
| SPP36-43r | 15 | a26 | 666 | 53 | 5 | 0.60 | 1140 | 0.0871 | 5.9 | 0.70 | 10.3 | 0.0582 | 8.4 | 0.57 | 538 | 30 | 538 | 44 | 536 | 185 | 100 | mag. |
| SPP36-43c | 15 | a27 | 9627 | 617 | 59 | 0.12 | 16040 | 0.1005 | 2.6 | 0.84 | 3.3 | 0.0606 | 2.0 | 0.80 | 617 | 16 | 619 | 15 | 625 | 43 | 99 | met. |
| SPP36-44 | 15 | a28 | 1689 | 131 | 14 | 0.55 | 1520 | 0.1008 | 2.2 | 0.83 | 4.6 | 0.0594 | 4.1 | 0.48 | 619 | 13 | 611 | 21 | 581 | 88 | 107 | mag. |
| SPP36-45 | 15 | a29 | 1751 | 703 | 26 | 0.51 | 8471 | 0.0364 | 2.9 | 0.25 | 6.7 | 0.0507 | 6.0 | 0.43 | 231 | 7 | 230 | 14 | 228 | 140 | 101 | mag. |
| SPP36-46r | 15 | a30 | 1178 | 183 | 24 | 1.44 | 1101 | 0.1064 | 3.4 | 0.90 | 5.9 | 0.0615 | 4.9 | 0.57 | 652 | 21 | 653 | 29 | 657 | 104 | 99 | mag. |
| SPP36-46c | 15 | a31 | 8238 | 509 | 55 | 0.14 | 7033 | 0.1144 | 2.1 | 0.97 | 2.9 | 0.0615 | 2.0 | 0.72 | 698 | 14 | 688 | 15 | 656 | 44 | 107 | met. |
| SPP36-47 | 15 | a32 | 13811 | 1061 | 104 | 0.46 | 23262 | 0.0951 | 3.5 | 0.77 | 4.1 | 0.0590 | 2.0 | 0.87 | 585 | 20 | 582 | 18 | 566 | 45 | 103 | mag. |
| SPP36-49 | 15 | a35 | 2261 | 547 | 25 | 1.92 | 3426 | 0.0327 | 2.5 | 0.23 | 3.9 | 0.0508 | 3.0 | 0.65 | 208 | 5 | 210 | 7 | 230 | 69 | 90 | mag. |
| SPP36-50 | 15 | a36 | 1732 | 127 | 13 | 0.74 | 2828 | 0.0967 | 2.7 | 0.78 | 5.3 | 0.0587 | 4.5 | 0.52 | 595 | 16 | 587 | 24 | 556 | 99 | 107 | mag. |
| SPP36-51 | 15 | a37 | 1699 | 424 | 18 | 1.51 | 3362 | 0.0339 | 2.3 | 0.24 | 4.9 | 0.0502 | 4.3 | 0.47 | 215 | 5 | 214 | 9 | 206 | 100 | 104 | mag. |
| SPP36-52 | 15 | a38 | 1476 | 361 | 15 | 1.61 | 2910 | 0.0312 | 2.2 | 0.22 | 4.0 | 0.0503 | 3.3 | 0.56 | 198 | 4 | 199 | 7 | 210 | 77 | 94 | mag. |
| SPP36-53r | 15 | a39 | 4730 | 355 | 33 | 0.22 | 7795 | 0.0955 | 2.5 | 0.79 | 3.6 | 0.0599 | 2.5 | 0.71 | 588 | 14 | 590 | 16 | 599 | 54 | 98 | met. |
| SPP36-54 | 15 | a40 | 3752 | 138 | 22 | 0.20 | 4365 | 0.1620 | 2.7 | 1.55 | 4.3 | 0.0693 | 3.3 | 0.63 | 968 | 24 | 950 | 27 | 908 | 69 | 107 | met. |
| SPP36-55c | 15 | a41 | 5977 | 199 | 32 | 0.18 | 8228 | 0.1656 | 2.7 | 1.64 | 3.6 | 0.0717 | 2.4 | 0.75 | 988 | 24 | 985 | 23 | 979 | 48 | 101 | met. |
| SPP36-56 | 15 | a42 | 1020 | 265 | 10 | 1.00 | 2026 | 0.0331 | 3.0 | 0.23 | 5.9 | 0.0501 | 5.1 | 0.50 | 210 | 6 | 209 | 11 | 201 | 119 | 104 | mag. |
| SPP36-57 | 15 | a43 | 5259 | 235 | 38 | 0.51 | 7680 | 0.1594 | 3.3 | 1.50 | 5.4 | 0.0684 | 4.2 | 0.62 | 954 | 30 | 932 | 33 | 881 | 87 | 108 | mag. |
| SPP36-58 | 15 | a44 | 2419 | 632 | 24 | 1.10 | 2654 | 0.0324 | 2.4 | 0.22 | 4.9 | 0.0501 | 4.3 | 0.48 | 206 | 5 | 205 | 9 | 198 | 101 | 104 | mag. |
| SPP36-59m | 15 | a45 | 1287 | 321 | 11 | 0.35 | 1564 | 0.0345 | 3.3 | 0.24 | 9.7 | 0.0504 | 9.1 | 0.34 | 219 | 7 | 218 | 19 | 215 | 211 | 102 | mag. |
| SPP36-59c | 15 | a46 | 2395 | 609 | 29 | 2.06 | 4739 | 0.0344 | 2.3 | 0.24 | 4.5 | 0.0503 | 3.9 | 0.50 | 218 | 5 | 217 | 9 | 209 | 90 | 104 | mag. |
| SPP36-60 | 15 | a47 | 2127 | 184 | 16 | 0.53 | 3663 | 0.0833 | 2.4 | 0.66 | 4.4 | 0.0576 | 3.8 | 0.53 | 516 | 12 | 515 | 18 | 513 | 82 | 100 | mag. |
| SPP36-61 | 15 | a48 | 8746 | 755 | 60 | 1.00 | 11861 | 0.0725 | 2.5 | 0.61 | 3.1 | 0.0612 | 1.9 | 0.80 | 451 | 11 | 485 | 12 | 648 | 40 | 70 | mag. |
| SPP36-62 | 15 | a49 | 2439 | 142 | 18 | 0.65 | 3894 | 0.1204 | 3.4 | 1.05 | 6.1 | 0.0635 | 5.1 | 0.55 | 733 | 23 | 731 | 32 | 725 | 107 | 101 | mag. |
| SPP36-63r | 15 | a50 | 12686 | 418 | 75 | 0.33 | 6093 | 0.1794 | 2.6 | 1.79 | 3.1 | 0.0725 | 1.8 | 0.82 | 1063 | 25 | 1043 | 21 | 999 | 37 | 106 | mag. |
| SPP36-63c | 15 | a51 | 8485 | 276 | 51 | 0.45 | 6534 | 0.1775 | 3.0 | 1.78 | 3.9 | 0.0726 | 2.4 | 0.78 | 1053 | 30 | 1037 | 25 | 1002 | 49 | 105 | mag. |
| SPP36-64r | 15 | a52 | 3990 | 221 | 22 | 0.03 | 6258 | 0.1070 | 2.6 | 0.92 | 3.8 | 0.0627 | 2.9 | 0.67 | 655 | 16 | 665 | 19 | 698 | 61 | 94 | met. |
| SPP36-64c | 15 | a53 | 7552 | 192 | 41 | 0.74 | 9451 | 0.1928 | 2.6 | 2.10 | 3.3 | 0.0789 | 2.0 | 0.79 | 1137 | 28 | 1148 | 23 | 1170 | 40 | 97 | mag. |
| SPP36-65 | 15 | a54 | 9396 | 314 | 54 | 0.39 | 8590 | 0.1689 | 2.7 | 1.67 | 3.4 | 0.0716 | 2.1 | 0.78 | 1006 | 25 | 996 | 22 | 973 | 44 | 103 | mag. |
| SPP36-66 | 15 | a55 | 2073 | 105 | 14 | 0.75 | 1488 | 0.1246 | 2.3 | 1.12 | 4.6 | 0.0650 | 4.0 | 0.50 | 757 | 16 | 762 | 25 | 775 | 83 | 98 | mag. |
| SPP36-67r | 16 | a1 | 964 | 54 | 5 | 0.82 | 1936 | 0.0825 | 2.8 | 0.67 | 8.0 | 0.0587 | 7.5 | 0.34 | 511 | 14 | 519 | 33 | 556 | 165 | 92 | mag. |
| SPP36-68 | 16 | a2 | 11794 | 255 | 46 | 0.30 | 2142 | 0.1796 | 2.3 | 1.89 | 2.7 | 0.0764 | 1.5 | 0.84 | 1065 | 23 | 1078 | 18 | 1106 | 30 | 96 | mag. |

# Results of U-Th-Pb LA-ICPMS analyses of zircons from sample SPP36 (continuation)

| Spot | Seq. | No. | $^{207}Pb$ [a] (cps) | U [b] (ppm) | Pb [b] (ppm) | Th/U [b] | $^{206}Pb/^{204}Pb$ | $^{206}Pb/^{238}U$ [c] | ±2s (%) | $^{207}Pb/^{235}U$ [c] | ±2s (%) | $^{207}Pb/^{206}Pb$ [c] | ±2s (%) | Rho [d] | Age (Ma) $^{206}Pb/^{238}U$ | ±2s | Age (Ma) $^{207}Pb/^{235}U$ | ±2s | Age (Ma) $^{207}Pb/^{206}Pb$ [c] | ±2s | conc [e] (%) | Origin [f] |
|---|---|---|---|---|---|---|---|---|---|---|---|---|---|---|---|---|---|---|---|---|---|---|
| SPP36-69 | 16 | a3 | 2040 | 78 | 13 | 0.02 | 1338 | 0.1608 | 4.9 | 1.53 | 7.5 | 0.0688 | 5.7 | 0.66 | 961 | 44 | 941 | 47 | 893 | 117 | 108 | met. |
| SPP36-70 | 16 | a4 | 5449 | 260 | 26 | 0.38 | 15143 | 0.0992 | 2.3 | 0.82 | 3.2 | 0.0597 | 2.2 | 0.72 | 610 | 13 | 606 | 15 | 594 | 48 | 103 | mag. |
| SPP36-71 | 16 | a5 | 2154 | 327 | 13 | 1.10 | 7138 | 0.0325 | 2.8 | 0.23 | 4.2 | 0.0502 | 3.1 | 0.67 | 206 | 6 | 206 | 8 | 206 | 72 | 100 | mag. |
| SPP36-72c | 16 | a6 | 9271 | 208 | 35 | 0.62 | 4641 | 0.1556 | 2.6 | 1.55 | 3.4 | 0.0721 | 2.2 | 0.77 | 932 | 23 | 949 | 21 | 988 | 45 | 94 | mag. |
| SPP36-73c | 16 | a7 | 16917 | 145 | 46 | 0.50 | 13326 | 0.2979 | 4.6 | 4.16 | 5.3 | 0.1013 | 2.8 | 0.85 | 1681 | 68 | 1666 | 45 | 1648 | 51 | 102 | mag. |
| SPP36-74c | 16 | a8 | 10380 | 205 | 38 | 0.51 | 23219 | 0.1785 | 3.4 | 1.82 | 4.0 | 0.0740 | 2.2 | 0.84 | 1059 | 33 | 1053 | 27 | 1043 | 44 | 102 | mag. |
| SPP36-75 | 16 | a9 | 1591 | 142 | 8 | 1.60 | 5090 | 0.0448 | 3.7 | 0.32 | 7.6 | 0.0521 | 6.6 | 0.48 | 283 | 10 | 283 | 19 | 291 | 151 | 97 | mag. |
| SPP36-76c | 16 | a10 | 2968 | 145 | 13 | 0.33 | 8572 | 0.0880 | 2.7 | 0.70 | 4.3 | 0.0577 | 3.4 | 0.61 | 543 | 14 | 539 | 18 | 519 | 75 | 105 | mag. |
| SPP36-77 | 16 | a11 | 2213 | 309 | 14 | 2.33 | 7335 | 0.0318 | 2.7 | 0.22 | 5.5 | 0.0506 | 4.8 | 0.49 | 202 | 5 | 203 | 10 | 221 | 110 | 91 | mag. |
| SPP36-78 | 16 | a12 | 2243 | 317 | 15 | 2.33 | 7473 | 0.0315 | 2.7 | 0.22 | 5.4 | 0.0501 | 4.6 | 0.51 | 200 | 5 | 200 | 10 | 201 | 107 | 99 | mag. |
| SPP36-79 | 16 | a13 | 3686 | 494 | 21 | 1.14 | 11858 | 0.0351 | 2.9 | 0.25 | 3.6 | 0.0516 | 2.2 | 0.80 | 222 | 6 | 226 | 7 | 269 | 50 | 82 | mag. |
| SPP36-80 | 16 | a14 | 3726 | 449 | 21 | 1.23 | 11962 | 0.0385 | 2.8 | 0.27 | 3.5 | 0.0516 | 2.2 | 0.79 | 244 | 7 | 246 | 8 | 270 | 49 | 90 | mag. |
| SPP36-81r | 16 | a15 | 4865 | 129 | 19 | 0.47 | 11966 | 0.1478 | 2.8 | 1.37 | 3.4 | 0.0674 | 1.9 | 0.83 | 889 | 23 | 878 | 20 | 849 | 39 | 105 | mag. |
| SPP36-81c | 16 | a16 | 5138 | 247 | 23 | 0.50 | 14476 | 0.0927 | 2.4 | 0.75 | 3.7 | 0.0586 | 2.9 | 0.64 | 572 | 13 | 567 | 16 | 550 | 62 | 104 | mag. |
| SPP36-82r | 16 | a17 | 1157 | 32 | 5 | 3.33 | 2140 | 0.0974 | 3.8 | 0.79 | 6.8 | 0.0589 | 5.7 | 0.56 | 599 | 22 | 592 | 31 | 564 | 124 | 106 | mag. |
| SPP36-82c | 16 | a18 | 6254 | 312 | 28 | 0.56 | 17783 | 0.0883 | 2.6 | 0.71 | 3.8 | 0.0580 | 2.7 | 0.70 | 545 | 14 | 542 | 16 | 528 | 59 | 103 | mag. |
| SPP36-83 | 16 | a19 | 6372 | 313 | 31 | 0.73 | 18239 | 0.0900 | 2.3 | 0.72 | 3.2 | 0.0580 | 2.1 | 0.74 | 556 | 12 | 551 | 14 | 531 | 47 | 105 | mag. |
| SPP36-84c | 16 | a20 | 993 | 61 | 6 | 0.81 | 7096 | 0.0877 | 3.1 | 0.69 | 5.6 | 0.0574 | 4.7 | 0.54 | 542 | 16 | 536 | 24 | 508 | 104 | 107 | mag. |
| SPP36-85 | 16 | a21 | 1377 | 79 | 4 | 0.90 | 6222 | 0.0425 | 4.2 | 0.30 | 9.7 | 0.0513 | 8.8 | 0.43 | 268 | 11 | 267 | 23 | 254 | 202 | 106 | mag. |
| SPP36-86r | 16 | a22 | 27103 | 114 | 62 | 0.73 | 11513 | 0.4851 | 2.6 | 11.81 | 3.2 | 0.1765 | 1.9 | 0.81 | 2549 | 55 | 2589 | 31 | 2621 | 31 | 97 | mag. |
| SPP36-86c | 16 | a23 | 125646 | 366 | 176 | 0.15 | 51509 | 0.4587 | 2.4 | 11.53 | 2.6 | 0.1823 | 1.1 | 0.91 | 2434 | 48 | 2567 | 25 | 2674 | 18 | 91 | met. |
| SPP36-87 | 16 | a24 | 1369 | 83 | 7 | 1.03 | 4089 | 0.0766 | 2.9 | 0.59 | 5.6 | 0.0558 | 4.9 | 0.51 | 476 | 13 | 471 | 21 | 445 | 108 | 107 | mag. |
| SPP36-88 | 16 | a25 | 6218 | 320 | 29 | 0.27 | 17464 | 0.0935 | 2.5 | 0.75 | 3.5 | 0.0585 | 2.4 | 0.72 | 576 | 14 | 571 | 15 | 549 | 52 | 105 | met. |
| SPP36-89r | 16 | a26 | 2124 | 106 | 13 | 1.81 | 5981 | 0.0887 | 2.8 | 0.72 | 4.7 | 0.0588 | 3.8 | 0.59 | 548 | 14 | 550 | 20 | 558 | 83 | 98 | mag. |
| SPP36-90 | 16 | a27 | 31911 | 113 | 59 | 0.59 | 33181 | 0.4599 | 2.8 | 10.13 | 3.1 | 0.1597 | 1.4 | 0.89 | 2439 | 56 | 2446 | 29 | 2452 | 24 | 99 | mag. |
| SPP36-91r | 16 | a28 | 2390 | 116 | 10 | 0.46 | 6837 | 0.0865 | 2.7 | 0.69 | 4.6 | 0.0579 | 3.8 | 0.58 | 535 | 14 | 533 | 19 | 525 | 83 | 102 | mag. |
| SPP36-92 | 16 | a29 | 868 | 69 | 4 | 1.32 | 3495 | 0.0411 | 2.5 | 0.29 | 8.0 | 0.0514 | 7.6 | 0.31 | 260 | 6 | 260 | 19 | 259 | 175 | 100 | mag. |
| SPP36-93 | 16 | a30 | 71368 | 118 | 5 | 1.96 | 19235 | 0.0307 | 2.5 | 0.21 | 4.6 | 0.0496 | 3.8 | 0.55 | 195 | 5 | 193 | 8 | 179 | 89 | 109 | mag. |
| SPP36-94 | 16 | a31 | 3925 | 211 | 19 | 0.66 | 1855 | 0.0855 | 2.6 | 0.68 | 3.4 | 0.0575 | 2.2 | 0.77 | 529 | 13 | 526 | 14 | 511 | 48 | 103 | mag. |
| SPP36-95 | 16 | a32 | 8155 | 167 | 31 | 0.44 | 18532 | 0.1790 | 3.3 | 1.80 | 3.9 | 0.0729 | 2.1 | 0.84 | 1061 | 32 | 1045 | 26 | 1012 | 43 | 105 | mag. |
| SPP36-96 | 16 | a33 | 1422 | 244 | 9 | 1.29 | 4688 | 0.0315 | 2.9 | 0.22 | 5.6 | 0.0504 | 4.7 | 0.52 | 200 | 6 | 201 | 10 | 213 | 110 | 94 | mag. |
| SPP36-97c | 16 | a34 | 1449 | 138 | 5 | 0.90 | 2820 | 0.0306 | 3.7 | 0.21 | 9.4 | 0.0504 | 8.7 | 0.40 | 194 | 7 | 196 | 17 | 212 | 201 | 92 | mag. |
| SPP36-98r | 16 | a35 | 3117 | 182 | 14 | 0.07 | 8925 | 0.0806 | 2.6 | 0.64 | 4.0 | 0.0579 | 3.0 | 0.65 | 500 | 13 | 505 | 16 | 527 | 67 | 95 | met. |
| SPP36-98c | 16 | a36 | 1287 | 54 | 4 | 0.00 | 2490 | 0.0781 | 5.2 | 0.62 | 11.2 | 0.0576 | 10.0 | 0.46 | 485 | 24 | 490 | 45 | 516 | 219 | 94 | met. |
| SPP36-99 | 16 | a37 | 12017 | 289 | 47 | 0.68 | 5203 | 0.1521 | 2.5 | 1.48 | 3.1 | 0.0704 | 1.7 | 0.83 | 913 | 22 | 921 | 19 | 941 | 36 | 97 | mag. |
| SPP36-100 | 16 | a38 | 6222 | 115 | 21 | 0.09 | 13417 | 0.1899 | 3.4 | 2.01 | 4.2 | 0.0768 | 2.5 | 0.80 | 1121 | 35 | 1120 | 29 | 1117 | 51 | 100 | met. |

# Results of U-Th-Pb LA-ICPMS analyses of zircons from sample CHW07

| Spot | Seq. | No. | $^{207}Pb$ [a] (cps) | U [b] (ppm) | Pb [b] (ppm) | Th [b] U | $^{206}Pb/^{204}Pb$ | $^{206}Pb^{c}/^{238}U$ | ±2s (%) | $^{207}Pb^{c}/^{235}U$ | ±2s (%) | $^{207}Pb^{c}/^{206}Pb$ | ±2s (%) | Rho [d] | Age (Ma) $^{206}Pb/^{238}U$ | ±2s | $^{207}Pb/^{235}U$ | ±2s | $^{207}Pb^{c}/^{206}Pb$ | ±2s | conc [e] (%) | Origin [f] |
|---|---|---|---|---|---|---|---|---|---|---|---|---|---|---|---|---|---|---|---|---|---|---|
| CHW07-1r | 4 | a17 | 2368 | 105 | 11 | 1.06 | 4594 | 0.0911 | 2.3 | 0.75 | 3.6 | 0.0596 | 2.8 | 0.64 | 562 | 12 | 567 | 16 | 587 | 60 | 96 | mag. |
| CHW07-1c | 4 | a18 | 3426 | 222 | 21 | 0.54 | 8382 | 0.0916 | 2.2 | 0.74 | 2.8 | 0.0582 | 1.8 | 0.77 | 565 | 12 | 560 | 12 | 537 | 40 | 105 | mag. |
| CHW07-2 | 4 | a19 | 4184 | 233 | 28 | 0.62 | 7545 | 0.1157 | 3.4 | 0.99 | 4.4 | 0.0620 | 2.8 | 0.77 | 706 | 23 | 698 | 22 | 674 | 60 | 105 | mag. |
| CHW07-4r | 4 | a21 | 395 | 84 | 4 | 0.63 | 1462 | 0.0398 | 3.0 | 0.29 | 7.4 | 0.0529 | 6.8 | 0.40 | 252 | 7 | 259 | 17 | 324 | 154 | 78 | mag. |
| CHW07-5 | 4 | a23 | 4444 | 431 | 39 | 0.58 | 5934 | 0.0849 | 2.5 | 0.67 | 3.2 | 0.0574 | 2.0 | 0.78 | 525 | 13 | 522 | 13 | 507 | 44 | 104 | mag. |
| CHW07-6 | 4 | a24 | 832 | 85 | 8 | 0.91 | 519 | 0.0828 | 3.1 | 0.65 | 5.6 | 0.0571 | 4.6 | 0.55 | 513 | 15 | 509 | 22 | 494 | 102 | 104 | mag. |
| CHW07-7 | 4 | a25 | 1319 | 56 | 9 | 0.46 | 3565 | 0.1625 | 2.3 | 1.63 | 4.2 | 0.0729 | 3.5 | 0.56 | 971 | 21 | 983 | 27 | 1011 | 70 | 96 | mag. |
| CHW07-8r | 4 | a26 | 2114 | 314 | 19 | 0.57 | 1165 | 0.0582 | 2.3 | 0.43 | 3.6 | 0.0537 | 2.8 | 0.64 | 365 | 8 | 364 | 11 | 358 | 62 | 102 | mag. |
| CHW07-9r | 4 | a27 | 2606 | 215 | 23 | 0.38 | 2772 | 0.1084 | 2.8 | 0.92 | 4.2 | 0.0616 | 3.0 | 0.68 | 664 | 18 | 663 | 20 | 661 | 65 | 100 | mag. |
| CHW07-10 | 4 | a28 | 5657 | 417 | 50 | 1.02 | 17891 | 0.1021 | 2.2 | 0.87 | 2.9 | 0.0617 | 1.8 | 0.78 | 627 | 13 | 635 | 14 | 663 | 38 | 95 | mag. |
| CHW07-11c | 4 | a29 | 3562 | 146 | 26 | 0.39 | 3062 | 0.1778 | 2.9 | 1.79 | 3.5 | 0.0729 | 2.0 | 0.82 | 1055 | 28 | 1041 | 23 | 1012 | 41 | 104 | mag. |
| CHW07-12 | 4 | a30 | 7293 | 359 | 70 | 0.77 | 1795 | 0.1812 | 2.4 | 1.77 | 3.2 | 0.0710 | 2.0 | 0.77 | 1074 | 24 | 1036 | 21 | 958 | 41 | 112 | mag. |
| CHW07-13 | 4 | a31 | 1857 | 151 | 17 | 0.48 | 6096 | 0.1121 | 3.0 | 0.94 | 4.9 | 0.0608 | 3.8 | 0.62 | 685 | 20 | 673 | 24 | 633 | 83 | 108 | mag. |
| CHW07-14 | 4 | a32 | 705 | 190 | 8 | 0.68 | 2730 | 0.0410 | 2.6 | 0.29 | 6.2 | 0.0514 | 5.6 | 0.42 | 259 | 7 | 259 | 14 | 258 | 130 | 100 | mag. |
| CHW07-15 | 4 | a33 | 805 | 282 | 11 | 1.19 | 3147 | 0.0324 | 3.0 | 0.22 | 6.2 | 0.0500 | 5.4 | 0.49 | 205 | 6 | 204 | 12 | 194 | 126 | 106 | mag. |
| CHW07-16r | 4 | a34 | 214 | 43 | 2 | 1.47 | 585 | 0.0320 | 6.3 | 0.23 | 8.8 | 0.0514 | 6.2 | 0.72 | 203 | 13 | 207 | 17 | 259 | 142 | 78 | mag. |
| CHW07-16c | 4 | a35 | 569 | 153 | 6 | 1.49 | 2183 | 0.0310 | 3.4 | 0.22 | 7.1 | 0.0505 | 6.2 | 0.47 | 197 | 7 | 199 | 13 | 217 | 144 | 91 | mag. |
| CHW07-17c | 4 | a36 | 7933 | 291 | 54 | 0.27 | 5575 | 0.1880 | 4.4 | 1.90 | 4.9 | 0.0735 | 2.2 | 0.90 | 1110 | 45 | 1083 | 33 | 1027 | 44 | 108 | mag. |
| CHW07-18 | 4 | a37 | 297 | 28 | 3 | 0.39 | 1009 | 0.0893 | 3.6 | 0.73 | 10.3 | 0.0594 | 9.6 | 0.35 | 551 | 19 | 557 | 45 | 581 | 209 | 95 | met. |
| CHW07-19 | 4 | a38 | 1159 | 141 | 7 | 1.46 | 221 | 0.0303 | 2.8 | 0.55 | 26.9 | 0.1315 | 26.7 | 0.11 | 192 | 5 | 444 | 102 | 2118 | 469 | 9 | mag. |
| CHW07-20r | 4 | a39 | 3329 | 309 | 29 | 0.45 | 11091 | 0.0939 | 3.5 | 0.77 | 4.7 | 0.0596 | 3.1 | 0.75 | 579 | 20 | 581 | 21 | 589 | 67 | 98 | mag. |
| CHW07-21 | 4 | a40 | 2225 | 82 | 15 | 0.30 | 5804 | 0.1785 | 3.1 | 1.85 | 5.0 | 0.0752 | 4.0 | 0.61 | 1059 | 30 | 1064 | 34 | 1075 | 80 | 98 | mag. |
| CHW07-22c | 4 | a41 | 6578 | 553 | 59 | 0.34 | 5063 | 0.1094 | 3.4 | 0.94 | 6.7 | 0.0620 | 5.8 | 0.51 | 669 | 22 | 670 | 33 | 674 | 123 | 99 | unc. |
| CHW07-23r | 4 | a42 | 349 | 35 | 4 | 2.21 | 1013 | 0.0884 | 3.9 | 0.69 | 8.0 | 0.0569 | 7.0 | 0.49 | 546 | 21 | 535 | 34 | 487 | 154 | 112 | mag. |
| CHW07-23c | 4 | a43 | 650 | 43 | 6 | 0.76 | 2063 | 0.1249 | 3.7 | 1.08 | 6.1 | 0.0626 | 4.9 | 0.60 | 759 | 27 | 743 | 33 | 696 | 105 | 109 | mag. |
| CHW07-24 | 4 | a44 | 951 | 325 | 13 | 1.50 | 3737 | 0.0321 | 3.5 | 0.22 | 5.6 | 0.0503 | 4.4 | 0.62 | 204 | 7 | 204 | 10 | 207 | 103 | 99 | mag. |
| CHW07-25 | 4 | a45 | 489 | 166 | 6 | 1.43 | 1941 | 0.0313 | 4.3 | 0.21 | 8.0 | 0.0498 | 6.8 | 0.54 | 198 | 8 | 197 | 15 | 184 | 158 | 108 | mag. |
| CHW07-26 | 4 | a46 | 7878 | 356 | 56 | 0.15 | 22425 | 0.1642 | 3.1 | 1.60 | 3.7 | 0.0706 | 2.1 | 0.82 | 980 | 28 | 970 | 23 | 947 | 43 | 103 | met. |
| CHW07-27 | 4 | a47 | 3047 | 240 | 25 | 0.42 | 1864 | 0.1028 | 4.0 | 0.88 | 6.5 | 0.0622 | 5.1 | 0.61 | 631 | 24 | 642 | 31 | 682 | 110 | 92 | mag. |
| CHW07-28 | 4 | a48 | 9925 | 37 | 25 | 0.49 | 8725 | 0.5782 | 2.9 | 17.87 | 3.5 | 0.2241 | 2.0 | 0.83 | 2941 | 68 | 2983 | 34 | 3011 | 31 | 98 | mag. |
| CHW07-29c | 4 | a49 | 13338 | 543 | 103 | 0.43 | 36382 | 0.1843 | 3.1 | 1.86 | 3.5 | 0.0731 | 1.6 | 0.89 | 1090 | 31 | 1066 | 23 | 1016 | 32 | 107 | mag. |
| CHW07-30r | 4 | a50 | 537 | 167 | 7 | 1.29 | 2115 | 0.0340 | 3.6 | 0.24 | 6.7 | 0.0509 | 5.7 | 0.53 | 215 | 8 | 217 | 13 | 234 | 131 | 92 | mag. |
| CHW07-31 | 4 | a51 | 2060 | 100 | 20 | 0.93 | 5737 | 0.1810 | 2.8 | 1.80 | 5.5 | 0.0723 | 4.7 | 0.52 | 1072 | 28 | 1047 | 36 | 995 | 95 | 108 | mag. |
| CHW07-32r | 4 | a52 | 3477 | 363 | 36 | 0.16 | 3700 | 0.1056 | 3.1 | 0.88 | 4.5 | 0.0604 | 3.3 | 0.68 | 647 | 19 | 641 | 22 | 618 | 72 | 105 | met. |
| CHW07-32c | 4 | a53 | 4123 | 184 | 32 | 0.34 | 11476 | 0.1764 | 3.8 | 1.73 | 4.5 | 0.0712 | 2.5 | 0.84 | 1047 | 37 | 1020 | 29 | 962 | 51 | 109 | mag. |
| CHW07-33c | 4 | a54 | 6368 | 364 | 51 | 0.34 | 18450 | 0.1387 | 3.4 | 1.32 | 4.3 | 0.0688 | 2.6 | 0.79 | 837 | 27 | 853 | 25 | 894 | 54 | 94 | mag. |
| CHW07-33r | 4 | a55 | 4236 | 418 | 41 | 0.14 | 14155 | 0.1039 | 2.9 | 0.85 | 3.5 | 0.0596 | 1.9 | 0.84 | 637 | 18 | 627 | 16 | 590 | 41 | 108 | met. |
| CHW07-34c | 5 | a1 | 263 | 187 | 19 | 0.19 | 873 | 0.1079 | 3.9 | 0.95 | 11.9 | 0.0638 | 11.2 | 0.33 | 661 | 24 | 678 | 61 | 736 | 238 | 90 | mag. |
| CHW07-35r | 5 | a2 | 206 | 394 | 17 | 1.48 | 799 | 0.0350 | 4.5 | 0.25 | 10.9 | 0.0519 | 9.9 | 0.41 | 222 | 10 | 227 | 22 | 283 | 227 | 78 | mag. |
| CHW07-36 | 5 | a3 | 779 | 200 | 34 | 0.81 | 2168 | 0.1545 | 3.0 | 1.56 | 6.1 | 0.0733 | 5.3 | 0.49 | 926 | 26 | 955 | 38 | 1023 | 107 | 91 | mag. |
| CHW07-37 | 5 | a4 | 133 | 176 | 7 | 0.94 | 515 | 0.0340 | 4.0 | 0.23 | 10.7 | 0.0497 | 9.9 | 0.37 | 216 | 9 | 213 | 21 | 179 | 232 | 120 | mag. |
| CHW07-38 | 5 | a5 | 26 | 27 | 1 | 0.68 | 92 | 0.0313 | 13.0 | 0.22 | 20.5 | 0.0509 | 15.8 | 0.63 | 199 | 25 | 201 | 38 | 235 | 365 | 84 | mag. |
| CHW07-39 | 5 | a6 | 56 | 58 | 2 | 0.82 | 227 | 0.0320 | 5.4 | 0.22 | 16.1 | 0.0497 | 15.2 | 0.33 | 203 | 11 | 202 | 30 | 183 | 354 | 111 | mag. |
| CHW07-40 | 5 | a7 | 744 | 192 | 22 | 1.31 | 2479 | 0.0946 | 3.6 | 0.79 | 6.6 | 0.0603 | 5.5 | 0.55 | 582 | 20 | 589 | 30 | 613 | 120 | 95 | mag. |
| CHW07-41 | 5 | a8 | 110 | 95 | 4 | 1.64 | 450 | 0.0317 | 4.3 | 0.22 | 14.6 | 0.0503 | 13.9 | 0.29 | 201 | 8 | 201 | 27 | 208 | 323 | 97 | mag. |
| CHW07-42r | 5 | a9 | 28 | 17 | 1 | 2.51 | 100 | 0.0331 | 10.5 | 0.24 | 18.2 | 0.0530 | 14.9 | 0.57 | 210 | 22 | 220 | 37 | 329 | 339 | 64 | mag. |
| CHW07-43 | 5 | a10 | 303 | 69 | 7 | 0.73 | 1007 | 0.0953 | 4.5 | 0.78 | 8.3 | 0.0592 | 7.0 | 0.54 | 587 | 25 | 584 | 38 | 574 | 153 | 102 | mag. |
| CHW07-44 | 5 | a11 | 218 | 125 | 4 | 0.36 | 848 | 0.0348 | 2.5 | 0.25 | 10.0 | 0.0511 | 9.7 | 0.25 | 221 | 5 | 223 | 20 | 244 | 223 | 90 | mag. |
| CHW07-45 | 5 | a12 | 423 | 66 | 6 | 0.84 | 453 | 0.0868 | 5.0 | 0.68 | 9.6 | 0.0572 | 8.3 | 0.52 | 536 | 26 | 530 | 41 | 500 | 182 | 107 | mag. |
| CHW07-46r | 5 | a13 | 1763 | 201 | 23 | 0.04 | 5675 | 0.1222 | 2.9 | 1.05 | 5.2 | 0.0624 | 4.3 | 0.56 | 743 | 21 | 729 | 27 | 688 | 91 | 108 | met. |
| CHW07-46c | 5 | a14 | 1406 | 82 | 12 | 0.12 | 3954 | 0.1528 | 6.3 | 1.47 | 8.1 | 0.0696 | 5.1 | 0.78 | 916 | 54 | 916 | 50 | 916 | 105 | 100 | met. |
| CHW07-47 | 5 | a15 | 71 | 25 | 1 | 1.29 | 231 | 0.0326 | 3.3 | 0.24 | 11.4 | 0.0523 | 10.9 | 0.29 | 207 | 7 | 215 | 22 | 300 | 248 | 69 | mag. |
| CHW07-48r | 5 | a16 | 602 | 72 | 7 | 0.46 | 2019 | 0.0902 | 3.9 | 0.74 | 8.0 | 0.0598 | 7.1 | 0.48 | 557 | 21 | 565 | 35 | 596 | 153 | 94 | mag. |
| CHW07-48c | 5 | a17 | 590 | 45 | 7 | 0.24 | 1711 | 0.1593 | 3.9 | 1.50 | 7.6 | 0.0684 | 6.6 | 0.51 | 953 | 35 | 931 | 48 | 880 | 136 | 108 | mag. |
| CHW07-49 | 5 | a18 | 37 | 14 | 1 | 1.55 | 144 | 0.0362 | 6.8 | 0.25 | 34.8 | 0.0505 | 34.2 | 0.20 | 229 | 15 | 228 | 74 | 218 | 791 | 105 | mag. |
| CHW07-50 | 5 | a19 | 71 | 26 | 1 | 0.90 | 296 | 0.0307 | 4.9 | 0.21 | 18.2 | 0.0502 | 17.6 | 0.27 | 195 | 9 | 196 | 33 | 205 | 408 | 95 | mag. |
| CHW07-53 | 5 | a22 | 177 | 41 | 2 | 1.78 | 510 | 0.0330 | 4.5 | 0.34 | 13.6 | 0.0740 | 12.8 | 0.33 | 209 | 9 | 294 | 35 | 1041 | 259 | 20 | mag. |
| CHW07-54r | 5 | a23 | 52 | 12 | 0 | 1.62 | 164 | 0.0353 | 6.0 | 0.25 | 13.8 | 0.0523 | 12.4 | 0.43 | 224 | 13 | 230 | 29 | 300 | 284 | 75 | mag. |
| CHW07-54c | 5 | a24 | 108 | 32 | 1 | 1.52 | 448 | 0.0318 | 3.7 | 0.22 | 10.2 | 0.0497 | 9.5 | 0.36 | 202 | 7 | 200 | 19 | 180 | 221 | 112 | mag. |
| CHW07-55r | 5 | a27 | 2127 | 197 | 19 | 0.36 | 7249 | 0.0941 | 2.3 | 0.77 | 3.7 | 0.0590 | 2.9 | 0.62 | 580 | 13 | 577 | 17 | 567 | 64 | 102 | mag. |
| CHW07-55c | 5 | a28 | 571 | 55 | 5 | 0.42 | 2042 | 0.0924 | 3.2 | 0.73 | 6.5 | 0.0572 | 5.6 | 0.49 | 570 | 17 | 555 | 28 | 497 | 124 | 115 | mag. |
| CHW07-56 | 5 | a29 | 399 | 121 | 4 | 0.83 | 148 | 0.0326 | 4.0 | 0.24 | 9.2 | 0.0534 | 8.3 | 0.44 | 207 | 8 | 218 | 18 | 345 | 187 | 60 | mag. |
| CHW07-57r | 5 | a30 | 678 | 141 | 7 | 1.34 | 2423 | 0.0391 | 2.6 | 0.27 | 5.9 | 0.0504 | 5.3 | 0.44 | 247 | 6 | 244 | 13 | 216 | 122 | 115 | mag. |
| CHW07-58 | 5 | a31 | 969 | 291 | 10 | 0.55 | 3785 | 0.0329 | 3.5 | 0.24 | 6.9 | 0.0526 | 5.9 | 0.50 | 208 | 7 | 217 | 13 | 313 | 135 | 67 | mag. |
| CHW07-59 | 5 | a32 | 8827 | 657 | 64 | 0.02 | 8880 | 0.1060 | 3.4 | 0.86 | 4.2 | 0.0591 | 2.4 | 0.82 | 650 | 21 | 632 | 20 | 570 | 52 | 114 | met. |
| CHW07-60c | 5 | a33 | 215 | 19 | 5 | 7.78 | 791 | 0.0857 | 3.5 | 0.66 | 11.3 | 0.0556 | 10.8 | 0.31 | 530 | 18 | 512 | 47 | 435 | 240 | 122 | mag. |
| CHW07-61r | 5 | a34 | 914 | 183 | 7 | 1.66 | 2801 | 0.0311 | 3.2 | 0.23 | 7.2 | 0.0541 | 6.5 | 0.44 | 197 | 6 | 212 | 14 | 375 | 145 | 53 | mag. |
| CHW07-61m | 5 | a35 | 366 | 88 | 4 | 1.78 | 1478 | 0.0327 | 3.5 | 0.22 | 9.0 | 0.0497 | 8.3 | 0.39 | 207 | 7 | 205 | 17 | 180 | 193 | 115 | mag. |
| CHW07-61c | 5 | a36 | 2152 | 449 | 15 | 0.16 | 8415 | 0.0359 | 3.3 | 0.26 | 4.8 | 0.0516 | 3.5 | 0.68 | 227 | 7 | 231 | 10 | 268 | 80 | 85 | mag. |
| CHW07-62 | 5 | a37 | 872 | 115 | 7 | 0.89 | 3373 | 0.0557 | 2.7 | 0.40 | 6.3 | 0.0519 | 5.7 | 0.42 | 349 | 9 | 340 | 18 | 280 | 131 | 125 | mag. |
| CHW07-63r | 5 | a38 | 1254 | 247 | 9 | 0.78 | 4910 | 0.0323 | 2.5 | 0.23 | 6.5 | 0.0509 | 5.9 | 0.39 | 205 | 5 | 208 | 12 | 236 | 137 | 87 | mag. |
| CHW07-63c | 5 | a39 | 390 | 67 | 3 | 1.07 | 1319 | 0.0353 | 3.7 | 0.25 | 7.2 | 0.0519 | 6.2 | 0.51 | 224 | 8 | 229 | 15 | 282 | 141 | 79 | mag. |
| CHW07-64r | 5 | a40 | 6122 | 333 | 33 | 0.22 | 3403 | 0.1051 | 2.5 | 0.86 | 5.1 | 0.0593 | 4.5 | 0.49 | 644 | 16 | 630 | 24 | 579 | 97 | 111 | mag. |
| CHW07-65 | 5 | a41 | 477 | 105 | 4 | 0.68 | 1929 | 0.0314 | 3.5 | 0.21 | 8.8 | 0.0497 | 8.1 | 0.39 | 199 | 7 | 198 | 16 | 181 | 189 | 110 | mag. |
| CHW07-66 | 5 | a42 | 388 | 54 | 2 | 0.78 | 725 | 0.0268 | 3.1 | 0.20 | 7.5 | 0.0540 | 6.8 | 0.42 | 170 | 5 | 184 | 13 | 370 | 153 | 46 | mag. |

# Results of U-Th-Pb LA-ICPMS analyses of zircons from sample CHW07 (continuation)

| Spot | Seq. | No. | $^{207}Pb$ [a] (cps) | U [b] (ppm) | Pb [b] (ppm) | Th/U [b] | $^{206}Pb/^{204}Pb$ | $^{206}Pb/^{238}U$ [c] | ±2s (%) | $^{207}Pb/^{235}U$ [c] | ±2s (%) | $^{207}Pb/^{206}Pb$ [c] | ±2s (%) | Rho [d] | Age (Ma) $^{206}Pb/^{238}U$ | ±2s | $^{207}Pb/^{235}U$ | ±2s | $^{207}Pb/^{206}Pb$ [c] | ±2s | conc [e] (%) | Origin [f] |
|---|---|---|---|---|---|---|---|---|---|---|---|---|---|---|---|---|---|---|---|---|---|---|
| CHW07-67 | 5 | a43 | 2141 | 150 | 13 | 0.45 | 7644 | 0.0857 | 2.7 | 0.66 | 5.0 | 0.0562 | 4.2 | 0.54 | 530 | 14 | 518 | 21 | 462 | 94 | 115 | mag. |
| CHW07-68c | 5 | a44 | 2906 | 81 | 14 | 0.40 | 8347 | 0.1666 | 2.9 | 1.63 | 5.2 | 0.0712 | 4.4 | 0.55 | 993 | 26 | 984 | 33 | 963 | 89 | 103 | mag. |
| CHW07-68r | 5 | a45 | 6610 | 365 | 32 | 0.08 | 8800 | 0.0927 | 2.3 | 0.77 | 3.1 | 0.0601 | 2.1 | 0.74 | 572 | 13 | 579 | 14 | 607 | 46 | 94 | met. |
| CHW07-69 | 5 | a46 | 1392 | 85 | 7 | 0.45 | 923 | 0.0823 | 2.7 | 0.64 | 5.5 | 0.0562 | 4.8 | 0.49 | 510 | 13 | 501 | 22 | 461 | 107 | 111 | mag. |
| CHW07-70 | 5 | a47 | 827 | 154 | 6 | 1.32 | 3165 | 0.0312 | 2.8 | 0.22 | 5.1 | 0.0513 | 4.3 | 0.54 | 198 | 5 | 202 | 9 | 254 | 98 | 78 | mag. |
| CHW07-71 | 5 | a48 | 2679 | 147 | 13 | 0.48 | 3601 | 0.0877 | 2.5 | 0.74 | 4.3 | 0.0608 | 3.5 | 0.58 | 542 | 13 | 560 | 19 | 632 | 76 | 86 | mag. |
| CHW07-72r | 5 | a49 | 1064 | 52 | 6 | 0.66 | 3306 | 0.0976 | 3.0 | 0.77 | 6.4 | 0.0574 | 5.7 | 0.46 | 601 | 17 | 581 | 29 | 507 | 126 | 118 | mag. |
| CHW07-72c | 5 | a50 | 2313 | 117 | 14 | 1.31 | 7676 | 0.0939 | 2.6 | 0.78 | 4.1 | 0.0602 | 3.2 | 0.64 | 579 | 15 | 586 | 19 | 612 | 69 | 95 | mag. |
| CHW07-73r | 5 | a51 | 2052 | 99 | 10 | 0.37 | 2110 | 0.1021 | 3.1 | 0.83 | 4.8 | 0.0592 | 3.7 | 0.64 | 627 | 18 | 616 | 22 | 576 | 80 | 109 | mag. |
| CHW07-74 | 5 | a52 | 1194 | 199 | 8 | 1.30 | 4245 | 0.0303 | 3.3 | 0.21 | 5.8 | 0.0496 | 4.8 | 0.57 | 192 | 6 | 191 | 10 | 177 | 111 | 108 | mag. |
| CHW07-75 | 5 | a53 | 546 | 97 | 3 | 0.48 | 2169 | 0.0308 | 3.3 | 0.22 | 8.7 | 0.0511 | 8.0 | 0.39 | 196 | 6 | 199 | 16 | 244 | 185 | 80 | mag. |
| CHW07-76r | 5 | a54 | 19563 | 466 | 74 | 0.21 | 61209 | 0.1630 | 3.0 | 1.58 | 3.6 | 0.0702 | 2.0 | 0.84 | 974 | 27 | 961 | 22 | 933 | 40 | 104 | met. |
| CHW07-76c | 5 | a55 | 37681 | 459 | 75 | 0.43 | 1810 | 0.1608 | 2.4 | 1.47 | 6.6 | 0.0664 | 6.2 | 0.36 | 961 | 21 | 919 | 41 | 819 | 129 | 117 | mag. |
| CHW07-77 | 6 | a1 | 2642 | 234 | 15 | 1.09 | 1401 | 0.0574 | 2.2 | 0.43 | 3.8 | 0.0546 | 3.1 | 0.57 | 360 | 8 | 365 | 12 | 396 | 70 | 91 | mag. |
| CHW07-78 | 6 | a2 | 4301 | 222 | 21 | 0.62 | 2713 | 0.0894 | 2.4 | 0.72 | 3.6 | 0.0584 | 2.6 | 0.67 | 552 | 13 | 550 | 15 | 543 | 58 | 102 | mag. |
| CHW07-79r | 6 | a3 | 1837 | 60 | 9 | 0.61 | 5543 | 0.1395 | 3.1 | 1.26 | 4.8 | 0.0655 | 3.6 | 0.65 | 842 | 25 | 828 | 28 | 790 | 77 | 107 | mag. |
| CHW07-79c | 6 | a4 | 5076 | 117 | 20 | 0.44 | 13714 | 0.1622 | 2.5 | 1.65 | 3.5 | 0.0737 | 2.5 | 0.71 | 969 | 22 | 989 | 23 | 1033 | 51 | 94 | mag. |
| CHW07-80r | 6 | a5 | 1413 | 63 | 11 | 3.45 | 4544 | 0.1072 | 2.0 | 0.92 | 5.5 | 0.0624 | 5.1 | 0.37 | 656 | 13 | 664 | 27 | 688 | 109 | 95 | mag. |
| CHW07-81r | 6 | a6 | 5148 | 198 | 24 | 0.52 | 2615 | 0.1171 | 3.5 | 1.01 | 4.4 | 0.0628 | 2.7 | 0.79 | 714 | 24 | 711 | 23 | 702 | 57 | 102 | mag. |
| CHW07-81c | 6 | a7 | 4285 | 133 | 21 | 0.48 | 12344 | 0.1512 | 2.4 | 1.45 | 4.1 | 0.0694 | 3.3 | 0.58 | 908 | 20 | 908 | 25 | 910 | 69 | 100 | mag. |
| CHW07-82c | 6 | a8 | 8823 | 241 | 37 | 0.16 | 24645 | 0.1593 | 2.5 | 1.56 | 3.4 | 0.0711 | 2.4 | 0.72 | 953 | 22 | 955 | 21 | 962 | 49 | 99 | met. |
| CHW07-83r | 6 | a9 | 442 | 83 | 3 | 1.11 | 1746 | 0.0334 | 2.6 | 0.24 | 8.8 | 0.0510 | 8.4 | 0.29 | 212 | 5 | 215 | 17 | 241 | 193 | 88 | mag. |
| CHW07-83c | 6 | a10 | 1094 | 200 | 11 | 3.57 | 4340 | 0.0305 | 3.0 | 0.21 | 5.1 | 0.0504 | 4.2 | 0.59 | 193 | 6 | 195 | 9 | 213 | 96 | 91 | mag. |
| CHW07-84c | 6 | a11 | 5048 | 193 | 24 | 0.12 | 4811 | 0.1306 | 1.9 | 1.16 | 3.1 | 0.0645 | 2.5 | 0.62 | 791 | 14 | 783 | 17 | 759 | 52 | 104 | met. |
| CHW07-85 | 6 | a12 | 3918 | 616 | 22 | 0.24 | 3413 | 0.0366 | 3.1 | 0.25 | 4.3 | 0.0504 | 3.0 | 0.71 | 231 | 7 | 230 | 9 | 213 | 70 | 109 | unc. |
| CHW07-86r | 6 | a13 | 318 | 60 | 2 | 0.82 | 571 | 0.0313 | 2.6 | 0.22 | 8.8 | 0.0505 | 8.4 | 0.30 | 199 | 5 | 200 | 16 | 218 | 194 | 91 | mag. |
| CHW07-87m | 6 | a14 | 3032 | 90 | 13 | 0.44 | 1489 | 0.1378 | 2.2 | 1.28 | 4.1 | 0.0676 | 3.4 | 0.55 | 832 | 17 | 839 | 23 | 857 | 71 | 97 | mag. |
| CHW07-88r | 6 | a15 | 6710 | 313 | 33 | 0.54 | 22302 | 0.1010 | 2.2 | 0.83 | 3.3 | 0.0597 | 2.5 | 0.66 | 620 | 13 | 615 | 15 | 594 | 54 | 104 | mag. |
| CHW07-89 | 6 | a16 | 3435 | 34 | 11 | 0.82 | 4977 | 0.2939 | 3.1 | 4.10 | 5.2 | 0.1011 | 4.1 | 0.61 | 1661 | 46 | 1654 | 43 | 1644 | 76 | 101 | mag. |
| CHW07-90 | 6 | a17 | 9844 | 520 | 48 | 0.08 | 30124 | 0.0984 | 3.2 | 0.82 | 3.8 | 0.0602 | 2.0 | 0.85 | 605 | 19 | 607 | 18 | 612 | 44 | 99 | met. |
| CHW07-91r | 6 | a18 | 511 | 26 | 3 | 1.62 | 1741 | 0.1026 | 2.7 | 0.84 | 8.9 | 0.0596 | 8.5 | 0.31 | 629 | 16 | 621 | 42 | 589 | 185 | 107 | mag. |
| CHW07-91c | 6 | a19 | 4780 | 106 | 18 | 0.35 | 10396 | 0.1655 | 3.4 | 1.68 | 4.4 | 0.0738 | 2.7 | 0.78 | 987 | 31 | 1002 | 28 | 1035 | 55 | 95 | mag. |

# Results of U-Th-Pb LA-ICPMS analyses of zircons from sample CHW26

| Spot | Seq. | No. | $^{207}Pb$ [a] (cps) | U [b] (ppm) | Pb [b] (ppm) | Th [b] U | $^{206}Pb/^{204}Pb$ | $^{206}Pb/^{238}U$ [c] | ±2s (%) | $^{207}Pb/^{235}U$ [c] | ±2s (%) | $^{207}Pb/^{206}Pb$ [c] | ±2s (%) | Rho [d] | Age (Ma) $^{206}Pb/^{238}U$ | ±2s | Age (Ma) $^{207}Pb/^{235}U$ | ±2s | Age (Ma) $^{207}Pb/^{206}Pb$ [c] | ±2s | conc [e] (%) | Origin [f] |
|---|---|---|---|---|---|---|---|---|---|---|---|---|---|---|---|---|---|---|---|---|---|---|
| CHW26-1m | 6 | a20 | 15527 | 45 | 29 | 0.81 | 6672 | 0.5378 | 2.3 | 13.81 | 2.7 | 0.1863 | 1.4 | 0.87 | 2774 | 53 | 2737 | 26 | 2710 | 22 | 102 | mag. |
| CHW26-2r | 6 | a21 | 613 | 102 | 5 | 2.48 | 2266 | 0.0329 | 3.2 | 0.23 | 7.1 | 0.0501 | 6.3 | 0.45 | 209 | 7 | 208 | 13 | 202 | 146 | 104 | mag. |
| CHW26-3 | 6 | a22 | 5149 | 244 | 26 | 0.62 | 16940 | 0.0990 | 3.4 | 0.82 | 4.3 | 0.0599 | 2.7 | 0.78 | 609 | 20 | 607 | 20 | 598 | 58 | 102 | mag. |
| CHW26-4 | 6 | a23 | 284 | 54 | 2 | 0.93 | 1129 | 0.0309 | 3.5 | 0.21 | 7.3 | 0.0503 | 6.4 | 0.48 | 196 | 7 | 197 | 13 | 210 | 149 | 93 | mag. |
| CHW26-5 | 6 | a24 | 960 | 43 | 5 | 1.21 | 2999 | 0.1084 | 2.5 | 0.95 | 6.2 | 0.0637 | 5.6 | 0.41 | 663 | 16 | 679 | 31 | 733 | 119 | 91 | mag. |
| CHW26-6 | 6 | a25 | 4135 | 204 | 24 | 1.14 | 4213 | 0.1011 | 2.2 | 0.84 | 3.7 | 0.0602 | 3.0 | 0.60 | 621 | 13 | 618 | 17 | 609 | 64 | 102 | mag. |
| CHW26-8 | 6 | a27 | 2933 | 57 | 12 | 0.84 | 6874 | 0.1938 | 2.3 | 1.99 | 5.2 | 0.0746 | 4.7 | 0.45 | 1142 | 25 | 1114 | 36 | 1058 | 94 | 108 | mag. |
| CHW26-11c | 6 | a30 | 443 | 11 | 2 | 0.42 | 1286 | 0.1529 | 14.2 | 1.46 | 20.3 | 0.0692 | 14.5 | 0.70 | 917 | 123 | 914 | 131 | 905 | 300 | 101 | mag. |
| CHW26-11r | 6 | a31 | 2978 | 131 | 13 | 0.07 | 1366 | 0.1027 | 3.4 | 0.86 | 5.5 | 0.0610 | 4.3 | 0.62 | 630 | 20 | 632 | 26 | 639 | 93 | 99 | met. |
| CHW26-12c | 6 | a32 | 653 | 40 | 4 | 1.11 | 2257 | 0.0853 | 3.4 | 0.68 | 7.8 | 0.0576 | 7.0 | 0.44 | 528 | 17 | 525 | 32 | 514 | 153 | 103 | mag. |
| CHW26-13c | 6 | a33 | 839 | 49 | 4 | 0.67 | 2965 | 0.0842 | 2.8 | 0.66 | 6.9 | 0.0565 | 6.3 | 0.41 | 521 | 14 | 512 | 28 | 474 | 138 | 110 | mag. |
| CHW26-14r | 6 | a34 | 3001 | 139 | 15 | 0.71 | 1915 | 0.1033 | 2.3 | 0.89 | 3.8 | 0.0624 | 3.0 | 0.60 | 634 | 14 | 646 | 18 | 688 | 64 | 92 | mag. |
| CHW26-15c | 6 | a35 | 5079 | 171 | 26 | 0.84 | 1576 | 0.1391 | 3.0 | 1.27 | 3.7 | 0.0662 | 2.2 | 0.81 | 839 | 24 | 832 | 21 | 814 | 46 | 103 | mag. |
| CHW26-16 | 6 | a36 | 4638 | 194 | 23 | 0.54 | 15074 | 0.1148 | 2.1 | 0.98 | 3.2 | 0.0617 | 2.4 | 0.65 | 700 | 14 | 692 | 16 | 665 | 52 | 105 | mag. |
| CHW26-17 | 6 | a37 | 8077 | 379 | 40 | 0.38 | 26733 | 0.1060 | 2.5 | 0.88 | 3.5 | 0.0605 | 2.5 | 0.70 | 649 | 15 | 643 | 17 | 620 | 53 | 105 | mag. |
| CHW26-18 | 6 | a38 | 940 | 164 | 6 | 0.86 | 3716 | 0.0347 | 2.2 | 0.24 | 6.6 | 0.0504 | 6.2 | 0.33 | 220 | 5 | 219 | 13 | 213 | 144 | 103 | mag. |
| CHW26-19r | 6 | a39 | 4021 | 167 | 17 | 0.73 | 1045 | 0.0989 | 2.2 | 0.83 | 5.3 | 0.0607 | 4.9 | 0.41 | 608 | 13 | 612 | 25 | 627 | 105 | 97 | mag. |
| CHW26-20r | 6 | a40 | 4208 | 37 | 7 | 1.57 | 492 | 0.1036 | 7.7 | 0.82 | 11.1 | 0.0571 | 8.0 | 0.69 | 636 | 47 | 605 | 52 | 494 | 177 | 129 | mag. |
| CHW26-20c | 6 | a41 | 2063 | 97 | 12 | 1.62 | 2170 | 0.1007 | 4.2 | 0.85 | 5.9 | 0.0614 | 4.2 | 0.71 | 618 | 25 | 626 | 28 | 653 | 90 | 95 | mag. |
| CHW26-21 | 6 | a42 | 971 | 152 | 6 | 1.43 | 1522 | 0.0309 | 4.9 | 0.22 | 7.4 | 0.0507 | 5.6 | 0.66 | 196 | 9 | 199 | 13 | 227 | 130 | 86 | mag. |
| CHW26-22 | 6 | a43 | 10120 | 445 | 51 | 0.79 | 23047 | 0.1056 | 4.2 | 0.89 | 5.1 | 0.0610 | 2.9 | 0.82 | 647 | 26 | 646 | 25 | 640 | 63 | 101 | mag. |
| CHW26-23 | 6 | a44 | 2255 | 298 | 11 | 0.68 | 2976 | 0.0355 | 4.3 | 0.25 | 7.0 | 0.0505 | 5.5 | 0.61 | 225 | 9 | 225 | 14 | 219 | 128 | 103 | mag. |
| CHW26-24 | 6 | a45 | 9346 | 194 | 33 | 0.49 | 3852 | 0.1639 | 2.5 | 1.67 | 3.3 | 0.0741 | 2.1 | 0.77 | 978 | 23 | 999 | 21 | 1044 | 42 | 94 | mag. |
| CHW26-25c | 6 | a46 | 2581 | 131 | 13 | 0.67 | 8822 | 0.0912 | 3.1 | 0.73 | 4.2 | 0.0583 | 2.8 | 0.74 | 563 | 17 | 559 | 18 | 542 | 61 | 104 | mag. |
| CHW26-26r | 6 | a47 | 5622 | 251 | 27 | 0.58 | 18385 | 0.1026 | 2.3 | 0.86 | 3.3 | 0.0609 | 2.4 | 0.68 | 629 | 14 | 631 | 16 | 635 | 52 | 99 | mag. |
| CHW26-26c | 6 | a48 | 14789 | 290 | 64 | 1.14 | 25531 | 0.1843 | 2.5 | 1.91 | 3.3 | 0.0752 | 2.2 | 0.75 | 1090 | 25 | 1084 | 22 | 1073 | 44 | 102 | mag. |
| CHW26-27 | 6 | a49 | 610 | 113 | 5 | 2.28 | 1625 | 0.0310 | 3.4 | 0.21 | 8.6 | 0.0501 | 7.9 | 0.39 | 197 | 7 | 197 | 15 | 201 | 183 | 98 | mag. |
| CHW26-28m | 6 | a50 | 989 | 37 | 4 | 0.32 | 3111 | 0.1145 | 3.2 | 1.00 | 5.5 | 0.0636 | 4.5 | 0.58 | 699 | 21 | 706 | 28 | 730 | 95 | 96 | mag. |
| CHW26-29 | 6 | a51 | 201 | 9 | 1 | 0.74 | 675 | 0.1219 | 11.9 | 1.06 | 16.6 | 0.0632 | 11.7 | 0.71 | 742 | 84 | 735 | 91 | 716 | 248 | 104 | mag. |
| CHW26-30c | 6 | a53 | 258 | 17 | 1 | 0.58 | 587 | 0.0388 | 24.9 | 0.29 | 40.7 | 0.0547 | 32.2 | 0.61 | 245 | 60 | 261 | 98 | 398 | 721 | 62 | mag. |
| CHW26-33m | 7 | a1 | 1519 | 77 | 7 | 0.05 | 4930 | 0.1004 | 3.6 | 0.85 | 5.6 | 0.0618 | 4.4 | 0.63 | 617 | 21 | 627 | 27 | 666 | 93 | 93 | met. |
| CHW26-34 | 7 | a2 | 1612 | 85 | 9 | 1.04 | 5327 | 0.0936 | 2.9 | 0.78 | 5.1 | 0.0601 | 4.1 | 0.57 | 577 | 16 | 583 | 23 | 607 | 90 | 95 | mag. |
| CHW26-35 | 7 | a3 | 1701 | 80 | 9 | 0.70 | 5660 | 0.1003 | 2.3 | 0.83 | 5.1 | 0.0600 | 4.5 | 0.46 | 616 | 14 | 614 | 24 | 604 | 98 | 102 | mag. |
| CHW26-36r | 7 | a4 | 108 | 33 | 1 | 1.28 | 445 | 0.0315 | 5.1 | 0.21 | 14.9 | 0.0490 | 14.0 | 0.34 | 200 | 10 | 196 | 27 | 146 | 328 | 137 | mag. |
| CHW26-37 | 7 | a5 | 322 | 48 | 2 | 1.12 | 1227 | 0.0382 | 3.5 | 0.27 | 9.5 | 0.0516 | 8.8 | 0.37 | 242 | 8 | 244 | 21 | 268 | 202 | 90 | mag. |
| CHW26-38 | 7 | a6 | 821 | 81 | 9 | 1.03 | 2712 | 0.0893 | 3.1 | 0.74 | 5.8 | 0.0603 | 5.0 | 0.52 | 551 | 16 | 564 | 26 | 615 | 107 | 90 | mag. |
| CHW26-39 | 7 | a7 | 179 | 11 | 1 | 0.82 | 631 | 0.0910 | 4.6 | 0.74 | 16.0 | 0.0586 | 15.3 | 0.29 | 562 | 25 | 560 | 71 | 551 | 334 | 102 | mag. |
| CHW26-40r | 7 | a8 | 312 | 19 | 1 | 0.80 | 2359 | 0.0422 | 11.2 | 0.30 | 41.2 | 0.0511 | 39.7 | 0.27 | 267 | 29 | 265 | 101 | 246 | 914 | 108 | mag. |
| CHW26-40c | 7 | a9 | 1623 | 333 | 12 | 1.05 | 6414 | 0.0304 | 2.5 | 0.21 | 4.6 | 0.0504 | 3.8 | 0.55 | 193 | 5 | 194 | 8 | 213 | 88 | 91 | mag. |
| CHW26-41r | 7 | a10 | 2971 | 152 | 17 | 0.80 | 5662 | 0.1057 | 2.6 | 0.90 | 4.5 | 0.0617 | 3.6 | 0.59 | 648 | 16 | 651 | 22 | 664 | 77 | 98 | mag. |
| CHW26-42 | 7 | a11 | 265 | 53 | 2 | 0.58 | 1538 | 0.0302 | 3.2 | 0.22 | 10.6 | 0.0518 | 10.1 | 0.30 | 192 | 6 | 199 | 19 | 276 | 230 | 70 | mag. |
| CHW26-43r | 7 | a12 | 2872 | 181 | 16 | 0.44 | 5779 | 0.0883 | 3.0 | 0.73 | 5.6 | 0.0597 | 4.7 | 0.54 | 546 | 16 | 555 | 24 | 591 | 102 | 92 | mag. |
| CHW26-44 | 7 | a13 | 1193 | 62 | 6 | 0.51 | 3992 | 0.1006 | 2.9 | 0.83 | 6.8 | 0.0597 | 6.1 | 0.43 | 618 | 17 | 612 | 32 | 592 | 132 | 104 | unc. |
| CHW26-45m | 7 | a14 | 14633 | 324 | 59 | 0.32 | 38731 | 0.1801 | 2.8 | 1.86 | 3.2 | 0.0748 | 1.4 | 0.89 | 1068 | 28 | 1066 | 21 | 1064 | 29 | 100 | met. |
| CHW26-46c | 7 | a15 | 2903 | 580 | 23 | 2.05 | 2006 | 0.0287 | 2.8 | 0.20 | 7.0 | 0.0502 | 6.4 | 0.40 | 183 | 5 | 184 | 12 | 205 | 149 | 89 | mag. |
| CHW26-47 | 7 | a16 | 1023 | 175 | 8 | 1.43 | 4089 | 0.0345 | 3.2 | 0.24 | 6.8 | 0.0501 | 6.0 | 0.47 | 219 | 7 | 217 | 13 | 199 | 138 | 110 | mag. |
| CHW26-48 | 7 | a17 | 1495 | 101 | 8 | 0.58 | 1880 | 0.0793 | 3.0 | 0.62 | 5.6 | 0.0563 | 4.7 | 0.54 | 492 | 14 | 487 | 22 | 462 | 104 | 106 | mag. |
| CHW26-49r | 7 | a18 | 3681 | 177 | 18 | 0.28 | 11903 | 0.1024 | 2.6 | 0.87 | 4.0 | 0.0615 | 3.1 | 0.64 | 629 | 15 | 635 | 19 | 658 | 65 | 95 | met. |
| CHW26-50r | 7 | a19 | 2305 | 124 | 13 | 0.61 | 559 | 0.0969 | 5.2 | 0.82 | 7.4 | 0.0614 | 5.3 | 0.70 | 596 | 29 | 608 | 35 | 652 | 114 | 91 | mag. |
| CHW26-51c | 7 | a20 | 2685 | 127 | 13 | 0.41 | 1738 | 0.1051 | 2.2 | 0.88 | 3.6 | 0.0606 | 2.8 | 0.61 | 644 | 14 | 640 | 17 | 624 | 61 | 103 | mag. |
| CHW26-52r | 7 | a21 | 1721 | 105 | 10 | 0.56 | 708 | 0.0873 | 3.0 | 0.70 | 5.4 | 0.0582 | 4.5 | 0.56 | 540 | 16 | 539 | 23 | 538 | 98 | 100 | mag. |
| CHW26-52c | 7 | a22 | 10623 | 236 | 44 | 0.58 | 17857 | 0.1748 | 2.8 | 1.75 | 3.4 | 0.0725 | 1.9 | 0.83 | 1038 | 27 | 1026 | 22 | 1000 | 38 | 104 | mag. |
| CHW26-53 | 7 | a23 | 1392 | 66 | 8 | 0.70 | 4516 | 0.1083 | 2.8 | 0.92 | 5.7 | 0.0613 | 4.9 | 0.50 | 663 | 18 | 660 | 28 | 649 | 105 | 102 | mag. |
| CHW26-54 | 7 | a24 | 1232 | 45 | 2 | 1.15 | 4952 | 0.0321 | 3.8 | 0.22 | 12.0 | 0.0500 | 11.4 | 0.32 | 204 | 8 | 203 | 22 | 194 | 265 | 105 | mag. |
| CHW26-55 | 7 | a25 | 1833 | 38 | 4 | 0.48 | 2738 | 0.0944 | 3.3 | 0.78 | 7.5 | 0.0598 | 6.7 | 0.44 | 581 | 18 | 584 | 34 | 596 | 146 | 98 | met. |
| CHW26-56 | 7 | a26 | 2773 | 150 | 14 | 0.14 | 9144 | 0.0960 | 2.9 | 0.79 | 4.9 | 0.0597 | 4.0 | 0.59 | 591 | 16 | 591 | 22 | 594 | 87 | 99 | met. |
| CHW26-57 | 7 | a27 | 1943 | 85 | 10 | 0.44 | 2074 | 0.1116 | 3.1 | 0.95 | 5.2 | 0.0615 | 4.2 | 0.59 | 682 | 20 | 676 | 26 | 655 | 90 | 104 | mag. |
| CHW26-58c | 7 | a28 | 12969 | 582 | 65 | 0.37 | 14608 | 0.1113 | 3.1 | 0.95 | 3.7 | 0.0616 | 2.0 | 0.84 | 680 | 20 | 676 | 18 | 660 | 42 | 103 | mag. |
| CHW26-59r | 7 | a29 | 3772 | 203 | 19 | 0.48 | 12600 | 0.0904 | 2.9 | 0.74 | 4.4 | 0.0598 | 3.3 | 0.66 | 558 | 15 | 565 | 19 | 595 | 72 | 94 | mag. |
| CHW26-60 | 7 | a30 | 1914 | 110 | 10 | 0.59 | 6542 | 0.0814 | 2.6 | 0.66 | 4.9 | 0.0584 | 4.1 | 0.54 | 505 | 13 | 512 | 20 | 544 | 89 | 93 | mag. |
| CHW26-61 | 7 | a31 | 1823 | 151 | 6 | 1.72 | 3246 | 0.0297 | 2.6 | 0.21 | 5.6 | 0.0504 | 4.9 | 0.46 | 189 | 5 | 191 | 10 | 214 | 114 | 88 | mag. |
| CHW26-62 | 7 | a32 | 1909 | 267 | 11 | 0.66 | 7459 | 0.0383 | 3.9 | 0.27 | 5.5 | 0.0514 | 3.9 | 0.71 | 242 | 9 | 244 | 12 | 260 | 89 | 93 | mag. |
| CHW26-63r | 7 | a33 | 8801 | 373 | 40 | 0.13 | 8116 | 0.1149 | 3.0 | 1.00 | 3.6 | 0.0631 | 1.9 | 0.84 | 701 | 20 | 704 | 19 | 713 | 41 | 98 | met. |
| CHW26-64 | 7 | a34 | 1644 | 123 | 4 | 1.07 | 549 | 0.0299 | 3.1 | 0.20 | 7.0 | 0.0489 | 6.2 | 0.45 | 190 | 6 | 186 | 12 | 142 | 146 | 134 | mag. |
| CHW26-65 | 7 | a35 | 4067 | 169 | 21 | 0.45 | 4894 | 0.1208 | 2.9 | 1.04 | 4.4 | 0.0622 | 3.3 | 0.66 | 735 | 20 | 722 | 23 | 680 | 71 | 108 | met. |
| CHW26-66 | 7 | a36 | 1412 | 68 | 8 | 0.72 | 3772 | 0.1050 | 3.0 | 0.87 | 5.3 | 0.0604 | 4.4 | 0.56 | 644 | 18 | 638 | 25 | 618 | 94 | 104 | mag. |
| CHW26-67 | 7 | a37 | 396 | 64 | 8 | 1.28 | 1350 | 0.0997 | 3.6 | 0.81 | 10.0 | 0.0592 | 9.4 | 0.36 | 612 | 21 | 605 | 47 | 575 | 204 | 106 | mag. |
| CHW26-68 | 7 | a38 | 1986 | 318 | 13 | 0.88 | 7481 | 0.0383 | 2.5 | 0.27 | 4.8 | 0.0511 | 4.0 | 0.53 | 242 | 6 | 243 | 10 | 246 | 93 | 99 | mag. |
| CHW26-69 | 7 | a39 | 1175 | 58 | 6 | 0.73 | 3871 | 0.0955 | 2.8 | 0.80 | 5.1 | 0.0604 | 4.3 | 0.54 | 588 | 16 | 594 | 23 | 619 | 92 | 95 | mag. |
| CHW26-70 | 7 | a40 | 1553 | 81 | 8 | 0.87 | 5356 | 0.0865 | 4.1 | 0.68 | 7.1 | 0.0573 | 5.8 | 0.58 | 535 | 21 | 529 | 30 | 505 | 127 | 106 | mag. |
| CHW26-71 | 7 | a41 | 1516 | 96 | 4 | 1.70 | 2013 | 0.0299 | 3.3 | 0.21 | 6.5 | 0.0511 | 5.5 | 0.52 | 190 | 6 | 194 | 12 | 244 | 128 | 78 | mag. |
| CHW26-72 | 7 | a42 | 46068 | 99 | 71 | 0.76 | 40349 | 0.5908 | 3.4 | 18.44 | 4.1 | 0.2264 | 2.1 | 0.85 | 2993 | 83 | 3013 | 40 | 3027 | 34 | 99 | mag. |
| CHW26-73 | 7 | a43 | 3105 | 20 | 1 | 2.03 | 2415 | 0.0342 | 5.6 | 0.24 | 19.3 | 0.0509 | 18.4 | 0.29 | 217 | 12 | 219 | 39 | 237 | 426 | 92 | mag. |
| CHW26-74 | 7 | a44 | 1509 | 72 | 9 | 1.00 | 5047 | 0.1037 | 2.4 | 0.85 | 5.2 | 0.0597 | 4.6 | 0.46 | 636 | 14 | 627 | 25 | 593 | 100 | 107 | mag. |
| CHW26-75 | 7 | a45 | 4384 | 236 | 23 | 0.52 | 1845 | 0.0940 | 4.0 | 0.76 | 4.8 | 0.0586 | 2.6 | 0.84 | 579 | 22 | 574 | 21 | 553 | 57 | 105 | mag. |

# Results of U-Th-Pb LA-ICPMS analyses of zircons from sample CHW26 (continuation)

| Spot | Seq. | No. | $^{207}Pb$ [a] (cps) | U [b] (ppm) | Pb [b] (ppm) | Th/U [b] | $^{206}Pb/^{204}Pb$ | $^{206}Pb/^{238}U$ [c] | ±2s (%) | $^{207}Pb/^{235}U$ [c] | ±2s (%) | $^{207}Pb/^{206}Pb$ [c] | ±2s (%) | Rho [d] | Age (Ma) $^{206}Pb/^{238}U$ | ±2s | $^{207}Pb/^{235}U$ | ±2s | $^{207}Pb/^{206}Pb$ [c] | ±2s | conc [e] (%) | Origin [f] |
|---|---|---|---|---|---|---|---|---|---|---|---|---|---|---|---|---|---|---|---|---|---|---|
| CHW26-76 | 7 | a46 | 11437 | 613 | 61 | 0.12 | 11337 | 0.1055 | 2.7 | 0.88 | 3.2 | 0.0607 | 1.6 | 0.87 | 647 | 17 | 643 | 15 | 630 | 34 | 103 | mag. |
| CHW26-77 | 7 | a47 | 4314 | 107 | 9 | 0.45 | 1494 | 0.0841 | 5.0 | 0.68 | 6.4 | 0.0590 | 3.9 | 0.79 | 521 | 25 | 529 | 27 | 567 | 85 | 92 | mag. |
| CHW26-78r | 7 | a48 | 1441 | 67 | 7 | 0.87 | 2321 | 0.0998 | 3.1 | 0.83 | 4.9 | 0.0605 | 3.7 | 0.65 | 613 | 18 | 615 | 23 | 620 | 80 | 99 | mag. |
| CHW26-78c | 7 | a49 | 1516 | 26 | 3 | 1.46 | 1720 | 0.1007 | 3.5 | 0.83 | 8.2 | 0.0596 | 7.4 | 0.43 | 618 | 21 | 612 | 38 | 590 | 160 | 105 | mag. |
| CHW26-79 | 7 | a50 | 1281 | 61 | 2 | 1.39 | 1161 | 0.0301 | 3.9 | 0.21 | 12.8 | 0.0497 | 12.1 | 0.31 | 191 | 7 | 191 | 22 | 182 | 283 | 105 | mag. |
| CHW26-80 | 7 | a51 | 1071 | 10 | 5 | 0.82 | 1595 | 0.4161 | 6.2 | 7.90 | 11.8 | 0.1378 | 10.0 | 0.53 | 2243 | 118 | 2220 | 112 | 2199 | 174 | 102 | mag. |
| CHW26-81 | 7 | a52 | 2583 | 128 | 14 | 0.39 | 1869 | 0.1113 | 2.5 | 0.94 | 4.1 | 0.0610 | 3.2 | 0.62 | 680 | 16 | 671 | 20 | 638 | 68 | 107 | mag. |
| CHW26-82 | 7 | a53 | 1215 | 25 | 3 | 0.10 | 255 | 0.1445 | 14.2 | 1.50 | 19.8 | 0.0755 | 13.8 | 0.72 | 870 | 117 | 932 | 129 | 1081 | 277 | 80 | unc. |
| CHW26-84 | 7 | a55 | 149 | 44 | 1 | 0.21 | 208 | 0.0379 | 16.1 | 0.26 | 27.7 | 0.0502 | 22.5 | 0.58 | 240 | 38 | 236 | 60 | 203 | 523 | 118 | mag. |
| CHW26-85r | 8 | a1 | 3512 | 175 | 18 | 0.27 | 1693 | 0.1040 | 3.4 | 0.87 | 4.2 | 0.0604 | 2.5 | 0.81 | 638 | 21 | 633 | 20 | 619 | 53 | 103 | mag. |
| CHW26-85c | 8 | a2 | 3834 | 67 | 19 | 2.23 | 10091 | 0.1954 | 4.4 | 2.04 | 5.5 | 0.0757 | 3.3 | 0.80 | 1150 | 46 | 1129 | 38 | 1087 | 67 | 106 | mag. |
| CHW26-86 | 8 | a3 | 1646 | 83 | 10 | 1.42 | 5483 | 0.1011 | 2.9 | 0.84 | 5.9 | 0.0600 | 5.1 | 0.50 | 621 | 17 | 617 | 27 | 603 | 110 | 103 | mag. |
| CHW26-87 | 8 | a4 | 939 | 109 | 6 | 0.83 | 3559 | 0.0501 | 2.5 | 0.36 | 5.9 | 0.0525 | 5.3 | 0.43 | 315 | 8 | 314 | 16 | 308 | 120 | 102 | mag. |
| CHW26-88 | 8 | a5 | 1495 | 66 | 6 | 0.49 | 3760 | 0.0860 | 3.0 | 0.67 | 6.0 | 0.0565 | 5.2 | 0.50 | 532 | 15 | 521 | 25 | 473 | 114 | 112 | mag. |
| CHW26-89 | 8 | a6 | 2070 | 204 | 9 | 2.67 | 2660 | 0.0302 | 3.2 | 0.20 | 5.1 | 0.0487 | 3.9 | 0.63 | 192 | 6 | 187 | 9 | 133 | 93 | 144 | mag. |
| CHW26-90 | 8 | a7 | 5603 | 228 | 28 | 0.59 | 8644 | 0.1152 | 2.4 | 0.98 | 3.3 | 0.0619 | 2.3 | 0.73 | 703 | 16 | 695 | 17 | 670 | 48 | 105 | mag. |
| CHW26-91 | 8 | a8 | 3186 | 150 | 15 | 0.66 | 6406 | 0.0903 | 4.9 | 0.72 | 13.3 | 0.0576 | 12.3 | 0.37 | 557 | 26 | 549 | 58 | 514 | 271 | 108 | mag. |
| CHW26-92 | 8 | a9 | 1427 | 89 | 3 | 1.32 | 1656 | 0.0314 | 2.7 | 0.22 | 7.0 | 0.0512 | 6.5 | 0.38 | 199 | 5 | 203 | 13 | 249 | 149 | 80 | mag. |
| CHW26-93c | 8 | a10 | 1650 | 69 | 7 | 0.34 | 2178 | 0.0963 | 3.1 | 0.79 | 6.2 | 0.0596 | 5.4 | 0.49 | 593 | 17 | 592 | 28 | 590 | 117 | 101 | mag. |
| CHW26-94 | 8 | a11 | 3334 | 135 | 17 | 1.67 | 11354 | 0.0994 | 2.4 | 0.81 | 4.6 | 0.0588 | 4.0 | 0.53 | 611 | 14 | 600 | 21 | 561 | 86 | 109 | mag. |
| CHW26-95 | 8 | a12 | 1418 | 83 | 3 | 1.45 | 1663 | 0.0321 | 2.1 | 0.22 | 8.0 | 0.0504 | 7.7 | 0.26 | 203 | 4 | 204 | 15 | 211 | 179 | 96 | mag. |
| CHW26-96r | 8 | a13 | 1200 | 54 | 2 | 0.50 | 1101 | 0.0332 | 6.8 | 0.24 | 11.6 | 0.0515 | 9.4 | 0.59 | 211 | 14 | 215 | 23 | 265 | 216 | 80 | mag. |
| CHW26-97 | 8 | a14 | 1179 | 190 | 7 | 0.71 | 4602 | 0.0338 | 2.0 | 0.24 | 4.7 | 0.0508 | 4.2 | 0.43 | 215 | 4 | 216 | 9 | 231 | 97 | 93 | mag. |
| CHW26-98 | 8 | a15 | 1140 | 56 | 2 | 0.60 | 1311 | 0.0322 | 7.0 | 0.29 | 15.9 | 0.0657 | 14.3 | 0.44 | 204 | 14 | 260 | 37 | 797 | 300 | 26 | mag. |
| CHW26-99r | 8 | a16 | 1331 | 53 | 6 | 0.31 | 1672 | 0.1089 | 2.8 | 0.93 | 9.0 | 0.0620 | 8.6 | 0.31 | 667 | 18 | 668 | 45 | 674 | 184 | 99 | mag. |
| CHW26-100 | 8 | a17 | 2632 | 134 | 14 | 0.61 | 8838 | 0.0954 | 2.2 | 0.78 | 3.7 | 0.0594 | 3.0 | 0.60 | 587 | 13 | 586 | 17 | 580 | 65 | 101 | mag. |
| CHW26-101 | 8 | a18 | 1990 | 116 | 10 | 0.57 | 6701 | 0.0824 | 2.5 | 0.67 | 4.7 | 0.0589 | 4.0 | 0.54 | 510 | 12 | 520 | 19 | 564 | 86 | 90 | mag. |
| CHW26-102r | 8 | a19 | 6051 | 128 | 16 | 0.88 | 9397 | 0.0975 | 3.8 | 0.83 | 7.0 | 0.0621 | 5.9 | 0.54 | 600 | 22 | 616 | 33 | 676 | 126 | 89 | mag. |
| CHW26-103 | 8 | a20 | 5795 | 110 | 23 | 0.42 | 14574 | 0.2016 | 2.6 | 2.20 | 3.3 | 0.0791 | 2.1 | 0.78 | 1184 | 28 | 1180 | 24 | 1174 | 42 | 101 | mag. |
| CHW26-104 | 8 | a21 | 3839 | 203 | 19 | 0.23 | 12685 | 0.0956 | 2.5 | 0.78 | 4.2 | 0.0591 | 3.5 | 0.58 | 588 | 14 | 585 | 19 | 571 | 75 | 103 | mag. |
| CHW26-105 | 8 | a22 | 1491 | 90 | 3 | 1.01 | 1052 | 0.0323 | 2.9 | 0.23 | 7.7 | 0.0507 | 7.2 | 0.37 | 205 | 6 | 207 | 15 | 226 | 166 | 91 | mag. |
| CHW26-106r | 8 | a23 | 928 | 50 | 5 | 0.73 | 1969 | 0.0887 | 2.2 | 0.73 | 7.3 | 0.0594 | 7.0 | 0.30 | 548 | 11 | 555 | 32 | 582 | 151 | 94 | mag. |
| CHW26-106c | 8 | a24 | 1854 | 80 | 8 | 0.43 | 1439 | 0.0949 | 3.5 | 0.77 | 5.1 | 0.0591 | 3.7 | 0.69 | 585 | 20 | 581 | 23 | 569 | 80 | 103 | mag. |
| CHW26-107r | 8 | a25 | 3112 | 181 | 17 | 0.41 | 10469 | 0.0917 | 2.5 | 0.75 | 4.2 | 0.0593 | 3.4 | 0.59 | 566 | 14 | 568 | 19 | 579 | 74 | 98 | met. |
| CHW26-107c | 8 | a26 | 2324 | 119 | 11 | 0.36 | 1609 | 0.0899 | 2.5 | 0.74 | 4.9 | 0.0599 | 4.1 | 0.52 | 555 | 14 | 563 | 21 | 599 | 90 | 93 | met. |
| CHW26-108 | 8 | a27 | 1828 | 105 | 5 | 1.60 | 2740 | 0.0358 | 2.4 | 0.25 | 5.1 | 0.0514 | 4.6 | 0.46 | 227 | 5 | 230 | 11 | 258 | 105 | 88 | mag. |
| CHW26-109r | 8 | a28 | 2209 | 109 | 14 | 1.34 | 7360 | 0.1034 | 2.4 | 0.86 | 4.3 | 0.0601 | 3.5 | 0.56 | 634 | 15 | 628 | 20 | 607 | 77 | 105 | mag. |
| CHW26-109c | 8 | a29 | 14165 | 550 | 66 | 0.84 | 30553 | 0.1059 | 3.0 | 0.90 | 4.4 | 0.0616 | 3.2 | 0.69 | 649 | 19 | 652 | 21 | 661 | 68 | 98 | mag. |
| CHW26-110c | 8 | a30 | 11784 | 370 | 50 | 0.93 | 1522 | 0.1140 | 3.0 | 0.97 | 5.1 | 0.0618 | 4.1 | 0.58 | 696 | 20 | 689 | 26 | 667 | 88 | 104 | mag. |
| CHW26-111 | 8 | a31 | 4803 | 233 | 28 | 1.11 | 15995 | 0.1015 | 2.9 | 0.84 | 3.7 | 0.0600 | 2.4 | 0.77 | 623 | 17 | 619 | 17 | 605 | 51 | 103 | mag. |
| CHW26-112 | 8 | a32 | 2612 | 180 | 15 | 0.50 | 1708 | 0.0827 | 2.0 | 0.65 | 4.8 | 0.0566 | 4.3 | 0.42 | 512 | 10 | 506 | 19 | 477 | 96 | 107 | mag. |
| CHW26-113 | 8 | a33 | 1381 | 55 | 6 | 0.29 | 1249 | 0.1076 | 4.0 | 0.92 | 9.3 | 0.0617 | 8.4 | 0.43 | 659 | 25 | 660 | 46 | 664 | 180 | 99 | unc. |

Diameter of laser spot = 20µm; depth of crater 10-15 µm.

[a] Within run background-corrected mean $^{207}Pb$ signal in counts per second.

[b] U and Pb content and Th/U ratio were calculated relative to GJ-1 reference (LA-ICPMS values, Gerdes, unpublished).

[c] corrected for background, common Pb and within-run Pb/U fractionation and subsequently normalised to GJ-1 (ID-TIMS value/measured value). $^{207}Pb/^{235}U$ was calculated using $^{207}Pb/^{206}Pb/(^{238}U/^{206}Pb \times 1/137.88)$. Uncertainties propagated following GERDES and ZEH (2006, 2008).

[d] Rho is the error correlation defined as $err^{206}Pb/^{238}U / err^{207}Pb/^{235}U$

[e] Percent concordance = $^{206}Pb/^{238}U$ age / $^{207}Pb/^{206}Pb$ age x 100

[f] Zircon origin was determined by a combination of geochemical evidence (Th/U ratio) and interpretation of internal zoning (CL images). mag.: magmatic; met.: metamorphic; unc.: uncertain. More explanations in the text.

# Appendix 7.2

Ahrens-Wetherill concordia plots
of U-Pb age data of detrital zircons

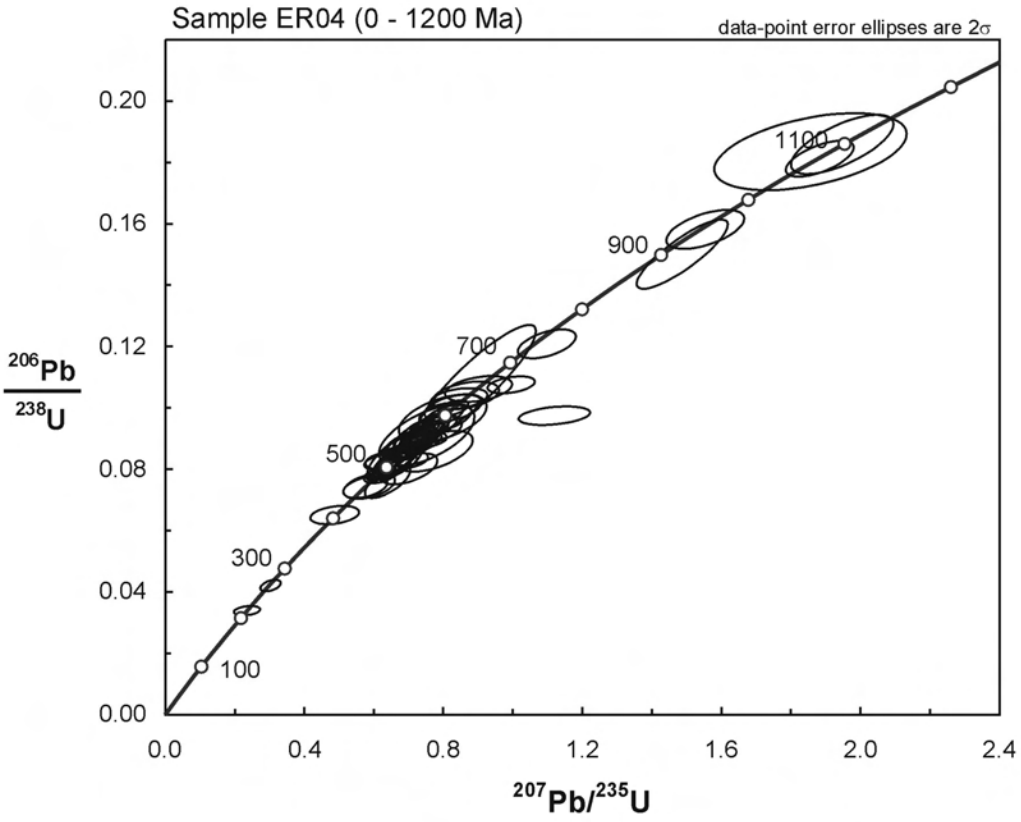
Sample ER04 (0 - 1200 Ma)
data-point error ellipses are 2σ
0.20
0.16
0.12
0.08
0.04
0.00
206Pb/238U
1100
900
700
500
300
100
0.0
0.4
0.8
1.2
1.6
2.0
2.4
207Pb/235U

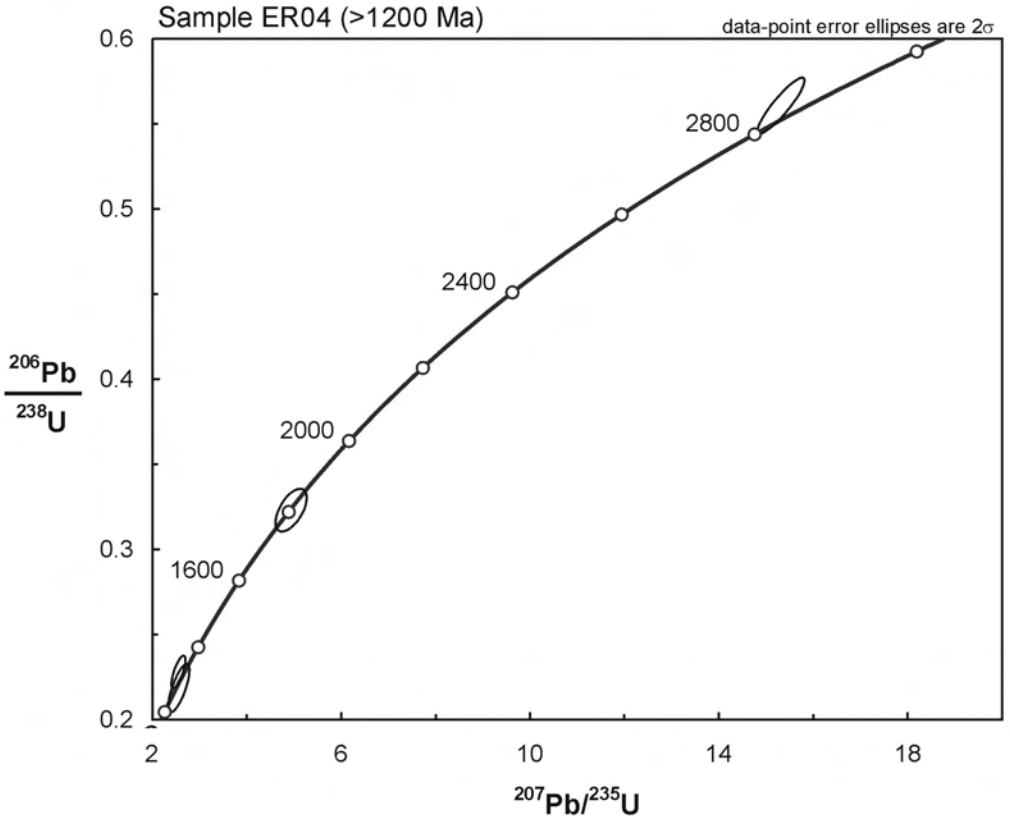
Sample ER04 (>1200 Ma)
data-point error ellipses are 2σ
0.6
0.5
0.4
0.3
0.2
206Pb/238U
2800
2400
2000
1600
2
6
10
14
18
207Pb/235U

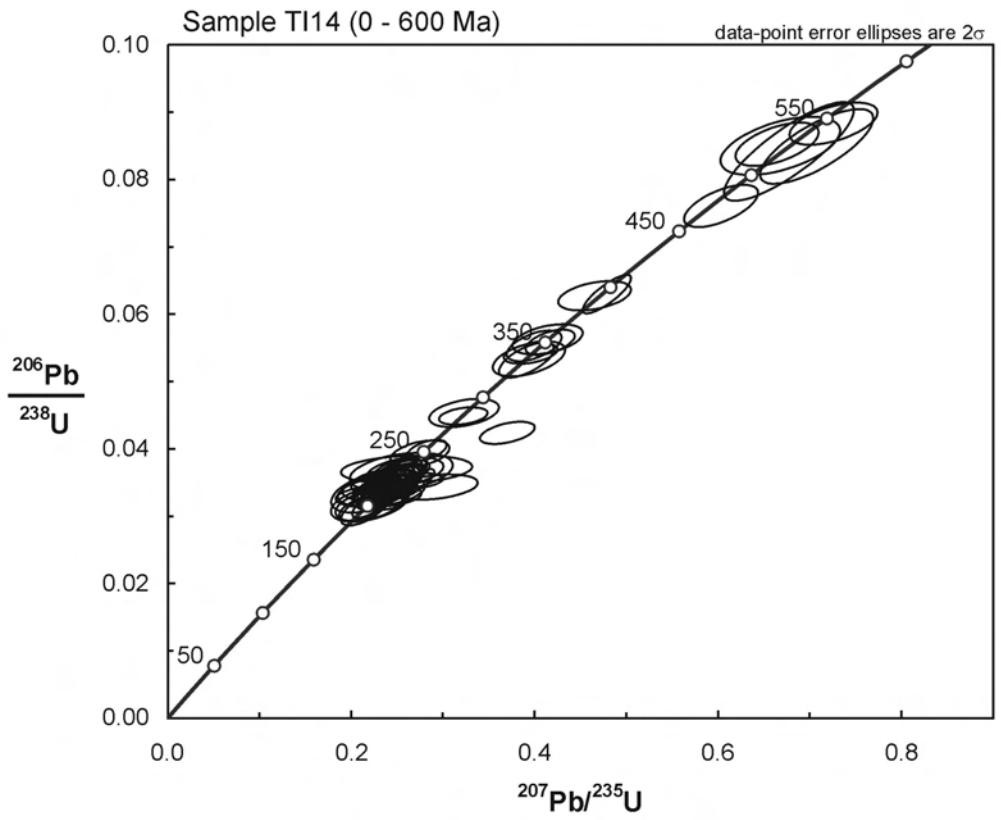
Sample TI14 (0 - 600 Ma)
data-point error ellipses are 2σ
0.10
0.08
0.06
0.04
0.02
0.00
0.0
0.2
0.4
0.6
0.8
206Pb/238U
207Pb/235U
50
150
250
350
450
550

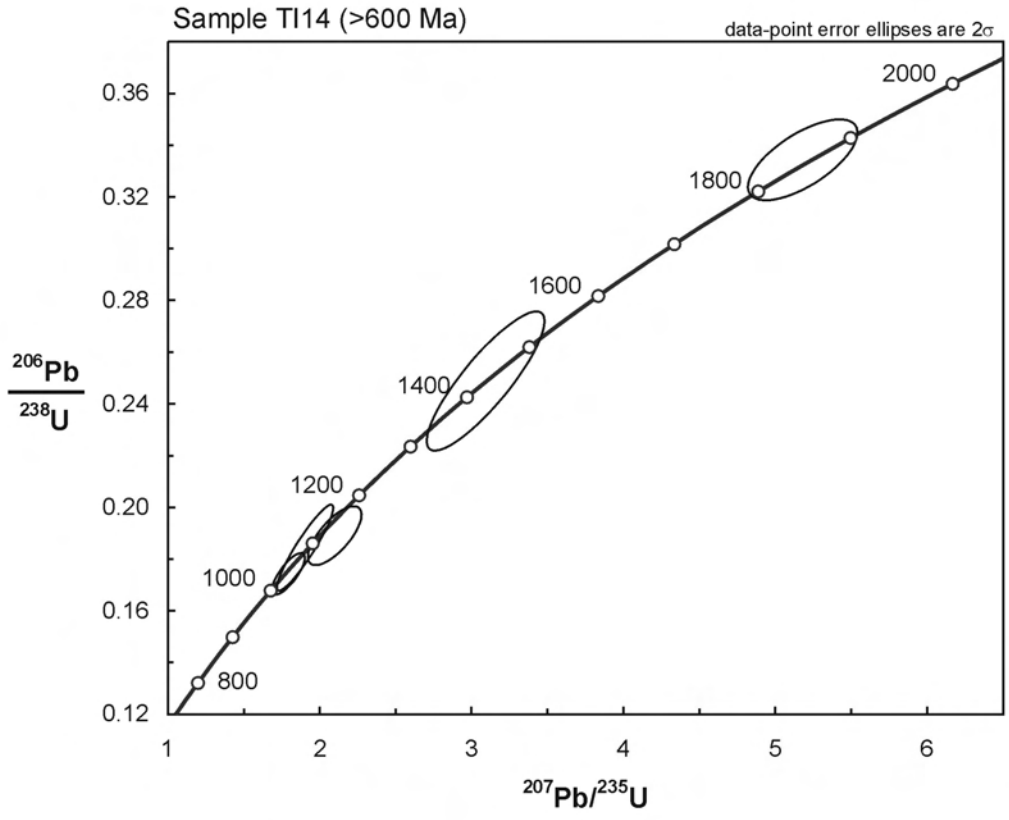
Sample TI14 (>600 Ma)
data-point error ellipses are 2σ
0.36
0.32
0.28
0.24
0.20
0.16
0.12
1
2
3
4
5
6
206Pb/238U
207Pb/235U
800
1000
1200
1400
1600
1800
2000

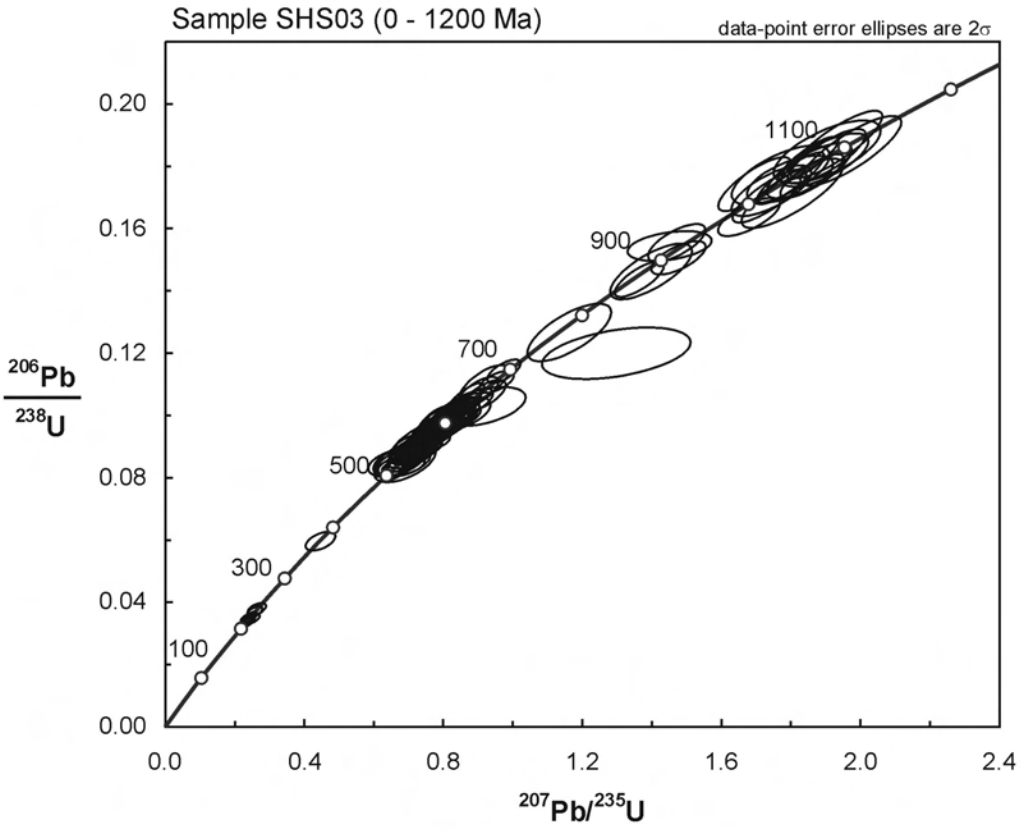
Sample SHS03 (0 - 1200 Ma)
data-point error ellipses are 2σ
0.20
0.16
0.12
0.08
0.04
0.00
206Pb/238U
1100
900
700
500
300
100
0.0
0.4
0.8
1.2
1.6
2.0
2.4
207Pb/235U

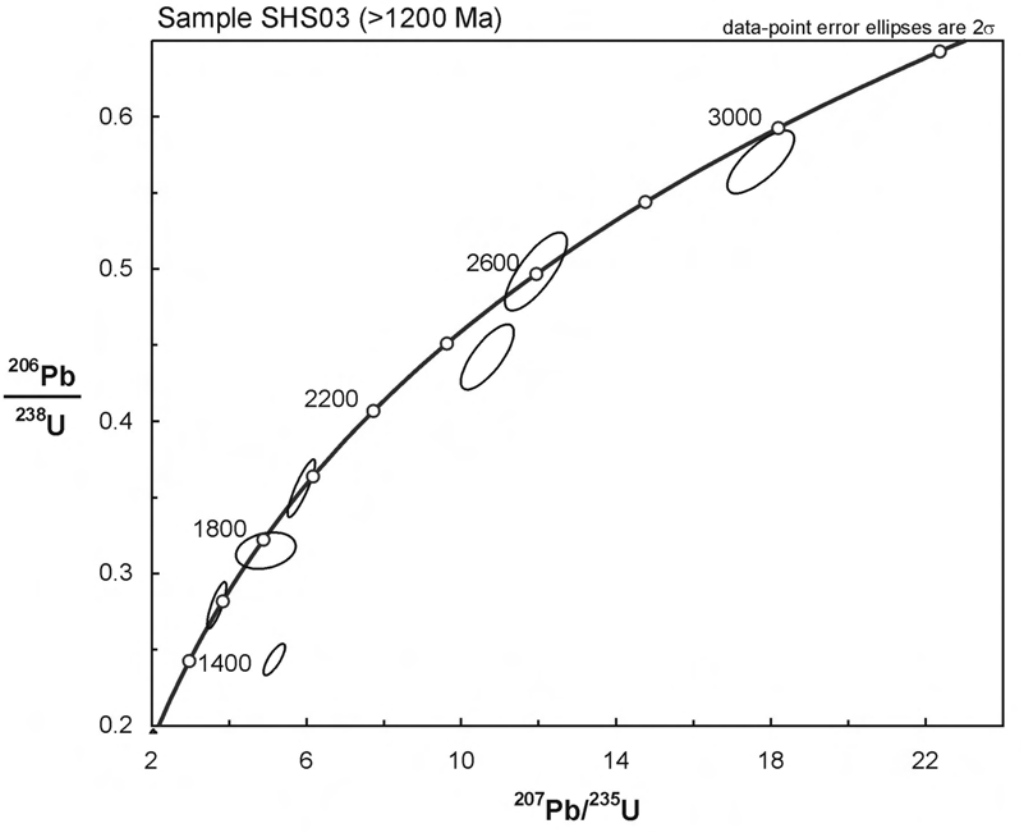
Sample SHS03 (>1200 Ma)
data-point error ellipses are 2σ
0.6
0.5
0.4
0.3
0.2
206Pb/238U
3000
2600
2200
1800
1400
2
6
10
14
18
22
207Pb/235U

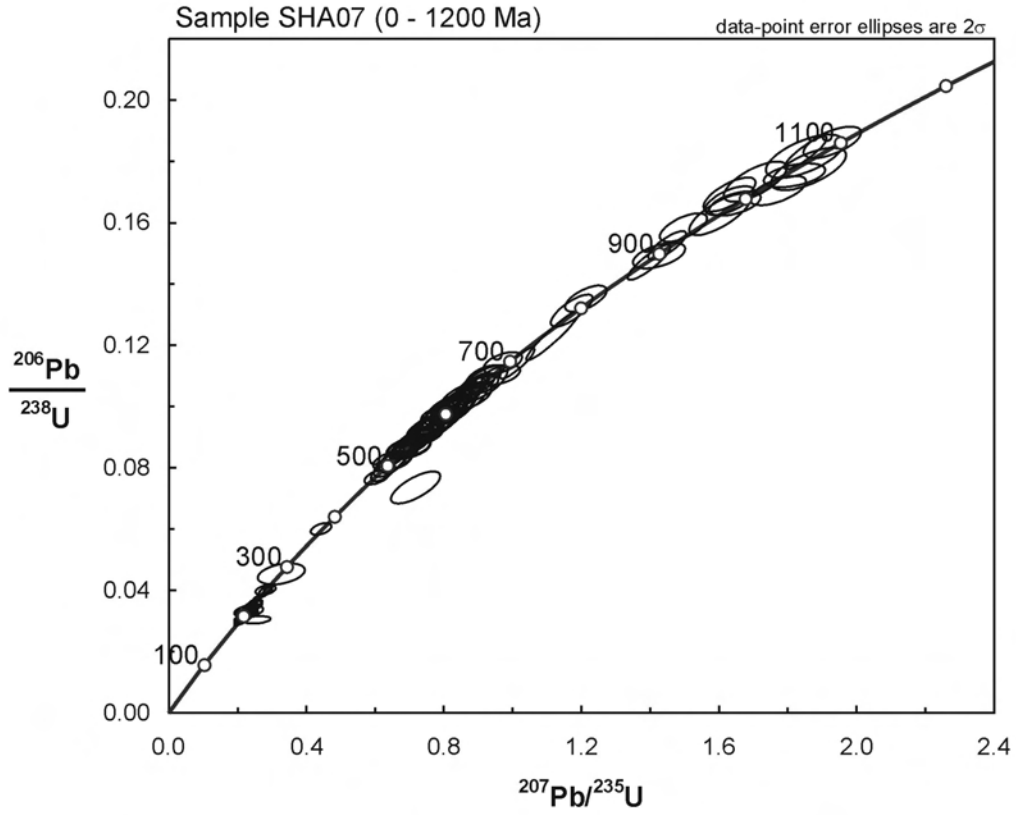
Sample SHA07 (0 - 1200 Ma)
data-point error ellipses are 2σ
0.20
0.16
0.12
0.08
0.04
0.00
0.0
0.4
0.8
1.2
1.6
2.0
2.4
100
300
500
700
900
1100
206Pb/238U
207Pb/235U

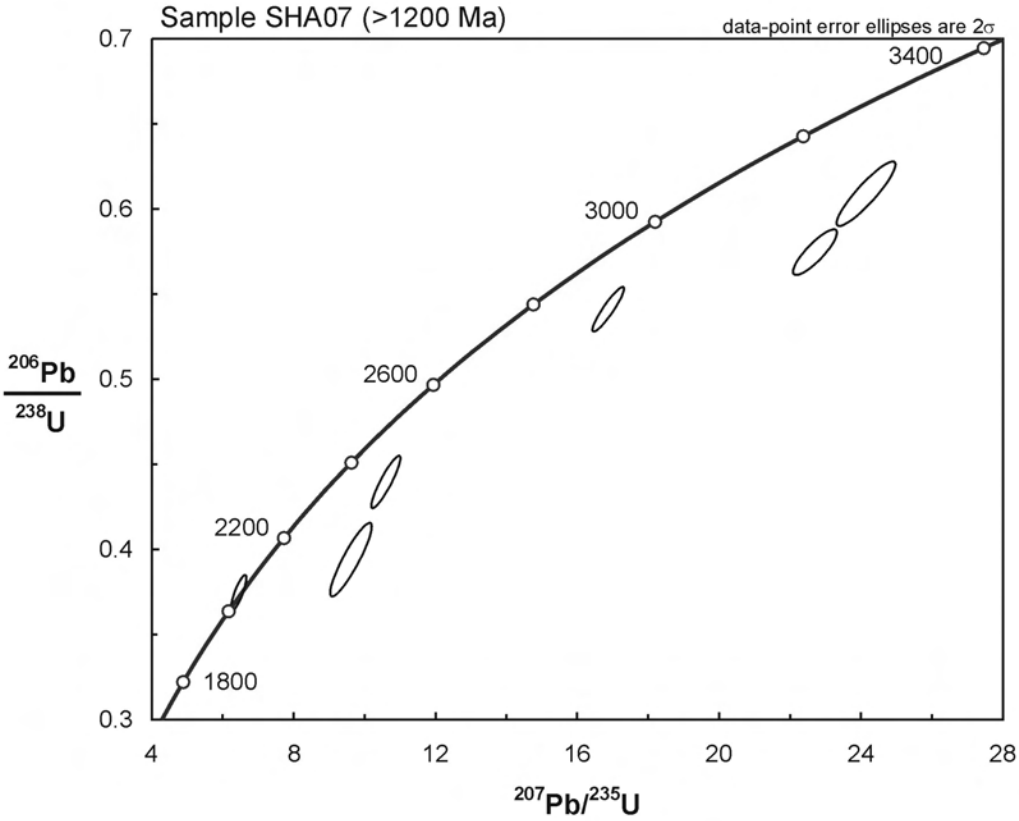
Sample SHA07 (>1200 Ma)
data-point error ellipses are 2σ
0.7
0.6
0.5
0.4
0.3
4
8
12
16
20
24
28
1800
2200
2600
3000
3400
206Pb/238U
207Pb/235U

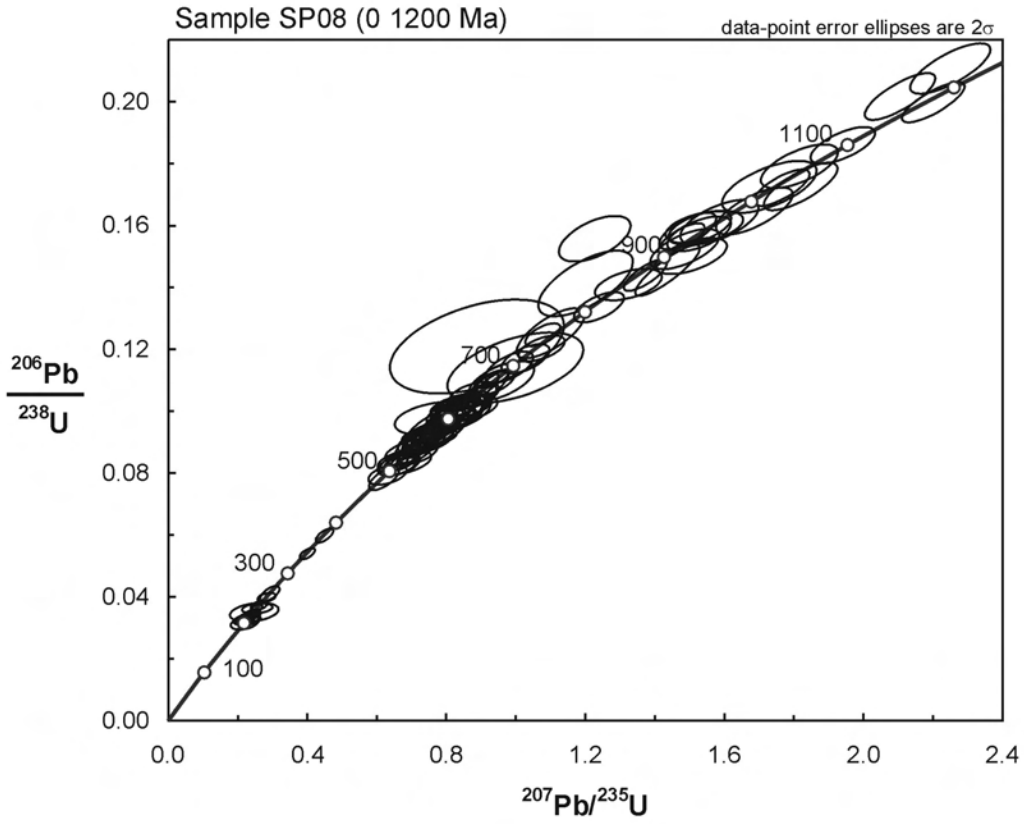
Sample SP08 (0 1200 Ma)
data-point error ellipses are 2σ
0.20
0.16
0.12
0.08
0.04
0.00
0.0
0.4
0.8
1.2
1.6
2.0
2.4
1100
900
700
500
300
100
206Pb/238U
207Pb/235U

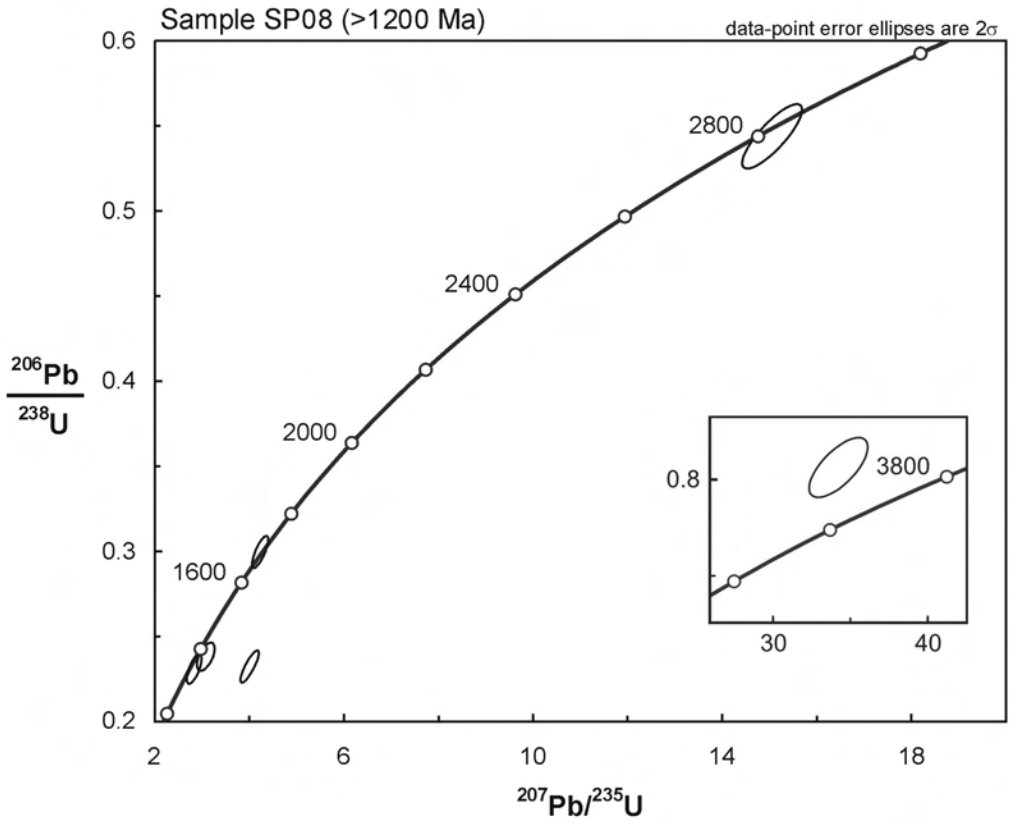
Sample SP08 (>1200 Ma)
data-point error ellipses are 2σ
0.6
0.5
0.4
0.3
0.2
2
6
10
14
18
2800
2400
2000
1600
0.8
3800
30
40
206Pb/238U
207Pb/235U

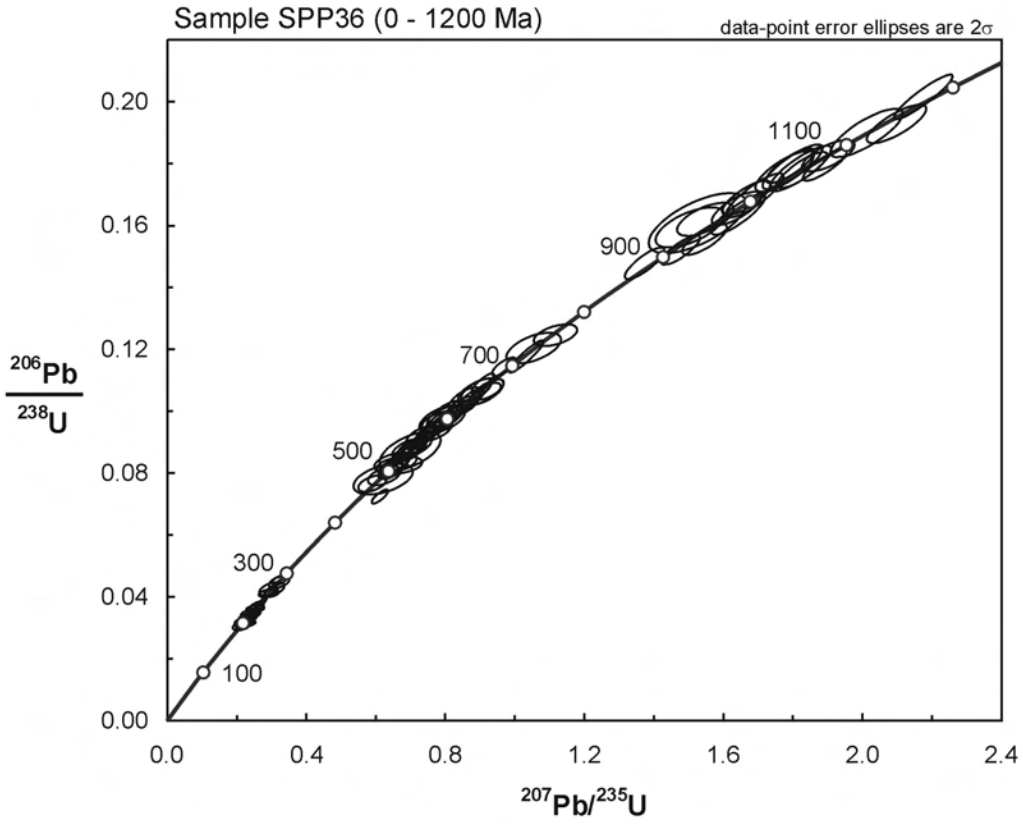
Sample SPP36 (0 - 1200 Ma)
data-point error ellipses are 2σ
0.20
0.16
0.12
0.08
0.04
0.00
206Pb/238U
1100
900
700
500
300
100
0.0
0.4
0.8
1.2
1.6
2.0
2.4
207Pb/235U

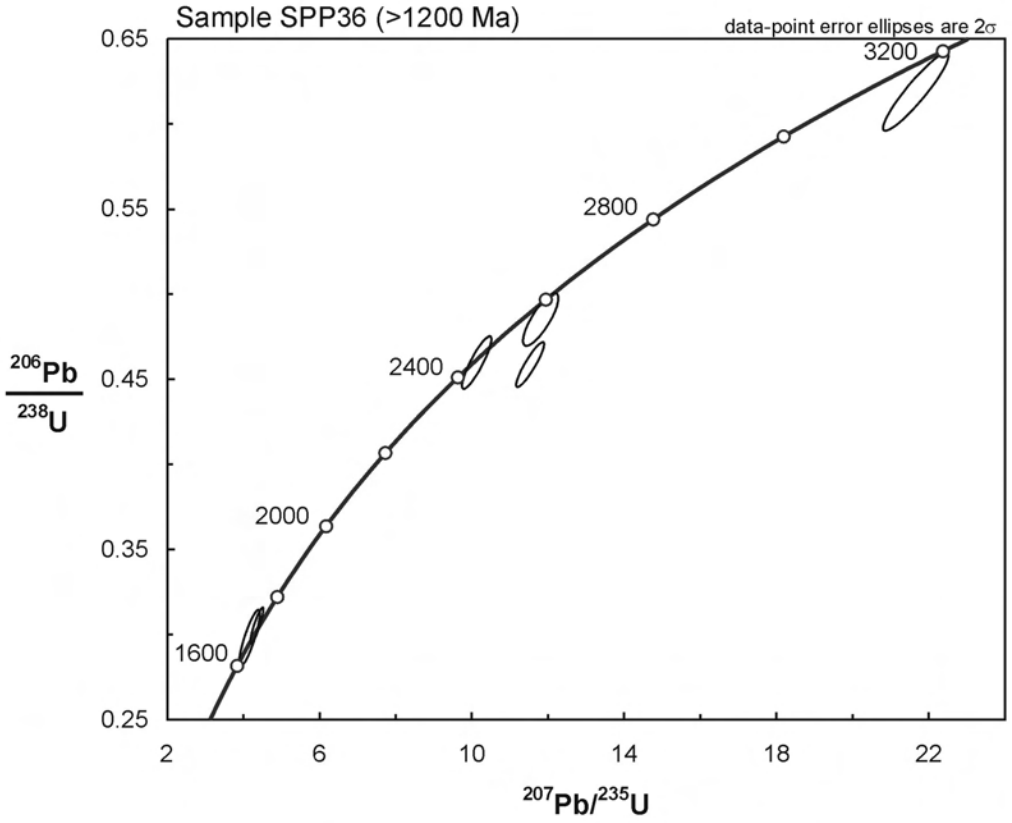
Sample SPP36 (>1200 Ma)
data-point error ellipses are 2σ
0.65
0.55
0.45
0.35
0.25
206Pb/238U
3200
2800
2400
2000
1600
2
6
10
14
18
22
207Pb/235U

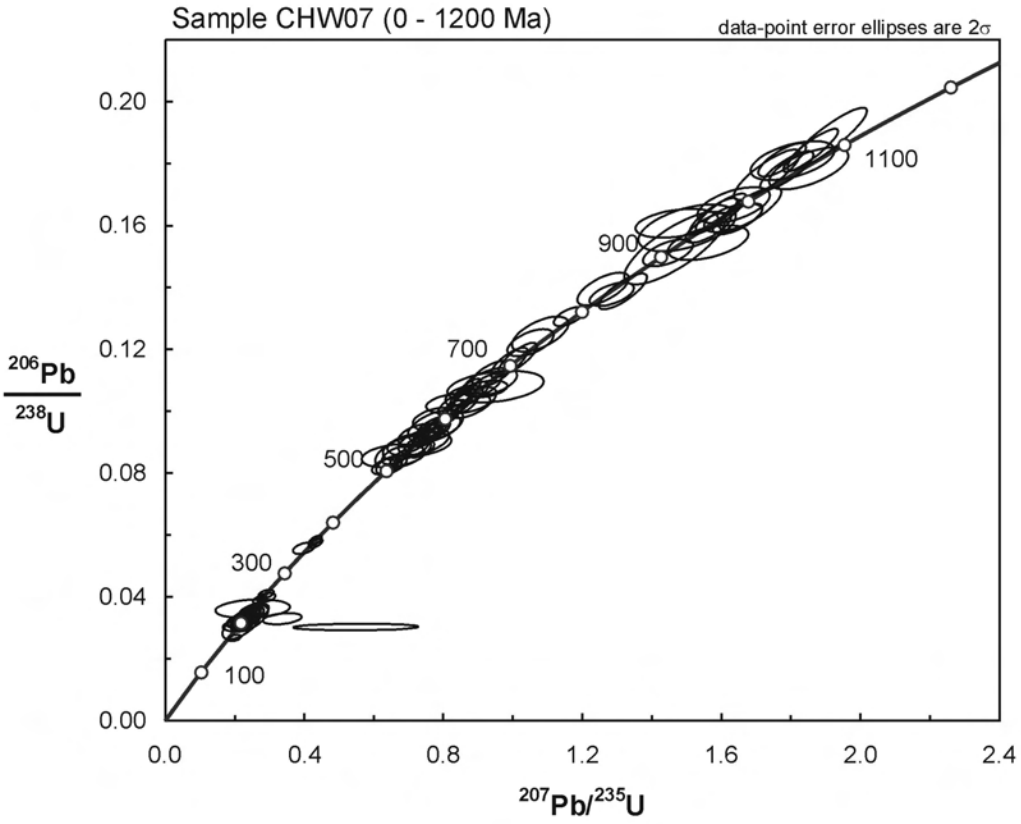
Sample CHW07 (0 - 1200 Ma)
data-point error ellipses are 2σ
0.20
0.16
0.12
0.08
0.04
0.00
206Pb/238U
1100
900
700
500
300
100
0.0
0.4
0.8
1.2
1.6
2.0
2.4
207Pb/235U

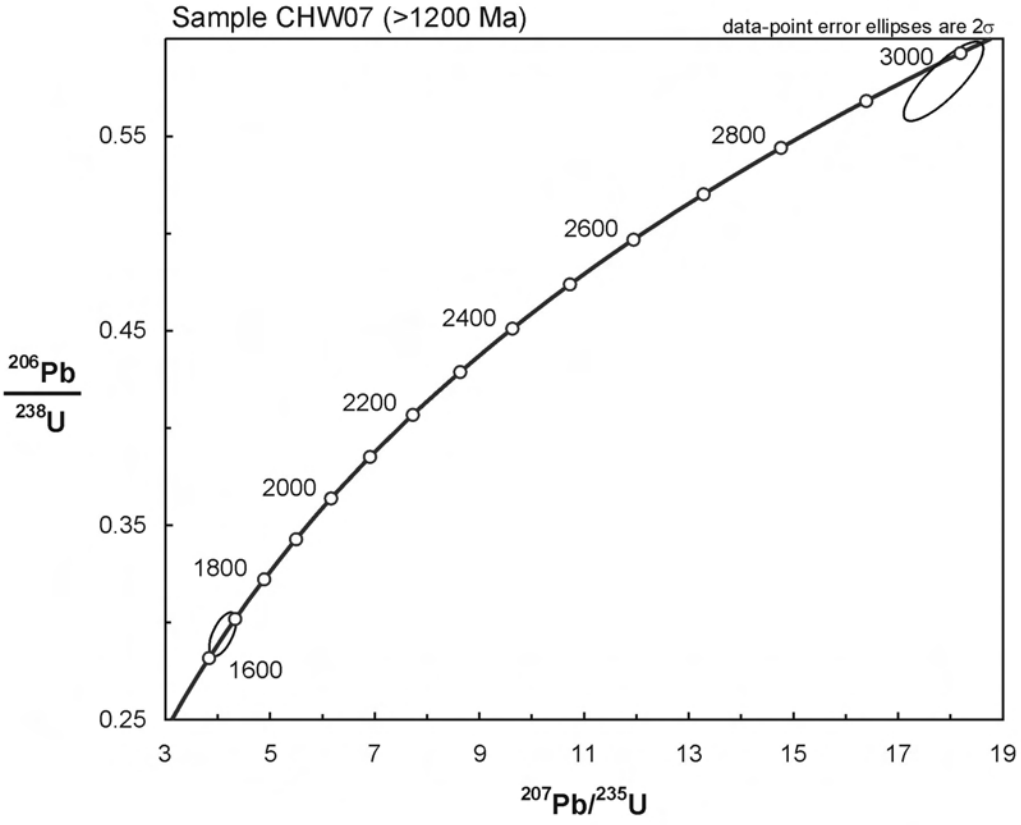
Sample CHW07 (>1200 Ma)
data-point error ellipses are 2σ
0.55
0.45
0.35
0.25
206Pb/238U
3000
2800
2600
2400
2200
2000
1800
1600
3
5
7
9
11
13
15
17
19
207Pb/235U

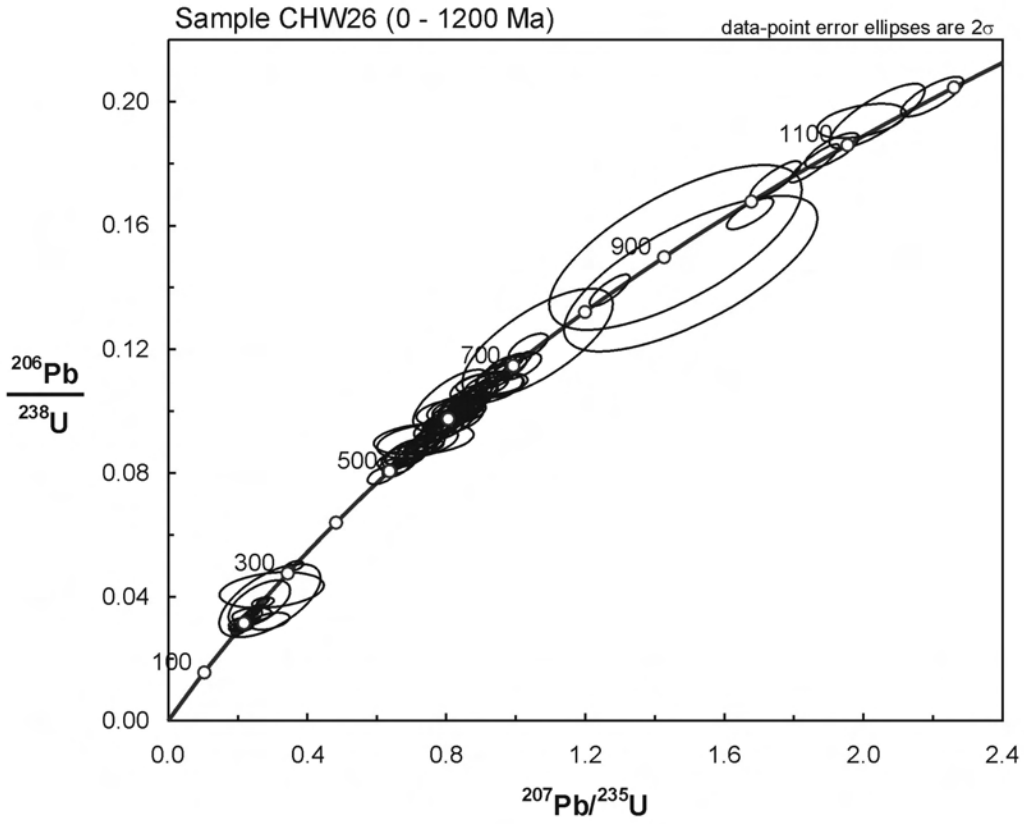
Sample CHW26 (0 - 1200 Ma)
data-point error ellipses are 2σ
0.20
0.16
0.12
0.08
0.04
0.00
206Pb/238U
1100
900
700
500
300
100
0.0
0.4
0.8
1.2
1.6
2.0
2.4
207Pb/235U

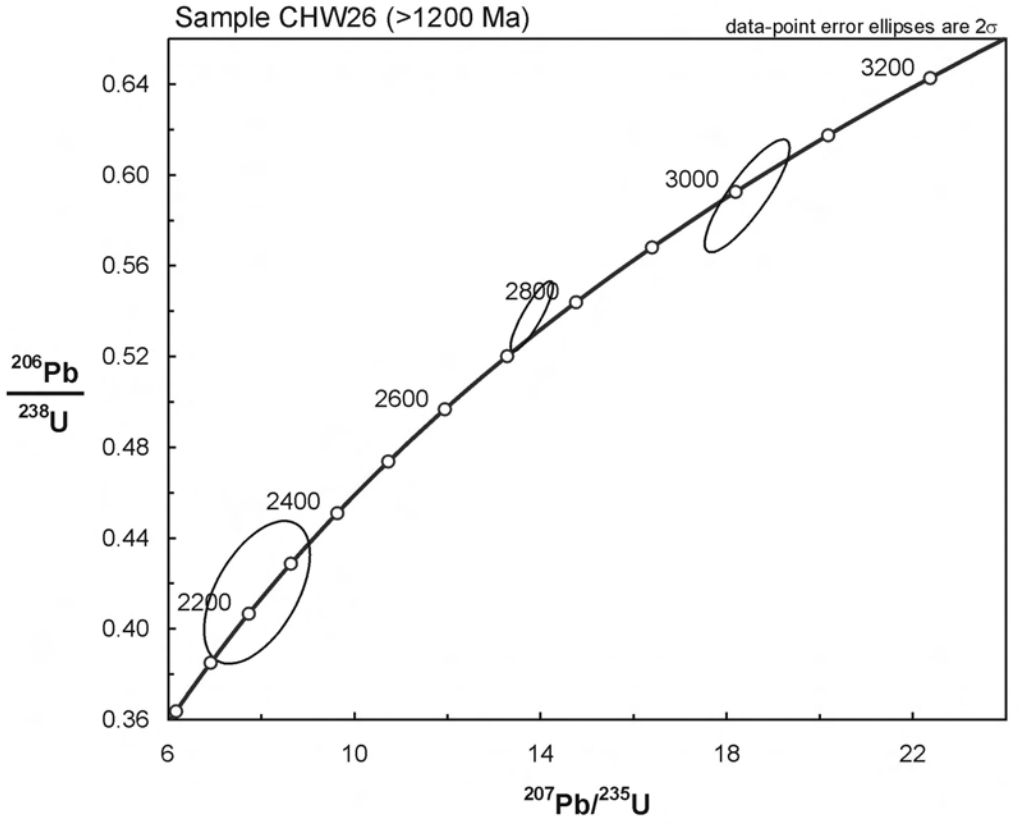
Sample CHW26 (>1200 Ma)
data-point error ellipses are 2σ
0.64
0.60
0.56
0.52
0.48
0.44
0.40
0.36
206Pb/238U
3200
3000
2800
2600
2400
2200
6
10
14
18
22
207Pb/235U

# Appendix 7.3

Cathodoluminescence-images
of analysed zircons from the SPF

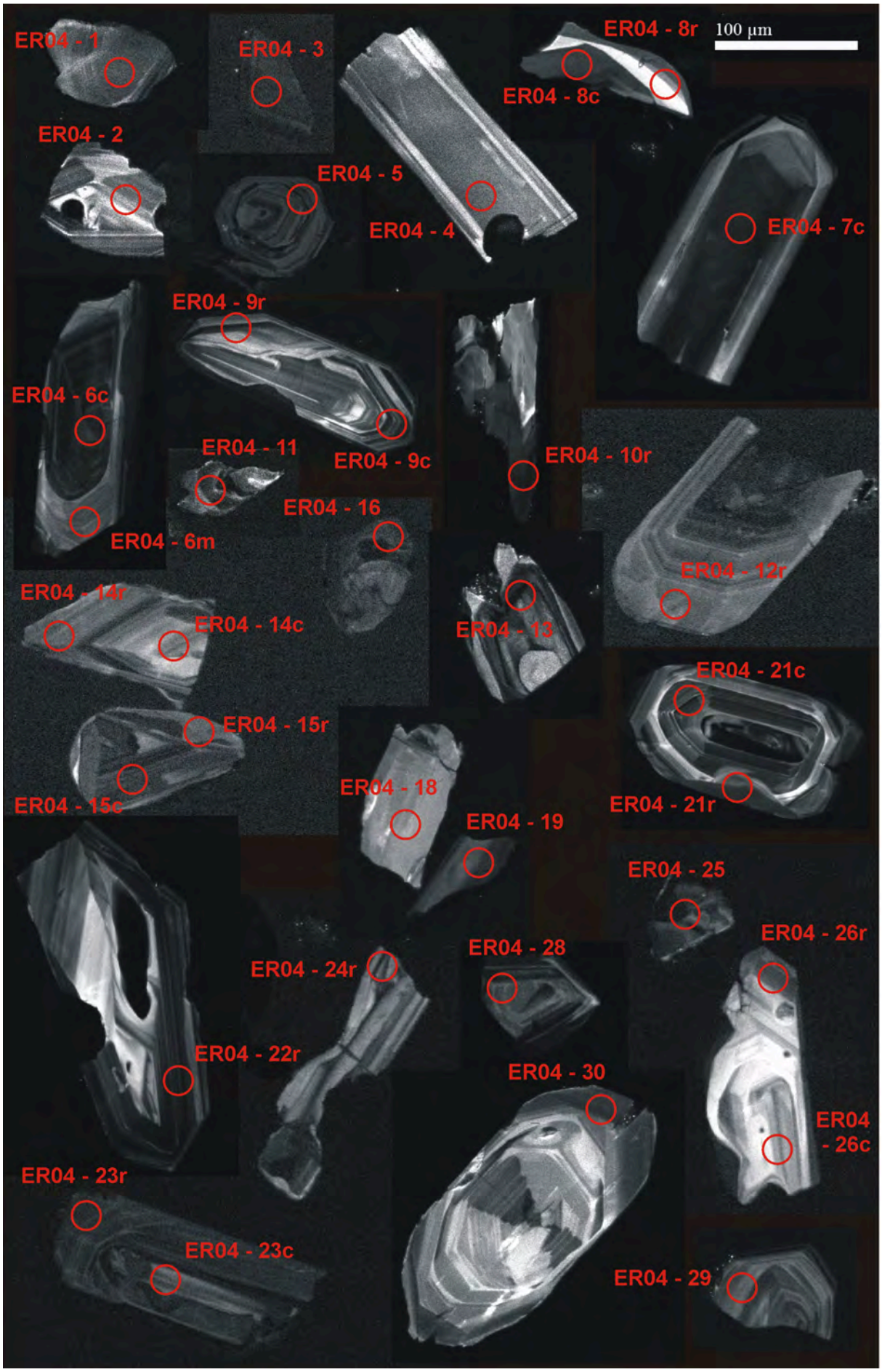
ER04 - 1
ER04 - 3
ER04 - 8r
100 µm
ER04 - 8c
ER04 - 2
ER04 - 5
ER04 - 4
ER04 - 7c
ER04 - 9r
ER04 - 6c
ER04 - 11
ER04 - 9c
ER04 - 10r
ER04 - 16
ER04 - 6m
ER04 - 12r
ER04 - 14r
ER04 - 14c
ER04 - 13
ER04 - 21c
ER04 - 15r
ER04 - 15c
ER04 - 18
ER04 - 19
ER04 - 21r
ER04 - 25
ER04 - 26r
ER04 - 28
ER04 - 24r
ER04 - 22r
ER04 - 30
ER04 - 26c
ER04 - 23r
ER04 - 23c
ER04 - 29

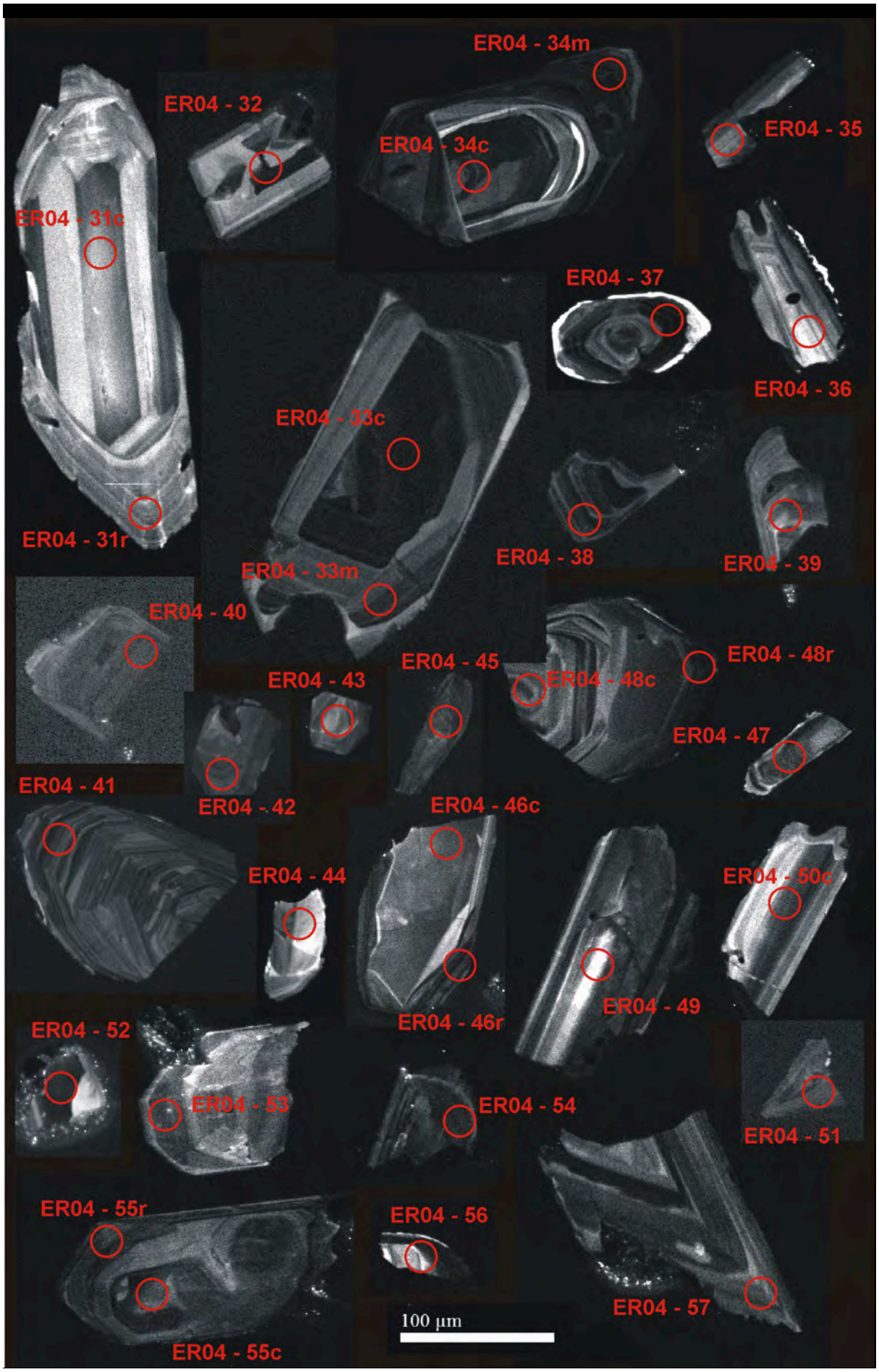
ER04 - 34m
ER04 - 32
ER04 - 34c
ER04 - 35
ER04 - 31c
ER04 - 37
ER04 - 36
ER04 - 33c
ER04 - 31r
ER04 - 38
ER04 - 39
ER04 - 33m
ER04 - 40
ER04 - 45
ER04 - 48r
ER04 - 43
ER04 - 48c
ER04 - 47
ER04 - 41
ER04 - 42
ER04 - 46c
ER04 - 44
ER04 - 50c
ER04 - 49
ER04 - 52
ER04 - 46r
ER04 - 53
ER04 - 54
ER04 - 51
ER04 - 55r
ER04 - 56
ER04 - 57
100 µm
ER04 - 55c

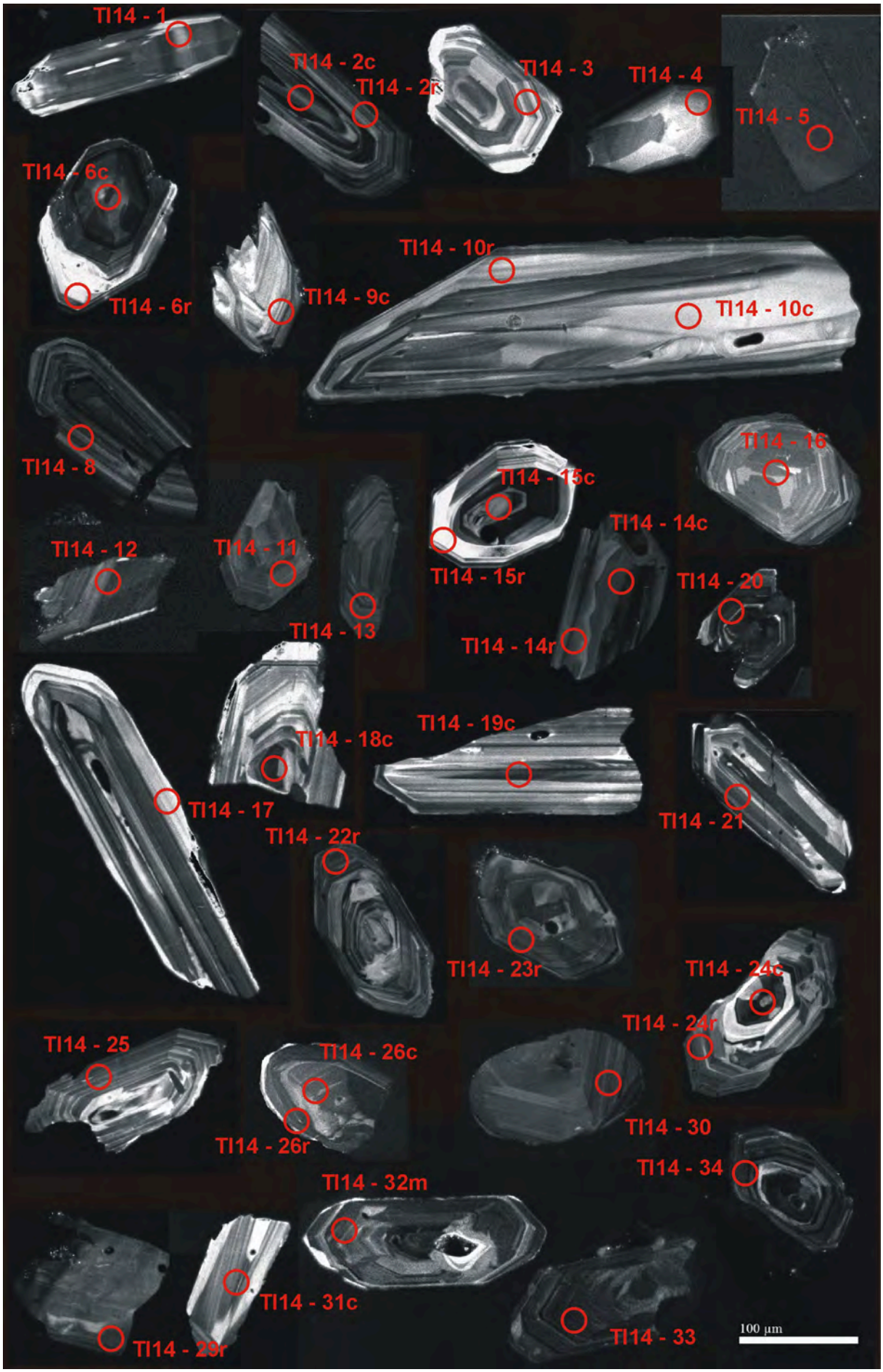
TI14 - 1
TI14 - 2c
TI14 - 2r
TI14 - 3
TI14 - 4
TI14 - 5
TI14 - 6c
TI14 - 6r
TI14 - 9c
TI14 - 10r
TI14 - 10c
TI14 - 8
TI14 - 16
TI14 - 15c
TI14 - 14c
TI14 - 12
TI14 - 11
TI14 - 15r
TI14 - 20
TI14 - 13
TI14 - 14r
TI14 - 18c
TI14 - 19c
TI14 - 17
TI14 - 21
TI14 - 22r
TI14 - 23r
TI14 - 24c
TI14 - 24r
TI14 - 25
TI14 - 26c
TI14 - 30
TI14 - 26r
TI14 - 34
TI14 - 32m
TI14 - 31c
TI14 - 33
TI14 - 29r
100 µm


TI14 - 36
TI14 - 35r
TI14 - 38c
TI14 - 38r
TI14 - 43
TI14 - 37
TI14 - 44
TI14 - 39c
TI14 - 40c
TI14 - 41r
TI14 - 42c
TI14 - 47
TI14 - 45c
TI14 - 46
TI14 - 39r
TI14 - 50c
TI14 - 49c
TI14 - 48
TI14 - 52
TI14 - 59
TI14 - 49r
TI14 - 53
TI14 - 58r
TI14 - 55c
TI14 - 58c
TI14 - 60c
TI14 - 56c
TI14 - 56r
TI14 - 57
100 µm
TI14 - 60r


SHS03 - 4r
SHS03 - 1c
SHS03 - 2
SHS03 - 4c
SHS03 - 1r
SHS03 - 3r
SHS03 - 6
SHS03 - 5
SHS03 - 12r
SHS03 - 15
SHS03 - 8c
SHS03 - 10r
SHS03 - 11
SHS03 - 18r
SHS03 - 8r
SHS03 - 7r
SHS03 - 22r
SHS03 - 22c
SHS03 - 13c
SHS03 - 9
SHS03 - 16c
SHS03 - 23r
SHS03 - 19
SHS03 - 14r
SHS03 - 17r
SHS03 - 16r
SHS03 - 20r
SHS03 - 24c
SHS03 - 21r
SHS03 - 26r
SHS03 - 21c
SHS03 - 25
SHS03 - 27
100 µm

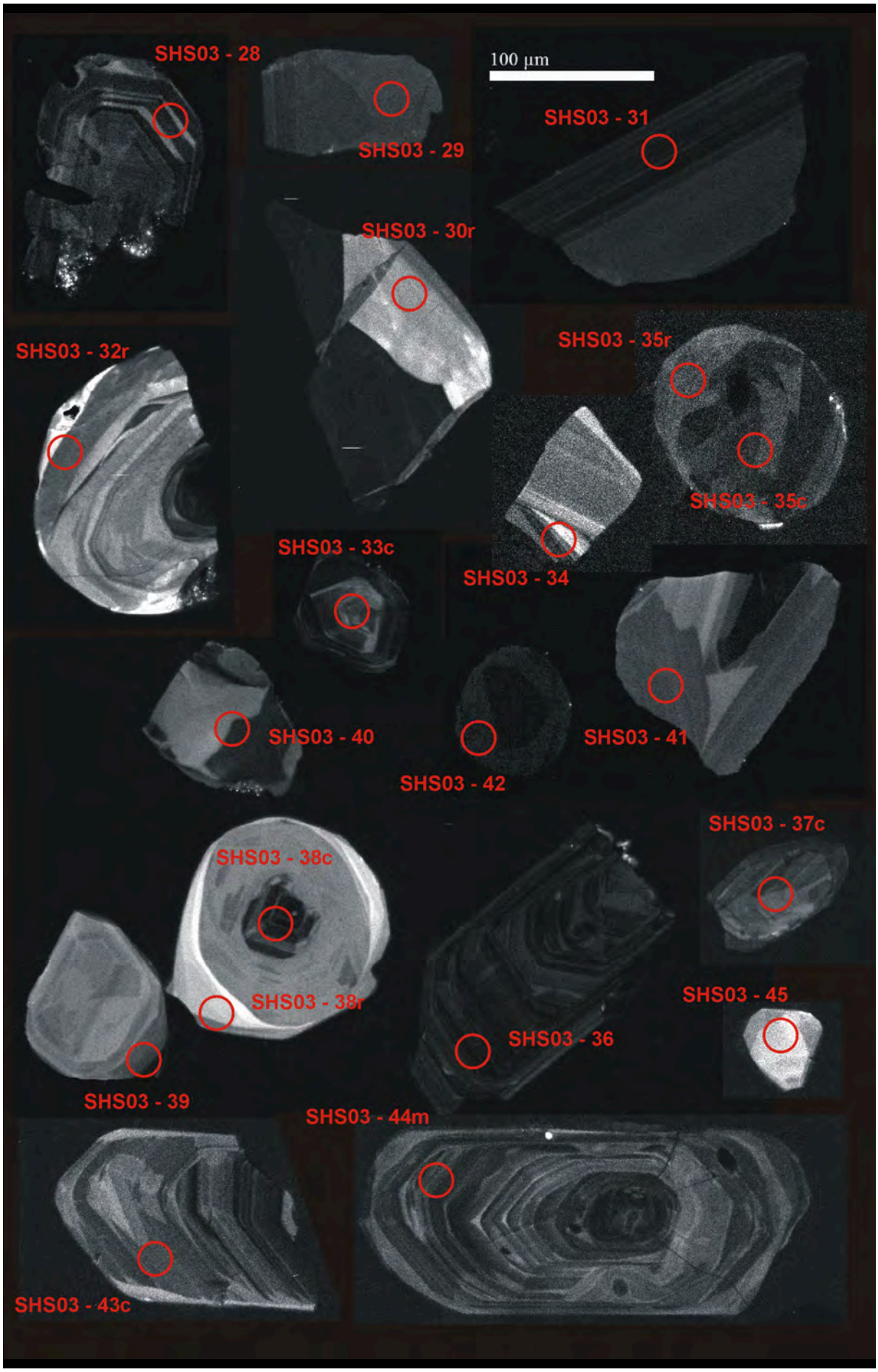
SHS03 - 28
100 µm
SHS03 - 29
SHS03 - 31
SHS03 - 30r
SHS03 - 32r
SHS03 - 35r
SHS03 - 35c
SHS03 - 33c
SHS03 - 34
SHS03 - 40
SHS03 - 41
SHS03 - 42
SHS03 - 37c
SHS03 - 38c
SHS03 - 38r
SHS03 - 45
SHS03 - 36
SHS03 - 39
SHS03 - 44m
SHS03 - 43c


SHS03 - 51
SHS03 - 53
SHS03 - 52c
SHS03 - 49r
SHS03 - 52r
SHS03 - 50m
SHS03 - 48m
SHS03 - 46c
SHS03 - 55r
SHS03 - 54
SHS03 - 47
SHS03 - 46r
SHS03 - 57
SHS03 - 56c
SHS03 - 63r
SHS03 - 68c
SHS03 - 58c
SHS03 - 60c
SHS03 - 59
SHS03 - 65m
SHS03 - 66m
SHS03 - 69
SHS03 - 64r
SHS03 - 71
SHS03 - 62
SHS03 - 67c
SHS03 - 70
SHS03 - 72c
SHS03 - 72r
SHS03 - 73
100 µm

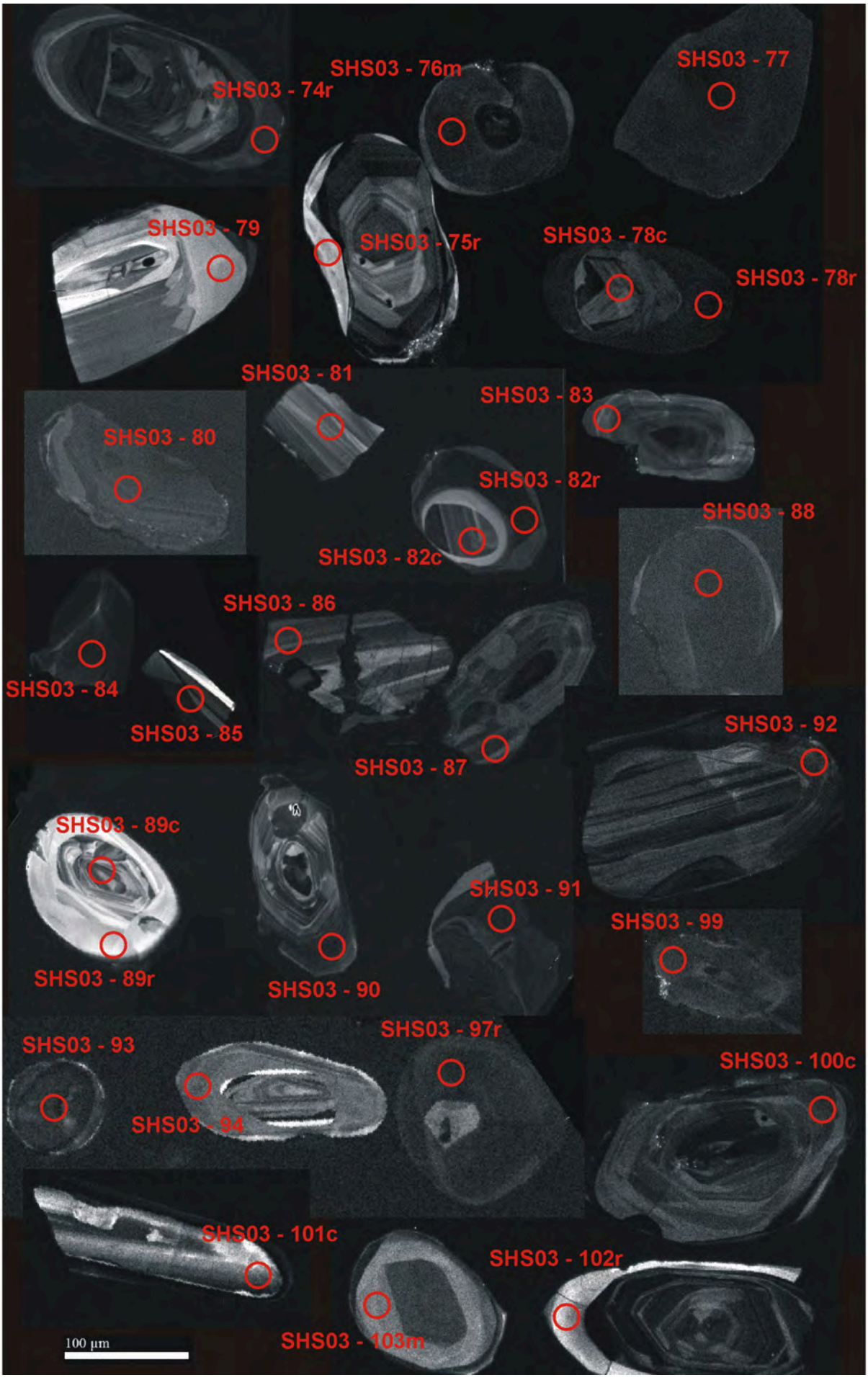
SHS03 - 74r
SHS03 - 76m
SHS03 - 77
SHS03 - 79
SHS03 - 75r
SHS03 - 78c
SHS03 - 78r
SHS03 - 81
SHS03 - 83
SHS03 - 80
SHS03 - 82r
SHS03 - 88
SHS03 - 82c
SHS03 - 86
SHS03 - 84
SHS03 - 85
SHS03 - 87
SHS03 - 92
SHS03 - 89c
SHS03 - 91
SHS03 - 99
SHS03 - 89r
SHS03 - 90
SHS03 - 97r
SHS03 - 93
SHS03 - 100c
SHS03 - 94
SHS03 - 101c
SHS03 - 102r
SHS03 - 103m
100 µm


100 µm
SHA07 - 2r
SHA07 - 7
SHA07 - 6
SHA07 - 4
SHA07 - 8
SHA07 - 9c
SHA07 - 3
SHA07 - 5c
SHA07 - 11
SHA07 - 1r
SHA07 - 13
SHA07 - 15c
SHA07 - 10
SHA07 - 12
SHA07 - 15r
SHA07 - 22
SHA07 - 14
SHA07 - 21
SHA07 - 17
SHA07 - 16
SHA07 - 19
SHA07 - 18
SHA07 - 20
SHA07 - 26
SHA07 - 23
SHA07 - 24
SHA07 - 28
SHA07 - 29
SHA07 - 25r
SHA07 - 31
SHA07 - 27
SHA07 - 30r
SHA07 - 32
SHA07 - 30c
SHA07 - 43
SHA07 - 34
SHA07 - 33
SHA07 - 40
SHA07 - 35c
SHA07 - 42
SHA07 - 37r
SHA07 - 39
SHA07 - 36
SHA07 - 44
SHA07 - 37c
SHA07 - 38c
SHA07 - 41

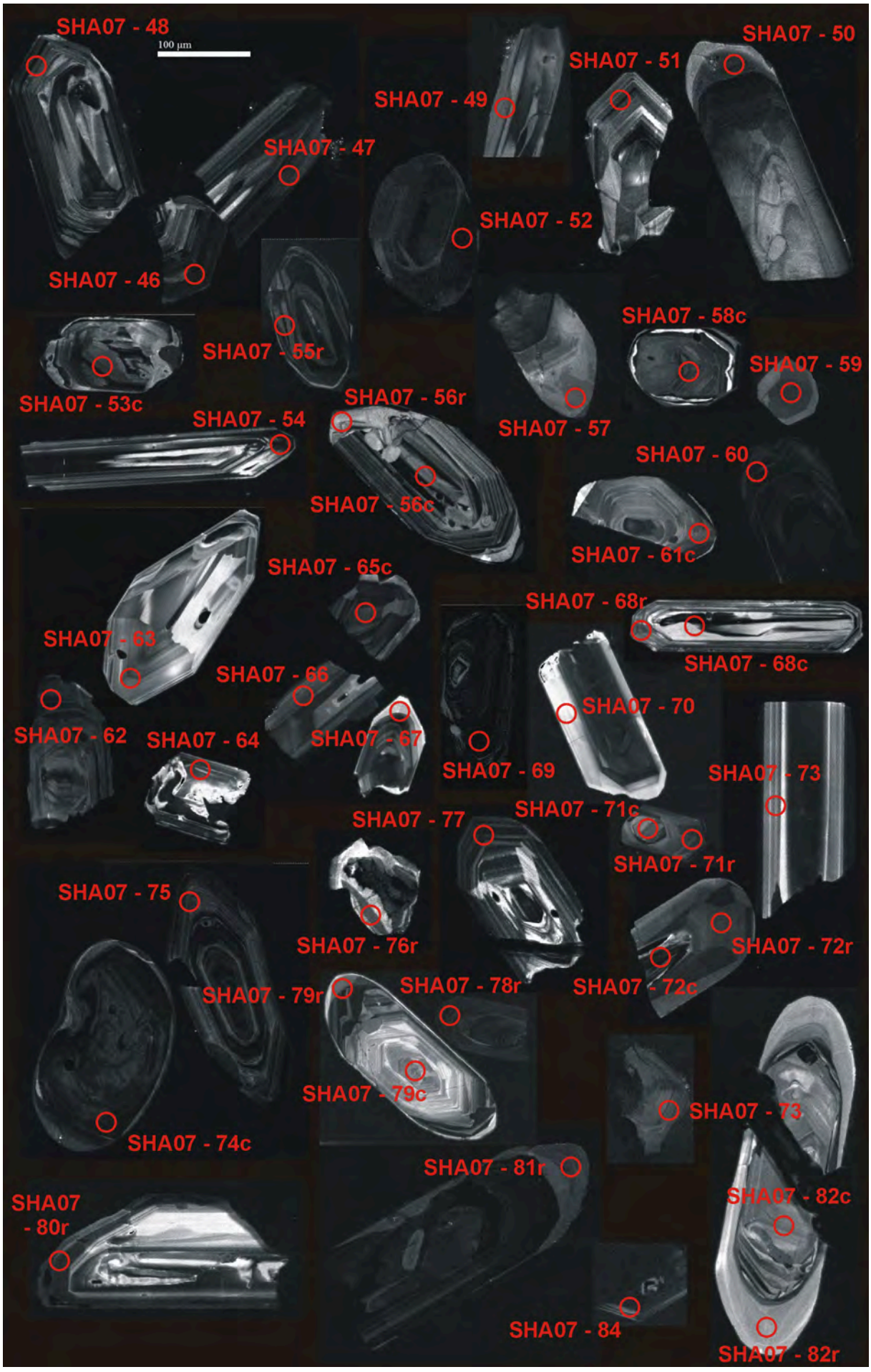
SHA07 - 48
100 µm
SHA07 - 50
SHA07 - 51
SHA07 - 49
SHA07 - 47
SHA07 - 52
SHA07 - 46
SHA07 - 58c
SHA07 - 55r
SHA07 - 59
SHA07 - 53c
SHA07 - 56r
SHA07 - 54
SHA07 - 57
SHA07 - 60
SHA07 - 56c
SHA07 - 61c
SHA07 - 65c
SHA07 - 68r
SHA07 - 63
SHA07 - 68c
SHA07 - 66
SHA07 - 70
SHA07 - 62
SHA07 - 64
SHA07 - 67
SHA07 - 69
SHA07 - 73
SHA07 - 77
SHA07 - 71c
SHA07 - 71r
SHA07 - 75
SHA07 - 76r
SHA07 - 72r
SHA07 - 79r
SHA07 - 78r
SHA07 - 72c
SHA07 - 79c
SHA07 - 73
SHA07 - 74c
SHA07 - 81r
SHA07 - 82c
SHA07 - 80r
SHA07 - 84
SHA07 - 82r

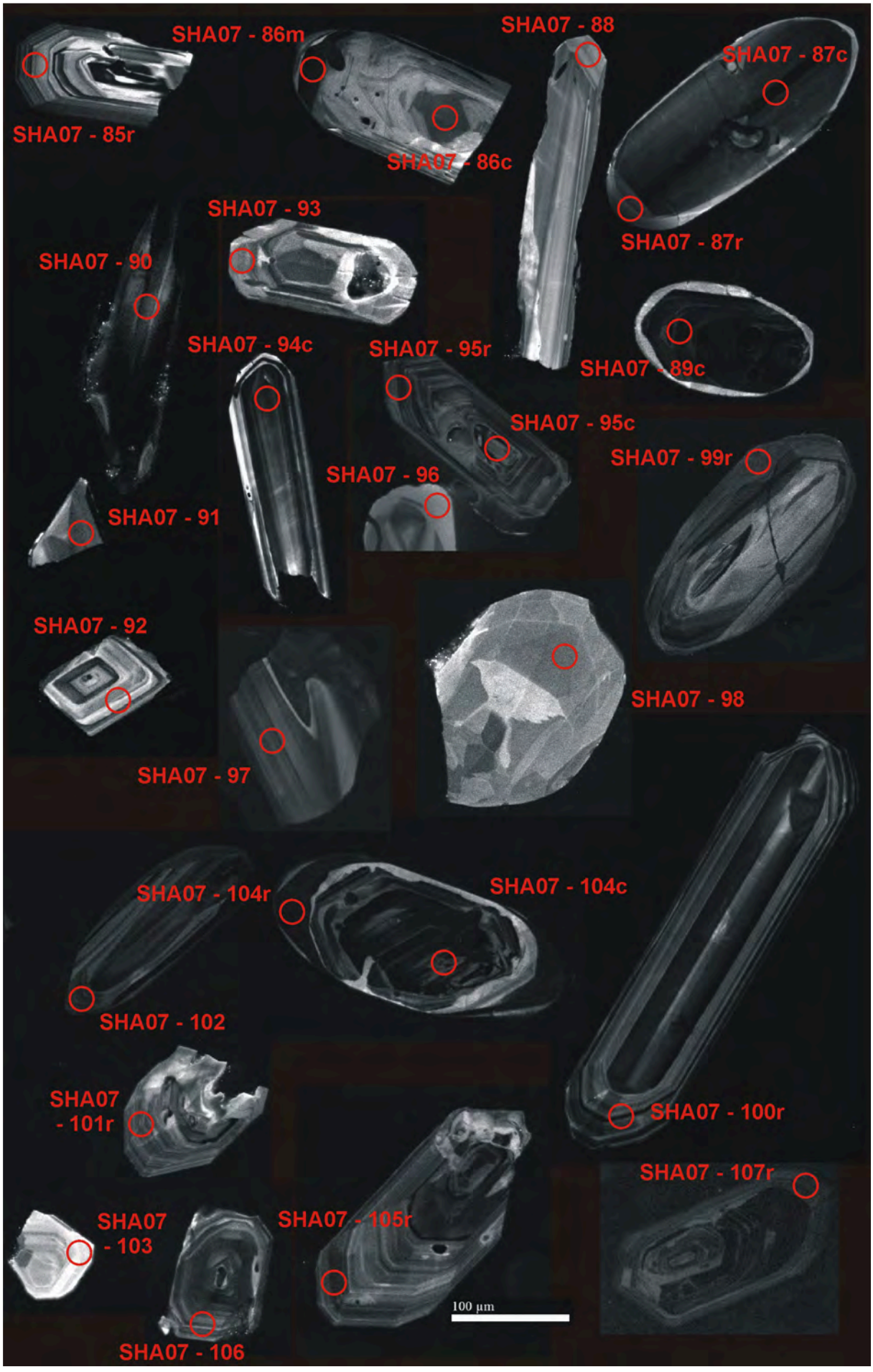
SHA07 - 86m
SHA07 - 88
SHA07 - 87c
SHA07 - 85r
SHA07 - 86c
SHA07 - 93
SHA07 - 90
SHA07 - 87r
SHA07 - 94c
SHA07 - 95r
SHA07 - 89c
SHA07 - 95c
SHA07 - 99r
SHA07 - 96
SHA07 - 91
SHA07 - 92
SHA07 - 98
SHA07 - 97
SHA07 - 104r
SHA07 - 104c
SHA07 - 102
SHA07 - 101r
SHA07 - 100r
SHA07 - 107r
SHA07 - 103
SHA07 - 105r
100 µm
SHA07 - 106

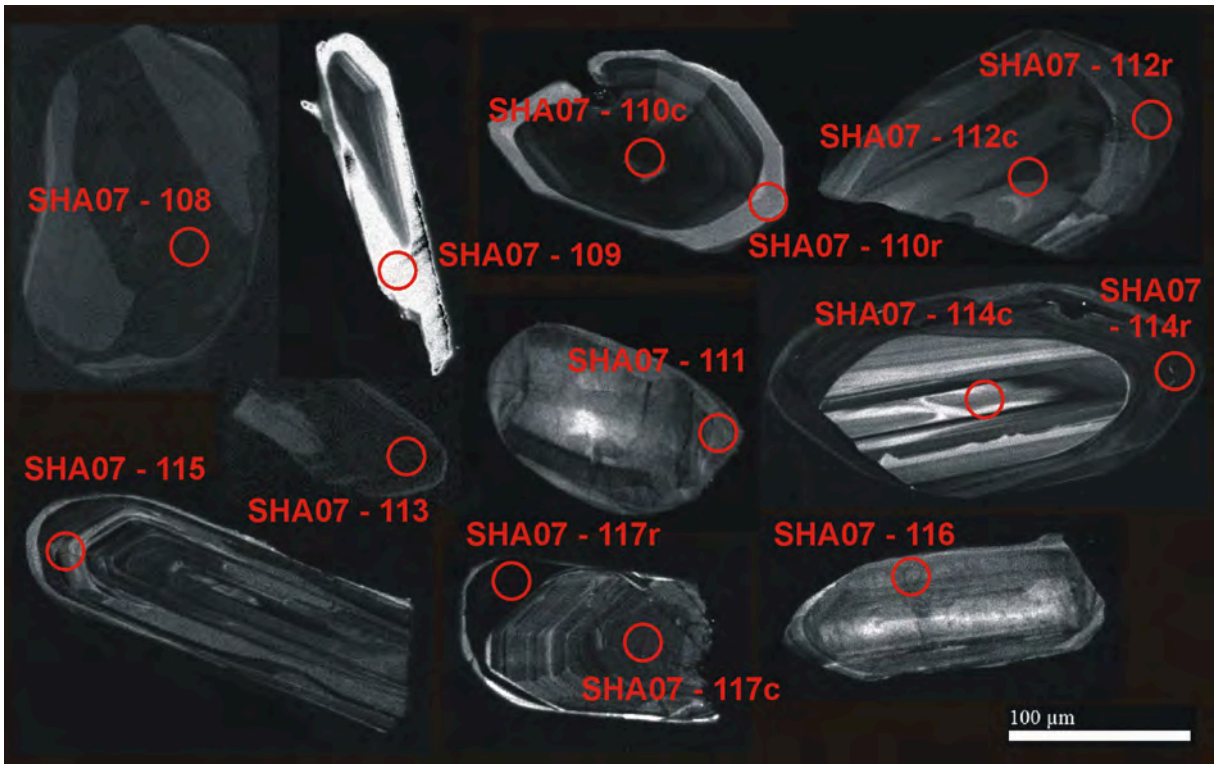
SHA07 - 108
SHA07 - 109
SHA07 - 110c
SHA07 - 110r
SHA07 - 112r
SHA07 - 112c
SHA07 - 111
SHA07 - 114c
SHA07 - 114r
SHA07 - 115
SHA07 - 113
SHA07 - 117r
SHA07 - 117c
SHA07 - 116
100 µm


SP08 - 1r
SP08 - 1m
SP08 - 1c
SP08 - 2r
SP08 - 2m
SP08 - 3
SP08 - 4
SP08 - 13r
SP08 - 13c
SP08 - 6r
SP08 - 6c
SP08 - 11
SP08 - 5
SP08 - 7r
SP08 - 7m
SP08 - 12
SP08 - 8
SP08 - 10
SP08 - 15
SP08 - 9
SP08 - 16
SP08 - 19r
SP08 - 18r
SP08 - 17
SP08 - 19c
SP08 - 21c
SP08 - 18c
SP08 - 24
SP08 - 20
SP08 - 22
SP08 - 23
SP08 - 31
SP08 - 29r
SP08 - 29c
SP08 - 32
SP08 - 25
SP08 - 27c
SP08 - 27r
SP08 - 26r
SP08 - 30
SP08 - 28
SP08 - 36r
SP08 - 26c
SP08 - 34
SP08 - 35c
SP08 - 36m
SP08 - 35r
SP08 - 35m
100 µm


SP08 - 37
SP08 - 38
SP08 - 39
SP08 - 40c
SP08 - 40r
SP08 - 40m
SP08 - 41
SP08 - 42r
SP08 - 44
SP08 - 45
SP08 - 43
SP08 - 47
SP08 - 46c
SP08 - 46r
SP08 - 48c
SP08 - 50
SP08 - 54
SP08 - 51
SP08 - 55r
SP08 - 49
SP08 - 53
SP08 - 52
SP08 - 59
SP08 - 56c
SP08 - 57
SP08 - 60r
SP08 - 62r
SP08 - 56r
SP08 - 61
SP08 - 62r
SP08 - 62c
SP08 - 62c
SP08 - 64
SP08 - 65
SP08 - 66c
SP08 - 67
SP08 - 68
SP08 - 69c
SP08 - 69r
SP08 - 71
SP08 - 70
100 µm

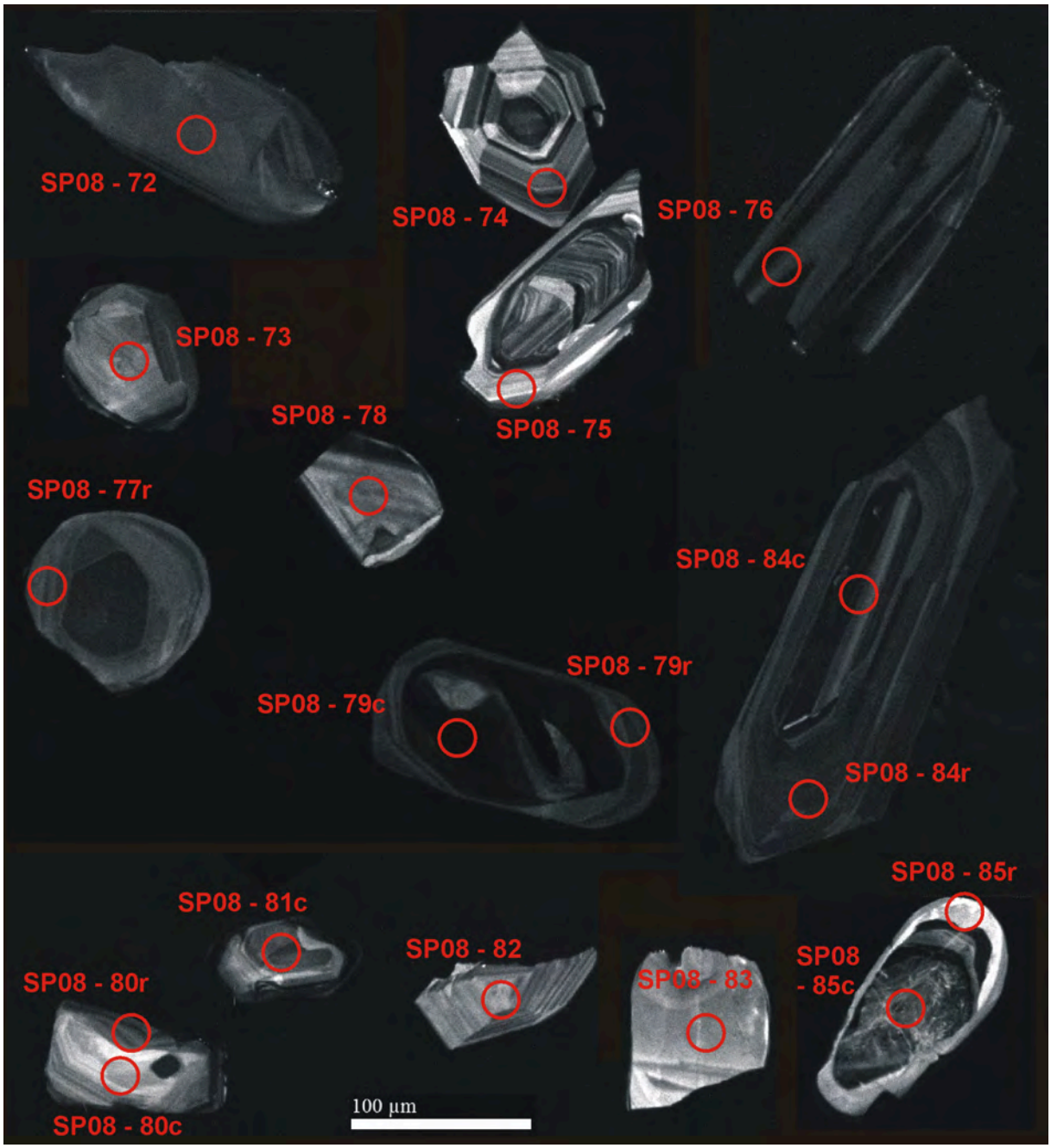
SP08 - 72
SP08 - 74
SP08 - 76
SP08 - 73
SP08 - 75
SP08 - 78
SP08 - 77r
SP08 - 84c
SP08 - 79r
SP08 - 79c
SP08 - 84r
SP08 - 85r
SP08 - 81c
SP08 - 82
SP08 - 83
SP08 - 85c
SP08 - 80r
SP08 - 80c
100 µm

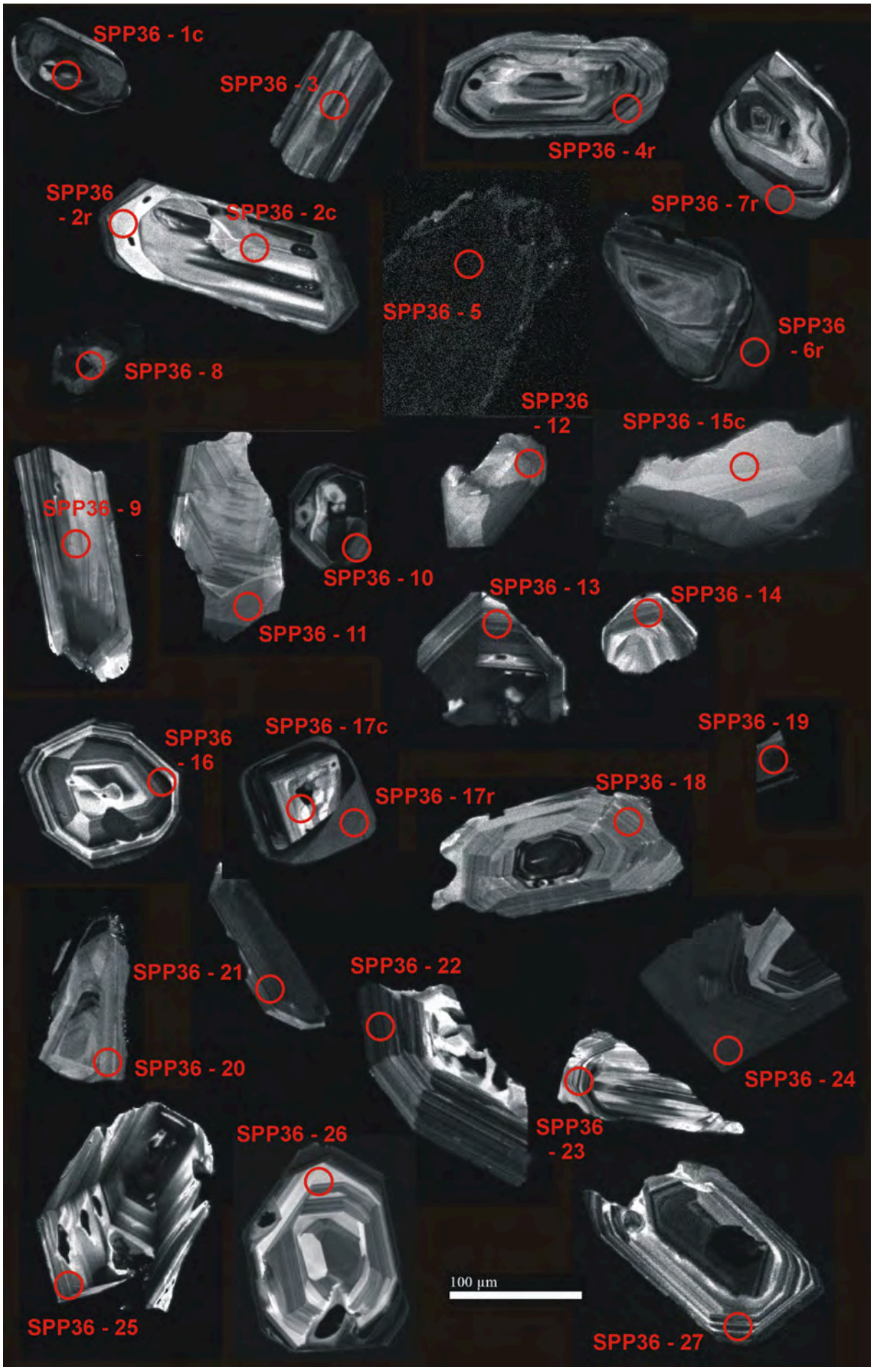
SPP36 - 1c
SPP36 - 3
SPP36 - 4r
SPP36 - 2r
SPP36 - 2c
SPP36 - 7r
SPP36 - 5
SPP36 - 6r
SPP36 - 8
SPP36 - 12
SPP36 - 15c
SPP36 - 9
SPP36 - 10
SPP36 - 13
SPP36 - 14
SPP36 - 11
SPP36 - 16
SPP36 - 17c
SPP36 - 19
SPP36 - 17r
SPP36 - 18
SPP36 - 21
SPP36 - 22
SPP36 - 20
SPP36 - 24
SPP36 - 23
SPP36 - 26
100 µm
SPP36 - 25
SPP36 - 27

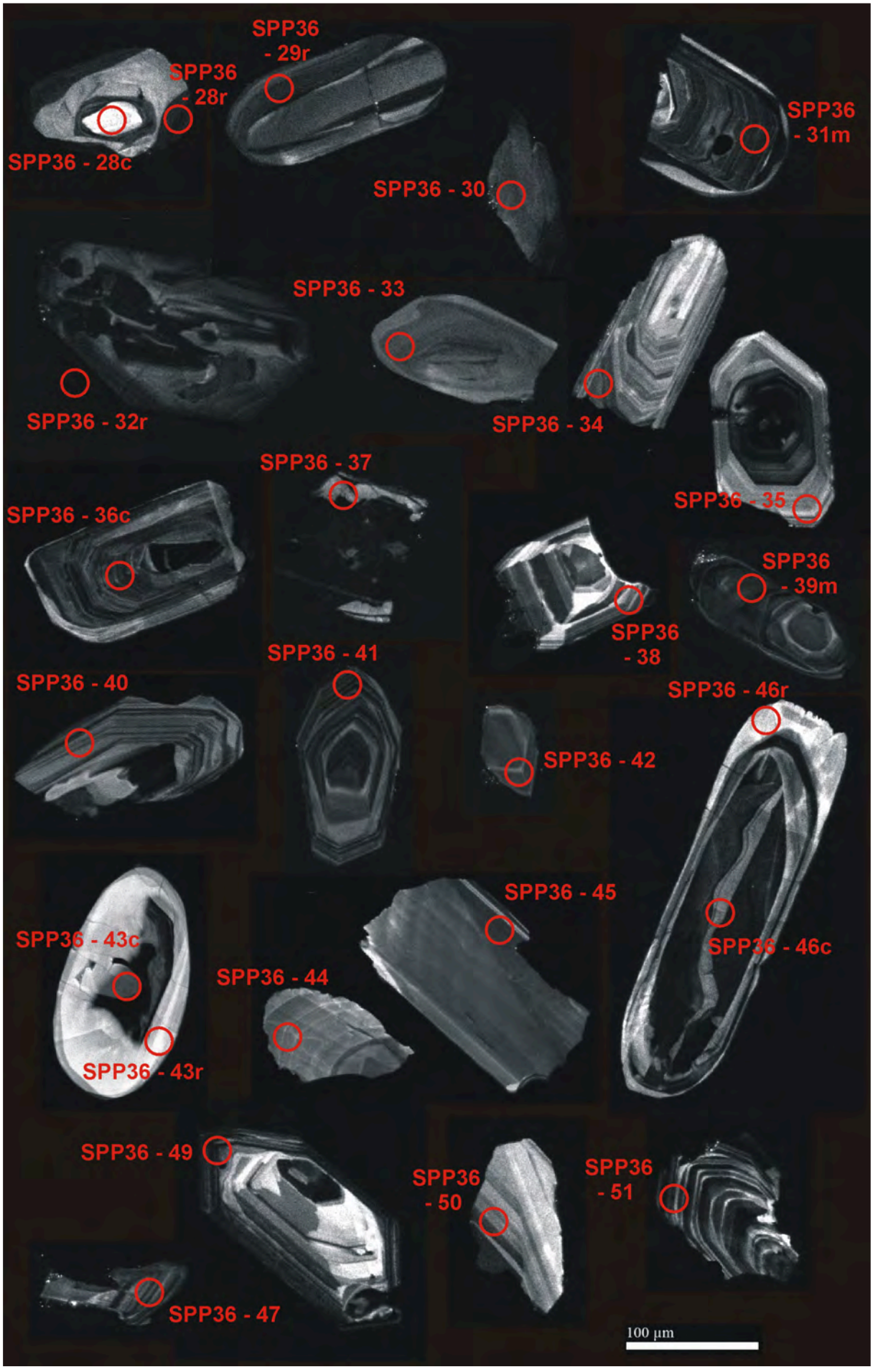
SPP36 - 29r
SPP36 - 28r
SPP36 - 28c
SPP36 - 31m
SPP36 - 30
SPP36 - 33
SPP36 - 32r
SPP36 - 34
SPP36 - 37
SPP36 - 36c
SPP36 - 35
SPP36 - 39m
SPP36 - 38
SPP36 - 41
SPP36 - 40
SPP36 - 46r
SPP36 - 42
SPP36 - 45
SPP36 - 43c
SPP36 - 46c
SPP36 - 44
SPP36 - 43r
SPP36 - 49
SPP36 - 50
SPP36 - 51
SPP36 - 47
100 µm

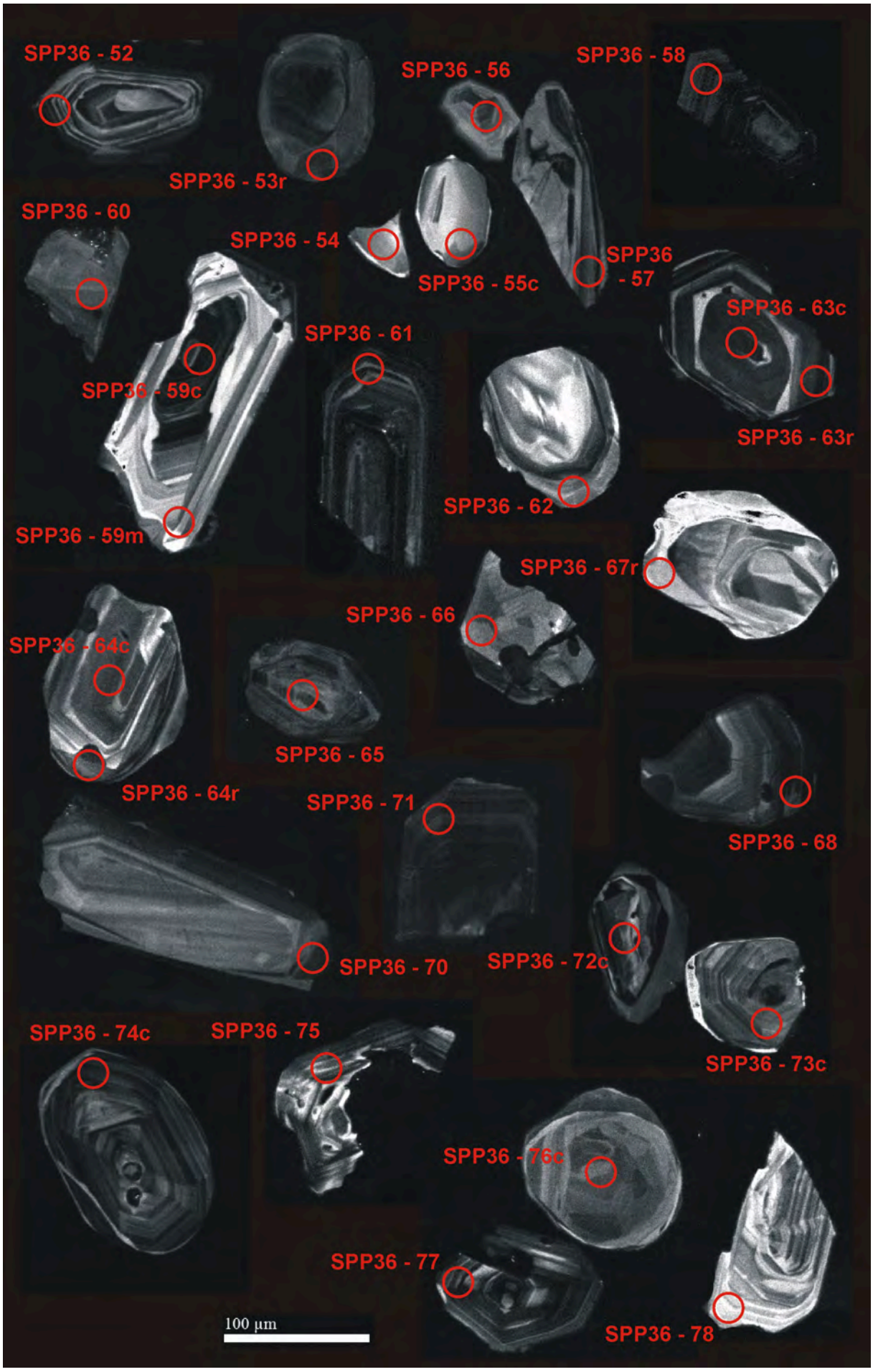
SPP36 - 52
SPP36 - 53r
SPP36 - 56
SPP36 - 58
SPP36 - 60
SPP36 - 54
SPP36 - 55c
SPP36 - 57
SPP36 - 63c
SPP36 - 61
SPP36 - 59c
SPP36 - 63r
SPP36 - 62
SPP36 - 59m
SPP36 - 67r
SPP36 - 66
SPP36 - 64c
SPP36 - 65
SPP36 - 64r
SPP36 - 71
SPP36 - 68
SPP36 - 70
SPP36 - 72c
SPP36 - 74c
SPP36 - 75
SPP36 - 73c
SPP36 - 76c
SPP36 - 77
SPP36 - 78
100 µm

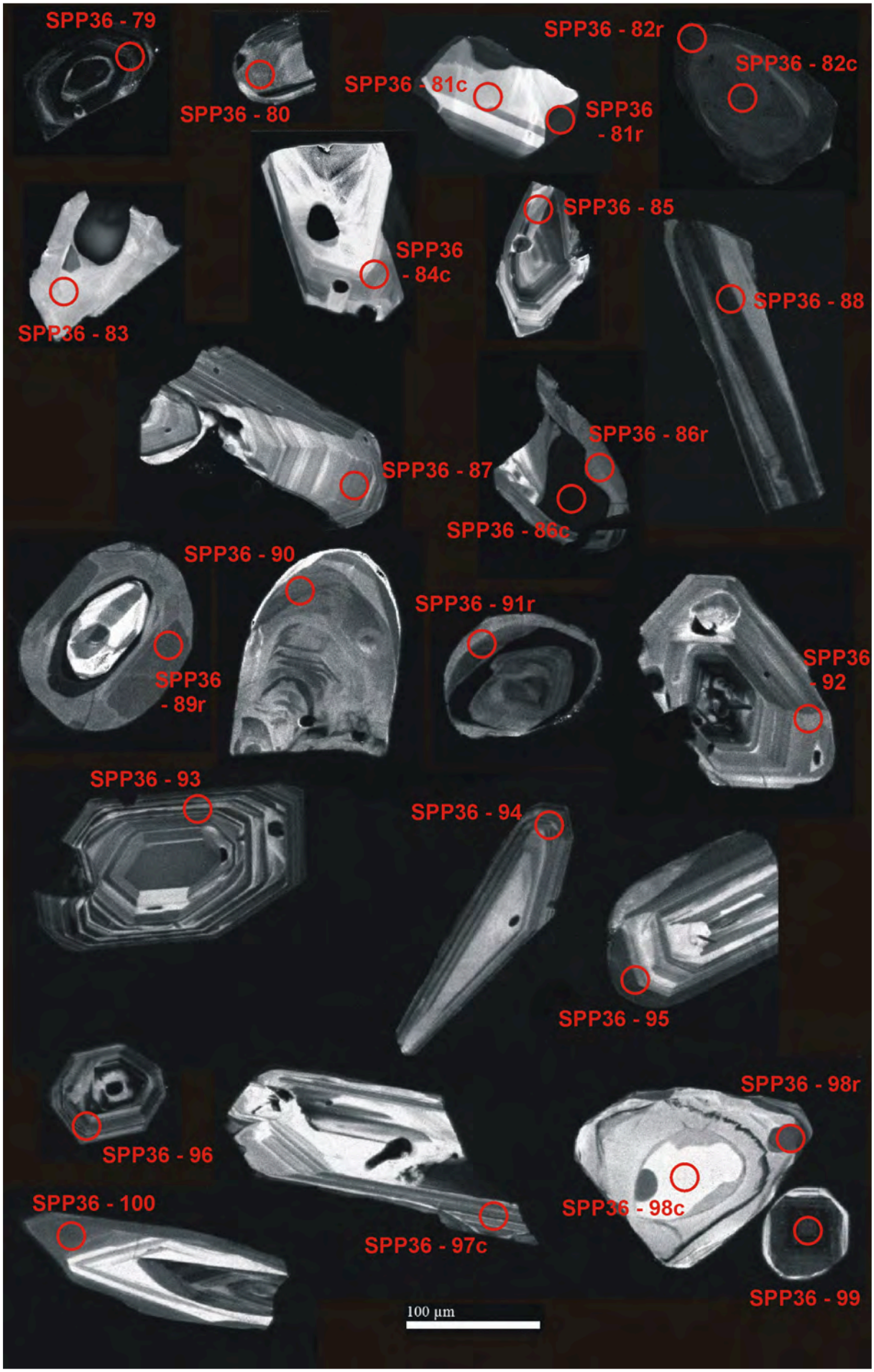
SPP36 - 79
SPP36 - 80
SPP36 - 81c
SPP36 - 81r
SPP36 - 82r
SPP36 - 82c
SPP36 - 83
SPP36 - 84c
SPP36 - 85
SPP36 - 88
SPP36 - 86r
SPP36 - 87
SPP36 - 86c
SPP36 - 90
SPP36 - 89r
SPP36 - 91r
SPP36 - 92
SPP36 - 93
SPP36 - 94
SPP36 - 95
SPP36 - 96
SPP36 - 98r
SPP36 - 98c
SPP36 - 100
SPP36 - 97c
SPP36 - 99
100 µm

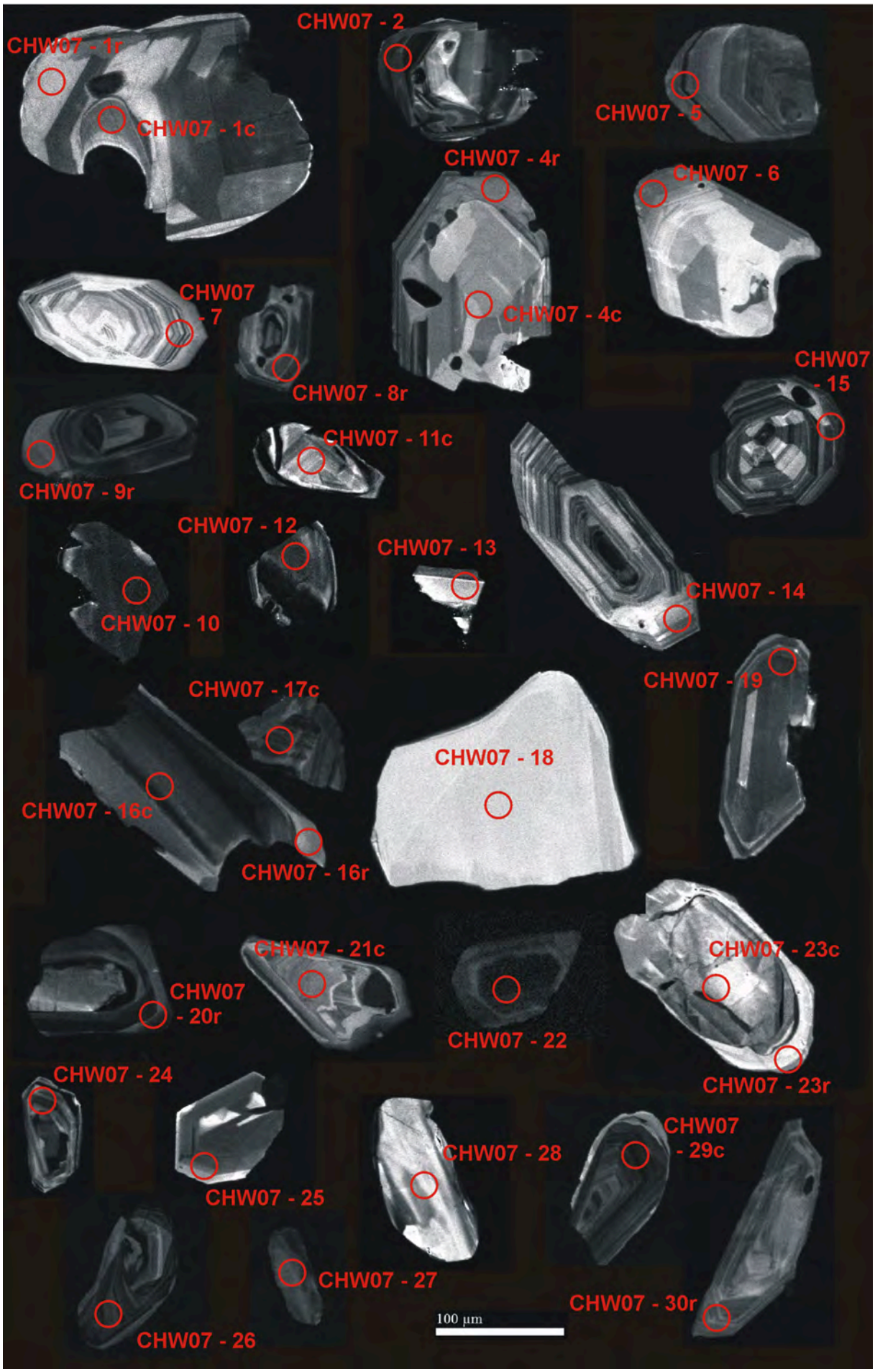
CHW07 - 1r
CHW07 - 1c
CHW07 - 2
CHW07 - 5
CHW07 - 4r
CHW07 - 6
CHW07 - 7
CHW07 - 4c
CHW07 - 8r
CHW07 - 15
CHW07 - 11c
CHW07 - 9r
CHW07 - 12
CHW07 - 13
CHW07 - 14
CHW07 - 10
CHW07 - 19
CHW07 - 17c
CHW07 - 18
CHW07 - 16c
CHW07 - 16r
CHW07 - 21c
CHW07 - 23c
CHW07 - 20r
CHW07 - 22
CHW07 - 24
CHW07 - 23r
CHW07 - 28
CHW07 - 29c
CHW07 - 25
CHW07 - 27
CHW07 - 30r
CHW07 - 26
100 µm

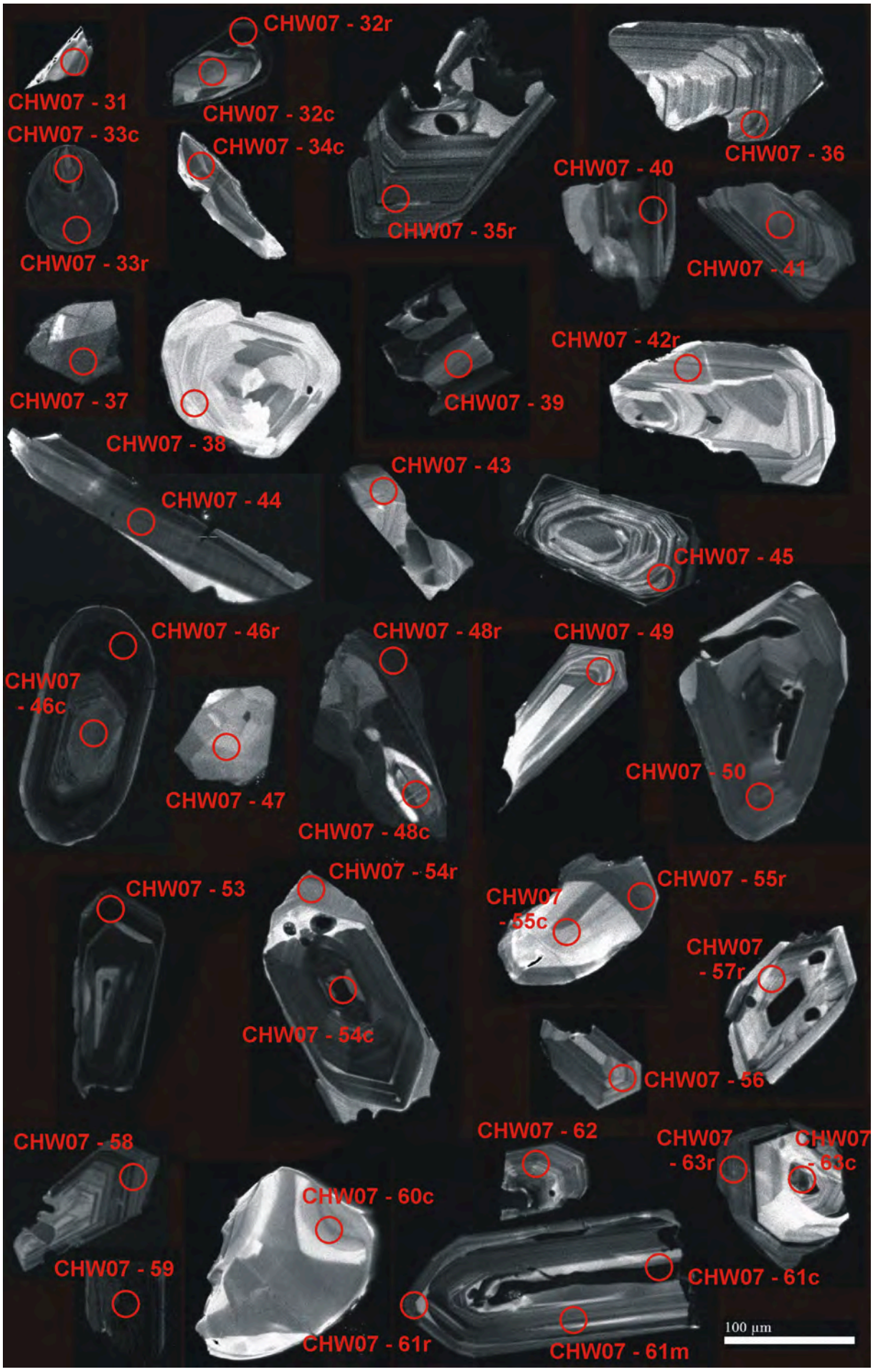
CHW07 - 32r
CHW07 - 31
CHW07 - 32c
CHW07 - 33c
CHW07 - 34c
CHW07 - 36
CHW07 - 40
CHW07 - 35r
CHW07 - 33r
CHW07 - 41
CHW07 - 42r
CHW07 - 37
CHW07 - 39
CHW07 - 38
CHW07 - 43
CHW07 - 44
CHW07 - 45
CHW07 - 46r
CHW07 - 48r
CHW07 - 49
CHW07 - 46c
CHW07 - 50
CHW07 - 47
CHW07 - 48c
CHW07 - 54r
CHW07 - 53
CHW07 - 55r
CHW07 - 55c
CHW07 - 57r
CHW07 - 54c
CHW07 - 56
CHW07 - 58
CHW07 - 62
CHW07 - 63r
CHW07 - 63c
CHW07 - 60c
CHW07 - 59
CHW07 - 61c
CHW07 - 61r
CHW07 - 61m
100 µm

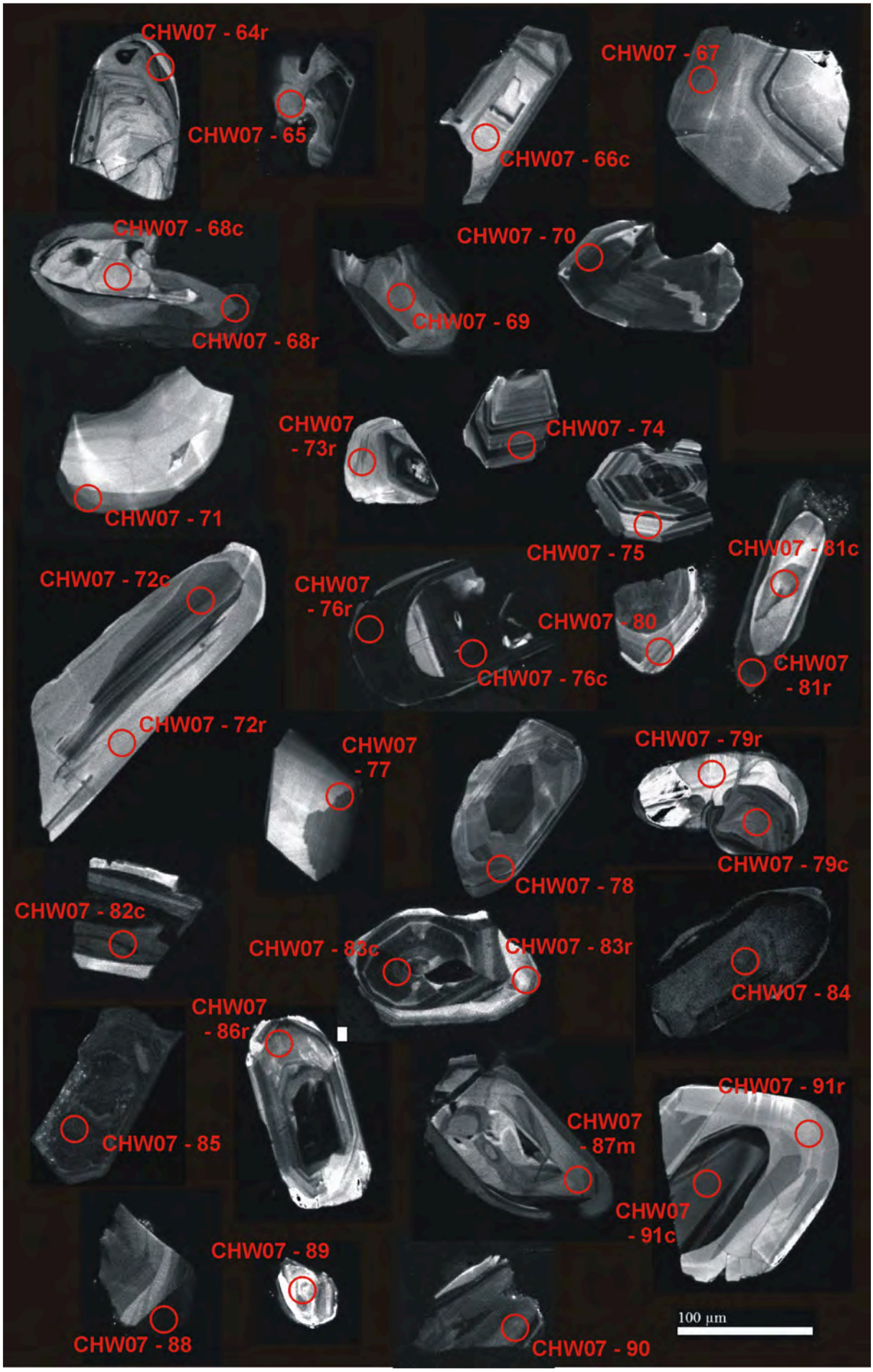
CHW07 - 64r
CHW07 - 65
CHW07 - 67
CHW07 - 66c
CHW07 - 68c
CHW07 - 68r
CHW07 - 70
CHW07 - 69
CHW07 - 71
CHW07 - 73r
CHW07 - 74
CHW07 - 75
CHW07 - 81c
CHW07 - 72c
CHW07 - 76r
CHW07 - 80
CHW07 - 76c
CHW07 - 81r
CHW07 - 72r
CHW07 - 77
CHW07 - 79r
CHW07 - 78
CHW07 - 79c
CHW07 - 82c
CHW07 - 83c
CHW07 - 83r
CHW07 - 84
CHW07 - 86r
CHW07 - 85
CHW07 - 87m
CHW07 - 91r
CHW07 - 91c
CHW07 - 89
CHW07 - 88
CHW07 - 90
100 µm

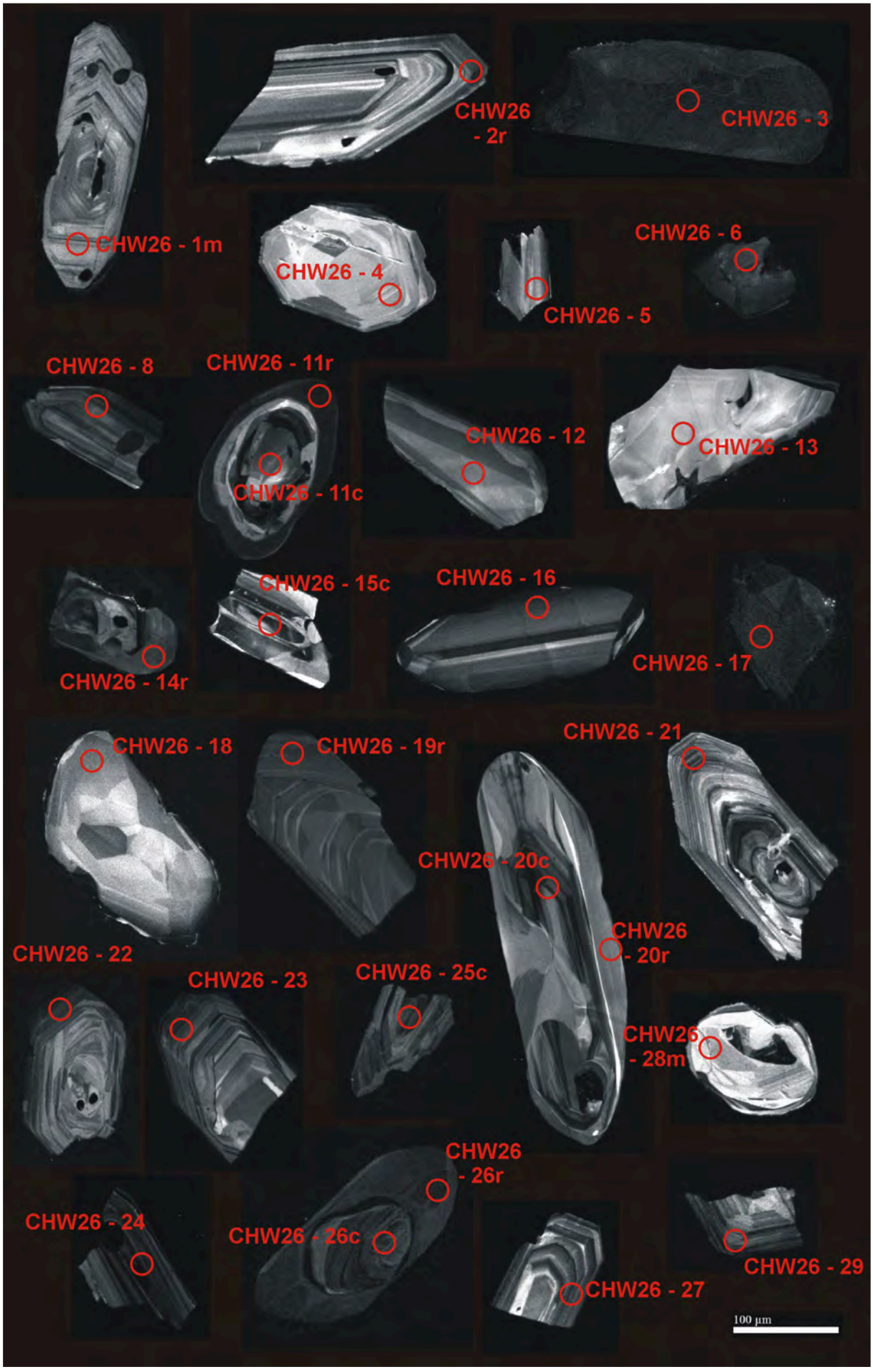
CHW26 - 1m
CHW26 - 2r
CHW26 - 3
CHW26 - 4
CHW26 - 5
CHW26 - 6
CHW26 - 8
CHW26 - 11r
CHW26 - 11c
CHW26 - 12
CHW26 - 13
CHW26 - 14r
CHW26 - 15c
CHW26 - 16
CHW26 - 17
CHW26 - 18
CHW26 - 19r
CHW26 - 20c
CHW26 - 20r
CHW26 - 21
CHW26 - 22
CHW26 - 23
CHW26 - 25c
CHW26 - 26r
CHW26 - 26c
CHW26 - 27
CHW26 - 28m
CHW26 - 29
CHW26 - 24
100 µm

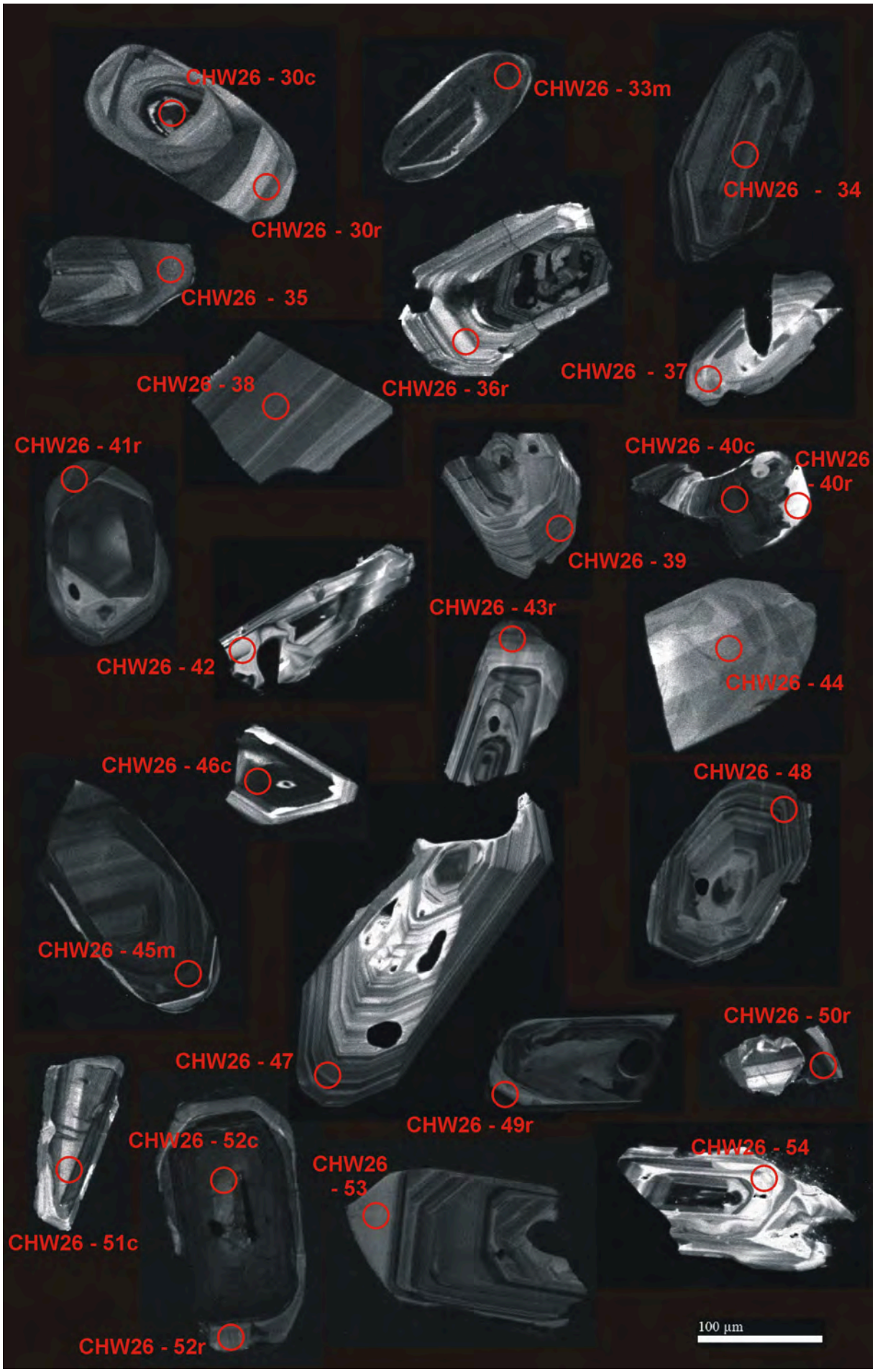
CHW26 - 30c
CHW26 - 33m
CHW26 - 34
CHW26 - 30r
CHW26 - 35
CHW26 - 36r
CHW26 - 37
CHW26 - 38
CHW26 - 41r
CHW26 - 40c
CHW26 - 40r
CHW26 - 39
CHW26 - 43r
CHW26 - 42
CHW26 - 44
CHW26 - 46c
CHW26 - 48
CHW26 - 45m
CHW26 - 50r
CHW26 - 47
CHW26 - 49r
CHW26 - 52c
CHW26 - 54
CHW26 - 53
CHW26 - 51c
CHW26 - 52r
100 µm

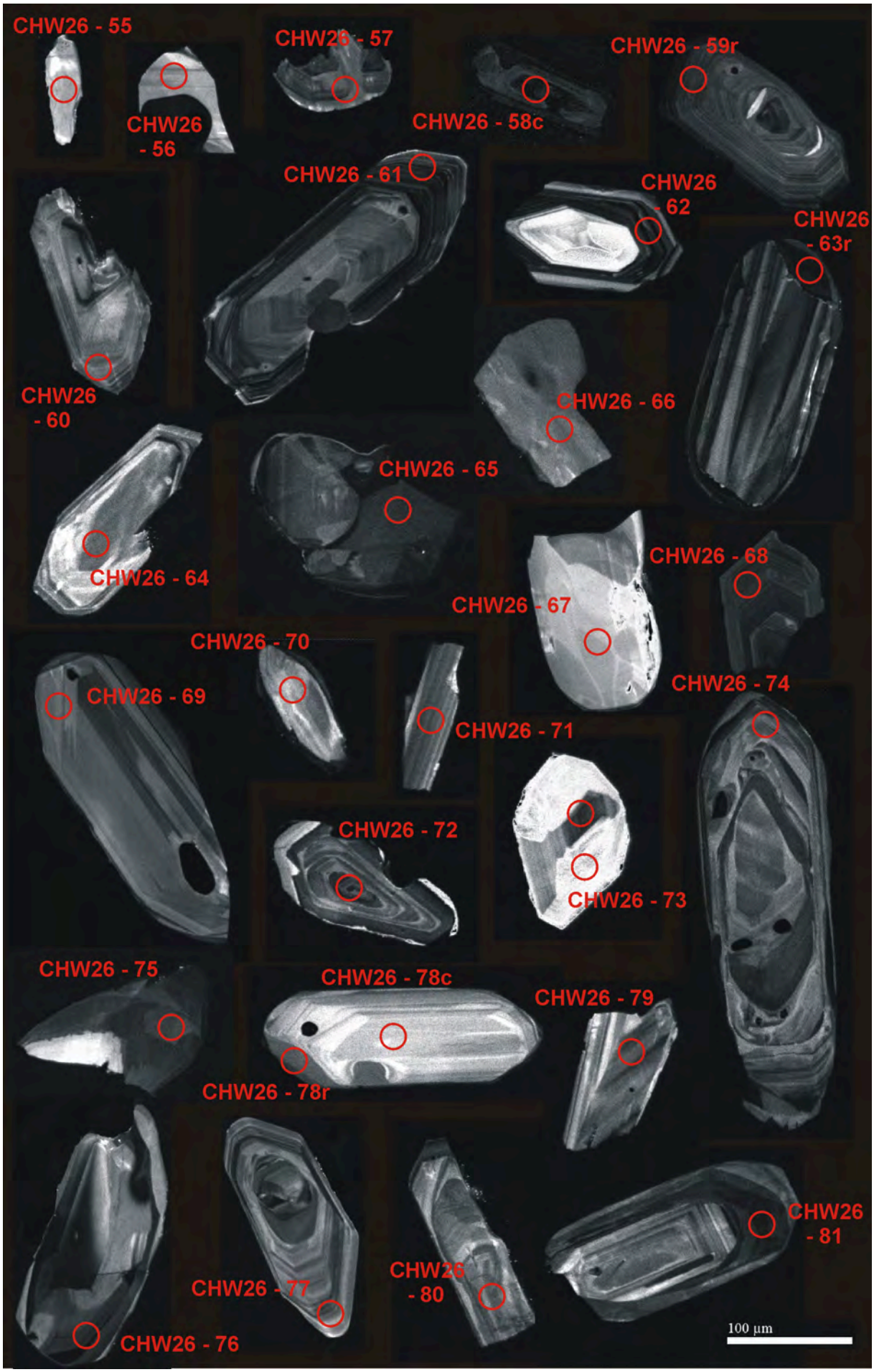
CHW26 - 55
CHW26 - 57
CHW26 - 59r
CHW26 - 56
CHW26 - 58c
CHW26 - 61
CHW26 - 62
CHW26 - 63r
CHW26 - 60
CHW26 - 66
CHW26 - 65
CHW26 - 64
CHW26 - 68
CHW26 - 67
CHW26 - 70
CHW26 - 69
CHW26 - 74
CHW26 - 71
CHW26 - 72
CHW26 - 73
CHW26 - 75
CHW26 - 78c
CHW26 - 79
CHW26 - 78r
CHW26 - 81
CHW26 - 77
CHW26 - 80
CHW26 - 76
100 µm

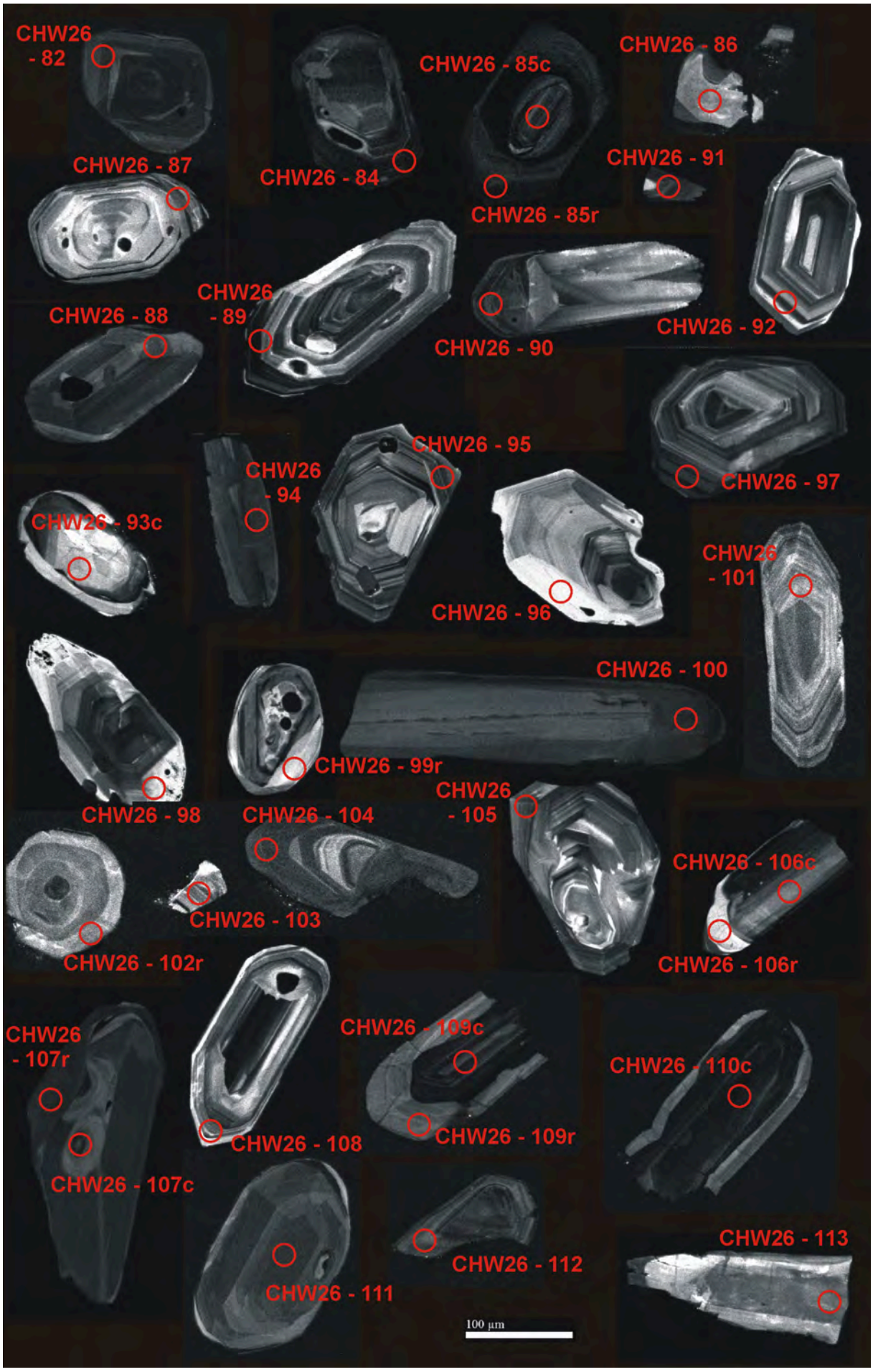
CHW26 - 82
CHW26 - 85c
CHW26 - 86
CHW26 - 87
CHW26 - 84
CHW26 - 91
CHW26 - 85r
CHW26 - 89
CHW26 - 88
CHW26 - 92
CHW26 - 90
CHW26 - 95
CHW26 - 94
CHW26 - 97
CHW26 - 93c
CHW26 - 101
CHW26 - 96
CHW26 - 100
CHW26 - 99r
CHW26 - 98
CHW26 - 104
CHW26 - 105
CHW26 - 106c
CHW26 - 103
CHW26 - 102r
CHW26 - 106r
CHW26 - 107r
CHW26 - 109c
CHW26 - 110c
CHW26 - 108
CHW26 - 109r
CHW26 - 107c
CHW26 - 113
CHW26 - 112
CHW26 - 111
100 µm

# Appendix 8

Sm-, Nd- and Sr-isotope data of mudstones

| Sample | Sr (OES) [µg/g] | Sr SD [µg/g] | Nd (MS) [µg/g] | Nd SD [µg/g] | Sm (MS) [µg/g] | Sm SD [µg/g] |
|---|---|---|---|---|---|---|
| **SHA11** | 93.0 | 0.5 | 26.0 | 0.2 | 5.19 | 0.04 |
| **TI13** | 87.7 | 0.2 | 33.4 | 0.1 | 6.84 | 0.05 |
| **CHW15** | 148.1 | 0.5 | 32.1 | 0.2 | 6.35 | 0.05 |
| **SHC29** | 52.0 | 0.4 | 41.6 | 0.1 | 8.18 | 0.04 |
| **SPP02 /1** | 37.80 | 0.02 | 41.5 | 0.2 | 8.29 | 0.04 |
| **SPP02 /2** | 37.86 | 0.06 | 41.5 | 0.3 | 8.23 | 0.05 |

| Sample | Sample Weight [g] | Spike Weight [g] | Spike | $^{87}Sr/^{86}Sr$ [fc] | 2se | Sr [µg/g] |
|---|---|---|---|---|---|---|
| **SHA-11** | 0.06953 | 0.05085 | Rb-Sr-15 | 7.14E-01 | 0.000017 | 86.932414 |
| **TI13** | 0.0594 | 0.05377 | Rb-Sr-15 | 7.19E-01 | 0.000013 | 84.153028 |
| **CHW15** | 0.06129 | 0.06909 | Rb-Sr-15 | 7.14E-01 | 0.000024 | 142.000321 |
| **SHC29** | 0.0503 | 0.02855 | Rb-Sr-15 | 7.52E-01 | 0.000026 | 50.808015 |
| **SPP02** | 0.07014 | 0.02975 | Rb-Sr-15 | 7.60E-01 | 0.000071 | 35.479739 |

| Sample | Sample Weight [g] | Spike Weight [g] | Spike | $^{144}Nd$ [µmol] | $^{143}Nd/^{144}Nd$ [fc] | 2se | $^{145}Nd/^{144}Nd$ [fc] | 2se | Nd [µg/g] |
|---|---|---|---|---|---|---|---|---|---|
| **SHA-11** | 0.06953 | 0.10641 | Sm-Nd-1 | 3.14E-09 | 0.512442 | 0.000009 | 0.348397 | 0.000007 | 27.4 |
| **TI13** | 0.0594 | 0.12057 | Sm-Nd-1 | 3.52E-09 | 0.512587 | 0.000014 | 0.348401 | 0.000008 | 36.0 |
| **CHW15** | 0.06129 | 0.11515 | Sm-Nd-1 | 3.45E-09 | 0.512313 | 0.000020 | 0.348389 | 0.000015 | 34.1 |
| **SHC29** | 0.0503 | 0.12489 | Sm-Nd-1 | 3.72E-09 | 0.512270 | 0.000029 | 0.348440 | 0.000023 | 44.8 |
| **SPP02** | 0.07014 | 0.15301 | Sm-Nd-1 | 5.13E-09 | 0.512294 | 0.000023 | 0.348433 | 0.000017 | 44.3 |

| Sample | Sample Weight [g] | Spike Weight [g] | Spike | $^{147}Sm$ [µmol] | Sm [µg/g] |
|---|---|---|---|---|---|
| **SHA-11** | 0.06953 | 0.10641 | Sm-Nd-1 | 3.94E-10 | 5.68 |
| **TI13** | 0.0594 | 0.12057 | Sm-Nd-1 | 4.36E-10 | 7.35 |
| **CHW15** | 0.06129 | 0.11515 | Sm-Nd-1 | 4.14E-10 | 6.78 |
| **SHC29** | 0.0503 | 0.12489 | Sm-Nd-1 | 4.37E-10 | 8.71 |
| **SP-L1.1** | 0.07014 | 0.15301 | Sm-Nd-1 | 6.24E-10 | 8.92 |

# Appendix 9

U-Pb (SHRIMP) ages and CL-images of zircons
from the tuffaceous sandstone sample SHA12 (uppermost SPF)

U-Pb (SHRIMP) isotope data of magmatic Zircons from sample SHA12 (uppermost SPF)

| Spot | $^{206}Pb_c$ | U | Th | $\frac{^{232}Th}{^{238}U}$ | $^{206}Pb^*$ | $\frac{^{206}Pb}{^{238}U}$ [a] | $\frac{^{207}Pb}{^{206}Pb}$ [a] | Disc. | $\frac{^{238}U}{^{206}Pb^*}$ [a] | ± | $\frac{^{207}Pb^*}{^{206}Pb^*}$ [b] | ± | $\frac{^{207}Pb^*}{^{235}U}$ [c] | ± | $\frac{^{206}Pb^*}{^{238}U}$ [a] | ± | err. corr. |
|---|---|---|---|---|---|---|---|---|---|---|---|---|---|---|---|---|---|
| | (%) | (ppm) | (ppm) | | (ppm) | age [Ma] | age [Ma] | (%) | | (%) | | (%) | | (%) | | (%) | |
| SHA12 - 1.1 | 0.47 | 346 | 292 | 0.87 | 8.77 | 186.5 ± 3.5 | 115 ±110 | -38 | 34.07 | 1.9 | 0.0483 | 4.8 | 0.196 | 5.2 | 0.02936 | 1.9 | 0.365 |
| SHA12 - 1.2 | 0.73 | 344 | 297 | 0.89 | 8.79 | 187.4 ± 3.4 | -22 ±150 | -112 | 33.91 | 1.8 | 0.0456 | 6.2 | 0.186 | 6.5 | 0.02949 | 1.8 | 0.284 |
| SHA12 - 2.1 | 1.03 | 193 | 222 | 1.19 | 4.91 | 186.3 ± 3.7 | 2 ±220 | -99 | 34.1 | 2 | 0.0461 | 9.1 | 0.186 | 9.3 | 0.02933 | 2 | 0.215 |
| SHA12 - 2.2 | 1.22 | 48 | 26 | 0.55 | 1.27 | 191.3 ± 4.9 | -258 ±400 | -235 | 33.21 | 2.6 | 0.0415 | 16 | 0.172 | 16 | 0.03012 | 2.6 | 0.161 |
| SHA12 - 3.1 | 0.04 | 331 | 265 | 0.83 | 8.36 | 187.0 ± 3.4 | 146 ± 67 | -22 | 33.98 | 1.8 | 0.049 | 2.9 | 0.1987 | 3.4 | 0.02943 | 1.8 | 0.538 |
| SHA12 - 4.1 | -- | 332 | 222 | 0.69 | 8.83 | 196.5 ± 3.5 | 240 ± 67 | 22 | 32.31 | 1.8 | 0.051 | 2.9 | 0.2176 | 3.4 | 0.03095 | 1.8 | 0.530 |
| SHA12 - 5.1 | 0.28 | 485 | 503 | 1.07 | 12.3 | 187.8 ± 3.3 | 109 ± 83 | -42 | 33.83 | 1.8 | 0.0482 | 3.5 | 0.1965 | 3.9 | 0.02956 | 1.8 | 0.449 |
| SHA12 - 6.1 | 0.23 | 440 | 423 | 0.99 | 11 | 184.2 ± 3.3 | 144 ±110 | -22 | 34.51 | 1.8 | 0.0489 | 4.6 | 0.1955 | 4.9 | 0.02898 | 1.8 | 0.365 |
| SHA12 - 6.2 | 0.92 | 174 | 138 | 0.82 | 4.08 | 172.4 ± 3.5 | 109 ±230 | -37 | 36.9 | 2.1 | 0.0482 | 9.9 | 0.18 | 10 | 0.0271 | 2.1 | 0.204 |
| SHA12 - 7.1 | 0.28 | 283 | 174 | 0.64 | 7.12 | 185.8 ± 3.4 | 233 ± 86 | 26 | 34.2 | 1.9 | 0.0508 | 3.7 | 0.2049 | 4.2 | 0.02924 | 1.9 | 0.443 |
| SHA12 - 8.1 | 0.61 | 383 | 347 | 0.94 | 10 | 192.8 ± 3.5 | 39 ±140 | -80 | 32.94 | 1.8 | 0.0468 | 6 | 0.196 | 6.2 | 0.03036 | 1.8 | 0.293 |

Errors are 1-sigma; $Pb_c$ and $Pb^*$ indicate the common and radiogenic portions, respectively.

Error in Standard calibration was 0.64%

[a] Common Pb corrected using measured $^{204}Pb$.

[b] Common Pb corrected by assuming $^{206}Pb/^{238}U$-$^{207}Pb/^{235}U$ age-concordance

[c] Common Pb corrected by assuming $^{206}Pb/^{238}U$-$^{208}Pb/^{232}Th$ age-concordance

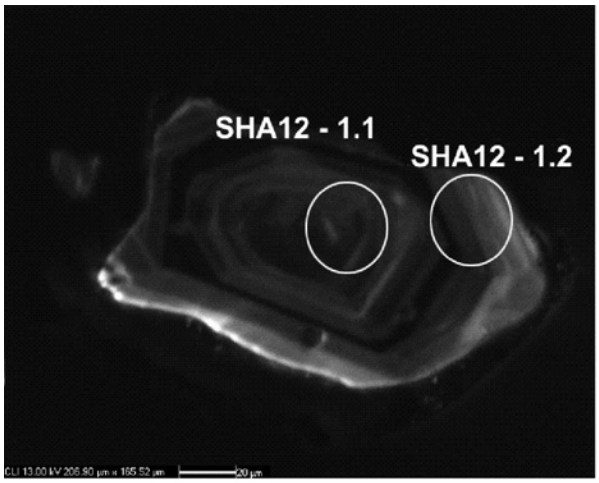
SHA12 - 1.1
SHA12 - 1.2

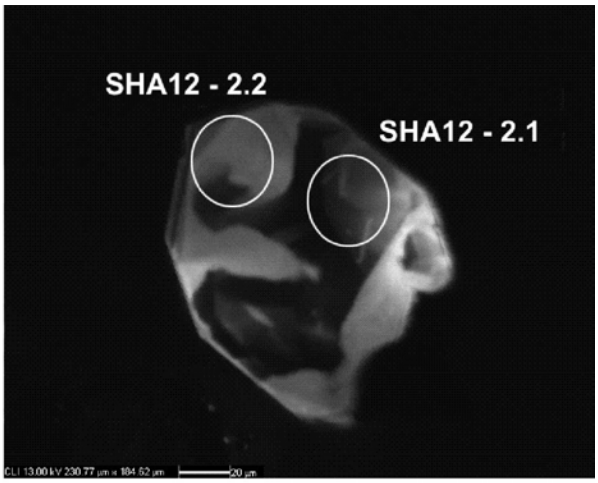
SHA12 - 2.2
SHA12 - 2.1

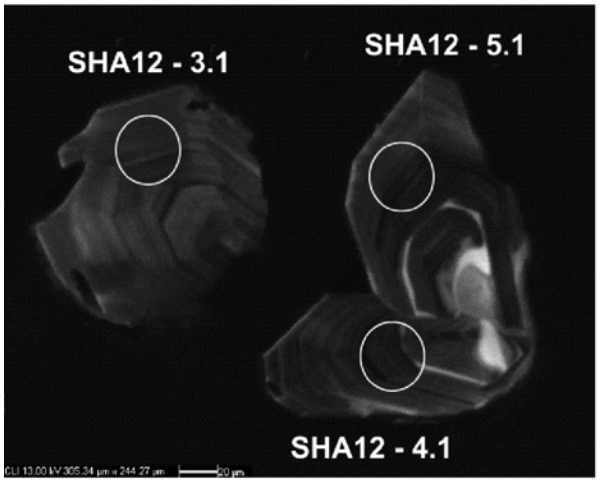
SHA12 - 3.1
SHA12 - 5.1
SHA12 - 4.1

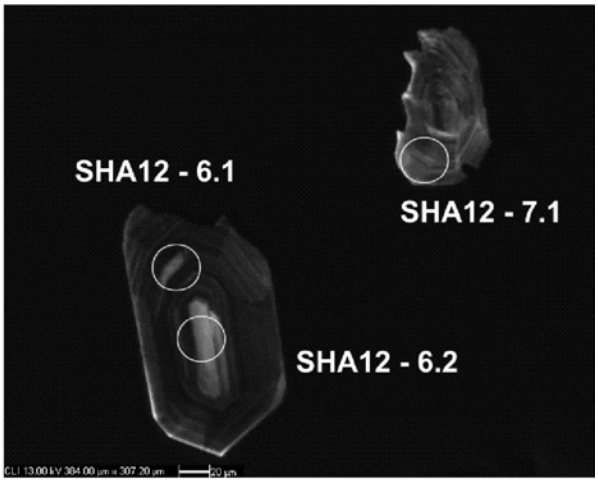
SHA12 - 6.1
SHA12 - 7.1
SHA12 - 6.2

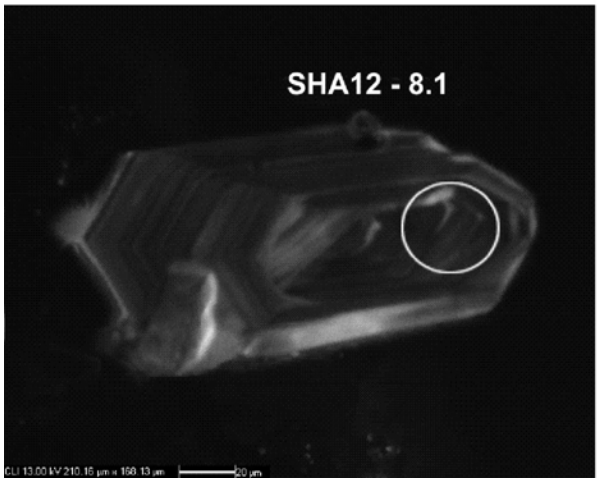
SHA12 - 8.1

# Appendix 10

X-ray diffractograms of tuffaceous sandstones

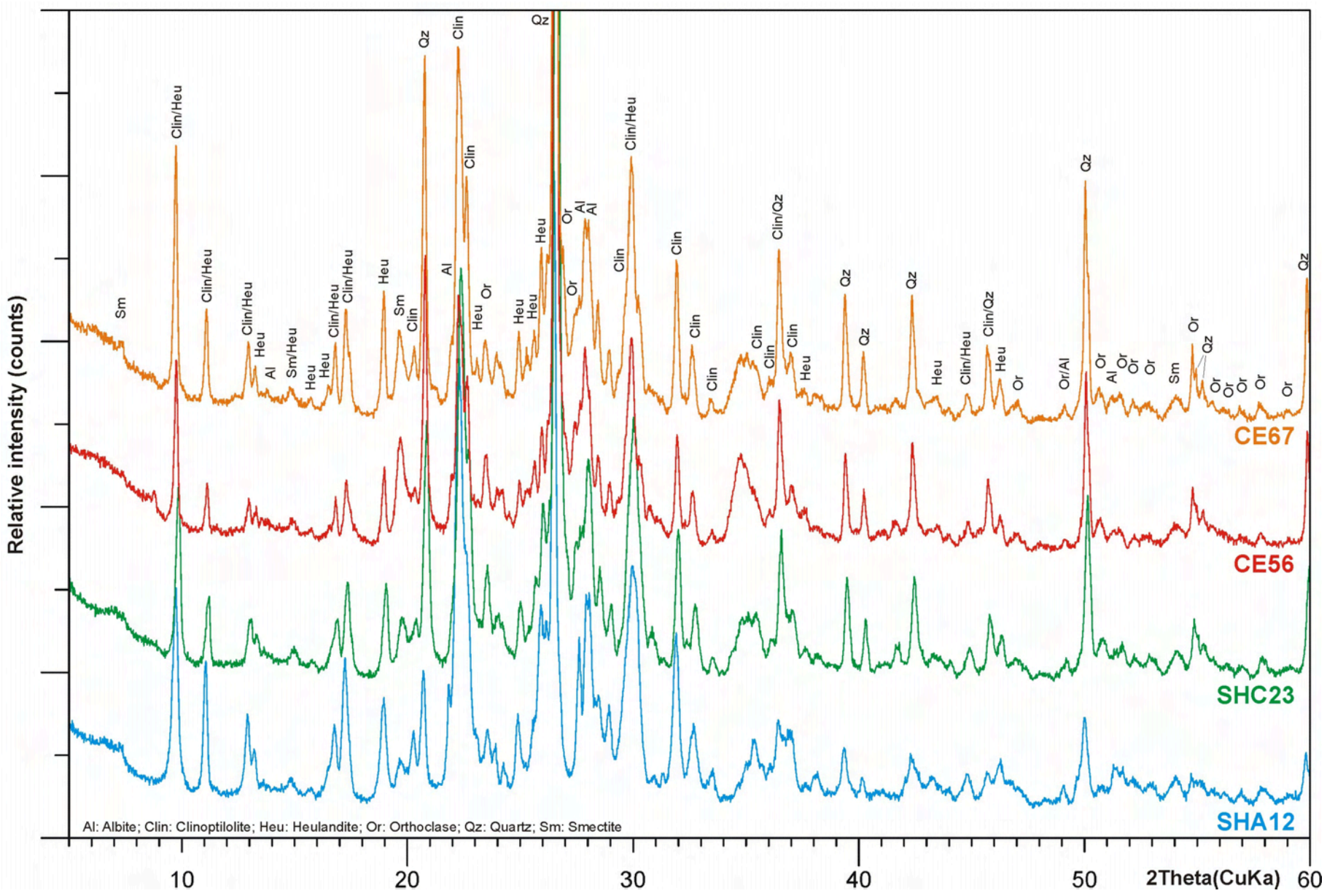
Relative intensity (counts)
Sm
Clin/Heu
Clin/Heu
Clin/Heu
Heu
Al
Sm/Heu
Heu
Heu
Clin/Heu
Clin/Heu
Heu
Sm
Clin
Qz
Al
Clin
Clin
Heu
Or
Heu
Heu
Heu
Qz
Or
Or
Al
Al
Clin
Clin/Heu
Clin
Clin
Clin
Clin
Clin
Clin/Qz
Clin
Heu
Qz
Qz
Qz
Heu
Clin/Heu
Clin/Qz
Heu
Or
Or/Al
Qz
Or
Al
Or
Or
Or
Sm
Or
Qz
Or
Or
Or
Or
Qz
CE67
CE56
SHC23
SHA12
Al: Albite; Clin: Clinoptilolite; Heu: Heulandite; Or: Orthoclase; Qz: Quartz; Sm: Smectite
10
20
30
40
50
2Theta(CuKa)
60

# Appendix 11

Geological cross section of the working area in NVL

# Geological cross-section of North Victoria Land

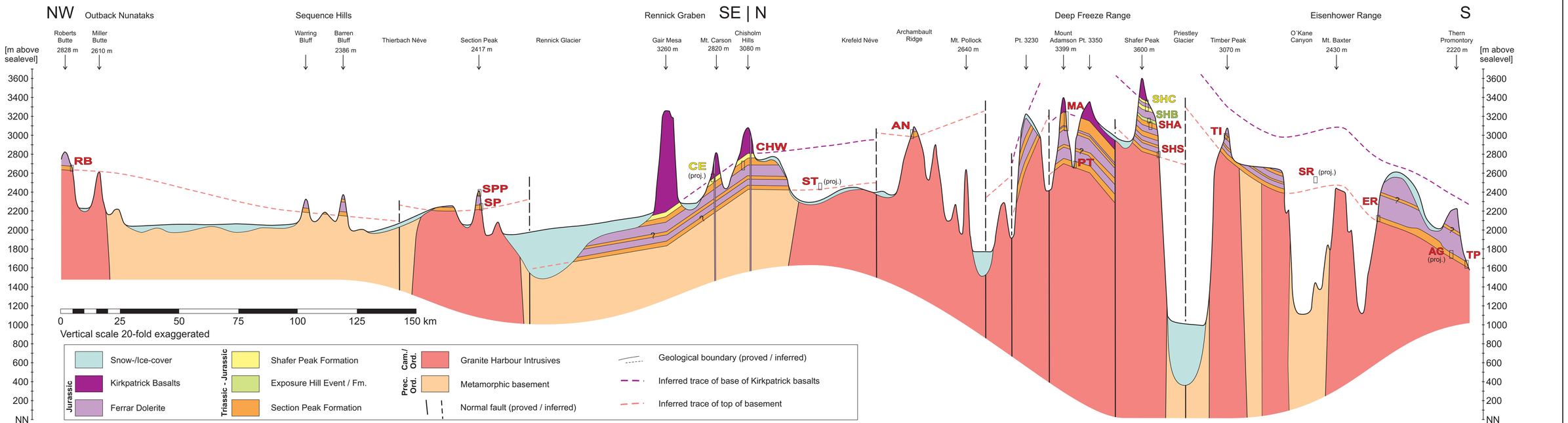

**Selbständigkeitserklärung**

Ich erkläre, dass ich die vorliegende Arbeit selbständig und unter Verwendung der angegebenen Hilfsmittel, persönlichen Mitteilungen und Quellen angefertigt habe.

Augsburg, 1. Oktober 2010 .....

Martin Elsner